Understanding Complex Systems

Ramon G. Rubio · Yuri S. Ryazantsev
Victor M. Starov · Guo-Xiang Huang
Alexander P. Chetverikov · Paolo Arena
Alex A. Nepomnyashchy · Alberto Ferrus
Eugene G. Morozov *Editors*

Without Bounds: A Scientific Canvas of Nonlinearity and Complex Dynamics

Springer

Springer Complexity

Springer Complexity is an interdisciplinary program publishing the best research and academic-level teaching on both fundamental and applied aspects of complex systems – cutting across all traditional disciplines of the natural and life sciences, engineering, economics, medicine, neuroscience, social and computer science.

Complex Systems are systems that comprise many interacting parts with the ability to generate a new quality of macroscopic collective behavior the manifestations of which are the spontaneous formation of distinctive temporal, spatial or functional structures. Models of such systems can be successfully mapped onto quite diverse "real-life" situations like the climate, the coherent emission of light from lasers, chemical reaction-diffusion systems, biological cellular networks, the dynamics of stock markets and of the internet, earthquake statistics and prediction, freeway traffic, the human brain, or the formation of opinions in social systems, to name just some of the popular applications.

Although their scope and methodologies overlap somewhat, one can distinguish the following main concepts and tools: self-organization, nonlinear dynamics, synergetics, turbulence, dynamical systems, catastrophes, instabilities, stochastic processes, chaos, graphs and networks, cellular automata, adaptive systems, genetic algorithms and computational intelligence.

The three major book publication platforms of the Springer Complexity program are the monograph series "Understanding Complex Systems" focusing on the various applications of complexity, the "Springer Series in Synergetics", which is devoted to the quantitative theoretical and methodological foundations, and the "SpringerBriefs in Complexity" which are concise and topical working reports, case-studies, surveys, essays and lecture notes of relevance to the field. In addition to the books in these two core series, the program also incorporates individual titles ranging from textbooks to major reference works.

Understanding Complex Systems

Founding Editor: S. Kelso

Future scientific and technological developments in many fields will necessarily depend upon coming to grips with complex systems. Such systems are complex in both their composition – typically many different kinds of components interacting simultaneously and nonlinearly with each other and their environments on multiple levels – and in the rich diversity of behavior of which they are capable.

The Springer Series in Understanding Complex Systems series (UCS) promotes new strategies and paradigms for understanding and realizing applications of complex systems research in a wide variety of fields and endeavors. UCS is explicitly transdisciplinary. It has three main goals: First, to elaborate the concepts, methods and tools of complex systems at all levels of description and in all scientific fields, especially newly emerging areas within the life, social, behavioral, economic, neuro- and cognitive sciences (and derivatives thereof); second, to encourage novel applications of these ideas in various fields of engineering and computation such as robotics, nano-technology and informatics; third, to provide a single forum within which commonalities and differences in the workings of complex systems may be discerned, hence leading to deeper insight and understanding.

UCS will publish monographs, lecture notes and selected edited contributions aimed at communicating new findings to a large multidisciplinary audience.

For further volumes:
http://www.springer.com/series/5394

Ramon G. Rubio • Yuri S. Ryazantsev
Victor M. Starov • Guo-Xiang Huang
Alexander P. Chetverikov • Paolo Arena
Alex A. Nepomnyashchy • Alberto Ferrus
Eugene G. Morozov
Editors

Without Bounds: A Scientific Canvas of Nonlinearity and Complex Dynamics

Springer

Editors
Ramon G. Rubio
Dpt. Quimica-Fisica-I
UCM
Madrid, Spain

Yuri S. Ryazantsev
Instituto Pluridisciplinar
UCM
Madrid, Spain

Victor M. Starov
Dpt. of Chemical Engineering
Loughborough University
Loughborough, United Kingdom

Guo-Xiang Huang
Physics Dpt.
East China Normal University
Shanghai
China, People's Republic

Alexander P. Chetverikov
Faculty of Physics
Saratov State University
Saratov, Russia

Paolo Arena
Dpt. di Ingegneria Elettrica
Elettronica
Università di Catania
Catania, Italy

Alex A. Nepomnyashchy
Dept. of Mathematics
Technion
Haifa, Israel

Alberto Ferrus
Instituto Cajal
CSIC
Madrid, Spain

Eugene G. Morozov
Shirshov Institute of Oceanology
Moscow, Russia

ISSN 1860-0832 ISSN 1860-0840 (electronic)
ISBN 978-3-642-34069-7 ISBN 978-3-642-34070-3 (eBook)
DOI 10.1007/978-3-642-34070-3
Springer Heidelberg New York Dordrecht London

Library of Congress Control Number: 2013937955

Printed on acid-free paper

Springer is part of Springer Science+Business Media (www.springer.com)

Preface

It is with great pleasure that we have gathered the chapters of this book on Nonlinearity and Complex Dynamics to honor our colleague and friend Prof. Manuel G(arcía) Velarde, offered to him as a token of friendship, on the occasion of his seventieth anniversary. The contents are a follow-up of a Week of Science celebrated in September 2011 at Instituto Pluridisciplinar (IP), Universidad Complutense of Madrid (UCM), Spain. With four other UCM professors he was co-founder and there he had been for the past 20 years of his scientific career as (PROPIO) professor of physics [www.ucm.es/info/fluidos]. The IP-UCM was possible, thanks to an adventurous action of the then UCM Rector Gustavo Villapalos, a professor of law.

The Week of Science was also dedicated to honor several of his fellow colleagues at Prof. Velarde's request, as they were celebrating birthdays about the same week. They are Prof. Werner Ebeling (Berlin), Prof. Ivan B. Ivanov (Sofia), Prof. Grégoire Nicolis (Brussels), Prof. John J. Kozak (Chicago), Dr. Benoit Scheid (Brussels), Music composer Maestro Tomás Marco, and Dr. Rafael García Serrano, Museum Curator of "Museo del traje" (Madrid), formerly Curator of "Museum of Santa Cruz," Toledo. All of them have been frequent visitors of IP-UCM.

The Week of Science was an opportunity to appreciate the broad spectrum of interests of Prof. Velarde, both in science and culture. Surfer and architect Pablo Díaz offered a fascinating talk on surf waves all around the world. It was also the opportunity to learn about his love of Music, not just J. S. Bach (Cello suite ♯1, BWV 1007 in G major, was played by Maestro Angel Ga. Jermann, Professor at Real Conservatorio Superior de Música, Madrid). Here it follows a song much loved by Manuel:

Folks call me a maverick.
Guess I ain't too diplomatic...
Well, I have been accused
Of makin' my own rules.
There must be rebel blood
Just a runnin' through my veins.

But I ain't no hypocrite
What you see is what you get.
And that's the only way I know
To play the game.
Old Noah took much ridicule
For building his great ark.
But after forty days and forty nights
He was lookin' pretty smart.
Sometines it's best to brave the wind and rain
By havin' strength to go against the grain.

("Against the grain", lyrics by Bruce Bouton, Larry Cordle, and Carl Jackson; sung by Garth Brooks.)

It was then naturally fitting well with his approach to life that in September 2007 Manuel organized a conference in Toledo for the **Academia Europaea** [www.acadeuro.org] with the theme of "The Dialogue of Three Cultures and our European heritage. Toledo crucible of the Cultures at the dawn of the Renaissance" [www.ucm.es/info/fluidos, see Int. Conf. Toledo 2007]. The conference covered topics from geography, history, poetry, linguistics, art, medicine, pharmacology, geometry, mathematics, astronomy, and hydraulics. The conference started at the Cathedral of Toledo in a large room (the Sacristy) covered with more than a dozen paintings by *El Greco* and a cieling decorated by *L. Jordaens*. The inaugural speeches were delivered in Latin. As he has said, one thing he wanted to understand was what brought Toledo then (1200) for quite some time at the cultural and scientific zenith in Europe, to almost vanishing in a rather short time interval.

In 2002, a special issue of the *International Journal of Bifurcation and Chaos* (vol. 12, n. 11, 348 pp.) was edited by Prof. G. Nicolis to celebrate Manuel's sixtieth birthday. Under the topic tittle *Spatio-Temporal Complexity*, it included 28 original research papers contributed by 67 scientists from Europe, the Americas, Asia, Africa, and the Middle East. This book follows the same path celebrating his seventieth birthday.

Finally, we have received with joy the news of his appointment as director of a newly created "Research Chair" at Universidad Alfonso X el Sabio [www.uax.es] where Prof. Velarde is starting yet another period of his life. This has been made possible, thanks to Rector Jose Domínguez de Posada, a professor of civil engineering, Dr. Juan José Montoya, MD, Director of the UAX Foundation, and UAX President Don Jesús Núnez Velázquez.

The editors wish to express their appreciation to Manuel's secretary Mrs María J. Martín for her kindness and her endless patience in the preparation of this book with a dedication well beyond the call of duty.

The Editors

INSTITUTO PLURIDISCIPLINAR-UCM, MADRID (SPAIN)

SEPTEMBER 12-16, 2011

A WEEK OF SCIENCE

TO CELEBRATE THE

70th BIRTHDAY (SEPT. 7th, real; 14th, legal; 2011) OF

Prof. MANUEL G. VELARDE

(http://www.ucm.es/info/fluidos)

AND AT HIS REQUEST TO ALSO CELEBRATE THE BIRTHDAY OF HIS COLLEAGUES AND FRIENDS

Prof. IVAN B. IVANOV (SEPT. 6TH), Prof. GREGOIRE NICOLIS (SEPT. 11th), Maestro TOMAS MARCO (SEPT. 12th), Prof. JOHN J. KOZAK (SEPT. 14th), Prof. WERNER EBELING (SEPT. 15th), Dr. BENOIT SCHEID (SEPT. 15th), and Museum Curator DR. RAFAEL GARCIA SERRANO (SEPT. 16th)

SCIENTIFIC COMMITTEE:

M. ADLER (MARNE-LA-VALLEE), P. ARENA (CATANIA), J. BRAGARD (PAMPLONA), A. CASTELLANOS (SEVILLA), A. P. CHETVERIKOV (SARATOV), P. COLINET (BRUSSELS), J. S. DEHESA (GRANADA), E. DEL RIO (UPM, MADRID), V. FAIREN (UNED, MADRID), G.-X. HUANG (SHANGHAI), R. G. RUBIO (UCM, MADRID) (Chair), S. KALLIADASIS (IMPERIAL COLLEGE, LONDON), A. A. NEPOMNYASHCHY (HAIFA), J. M. REDONDO (BARCELONA), Yu. S. RYAZANTSEV (MADRID) (co-Chair), V. M. STAROV (LOUGHBOROUGH), U. THIELE (LOUGHBOROUGH) A. WIERSCHEM (ERLANGEN)

OUTLINE

MONDAY SEPTEMBER 12

MULTIFLOW TRAINING DAY-

SYMPOSIUM ON FLUID PHYSICS AND RELATED NONLINEAR PHENOMENA AT INTERFACES AND IN OTHER GEOMETRIES

TUESDAY SEPTEMBER 13

MULTIFLOW TRAINING DAY-SYMPOSIUM ON WETTING AND SPREADING DYNAMICS

SPONSORED BY RAMON ARECES FOUNDATION AND SPRINGER-VERLAG IN COLLABORATION WITH MULTIFLOW CONSORTIUM (EU) AND (FASES) ESA

Presentation of special issue of EUROPEAN PHYSICAL JOURNAL-SPECIAL TOPICS- DISCUSSION AND DEBATE on WETTING AND SPREADING PHENOMENA AND PROBLEMS,

Coordinated by Prof. Manuel G. VELARDE.

WEDNESDAY SEPTEMBER 14 (morning)

(Continued) **MULTIFLOW TRAINING DAY-**

SYMPOSIUM ON FLUID PHYSICS AND RELATED NONLINEAR PHENOMENA AT INTERFACES AND IN OTHER GEOMETRIES

WEDNESDAY SEPTEMBER 14 (afternoon)

SYMPOSIUM (AND ROUND TABLE) ON SOLITONS, SOLECTRONS AND SOME NOVEL ASPECTS OF ELECTRIC TRANSPORT

WEDNESDAY SEPTEMBER 14 (evening)

SCIENCE AS PART OF CULTURE

L. Pismen: Swings of science: from complexity to simplicity and back

Cello Recital: **Angel Ga. Jerman**: J. S. Bach: Cello suite #1, BWV 1007 in G major

AGAPE/BANQUET- 9 pm

THURSDAY SEPTEMBER 15 (morning)

SPARK SYMPOSIUM (AND ROUND TABLE) ON BIOPHYSICS, NEURODYNAMICS AND ROBOTS

THURSDAY SEPTEMBER 15 (afternoon)

SYMPOSIUM (AND ROUND TABLE) ON COMPLEX SYSTEMS

FRIDAY SEPTEMBER 16 (morning and afternoon)

MULTIFLOW TRAINING DAY ON FLOWS AND COMPUTATIONAL METHODOLOGIES-

ERCOFTAC SYMPOSIUM ON GEOPHYSICAL AND ASTROPHYSICAL FLOWS AND RELATED PROBLEMS

Contents

Part I
Personal Reminiscences

M.G. Velarde: Succint Biography. Doing Science in Spain as a Maverick

Yu.S. Ryazantsev

Professor Manuel G(arcía) VELARDE, born in Almería, Spain (1941), graduated in Physics from Universidad Complutense (UCM, Madrid, 1963), got the Ph.D. from the same university in November 1968 (following guidance by Prof. M. Castans, Prof. I. Prigogine and Prof. G. Nicolis) and in January 1970 (under guidance of Prof. P. Résibois) from the Université Libre de Bruxelles (ULB). His first paper was published in 1968. Since then, until 2012, Prof. Velarde has published over 330 research papers, over 140 book chapters or contributions to Conference Proceedings, about 20 books (12 as author and 12 as scientific coordinator) and more than 135 lay audience articles [cf.: www.ucm.es/info/fluidos]. Such a prolific research output covers a wide spectrum of phenomena, problems and several disciplines. It embraces kinetic theory, statistical mechanics, thermodynamics, fluid physics, geophysics, optics and lasers, ferromagnetism, electron transport theory, acoustics, elasticity, wave theory, reaction-diffusion science, biophysics, active lattice dynamics, and neuro-dynamics, all phenomena and methodologies treated from the unifying perspective of nonlinear dynamics. Particular problems he studied were the foundations of nonlinear non-equilibrium thermodynamics of transport processes and instabilities (with J. Ross and X.-L. Chu); various aspects of phase transitions and cooperative phenomena in spin systems and in Bose–Einstein condensates (with G.-X. Huang); cross-transport (Soret and Dufour) processes and their role coupled to flows and instability (research initiated with R.S. Schechter); thermo-hydrodynamic instabilities leading to convective patterns, their defects and their evolution; the motions of active self-propelling drops (with Yu.S. Ryazantsev and Alex Ye. Rednikov); wetting and spreading dynamics of liquids over other liquids or over solid substrates, porous or not (a long lasting and still ongoing collaboration with V.M. Starov, recently augmented with the collaboration

Yu.S. Ryazantsev (✉)
Instituto Pluridisciplinar, Universidad Complutense de Madrid,
Paseo Juan XXIII, 1, Madrid-28040, Spain
e-mail: yriazant@aero.upm.es

R.G. Rubio et al. (eds.), *Without Bounds: A Scientific Canvas of Nonlinearity and Complex Dynamics*, Understanding Complex Systems,
DOI 10.1007/978-3-642-34070-3_1,

of R.G. Rubio); interfacial phenomena, also leading to pattern formation or waves; non-linear interfacial waves and interfacial solitons; solitons in elastic rods; internal waves in the atmosphere and the ocean with special attention paid to the phenomena observed in the Straight of Gibraltar (a lasting collaboration with E.G. Morozov); oscillatory phenomena in lasers; oscillatory processes in bio–physico–chemical systems and in reaction-diffusion systems, continuous and discrete; pattern and wave formation and their replication in synergetic active lattices (a decade of collaboration with V. I. Nekorkin); models of the cerebellar dynamics and other brain dynamic functions (learning, memotaxis) with potential for application in robots (with V.A. Makarov in a collaborative research sponsored by an EU Consortium); a new form of soliton-mediated (solectron) electric conduction in crystal lattices, etc.

The above mentioned research was done during three distinct periods of time. From 1965 to 1972, it was a training period, first as a Ph.D. student at ULB (Belgium) and, subsequently, as a postdoctoral researcher at the University of Texas at Austin (USA). As Manuel has confided me his approach to science and beyond was shaped by the influence of three extraordinary persons and scientists: Ilya Prigogine, Grégoire Nicolis and Pierre Résibois.

The second period (1971–1992) refers to teaching, research and a heavy administrative endeavor. In the Fall of 1971 he was appointed Associate Professor of Physics at the recently created Universidad Autonoma de Madrid (UAM). Subsequently, there he became Full Professor. At UAM, under the leadership of Prof. Nicolás Cabrera, he participated with a group of enthusiastic scientists in the building up of the Department of Physics. While at UAM, Prof. Velarde published three major papers, one in *Advances in Chemical Physics* (1974, with R.S. Schechter, and J.K. Platten: The two-component Benard problem), another in *Reviews of Modern Physics* (1977, with C. Normand and Y. Pomeau: Convective Instability. A physicist's approach), and the third in *Scientific American* (1980, with C. Normand: Convection). In retrospect, it can be said that those three publications helped establishing a research area in Physics. It was also at that time that appeared his (pioneering, at least in Spain) interest in carrying, close to experiment, pluri-, inter-, and trans-disciplinary research using *nonlinear* dynamics. Among his papers is worth mentioning one in *Journal of Mathematical Biology* (1979, with V. Fairén) where a simple, albeit nonlinear mathematical model accounts for the time periodic oscillations in the aerobic/anaerobic respiratory process of a bacterial culture experimentally studied by H. Degn in Odense.

During 1982–1992, Prof. Velarde worked at UNED, the Spanish Open University, where he created the Department of Physics, reaching soon international standard. He supervised there more than a dozen Ph.D. students. He also spent much effort and time in carrying science to the lay audience by traveling and delivering hundreds of public lectures for the lay audience, elementary and high schools, all over Spain. For this endeavor, Prof. Velarde was awarded the *Capire Prize* (1987) and for his research achievements the *Physics Prize* of the Spanish Royal Academy of Sciences (1991).

The third period (1993–2011) has been his most productive one due to the exceptional circumstances offered by his appointment as PROPIO Professor of

Physics (a program similar to the Royal Society Chairs in the UK) at the Instituto Pluridisciplinar of the Universidad Complutense de Madrid (UCM). Besides numerous regular scientific publications, Prof. Velarde coauthored several research frontier books: 2001: **Nonlinear Dynamics of Surface-Tension-Driven Instabilities**, Wiley-VCH, N.Y., 512 pp. (with P. Colinet and J. Cl. Legros); 2002: **Interfacial Phenomena and Convection**, Chapman & Hall/CRC, Londres, 365 pp. (with A. A. Nepomnyashchy and P. Colinet); 2002: **Synergetic Phenomena in Active Lattices. Patterns, Waves, Solitons, Chaos**, Springer-Verlag, Berlin, 357 pp. (with V. I. Nekorkin); 2003: **Liquid Interfacial Systems. Oscillations and Instability**, M. Dekker, Inc., N.Y., 367 pp. (con R. V. Birikh, V. A. Briskman and J. Cl. Legros). 2007: **Wetting and Spreading Dynamics**, Taylor & Francis, N. Y., 515 pp. (with V. M. Starov and C. J. Radke); and 2012: **Falling Film Flows**, Springer-Verlag, London, 440 pp. (with S. Kalliadasis, Ch. Ruyer-Quil and B. Scheid).

Guess and improve, or otherwise trial and error, seems to have been all along his life a powerful drive in Manuel' scientific exploration. This together with the idea that past a threshold a new state worth exploring was there. Take the love problem it was for him the self-propulsion of a drop, among the many others he explored in hydrodynamics. The problem has a long history. When a solid body, say a sphere, or a drop moves in a fluid it experiences drag and its behavior follows a law established by G.G. Stokes (1851), and J.S. Hadamard (1911) and W. Rybczynski (1911). The law was subsequently extended by B.G. Levich (1962) to account for the role of surfactants. The new idea was that if the drop acts as an engine in a car, reacts upon receiving energy or matter from outside, then past a threshold in the reaction rate strength above a critical value of the surface tension non uniformity, the initial state, motionless or other, gives way to selfpropulsion as the drag can be overcome. This is a consequence of the broken symmetry induced by a spontaneous fluctuation. Such symmetry breakdown and new state could be sustained with an appropriate dynamic input-output energy balance. I had the pleasure of exploring this problem with Manuel and a young fellow friend Alex. Ye. Rednikov. We still today keep an eye on the problem though our joint papers date to 1994!

Noteworthy also is that in about a dozen papers (including theory, numerics, and experimental data), in collaboration with X.-L. Chu, A.A. Nepomnyashchy, C.I. Christov and H. Linde, Prof. Velarde developed the "dissipative soliton" concept (his coinage), showing its ubiquity in fluid physics and beyond. This was a significant generalization of the original soliton concept introduced for integrable systems. The soliton may be a consequence of a suitable initial nonlinear excitation (velocity depends on amplitude) that in balance with dispersion (velocity depends on color/wavelength) survives for ever in a conservative system. Manuel suggested that in a driven-dissipative system an appropriate input–output energy dynamic balance could sustain the above mentioned soliton. Experiments carried by A. Wierschem and H. Linde confirmed his prediction. It was a breakthrough in our understanding of nonlinear waves in dissipative flows and other systems.

Since 2005 a new concept, he also invented, is being developed with W. Ebeling and A.P. Chetverikov, and several other international colleagues. It is the "solectron" quasiparticle, a bound state of an electron to a lattice soliton, as a natural

generalization to *anharmonic* crystal lattices of the (nowadays textbook) polaron concept long ago introduced by L.D. Landau and S.I. Pekar for the *harmonic* cases. His theory points to the possibility of supersonic electron transfer and a kind of electric superconduction that for biomolecular wires and the like, synthetic or otherwise, would be at ambient temperature.

He was awarded the *Honorary Doctorate* from the Université de Provence (Aix-Marseille I) in 1994 and from the University of Saratov in 2010 (ceremony in 2011). At the former he had been Visiting Professor over extended periods of time. He also received the *Rammal Medal* of the Société Francaise de Physique and the Fondation de l'Ecole Normale Supérieure (1996), the *Dupont Science Prize* (2003) [www.premiodupont.org] and the *Medal* of the Spanish Physical Society (2009). He was elected to membership of the **Academia Europaea** (1993; Council member, 2002), to Rector of the International Center for Mechanical Sciences (CISM, Udine, Italy [www.cism.it]; 2002–2004) and (as cofounder) to the Scientific Board of the recently created International Center "Nonlinear Dynamics and Complex Systems", Pescara, Italy [www.nodycosy.unich.it]. He has been research scientist or invited professor in several universities and institutions (CEN-Saclay, Los Alamos National Laboratory, U. Paris VI, XI, Marne-la-Vallée, Grenoble and CNRS, Marseille/I, II, III, NTH-Trondheim, Cambridge U., UC Berkeley, UC Santa Barbara, UC Irvine, Stanford U., Academia Sinica and Normal U. Beijing, HUST-Wuhan, ECNU-Shanghai, etc.).

Professor Velarde has served the international scientific community and the profession as member of several committees and editorial boards (IUPAP, IUTAM, EPS, NATO, EU, ESA, ELGRA/Vice President and President, LABEX Jury (France) President, etc.).

M.G. Velarde: Highlights of Research Achievements

Yu.S. Ryazantsev

For a list of publications with full details see www.ucm.es/info/fluidos, under Personnel, Manuel G. Velarde, cv.

1965–1969–1971: Established domain of validity of Gibbs local equilibrium assumption at the core of the Non-Equilibrium Thermodynamics of L. Onsager and I. Prigogine.

1966–1973: Studied the core nature of non-analytic density expansions of transport coefficients, like self-diffusion, originating in the BBGKY hierarchy and I. Prigogine's non-equilibrium Statistical Mechanics.

1971–1973: Theory of convective instability and criteria to eliminate undesirable effects when measuring the cross-transport thermal diffusion coefficient (Soret effect). Verified in numerous experiments first by H.J.V. Tyrrell (Chelsea College, London) [Trans. Faraday Soc. 71 (1975) 42]. Criteria still used in 2002 and later on by J.V. Sengers (Maryland, College Park), etc.

1972–2011: Theory of instability for fluid systems (nematic liquid crystals, EHD, MHD, falling liquid films, etc.), including features of transverse and longitudinal/dilational interfacial waves.

1979: Mathematical model description of aerobic-anaerobic alternance in the respiration process of *Klebsiella aerogenes* (bacterial culture) motivated and in agreement with experiments by H. Degn (Odense).

1981–1982: Theory providing known and new features of Q-switch laser with absorber. Agreement with experiments by E. Arimondo (Pisa), by C.O. Weiss (Braunschweig), and others using CO2-SF6 laser.

1994: Non-linear non-equilibrium thermodynamic theory of convective instability in agreement with experiment by M. Zamora (Seville) [J. Fluid Mech. 167 (1986) 427].

Yu.S. Ryazantsev (✉)
Instituto Pluridisciplinar, Universidad Complutense de Madrid, Paseo Juan XXIII, 1, Madrid-28040, Spain
e-mail: yriazant@aero.upm.es

R.G. Rubio et al. (eds.), *Without Bounds: A Scientific Canvas of Nonlinearity and Complex Dynamics*, Understanding Complex Systems,
DOI 10.1007/978-3-642-34070-3_2,

1994: Thresholds for self-propulsion of drops due to surface tension gradients, variable effective gravity, micro-gravity and g-jitter, thus illuminating the path for space experiments. In agreement with experiments by J.W. Bush (Cambridge) [J. Fluid Mech. 352 (1997) 283] and by A. M-Tatsis (Imperial College, London) in microgravity experiments. Theory has been incorporated in ESA and NASA specialists books: in 1997 by S.S. Sadhal (USC, LA) and in 2001 by R.S. Subramanian (Clarkson College, Potsdam, NY).

1995: Introduction of the "dissipative soliton" concept to describe onset and features of non-linear surface waves due to surface tension gradients (Marangoni effect). It has proven to be of universal value well beyond its original hydrodynamics context, as there are now books and international meetings organized with precisely that same title. Although he had used this concept in several papers already in 1991, it was in a paper published in 1995 in Physica D where the term appeared in the title of the paper.

1996: Avalanche-collapse model for "excitability" in non-linear dynamics, in agreement with laser experiments by F.T. Arecchi (Florence) using a laser with intracavity absorber [Europhys. Lett. 38 (1997) 85].

1996: Theory about the onset of form by replication (with controllable degree of fidelity) in active systems. Results incorporated in books in 1999 and in 2003 by A.C. Scott (Tucson U., AZ) with discussion supporting their significance to understand early stages of prebiotic evolution.

1997–Present: Theory describing universal laws of wetting and spreading processes over smooth and porous, isothermal and heated substrates, verified by experiments.

1999: Theory describing features of huge internal waves (100 m amplitude along the pycnocline) in the Strait of Gibraltar and other straits, in agreement with field data from several authors.

2001: Theory of generalized stochastic (coherence) resonance: there are systems with excitability-oscillatory behavior that take advantage of noise to operate meaningfully with no need of external drive, in agreement with experiment by O. Piro [Phys. Rev. Lett. 92 (2004) 073901], who has proposed a thermo-optical device.

2001: Theory of universal features of wavy phenomena, leading to dewetting and film rupture over smooth and porous, isothermal and heated substrates. Agreement with the available data of 1949 by P. Kapitza, by G. Reiter (1992–1993), and by J. Becker (2003).

2001–2003: Theory of significant features of solitonic collisions in Bose–Einstein condensates.

2002–2011: Mathematical models of neurons, cerebellar function and CPGs (memory and learning) in agreement with available data.

2009–2012: Theory of "memotaxis", a novel strategy concept for search and survival. Observed by R. Strauss in Mainz in *Drosophila melanogaster* under humidity and/or temperature gradients. Implemented in robots by P. Arena and engineers in Catania (EU Consortium SPARK).

2010–2011: Theory of "internal representation layers" in mathematical brain models of perception for action. Implemented in robots by P. Arena and engineers in Catania (EU Consortium SPARK).

2005–Present: Theory of a new form of fast, long range electron transfer assisted by solitons (e.g. a transition from Ohmic to field-independent non-Ohmic, generally, supersonic conduction). Coined the concepts of electron "surfing" and "solectron" (2005) to account for the coupling of nonlinear elasticity to quantum mechanics, as a generalization of Landau and Pekar's "polaron" (nowadays textbook) concept. The theory predicts a kind of ballistic/losses-free electric transport at ambient temperatures. It also leads to a new form of "electron pairing" both in momentum space and in real space (accounting for Coulomb repulsion and Pauli's exclusion principle).

Gallery of Portraits and Other Pictures

M.G. Velarde

The pictures illustrate how science is part of culture, and the cosmopolitan life at the Instituto Pluridisciplinar of Universidad Complutense of Madrid (Spain).

Fig. 1 A portrait of the scientist as a senior man

M.G. Velarde
Instituto Pluridisciplinar, UCM, Paseo Juan XXIII, 1, Madrid-28040, Spain
e-mail: mgvelarde@ucm.es; mgvelarde@uax.es

R.G. Rubio et al. (eds.), *Without Bounds: A Scientific Canvas of Nonlinearity and Complex Dynamics*, Understanding Complex Systems,
DOI 10.1007/978-3-642-34070-3_3,

Fig. 2 With wife María del Pilar

Fig. 3 "Slow down you fool you might win" (Pugh). With María del Pilar and daughter Esther-Adelaida on the way from Santa Fe to Taos, in New Mexico

Fig. 4 With a local folk in the wild West a year in the 1980s when Manuel was Consultant to the Los Alamos National Laboratory in New Mexico. The town is Fort Sumner where Billy the Kid (William H. Bonney) was assassinated by former fellow friend and then Sheriff Pat F. Garrett. Daughter Esther-Adelaida is inside the stage coach

Fig. 5 Will Zimmerman and Manuel at the farewell party for Will and fiancée Julia Rees, after their postdoc stay in Madrid. At present both are professors at Sheffield University. The picture at the center in the hands of Manuel was done by Will's mother, an accomplished artist who had only ever done one portrait of any of Will's mentors or collaborators

Fig. 6 With Guoxiang Huang at Manuel's home in Madrid

Fig. 7 With Werner Ebeling at Institut für Physik, Humboldt Universität in Berlin

Fig. 8 With Takuji Kawahara in Kyoto. The Kinkaku-ji temple is seen in the back

Fig. 9 With S. Kaliszky, his predecessor as Rector of CISM (Udine, Italy)

Fig. 10 Trading books and knowledge about fluids for coffee and knowledge about coffee and complexity with chemist Ernesto Illy (owner of Illy-Caffè) at the XVIIth Century Palazzo del Torso (Udine, Italy). On December 15th, 2004, Dr. Illy gave the invited lecture at the farewell ceremony of Manuel as Rector of C.I.S.M.

Fig. 11 G. Nicolis and Manuel during the "Week of Science", September, 2011, synchronizing watches trying to make sure the impossible task of precluding the schedule becoming chaotic

Fig. 12 With astronaut Claude Nicollier at a public lecture at Ateneo de Madrid, where Manuel had a chair following the tradition of S. Ramón y Cajal, J. Echegaray and others, who also held chairs at the same learned institution

Fig. 13 With violonist Igor Oistrach at Manuel's home in Madrid

Fig. 14 With Michael Berry at a discussion with painters, musicians, and literary people in Madrid

Fig. 15 With I. Prigogine, poet Carlos Bousoño (*right* to IP) and sculptor Eduardo Chillida *far right*, *left* of Manuel, at the home of MD Neurophysiologist Alberto Portera (with the camera)

Fig. 16 With (*left* to *right*) former UCM Rector R. Puyol, Maestros Tomas Marco, Cristobal Halffter and Luis de Pablo, and MD Alberto Portera, after ceremony of award of Honorary Doctorate to the three music composers

Fig. 17 With (*left* to *right*) sculptor Eduardo Chillida, María del Pilar and other friends

Fig. 18 Ceremony of *Honorary Doctorate* (1985) offered to Prof. Ilya Prigogine by the Spanish Open University (UNED). Noteworthy is that the Rector of UNED presiding was the first lady ever Rector of a University in the history of Spain, Prof. Elisa Pérez Vera, at present a member of the Supreme Court (Tribunal Constitucional) of Spain

Fig. 19 With W. Ebeling (*left*) and A.P. Chetverikov (*right*) after Manuel was awarded an *Honorary Doctorate*. They are besides the statue of N.G. Chernyshevsky, after whom is named the Saratov State University, a friend of F.M. Dostoyevski and author of a celebrated book "What is to be done", where he argues about "rational egoism" leading to solidarity, a *motto* later on taken up by V.I. Lenin

Fig. 20 With Ivan B. Ivanov (*left*) and María del Pilar (*center*) at Rila Monastery in Bulgaria (1986)

Fig. 21 With Orlin D. Velev (*left*), Victor M. Starov and wifes María del Pilar (*center*) and Nadia (*right*) in Sofia (1986)

Fig. 22 With E.G. Morozov (*left*) and K. Trulsen (*center*) at IP-UCM

Fig. 23 With Milton Van Dyke and their wifes, Sylvia (*center right*) and María del Pilar (*center left*) in Santander (Spain)

Fig. 24 With V.A. Briksman (*left*) and V.Ya. Shkadov (*center*) in Moscow at the home of the latter

Fig. 25 With (*left* to *right*): H. Haken, A. Fdez.-Molina, W. Ebeling and R.R. Llinás, at IP-UCM

Fig. 26 With John B. Fenn (*center left*), Rudolph (Rudy) Marcus (*center right*), and Vicente López (*left*, former postdoc of the latter), at the time Manuel was Rector of the International Center for Mechanical Sciences (CISM, Udine, Italy). John was awarded the *Nobel Prize for Chemistry* in 2002 for experimental discoveries made past 70 and after being "forced" to retire from Yale University to Commonwealth University of Virginia at Richmond. Rudy was awarded the *Nobel Prize for Chemistry* in 1992 for his theory of electron transfer (ET) a topic now of Manuel's love

Fig. 27 Very serious planning of a trip to Granada, Spain, to visit the Alhambra, with, from *left* to *right*, Roberto Lima (Brazil), Renate (Mrs) Röpke and Gerd Röpke (Germany) and Barbara (Mrs) Ebeling

Fig. 28 Sacred tradition: black/white board discussions, here with G. Tsironis (*left*), W. Ebeling (*center*) and A.P. Chetverikov (*right*) at IP-UCM

Fig. 29 Portrait of the scientist as a donkey on duty for Masters Y. Pomeau (*left*) and P. Clavin (*center*). Or are they following Manuel? And for what curious purpose? Is it because of the ongoing economic crisis also affecting scientists? Paul did the babysitting for Manuel's children four decades ago in Brussels

Fig. 30 With a group of participants at one of the CNRS meetings organized by P. Clavin and Y. Pomeau in the French, rebuilt by Belgians, village of Peyresq, in the Provence, South of France. Manuel's wife, María del Pilar, is standing at the *center* of the picture (with dark glasses) together with Marie-Christine (Micrie, Mrs) Clavin (*below left* above Manuel) and Chantal (Mrs) Pomeau (*right* besides Yves). Len Pismen is seated on the *right*. Recently, Len, Yves, Manuel with Eshel Ben-Jacob, under the guidance and coordination of Springer Editor Dr. Chris Caron, have launched a forum of *Discussion and Debate* in the *European Physical Journal, Special Topics Series* (www.epj.org)

Fig. 31 Lecturers at the first NATO-ASI held in Spain (1983) at El Escorial. *Left* to *right first row*: P.C. Fife, M.O. Scully, G. Nicolis, P. Clavin, and several other colleagues

Fig. 32 With P.G. de Gennes (*center*, smoking), composer T. Marco (*right* to Manuel), Yuri S. Ryazantsev, C.I. Christov, A. Ye Rednikov, among others, at IP-UCM

Fig. 33 With P.G. de Gennes and wife Annie at a most typical olive oil based restaurant, "Casa Juanito" in Baeza (Andalucía). Also in the picture Y. Pomeau, P. Clavin and V. Sánchez. Juanito (next to Micrie Clavin) and his wife Luisa (next to de Gennes) both dressed white are at the *center* of the picture

Fig. 34 With J. Laskar (standing extreme *left*), B. Mandelbrot, A. Libchaber, H. Linde and several other colleagues. Seated below A. Wierschem next to G. Nicolis (*right*). Katy Nicolis is seated at extreme *left*, at IP-UCM

Fig. 35 With (*left* to *right*): R.S. MacKay, María del Pilar (*center*), an MD lady friend, W. Ebeling and A.A. Nepomnyashchy, in Madrid

Fig. 36 *Left* to *right* (standing): V.I. Nekorkin, W. Ebeling, L. Fortuna, P. Arena, V.A. Makarov, A. Giaquinta, U. Thiele. Seated: H. Cruse, R.V. Birikh, at IP-UCM

Fig. 37 From *left* to *right* with R.V. Birikh, G.R. Sarma, J.C. Legros, R. Narayanan, P. Colinet, V.A. Briksman, U. Thiele and J. Bragard at IP-UCM

Fig. 38 The 3rd Physicochemical Hydrodynamics Conference held in Madrid (1980) and the first Benjamin G. Levich attended after being allowed to emigrate from the former Soviet Union. BGL is at the center in the picture next to S. Ostrach (*left*) and B. Spalding (*right*) next to Manuel

Fig. 39 Group photo of lecturers and other participantes at a School on Fluid Physics and Nonlinearity held in Marrakech in April 1998. Coorganzied with Mohamed Belhaq (Professor of Mechanics at Hassan II University in Casablanca), who appears third row from *top*, fourth from *left*. It was sponsored by the European Physical Society (EPS), the Third World Academy of Sciences (TWAS), the UNESCO and the cooperation bilateral treaty of Morocco and Spain (Minister of Foregin Affairs of Spain)

Fig. 40 Birthday dinner during the "Week of Science" (September 2011) in the garden of the "Museo del traje", Ciudad Universitaria, UCM Campus. Standing: from *left* to *right* P. Schuster (Austria), A.P. Chetverikov (Russia), Michèle Vignes-Adler (France), P. Gaspard (Belgium), Larissa Brizhik (Ukraine), Leonor Cruzeiro (Portugal) with singers W. Ebeling and G. Röpke. Seated: from *left* to *right* Annie Steinchen-Sanfeld (Belgium and France), A. Acrivos (Greece and USA), Jennie (Mrs) Acrivos (Cuba and USA). Seated seen from the back, *left* to *right*: María del Pilar, Mrs. García Serrano and Museum Curator Rafael García Serrano

Fig. 41 *Right to left*: M. de Leener, J. Brocas and MGV, all from the School of Ilya Prigogine (ULB, Belgium), on their way to Copenhagen to attend the IUPAP Statistical Physics Conference in 1966

Fig. 42 With M. de Leener (*right*)—both students of P. Resibois—in Copenhagen at the week of the IUPAP Statistical Physics Conference in 1966

Fig. 43 With the President of University of Aix-Provence (Marseille I) at the ceremony of his Honorary Doctorate in 1994

Fig. 44 With (*left to right*) Yu. S. Ryazantsev, Cuban Cosmonaut A. Tamayo and J. Padday, at the IUPAP Conference on Teaching Thermodynamics and Statistical Physics held in Badajoz (Spain) in 1992

Fig. 45 With Zhang Ji-Yue (Northwestern University) at a Museum in Xian in January 1986

Fig. 46 At the Great Wall near Beijing, in 1986

Fig. 47 With Hao Bai-Lin at the Yellow Crane Tower, a pagoda by the Yangzi river, near Wuhan in January 1986

Fig. 48 With N. F. Ramsey and their spouses, Ellie and Maria del Pilar, in the garden at the Queen Sofia Museum of Modern art in Madrid

Fig. 49 At the ceremony of Honorary Doctorate offered by UNED to Hermann Haken in 1987

Fig. 50 *Left to right*: F. de Elzaburu, E. de Bono, P. Manzelli, MGV and J. P. Changeux, after the reception of the Capire prize in 1987 (awarded to dB, C and V)

Fig. 51 With V. Anishchenko and W. Ebeling at the dasha of the first by the Volga river, near Saratov, in 2011

Fig. 52 With G. Z. Gershuni and E. M. Zhukhovitsky when attending a Conference held on a ship from Perm to Moscow

Fig. 53 *Left to right*: E. Riande, A. Acrivos, MGV, A. Sanfeld, G. I. Barenblatt and M. Van Dyke during a Summer School held in Almeria (Spain)

Fig. 54 *Left to right*: J. Alaez, Y. Pomeau, MGV, H. Peregrine and D. G. Crighton, during a Summer School held in Almeria (Spain)

Thirteen Years of Collaboration with Manuel on Complexity in Biorobotics and Brain Science

P. Arena

This contribution aims at testifying a long history of mutual and really fruitful collaboration of myself with Prof. Manuel G. Velarde: a history based on our common interests in complex adaptive systems, intelligence in Biology and in Robotics.

I remember as it were yesterday my first phone conversation with Manuel. I received his call towards the fall of 1999. At that time he was in contact with Leon Chua (one of the most brilliant minds I've ever met), regarding his interest in neural dynamics and robots. Leon was enthusiastic with my implementation of cellular nonlinear networks applied to analog locomotion control in artificial robots [1]. I was working with Prof. Luigi Fortuna, former teacher in my undergraduate studies, subsequently my PhD supervisor and now my colleague (this is a honour for me indeed!). We had implemented this robot control structure in analogue hardware under the Cellular Nonlinear Network (CNN) paradigm, introduced by Leon. The real demonstrations and accompanying videos of the walking multipode, showing also a real time gait adaptation, were shown worldwide by Leon as one of the best examples of simple brain dynamics implemented really working prototypes. In one of those occasions Leon stimulated the brilliant Manuel's mind to contact myself, as a potentially suitable counterpart for exploring working solutions for models of biological intelligence.

The first meeting together as a result of our phone conversation, without loosing time, as his habit, he invited Luigi and me to a meeting in Madrid entitled "Dinámica Cerebelosa, Sistemas Dinámicos y Robots neuro-motivados" (Fig. 1). Luigi and I brought our *Rexabot* with us, showing its capabilities (Fig. 2). We were proud to show one the first examples of reaction-diffusion systems in action and interaction. The meeting was highly rewarding for myself, since I discovered Biology as a kind of treasure from which to draw a lot of inspiration for technology. Manuel gave me

P. Arena (✉)
DIEEI, University of Catania, Viale A. Doria 6, 95125 Catania, Italy
e-mail: parena@diees.unict.it

R.G. Rubio et al. (eds.), *Without Bounds: A Scientific Canvas of Nonlinearity and Complex Dynamics*, Understanding Complex Systems,
DOI 10.1007/978-3-642-34070-3_4, © Springer-Verlag Berlin Heidelberg 2013

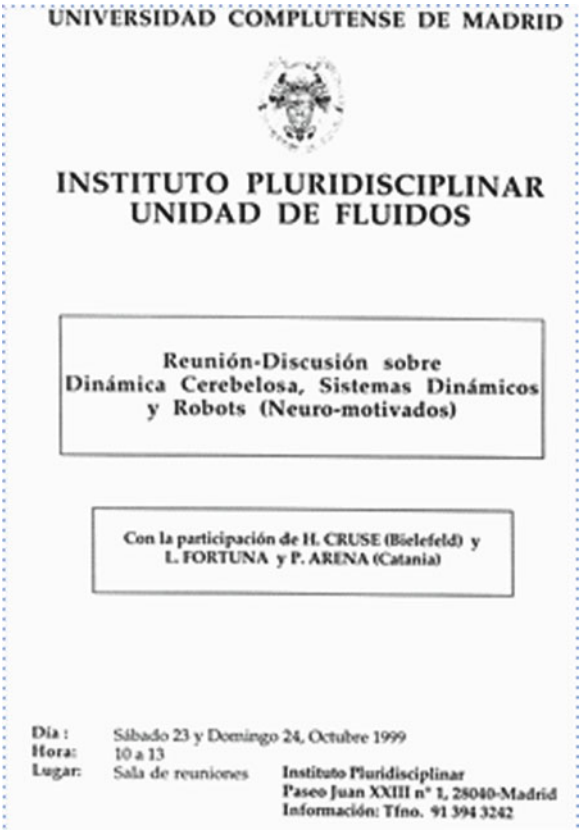
UNIVERSIDAD COMPLUTENSE DE MADRID

INSTITUTO PLURIDISCIPLINAR
UNIDAD DE FLUIDOS

Reunión-Discusión sobre
Dinámica Cerebelosa, Sistemas Dinámicos
y Robots (Neuro-motivados)

Con la participación de H. CRUSE (Bielefeld) y
L. FORTUNA y P. ARENA (Catania)

Día : Sábado 23 y Domingo 24, Octubre 1999
Hora: 10 a 13
Lugar: Sala de reuniones

Instituto Pluridisciplinar
Paseo Juan XXIII nº 1, 28040-Madrid
Información: Tfno. 91 394 3242

Fig. 1 Workshop-discussion meeting at IP-UCM over week-end days (1999)

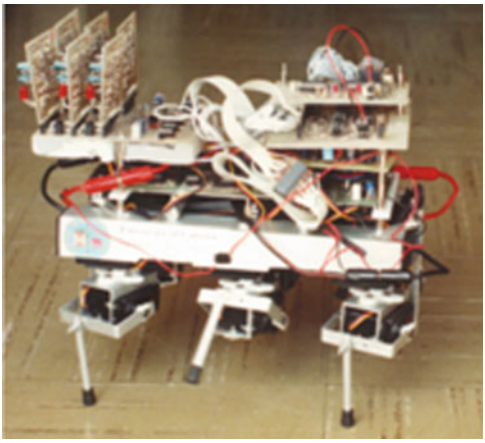

Fig. 2
ReXabot:reaction-diffusion CNN controlled robot

the opportunity of meeting Prof. Holk Cruse, one of the most important biologists interested in animal and artificial locomotion. At that meeting Prof. Joseph Ayers, the worldwide expert in lobster neurobiology, was also invited. All of us together found a large interest convergence on trying to model and subsequently implement in artifacts the biological principles of locomotion, with the aim to go up from a purely mechanistic approach to the implementation of a embryonic form of intelligence.

Manuel was convinced of the fact that a real intelligent robot should be able to make mistakes, not only to take good decisions, that are for the large majority of cases a result of pre-programmed actions. Intelligence has to draw its basis from the capability to learn from wrong decisions and, even after learning, the robot has to be given the possibility to commit mistakes, and from then to gain opportunities to learn more. We completely agreed with that view. The unique problem was given by the potential problems to the robot mechanics and electronics caused by letting it making wrong decisions. On the other hand, learning on line from the results of own actions in a real environment could have been a real mean to test the real robot capabilities and the joint behavior of algorithms and hardware. This rule guided us in the following years of our collaboration.

These very rewarding meetings continued, thanks to Manuel's initiative. He invited me again the following year, together with Prof. Sten Grillner, one of the most important neuroscientists, the father of Lamprey neurobiology and Orian Ekeberg, his collaborator in charge of implementing the biological model into dynamic robot simulations. This was across the year 2000, when our students, Luigi and myself in Catania had just developed our artificial lamprey underwater robot. Our Lamprey brain was loosely inspired by the basic locomotion generation principles proposed by Grillner.

Also at that time I became associate Professor and the influence of these meetings was really important for my future research. I soon realised that, in order to maximise the search for new results, minimising the time needed to obtain them, a tight collaboration among the different scientific fields present at those meetings was necessary.

In 2002, as reported in the leaflet below (Fig. 3), Manuel succeeded in organising an impressive meeting within the "2° Ciclo de invierno de ciencia y tecnología". There Luigi and myself showed again one of our robot prototypes. One of the invited speakers was Prof. Walter Freeman, the father of the modern view of olfactory neurodynamics in mammals, whose idea on the arousal of concepts as the result of competition among different attractors in a multidimensional chaotic landscape formed by the neuronal population, fostered a lot my ideas on complex neural circuit architecture modelling.

The discussion at that meeting was quite stimulating: we had both formal and informal discussions with Manuel and Walter: the latter, looking at our walking machine showing a number of different locomotion patterns in real time, was positively surprised but pointed out a critical comment that was providential, since it largely stimulated my future research: "your robots"—he said—"succeed in locomotion, but do show neither attention nor intentionality, the fundamental

Fig. 3 Program flyer of Workshop (2002)

ingredients to go up from a purely reflex based adaptive system to a perceptual machine". Walter was convinced that our approach of using complex systems, implemented through adaptive analogue circuits mimicking neural dynamics, could have been a suitable tool to approach the perception process. Complex dynamics are able to generate an impressively large number of different solutions, that subsequently can be shaped to fit the body–environment interaction, from the level of reflexes, to that one of cognitive interaction. These ideas, focalised in the course of those meetings, were subsequently deepened and developed.

The CISM School in Udine. In 2003 an interesting single partner project, funded to our group in Catania from the Office of the Naval Research, allowed us to invest resources to build more efficient legged prototypes and neural circuits. In those years Manuel was the Rector of the International Centre for Mechanical Sciences (CISM), in Udine (Italy). He invited me to coordinate an International School on "Dynamical Systems, wave-based computation and neuro-inspired robots": this title summarises the new emerging scientific field that we were going to introduce (Fig. 4). At that school all the results produced in the past few years were efficiently summarised and presented, and also other key persons that could complete the panorama and

Fig. 4 Flyer announcing School (2003) at CISM (Udine, Italy)

help us to more deeply understand the future directions of this stimulating research gave interesting invited talks. Among them were Dr. Tatiana Deliagina, a close collaborator of Sten Grillner, and Prof. Barbara Webb, whom I had met for the first time in 2000 at an SPIE conference in Boston. The former gave interesting lectures on the neurobiological basis of Central Pattern Generator, whereas the latter talked about sensory motor integration in insects and the related models. A number of students from all over Europe were also able to attend. They were allowed to develop practical applications, using Lego Mindstorm, of the model presented during the lectures. This was very rewarding and stimulating both for students and for us, involved with them in the implementation and discussions. At the suggestion and sponsorship of Manuel, Luigi and I offered a public lecture with robot demonstrations at the beautiful *Palazzo della Provincia* in Udine. A book was later on published, with the lecture notes of this school [2].

The SPARK Project. The overall participation and organisation of that school convinced me that it was time to submit a proposal for a grant to the European Commission. There was a recently announced call on "Cognitive systems, interaction and Robotics", where one of the main issues to cover for a successful proposal was to address a new type of adaptive interaction with the environment: nothing better than our emerging approach based on complex dynamics generating complex activity patterns. Moreover, through all those meetings organised by Manuel and together with him, a good consortium, with really competent scientists, in charge for working towards the same direction from different scientific fields, was ready to be formed.

I personally worked really a lot, for a number of months to carefully prepare the proposal which we called *Spatial-temporal Patterns for action-oriented perception in roving robots* (acronym SPARK). This was an ambitious project aimed at

implementing our ideas on the new approach of using complex dynamics to represent a new paradigm for action-oriented perception. The consortium comprised six partners, who personally knew one another and I was sure of their willingness of working at the different sides of that puzzle of complex nonlinear dynamics and perception in algorithms and animals. The heart of the consortium was composed by our group in Catania, Manuel's knot in Madrid, Holk's group in Bielefeld and Barbara's team in Edinburgh; two small companies ANAFOCUS and ANALOGIC, devoted to develop, respectively, hardware and software tools, based on cellular nonlinear networks, took part in this adventure. The proposal was successful and we were allowed to work together with enthusiasm. I have to acknowledge and thank the wonderful character of our project Officer, Dr. Hans-George Stork, who continuously encouraged us to make good research while maintaining the project outline and deadlines. He himself participated non only in our meetings but also in other initiatives, like schools, and this demonstrates his approach: as a mathematician checking the project development by very professionally following also technical activities. During the project activities I worked a lot together with Manuel, and also against his volcanic character to think about a lot of things simultaneously. At that time I remember that he was going to loose his primary interest in Spatial Temporal Dynamics and reaction-diffusion systems (which was the main common argument in SPARK): he was more and more involved in studying superconductivity! But I convinced him to continue to work on the reaction-diffusion side, which led to important breakthroughs within the project. The SPARK activities were really intense and full of significant results on spatial-temporal dynamics applied to perceptual robots: one of them was the reformulation of the "Winnerless Competition" principle into the Cellular Nonlinear Network paradigm [3, 4], for the subsequent application to the generation of perceptual behaviors into a roving robot. The wandering of state variables among a number of saddle nodes, maintaining, at the same time, an overall stable trajectory was used for the representation of perceptual states in moving machines. This strategy followed a "twin" approach which used the paradigm of Turing Patterns in reaction-diffusion cellular Nonlinear Networks. This computational structure, able to generate hundreds of different patterns and steady state attractors in nonlinear cellular circuits, even constituted by a relatively small number of cells, gave the possibility of implementing emerging solutions to the perception-for-action cycle in our robot prototypes. The practical evaluation of the capabilities of the robot to find new solutions to solve a given job in front of unforeseen drawbacks was a real success. The SPARK project was considered by the EU reviewers a show-case in the panorama of the EU funded projects. Three years of joint efficient research, together with Manuel and other impressively active neuroscientists led to a really well settled consortium. We were used to meet every 4 months and every half year a 1-week meeting, called SPARK brainstorming week was organised, where to discuss theoretical results, but also to create links to biology and to robotic implementation. The SPARK project started with the idea of applying complex dynamics to represent brain dynamics from a high level perspective, but the lessons learned from Neurobiology led both Manuel and myself to realise that, whatever perspective from which to face with the problem

Fig. 5 Manuel and myself at one of our SPARK meetings in Madrid in wintertime

of intelligence, we had to take in large consideration the brain functions. And, most important, the continuous meeting with Holk and Barbara convinced us that the basics of intelligence, considered not only as a purely, fixed reflex, adaptive behavior, but as the capability of decision making, resolving contradictory cues, and so on, could be found not only in sophisticated mammal brain, but also in tiny, ganglionic assemblies of neural cells, as insect brains are made of. Insects became our main source of inspiration for our immediate future research activity. Most importantly, some basic brain functions are better to be focalised and characterised in small brains than in larger ones. Moreover models genetic tools were available to control behavioral repertoires, to try to close the feedback among brain structure, function and behaviors in the insect brain. To proceed in this direction we needed a neurogenetics expert. Holk suggested us to meet and discuss with one of the worldwide experts in the *Drosophila melanogaster* brain neurobiology and genetics, Prof. Roland Strauss.

The SPARK II Project. At that time, the beginning of 2007 (Fig. 5), strong from the really positive experience with SPARK, I was also encouraged by Manuel and Holk to submit another EU initiative, that, building upon the acquired experience, could be focused on the high risky but at the same time mostly fascinating proposal to design an insect brain computational model: the SPARK II project was conceived, submitted and approved. SPARK II started at the beginning of 2008, with the collaboration of Roland as a new partner.

One of the most important steps towards understanding and modelling brain functions is spatial working memory and the capability to take decisions on the basis of previous experience, especially in front of noisy and incomplete sensory information. Manuel started formalising the following, simple but efficient idea: if someone took a decision based on a certain actual information, and pursues this decision for a certain amount of time, even in front of contradictory and noisy cues, he, for a while continues to maintain that decision notwithstanding sensory information that could suggest different responses. Manuel formalised this principle which generalised the phenomenon of bacterial *chemotaxis* introducing the concept of *memotaxis*. The first mathematical model was published in early 2008 in the "Revista Espanola de Física" (Fig. 6), together with some preliminary results on our


Temas de Física

Quimiotaxis, infotaxis y memotaxis: estrategias de exploración y supervivencia

Nazareth P. Castellanos, Davide Lombardo, Valeri A. Makarov, Manuel García Velarde y Paolo Arena

La exploración y búsqueda de alimentos por organismos simples como, por ejemplo una bacteria, puede reducirse a un conjunto de reglas basadas en el gradiente de concentración, lo que se conoce como quimiotaxis. Pero esta estrategia está limitada a que haya una alta razón señal-ruido (SNR, siglas en inglés). Una estrategia complementaria es la memotaxis, que requiere una capacidad computacional mínima y puede ser fácilmente implementada en "hardware". Bajo esta estrategia subyace un sistema dinámico que modela la memoria a corto plazo. Cuando interactúa con el entorno este sistema dinámico recoge información de los pasos que ha realizado con éxito (aquellos que aparentemente le acercan a la meta buscada) y es capaz de corregir decisiones equivocadas [illegible] que en ciertas situaciones como baja SNR pueda [illegible] sobre el que se implementa tal algoritmo pueda [illegible] taxis. Mostramos numérica y experimentalmente [illegible] rablemente la aleatoriedad observada con la [illegible] una ganancia en el rendimiento del robot. Tam[illegible] es otro algoritmo de búsqueda.

REVISTA ESPAÑOLA DE FISICA

VOLUMEN 22, NÚMERO 3, 2008

Fig. 6 Part of front page of paper on "memotaxis" (in Spanish)

Fig. 7 Manuel, Giacomo Rizzolati and myself (standing in the *right*) at the school on nonlinear dynamics and robots at El-Escorial

robots, but the complete methodology is still under development and we have really interesting results in biological experiments which are currently under investigation to assess the presence of this phenomenon at the decision level in animals.

The following summer Manuel and myself organised, with the support of the European network for the advancement of artificial cognitive systems "EU-Cognition", a summer school entitled: "Non-Linear Dynamics and Robots: From Neurons to Cognition" (Figs. 7, 8 and 9). The School was organised within the "Cursos de Verano" at El Escorial, a wonderful place in the neighborhood of Madrid. This was 1 week of intense scientific work: mornings and early afternoons were devoted to teach to students and applicants. Those served as stimulus for the evening meetings within our SPARK II consortium. The school hosted invited speakers like Prof. Giacomo Rizzolati, who gave an interesting lecture on mirror neurons, stimulating our ideas on the possible counterpart in the insect brain. The picture (Fig. 7) illustrates one of the moments of the seminars organised within such a school at El Escorial, with Manuel as the Chairperson. The following successful joint collaboration within the SPARK II project led to the formalization of an insect brain computational model endowed with Memotaxis, neural spiking networks and the capability of on-line learning in robot prototypes. Practical demonstrations were really stimulating for interesting future collaborations which are still continuing, even if informally.

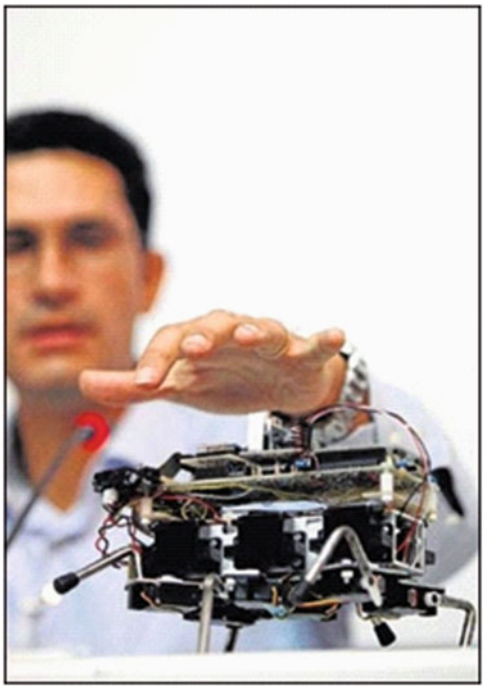

Fig. 8 Myself and MiniXex

Fig. 9 School "Nonlinear dynamics and robots: From neurons to cognition": El-Escorial, summer 2008

There are men which are able to strongly influence research interests and scientific careers: they represent true *bifurcation points*. This was Manuel in my past 13 years of research.

Manuel for a long period, acted as a kind of modern “mecenas”, inviting several experts together for the only interest in science, and I was honored to join many times his interesting meetings, with the opportunity to meet outstanding people who contributed in shaping my actual interests in bio inspired systems, neurodynamics and Robots. Thanks Manuel for all of this and, last but not least, for your friendship, a basic element of our successful joint activity (Fig. 9).

References

1. Arena, P., Fortuna, L., Branciforte, M.: Reaction-diffusion CNN algorithms to generate and control artificial locomotion. IEEE Trans. Circ. Syst. I Fund. Theor. Appl. **46**, 259–266 (1999)
2. Arena, P. (ed.): Dynamical Systems, Wave-Based Computation and Neuro-Inspired Robots. CISM Courses and Lectures, vol. 500. Springer, New York (2008) [ISBN-10: 3211787747]
3. Arena, P., Fortuna, L., Lombardo, D., Patanè, L., Velarde, M.G.: The winnerless competition paradigm in cellular nonlinear networks: models and applications. Int. J. Circ. Theor. Appl. **37**, 505–528 (2009)
4. Arena, P., Fortuna, L., Lombardo, D., Patanè, L., Velarde, M.G.: The WLC principle for action-oriented perception. In: Proceedings of Microtechnologies for the New Millennium (SPIE 07), Gran Canaria (Spain), 2–4 May 2007

My Relation with Professor Manuel G. Velarde

X.-L. Chu

I first knew Manuel by his scientific work. In 1983 when I started my postgraduate study, Prof. Bailin Hao, my advisor in China, who is also a good friend of Manuel, gave me a few topics to choose as my research direction. As the introduction to one of the possible research areas, a review article on the stability of fluid motion by Normand, Pomeau and Velarde in Review of Modern Physics caught my attention. This review article became not only the introduction to my research career, but also the introduction to my relation with Manuel, who eventually became my Ph.D. thesis advisor, a father-like tutor of life and a great friend.

After reading the research papers published by Manuel's team, I did a few small pieces of follow-up work on fluid interface stabilities in 1983 and 1984. Through the connection of Prof. Hao, Manuel and I started to exchange preprints of research papers. In December 1985, Manuel came to China at Prof. Hao's invitation and arrangement. Our first meeting in person was at Beijing Airport. I remember that Prof. Hao, who met Manuel not long ago, asked about Manuel's newly kept moustache and beard. Manuel said that it was common in Spain that people start to keep them at early age and shave it at age of 60 as symbol of starting new life. I didn't have chance to see Manuel at his 60th birthday, but, Manuel, you are at 70 now and you have never slowed down a little bit in your path pursuing exploration at the forefront of science.

In recent years my connections with Manuel are through emails. In every mail from Manuel, he talks with great enthusiasm about his recent works and recent published papers, just like the way he talked when I was in Madrid. From the words and lines in Manuel's mail, I can always feel slashing out of his energy, which have been inspirational for me and motivated me to take challenges in my work and life

X.-L. Chu (✉)
System Engineer, Alcatel-Lucent USA Inc., 1960 LUCENT LN, 1c-222,
NAPERVILLE, IL 60563-1594, USA
e-mail: xiaolin.chu@alcatel-lucent.com

R.G. Rubio et al. (eds.), *Without Bounds: A Scientific Canvas of Nonlinearity and Complex Dynamics*, Understanding Complex Systems,
DOI 10.1007/978-3-642-34070-3_5, © Springer-Verlag Berlin Heidelberg 2013

all the time, whether the time I was doing my Ph.D. research at the Spanish Open university (UNED) in Madrid, or later research and development in industry.

In his first trip to China, Manuel visited Beijing, Xi'an and Wuhan. He lectured at all three places, and visited opera houses, music schools, museums and historical monuments. In my home town Wuhan, the university (HUST) had organized a Winter school. Manuel and Prof. Hao gave series of talks on non-equilibrium systems to young scientists and graduate students from different places of China. In this school, they brought in the new ideas and research forefront at that time. Manuel's broad knowledge in science and his lecture full of energy impressed all participants.

In the summer of 1986, I arrived in Madrid and started working on my Ph.D. thesis under Manuel's guidance. I still remember Manuel's words, "you are the first Ph.D. student in science from China to Spain and we have to make this a success thus setting the standard". Indeed, he had put all types of efforts to help me overcome hurdles of working and living in a totally new environment. When I arrived, Manuel sent me to a Summer school in the University of Salamanca to learn Spanish. He wrote to the Rector of the University to get my tuition waived. After I finished 4 weeks intense Spanish courses and came back to Madrid from Salamanca, Manuel used his relations to find a Colegio Mayor (campus student dorm) close to the office. In order to get the best computing facilities, Manuel called his colleagues in the Atomic Energy Center (JEN) in Madrid, to setup an account for me to use the fastest available computer at that time. This was no easy matter due to my Chinese citizenship. But Manuel managed to overcome the difficulty.

In about 3 years, I had chance to work closely with Manuel. Like many other people around him, I was immediately impressed and infected by his passionate style of working. His broadness in knowledge, his persistence in pursuing the best results and his sensitivity in capturing new ideas has made him always steps ahead of others. Remember once Manuel invited a great experimental scientist from Berlin (former GDR-Germany), Dr. Harmut Linde to Madrid. Dr. Linde showed us his experiment results, movies of spontaneous surface waves of liquid layer. Manuel immediately pointed out that the waves in Linde's experiments were "solitary" waves, a special kind of non-linear waves. In the next a few months, Manuel started to guide us in the direction of solitary waves. We kept discussing all the time on solitary waves, read all the available literature on the subject and tried different approaches to formulate mathematically the onset of spontaneously growing solitary waves. Finally we found a simple and intuitive way to combine the linear stability theory and the Korteweg-de Vries equation, providing a qualitative explanation of Linde's experiments.

Weekend and holidays could be home-sick time for a person away from family. To help me deal with this, Manuel and his family often invite me to spent time with them. During my staying in Spain, I don't remember how many weekends and holidays I had been with Manuel's family, where I was treated as one of them. Together we went to swimming pool, watching classic movies in the home theater, ate in the community restaurants (kind of country club), partying with relatives and family friends. Maria del Pilar, Alberto, Uriel and Esther (their three children) thank you all for making me feel the family warm while I was away from my family in

China. I love all you. Still miss the charcoal grilled lamb ribs made in Manuel's back yard, without any BBQ sauce, but only drops of juice squeezed from fresh lemon and a pinch of salt.

During my 3 years staying in Spain, one of the most memorable activities besides research, is to go with Manuel in a tour-program, schools and cultural centers all around Spain, called "Barraca de la Ciencia". This was an invention of Manuel. He drove out to the high schools all over the Spain, pulling a trailer packed with equipments for lectures with demos (with participation of the audience), projection of films and slide projections. In many cases, we had to drive through country side roads to small towns and villages far from cities. As an internationally well-known scientist and leading researcher of the field he was working, I believe his words had sew seeds of science in many hearts of high school students, and motivated young people to choose the research career.

To give lectures to elementary or high school students is not part of work of a normal university professor, and intense travel and lecturing stretched Manuel's already busy schedule. It's hard to image anyone can take the extra duty like this and insist for many years, without taking education as a mission of his life. I had some discussions with Manuel on why and how he invented this program. After a long talk starting from the word "Barraca" and through the history of science education all over the world, Manuel concluded in a cold way, "It's fun to travel and talk to children and young people". I have to say that, those trips with Manuel added a lot of fun to my life in Spain. I had chance to see not only big cities and tourist hot spots in Spain, but also a lot of small villages. I had chance to dine in village restaurants, and eat partridges with lead bullets in it. I had chance to taste all kinds of house wines from different restaurants. After about 3 years, I learnt more about Spain than many other foreign students who just spent time in school and big cities. I felt Spain was my second homeland.

Manuel always treated his students in a father like way. He cares about his students not only the courses taken, progress in research, but also the student's career and life beyond the period of study. During my study in Spain, Manuel sent me to visit many research labs and institutes in Europe to start collaboration. He also sent me to several international conferences to broaden my knowledge base, to meet other scientists and show up myself alone in self-defense. When preparing defending my thesis, Manuel organized an international jury committee, with scientists from many different countries, including Prof. Hao who chaired the Jury (Ph.D. granted in October 1988). After I finished my study in Spain, I returned home to meet wife, child and family. I prefer to skip saying how he managed using the old fashion telex communication with the Rector of HUST to get me again out of China in a quite difficult situation, as Manuel wanted me to do postdoc research at Stanford University, with Prof. John Ross, whom he knew for a long time. I was lucky to serve as a bridge between these two great scientists, as we published together several papers originating from work done while Manuel visiting Stanford and John visiting Madrid. After Stanford Manuel secured another postdoc period at Illinois Institute of Technology, with Professors Darsh Wasan and Alex Nikolov, who also were old acquaintances of him.

Manuel made his best efforts to pave a way for me to become an independent and critical mind and a qualified researcher in science. Although I eventually changed career to the industry, my education, especially the training as Ph.D. student in Spain, has helped me to deal with all possible tasks in my everyday's job. Three years spent in Spain is a portion of the best memory in my life.

Happy 70th birthday, Manuel.

My Scientific and Personal Relation with Manuel G. Velarde

E. del Rio

I knew Manuel through a call for potential Ph.D. students in 1987. A number of students applied for and fortunately I passed the selection process, then Manuel was my Ph.D. supervisor and I joined Manuel's group. We were several Ph.D. students and quite a number of postdocs and a number of visitors coming from all around the world. Since Manuel works in non-stop regime, the whole environment of Manuel stayed at a high energy state with no chance to fall into a low energy level. It was a extraordinary experience from scientific, cultural and personal points of view.

It is impossible to mention all people that I met in the IP-UCM, but Christo Christov (Uncle Christo for us) has a special place in my memory. Uncle Christo used a PC-486, at that time, the Intel most powerful central processing unit. Using Linux the suitably *tuned* 486 by Uncle Christo worked as fast as a Cray.

I worked on various aspects of the dynamics of the nonlinear (cubic) Helmholtz and (quadratic) Duffing oscillators subjected to external forcing. The former is the underlying dynamical system of the (soliton-bearing) Boussinesq-Korteweg-de Vries (B-KdV) equation. Manuel was interested in understanding all about it as he was searching for all possible aspects of the evolution of a liquid surface driven by external constraints. A liquid surface is like a membrane and hence a potential oscillator with asymmetry where the Helmholtz dynamical system unfolds in space-time. I was amazed by learning that he is recently using the same nonlinear models and concepts, we discussed together so long ago, in a new theory of electron transport in anharmonic crystal lattices in solid state physics.

Manuel introduced me to Nikolai Rulkov and one of problems we worked was the chaotic synchronisation problem. I made an analog circuit (analog computer) to test the theory. By the way, I still have the circuit in my lab. It might be interesting to check if the circuit still works. I remember when President Boris Yelsin was on a

E. del Rio (✉)
Departamento de Física Aplicada, ETSI Aeronáuticos, Universidad Politécnica de Madrid, Cardenal Cisneros 3, 28040 Madrid, Spain
e-mail: ezequiel.delrio@upm.es

R.G. Rubio et al. (eds.), *Without Bounds: A Scientific Canvas of Nonlinearity and Complex Dynamics*, Understanding Complex Systems,
DOI 10.1007/978-3-642-34070-3_6, © Springer-Verlag Berlin Heidelberg 2013

tank in Moscow and all of us were waiting for Nikolai to ask what was happening in Russia.

I recall Dr. Harmut Linde visiting the IP-UCM to show us experimental results on waves in liquid layers. Suddenly in the middle of the seminar presentation Manuel pointed out that the Linde waves were solitons like those he knew of the B-KdV wave equation mentioned above and we all were involved in a scientific discussion on solitons. I observed the discussion without understanding what they were talking about, because it was for me the first time that I heard the soliton word, but I understood that was a privilege for my to be there. This line of thought and the consideration of a liquid surface as a vibrating membrane led to the Ph.D. research later done by A. Wierschem. Eventually, I wrote papers with Manuel on dissipative solitons and dynamical ratchets. Recently, Manuel pushed me to investigate the connection between solitons and the gaits generator in insects and also the possibility to make a mechanical insect based on this idea, so I expected that my next paper with Manuel will be about a legged soliton!

I also remember Dr. Linde giving to Manuel a portion from the "Berlin wall" when it fell. Years ago nobody couldn't imagine what, two decades after the fall of the Berlin wall, the main task of the European democracies would be to obey the markets against of the dreams born when it fell.

It is impossible to forget Prof. Ilya Prigogine visiting the IP-UCM and his exciting lectures and scientific discussions.

Aspects of an anecdote show Manuel's character and the way he treated his Ph.D. students. Doing the research and getting the Ph.D. was not the problem save that he used to have with the candidate a private hearing, closed doors, with the Jury. It was something he had learned at ULB in Brussels where he got one of his Ph.Ds. The problem was that the respective duration of the presentation and the discussion were not fixed, a priori, and my hearing lasted some 3 h. I was awarded my Ph.D. in 1993. Since then we have collaborated for about a decade within an European Consortium SPARK on nonlinear dynamics for robots and we have published papers on subjects different from that of my Ph.D. work.

Besides the research activities, Manuel organized a number of Summer Schools first in Almería, later in Santander, and, more recently, at El Escorial. Manuel's schools were characterized by lectures given by high qualified speakers followed by long scientific discussions with students and speakers. Usually, the discussion ended just before the dinner time. Too much time and master classes for the actual Bologna framework!!

In spite of Manuel being 70 years old, he is a young pioneer in science and culture.

Manolo García Velarde: Three Relevant Traits of His Multifaceted Persona

F. Mayor-Zaragoza

1 Highly Unusual

He is infrequent in his ways, in his focus, in his opinions. He is the essence of non-linearity.

His appearance, mostly because his spiked hair, almost electric, is impressive. When looking at him, one may rapidly think that someone like him must do amazing things. For sure, complexity requires to be addressed by this kind of people.

From the physics of fluids, interfaces, and wetting dynamics, ... to science as a part of culture, to science as a tool for academic training, a tool for creative activities with children.

Like Federico García Lorca with his theatre "on his back" (and Manuel Bartolomé Cossío with his "misiones pedaggicas"), Manuel García Velarde traveled, with his science "on his back", across Spain.

Off the common tracks. He is highly unusual.

2 Excessive

Progress mainly consists of believing—and endeavoring—that the impossible today could become possible tomorrow. In 2011, Dilma Roussef, President of Brazil, said in her investiture speech that, "For our dreams to become true we must know how to overcome the frontier lines of what it is possible". Nothing is inexorable. The

F. Mayor-Zaragoza (✉)
Professor of Biochemistry (retired), Former Minister of Education and Science, Spain, and Former Director General UNESCO

President Foundation "Culture of Peace", c/ Velázquez 14, 3° dcha., 28001 Madrid, Spain
e-mail: fmayor@fund-culturadepaz.org; http://www.fund-culturadepaz.org

R.G. Rubio et al. (eds.), *Without Bounds: A Scientific Canvas of Nonlinearity and Complex Dynamics*, Understanding Complex Systems,
DOI 10.1007/978-3-642-34070-3_7,

creative ability that distinguishes every human being can, if capable of seeing the invisible, of making real the impossible. Whatever is coming next needs to be made. For that, we all have to work together and follow the guidelines of those whom, in the scientific context, have gone farthest. Reality needs to be deeply understood in order to be deeply transformed. Otherwise, changes may be just superficial, epidermic. Manolo García Velarde knows that one must flee from the spotlight of the media to be able to know the scenery as a whole. As stated by Bernard Lawn in 1985 when he received the Nobel Peace Prize, "Only to the extent in which we are capable of seeing the invisible, we are capable of doing the impossible". Only excess is historic, only excess allows, with a great deal of human tension, to create, to invent a future, to the nobleness of human dignity.

3 Perseverant

To all of the above, he sums up tenacity. Manuel García Velarde is not discouraged. He can sometimes, feel deceived. Nonetheless, he is never hopeless. He does come back once and again. In his seventees, he continues engaged projecting from the highest level of physics research, to reach the lay citizenry, to conquer the audiences of children. Let it be for many years to come.

Manuel Garca Velarde, unusual, excessive, perseverant, ... and much more.

Reminiscences from an Expatriate Scientist

C. Montes

The Workshop "A WEEK OF SCIENCE" celebrating the 70th birthday (September 7th, real; 14th, legal; 2011) of Prof. Manuel G. Velarde, was an outstanding meeting. For me, Carlos Montes, Directeur de Recherche au CNRS (emeritus since 2006), was the best opportunity to embrace my friend Manuel. I know him from the early seventeens because we have a strong common history. We are both Spanish physicists emigrating from our country in order to carry out research in physics. At the end of the sixteens this was not possible in Spain. Both fulfilled research in nonlinear physics and we meet together many times in international conferences and workshops devoted to this area. However our careers deviated in the sense that he choosed to return to Spain in order to develop the research from the bottom, which represented an immense task, and to become the leader in hydrodynamics and nonlinear physics, and I take the chance of developing the research in France as a fellow of the Centre National de la Recherche Scientifique, which remains for me the best research institution in the world. We only do work for the scientific community, like the artists, without thinking about material fallouts. This is a privilege and a singularity which compel us to an exemplary behaviour. Velarde's work on dissipative solitons, hydrodynamic instabilities and convection remains a reference for me in my field of plasma physics and nonlinear optics. I will not enumerate here all the research work done by Manuel but my purpose is to testify his honesty. He was the first Spanish physicist who invited me to lecture on kinetic theory in plasmas in the University Autonoma of Madrid in the Spring of 1976. I remained grateful to him and I can assert that besides considering him as one of the best Spanish physicists he is "un autentico caballero".

C. Montes (✉)
Laboratoire de Physique de la Matière Condensée, CNRS, Université de Nice - Sophia Antipolis, 06108 Nice Cedex 2, France
e-mail: carlos.montes@unice.fr

R.G. Rubio et al. (eds.), *Without Bounds: A Scientific Canvas of Nonlinearity and Complex Dynamics*, Understanding Complex Systems,
DOI 10.1007/978-3-642-34070-3_8, © Springer-Verlag Berlin Heidelberg 2013

An Extraordinary Year of My Life

A.Ye. Rednikov

Most of the time, life goes on at a regular pace. This does not mean that nothing interesting happens. It is just regular, normal happy daily life. But there are times when things accelerate and impressions overflow. The periods like this leave a deep impact on one's life. For me, the first year of my postdoc with Manuel, in 1992, at Instituto Pluridisciplinar (IP) of the Universidad Complutense of Madrid (UCM), was definitely one of such occasions. In a word, it was a shock, in a good sense of the word, both scientific and cultural. Well, why it was also cultural, it can be easily understood by imagining someone from Russia (then part of Soviet Union) at the heyday of her post-communist crisis suddenly finding himself in the splendid Madrid. The scientific part of the shock was no less strong. Here it is first of all my sudden and unavoidable exposure to a constant need to cope with new problems and ideas constantly discussed around, to communicate with an increasing number of scientists staying with Manuel either on a long-term basis or just coming as short-term visitors. For someone like me, who is generally predisposed to working quietly in his corner on his small problems, it was quite an enlightening challenge.

Manuel's team was rather diverse. It happened that quite a number of scientists coming from different countries started their stay with Manuel nearly at the same time as me, so that I was directly submerged into a remarkable ambience. For such diversity, we even used to be jokingly called a Zoo by the locals. Each one was a unique personality. The Spanish part of the team was, among other things, of an invaluable help in all aspects of the new life. Juan Luis Valero remained closely associated in my mind with the word "because", which he used in each second phrase and whose pronunciation he accentuated by lifting a finger. From this, I decided for myself that the Spanish people had a strong feeling for the cause and effect relationship. Angel Rodríguez Lozano was perceived by me as a true Spanish nobleman, hidalgo. Ezequiel del Río, constantly laughing and joking around, finally

A.Ye. Rednikov (✉)
Université Libre de Bruxelles, Brussels, Belgium
e-mail: aredniko@ulb.ac.be

R.G. Rubio et al. (eds.), *Without Bounds: A Scientific Canvas of Nonlinearity and Complex Dynamics*, Understanding Complex Systems,
DOI 10.1007/978-3-642-34070-3_9, © Springer-Verlag Berlin Heidelberg 2013

turned out to be quite a serious man with a continuing scientific career. At a later stage, we were joined by another colorful Spanish guy, Juan Antonio Mendez (simply Ivan Antonych between Russian speakers), the first experimentalist-in-chief of Manuel's new lab at the IP-UCM. I could not imagine my time in Madrid without Christo Christov, a person of multiple talents, not only scientific, always ready to lend a helping hand, which I often abused. "Uncle Christo knows", he used to repeat when asked a scientific question, which turned into "Uncle Christo helps everyone" when asked for computer help. I was deeply impressed by the personalities of George Khomenko, with his elitist but at the same time friendly style and perfect (at least to my ears) English, of whom I retained in the memory a fancy word "helicity", Xiao-Lin Chu, who used to speak with the calm confidence of a person sure of having made a great job, Will Zimmerman, with his Macintosh, symbolic software and viscous fingering, all new to me at the epoch, and the mysterious Julia Rees, with an awesome experience of Antarctic expeditions. Hartmut Linde was capable of endlessly discussing his extensive experimental results on waves and convective patterns. Each time we finally had the impression of more or less grasping what was going on and the discussion was turning to an end, he would be able to pull out of his vast archive yet another figure that mercilessly undermined our conclusions. At the epoch, I used to think of him, "Wow, what amazing working capacity and vivid interest in science at his age!" Now that I met him at the Week of Science (September 2011) in Madrid nearly 20 years later, I cannot help but state that he is still the same! Marcel Hennenberg was a classic from the beginning of my thesis. No, I had not known him personally before Madrid. It was just his papers on Marangoni instability of drops that I had had to read. My Moscow Ph.D. thesis supervisor Yuri S. Ryazantsev, who recommended me to Manuel, was also among us, and we were even closer than in Moscow. Yuri Sergueevich now taught me not only his rigorous approach to science, but also life, the latter sometimes together with his wife Petra, of whom I was always a little bit afraid perceiving her as too a strict lady. We often joked that it was Petra who was at the origin of the chain of events that brought me to Madrid. A "child of the war", as they use to call the children evacuated from Spain to the Soviet Union during the Spanish Civil War, she returned to Spain, already a M.D. in gynecology, in the beginning of the 1990s. At the top of this team was Manuel, who amazed me from the very beginning by his style and personality. His active and fruitful involvement in so many scientific subjects, insatiable interest in science, inexhaustible energy, multiple organizational activities (e.g. public physics lectures at the "Ateneo" of Madrid) were truly incredible, and nothing of this has changed since then.

We enjoyed close ties, both scientifically and administratively, with the group of Amable Lian at the nearby Aeronautics School of the Polytechnic University of Madrid (UPM). Paco Higuera from this group and Amable himself were always considered by me with reverence for their mastering of fluid dynamics, the reverence increasing even more after Amable once pointed out to me a mistake during a weekly seminar we used to have in common between the two groups.

Somewhat paradoxically, I had to come to Madrid with Manuel in order to make acquaintances of many scientists from my own country and even from my native city

of Nizhny Novgorod. I studied in Moscow and had little scientific contacts at home. In Madrid, I met representatives of the famous Nizhny Novgorod scientific school in the field of nonlinear dynamics, Nikolai F. Rulkov, Mikhail I. Rabinovich and Vladimir I. Nekorkin, the latter becoming a close friend. I also met representatives of a no less famous Perm scientific school in the field of hydrodynamic instability, Gregory Z. Gershuni, Vladimir A. Briskman and Rudolf V. Birikh. The latter two used to come on short visits and seemed to me as brothers, even though they were not. I knew the famous Birikh solution from my student years and in Madrid I got an occasion to meet the classic himself. Alex A. Nepomnyashchy, also originally from Perm but by then already from Haifa in Israel, impressed me right away by his profound knowledge and by an all-on-blackboard lecture-seminar on the derivation of a long wave equation for Marangoni–Bénard convection. I also had occasions to meet high-ranking Russian Academicians, to whom in Moscow I would not be allowed even at a gunshot distance, but there at the IP-UCM in Madrid, I found them surprisingly accessible. In particular, I was delighted to meet academician Belotserkovsky, the Rector of the Moscow Phystech (the MIT equivalent in Russia) at the time I started my studies there. Also the late Alex. G. Golovin younger than me at Phystech and another of Yuri's former students was one of the visitors at IP-UCM then coming from the Technion in Haifa.

We lived as a really close community, sharing lunches, seminars, frequent discussions at the blackboard (a sacred tradition with Manuel, however busy he might be), spending a lot of our leisure time together, visiting each other at home, going to workshops and summer schools organized by Manuel, of which a summer school in Almería, the native land of Manuel, was truly unforgettable. It was intense as never again. On top of that, with Hartmut, Xiao-Lin and George (later, Marcel), we were renting together a mansion in Pozuelo de Alarcon, quite near Manuel's home, in the suburbs of Madrid, where discussions about waves and solitons often recommenced with a new enthusiasm during the evenings we spent in the chimney corner. Frankly speaking, I did not understand too much in the beginning, which was quite an incentive to learn and later to contribute to these subjects. We were often invited to Manuel's house. Once we even had a weekend seminar over there in Manuel's home office by a Japanese visitor who happened to be in Madrid just for a few days. I remember his spacious loft office, where not so much space was actually available due to tons of books lying about everywhere on the floor. After the seminar, we were served lunch by Manuel's charming wife María del Pilar.

So was my first year with Manuel. Later, I was lucky enough to enjoy a few more years in Madrid, but it became more like a regular life, while the first year remained in my memory as especially extraordinary. Papers on self propulsion of drops, Marangoni-driven instabilities, nonlinear waves, … came from tough, deep, detailed, infinitely long blackboard's discussions with him and Yuri Sergueevich, and after on joined by Pierre Colinet and Vadim N. Kurdyumov, another former student of Yuri.

Reminiscence of My Time in Manuel's Group at the Instituto Pluridisciplinar

A. Wierschem

I joined Manuel's group at the Instituto Pluridisciplinar (IP) in April 1994. The year before, Manuel had been one of its cofounders at Universidad Complutense de Madrid (UCM). Although up to then I had not worked in fluid dynamics, he accepted me under the condition to build up a lab from scratch to carry out experiments on convection. I agreed enthusiastically, yet not every Ph.D. student has the opportunity to carry out his research in a new lab—and on top of this, a lab one has a lot of freedom to design.

Once arrived at the Instituto Pluridisciplinar, I soon realized what a tremendously vivid and international group Manuel headed. In addition to Ph.D. students and postdocs there were numerous visitors from different parts of the world, engaged in diverse subjects. Some stayed for a few days, some for several months—and many came back regularly. Many of the visitors that were at that time young researchers are now established scientists, others were at that time already well established and well known—and here they presented their new studies and one could discuss with them! For me as a young Ph.D. student this was great! I remember pretty well the inspiring and lively discussions. There were tough arguments, and tremendous (or better terrific!) blackboard discussions on the scientific topics that at the same time were always full of respect for the person. Here science counted and arguments, not personal belief or the like.

So this is where I started to learn about fluid mechanics, convection, nonlinear dynamics and many analytical and experimental methods. But one could also pick up things about lasers, neurons, making maps, ... It was an invaluable experience to see the wealth of ideas and the crosslinks between the diverse subjects that Manuel and all the others in his group elaborated. But Manuel was not only a very dedicated scientist and teacher; he also created a lot of opportunities. As a student of his, one

A. Wierschem (✉)
Institute of Fluid Mechanics, Friedrich-Alexander University Erlangen-Nuremberg, Cauerstrasse 4, 91058 Erlangen, Germany
e-mail: andreas.wierschem@lstm.uni-erlangen.de

R.G. Rubio et al. (eds.), *Without Bounds: A Scientific Canvas of Nonlinearity and Complex Dynamics*, Understanding Complex Systems,
DOI 10.1007/978-3-642-34070-3_10,

could participate in summer schools he organized, visit laboratories of collaborators and friends of him all around Europe, to learn also from their expertise.

In this vibrant environment that Manuel created and pushed forward, there was also a close link between experiment and theory. It helped me a lot to better understand what I observed in my system. Due to the quick feedback between the two lines of action, experiments could be designed to check new theoretical predictions. Most remarkable was Manuel's prejudicial approach, deep insight, by suggesting what he thought was to be seen in experiments. On the other hand, the experimental observation helped him in what to take into account and what to focus on.

Another anecdote yet vital for my academic career was the following. I went to Madrid with a fellowship of the Daimler-Benz Foundation. At Manuel's suggestion, I registered in one of the Ph.D. programs of UCM. Due to unexpected (or may be not so) I had to withdraw from it. When he knew about the problem, he phoned his friend Prof. W. Ebeling at Humboldt University in Berlin and in a matter of days I was registered in their Ph.D. program, and there I got my doctoral degree in October 1977.

When I was asked to participate in the week of science in Madrid to celebrate Manuel's 70th birthday, I did not hesitate an instant. I was delighted to meet again him and so many other persons again, to which I owe so many things. Now, if you ask me, how did my stay in Manuel's group affect my professional life, I may answer: "Well, quite much. I learned a lot from him and deeply enjoyed the fruitful interaction in a stimulating environment. Besides, Manuel introduced me to fluid dynamics, something I still deal with almost 20 years later".

My Year with Manuel

W. Zimmerman

It really started 20 months earlier, when Manuel gave a seminar to the Homsy research group at Stanford University. Manuel captivated me with his description of the "solitary" wave and the new nonlinear wave equation he was deriving in active media. He came to my seminar not long after, where I was declaring my intention to finish my doctorate soon. I considered myself a new breed of fluid dynamicist—a computational modeller. Manuel could see the utility of our collaboration, so he invited me to Madrid. I had not yet made plans for my career nor life after the submission of that life changing document—the doctoral thesis—so I agreed to go if we could secure funding. Thus I applied to NATO for a fellowship, which had to be held in a NATO member state. When I learned it was successful, I accelerated my analysis and writing of the thesis so as to start the fellowship within the window of opportunity.

Academic colleagues and friends tried to talk me out of going, for two sensible reasons. First, Silicon Valley was nirvana for my type—geeks. I had the best computing facilities in the world on my doorstep, and access to clever people through my networking. Second, I was not a traditional fluid dynamicist—a theorist—so how would I cope without top notch computers and with the expectation of contributing on theory? I was really very worried about this, so I bought every book on fluid dynamics theory in the Stanford Bookstore, while hatching a plot. I did not have to accept the fellowship. I could always decline if I found it too difficult dealing with the cultural differences and the lack of facilities for my expertise. I would also take my trusting Macintosh desktop with me, which I could programme at low level and had a very useful range of software I had acquired over the years for analysis. So I decided to visit Madrid as a tourist, without telling Prof. Velarde, and see if

W. Zimmerman (✉)
Professor of Biochemical Dynamical Systems, University of Sheffield,
17 Mappin Street, Sheffield S1 4DT, UK
e-mail: w.zimmerman@sheffield.ac.uk

R.G. Rubio et al. (eds.), *Without Bounds: A Scientific Canvas of Nonlinearity and Complex Dynamics*, Understanding Complex Systems,
DOI 10.1007/978-3-642-34070-3_11, © Springer-Verlag Berlin Heidelberg 2013

I could make the necessary arrangements for living. I had travelled in Europe as a student, so surely would be able to brave Spain alone, wouldn't I?

When I arrived at the Madrid airport, I found that my usual strategy of reporting to the Youth Hostel was completely insufficient. No vacancies at either site, so I started calling the list of cheap hotels recommended by the Hostel. No luck. Everything was full, even though it was early afternoon. So I had a problem. Who did I know in Madrid? Only Prof. Velarde, but I was completely unexpected. So I had to call him. He was surprised that I turned up without warning, but very helpful. He arranged a room for me at the Residencia of the Research Council (CSIC) for that night, and gave me the contact of his travel agent who then booked me a hotel for the week. His research group then hunted around among their contacts for a vacancy for a room among friends, and showed no end of hospitality. I did not have the heart to tell anyone that I, a kid from the "sticks", was anxious about staying in a foreign country, language and culture, so was not really committed to staying the course. I was overwhelmed by kindness. Manuel invited me to his house some evenings and weekends, and did not mind that I stayed for hours playing their piano. María del Pilar was always concerned for my well-being, and tried to include me in her circle. The group and my flatmates kept including me in social events and outings, which built that feeling of belonging.

Of course it was a seminal year for my outlook and philosophy as a researcher as well. The ensemble cast of visitors that Prof. Velarde assembled was fascinating. He had co-founded a new institute (Instituto Pluridisciplinar) at Universidad Complutense de Madrid (UCM) which included visiting researchers, typically on sabbatical, with global reach and excellent track records in their fields, but of course overlapping with his interests, yet that was hardly any limitation. The size and the scope of experts assembled was simply breath-taking. Fortunately for me, I had a skill, practically born with it, which put me at the center of the team at a vantage to overlook this breadth of ideas and explosion of creativity—I was a native English speaker, and modestly a good writer. So practically every manuscript for publication produced in the team that year was passed by me to check the English. I read them carefully for grammar and spelling, but also content. I did background reading with my trove of books and acquired relevant journal articles to understand these manuscripts. I was proud when I caught a conceptual error. I preened when I noticed a whole page was missing from a manuscript.

But I learned, from this experience, and from observing Prof. Velarde's *modus operandi*, probably the single most important formative lesson for my research career. Every researcher has to build their own philosophy of how to research, but also what to research. I was under the misapprehension that research is what the community of researchers do, so one simply picked a spot that seemed unworked on, and pushed it along. Yet, Prof. Velarde had a completely different approach. He would have a new idea (at least daily), discuss it with the great minds about him, and see who would pick up on it. And the idea was not a simple advance on what was done previously. It would draw connections that had never been made before, and try to leap to a new paradigm for what should be done. I am certain that he invented his recent groundbreaking concept of the "solectron" is this style.

So I had learned what was a viable topic for research—anything you like, as long as you can dream up why your new concept could be a paradigm shift, and as long as you can resource the project by convincing someone else to push along the first few steps with you. Since then, I have never seen the point of incremental research. The idea may brash, it may be wholly wrong, but it has to be new and have a plausible story. After that, perhaps you cook it yourself, your perhaps you convince a colleague, research associate or student to take up the baton for awhile. You create a project by assembling the resources and thinking through what experimental plan or theoretical/computational developments are necessary to add support and grow momentum. But it starts with your own enthusiasm for the idea. I have started literally hundreds of projects since. Manuel had shown me how to be bold. My previous training had taught me how to be a careful researcher, but not what to research. Manuel demonstrated that you follow your inner muse, wherever it leads. As long as you conduct the research carefully, and choose targets that matter if your research idea pans out, then there really are only limits of the imagination.

Of course the wider team that Manuel assembled was terrific too. I will be forever indebted to the late Christo Christov and George Khomenko for their collaboration, and brilliant ideas, which we continued to develop for the rest of their lives. Manuel, unwittingly, introduced me to my wife-to-be, which has had the most profound effect of all. Indeed, Julia Rees had been invited by Manuel to lecture on her fascinating work on the atmospheric boundary layer at Antarctica. Yet, my most compelling engineering science advances I owe to my year with Manuel, and his subsequent nurturing of my understanding of nonlinear waves that Manuel fostered over the next several years with return invitations to Madrid and several summer schools which were like family reunions. Eventually, the pressures of my family life made it difficult to keep up our meetings, and my research took a profoundly practical and now commercial bent, but with nonlinear waves at the core of my biggest achievements so far.

Without going into details, my first two patents (and three and four, which are confidential at the moment), exploit nonlinear wave dynamics in an essential fashion. As Manuel encouraged and collaborated with my exploration of the theory of nonlinear wave dynamics in fluid systems, with the derivation of new propagation equations and computational/theoretical solutions, I started imagining how nonlinear wave phenomena could be exploited in the chemical and process industries. I took up the study of fluidics so that I could design and engineer oscillating systems easily, and then use them as components in more complicated physicochemical systems.

I had noticed that the sector was very conservative, and most conventional systems were designed to work at steady state. But a steady state could be viewed as performance that is limited by two (or more) generalized opposing forces being held in balance. One such force might lead to a beneficial outcome, but the opposing force constrained the benefit or provided a countervailing disadvantage. But oscillations change that balance—perhaps re-establishing it with an order of magnitude better performance. Or perhaps making it worse, but that would depend on the parameters controlling the oscillation: frequency, amplitude, and

sometimes phase. I have made a series of discoveries exploiting nonlinear fluidic oscillations inducing beneficial change. The headline invention was energy efficient microbubbles (which won the 2009 IChemE Moulton Medal and the 2010 Royal Society Innovation award), but I imagine my second invention of low power plasma microreactors will make an even bigger impact. All because Manuel instilled the desire to understand the theory of nonlinear waves more deeply, and the engineer in me seeking to answer the question of "what good is that?" I am not sure that I would have had courage enough to try, if I had not seen Manuel's example of what boldness could achieve.

Our Adventure with Manuel

W. Zimmerman

The European Geophysical Society Annual Congress was held in Edinburgh in April 1992. It was my first international conference as a "grown up" researcher—a post-doc. As Manuel was planning on attending, he suggested that we take a contingent from the nascent Instituto Pluridisciplinar. His support letter was essential to the conference waiving my fee as a young academic to present a paper on our joint work—a mathematical analysis of dissipative solitary waves in situations that occur in oceans and atmospheres.

The solitary wave has received substantial attention since first noticed by John Scott Russell in 1834 when he reported sighting the phenomenon while walking along the Grand Union Canal outside Edinburgh. I am aware that Manuel has organized symposia to celebrate the widespread of its applicability in science and engineering as a paradigm for nonlinear wave propagation, is a regular public speaker on its importance and history, as well as deep expert in the underpinning concepts, which has influenced his creation of the "Solectron" theory.

Since we had a free afternoon in the conference, Manuel proposed that he, Julia Rees (a British applied mathematician on sabbatical in Madrid, whom Manuel introduced me to, and later became my wife) and I take an excursion to the Grand Union Canal to pay homage to the site, as well as to hunt up a memorial to it that he heard existed. So we looked on as Manuel went to the conference information desk, and enquired of two undergraduate students manning it, whether they could direct him to the site on the Grand Union Canal where John Scott Russell first discovered the solitary wave (in 1834). They did not know, but helpfully told us of a nice restaurant on near the canal which was in the conference information pack, and where to pick up a taxi.

W. Zimmerman (✉)
Professor of Biochemical Dynamical Systems, University of Sheffield, 17 Mappin Street, Sheffield S1 4DT, UK
e-mail: w.zimmerman@sheffield.ac.uk

R.G. Rubio et al. (eds.), *Without Bounds: A Scientific Canvas of Nonlinearity and Complex Dynamics*, Understanding Complex Systems,
DOI 10.1007/978-3-642-34070-3_12, © Springer-Verlag Berlin Heidelberg 2013

Fig. 1 Manuel posing along the Grand Union Canal in April 1992. The photo has been blown up into a poster and occupies a prominent spot in my office in the Kroto Research Institute

When we entered the taxi, Manuel asked the driver, could take us to the site on the Grand Union Canal where John Scott Russell first discovered the solitary wave? When he looked puzzled, I said that we knew of a restaurant near there, and he recognized that, so the taxi duly delivered us to the restaurant. After having a nice lunch, when the waiter came to take orders for afters/coffees, Manuel asked him, a young lad, whether he could direct us to the site on the Grand Union Canal where John Scott Russell first discovered the solitary wave. Amazingly, the waiter said that as a youngster, he used to play along the canal, and he knew precisely where the dedication plaque was, but that was the only memorial he knew of. Furthermore, he was just getting off work, so he was delighted as a Scotsman to host our international contingent to see it.

So we traipsed along the canal, and eventually crossing stiles, over a pedestrian overpass, and then down a ladder below the overpass to find a small, gold coloured plate embedded in the stone wall of the canal (see Fig. 1). Fortunately, I had my camera along for the excursion and recorded Manuel posing next to the memorial plaque. The photo was blown up into a poster by my parents, and occupies a prominent spot in my office in the Kroto Research Institute. I tell this tale to new research students as a parable for how a scientist pursues his objectives. Quite what we hope to find may be blurred in intention, questioned by others as offbeat and unlikely to yield any progress. Nevertheless, the chase itself was enjoyable (it was a nice lunch and excellent scenery), the going may be rough and you might wonder whether the effort is all worth it, and sometimes all you get out of actually achieving your goal is the equivalent of a footnote. But you pursue it with dogged determination, as the "game is worth the candle." Sometimes you do uncover nuggets of gold.

I do have to be careful who I tell this story to, as there is no intent to belittle the plaque, but it really is quite insignificant in size as a memorial, and only the natives know where it is. Nevertheless, it is important to some people. I told this story to Norman Zabusky when I visited Rutgers in June of 1992, and I am afraid he did not find it humorous at all. It seems he was there for the dedication of the plaque as the guest of honor, so why shouldn't people be making pilgrimages to see it?

As I write this, a research student of Julia's, co-supervised by me, is defending her doctorate on some experimental work on solitary waves in a micro device I designed, as well as some nonlinear wave analysis and inverse methods, which may someday lead to the device being utilized in process monitoring/control systems. Who is to say that our "little" excursion along the Grand Union Canal is not still bearing fruit?

Part II
Scientific Contributions: Flows, Instabilities and Convective Patterns

A Peculiar Observation Arising from the Stokes Approximation in Certain Closed Flows

W. Guo, R. Narayanan, and G. Labrosse

1 The Stokes Eigen Problem

The Stokes approximation is one which is applied in the creeping flow limit to a number of fluid mechanics problems (cf. for example, Shankar and Deshpande [1], Pan and Acrivos [2], Duda and Vrentas [3], Subramaniam and Balasubramaniam [4] etc.) and can often give satisfactory explanations for a number of phenomena. For example, the prediction of Moffatt eddies in a two dimensional driven cavity, the prediction of branching behavior in nonlinear Rayleigh–Bénard convection when the inertial terms are dropped as in the large Prandtl number limit and the migration of drops in a microgravity environment due to thermocapillary forces are all examples of where the Stokes approximation in closed flows gives a good prediction of qualitative behavior.

However in making the Stokes approximation, there are instances in which spurious phenomena arise. The objective of this very brief communication is to give one such example.

Consider a rectangular 3-D cavity with all walls, save one which moves at a constant low speed, to be stress free. After a steady flow is established let the moving wall be suddenly replaced by a stress free boundary too; all boundaries then become stress free. Now the fluid in the container continues to flow though it dies down exponentially in time on account of its kinematic viscosity. This surely comes as no surprise, and can be particularly seen if we assume that the entire flow regime

W. Guo · R. Narayanan (✉)
Dept. Chemical Engineering, University of Florida, Gainesville, FL 32611, USA

Université Paris 11, Orsay Cedex 91403, France
e-mail: ranga@ufl.edu

G. Labrosse
Université Paris 11, Orsay Cedex 91403, France
e-mail: labrossenator@gmail.com

R.G. Rubio et al. (eds.), *Without Bounds: A Scientific Canvas of Nonlinearity and Complex Dynamics*, Understanding Complex Systems,
DOI 10.1007/978-3-642-34070-3_13,

could be computed from the modeling equations using only the Stokes equations. However what might be surprising is that the companion pressure field instantly becomes a constant in time everywhere in the flow field. In other words the flow dissipates in time but the pressure field equilibrates instantly to its average value regardless of the size of the container.

The problem can be traced algebraically to the fact that the Laplacian of the pressure field is zero in this creeping flow limit while the normal gradient of the pressure is zero on the entire boundary, it being vorticity-free, yielding a constant value for the pressure field everywhere. In physical terms there are really two reasons for this anomalous behavior and both act together. The first is that a recirculating flow must mean that the fluid has to come to a stop as it makes a turn and this conjures an image of local acceleration or deceleration whether or not the flow is steady. But the Stokes model does not accommodate any local inertial acceleration or deceleration that would ordinarily arise from the term, for it only allows a time dependent acceleration. Now if the inertial terms were included it would cause the pressure field to decay in a manner similar to the velocity field whether or not there is a source of pressure from the boundary. In other words, in order to get the pressure field to decay when the flow field in an incompressible fluid decays, either the inertial terms need to be included or the boundary must have a source of pressure as in the case of a non-vanishing vorticity boundary condition or both must occur. In our example neither is the inertial term included nor is there a source of pressure. Another reason for the strange behavior when the driving wall is replaced by a constant stress wall is that the flow is assumed to be incompressible and all pressure signals must travel at unbounded speed thus leading to a situation where the pressure field equilibrates instantly and becomes a constant no matter how far the flow field is from the erstwhile moving wall. However if the flow were assumed to be compressible with the Stokes approximation, the pressure field would not instantly become a constant.

Now the above example is given in a rectangular cavity and it follows without much thought that in every case, where the normal component of the pressure gradient on the surface is zero, the pressure field must instantly become a constant. However it does not follow that the zero vorticity wall condition leads to the vanishing of the normal gradient of pressure in any three-dimensional container of arbitrary shape.

2 Some Computations and Inferences

To give the reader a graphical idea of the flows and pressure fields we have performed some computations, solving the Stokes problem with a consistent Spectral Stokes solver [5]. The steady flow in a driven 2-D rectangular cavity is computed where the upper wall is in motion with a speed $(1 - x^2)^2$. Note that this boundary condition pertains to the regularization of the boundary in such a manner

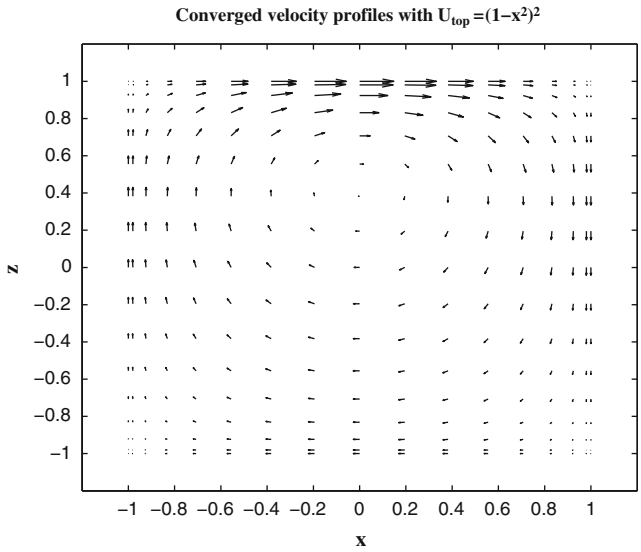

Fig. 1 Converged velocity profiles for $U_{top} = (1 - x^2)^2$

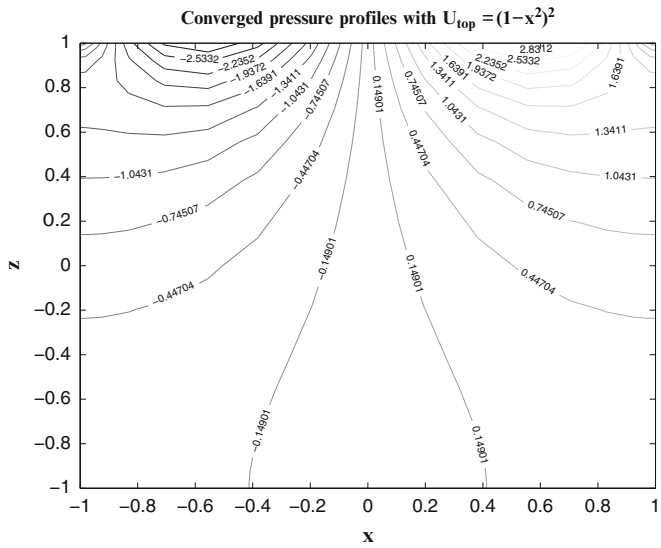

Fig. 2 Converged pressure profiles for $U_{top} = (1 - x^2)^2$

that there is no singularity in the no-slip condition at both corners. More on the regularization condition can be seen in [6] and [7].

Having computed the steady profile (see Figs. 1 and 2) the moving wall is then assumed to be suddenly replaced by a half-speed wall. All other walls are assumed

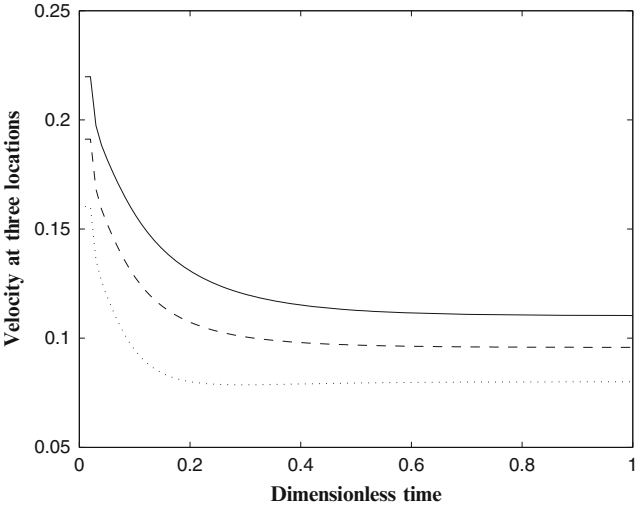

Fig. 3 Norm of the velocity vs. dimensionless time where the moving upper wall speed is suddenly reduced to $U_{top} = \frac{(1-x^2)^2}{2}$. The three curves represent the change in velocity with dimensionless time at three different horizontal locations in the middle z plane

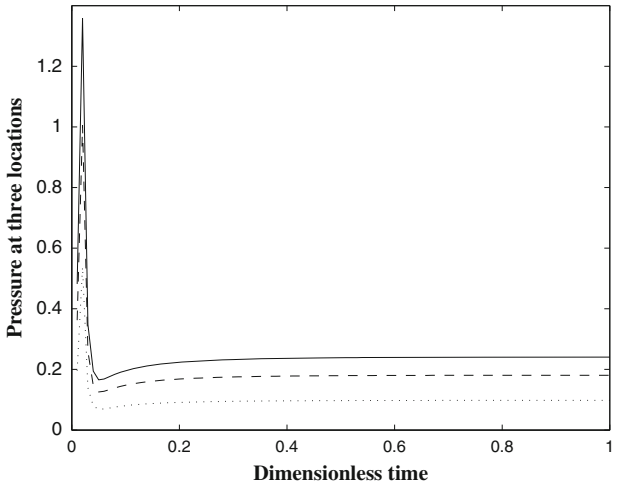

Fig. 4 Pressure vs. dimensionless time where the moving upper wall speed is suddenly reduced to $U_{top} = \frac{(1-x^2)^2}{2}$. The three curves represent the change in pressure with dimensionless time at three different horizontal locations in the middle z plane

to have their tangential components free of vorticity. By computing the norm of the velocity in the mid plane at various transverse positions we can see in Fig. 3 the decay in velocity in scaled time. The corresponding pressure field (Fig. 4) acts likewise.

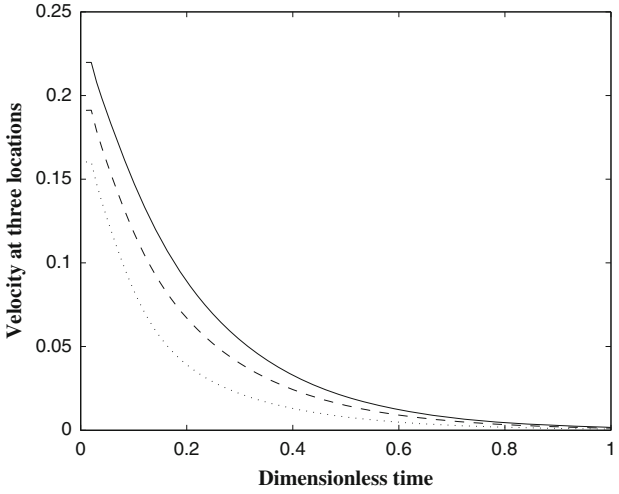

Fig. 5 Norm of the velocity vs. dimensionless time where the moving upper wall is suddenly replaced by a stress free wall. The three curves represent the velocity change with dimensionless time at three different horizontal locations in the middle z plane

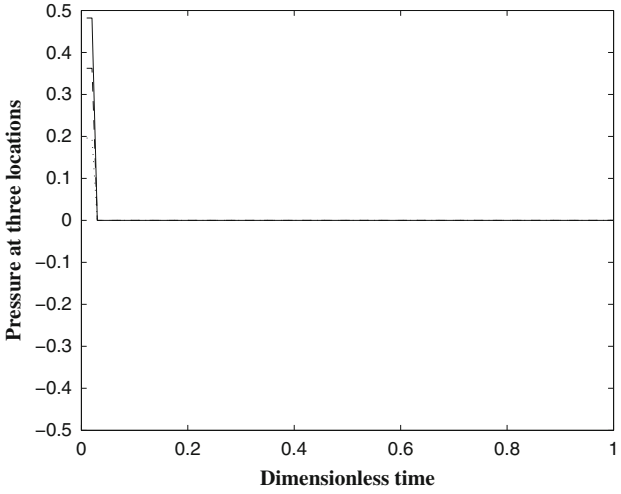

Fig. 6 Pressure vs. dimensionless time where the moving upper wall is suddenly replaced by a stress free wall. The three curves represent the pressure change with dimensionless time at three different horizontal locations in the middle z plane

A second case is considered when the moving wall is replaced by a constant vorticity boundary but something different is seen here. While the velocity at the mid plane still decays exponentially (Fig. 5) the pressure field approaches a constant value almost instantly in time (Fig. 6) with any deviation arising from numerical approximations. The calculations were compared with a series solution.

It may be noted that the vorticity-free boundary conditions are certainly not realizable in an experiment but many classical problems routinely assume these conditions to understand physical phenomena. One example is the Bénard problem [8]. While the proof that leads to the peculiarity discussed in this short note is trivial, the observation is nonetheless curious as the problem is mathematically well-posed. This does not mean that the Stokes approximation ought to be discarded for it is, as noted earlier, useful in studying a number of problems. But it certainly means that it comes with its baggage.

Acknowledgement We acknowledge, with gratitude, support from NSF 0968313.

References

1. Shankar, P.N., Deshpande, M.D.: Fluid mechanics in the driven cavity. Annu. Rev. Fluid. **32**, 93–136 (2000)
2. Pan, F., Acrivos, A.: Steady flows in rectangular cavities. J. Fluid Mech. **28**, 643–655 (1967)
3. Duda, J.L., Vrentas, J.S.: Steady flow in the region of closed streamlines in a cylindrical cavity. J. Fluid Mech. **45**, 247–260 (1971)
4. Subramaniam, R.S., Balasubramaniam, R.: The Motion of Bubbles and Drops in Reduced Gravity. Cambridge University Press, Cambrigde (2001)
5. Leriche, E., Labrosse, G.: Higher-order direct stokes solvers with or without temporal splitting: numerical investigations of their comparative properties. SIAM J. Sci. Comput. **22**, 1386–1410 (2000)
6. Shen, J.: Hopf bifurcation of the unsteady regularized driven cavity flow. J. Comput. Phys. **95**, 228–245 (1991)
7. Chénier, E., Delcarte, C., Kasperski, G., Labrosse, G.: Sensitivity of the liquid bridge hydrodynamics to local capillary contributions. Phys. Fluids **14**(9), 3109–3117 (2002)
8. Chandrasekhar, S.: Hydrodynamic and Hydromagnetic Stability. Clarendon, Oxford (1961)

Influence of Periodic and Quasi-periodic Gravitational Modulation on Convective Instability of Reaction Fronts in Porous Media

K. Allali and M. Belhaq

1 Introduction

Various kinds of instabilities that can influence the propagation of reaction fronts can be encountered in several physical problems, including the thermo-diffusional instability, the hydrodynamical instability as well as the convective instability. For instance, the thermo-diffusional instability appears as a result of competition between the heat production in the reaction zone and heat transfer to the cold reactants. To investigate this type of instability, the density of the medium can be taken as constant to remove the influence of hydrodynamics and to simplify the model. The stability conditions in this case were studied in [1–5]. In hydrodynamic instability of reaction fronts, the density of the medium is variable and usually considered as a given function of the temperature. In this case, the instability is caused by heat expansion of the gas or liquid in a neighborhood of the reaction zone [6–10]. Due to the fact that instabilities of reaction fronts are undesirable phenomena, several works have been devoted to studying the effect of a periodic vibration on the convective instability of these reaction fronts. For instance, it was shown that high-frequency vibrations can influence stability of various convective flows, namely periodic modulations can have a stabilizing effect for low frequencies and a destabilizing effect for high ones [11].

It is worth noticing that the case of reaction fronts with liquid reactant and solid product was considered in [12], while the case where the reactant and the product are liquids was analyzed in [13, 14]. It was concluded in these cases that a periodic

K. Allali
Department of Mathematics, University Hassan II-Mohammedia, P.O. Box 146, FST-Mohammadia, Morocco

M. Belhaq (✉)
Department of Mechanics, University Hassan II-Casablanca, P.O. Box 5366, Maârif, Casablanca, Morocco
e-mail: mbelhaq@yahoo.fr

R.G. Rubio et al. (eds.), *Without Bounds: A Scientific Canvas of Nonlinearity and Complex Dynamics*, Understanding Complex Systems,
DOI 10.1007/978-3-642-34070-3_14, © Springer-Verlag Berlin Heidelberg 2013

vibration can affect the onset of convection. Specifically, it was indicated that the case where the polymerization front in liquids is different from the case when the polymer is solid. The difference is that in liquids, the convective instability may exist also in descending fronts [15].

The case of reaction fronts in porous media has also been tackled and the influence of periodic vibration on convective instability has been investigated. The linear stability analysis and direct numerical simulations were performed and the effect of vibration on the onset of convection was examined. In addition, in the case of a porous medium saturated by a fluid, the effect of vertical vibrations on thermal stability of a conductive solution was examined in [16]; for other directions of vibration, depending on the vibrational parameter and the angle of vibration, stabilizing and destabilizing effects were discussed [17].

Mechanical and thermal vibrations have also been studied in connection with the Rayleigh–Bénard convection [18, 19], directional solidification [20, 21], and doubly diffusive convection [22]. In spite of numerous results on the influence of vibrations on convective instability, some questions still remain open. In particular, normal vibrations cannot stabilize the conductive state in an unbounded domain [23], while tangential vibration is only effective for vibration frequencies that are not too large [24].

It is worth noticing that the problem of convective instability under the influence of periodic gravity or periodic heating of a liquid layer or the effect of periodic magnetic field on magnetic liquid layer has been widely analyzed during the last decades; see for instance [18, 25–34] and references therein.

While the influence of a periodic modulation on the convective instability was extensively studied in various physical problems and using different types of modulation, only few works have been devoted to study the effect of a quasi-periodic (QP) vibration on such a convective instability. To the best of our knowledge, Boulal et al. [35] were the first who investigated the effect of a QP gravitational modulation with two incommensurate frequencies on convective instability from analytical view point. They considered the problem of stability of a heated fluid layer. The threshold of convective instability was determined in the case of heating from below or from above, and it was shown that the frequencies ratio of QP vibration strongly affects the convective instability threshold. Motivated by the successful treatment in studying QP convective instability in the later problem, similar studies were performed. The influence of QP gravitational modulation on convective instability in Hele-Shaw cell was examined in [36], and its influence on thermal instability in a horizontal Newtonian magnetic liquid layer with non-magnetic rigid boundaries (in the presence of a vertical magnetic field) was analyzed in [37]. It was shown that in the case of a heating from below, a QP modulation produces a stabilizing or a destabilizing effect depending on the frequencies ratio.

In these works [35–37], the original QP partial differential equations modeling the problem are reduced to a QP Mathieu equation using Galerkin method truncated to the first order. Due to the fact that the Floquet theory cannot be applied in the QP forcing case, the approach used to obtain the marginal stability curves was based on the application of the harmonic balance method and Hill's determinants [38, 39].

Recently, the effect of QP gravitational modulation on convective instability of reaction fronts in porous media was studied in [40]. The QP modulation has been chosen as a sum of two modulations having two incommensurate frequencies. It was concluded that in a certain regions corresponding to small values of the amplitude vibration, a stabilizing effect can be achieved, whereas large amplitudes of vibration induce a destabilizing effect. The results also shown that for a given value of the critical Rayleigh number and for large frequencies, the front can undergo abrupt change of stability by varying the amplitude of vibration.

The aim of this chapter is to give an overview on the effect of different gravitational modulations on the convective instability of reaction front. We first consider the case where the amplitude of the periodic vibration is modulated. In this situation, two cases are considered. In the first case, the frequency of the modulation is assumed to be twice the frequency of the vibration itself, while in the second case, the frequency of the modulation is supposed to be half that of the vibration. In a second case, we discuss the effect of QP gravitational modulation on the convective instability of reaction front. These studies are motivated by applications arising in some physical problems, as for instance, frontal polymerization [41] or problem related to environmental pollution [42]. The QP vibration may eventually result from a simultaneous existence of a basic vibration applied to the system with a frequency ν_1 and of an additional residual vibration having a frequency ν_2, such that ν_1 and ν_2 are incommensurate. Indeed, this residual vibration may come from various sources as machinery, friction or just a modulation phenomenon leading to the modulation of the amplitude of the basic vibration.

It what follows we consider a periodic vibration and QP one with two incommensurate frequencies in the vertical direction upon the system containing a reaction reactant and a reaction product. This excitation causes the acceleration, b, perpendicular to the reactant–product interface. In order to investigate the influence of different vibration (periodic, QP and with modulation of amplitude), we consider the time dependence of the instantaneous acceleration acting on the fluids given by $g + b(t)$, where g is the gravity acceleration and $b(t)$ can be a periodic, modulated periodic or QP force. In other words, wa shall consider the following three cases: $b(t) = \lambda sin(\nu t)$, $b(t) = \lambda_1 sin(\nu_1 t) + \lambda_2 sin(\nu_2 t)$ and $b(t) = \lambda cos(\nu_2 t) sin(\nu_1 t)$ where $\lambda, \lambda_1, \lambda_2$ and ν, ν_1, ν_2 are respectively, the amplitudes and the frequencies of the considered vibration. Here, we consider reaction fronts in a porous medium with the fluid motion described by the Darcy law and the Boussinesq approximation, which takes into account the temperature dependence of the density only in the volumetric forces.

It is worthy to notice that the problem of reducing the original Navier–Stokes equations to a standard QP Mathieu equation using Galerkin method, harmonic balance method and Hill's determinants [35–37] cannot be exploited here due to the coupling of the concentration and the heat equations (reaction-diffusion problem coupled with the Darcy equation). Therefore, to obtain the convective stability boundary, we first reduce the original reaction-diffusion problem to a singular perturbation one using the so-called matched asymptotic expansion (see Appendix),

we perform a linear stability analysis, and then solve the reduced interface problem using numerical simulations.

This chapter is organized as follow. Section 2 is devoted to state the problems and to perform the linear stability analysis. In Sect. 3, we analyze the influence of different gravitational modulation on the convective instability of reaction front, and we conclude in the last section.

2 Governing Equations and Linear Stability Analysis

2.1 The Model

We consider an upward propagating reaction front in a porous medium filled by an incompressible reacting fluid submitted to a periodic or QP gravitational vibration, as shown in Fig. 1. The model of a such process can be described by a reaction-diffusion system coupled with the hydrodynamic equations under the Darcy law:

$$\frac{\partial T}{\partial t} + \mathbf{v}.\nabla T = \kappa \Delta T + qK(T)\phi(\alpha), \tag{1}$$

$$\frac{\partial \alpha}{\partial t} + \mathbf{v}.\nabla \alpha = d\Delta\alpha + K(T)\phi(\alpha), \tag{2}$$

$$\mathbf{v} + \frac{K}{\mu}\nabla p = \frac{g\beta K}{\mu}\rho(T - T_0)(1 + b(t))\boldsymbol{\gamma}, \tag{3}$$

$$\nabla.\mathbf{v} = 0. \tag{4}$$

with the following boundary conditions:

$$T = T_i\ , \alpha = 1 \text{ and } v = 0 \text{ when } y \to +\infty, \tag{5}$$

$$T = T_b\ , \alpha = 0 \text{ and } v = 0 \text{ when } y \to -\infty. \tag{6}$$

Here T is the temperature, α the depth of conversion, $\mathbf{v} = (v_x, v_y)$ the fluid velocity, p the pressure, κ the coefficient of thermal diffusivity, d the diffusion, q the adiabatic heat release, g the gravity acceleration, ρ the density, β the coefficient of thermal expansion, μ the viscosity and γ is the unit vector in the upward direction. In addition, T_0 is the mean value of temperature, T_i is an initial temperature while T_b is the temperature of the burned mixture given by $T_b = T_i + q$. The function $K(T)\phi(\alpha)$ is the reaction rate where the temperature dependence is given by the Arrhenius law [10]:

$$K(T) = k_0 \exp\Big(-\frac{E}{R_0 T}\Big) \tag{7}$$

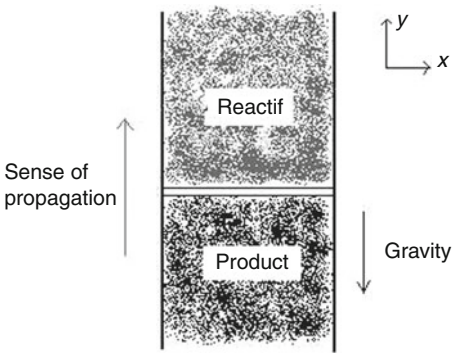

Fig. 1 Sketch of the reaction front propagation

where E is the activation energy, R_0 the universal gas constant and k_0 is the pre-exponential factor. For the asymptotic analysis of this problem we assume that the activation energy is large and we consider zero order reaction for which

$$\phi(\alpha) = \begin{cases} 1 \text{ if } \alpha < 1 \\ 0 \text{ if } \alpha = 1 \end{cases} . \tag{8}$$

The gravitational modulation force $b(t)$ is given depending of the nature of modulation. If it is periodic, $b(t) = \lambda sin(\nu t)$, and if it is QP, $b(t) = \lambda_1 sin(\nu_1 t) + \lambda_2 sin(\nu_2 t)$.

2.2 The Dimensionless Model

In order to write down the dimensionless model, we now introduce the spatial variables $x' = \frac{xc_1}{\kappa}$, $y' = \frac{yc_1}{\kappa}$, time $t' = \frac{tc_1^2}{\kappa d}$, velocity $\frac{\mathbf{v}}{c_1}$, pressure $\frac{p\kappa\mu}{K}$ with $c_1 = c/\sqrt{2}$ and frequency $\sigma = \frac{\kappa}{c_1^2}\nu$. Denoting $\theta = \frac{T - T_b}{q}$ and keeping for convenience the same notation for the other variables, we obtain the system

$$\frac{\partial\theta}{\partial t} + v\nabla\theta = \Delta\theta + W_Z(\theta)\,\phi(\alpha), \tag{9}$$

$$\frac{\partial\alpha}{\partial t} + v\nabla\alpha = \Lambda\Delta\alpha + W_Z(\theta)\,\phi(\alpha), \tag{10}$$

$$v + \nabla p = R_p(\theta + \theta_0)\begin{pmatrix}0\\1\end{pmatrix}(1 + b_d(t)), \tag{11}$$

$$div(v) = 0 \tag{12}$$

with the following conditions at infinity:

$$\theta = -1\,,\, \alpha = 0 \text{ and } v = 0 \text{ when } y \to +\infty, \tag{13}$$

$$\theta = 0\,,\, \alpha = 1 \text{ and } v = 0 \text{ when } y \to -\infty. \tag{14}$$

Here $\Lambda = d/\kappa$ is the inverse of the Lewis number, $R_p = \dfrac{Kc_1^2P^2R}{\mu^2}$, where R is the Rayleigh number and P the Prandtl number that are defined by $R = \dfrac{g\beta q\kappa^2}{\mu c_1^3}$ and $P = \dfrac{\mu}{\kappa}$. In addition, we use the parameters $\delta = \dfrac{R_0T_b}{E}$ and $\theta_0 = \dfrac{T_b - T_0}{q}$. The reaction rate is given by:

$$W_Z(\theta) = Z\exp\Big(\frac{\theta}{Z^{-1} + \delta\theta}\Big), \tag{15}$$

where $Z = \dfrac{qE}{R_0T_b^2}$ stands for Zeldovich number. The dimensionless modulation force is given by $b_d(t) = \lambda sin(\sigma t)$ in the periodic modulation case, or $b_d(t) = \lambda_1 sin(\sigma_1 t) + \lambda_2 sin(\sigma_2 t)$ in the QP modulation case.

2.3 Linear Stability Analysis

2.4 Approximation of Infinitely Narrow Reaction Zone

To study the problem analytically, we reduce it to a singular perturbation problem where the reaction zone is supposed to be infinitely narrow and the reaction term is neglected outside the reaction zone. This method, called Zeldovich–Frank-Kamenetskii approximation, is a well-known approach for combustion problems [10, 43]. We will carry out a formal asymptotic analysis with $\epsilon = \dfrac{1}{Z}$ taken as a small parameter to obtain a closed interface problem. Let us denote by $\zeta(t, x)$ the location of the reaction zone in the laboratory frame reference. The new independent variable in the direction of the front propagation is written as

$$y_1 = y - \zeta(t, x). \tag{16}$$

We introduce new functions $\theta_1, \alpha_1, \mathbf{v}_1, p_1$ as follows

$$\begin{aligned} \theta(t, x, y) &= \theta_1(t, x, y_1), \quad \alpha(t, x, y) = \alpha_1(t, x, y_1), \\ \mathbf{v}(t, x, y) &= \mathbf{v}_1(t, x, y_1), \quad p(t, x, y) = p_1(t, x, y_1) \end{aligned} \tag{17}$$

and we re-write the equations in the form (the index 1 for the new functions is omitted):

$$\frac{\partial\theta}{\partial t} - \frac{\partial\theta}{\partial y_1}\frac{\partial\zeta}{\partial t} + \mathbf{v}.\widetilde{\nabla}\theta = \widetilde{\Delta}\theta + W_Z(\theta)\phi(\alpha), \tag{18}$$

$$\frac{\partial\alpha}{\partial t} - \frac{\partial\alpha}{\partial y_1}\frac{\partial\zeta}{\partial t} + \mathbf{v}.\widetilde{\nabla}\alpha = W_Z(\theta)\phi(\alpha), \tag{19}$$

$$\mathbf{v} + \widetilde{\nabla}p = R_p(\theta+\theta_0)(1+b_d(t))\boldsymbol{\gamma}, \tag{20}$$

$$\frac{\partial v_x}{\partial x} - \frac{\partial v_x}{\partial y_1}\frac{\partial\zeta}{\partial x} + \frac{\partial v_y}{\partial y_1} = 0, \tag{21}$$

where we have set

$$\widetilde{\Delta} = \frac{\partial^2}{\partial x^2} + \frac{\partial^2}{\partial y_1^2} - 2\frac{\partial\zeta}{\partial x}\frac{\partial^2}{\partial x\partial y_1} + \Big(\frac{\partial\zeta}{\partial x}\Big)^2\frac{\partial^2}{\partial y_1^2} - \frac{\partial^2\zeta}{\partial x^2}\frac{\partial}{\partial y_1}, \tag{22}$$

$$\widetilde{\nabla} = \Big(\frac{\partial}{\partial x} - \frac{\partial\zeta}{\partial x}\frac{\partial}{\partial y_1}, \frac{\partial}{\partial y_1}\Big). \tag{23}$$

We use the method of matched asymptotic expansions. To do so, we assume that the outer solution of the problem can be written in the form

$$\begin{aligned} &\theta = \theta^0 + \epsilon\theta^1 + \ldots, \quad \alpha = \alpha^0 + \epsilon\alpha^1 + \ldots, \\ &\mathbf{v} = \mathbf{v}^0 + \epsilon\mathbf{v}^1 + \ldots, \quad p = p^0 + \epsilon p^1 + \ldots. \end{aligned} \tag{24}$$

Here $(\theta^0, \alpha^0, \mathbf{v}^0)$ is a dimensionless form of the basic solution.

In order to obtain jump conditions in the reaction zone, we consider the inner problem and we introduce the stretching coordinate $\eta = y_1/\epsilon$, with $\epsilon = 1/Z$. On the other hand, the inner solution is sought in the form

$$\begin{aligned} &\theta = \epsilon\tilde{\theta}^1 + \ldots, \quad \alpha = \tilde{\alpha}^0 + \epsilon\tilde{\alpha}^1 + \ldots, \\ &\mathbf{v} = \tilde{\mathbf{v}}^0 + \epsilon\tilde{\mathbf{v}}^1 + \ldots, \quad p = \tilde{p}^0 + \epsilon\tilde{p}^1 + \ldots, \quad \zeta = \tilde{\zeta}^0 + \epsilon\tilde{\zeta}^1 + \ldots. \end{aligned} \tag{25}$$

Substituting these expansions into (18)–(21), we obtain the first-order inner problem:

$$\Big(1 + \Big(\frac{\partial\tilde{\zeta}^0}{\partial x}\Big)^2\Big)\frac{\partial^2\tilde{\theta}^1}{\partial\eta^2} + \exp\Big(\frac{\tilde{\theta}^1}{1+\delta\tilde{\theta}^1}\Big)\phi(\tilde{\alpha}^0) = 0, \tag{26}$$

$$-\frac{\partial\tilde{\alpha}^0}{\partial\eta}\frac{\partial\tilde{\zeta}^0}{\partial\eta} - \frac{\partial\tilde{\alpha}^0}{\partial\eta}\Big(\tilde{v}_x^0\frac{\partial\tilde{\zeta}^0}{\partial x} - \tilde{v}_y^0\Big) = \exp\Big(\frac{\tilde{\theta}^1}{1+\delta\tilde{\theta}^1}\Big)\phi(\tilde{\alpha}^0), \tag{27}$$

$$\frac{\partial\tilde{p}^0}{\partial\eta} = 0, \tag{28}$$

$$\tilde{v}_x^0 + \frac{\partial \tilde{p}^0}{\partial x} - \frac{\partial \tilde{\xi}^0}{\partial t}\frac{\partial \tilde{p}^1}{\partial \eta} = 0, \tag{29}$$

$$\tilde{v}_y^0 + \frac{\partial \tilde{p}^1}{\partial \eta} = -R_p\theta_0(1 + b_d(t)), \tag{30}$$

$$-\frac{\partial \tilde{v}_x^0}{\partial \eta}\frac{\partial \tilde{\xi}^0}{\partial x} + \frac{\partial \tilde{v}_y^0}{\partial \eta} = 0. \tag{31}$$

Then, the matching conditions are

$$\eta \to +\infty: \quad \tilde{\theta}^1 \sim \theta^1|_{y_1=0+} + \eta\frac{\partial \theta^0}{\partial y_1}|_{y_1=0+}, \quad \tilde{\alpha}^0 \to 0, \quad \tilde{\mathbf{v}}^0 \to \mathbf{v}^0|_{y_1=0+}, \tag{32}$$

$$\eta \to -\infty: \quad \tilde{\theta}^1 \to \theta^1|_{y_1=0-}, \quad \tilde{\alpha}^0 \to 1, \quad \tilde{\mathbf{v}}^0 \to \mathbf{v}^0|_{y_1=0-}. \tag{33}$$

From (28) we obtain that $\tilde{p}^0$ does not depend on η, which implies that the pressure is continuous through the interface. Next, denoting by s the quantity

$$s = \tilde{v}_x^0\frac{\partial \tilde{\xi}^0}{\partial x} - \tilde{v}_y^0, \tag{34}$$

we obtain from (31) that s does not depend on η. Finally from (29), (30) and (34) we easily obtain that $\tilde{v}_x^0$ and $\tilde{v}_y^0$ do not depend on η, which provides the continuity of the velocity through the interface.

We next derive the jump conditions for the temperature from (26), in the same way as it is usually done for combustion problems. From (27) it follows that $\tilde{\alpha}^0$ is a monotone function and $0 < \tilde{\alpha}^0 < 1$. Since we consider zero-order reaction, we have $\phi(\tilde{\alpha}^0) \equiv 1$. We conclude from (26) that $\tilde{\theta}^1$ is also a monotone function. Thus, multiplying (26) by $\dfrac{\partial \tilde{\theta}^1}{\partial \eta}$ and integrating, we obtain

$$\Big(\frac{\partial \tilde{\theta}^1}{\partial \eta}\Big)^2\Big|_{\eta=+\infty} - \Big(\frac{\partial \tilde{\theta}^1}{\partial \eta}\Big)^2\Big|_{\eta=-\infty} = -\frac{2}{A}\int_{-\infty}^{\theta^1} \exp\Big(\frac{\tau}{1+\delta\tau}\Big)d\tau, \tag{35}$$

where we have set

$$A = 1 + \Big(\frac{\partial \tilde{\xi}^0}{\partial x}\Big)^2. \tag{36}$$

Next, subtracting (26) from (27) and integrating, we obtain

$$\frac{\partial \tilde{\theta}^1}{\partial \eta}\Big|_{\eta=+\infty} - \frac{\partial \tilde{\theta}^1}{\partial \eta}\Big|_{\eta=-\infty} = -\frac{1}{A}\Big(\frac{\partial \tilde{\xi}^0}{\partial t} + s\Big). \tag{37}$$

Using now the matching conditions and truncating the expansion as:

$$\theta^0 \approx \theta, \quad \theta^1|_{y_1=0-} \approx Z\theta|_{y_1=0} \quad \zeta^0 \approx \zeta, \quad \mathbf{v} \approx \mathbf{v}^0, \tag{38}$$

we obtain the jump conditions

$$\Big(\frac{\partial\theta}{\partial y_1}\Big)^2\Big|_{y_1=0+} - \Big(\frac{\partial\theta}{\partial y_1}\Big)^2\Big|_{y_1=0-} = 2Z\Big(1+\Big(\frac{\partial\zeta}{\partial x}\Big)^2\Big)^{-1} \int_{-\infty}^{\theta|_{y_1=0}} \exp\Big(\frac{\tau}{Z^{-1}+\delta\tau}\Big)d\tau, \tag{39}$$

$$\frac{\partial\theta}{\partial y_1}\Big|_{y_1=0+} - \frac{\partial\theta}{\partial y_1}\Big|_{y_1=0-} = -\Big(1+\Big(\frac{\partial\zeta}{\partial x}\Big)^2\Big)^{-1}\Big(\frac{\partial\zeta}{\partial t} + (v_x\frac{\partial\zeta}{\partial x} - v_y)\Big|_{y_1=0}\Big). \tag{40}$$

2.5 Formulation of the Interface Problem

Let us summarize the interface problem. We have for $y > \zeta$ (in the unburnt medium)

$$\frac{\partial\theta}{\partial t} + \mathbf{v}.\nabla\theta = \Delta\theta, \tag{41}$$

$$\alpha \equiv 0, \tag{42}$$

$$\mathbf{v} + \nabla p = R_p(\theta+\theta_0)(1+b_d(t))\boldsymbol{\gamma}, \tag{43}$$

$$\nabla.\mathbf{v} = 0. \tag{44}$$

The equations in the burnt medium ($y < \zeta$) lead to the following system:

$$\frac{\partial\theta}{\partial t} + \mathbf{v}.\nabla\theta = \Delta\theta, \tag{45}$$

$$\alpha \equiv 1, \tag{46}$$

$$\mathbf{v} + \nabla p = R_p(\theta+\theta_0)(1+b_d(t))\boldsymbol{\gamma}, \tag{47}$$

$$\nabla.\mathbf{v} = 0. \tag{48}$$

We finally complete this system by the following jump conditions at the interface $y = \zeta$:

$$[\theta] = 0, \quad \Big[\frac{\partial\theta}{\partial y}\Big] = \frac{\frac{\partial\zeta}{\partial t}}{1+\Big(\frac{\partial\zeta}{\partial x}\Big)^2}, \tag{49}$$

$$\Big[\Big(\frac{\partial\theta}{\partial y}\Big)^2\Big] = -\frac{2Z}{1+(\frac{\partial\zeta}{\partial x})^2}\int_{-\infty}^{\theta(\zeta)}\exp\Big(\frac{s}{1/Z+\delta s}\Big)ds, \tag{50}$$

$$[\mathbf{v}] = 0. \tag{51}$$

Here we denote by [ ] the quantity

$$[f] = f|_{\zeta-0} - f|_{\zeta+0}. \tag{52}$$

The above free boundary problem is completed with the conditions at infinity:

$$y \to +\infty, \quad \theta = -1 \text{ and } \mathbf{v} = 0, \tag{53}$$

$$y \to -\infty, \quad \theta = 0 \text{ and } \mathbf{v} = 0. \tag{54}$$

2.6 Travelling Wave Solution

In this subsection we perform the linear analysis of the steady-state solution for the interface problem. This problem has a travelling wave solution:

$$\theta(t, x, y) = \theta_s(y - ut), \quad \alpha(t, x, y) = \alpha_s(y - ut) \text{ and } \mathbf{v} = 0, \tag{55}$$

where

$$\theta_s(t, y) = \begin{cases} 0 & \text{if } y < 0 \\ e^{-uy} - 1 & \text{if } y > 0 \end{cases}, \tag{56}$$

and

$$\alpha_s(t, y) = \begin{cases} 1 & \text{if } y < 0 \\ 0 & \text{if } y > 0 \end{cases}. \tag{57}$$

where the number u stands for the wave speed. It can easily be computed using the jump conditions of the free boundary problem.

We now introduce the coordinates in the moving frame defined by $y_1 = y - ut$. In this referential, the above travelling wave is a stationary solution of the problem

$$\frac{\partial \theta}{\partial t} + u\frac{\partial \theta}{\partial y} + \mathbf{v}.\nabla\theta = \Delta\theta, \tag{58}$$

$$\mathbf{v} + \nabla p = R_p(\theta + \theta_0)(1 + b_d(t))\boldsymbol{\gamma}, \tag{59}$$

$$\nabla.\mathbf{v} = 0, \tag{60}$$

together with the jump condition found in the previous subsection.

We now consider a small perturbation of this stationary solution. For that purpose we consider a perturbation of the reaction front of the form

$$\zeta(t, x) = ut + \xi(t, x), \text{ with } \xi(t, x) = \epsilon_1(t)e^{ikx}. \tag{61}$$

To study the stability of the solution of our problem, we look for a solution of the problem in the form of the perturbed stationary solution:

$$\theta = \theta_s + \tilde{\theta}, \quad v = v_s + \tilde{v}, \tag{62}$$

where

$$\begin{aligned} \tilde{\theta}(t,x,y) &= \theta_j(y,t)e^{ikx}, \text{ for } j = 1,2, \\ \tilde{v}(t,x,y) &= v_j(y,t)e^{ikx}, \text{ for } j = 1,2. \end{aligned} \tag{63}$$

Here the index $j = 1$ corresponds to functions for $z < 0$ and $j = 2$ for $z > 0$.

We exclude the pressure p and the component v_x of the velocity from the interface problem applying two times the operator $curl$. Thus, we obtain the following problem:

For the burnt media ($y < 0$):

$$v_1'' - k^2 v_1 = -R_p k^2 (1 + b_d(t))\theta_1, \tag{64}$$

$$\frac{\partial \theta_1}{\partial t} - \theta_1'' - u\theta_1' + k^2\theta_1 = 0. \tag{65}$$

For the unburnt media ($y > 0$):

$$v_2'' - k^2 v_2 = -R_p k^2 \theta_2 (1 + b_d(t)), \tag{66}$$

$$\frac{\partial \theta_2}{\partial t} - \theta_2'' - u\theta_2' + k^2\theta_2 = u\exp(-uy)v_2, \tag{67}$$

go back to the margin where u stands for the stationary front velocity. Taking into account that

$$\theta \,\big|_{\xi=\pm 0} = \theta_s(\pm 0) + \xi\theta_s'(\pm 0) + \tilde{\theta}(\pm 0), \tag{68}$$

and

$$\frac{\partial \theta}{\partial y}\,\big|_{\xi=\pm 0} = \theta_s'(\pm 0) + \xi\theta_s''(\pm 0) + \frac{\partial \tilde{\theta}}{\partial y}(\pm 0), \tag{69}$$

we obtain the following jump conditions:

$$\theta_2(0,t) - \theta_1(0,t) = u\epsilon_1(t), \tag{70}$$

$$\theta_2'(0,t) - \theta_1'(0,t) = -\epsilon_1(t)u^2 - \epsilon_1'(t) + v_1(0,t), \tag{71}$$

$$\epsilon_1(t)u^2 + \theta_2'(0,t) = -\frac{Z}{u}\theta_1(0,t), \tag{72}$$

$$v_2^{(i)}(0,t) = v_1^{(i)}(0,t) \quad i = 0,1. \tag{73}$$

3 Numerical Results and Discussion

3.1 Case of Periodic Vibration

In this case, $b_d(t) = \lambda cos(\sigma t)$. To find the convective instability boundary, we solve numerically the problem (64)–(67) with the jump conditions (70)–(73). The numerical accuracy is controlled by decreasing the time and space steps.

For fixed Z and k we vary R_p. If the Rayleigh number R_p is less than a critical value R_c, the solution is decreasing in time. If $R_p > R_c$, the solution increases, and for $R_p = R_c$ it is periodic in time (Fig. 2, bottom). Similar behavior is observed in the case without vibrations (Fig. 2, top). When the Rayleigh number exceed the critical value the perturbation grows in time and when the Rayleigh number is bellow the critical value the perturbation decays. There are no oscillations because the amplitude of vibrations is equal to zero.

Figure 3 shows the critical value of the Rayleigh number as a function of the amplitude of vibrations for different frequencies. If $\lambda = 0$, we obtain the same value $R_c = 26$ as in the absence of vibrations [44]. For small positive λ, vibrations stabilize the solution: R_c is an increasing function. For larger values of λ, vibrations destabilize the solution: R_c is a decreasing function. When we increase the frequency σ, the front becomes more stable.

Figure 4 shows the critical value of the Rayleigh number as a function of the frequency of vibrations for different amplitudes. If $\lambda = 0$, the curve takes a constant value $R_c = 26$ corresponding to the absence of vibration. If $\lambda \neq 0$, all curves are increasing functions, i.e. when the frequency increases the front become more stable. It can be seen that all curves have a asymptotic behavior when the frequency is sufficiently large, which means that high-frequency vibration can stabilize the front.

3.2 Case of Periodic Vibration with Modulation of Amplitude

In this case, $b_d(t) = \lambda cos(\sigma_2 t) sin(\sigma_1 t)$ where now the amplitude of the vibration is modulated and is written as $\lambda cos(\sigma_2 t)$. The interface problem is solved numerically leading to the critical Rayleigh number. Figure 5 shows the critical Rayleigh number as function of the amplitude for some different choice of the frequencies ratio. It is worth noticing that in the absence of vibration modulation ($\sigma_2 = 0$), we find the same result as in [16] which is consistent with the current analysis. Results in Fig. 5 indicate that for relatively small values of the modulation amplitude λ and for a value of the frequency modulation equal to half the frequency of the vibration ($\sigma_2 = \sigma_1/2$), the reaction front undergoes a destabilizing effect. In contrast, a stabilizing effect is gained when the frequency modulation is twice that of the vibration ($\sigma_2 = 2\sigma_1$). In other words, the front is less stable when ($\sigma_2 = \sigma_1/2$) and it is more stable when ($\sigma_2 = 2\sigma_1$).

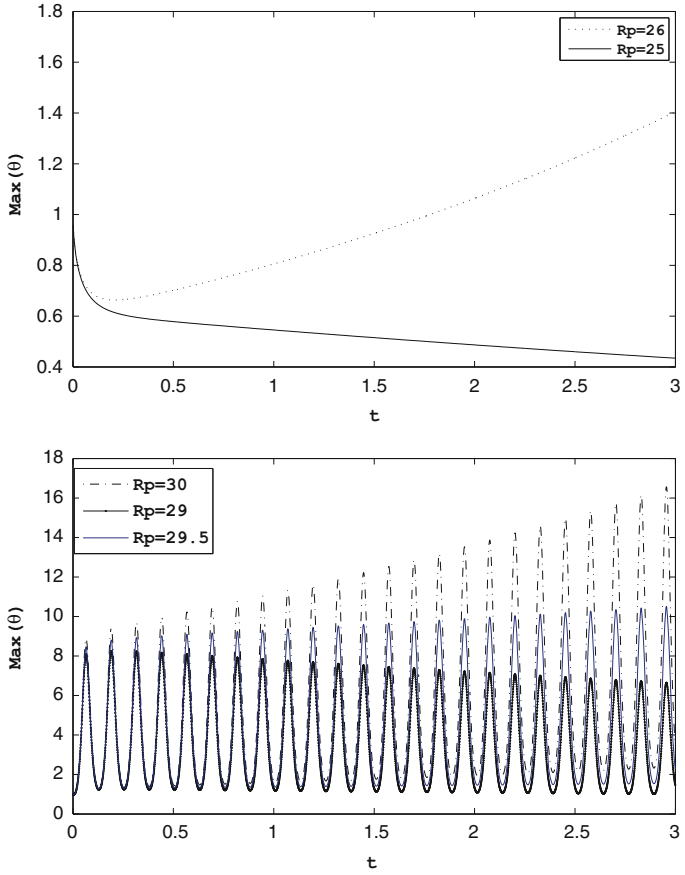

Fig. 2 Temperature maximum as a function of time for $k = 3.14$, $Z = 8$, $u = 1.4142$, $\lambda = 0$ (*top*) and for $k = 3.14$, $Z = 8$, $u = 1.4142$, $\lambda = 5$, $\sigma = 50$ (*bottom*)

Figure 6 depicts the critical Rayleigh number as function of the frequency of the vibration, σ_1, in the case where ($\sigma_2 = 2\sigma_1$). This figure shows that when $\sigma_2 = 2\sigma_1$, increasing the frequency of the vibration, σ_1, causes the critical Rayleigh number to increase stepwise leading the reaction front to substantially gain stability.

3.3 Case of Quasi-periodic Modulation

In this case, the form of the QP gravitational modulation is written as $b_d(t) = \lambda_1 sin(\sigma_1 t) + \lambda_2 sin(\sigma_2 t)$, where λ_1, λ_2 and σ_1, σ_2 are the amplitudes and the frequencies, respectively. Figure 7 depicts the variation of the maximum of temperature as function of time. It can be seen from these plots that if the Rayleigh

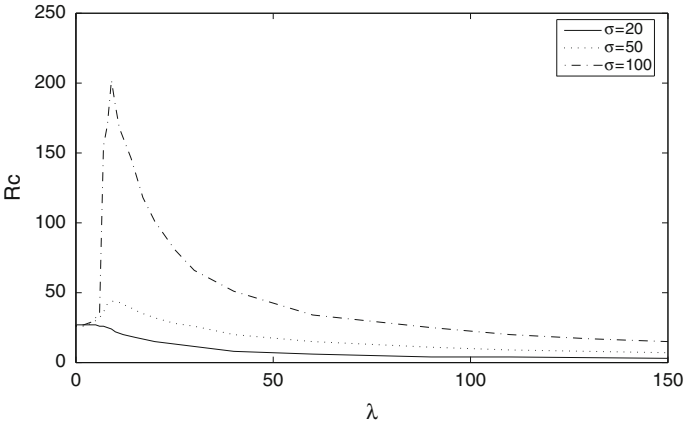

Fig. 3 Convective instability boundary: critical Rayleigh number as a function of the amplitude of vibrations for $k = 3.14$, $Z = 8$ and $u = 1.4142$ and for different values of the frequency σ

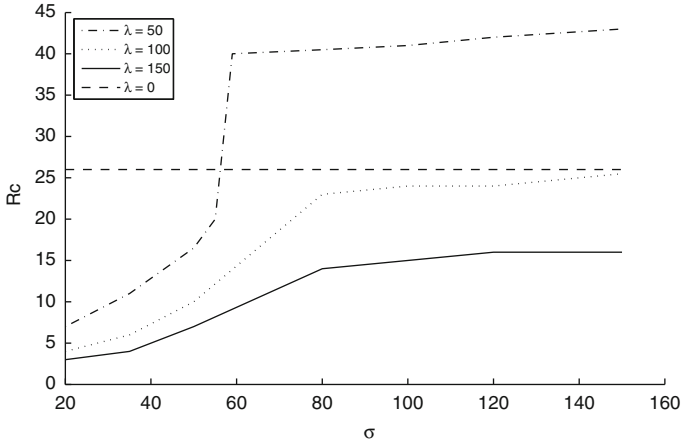

Fig. 4 Convective instability boundary: critical Rayleigh number as a function of the frequency of vibrations for $k = 3.14$, $Z = 8$ and $u = 1.4142$ and for different values of the amplitude λ

number R_p is less than a critical value R_c, the solution is decreasing in time which corresponds to a stable (bounded) variation of the maximum of temperature. For values of R_p larger than R_c, the maximum of temperature presents unbounded oscillations which corresponds to unstable solutions. To detect this instability, we start our computations with small Rayleigh numbers and then we increase it slowly until the critical value of the Rayleigh number is captured. The figure shows that the maximum of temperature variation is decreasing for $R_p = 26$ and increasing for $R_p = 28$ indicating that the critical Rayleigh number is approximatively located between, i.e. $R_c \approx 27$.

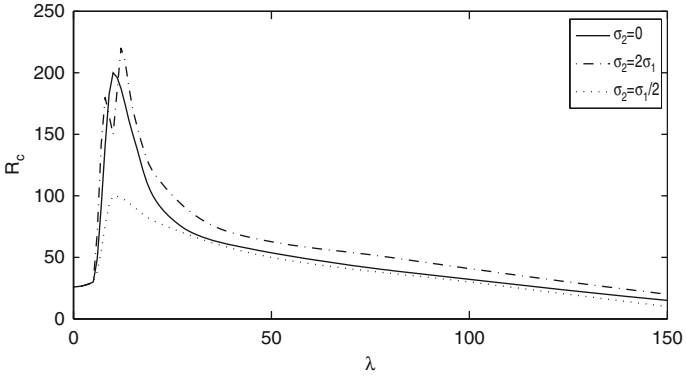

Fig. 5 Critical Rayleigh number as function of the amplitude λ for different values of frequencies ratio and for $\sigma_1 = 100$

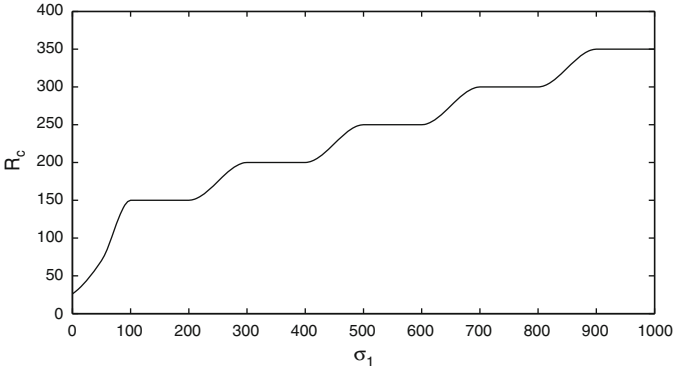

Fig. 6 Critical Rayleigh number as function of the frequency σ_1 for $\lambda = 10$ and for $\sigma_2 = 2\sigma_1$

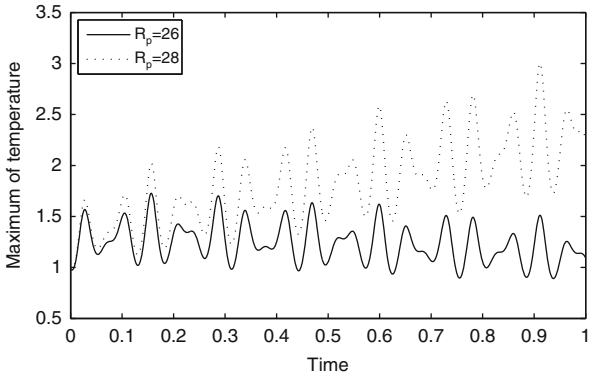

Fig. 7 Maximum of temperature as function of time for $\lambda_1 = 2$, $\lambda_2 = 2$, $\sigma_1 = 100$ and $\sigma_2 = \sqrt{2}\sigma_1$

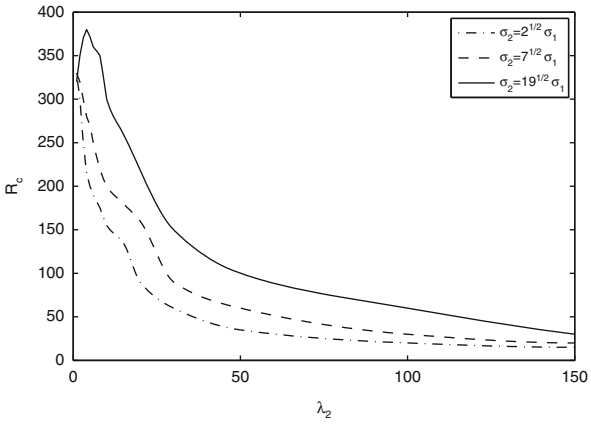

Fig. 8 Critical Rayleigh number as function of the amplitude λ_2 for $\lambda_1 = 5$ and $\sigma_1 = 500$

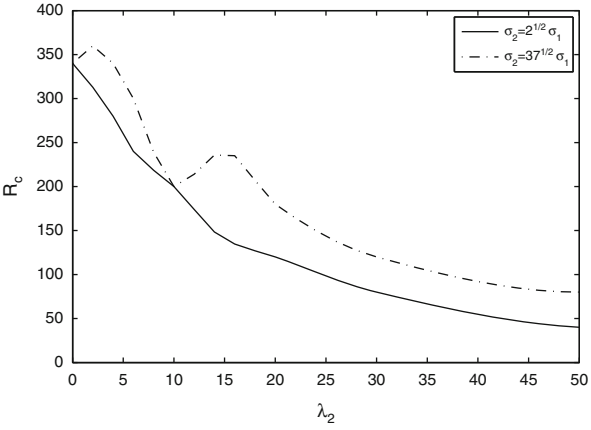

Fig. 9 Critical Rayleigh number as function of the amplitude λ_2 for $\lambda_1 = 5$ and $\sigma_1 = 250$

Figure 8 shows, for $\lambda_1 = 5$ and $\sigma_1 = 500$, the variation of the critical Rayleigh number as function of the amplitude λ_2. The plots indicate that for small values of the frequencies ratio $\sigma = \sigma_2/\sigma_1$, as the amplitude λ_2 increases, the critical Rayleigh number decreases from a certain value of $R_p(\approx 325)$. If σ is increased substantially, a stabilizing effect appears in a region corresponding to small values of λ_2. In this zone, one can expect a regaining of stability of reaction fronts. For higher values of λ_2 the critical Rayleigh number decreases for different σ indicating that large values of λ_2 induce a destabilizing effect. Figure 9 illustrates similar results for $\sigma_1 = 250$. It is seen in this figure that for higher values of σ, a stabilizing effect appears in two successive regions corresponding, respectively, to small and moderate values of the amplitude λ_2. This result means that increasing σ, stability may be gained in certain specific intervals of λ_2.

Finally, Fig. 10 shows, for given amplitudes and for different values of the frequencies ratio σ, the critical Rayleigh number as function of σ_1. This figure

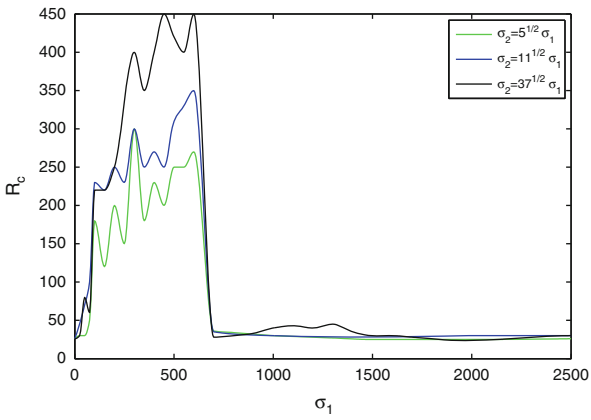

Fig. 10 Critical Rayleigh number as function of frequency σ_1 for $\lambda_1 = \lambda_2 = 5$

indicates clearly that in the absence of QP vibration ($\sigma_1 = 0, \sigma_2 = 0$), the curves start at the value $R_c = 26$ corresponding to the unmodulated case, which is in good agreement with the previous works [16, 44] and hence validating the numerical simulations. This figure also depicts an interesting phenomenon, that is, in a certain interval of σ_1, the value of the critical Rayleigh number increases from the unmodulated case $R_c = 26$ with oscillatory variation. Increasing σ, the oscillating variation of the critical Rayleigh number increases creating a repeated alternating zones where stability is gained. At a certain value of $\sigma_1 \approx 700$, the critical Rayleigh number suddenly drops to meet the unmodulated case, $R_c = 26$. Above $\sigma_1 \approx 700$, the frequencies ratio has no effect on the critical Rayleigh number and the problem becomes equivalent to the unmodulated case.

We have shown that in the presence of a QP vibration, the convection instability of reaction fronts in porous media can be controlled and the reaction fronts may remain stable in certain regions, and for certain combinations of the amplitudes and the frequencies ratio of the QP vibration.

4 Summary

In this chapter we have presented an overview on the effect of a vertical periodic and QP gravitational modulation on the convective instability of reaction fronts in porous media. Attention was focused on two cases. The case where the gravitational vibration is periodic and its amplitude is modulated, and the case where the vibration is QP having two incommensurate frequencies. In both cases the heating is acted from below such that the sense of reaction is opposite to the gravity sense. To approximate the convective instability threshold, the original reaction-diffusion problem is first reduced to a singular perturbation one using the matched asymptotic expansion. Then, the linear stability analysis of the steady-state solution

for the interface problem is performed. The obtained reduced problem is solved numerically.

In the case where the modulation of the vibration is periodic, it was shown that for relatively small values of the modulation amplitude and for a value of the frequency modulation equal to half the frequency of the vibration ($\sigma_2 = \frac{\sigma_1}{2}$), the reaction front undergoes a destabilizing effect. In contrast, a stabilizing effect is gained when the frequency modulation is twice that of the vibration ($\sigma_2 = 2\sigma_1$). It was also shown that increasing the frequency of the vibration, σ_1, causes the critical Rayleigh number to increase stepwise leading the reaction front to substantially gain stability.

In the case of QP gravitational modulation, it was shown that for relatively small values of the amplitudes λ_1 and λ_2 of the QP vibration, an increase of the frequencies ratio $\sigma = \frac{\sigma_2}{\sigma_1}$ has a stabilizing effect. The results also revealed that for given values of λ_1 and λ_2 and below a critical value of the frequency σ_1, an increase of the frequencies ratio σ produces a stabilizing effect. In this interval of σ_1, the convection threshold grows from the critical Rayleigh number of the unmodulated case, $R_c = 26$, with oscillating variation. This alternating variation of the critical Rayleigh number indicates that for appropriate values of parameters, a more pronounced stabilizing effect can be gained. At a certain critical value of σ_1, the critical Rayleigh number drops to the unmodulated case. Above the critical value of σ_1, the frequencies ratio has no effect on the critical Rayleigh number showing that for higher values of the frequency σ_1, the QP vibration has no effect and the problem tends to the unmodulated case. The results of this work shown that in the presence of a QP vibration, the convection instability of reaction fronts in porous media can be controlled and the reaction fronts may be sustained in stability regions for appropriate values of the amplitudes and frequencies of the vibration.

5 Appendix

5.1 The Method of Matched Asymptotic Expansions

In a large class of singular perturbed problems, the domain may be divided into two subdomains. On one of these, the solution is accurately approximated by an asymptotic series found by treating the problem as a regular perturbation. The other subdomain consists of one or more small areas in which that approximation is inaccurate, generally because the perturbation terms in the problem are not negligible there. These areas are referred to as transition layers, or boundary or interior layers depending on whether they occur at the domain boundary (as is the usual case in applications) or inside the domain.

An approximation in the form of an asymptotic series is obtained in the transition layer(s) by treating that part of the domain as a separate perturbation problem. This approximation is called the “inner solution,” and the other is the “outer solution,”

named for their relationship to the transition layer(s). The outer and inner solutions are then combined through a process called "matching" in such a way that an approximate solution for the whole domain is obtained. More details can be found in [45, 46].

5.2 Simple Example

Consider the equation

$$\epsilon y'' + (1+\epsilon)y' + y = 0,$$

where y is a function of t, $y(0) = 0$, $y(1) = 1$ and $0 < \epsilon \ll 1$.

Outer and Inner Solutions

Since ϵ is very small, the first approach is to find the solution to the problem

$$y' + y = 0,$$

which is

$$y = Ae^{-t}$$

for some constant A. Applying the boundary condition $y(0) = 0$, we would have $A = 0$; applying the boundary condition $y(1) = 1$, we would have $A = e$. At least one of the boundary conditions cannot be satisfied. From this we infer that there must be a boundary layer at one of the endpoints of the domain.

Suppose the boundary layer is at $t = 0$. If we rescal $\tau = t/\epsilon$, the problem becomes

$$\frac{1}{\epsilon}y''(\tau) + (1+\epsilon)\frac{1}{\epsilon}y'(\tau) + y(\tau) = 0,$$

which, after multiplying by ϵ and taking $\epsilon = 0$, is

$$y'' + y' = 0$$

with the solution

$$y = B - Ce^{-\tau}$$

for some constants B and C. Since $y(0) = 0$, we have $C = B$, so the inner solution is

$$y_I = B\left(1 - e^{-\tau}\right) = B\left(1 - e^{-t/\epsilon}\right).$$

Matching

Notice that we have assumed the outer solution to be

$$y_O = e^{1-t}.$$

The idea of matching is for the inner and outer solutions to agree at some value of t near the boundary layer as ϵ decreases. For example, if we fix $t = \sqrt{\epsilon}$, we have the matching condition

$$\lim_{\epsilon \to 0} y_I\left(\sqrt{\epsilon}\right) = \lim_{\epsilon \to 0} y_O\left(\sqrt{\epsilon}\right),$$

thereby $B = e$. Note that instead of $t = \sqrt{\epsilon}$, we could have chosen any other power law $t = \epsilon^k$ with $0 < k < 1$. To obtain our final matched solution, valid on the whole domain, one popular method is the uniform method. In this method, we add the inner and outer approximations and subtract their overlapping value, $y_{overlap}$. In the boundary layer, we expect the outer solution to be approximate to the overlap, $y_O \sim y_{overlap}$. Far from the boundary layer, the inner solution should approximate it, $y_I \sim y_{overlap}$. Hence, we want to eliminate this value from the final solution. In our example, $y_{overlap} \sim e$. Therefore, the final solution is,

$$y(t) = y_I + y_O - e = e\left(1 - e^{-t/\epsilon}\right) + e^{1-t} - e = e\left(e^{-t} - e^{-t/\epsilon}\right).$$

Accuracy

Substituting the matched solution in the differential equation yields

$$\epsilon y'' + (1+\epsilon)\, y' + y = 0,$$

which implies, due to the uniqueness of the solution, that the matched asymptotic solution is identical to the exact solution up to a constant multiple, as it satisfies the original differential equation. This is not necessarily always the case, any remaining terms should go to zero uniformly as $\epsilon \to 0$. As to the boundary conditions, $y(0) = 0$ and $y(1) = 1 - e^{1-1/\epsilon}$, which quickly converges to the value given in the problem.

Not only does our solution approximately solve the problem at hand; it closely approximates the exact solution. It happens that this particular problem is easily found to have exact solution

$$y(t) = \frac{e^{-t} - e^{-t/\varepsilon}}{e^{-1} - e^{-1/\varepsilon}},$$

which, as previously noted, has the same form as the approximate solution. Note also that the approximate solution is the first term in a binomial expansion of the exact solution in powers of $y(1) = e^{1-1/\epsilon}$.

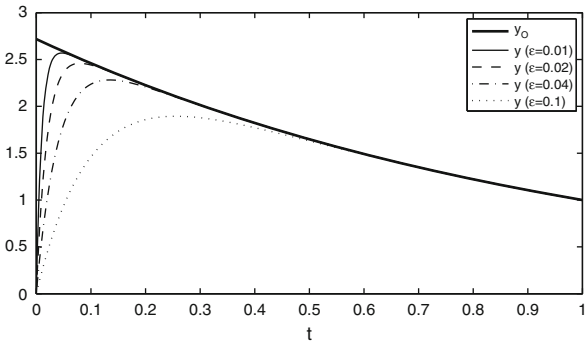

Fig. 11 Convergence approximation

Figure 11 shows convergence of the exact solution for various ϵ and the outer solution. Note that since the boundary layer becomes narrower with decreasing ϵ, the approximations converge to the outer solution pointwise, but not uniformly.

Location of Boundary Layer

Conveniently, we can see that the boundary layer, where y' and y'' are large, is near $t = 0$, as supposed earlier. If we had supposed it to be at the other endpoint and proceeded by making the rescaling $\tau = (1 - t)/\epsilon$, we would have found it impossible to satisfy the resulting matching condition. For many problems, this kind of trial and error is the only way to determine the true location of the boundary layer.

References

1. Aldushin, A.P., Kasparyan, S.G.: Thermodiffusional instability of a combustion front. Sov. Phys. Dokl. **24**, 29–31 (1979)
2. Barenblatt, G.I., Zeldovich, Y.B., Istratov, A.G.: Diffusive-thermal stability of a laminar flame. Zh. Prikl. Mekh. Tekh. Fiz. **4**, 21 (1962) (in Russian)
3. Margolis, S.B., Kaper, H.G., Leaf, G.K., Matkowsky, B.G.: Bifurcation of pulsating and spinning reaction fronts in condensed two-phase combustion. Combust. Sci. Technol. **43**, 127–165 (1985)
4. Matkowsky, B.J., Sivashinsky, G.I.: Propagation of a pulsating reaction front in solid fuel combustion. SIAM J. Appl. Math. **35**, 465–478 (1978)
5. Shkadinsky, K.G., Khaikin, B.I., Merzhanov, A.G.: Propagation of a pulsating exothermic reaction front in the condensed phase. Combust. Expl. Shock Waves **7**, 15–22 (1971)
6. Clavin, P.: Dynamic behavior of premixed flame fronts in laminar and turbulent flows. Progr. Energ. Combust. Sci. **11**, 1–59 (1985)
7. Istratov, A.G., Librovich, V.B.: Effect of the transfer processes on stability of a planar flame front. J. Appl. Math. Mech. **30**, 451–466 (1966) (in Russian)
8. Landau, L.D., Lifshitz, E.M.: Fluid Mechanics, p. 683. Pergamon, New York (1987)
9. Matalon, M., Matkowsky, B.J.: Flames in fluids: their interaction and stability. Combust. Sci. Technol. **34**, 295–316 (1983)

10. Zeldovich, Y.B., Barenblatt, G.I., Librovich, V.B., Makhviladze, G.M.: The Mathematical Theory of Combustion and Explosions, p. 597. Consultants Bureau, New York (1985)
11. Wadih, M., Roux, B.: The effects of gravity modulation on the stability of a heated fluid layer. J. Fluid Mech. **40**(4), 783–806 (1970)
12. Allali, K., Volpert, V., Pojman, J.A.: Influence of vibrations on convective instability of polymerization fronts. J. Eng. Math. **41**(1), 13–31 (2001)
13. Allali, K., Bikany, F., Taik, A., Volpert, V.: Influence of vibrations on convective instability of reaction fronts in liquids. Math. Model. Nat. Phenom. **5**(7), 35–41 (2010)
14. Allali, K., Bikany, F., Taik, A., Volpert, V.: Linear stability analysis of reaction fronts propagation in liquids with vibrations. Int. Electron. J. Pure Appl. Math. **1**(2), 196–215 (2010)
15. Garbey, M., Taik, A., Volpert, V.: Influence of natural convection on stability of reaction fronts in liquids. Q. Appl. Math. **53**, 1–35 (1998)
16. Aatif, H., Allali, K., El Karouni, K.: Influence of Vibrations on convective instability of reaction fronts in Porous media. Math. Model. Nat. Phenom. **5**(5), 123–137 (2010)
17. Zenkovskaya, S.M., Rogovenko, T.N.: Filtration convection in a high-frequency vibration field. J. Appl. Mech. Tech. Phys. **40**, 379–385 (1999)
18. Gershuni, G.Z., Zhukhovitskii, E.M.: The Convective Stability of Incompressible Fluids. Keter Publications, Jerusalem, pp. 203–230 (1976)
19. Gresho, P.M., Sani, R.L.: The effects of gravity modulation on the stability of a heated fluid layer. J. Fluid Mech. **40**(4), 783–806 (1970)
20. Murray, B.T., Coriell, S.R., McFadden, G.B.: The effect of gravity modulation on solutal convection during directional solidification. J. Cryst. Growth **110**, 713–723 (1991)
21. Wheeler, A.A., McFadden, G.B., Murray, B.T., Coriell, S.R.: Convective stability in the Rayleigh-Bénard and directional solidification problems: high-frequency gravity modulation. Phys. Fluids A **3**(12), 2847–2858 (1991)
22. Gershuni, G.Z., Kolesnikov, A.K., Legros, J.C., Myznikova, B.I.: On the vibrational convective instability of a horizontal, binary-mixture layer with Soret effect. J. Fluid Mech. **330**, 251–269 (1997)
23. Woods, D.R., Lin, S.P.: Instability of a liquid film flow over a vibrating inclined plane. J. Fluid Mech. **294**, 391–407 (1995)
24. Or, A.C.: Finite-wavelength instability in a horizontal liquid layer on an oscillating plane. J. Fluid Mech. **335**, 213–232 (1997)
25. Aniss, S., Souhar, M., Belhaq, M.: Asymptotic study of the convective parametric instability in Hele-Shaw cell. Phys. Fluids **12**, 262–268 (2000)
26. Aniss, S., Belhaq, M., Souhar, M.: Effects of a magnetic modulation on the stability of a magnetic liquid layer heated from above. ASME J. Heat Transf. **123**, 428–432 (2001)
27. Aniss, S., Belhaq, M., Souhar, M., Velarde, M.G.: Asymptotic study of Rayleigh-Bénard convection under time periodic heating in Hele-Shaw cell. Phys. Scr. **71**, 395–401 (2005)
28. Bhadauria, B.S., Bhatia, P.K., Debnath, L.: Convection in Hele-Shaw cell with parametric excitation. Int. J. Non-Linear Mech. **40**, 475–484 (2005)
29. Clever, R., Schubert, G., Busse, F.H.: Two-dimensional oscillatory convection in a gravitationally modulated fluid layer. J. Fluid Mech. **253**, 663–680 (1993)
30. Gresho, P.M., Sani, R.L.: The effects of gravity modulation on the stability of a heated fluid layer. J. Fluid Mech. **40**(4), 783–806 (1970)
31. Rogers, J.L., Schatz, M.F., Bougie, J.L., Swift, J.B.: Rayleigh-Bénard convection in a vertically oscillated fluid layer. Phys. Rev. Lett. **84**(1), 87–90 (2000)
32. Rosenblat, S., Tanaka, G.A.: Modulation of thermal convection instability. Phys. Fluids **7**, 1319–1322 (1971)
33. Venezian, G.: Effect of modulation on the onset of thermal convection. J. Fluid Mech. **35**(2), 243–254 (1969)
34. Wadih, M., Roux, B.: The effects of gravity modulation on the stability of a heated fluid layer. J. Fluid Mech. **40**(4), 783–806 (1970)
35. Boulal, T., Aniss, S., Belhaq, M., Rand, R.H.: Effect of quasiperiodic gravitational modulation on the stability of a heated fluid layer. Phys. Rev. E **52**(76), 56320 (2007)

36. Boulal, T., Aniss, S., Belhaq, M., Azouani, A.: Effect of quasi-periodic gravitational modulation on the convective instability in Hele-Shaw cell. Int. J. Non-Linear Mech. **43**, 852–857 (2008)
37. Boulal, T., Aniss, A., Belhaq, M.: Quasiperiodic gravitational modulation of convection in magnetic fluid. In: Wiegand, S., Köhler, W., Dhont, J.K.G. (eds.) Thermal Non-Equilibrium. Lecture Notes of the 8th International Meeting of Thermodiffusion, 9–13 June 2008, Bonn, Germany, p. 300 (2008) [ISBN: 978-3-89336-523-4]
38. Rand, R.H., Guennoun, K., Belhaq, M.: 2:2:1 Resonance in the quasi-periodic Mathieu equation. Nonlinear Dynam. **31**(4), 367–374 (2003)
39. Sah, S.M., Recktenwald, G., Rand, R.H., Belhaq, M.: Autoparametric quasiperiodic excitation. Int. J. Non-linear Mech. **43**, 320–327 (2008)
40. Allali, K., Belhaq, M., El Karouni, K.: Influence of quasi-periodic gravitational modulation on convective instability of reaction fronts in porous media. Comm. Nonlinear Sci. Numer. Simulat. **17**(4), 1588–1596 (2012)
41. Volpert, V.A., Volpert, V.A., Ilyashenko, V.M., Pojman, J.A.: Frontal polymerization in a porous medium. Chem. Eng. Sci. **53**(9), 1655–1665 (1998)
42. Abdul Mujeebu, M., Abdullah, M.Z., Abu Bakar, M.Z., Mohamad, A.A., Muhad, R.M.N., Abdullah, M.K.: Combustion in porous media and its applications a comprehensive survey. J. Environ. Manage. **90**, 2287–2312 (2009)
43. Zeldovich, Y.B., Frank-Kamenetsky, D.A.: The theory of thermal propagation of flames. Zh. Fiz. Khim. **12**, 100–105 (1938)
44. Allali, K., Ducrot, A., Taik, A., Volpert, V.: Convective instability of reaction fronts in porous media. Math. Model. Nat. Phenom. **2**(2), 20–39 (2007)
45. Nayfeh, A.H.: Perturbation Methods. Wiley Classics Library, Wiley-Interscience, New York (2000)
46. Verhulst, F.: Methods and Applications of Singular Perturbations: Boundary Layers and Multiple Timescale Dynamics. Springer, New York (2005)

Genesis of Bénard–Marangoni Patterns in Thin Liquid Films Drying into Air

P. Colinet, F. Chauvet, and S. Dehaeck

1 Introduction

Significant progress in the understanding of pattern formation in spatially extended systems has been possible thanks to well-controlled detailed experimental studies of Rayleigh–Bénard convection, i.e. the buoyancy-induced hydrodynamic instability of a fluid layer heated from below (see e.g. the classical reviews [1, 2]). Roll-like cellular patterns and their transitions to more complex structures and turbulent-like behavior were indeed extensively studied, with or without additional effects [3], sometimes up to very high Rayleigh numbers (see [4] and references therein). In parallel, surface-tension-driven (thermo- or soluto-capillary) instabilities have also been studied in details (see e.g. [5–7], as well as the contributions of H. Linde, K. Eckert and A. Wierschem in this volume), providing a wide variety of new structures and transitions, even though eventually covering a more narrow range of supercriticalities than buoyancy-driven convection.

Not much attention has been devoted however to pattern forming systems in which the typical wavelength (measured, say, by the spatial period of the fastest growing mode, or by a nonlinearly determined spatial scale) is continuously varied in time. As Bénard convection cells typically scale with the depth of the liquid layer, one could think of varying the latter by injecting/retracting fluid or, as done

P. Colinet (✉) · S. Dehaeck
Université Libre de Bruxelles, TIPs (Transfers, Interfaces and Processes), CP 165/67, Av. F.D. Roosevelt, 50, 1050 Brussels, Belgium
e-mail: pcolinet@ulb.ac.be; sam.dehaeck@gmail.com

F. Chauvet
Université Libre de Bruxelles, TIPs (Transfers, Interfaces and Processes), CP 165/67, Av. F.D. Roosevelt, 50, 1050 Brussels, Belgium

Université Paul Sabatier, Laboratoire de Génie Chimique, 118 route de Narbonne, 31062 Toulouse cedex 9, France
e-mail: fchauvet@gmail.com

R.G. Rubio et al. (eds.), *Without Bounds: A Scientific Canvas of Nonlinearity and Complex Dynamics*, Understanding Complex Systems,
DOI 10.1007/978-3-642-34070-3_15, © Springer-Verlag Berlin Heidelberg 2013

here, by allowing the liquid layer to evaporate. Indeed, during the evaporation of a pure liquid layer into dry air, the liquid/gas interface is cooled because of the energy consumption for the phase change. This temperature difference across the liquid layer can generate surface-tension-driven convection and/or buoyancy-driven convection in the liquid, depending on the layer thickness. Here, as in [8], we mostly focus on surface-tension-driven convection or Bénard–Marangoni (BM) convection arising typically for 1 mm thick (or thinner) liquid layers, even though one cannot exclude an influence of buoyancy for the thicker liquid layers we initiate the experiments with. The continuously decreasing liquid depth forces an increase of the number of convection cells per unit area, and it is of primary interest to investigate how these are created and which kind of dynamical regimes such process leads to. Other questions addressed here, even though not always in full details, are the following: (i) can the observed pattern dynamics be considered as quasi-steady, i.e. instantaneously (or adiabatically) adapting to the continuously decreasing liquid depth? (ii) what is the level of disorder of the observed patterns and on which parameters does it depend? (iii) is the problem of an evaporating liquid layer formally equivalent, possibly under some well-controlled hypotheses, to that of a non-volatile liquid layer heated from below (i.e. the classical BM instability)?

Note that the last of these questions has recently been investigated by the authors [9], who showed that the instability threshold is quite accurately described by a generalized Pearson's theory [10], provided the heat transfer coefficient at the free surface (i.e. in dimensionless form, the Biot number) is suitably defined to incorporate heat spreading along the interface by vapor diffusion in the gas and associated latent heat exchange. Interestingly, this effect formally turns out to act as an effective thermal conductivity of the gas phase, which can be quite large for very volatile liquids [9]. Such reduction to a one-sided approach is actually possible thanks to the smallness of relaxation time scales in the gas (compared to those in the liquid layer), allowing to slave the dynamics of temperature and concentration fluctuations in the gas to the interfacial temperature fluctuations (see also [6, 11]). Note also that contrary to the original Pearson's theory, the free surface Biot number is found to depend on the wavenumber of the fluctuations, hence rendering the stability problem non-local. When the gas phase is much thicker than the liquid depth, as considered hereafter, the Biot number is simply proportional to the wavenumber, with a coefficient depending only on thermo-physical properties of the fluids involved (including the diffusion coefficient of the vapor in the air) and on ambient temperature and pressure. In view of these recent results, the preliminary answer to question (iii) above seems to be positive, in that the two-layer problem of a liquid evaporating into a non-soluble inert gas can indeed be reduced, under quite reasonable assumptions [9, 11], to a much simpler problem involving liquid phase quantities only. The only noteworthy difference compared to the Pearson's problem of a liquid layer heated from below is that the free surface heat transfer is described by a (non-local) generalization of Newton's cooling law accounting for the phase change process.

The paper is organized as follows: the experimental set-up and procedures are described in Sect. 2, while the main results obtained in this preliminary study are

reported in Sect. 3, together with discussions allowing to bring some elements of answer to the questions raised above. Further conclusions and perspectives follow in Sect. 4.

2 Experimental Set-Up and Procedures

Each experimental run is started by pouring a certain amount of volatile liquid in a cylindrical container to form an approximately 1 mm thick liquid layer. Volatile liquids used are Hydrofluoroethers, HFE-7000, 7100, 7200 and 7300 from the company 3M, which have similar physical properties except for their saturation pressure at ambient temperature. The HFE-7000 is the most volatile with $p_{\mathrm{sat}}(24°\mathrm{C}) = 0.61$ bar and the less volatile is HFE-7300 with $p_{\mathrm{sat}}(24°\mathrm{C}) = 0.06$ bar. The container is made of a PVC cylinder glued to a 10 mm thick aluminum plate. The height of the cylinder is $H = 1$ cm, its diameter is 63.5 mm and its thickness is 6 mm.

In addition to the effect of volatility (dependent on the HFE used), we also vary the evaporation rate independently by changing the "transfer distance" H in the gas, roughly equal to the height above which the residual concentration of vapor is negligible (the HFE vapor, being heavier than air, spills over the container wall and is entrained downwards by gravity). Variation of H is accomplished by topping another PVC cylinder (of the same diameter) on the one glued to the plate, wrapping them with a scotch tape in order to avoid any vapor leak. Using additional cylinders of various heights allows setting H to 1–5 cm. In these conditions, the evaporation process is limited by diffusion of vapor into air (implying in particular that the gas may be considered as saturated near the interface, and that the temperature drop across the liquid layer may be neglected when evaluating the corresponding interfacial vapor pressure [11]) and the evaporation rate remains quasi-constant until the layer is too thin and dewetting begins.

The liquid film thickness e and evaporation rate E are measured by weighting, using a precision balance. As described in [9], the mass of the liquid meniscus against the lateral wall has to be taken into account, together with the mass of the vapor contained within the cylinder, in order to obtain an accurate estimation of the instantaneous liquid thickness $e(t)$. The evaporation rate itself, E, is simply computed from the time derivative of the total mass, using a linear fit.

As convection in the pure liquid is necessarily associated with temperature variations, we use a Focal Plane Array IR camera-type (Thermosensorik, InSb 640 SM) facing the liquid/gas interface, to follow the time evolution of the whole cellular pattern. IR images and liquid mass are recorded at a frequency of 1 Hz during the drying of the liquid layer. Occasionally, the pattern evolution is also recorded using a Schlieren set-up, such as shown in Fig. 1, depicting the typical sequence observed. Convection appears right after filling and the pattern is strongly time-dependent (chaotic or "turbulent" regime), evolving into more stable hexagonal-like arrangements when the thickness decreases, until the convective state turns into a

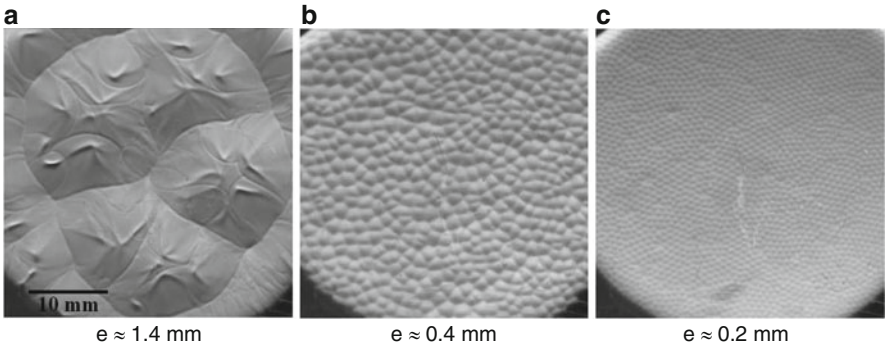

Fig. 1 Typical patterns (here observed using a Schlieren set-up working in double transmission through the film and reflection on the bottom mirror) generated during drying of a liquid film (the thickness e is indicated for each snapshot). The IR pattern evolution is qualitatively similar

"conductive" one (not shown in Fig. 1). During the convective regime, the number of cells sharply increases and their size decreases, partly due to a rapid process of cell nucleation/mitosis (see later).

Having recorded the pattern evolution, the wavenumber $q(t)$ is extracted as the mean position of the fundamental peak in the azimuthally averaged FFT spectra of the images. Then, it is possible to compute the dimensionless wavenumber $k(t) = q(t)e(t)$. From the measurement of e it is also possible to estimate the temperature difference across the liquid layer (neglecting heat coming from the air and lateral losses) as $\Delta T = E\mathscr{L}e/\lambda S$, where $\mathscr{L}$ is the latent heat of vaporization, λ is the liquid thermal conductivity and S is the container cross-section. This estimation assumes a linear (purely conductive) temperature distribution in the liquid layer, which actually corresponds to the usual definition of the Marangoni number $Ma = -\gamma_T \Delta T e/\eta\kappa$ (where γ_T is the surface tension variation with temperature, η is the liquid dynamic viscosity and κ is the liquid thermal diffusivity) characterizing the destabilizing effect of thermocapillarity. The supercriticality can then be computed as $\epsilon = (Ma - Ma_c)/Ma_c$, where Ma_c is the critical Marangoni number corresponding to the transition between convective and conductive states (observed at the critical thickness e_c, see [9] for details).

3 Preliminary Results and Discussions

The dimensionless mean wavenumber k as a function of the supercriticality ϵ is plotted in Fig. 2a for all the liquids and all the evaporation rates tested. For a given liquid the curves corresponding to different evaporation rates coincide rather well, evidencing that wavenumber selection does not depend on the evaporation rate, but rather on the particular liquid tested.

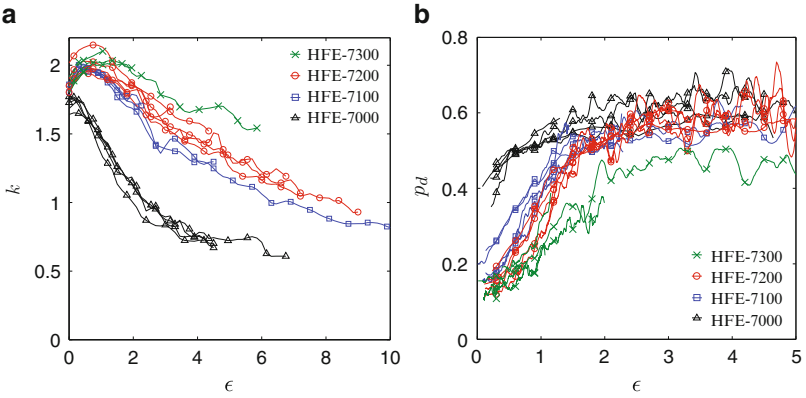

Fig. 2 (**a**) Dimensionless wavenumber k as a function of the supercriticality ε. (**b**) Concentration of defects p_d as a function of the supercriticality ε (fluctuations at high supercriticality are due to an insufficient number of cells). Results are given for all the HFEs and all the evaporation rates tested

This observation clearly suggests a quasi-static evolution, where the wavenumber of the pattern adiabatically adjusts to the instantaneous value of the supercriticality $\varepsilon(t)$. This could indeed be expected as the timescale for liquid depth variation $\sim e/\dot{e}$ turns out to be much larger than the thermal "vertical" time scale $\sim e^2/\kappa$, for all cases investigated here. Yet, the fact that $e/\dot{e}$ remains much smaller than the "lateral" time scale $\sim L^2/\kappa$ (where L is the container diameter), representative of the time needed for global wavenumber adjustments and defect elimination, seems in contradiction with this hypothesis. Another puzzling observation is that, in addition to being unusually fast, the wavenumber selection appears to be rather sharp, i.e. the value of $k(\varepsilon)$ is quite well determined (while relatively wide bands of stable wavenumbers are typically predicted by nonlinear theories [2]), independently of the history of the pattern (for a given liquid). These experimental facts certainly deserve further investigation, including theoretical and numerical analysis.

Note in this respect that the shape of the curves in Fig. 2a has a striking similarity with numerical predictions of Merkt and Bestehorn [12], even though the latter are based on a constant (wavenumber-independent) value of the Biot number. In particular, our experimental results always yield a maximum value of k at small ε for the less volatile liquids (HFE-7100, 7200 and 7300), while Merkt and Bestehorn [12] also observe this non-monotonic behavior at small values of the Biot number.

Now, using an image processing algorithm detecting the centers of the convective cells, the Voronoi diagrams are constructed for each image, allowing to determine the geometry of each convective cell in the pattern. Some of these diagrams are shown in Fig. 3 at the end of the convective regime. As usual, typical defects consisting of pentagons-heptagons pairs are visible, although they here seem to naturally form chains of variable length, probably as a result of the particular pattern genesis observed here. Looking attentively, it seems that most of these penta–hepta

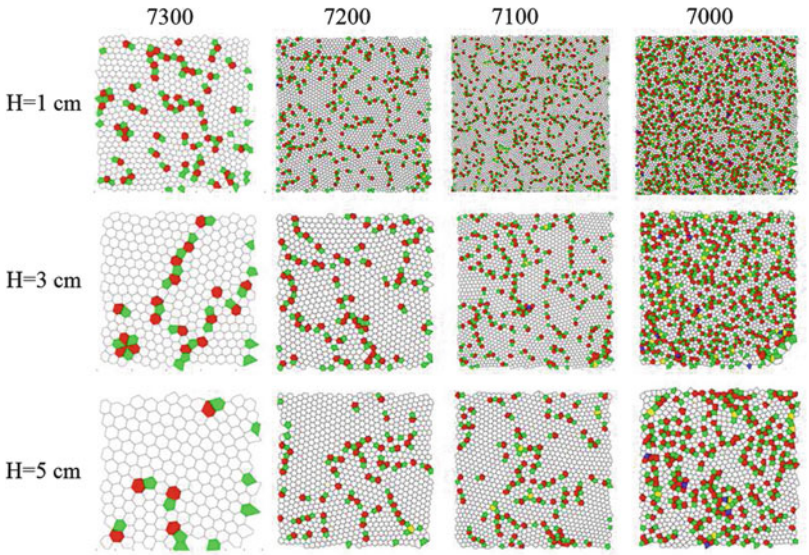

Fig. 3 Voronoi diagrams of the patterns at the end of the convective regime ($\varepsilon \simeq 0.1$) for all the HFEs and three evaporation rates (inversely proportional to the container height H). Hexagonal cells are in *white*, pentagonal cells are in *green* and heptagonal cells are in *red*

chains form grain boundaries between hexagonal patterns rotated by about 30° with respect to each other. Moreover, some localized defects as a "flower defect" are observed for the HFE-7300 and $H = 3$ cm case.

From these Voronoi diagrams, a "degree of disorder", p_d, can then be defined as the number of defects (pentagons and heptagons) divided by the total number of cells. This concentration of defects is plotted in Fig. 2b, versus the supercriticality ε. Figures 2b and 3 show that the more a liquid is volatile, the more the pattern is disordered (at a given value of the supercriticality). Counter-intuitively however, just as for the wavenumber selection in Fig. 2a, the degree of disorder appears not to depend on the evaporation rate, but rather only on the type of liquid used. Again, this goes in favor of a quasi-static evolution of the patterns, which appear to adapt to the instantaneous value of the supercriticality (note that this is the only parameter which varies with the thickness $e(t)$, as will be discussed in the next section).

During the drying of the liquid layer, a rapid process of nucleation of new cells is observed, as expected, together with much less frequent cell collapse (and disappearance) processes. Using a specific image processing algorithm to detect the location of these events, it appears that cell nucleation and collapse occur much more frequently near the defects than in areas consisting of "islands" of quasi-perfect hexagonal cells. Furthermore, the cells undergoing a split, or "mother cells", turn out to be mostly heptagonal (some splits of hexagonal cells are observed, but they are always connected to defects) and never pentagonal. The "daughter cells" were found

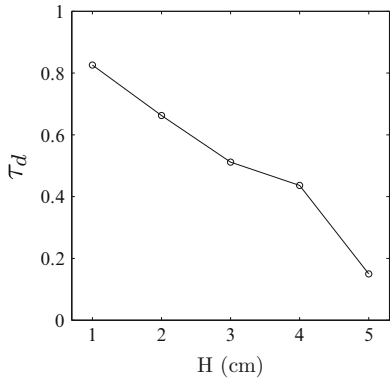

Fig. 4 Ratio (computed at the end of the convective regime) of the net rate of nucleation of new cells (from defects) to the net rate of increase of the total number of cells, as a function of the height of the container (which is inversely proportional to the evaporation rate), for the case of HFE-7200 (moderate volatility)

to be in most cases pentagonal and sometimes hexagonal but never heptagonal. The overall process seems to allow the collective shrinkage of hexagonal cells organized in "islands" separated by chains or assemblies of defects playing the role of a kind of "friction zone" perpetually adapting to the morphology of hexagon islands.

Finally, we have computed the net rate of nucleation of new cells (cells created by nucleation minus cells lost by collapse), divided by the rate of increase of the total number of cells in the pattern. This dimensionless quantity, denoted by τ_d, has been calculated at the end of the convective regime for the case of HFE-7200 and for the five evaporation rates, and is represented in Fig. 4.

It is seen that the larger the evaporation rate (i.e. the faster the film thickness decrease), the larger the ratio τ_d, indicating that most of the new convective cells originate from splitting/mitosis (i.e. from defects already present in the pattern). This proportion reaches more than 80% at the largest evaporation rate studied here. For smaller evaporation rates, wavenumber adjustment is rather achieved by another mechanism consisting in a drift and a compression of islands of defect-free hexagonal cells. In that case, the new cells are actually mostly created at the periphery of the container (it is quite well visible on accelerated videos), and subsequently drift towards its center.

4 Further Conclusions and Perspectives

To conclude, we first stress that global wavenumber selection and defect concentration here appear not to depend on the pattern quenching rate (as demonstrated in Fig. 2), while the relative proportion of mechanisms allowing these pattern modifications (i.e. nucleation and drift) do depend on it (see Fig. 4). This surprising observation casts some doubt on the positiveness of the answer to the first question raised in the introduction, namely about the quasi-steady character of the evolution of the patterns while the liquid layer decreases. As already mentioned in the previous section, it might also appear unusual that the pattern would relax to some "unique"

state (determined by the instantaneous value of the supercriticality) on a time scale much shorter than the lateral diffusion time. One way to reconcile these observations might therefore be that averaged characteristics such as the mean wavenumber or the defect concentration indeed appear to be independent of the quenching speed, while more local characteristics of the patterns do depend more visibly on it. This is currently under detailed investigation, and will be reported elsewhere.

As for the second question raised in the introduction, namely about the type of disorder in the continuously quenched patterns observed here, it is also certainly too early to reach definitive conclusions. Yet, our experiments have allowed to evidence the genericity of chains of penta–hepta defects in such patterns, as well as their role as grain boundaries between islands made of hexagonal structures with different orientations. To our knowledge, these structures have not been theoretically studied in details in the past, which might be undertaken on the basis of amplitude equations, or model order-parameter equations such as (generalized) Swift–Hohenberg and Sivashinsky-type PDEs (suitably modified to mimic the effect of varying liquid layer thickness). In addition, these chains of defects also appear to act as nuclei for the creation of new convection cells, via splitting/mitosis of (mostly heptagonal) mother cells, to yield (mostly pentagonal) daughter cells. It would also be of interest to discuss these observations in view of earlier results about the hexagons/squares transition (and associated lines of pentagons) obtained by K. Nitschke-Eckert for BM convection in non-volatile liquids [13, 14].

Finally, as far as our last question is concerned, it was already mentioned in the introduction that in view of recent results [9, 11], a formal equivalence indeed appears to exist between the full two-phase problem of a drying liquid film and the one-phase model first proposed by Pearson [10]. Namely, defining the free surface heat transfer coefficient such as to account for evaporation processes and vapor diffusion in the gas phase (including the associated latent heat exchanges between hot and cold regions of the free surface), the simplest of such generalized one-sided models has been convincingly validated by accurate experiments, as far as the threshold of instability is concerned [9]. Importantly, under quite reasonable assumptions (including a flat free surface, small gas viscous stresses, and a large gas-to-liquid thickness ratio), the influence of evaporation can be accurately described using a single additional dimensionless parameter, independent of liquid and gas depths (actually, this is the coefficient of the dimensionless wavenumber in the expression of the Biot number, as mentioned in the introduction). Hence, in addition to the usual Prandtl and Marangoni numbers, one has an additional dimensionless number, which actually turns out to allow a quantitative description of the cross-over between non-volatile liquids (critical Marangoni number of about 80) and volatile liquids in contact with their pure vapor (very large critical Marangoni number, due to the fact that the interfacial temperature is homogeneous in a one-component system, unless small kinetic effects are taken into account).

Therefore, a natural prolongation of the present work will be to examine whether the nonlinear patterns observed experimentally in drying liquid films can be rationalized in terms of these three numbers only. In particular, for a given liquid evaporating into air at ambient temperature and pressure, only the Marangoni

number (hence the supercriticality ε) is expected to vary with time (through the variation of the liquid film thickness). Provided the rate of liquid loss is not too fast (as in our experiments), the pattern transitions should be observed at values of ε independent of the evaporation rate (controlled, as in the present study, by modifying the "diffusion length" in the gas). This includes the threshold of transition between quasi-steady patterns and "interfacial turbulence" (see e.g. the time-dependent polygonal patterns with sharp boundaries predicted or observed in [5–8, 12], and also Fig. 1a), which is far from being completely understood. Such promising perspectives are associated with quite interesting fundamental questions, such as the role of (viscous and thermal) dissipation in highly supercritical surface-tension-driven convection, the direction of energy transfer between short and large-scale structures, the role of external length scales such as the liquid depth or the lateral size of the container . . .

Acknowledgement Several of the basic questions dealt with here (some of them still pending!) actually emerged already during the post-doctoral stay of the first author in Instituto Pluridisciplinar of Universidad Complutense de Madrid, where so many exciting and fruitful discussions took place not only with M.G. Velarde, but also with A.A. Nepomnyashchy, A. Rednikov, M. Bestehorn, R. Narayanan, H. Linde, L.M. Pismen, Y. Pomeau, G. Nicolis, U. Thiele, S. Kalliadasis, A. Wierschem, J. Bragard, M. Argentina, K. Eckert and V.M. Starov (non-exhaustive list). The first author is extremely grateful to M.G. Velarde for having allowed him to meet so many brilliant scientists, which, together with the exceptional scientific atmosphere of the Instituto Pluridisciplinar, have greatly contributed to his future scientific career. In addition, the authors of the present paper gratefully acknowledge financial support of ESA and BELSPO PRODEX projects, EU–FP7 MULTIFLOW Initial Training Network, ULB–BRIC, and Fonds de la Recherche Scientifique—FNRS.

References

1. Normand, C., Pomeau, Y., Velarde, M.G.: Convective instability: a physicist's approach. Rev. Mod. Phys. **49**, 581–624 (1977)
2. Cross, M.C., Hohenberg, P.C.: Pattern formation outside of equilibrium. Rev. Mod. Phys. **65**, 851–1112 (1993)
3. Bodenschatz, E., Pesch, W., Ahlers, G.: Recent developments in Rayleigh-Bénard convection. Annu. Rev. Fluid Mech. **32**, 709–778 (2000)
4. Niemela, J.J., Skrbek, L., Sreenivasan, K.R., Donnelly, R.J.: Turbulent convection at very high Rayleigh numbers. Nature **404**, 837–840 (2000)
5. Schatz, M.F., Neitzel, G.P.: Experiments on thermocapillary instabilities. Annu. Rev. Fluid Mech. **33**, 93–127 (2001)
6. Colinet, P., Legros, J.-C., Velarde, M.G.: Nonlinear Dynamics of Surface-Tension-Driven Instabilities. Wiley-VCH, Berlin (2001)
7. Nepomnyashchy, A.A., Velarde, M.G., Colinet, P.: Interfacial Phenomena and Convection. Chapman & Hall/CRC, London (2002)
8. Mancini, H., Maza, D.: Pattern formation without heating in an evaporative convection experiment. Europhys. Lett. **66**, 812–818 (2004)
9. Chauvet, F., Dehaeck, S., Colinet, P.: Threshold of Bénard-Marangoni instability in drying liquid films. Europhys. Lett. **99**, 34001 (2012)

10. Pearson, J.R.A.: On convection cells induced by surface tension. J. Fluid Mech. **4**, 489–500 (1958)
11. Haut, B., Colinet, P.: Surface-tension-driven instabilities of a pure liquid layer evaporating into an inert gas. J. Colloid Interface Sci. **285**, 296–305 (2004)
12. Merkt, D., Bestehorn, M.: Bénard-Marangoni convection in a strongly evaporating fluid. Physica D **185**, 196–208 (2003)
13. Nitschke, K., Thess, A.: Secondary instability in surface-tension-driven convection. Phys. Rev. E **52**, 5772–5775 (1995)
14. Eckert, K., Bestehorn, M., Thess, A.: Square cells in surface-tension-driven Bénard convection: experiment and theory. J. Fluid Mech. **356**, 155–197 (1998)

Pattern Formation Emerging from Stationary Solutal Marangoni Instability: A Roadmap Through the Underlying Hierarchic Structures

H. Linde, K. Schwarzenberger, and K. Eckert

1 Introduction

The complexity of interfacial convection has long exerted a pull and, at the same time, is the reason why this type of flow still belongs to the class of problems in chemical engineering and non-linear physics which are not fully resolved. This flow arises from the Marangoni instability which typically occurs when surface-active solutes, or heat, undergo a mass or heat transfer across an interface. During these processes various types of both quasi-steady and time-dependent flow structures have been observed [1–12]. This enormous diversity of patterns is responsible for the common but fuzzy term "interfacial turbulence". The foundation for a theoretical understanding of such structures was laid by Sternling and Scriven in their seminal paper in 1959 [13]. According to them, Marangoni instability can set in either via a *stationary* or an *oscillatory* mode. While most of the earliest studies show photographs of such structures emerging from the stationary mode, only the oscillatory regime has received an in-depth characterization: Linde and co-workers [14–19] first succeeded both in their heat- and mass-transfer-experiments in clearly identifying the oscillatory regime, showing signs of anomalous dispersion, and called them "Sternling–Scriven-oscillation". The main feature of these oscillatory modes is their wavelike character with three different dispersion relations (anomalous dispersion, normal dispersion and dispersion-free waves), cf. the overview given in [18, 19]. It has been proved that waves with anomalous dispersion relation—and even

H. Linde
Str. 201, Nr. 6, 13156 Berlin, Germany
e-mail: Hartmut.Linde@yahoo.de

K. Schwarzenberger · K. Eckert (✉)
Institute of Fluid Mechanics, Technische Universität Dresden, 01062 Dresden, Germany
e-mail: kerstin.eckert@tu-dresden.de

R.G. Rubio et al. (eds.), *Without Bounds: A Scientific Canvas of Nonlinearity and Complex Dynamics*, Understanding Complex Systems,
DOI 10.1007/978-3-642-34070-3_16,

dispersion-free waves—behave at moderate and highly supercritical conditions like dissipative solitons. This classification is based on the phase shift which they experience during collisions. This phase shift is negative for acute angle collisions and positive for obtuse angle collisions, i.e similar to Mach reflections at the walls. It was possible [18] to measure experimentally the critical Marangoni number in gas/liquid-systems for this oscillatory regime during stationary heat transfer following the theory of [20]. The experimental value of the critical Marangoni number $Ma_{cr} \sim 10^5$ for the onset of the instability in the nitrogen/biphenyl-system showed a good agreement between experiment and theory. It was determined for heat transfer from above when the thickness of the liquid phase was smaller than that of the boundary layer.

In contrast, the route towards the complex convection patterns starting from *stationary* primary Marangoni instability has been much less explored and is not as well understood, although several instability analyses are available [20–26]. Of those the theory developed by Reichenbach and Linde [20] correctly determined a critical Marangoni number of ~ 100 for the onset of Marangoni cells in the thermal case with a thin liquid layer. This corresponds with the classical value by Pearson [27] for the roll cell regime. The calculations were based on the material parameters of the nitrogen/biphenyl-system, which was already suited for a comparison of theory and experiment concerning the oscillatory regime, now with heat transfer from *below*. However, the validity of these theoretical works is restricted to the threshold of the Marangoni instability while typical experiments operate at high supercriticality.

The correlation between the mass transfer coefficient and the driving force for interfacial convection was estimated in numerous experimental studies in chemical engineering which are reviewed by Golovin [28]. Using scaling analysis he showed that the chaotically pulsating cells obey a linear scaling of the Sherwood number as a function of the Marangoni number, i.e. $Sh \sim Ma \cdot Sc^{-1/2}$. By contrast, the spatially ordered convective cells which are arranged in cellular networks follow a reduced $Sh \sim Ma^{1/3} \cdot Sc^{1/6}$ dependence. Scaling experiments laying between 1/3 and 1 are attributed to a combination of both chaotic and regular cells.

By critically reviewing a wide range of experimental systems sensitive to the stationary mode of the primary Marangoni instability, we propose a new classification system for highly complex and unsteady patterns. It allows us to sort all pattern classes known from the literature, such as regular or pulsating Marangoni cells [1,3,4,7,9,28] or what [1] termed "ripples" into a unified classification, consisting of a low number of generic patterns occurring at different hierarchies. We claim that a considerable part of what is called "interfacial turbulence" arises from the periodic decay and re-amplification of these structures, resembling someone climbing up and down along a step ladder. Note that other types of convection, such as density-driven instabilities, can result in complex interactions with Marangoni instabilities [9, 29–34]. For example, not only forced convection but also Rayleigh–Taylor instability can activate irregular interfacial convection both in Marangoni-unstable and even in Marangoni-stable systems [4, 9, 35]. The chaotic appearance of these coupled instabilities is another important feature falling under the topic "interfacial

turbulence". However, the concept of this report is exclusively based on systems where the density stratification remains stable during the experiment.

Most of the photographs in this work rest on published [4, 9, 36, 37] and unpublished material [38] in systems with mass transfer. The structures were made visible by means of the shadowgraph technique operating in transmission [36] through the superposed liquid–liquid systems. The non-trivial superposition of the two liquids in large three-dimensional cuvettes was conducted by means of a special apparatus [9, 16, 36]. For a low number of experiments a Hele–Shaw cell was also used [3, 39]. To characterize the system's driving force the solutal Marangoni number Ma is used as the determining parameter for interfacial convection

$$Ma = \frac{\mathrm{d}\sigma/\mathrm{d}c \cdot \mathrm{d}c/\mathrm{d}x \cdot \delta^2}{\eta \cdot D}, \tag{1}$$

where $\mathrm{d}\sigma/\mathrm{d}c$, $\mathrm{d}c/\mathrm{d}x$, δ, D and η refer to the change of interfacial tension σ with concentration c, the concentration gradient, the characteristic length, the diffusion coefficient and the dynamic viscosity. If the acting driving force is beyond the critical condition for its onset, i.e. $Ma \gg Ma_{cr}$, a nonlinear evolution of the stationary primary Marangoni instability towards the formation of the observed superstructures is possible [40].

The paper is organized as follows. In Sect. 2 we postulate our understanding of this nonlinear evolution in the form of four theses. The three main types of pattern and their different hierarchy levels are explained in Sect. 3. By choosing one system as a representative example, we demonstrate in Sect. 4 that these patterns evolve over time via periodic decays and subsequent re-amplifications. Finally, unresolved issues are summarized in Sect. 5.

2 The Central Theses

Based on a critical analysis of our own experiments and a review of the literature we claim to have identified four main pieces making up the puzzle of interfacial convection in such systems with a stationary primary Marangoni instability according to [13]:

1. Interfacial convection in these systems is built up of three basic structures: (a) Marangoni roll cells, (b) relaxation oscillations and (c) synchronized relaxation oscillation waves. Marangoni roll cells are the canonic structure which probably possess the highest kinetic energy. As the driving force decreases the cells can degenerate in either relaxation oscillations or synchronized relaxation oscillation waves.
2. Each of these structures may occur in n different hierarchy steps of different size, which we call the nth order, referring to the number of substructures which are embedded into it. Substructure(s) of all three types can occur in any of the three patterns.

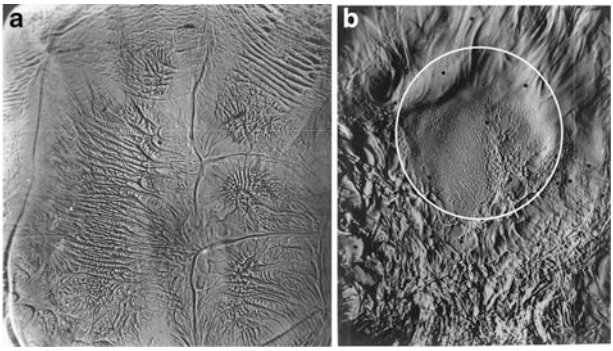

Fig. 1 (**a**) Large-scale Marangoni cells with a substructure in the form of second-order relaxation oscillation waves which are again sub-structured with smaller cells in the system *acetone/(glycerol–water mixture)* and acetic acid as the diffusing species. (**b**) Small-scale Marangoni cells in the center (*encircled*) as substructures of the spreading of third-order relaxation oscillations, surrounded by fast-moving first-order relaxation oscillations and disturbances resulting from the foregoing lively spreading in the system *benzene/water* with dioxane as the diffusing species

3. The driving force of all these structures is the Marangoni shear stress, $\mathrm{d}\sigma/\mathrm{d}c \cdot \partial c/\partial x$, operating on different length scales.
4. Interfacial convection can consist of numerous periodic cycles of amplification and decay of the three basic structures. The complexity in large containers, whose size exceeds the largest wavelength, arises from the fact that structures of different types or of a different hierarchy might occur simultaneously in different regions of the container.

In anticipation of what we are about to demonstrate, Fig. 1 illustrates some of these theses by showing

- Large-scale structures into which small-scale structures are embedded.
- The parallel existence of different sorts of pattern. In Fig. 1a these are large-scale cells and relaxation oscillation waves (again sub-structured with small cells) while in Fig. 1b cells and highly unsteady relaxation oscillations coexist.

The following four chapters substantiate these theses.

3 The Building Blocks of Interfacial Convection

3.1 Roll Cells

The quasi-stationary Marangoni roll cells are the basic structure. They are driven by a concentration difference in the transferring solute between the cell center and periphery along the interface. A higher solute concentration implies a lower

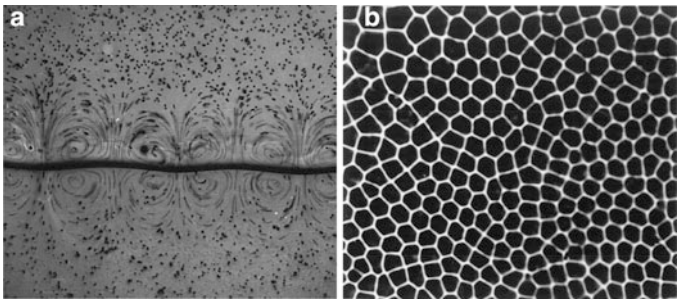

Fig. 2 *Left*: Visualization of the flow structure of Marangoni roll cells in a Hele–Shaw cell by means of tracer particles. *Right*: Network of Marangoni roll cells at an extended interface

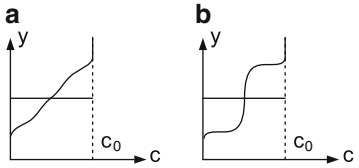

Fig. 3 Schematic showing the concentration profile normal to the interface for an active Marangoni roll cell (**a**) and shortly after the decay of the Marangoni convection (**b**). For simplicity, the partition ratio of the solute concentration between the two liquid phases was assumed to be equal to unity

interfacial tension σ for the solutes of interest there. The resulting Marangoni shear stress, $\mathrm{d}\sigma/\mathrm{d}c \cdot \partial c/\partial x$, is the driving force of convection. It can be directed both from the center towards the periphery, i.e. $\sigma_c < \sigma_p$, or vice versa. In the first case, a *c cell*, the flow at the interface is from the **c**enter towards the periphery. In the second one, a *p cell*, the interfacial flow is directed from the **p**eriphery to the center. In three-dimensional cuvettes, the *c cell* case is the most frequent [5] while the *p cells* appear only for very high Marangoni numbers. Irrespective of the orientation of the Marangoni shear stress, a toroidal Marangoni convection is driven, the boundaries of which form the cell border. Adjoining convection cells at the extended interface form a spatially fixed and dense network of polygonal cells as shown in Fig. 2b. In a two-dimensional situation, such as that in the Hele–Shaw cell, the torus degenerates into the double vortex structure, cf. Fig. 2a.

The concentration profile which feeds the active Marangoni roll cell is shown schematically in Fig. 3a. Small fluctuations create a concentration increment at the interface, which is reinforced when the Marangoni number exceeds the critical one, leading to the roll cell convection described. This convection provides an intense mixing which enhances the mass transfer and simultaneously flattens the concentration gradients. Therefore, after a while, the driving Marangoni stress falls to a sub-critical level and the roll cell breaks down, cf. Fig. 3b. In the subsequent relaxation time the concentration gradient is restored by diffusion and the cycle starts again. This process is particularly noteworthy if the experimental container

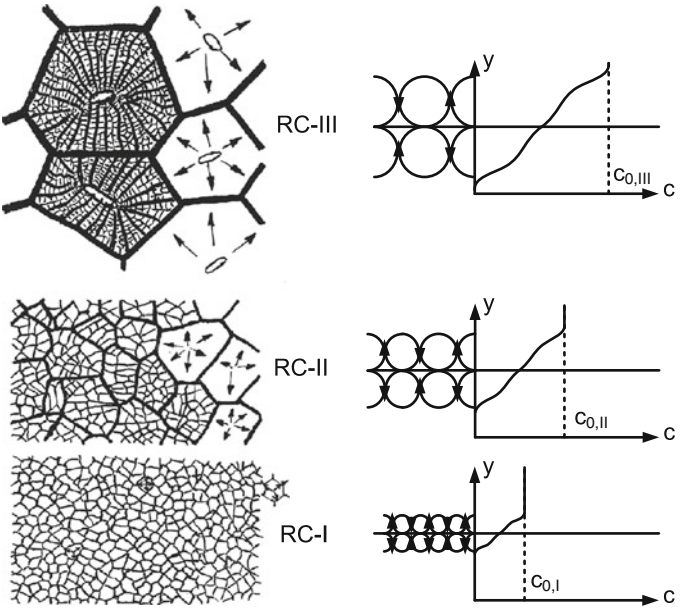

Fig. 4 Schematic showing different orders of Marangoni roll cells with their corresponding concentration profiles normal to the interface

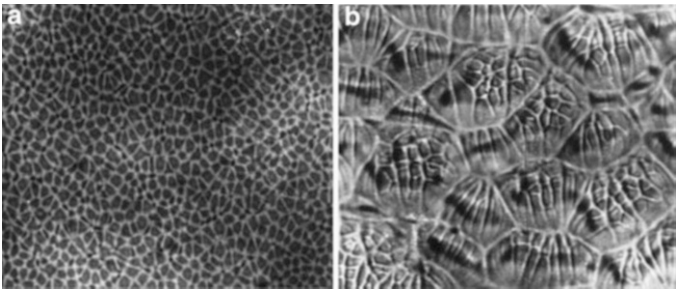

Fig. 5 Marangoni roll cells of the first (**a**) and second order (**b**) in the system *cyclohexanol/water* with butanol as the diffusing species

matches the wavelength of the convection unit, i.e. the roll cell occupies the whole interface. In that case, the decays and re-amplifications succeed in a strictly periodic manner.

Depending on the characteristic length scales across which significant σ differences occur, different hierarchy levels are attained, schematically depicted in the cartoon in Fig 4. The arrows which are drawn in some cells mark the quasi-stationary flow from the center to the periphery. Marangoni roll cells of the first order, in the following abbreviated as *RC-I*, are the smallest ones and not substructured, as can be seen in Fig. 5a. They occur when the critical Marangoni

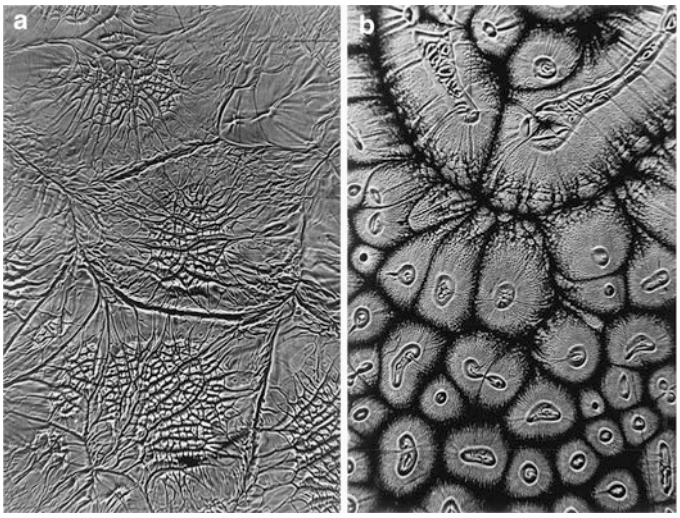

Fig. 6 (**a**) Third-order Marangoni roll cells in the system *acetone/(glycerol–water mixture)* (**b**) and different concentrations of acetic acid as the diffusing species

number is exceeded. The typical size distribution ranges from 0.1 to 5 mm. As the Marangoni number increases, second- or third-order roll cells may appear. The *RC-IIs* (Fig. 5b) are characterized by the presence of one substructure in its interior. This can be an *RC-I* or equally a first-order relaxation oscillation or a first-order relaxation oscillation wave (see later). This substructure is instantaneously formed at the place where the bulk flow driven by the Marangoni stress impinges on the interface. From there it is advected by the larger-scale Marangoni convection of the higher hierarchy level, here of the second order, towards the periphery (in case of a *c cell*). Thereby, the size of the advected substructure increases with its residence time at the interface. Finally, in the region where the downflow from the interface to the bulk occurs, the substructure is compressed.

The third-order roll cells (*RC-III*) underlie the same mechanisms as *RC-IIs*. However, they now host two drifting substructures. Figure 6 shows two examples for the case where the substructure consists exclusively of *RC-Is* and *RC-IIs*. In contrast to *RC-IIs*, the stronger interfacial convection leads to a ladder-like structure elongated along the flow direction. Furthermore, distinct deformations of the concentration distribution and, to some extent, of the interface itself occur around the place where the bulk fluid impinges on the interface (cf. Fig. 6b). This figure also shows clearly the coarsening which the substructure undergoes during its advection from the center towards the periphery.

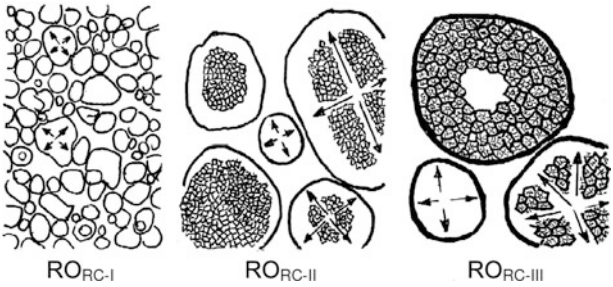

Fig. 7 Schematic showing relaxation oscillations (RO_{RCs}) of the first to third orders. The *arrows* indicate the direction of the spreading motion

3.2 Chaotic Relaxation Oscillations

The second pattern we have identified is the relaxation oscillation of Marangoni roll cells (RO_{RC}) which appear in a chaotic manner if the container size is much larger than the size of the individual convection units. Again, different hierarchy levels can be attained, the basic features of which are shown schematically in Fig. 7. In principle, $RO_{RC\text{-}Is}$ to $RO_{RC\text{-}IIIs}$ are considered as higher-frequency decays and re-amplifications of individual *RCs* of the same hierarchy class, i.e. *RC-I* to *RC-III*. In other words, the toroidal flow of the *RCs* cannot develop completely and it degenerates into a spreading motion along the interface. Therefore, the appearance of the chaotic RO_{RCs} differs in several respects from that of the quasi-stationary *RCs*. In contrast to the *RCs*, the borders of contiguous RO_{RCs} are round instead of polygonal and move unsteadily in space. If this spreading motion is locally limited by external walls, the frequency spectrum of these RO_{RCs} can be tuned from a multi-mode chaotic one into a more regular one consisting of a few number of modes, only, e.g. see [33].

The spreading motion is indicated with arrows in some convection units in Figs. 7 and 8. After the spreading area reaches its maximum extent, the forcing is insufficient to sustain a further spreading and the motion ceases. Thus, the RO_{RCs} can either occur as an eruptive interfacial motion arising autonomously in time and space or as a pulsating network, as nicely shown in Fig. 8a. In that case, individual relaxation oscillations lose the competition with neighbouring RO_{RCs} and are compressed by their spreading motion. Because the relaxation oscillations in Fig. 8a are free of any internal substructure we identify them as a first-order pattern, i.e. $RO_{RC\text{-}I}$, placed on the lowest level of the hierarchy. The $RO_{RC\text{-}IIs}$ in Fig. 8b host small Marangoni roll cells which are advected by the large-scale spreading motion. An example of a $RO_{RC\text{-}III}$ with a substructure of *RC-IIs* and *RC-Is* is shown in Fig. 8c wherein the superimposed interfacial flow again leads to a ladder-like alignment of the embedded *RC-I*, most notably in the middle of the image.

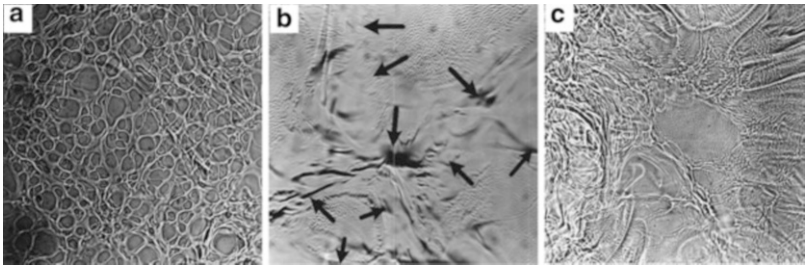

Fig. 8 (**a**) Pulsating $RO_{RC\text{-}Is}$ in the system *isoamyl alcohol/water* with sodium dodecyl sulfate as the diffusing species. (**b**) $RO_{RC\text{-}IIs}$ in the system *benzene/water* with dioxane as the diffusing species. The spreading direction is indicated by *arrows*. The substructure in the form of *RC-Is* is visible. (**c**) $RO_{RC\text{-}IIIs}$ in the same system as in (**b**). The substructure consists of *RC-IIs* and *RC-Is*

The RO_{RCs} have a considerably shorter lifetime than their quasi-stationary *RC* counterparts. The reason is probably that the timespan for which the Marangoni stress can be sustained is shorter or of the order of the eddy-turnover time of the Marangoni torus in the *RC*. This may occur when the delivery of the diffusing species is not sufficient to sustain the critical condition for the stationary state any more [37, 40]. Therefore, we assume that the RO_{RCs} require a smaller driving Marangoni shear stress than the *RCs* and hence locate this type of pattern on a lower level in the order of regimes.

3.3 Synchronized Relaxation Oscillation Waves

The most peculiar structure, significantly differing from the foregoing ones, is that of what we call synchronized relaxation oscillation waves, *ROWs*. Figure 9 shows examples of *ROW-Is*. The waves are free of any substructure in between, therefore being termed first-order. Mostly, they appear as planar (a) or concentric waves (b), the latter being nothing else than what [1] termed *ripples*. Both types are divided by nearly equidistant relaxation zones and can occur either as the prevailing structure or in the form of a substructure. The *ROWs* feature another interesting phenomenon depicted in Fig. 9c. Disturbances from surrounding structures, such as chaotic $RO_{RC\text{-}Is}$, cause the broken wave fronts to adopt a spiral form. A trend towards spiral-shaped waves is also observed at the open ends of *ROW-Is* generated by nucleation. The existence of a tendency to form spirals is already known from the chemical waves of reaction-diffusion systems such as the Belousov–Zhabotinsky reaction [41, 42]. This analogy supports the classification of the *ROWs* as an essentially new category of interfacial convection.

This wavelike type of Marangoni convection can also develop under sub-critical conditions when disturbing eddies are absent, i.e. if the driving force is too low for cellular convection. Typically, the *ROWs* appear either as a product of ageing

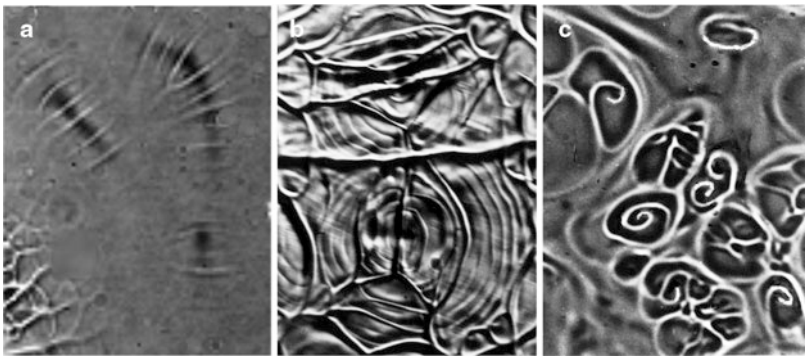

Fig. 9 (**a**) Planar *ROW-I*, in the system *cyclohexanol/water* with butanol as the diffusing species. (**b**) Substructure of concentric *ROW-I* in the system *acetone/(glycerol–water mixture)* and acetic acid as the diffusing species. (**c**) Spiral chaos due to broken waves in the system *isoamyl alcohol/water* with sodium dodecyl sulfate as the diffusing species

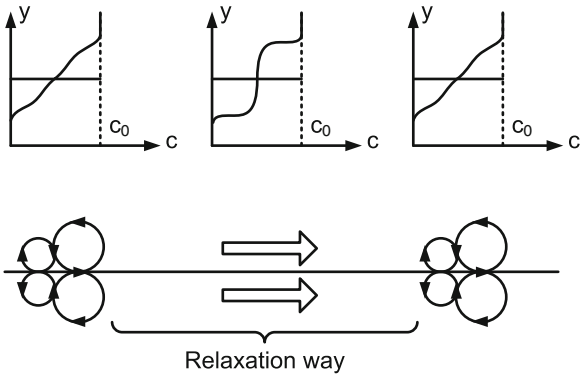

Fig. 10 Schematic showing basic features of the synchronized relaxation oscillation waves (*ROWs*) and the underlying concentration profiles normal to the interface

and decaying *RCs* or through a synchronization of RO_{RCs}. Another possibility is the nucleation of *ROW-Is* in relaxation zones after the decay of other structures. Obviously, they are an efficient way to exploit weaker Marangoni stresses which are not sufficient to drive either *RCs* or RO_{RCs}. Figure 10 shows elementary features of the waves, which differ from the cellular convection typically considered as the embodiment of stationary Marangoni instability. The flow profile is considered *asymmetric* in the direction of travel. Indeed, the shape of the *ROWs* might be more complex than the scheme in this drawing. For instance, there are signs of a secondary convection on a larger scale around a cluster of travelling *ROWs*. Note e.g. the dark line in Fig. 9a which appears at the back of one such cluster going through the middle of the individual waves. Furthermore, boundaries between clusters of *ROWs* have been observed in some experiments. Both lines indicate a concentration gradient which may force a convection directed towards the interface at the back line and into the phases at the periphery of the *ROWs*.

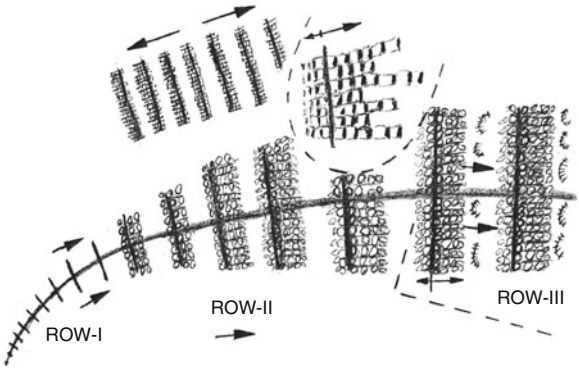

Fig. 11 Schematic showing the route of progressive sub-structuring of *ROW*'s

The interfacial convection underlying the *ROWs* consumes its driving concentration gradient while travelling along the interface. The relatively small concentration gradients needed for this sort of pattern are easily restored by diffusion along the relaxation way so that the next wave follows after a short distance, as depicted in Fig. 10. The process of the consumption and regeneration of the driving force was already discussed for simple Marangoni roll cells in Sect. 3.1. However, there is a difference in the periodicity for the travelling *ROWs*. While the cells are re-amplified after a certain relaxation *time* of sub-critical Marangoni stress, the progression of the Marangoni driving force in the *ROWs* now depends on their *location*.

A sub-structuring of *ROWs* takes place either by the amplification of lower-order *ROWs* or by a transition from higher-order *RCs* and RO_{RCs}. Figure 11 overviews the route of progressive sub-structuring until the third order, *ROW-III*, is reached. The wavelength of the *ROWs* grows along this route. Together with the formation of the sub-structure, the visual impression of this process resembles the development of a feather. *ROW-II* is sub-structured by *RC-Is* with a ladder-like alignment due to the higher-order interfacial convection. According to the asymmetric flow (cf. Fig. 10), the sub-structure is mainly located ahead of the wave front with a smaller part behind it. For *ROW-III* an additional sub-structuring occurs in the relaxation zones where smaller clusters of *ROW-II* are formed. Examples of *ROW-II* and *ROW-III* are shown in Figs. 12 and 13. Note the existence of the nearly equidistant relaxation zones at every hierarchy level, with the driving force being exhausted behind the waves and restored in front of them.

4 Time-Sequence of Structure Formation

Based on the three canonic structures, *RC*, RO_{RC} and *ROW*, it is possible to describe any experiment with solvents/solutes sensitive to stationary primary Marangoni instability according to [13] if other types of density-driven convection such as the Rayleigh–Taylor instability are absent. This affords the possibility to characterize

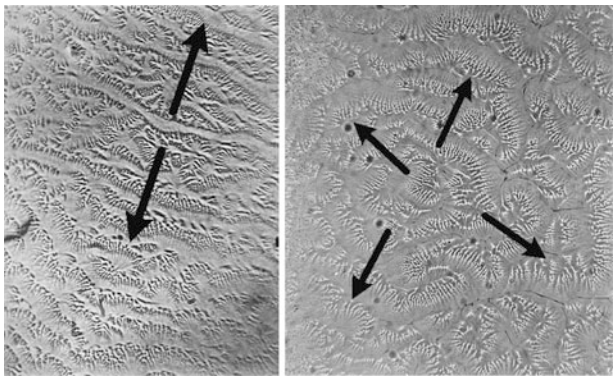

Fig. 12 Different examples for *ROW-II* in the system *isoamyl alcohol/water* with methanol as the diffusing species. The direction of travel is indicated by *arrows*

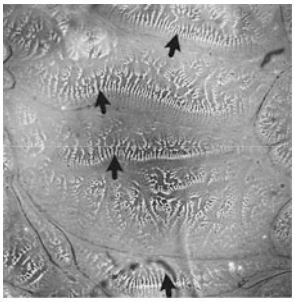

Fig. 13 *ROW-III* in the system *isoamyl alcohol/water* with methanol as the diffusing species. *Black arrows* show the direction of travel

the sequence of patterns with the help of a diagram as depicted in Fig. 14. This scheme contains the generic structures in their different hierarchy levels ordered qualitatively according to the probable level of the Marangoni stress which we assume to be responsible for the respective structure. Generally, the type of structure which can be attained depends on the Marangoni stress acting on the system. Furthermore, some structures may also be skipped during the re-amplification or decay of the convection. Due to the extension of the interface, the intensity of the large-scale Marangoni convection varies locally. This allows for new branches of temporal evolution in a single experiment whereby diverse structures may coexist in different regions of the interface. Hence, the scheme in Fig. 14 should not be considered as a fixed chronology but rather as a roadmap where every system follows its own path in the course of its nonlinear evolution.

The first excitation of the instabilities after the shock-like superposition of both phases is omitted in the description of a system's cycle. Here, extremely high concentration gradients operate in a small boundary layer. As a result, an "initial oscillation" can be observed in many systems. This oscillation acts for a short time span in the form of spreading movements without a substructure, which decay and

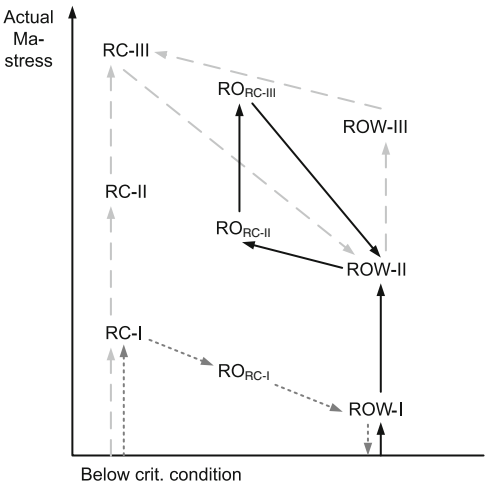

Fig. 14 Schematic showing the order of structures according to their underlying driving force. Routes for different experimental systems are inserted

revive in a high frequency. The wavelength of these spreadings roughly matches the thickness of the boundary layer.

The fading of the initial oscillation is usually succeeded by the instability cascade moving up and down several times at which point the re-amplifications start via the lower-order structures. The decays can either be complete, i.e. falling below the critical condition for the onset of any interfacial convection, or they can cease at intermediate states. As this repeating process comprises several hierarchical levels, we refer to it as a hyper-cycle. The lines in Fig. 14 describe examples of different hyper-cycles. One of those characteristic sequences, the solid line, is detailed by the corresponding shadowgraph images in Fig. 15. The relevant material data of the underlying chemical system *benzene/water* with dioxane as the diffusing species, is summarized in Table 1.

Vivid eruptive motions in the form of third-order relaxation oscillations, $RO_{RC\text{-}IIIs}$, cover the interface in Fig. 15a, then they decay in Fig. 15b. In Fig. 15c, the relaxation oscillations are replaced by patches of *ROW-II*. In between, there are regions of a calm interface where a further nucleation of waves can occur. The motion of the waves can be seen nicely in Fig. 15d, e. The waves are already distorted in Fig. 15f by the re-excitation of the chaotic relaxation oscillations $RO_{RC\text{-}II}$ which become dominant in Fig. 15g. Figure 15h shows the amplification of the relaxation oscillations until the third order, $RO_{RC\text{-}III}$, is reached again in Fig. 15i.

By tuning the driving force, hyper-cycles of a higher order (dashed line) or lower order (dotted line) can be achieved in Fig. 14. For instance, by choosing a high solvent viscosity, one restricts the system to the lowest steps. In turn, increasing the surface activity or the concentration of the diffusing species, more hierarchy levels become accessible.

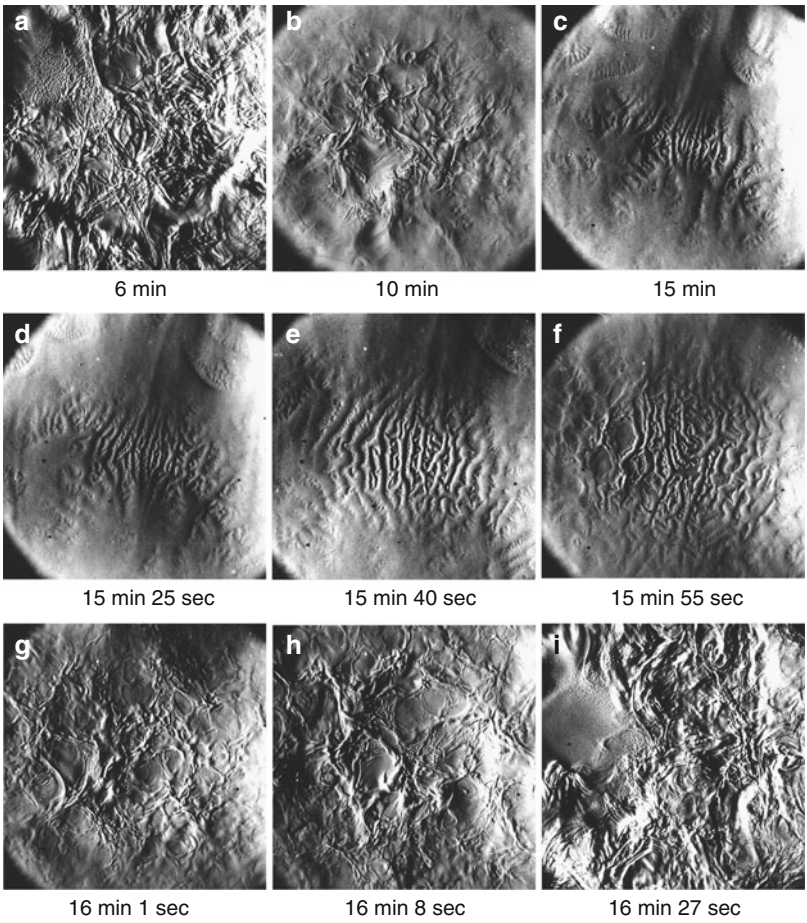

Fig. 15 Time series of pattern formation in the system *benzene/water* with 10% dioxane. The time after the contact of the phases is indicated under the respective images

Table 1 Material data for the system *benzene/water* with dioxane as the diffusing species at 20°C: kinematic viscosity ν, density ρ and interfacial tension at phase equilibrium σ_{eq} with benzene as the second phase

	$\nu\,[10^{-6}\,\mathrm{m^2/s}]$	$\rho\,[10^{3}\,\mathrm{kg/m^3}]$	$\sigma_{eq}\,[10^{-3}\,\mathrm{N/m}]$
Benzene saturated with water	0.74	0.879	
Water saturated with benzene	1.00	0.999	31.3
Water + 5% dioxane saturated with benzene	1.11	1.004	24.8
Water + 10% dioxane saturated with benzene	1.22	1.008	21.4

5 Outlook

In this work, structure was given to several aspects of interfacial convection, thereby providing a clearer overview of the sometimes confusing diversity of the so-called "interfacial turbulence"-problem. However, several questions remain open. The hierarchy of the basic structures according to their underlying driving force was proposed based on ideas suggested by experimental observation, but shall not be regarded as a proven fact. One of the most exciting issues is the selection of distinctly different sorts of pattern, such as RO_{RC} and *ROW*, during the nonlinear evolution. It is likely that those structures are preferred which dissipate available resources most effectively. However, neither the transition between these pattern, nor the velocity field of the RO_{RCs} and *ROWs* are really understood. Detailed velocity measurements [43] have the potential to advance our understanding of the corresponding internal processes.

Acknowledgement The financial support for two of us (K.S. and K.E.) by the Deutsche Forschungsgemeinschaft in the form of the Priority Programme 1506 and by Deutsches Zentrum für Luft- und Raumfahrt (Grants no. 50WM0638 and 50WM1144) is gratefully acknowledged.

References

1. Orell, A., Westwater, J.W.: Spontaneous interfacial cellular convection accompanying mass transfer: ethylene glycol – acetic acid – ethyl acetate. AIChE J. **8**, 350–356 (1962)
2. Sawistowski, H., Goltz, G.: The effect of interface phenomena on mass-transfer rates in liquid-liquid extraction. Chem. Eng. Res. Des. **41**, 174–181 (1963)
3. Linde, H., Pfaff, S., Zirkel, C.: Strömunguntersuchungen zur hydrodynamischen Instabilität flüssig-gasförmiger Phasengrenzen mit Hilfe der Kapillarspaltmethode. Z. für Phys. Chemie **225**, 72–100 (1964)
4. Linde, H., Schwarz, E.: Untersuchungen zur Charakteristik der freien Grenzflächenkonvektion beim Stoffübergang an fluiden Grenzen. Z. für Phys. Chem. **224**, 331–352 (1963)
5. Linde, H., Schwarz, E.: Über grossräumige Rollzellen der freien Grenzflächenkonvektion. Monatsberichte Deutsche Akad. der Wiss. Berl. **7**, 330–338 (1964)
6. Austin, L., Ying, W., Sawistowski, H.: Interfacial phenomena in binary liquid-liquid systems. Chem. Eng. Sci. **21**, 1109–1110 (1966)
7. Bakker, C.A.P., van Buytenen, P.M., Beek, W.J.: Interfacial phenomena and mass transfer. Chem. Eng. Sci. **21**, 1039–1046 (1966)
8. Thomas, W., Nicholl, E. McK.: An optical study of interfacial turbulence occurring during the absorption of CO_2 into monoethanolamine. Chem. Eng. Sci. **22**, 1877–1878 (1967)
9. Schwarz, E.: Zum Auftreten von Marangoni-Instabilität. Wärme Stoffübertrag. **3**, 131–133 (1970)
10. Imaishi, N., Fujinawa, K.: An optical study of interfacial turbulence accompanying chemical absorption. Int. J. Chem. Eng. **20**, 226–231 (1980)
11. Agble, D., Mendes-Tatsis, M.: The effect of surfactants on interfacial mass transfer in binary liquid-liquid systems. Int. J. Heat Mass Transf. **43**, 1025–1034 (2000)
12. Sun, Z.F., Yu, K.T., Wang, S.Y., Miao, Y.Z.: Absorption and desorption of carbon dioxide into and from organic solvents: Effects of Rayleigh and Marangoni instability. Ind. Eng. Chem. Res. **41**, 1905–1913 (2002)

13. Sternling, C.V., Scriven, L.E.: Interfacial turbulence: Hydrodynamic instability and the Marangoni effect. AIChE J. **5**, 514–523 (1959)
14. Loeschcke, K., Schwarz, E., Linde, H.: Ein oszillatorisches Regime der Marangoni-Instabilität. Abhandlungen Dtsch. Akad. Wiss. Berl. **6b**, 720–733 (1966)
15. Linde, H., Loeschcke, K.: Rollzellen und Oszillation beim Wärmeübergang zwischen Gas und Flüssigkeit. Zellgrössen und Frequenzen im Vergleich mit der Theorie der Marangoni Instabilität von Sterling und Scriven. Chem. Ing. Tech. **39**, 65–74 (1967)
16. Linde, H., Schwarz, E., Gröger, K.: Zum Auftreten des oszillatorischen Regimes der Marangoni-Instabilität beim Stoffübergang. Chem. Eng. Sci. **22**, 823–836 (1967)
17. Linde, H., Kunkel, M.: Einige neue qualitative Beobachtungen beim oszillatorischen Regime der Marangoni-Instabilität. Heat Mass Transf. **2**, 60–64 (1969)
18. Linde, H., Velarde, M.G., Wierschem, A., Waldhelm, W., Loeschcke, K., Rednikov, A.Y.: Interfacial wave motions due to Marangoni instability. J. Colloid Interface Sci. **188**, 16–26 (1997)
19. Linde, H., Velarde, M.G., Waldhelm, W., Loeschcke, K., Wierschem, A.: On the various wave motions observed at a liquid interface due to Marangoni stresses and instability. Ind. Eng. Chem. Res. **44**, 1396–1412 (2005)
20. Reichenbach, J., Linde, H.: Linear perturbation analysis of surface-tension-driven convection at a plane interface (Marangoni instability). J. Colloid Interface Sci. **84**, 433–443 (1981)
21. Hennenberg, M., Bisch, P., Vignes-Adler, M., Sanfeld, A.: Mass transfer, Marangoni effect, and instability of interfacial longitudinal waves: I. Diffusional exchanges. J. Colloid Interface Sci. **69**, 128–137 (1979)
22. Hennenberg, M., Bisch, P., Vignes-Adler, M., Sanfeld, A.: Mass transfer, Marangoni effect, and instability of interfacial longitudinal waves. II. Diffusional exchanges and adsorption-desorption processes. J. Colloid Interface Sci. **74**, 495–508 (1980)
23. Mendes-Tatsis, M.A., Perez De Ortiz, E.S.: Marangoni instabilities in systems with an interfacial chemical reaction. Chem. Eng. Sci. **51**, 3755–3761 (1996)
24. Slavtchev, S., Hennenberg, M., Legros, J.-C., Lebon, G.: Stationary solutal Marangoni instability in a two-layer system. J. Colloid Interface Sci. **203**, 354–368 (1998)
25. Nepomnyashchy, A.A., Velarde, M.G., Colinet, P.: Interfacial phenomena and convection. Chapman & Hall/CRC, Pitman Series, Boca Raton (2002)
26. Slavtchev, S., Kalitzova-Kurteva, P., Mendes, M.: Marangoni instability of liquid-liquid systems with a surface-active solute. Colloids Surf. A Physicochem. Eng. Asp. **282–283**, 37–49 (2006)
27. Pearson, J.: On convection cells induced by surface tension. J. Fluid Mech. **4**, 489–500 (1958)
28. Golovin, A.: Mass transfer under interfacial turbulence: Kinetic regulaties. Chem. Eng. Sci. **47**, 2069–2080 (1992) (and references therein)
29. Berg, J.C., Morig, C.R.: Density effects in interfacial convection. Chem. Eng. Sci. **24**, 937–946 (1969)
30. Gumerman, R.J., Homsy, G.M.: Convective instabilities in concurrent two phase flow: Part I. Linear stability. AIChE J. **20**, 981–988 (1974) (and the subsequent articles in this series)
31. Tanny, J., Chen, C.C., Chen, C.F.: Effects of interaction between Marangoni and double-diffusive instabilities. J. Fluid Mech. **303**, 1–21 (1995)
32. Grahn, A.: Two-dimensional numerical simulations of Marangoni-Bénard instabilities during liquid-liquid mass transfer in a vertical gap. Chem. Eng. Sci. **61**, 3586–3592 (2006)
33. Sczech, R., Eckert, K., Acker, M.: Convective instability in a liquid-liquid system due to complexation with a crown ether. J. Phys. Chem. A **112**, 7357–7364 (2008)
34. Schwarzenberger, K., Eckert, K., Odenbach, S.: Relaxation oscillations between Marangoni cells and double diffusive fingers in a reactive liquid-liquid system. Chem. Eng. Sci. **68**, 530–540 (2012)
35. Linde, H.: Versuche zur Deutung des Einflusses der erzwungenen Konvektion auf die Grenzflächendynamik beim Stoffübergang. Abhandlungen Dtsch. Akad. Wiss. Berl. **6b**, 710–719 (1966)

36. Schwarz, E.: Hydrodynamische Regime der Marangoni-Instabilität beim Stoffübergang über eine fluide Phasengrenze. Ph.D. thesis, HU Berlin (1967)
37. Linde, H., Schwartz, P., Wilke, H.: Dissipative structures and nonlinear kinetics of the Marangoni-instability. In: Dynamics and Instability of Fluid Interfaces. Springer, Berlin (1979)
38. Linde, H., Schwarz, E.: Divers photographic images. Recorded during the thesis of E. Schwarz
39. Shi, Y., Eckert, K.: A novel Hele-Shaw cell design for the analysis of hydrodynamic instabilities in liquid-liquid systems. Chem. Eng. Sci. **63**, 3560–3563 (2008)
40. Linde, H., Schwartz, P.: Zeitabhängiges Verhalten und Regelmässigkeit bei hydrodynamischen dissipativen Strukturen. Nova Acta Leopoldina NF **61**, 105–125 (1989)
41. Keener, J.P., Tyson, J.J.: Spiral waves in the Belousov-Zhabotinskii reaction. Phys. D Nonlinear Phenom. **21**, 307–324 (1986)
42. Linde, H.: Topological similarities in dissipative structures of Marangoni-instability and Belousov-Zhabotinsky-reaction. In: Self-Organization: Autowaves and Structures Far from Equilibrium, Springer, Berlin (1984)
43. Schwarzenberger, K., Köllner, T., Linde, H., Odenbach, S., Boeck, T., Eckert, K.: On the transition from cellular to wave-like patterns during solutal Marangoni convection. Eur. Phys. J. Special Topics **219**, 121–130 (2013)

Observation of the Thermocapillary Motion of a Droplet in a Laser Beam

P. López, Yu.S. Ryazantsev, R.G. Rubio, F. Ortega, M.G. Velarde, and J.M. Redondo

1 Introduction

The motion of drops and bubbles due to the thermocapillary effect is a quite known phenomenon and has been observed long before the beginning of its scientific study. The information on history and main results of the researches of the thermocapillary effect can be found, for example, in [1]. Firstly, it was studied experimentally in [2] where the approximate formula for the thermocapillary force acting on a bubble which was placed in a temperature gradient was obtained. After the pioneering work by Young et al. [2], the thermocapillary effect for drops and bubbles was studied theoretically and experimentally in many works (see, for example, [3]). A comprehensive analysis of the problem can be found in the monograph by Subramanian and Balasubramanian [4].

The thermocapillary motion is caused by the temperature dependence of the surface tension. The presence of a temperature gradient on the fluid interface causes the appearance of the gradient of the surface tension and the motion of the interface which, due to viscosity, gives rise to the motion of the fluids close to the interface.

P. López
Instituto Pluridisciplinar and Dpto. de Matemática Aplicada, Facultad de CC. Biológicas, Universidad Complutense de Madrid (UCM), Ciudad Universitaria, Madrid-28040, Spain
e-mail: maplopez@bio.ucm.es

Yu.S. Ryazantsev (✉) · M.G. Velarde
Instituto Pluridisciplinar, UCM, Paseo Juan XXIII, 1, Madrid-28040, Spain
e-mail: yriazant@aero.upm.es; mgvelarde@pluri.ucm.es

R.G. Rubio · F. Ortega
Dpto. de Química Física, Facultad de CC. Químicas, UCM, Ciudad Universitaria, Madrid-28040, Spain
e-mail: rgrubio@quim.ucm.es

J.M. Redondo
Dpto. de Física Aplicada, Universidad Politécnica de Cataluna, Campus Norte, Barcelona, Spain

R.G. Rubio et al. (eds.), *Without Bounds: A Scientific Canvas of Nonlinearity and Complex Dynamics*, Understanding Complex Systems,
DOI 10.1007/978-3-642-34070-3_17,

In the general case, the non homogeneity of the temperature distribution on the interfaces causes different types of fluid flows near the interface depending on the form of the surface and the temperature distribution. The resulting motion and the characteristics of the flow also depend on the presence of body forces, for example, gravity.

In case of a free droplet or bubble placed in other liquid, the droplet can move as a whole. The source of the traction is the gradient of the surface tension which appears due to the non-uniformity of the temperature at the liquid interface. The thermocapillary motion of the drop with constant velocity can be observed when the thermocapillary force compensates totally the hydrodynamic forces due to viscous stationary flow of the fluid out and inside the drop. The general case of such effect is the motion or quiescent state of the drop or bubble in the fluid in the presence of gravity when the sum of the thermocapillary, mass and hydrodynamic forces is equal to zero.

Up to now, most of experiments on thermocapillary movement of a single drop have been carried out in a system where the motion was initiated by an external temperature gradient (for example, the non-uniform distribution of temperature was created by solid surfaces with different temperature). But the source of the temperature gradient which causes the thermocapillary motion could be different and the non-uniform temperature field could appear due to not isothermal processes inside or at the drop surface [5, 6]. Lasers are quite effective energy sources, allowing to create the necessary non-homogeneous distribution of temperature in non-uniform liquid systems with drops and bubbles. The laser beam can supply the thermal energy at the interface surface and generate and control the gradient of the temperature which in its turn can induce the thermocapillary motion in the chosen zone [7–9]. But, apparently, in the literature there is no data on study of the movement of a single drop in a laser beam in strictly controllable conditions close to the ideal. Such data will help to specify a design procedure of processes in which laser is used as the tool for moving, crushing and coalescence of drops.

An approximate theoretical analysis of the movement of a drop or bubble in a laser beam has been made, and a simple expression for the velocity of such motion was obtained in [8, 10, 11]. The rough estimation of the velocity of the thermocapillary motion can be given using the following approximate formula [10, 11]:

$$U = \frac{1}{6}\frac{\sigma_T J}{6(2\lambda_1 + \lambda_2)(2\mu_1 + 3\mu_2)},\ \sigma_T = \left(\frac{d\sigma}{dT}\right)_{surface} \tag{1}$$

where index 1 corresponds to salt solutions and index 2 correspond to drop. The drop velocity U is expressed in terms of drop diameter per unit time (second), J is the intensity of the laser radiation flux (cal/cm^2 s), $\lambda_{1,2}$ is the thermal conductivity of the two fluids (cal/cm s °C), $\mu_{1,2}$ is the shear viscosity of the two fluids (g/cm s), σ is the surface tension (g/s^2), T is the temperature (°C), and a is the radius of the drop (cm).

The expression (1) for the velocity is based on the use of some important simplifications of the problem. The movement of the droplet is steady and it moves in an infinite space which is filled with an homogeneous fluid of constant temperature and zero velocity at infinity. The flux of the laser radiation is totally absorbed by the droplet surface, and the reflection and refraction of the rays on its surface are considered negligible. The non homogeneous distribution of the laser intensity in the cross section of the beam is supposed to be negligible. And, finally, the physical characteristics of the fluid system (viscosities, densities and thermo conductivities) are considered to be constant. Apparently, the roughest one is the assumption of the full absorption of the radiation on the surface. These simplifying assumptions show that although the simple model takes into consideration the most important characteristics of the phenomenon, it can give only a rather approximate qualitative picture of it.

2 Experimental Methodology

The experimental study of the thermocapillary motion needs experimental conditions maximally free of complicating factors and gravity places the main limitations on the kind of experiments to do (vertical temperature gradients and relatively small drops in order to minimize buoyant convection in the fluid and the gravitational contribution to the drop motion).

The buoyant convection is one of the main perturbing factors which should be avoided or compensated in the experimental research of thermocapillary movement of drops. One of the ways to avoid the natural convection is the choice of such experimental conditions in which the normal convection does not appear. It corresponds to cases which are characterized by a sufficiently small gradient of the temperature [2, 3]. Or to compensate the natural convection by the use of limiting walls [12]. Or the weightlessness condition in drop towers, sounding rockets and space laboratory, which also permit to avoid the natural convection due to microgravity conditions.

We study experimentally the thermocapillary motion of a drop in a laser beam in terrestrial conditions using the Plateau configuration: the liquid drop is placed inside a fluid system in which there is a vertical gradient of density with a very stable density interface (see Fig. 1). In this case, the drop will be suspended in a thin horizontal fluid layer of equal density and can move in it under the influence of the thermocapillary force which is provoked by the non homogeneous heating of the drop due to the thermal action of the laser beam. The use of the Plateau method makes it possible to reduce drastically the influence of buoyancy.

Figure 1 illustrates the set-up, where T_1 and T_2 are the temperatures in two opposite points of the drop, U is the thermocapillary velocity and J is the flux of laser radiation. In general, the surface tension decreases with the growth of temperature and the drop moves towards the laser beam. This figure also shows schematically the geometry of the experimental fluid system which consists of two

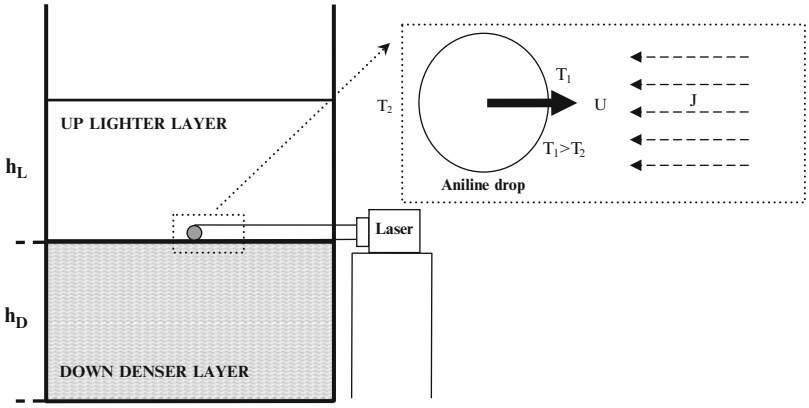

Fig. 1 Scheme of the experimental fluid system with the stable density interface and the aniline droplet on it. To zoom in the *marked square* shows the thermocapillary migration of the droplet under a laser beam of intensity J

liquid layers that are at rest inside a glass container with height H, longitude L and cross section b of 6 cm, 8 cm and 3 cm respectively. The upper layer is a low concentration salt solution of height 3 cm and density 1.019 g/cm^3 which is supposed to be not contaminated by surfactants. The bottom layer is a denser salt solution with density 1.44 g/cm^3 and height 3 cm. This experimental fluid system is characterized by a stable density interface, an horizontal plane corresponding to the density jump which will retain its position and over which a droplet will be located. The fluid of the drop is aniline, which is a colourless liquid of density 1.022 g/cm^3. The solution of the upper layer is lighter than the aniline and, therefore, the aniline drop placed in any point of the upper layer falls slowly down to reach the stable interface and, finally, stays on it.

To prepare this two fluid layer system, a thin metal tube with curved lower end (at 90°) and diameter 3 mm was introduced into the experimental container. The other end of the tube was fitted to a glass recipient with a tap. First, the glass recipient is filled with the lighter solution. Then the faucet is turned on and the lighter solution is deposited inside the experimental container. The tap is turned off. Second, the empty glass recipient is filled with the denser salt solution. The tap is turned on again, the lighter solution rises up inside the experimental container while the denser one stays down. Finally, the experimental fluid system is made by two homogeneous fluid layers separated by a stable density interface. The thermocapillary effect for aniline drops of different diameters (from 3 to 10 mm) can be studied with this experimental setup. And it can be seen that the smaller drop is spherical but the biggest one is slightly deformed. To observe the thermocapillary motion of the drop in the conditions described above, the experimental setup should satisfy a number of special requirements.

In this Plateau system with a salt concentration jump, the thermal buoyant force acting on the drop will be compensated by the step distribution of the density of

the working liquid. The initial abrupt jump of concentration between up and down fluid layers is diffused very slowly with time owing to molecular diffusion and the aniline drop will be retained very close to the horizontal stable interface. Therefore, we have a suspended drop in a brine gradient and the horizontal laser beam comes to this aniline drop, heats it non homogeneously and modifies its surface tension which induces the thermocapillary migration of the drop.

At a given choice of laser frequency, its absorption by the experimental salt solutions in the container can be sufficiently low and their heating during the experiment will be negligible and lesser than the absorption by the drop. However, the coefficient of absorption of the drop should be high enough so that the drop heating becomes non-uniform with a maximum on the forward surface of the drop. And also, the intensity of the laser beam should be sufficiently high to assure a high drop absorption.

The thermocapillary motion of the drop should be initiated by its strongly non homogeneous heating by the flux of the laser radiation coming to its surface. As a source of radiation we used the coherent Verdi V5 Laser system with a wavelength of 532 nm (green colour), an output power up to 2 W and a beam divergence less than 0.5 mrad. The initial diameter of the laser beam is equal to 2.25 mm ($\pm 10\%$) and it can be increased with the use of suitable optics.

As mentionated before, the roughest estimation is the assumption of the full absorption of the radiation by the drop surface. To obtain the optimal conditions for the observation of the thermocapillary motion, the absorption of laser radiation by the liquid of the drop should be as much as possible to ensure a strongly non homogeneous distribution of temperature on the surface drop. The working liquid aniline appears to be a suitable liquid for use in the proposed experiment because is almost immiscible in water (and salt solutions) and its absorption coefficient can be modified by adding some chemical substance.

First, we obtained the aniline absorbance spectra. A Hewlett Packard 8452A Diode Array Spectrophotometer was used which is capable of acquiring complete UV/Visible absorbance spectra. The system is a single beam instrument which permits to obtain the dependence of the absorption coefficient on wave length in standard form

$$A(\lambda) = log\left(\frac{I_o(\lambda)}{I(\lambda)}\right). \tag{2}$$

Here, I_0 and I are the initial flux and the final flux of laser radiation which passed through the cuvette with the tested liquid respectively. $A(\lambda)$ is the absorption coefficient (1/length) as a function of the wave length λ.

The absorbance spectroscopy of aniline shows that pure aniline absorbs in the K (220–250 nm) and the B (250–290 nm) bands and has a very intense absorption peak at $\lambda_{max} \approx 310$ nm. The aniline absorption of radiation with wavelength 532 nm corresponding to the Verdi V5 Laser is comparatively low (see Fig. 2).

To obtain a liquid of greater absorption, nigrosine can be added to aniline because it colours in black. Nigrosine is a dark black pigment which is used in dying of the leather, wood, inks and textiles. There are water-, alcohol- and oil-soluble

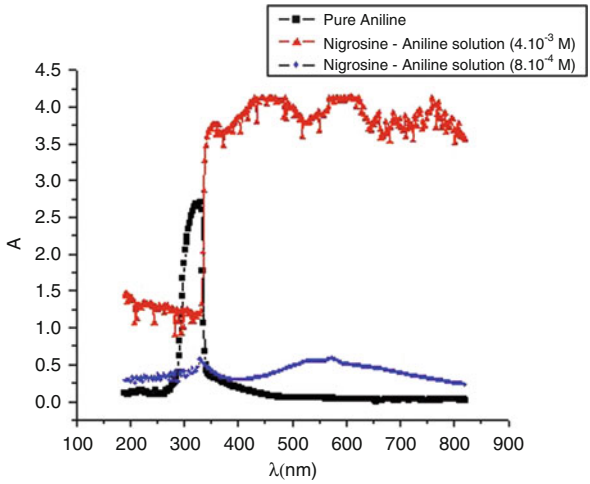

Fig. 2 Spectra of pure aniline (*black curve*) and solution of nigrosine in aniline (2.5 g/l, cuvette 1 cm width, *red curve*; 0.5 g/l, cuvette 0.1 cm width, *blue curve*)

Table 1 Absorbance of liquids used in the experiment for 532 nm

Substance	Absorbance (cm^{-1})
Pure aniline (cuvette 1 cm width)	$4.79\ 10^{-2}$
Nigrosine–aniline (2.5 g/l, cuvette 1 cm width)	$\gg 3.786$
Nigrosine–aniline (0.5 g/l, cuvette 0.1 cm width)	5.514
Water (cuvette 1 cm width)	$7.63\ 10^{-5}$

nigrosines. The alcohol-soluble one, which is a black uniform smooth powder, seems to be the more suitable in our case. When nigrosine powder is added to aniline, it colours in intense black but undissolved particles should be removed by appropriate centrifugation. The nigrosine–aniline solution has a high absorption (Fig. 2) and can be used as the liquid of the drop in the proposed experiment.

Figure 2 shows three absorbance spectra. The black line corresponds to the pure aniline absorbance spectra in a test cell with 1 cm of longitudinal dimension. The absorption peak can be seen, which is narrow and located at 330 nm.

The red curve corresponds to a nigrosine–aniline solution with 2.5 g/l with the longitudinal dimension of the probe cell equal to 1 cm. It is seen that absorption is so high that saturation is attained. Blue curve corresponds to a nigrosine–aniline solution with 0.5 g/l; the longitudinal dimension of the cell is equal to 0.1 cm. In the case of the nigrosine–aniline solution the zone of strong absorption appears located in the interval from 330 to 820 nm which includes the green line $\lambda = 532$ nm of the laser.

The analysis of the absorption of laser radiation with wavelength 532 nm shows that the absorption of the solution strongly grows with the increase of the concentration of nigrosine. Table 1 shows the absorbance coefficient of different liquids used in experiment for $\lambda = 532$ nm.

Approximate extrapolation of data about absorption of laser radiation for a solution with nigrosine concentration 0.5 g/l shows that the factor of absorption

can change from 5.514 cm^{-1} to a value of an order of 20 cm^{-1} in the range of concentration 0.5–2.5 g/l. Such level of absorption of laser radiation by aniline–nigrosine drop could make a strongly non homogeneous distribution of temperature inside it as well as at its surface and causes the thermocapillary motion of the drop.

3 Results and Discussion

The thermocapillary movement of a single droplet of nigrosine–aniline solution caused by a laser beam was observed. The experiment was filmed by a video camera. The diameter of the droplet was 5 mm. The concentration of the nigrosine–aniline solution was 0.5 g/l. The radius of the laser beam was equal to 1.125 cm, the laser power was about 700 mW and the wave length is 532 nm (a green beam).

Figure 3 shows a time sequence of frames corresponding to the experiment carried out. In the beginning the droplet has been placed on a level of neutral buoyancy and began to move after a short relaxation time due to the inclusion of the laser beam. The thermocapillary migration of the aniline droplet is evident in the time sequence of frames. During the movement the droplet keeps its spherical form and remains very close to this zero buoyancy plane in spite of its temperature change. Simple approximate estimations show that the density of the drop will be decreased. However, vertical displacement of the drop during the time interval of order 10 min will not be more than 0.4 mm.

The vertical gradient of density in the vicinity of the zero buoyancy plane was very high, because the salt concentration gradient on the drop trajectory decreases in time very slowly because of diffusion of the initial jump.

Figure 4 shows the time evolution of droplet velocity along its trajectory during the experiment. The experimental value of the drop velocity is of the same order of magnitude obtained by other studies. For example, the velocity of the thermocapillary migration is about [0.2, 0.3] mm/s under low Reynolds and thermal Marangoni numbers [12]. Finally, drop velocity is not constant or uniform in time and it follows a linear behaviour. Therefore, there is a drop acceleration which is about 3.10^{-5} cm/s^2.

The experimental conditions do not correspond exactly to the conditions in which the simple formula (1) for the velocity of the thermocapillary motion of the drop in laser beam is based. The main differences are: on the one hand in the experiment the cross section of the beam is smaller than the cross section of the drop. Secondly, the absorption coefficient of the liquid in the drop is not very high. Therefore the absorption of radiation takes place in the bulk of drop but not on the surface. Thirdly, the symmetry axes of the drop and the laser beam do not coincide all the time during the motion. In view of the above, the comparison of other experimental data on the drop velocity with the theoretical estimate based on formula (1) is not to be expected. A rough evaluation indicates that the difference can be one-or-two orders of magnitude.

Fig. 3 Time sequence with several frames. The aniline droplet, located on a stable density interface, moves towards the green laser beam, that is, in the direction of the temperature gradient

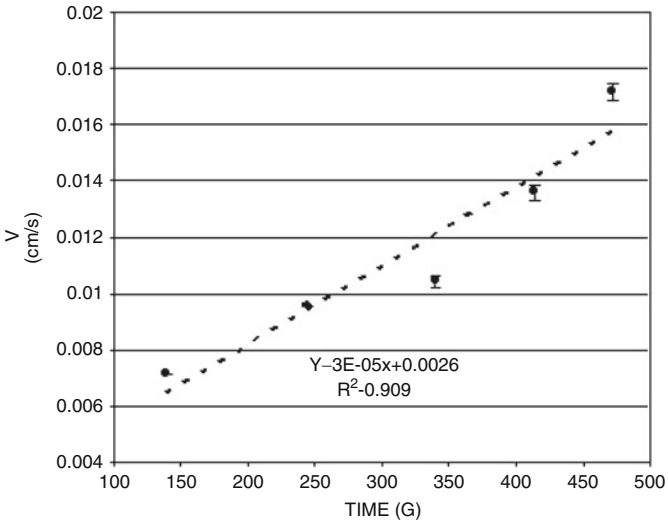

Fig. 4 Velocity of the aniline droplet related to the thermocapillary migration due to the laser heating. Drop diameter is 5 mm and laser intensity is about 700 mW. The *straight line* is fitted by least squares

4 Conclusions

The main result of this test experiment is that we observed the thermocapillary movement of a single droplet of nigrosine–aniline solution caused by a laser beam heating. This experiment seems to be the first one in which the thermocapillary

motion of a single droplet is initiated by a laser and observed in a pure form because the phenomenon was not complicated by the natural convection, gravity, the presence of other droplets, the drop vaporization or the presence of limiting walls.

The experimental velocity of the drop was about $U = 0.8 - 2.0$ diam/min.

References

1. Castagnolo, D., Monti, R.: Thermal Marangoni flow. In: Monti, R. (ed.) Physics of Fluids in Microgravity. Earth Space Institute Book Series, vol. 7, pp. 78–121. Taylor & Francis, Boca Raton (2001)
2. Young, N.O., Goldstein, J.S., Block, M.J.: The motion of bubbles in a vertical temperature gradient. J. Fluid Mech. **6**, 350–356 (1959)
3. Barton, K.D., Subramanian, R.S.: The migration of liquid drop in a vertical temperature gradient. J. Colloid Interface Sci. **133**, 211–221 (1989)
4. Subramanian, R.S., Balasubramanian, R.: The motion of bubbles and drops in reduced gravity. Cambridge University Press, Cambridge (2001)
5. Ryazantsev, Yu.S.: On thermocapillary motion of the reacting drop in chemically active surrounding. Izv. Akad. Nauk SSSR Mekhanika Zhidk. Gaza **2**, 180–183 (1985) [translated from Russian]
6. Rednikov, A.Ye., Ryazantsev, Yu.S., Velarde, M.G.: Active drop and drop motion due tu nonequilibrium phenomena. J. Non-Equilib. Thermodyn. **19**, 95–113 (1994)
7. Bezuglyi, B.A., Ivanova, N.A.: Pumping of a fluid through a microchannel by means of a bubble driven by a light beam. Fluid Dynam. **42**, 91–96 (2007)
8. Bezuglyi, B.A., Ivanova, N.A.: Creation, transportation, and coalescence of liquid drops by means of a light beam. Fluid Dynam. **41**, 278–285 (2006)
9. Subramanian, R.S., Balasubramaniam, R.: The motioons of bubbles and drops in reduced gravity. Cambridge University Press, Cambridge (2001)
10. Oliver, D.L.R., DeWitt, K.J.: Surface tension driven flows for a droplet in a microgravity environment. Int. J. Heat Mass Transf. **31**, 1534–1537 (1988)
11. Rednikov, A.Ye., Ryazantsev, Yu.S.: On thermocapillary motion of a drop under action of a radiation. J. PMTF **2**, 179–183 (1989)
12. Bratukhin, Yu.K., Kostarev, K.G., Viviani, A., Zuev, A.L.: Experimental study of Marangoni bubble migration in normal gravity. Exp. Fluids **38**, 594–605 (2005)

Influence of Heat Flux Modulation on Thermocapillary Instability in a Binary Mixture with the Soret Effect

I.S. Fayzrakhmanova, S. Shklyaev, and A.A. Nepomnyashchy

1 Introduction

Since the pioneering paper by Faraday [1], the behavior of fluids under external periodic actions has been a focus of interest. One of the reasons of this persistent attention is a variety of eigen-oscillations inherent to fluids and, therefore, a possibility of excitation of different kinds of resonances. In the context of the Marangoni convection these researches were initiated by Gershuni et al. [2], the survey of the results can be found in [3].

As one of the above-mentioned eigen-oscillations, the longwave Marangoni oscillatory convection in a binary liquid layer [4] can be mentioned. In [5] and [6] we studied the behavior of this system under low-frequency vibration. However, modulation of a heat flux on the lower boundary, which is the subject of the present paper, can be simpler accomplished experimentally and studied theoretically.

The chapter is organized as follows. We start with the problem statement in Sect. 2; the base state is found and the stability problem is formulated. Sections 3

I.S. Fayzrakhmanova
Department of Mathematics, Technion – Israel Institute of Technology, Haifa 32000, Israel

Department of General Physics, Perm State Technical University, Perm 614990, Russia

S. Shklyaev
Institute of Continuous Media Mechanics, Ural Branch of Russian Academy of Sciences, Perm 614013, Russia

A.A. Nepomnyashchy (✉)
Department of Mathematics, Technion – Israel Institute of Technology, Haifa 32000, Israel

Minerva Center for Nonlinear Physics of Complex Systems, Technion – Israel Institute of Technology, Haifa 32000, Israel
e-mail: nepom@techunix.technion.ac.il

R.G. Rubio et al. (eds.), *Without Bounds: A Scientific Canvas of Nonlinearity and Complex Dynamics*, Understanding Complex Systems,
DOI 10.1007/978-3-642-34070-3_18, © Springer-Verlag Berlin Heidelberg 2013

and 4 are devoted to the analysis of the problem for longwave and shortwave perturbations, respectively. Brief summary of the results is presented in Sect. 5.

2 Problem Statement and Governing Equations

We consider an infinite layer of an incompressible binary liquid of thickness d. At the lower rigid boundary ($z = 0$) the heat flux is modulated with an amplitude $k_{th}B$ and frequency Ω about its mean value $k_{th}a$. (Here k_{th} is the thermal conductivity, therefore $-a$ has the meaning of the mean vertical temperature gradient and B is the amplitude of its oscillation.) At the upper free nondeformable surface the thermal flux is kept equal to $k_{th}a$. When the deviations of the temperature and concentration from their respective reference values C_* and T_* are sufficiently small, the surface tension σ can be linearized as follows:

$$\sigma(T, C) = \sigma_0 - \sigma_T(T - T_*) + \sigma_C(C - C_*). \tag{1}$$

The temperature gradient induces a gradient of solute concentration owing to the presence of the Soret effect.

We choose κ/d, d^2/κ, d, ad, $\sigma_T ad/\sigma_C$, $\rho\nu\kappa/d^2$ as the scales for the velocity, time, length, temperature, solute concentration, and pressure, respectively. Here κ, ν, and ρ are the thermal diffusivity, kinematic viscosity, and density of the mixture, respectively.

The dimensionless boundary value problem governing the motion of the binary liquid reads

$$\nabla \cdot \mathbf{v} = 0, \tag{2}$$

$$\frac{\partial \mathbf{v}}{\partial t} + \mathbf{v} \cdot \nabla \mathbf{v} = P\left(-\nabla p + \nabla^2 \mathbf{v}\right), \tag{3}$$

$$\frac{\partial T}{\partial t} + \mathbf{v} \cdot \nabla T = \nabla^2 T, \tag{4}$$

$$\frac{\partial C}{\partial t} + \mathbf{v} \cdot \nabla C = L\left(\nabla^2 C + \chi \nabla^2 T\right), \tag{5}$$

$$\begin{aligned} \mathbf{v} = 0,\ \partial_z T = -(1 + b\cos\omega t), \\ \partial_z C = \chi(1 + b\cos\omega t) \text{ at } z = 0, \end{aligned} \tag{6}$$

$$w = 0,\ \partial_z \mathbf{u} = -M\nabla_2(T - C),\ \partial_z T = -1,\ \partial_z C = \chi \text{ at } z = 1, \tag{7}$$

where $\mathbf{v} = \mathbf{u} + w\mathbf{e}_z$, ∇_2 stands for a two-dimensional projection of the gradient operator onto the plane $x - y$, the rest of notations are conventional.

The boundary value problem (2)–(7) is governed by six dimensionless parameters

$$P = \frac{\nu}{\kappa},\ L = \frac{D}{\kappa},\ M = \frac{\sigma_T a d^2}{\nu \rho_0 \kappa},\ \chi = \frac{\alpha_D \sigma_C}{\sigma_T},\ b = \frac{B}{a},\ \omega = \frac{d^2 \Omega}{\kappa}, \tag{8}$$

which are the Prandtl, Lewis, Marangoni, Soret numbers, the amplitude and frequency of the heat flux modulation, respectively. Here D is the mass diffusivity, α_D is the Soret coefficient.

This boundary value problem has a solution corresponding to the quiescent fluid

$$\mathbf{v}_0 = 0,\ T_0 = -z + b\mathrm{Re}\left[e^{i\omega t}\frac{\cosh\alpha(1-z)}{\alpha\sinh\alpha}\right],$$
$$C_0 = \chi z + b\chi\mathrm{Re}\left\{\frac{e^{i\omega t}}{\alpha^2-\gamma^2}\left[\frac{\gamma\cosh\gamma(1-z)}{\sinh\gamma} - \frac{\alpha\cosh\alpha(1-z)}{\sinh\alpha}\right]\right\}, \tag{9}$$

where $\alpha = \sqrt{i\omega}$, $\gamma = \sqrt{i\omega/L}$. Below we are interested in the stability analysis of this state for a low-frequency modulation, $\omega \ll \min\{1, P, L\}$. Therefore, omitting $O(\omega)$ terms one can reduce (9) to

$$T_0 \approx -z + b\frac{\sin\omega t}{\omega} + b\cos\omega t\frac{2-6z+3z^2}{6},$$
$$C_0 \approx \chi z - \chi b\cos\omega t\frac{2-6z+3z^2}{6}. \tag{10}$$

The first term in the oscillatory part of the temperature is large ($\sim \omega^{-1}$); its origin is clear: during the first (last) half of the period $0 < t < \pi/\omega$ ($\pi/\omega < t < 2\pi/\omega$), which is large, the heat flux on the bottom directed to the layer is positive (negative), leading to a strong increase (decrease) in the mean temperature. However, this term is spatially uniform and therefore it does not influence the layer stability.

In order to study the stability of the base state (9) with respect to infinitesimal two-dimensional disturbances, we linearize (2)–(7) around the base state and represent an arbitrary field f of perturbations in the form

$$f(t, x, z) = e^{ikx}\tilde{f}(t, z), \tag{11}$$

with a wavenumber k. The evolution of small perturbations is governed by the following boundary value problem:

$$\frac{\partial\Delta\tilde{\psi}}{\partial t} = P\Delta^2\tilde{\psi}, \tag{12}$$
$$\frac{\partial\tilde{T}}{\partial t} = ik\tilde{\psi}\frac{\partial T_0}{\partial z} + \Delta\tilde{T}, \tag{13}$$

$$\frac{\partial \tilde{C}}{\partial t} = ik\tilde{\psi}\frac{\partial C_0}{\partial z} + L\left(\Delta\tilde{C} + \chi\Delta\tilde{T}\right), \tag{14}$$

$$\tilde{\psi} = \partial_z\tilde{\psi} = \partial_z\tilde{T} = \partial_z\tilde{C} = 0 \text{ at } z = 0, \tag{15}$$

$$\tilde{\psi} = \partial_z\tilde{T} = \partial_z\tilde{C} = 0,\ \partial_z^2\tilde{\psi} = -ikM(\tilde{T} - \tilde{C}) \text{ at } z = 1, \tag{16}$$

where $\Delta \equiv \partial_z^2 - k^2$ and the stream function $\tilde{\psi}$ is introduced according to the relations $\tilde{w} = -\partial_x\tilde{\psi}$, $\tilde{u}_x = \partial_z\tilde{\psi}$.

Depending on the wavenumber we classify the disturbances as longwave ($k^2 \sim \omega$) and shortwave ($k^2 \gg \omega$) ones. For the longwave perturbations (Sect. 3) the Prandtl number is unimportant, in Sect. 4 (the shortwave mode) we assume $P = 2$. Although for most binary liquids the Lewis number is rather small, we do not assume it to be asymptotically small; in computations $L = 0.01$ is set.

3 Longwave Approximation

The boundary value problem can be substantially simplified for the longwave instability, which plays an important role in the absence of modulation. To study the evolution of longwave perturbations, we introduce the following rescalings:

$$\tau = \omega t,\ k = \sqrt{\omega}K,\ \tilde{\psi} = \sqrt{\omega}\tilde{\Psi}, \tag{17}$$

and expand the fields of perturbations into power series in small ω

$$(\tilde{\Psi}, \tilde{T}, \tilde{C}) = (\tilde{\Psi}_0, \tilde{T}_0, \tilde{C}_0) + \omega(\tilde{\Psi}_2, \tilde{T}_2, \tilde{C}_2) + \ldots. \tag{18}$$

The derivation of the amplitude equation is similar to that carried out in [5], therefore here we present only milestones of the calculations, referring to the cited paper for the details.

The solution in the zeroth order is given by

$$\tilde{T}_0 = a_1(\tau),\ \tilde{C}_0 = a_2(\tau),\ \tilde{\Psi}_0 = \frac{iKM}{4}(\tilde{T}_0 - \tilde{C}_0)z^2(1 - z), \tag{19}$$

where $a_1(\tau)$ and $a_2(\tau)$ are yet-to-be-determined. The solvability condition in the second order results in the following amplitude equation:

$$\ddot{h} - K^2 mA(\chi + 1)(h\cos\tau)_\tau - \dot{h}K^2\alpha - K^4 h\left(\Theta + m\chi_L A\cos\tau\right) = 0, \tag{20}$$

where a dot denotes the derivatives over τ, $h = a_2 - a_1$ is the surface tension perturbation, $m = M/48$, $A = 2b/5$, $\chi_L = \chi + L + \chi L$, $\alpha = m(\chi + 1) - L - 1$, $\Theta = m\chi_L - L$. If $\Theta < 0$, this second order ordinary differential equation for h is similar to the well-known Mathieu equation with damping [7].

According to the Floquet theory, the solution of (20) is represented in the form:

$$h(\tau) = e^{s\tau} H_0(\tau), \tag{21}$$

where $H_0(\tau)$ is periodic with the period 2π, s is the complex Floquet exponent; below we discuss only the perturbation with the largest s_r. (Hereafter subscripts r and i denote the real and imaginary parts, respectively.) At the stability boundary $s_r = 0$ and the perturbations are classified according to the value of s_i in the following way: (1) subharmonic mode with $s_i = 1/2$; (2) synchronous mode with $s_i = 0$; (3) quasi-periodic modes with $0 < |s_i| < 1/2$.

The Floquet exponents are calculated analytically in several limiting cases and numerically for arbitrary values of the parameters.

Analysis of limiting cases is similar to that performed in [5], therefore the results are discussed briefly. First, at small A and

$$-1 < \chi < \chi_o,\ \chi_o = -\frac{L^2}{1 + L + L^2}, \tag{22}$$

when the longwave oscillatory mode is critical for the unmodulated heat flux [4], the resonant excitation of subharmonic (SH) mode takes place. Namely, for a perturbation whose wavenumber is close to the resonant one

$$K^2\Omega_k \approx \frac{1}{2} + O(A),\ \Omega_k = \sqrt{-\frac{\chi(1 + L + L^2) + L^2}{1 + \chi}}, \tag{23}$$

($K^2\Omega_k$ is the frequency of neutral oscillations for $A = 0$) a destabilization takes place. The correction to the Marangoni number of the oscillatory mode [4]

$$m_o = \frac{1 + L}{1 + \chi}, \tag{24}$$

is negative and proportional to A. There also exists a synchronous mode, but the corresponding correction to m_o is proportional to A^2.

Secondly, beyond the interval given by (22) or at negative m, when the monotonic mode is critical for $A = 0$, the stability threshold for True Longwave (TLW) mode with $K = 0$ remains the same as it was found in [4]:

$$m_m = \frac{L}{\chi + L + \chi L}. \tag{25}$$

Finally, in the opposite limiting case, $K \gg 1$, the Wentzel-Kramers-Brillouin method can be applied. To that end we represent the solution to (20) in the form:

$$h = \exp\left[K^2 \Phi(\tau)\right],$$

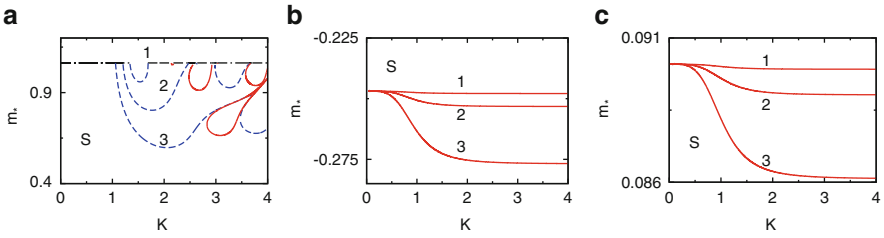

Fig. 1 Neutral stability curves for the longwave perturbations. Lines 1, 2, and 3 correspond to $A = 0.2,\ 0.5$, and 1, respectively. The domains of stability are marked with "S." (**a**) Competition of the subharmonic (the *dashed lines*), synchronous (the *solid lines*), and quasiperiodic (the *dashed-dotted line*) modes for $\chi = -0.05$. Note, that the quasiperiodic mode is shown for $A = 0.2$ only, for higher values of A the breaks in the *dashed-dotted lines* increase; (**b**) the synchronous mode for $\chi = -0.05$ at negative m; (**c**) $\chi = 0.1$, the synchronous mode

which results in the following quadratic equation for the rescaled "growth rate" $\Lambda = \dot{\Phi}$ (an actual instantaneous growth rate in the unrescaled time t is Λk^2, see Sect. 4):

$$\Lambda^2 - \Lambda\left[mA(\chi+1)\cos\tau + \alpha\right] - \left[\Theta + m\chi_L A\cos\tau\right] = 0. \tag{26}$$

At the stability boundary the real part of the Floquet exponent vanishes:

$$s_r = \frac{K^2}{2\pi}\Phi_r(2\pi) = 0, \tag{27}$$

$$\Phi(2\pi) = \pi\alpha + \frac{1}{2}\int_0^{2\pi}\sqrt{\left[m(\chi+1)A\cos\tau + \alpha\right]^2 + 4\left[m\chi_L A\cos\tau + \Theta\right]}. \tag{28}$$

The corresponding stability boundary is sought numerically. Depending on the value of $\Phi_i(2\pi)$ the mode is termed as either Intermediate Longwave Synchronous mode (ILW-S) for $\Phi_i(2\pi) = 0$ or Intermediate Longwave Quasiperiodic mode (ILW-Q) otherwise. As it will be shown in Sect. 4, these modes match with the shortwave perturbations.

For numerical computations the shooting method is applied; results of calculations are shown in Figs. 1 and 2. It is clear that at χ satisfying the condition (22), the SH mode is critical, even though the destabilization for the synchronous mode also occurs. Between the SH and synchronous modes there are islands of the quasiperiodic mode, for which the Marangoni number is given by (24) independently of A. Similarly to Ref. [5], with the increase in A only s_i changes, see Fig. 2b in the cited paper. As the amplitude of the modulation grows, the intervals in K, where the quasiperiodic mode is critical, shrinks because of the strong destabilization with respect to both the SH and synchronous modes.

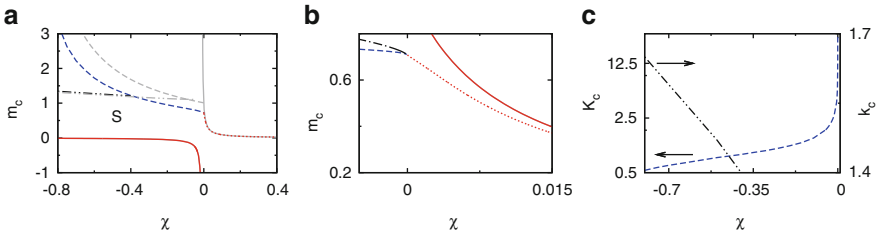

Fig. 2 Results of numerical calculations within the Floquet theory at $A = 0.5$. (**a**) Stability domain in the plane $\chi - m_c$; the *solid, dotted,* and *dashed lines* correspond to the longwave perturbations: the true longwave (TLW), intermediate longwave (ILW-S) (both are synchronous), and subharmonic (SH) modes, respectively; the *dashed-double-dotted line* corresponds to the shortwave quasiperiodic mode, see Sect. 4. The *grey lines* show the stability boundaries for the monotonic (the *solid lines*) and oscillatory (the *dashed line*) longwave modes and oscillatory shortwave mode (the *dashed-double-dotted line*) at $A = 0$; (**b**) the zoomed in fragment of panel (**a**) with a competition between TLW and ILW-S modes and emergence of the SH mode shown. The *dashed-dotted line* corresponds to the ILW-Q mode; (**c**): the critical rescaled wavenumber K_c for the SH mode (*the dashed line*, left axis) and the critical wavenumber k_c for the shortwave quasiperiodic mode (the *dashed-double-dotted line*, right axis)

Neutral stability curves corresponding to synchronous perturbations for negative m or beyond the interval (22) always attain the critical (maximum at $m < 0$ and minimum otherwise) value either at $K = 0$ (TLW mode) or at $K \gg 1$ (ILW-S mode).

Variation of the critical Marangoni number with χ is demonstrated in Fig. 2a; for the sake of comparison, the results in the absence of modulation are also presented. It is clear, that the destabilization of the layer takes place mainly within the range of χ given by (22), when the SH mode is critical. There is also a weak destabilization at small $|\chi|$, shown in Fig. 2b, when the ILW-S mode is critical. It is worth noting, that the SH mode emerges from the point of intersection of ILW-S and ILW-Q modes, see Fig. 2b; the critical wavenumber for the SH mode is large in the vicinity of this point (Fig. 2c).

4 Shortwave Instabilities

For finite values of k and low frequency ω, the WKB method is efficient for the numerical study of (12)–(16). To that end the solution is represented in the form

$$\tilde{f} = \left(\hat{f} + \omega \hat{f}_1 + \ldots\right) \exp\left[\omega^{-1}\phi(\tau)\right],$$

where $\tilde{f} = (\tilde{\psi}, \tilde{T}, \tilde{C})$ and ϕ is an analog of the eikonal function in geometric optics. Substituting this ansatz into (12)–(16), in the zeroth order with respect to ω one arrives at the boundary value problem, which can be produced from (12)–(16) by replacing the time-derivatives with a "growth rate" $\lambda = \dot{\phi}$. Indeed, for the low

frequency the variation of the heat flux is so slow, that a perturbation has enough time to tune to the instantaneous value of the heat flux and, therefore, it evolves with the momentarily growth rate $\lambda(\tau)$.

Applying the Floquet theory, one treats the layer to be stable, if the mean value of the growth rate over the modulation period is purely imaginary:

$$\int_0^{2\pi} \lambda_r(\tau) d\tau = 0, \tag{29}$$

where the branch with the maximal growth rate should be chosen (in fact, the choice of the branch can be a little more complicated, see the detailed analysis in [6]).

It should be emphasized that for $k \ll 1$ this stability criterion reduces to (28), i.e. the ILW modes indeed ensure matching between longwave and shortwave modes. Numerical simulations (the shooting method is used) demonstrate that for $A = 0.5$ and $\chi > -0.4$ either ILW-Q or ILW-S mode is always critical within the WKB theory; perturbations with nonzero k provide larger values of the Marangoni number. Therefore, the competition of longwave modes, shown in Fig. 2a, determines the stability boundaries in that case. However, for negative Soret numbers with sufficiently large absolute values [either a strong negative Soret effect for positive σ_C or negative σ_C and a strong positive Soret effect, see (8)], $\chi < -0.4$, the shortwave quasiperiodic mode becomes critical instead of the SH one. The corresponding stability boundary is also shown in Fig. 2a. This shortwave mode stems from the shortwave oscillatory mode found in [8]. It is clear from Fig. 2a that the heat flux modulation slightly changes the stability boundary for this mode, whereas for the longwave SH mode the resonant destabilization is well-pronounced. Therefore, the modulation augments the interval of χ, where the SH mode is critical.

Note that (29), which is called "asymptotic stability criterion" [9], assumes that a perturbation is introduced initially and after that evolves without any energy supply. However, in any realistic system, some kind of noise takes place, which serves as an energy source for the initially excited perturbation. This noise becomes especially important for a low-frequency modulation, when the time periods of growth and decay of perturbations last for a long time and the noise, for instance, is able to stop an exponential perturbation decrease during the decaying stage. It is clear that the asymptotic theory operates with an idealized system and therefore overestimates the stability threshold.

Generally speaking, in the presence of noise there is no standard criterion of the stability, a threshold should depend on such factors as the amplitude of noise, system nonlinearity, etc. However, in the limiting case of finite noise one can use the so-called "empirical" criterion [9], according to which the system is treated as unstable as soon as $\lambda_r(\tau_*)$ becomes positive at certain time moment τ_*. Finite level of noise instantaneously makes this perturbation growing fast and therefore the system leaves the vicinity of the base solution. It is intuitively clear that this criterion provides an underestimation of the stability threshold.

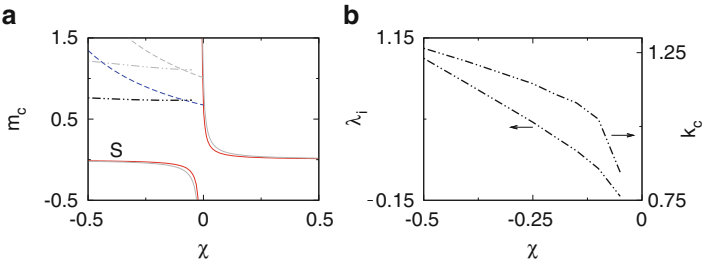

Fig. 3 Panel (**a**) Stability map for the system with noise at $A = 0.5$. The *solid* and *dashed lines* correspond to the longwave monotonic, (30), and longwave oscillatory modes, (31), respectively; the *dashed-double-dotted line* depicts the stability boundary for the shortwave oscillatory mode. The *grey lines* depict the stability boundary for $A = 0$, longwave monotonic mode (the *solid line*), (25), longwave oscillatory mode (the *dashed line*), (24), and shortwave oscillatory mode (the *dashed-double-dotted line*). The domain of stability is marked by "S." Panel (**b**) Variation of the wavenumber k_c (the right axis) and frequency (the left axis) of critical perturbations for the shortwave oscillatory mode with χ

Again, further simplification is possible for $k \to 0$. In this case (26) is still valid and the real part of $\Lambda = \lambda/k^2$ vanishes at the stability boundary. Both monotonic and oscillatory modes are possible with their respective stability thresholds given by

$$m_m^{(e)} = \frac{L}{(1+A)(\chi + L + \chi L)} \tag{30}$$

and

$$m_o^{(e)} = \frac{1+L}{(1+A)(1+\chi)}. \tag{31}$$

In both cases $\tau_* = 0$. Longwave oscillatory mode takes place, when the squared frequency of marginal oscillations Ω_k^2 [see (23)] is positive, i.e. under condition (22); both the frequency and the interval of existence for this mode are exactly the same as for the unmodulated heat flux [4]. Moreover, the stability thresholds given by (30) and (31) differ from the respective values for $A = 0$, (25) and (24), only by an additional factor $(1 + A)$ in the denominators. Note, that in view of the relation $A = 2b/5$ (see Sect. 3), this result does not coincide with a naive prediction based on the introduction of the instantaneous Marangoni number via the time-dependent heat flux. The difference originates from the different variation with z of the mean and oscillatory parts of T_0 and C_0, (10). The stability region in the plane $\chi - m$ for the longwave perturbations is shown in Fig. 3.

Similarly to the noise-free case, numerical simulations indicate that for $A = 0.5$ and χ greater than a certain value $\chi_c^{(e)}$, the critical perturbations are materialized at $k = 0$, see Fig. 3. In contrast to the noise-free system, this $\chi_c^{(e)}$ is almost independent of the modulation amplitude A. Moreover, a destabilization for the shortwave oscillatory mode is well pronounced. The naive assumption that $m_c(A) = m_c(A = 0)/(1 + A)$, though it is not exact, provides a fairly good prediction for the dashed-double-dotted line in Fig. 3a. The critical wavenumber

and frequency of neutral oscillations become smaller in presence of modulation, see Fig. 3b, but they vary with χ in a qualitatively similar manner to that found for the shortwave oscillatory mode in [8].

5 Conclusions

The influence of a low-frequency modulation of a heat flux on the surface-tension-driven convection in a layer of a binary mixture is investigated. Applying the Floquet theory (the asymptotic stability criterion), we demonstrated that for the Soret number χ larger than a certain negative value χ_c, the instability of the layer can be caused by each of the following three longwave modes: Subharmonic mode (SH) and two synchronous modes, True Longwave mode (TLW) and Intermediate Longwave mode (ILW-S). The increase in the modulation amplitude A leads to a strong destabilization with respect to the SH mode, for ILW-S the destabilization takes place as well, whereas the stability threshold for the TLW mode does not depend on A at all. At negative and rather small values of $\chi < \chi_c$, the shortwave quasiperiodic perturbations become critical. The modulation of the heat flux increases the critical value of $|\chi_c|$.

We also have applied the so-called empirical criterion, when the layer is assumed unstable as soon as the instantaneous growth rate becomes positive during the vibration period. Again, destabilization of the layer is found; longwave disturbances, either monotonic or oscillatory, are critical. Similarly to the Floquet analysis, at $0 > \chi_c^{(e)} > \chi$ the shortwave oscillatory mode dominates; but in presence of noise $|\chi_c^{(e)}|$ does not change much as the amplitude of modulation increases. This makes the destabilization for the noisy system more pronounced.

References

1. Faraday, M.: On a peculiar class of acoustic figures; and on certain forms assumed by groups of particles upon vibrating elastic surfaces. Philos. Trans. R. Soc. Lond. **121**, 299 (1831)
2. Gershuni, G.Z., Nepomnyashchy, A.A., Velarde, M.G.: On dynamic excitation of Marangoni convection. Phys. Fluids A **4**, 2394 (1992)
3. Birikh, R.V., Briskman,V.A., Velarde, M.G., Legros, J.-C.: Liquid Interfacial Systems. Oscillations and Instability. Marcel Dekker, New York (2003)
4. Oron, A., Nepomnyashchy, A.A.: Long-wavelength thermocapillary instability with the Soret effect. Phys. Rev. E **69**, 016313 (2004)
5. Fayzrakhmanova, I.S., Shklyaev, S., Nepomnyashchy, A.A.: Influence of a low frequency vibration on a longwave Marangoni instability in a binary mixture with the Soret effect. Phys. Fluids **22**, 104101 (2010)
6. Fayzrakhmanova, I.S., Shklyaev, S., Nepomnyashchy, A.A.: Influence of low-frequency vibration on thermocapillary instability in a binary mixture with the Soret effect: long-wave versus short-wave perturbations. J. Fluid Mech. **714**, 190 (2013)

7. Nayfeh, A.H.: Perturbation Methods. Wiley, New York (1973)
8. Shklyaev, S., Nepomnyashchy, A.A., Oron, A.: Marangoni convection in a binary liquid layer with Soret effect at small Lewis number: linear stability analysis. Phys. Fluids **21**, 054101 (2009)
9. Homsy, G.M.: Global stability of time-dependent flows. Part 2. Modulated fluid layers. J. Fluid Mech. **62**, 387 (1974)

Onset of Stationary Flows of a Cohesive Granular Material in a Channel

A. de Ryck and O. Louisnard

1 Introduction

Bulk solid handling is still an affair of concern in process industry due to its lack of reliability and assessed constitutive equations to describe and predict powder flows.

The behaviour of gravitational flows are given by the competition of the following forces: the weight of the grains, the particle–particle friction, their non-overlapping and the attractive forces between them (van-der-Waals or capillary forces).

Using a continuum mechanics frame, we adopt, as constitutive equation to describe such a flow, a co-linear relationship between the stress and strain-rate tensors (σ and $\dot{\gamma}$ respectively):

$$\sigma = -PI + [c + \mu(I)P]\frac{\dot{\gamma}}{|\dot{\gamma}|}, \tag{1}$$

where $P = \sigma_{ii}$ is the mean pressure and $|\dot{\gamma}| = \sqrt{\dot{\gamma}_{ij}\dot{\gamma}_{ij}/2}$. This relation extends the model developed by Jenike [1] (Coulomb failure criterion generalized into a conical yield criterion, pressure isotropy) to the case of cohesive powders. The cohesion c is supposed constant.

Some viscosity is introduced by a dependency of the coefficient of friction μ with the deformation rate. Following Da Cruz [2], μ is supposed to vary with the Inertial number I, given by the ratio of the inertial time scale to the macroscopic deformation time scale ($|\dot{\gamma}|^{-1}$):

A. de Ryck (✉) · O. Louisnard
Université de Toulouse, Mines Albi, Centre Rapsodee, UMR CNRS 5302, route de Teillet, 81000 Albi, France
e-mail: deryck@mines-albi.fr

R.G. Rubio et al. (eds.), *Without Bounds: A Scientific Canvas of Nonlinearity and Complex Dynamics*, Understanding Complex Systems,
DOI 10.1007/978-3-642-34070-3_19, © Springer-Verlag Berlin Heidelberg 2013

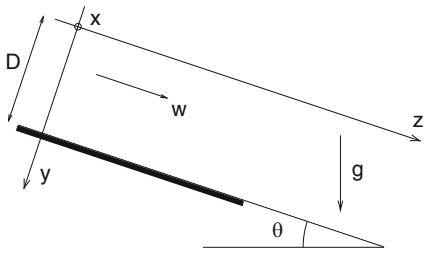

Fig. 1 Side view of a stationary parallel flow in a channel

$$I = \frac{|\dot{\gamma}|\, d}{\sqrt{P/\rho}}, \tag{2}$$

where ρ is the apparent specific mass of the powder and d the particle size.

This rheology, proposed by Jop et al. [3] is applied in the case of a surface flow (the depth of the flowing layer is supposed less than the depth of the granular bed), stationary and parallel to the direction of the free surface greatest slope (inclination angle θ). The flow is maintained between two vertical parallel walls with a gap distance $2a$ between them. μ_w is the grain-particle coefficient of friction.

2 Liminary Results

2.1 Set of Equations

Under the conditions set in introduction, the equation for the dynamics reduces to the equilibrium equation $\overrightarrow{\nabla}\sigma = \rho\overrightarrow{g}$. In the normal and along the channel slope (Oy and Oz in Fig. 1), it leads respectively to an hydrostatic mean pressure: $P = \rho g y \cos\theta$ and to:

$$\frac{\partial}{\partial x}\left((c + \mu P)\sin\alpha\right) + \frac{\partial}{\partial y}\left((c + \mu P)\cos\alpha\right) - \rho g \sin\theta = 0, \tag{3}$$

where α is the local angle of an iso-velocity line, $w(x, y) = constant$, with respect to the horizontal Ox ($\tan\alpha = \frac{\partial w}{\partial x}\frac{\partial w}{\partial y}^{-1}$).

This last equation leads to a parametric ordinary differential equation for the iso-velocity lines in plane normal to the flow direction (x-y plane), see de Ryck [4] for details.

Together with the appropriate boundary conditions on the lateral walls or the free surface, the velocity field may be obtained with the set of iso-w lines.

2.2 Constant Coefficient of Friction

In the case of a constant coefficient of friction, the system may be integrated and we obtain for the iso-velocity lines [5]:

$$x = (h + \ell_{\mu\theta})\frac{s + \frac{R}{k}\sin(ks)}{1 + R}, \tag{4}$$

$$y + \ell_{\mu\theta} = (h + \ell_{\mu\theta})\frac{R + \cos(ks)}{1 + R}. \tag{5}$$

These equations are those of a trochoid parameterized by s, whose maximal depth (for $x = 0$) is h. In order to shorten the expressions, we introduce $\ell_{\mu\theta} = \frac{\ell}{\mu\cos\theta} = \frac{c}{\mu\rho g\cos\theta}$, $R = \frac{\tan\theta}{\mu}$ and $k = \sqrt{R^2 - 1}$.

The depth h is determined by the boundary conditions. The iso-velocity may attain the free surface with an angle $\alpha = \pi/2$, or the lateral walls of the channel with an angle $\alpha = \pi/2$ if the walls are rough, or $\alpha = \alpha_w$ if the walls are smooth. In all these cases, there is only one *single* solution. Therefore, it is deduced that the flow has the form of the sliding of two rigid blocks along this unique interface, which description corresponds to the rigid-plastic model by Coulomb. This result comes from, as shown in Blumenfeld and Edwards [6], that in the case of a parallel and steady-state flow with a constant coefficient of friction, it is not possible to have an extremum in the velocity profile. As a consequence, only plug flows occur in such conditions.

2.3 Flow for μ = Constant

To fully describe the flow, the localization of this iso-velocity line is obtained by writing the force balance on the plug sliding on it. Three cases may be distinguished.

2.3.1 Iso-velocity Attaining the Free Surface

The equilibrium is written by equating the shear force integrated along the boundary iso-velocity line between the plug and dead zones, with the weight per unit z-length:

$$\int_0^{s_w} (c + \mu\rho g\cos\theta y)\sqrt{\left(\frac{dx}{ds}\right)^2 + \left(\frac{dy}{ds}\right)^2}\,ds = \int_0^{s_w} \rho g\sin\theta y\frac{dx}{ds}ds, \tag{6}$$

Using $(h + \ell_{\mu\theta})^2 = \left(\frac{dx}{ds}\right)^2 + \left(\frac{dy}{ds}\right)^2$ and (4) and (5), y may be written as $y = \frac{1}{R}(\frac{dx}{ds} + \lambda)$, with:

$$\lambda = (R-1)h - \ell_{\mu\theta}, \tag{7}$$

so that (6) becomes:

$$\int_0^{s_w} \left(\frac{dy}{ds}\right)^2 ds = \lambda a. \tag{8}$$

At the free surface, the no-stress condition leads to $\frac{dx}{ds}|_{y=0} = 0$. Then, we have $\lambda = 0$. As a consequence, from (8), $y \equiv 0$. There is no flow with such a boundary condition. If a plug flow exists, it has to occur on a sliding surface which attains the lateral walls at a finite depth. Thus, there is a parietal sliding on a depth h_w.

2.3.2 Rough Lateral Walls

For a rough wall, we have $\mu_w(h_w) = \mu(\pm a, h_w)$, then $\frac{dx}{ds}|_{x=\pm a} = 0$ and consequently $h_w = \frac{\lambda}{R}$. We also have $a = \frac{h+\ell_{\mu\theta}}{1+R}(1+s_w)$ where $s_w = \arccos(-1/R)/k$. The equilibrium equation leads to a third relation between h, h_w and R. It contains a new term compared to (6) due to the frictional stress at the lateral walls:

$$\int_0^{s_w} \left(\frac{dy}{ds}\right)^2 ds + \int_0^{h_w} (\ell_{\mu\theta} + y)dy = Rh_w a. \tag{9}$$

This leads to an implicit relationship between the inclination angle θ and both the coefficient of friction and the cohesion c scaled by $\rho g a$:

$$\frac{\ell}{a} = \sin\theta \left(1 - \sqrt{\frac{s_w + R^{-2}}{s_w + 1}}\right). \tag{10}$$

The latter equation shows that there is a unique slope angle θ_o allowing a stationary flow for a given cohesive length $\ell = \frac{c}{\rho g} < a$. For $\theta < \theta_o$, the flows are decelerated. Above this value, they are accelerated. If the cohesive length ℓ is greater than the half-width of the channel, there is no more steady-state flows feasible. Figure 2 presents this angle versus ℓ/a for different bulk friction angle ϕ, given by $\mu = \tan\phi$. As soon as this slope is obtained, the dimensionless depth of the flowing zone h/a, and the dimensionless depth at the walls h_w/a are easily determined (Fig. 3).

These depths tend towards zero when $c \to 0$. For a non-cohesive powder, the minimal inclination angle is given by the bulk friction angle ϕ and the flow at this threshold is superficial ($h \to 0$). With rough channel walls, there is no more flow for $\ell \geq a$ and the depth of the flow at this limit diverges.

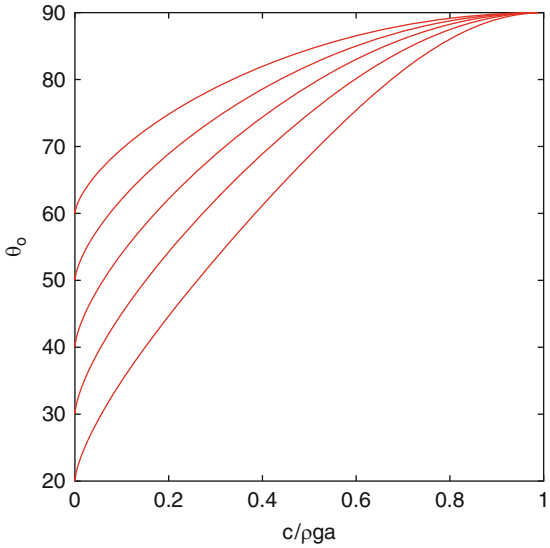

Fig. 2 Minimal slope angle for a steady-state flow in a channel of width $2a$ versus the dimensionless cohesion $\frac{c}{\rho g a}$, for different bulk friction angles (from *bottom* to *top*, $\phi = 20$, 30, 40, 50 and 60°

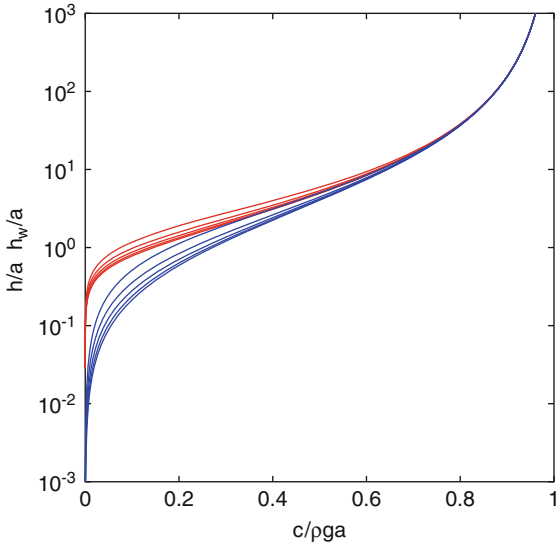

Fig. 3 Depth of the flow at the centre h (*top bundle* of curves) and at the walls h_w (*bottom bundle*) scaled by a, versus the cohesion c scaled by $\rho g a$. In each bundle, from *bottom* to *top*, $\phi = 20$, 30, 40, 50 and 60°

2.3.3 Smooth Lateral Walls

For smooth and non-adhesive walls, the friction condition, using the relation $\sin\alpha = \frac{k \sin ks}{R + \cos ks}$, leads to $\frac{dy}{ds}|_w = -\frac{\mu_w}{\mu} h_w$. The equilibrium equation writes:

$$\int_0^{s_w} \left(\frac{dy}{ds}\right)^2 ds + \frac{\mu_w}{\mu}\frac{h_w^2}{2} = \lambda a, \tag{11}$$

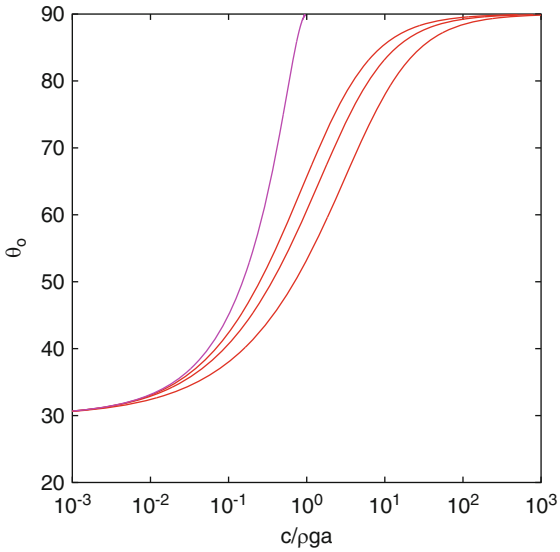

Fig. 4 Minimal slope angle for a steady-state flow in a channel of width $2a$ versus the cohesion c scaled by $\rho g a$, for $\phi = 30°$. The *upper curve* is for the rough case. The three others are for the smooth case with, from *bottom* to *top*, $\phi_w = 10$, 20 and 30°

leading to the following set of equations:

$$\begin{aligned} \frac{\mu_w}{\mu} h_w (\ell_{\mu\theta} + \frac{ka}{\sin ks_w}) - 2R\ell_{\mu\theta} a = 0, \\ \ell_{\mu\theta} = ak \frac{R + \cos ks_w - \frac{\mu}{\mu_w} k \sin ks_w}{ks_w + R \sin ks_w}, \\ h_w = a \frac{k^2 \sin ks_w}{ks_w + R \sin ks_w}. \end{aligned} \tag{12}$$

The results is described without loss of generality using an internal angle of friction $\phi = 30°$. They are displayed in Figs. 4 and 5. Figure 4 shows the slope angle for a steady-state flow as a function of ℓ/a for respectively $\phi_w = 10$, 20 and 30° from bottom to top (where $\phi_{(w)} = \tan^{-1} \mu_{(w)}$). The highest curve corresponds to the rough case (cf. Fig. 2) and is displayed for comparison. The absence of adhesion at the walls reduces the minimal slope to obtain the stationary flow in the channel, and flows may occur for $\ell > a$. The less the wall friction is (compared to the bulk friction), the less the slope is. Figure 5 gives the corresponding depths.

3 Flow for a Non Constant Coefficient of Friction

For a cohesive powder and a coefficient of friction depending on the inertial number, we obtain a sheared zone between a dead zone below it and a plug on it. Figure 6 illustrates this for a given instance. It displays the depth velocity profile on the

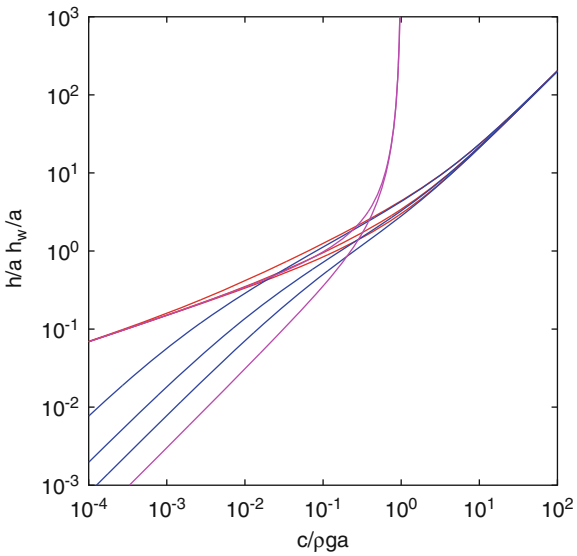

Fig. 5 Depths h and h_w scaled by a at the onset of stationary flow in a channel of width $2a$, versus ℓ/a, for $\phi = 30°$. The two diverging curves at $\ell = a$ are for the rough case. For the smooth case, three solutions are displayed for $\phi_w = 10$, 20 and 30°

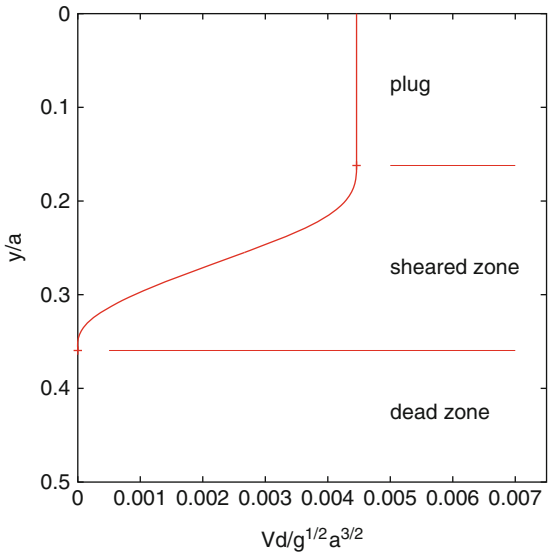

Fig. 6 Scaled depth velocity profile at the middle of the channel with $\ell = 180\mu_s a$, $\mu(I) = \mu_s (1 + 0,685/(0,279/I + 1))$ and $R = 1,09$. The sheared zone is confined between a dead zone below it and a plug flow on it. For more details on the thickness of this shear band, see [7]

middle plane of the channel, for the particular relationship $\mu = \mu_s + \frac{\mu_\infty - \mu_s}{I_o/I+1}$. The exact form of the velocity profile depends on the relation $\mu(I)$, but the boundary iso-velocities with the dead and plug zones only depend on the behaviour of the friction coefficient close to $I \to 0$. The full study on the localisation of these limits is done in de Ryck and Louisnard [7]. It emerges that the minimal slope to obtain a steady-state flow corresponds to the situation where the thickness of the sheared zone tends toward zero. It formally corresponds to the case $\mu = constant$. The results obtained

in Sect. 2.3 then apply and give the minimal slope and depth at threshold for all the cases described by a $\mu(I)$ rheology using $\mu = \mu(I \to 0)$.

4 Weak and High Cohesions

In the case of a weak cohesion, i.e. $\ell \ll a$, (10) or the set of (12) may be developed to yield the analytical expressions of the minimal inclination angle (in radians) and of the depths. These quantities, in the limit of weak cohesion, do not depend on the nature of the lateral walls, except for h_w, which depends on the ratio μ/μ_w in the smooth case:

$$\begin{aligned} \theta_o &\approx \phi + \sin 2\phi \left(\frac{\pi}{4\sin\phi}\frac{\ell}{a}\right)^{2/3}, \\ h &\approx \left(\frac{16}{\pi^2 \sin\phi}\ell a^2\right)^{1/3}, \\ \left[\begin{array}{ll} h_w \approx \frac{\ell}{\sin\phi} & \text{rough case} \\ h_w \approx 4(\mu/\mu_w)^2 \frac{\ell}{\sin\phi} & \text{smooth case} \end{array}\right. & . \end{aligned} \tag{13}$$

For high cohesion, the rough and smooth cases must be distinguished, and it is obtained:

$$\begin{aligned} \theta_o &= \frac{\pi}{2} - \frac{2}{\pi \tan\phi}(1-\ell/a)^2, \\ h &\approx \frac{\pi}{2} a (1-\ell/a)^{-1}, \\ h - h_w &\approx a, \end{aligned} \tag{14}$$

when $\ell \to a^-$ (rough case) and:

$$\begin{aligned} \theta_o &= \frac{\pi}{2} - \left(2\mu_w \frac{\ell}{a}\right)^{-1}, \\ h &\approx 2\ell, \\ h - h_w &\approx \frac{\mu_w}{\mu} a, \end{aligned} \tag{15}$$

when $\ell \to \infty$ in the smooth case.

5 Conclusions

For the description of cohesive granular parallel and steady-state flows in channels of finite width, using a rheology based on a dependency of the friction coefficient with the inertial number, we obtain that the minimal slope is independent on the $\mu(I)$ relationship and only depends on three parameters: ϕ the internal friction

angle, ℓ/a, the ratio of the cohesive length on the (half)-width of the channel and, in the smooth and non-adhesive wall case, on the ratio of wall to internal friction μ_w/μ. The depths at this threshold depend on the same set of parameters.

Finally, it can be noticed that the size of the grains do not explicitly appears in that study. It has an influence through the cohesion c. Nevertheless, if the channel width becomes of order the size of the particles, the confinement effect has to be taken into account [4].

Acknowledgement It is a pleasure to thank Renaud Ansart, John A. Dodds, Haiping Zhu and Aibing Yu for fruitful discussions on that domain. A. de R. is glad to thank Manuel G. Velarde for the opportunity of a one-year position at the Unidad de Fluidos, Instituto Pluridisciplinar, working on spreading and Marangoni phenomena at that time.

References

1. Jenike, A.W.: A theory of flow of particulate solids in converging and diverging channels based on a conical yield function. Powder Technol. **50**, 229–236 (1987)
2. Da Cruz, F., Emam, S., Prochnow, M., Roux, J.-N., Chevoir, F.: Rheophysics of dense granular materials: discrete simulations of plane shear. Phys. Rev. E **72**, 021309 (2005)
3. Jop, P., Forterre, Y., Pouliquen, O.: A constitutive law for dense granular flows. Nature **441**, 727–730 (2006)
4. de Ryck, A.: Granular flows down inclined channels with a strain-rate dependent friction coefficient. Part II: cohesive materials. Granular Matter **10**, 361–367 (2008)
5. de Ryck, A., Ansart, R., Dodds, J.A.: Granular flows down inclined channels with a strain-rate dependent friction coefficient. Part I: non-cohesive materials. Granular Matter **10**, 353–360 (2008)
6. Blumenfeld, R., Edwards, S.F., Schwartz, M.: Da vinci fluids, catch-up dynamics and dense granular flow. Eur. Phys. J. E **32**, 333–338 (2010)
7. de Ryck, A., Louisnard, O.: Depth and minimal slope for surface flows of cohesive granular materials on inclined channels. J. Fluid Mech. (submitted) (2012)

Part III
Scientific Contributions: Interfacial Phenomena, Wetting and Spreading Problems

Thermography Applied to Interfacial Phenomena, Potentials and Pitfalls

M. Antoni and K. Sefiane

1 Introduction

The IR technique is an advanced non-contact and non destructive test method. It is based on the fact that all objects, above absolute zero, emit infrared, radiant heat, at a rate that is directly related to the temperature of the object. The radiant incident energy on a surface is partially reflected, partially absorbed and partially transmitted through the material. The sensors of a thermographic IR camera detect the wavelength of the energy emitted by an object and, by the use of integral equations, the temperature can be obtained once the body material and surface properties are known. It is recognised that there are a few affordable materials (still quite expensive) transparent to IR radiation like germanium and zinc selenide, and all lenses must be made of these materials to work with IR cameras. What the IR camera measures is the heat flux emitted by a body. By this measurement, and knowing the body emissivity and surface characteristics, one can infer the body temperature. When the emissivity of a body is low (typically smaller than 0.1), as for metals, and its temperature is close to ambient, it is very likely that the IR camera will detect the transmitted and reflected components characteristic of the ambient surrounding the target material. In order to avoid this, it must be remembered that the radiant heat flux is proportional to the fourth power of temperature; therefore, the ambient could be masked if the body temperature is sufficiently above ambient. This is the reason why it is common practice to mount the object whose temperature must be measured, on a heated stage set at a temperature sufficiently higher than the ambient one.

M. Antoni
Aix-Marseille Université, UMR-CNRS 7246 MADIREL Centre St. Jérôme - BP 461 - Marseille 13397 Cedex 20, France

K. Sefiane (✉)
School of Engineering, University of Edinburgh, Kings Buildings, Edinburgh EH9 3JL, UK
e-mail: K.Sefiane@ed.ac.uk

R.G. Rubio et al. (eds.), *Without Bounds: A Scientific Canvas of Nonlinearity and Complex Dynamics*, Understanding Complex Systems,
DOI 10.1007/978-3-642-34070-3_20,

IR technique is a suitable solution to measuring interfacial temperature of systems undergoing heat and mass transfers. In the past, this technique has been used to measure surface temperature of liquids but, in some physical phenomena, geometrical configurations can make things slightly more difficult. For example droplets and menisci interfaces are usually curved objects and the accurate determination of the emissivity of such systems must be solved. Despite these difficulties, IR thermography has proven to be a powerful tool in measuring absolute temperature in many studies in particular for evaporating and boiling systems where phase change is present. For a better understanding of these phase changes processes, the interfacial temperature is a key facto, especially at small scales. The access to the interface temperature at the micro-scale has been a challenging task. The use of conventional thermocouples has been pushed to the limit using miniaturisation. Fang and Ward [1] have investigated the cooling effect resulting from the evaporation of water in a reduced pressure environment by using micro-thermocouples near the interface. They show an increase in the cooling effect with the increase in the evaporation mass flux. It is interesting to note that with the thermocouple used (the smallest one of 80.3 μm diameter) they were able to read temperature within 30 μm from the interface. This clearly shows that in this area there is an important need for experimental techniques with higher resolution and less interference. Despite this attempt, the acquisition of information near interfaces remains quite difficult, because of small sizes and usually curved geometries. In this context, IR thermography is a potential candidate for bridging thus gap and allowing measurements that are very difficult to perform with conventional techniques.

IR thermography has been used recently, coupled with high-speed imaging, for local heat transfer measurement of mini and micro channels by Hetsroni et al. [2, 3]. IR thermography has also been used for local heat transfer measurement in complex geometry like plate finned tube heat exchangers as described in [4], to detect transition and separation regions of the boundary layer that strongly influence the heat transfer for such applications. Because of the fast time response of more recent cameras, IR technique is successfully applied also to study boiling (see [5,6]) and evaporation [7, 8]. The equipment used to perform such measurements is at the heart of the reliability and accuracy of these measurements. During the last 2 decades different types of IR cameras have been developed in order to meet the needs of always more demanding applications. It must be pointed out that most of efforts made in this area were for military application where detecting objects of a certain nature and/or live organisms in the dark is crucial. Detailed and exhaustive information on different technologies can be found in [9–12]. The most important part of the IR camera is undoubtedly the detector. There are two technologies being in use: single and multi detector. In single detector cameras a rotating prism, scanning the field of view line-by-line, records the flux emitted by the target object on the single detector that is therefore heavily loaded; moreover, the scanning mechanism introduces some noise in the system [12]. Focal Plane Array (FPA) IR cameras have lowered the price, raised both the resolution and the sensitivity of IR thermography compared to the single detector technology [9]. The drawback is that the detectors on the matrix receive an unwanted heat flux from the surrounding

objects in the ambient and from the detectors themselves as pointed out in [10, 11]. Besides, in FPA cameras, there is no internal temperature reference, like in the single detector thermal scanner, to which the signal is constantly compared [10, 11]. These two limitations could make the FPA technology a less useful tool for quantitative analysis in heat transfer studies where accuracy is among the crucial requirements. In the single detector camera, a cold shield (at around 70 K) is placed in front of the detector in order to remove all the unwanted flux not coming from the object under investigation. This low temperature can be controlled through the use of Peltier elements or liquid nitrogen. Because of its temperature, the flux produced by the cold shield can be neglected with respect to the incoming flux from the object being studied. In the array detectors the cold shield is also used but does not remove entirely the unwanted flux; in particular, the flux produced by the ambient inside the IR camera between the detector array and the lenses. In IR cameras used for quantitative measurements, a temperature sensor is placed on the lenses in order to correct this effect.

As outlined in [10], the FPA cameras can successfully be used for quantitative measurement only if they are calibrated frequently. The latest IR thermographic cameras have a spatial resolution of about $\sim 3\,\mu m$, this performance starts to compete with other techniques used to map temperature such as unsealed thermochromic liquid crystals [13, 14] and polymer dispersed thermochromic liquid crystals [15]. The time response of IR cameras with photon detectors is of the order of micro-seconds as shown by Conn and Avery [16] whereas the time response of thermochromic liquid crystals has been evaluated to be in a range of a few and hundreds of milliseconds [17, 18]. The limitations of conventional techniques such as thermocouples and tedious procedures with some new techniques like thermochromic liquid crystals, make a strong argument for adopting IR thermography to study interfacial phenomena. But in order to understand the opportunities and limitations associated with the use of IR thermography technique, one has to recall the fundamentals of this latter.

2 Radiation and Heat Transfer Theory

The signal acquired by the IR camera is an electromagnetic energy transferred through radiations. IR electromagnetic radiations are emitted by all objects with a temperature above absolute zero. Together with conduction and convection, they correspond to one mechanism of heat transfer from hot to cold regions. The higher is the temperature of the objects the larger is the intensity of the IR radiations and they are out of the visible range of the electromagnetic spectrum for temperatures below 500°C. Above, this temperature objects are glowing in the red range of the visible spectrum and energy emission is not lying any more only in the IR wavelengths. Besides emitted radiation, objects also react to incident light by absorbing or reflecting part of it or allowing it to cross through them. As a result, the perception

we have of an object is a combination of three different mechanisms: absorption, reflection and transmission each of them being characterized by the specific physical properties of the target object. The absorption of materials result from the exchanges between molecular vibrations and IR waves and the fraction of the incident energy it involves is described by its absorptivity α. The incident energy fraction reflected off the surface is given by the reflectivity ρ. Finally the one transported across the object is fixed by the transmissivity τ. As they correspond to fraction of the incident energy, coefficients α, ρ and τ are dimensionless quantities but that all depend on both wavelength and working temperature. They hence take values between zero and one depending on how an object absorbs, reflects or transmits the energy of the incident radiation.

Common objects are usually far from these limits since they are never ideal absorbers ($\alpha = 1$), reflectors ($\rho = 1$) or transmitters ($\tau = 1$) although important examples, like black bodies or perfectly polished silver surfaces, come very close to limit situations (respectively $\alpha \approx 1$ and $\rho = 0$). Due to the conservation of total energy, α, ρ and τ are not independent quantities and they obey the relation:

$$\alpha + \rho + \tau = 1. \tag{1}$$

The temperature of an object is evaluated by measuring the intensity of the emitted IR radiation by a thin surface layer where interactions between the object and the radiation take place. Reflected and transmitted radiations represent therefore potential sources of errors that have to be accounted for. For direct interfacial temperature measurements, thermography should hence ideally make possible to discriminate the contribution of interfaces from all others. This is technically possible only for those objects with the specificity to isotropically radiate the largest possible fraction of the energy they have absorbed regardless of the radiation wavelengths and the working temperature. Such ideal objects are known as perfect black bodies. According to Kirchhoff's point of view, perfect black bodies have absorbing layers of infinitely small thickness. But this requires severe conditions on light scattering. This view has been modified by Planck who demonstrated the necessity for the interfacial regions to have a sufficiently large thickness to prevent re-emission of the radiation and simultaneously limit scattering effects that could also contribute to help the radiation escaping back out.

One fundamental condition for temperature measurements to be relevant is thermal equilibrium between the considered object and the radiation field. This imposes that the amount of energy absorbed by a given area of the target object is the same than the one emitted by this same area when the object is completely opaque ($\tau = 0$). Absorption is then completely balanced by emission imposing the absorptivity α and the emissivity, noted ϵ in the following, to be the same. This condition, $\alpha = \epsilon = 1$ is known as Kirchhoff's law. It is true for all radiations and assumes the existence of a unique underlying equilibrium distribution of the radiation energy. For thermal radiation, this distribution, called spectral radiance, has been established by Planck for a perfect black body. It depends on both absolute

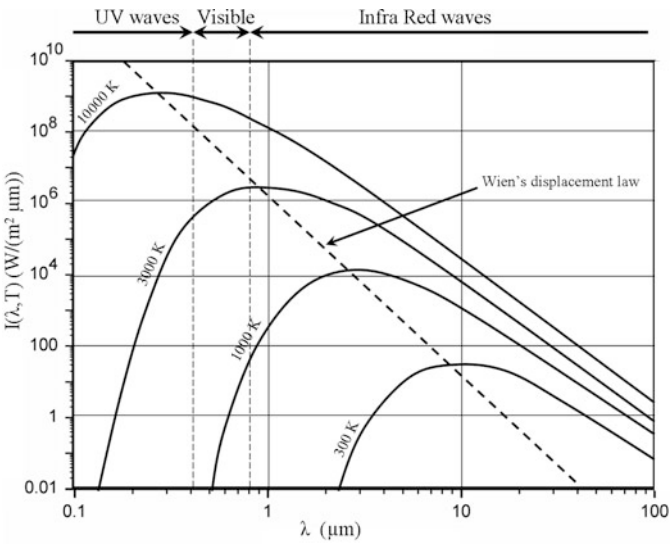

Fig. 1 Spectral radiance obtained from Plank's law for several values of temperature

temperature T and wavelength λ and is equivalent to an electromagnetic energy flux falling in a given solid angle per unit time and unit wavelength and writes:

$$I = (\lambda, \tau) = \frac{2hc^2}{\lambda^5} \frac{1}{exp\left(\frac{hc}{kt\lambda}\right) - 1} \tag{2}$$

where $I = (\lambda, \tau)$ is the spectral radiance, $h = 6.6210^{-34}$ Js Planck's constant, c speed light, $k = 1.3810^{-23}$ J/K Boltzmann's constant.

The behavior of $I = (\lambda, \tau)$ as a function of λ is illustrated in Fig. 1 showing the emission curves for a black body at different temperatures. The emitted radiation intensity increases with temperature and the maximum is reached for wavelength λ_{max} given by Wien's displacement law: $\lambda_{max} = b/T$ where $b = 2.89810^{-3}$ mK is the Wien's displacement constant. The Wien law states that this maximum shifts to the lower wavelengths when increasing the temperature and Fig. 1 clearly illustrates this effect. $I = (\lambda, \tau)$ rapidly decreases away from this value. This is actually one of the limitations of (2) since a black body at room temperature would almost present no radiation in the visible spectrum. In Fig. 1 it is also clear that the emission intensity of a specific wavelength λ is also a function of temperature. For example, at $T = 5,800$ K, like on the surface of the sun, $\lambda_{max} \approx 0.5\,\mu$m. This corresponds to a peak in the centre of the visible spectrum and explains why the sun's perception is white (it is actually turned to yellow due to the scattering of blue light in Earth's atmosphere). Conversely, for objects at 300 K, $\lambda_{max} = 9.7\,\mu$m, and no human eye detectable visible-spectrum radiation is emitted in this case. The total energy

radiated per unit surface W_{bb} of a black body is obtained after integration of (2) and is given by the Stefan–Boltzmann law,

$$W_{bb} = \sigma T^4, \tag{3}$$

where $\sigma = 5.6710^{-8}\,\mathrm{Js}^{-1}\,\mathrm{m}^{-2}\,\mathrm{K}^{-4}$ is the Stefan-Boltzmann constant. Equation (3) demonstrates that the energy radiated by a black-body increases with temperature to the fourth power.

Equations (1)–(3) provide the fundamental relations for the measure of temperature from the emitted radiation of perfect black bodies. So far, no considerations were made about the geometry of the radiant surface and it is important to keep in mind that (2) holds for any convex back bodies. Another important condition here is their surface temperature to be throughout the same for equilibrium conditions to be satisfied. In practice, real objects are never perfects emitters or reflectors and their thermal energy radiation W is always smaller than that of a black body. The grey body approximation is one possibility to describe such systems. Grey bodies are those objects with an emissivity smaller than one ($\epsilon < 1$) and taking sometimes constant value in a given wave length band. Stefan-Boltzmann's law is then modified in,

$$W = \epsilon\sigma T^4 \tag{4}$$

indicating that the total energy of a grey body is that of the black body at the same temperature but reduced in proportion of the value of the emissivity of the target material. The grey body model is of first importance in thermography measurements that generally operate in spectral windows within which emissivity can be considered as a constant. As it can be obtained from either emissivity charts or experimental calibrations they provide, in addition to the measurement of W, the necessary input for (4) from which temperature can finally be evaluated.

It is important to note here that if the grey body model provides better descriptions of real objects, it is still an approximation that is too restrictive with respect to true materials that are usually neither black bodies nor grey bodies. In most real cases, materials act as selective radiators in the sense that they can behave either like black, grey bodies or even as ideal reflectors depending on the considered wavelength and temperature ranges. In modern materials, emissivity can for example be controlled not only for specific wavelengths ranges but also monitored to become even temperature dependent. A sketch of the shape of the λ-dependence of the spectral radiance of these different materials is proposed in Fig. 2.

For experimental purposes, it is necessary to image a target object using a waveband that does not transmit through its surface. If this condition is satisfied then the temperature measurement represents conditions at the target surface. But if it is not, the measurement is made over a volume extending from the surface into the target. As discussed above, Planck demonstrated the necessity of such a non-zero thickness for the interface that must be sufficiently large for spectral radiance

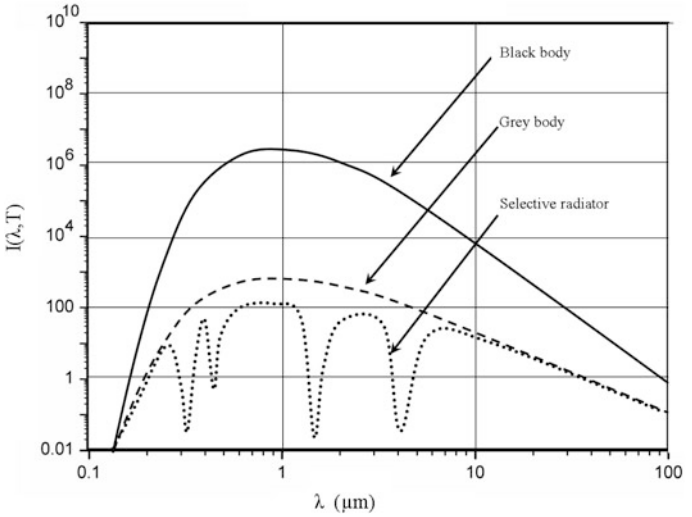

Fig. 2 Sketch of the wavelength dependence of the spectral radiance for a black body (at $T = 3,000$ K), a grey body and a selective radiator. All are supposed to be at the same temperature

of (2) to hold. The extent of radiation penetration and the temperature profile within the target may be approached by considering the equation of optical depth [19] also often called skin effect,

$$I_\mu = I exp(-\mu x), \tag{5}$$

where $I\mu$ the spectral radiance at distance x inside the target material, I is the radiance given in (2), x is distance into the target material and μ is optical penetration depth that is known for most classical materials. The distance $d\mu = 1/\mu$ is the penetration distance (i.e. the value of x such that $I\mu/I = 1/e$ with $e = 2.718$ the Euler constant). At this distance there is only 36.8% (ie. 1/e) of the initial radiance left. At five penetration distances into the target, the radiance has declined to 0.67% of its initial intensity. Conversely, the radiation of a molecule existing five penetration distances into the target has declined to 0.67% of the emitted radiance when it reaches the surface. If the volume bounded by the plane of the target surface and the plane $5d\mu$ into it are lumped together, it may be considered as a single opaque target over which the temperature measurement is made. If the target is thicker than $5d\mu$ and has no or negligible temperature variation with depth then the target may be estimated to be opaque and IR thermography may be safely applied. This was the case with Greenberg et al. [20] investigation into thin film polymer casting. It was first determined that the polymer film did not transmit radiation from objects behind it (in other words the lumped opaque approximation was valid). Secondly, modelling showed that for the films investigated, the temperature profile was a function of time only and did not vary

with depth. This allowed for accurate temperature measurements of the target despite it being partially transparent in the considered IR spectrum range.

IR thermography would not be a suitable technique for measurements into a penetration volume where there is a significant temperature gradient. For example, in evaporative cooling, a liquid interface becomes cooler than the liquid bulk. If this liquid is transparent an IR camera imaging the scene will measure high-temperature emissions from the bulk that are seen through the interface and will therefore show an erroneously high temperature. Several options can be followed to overcome this problem. (a) If $d\mu$ is small, temperature averaging can be safely used. (b) If the temperature gradient within the liquid is known, the high-temperature contributions may be subtracted from the signal by considering differential transmission volumes. (c) If the transmitting medium is a solid, painting its interfacing surface with a thermally thin layer of matt black paint could be another solution. (d) Operate at a different IR wavelength where the target object is opaque. Option (a) is acceptable if its condition holds. Option (b) is infeasible for most experimental situations. Option (c) is a simple solution that has been successfully applied by many authors in the investigation of the liquid-solid interface transient temperature during cooling by droplets. However, the technique is limited to obtaining only solid interface temperatures and may be unsuitable when surface coating are being investigated. Finally, option (d) is the simplest, least error prone and most desirable solution and should be attempted if possible. The use of IR filters that corresponds to IR absorption bands of the target material would be a suitable way to achieve this.

As just discussed, the surface temperature of materials strongly depends on intrinsic properties but they're also modified by the conditions around them. For example air flows will modify the heat transfer coefficients that will affect the results of IR imaging. Determining a material temperature from thermographic measurements hence implies a number of fundamental parameters to be accounted for. Among them: angle dependency and, as will be discussed below, the influence of the transmitting medium. In the construction of (2) one important condition is that the black body is a diffuse emitter (its thermal energy radiation is hence emitted equally in all directions). But an IR camera, like any common optical device, collects energy from within a conical field-of-view that is fixed by the optical capabilities of the camera (focal distance, optical resolution, lens geometry, camera sensors, etc.). The radiation that impinges on the camera corresponds hence to a projection onto its 2D FPA detector of a 3D measured object within this conical field of view. This means that the IR response of a given point of an object interface might strongly depend on the viewing angle. Objects with complex 3D geometries can indeed generate overall IR signals strongly distorted because of the different optical paths followed by the IR radiations within them. As a result, in IR thermography non zero viewing angle can lead to serious misinterpretations. Viewing the object with a normal incidence is however not always the optimal solution. Experiments actually suggest that the best IR signal quality is achieved when measurements are within the cone of maximum emissivity. This discussion indicates that in real materials, precise temperature measurements have to account for the angle at which the surface

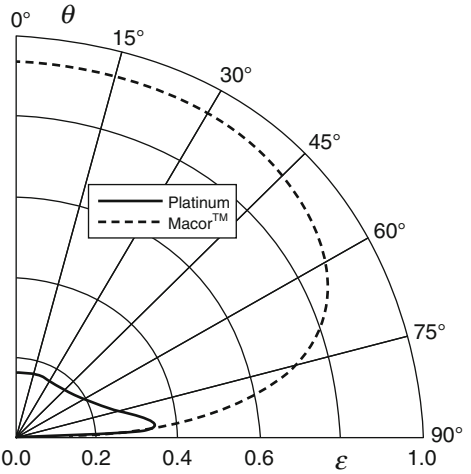

Fig. 3 Angle dependence of the emissivity for platinum and Macor

is observed. In the models, this directional dependence is included in the value of the emissivity ϵ. It is still assumed to be wavelength independent but now includes a dependence of the viewing angle θ. In general dielectric materials, emissivity is almost constant as long as $\theta < 60°$ and drops to zero when $\theta > 60°$ as shown in Fig. 3. Conductors and molten metals have generally much smaller emissivity and often display minimal values for normal incidences $\theta = 0°$. But for such materials the emissivity can remain constant up to viewing angles as large as 85°.

There are some situations where the effect of viewing angles is too important to be neglected. The investigation of Walsh et al. [21] involved temperature measurements on the surface of a piece of pipe. In order to avoid viewing angle emissivity errors, the thermograph images were analyzed digitally by an edge detection algorithm. With the edges of the pipe recognized by the high-temperature area showing up against the background. Temperature measurements were taken from the centre of the pipe, where the viewing angle would be at or close to 0°. The same approach has been followed for measuring the contact line location in evaporating water droplets [22]. A more difficult situation to resolve is in the application of IR thermography to explore interfacial temperature of menisci evaporating inside capillary tubes. In situations where the IR camera is situated such as it is looking into the capillary onto the meniscus, there exists the potential for low contact-angle fluids to possess emissivities with high radial variation. In studies where the temperature profile of a liquid which undergoing evaporative cooling is investigated, such as by Buffone et al. [23] there is an expectation for the wetting fluid to be coolest at the outer capillary radius. An example of such a result is shown Fig. 4. The radial temperature profile near the capillary wall obtained in this figure is consistent with a target with a decreasing emissivity as viewing angle increases but this uncontrolled variable can seriously increase the complexity of obtaining the true emissivity. There is no simple solution to this problem. Accurate determination of emissivity as a function of viewing angle for all wetting fluids could be paired

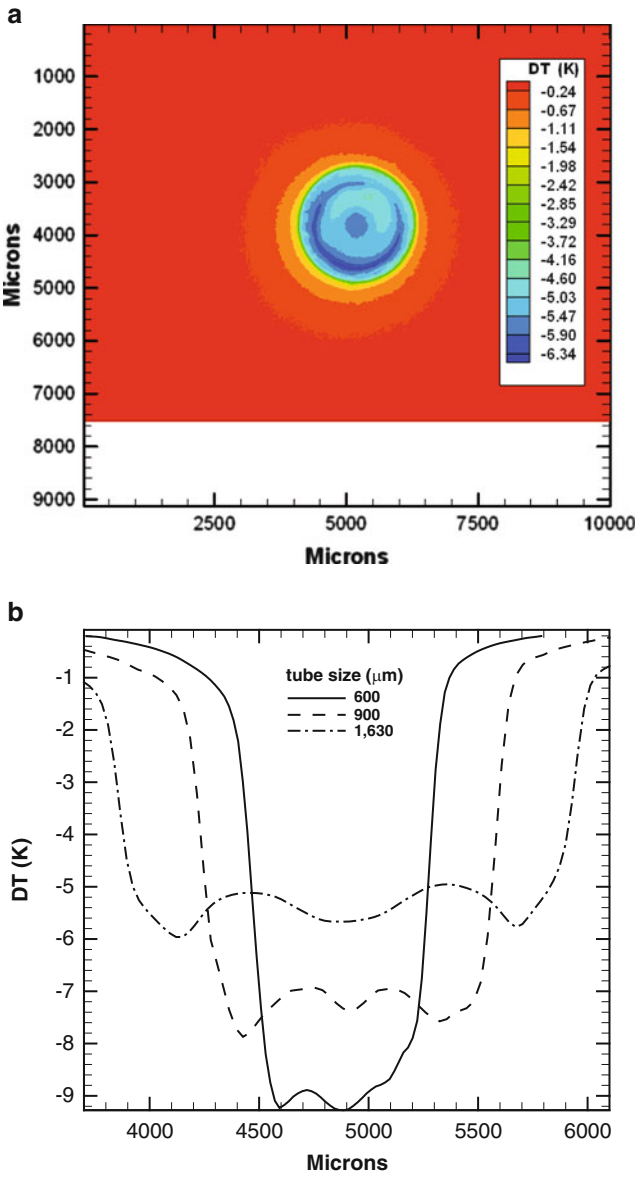

Fig. 4 IR image of a 900 μm diameter heated capillary and methanol as liquid. *Left figure*: Temperature difference with ambient along the horizontal sections of (*right figure*) for various tube size [23]

with modelling of the meniscus shape. Image processing could then identify the viewing angle as a function of radius and apply the correct corresponding emissivity value. Such data is not available in the literature however, and obtaining this data experimentally adds significant extra work and complexity.

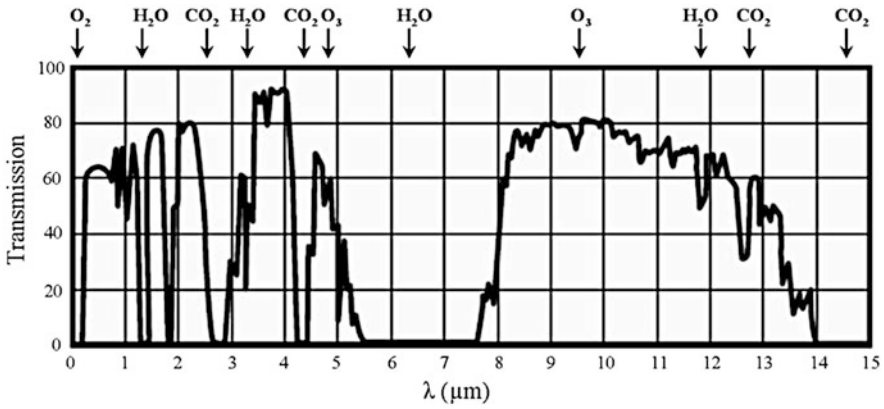

Fig. 5 Atmospheric transmission spectrum at sea level for saturated air

As stated above, the surface temperature of materials strongly depends on the conditions around them. For example a gas flow above a solid surface or the evaporation of a liquid will modify the heat transfer coefficients that will in turn affect the results of IR imaging. In this context, transmitting medium plays a key role in the relevance of the final interpretation of thermography images. It has to be transparent in the operating wavelength band otherwise the measured apparent temperature will be underestimated. This underestimation will be accentuated for large focal distance and will not be compensated by atmosphere radiation (remember that if an object absorbs radiations, it will also emit according to Kirchhoff's law). For a perfectly transparent transmitting medium, $\tau = 1$, no radiance is lost in its transmission and the target material radiation entirely reaches the camera. For standard experiments, this medium is air for which radiance attenuation depends unfortunately strongly on the wavelength. Water molecules and carbon dioxide are the main absorbing molecules and working in such conditions imposes the use of the so called atmospheric windows where atmospheric attenuation is minimal. These windows are mainly situated in three wavelength bands: 1.7–2.5, 3.4–4.1 and 7.5–11.5 μm as can be seen in Fig. 5 representing the absorption spectrum of air at sea level and for saturated air. The two first windows are commonly considered as Medium Wavelength Infrared (MWIR) and the third as Long-Wave Infrared (LWIR). The main components of air, N_2 and O_2, have no interactions with IR waves while polar species such as CO_2 and ubiquitous H_2O do have interactions. For this last reason the humidity and temperature of air are important parameters in obtaining the air transmissivity coefficient. This is also why the main gaps of Fig. 5 correspond to H_2O vibrational transitions that results in low air transmissivity. It is worth noting that suspensions in air like dust or particles also do contribute to lower the transmission quality due to scatting in both MWIR and LWIR. Most of commercial IR camera softwares packages take ambient temperature and humidity as inputs in order to automatically calculate and account for air transmission [24].

But particles are too specific to be accounted for. This is why clean air conditions are also usually required for reliable thermography measurements.

The non negligible effect of air clearly indicates that to measure the correct target object temperature from IR radiations, it is necessary to account for not only the emissivity of the material itself but also the impact of the transmitting medium attenuation and the radiation of surrounding objects. Depending on the working conditions these last contributions can overcome the target object signal and considerably hinder the interest of IR thermography techniques. The estimation of the impact of these contributions constitutes actually one essential step in the calibration procedure of the IR cameras. It is indeed only a careful control of these latter that will allow a one to one link between the measured emitted energy and the temperature of the target object. In the following, we assume for simplicity that all the surrounding of the object is at the same temperature T_{sur}. If T_{to} is the target object temperature and τ_{tm} the medium transmissivity, the emission of the object itself generates at the level of the IR camera detectors the radiation intensity $\epsilon\tau_{tm}W_{bb}(T_{to})$ whereas the contribution of surrounding diffuse (unfocussed and homogeneous) sources writes $(1-\epsilon)$ (here, the emissivity is assumed to be same for all emitting objects). Emission from atmosphere due to the object and surrounding radiation sources is moreover given by where is the temperature of the transmitting medium. The balance of radiant sources and losses yields the following equation:

$$W_{cam} = \epsilon\tau_{tm}W_{bb}(T_{to}) + (1-\epsilon)\tau_{tm}W_{bb}(T_{sur}) + (1-\tau_{tm})W_{bb}(T_{tm}), \qquad (6)$$

where W_{cam} is the radiation intensity measured by the FPA sensors of the IR camera and W_{bb} the one of the black body equivalent given by Stefan-Boltzmann's law. In most experiences, air is the transmitting medium and focal distances are relatively short (few centimeters). Air attenuation and surroundings radiations are then negligible and one can reasonably assume $W_{cam} = \epsilon\tau_{tm}W_{bb}(T_{to})$ without significant loss of accuracy. This is clearly not true for long focal distances where, depending of the circumstances, reflected emission from ambient sources and emission from the atmosphere may become so important that the target object signal will be completely modified. The use of engineering lookup tables becomes then essential. Reflection from ambient non-black and opaque body results in an ambient temperature radiance being detected by the IR camera sensors that will result in an incorrect target temperature calculation. As discussed above, the second term in (5) is one way to account for surrounding reflection sources assuming the temperature and emissivity to be uniform. But a scene may contain many sources of diffuse and specular reflections potentially composed of different materials and at different temperatures. As already discussed, the most direct way to tackle these reflections is to minimize the reflectance of both the target and its surroundings by a painting with a high-emissivity paint (typically matt black). This has been applied for example by Chauvet et al. [25] in obtaining the temperature profile along a square capillary containing an evaporating liquid. The outer surface of the capillary was painted matt black and, as the capillary thickness was small, temperature measurements could be

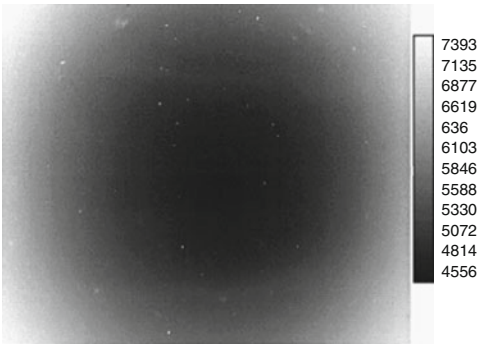

Fig. 6 Image of quasi-perfect mirror produced by an FPA camera. Scale in relative temperature [11]

made on the outer surface that would be equal to the internal sold-liquid, solid-liquid-vapour and solid-vapour interfaces along the capillary's length. Nevertheless, it was required to employ imaging techniques (here an image subtraction method) to account for remaining reflected radiances. A method employed by Howard et al. [26] and also by Mori et al. [27] saw both the target painted matt black (a section of pipe and a rotating blade, respectively) along with surroundings. In the example of Mori et al. [27], areas near the experiment apparatus were painted matt black. Walsh et al. [21] were achieved even greater control over reflectance by placing the small section of pipe inside a matt black box. This is not an ideal solution and potentially hinders accessibility to the apparatus, but is very simple to implement. A disadvantage of this technique is that the use of the high-emissivity paint coating can potentially change the heat transfer resistance of the system and influence the experimental results, [21]. Alternative methods to correct unwanted reflectance effect is also to use imaging techniques. But this requires specific image treatment software often supplied by IR camera providers.

One particular aspect of ambient disturbances shows up for short focal length optics when an IR camera is facing a reflective target surface. In such situations, it detects a radiance originating from the camera detector itself. This is known as the "Narcissus effect". It is particularly noticeable in cooled cameras where a concentrically increasing temperature gradient can be seen originating in the centre of the image, as shown in Fig. 6, for a quasi-perfect mirror. This is due to the centre sensors of the FPA array that detect a greater radiance from IR camera apparatus than outer ones which instead measure more ambient reflections. Image processing allows to monitor this effect by simple image subtractions. More refined processing techniques are able to remove the influence of the Narcissus effect from an image through consideration of the sources of reflected IR radiation. A pixel-by-pixel calibration can for example be achieved by the fitting of a standardization function [11].

3 Example of Applications: Evaporating and Boiling Liquids

The evaporation of liquids has been subject to an increasing interest in the scientific community and the full understanding of physical and chemical mechanisms involved in such two phase systems are still nowadays in many aspects open problems. One example among others is the description of the heat and mass exchanges occurring at liquid/vapor and liquid/solid interfaces. This interest has been driven by an increase in the range of applications underpinned by this phenomenon. The interaction of liquids with solids like in micro channel evaporating meniscus or in deposited droplet on a heated substrate impinges on a wide range of applications such as, spray cooling, nuclear applications and coating technologies. Many different scenarios show up in two phase evaporating systems, depending on the considered liquids, their temperature, the boundary conditions (like the capillary or the substrate temperature and geometry), etc. Fluid motion driven by temperature gradients imposed along a free liquid-gas interface is for example a well-documented phenomenon in micro-channels [28]. Transient regimes due to temperature differences have also been evidenced and explored as discussed below [22].

Liquid evaporation investigations use most frequently optical techniques that do not require complex calibration procedures. But they have many limitations, especially in the cases where thermal properties are important and must therefore be carefully monitored. In most cases indeed, complex liquid flows and temperature fields are at the origin of the overall boiling and/or evaporating dynamics. These phenomena clearly cannot be explained using conventional optical techniques that give access only to geometrical properties like contact angle or contact line location. Such measurements would indeed be limited by the optical resolution and the optical properties of the liquid. As a result, for small contact angles optical techniques cannot detect the presence of the then very thin liquid films often present in the wetting region. Nonetheless, these films must be precisely investigated since they are then main actors of contact line dynamics where evaporation rates are known to be the largest [7]. When investigating evaporation of liquids, IR thermography offers many advantages: e.g. Local temperature measurements, new approach to characterize contact line evolution and its location and the possibility to estimate local heat fluxes from simple models [7]. As usual optical techniques, IR thermography is a non-contact and non destructive measurement method with finite resolution. But as IR thermography gives access to temperatures it allows the study of evaporation sequences even when contact angles become very small ($\theta < 10°$) like it occurs for example in the case of a droplet sitting on a solid substrate at the very end of its lifetime [7]. This section will focus on two examples of two phase systems: evaporating droplets deposited on substrates and boiling in micro channels. Both examples involve free evolving interfaces but in different geometries. In the first case, wetting films are horizontal and the droplet is not fed by incoming

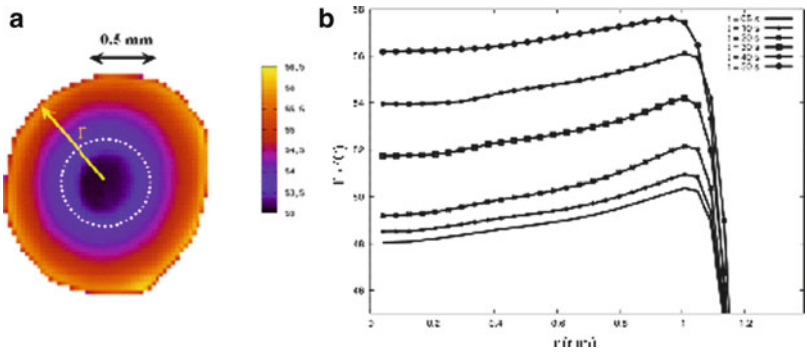

Fig. 7 (**a**) IR image of a 1.4 μL water droplet interface short after its deposition on a copper substrate at temperature $T_s = 60°C$. Radial coordinate is noted by r and temperature is given by the color scale. *Dashed line* is a circle of radius $r = 0.3$ mm with centre the droplet apex. (**b**) Time evolution of the interfacial temperature in radial coordinate [7]

liquid whereas in the case of microchannels, geometry is confined and liquid is often introduced in order to maintain the relevant phenomena in the field of view if the camera.

The IR camera used in the present investigation is a FLIR ThermaCAM SC3000 that has a thermal sensitivity of 20 mK at 30°C, an accuracy of 1% or 1 K of full scale for temperatures up to 150°C and 2% or 2 K of full scale for temperatures above 150°C. The system provides for automatic atmospheric transmission correction of temperature based on the input distance from the object, atmospheric temperature and relative humidity. The field of view at minimum focus distance (26 mm) is 10 mm · 7.5 mm and the instantaneous field of view is 1.1 mrad. The system can acquire images in real time and high speed (with a reduction of the picture size). The images acquired are transferred to a dedicated PC with a special built in ThermaCAM research software (by FLIR System). The spatial resolution of this equipment depends essentially on the IR camera spectral range (8–9 μm for the camera used), the field of view of the camera and the microscope. The IR images were obtained with an experimental set up where the IR camera was mounted directly above the systems under consideration, facing vertically downwards onto them.

As discussed in Sect. 2, emissivity is the key parameter in thermography since it is the one that will allow or not the evaluation of a temperature from the emitted radiations of a material. When investigating the properties of systems like the one in focus in this section, emissivity differences can be used not only to evaluate temperatures but also to discriminate opaque liquids from solids. Liquids and solids have indeed different emissivity and this makes possible a simple and accurate detection of liquid-solid coexisting regions allowing for example the study of contact angle and contact line dynamics. When calibrating the IR camera on the emissivity of the evaporating liquids, the resulting IR map will display important dips (or peaks) in temperatures for the solids (see Fig. 7b). In the case of copper substrates this can even give rise to negative absolute temperatures that clearly

indicate measurements out of the calibration of the IR camera. Therefore special care has to be devoted to this calibration and to the choice of the liquids. In the case of deposited droplets, transparent liquids will for example integrate IR radiance contributions of the substrate. This will make the analysis of the IR maps in term of temperatures completely arbitrary if adapted emissivity models are not used.

4 Evaporating Droplets

When a water droplet of few micro liters is deposited on a moderately heated copper or aluminum substrate, it rapidly spreads and reaches a maximum contact radius depending on its composition and on the substrate properties. This spreading process is usually very fast and occurs within few milliseconds. After this first sequence, water droplets exhibit a quasi steady evolution where contact line radius remains constants. This second regime is called pinned droplet regime and, for water droplets on aluminum or copper substrates, it is also the longest since it corresponds to the evaporation of more than 80% of the initial volume. This second regime clearly depends on the substrate temperature Ts and the characteristic times of its evolution is slow enough (about 50 s when $Ts = 60°C$) to assume a well established equilibrium between the water droplet and the radiation field for the Boltzmann distribution to be valid. Droplets are millimeter sized and hence have spherical cap geometry as a result of the negligible effect of gravity regarding to capillary forces. Evaporation takes place as a result of the non-saturation of the vapour in the semi-open boundary domain. At the free surface, the vapour concentration is assumed to be the saturation concentration, in the vapour phase a steady diffusive regime sets in from the saturated layer to the unsaturated region. In practice, such microliter water droplets when deposited on a copper substrate can be deformed as illustrated in Fig. 7a despite the control of the copper substrate properties. Wetting of the copper by water differs from one experiment to the other even when realized in the same conditions. The main origin of these reproducibility limitations and of the resulting non axi-symmetry of the droplets is the deposition procedure that is used. It consists here in a micro syringe delivering the required amount of water in a pending droplet configuration. This pending droplet in then captured and deposited on the substrate using a micrometer translating table moved manually. This procedure is the simplest and the most precise that can be achieved by hand. Automated droplet deposition devices could probably improve significantly the reproducibility level of the experiments.

Right after the deposition of the droplet, the IR images reveal temperature gradients along the water-air interface with the apex being colder than the contact line as illustrated in Fig. 7a. This temperature profile evolves with time and is found to be consistent for all investigated substrate temperatures. As the water used for this droplet was initially at room temperature (here 20°C), a finite time is necessary to heat it up but its temperature remains smaller than T_s for the complete evaporation duration. Due to this and to a far field temperature, also smaller than Ts, the droplets' apex ($r = 0\,\text{mm}$) remains cooler than the contact line region ($r \approx 1\,\text{mm}$) as

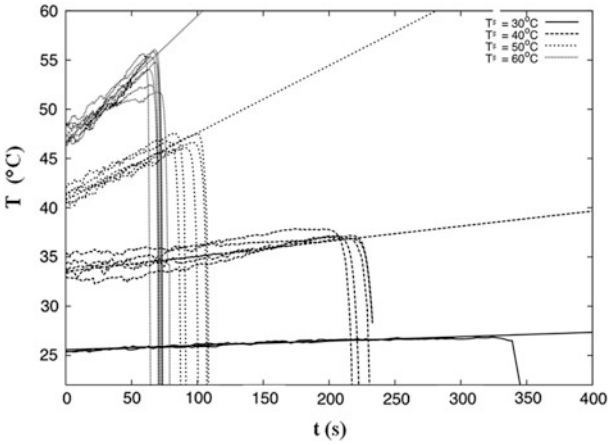

Fig. 8 Radial droplet interface temperature as a function of time for $r = 0.3$ mm and for different values of T_s. Several experiments are displayed for each value of T_s (but for $T_s = 30°C$). The *straight lines* are linear fittings of the temperature rise of the ensemble averaged measurements in the pinned droplet regimes [7]

can be seen in Fig. 7b. Although true for the experiment of Fig. 7, this observation cannot be generalized since viewing angle and depth of field of the IR cameras optics come into play. The focus is often performed, for practical reasons, onto the contact line and not on the droplet's apex and, due to finite depth of field, this can lead to underestimated temperatures at the apex. For the experiments of Fig. 7, the complete droplet interface is in the camera's depth of field and viewing angles are small enough for the temperatures to take relevant values.

Sequences of images like the one of Fig. 7a are obtained for each experiments and dedicated image treatment software is used to extract the time evolution of the radial temperature profiles. One interesting measurement here is the time evolution of the droplet interfacial temperature for a given value of r in the pinned regime. Figure 8 displays this temperature at radial position $r = 0.3$ mm for different values of T_s. It is important noting here that the ones obtained here results from the averaged temperature along the circle of radius $r = 0.3$ mm (white dashed line in Fig. 7a). For each value of T_s, several experiments are represented to illustrate their reproducibility, and the linear fittings are obtained from ensemble averages in the pinned regime are also plotted to better visualize the heating trends. Figure 8 shows that interfacial temperature is linearly rising with a slope that increases with the substrate temperature. Simple scaling laws have been evidenced to describe this behavior [7]. The sharp decline of these curves for later times indicates the complete evaporation of the droplet and reveals the bare copper surface from which the droplet lifetime and contact line evolution can be studied. The same measurements for other values of r show almost identical trends as long as $r < 0.7$ mm [7]. This demonstrates that far from the contact line, temperature rising rates do not significantly depend on r and that the substrate inflowing energy yields a quiet

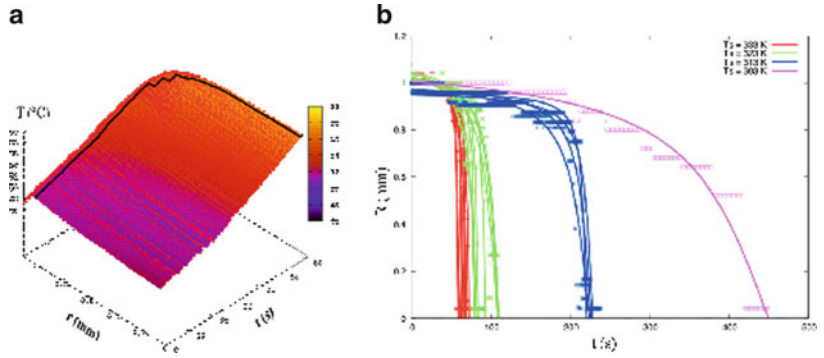

Fig. 9 (**a**) 3D plot of the droplet interface temperature as a function of time t and radial coordinate r when $T_s = 60°C$. *Full black line* is the contact line. (**b**) Evolution of the contact line radius R for different substrate temperatures. Several experiments are shown in this figure and *full lines* are hyperbolic tangent interpolations of ensemble averaged data [7]

homogeneous heating up at least in this region of the interface. But this behavior is no more true for $r > 0.7$ mm where the growth rate of interfacial temperature becomes strongly r dependent. This is due to different heat transport mechanisms. The main reason here is reducing droplet thickness when approaching the contact line that makes heat transfers easier as thermal resistance is reduced. But the important observation here is that thermography now makes possible to provide quantitative analysis of the local outgoing mass flow as will be discussed next. It is worth noting that the data of Fig. 8 are space-averaged along the circle $r = 0.3$ mm as just mentioned. All temperature fluctuations like for example hydrothermal waves are hence smoothed out and cannot be detected any more. Such waves have been for example evidenced with IR thermography in the case of FC-72 evaporating droplets on titanium substrates (see next).

IR thermography also allows the tracking of the time evolution of the contact line. Figure 9a shows a 3D plot of the interfacial temperature as a function of time and r when $T_s = 60°C$. It indicates a global heating of the droplet from about 48°C up to 59°C. The contact line location is also displayed in this figure. A careful inspection of it shows mainly two regimes. A pinned regime when $t < 50$ s where the contact line radius is constant and a depinning regime when $t > 50$ s where contact line moves rapidly before complete evaporation of the droplet. In this very last period of the droplet life time, temperature in the vicinity of contact line is almost constant and takes value 59°C. The contact radius evolution $R(t)$ is shown in Fig. 9b for several substrate temperatures and shows that the droplets remain pinned for most of their lifetime for sufficiently large values of T_s. This result is in a good agreement with the measurements performed with optical techniques. But with the interest here that the use of IR thermography in this specific case allows the detection of water even when the droplet is reduced to a very thin film which is no more accessible to optical techniques.

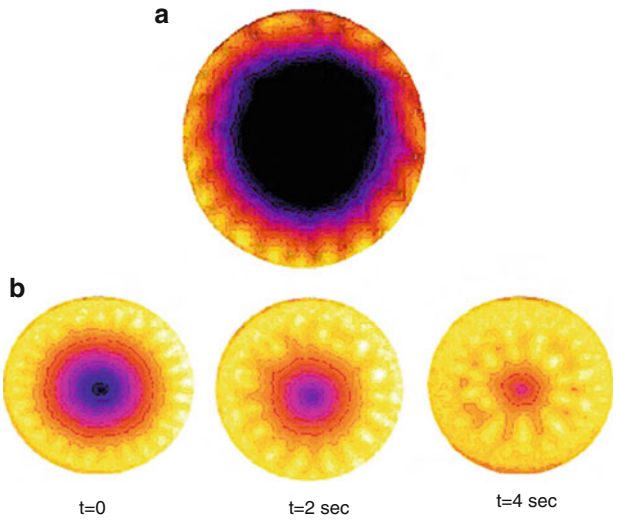

Fig. 10 (**a**) Evaporating methanol droplets, thermal waves numbered across the droplet circumference. (**b**) Evolution of the patterns observed during the evaporation of a FC-72 droplet on a titanium substrate. Contact line diameter is about 3 mm in these images [8]

IR thermography technique has also been used to study temperature pattern formation driven by the spontaneous evaporation of sessile droplets and interpreted in terms of hydrothermal waves. We present in what follows some key findings for droplets of methanol, ethanol and FC-72 and made possible by the use of this technique. New results were obtained showing the influence of the temperature and the thermal conductivity of the substrate on the number of waves observed at the free surface of such evaporating droplets in the pinned regime [8]. A correlation was in particular evidenced between the influence of the liquid volatility and the number of hydrothermal waves that can be seen in Fig. 11. These experimental data reveal the presence of traveling waves that have been described with a three-dimensional stability analysis in spherical coordinates. New scaling factors and dimensionless numbers were introduced in order to account for the thermal diffusivity in the substrate as well as the evaporation rate [29]. Similar experiments for water show only a very weak hydrothermal activity. This is due to the fact that for water droplets, the temperature gradients on the interface are only about 1°C. In contrast, the results obtained for the other liquids tested were more interesting since temperature gradients could reach values larger than 5°C. Methanol and ethanol appeared to show distinct thermal fluctuations that were observed to vary temporally as illustrated in Fig. 10a for methanol. These spoke like wave trains appear to move in a direction that is parallel to the droplet periphery, rotating around the droplet. For ethanol, the number of waves observed and the respective travelling velocities were found to vary depending on the substrate that was used [8]. As the droplet evaporated, their number decreased, whilst the temperature fluctuations for each wave increased. The more volatile methanol droplets were found to display much

higher numbers of waves than ethanol ones, when tested using the same procedure. For example, in the case of a titanium substrate, held at 26°C, the number of waves visible in methanol droplets ranged from around 40 at an early stage in the droplet evaporation, down to 20 at the latter stage of its lifetime. In comparison, ethanol displayed a wave range only between 14 and 7.

In the case of FC-72 a rather different hydrothermal pattern was observed as illustrated in Fig. 10b. Hydrothermal cells emerge from the apex region of the droplets and then drift toward the edge. The size of these cells is found to be smaller for those closer to the edge of the droplet as can be seen in Fig. 10b for different times. The pattern formation was analyzed further by examining the dependence of the size of the cells on the local height of the droplet. It was shown that the size of the cells increases, approximately linearly, with the droplet height [8, 30].

5 Boiling and Two-Phase Flows in Micro-Channels

IR thermography finds also important applications in measuring temperatures on the walls of channels with boiling taking place within. Conversely to evaporating droplets, it is the temperature of a solid, here glass, that will be investigated in this section. Illustrations with ethanol and FC-72 will be presented below for glass microchannels. We present in what follows some key findings made possible by the use of IR technique in such microchannels and refer the reader to specialised texts on two phase flows and boiling phenomena [31].

Two-phase flow instabilities in single high-aspect-ratio rectangular micro-channels were experimentally investigated using FC-72 and ethanol in micro-channels with varying hydraulic diameters (noted d_h in the following) and in a wide range of heat fluxes and liquid mass fluxes (noted q) [32]. One interesting result from these studies is the identification of low-frequency fluctuations (resp. high-frequency fluctuations), the flow patterns corresponding to these situations are illustrated in Fig. 11a (resp. Fig. 11b) depending on the mass flux, on d_h and q. Based on direct visual inspection it appears that the low-frequency fluctuation is the major fluctuation mode at lower mass flux and resulted from the periodic reverse and rewetting flow, Fig. 11. The high-frequency fluctuation, on the other hand, is caused by the vapour slug cluster passage during the rewetting flow and the vapour collision at downstream. One example of flow regimes for FC-72 boiling in a micro-channel is illustrated in Fig. 12 where vapour collision with large-scale nucleation and droplet evaporation are clearly visible. The two phase flow within microchannels exhibit three-phase contact lines where heat/mass transfer is intense. Around these regions there are large temperature gradients on the wall. These temperature gradients are picked up when using the IR camera from the outside because of the small thickness and good conductivity of the channel walls.

Micro-channel surface temperature is fluctuating because of the periodic reverse and rewetting flow and the consequent local partial dry-out. IR thermography measurements established that the low frequency pressure drop and the averaged

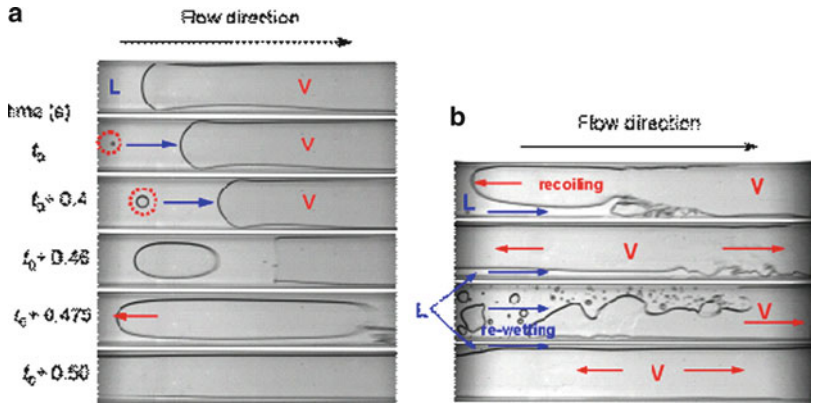

Fig. 11 Flow regimes of ethanol boiling in a micro-channel with $dh = 1,454\,\mu\text{m}$, (**a**) slug and annular flow at $G = 11.2\,\text{kg}\,\text{m}^{-2}\,\text{s}^{-1}$ and $q = 11.0\,\text{kW}\,\text{m}^{-2}$, (**b**) wispy-annular flow at $G = 11.2\,\text{kg}\,\text{m}^{-2}\,\text{s}^{-1}$ and $q = 15.0\,\text{kW}\,\text{m}^{-2}$ [33]

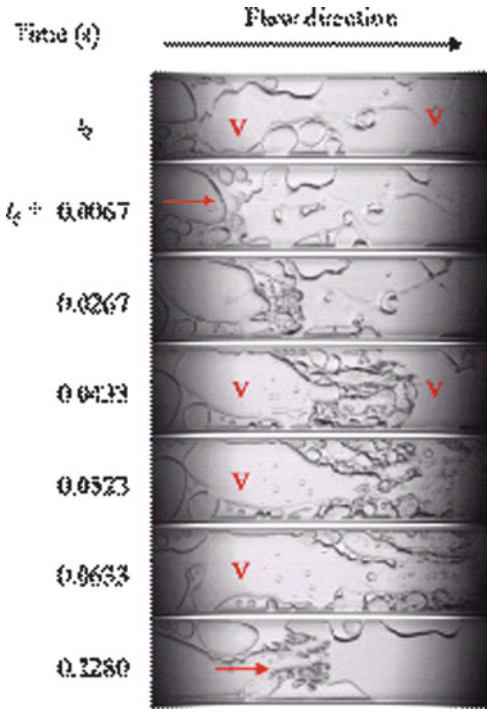

Fig. 12 Flow regimes of FC-72 boiling in the channel with $d_h = 1,454\,\mu\text{m}$ at $G = 44.8\,\text{kg}\,\text{m}^{-2}\,\text{s}^{-1}$ and $q = 18.31\,\text{kW}\,\text{m}^{-2}$ [33]

channel wall temperature (noted T_w) fluctuations are in-phase. Temperature fluctuation amplitude is higher at downstream where the vapour phase exists. In addition, micro-channel wall temperature distribution of FC-72 is remarkably different from ethanol. Ethanol flow boiling shows stable fluctuation mode where the pressure drop

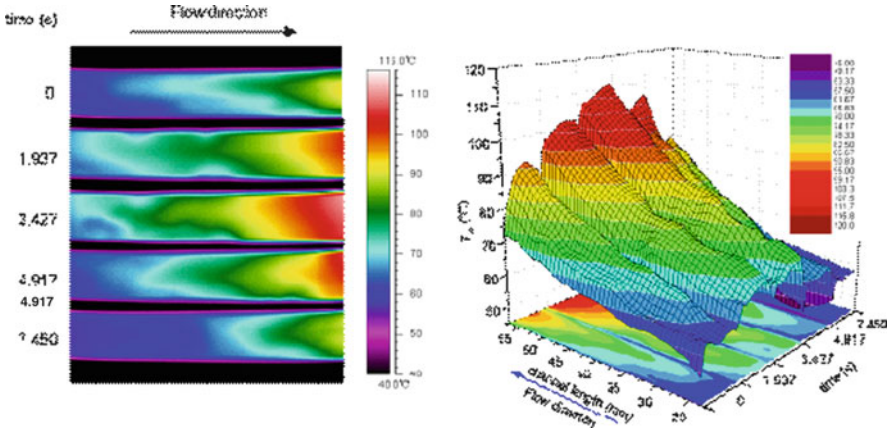

Fig. 13 Infrared sequences of channel surface temperatures and the 3-dimensional plot; $d_h = 571\,\mu\text{m}$, $G = 11.2\,\text{kW m}^{-2}$, $q = 2.07\,\text{kW m}^{-2}$; FC-72 [33]

and temperature oscillate regularly. Very high T_w fluctuation amplitude is reached, implying much longer recoiling and re-wetting period of ethanol than FC-72. The channel wall temperature gradient is lessened by increasing heat flux. For FC-72, T_w fluctuates chaotically with low amplitudes while the wall temperature gradient exists in the channel axial direction. For ethanol, however, T_w fluctuates regularly with high fluctuation amplitudes and low channel wall temperature gradient appears during the rewetting period. These differences are explained by the very low surface tension of FC-72 and its complete wetting of glass walls.

The channel surface temperature distributes differently depending on the flow regime taking place within it. A high-frequency low-amplitude fluctuations mode is present in the flow, as illustrated in Fig. 13 in the case of FC-72. A higher heat flux is applied on the channel surface, temperature gradually grows along the channel stream-wise direction and high values of T_w are achieved near the channel exit where large amount of vapour exists. Nucleation is taking place within the liquid film, vapour collision is then the major fluctuation source and the entrained liquid in the vapour core is evaporating fiercely due to high heat flux. Because the reverse flow is largely suppressed by higher mass flux, the vapour-occupied portion in the channel constantly exists. In this circumstance, the high temperature area should be monitored with special attention because the constantly high channel wall temperature could easily result in surface destruction. The channel wall temperature fluctuations indicate that the temperature fluctuation amplitude is higher at downstream. This is because the downstream channel is more likely to be occupied by the vapour phase, thus is easier to be affected by the liquid and vapour distribution.

Thermographic results corresponding to the regular temperature fluctuation are exhibited in Fig. 14 still for FC-72. The low-frequency high-amplitude instabilities are resulted from the recoiling and rewetting mechanism. Uniform temperature

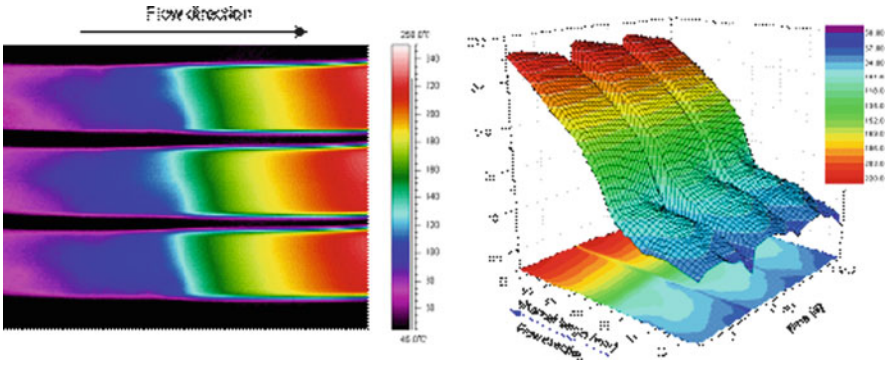

Fig. 14 Infrared sequences of channel surface temperatures and the 3-dimensional plot; $d_h = 571\,\mu\text{m}$, $G = 11.2\,\text{kW m}^{-2}$, $q = 4.30\,\text{kW m}^{-2}$; FC-72 [33]

profiles during rewetting can be found. In addition, more intense fluctuation level is triggered by increasing the heat flux. Meanwhile, the temperature gradient along the channel is lessened. As the heat flux increases, the pressure drop fluctuation and channel wall temperature oscillation become increasingly chaotic. There appear some low-amplitude instabilities, which are caused by the random bubble nucleation and vapour collision.

The above section illustrates the use of IR thermography in investigating and understanding multiphase flows and heat transfer at the microscale. In the specific case presented above, the IR technique allowed spatial and temporal monitoring of wall temperature. The data acquired helped understanding and quantifying two flow instabilities taking place inside the microchannel.

6 Conclusions

While much of the discussion in this chapter has focussed on methods of applying IR thermography and accounting for the many and complex sources of measurement distortion, it is important to present this in context of the advantages to be gained from the technique's use. The two key advantages of IR thermography are (a) the non-intrusive nature of the temperature measurements and (b) the two-dimensional temperature measurements obtained. It is this first characteristic that has allowed the IR thermography technique to be applied extensively in the investigation of thermo-fluid-dynamics, as it allows evaluation of the entire flow system without any alteration in the flow dynamics. The technique has also found increasing applications in experiments outside of convective heat transfer investigations, such as its application in examining boiling heat transfer and systems undergoing phase changes. Here the use of an IR camera allows evaluation of temperature at the solid-liquid interface of the heater in flow boiling as well as mass flows in the case of deposited droplets. It is this ability to produce images that allow for powerful

visualisations of complex systems that is perhaps one of the strongest, albeit somewhat intangible, merits of IR thermography. Investigations into heat transfer situations involving pool or channels flow boiling, micro-channels and mass transfer have the highest potential to be gained from the application of IR thermography, as the evaluation of interfacial temperature allows for evaluation of heat and mass fluxes and contact line dynamics.

Sources of errors and the methods used to account for them have been discussed. Digital recording of results allows for significant flexibility in the identification and correction of errors through signal processing. However, there are some issues which remain as yet unsolved for the purposes of interfacial temperature measurements. The largest of these is the influence of target emissivity (or absorptivity), reflectivity and transmissivity on measured temperatures. This chapter aimed to provide basic elements for quantifying the penetration of IR temperature measurements through the concept of penetration depth; however their application relies only on the availability of optical data. The availability of data on the IR spectrum properties of material is limited and exacerbates this problem. IR penetration for non-opaque materials cannot be quantified, and the planning of an experiment is hindered if the IR camera operating wavelength required of the apparatus materials is not known. Future work aiming to resolve this shortcoming could examine the potential for extensively available IR spectroscopy data to be applied to IR thermography experiment design. Additionally, it may be possible to predict material IR properties from vibrational and rotational transition energies. The growth of use of any new technique depends strongly on the ease of its uptake, and in this regard IR thermography requires further work to mature. A final limitation is the requirement for experimental arrangements that minimise background reflection and maximise target emissivity in order to obtain accurate readings is an additional limitation. In the examination of large pieces of apparatus, painting the surroundings in matt black paint may be an undesirable imposition. In experiments involving smaller apparatus, accuracy considerations requiring the use of a “black box” reduce accessibility and visibility. Furthermore, painting solid interfaces in matt black paint is infeasible in investigations involving surface treatments and may cause error in the alteration of heat transfer characteristics.

IR thermography presents a number of limitations as any other investigation techniques. But it is up to date the most powerful tool for obtaining interfacial temperatures within large field of views and, when experimental conditions are favourable, a technique able to provide great details for the studied systems. The accuracy of temperature measurements requires consideration of sources of error, including the Narcissus effect, reflected IR waves from background sources and obtaining the target emissivity. These are accounted for through calibration and signal processing. On top of this, the impressive range of temperature covered by the IR cameras (from −20 to 2,000°C) makes it very easy to analyze situations such as the ones with an extra heating provided when large temperature variations are expected. IR thermography has been extensively applied for the measurement of convective heat transfer coefficients but due to its great potential its use outside of this field is nowadays rapidly growing.

References

1. Fang, G., Ward, C.A.: Temperature measurement close to the interface of an evaporating liquid. Phys. Rev. E **59**, 417–428 (1998)
2. Hetsroni, G., Mewes, D., Enke, C., Gurevich, M., Mosyak, A., Rozenblit, R.: Heat transfer to two-phase flow in inclined tubes. Int. J. Multiphase Flow **29**, 173–194 (2003)
3. Hetsroni, G., Mosyak, A., Segal, Z., Pogrebnyak, E.: Two-phase flow patterns in parallel micro-channels. Int. J. Multiphase Flow **29**, 341–360 (2003)
4. Herchang, A., JiinYuh, J., Jer-Nan, Y.: Local heat transfer measurements of plate finned-tube heat exchangers by infrared thermography. Int. J. Heat Mass Transf. **45**, 4069–40782 (2002)
5. Sgheiza, J.E., Myers, J.E.: Behavior of nucleation sites in pool boiling. AIChE J. **31**, 1605–1613 (1985)
6. Theofanous, T.G., Tu, J.P., Dinh, A.T., Dinh, T.N.: The boiling crisis phenomenon: Part I: nucleation and nucleate boiling heat transfer. Exp. Therm. Fluid Sci. **26**, 775–792 (2002)
7. Girard, F., Antoni, M., Sefiane, K.: Infrared thermography investigation of an evaporating sessile water droplet on heated substrates. Langmuir **26**, 4576–4580 (2010)
8. Sefiane, K., Moffat, R., Steinchen, A.: On hydrothermal waves observed during evaporation of sessile droplets. Colloids Surf. A Physicochem. Eng. Asp. **365**, 95–108 (2010)
9. Rogalski, A.: Infrared detectors: an overview. Infrared Phys. Technol. **43**, 187–210 (2002)
10. Rainieri, S., Pagliarini, G.: Data processing technique applied to the calibration of a high performance FPA infrared camera. Infrared Phys. Technol. **43**, 345–351 (2002)
11. Horny, N.: FPA camera standardization. Infrared Phys. Technol. **44**, 109–119 (2003)
12. Kaplan, H.: Practical Applications of Infrared Thermal Sensing and Imaging Equipment. SPIE, Bellingham (2007)
13. Höhmann, C., Stephan, P.: Microscale temperature measurement at an evaporating liquid meniscus. Exp. Therm. Fluid Sci. **26**, 157–162 (2002)
14. Farina, D.J., Hacher, J.M., Moffat, R.J., Eaton, J.K.: Illuminant invariant calibration of thermochromic liquid crystals. Exp. Therm. Fluid Sci. **9**, 1–12 (1994)
15. Hay, J.L., Hollingsworth, D.K.: A comparison of trichromic systems for use in the calibration of polymer-dispersed thermochromic liquid crystals. Exp. Therm. Fluid Sci. **12**, 17–12 (1996)
16. Conn G.K.T., Avery D.G.: Infrared Methods: Principles and Applications. Academic, New York (1960)
17. Parker, R.: Transient surface temperature response of liquid crystals films. Mol. Cryst. Liq. Cryst. **20**, 99–106 (1973)
18. Ireland P.T., Jones T.V.: The response time of a surface thermometer employing encapsulated thermochromic liquid crystals. J. Phys. E Sci. Instrum. **20**, 1195–1199 (1987)
19. Kitchin, C.R.: Stars, Nebulae, and the Interstellar Medium: Observational Physics and Astrophysics. A. Hilger, Bristol (1987)
20. Greenberg, A.R., Shojaie, S.S., Krantz, W.B., Tantekin-Ersolmaz, S.B.: Use of infrared thermography for temperature-measurement during evaporative casting of thin polymeric films. J. Memb. Sci. **107**, 249–261 (1995)
21. Walsh, P.A., Walsh E.J., Muzychka Y.M.: Heat transfer model for gas-liquid slug flows under constant flux. Int. J. Heat Mass Transf. **53**, 3193–3201 (2010)
22. Girard, F., Antoni, M., Sefiane, K.: On the effect of Marangoni flow on evaporation rates of heated water drops. Langmuir **24**, 9207–9210 (2008)
23. Buffone, C., Sefiane, K.: IR measurements of interfacial temperature during phase change in a confined environment. Exp. Therm. Fluid Sci. **29**, 65–74 (2004)
24. Hamamatsu: Characteristics and Use of Infrared Detectors. Hamamatsu Photonics K.K., Bridgewater (2004)
25. Chauvet, F., Cazin, S., Duru, P., Prat, M.: Use of infrared thermography for the study of evaporation in a square capillary tube. Int. J. Heat Mass Transf. **53**, 1808–1818 (2010)
26. Howard, J.A., Walsh, P.A., Walsh, E.J.: Prandtl and capillary effects on heat transfer performance within laminar liquid-gas slug flows. Int. J. Heat Mass Transf. **54**, 4752–4761 (2011)

27. Mori, M., Novak, L., Sekavčnik, M.: Measurements on rotating blades using IR thermography. Exp. Therm. Fluid Sci. **32**, 387–396 (2007)
28. Buffone, C., Sefiane, K.: Controlling evaporative thermocapillary convection using external heating: an experimental investigation. Exp. Therm. Fluid Sci. **32**, 1287–1300 (2008)
29. Dunn, G., Wilson, S. K., Duffy, B., David, S., Sefiane, K.: The strong influence of substrate conductivity on droplet evaporation. J. Fluid Mech. **23**, 329–351 (2009)
30. Mancini, H., Maza, D.: Pattern formation without heating in an evaporative convection experiment. Europhys. Lett. **66**, 812–818 (2004)
31. Collier, J.G., Thome, J.R.: Convective Boiling and Condensation. Oxford Engineering Science. Oxford University Press, New York (1996) [ISBN 13: 9780198562962]
32. Wang, Y., Sefiane, K.: Effects of heat flux, vapour quality, channel hydraulic diameter on flow boiling heat transfer in variable aspect ratio micro-channels using transparent heating. Int. J. Heat Mass Transf. **55**, 2235–2243 (2012)
33. Wang, Y.: Liquid vapour phase change and multiphase flow heat transfer in single micro-channels using pure liquids and nano-fluids. Ph.D. thesis, University of Edinburgh (2011)

Shear Rheology of Interfaces: Micro Rheological Methods

A.J. Mendoza, R.C. Jordán, F.M. Pedrero, H. Agogo, R.G. Rubio, F. Ortega, and M.G. Velarde

1 Introduction

Many of the diverse properties of soft materials (polymer solutions, gels, filamentous proteins in cells, etc.) stem from their complex structures and dynamics that have multiple characteristic length and time scales. A wide variety of technologies, from paints to foods, from oil recovery to processing of plastics, evaporation of complex fluids, design of multiphase chemical reactors, rely heavily on understanding the flow of complex fluids [1, 2]. The viscoelastic responses of complex materials depend on the time scale at which the sample is probed. Measurements of the complex shear modulus, $G^*(\omega)$, as a function of frequency are most frequently used for obtaining the elasticity and viscosity. Typical experiments using standard rheometers for bulk systems apply a small oscillatory strain on the sample, and usually probe frequencies from mHz up to tens of Hz.

Although standard rheological measurements have been very useful in characterizing soft materials and complex fluids, they suffer from some drawbacks, e.g. the need of sample volumes larger than one milliliter, which make them unsuitable for rare or precious materials, and for biological samples that are available in minute quantities. Furthermore, only average measurements of the system response are

A.J. Mendoza · R.C. Jordán · H. Agogo · R.G. Rubio (✉)
Departamento de Química Física I, Facultad de CC. Químicas and Instituto Pluridisciplinar, Universidad Complutense de Madrid, 28040 Madrid, Spain
e-mail: rgrubio@quim.ucm.es

F.M. Pedrero · F. Ortega
Departamento de Química Física I, Facultad de CC. Químicas, Universidad Complutense de Madrid, 28040 Madrid, Spain
e-mail: fortega@quim.ucm.es

M.G. Velarde
Instituto Pluridisciplinar, Universidad Complutense de Madrid, 28040 Madrid, Spain
e-mail: mgvelarde@pluri.ucm.es

R.G. Rubio et al. (eds.), *Without Bounds: A Scientific Canvas of Nonlinearity and Complex Dynamics*, Understanding Complex Systems,
DOI 10.1007/978-3-642-34070-3_21,

obtained using conventional rheometers due to the typical size of their probes, which makes them useless for local measurements in inhomogeneous systems. Microrheological techniques are being used during the last two decades for probing the material response on micrometer length scales, and using microliter sample volumes. The following advantages over macrorheology are worth mentioning: (a) much higher range of frequencies available without using the time-temperature superposition that is valid only for a limited number of systems [2]; (b) the capability of measuring material inhomogeneities that cannot be studied using macrorheological methods, and (c) rapid thermal and chemical homogenization that allow the transient rheology of evolving systems to be studied [3]. Microrheology methods typically use embedded nano- or microparticles to locally deform the samples hence macro- and microrheology probe different aspects of the material. Macrorheology measurements explore extremely long (macroscopic) length scales compared to the characteristic length scales of the system, microrheology effectively measures material properties on the scale of the probe itself (since flow and deformation fields decay on this length scale). Detailed descriptions of the methods and applications of microrheology to the study of bulk systems have been given in review articles published in recent years [4–11]. In the present work we will focus on techniques that use micron-size particles, and their application to the study of the dynamic behavior of fluid interfaces.

Interfaces play a dominant role in the behavior of many complex fluids. Interfacial rheology has been found to be a key factor in the stability of foams and emulsions, compatibilization of polymer blends, flotation technology, fusion of vesicles, mass transport through interfaces, drug delivery from micro- and nanocapsules, etc. [12,13]. In most cases interfacial rheology has been controlled by a careful selection of surfactants. However, the environmental regulations in the EU are becoming stricter, and conventional synthetic surfactants have to be substituted by environmentally friendly chemicals. One of the most promising possibilities is to stabilize the interfaces using natural or biodegradable particles trapped at the interfaces, due to the high trapping energy of microparticles at fluid interfaces [14].

The dynamics of fluid interfaces is a rather complex problem because, even for the simplest fluid–fluid interface, different dynamic modes have to be taken into account: the capillary (out of plane) mode, and the in-plane mode, which contains dilational (or extensional) and shear contributions. For more complex interfaces, such as thicker ones, other dynamic modes (bending, splaying) have to be considered [15]. Moreover, the coupling of the above mentioned modes with adsorption/desorption kinetics may be very relevant for interfaces that contain soluble or partially soluble surfactants, polymers or proteins [16–18].

Till recently interfacial shear rheology has been studied using macroscopic interfacial rheometers which have a lower sensibility limit of about $10^{-6}\,\mathrm{N\,s\,m^{-1}}$ [16, 19–21], however many important systems have surface shear viscosities below this limit, and microrheological techniques have been developed to overcome this limit down to values as low as $10^{-10}\,\mathrm{N\,s\,m^{-1}}$. In spite that the measurement of diffusion coefficients of particles attached to interfaces is relatively straightforward with modern microrheological techniques (see below), one has to rely on

hydrodynamic models of the viscoelastic surroundings probed by the particles in order to obtain variables such as monolayer elasticity or shear viscosity. The more complex the structure of the interface the stronger are the assumptions of the model, which reduces its range of applicability and makes more difficult to test its validity. In the present work we will briefly review two experimental techniques frequently used to study the dynamics of microparticles trapped at interfaces, and the use of microparticles as probes for studying the shear rheology of monolayers at fluid interfaces. We will also summarize two of the available theoretical approaches for calculating the shear microviscosity of fluid monolayers from particle tracking experiments. Finally the relatively few experimental results available for fluid interfaces using the two techniques will be discussed and analyzed using the two theories. The results will show that we are far from understanding microrheology results, and therefore more experimental and theoretical work is necessary.

2 Experimental Techniques

For studying the viscoelasticity of the probe environment there are two broad types of experimental methods: active methods, which involve probe manipulation, and passive methods, that relay on thermal fluctuations. Passive techniques are typically more useful for measuring low values of predominantly viscous moduli, whereas active techniques can extend the measurable range to samples with significant elasticity modulus. In this work we will focus on one passive technique: particle tracking by video microscopy, and one active technique: optical tweezers.

2.1 Fundamentals of Video Microscopy Particle Tracking

The main idea in particle tracking is to follow the trajectories of probes introduced into (onto) the system by video microscopy. The trajectories of the particles, either in bulk or on surfaces, allow one to calculate the mean square displacement, MSD, which is related to the diffusion coefficient, D, and the dimensions in which the translational motion takes place, d, by

$$\left\langle \Delta r^2(\tau) \right\rangle = 2d D \tau^{\alpha}, \tag{1}$$

where the brackets indicate the average over all the particles.

In case of diffusion in a purely viscous material (or interface), α is equal to 1, and the usual linear relation is obtained between the MSD and the lag time τ. For highly viscous materials or interfaces (like condensed surfactant or lipid monolayers and dense polymer monolayers), or when the system is dominated by the probe particles interactions (being this particularly important at high particle surface coverage) (1) does not fully apply. The movement of nano- and micro-particles in these solid-like

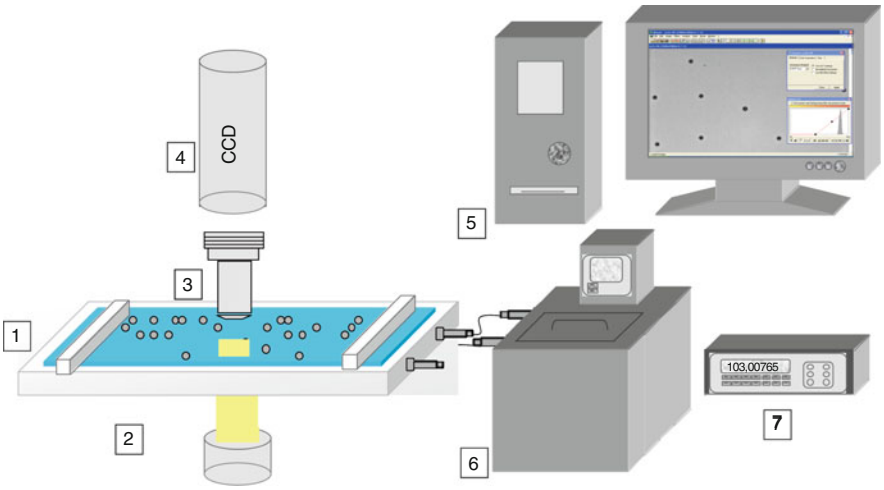

Fig. 1 Typical particle tracking setup for 2D microrheology experiments: (1) Langmuir trough; (2) illumination; (3) microscope objective; (4) CCD camera; (5) computer; (6) thermostat; (7) electronics for measuring the surface pressure

interfaces cannot simply be interpreted assuming sub-diffusivity $\alpha < 1$. In fact if we consider a Maxwell viscoelasticity model the mean square displacement adopts the form of

$$\left\langle \Delta r^2(\tau) \right\rangle = \sigma/E + \sigma\tau/\eta, \tag{2}$$

where σ is the stress, E is the elasticity modulus and η the viscosity coefficient and all of them refer to pure shear deformations. The characteristic Maxwell time is given by $\tau_c = \eta/E$. Anomalous diffusion $\alpha < 1$ has been invoked in many systems of biological interest where the Brownian motion of the particles is hindered by obstacles, or even constrained to defined regions (corralled motion) [22]. The diffusion coefficient is related to the friction coefficient, f, by the Einstein relation

$$D = \frac{k_B T}{f}. \tag{3}$$

In 3D f is given by Stokes law, $f = 6\pi\eta$, and for pure viscous fluids the shear viscosity can be directly obtained from the diffusion coefficient. However, as we will discuss below, Stokes law does not apply to interfaces.

Figure 1 shows a sketch of a typical setup for interface particle tracking experiments. A CCD camera (typically 30 fps) is connected to a microscope that permits to image the interface prepared onto a Langmuir through. The series of images are transferred to a computer to be analyzed and to extract the trajectories of a set of particles. A common problem is that the Brownian motion of the particles is often superimposed to a collective motion of the fluid arising from thermal

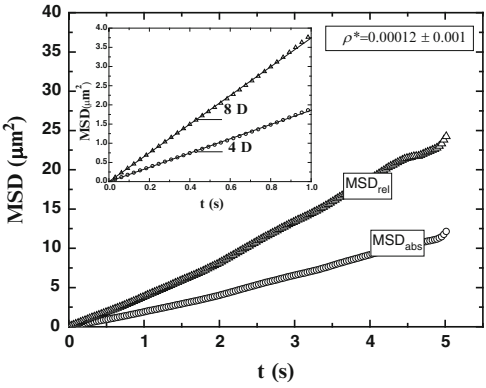

Fig. 2 Mean square displacements and relative square displacement for latex particles at the water/n-octane interface. Experimental details: set of 300 latex particles of 1 μm of diameter, surface charge density: $-5.8\,\mu\,\mathrm{C\,cm^{-2}}$, and reduced surface density, $\rho^* = 1.2 \cdot 10^{-3} (\rho^* = \rho a^2)$, 25°C

gradients, and then it is useful the use of the relative mean square displacement of pairs of particles defined by

$$\mathrm{MSD}_{rel} \equiv \left\langle \Delta r_{rel}^2(\tau) \right\rangle = \left\langle \left(\Delta \mathbf{r}_{ij}(t+\tau) - \Delta \mathbf{r}_{ij}(t) \right)^2 \right\rangle = 4dD\tau. \tag{4}$$

The above averages are taken over all the pairs of particles and initial times, t, of the system. In this way any collective motion is eliminated or reduced.

Figure 2 shows a typical set of results for the MSD of a system of latex particles (1 μm of radius) spread at the water/n-octane interface at low particle surface densities (gas-like phase) [23]. The analysis of MSD and MSD_{rel} in terms of (1) and (4) and in the linear range allows one to obtain D. However, it must be taken into account that for laden interfaces, even below the threshold of aggregation or fluid–solid phase transitions, the MSD shows a sub-diffusive behavior ($\alpha < 1$ in (1)). Therefore, only physically meaningful values of D can be obtained in the limit of short times, and this should be taken into account when extracting the surface microrheology parameters from D.

When the samples are heterogeneous at the scale of particle size (a situation rather frequent, specially in biological systems [22, 24–26]), single particle tracking gives erroneous results and the so-called "two-point" correlation method is recommended [27]. In this method the fluctuations of pairs of particles at a distance R_{ij} are measured for all the possible values of R_{ij} within the system. Vector displacements of individual particles are calculated as a function of lag time, τ, and initial absolute time, t: Then the ensemble averaged tensor product of the vector displacements is calculated [9]:

$$\begin{aligned} D_{\alpha,\beta}(r,\tau) &= \left\langle \Delta r_\alpha^i(r,\tau) \Delta r_\beta^j(r,\tau) \delta \left[r - R_{ij}(t) \right] \right\rangle_{i \neq j,t} \\ \Delta r_{\alpha,\beta}^{i,j}(r,\tau) &= r_{\alpha,\beta}^{i,j}(t+\tau) - r_{\alpha,\beta}^{i,j}(t), \end{aligned} \tag{5}$$

where i and j label two particles, α and β are coordinate axes and R_{ij} is the distance between particles i and j. The average corresponding to $i = j$ represents

the one-particle mean-squared displacement. Two-point microrheology probes dynamics at different lengths from distances much larger than the particle radius down to the particle size which reflects extrapolation of long-wavelength thermal fluctuations of the medium to the particle size [28].

For the case in which the particles are embedded in a viscoelastic fluid, particle tracking experiments allow one to obtain the viscoelastic moduli of the fluids. Manson and Weitz first in an ad-hoc way, and later Levine and Lubensky in a more rigorous way, proposed a generalization of the Stokes–Einstein equation (GSE) [29, 30]:

$$\left\langle \Delta\tilde{r}^2(s) \right\rangle = \frac{2k_B T}{3\pi a s \tilde{G}(s)}, \tag{6}$$

where $\tilde{G}(s)$ is the Laplace transform of the stress relaxation modulus, s is the Laplace frequency, and a is the radius of the particles. An alternative expression for the GSE equation can be written in the Fourier domain [31]. Different methods have been devised to obtain $\tilde{G}(s)$ from the experimental MSD [31–35]. The GSE equation is valid under the following approximations: (a) the medium around the sphere may be treated as a continuum material, which requires that the size of the particle be larger than any structural length scale of the material; (b) no slip boundary conditions; (c) the fluid surrounding the sphere is incompressible; and (d) there are no inertial effects. Very recently, Felderhof has presented an alternative method for calculating the shear complex modulus from the velocity autocorrelation function, that can be calculated from the particle trajectories [36].

For interfaces the situation is more complex, and the calculation of the surface shear viscosity has relied on the use of hydrodynamic models of the interface (see below). Only very recently Song et al. [37] have performed computer simulations that indicate that the GSE can be applied to fluid interfaces. Furthermore, the same group has applied the GSE to the study of interfaces in oil–water emulsions [37–39]. So far, no comparison has been made between the surface shear viscosity calculated by hydrodynamic models and the GSE.

2.2 *Fundamentals of the Optical Tweezers Technique*

This technique uses a highly focused laser beam to trap a colloidal particle, as a consequence of the momentum transfer associated with bending light. The most basic design of an optical tweezers is shown in Fig. 3a: A laser beam (usually in the IR range) is focused by a high-quality microscope (high numerical aperture objective) to a spot in a plane in the fluid. Figure 3b shows a detailed scheme of how an optical trap is created. Light carries a momentum in the direction of propagation that is proportional to its energy, and any change in the direction of light, by reflection or refraction, will result in a change of the momentum. If an object bends the light, conservation momentum requires that the object must undergo an equal and opposite momentum change, which gives rise to a force acting on the subject. When the light interacts with a bead, the sum of the forces acting on the particle

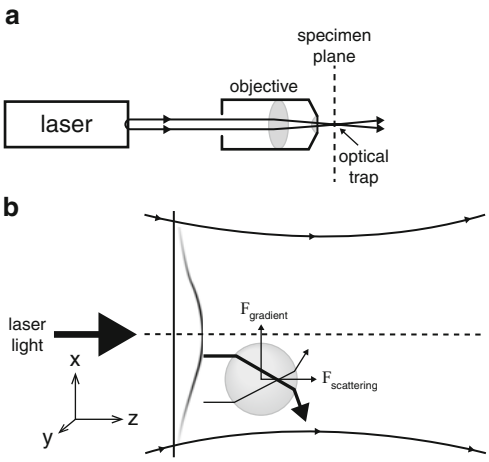

Fig. 3 (**a**) Basic design of an optical tweezers instrument; (**b**) Details of the physical principles leading to the optical trap

can be split into two components: F_{sc}, the scattering force, pointing in the direction of the incident beam, and F_g, the gradient force, arising from the gradient of the Gaussian intensity profile and pointing in the plane perpendicular to the incident beam towards the center of the beam. F_g is a restoring force that pulls the bead into the center of the beam. If the contribution to F_{sc} of the refracted rays is larger than that of the reflected rays then a restoring force is also created along the beam direction and a stable trap exists. A detailed description of the theoretical basis and of modern experimental setups has been given in [40–42] that also include a review of applications of optical tweezers to problems of biophysical interest: ligand–receptor interactions, mechanical response of single chains of biopolymers, force spectroscopy of enzymes and membranes, molecular motors, and cell manipulation. A recent application of optical tweezers to study the non-linear mechanical response of red-blood cells is given by Yoon et al. [43]. Finally, optical tweezers are also suitable for the study of interfacial rheology [44].

3 Dynamics of Particles at Interfaces

3.1 Diffusion Coefficient of Particles Adsorbed at Fluid Interfaces

A problem that appears to be ignored in the analysis of particle dynamics at interfaces is the strong influence of the interactions with other particles that leads to a decrease of the apparent D, so in what follows we will only refer to the infinite dilution diffusion coefficient. We have already mentioned that quite frequently one finds a subdiffusive behavior of the MSD of particles trapped at fluid interfaces. Figure 4 shows an example of the results obtained by tracking the trajectories of a single particle at an octane/water interfaces in an optical trap. Since no linear range

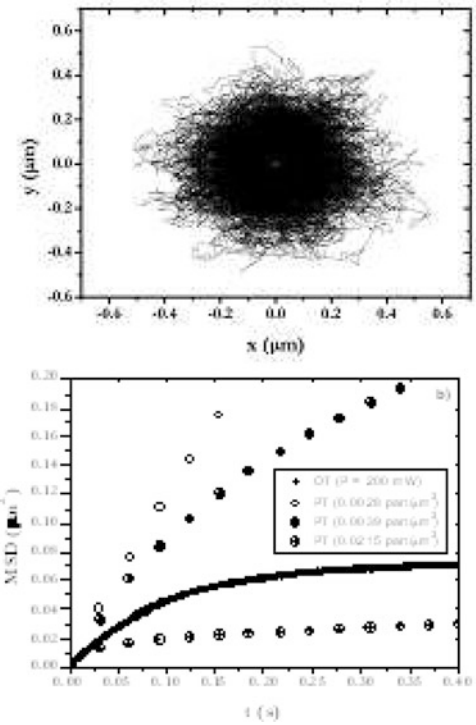

Fig. 4 *Up figure*: Typical trajectory observed for a latex macroparticle (radius 1 μm) in an optical trap at the octane/water interface and 25°C; x and y are the displacements from the center of the trap in the x and y axis. *Down figure*: Example of subdiffusive dynamics of latex microparticles of 2.9 μm of radius obtained by video microscopy particle tracking, PT, at different particle surface densities, and for a single particle in an optical trap. The continuous lines are the fits to the Langevin equation (8). All the results were taken at the octane/water interface at 25°C

is observed, D has been obtained by fitting the MSD results to the solution of the Langevin equation including an elastic force:

$$m\frac{dv}{dt} = -\xi v + f(t) - kx, \tag{7}$$

where m is the mass of the particle, v its velocity, ξ the friction coefficient, k the characteristic force constant of the elastic force acting on the particle, and $f(t)$ is the random force, so that time average $< f(t) >= 0$. Even though the potential well is not strictly parabolic, it is a very good approximation for laser intensities such that the particle are trapped relatively deep inside the potential well. The solution of (7) was given by Chandrasekar [45], and fits very well the data shown in Fig. 4. An important point is that the fits allow one to obtain the diffusion coefficient at infinite dilution, D_0. For diluted particle monolayers in which a linear dependence of the MSD is observed in the particle tracking experiments, the agreement with the values of D_0 obtained using the optical tweezers technique agree within the experimental error. This is a very important result because, as discussed below, the interfacial shear viscosity is calculated, using hydrodynamic theories, from D_0. Therefore, the fact that two different microrheological techniques lead to the same values of the diffusion coefficient, ensures that the viscosity obtained will also be the same.

3.2 *Fischer's Theory for the Shear Micro-Rheology of Monolayers at Fluid Interfaces*

For particles trapped at interfaces Einstein's equation, (3), is still valid. Nevertheless, Stokes equation for f is no longer valid because at interfaces f is a function of the viscosities of the phases ($\eta's$), the geometry of the particle (e.g., the radius "a" for spheres), the contact angle between the probe particle and the interface (θ), etc. There is no rigorous solution for the slow viscous flow equations for steady translational motion of a sphere in an ideal 2D fluid, e.g. a monolayer (Stokes paradox), hence we will briefly describe one of the most recent theoretical approaches for describing f.

Fischer et al. [46] assumed that a surfactant monolayer behaves as incompressible because Marangoni forces (forces due to surface tension gradients) strongly suppress any motion at a surface that compress or expands the interface due to any gradient in the surface pressure. Such gradients are instantly compensated by the fast motion of the surfactant at the interface, thus leading to a constant surface pressure, and therefore the monolayer behaves as an incompressible body (Fischer assumes that the velocity of the 2D surfactant diffusion is faster than the motion of the beads). The fact that the drag on a disk in a monolayer is that of an incompressible surface has been verified experimentally [47, 48], although this hypothesis could fail for highly viscous polymer monolayers.

Fischer et al. have numerically solved the problem of a sphere trapped at an interface with a contact angle θ moving in an *incompressible* surface [46]. They showed that contributions due to Marangoni forces account for a significant part of the total drag. This effect becomes most pronounced in the limit of vanishing surface compressibility. They solved the fluid dynamics equations for a 3D object moving in a monolayer of surface shear viscosity, η_s between two infinite viscous phases. The monolayer surface is assumed to be flat (no electrocapillary effects). Then the translational drag coefficient, k_T, was expressed as a series expansion of the Boussinesq number, $B = \eta_s/((\eta_1 + \eta_2)a)$, a being the radius of spherical particle:

$$k_T = k_T^0 + Bk_T^1 + O(B^2). \tag{8}$$

For $B = 0$, and for an air–water interface ($\eta_1, \eta_2 = 0$), the numerical results for $k_T^{(0)}$ and $k_T^{(1)}$ are fitted with an accuracy of 3% by the following expressions:

$$k_T^0 \approx 6\pi \sqrt{\tanh\left(32\left(\frac{d}{R}+2\right)/(9\pi^2)\right)} \tag{9}$$

$$k_T^{(1)} \approx \begin{cases} -4ln\left(\frac{2}{\pi}\arctan\left(\frac{2}{3}\right)\right)\left(\frac{a^3/2}{(d+3a)^{3/2}}\right) & (d/a > 0) \\ -4ln\left(\frac{2}{\pi}\arctan\left(\frac{d+2a}{3a}\right)\right) & (d/a < 0) \end{cases} \tag{10}$$

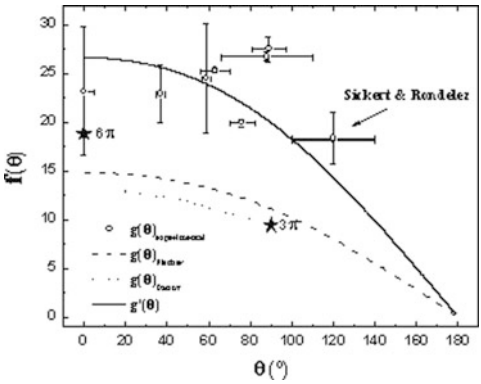

Fig. 5 Friction coefficients calculated from the experimental diffusion coefficients measured by particle tracking experiments (*symbols*), by Fischer's theory (*dashed line*), and by the corrected Fischer's theory (*continuous line*)

where d is the distance from the apex of the bead to the plane of the interface (which defines the contact angle). Note that if d goes to infinity, $k_T^0 = 6\pi$, which is the correct theoretical value for a sphere in bulk (Stokes law). They found that, even in the absence of any appreciable surface viscosity, the drag coefficient of an incompressible monolayer is higher than that of a free interface.

Figure 5 shows the friction coefficient for latex particles at the water–air interface obtained from single particle tracking for polystyrene latex particles. It also shows the values calculated from Fischer's theory, pointing out that the theoretical values are smaller than the experimental values over the whole θ range. An empirical factor of $f(\theta)_{exp}/f(\theta)_{Fischer} = 1.8 \pm 0.2$ brings the values calculated with Fischer's theory in good agreement with the experiments at all the contact angle values. A similar situation was found for the water-n-octane interface with a smaller correction factor $f(\theta)_{exp}/f(\theta)_{Fischer} = 1.2 \pm 0.1$. So far the physical origin of this correction factor is unknown.

4 Particle Tracking Results

Sickert and Rondelez were among the first to calculate the surface shear viscosity of monolayers by tracking the trajectories of spherical particles embedded in Langmuir monolayers at the air/water interface [49]. They have measured the surface viscosity of three monolayers formed by pentadecanoic acid (PDA), L-α-dipalmitoylphosphatidylcholine (DPPC) and N-palmitoyl-6-n-penicillanic acid (PPA) respectively. The values of the shear viscosities for PDA, DPPC and PPA reported were in the range of 1 to 11.10^{-10} N s m^{-1} in the liquid expanded region of the monolayer, that, as already said, are beyond the range of macroscopic mechanical methods. More recently, Bonales et al. have calculated the shear viscosity of two polymer Langmuir films, and compared these values with those obtained by canal viscosimetry [50]. Hilles et al. [51] studied the glass transition in Langmuir films. Figure 6 shows the results obtained for a monolayer of poly(4-hydroxystyrene) at

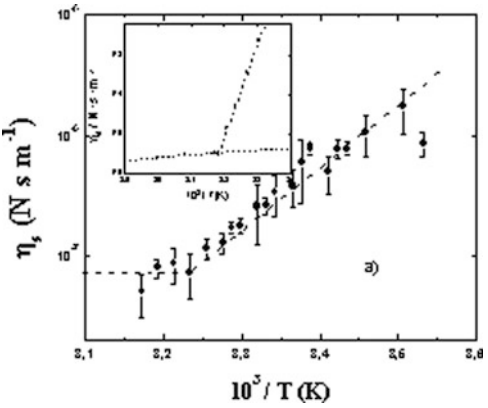

Fig. 6 Temperature dependence of the surface shear viscosity of a monolayer of poly(4-hydroxystyrene) at the air–water interface obtained by particle tracking (the insets show the corresponding values measured with a macroscopic canal viscometer. Experiments done at $\Pi = 8\,\mathrm{mN \cdot m^{-1}}$

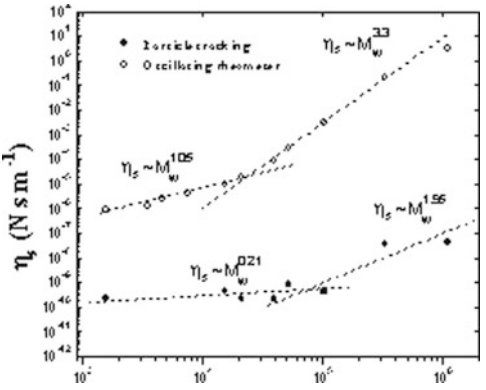

Fig. 7 Surface shear viscosity for monolayers of poly(t-butyl acrylate) as a function of the molecular weight and for a surface pressure $\Pi = 16\,\mathrm{mN \cdot m^{-1}}$. The *lower curve* corresponds to data obtained from video microscopy particle tracking. The *upper curve* was obtained from conventional oscillatory interfacial rheometers

an air–water interface. For all the monolayers reported in Refs. [50, 51] the surface shear viscosity calculated from Fischer's theory using the D values obtained from the MSD results was lower than that measured with the macroscopic canal surface viscometer. Similar qualitative conclusions were reached at by Sickert et al. for their monolayers [52]. These authors have later reanalyzed their original data [49] and they found that the relation $D_0/D_{\to 0}$ (D_0 being the diffusion coefficient of the beads at a free compressible surface, and $D_{\to 0}$ the value of an incompressible monolayer which surface concentration is tending to zero) is, theoretically, not equal to 1 but to about 0.8, which is confirmed by their experiment, and also confirms the observations of Barentin et al. [19] and Lee et al. [3] for different systems. In spite of the apparent success of Fischer's theory, the surface viscosity values are rather low when compared to the results obtained by macrorheology methods (see below).

As above mentioned there is a quantitative inconsistency between macro and micro-rheology results. Figure 7 shows clearly the large difference found between micro- and macrorheology for monolayers of poly(t-butyl acrylate) near the collapse surface concentration, Γ^{**} [16]. The macrorheology results have been obtained using two different interfacial oscillatory rheometers [21].

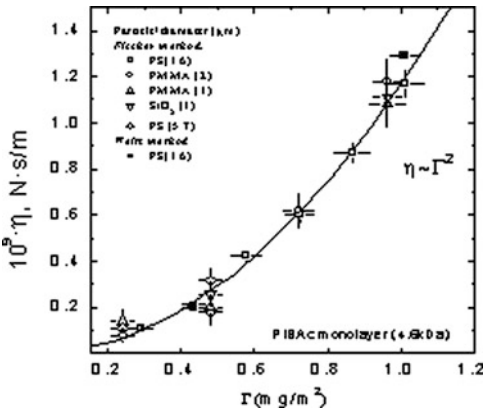

Fig. 8 Surface concentration dependence of the surface shear rheology for a monolayer of poly(t-butyl acrylate). The *symbols* are experimental results obtained by video microscopy particle tracking using particles of different chemical nature and size and using both Fischer's theory and the Generalized Stokes Einstein theory (Weitz method)

Figure 8 shows that the interfacial shear viscosities obtained with particles of rather different chemical nature and size agree within the experimental uncertainty. This discards that the origin of the discrepancies between macro- and microrheology can stem from the interactions between the particles and the monolayer molecules. Moreover, the values calculated from the modified-Fischer's theory or by direct application of the GSE equation lead to almost indistinguishable surface shear viscosities.

This discrepancy between micro- and macrorheology in the study of monolayers seems to be a rather frequent situation and no clear theoretical answer has been found so far for this fact. This type of disagreement has been also found in 3D systems, where in some cases the origin of the problem has been identified to be the inhomogeneity of the system [25, 26]. In the analysis of the particle tracking at interfaces shown above, it has been assumed that systems are homogeneous, which might not be the case. Prasad and Weeks have applied the two-particle correlation method (5) to the motion of particles trapped to the air–water interface covered with a Langmuir monolayer of human serum albumin (HSA) as a function of surface concentration [53]. They found that for high surface concentrations the one and two particle (correlated) measurements give different values of the viscosity. They explained this by suggesting that the monolayer was inhomogeneous. Both methods agree when the particle size is of the same order than the scale of the inhomogeneities of the system. However, the authors did not compare particle tracking results with macrorheology. In conclusion we need to be very careful when extracting surface viscosities in this kind of systems from single particle tracking, and whenever possible one should use two-particle correlated analysis.

However, the problem might be not only due to the length scale of the rheology but also because the active or passive character of the technique used. In fact, Lee et al. [3] combined active and passive microrheology methods to study protein (β-lactoglobulin) layers at the air–water interface. They used *magnetic nanowire microrheology* and *particle tracking* with correlated analysis as a function of adsorption time, and found that the surface viscosity obtained is about one order

of magnitude larger when measured with the active technique. Both techniques are micro-rheology methods but give quite different values for the surface viscosity. However, as indicated above, in our case both video microscopy and optical tweezers give the same values of D_0 from which the interfacial surface viscosity is calculated, therefore the use of passive or active techniques does not seem to be the source of the discrepancy between macro- and microrheology.

It is also needed to bear in mind that ideal 2D systems do not exist; the interface is a region of certain thickness which makes the interpretation of the results quite slippery. For example, Prasad et al. [54] have measured the surface viscosity of a commercial dishwasher surfactant (soluble) in a soap film by single and correlated particle tracking as a function of the film thickness. They found unphysical values for the surface viscosity for thickness larger than a certain value. Above this critical thickness, single particle tracking gives negative values for the surface viscosity, and two-particle correlated MSD gives large positive values compared to the values found in thin films. It would be possible to extend this idea to thick monolayers (for example, for some polymer monolayers), and consider that the motion of the beads does not take place in a 2D environment but in a quasi-3D one. This would make quite tricky the interpretation of the particle tracking results obtained using the theories outlined in the previous paragraphs.

It has also been shown that sometimes for very dense layers of polymers, the probes move faster than they do in layers formed at lower surface concentrations of the same polymer [3]. In these cases we can imagine that the particle probes could be expelled out of the interface and keep under (onto) the layer giving erroneous values of the diffusion coefficient, and of the surface viscosity calculated from the MSD.

5 Conclusions

Microrheology techniques, and specially particle tracking, are probably the only suited techniques for the study of the rheology in many systems of interest, as for example the dynamics inside cell membranes or in the expanded region of monolayers. However one must be very careful in interpreting the results obtained from single particle tracking and the available theories. Whenever possible the correlated two-particle MSD should be used. It is clear from the results that for fluid interfaces much more experimental and theoretical work is needed to explain why the shear surface microviscosity is much smaller than the one measured with conventional surface rheometers. Despite all the problems mentioned, in our opinion it is worth continuing working on this microrheological techniques for its potentiality in the study of the dynamics of systems of biological importance.

Acknowledgement This work has been supported in part by MICINN under Grant FIS2012-38231-C02-01, by ESA under Grant FASES MAP-AO-00-052, and Pasta A.J. Mendoza and R. Chuliá are grateful to U.E. (Grant Marie-Curie-ITN "MULTIFLOW") for a Ph.D. and

a post-doc contract, respectively. F. Martínez Pedrero is grateful to the PICATA program (UCM) for a post-doc contract. We are grateful to Th.M. Fischer, R. Miller and L. Liggieri for helpful discussions.

References

1. Larson, R.G.: The Structure and Rheology of Complex Fluids. Oxford University Press, New York (1999)
2. Riande, E., Díaz-Calleja, R., Prolongo, M.G., Masegosa, R.M., Salom, C.: Polymer Viscoelasticity. Stress and Strain in Practice. Marcel Dekker, New York (2000)
3. Lee, M.H., Reich, D.H., Stebe, K.J., Leheny, R.L.: Combined passive and active microrheology study of protein-layer formation at an air-water interface. Langmuir **25**, 7976–7982 (2009)
4. Crocker, J.C., Grier, D.G.: Methods of digital video microscopy for colloidal studies. J. Colloid Interface Sci. **179**, 298–310 (1996)
5. MacKintosh, F.C., Schmidt, C.F.: Microrheology. Curr. Opin. Colloid Interface Sci. **4**, 300–307 (1999)
6. Mukhopadhyay, A., Granick S.: Micro- and nanorheology. Curr. Opin. Colloid Interface Sci. **6**, 423–429 (2001)
7. Breedveld, V., Pine, D.J.: Microrheology as a tool for high-throughput screening. J. Mater. Sci. **38**, 4461–4470 (2003)
8. Waigh, T.A.: Microrheology of complex fluids. Rep. Prog. Phys. **68**, 685–742 (2005)
9. Gardel, M.L., Valentine, M.T., Weitz, D.A.: Microrheology. In: Brauer, K. (ed.) Microscale Diagnostic Techniques, pp. 1–49. Springer, Berlin (2005)
10. Cicuta, P., Donald, A.M.: Microrheology: a review of the method and applications. Soft Matter **3**, 1449–1455 (2007)
11. Bonales, L.J., Maestro, A., Rubio, R.G., Ortega, F.: Microrheology of complex systems. In: Schulz, H.E., Andrade Simoes, A.L., Jahara Lobosco, R. (eds.) Hydrodynamics. Advanced Topics. INTECH, Rijeka (2011)
12. Langevin, D.: Influence of interfacial rheology on foam and emulsion properties. Adv. Colloid Interface Sci. **88**, 209–222 (2000)
13. Guzmán, E., Chuliá-Jordán, R., Ortega, F., Rubio, R.G.: Influence of the percentage of acetylation on the assembling of LbL multilayers of poly(acrylic acid) and chitosan. Phys. Chem. Chem. Phys. **13**, 18200–18207 (2011)
14. Binks, B., Horozov, S. (eds.): Colloidal Particles at Liquid Interfaces. Cambridge University Press, Cambridge (2006)
15. Miller R., Liggieri L. (eds.): Interfacial Rheology. Brill, Leiden (2009)
16. Munoz, M.G., Monroy, F., Ortega F., Rubio, R.G., Langevin, D.: Monolayers of symmetric triblock copolymers at the air-water interface. 2. Adsorption kinetics. Langmuir **16**, 1094–1101 (2000)
17. Díez-Pascual, A.M., Monroy F., Ortega F., Rubio, R.G., Miller R., Noskov, B.A.: Adsorption of water-soluble polymers with surfactant character. Dilational viscoelasticity. Langmuir **23**, 3802–3808 (2007)
18. Langevin, D. (ed.): Light Scattering by Liquid Surfaces and Complementary Techniques. Marcel Dekker, New York (1989)
19. Barentin, C., Muller, P., Ybert, C., Joanny, J.-F., di Meglio, J.-M.: Shear viscosity of polymer and surfactant monolayers. Eur. Phys. J. E **2**, 153–159 (2000)
20. Gavranovic, G.T., Deutsch, J.M., Fuller, G.G.: Two-dimensional melts: chains at the air-water interface. Macromolecules **38**, 6672–6679 (2005)
21. Maestro, A., Ortega, F., Monroy, F., Krägel, J., Miller, R.: Molecular weight dependence of the shear rheology of poly(methyl methacrylate) Langmuir films: a comparison between two different rheometry techniques. Langmuir **25**, 7393–7400 (2009)

22. Saxton, M.J., Jacobson, K.: Single-particle tracking: applications to membrane dynamics. Annu. Rev. Biophys. Biomol Struct. **26**, 373–399 (1997)
23. Bonales, L.J., Rubio, J.E.F., Ritacco, H., Vega, C., Rubio, R.G., Ortega, F.: Freezing transition and interaction potential in monolayers of microparticles at fluid interfaces. Langmuir **27**, 3391–3400 (2011)
24. Konopka, M.C., Weisshaar, J.C.: Heterogeneous motion of secretory vesicles in the actin cortex of live cells: 3D tracking to 5-nm accuracy. J. Phys. Chem. A **108**, 9814–9826 (2004)
25. Alexander, M., Dalgleish, D.G.: Diffusing wave spectroscopy of aggregating and gelling systems. Curr. Opin. Colloid Interface Sci. **12**, 179–186 (2007)
26. Hasnain, I., Donald, A.M.: Microrheology characterization of anisotropic materials. Phys. Rev. E **73**, 031901 (2006)
27. Chen, D.T., Weeks, E.R., Crocker, J.C., Islam, M.F., Verma, R., Gruber, J., Levine, A.J., Lubensky, T.C., Yodh, A.G.: Phys. Rev. Lett. **90**, 108301 (2003)
28. Liu, J., Gardel, M.L., Kroy, K., Frey, E., Hoffman, B.D., Crocker, J.C., Bausch, A.R., Weitz, D.A.: Microrheology probes length scale dependent rheology. Phys. Rev. Lett. **96**, 118104 (2006)
29. Mason, T.G., Weitz, D.A.: Optical measurements of frequency-dependent linear viscoelastic moduli of complex fluids. Phys. Rev. Lett. **74**, 1250–1253 (1995)
30. Levine, A.J., Lubensky, T.C.: One- and two-particle microrheology. Phys. Rev. Lett. **85**, 1774–1777 (2000)
31. Mason, Th.G.: Estimating the viscoelastic moduli of complex fluids using the generalized Stokes-Einstein equation. Rheol. Acta **39**, 371–378 (2000)
32. Dasgupta, B.R., Tee, S.Y., Crocker, J.C., Frisken, B.J., Weitz, D.A.: Microrheology of polyethylene oxide using diffusion wave spectroscopy and single scattering. Phys. Rev. E **65**, 051505 (2002)
33. Evans, R.M., Tassieri, M., Auhl, D., Waigh, Th.A.: Direct conversion of rheological compliance measurements into storage and loss moduli. Phys. Rev. E **80**, 012501 (2009)
34. Mason, Th.G.: Estimating the viscoelastic moduli of complex fluids using the generalized Stokes-Einstein equation. Rheol. Acta **39**, 371–378 (2000)
35. Wu, J., Dai, L.L.: One-particle microrheology at liquid-liquid interfaces. Appl. Phys. Lett. **89**, 094107 (2006)
36. Felderhof, B.U.: Estimating the viscoelastic moduli of a complex fluid from observation of Brownian motion. J. Chem. Phys. **131**, 164904 (2009)
37. Song, Y., Luo, M., Dai, L.L.: Understanding nanoparticles diffusion and exploring interfacial nanorheology using molecular dynamics simulations. Langmuir **26**, 5–9 (2009)
38. Wu, Ch-Y., Tarimala, S., Dai, L.L.: Dynamics of charged microparticles at oil-water interfaces. Langmuir **22**, 2112–2116 (2006)
39. Wu, Ch-Y., Song, Y., Dai, L.L.: Two-particle microrheology at oil-water interfaces. Appl. Phys. Lett. **95**, 144104 (2009)
40. Ou-Yang, H.D., Wei, M.T.: Complex fluids: probing mechanical properties of biological systems with optical tweezers. Ann. Rev. Phys. Chem. **61**, 421–440 (2010)
41. Borsali, R., Pecora, R. (eds.): Soft-Matter Characterization, vol. 1. Springer, Berlin (2008)
42. Resnick, A.: Use of optical tweezers for colloid science. J. Colloid Interface Sci. **262**, 55–59 (2003)
43. Yoon, Y.-Z., Kotar, J., Yoon, G., Cicuta, P.: The nonlinear mechanical response of the red blood cell. Phys. Biol. **5**, 036007 (2008)
44. Steffen, P., Heinig, P., Wurlitzer, S., Khattari, Z., Fischer, Th.M.: The translational and rotational drag on Langmuir monolayer domains. J. Chem. Phys. **115**, 994–997 (2001)
45. Chandrasekhar, S.: The theory of Brownian motion. Rev. Mod. Phys. **21**, 383 (1949)
46. Fischer, Th.M., Dhar, P., Heinig, P.: The viscous drag of spheres and filaments moving in membranes or monolayers. J. Fluid Mech. **558**, 451–475 (2006)
47. Fischer, Th.M.: Comment on "Shear viscosity of Langmuir monolayers in the low density limit". Phys. Rev. Lett. **92**, 139603 (2004)

48. Wurlitzer, S., Schmiedel, H., Fischer, Th.M.: Electrophoretic relaxation dynamics of domains in Langmuir-monolayer. Langmuir **18**, 4393 (2002)
49. Sickert, M., Rondelez, F.: Shear viscosity of Langmuir monolayers in the low density limit. Phys. Rev. Lett. **90**, 126104 (2003)
50. Bonales, L.J., Ritacco, H., Rubio, J.E.F., Rubio, R.G., Monroy, F., Ortega, F.: Dynamics in ultrathin films: particle tracking microrheology of Langmuir monolayers. Open Phys. Chem. J. **1**, 25–32 (2007)
51. Hilles, H.M., Ritacco, H., Monroy, F., Ortega, F., Rubio, R.G.: Temperature and concentration effects on the equilibrium and dynamic behavior of a Langmuir monolayer: from fluid to gel-like behavior. Langmuir **25**, 11528–11532 (2009)
52. Sickert, M., Rondelez, F., Stone, H.A.: Single-particle Brownian dynamics for characterizing the rheology of fluid Langmuir monolayers. Eur. Phys. Lett. **79**, 66005 (2007)
53. Prasad, V., Koehler, S.A., Weeks, E.R.: Two-particle microrheology of quasi-2D viscous systems. Phys. Rev. Lett. **97**, 176001 (2006)
54. Prasad, V., Weeks, E.R.: Two-dimensional to three-dimensional transition in soap films demostrated by microrheology. Phys. Rev. Lett. **102**, 178302 (2009)

Cohesive and Non-cohesive Adsorption of Surfactants at Liquid Interfaces

R.I. Slavchov, I.M. Dimitrova, and I.B. Ivanov

1 Introduction

Long ago, Adam showed that the spread monolayers of nonionic surfactants exhibit a state with the properties of a two-dimensional (2D) liquid [1], e.g., with compressibility intermediate between that of the 2D gaseous and the 2D solid states of the adsorption layers. Consequently, he called this 2D phase "liquid expanded (LE)" [1–3]. The reasons for its existence and its basic structure were revealed by Langmuir [2]. He argued that the hydrocarbon tails of the surfactant in the LE state form a very thin liquid oil film spread over the interface.

The concept of LE monolayer is not widely accepted for the most important from technological point of view soluble adsorption layers at liquid interfaces. The most popular adsorption isotherms used in the literature for soluble surfactants (Volmer, de Boer-van der Waals, Langmuir's isotherm for soluble surfactants, Frumkin) do not involve the LE state and the phase transition from 2D gas to LE. The reason of the neglect of such phase transition is the fact that it is not easy to observe it with surface tension data: it occurs as a small kink (discontinuity of the first derivative) in the dependence of the surface tension σ on the concentration C which is often obscured by the experimental error. Several studies exist which give evidence that LE state is, in fact, common feature not only of insoluble, but also to soluble monolayers [4–7]. Still, to the best of our knowledge, answers have not been given to the following basic questions: which soluble surfactants exhibit the LE state and which ones do not? How to prove the existence of LE state and when to expect it? How are the parameters of the LE state related to the surfactant structure and the

R.I. Slavchov · I.M. Dimitrova
Department of Physical Chemistry, Sofia University, 1164 Sofia, Bulgaria

I.B. Ivanov (✉)
Laboratory of Chemical Physics and Engineering, Sofia University, 1164 Sofia, Bulgaria
e-mail: ii@lcpe.uni-sofia.bg

R.G. Rubio et al. (eds.), *Without Bounds: A Scientific Canvas of Nonlinearity and Complex Dynamics*, Understanding Complex Systems,
DOI 10.1007/978-3-642-34070-3_22, © Springer-Verlag Berlin Heidelberg 2013

medium properties (temperature, composition, etc.)? A previous work of ours dealt with the LE state in monolayers of ionic surfactants [6]. In this work, we turn to uncharged adsorption layers of soluble nonionic surfactants.

Two types of surface pressure isotherms (surface pressure $\pi^S \equiv \sigma_0 - \sigma$ vs. concentration C) will be considered in this chapter: cohesive and non-cohesive. The non-cohesive type of isotherms start at $\pi^S = 0$ and $C = 0$ with a linear portion. At larger concentrations, the dependence π^S vs. C smoothly becomes curved, with negative deviations from the ideal behavior, corresponding to repulsion (cf. Figs. 2a and 3 below).

In the case of cohesive type of isotherm, the initial linear portion starts again at $\pi^S = 0$ and $C = 0$. Then, at relatively low concentrations, $\pi^S(C)$ undergoes a kink, followed by a second linear portion of larger slope and negative intercept $-\pi_{coh}$ (cf. Fig. 2a). The first linear portion corresponds to 2D gaseous layer, where Henry's adsorption isotherm holds. The second linear portion corresponds to LE layer. With *insoluble* surfactants, the LE layer at larger compressions undergoes phase transition to a solid like layer [1–3,8]. With *soluble* surfactants, the adsorption isotherm eventually curves due to repulsion between the hydrophilic heads and π^S stops changing when the critical micelle concentration (*cmc*) is reached. These events will be discussed in details in Sect. 3.

Langmuir's suggestion for the structure of the LE layer was that, in fact, an oil-like film is formed by the surfactant hydrophobic tails at which the hydrophilic groups are "adsorbed" [2]. He argued that this layer "must be regarded as essentially a typical hydrocarbon liquid in which the molecules possess all natural freedom of motion of such liquids" [2]. Kaganer et al. also pointed out that the LE layer is structureless and "there is no detectable X-ray diffraction signal. In this phase, the heads of the molecules are translationally disordered and the chains are conformationally disordered" [8]. Langmuir showed that his model explains the main feature of the 2D equation of state (EOS): the existence of what he called "spreading pressure of the monolayer" (we prefer the notion cohesive pressure, π_{coh}, introduced later by Davies [9, 10]). Later, Langmuir's model was extended several times. For example, the repulsion between the surfactant polar head-groups was treated by Smith [11], and the dependence of the cohesive pressure on the adsorption was analyzed by Davies [9, 10]. In *soluble* monolayers, first order phase transitions of the LE phase both to 2D-gaseous and to 2D-solid state were directly observed by Brewster angle microscopy and dynamic surface tension measurements [5]. For the current state of the art of the phase behavior of *insoluble* monolayers, the reader is referred to the available reviews in the literature [8, 12].

Langmuir analyzed further the equation of state (π^S vs. surface area A) of films of myristic acid spread on a dilute HCl solution around the point of phase transition to the solid-like layer. He argued that the data for this region can be explained if one assumes that surface aggregates (micelles) of 13 molecules are in equilibrium at the surface with single molecules [2]. Kumpulainen et al. [4] applied this idea to explain their tensiometric data obtained for soluble surfactants. Large surface aggregates were detected experimentally by optical methods, e.g., fluorescence micrography [13].

In this paper we are interested mainly in the linear part of the LE adsorption isotherm $\pi^S(C)$. Its linearity suggests that the adsorption is of Henry's type, i.e., the adsorbed layer can be considered as being ideal but with adsorption constant larger than that of the gaseous layer. By using this assumption, we analyzed thoroughly the experimental data for 50 systems and obtained reasonable and self-consistent results. This would have been impossible, had the nature of the LE adsorbed layer have been different.

In Sect. 2, we will briefly present a model and an equation for the adsorption constant K_a of nonionic surfactant at liquid interface. This model turns out to be a useful instrument for the analysis of the tensiometric data for these surfactants. In Sect. 3, we present our concept for cohesive and non-cohesive isotherms. The equations of state and the procedures for processing tensiometric data for both types of isotherms are described in Sect. 3.3. In Sect. 4, the dependence of the adsorption constant of cohesive and non-cohesive systems on the surfactant structure and on temperature is interpreted with our model for the adsorption constant. The dependence of the cohesive pressure on the surfactant hydrocarbon chain length is also discussed.

2 Henry's Adsorption Constant, Adsorption Energy and Thickness

2.1 Henry's Adsorption Isotherm

Consider an ideal nonionic surfactant solution of concentration C in equilibrium with an ideal gaseous adsorbed monolayer of the same surfactant with adsorption Γ. The surfactant chemical potentials in the two states are

$$\mu^B = \mu_0^B + k_B T \ln C, \tag{1}$$

$$\mu^S = \mu_0^S + k_B T \ln \Gamma. \tag{2}$$

Here superscripts "B" and "S" denote bulk and surface phase, and μ_0^S and μ_0^B are the corresponding standard chemical potentials. At equilibrium, μ^B and μ^S must be equal, which leads to Henry's adsorption isotherm:

$$\Gamma = K_a C, \tag{3}$$

where, the *adsorption constant* K_a of the surfactant in the gaseous adsorption layer is defined by the relation

$$k_B T \ln K_a \equiv \mu_0^B - \mu_0^S. \tag{4}$$

As it is obvious from the derivation, Henry's adsorption isotherm (3) is valid only for adsorption layer consisting of non interacting surfactant molecules, i.e., in a very dilute adsorption layer.

Davies and Rideal [10] proposed the following relation of K_a with the molecular parameters of the surfactant:

$$K_a = \delta_a \exp\left(E_a / k_B T\right), \tag{5}$$

where δ_a is referred to as "thickness of the adsorbed layer", and E_a as adsorption energy. They proposed to use for the thickness δ_a the length of the surfactant's hydrophobic tail, an assumption adopted later by others (e.g., [4, 14–16]). For the adsorption energy E_a of surfactants with straight hydrocarbon chain Davies and Rideal used the expression

$$E_a = E_0 + u_{CH_2} n_C. \tag{6}$$

Here n_C is the number of carbon atoms in the hydrophobic chain and u_{CH_2} is the (positive) free energy of transfer of a methylene (-CH_2-) group from the solution into the adsorption layer. E_0 is the n_C-independent part of E_a which was ascribed solely to the adsorption energy E_{head} of the hydrophilic head (cf. (4.3) in [10]). Both assumptions of Davies and Rideal for δ_a and E_a are disputable. More rigorous treatment based on classical statistical thermodynamics was given in [17] based on Gibbs definition of adsorption. We will re-derive the results from [17] using an alternative, quantum mechanical approach.

2.2 Geometry of a Surfactant Molecule

A detailed molecular adsorption model should involve the geometrical parameters of the surfactant hydrophobic chain: cross-sectional area $\alpha_\perp$ and length l_{CH_2} per -CH_2- group in the stretched hydrocarbon chain. Therefore, it is pertinent to discuss first their values. The area per molecule of dense-packed molecules, measured in insoluble monolayer of alcohols at the point of collapse, is $18 \pm 0.5\,\text{Å}^2$ [11, 18]. This is in good agreement with the crystallographic radius of solid alkanes, $18.5\,\text{Å}^2$ [19, 20]. If at the point of collapse the structure of the dense adsorption layer is hexagonal, the area of collapse must be larger than the actual cross-sectional area $\alpha_\perp$ of the surfactant by a factor of 1.10 (the ratio of the area of a hexagon and the circle inscribed inside it). With this correction, the value $18.5\,\text{Å}^2$ cited above becomes $\alpha_\perp = 16.5\,\text{Å}^2$. The corresponding cross-sectional radius is $R_\perp = 2.29\,\text{Å}$. For the length l_{CH_2} per -CH_2- group of a stretched hydrocarbon chain, the value $1.26\,\text{Å}$ is accepted [21]. The lateral area (along the chain) per -CH_2- group is then $\alpha_\parallel = 2\pi l_{CH_2} R_\perp = 18.1\,\text{Å}^2$, which is close to $\alpha_\perp = 16.5\,\text{Å}^2$.

2.3 Interaction Potential of a Surfactant Molecule with the Interface

To evaluate the general expression (4) for K_a, we must find the change in the standard Gibbs free energy of a surfactant molecule when it is transferred from the solution to the interface. The interaction potential $u(z)$ between the surfactant molecule and the interface was modeled by Ivanov et al. [17] by assuming that the surfactant is a solid cylindrical rod, approaching the interface by keeping its normal orientation with respect to it. While its head is at distance $z > n_C l_{CH_2}$, the rod is in the bulk solution and do not interact with the interface (state I in Fig. 1). At $z < n_C l_{CH_2}$, the surfactant penetrates the interface, where according to [17] the following effects contribute to $u(z)$:

- **(i)** When the cap of the hydrocarbon chain touches the surface, a portion of the water|hydrophobic phase interface, of area $\alpha_\perp$, disappears (Fig. 1, state II). The contribution of this process to $u(z)$ was modeled in [17] as a contact potential at $z = n_C l_{CH_2}$:

$$u_{(i)}(z) = \begin{cases} \sigma_0 \alpha_\perp, & z < n_C l_{CH_2}, \\ 0, & z > n_C l_{CH_2}, \end{cases} \tag{7}$$

  where σ_0 is the surface tension of the pure water|hydrophobic phase interface. For water|alkane interface at room temperature, $\sigma_0 \approx 50$ mN/m, so the energy $\sigma_0 \alpha_\perp$ is about $2 \times k_B T$, which is by no means negligible. This contribution was first accounted for independently by Ivanov et al. [17] and Kumpulainen et al. [4].
- **(ii)** For the energy u_{CH_3} of transfer of the -CH_3 group, we assume proportionality to the contact area of this group with water [22]. To calculate this area, one can approximate the shape of -CH_3 as a cylinder with a cap. The lateral area of the cylinder is assumed equal to that of a -CH_2- group, $\alpha_\parallel$, and the cap area is assumed equal to the cross-sectional area $\alpha_\perp$ of the hydrocarbon tail. The two areas are almost equal and the energy corresponding to each is $u_{CH_2}\alpha_\parallel$. The energy pertaining to the *cap* only can be represented as a contact potential with the same z-dependence as $u_{(i)}$ in (7):

$$u_{(ii)}(z) = \begin{cases} u_{CH_2}, & z < n_C l_{CH_2}, \\ 0, & z > n_C l_{CH_2}, \end{cases} \tag{8}$$

  The second part of u_{CH_2} (pertaining to the lateral area of -CH_3) is not included in (8); it will be included in the next term, the potential $u_{(iii)}$.
- **(iii)** Assuming for simplicity that the carbon chain remains normal to the interface, one can model the hydrophobic energy due to -CH_2- adsorption (plus the lateral energy of the -CH_3 group) as linear function of the distance z between the surfactant head and the interface:

$$u_{(iii)}(z) = u_{CH_2} z / l_{CH_2}, \qquad n_C l_{CH_2} > z > 0. \tag{9}$$

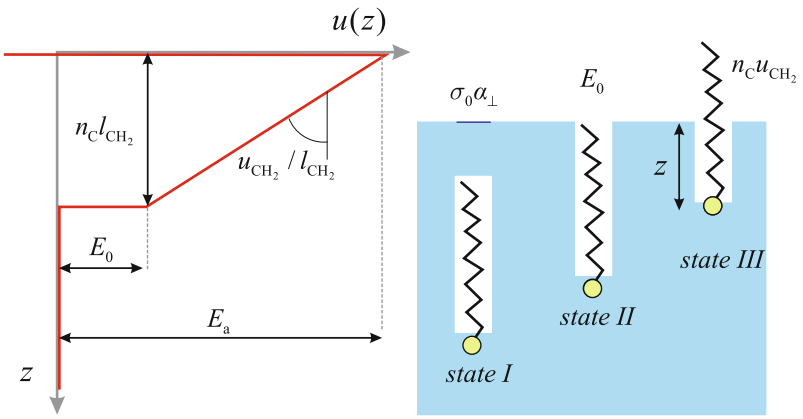

Fig. 1 Molecular interaction potential $u(z)$ of a surfactant molecule with the interface as a function of the distance z between the polar head-group and the interface, cf. (10). According to our model, at distances $z > n_C l_{CH_2}$ (*state I*) there is no significant interaction. At $z = n_C l_{CH_2}$ (*state II*), energy is gained due to the disappearance of clean water surface of area $\alpha_\perp$, and the transfer energy of the cap of the -CH_3 group, cf. (8). At shorter distances (*state III*), there is linear dependence of u on z related to the energy of transfer $n_C u_{CH_2}$ of the hydrocarbon chain from water to the hydrophobic phase, cf. (9)

- **(iv)** Although the hydrophilic head remains immersed in the hydrophilic phase, it also interacts with the interface. This interaction involves probably both short-ranged and long-ranged (such as van der Waals and electrostatic) forces and is strongly specific. Since these forces are not yet fully understood, we will account for their contribution to the adsorption energy E_a by an empirical constant E_{head}.
- **(v)** One finally assumes that the surfactant cannot desorb into the hydrophobic phase, i.e. $u(z) = \infty$ at $z < 0$.

We made above implicitly a simplification of the stage of the penetration of the interface by the -CH_3 group. In fact, stages **(i)** and **(ii)** above cannot be separated. They are part of a continuous process starting in the moment when the -CH_3 group touches the interface and ending when the whole group is in the hydrophobic phase. It is hardly possible to describe correctly this process at least because the exact geometry of the -CH_3 group is unknown. That is why we used the approximate model described in paragraphs **(i)** and **(ii)** above.

Combining the contributions **(i)–(v)**, one obtains an approximate expression for the interaction potential of a surfactant molecule with the interface [17] (see Fig. 1):

$$u(z) = \begin{cases} \infty & 0 > z, \\ -E_a + u_{CH_2} z / l_{CH_2}, & n_C l_{CH_2} > z > 0, \\ 0, & z > n_C l_{CH_2}, \end{cases} \tag{10}$$

where the adsorption energy E_a is given by

$$E_a = E_{head} + \alpha_\perp \sigma_0 + u_{CH_2}(n_C + 1). \tag{11}$$

In (10), the free energy of the surfactant in the bulk solution is used as reference state. Comparison of (11) and (6) leads to an explicit expression for the empirical constant E_0 of Davies and Rideal [10]:

$$E_0 = E_{head} + u_{CH_2} + \alpha_\perp \sigma_0. \tag{12}$$

It encompasses not only E_{head} as assumed by Davies and Rideal, but also the other contributions to E_a, unrelated to the adsorption of the -CH_2- chain (namely, $u_{CH_2} + \alpha_\perp \sigma_0$).

2.4 *Partition Functions of a Surfactant Molecule at the Interface*

We will account now for the effects of the kinetic energies on the adsorption by investigating the partition function of the surfactant molecule at the interface. We use the model (10) for the interaction potential $u(z)$. Since the "width" of the potential well is very small (in fact zero as z goes to zero), one might expect quantum mechanical effects to play certain role for the value of K_a. Therefore, we adopt a quantum mechanical approach to the problem.

Let us denote the energies of interaction of the surfactant molecule with the medium in the bulk and at the surface by u^B and u^S respectively (with account to Fig. 1, $u^B - u^S = E_a$). For ideal systems one can deduce the standard chemical potentials in the bulk and at the surface, μ_0^S and μ_0^B from Eqs. (4.26) and (7.8) of Hill [23]:

$$\mu_0^B = u^B - k_B T \ln q_{trans}^B - k_B T \ln q_{rot}^B, \tag{13}$$

$$\mu_0^S = u^S - k_B T \ln q_{trans}^S q_{vibr,z}^S - k_B T \ln q_{rot}^S, \tag{14}$$

where q^B and q^S are the respective quantum partition functions. We account for the translational and rotational degrees of freedom in the bulk and at the surface (indicated with subscript), and for the partition function $q_{vibr,z}^S$ standing for the vibration of the molecule at the surface in the potential well defined by $u(z)$, (10).

- **(i)** *Translational degrees of freedom.* A surfactant molecule in the bulk moves freely in 3 directions, while at the surface transition is possible only in x and y directions. Therefore,

$$q_{trans}^B = \Lambda^{-3}, \qquad q_{trans}^S = \Lambda^{-2}, \tag{15}$$

where $\Lambda = h/(2\pi m k_B T)^{1/2}$ is de Broglie thermal wavelength [23], m is molecular mass and h is Planck constant.

- **(ii)** *Vibration in z direction*. For the potential in Fig. 1, the surfactant molecules oscillate in a triangular potential well:

$$u(z) = \begin{cases} u_{CH_2} z / l_{CH_2}, & z > 0, \\ \infty, & z < 0. \end{cases} \tag{16}$$

For vibrations in such potential, one can apply the Wentzel–Kramers–Brillouin approximation [24] for the energies ϵ_v of the quantum states with quantum numbers $v = 1 \div \infty$:

$$\epsilon_v = \epsilon_1 \left(\frac{4v - 1}{3} \right)^{2/3}, \tag{17}$$

where the energy of the basic state ϵ_1 is given by

$$\epsilon_1 = \frac{3^{4/3} h^{2/3}}{8 m^{1/3}} \frac{u_{CH_2}^{2/3}}{l_{CH_2}^{2/3}}. \tag{18}$$

If $\epsilon_1 \ll k_B T$, the Euler's summation formula can be used to calculate the partition function $q_{vibr,z}^S$ (e.g. (44.5) and (44.6) in the book of Levich [25]):

$$q_{vibr,z}^S \equiv \sum_{v=1}^{\infty} \mathrm{e}^{-\epsilon_v / k_B T} \approx \int_1^{\infty} \mathrm{e}^{-\epsilon_v / k_B T} \mathrm{d}v + \frac{1}{2} \mathrm{e}^{-\epsilon_1 / k_B T}. \tag{19}$$

The integral in the right side can be taken analytically. Thus one obtains:

$$q_{vibr,z}^S = \frac{9\sqrt{\pi}}{16} \left(\frac{\epsilon_1}{k_B T} \right)^{-3/2} \left(1 + \sqrt{\frac{4}{\pi} \frac{\epsilon_1}{k_B T}} \mathrm{e}^{-\epsilon_1 / k_B T} - \mathrm{erf} \sqrt{\frac{\epsilon_1}{k_B T}} \right) + \frac{1}{2} \mathrm{e}^{-\epsilon_1 / k_B T}, \tag{20}$$

where "erf" is the error function. By taking now the limit $\epsilon_1 \ll k_B T$ one obtains

$$q_{vibr,z}^S = \frac{k_B T}{\Lambda} \frac{l_{CH_2}}{u_{CH_2}} - \frac{1}{4}. \tag{21}$$

The first term in the right hand side of (21) coincides with the result of Ivanov et al. [17] obtained by classical mechanical derivation and Gibbs' definition of adsorption. The 1/4 is a quantum mechanical correction. For a hydrocarbon chain at water|oil interface (W|O), $u_{CH_2} = 1.39 \times k_B T$ [21] and the value of the first term is about 12 for hexanol at 25°C. Therefore, the quantum correction is typically less than 2% and can be neglected. Then,

$$q_{vibr,z}^S = \frac{k_B T}{\Lambda} \frac{l_{CH_2}}{u_{CH_2}}. \tag{22}$$

This justifies the classical derivation of the adsorption constant K_a in Ref. [17].

- **(iii)** *Rotation*. In order to estimate the contribution of the rotation to the adsorption constant K_a, it is sufficient to calculate the partition functions for the initial (in the bulk) and the final (at the surface) states. For simplicity we will assume that the molecule rotates as a solid stick of inertial moment I. The Hamiltonian of a freely rotating stick in spherical coordinates (r, ϑ, φ) is [23]:

$$H = \frac{1}{2I}\left(p_\vartheta^2 + p_\varphi^2/\sin^2\vartheta\right).$$

Here p_ϑ and p_φ are the corresponding momenta of the stick. This corresponds to bulk partition function ((8)–(27) of [23]):

$$q_{rot}^B = \frac{1}{h^2}\int_{-\infty}^{\infty}\int_{-\infty}^{\infty}\int_0^{\pi}\int_0^{2\pi} \mathrm{e}^{-H/k_BT}\mathrm{d}\varphi\mathrm{d}\vartheta\mathrm{d}p_\varphi\mathrm{d}p_\vartheta = 8\pi^2 k_BTI/h^2. \quad (23)$$

We will assume also that the rotation of the surfactant at the interface $z = 0$ is again free but restricted to the semi-space $z < 0$. This yields for the surface partition function q_{rot}^S:

$$q_{rot}^S = \frac{1}{h^2}\int_{-\infty}^{\infty}\int_{-\infty}^{\infty}\int_0^{\pi/2}\int_0^{2\pi} \mathrm{e}^{-H/k_BT}\mathrm{d}\varphi\mathrm{d}\vartheta\mathrm{d}p_\varphi\mathrm{d}p_\vartheta = 4\pi^2 k_BTI/h^2. \quad (24)$$

- **(iv)** It is difficult to calculate the contribution of all intramolecular vibrational and rotational states to the adsorption constant K_a. We believe, however, that they are implicitly accounted for in the empirical values of the transfer energy u_{CH_2} and in the constant E_{head} in (12).

Substituting the results (15), (22)–(24) into the expressions (13) and (14) for the standard chemical potentials, we obtain

$$K_a \equiv \exp\frac{\mu_0^B - \mu_0^S}{k_BT} = \frac{k_BTl_{CH_2}}{2u_{CH_2}}\exp\frac{E_a}{k_BT}. \quad (25)$$

Comparison with (5) yields for the adsorption thickness δ_a the expression

$$\delta_a = \frac{k_BT}{2}\frac{l_{CH_2}}{u_{CH_2}}. \quad (26)$$

This differs from the corresponding expression in [17] with the factor 1/2 originating from (24) for q_{rot}^S. With the values $l_{CH_2} = 1.26\,\text{Å}$ and $u_{CH_2}^{WO} \approx 1.39k_BT$ (cf. [21] and Sect. 4.2 below), one obtains for simple surfactants at W|O $\delta_a = 0.45\,\text{Å}$. For water|gas surface (W|G), $u_{CH_2}^{WG} \approx 1.04k_BT$, so that the adsorption thickness is higher: $\delta_a = 0.63\,\text{Å}$. These values of δ_a are quite different from those based on the assumption of Davies and Rideal that δ_a is

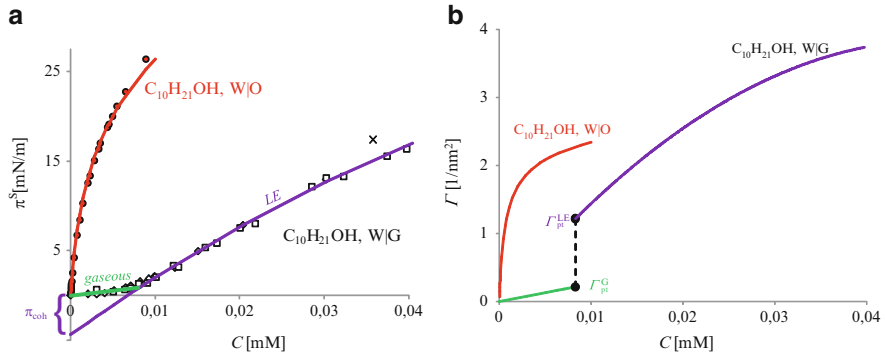

Fig. 2 (**a**) Surface pressure isotherm (π^S vs. C) of $C_{10}H_{21}OH$ at W|dodecane and W|G interfaces. At W|G, the decanol behaves as a cohesive surfactant and demonstrates $\pi^S(C)$ isotherm of LE-type. The LE line is a regression with quadratic polynomial with non-zero intercept, cf. (32). In the Henry region, (30) is followed, indicating gaseous state of the monolayer. At W|O the same surfactant follow the HFL isotherm with $\alpha = 16.5\,\text{Å}^2$. Adsorption constant was the only fitting parameter ($K_a = 6.54 \times 10^{-3}$ m). (**b**) The corresponding adsorption isotherms, $\Gamma(C)$, obtained as $\Gamma = \mathrm{d}\pi^S/\mathrm{d}k_BT\ln C$. Marked by dots are the points of phase transition of the gaseous and the LE phase (Γ_{pt}^{G} and Γ_{pt}^{LE} respectively)

equal to the length of the hydrophobic chain (e.g., for dodecanol they recommend $\delta_a = 12 \times l_{CH_2} = 15\,\text{Å}$)

3 Cohesive and Non-cohesive Adsorption of Surfactants

We analyzed numerous experimental data for surface pressure $\pi^S(=\sigma_0-\sigma)$ vs. concentration C and found that at low concentrations virtually all of them exhibit one of two distinctive types of behavior. In some cases (Fig. 2a, line W|O), the plot starts with a linear section with zero intercept. In other cases (Fig. 2a, lines W|G) there are two sections: one with intercept zero and a second one having finite negative intercept ($-\pi_{coh}$), the two region divided by a distinctive kink. For reasons, which will become clear in this section, we will call the first type of adsorption behavior *non-cohesive*, and the second one -*cohesive*.

3.1 Non-cohesive Adsorption and Helfand–Frisch–Lebowitz Model

The governing molecular property of the surfactant in the non-cohesive case is its actual molecular area α (i.e., the effective cross-sectional area, cf. Sect. 2.2).

The most widely used models for non-cohesive adsorption of surfactants at liquid surfaces are the Langmuir model (rigorously valid only for localized adsorption at solid surfaces [23, 26]) and Volmer model (which is in fact the exact solution of the problem for one-dimensional fluid of rods [27, 28] but not for adsorption of circular discs at planar interface). A more natural model for the non-cohesive adsorption layer of small molecules seems to be a two-dimensional fluid of hard discs. A nearly exact surface equation of state (EOS) of this system was derived by Helfand, Frisch and Lebowitz (HFL) [29, 30]:

$$\frac{\pi^S}{k_B T} = \frac{\Gamma}{(1-\alpha\Gamma)^2}. \tag{27}$$

From (27), the dependence of the chemical potential μ^S of the surfactant at the interface on the adsorption Γ can be obtained by integration of the Gibbs isotherm, $\mathrm{d}\pi^S = \Gamma \mathrm{d}\mu^S$. This yields:

$$\mu^S = \mu_0^S + k_B T \ln \gamma^S \Gamma, \qquad \ln \gamma^S = -\ln(1-\alpha\Gamma) + \frac{\alpha\Gamma\,(3-2\alpha\Gamma)}{(1-\alpha\Gamma)^2}. \tag{28}$$

Here γ^S is the surface activity coefficient. The condition $\mu^S = \mu_0^S + k_B T \ln \Gamma$ at $\Gamma \to 0$ was used for the determination of the integration constant. The adsorption isotherm $\Gamma(C)$ corresponding to HFL model follows from the equilibrium condition $\mu^S = \mu^B$, where μ^S is given by (28) and the chemical potential of the surfactant in an ideal bulk solution is $\mu^B = \mu_0^B + k_B T \ln C$; the result is:

$$K_a C = \frac{\Gamma}{1-\alpha\Gamma} \exp\left[\frac{\alpha\Gamma\,(3-2\alpha\Gamma)}{(1-\alpha\Gamma)^2}\right]. \tag{29}$$

For non-ideal bulk solution, the concentration C in (29) must be replaced with activity γC, where γ is the bulk activity coefficient. The adsorption isotherm (29) was derived first by Ivanov et al. [17] (Helfand et al. derived in fact only the EOS (27) [29]), but since (29) is based on HFL model, we will still call it "HFL adsorption isotherm". Equations (27) and (29) define parametrically the surface tension isotherm $\pi^S(C)$ (with parameter Γ). When both (27) and (29) are used for the interpretation of $\pi^S(C)$ data, we will term their combination "HFL model".

The HFL model is suitable especially for the case of adsorption at W|O, where attraction between hydrocarbon chains is known [9, 22] to be very small. We will show below that non-cohesive behavior is not rare also at W|G, although there is no guarantee that attractive interaction is completely absent in this case. Nevertheless, we will use (27) and (29) for non-cohesive surfactants at W|G as a tool for analysis of their adsorption constant K_a. At that, we will obtain also values of the actual molecular area α, but will not analyze them since it is possible that they depend significantly on the neglected attractive interactions.

3.2 Cohesive Adsorption: Phenomenological Relations

As already mentioned, a typical feature of the cohesive isotherms is the existence of a kink in the $\pi^S(C)$ isotherm at low concentration (cf. Fig. 2, octanol at W|G). The lack of such kink is indicative of non-cohesive adsorption (cf. Fig. 2, octanol at W|O). Henry's region before the kink corresponds to gaseous state of the monolayer. The behavior right after the kink is close to linear, with negative intercept, $-\pi_{coh}$. Cohesive adsorption behavior was discovered by Adam [1,3] who noticed that, with insoluble surfactants, between the gaseous and solid-like state of the adsorption layer, a state with intermediate compressibility occurs. He called it "liquid expanded (LE) state". Langmuir showed that the quantitative interpretation of the experimental EOS needs the introduction of a negative surface pressure, which he called "spreading pressure" [2]. Although our analysis of the adsorption behavior of soluble surfactants is rather different from that of Langmuir, we will still call the adsorption layer "liquid expanded", but we will use for the negative intercept the notion cohesive pressure π_{coh} introduced by Davies [9,10].

3.3 Processing of Experimental Data

Since the data interpretation in the two cases (cohesive and non-cohesive) involves a number of steps, we will now illustrate in details the computational procedures on the examples in Fig. 2, decanol at W|G and W|octane.

a. Non-cohesive Adsorption

The interfacial tension data of Aveyard and Briscoe [31] for fatty alcohols at W|O interface were presented by the authors as function of the concentration C^O of the surfactant in the oil phase, where the alcohols are more soluble. In order to be able to compare the adsorption in these systems with adsorption at W|G, we recalculated the corresponding concentration C^W of octanol in the water by using the equilibrium condition $C^W = \gamma^O C^O / K_p$, where K_p is the partition coefficient. The activity coefficient γ^O cannot be neglected for the alkane solutions, as they were concentrated and alcohols are known to tetramerize in oil solutions [32]. For dodecanol in octane at 30°C the tetramerization constant is $K_{1,4} = 780M^{-3}$ [32]. We assumed that this value is valid for all considered alcohol solutions in alkanes, since the tetramerization is probably determined by the interaction between the hydrophilic heads. The activity coefficient γ^O was calculated by solving the equation $C^O = \gamma^O C^O + 4K_{1,4}\left(\gamma^O C^O\right)^4$ following from the monomer–tetramer model [32]. The partition coefficient for the transfer of a surfactant molecule from oil to water follows an exponential dependence on n_C [33]. Data for alcohols are concordant with the equation $\ln K_p = -4.90 + 1.31 \times n_c$ ($K_p = 3,700$ for decanol

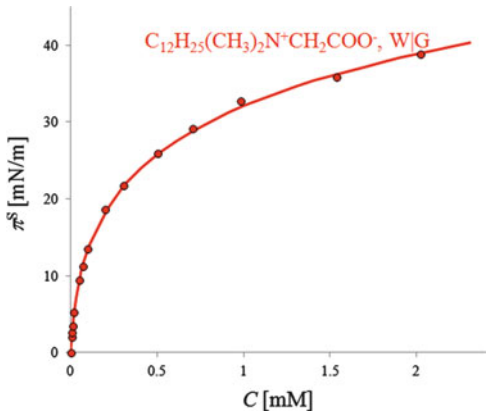

Fig. 3 Surface pressure isotherm (π^S vs. C) of $C_{12}H_{25}Me_2N^+CH_2COO^-$ at W|G interface. An example for non-cohesive isotherm at W|G. Line: HFL isotherm according to (27) and (29) with $\alpha = 19.6\,\text{Å}^2$ and $K_a = 1.83 \times 10^{-4}$ m. Experimental data is from [34]

in Fig. 2a). The so-obtained π^S vs. C^W data are perfectly fitted by the HFL model (line "W|O" in Fig. 2a), by using fixed actual molecular area $\alpha = 16.5\,\text{Å}^2$ of the hydrocarbon chain. The adsorption constant K_a is the only free parameter in (27) and (29): $K_a = 6.54 \times 10^{-3}$ m. The K_a values, determined by such one-parametric fit, have a very small error (less than 1% for ln K_a).

Only surfactants of relatively large head-groups follow non-cohesive behavior at W|G. In the cases of non-cohesive adsorption at W|G, the data processing does not require calculation of activities, as all investigated solutions were diluted (Fig. 3). Unlike the case of alcohols at W|O, for surfactants at W|G there is no independent source of information for α. Besides, it is not certain that HFL model is exact in this case since the disregarded intermolecular attraction may affect the value of the α-parameter of HFL. Therefore, we could not use the HFL model with only one parameter as it was with W|O, and instead we determined both K_a and α as adjustable parameters at W|G. The typical error in the values of these two parameters is $\pm 7\%$ for ln K_a and $\pm 2\,\text{Å}^2$ for α in cases when sufficient experimental data are disposable. The errors could be even higher (up to $\pm 20\%$ for ln K_a) when no measurements in the low-concentration region are available (this is usually the case).

b. Cohesive Adsorption

The W|G data in Fig. 2, which are typical example for cohesive adsorption, refer again to adsorption of decanol. Before the kink, a close-to-linear dependence of π^S on C without intercept is observed. This is the gaseous region, which is treated by using the Henry's EOS, cf. (3):

$$\pi^S = k_B T K_a^G C_s. \tag{30}$$

The data in the gaseous region are scarce and rather scattered; therefore, ln K_a^G is determined with a high error, $\pm 10\%$ at best.

After the kink, at intermediate concentrations, a second region is observed (Fig. 2). Some measurements exhibit in this region enough experimental points to depict a well-defined linear dependence $\pi^S(C)$, but with negative intercept [4]. Denoting this intercept by π_{coh}, one can write the following surface pressure isotherm for this linear region:

$$\pi^S = -\pi_{coh} + k_B T K_a^{LE} C. \tag{31}$$

In cases when the experimental data are scarce or scattered and the linear region is not well visible, we preferred use a square polynomial fit (LE curve in Fig. 2) with the equation:

$$\pi^S = -\pi_{coh} + k_B T K_a^{LE} C + k_B T B_2 \left(K_a^{LE}\right)^2 C^2, \tag{32}$$

which is, in fact, a virial expansion of the surface pressure isotherm (B_2 is the second virial coefficient). We believe that when the quadratic fit with (32) of given set of surface tension data yields a negative intercept $-\pi_{coh}$, the respective surfactant forms a *liquid expanded* layer. The value of $\ln K_a^{LE}$ determined by this fit is typically with error of the order of $\pm 15\%$. The accuracy of the π_{coh} value is also $\pm 15\%$. However, sometimes the error of π_{coh} can be due, at least in part, to systematic error of the surface tension measurements (cf. [6] for discussion).

From the phenomenological surface pressure isotherms (30) and (32), and the Gibbs isotherm one can calculate the respective adsorption isotherms of the gaseous and the LE state:

$$\Gamma = K_a^G C \quad \text{for gaseous state,} \tag{33}$$

$$\Gamma = K_a^{LE} C + 2B_2 \left(K_a^{LE}\right)^2 C^2 \quad \text{for LE state.} \tag{34}$$

In Fig. 2b, the isotherms (33) and (34) for $C_{10}H_{21}OH$ at W|G are plotted along with the result obtained for the same surfactant at W|O by means of HFL adsorption isotherm (29). The adsorption parameters for this plot were determined from the $\pi^S(C)$ data in Fig. 2a. The break of the curve $\Gamma(C)$ corresponds to phase transition from gaseous to LE state (dashed line in Fig. 2b).

4 Analysis of the Experimental Data for the Cohesive Pressure π_{coh} and the Adsorption Constant K_a

Let us now consider the experimental results for the adsorption of some homologous series of nonionic surfactants, analyzed in the framework of the ideas presented in the previous Sects. 2 and 3. We have processed the tensiometric data for 46 nonionic surfactants from nine homologous series at different interfaces and conditions (Fig. 6; cf. "List of symbols and abbreviations" (Table 1) for surfactants' names).

Table 1 List of symbols and abbreviations

B_2	Second virial coefficient
C	Surfactant concentration in the aqueous solution
E_a	Adsorption energy
E_{head}	Energy of transfer of surfactant's head from the bulk to the interface
k_B	Boltzmann constant
K_a	Henry's adsorption constant ($\Gamma = K_a C$)
l_{CH_2}	Length per -CH_2- group (1.26 $\mathring{A}$)
n_C	Number of carbon atoms in surfactant's hydrophobic chain
q	Partition function
T	Temperature
u_{CH_2}	Free energy for transfer of -CH_2- from water to hydrophobic phase
z	Cartesian coordinate
α	Actual area of a molecule
β	Attraction parameter
γ	Activity coefficient
Γ	Surfactant adsorption
δ_a	Adsorption thickness
μ	Chemical potential
π_{coh}	Cohesive pressure
π^S	Surface pressure, $\pi^S = \sigma_0 - \sigma$
σ	Surface tension
σ_0	Surface tension of the pure interface in the absence of surfactant
2D	Two-dimensional
cmc	Critical micelle concentration
EOS	Equation of state
HFL	Helfand–Frisch–Lebowitz model
LE	Liquid expanded state of the adsorption layer
W|G	Water–gas interface
W|O	Water–oil interface
-CH_2-	Methylene group
-CH_3-	Methyl group
$C_nH_{2n+1}OH$	Alkan-l-ol
$C_{n-1}H_{2n-1}COOH$	Alkanoic acid
$C_nH_{2n+1}Me_2PO$	An-alkyl dimethyl phosphine oxides
$C_8H_{17}SOC_2H_4OH$	Octylsulfinylethanol
$C_{10}H_{21}$Mal	n-Decyl β-maltopyranoside
$C_{10}H_{21}$Glu	n-Decyl β-glucopyranoside
$C_{10}H_{21}$SMal	n-Decyl β-D-thiomaltopyranoside
$C_nH_{2n+1}Me_2N^+CH_2COO^-$	N-n-alkyl-N, N-dimethylglycine
C_8H_{17}PEM	Maleic acid mono [2-(4-n-alkylpiperazinyl)ethyl ester]

All investigated surfactants ($C_nH_{2n+1}OH$) display at W|O non-cohesive adsorption behavior. There are some surfactants, mainly with short hydrocarbon chains and bulky head-groups ($C_nH_{2n+1}Me_2N^+CH_2COO^-$, short-chain $C_nH_{2n+1}Me_2PO$ etc.), which behave non-cohesively even at W|G interface. Cohesive (LE) type of surface pressure isotherms were found with most surfactants at W|G, like $C_{n-1}H_{2n-1}COOH$ at low pH, $C_nH_{2n+1}OH$, long-chained $C_nH_{2n+1}PEM$. Moreover, two homologous series of surfactants, $C_nH_{2n+1}Me_2PO$ and $C_nH_{2n+1}Me_2PEM$, exhibit transition from non-cohesive to cohesive behavior with the increase of the hydrocarbon chain length: for the W|G adsorption layers of $C_nH_{2n+1}Me_2PO$ with $n_C = 8 \div 10$ there is no LE region, while the homologues with $n_C = 11 \div 15$ exhibit gaseous-LE phase transition. The behavior of $C_nH_{2n+1}PEM$ is similar to that of $C_nH_{2n+1}Me_2PO$: $n_C = 8$ is non-cohesive, $n_C = 9 \div 11$ are cohesive.

4.1 The Cohesive Pressure π_{coh}

We will base our interpretation of the cohesive isotherms and the phenomenological equations (31) and (32) on Langmuir's concept for liquid expanded monolayer [2]. Langmuir's idea for the origin of the intercept $-\pi_{coh}$ (e.g. [3]) can be quantified as follows. Let σ_0^{WO} be the interfacial tension of the pure W|O interface, and σ_0^{OG} be the oil|gas surface tension. The surfactant hydrophobic tails are adsorbed at the W|G interface and form a structureless oil-like film whose total tension must be $\sigma_0^{WO} + \sigma_0^{OG}$. The hydrophilic heads are adsorbed at the W|O interface of this oil film. In the initial part of the LE region of the dependence π^S vs. C, the "adsorption" of the heads must be ideal. Then, one can write for the tension of the adsorption layer [4]

$$\sigma = \sigma_0^{OG} + \sigma_0^{WO} - k_B T K_a^{LE} C. \tag{35}$$

Here, the last term, stemming from (3), is due to (ideal) adsorption of surfactant's hydrophilic heads. However, by definition, the surface pressure at W|G is $\pi^S = \sigma_0^{WG} - \sigma$. Inserting here σ from (35), and comparing the result with (31), one obtains

$$\pi_{coh} = \sigma_0^{WO} + \sigma_0^{OG} - \sigma_0^{WG} \tag{36}$$

According to these simple considerations, the intercept $-\pi_{coh}$ coincides with the spreading coefficient of a hydrocarbon on water [2]. Therefore, the negative cohesive pressure $-\pi_{coh}$ was at first referred to as *spreading pressure*; the term "cohesive pressure" was introduced by Davies [9].

The simple considerations above give correctly only the order of the value of π_{coh}, but in fact they cannot explain the dependence of π_{coh} on the surfactant tail-length and head-group. The experimental dependence of π_{coh} on n_C is plotted in Fig. 4. The cohesive pressure increases with e.g. $\Delta\pi_{coh} = 0.7$ mN/m per -CH_2- group. This increment corresponds to surface energy per -CH_2- group equal to $\alpha_\perp \Delta\pi_{coh} \approx k_B \times 8$, in good agreement with the experimental finding that "the effect of each additional CH_2 group in the chain is equivalent to a lowering of

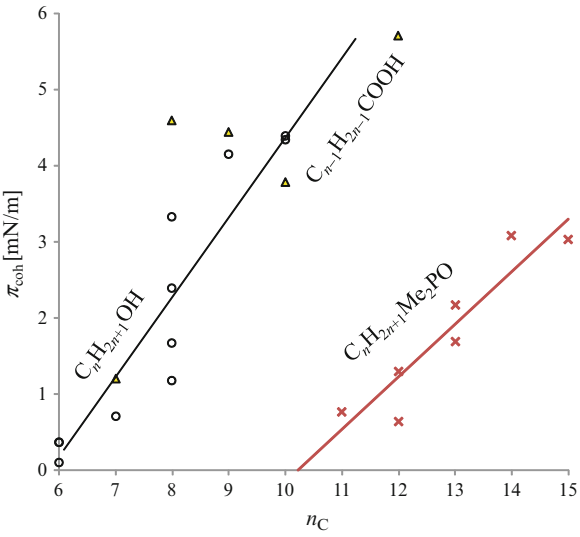

Fig. 4 Dependence of the cohesive pressure π_{coh} on hydrocarbon chain-length n_C for 3 homologous series: alkanols (*circles*), alkanoic acids (*triangles*) and alkyldimethyl phosphine oxides (*crosses*). The dependence is close to linear. For $C_nH_{2n+1}Me_2PO$, the value of n_C at which $\pi_{coh} = 0$ corresponds well with the transition length at which this homologous series becomes non-cohesive: the isotherm of $C_{10}H_{21}Me_2PO$ has no LE region. Tensiometric data from [35–37] were used to calculate π_{coh}

temperature of about 8°C" [2]. It is remarkable that the transition from cohesive to non-cohesive behavior of $C_nH_{2n+1}Me_2PO$ coincides with the value of n_C at which π_{coh} becomes zero (n_C between 10 and 11: $C_{11}H_{23}Me_2PO$ forms cohesive layers and $C_{10}H_{21}Me_2PO$ is non-cohesive). With alkanols and alkanoic acids, the values of π_{coh} are rather uncertain due to the insufficient experimental data. However, their behavior appears to be similar. One can predict from Fig. 4 that pentanol and pentanoic acid will form non-cohesive monolayers.

4.2 *Effect of the Surfactant Structure on the Adsorption Constant K_a*

The data for non-cohesive adsorption of $C_nH_{2n+1}OH$ ($n_C = 8 \div 18$) at W|O (oil phases are various alkanes) were processed by means of HFL model, (27) and (29), with $\alpha = 16.5\,\text{Å}^2$, as explained in Sect. 3. The adsorption constant K_a was the only free adjustable parameter. The dependence of $\ln K_a$ on n_C is shown in Fig. 5. It is linear with slope $u_{CH_2}/k_BT = 1.39$, corresponding to the known energy of transfer from water to oil phase [21]. For non-cohesive adsorption at W|G interface, again HFL model was used, but with two free parameters, α and K_a. The values obtained for α depend only on the head-group of the surfactant:

$$
\begin{aligned}
&C_nH_{2n+1}Me_2N^+CH_2COO^- \quad \text{with} \quad n_C = 8 \div 16 : \alpha = 18.8 \pm 1.5\text{Å}^2,\\
&C_nH_{2n+1}Me_2PO \quad \text{with} \quad n_C = 8 \div 10 : \qquad \alpha = 22 \pm 1\text{Å}^2,\\
&C_8H_{17}PEM : \qquad \alpha = 25\text{Å}^2.
\end{aligned}
$$

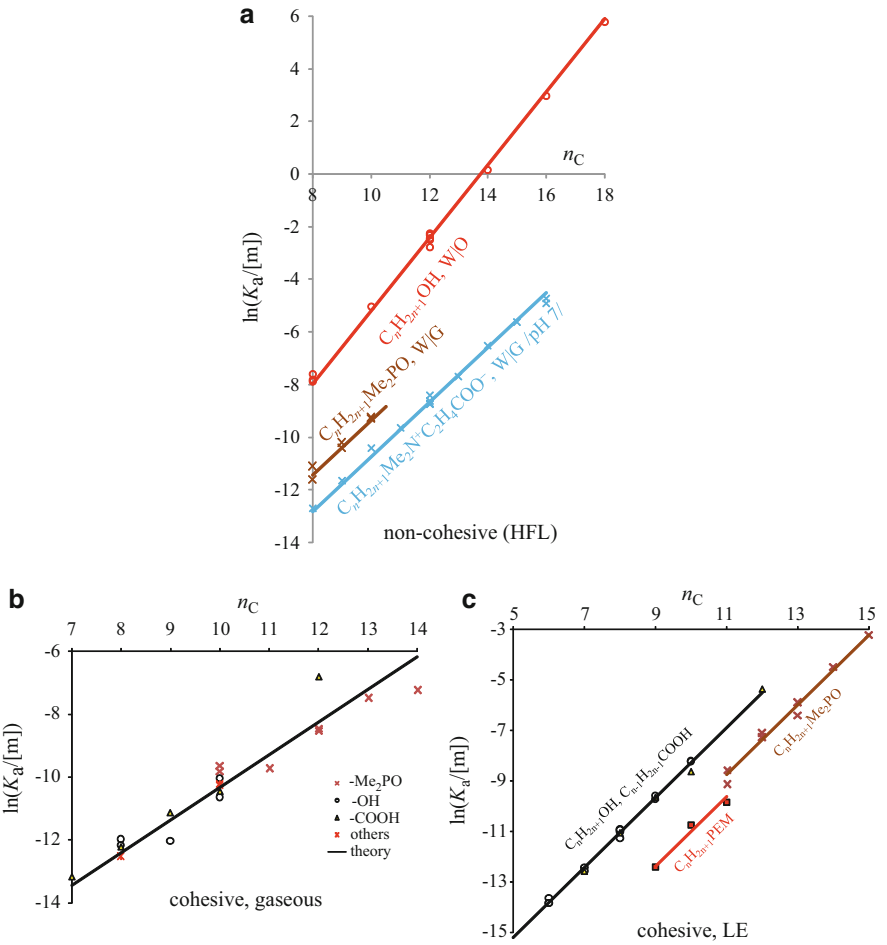

Fig. 5 Dependence of the logarithm of the adsorption constant $\ln K_a$ on the chain length n_C. (**a**) Non-cohesive adsorption: results from fit of tensiometric data with HFL model (similar to the fits in Figs. 2a and 3). The *lines* represent fits with (37) with fixed slopes ($u_{CH_2}/k_BT = 1.39$ for W|O and 1.04 for W|G data). (**b**) Cohesive adsorption, gaseous region. All data fall on a single line with slope 1.04 and intercept $\ln(K_a^\circ/[\mathrm{m}]) = -20.7$, cf. (37). (**c**) Cohesive adsorption, LE-region. Lines are fits with fixed slopes, 1.39. Data for alkanoic acids at low pH and alkanols fall on a single curve with intercept −22.2, while the intercepts for $C_nH_{2n+1}Me_2PO$ and $C_nH_{2n+1}PEM$ are significantly smaller. The tensiometric data used is from different sources (cf. Fig. 6 for the complete list)

In contrast to $C_nH_{2n+1}OH$ at W|O, the linear dependence of $\ln K_a$ on n_C for $C_nH_{2n+1}Me_2N^+CH_2\ COO^-$ and $C_nH_{2n+1}Me_2PO$ at W|G has slope $u_{CH_2}/k_BT = 1.04$ (Fig. 5a), typical for the transfer of a methylene group from water to gas [21].

Cohesive surface tension isotherms are observed only at W|G. Data for $C_nH_{2n+1}OH$, $C_{n-1}H_{2n-1}COOH$, long-chained $C_nH_{2n+1}Me_2PO$ and $C_nH_{2n+1}PEM$,

$C_8H_{17}SOC_2H_4OH$, $C_{10}H_{21}SMal$, $C_{10}H_{21}Mal$ and $C_{10}H_{21}Glu$ were processed. The experimental data for $\ln K_a^G$ vs. n_C for the gaseous region of all these surfactants fall on a single straight line with slope $u_{CH_2}/k_BT = 1.04$ (Fig. 5b), and with intercept $\ln(K_a^o/[\mathrm{m}]) = -20.7$. The LE region was processed with (32). With all these surfactants, the slope of the dependence of $\ln K_a^{LE}$ on n_C is $u_{CH_2}/k_BT = 1.39$ (Fig. 5c), i.e., the same as for the adsorption at W|O interface. This is certainly due to the fact that the transfer of -CH_2- is from water to LE adsorption layer, i.e., into an oil-like environment. The value of the intercept $\ln K_a^\circ$ of this dependence is the same for $C_nH_{2n+1}OH$ and $C_{n-1}H_{2n-1}COOH$. However, the $C_nH_{2n+1}Me_2PO$ have significantly lower values of $\ln K_a^\circ$ than the corresponding acids and alcohols, and with $C_nH_{2n+1}PEM$, $\ln K_a^o$ is even smaller (Fig. 5).

We now turn to the interpretation of the value of the intercepts $\ln K_a^\circ$ of the lines in Fig. 5. To compare the statistical model of K_a to the experimental data in Fig. 5, it is convenient to represent (5), (11) and (26) in logarithmic form:

$$\ln K_a = \ln K_a^\circ + n_C u_{CH_2}/k_BT, \tag{37}$$

where the intercept $\ln K_a^\circ$ of the experimental dependence of $\ln K_a$ on n_C is given by

$$\ln K_a^\circ \equiv \ln \delta_a + (E_{head} + u_{CH_2} + \alpha_\perp \sigma_\perp)/k_BT. \tag{38}$$

Here δ_a is the adsorption length, (26). The experimental value of the intercept $\ln K_a^\circ$ can be determined directly when data for several members of a homologous series are available (cf. Fig. 5). However, in few cases (e.g. for $C_8H_{17}SOC_2H_4OH$, $C_{10}H_{21}Mal$ etc.), data were available only for a single surfactant. Then, $\ln K_a^\circ$ was calculated from (37) with the known value of u_{CH_2}/k_BT (1.39 or 1.04) and the experimental $\ln K_a$ for this surfactant. The results for $\ln K_a^\circ$ for nine homologous series are presented in Fig. 6. The following comments of these results seem pertinent:

- 1. For all non-cohesive surfactants at W|G and for the gaseous region of all cohesive surfactants, the difference between theoretical and experimental values of $\ln K_a^\circ$ is about u_{CH_2}/k_BT (cf. Fig. 6). One possible reason for this difference is that the first carbon atom from the hydrocarbon tail is immersed in the water—that is why we called it "immersion energy". Such position of the surfactant molecule is natural for -COOH, where there is one C-atom in the carboxylic group. For the other examples in the Fig. 6, the immersion of the first C-atom might be due to the interaction of the head-group with the interface, i.e. to the neglected term E_{head} in (38). The analysis of this effect is complicated and will be postponed to a subsequent publication.
- 2. The comparison of the experimental and theoretical values of K_a in the LE region for the surfactants in Fig. 6 at W|G was done with intercept $\ln K_a^\circ$ calculated with $\sigma_0 = 50$ mN/m instead of 72.2 mN/m, as if the surfactant adsorbs at W|O interface. This in accord with Langmuir's interpretation of LE state.

surfactant, number of C-atoms, interface[a]	$\ln(K_a^o/[m])$ experimental	u_{CH_2}	immersion energy E_{head}	$\ln(K_a^o/[m])$ calculated Eq. (38)
non-cohesive surface tension isotherms[b] sigma$_0$ = 72.2 mN/m at W|G and sigma$_0$ = 50 mN/m at W|O				
$C_nH_{2n+1}Me_2PO$ $n_C = 8\div10$, W|G [35,37]	–19.7±0.1	1.04	$-u_{CH_2}$	–20.7
$C_nH_{2n+1}Me_2N^+CH_2COO^-$ $n_C = 8\div16$, W|G [35,34][e]	–21.1±0.2	1.04		
$C_8H_{17}PEM$ $n_C = 8$, W|G [35]	–21.3±0.3	1.04		
$C_nH_{2n+1}OH$ $n_C = 8\div18$, W|O [31]	–19.0±0.2	1.39	$-u_{CH_2}$	–21.7
cohesive surface tension isotherms – gaseous region[c] sigma$_0$ = 72.2 mN/m				
C_nH_{2n+1}–OH, –Me_2PO, –SOC_2H_4OH, –Mal, –SMal, –Glu $C_{n-1}H_{2n-1}COOH$ W|G [4,35-38]	–20.7±0.3	1.04	$-u_{CH_2}$	–20.7
cohesive surface tension isotherms – LE region[d] sigma$_0$ = 50 mN/m				
$C_nH_{2n+1}OH$ $n_C = 7\div12$, W|G [35,36]	–22.1±0.3	1.39	$-u_{CH_2}$	–21.9
$C_{n-1}H_{2n-1}COOH$ $n_C = 7\div10$, W|G [35][f]	–22.2±0.2	1.39	$-u_{CH_2}$	–21.9
$C_8H_{17}SOC_2H_4OH$, W|G [38]	–22.4	1.39	$-u_{CH_2}$	–21.9
$C_{10}H_{21}SMal$, W|G [4]	–21.8	1.39	$-u_{CH_2}$	–21.9
$C_{10}H_{21}Mal$, $C_{10}H_{21}Glu$, W|G [4]	–23.0, –22.8	1.39	$-2u_{CH_2}$	–23.3
$C_nH_{2n+1}Me_2PO$ $n_C = 11\div15$, W|G [35,37]	–24.0±0.25	1.39	$-3u_{CH_2}$	–24.7
$C_nH_{2n+1}PEM$ $n_C = 9\div11$, W|G [35]	–24.9±0.2	1.39	$-3u_{CH_2}$	–24.7

[a] Cf. "List of symbols and abbreviations" for surfactants' names
[b] Data for non-cohesive surfactants, W|G or W|O interface.
[c] Data for the gaseous region of cohesive surfactants.
[d] Data for the liquid expanded (LE) region of non-cohesive surfactants.
[e] Data for pH = 7; the compound is in its zwitterionic (betaine) form.
[f] Data for undissociated acids (low pH).

Fig. 6 Experimental and theoretical intercepts of the linear dependences $\ln k_a$ vs. n_C for different homologous series

- 3. With cohesive surfactants of bulky head-groups (e.g., $C_nH_{2n+1}Me_2PO$ and $C_nH_{2n+1}PEM$), the value of $\ln K_a^\circ$ in the LE region is considerably lower than the one predicted by (38). The immersion energy for these surfactants is about $2 \div 3 \times u_{CH_2}$.
- 4. The only nonionic surfactants at W|O for which we had truly reliable data are the fatty alcohols. Their adsorption constants was found somewhat larger than the theoretical value predicted by (38) (again with one immersed C-atom): the experimental $\ln(K_a^\circ/[\mathrm{m}])$ is -19.0 vs. the theoretical value -21.7.

One way to check the reliability of the values of the transfer energy u_{CH_2} determined from the slopes of the lines in Fig. 5 is the following analysis of the experimental dependence of the surface pressure on the surfactant concentration and chain-length n_C for the two types of adsorption: cohesive and non-cohesive. Any adsorption isotherm can be written as:

$$\gamma^S(\alpha\Gamma, \beta)\Gamma = K_a C; \tag{39}$$

here γ^S is surface activity coefficient and β is attraction parameter [30]. Accounting for (37) for K_a, one obtains:

$$\gamma^S(\alpha\Gamma, \beta)\Gamma = K_a^\circ \exp\left(u_{CH_2} n_C / k_B T\right) C. \tag{40}$$

To simplify the analysis of the dependence $\Gamma(C; n_C)$, let us for the time being neglect the dependence of α and β on n_C. Then, one concludes from (40) that $\Gamma = \Gamma\left[C \times \exp\left(n_C u_{CH_2}/T\right)\right]$. If one substitutes this dependence into the EOS $\pi^S(\Gamma)$, one concludes that the surface pressure will depend on n_C mainly through the product $C \exp\left(n_C u_{CH_2}/T\right)$, with $u_{CH_2} = 1.04 \times k_B T$ for non-cohesive adsorption and $u_{CH_2} = 1.39 \times k_B T$ for the LE region of cohesive isotherms. This hypothesis is checked in Fig. 7 on the examples of $C_nH_{2n+1}Me_2N^+CH_2COO^-$ at W|G (non-cohesive) and $C_{n-1}H_{2n-1}COOH$ at W|G at low pH (cohesive). The data were normalized to dodecyl hydrophobic chain by subtracting 12 from n_C in the exponent, i.e., by plotting $C \exp\left[u_{CH_2}\left(n_C - 12\right)/T\right]$ on the x-axis of Fig. 7. As seen from the Figure, the results fall on a single master curve for each type of system. The slight deviations from these master-curves are due to the dependence of α and β, and π_{coh} in the case of LE, on the hydrocarbon chain length n_C, which turns out to be weaker than the main dependence on n_C in (40), as assumed above.

4.3 Temperature Dependence of the Adsorption

The transfer energy of a -CH_2- group from water to hydrophobic phase was extensively discussed in the classical studies on the so-called "hydrophobic effect" [21, 22]. The thermodynamic analysis of data for the temperature dependence of a large number of "hydrophobic" phenomena, such as solubility of alkanes in

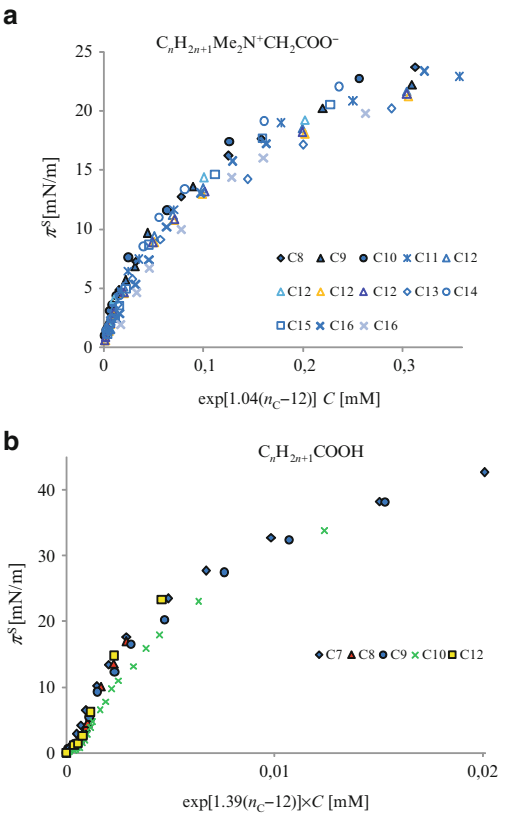

Fig. 7 Scaling of the surface tension isotherms (π^S vs. C) of homologous series of (**a**) cohesive and (**b**) non-cohesive surfactants. All data are for W|G surface. However, the data for the non-cohesive $C_nH_{2n+1}Me_2N^+CH_2COO^-$ series scales with $\exp(1.04n_C) \times C$, while the data for the LE region of $C_{n-1}H_{2n-1}COOH$ scales with $\exp(1.39n_C) \times C$, i.e., with the value $u_{CH_2}/k_BT = 1.39$ typical for W|O interface. All isotherms are reduced to a standard isotherm of the C_{12}-homologue of the respective series, see text for details. Data from [34, 35]

water, *cmc* of surfactants, etc., showed that this transfer energy is predominantly of entropic origin. It seems obvious that the nature of the free energy u_{CH_2} for *adsorption* of a methylene group in our expressions (37) and (38) is also related to the "hydrophobic" phenomena. We will use this fact to predict the temperature dependence of the adsorption constant K_a, by analyzing the tensiometric data of Vochten and Petre for the adsorption of heptanol at W|G interface [36]. The surface tension isotherms of heptanol in Fig. 8 exhibit non-zero intercepts: therefore, they are of the cohesive type. Hence, we processed the data according to the procedure outlined in Sect. 3.3 (cf. also Fig. 2a) in order to obtain the adsorption constants in the LE region at various temperatures. The results are shown in Fig. 9. We will interpret them now by using our (37) and (38) above.

The adsorption constant K_a involves large enthalpic contributions from two terms in (37) and (38), namely, the hydrophobic term $(n_C + 1)u_{CH_2}$ and the surface contribution $\alpha_\perp \sigma_0(T)/k_BT$. The hydrophobic term $(n_C + 1)u_{CH_2}$ in (37) and (38), which is the transfer free energy of the heptyl chain from water to the LE adsorption layer, must be very close to the Gibbs energy, $\Delta\mu_{0,hept}$, for transfer of a heptane

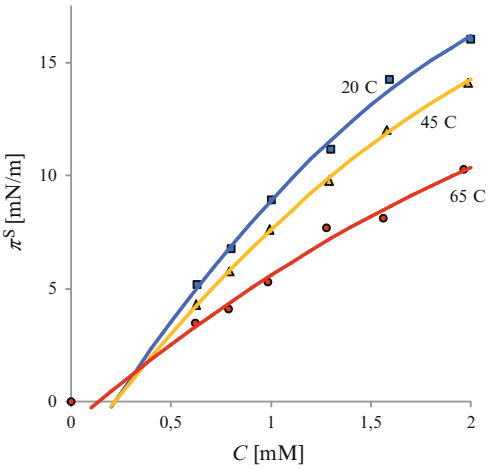

Fig. 8 Effect of the temperature on the cohesive surface pressure isotherm (π_S vs. C) of heptanol at W|G interface. Data by Vochten and Petre [36]

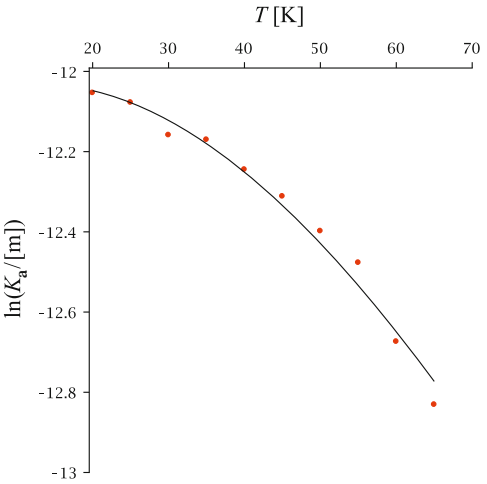

Fig. 9 Temperature dependence of the adsorption constant of heptanol at W|G in the LE region: ln K_a vs. T. The line is calculated from (43), with no adjustable parameters. Experimental points are calculated from the tensiometric data of Vochten and Petre [36]

molecule from water to heptane. The relation between these quantities must be obviously

$$\Delta\mu_{0,hept} = k_B T \ln x_s \approx -(n_C + 1)u_{CH_2}, \tag{41}$$

where x_s is the heptane molar fraction in a saturated aqueous solution. The last equation allows expressing u_{CH_2} by the measurable quantity x_s. Substituting the result in our (37) and (38) for K_a, one obtains:

$$\ln K_a = \frac{E_{head}}{k_B T} + \ln \delta_a + \frac{\alpha_\perp \sigma_0(T)}{k_B T} - \ln x_s(T). \tag{42}$$

It is convenient to normalize this equation to the standard temperature 298 K:

$$\ln K_a(T) = \ln K_a^{298} + \frac{\alpha_\perp}{k_B}\left(\frac{\sigma_0(T)}{T} - \frac{\sigma_0^{298}}{298}\right) - \ln\frac{x_s(T)}{x_s^{298}}. \tag{43}$$

Here we have neglected the weak temperature dependence of the term $\ln\delta_a + E_{head}/k_BT$ in (42). This normalization minimizes the error coming from the approximation (41). For heptanol, all quantities in the right-hand side of (43) can be easily found. The value of the constant $\ln\left(K_a^{298}/[m]\right) = -12.08$ was determined from the surface tension data at 25°C of Vochten and Petre [36]. For the LE state, the tension $\sigma_0(T)$ of the clean interface can be calculated from the equation:

$$\sigma_0 = \sigma_0^{298} - s_0(T - 298), \tag{44}$$

which is based on tensiometric data for water|alkane interface [39]. Here $s_0 = 0.09\,\mathrm{mJ/Km^2}$ is entropy and $\sigma_0^{298} = 50\,\mathrm{mJ/m^2}$ is the interfacial tension of W|alkane at 25°C [39]. The molecular area is $\alpha_\perp = 16.5\,\mathring{A}^2$. Finally, from [40], the temperature dependence of $\ln x_s$ in the range 20°C÷70°C is:

$$\ln x_s = \ln x_s^{298} + \frac{\Delta h_s^{298} - 298\Delta c_{p,s}}{R}\left(\frac{1}{T} - \frac{1}{298}\right) - \frac{\Delta c_{p,s}}{R}\ln\frac{T}{298}, \tag{45}$$

where x_s^{298} is the solubility at 298 K ($\ln x_s^{298} = -14.61$), $\Delta h_s^{298} = 2149\,\mathrm{J/mol}$ is the molar enthalpy of dissolution at 298 K, $\Delta c_{p,s} = -473.6\,\mathrm{J/molK}$ is the heat capacity of dissolution [40], R is gas constant. Substituting (44) and (45) in (43) yields an explicit expression for $\ln K_a(T)$. The results for $\ln K_a(T)$ calculated in this way from (43) are shown by continuous curve in Fig. 9 and compared with experimental results. The agreement is good.

From (43), the enthalpy of adsorption Δh_a can be calculated according to Gibbs–Helmholtz relation:

$$\Delta h_a = -k_BT^2\frac{\partial \ln K_a}{\partial T} = \alpha_\perp h_0 - \Delta h_s/N_A, \tag{46}$$

where $h_0 = \sigma_0 + Ts$ is the enthalpy per unit area of the W|O interface and $\Delta h_s = \Delta h_s^{298} + (T-298)\Delta c_{p,s}$ is the molar enthalpy of dissolution of heptane. The second "hydrophobic" term on the right hand side of (46), $\Delta h_s/N_A$, is a linear function of T; it is zero at 30°C, and reaches $6 \div 7 \times k_BT$ at 70°C. The first "surface" term, $\alpha_\perp h_0 = 1.3\times10^{-20}\,\mathrm{J}$, is about $3\times k_BT$. Therefore, the surface term is by no means negligible. On the contrary, it is the leading effect at room temperature.

The cohesive pressure π_{coh} of heptanol also varies with T. It can be shown that, starting from 3.0 mN/m at 20°C, it decreases with slope $0.044\,\mathrm{mN/m}\times\mathrm{K}$. One can then expect that π_{coh} will become zero at 90°C and the LE state will cease to exist, and the adsorption layer will become non-cohesive. This effect is similar to the effect of the decrease of the number of -CH_2- groups on π_{coh} in Fig. 4.

5 Conclusions

Our analysis of the experimental data for the surface and interfacial tension of more than 50 nonionic surfactants revealed that the data can be described by one of two characteristic isotherms: of cohesive and non-cohesive type. Three phenomenological criteria were formulated for relating given set of tensiometric data to one of these types.

The most important ***first criterion*** is the existence of a kink in the cohesive isotherms at low concentration (cf. Fig. 2a). The low-concentration region before the kink corresponds to gaseous state of the adsorption layer [4]. The $\pi^S(C)$-dependence after the kink exhibits negative intercept $-\pi_{coh}$ (Fig. 2a). This intercept $-\pi_{coh}$ is in fact Langmuir's *cohesive (spreading) pressure* [2, 10]. The kink itself probably corresponds to a first order phase transition [4, 5]. If no kink is present, the surface tension isotherm is non-cohesive.

Unfortunately, it is often problematic to obtain reliable measurements in the gaseous region of a cohesive isotherm, and consequently it is not always easy to observe the kink. If such is the case, a ***second criterion*** can be used: all surfactants which form non-cohesive monolayers follow (at least qualitatively) the HFL isotherm, with area parameter equal or very close to the actual area of the surfactant tail ($\alpha = 16.5\,\mathring{A}^2$ for surfactants with linear hydrocarbon tail and small polar head-group), cf. Fig. 2. In contrast, the data for cohesive films cannot be interpolated satisfactory with HFL model.

The ***third criterion*** is related to the linear dependence of the logarithm of adsorption constant $\ln K_a$ on the number n_C of carbon atoms of the surfactant, cf. (Fig. 5a). The slope of this dependence for non-cohesive type of isotherms is $\mathrm{d}\ln K_a/\mathrm{d}n_C = 1.04$. For the LE region of *cohesive* isotherms at W|G, the slope is 1.39 (Fig. 5c)—a value typical, in fact, for the W|O interface. The different slopes are related to the different transfer energies u_{CH_2} of a methylene group from water to gas and from water to LE adsorption layer. The latter is in fact a transfer to an oil-like environment.

The adsorption at W|O interface always exhibits non-cohesive behavior. Cohesive isotherms are typical for W|G only. However, not always the adsorption at W|G is cohesive (cf. Fig. 6), e.g., the isotherms of $C_nH_{2n+1}Me_2N^+CH_2COO^-$ at W|G exhibit no LE region (Fig. 7a). We have also found that within certain homologous series of surfactants, both types can be found: short-chain homologues are non-cohesive, while long-chained ones are cohesive (a typical example is $C_nH_{2n+1}Me_2PO$, cf. Fig. 5). The chain-length at which the transition from cohesive to non-cohesive behavior occurs corresponds to zero cohesive pressure (Fig. 4).

We further compared in Fig. 6 the experimentally determined adsorption constants to the model, previously developed by us (presented in Sect. 2). The model does not involve adjustable parameters. In most cases, the comparison is satisfactory, if one assumes that one C-atom from the hydrocarbon chain remains immersed into water (Fig. 6). We further checked our model by comparing its predictions to experimental data for the temperature T dependence of the adsorption constant

(Fig. 9). Independent data for the dependence on T of the transfer energy of the hydrocarbon chain from water to oil phase were used to model the transfer from water to liquid expanded monolayer at W|G. The agreement reached without using adjustable parameters is very good. This proves beyond doubt both Langmuir's concept for the LE state, and our model of the adsorption constant.

We also observed couple of effects which are waiting for explanation. The first one is the dependence of the cohesive pressure on the surfactant's chain-length and head-group (Fig. 4). An important open question is the equation of state of dense LE monolayer of nonionic surfactants. The comparison between results presented here for the nonionic surfactants and those obtained previously in [6] for ionic surfactants is also forthcoming.

Acknowledgement This work was supported by Bulgarian National Science Fund Grants DDVU 02/12 and DDVU 02/54.

References

1. Adam, N.K.: Proc. Roy. Soc. A **101**, 516 (1922)
2. Langmuir, I.: J. Chem. Phys. **1**, 756–776 (1933)
3. Adam, N.K.: The Physics and Chemistry of Surfaces. Clarendon, Oxford (1941)
4. Kumpulainen, A.J., Persson, C.M., Eriksson, J.C., Tyrode, E.C., Johnson, C.M.: Langmuir **21**, 305–315 (2005)
5. Mufazzal Hossain, Md., Suzuki, T., Iimura, K., Kato, T.: Langmuir **22**, 1074–1078 (2006)
6. Slavchov, R.I., Karakashev, S.I., Ivanov, I.B.: Ionic surfactants and ion-specific effects: adsorption, micellization, thin liquid films, Chapter 2. In: Römsted L. (ed.)Surfactant Science and Technology: Retrospects and Prospects. Taylor and Francis, LLC, Boca Raton (2013)
7. Aratono, M., Uryu, S., Hayami, Y., Motomura, K., Matuura, R.: J. Colloid Interface Sci. **98**, 33–38 (1984)
8. Kaganer, V.M., Möhwald, H., Dutta, P.: Rev. Mod. Phys. **71**, 779–819 (1999)
9. Davies, J.T.: J. Colloid Sci. **11**, 377–390 (1956)
10. Davies, J.T., Rideal, E.: Interfacial Phenomena. Academic, New York (1963)
11. Smith, T.: J. Colloid Interface Sci. **23**, 27–35 (1967)
12. Möhwald, H.: Rep. Rog. Phys. **56**, 653–685 (1993)
13. Fischer, T.M., Lösche, M.: Lect. Notes Phys. **634**, 383 (2004)
14. Shchukin, E.D., Pertsov, A.V., Amelina, E.A.: Colloid Chemistry. University Press, Moscow (1982) [in Russian]. Elsevier, Amsterdam (2001) [in English]
15. Kralchevsky, P.A., Danov, K.D., Broze, G., Mehreteab, A.: Langmuir **15**, 2351–2365 (1999)
16. Danov, K.D., Kralchevsky, P.A., Ananthapadmanabhan, K.P., Lips, A.: J. Colloid Interface Sci. **300**, 809–813 (2006)
17. Ivanov, I.B., Ananthapadmanabhan, K.P., Lips, A.: Adv. Colloid Interface Sci. **123–126**, 189–212 (2006)
18. Lange, H., Jeschke, P.: Surface monolayers, Chapter 1, pp. 1–44. In: Schick, M.J. (ed.) Nonionic Surfactants. Physical Chemistry. Surfactant Science Series, vol. 21. Marcel Dekker, New York (1987)
19. Hückel, W.: Theoretical Principles of Organic Chemistry, vol. II, p. 435. Elsevier, New York (1958)
20. Kitaigorodskii, A.I.: Organic Chemical Crystallography. Consultant Bureau, New York (1961)
21. Tanford, C.: The Hydrophobic Effect. Wiley, New York (1980)

22. Israelachvili, J.N.: Intermolecular and Surface Forces. Academic, New York (2011)
23. Hill, T.L.: An Introduction to Statistical Thermodynamics. Addison-Wesley, Reading (1962)
24. Davies, J.H.: The Physics of Low-Dimensional Semiconductors - An Introduction. Cambridge University Press, Cambridge (1998)
25. Levich, V.G.: Introduction to Statistical Physics. Gos. Izd. Tekhn.-Teor. Lit., Moscow (1954)
26. Langmuir, I.: J. Am. Chem. Soc. **40**, 1361–1403 (1918)
27. Volmer, M.: Z. Phys. Chem. **115**, 253–260 (1925)
28. Tonks, L.: Phys. Rev. **50**, 955–963 (1936)
29. Helfand, E., Frisch, H.L., Lebowitz, J.L.: J. Chem. Phys. **34**, 1037–1042 (1961)
30. Ivanov, I.B., Danov, K.D., Dimitrova, D., Boyanov, M., Ananthapadnamabhan, K.P., Lips, A.: Colloids Surf. A **354**, 118–133 (2010)
31. Aveyard, R., Briscoe, B.J.: J. Chem. Soc. Faraday Trans. 1 **68**, 478–491 (1972)
32. Aveyard, R., Briscoe, B.J., Chapman, J.: J. Chem. Soc. Faraday Trans. 1 **69**, 1772–1778 (1973)
33. Villalonga, F.A., Koftan, R.J., O'Connell, J.P.: J. Colloid Interface Sci. **90**, 539 (1982)
34. Wüstneck, R., Miller, R., Kriwanek, J., Holzbauer, H.-R.: Langmuir **10**, 3738 (1994)
35. Fainerman, V.B., Miller, R., Aksenenko, E.V., Makievski, A.V.: Equilibrium adsorption properties of single and mixed surfactant solutions, Chapter 3, pp. 189–286. In: Fainerman, V.B., MRobius, D., Miller, R. (eds.) Surfactants – Chemistry, Interfacial Properties, Applications
36. Vochten, R., Petre, G.: J. Colloid Interface Sci. **42**, 320–327 (1973)
37. Warszynski, P., Lunkenheimer, K.: J. Phys. Chem. B **103**, 4404–4411 (1999)
38. Aratono, M., Uryu, S., Hayami, Y., Motomura, K., Matuura, R.: J. Colloid Interface Sci. **98**, 33–38 (1984)
39. Goebel, A., Lunkenheimer, K.: Langmuir **13**, 369–372 (1997)
40. Tsonopoulos, C.: Fluid Phase Equilib. **156**, 21–33 (1999)

Surface Wetting: From a Phenomenon to an Important Analytical Tool

V. Dutschk

1 Theoretical Concepts of Wetting

Surface wetting as a physical phenomenon has been known for a long time and is the ability of a liquid to keep a contact with a solid surface resulting from intermolecular interactions. The degree of wetting is called *wettability* and is determined by a force balance between adhesive forces, acting between the liquid and solid phases, and cohesive forces, acting in the wetting liquid.

Some 100 years ago, Gibbs [1] elaborated the fundamentals of the thermodynamic theory of capillary; his paper *On the equilibrium of heterogeneous substances* was taken as a basis for all subsequent theoretical and experimental wetting work. Since then, diligent work has been done to describe the wetting behaviour of heterogeneous systems, thereby to determine the surface energies of liquid and solid bodies, and in this manner to predict the adhesion behaviour. Over a period of years, heaps of literature have been accumulated on these problems, proposing various measurement techniques and different evaluation possibilities, including criticism of one or other computational algorithm or fundamental idea.

Following is a brief discussion of the fundamental results.

1.1 Surface Tension and Surface Energy

It is common knowledge that inside a liquid a molecule undergoes a different equilibrium position than at the liquid surface, due to its neighbours, and that work has to be done to direct this molecule toward the surface. As this takes

V. Dutschk (✉)
Engineering of Fibrous Smart Materials (EFSM), Faculty for Engineering Technology (CTW), University of Twente, P.O. Box 217, 7500 AE, Enschede, The Netherlands
e-mail: v.dutschk@utwente.nl

R.G. Rubio et al. (eds.), *Without Bounds: A Scientific Canvas of Nonlinearity and Complex Dynamics*, Understanding Complex Systems,
DOI 10.1007/978-3-642-34070-3_23,

place, the surface will increase by this molecule which now has a potential energy elevated by the amount of this work. The corresponding increase in energy, being related to the unit of area, is referred to as *specific surface energy*. The force needed to do this work and related to the unit of length is referred to as *surface tension*. Most textbooks assume the surface tension to be identical to the specific surface energy. Strictly speaking, these terms are not identical. While the term *surface tension* (a unit of measurement: force per length, the force being determined by specifying amount and direction) originates from classical mechanics, the term *surface energy* (a unit of measurement: energy per area, the energy being fully considered by specifying a number) results from the energy approach. The thermodynamic definition of the surface tension γ expresses it in terms of the change in free energy (F) as the interfacial area (A) of two coexisting phases is changed at constant volume (V)

$$\gamma = \left(\frac{\partial F}{\partial A}\right)_{T,V}. \tag{1}$$

In the theory of capillarity, the surface tension is associated with the tension of two-dimensional membrane located at the boundary between two phases. In the absence of a field, the tensor of excess surface stresses (which is used to introduce the surface tension) is two-dimensional for plane surfaces. However, for a spherical surface, the transverse surface tension appears, i.e. the normal component of the tensor of excess surface stresses, which can be nullified by a simple selection of the position of the dividing surface as a tension surface [2]. In the presence of external field, even such simple as gravitational, the transverse surface tension can hardly be eliminated by some conditional procedures. As a result of the permanent presence of three-dimensional aspect, the theory of interfacial phenomena begins to lose its inherent simplicity and attractiveness.

Liquids with high surface tension, usually reflecting strong intra-molecular bonds, or liquids on low-energy solid surfaces, usually form nearly spherical droplets, whereas liquids with low surface tension, or liquids on high-energy surfaces, usually spread over the surfaces. This phenomenon is a result of minimization of interfacial energy. Thus, if a surface has a high free energy, most liquids will spread on the surface since this will usually lower the free energy. Wetting phenomena have been widely studied both theoretically and experimentally in connection with the physics of surfaces and interfaces.

1.2 Young Equation

Whether a liquid will wet a solid depends on the surface tension of the solid γ_{SG}, that of the liquid γ_{LG}, strictly speaking *interfacial tension* since wetting describes a displacement of a solid–gas (air) interface with a solid–liquid interface, and the interfacial solid–liquid tension γ_{SL}. These quantities are connected with the

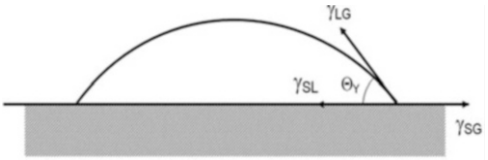

Fig. 1 Liquid drop on a solid surface: Θ_Y is the Young contact angle; γ_{LG} is the interfacial tension liquid–gas; γ_{SG} and γ_{SL} are interfacial tensions solid–gas and solid–liquid, respectively: ideal wetting situation

contact angle Θ_Y by the Young [3] equation where the contact angle stands for the equilibrium angle with the lowest energy state (Fig. 1)

$$\gamma_{SG} = \gamma_{SL} + \gamma_{LG} \cdot \cos \Theta_Y. \tag{2}$$

Since the quantities γ_{SG} and γ_{SL} are generally inaccessible to experiments, as opposed to γ_{LG}, the Young equation is often used for solving the inverse problem, i.e. to determine the difference ($\gamma_{SG} - \gamma_{SL}$, which is referred to as *wetting tension* or *adhesive tension*, by means of the experimental values θ and γ_{LG}. This is the free energy gained when a unit of the solid surface is wetted without changing the size of the liquid surface. The wettability directly depends on the interfacial tension γ_{SL}: the stronger the interfacial interactions, the lower the interfacial tension; the lower the interfacial tension, the better wetting.

1.3 Adsorbed Water Film

Contact angle estimation by means of the Young equation (2) is additionally complicated by the fact that the solid surface is able to adsorb water vapour from the air. The values of γ_{SG} depend on the thickness of the adsorbed water film. Adsorbed layers can change the interfacial behaviour by influencing adhesion due to the adsorption of electrolyte ions. Since water is also a weak electrolyte solution, which often forms a film on "dry" surfaces as an adsorbed layer under normal conditions, research into the relations between surface potentials or surface charges of solids acquires a particular meaning in the presence of an adsorbed water film. Studies in this direction was particularly initiated by Jacobasch [4]. Frumkin, Derjaguin and Churaev [5–8] wetting theory based on the surface forces seems to be best suited in this respect.

Relations between charged surfaces and molecular interaction forces are discussed in the context of this theory. Varying the balance of surface forces, it is possible to control the wetting behaviour. In 1938, Frumkin introduced the term *film tension* γ_f, which is equivalent to the term *solid surface tension* γ_{SG} and depends on the film thickness h [7] as shown in Fig. 2

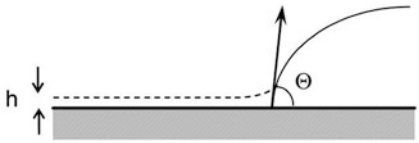

Fig. 2 Schematic representation of a solid surface with a thin wetting film

$$\gamma_f = \gamma_{SG}(h). \tag{3}$$

With a very large h (several hundred nanometers) is valid

$$\gamma_{SG} = \gamma_{SL} + \gamma_{LG}.$$

Assuming that the free energy determination of liquid films is based on a very thick liquid film, with

$$\gamma_f = \gamma_{SL} + \gamma_{LG},$$

rather than on the "dry" solid surface, Frumkin analysed the dependence $\gamma_f = \gamma_f(h)$. From this, the possibility of metastable states of liquid films was obtained with an incomplete wetting situation

$$\gamma_f < (\gamma_{SL} + \gamma_{LG}),$$

and the condition of a complete wetting was defined as

$$\gamma_f \geq (\gamma_{SL} + \gamma_{LG}).$$

At this point, the possible existence of γ_f values was postulated, which exceed the value $(\gamma_{LG} + \gamma_{SL})$ must be emphasised, while the Young equation lacks such a possibility.

1.4 Work of Adhesion

The work of adhesion between liquids and solids is described by the Dupré–Young equation

$$W_A = \gamma_{LG}(1 + \cos\theta). \tag{4}$$

The surface energy of solids can be, at least tentatively, determined by measuring the contact angle.

A different possibility to determine work of adhesion is to represent surface energy as a sum of two components: dispersion component γ_i^d (effect of London dispersion forces) and polar component γ_i^p (due to forces of a different kind). No less than two test liquids (a polar and a non-polar one) have to be used. This method

is based on Fowkes approach [9] which was later converted by Owens and Wendt [10] to the following form

$$\gamma_{12} = \gamma_1 + \gamma_2 - 2\sqrt{\gamma_1^d \cdot \gamma_2^d} - 2\sqrt{\gamma_1^p \cdot \gamma_2^p}.$$

For work of adhesion, hence, follows

$$W_A = 2\sqrt{\gamma_1^d \cdot \gamma_2^d} + 2\sqrt{\gamma_1^p \cdot \gamma_2^p}.$$

The surface tension of solids can be calculated by means of Young equation (2). However, the interfacial tension, γ_{SL} (or γ_{12}), as a result of the interactions between liquid and solid, cannot be determined directly in a wetting experiment. There are approaches which try to bypass the problem.

1.5 Critical Surface Tension

Since the state of surfaces is capable of influencing their wettability Zisman [10] introduced *critical surface tension* γ_c. Zisman examined the linear relation

$$\cos\theta = a - b \cdot \gamma_{LG},$$

with various test liquids. Then, γ_c results by linear extrapolation

$$\gamma_c = \lim_{\theta \to 0} \gamma_{LG}.$$

Measurements with non-polar liquids allow determination of the dispersion component γ_i^d and those with polar liquids determination of the polar one γ_i^p.

Based on the critical surface tension concept, Neumann [11] suggested to estimate surface free energies of solid substrates γ_{SG} from experimentally determined advancing contact angles of a known liquid (e.g. water) using the equation of state for solid–liquid interfacial tension developed in the frames of semi-empirical theory

$$\cos\theta = -1 + 2\sqrt{\gamma_{SG}/\gamma_{LG}} \cdot e^{-0.0001247(\gamma_{LG}-\gamma_{SG})^2}.$$

1.6 Fowkes and Good Theories

Fowkes proposed the possibility of splitting the surface energy into four terms γ_i^d and γ_i^p already mentioned in Sect. 1.4 as well as additional terms γ_i^i and γ_i^H (for

London, Debye, Keesom and hydrogen bond interactions[1]). For determination of the dispersion adhesion energy component, the Fowkes idea leads to the Good–Girifalco approach [12][2]

$$W_A^d = 2\sqrt{\gamma_1^d \cdot \gamma_2^d}. \tag{5}$$

For wetting non-polar liquids such as alkanes on rather non-polar polymers, surface energy is determined only by van der Waals forces: $\gamma_{non-polar} = \gamma^d$.

Fowkes also pointed out that "polar" forces (orientation and induction forces) hardly contribute to work of adhesion if contact formation happens between a polar liquid (i.e. water) and a non-polar liquid or solid surface. To determine the surface energy of polymers one then needs two liquids with the highest possible surface energy and the lowest possible tendency to formation of acid–base bonds, e.g. diiodomethane ($\gamma = \gamma^d = 50.8\,\mathrm{mJ/m^2}$) and 1-bromonaphthalene ($\gamma = \gamma^d = 44.4\,\mathrm{mJ/m^2}$). According to Fowkes, the contribution of Keesom and Debye forces to work of adhesion can be neglected, permitting the whole work of adhesion to be presented as a sum of two components: W_A^d and W_A^{ab}, where W_A^d is the work done by *non-specific* van der Waals forces (mainly by dispersion forces) and W_A^{ab} the work done by *specific* interactions (so-called acid–base interactions).

Contrary to the work done by *non-local* dispersion forces, the component W_A^{ab} of the work of adhesion is due to the formation of *local* donor–acceptor bonds at the interface. Because of its local nature, such an interaction can occur only with a direct contact of both bodies. Furthermore, the adhesion of rather non-polar polymers, such as polyolefin polymers or fluoroplastics, is only caused by the action of the van der Waals forces, whereas the contribution of the acid–base interactions to the total value of the work of adhesion of polar polymers can reach 70–80% [13].

The formation of an electric double layer in the contact area of two solid surfaces due to the formation of donor–acceptor bonds between them is the subject of Derjaguin's semi-empirical electric theory of adhesion [14, 15]. According to it, an exchange of electrons takes place at the contact site, which is due to different electronic structural levels of the contacting material.

Functional groups, such as hydroxyl group OH, carboxyl group COOH, phenyl ring, nitrile group CN, and amino group NH_2, act at the polymer surface as carriers of their adhesion activity much as they determine the mechanical properties of the polymer inside the latter.[3] The relation between the presence of the functional groups and the adhesiveness of some polymer materials is certainly no accident. Based on investigations of the semiconductor-polymer system, Jacobasch and Freitag [16] made up the following succession of donor–acceptor properties of the functional groups contained in polymers:

---

[1] Subsequently, Fowkes used the index "ab" (for *acid–base*) instead of "H". Hydrogen bonding is a special case of acid–base bonding.

[2] This one resulting from calculations according to Lifschitz theory.

[3] E.g. the presence of COOH, OH, or NH_2 groups which interact with polar groups of adjacent chains is responsible for a higher mechanical strength of the polymer.

$$–CN >= CO > –COOR > –C_6H_5 > –OR > –OH > NH_2,$$

where by the donor–acceptor properties change from left (donor) to right (acceptor).

Moreover, the same authors concluded that, in vacuum, the electrostatic component is predominant for the adhesion of polymers. The question was raised by Jacobasch [17] as to the validity of this deduction for actual interacting systems, i.e. for the contact formation in humid atmosphere (whereby conduction of the charge carriers is possible) and it still remains open. Generally speaking, functional groups in polymers may be made up in series according to their donor properties. Each previous member of the series functions as an electron pair donor with regard to the following member, which then acts as an electron pair acceptor.

Combining polymers, which are to interact with one another adhesively according to the acid–base principle, with consideration of the fact that the possibility of a non-symmetric electron density distribution in the contact area grows as the functional groups move away from one another in a series, makes it possible to derive the following empirical rule: to attain a good adhesion, thus great bond strengths, polymers must be purposefully combined with one another in such a way that their functional groups in a donor–acceptor series are as far as possible apart.

In view Fowkes's ideas, Berg called Fowkes a "pioneer" and the latter was highly esteemed for the development of his theory as well as its applications with practical problems of wetting and adhesion [18]. Fowkes' notion of necessary consideration of specific acid–base interactions was improved by Good [19, 20], who assumed that γ^{ab}, again, can be divided into two components by analogy with K_A and K_B constants according to Gutmann [21]: γ^+ (*acidic surface parameter* or Lewis acidic component) and γ^- (*basic surface parameter* or Lewis basic component).

(i) If both components γ^+ and γ^- of a substance can be neglected this substance is referred to as *non-polar* or *inert* (e.g. diiodomethane).
(ii) If either of both components is dominant this substance is defined as *monopolar* or *mono-functional* (e.g. ether).
(iii) If neither of both components can be neglected this substance is referred to as *bipolar* or *bifunctional* (e.g. water).

Table 1 shows that a considerable differences exist between the theoretical and experimental value for surface energy of water and glycerine.

For surface energy of water being a polar liquid, the following results [18] $\gamma^p + \gamma^i = 1.4\,\text{mJ/m}^2$ and $\gamma^d = 21.1\,\text{mJ/m}^2$. The surface energy of water determined experimentally amounts to approximately $73\,\text{mJ/m}^2$. Hence, it follows that the contribution of the specific acid–base interaction to the total surface energy of water comes to $\gamma^{ab} = 73 - (21.1 + 1.4) = 50.5\,\text{mJ/m}^2$. With water both components γ^+ and γ^- are uniform in size [18] $\gamma^+ = \gamma^- = 25.25\,\text{mJ/m}^2$.

Surface energy of chloroform, $CHCl_3$, and that of non-polar tetrachloromethane, CCl_4, are approximately equal ($\gamma = 29\,\text{mJ/m}^2$), work of adhesion with regard to water is, however, different W_A ($CHCl_3/H_2O$) $= 68.3\,\text{mJ/m}^2$ and W_A (CCl_4/H_2O) $= 54.7\,\text{mJ/m}^2$. The difference of $13.7\,\text{mJ/m}^2$ resulting from the formation of hydrogen

Table 1 Hamaker[a] constants and surface energies of some materials, calculated and determined experimentally [22]

Substance	Hamaker constant, $\times 10^{-20}$J	Surface energy γ, mJ/m^2	
		Theoretical	Experimental
Polystyrene (PS)	6.6	32.1	33.0
Polytetrafluoroethylene (PTFE)	3.8	18.5	18.3
Water	3.7	18.0	73.0
Glycerine	6.7	33.0	63.0

[a]The Hamaker constant is a interacting system specific parameter representing Van der Waals interaction between bodies

Table 2 Comparison between the surface energies of PS according to data found in the literature

Surface energy, mJ/m^2	Determination method						
	1	2	3	4	5	6	7
γ^d	42.0			44.0	26.5	26.5	
γ^p					8.1	8.3	
γ^{ab}	1.1						
γ	43.1	42.6	32.8		32.6	34.8	34.9
Reference	[23]	[24]	[25]	[25]	[17]	[17]	[26]

γ^d being the dispersion component, γ^p polar and γ^{ab} acid–base component of the surface energy; γ is the entire surface energy; measurement technique or theoretical approach, respectively: (1) Sessile drop method (geometric mean); (2) Owens–Wendt (harmonic mean); (3) according to Zisman; (4) according to Fowkes; (5) Owens–Wendt (geometric mean); (6) estimated from T_g value; (7) estimated through measuring surface forces between two polystyrene surfaces

bonds between chloroform and water—Cl_3C-H...OH_2—can be interpreted according to these ideas [19].

Surface energy of polystyrene, which is mono-polar, may be presented according to this approach as follows [18] $\gamma^d = 42\,\text{mJ/m}^2$; $\gamma^+ = 0$; $\gamma^- = 1.1\,\text{mJ/m}^2$.

Bibliographical values for the surface energy of polystyrene are summarized in Table 2.

Furthermore, significant non-dispersion contributions to the surface energy were found for polymethylmethacrylate (PMMA), polyvinylchloride (PVC), polyvinylchloride (PET), polyamide (PA 6) and none for polytetrafluoroethylene (PTFE), polyethylene (PE) and paraffin [18].

To determine acidic and basic components of work of adhesion, we need already three liquids. A new computational algorithm was proposed for this purpose by Good and Hawa [27] as an improvement of their own work. Therein, the acceptor γ^+ and donor γ^- parameters are calculated as solution of a system of nine equations for nine unknowns by means of three polar liquids at three solid surfaces.

Then work of adhesion W_A can be calculated as follows:

$$W_A = 2\sqrt{\gamma_1^d \cdot \gamma_2^d} + 2\sqrt{\gamma_1^+ \cdot \gamma_2^-} + 2\sqrt{\gamma_1^- \cdot \gamma_2^+}.$$

The behaviour of liquids on smooth solid surfaces is rather well understood. However, for rough solid surfaces the situation is much less clear, even though roughness occurs on practically all real surfaces of engineering or biological interest. The contact water angle is widely used as a criterion for evaluating surface hydrophobicity/hydrophilicity. However, recognition of the importance of surface hydrophobicity is growing in various industries, such as those of glass, automobiles, and electronics. To date, the contact angle and contact-angle hysteresis (the difference between the receding contact angle and the advancing contact angle) have been commonly employed as criteria for assessing the hydrophobicity or hydrophilicity of solid surfaces. An extensive overview about several models for predicting wetting behaviour can be found in [28].

2 Contact Angle Measurements

Two methods proved to be useful for characterisation of surfaces—sessile drop method and Wilhelmy plate method [29]. With the sessile drop method, a drop of test liquid or of melt is placed on the solid. After reaching equilibrium, the contact angle is read on an enlarged picture of the resting drop. With the Wilhelmy plate method, a sample with well-determined geometry is dipped in the test liquid, then the contact angle is determined from the changes in force occurring in the process. This method is especially suitable to characterise wetting kinetics on fibres by polymer melt. Velocity and degree of fibre wetting by polymer melt can be directly followed, allowing consideration of the rheological aspect when characterising strength properties of actual composite materials.

2.1 Quasi-static Contact Angle Measurements

The *sessile drop method* is used to investigate wetting of pure liquids on real surfaces in order to characterize the solid surfaces, or of aqueous solutions of surfactants, polymers and other water-soluble substances on model solid surfaces in order to characterize the solutions. The measurement data are the contact angle θ, drop base "d" and drop height "h" of the drop as shown in Fig. 3.

In an effort to obtain a more precise description of the surface energy, measurements of advancing angle θ_A and receding angle θ_R are increasingly used. The difference between the advancing and the receding angle is referred to as *contact angle hysteresis* ($\theta_A - \theta_R$). The latter provides additional information on surface morphology and chemical composition as well as on surface roughness. However, it should be remembered that contact angle measurements only allow determination of changes as against the standard.

It is well known that the state of a surface affects crucially its wettability. Therefore, controlling the surface properties such as roughness, surface structure

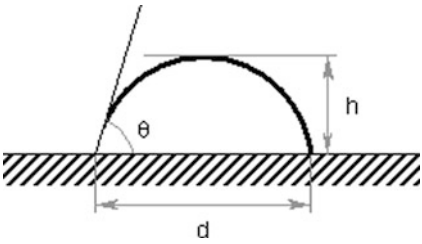

Fig. 3 Droplet "sitting" on a surface: sessile drop method

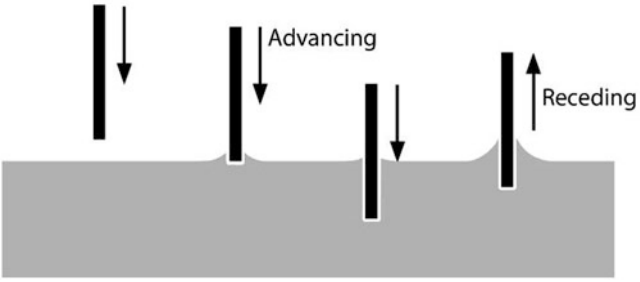

Fig. 4 Measurement of the advancing and receding contact angle of a fixed particle layer using the Wilhelmy plate method

and chemical composition is of great importance. Only in exceptional cases it is possible to infer the kind of surface alterations (roughness, chemical differences, charges, etc.) directly from contact angle alterations.

Advancing and receding contact angle measurements are possible force-driven if the drop volume will be increased or decreased. Since work of adhesion is by definition *reversible*, speaking in terms of thermodynamics, wetting and de-wetting should be identical, if there is enough time for balancing out the contact angle. There might not be any hysteresis if, beside van der Waals forces between liquid and solid surfaces (which are always present), no additional forces would participate in contact formation. Thus, a contact angle hysteresis can provide important information on molecular processes progressing at the interface (acid–base interactions).

An alternative method to evaluate wettability of a surface is to raise the liquid level gradually until it touches the handing plate or cylinder such as a single fibre suspended from a balance. The increase in weight is then noted, and this method is known as the *Wilhelmy plate technique*. The modified Wilhelmy plate method is gaining importance in view of the growing interest in determining the contact angles on nanoscalic materials—particles, fibres, nanotubes being added to polymeric compounds and other complex fluids [30, 31]. The principle of this method is balancing a thin plate immersed in liquid. If this technique is performed as a dynamic method, the partial contact angle values are attained reaching its maximum value—advancing contact angle θ_A, by immersing the plate into the liquid. If the plate is moved out of the liquid, receding contact angle θ_R is obtained (as shown in Fig. 4).

Based on the modified Wilhelmy plate method, wettability of porous media such as powders can be characterised by spontaneous capillary penetration of a liquid into pores spaces. Two experimental techniques are most commonly employed. The first one, height-time technique, see e.g. [32], measuring the height to which the liquid front advances in porous solids during the capillary rise process, and the second one, weight-time technique developed by Chwastiak [33], studying the increase in the weight of porous solids caused by the progression of the liquid inside their pores. In both cases, the experimental results were described by means of Washburn equation [34]. The literature on this topic is vast. The complex geometry of particle pore spaces creates numerous combinations of interfaces, capillaries, and wedges in which a liquid is retained, and results in a variety of air–liquid and solid–liquid configurations, making the interpretation of the results extremely difficult.

2.2 Dynamic Wetting Measurements

Contact angle as a thermodynamic equilibrium property, virtually all the published data for which reproducibility is claimed, are measurements of advancing contact angle within a minute of *three-phase contact* (TPC) line displacement. The second category is that of truly dynamic contact angles. If the TPC line as a phase boundary liquid–solid simultaneously moves relative to the adjacent solid surface, a dynamic contact angle will be observed. Dynamic contact angle means the contact angle as a function of time, which can significantly differs from the static contact angle.

Dynamic wetting measurements are possible either force-driven, if the drop volume will be increased/decreased or as time-dependent contact angle measurements with a constant volume. In the former case, advancing or receding angles[4] are formed to analyze the *contact angle hysteresis*, i.e. analysis of chemical and mechanical heterogeneities (as described in Sect. 2.1). In the latter case, the temporal contact angle change because of spontaneous spreading of the liquid is measured. If the spreading velocity is limited by the resistance of the TPC line, this phenomenon is referred to as *wetting dynamics* or *wetting kinetics* as shown in Fig. 5. The contact angle depending on the contact time of solid surface with measuring liquid is called *dynamic contact angle*.

For many applications, surfactants are introduced into the aqueous phase to increase the rate and uniformity of wetting. Despite their enormous technical importance, there is a lack of data in the literature about the spreading dynamics of aqueous surfactant solutions. The knowledge of how surfactant adsorption at the surfaces involved affects the spreading mechanism and dynamics is also limited. For more detail on wetting dynamics see [35–38]. Dynamic wetting measurements allow studying surfactants, polyelectrolytes or other surface-active substances as well as their mixtures and engineered surfaces [39].

[4]Strictly speaking, these are quasi-static measurements in the physical sense.

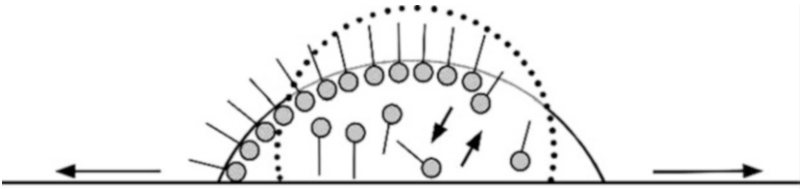

Fig. 5 A water drop containing surfactant molecules simultaneously spreading over a surface

3 Wetting Measurement in Technological Applications

Characterization of materials based on wetting measurements/interfacial thermodynamics is the most frequently used method in technological applications.

3.1 Fibre Wetting in Composite Processing

In fibre-reinforced composite processing, characterization of both—fibre surface properties and wetting behaviour of polymer on fibre is important [40]. From the experimentally determined contact angles of water, the surface free energies of fibre surface can be estimated using the equation of state for solid–liquid interfacial tension as described in Sect. 1.5. The modified Wilhelmy technique is also used to measure diameter of fibres [41].

Since the contact formation between fibre and matrix during composite processing occurs from the melt or solution, it is necessary to investigate fibre wettability for optimization of interfacial adhesion properties. Most thermoplastic polymers used in practice have a relatively high melting point, high softening temperature and high viscosity of the melt. This can cause an incomplete wetting of the reinforcing material by the melt and thus hamper the contact formation due to the fact that the actual contact zone becomes relatively small after the consolidation of the melt (the larger the contact area created the stronger the adherence). However, wetting measurements are indispensable as additional source of information for a comprehensive analysis of the interfacial properties of some practically relevant systems.

As described in [42], a Wilhelmy high-temperature wetting apparatus was used to study the adhesion between polymer blends and unsized glass fibres by determining the polymer melt wetting tension. The measurable quantity in the Wilhelmy experiment is the wetting tension $\gamma_L \cos\theta$ at the polymer melt/solid interface, which equals the force F per unit length of the perimeter p of the solid sample:

$$\gamma_L \cos\theta = \frac{F}{P} = \frac{g\Delta m}{p}$$

where γ_L is the surface tension of polymer melt, θ is contact angle, g is the gravitational constant, Δm is the change in mass before and after the fibre is immersed into the polymer melt. The high-temperature wetting apparatus [43] consists of a highly sensitive Sartorius microbalance (sensitivity of 1 μg), which is connected to a high-temperature cell through a stainless steel tube with an inner diameter 8 mm. The thin glass fibres used as solid probes are attached (using epoxy glue) to a metal wire, which is hooked onto another longer wire. The latter is fixed to the microbalance. In the high temperature cell the blends are heated under an inert gas flow. The temperature can be controlled with an accuracy of ±0.5°C. The polymer is brought into contact with the fibre by moving a motor-driven table at a constant velocity of 0.15 mm/min. The temperature in the cell, the velocity of the motor-driven table, recording of the change in mass by the microbalance before and after the fibre is immersed in the melt, and the atmosphere in the cell (inert gas pressure) are controlled by a computer. Before the fibre touches the polymer melt surface, its weight contribution is zeroed by the calibration routine of the balance. After the fibre has contacted the melt surface, the balance records the gain in weight caused by the wetting of the fibre.

The main difficulty in this experiment is the high viscosity of the polymer blend. Consequently, not only surface tension effects have to be considered in the Wilhelmy experiment but also hydrodynamic effects. Due to the forced fibre/liquid motion, non-negligible force contributions result from the shear stress exerted by the viscous flow of the liquid on the fibre. To exclude these hydrodynamic effects in wetting measurements, the fibre is held stationary at a constant penetration depth until viscous relaxation occurs. It is assumed that the meniscus of the liquid returns to equilibrium when a constant weight is reached. Only under these conditions, the measured force per unit length equals the wetting tension of the solid/polymer melt system. The fibre was immersed into the melt to a penetration depth of 0.15 mm. At this depth it was held stationary for 2 min, then the fibre was immersed to 0.30 mm depth and again held stationary for 2 min. At the last immersion stage, 0.45 mm depth was reached, glass fibre was held stationary for 5 min and after that it was emerged using the same sequence (0.15 mm/min emersion rate, two stops for 2 min each, at 0.30 and 0.15 emersion depths). Such immersion/emersion sequence allows polymer blend meniscus to relax, which results in a constant weight difference. Complete wetting was assumed when no weight difference was observed after the fibre was immersed and emerged at a given temperature. On average, the time required for one measurement was 30–45 min. A typical curve from a Wilhelmy balance experiment with the blends and a thin unsized glass fibre is shown in Fig. 6. Negligible weight differences between immersed and emerged states confirm a complete wetting mentioned above. This means that $\cos\theta = 1$ and surface tension of the blend γ_L (not wetting tension $\gamma_L \cos\theta$) was measured.

Temperature coefficients were determined from γ_L vs. T relationships as the slope of the curves.

In order to understand the processes that occur at the epoxy resin–polysulfone/glass fibre interface, surface tension of such blends was studied. The aim was to determine the temperature dependence of the blends surface

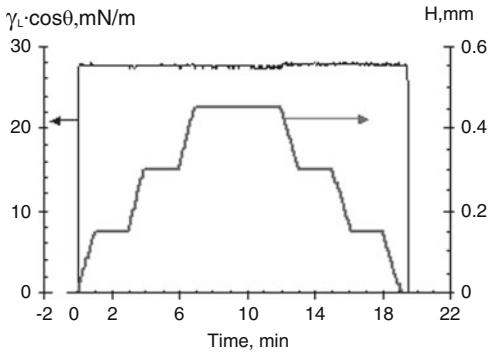

Fig. 6 Typical plot of wetting tension measurements obtained by the Wilhelmy technique for epoxy resin/polysulfone blends and unsized glass fibre ($d = 15.7\,\mu$m) at 190°C; H is the depth of fibre penetration. Reprinted from [42]

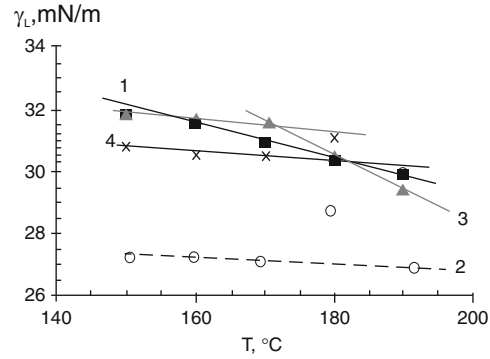

Fig. 7 Surface tension vs. temperature relationships for various epoxy resin–polysulfone systems. Polysulfone content: (1) 0 wt%, (2) 5 wt%, (3) 10 wt%, (4) 15 wt%. Reprinted from [42]

tension at the interface with glass fibres and how it was influenced by polysulfone concentration. It was found that surface tension decreases as the temperature increases which is quite typical for γ_L vs. T relationships and was already observed for different liquids, oligomers and highly viscous polymer melts. Temperature dependencies (Fig. 7) also contain information about the surface entropy, which is defined as $-(d\gamma_L/dT)$. It was found that incorporation of polysulfone significantly changed the surface entropy. In most cases, temperature coefficients of the blends were markedly lower than that of pure epoxy resin. It is also very interesting that incorporation of 5 wt% polysulfone resulted in the maximal decrease of $-(d\gamma_L/dT)$, while the surface entropies for the blend with 10 wt% modifier as well as that obtained for epoxy resin-15% polysulfone blend are closer to the $-(d\gamma_L/dT)$ value for epoxy resin. However, two $-(d\gamma_L/dT)$ values were obtained for epoxy resin-10% polysulfone blend. Its surface entropy, calculated for the 170–190°C temperature interval, is the highest, even when compared with the unmodified epoxy resin. It could be possibly explained by the unstable structure of the blends. It is assumed that the driving force for a good flow of a polymer is low viscosity, whereas for a good wetting of a substrate a low surface tension of the polymer is needed. In our case, the viscosity of the blends increased with polysulfone content increase which could possibly result in the retardation of the fibres impregnation

during composites production. On the other hand, surface tension values of the blends, except for 5 wt% polysulfone, were close to that of epoxy resin, so they should not lead to significant changes in the fibres wetting.

Overall conclusion of the studies can be drawn as follows, underlining the importance of wetting measurements in composite processing: A combination of wetting measurements based on the modified Wilhelmy plate method and rheological investigations in the system epoxy resin–polysulfone/glass fibre revealed that (1) activation energy for viscous flow as well as surface tension vs. polysulfone concentration relationships are nonadditive; (2) no significant changes in the kinetics of fibres wetting by the blends with increase in polysulfone content were observed; (3) all the ternary blends (epoxy resin–hardener–polysulfone) required at least 30 min at 180°C to achieve ultimate levels of the properties measured; (4) sea-island morphology of the blend with 5 wt% polysulfone and morphology with co-continuous phases in the case of blends with 10–15 wt% polysulfone were found after curing.

3.2 Wetting Studies on Human Hair

Dynamic penetration studies on differently modified human hair makes it possible to estimate the possibilities of water-soluble polymers to act as care components both in conventional shampoo formulations (free of the oil component) and in microemulsions. To estimate the spreading behaviour of water in terms of penetration rate, the capillary penetration method was used and improved. Methodological studies were accompanied by a study to determine water-absorbing capacity, water release by evaporation, topographic properties such as roughness and lustre of hair surfaces treated compared to the reference hair available as damaged (bleached) and undamaged.

The development was done with three different formulation concepts—a classical hair shampoo formulation, a micro emulsion based formulation and three market formulations claiming conditioning effects. Each formulation concept was represented by three different samples. The developed method is derived from a classical Washburn approach [34] originally developed to measure powder wetting. A bundle of parallel hair fibres in a measurement tube is connected to a micro balance. Water fills the measurement tube due to capillary effects once the hair gets in contact with the water and the weight of the tube increases. The weight increase over time is measured. It is dependent to the hydrophilic/hydrophobic properties of the surface. The influence of a hair care formulation on the surface of the hair can be detected by comparing untreated and modified hair samples.

The analysis can be made in an apparatus usually used for the measurements of surface tensions. The instrument has to offer a micro balance and the capability for time dependent measurements.

The hair of Asian type was purchased from Kerling International Haarfabrik in Backnang. Since healthy hair is by a sebum layer protected, hair under study was

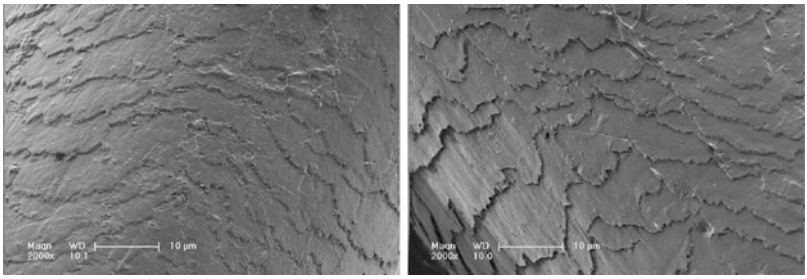

Fig. 8 SEM images of a reference hair (*left*) and a hair after bleaching (*right*)

damaged (roughened and hydrophilized) through bleaching in order to investigate the effect of individual polymer as additives in a care shampoo formulation. 10 ml of a 30% solution of H_2O_2 and 90 ml of a 30% solution of NH_3 were mixed. For deactivation of the mixture after hair bleaching $NaHSO_4$ was used. In Fig. 8, a reference hair as purchased and a hair after bleaching is shown.

The hair was cut into bundles of 10 cm lengths which are approximately two times longer than the measurement glass tubes. The hair was washed three times in a 1g/l solution of Marlipal 242/28 (Fatty alcohol-(C_{12}-C_{14})-polyethylene glycol-(2 EO)-ether sulphate sodium salt, INCl: sodium laureth sulfate) kindly provided by Sasol (Marl, Germany) in deionised water at 25°C (reference hair). After washing, the hair is reconditioned by pure deionised water until no traces of surfactant can be detected. Finally, the hair bundles are dried at 40°C in a vacuum oven for at least 2 h followed by drying overnight at room temperature.

For measurement glass tubes with an inner diameter of 2 mm and a length of 4 cm, hair portions of about 100 mg are separated. Every portion is arranged to a parallel hair bundle and pulled through the measurement glass tube with a sling. The hair is cut perpendicularly to the fibres at the bottom and the top ends of the glass tube. The hair bundle juts 3 mm out from the bottom end. The prepared measurement glass tubes are clearly marked and stored in a temperature-controlled laboratory maintained 24 ±1°C and 40 ±3% humidity.

A major drawback of the approach is the difficulty to get a constant packing (i.e. identical capillaries) in every glass tube especially with inhomogeneous fibres like human hair because small differences in the packing result in poor reproducibility of the experiments. Therefore, a calibration measurement with reference hair is required to scale measuring results to a comparable level. Thus, every tube is characterised by a calibration measurement with pure water. First, the weight of all filled glass tubes is determined. Then every sample is measured using the capillary rise technique according to the modified Washburn approach with deionised water. A typical graph for the weight vs. time curve is shown in Fig. 9.

The penetration rate is determined from the linear part of the weight vs. time curve by averaging at least 10 measurements. Next to the calibration measurement, the hair was reconditioned for the treatment with the hair care formulation. The measured sample is wetted completely with deionized water. After calibration,

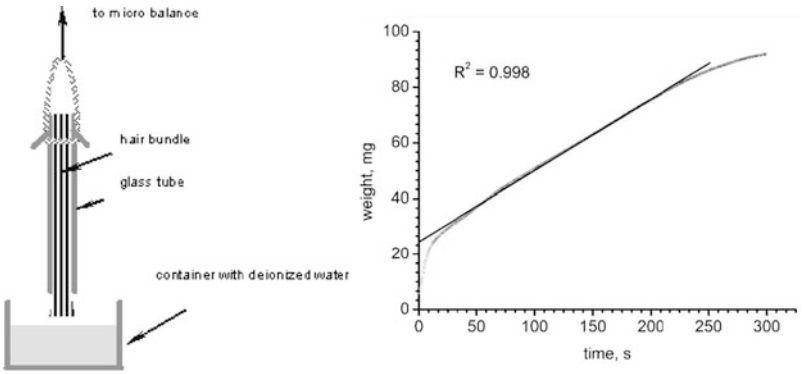

Fig. 9 Experimental set up (*left*) and single calibration measurement with pure water (*right*)

glass tubes are reconditioned at 40°C in an vacuum oven for 2 h followed by drying overnight at room temperature until the prior determined sample weight is reached again.

A solution of desired formulation was solved in deionized water to a concentration of 1 g/l. Each of 10 glass tubes is immersed into an usual test tube with 9 ml of the formulation solution for 30 min. After treatment, glass tubes containing hair bundles were rinsed several times with deionized water and dried according the drying procedure described above. The procedure was repeated 3 times until the surface tension of the rinsing water is identical with those of the pure water. Finally, the penetration rate of pure water is determined again as in the calibration procedure.

A comparison of the parameters investigated reveals that some polymers under investigation are well suitable as care components in a shampoo formulation. Moreover, it is possible to evaluate the influence of the oil component (paraffin, jojoba and silicone oil) in regard to the care effect. Jojoba and paraffin oil, in connection with the "care polymers" bring a positive effect for damaged hair, i.e. a considerable increase in the surface hydrophobicity, an improvement in lustre accompanied by surface smoothing and a time reduction in drying the hair. In the case of damaged hair, the conventional formulation with a care component gave better results than a micro-emulsion.

Additionally, contact angle of water on differently modified single hair was measured using the Wilhelmy plate method. In Fig. 10a, advancing and receding contact angles of pure water as well as their average values for reference hair were presented. In Fig. 10b, water contact angles as well as the water contact angle hysteresis for differently modified hair are summarized.

3.3 Wetting Measurements in Textile Characterization

It is well-known that the qualities of fabrics are closely dependent on their structure. Particularly, construction parameters, such as fineness of filaments and yarn, warp

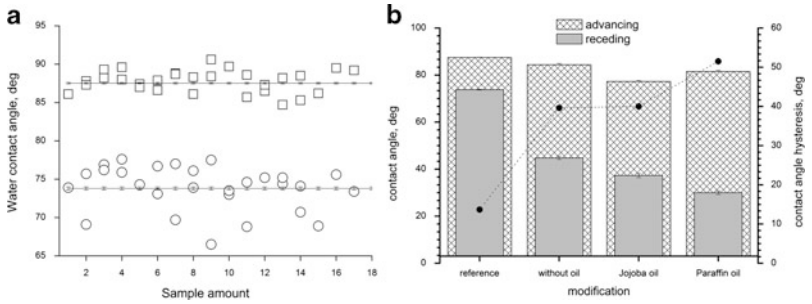

Fig. 10 Advancing and receding contact angles of water for reference hair cleaned with sodium laureth sulphate measured using the Wilhelmy plate method: the water advancing contact angle $\theta_A = 87.5°$ and the water receding contact angle $\theta_R = 73.8°$ (**a**), and contact angles for differently modified hair in comparison (**b**)

and weft density as well as the type of weave, control the texture and surface topography of fabrics. The fabric texture affects the porosity and strongly influences the textile characteristics such as fabric mass, thickness, draping ability, stress-strain behaviour or air permeability [44–46]. The surface topography of fabrics is responsible for their functionality—appearance and handle, wettability, soiling behaviour and cleanability [47, 48], abrasion resistance and wear [49]. There are very few systematic investigations of quantitative relations between construction parameters, topography of fabrics and their wettability, however.

The interaction between liquids and textile surfaces depends on the wettability of fibres, their surface geometry, the capillary geometry of the fibrous assembly, the amount and chemical nature of the liquid as well as on external forces. A randomly rough textile surface possesses pores, crevices, capillaries or other typical structures with their own characteristic wetting and penetration properties. As a consequence, the apparent contact angle on these surfaces will be affected by thermodynamics and kinetics associated with such intrinsic structures.

Wetting measurements in textile characterization are useful to evaluate changes before and after their modification in every respect. Dynamic contact angle measurements of aqueous surfactant and polymer solutions were used on textile surfaces in order to examine their soil-release properties [47, 48, 50].

Wetting measurements was used to estimate the degree of both, oily dirt sticking on the fabric after impregnation with different soil release polymers (SRP) and soil removal after washing. Cleanability of soiled textiles was evaluated as well by the soil additional density (SAD) analysis. The results demonstrated the application of dynamic wetting measurements in characterising both textile materials and interactions between them and aqueous solutions of soil release polymers. Differences between individual SRP were determined with respect to their spreading velocity on fabrics despite the similarity of their chemical composition and of the surface tension of their aqueous solutions. The weft-knitted double jersey fabric with the markedly higher filament fineness and surface porosity was found to show higher

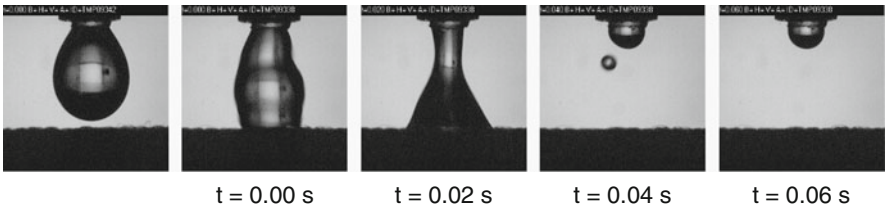

Fig. 11 Image sequence of a water drop applying to the surface of weft-knitted double jersey fabric treated with SRP [47]

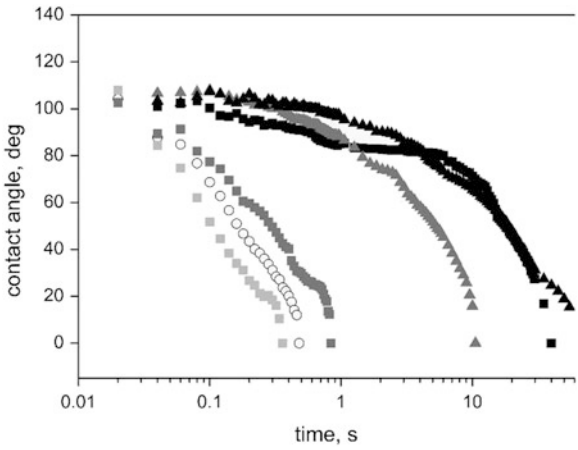

Fig. 12 Dynamic contact angles for the woven fabric F2 after soiling and washing with and without pre-treatment with SRP: (*circle*) untreated; (*light gray square*) after treatment with SRP; (*black square*) stained after treatment; (*gray square*) washed after treatment and staining; (*black triangle*) stained without treatment; (*gray triangle*) washed after staining without treatment

relative cleanability in soiling tests if treated with soil release polymers. In the case of untreated stained one, washing dramatically affects its cleanability (i.e. stain spreads over the whole surface) comparing with other textile materials.

The results for the spreading velocity (dr/dt) are conform with the data for the surface porosity for knitted fabrics: higher porosity leads to faster spreading. In the case of the woven fabric, the spreading velocity is, however, higher than that for knitted ones at comparable porosity, demonstrating the dependency of spreading characteristics on the kind of fabrics used. After treatment with SRP, recording of water contact angles was hardly possible due to complete hydrophilization of the fabrics surfaces. Figure 11 illustrates the image sequence of a water droplet applied to the surface of weft-knitted double jersey fabric treated with SRP. It is clearly seen that the water droplet completely penetrate into the textile surface after only 20 ms. Others SRP used show the same tendency.

Figure 12 shows (as an example) the dynamic water contact angles for a woven fabric. For the rather hydrophilic woven fabric, soiling hydrophobised its surface in both cases without and with pre-treatment with SRP. The fabric remains hydrophobic after its washing.

The SRP treatment of warp-knitted fabric and woven one also results in lowering their surface energy and improving their water absorptivity. The differences between

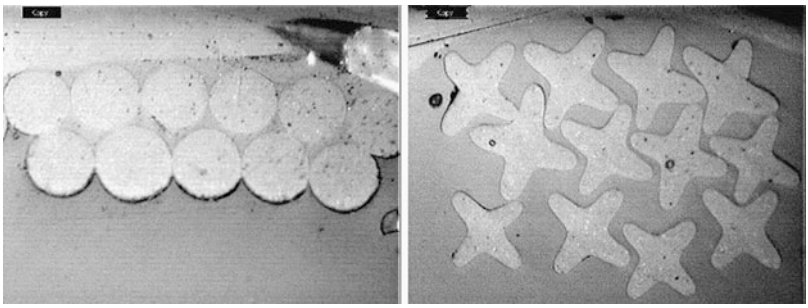

Fig. 13 Microscopic images of (cross-sectional view) of round (*left*) and cruciform (*right*) cross-sectional shaped filaments [51]

untreated and impregnated states were here, however, less marked than those for weft-knitted double jersey. It should be noted in this case, the weft-knitted double jersey fabric was made from textured "super-hydrophobic" properties to the fabric's surface.

In other studies [50–52], it was shown that the wetting, soiling and cleanability properties can be affected by using yarn of the same chemical nature with different structure and differently profiled polyester fibre, different types of weave and different weft density keeping the warp density constant. It is well known, that synthetic fibres which are predominantly spun by the melt spinning method with spinnerets having the non-circular hole geometry are called profiled or non-circular fibres. Various types of non-circular fibres have been developed to add functionalities and aesthetics to synthetic fibres leading to the change of their surface properties. The cross section of a synthetic fibre produced by the melt-spinning method can be easily varied by changes in the spinneret hole shape. In general, fibres consisting of non-circular cross-sectional shaped filaments show properties different from those of fibres with circular cross-sectional ones, including the bending stiffness, coefficient of friction, softness, lustre, comfort, pilling, bulkiness, handle, and performance. Microscopic images of different filament cross sections are illustrated in Fig. 13.

Variations in interlacing are also reflected in the fabric wettability considered in terms of the spreading rate as reported earlier [53]. The spreading rate decreased with increasing waviness for the plain weave, whereas it increased in the case of the twill one. It was concluded that the fabric wettability could be adjusted (in certain limits) by variation of density and interlacing keeping in mind the same chemical nature of microfilaments. Noticeable differences in the wetting behaviour of water are seen between the two types of weave if changes in porosity are considered. In the case of the plain weave, higher weft density leads to lower porosity and to higher water absorption time, as a consequence, shown in Fig. 14.

Moreover, water penetration into the plain texture is slightly slowed down with increasing porosity, reaches a maximum value of the absorption time (about 16 s) in the porosity range of approximately 1 $\mu m^3/\mu m^2$, and then accelerates towards the higher porosity values. It can be speculated about a "critical" value of the fabrics

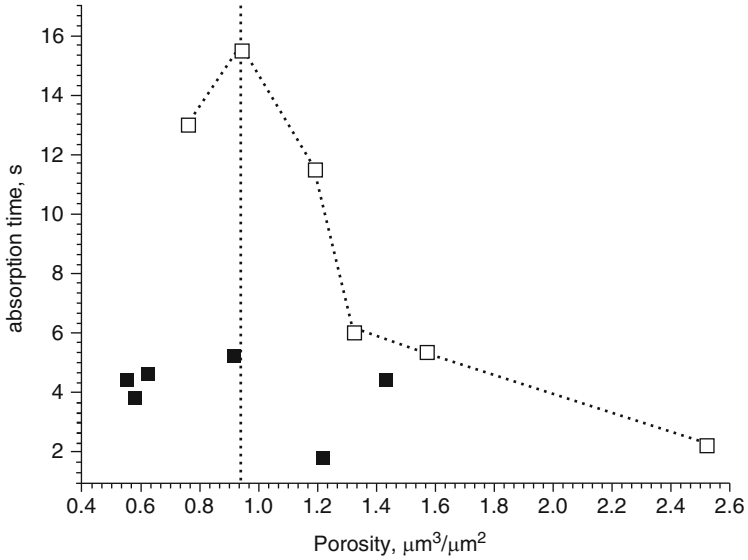

Fig. 14 Absorption time vs. surface porosity calculated as the ratio between the real pore volume and the corresponding geometric surface for (*white square*) plain and (*black square*) twill structures. Reprinted from [52], Copyright (2008), with permission from SAGE publications

porosity. Presumably, below this value water percolates with low velocity and above this with high a value. On the contrary, higher weft density of the twill weave results in higher porosity. The values of absorption time obtained for the twill texture are generally very low in about 2–5 s and almost independent of the porosity.

The differences in the penetration behaviour of water observed on two predetermined pattern of interlacing are caused by the different topographical structure since the chemical nature of filaments used was kept constant. It is noted, that the lateral distance between the threads is about 120 and 300 μm for the twill and plain weaves, respectively. The vertical dimension of the surface features is measured up to 20 μm for the plain topography and 40 μm for the twill topography. It is well known that in the case of moderately hydrophobic surfaces the complex internal geometry of real porous systems could enhance liquid penetration. The fabrics used were woven from polyester yarn. As reported earlier [35], this polymer is moderately hydrophobic with the water contact angle of 77° on its flat surface. The results obtained in the present study would suggest that water advanced in a stable flood (wicking regime) is observed [54]. The difference in the penetration behaviour (lower for the plain weave and faster for the twill weave) arises with the difference in the shape and size of the pores.

In essence, to achieve a more hydrophobic fabric texture, the technological parameters could be changed as follows: for both plain and twill structure, the weft density and filament fineness should be increased, and the yarn fineness should be reduced. Alternatively, the use of profiled fibres, e.g. cruciform, the fabric

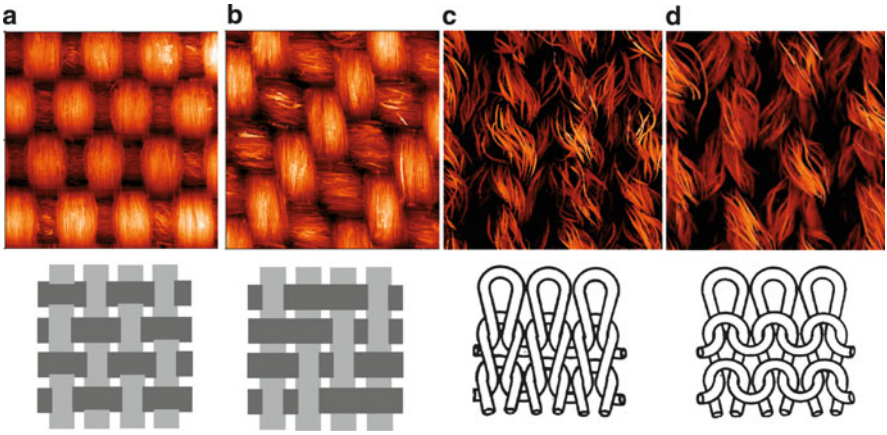

Fig. 15 Woven structures: (**a**) plain weave; (**b**) twill weave; and weft-knitted structures: (**c**) face side and (**d**) reversed side

manufacturing could lead to a more hydrophobic fabric texture on the basis of different roughness length scales [52].

An alternative method to evaluate the wettability of a textile surface is to raise the liquid level gradually until it just touches the hanging plate (or cylinder like single fibre) suspended from a balance. The increase in weight is then noted (cf. Sect. 2.1). Major advantages of the Wilhelmy plate technique are (1) the conditions of measurements are highly reproducible; (2) the speed of movement of the three-phase boundary is readily controlled; (3) the sensitivity of the technique is very high. Close agreement can be obtained between the Wilhelmy technique and careful measurements by the sessile drop technique. The plate method is especially useful when kinetic effects (adsorption, desorption, etc.) are important.

The liquid uptake measurements by means of the Wilhelmy plate technique were carried out with differently enzymatic treated fabrics of different type. A fabric sample is connected to a micro balance. Before the fabric sample touches the water surface, its weight contribution is zeroed by the calibration routine of the balance. After the fabric sample has penetrates into a liquid (defined depth of 1 mm), the balance records the gain in weight caused by the wetting of the textile and liquid uptake into the fabric due to capillary effects. Images of fabrics with the woven structure are illustrated in Fig. 15. The weight gain over time is measured. It is strongly dependent on the hydrophilic/hydrophobic properties of the surface. The influence of the fabrics modification can be detected by comparing differently modified samples. The liquid uptake rate is determined from the linear part of the mass square vs. time curve by averaging at least 3 measurements. The measurements were carried out with water and paraffin oil.

Comparing water and oil uptake rates with fabric surface topography parameters (roughness, surface porosity), it is possible to conclude about the effectiveness of

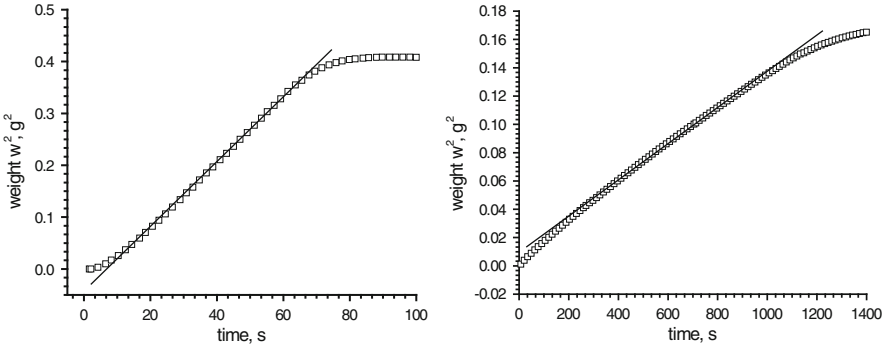

Fig. 16 Water (*left*) and paraffin oil (*right*) uptake rate of plain weaved fabric

modification in respect to cleanability and water evaporation capacity, i.e. drying rate.

A comparative analysis between different ether carbon acids with respect to wettability of fabrics, surface topography parameters and mechanical treatment by abrasion was done using the modified Wilhelmy plate method. To estimate the degree of hydrophobicity of textile surfaces before and after impregnation with protective finishes, dynamic wetting measurements were carried out with a dynamic absorption and contact angle tester. The water uptake rate is determined according to Washburn from the linear part of the mass square vs. time curve as shown in Fig. 16. Surface topography of fabrics was examined using an imaging measuring instrument for the optical analysis of roughness, MicroGlider (FRT, Germany), operating on principle of chromatic abberation. The measuring method was described in more detail in [47].

In Fig. 16, water and oil uptake is shown.

Some topography parameters such as mean roughness depth (Rz) and surface porosity (porosity of fibre surfaces without spaces between fibres) were obtained from the images with a size of 1 mm × 1 mm. The porosity is calculated as the ratio between the real pore volume and the corresponding geometric surface excluding spaces between fibres.

After impregnation of polyester materials with protective finishes carried out through immersion of these in the corresponding aqueous protective finish solution for 5 min, polyester fabrics were abrasively treated by using an abrasion test instrument APG 1000 (Maag Flockmaschinen, Germany). After abrading, wettability and surface topography of tested fabrics were re-examined (Table 3).

The modification of knitted fabrics with a finishing agent leads to a significant increase of the porosity, which is threefold higher for their unmodified face side than that for the modified one. Comparing macroscopic roughness parameters obtained for the modified twill woven fabric, a decrease is ascertain after its mechanical treatment by abrasion, and vice versa for the plain one. Differences between changes in roughness of three polyester textile materials with different initial topographic

Table 3 Topography parameters for fabrics used before and after abrading

	Surface porosity, $\mu m^3/\mu m^2$		
Type of fabrics	Unmodified	Modified with 2, before abrading	Modified with 2, after abrading
Plain	1.2	0.6	1.9
Twill	0.7	1.2	0.9
Knitted, face side	1.8	5.4	1.9
Knitted, reversed side	2.1	2.4	2.2

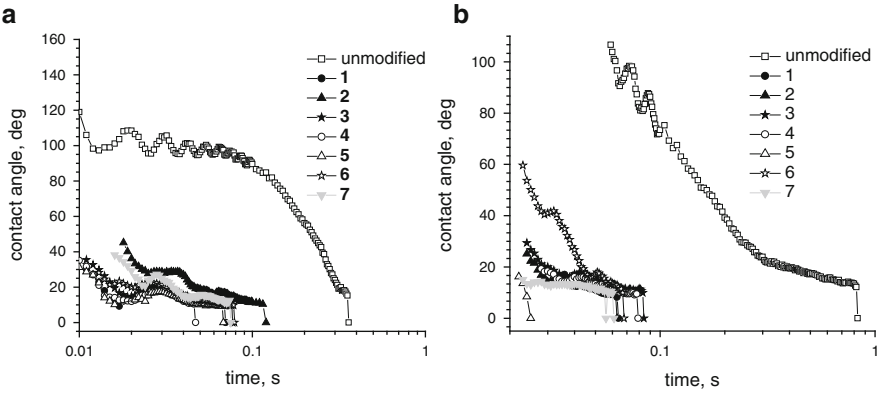

Fig. 17 Dynamic water contact angle for differently modified fabrics: (**a**) before their abrading; (**b**) after their modification by abrasion

structures being modified with a protective finish being ether carboxylic acid (isotridecanol ethoxylated carboxymethylated with pH 2.94 and surface tension of 26.4 mN/m) before and after their mechanical abrasion were determined despite the similarity of their chemical nature in the case of the soiling behaviour of such fabrics.

Figure 17a shows water contact angles for the fabrics before and after impregnation with different ether carbon acids (7 different substances obtained by Sasol Germany, Marl detailed in [49]) as measured using sessile drop method. The treatment of fabrics with these finishing agents results in lowering their water absorptivity. No significant differences were seen between different finishes with respect to hydrophilization of the fabrics. Water dynamic contact angles for unmodified fabrics and after their mechanical abrading are shown in Fig. 17b. A decrease of the water contact angle for unmodified fabrics indicates dramatic decreasing their abrasion resistance. Obviously, fabrics abrading, especially for knitted fabrics, results in increasing porosity followed by changing the wetting behaviour from highly hydrophobic to penetrating one.

Water uptake rate of the fabrics measured before and after abrading are summarized in Table 4 for the fabrics used. Interestingly, water penetrates fourfold faster

Table 4 Water uptake rate for differently modified fabrics before and after their abrading

	Water uptake rate $\times 10^5$, g^2/s						
	Before abrasion test			After abrasion test			
						Knitted	
♯	Plain	Twill	Knitted	Plain	Twill	f	l
0	0.04	0.15	1.84	8.01	1.39	99.83	174.0
1	0.03	0.02	1.71	0.60	0.71	5.96	23.17
2	0.04	0.02	9.97	0.65	1.0	120.0	151.0
3	0.03	0.06	35.4	8.79	10.0	254.0	140.0
4	0.01	0.01	0.34	7.79	7.59	5.46	33.95
5	0.1	0.06	20.8	0.69	1.7	112.0	137.0
6	0.1	0.14	53.4	7.68	1.36	314.0	492.0
7	0.002	0.02	0.73	7.84	7.63	270.0	160.0

(f) after abrading the face side of knitted fabric; (r) after abrading the reversed side of knitted fabric

into the woven fabric than into the knitted fabrics. The difference in the penetration behaviour arises from the difference in the shape and size of pores. From water uptake results, which are in agreement with dynamic contact angle measurements, the finishing agent **1** is the "best" for woven fabrics with the twill type of weave.

The finish **2** is also suitable with respect to changes in the wettability after abrading: the changes will be marginal. For knitted fabrics, the finish agents **1** and **4** seem to be the most suitable. From the contact angle measurements, the finishes **4** and **5** were obtained to be appropriate for this kind of polyester fabrics. In contrary to the wetting results describe above, the most suitable protective finishes for woven fabrics with the plain type of weave are not **3** and **7**, but **1**, **2** and **5**.

As differences between the wetting characteristics obtained from water uptake measurements are larger than those from the dynamic contact angle measurements, the water uptake rate seems to be more significant in estimating the "best" finishing agent. For all fabrics, the "best" finishing agent was revealed to be **1** in respect of changing the wetting characteristics.

The mechanical treatment of the fabrics by abrasion results in a decrease in hydrophilicity due to fuzzing (also called fuzzy and hairy, is a fabric condition characterized by a hairy appearance due to broken fibres or filaments.) caused by abrasive testing. To prevent unwanted changes in appearance of the fabrics usually occurring during washing, cleaning or in wear, fabrics can be modified with the following protective finishes: for plain woven fabrics, the finishing agents **3** and **7** would be the most suitable; for twill woven fabrics, the finishes **1** and **7** seems to be the "best"; for knitted fabrics, the finishes **4** and **5** can be used for modification. This analysis was done by assuming the slightest changes in fabrics wettability compared before and after abrading. A significant decrease of wettability indicates that some fuzzing defects appeared. A significant increase of wettability might be caused by gaping defects caused by irregular shrinkage of the yarns due to abrasive testing.

To explore the influence of different ether carboxylic acids provided by Sasol Germany as spin finishes for polyester fibres as well as protective finishes for

polyester fabrics, friction coefficient of polyester yarn produced by melt-spinning process and abrasion resistance of fabrics, respectively, were determined.

From friction measurements of fibre against steel, the spin finish **2** (Isotridecanol ethoxylated carboxymethylated) is evaluated as "the best" among other finishing agents with respect to decreasing the fibre friction.

The influence of textiles surface properties such as their topographical structure and degree of hydrophobicity on spreading and penetration behaviour of water before and after treatment with protective finishes as well as before and after mechanical treatment by abrasion was investigated.

The dynamic wetting and water uptake measurements were carried out to check the wetting characteristics of differently modified fabrics—impregnated with protective finishes and mechanically abraded. From these measurements, the water uptake rate seems to be a suitable parameter to estimate the abrading degree. The time of total absorption of water from the dynamic contact angle measurements as a wetting measure indicates changes in absorbing capacity after modification of fabrics with different protective finishes. The results described in this study support the usefulness of imaging techniques based on the principle of chromatic aberration as well as wetting measurements in characterising the surface of textile materials before and after their surface modification.

3.4 Wettability of Engineered Nanoparticles

A conceptually new methodology to collect information about wetting properties of technologically relevant nanoparticles using the Wilhelmy plate method along with modern optical techniques for surface roughness analysis is presented in brief. The results are based on several differently modified synthetic alumina particles as sun blockers for sunscreen products.

Emulsions are common formulation concepts employed to build stable systems consisting of two immiscible or partly immiscible liquids. They can be formed and stabilized only in the presence of well selected surfactants, polymers, proteins and their mixtures. Traditionally, surfactants composed of a hydrophilic and a hydrophobic part within the same molecule are used as emulsifiers. With increasing legal and consumer requirements to the emulsifiers being non-toxic, biodegradable, mild to skin and mucous, and with an attractive price/performance ratio, degrees of freedom in selecting and designing classical emulsifiers are limited. Consequently, industries such as cosmetics and pharmaceutics with high standards for product safety are seeking for alternatives to the conventional formulation concepts.

A new alternative approach uses nanoparticles according to the well-known principle of Pickering [55]. Especially, for products which contain particles in their formulation an additional or even complete stabilization by these particles will be a new and interesting concept. The key factor for the use of particles as stabilizing agent is their wetting by the two phases, namely the oil and aqueous phase. However, the affinity to each of the two phases should be different and is

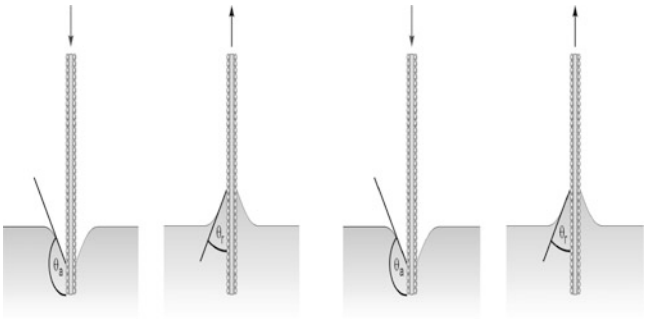

Fig. 18 Measurement of the advancing (*left*) and receding (*right*) dynamic contact angle of a fixed particle layer using the Wilhelmy plate method

expressed by the contact angle. The contact angle is an excellent measure describing the wettability of particles and their affinity interacting with liquids. Furthermore, it affects the stability of the emulsion through the energy of attachment in particles at the interfaces. In general, factors that affect surface chemistry and contact angles, will impact the stability and characteristics of the emulsion [56, 57].

Wettability of powders can be characterized by spontaneous capillary penetration of a liquid into pore spaces, however, the complex geometry of particle pore spaces creates numerous combinations of interfaces, capillaries, and wedges in which a liquid is retained, and results in a variety of air–liquid and solid–liquid configurations, making the result interpretation extremely difficult.

Pickering emulsions require sufficiently small particles which are usually at least tenfold smaller in size than the dispersed droplets of the emulsion. However, existing methods to characterize the particle wettability such as microsphere tensiometry, film and gel trapping techniques, and drop shape analysis fail in view of such small particles all with a similar size of less than 200 nm. In this study, wetting properties of differently modified alumina nanoparticles have been investigated by means of the modified Wilhelmy plate. This method seems to be suitable for a quick wettability characterization, and, therefore, this method may become a significant surface analytical tool in analyzing interfacial properties of powder materials.

Dispersible colloidal Boehmite alumina powders are used in this study, which are manufactured by Sasol (Brunsbüttel, Germany). The aluminas were modified by the manufacturer with *p*-toluene sulfonic acid (**1**) and alkylbenzene sulphonic acid (**2**). The surface coverage by two various modifying agents, the size of powder particles as well as of their primary aggregates in dispersion was investigated earlier in [58].

Water contact angles were measured to obtain the wettability of unmodified and modified alumina powders by the modified Wilhelmy plate method illustrated in Fig. 18.

The modified Wilhelmy plate method is gaining importance in view of the growing interest in determining the contact angles on nanoscalic materials—particles, fibres, nanotubes being added to polymeric compounds and other complex

Table 5 Values of advancing contact angles measured by the modified Wilhelmy method and sessile drop method as well as the ones corrected

		Modified Wilhelmy plate		Sessile drop method	
Particle type	Wenzel factor	θ, measured	θ, corrected	θ, measured	θ, corrected
1	1.994	18	62	10	60
2	3.815	54	81	91	90

Fig. 19 Topography images of modified plates (*left*) and (*right*) with particles **1** and **2**, respectively

fluids [30, 31]. The principle of this method is balancing a thin plate immersed in liquid. If this technique is performed as a dynamic method, the partial contact angle values are attained reaching its maximum value—advancing contact angle, by immersing the plate into the liquid. If the plate is moved out of the liquid, receding contact angle is obtained. In our measurements, alumina powders were attached to a double-sided adhesive tape. The measurements are performed at room temperature with deionized water. The air contained in pores cannot be displaced, as the plate roughness governed by attached particles is unavoidable, therefore, several immersion-emersion cycles were carried out. The receding contact angle seems to be more reliable because of its invariability during three measuring cycles. In addition, quasi-equilibrium contact angels were measured using the sessile drop method shown in Table 5.

The contact angle values measured using both methods seem to be underestimated because of the plate roughness, actually desired. The water-in-oil (W/O) a type of stable Pickering emulsion achieved using particles **2** cannot be explained with values lower than 90°. Assuming the Wenzel regime [59] during wetting, values measured were corrected using the Wenzel roughness factor $r_s = \cos\theta_{measured} / \cos\theta_{smooth}$. This factor was estimated from topographic images, shown in Fig. 19, taken with an image measuring instrument for the optical analysis of roughness MicroGlider (FRT, Germany). The roughness factor of a surface is the ratio between the real surface area and the geometric one. The correction of the measured contact angles with the roughness factor includes the assumption that the measured surface is completely wet, up to the scale of it' resolution. It is obvious that the determined roughness factor is bound by the resolution of the measuring device.

It is known that Wenzel regime is often not favoured energetically in the case of wet surfaces with roughness on many different length scales. It is likely that air is trapped in grooves of the surface and only a fraction of the surface comes into contact with the liquid. This case is referred to as the Cassie state [60]. It was shown

that the incomplete liquid–solid contact is driven by the surface slope [61]. Below a certain critical slope that depends on the true flat surface contact angle, Wenzel regime is favoured whereas above that value the Cassie state prevails.

Hence, slope distribution of the measured surface should be taken into account for further corrections of the measured contact angle on rough surfaces in order to determine wetting properties of the powder particles.

A theory for wetting was presented recently considering a Gaussian random surface [62]. Within the theory the average slope as well as the roughness factor are determined by the same parameter that is connected with the surface roughness power spectrum.

The results described above demonstrate the application of wetting measurements by the modified Wilhelmy plate in characterising dispersible colloidal powders. The difference between unmodified and modified alumina particles were determined with respect to their hydrophobicity/hydrophilicity. Analysing this in comparison with other properties of particles such as their electrical surface properties, the particle size in the dry and wetted states, and in an aqueous suspension, is an important factor in a development and mechanistic understanding the stability of emulsions.

References

1. Gibbs, J.W.: Trans. Conn. Acad. **3**, 108 (1873)
2. Rusanov, A.I., Shchekin, A.K.: Kolloidn. Zh. **61**, 437 (1999)
3. Young, T.: Philos. Trans. R. Soc. Lond. **95**, 65 (1805)
4. Weidenhammer, P., Jacobasch, H.-J.: Macromol. Symp. **126**, 51 (1997)
5. Churaev, N.V.: Adv. Colloid Interfacial Sci. **58**, 87 (1995)
6. Churaev, N.V.: Kolloidn Zh. **58**, 725 (1996)
7. Derjaguin, B.V., Churaev, N.V., Muller, V.M.: Surface Forces. Nauka, Moskau (1985)
8. Starov, V.M., Velarde, M.G., Radke, C.J.: Wetting and Spreading Dynamics. Taylor and Francis, Boca Raton (2007)
9. Fowkes, F.M.: J. Adhes. Sci. Tech. **1**, 7 (1987)
10. Owens, D.K., Wendt, R.C.: J. Appl. Polym. Sci. **13**, 1741 (1969)
11. Kwok, D.Y., Neumann, A.W.: Adv. Colloid Interface Sci. **81**, 167 (1999)
12. Good, R.J.: J. Colloid Interface Sci. **59**, 398 (1977)
13. Nardin, M., Schultz, J.: Compos. Interfaces **1**, 177 (1993)
14. Derjaguin, B.V.: Kolloidn. Zh. **69**, 155 (1934)
15. Derjaguin, B.V., Lazarev, W.: Kolloidn. Zh. **69**, 11 (1934)
16. Jacobasch, H.-J., Freitag, K.-H.: Acta Polym. **30**, 453 (1979)
17. Jacobasch, H.-J.: Oberflchenchemie faserbildender Polymerer. Akademie, Berlin (1984)
18. Berg, J.C.: Role of acid-base interactions in wetting and related phenomena. In: Berg, J.C. (ed.) Wettability, pp. 75–148. Marcel Dekker, New York (1993)
19. Good, R.J., van Oss, C.J.: The modern theory of contact angles and the hydrogen bond components of surface energies. In: Schrader, M.E., Loeb, G. (eds.) Modern Approach to Wettability: Theory and Applications, pp. 1–27. Plenum, New York (1991)
20. Good, R.J.: Contact angle, wettability, and adhesion: a critical review. In: Mittal, K.L. (ed.) Contact Angle, Wettability and Adhesion, pp. 3–36. VSP, Utrecht (1993)

21. Gutmann, V.: The Donor-Acceptor Approach to Molecular Interactions. Plenum, New York (1983)
22. Israelachvili, J.N.: Intermolecular and Surface Forces. Academic, San Diego (1991)
23. Good, R.J., Chaudhury, M.K.: Theory of adhesive forces across interfaces. 1. The Lifshitz-van der Waals component of interaction and adhesion. In: Lee, L.-H. (ed.) Fundamentals of Adhesion, pp. 137–150. Plenum, New York (1991)
24. Berlin, A.A., Bassin, B.E: Basics of Adhesion of Polymers. Chimia, Moskau (1974)
25. Kinloch, A.J.: Adhesion and Adhesives: Science and Technology. Chapman & Hall, London (1987)
26. Dutschk, V.: Surface forces and their contribution to adhesion and adherence in glass fibre reinforced polymer composites. Ph.D. thesis, University of Technology Dresden (2000)
27. Good, R.J., Hawa, A.K.: J. Adhes. **63**, 5 (1997)
28. Asthana, R., Sobczak, N.: J. Mater. **52**, 40 (2000)
29. Wilhelmy, L.: Ann. Phys. Chem. **CXIX**(6), 202 (1863)
30. Bachmann, J., Horton, R., van der Ploeg, R.R., Woche, S.: Soil Sci. Soc. Am. J. **64**, 564 (2000)
31. Kvítek, L., Pikal, P., Kovaříková, L., Hrbáč, J.: Acta Univ. Palacki. Olomuc. Chem. **41**, 27 (2002)
32. Good, R.J.: J. Colloid Interface Sci. **42**, 473 (1973)
33. Chwastiak, S.: J. Colloid Interface Sci. **42**, 298 (1973)
34. Washburn, E.W.: Phys. Rev. **17**, 273 (1921)
35. Dutschk, V., Sabbatovskiy, K., Stolz, M., Grundke, K., Rudoy, V.: J. Colloid Interface Sci. **267**, 456 (2003)
36. Dutschk, V., Breitzke, B.: Tenside Surfactants Deterg. **42**, 82 (2005)
37. Slavchov, R., Heinrich, G., Dutschk, V., Radoev, B.: Colloid Surf. A **354**, 252 (2009)
38. Lee, K.S., Ivanova, N., Starov, V.M., Hilal, N., Dutschk, V.: Kinetics of wetting and spreading by aqueous surfactant solutions (Review). Adv. Colloid Interfaces Sci. **144**, 54–65 (2008)
39. Dutschk, V.: Wetting dynamics of aqueous solutions on solid surfaces. In: Miller, R., Liggieri, L. (eds.) Drop and Bubble Interfaces, vol. 2. Progress in Colloid and Interface Science. Brill, Leiden (2011)
40. Plonka, R., Mäder, E., Gao, S.L., Bellmann, C., Dutschk, V., Zhandarov, S.: Compos. Part A **35**, 1207 (2004)
41. Bismarck, A., Kumru, M.E., Springer, J.: J. Colloid Interface Sci. **210**, 60 (1999)
42. Brantseva, T., Gorbatkina, Yu., Dutschk, V., Vogel, R., Grundke, K., Kerber, M.L.: J. Adhesion Sci. Technol. **17**, 2047 (2003)
43. Grundke, K., Uhlmann, P., Gietzelt, T., Redlich, B., Jacobasch, H.-J.: Colloids Surf. A **116**, 93 (1996)
44. Potluri, P., Parlak, I., Ramgulam, R., Sagar, T.V.: Comp. Sci. Technol. **66**, 297 (2006)
45. Milasius, V., Milašius, R., Kumpikaite, E., Olauškine, A.: Fibres Text. East. Eur. **11**, 48 (2003)
46. Kumpikaite, E.: Fibres Text. East. Eur. **15**, 35 (2007)
47. Calvimontes, A., Dutschk, V., Breitzke, B., Offermann, P., Voit, B.: Tenside Surfactants Deterg. **42**, 17 (2005)
48. Calvimontes, A., Dutschk, V., Koch, H., Voit, B.: Tenside Surfactants Deterg. **42**, 210 (2005)
49. Dutschk, V., Myat, S., Märtin, J., Stolz, M., Breitzke, B., Cherif, Ch., Heinrich, G.: Tenside Surfactants Deterg. **44**, 348 (2007)
50. Hasan, M.M.B., Dutschk, V., Calvimontes, A., Hoffmann, G., Heinrich, G., Cherif, Ch.: Tenside Surfactants Deterg. **45**, 274 (2008)
51. Hasan, M.M.B., Dutschk, V., Brünig, H., Mäder, E., Häußbler, L., Häßbler, R., Cherif, Ch., Heinrich, G.: J. Appl. Polym. Sci. **111**, 805 (2008)
52. Hasan, M.M.B., Calvimontes, A., Synytska, A., Dutschk, V.: Text. Res. J. **78**, 996 (2008)
53. Calvimontes, A., Synytska, A., Dutschk, V., Bell, Ch., Lehmann, B.: Melliand English **1–2**, E16 (2006)
54. Kissa, E.: Text. Res. J. **66**, 660 (1996)
55. Pickering, S.U.: J. Chem. Soc. **91**, 2001 (1907)
56. Lagaly, G., Reese, M., Abend, S.: App. Clay Sci. **14**, 83 (1999)

57. Melle, S., Lask, M., Fuller, G.G.: Langmuir **21**, 2158 (2005)
58. Dutschk, V., Stöckelhuber, K.-W., Albrecht, V., Geißbler, U., Simon, F., Petzold, G., Bellmann, K.: In: PARTEC2007, Proceedings, Nuremberg, 27–29 March 2007
59. Wenzel, R.N.: Ind. Eng. Chem. **28**, 988 (1936)
60. Cassie, A.B.D., Baxter, S.: Trans. Faraday Soc. **40**, 546 (1944)
61. Johnson, R.E., Dettre, R.H.: Adv. Chem. Ser. **43**, 112 (1964)
62. Yang, C., Tartaglino, U., Persson, B.N.J.: Eur Phys. J. E **25**, 139 (2008)

Wetting Transition and Line Tension of Oil on Water

H. Matsubara and M. Aratono

1 Introduction

Originally, wetting has attracted wide attention in the field of applied chemistry because of its crucial importance in industrial operations such as coating, painting, and lubrication. However, since the pioneering theoretical work of Cahn [1], it has become one of central academic research subjects in the field of soft matter science. In his theory, when two phases are sufficiently close to their critical solution point, the coexisting third phase must spread on the interface between these two phases. This theory is based on the scaling law of the interfacial tensions of coexisting phases near a critical point [2, 3] and has been verified by Cahn himself for a vapor/methanol/cyclohexane system [4]. Subsequently, this wetting transition has been extensively explored in the three-liquid-phase coexistence region of the water–oil–nonionic surfactant mixtures [5–17]. These experiments suggest an important relation between wetting transition and the structures of surfactant aggregates in bulk solutions. Widom, Gompper, and Schick have reviewed the theoretical works on wetting transition in ternary liquid mixtures based on the lattice model [18, 19].

In 1991, Brochard and co-workers classified wetting transition in a more simple and general manner by using the initial spreading coefficient and the long-range surface forces between the interfaces on both sides of the wetting film [20]. They showed the existence of three thermodynamically different possibilities for a wetting film: partial wetting, pseudo-partial wetting, and complete wetting (Fig. 1).

In the partial-wetting state, a liquid droplet placed on another material (substrate) does not spread even on the molecular level and remains as a lens as a result of a negative initial spreading coefficient (S_i). Both pseudo-partial wetting and

H. Matsubara · M. Aratono (✉)
Department of Chemistry, Faculty of Sciences, Kyushu University, Hakozaki, Higashi-ku, Fukuoka 812-8581, Japan
e-mail: aratono@chem.kyushu-univ.jp

R.G. Rubio et al. (eds.), *Without Bounds: A Scientific Canvas of Nonlinearity and Complex Dynamics*, Understanding Complex Systems,
DOI 10.1007/978-3-642-34070-3_24,

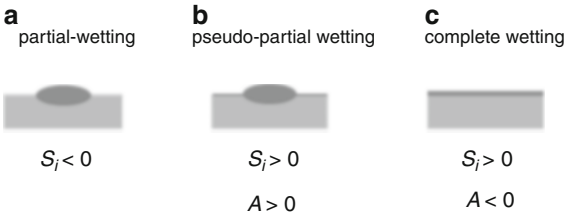

Fig. 1 A schematic representation of (**a**) Partial wetting, (**b**) pseudo-partial wetting, and (**c**) complete wetting of oil on water. S_i is the initial spreading coefficient introduced in (1) and A is the Hamaker constant

complete wetting have positive initial spreading coefficients, but are distinguished by their attractive (positive A) and repulsive (negative A) long-range surface forces. In pseudo-partial wetting, the competition between a positive initial spreading coefficient, which favors a thick film, and an attractive long-range surface force, which favors a thinner film, allows the formation of a molecular film (normally up to 100 nm). In complete wetting, a drop spreads as a uniform film.

In the following section, we will first summarize fundamental understandings of wetting transition of oil on water and then discuss the difference between existing wetting systems and the surfactant-assisted wetting which we have found and studied for the last 10 years. Mixing of oil molecules in surfactant adsorbed films triggers another first-order transition, freezing of pseudo-partial wetting film, upon cooling. Unique monolayer and bilayer solid film formations which depend on the chain length of oil and surfactant are also focused in Chap. 4. Finally, the close relation between above mentioned wetting and freezing transitions and the stability of the three-phase contact line is discussed in terms of the line tension of oil lenses.

2 Free Energy Profile Approach to Thin Liquid Film Formation

Cahn theory predicts the occurrence of the first-order wetting transition from the equilibrium spreading coefficient. However, wetting transitions are further classified into several different scenarios based on the initial spreading coefficient and the long-range van der Waals potential. For an oil droplet at the air–water interface, the initial spreading coefficient is given by

$$S_i = \gamma^{AW}(0) - \left(\gamma^{OW} + \gamma^{AO}\right), \tag{1}$$

where $\gamma^{AW}(0)$ is the air–water interfacial tension in the absence of the oil film. By combining the initial spreading coefficient and van der Waals potential, the free

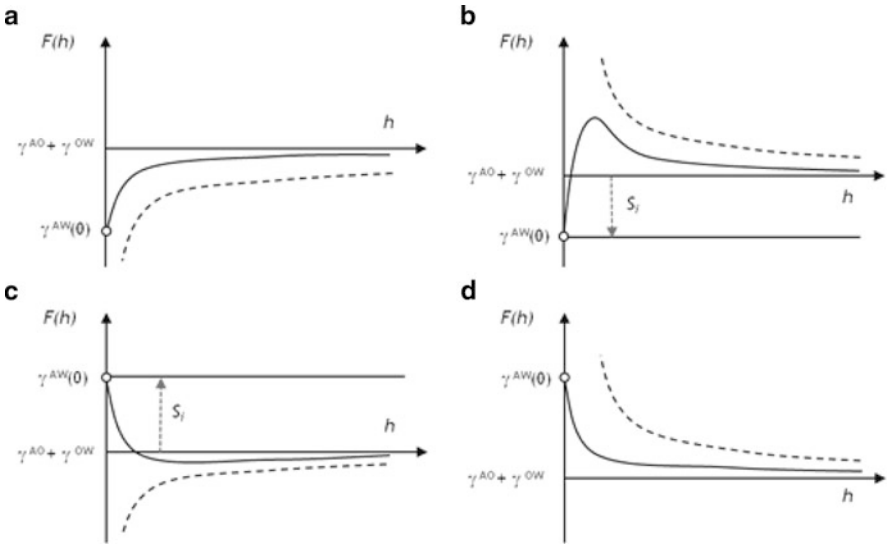

Fig. 2 Schematic representation of free energy $F(h)$ of the air–water interface as a function of the thickness h of an oil film. The long-range potential is shown as a *dotted line*. (**a**) $S_i < 0$ and $A > 0$ (partial wetting), (**b**) $S_i < 0$ and $A < 0$ (partial wetting), (**c**) $S_i > 0$ and $A > 0$ (pseudo-partial wetting), (**d**) $S_i > 0$ and $A < 0$ (complete wetting)

energy required to create a unit area of wetting film of an arbitrary thickness h from the complete wetting film ($h = \infty$) can be expressed as

$$F(h) = \gamma^{OW} + \gamma^{AO} - A/12\pi h^2, \tag{2}$$

where A is the Hamaker constant of air and water through the oil film [20]. This equals the sum of γ^{AO} and γ^{OW} for an infinitely thick film and $\gamma^{AW}(0)$ for zero thickness. Hence, the initial spreading coefficient and the equilibrium spreading coefficient respectively correspond to the intersection of y-axis and the global minimum of the free-energy profile when the sum of γ^{AO} and γ^{OW} is taken as the origin of the free energy.

The four possible free-energy profiles are depicted in Fig. 2. When the long-range potential is attractive (positive A), the free energy of the film decreases with decreasing film thickness. This leads to a minimum in the free energy at a finite thickness with a positive initial spreading coefficient (Fig. 2c) or at $h = 0$ with a negative initial spreading coefficient (Fig. 2a). In this case, the transition between partial wetting (a) and pseudo-partial wetting (c) can be induced by controlling the initial spreading coefficient. On the other hand, the transition between partial wetting (Fig. 2b) and complete wetting is also expected to occur by controlling the initial spreading coefficient when the long-range potential has a negative (repulsive) value. The later situation corresponds to the wetting transition discussed

in Introduction. Another type of transition to complete wetting can be achieved by changing the Hamaker constant from positive (Fig. 2c) to negative values (Fig. 2d).

3 Wetting of Alkane on Water

A second type of complete-wetting transition was first discovered by a French group for pentane on water [21]. The Hamaker constant of a pentane film on water has a positive value at room temperature because the dispersion contribution of the Hamaker constant

$$A_1 = \frac{3h\nu_e}{8\sqrt{2}} \times \frac{\left(n_3^2 - n_1^2\right)\left(n_3^2 + n_2^2\right)}{\left(n_3^2 + n_1^2\right)^{1/2}\left(n_3^2 + n_2^2\right)^{1/2}\left[\left(n_3^2 + n_1^2\right)^{1/2} + \left(n_3^2 + n_2^2\right)^{1/2}\right]}, \tag{3}$$

is superior to the zero-frequency contribution [22]

$$A_2 = \frac{3}{4}k_B T\left[\frac{\epsilon_3 - \epsilon_1}{\epsilon_3 + \epsilon_1}\right]\left[\frac{\epsilon_3 - \epsilon_2}{\epsilon_3 + \epsilon_2}\right], \tag{4}$$

where ϵ_j and n_j are the static dielectric constant and the refractive index of substance j, respectively, and ν_e denotes the characteristic absorption frequency. However, the absolute value of the dispersion term gradually decreases and the minimum in the free energy becomes shallower as the temperature increases. Finally, the thickness of the film diverges to a macroscopically thick film at 53°C where the total Hamaker constant changes sign.

With the same experimental system, Ragil et al. also found a first-order wetting transition from partial to pseudo-partial wetting at 25°C where the initial spreading coefficient passes through zero, corresponding to a change in the free energy profile depicted in Fig. 2a, c. A sequence of two transitions has also been experimentally observed with varying temperature for hexane on brine [23] and with varying salinity for heptane on brine [24]. A continuous transition from pseudo-partial to complete wetting for octane on glucose solutions has been induced by varying the glucose concentration [25]. The addition of electrolytes or glucose lowers the wetting-transition temperatures through the change in dielectric constant of aqueous phase.

Brochard theory correctly predicts whether a spread oil film thickens to macroscopic dimensions (complete wetting) or remains as a microscopic layer (pseudo-partial wetting), however, it does not explain the order of the wetting transitions. For example, according to the theory, the transition from partial wetting (Fig. 2a) to pseudo-partial wetting (Fig. 2c) should be a second-order transition because the initial spreading coefficient varies smoothly with temperature, salinity or

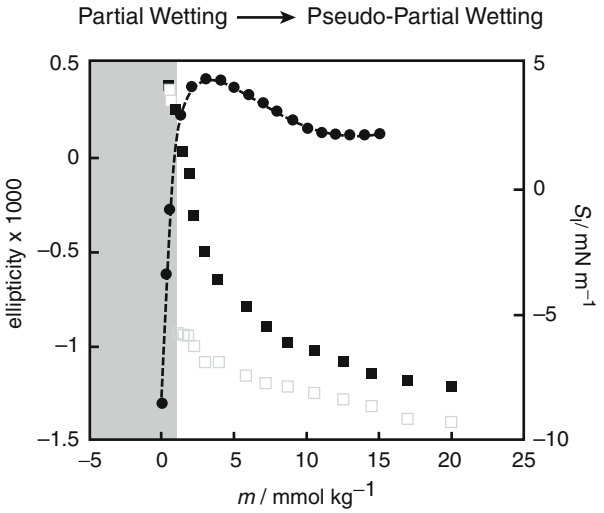

Fig. 3 The coefficient of ellipticity $\bar{\rho}$ for air–DTAB solution interface without hexadecane (*black square*) and with hexadecane (*white square*). The right hand axis shows initial spreading coefficient (*black circle*)

glucose concentration; this is in contrast to the experimental observation of first-order transitions. An investigation of the influence of the surfactant adsorption on the pseudo-partial wetting provides useful information regarding the short-range interaction and origin of the first-order transition because the initial spreading coefficient can be varied much more widely by the addition of a surfactant [26–31]. Increases in the carbon number of the oil give rise to the higher air–oil interfacial tension, whereas they do not significantly affect the dispersion interaction. As a result, liquid alkanes with chain length longer than that of octane do not spread on water surfaces because their initial spreading coefficients become negative. For longer alkanes, increasing the surfactant concentration, m, in the aqueous phase causes a first-order transition from partial wetting to pseudo-partial wetting. Figure 3 shows ellipsometric data for the cationic surfactant, dodecyltrimethylammonium bromide (DTAB), in the presence and absence of hexadecane [27]. The coefficient of ellipticity, $\bar{\rho}$, is related to the thickness of the surfactant/oil film. On the right-hand axis of Fig. 3, the initial spreading coefficients determined by interfacial tensiometry were plotted.

An analysis of data obtained using ellipsometry and tensiometry indicates that the thickness of the film above the wetting transition is approximately constant at a value of 0.7 nm, which is typical for an expanded monolayer of the pure surfactant. The mole fraction of the oil in this mixed monolayer, determined from a combination of the ellipsometric thickness (proportional to the total amount of oil and surfactant) and interfacial density of the surfactant molecules calculated by the adsorption equation, is found to vary from 2/3 just above the wetting transition

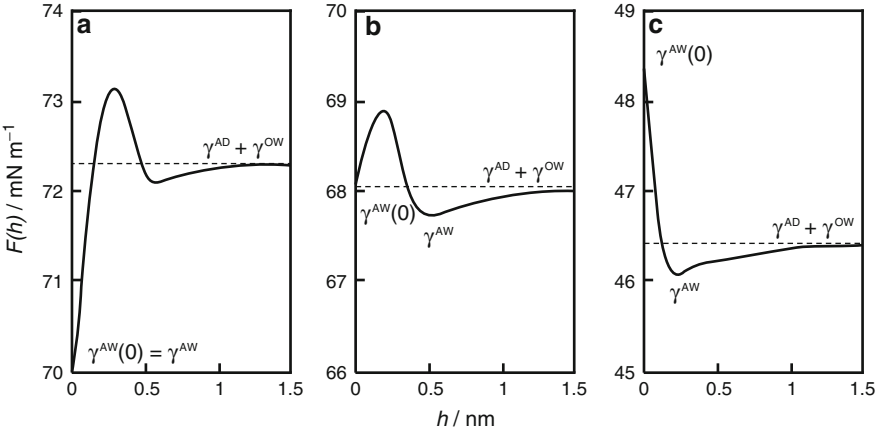

Fig. 4 Free energy profile for hexadecane on DTAB solutions. (**a**) 0.5, (**b**) 1.0 and (**c**) 8.0 mmol kg^{-1}. γ^{AW} Represents the equilibrium value of air–water interfacial tension. In these calculations, the h only counts the contribution of oil molecules to the wetting-film thickness. The shift of the free-energy minimum therefore indicates the mole fraction of surfactant in the monolayer increases with increasing the concentration

to 1/5 at the critical micelle concentration of the DTAB ($m = 15$ mmol kg^{-1}). To explain the first-order nature of the wetting transition, a theoretical model was proposed [29], in which the surface free energy consists of a long-range interaction and a short-range interaction described by a two-dimensional-lattice gas, taking into account the interaction between the oil and surfactant molecules (Fig. 4). The model provides quantitative agreement with the wetting-transition concentrations and the variation in composition of the wetting film with the bulk surfactant concentrations of alkanes on surfactant solutions.

The generality of wetting transitions of alkanes (decane, dodecane, hexadecane, butylcyclohexane, and squalane) on surfactant solutions (DTAB, tetradecyltrimethylammonium bromide (TTAB), hexadecyltrimethylammonium bromide (CTAB), dibucaine hydrochloride) has been explored by ellipsometry and interfacial tensiometry [30, 31]. These experiments suggest that the surfactant molecules adsorbed at the air–water interface cause wetting transitions by decreasing the required enthalpy for transferring oil molecules from the lens to the film by increasing the lateral dispersion interaction between hydrocarbon chains of the surfactant and oil molecules and by increasing the mixing entropy in the film. The wetting-transition concentration increases with increasing the surface tension of the oil for linear alkanes on the same surfactant solutions and decreases with increasing surfactant chain length for the same oil. The introduction of cyclohexane rings in the oil molecules contributes to lowering the wetting-transition concentration and the introduction of branches has the opposite effect (Fig. 5).

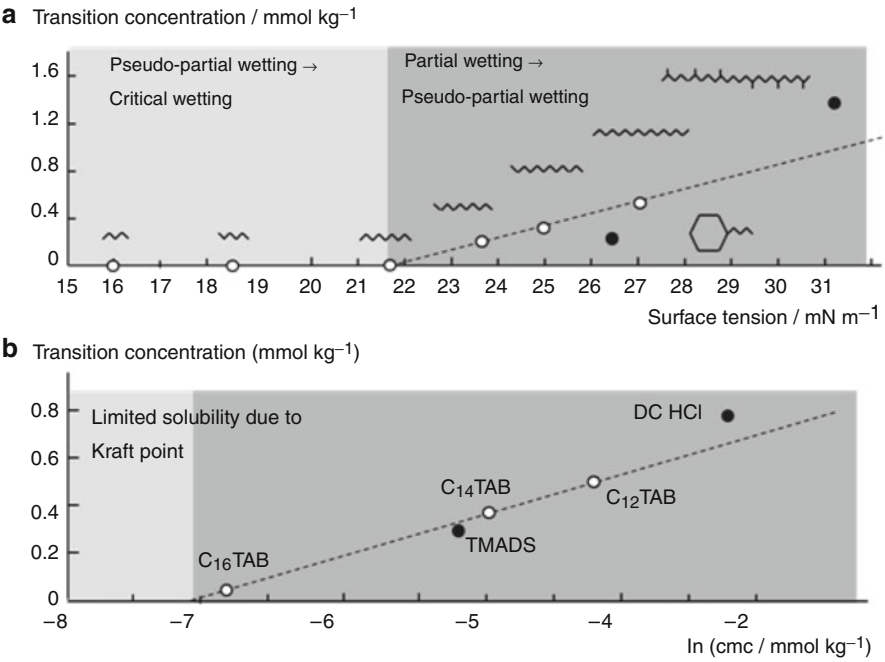

Fig. 5 (**a**) Transition concentrations on DTAB solution against surface tension of oil for decane, dodecane, hexadecane (*open circle*), squalane, and butylcyclohexane (*filled circle*), and (**b**) those of hexadecane on different surfactant solutions. TAMDS and DC HCl are respectively stand for tetramethylammonium dodecyl sulfate and dibucaine hydrochloride

4 Freezing Transition of Wetting Film

Cooling of the mixed monolayer of surfactant and alkane leads to another first-order phase transition whose character depends on the relative lengths of the hydrocarbon chains of the surfactant (k) and alkane (n). Wilkinson et al. and Sloutskin et al. showed that, for $k = 16$ and $11 < n < 17$, the low-temperature phase was a hexagonally packed solid phase with upright, conformationally ordered chains [32,33]; however, for $n > 18$, an unusual bilayer phase was formed in which a solid layer of pure alkane rested on a liquid-like lower phase [34]. Whether the ordered phase is of the monolayer or bilayer type can be readily determined by ellipsometry: the change in the coefficient of ellipticity at the phase-transition temperature is roughly three times as large in the latter case.

It is well known that longer members of alkane show the surface freezing, in which a crystalline monolayer is formed on top of the liquid bulk at temperatures above the bulk freezing point [35, 36]. For $16 < n < 30$, these monolayers are hexagonally packed, upright chains and exist at temperatures up to 3°C above the bulk freezing point depending on n [37–43]. From the fact that the crystallographic

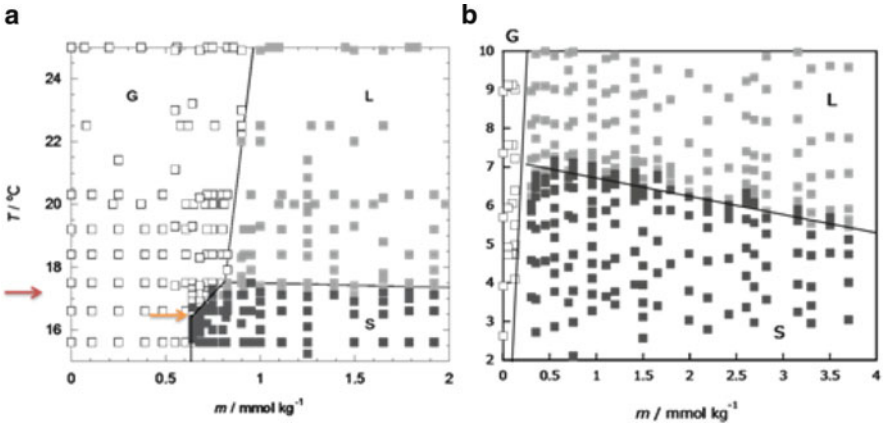

Fig. 6 The temperature–surfactant concentration diagrams for (**a**) DTAB/hexadecane and (**b**) TTAB/tetradecane systems. Each plot is the point where the ellipsometry was performed. The arrow on vertical axis of (**a**) indicates the surface freezing point of hexadecane and that on the G–S phase boundary is the bulk freezing point of hexadecane. These diagrams were reproduced from data published in [44] and [45]

structure of the ordered-phase of the bilayer determined by the grazing incidence X-ray diffraction was essentially the same as that of the surface-frozen phase of pure alkanes, Sloutskin et al. proposed that the mixed monolayer in the pseudo-partial wetting phase behaves like a liquid alkane that is wet by the solid alkane phase at temperatures below the surface freezing point of the alkane. For alkanes with chain lengths similar to or shorter than the surfactant, this wetting transition is pre-empted by freezing of the mixed monolayer.

The same conclusions have been drawn from the temperature-concentration diagrams of the surface phases determined by the discontinuous change in the ellipticity and the kink in the surface tension curves [44, 45]. The surface phases that exist for alkane molecules on a surfactant solution can be compared with the three phases of a two-dimensional fluid: gas (partial wetting), liquid (pseudo-partial wetting at high temperatures), and solid (pseudo-partial wetting at low temperatures) and, for brevity, we will use the terminology G, L, and S to identify these three phases.

The G/L transition has been identified by variation of the surfactant concentration at fixed temperature as seen in Fig. 3, and the L/S transition by variation of temperature at fixed surfactant concentration, therefore, one would expect these two phase boundaries to meet at a triple point. The triple point for the hexadecane film on DTAB solutions is located at $T = 17.3°C$ and $m = 0.75\,\mathrm{mmol\,kg^{-1}}$ as shown in Fig. 6a. It is important to note here that the L–S transition occurs at the temperature just below the surface freezing point of pure hexadecane and almost independent of the surface composition of DTAB. We introduced in the previous section that the composition of the mixed monolayer is rich in alkane

at low surfactant concentrations and rich in surfactant at high concentrations, therefore, the weak concentration dependence together with the similarity between the temperatures of the freezing transition and surface freezing in pure hexadecane provides supporting evidence that the lower mixed monolayer does not freeze at the L–S phase transition. On the contrary, the L–S phase boundary can be changed by the surfactant concentration principally in the tetradecane film on TTAB solutions, in which a mixed monolayer of alkane and surfactant freezes (Fig. 6b). It seems that the slope of the L–S phase boundary between these two systems is rather similar, however, the increase in the hydrocarbon chain length of surfactant by a carbon number of two (CTAB) gives rise to a much stronger dependence of the freezing temperature on the surfactant concentration [45].

5 Relation Between Wetting Transition and Line Tension

In general terms, line tension is the one-dimensional analogue of interfacial tension and can be interpreted as excess free energy associated with the line [46, 47]. For example, the stability of liquid-condensed (LC) domains surrounded by a liquid-expanded (LE) film in an insoluble monolayer is discussed from the viewpoint of the competition between the positive line tension acting on the edge of LC domains and the entropic loss associated with complete LC film formation [48, 49]. An important difference between line tension and interfacial tension is that the former can be negative in some situations; that is, the growth of the line becomes a thermodynamically acceptable process. The negative line tension deserves special attention because it promotes the fusion of cells [50] and the coalescence of emulsions [51, 52].

Rusanov classified line tension into three different types: the line tension in two-dimensional heterogeneous systems, the line tension at the three-phase (interface) contacts, and the effective line tension on deformable solids [53]. In two-dimensional systems, two interfacial phases are separated by a boundary line as two bulk phases separated by an interface. In this case, the mechanical definition of line tension becomes a simple expansion of that of interfacial tension. Consequently the line tension is always positive, as is the case for the interfacial tension.

On the other hand, the origin of the line tension in latter two cases involves the deformation of the interfacial profile near the three-phase contact. For an oil droplet on a solid substrate, the microscopic profile of the droplet is deviated from the macroscopic profile determined by the interfacial tensions near the three phase contact region because of the surface force between air–oil and oil–substrate interfaces [54–60]. When the surface force is attractive on the whole, the displacement of the interfacial profile occurs, bringing the two interfaces closer, and the length of the boundary line is increased due to the increase in the attractive interaction between the two interfaces (Fig. 7). The opposite situation is true in the case of repulsive surface forces.

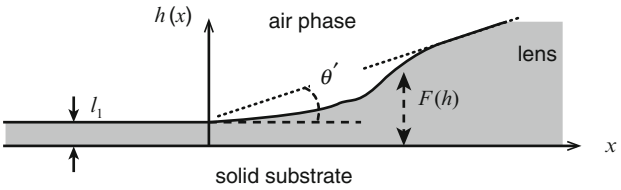

Fig. 7 Interface displacement model for a droplet on solid substrate. $\acute{\theta}$ Indicates the ideal contact angle derived from Young equation. The real contact angle becomes smaller than $\acute{\theta}$ by the attractive surface force $F(h)$

In the interface displacement model, the line tension is expressed as a functional of the interfacial profile $h(x)$

$$\tau = \int dx \left[\left(\frac{\gamma^{LV}}{2} \right) \left(\frac{dh}{dx} \right)^2 + F\left(h\left(x\right)\right) \right], \tag{5}$$

where the first term in the integrand accounts for the increase in the interfacial area, and the second term accounts for the surface forces acting through the liquid of thickness h. The integration proceeds from the thickness of the film in equilibrium with a lens ($x = -\infty$) to an infinitely thick film ($x = \infty$). By minimizing equation [55–57], the equilibrium line tension can be expressed as

$$\tau = \int dl \left[F\left(h\left(x\right)\right)\right]^{1/2}, \tag{6}$$

In the original paper of Indekeu, the square root of the free-energy profile, $F(h)$, is defined as the interface potential $V(h)$. Experimentally, the line tension is determined from the dependence of contact angle, θ, on the radius of the contact line, r, on the basis of a modified Young equation

$$\gamma^{SV} = \gamma^{SL} + \gamma^{LV} \cos\theta + \frac{\tau}{r}, \tag{7}$$

where γ^{SV}, γ^{SL}, and γ^{LV} are the solid–vapor, solid–liquid, and liquid–vapor interfacial tensions, respectively. The line tension is considerably small and is normally negligible as compared to the surface tension; however, since the line tension is proportional to the inverse of the radius of the lens, it plays an increasingly important role as the lens becomes smaller. Unfortunately, the line tensions measured by different researchers are still quite different and controversial [61–71]. Currently, this problem is being addressed by performing experiments on ideally smooth silicon wafer [72–75] or liquid surfaces [31, 76–79].

6 Line Tension at Wetting Transition

Indekeu successfully explained the theoretical connection between the line tension and wetting behavior of three-phase systems based on the interface displacement model and the surface free-energy profile [55–57]. For a first-order wetting transition to complete wetting (Fig. 8a), two minima exist at a finite and an infinite film thickness on the interfacial potential. Before the wetting transition, the negative contribution J_1 in the integral of (6) exceeds the positive contribution J_2. However, the magnitude of J_1 reduces as the transition point is approached, and finally, only the positive contribution remains in the integral. Hence, the line tension should be positive at the complete-wetting transition point. On the other hand, when the wetting transition occurs between two microscopic films of different thicknesses, the line tension changes sign from positive to negative, as expected from Fig. 8b. For a second-order transition from a film of finite thickness to a thick film, the line tension is negative and approaches zero at the wetting transition.

Using interferometry, Law and co-workers measured the contact angle of *n*-octane and *n*-octene droplets on a silicon wafer as a function of temperature [72, 73]. The silicon wafer was coated with hexadecyltrichlorosilane to control the wettability of the surface. They demonstrated that the line tension changes sign from negative to positive with a diverging slope near the first-order wetting transition. If the long-range surface force decays slowly as a function of the thickness, the line tension would be allowed to diverge at the transition point. Pompe measured the line tension of hexaethylene glycol on a silicon wafer and obtained positive values below a contact angle of 6° and negative values above [74]. In his experiment, the line tension was calculated from the profile of the liquid–vapor interface, as measured by high-resolution SFM imaging in tapping mode [80, 81]. The measured interfacial profile was fitted with a nonretarded van der Waals and exponentially decaying interactions.

There are a few experimental verification of the interfacial displacement model for wetting transitions on liquid surfaces. Dobbs calculated the line tension of shorter alkanes (butane to octane) by applying Cahn theory and showed that the magnitude of the line tension is of the order of 10^{-12} N, rising to a maximum of 5×10^{-12} N in the vicinity of first-order wetting transitions. Close to the critical wetting transitions, the line tension becomes negative and vanishes at the wetting transition [82]. We have recently confirmed the reversal of the sign of line tension associated with the wetting transition for a hexadecane lens on aqueous solutions of DTAB [77, 78] by using an interferometer originally developed by Aveyard and co-workers [76]. From the relation between the free energy profile and interface potential, it can be understood that a positive line tension in the partial-wetting regime corresponds to the maximum in the free-energy curve in Fig. 4a. The line tension assumes less-positive values as the wetting transition is approached; subsequently, in the pseudo-partial wetting regime, the integration along the van der Waals potential from the thickness of the mixed monolayer to an infinite thickness leads to a negative line tension (Fig. 4b). The images of hexadecane lenses

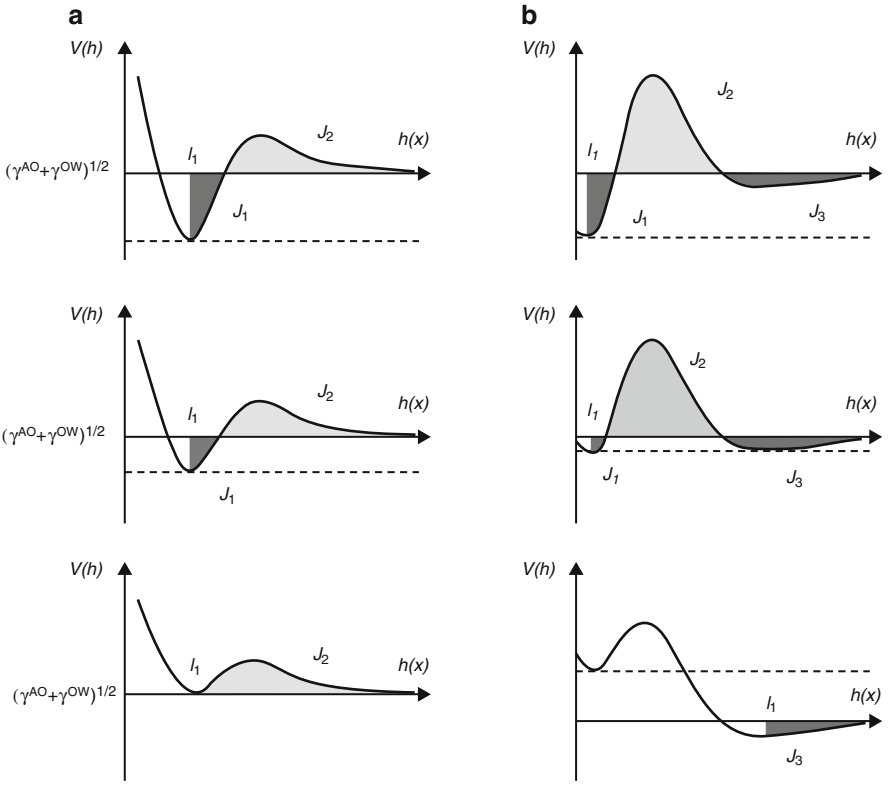

Fig. 8 Interface potential $V(h) = F(h)^{1/2}$ for (**a**) the first-order complete wetting transition and (**b**) thin–thick transition of wetting film. l_1 Represents the equilibrium thickness of the wetting film where the integral of (6) starts

obtained for two specific concentrations are shown in Fig. 9. Before the wetting transition (partial wetting), the small lenses formed by stirring merge spontaneously into a large lens as the equilibrium is approached. The behavior of the oil lens after the wetting transition (pseudo-partial wetting) leads to a remarkable contrast; large lenses break into small lenses without stirring. The manner in which the negative line tension promotes the spontaneous rise of the three-phase contact line is analogous to the stabilization of emulsions by the addition of surfactant molecules. From such a viewpoint, a surfactant that induces a wetting transition from partial to pseudo-partial wetting may be considered as a kind of line active agent.

Interestingly, the both L–S transitions again reverse the line tension sign [79]: oil lenses merge spontaneously in the S regime as well as the partial wetting regime (G). We are expecting that positive line tension values in the S regime results from the change in the long-range van der Waals potential due to the existence of the ordered monolayer; however, the precise shape of the interface potential is still unknown.

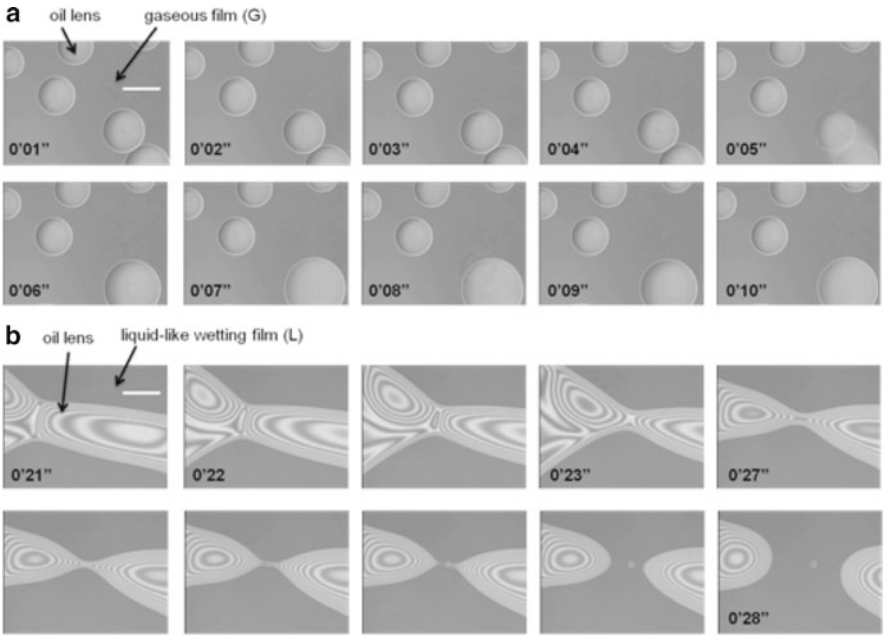

Fig. 9 Dynamics of lens coalescence (**a**) and fission (**b**) observed respectively in the G and L state. *White bar* shows 50 mm. The behavior of lenses in the S state is alike to (**a**) but takes quite long time to be equilibrated as mentioned in the text. Reprinted with permission from [79]

The coalescence of lenses proceeds quite slowly in the S regime, suggesting that a considerable increase in the surface viscosity occurred at the air–water (and air–oil) interface(s).

7 Conclusion

Throughout this chapter, we have summarized recent clarifications of the mechanisms of the first- and second-order wetting transitions developed by Cahn, Brochard, de Gennes and Indekeu. Short-range interactions determine whether the middle phase spreads or not and the long-range interactions determine whether the spreading film thickens to macroscopic dimensions or remains as a molecular or microscopic layer.

When three liquid phases (or two liquid phases and one gas phase) coexist, a first-order complete-wetting transition from partial wetting or pseudo-partial wetting occurs as the system approaches the consolute point of two of the liquid phases. For short-chain alkane droplets placed on water, the wetting transition from partial wetting to pseudo-partial wetting caused by varying the temperature is a first-order transition, and the subsequent thickening to a complete-wetting film is a

second-order transition. Drops of alkanes longer than octane exist solely in the pseudo-partial wetting state because of the positive initial spreading coefficient. This situation can be changed by adding salt or surfactant molecules to the aqueous phase.

Finally, a close relation between wetting transition and line tension, which theoretically equals an integral of the square of the free-energy profile of the wetting film, was discussed. In particular, the sign of the line tension changes at the transition between partial wetting, pseudo-partial wetting and freezing films, and as a result, a spontaneous rise of the three-phase contact line is thermodynamically allowed.

According to the aforementioned contributions, a much greater understanding has developed for the wetting transition of oil on water surface, including the freezing transition of wetting films, however, there are some problems that remain regarding the experimental and theoretical treatments of line tension. For example, we have not achieved convincing expression of one dimensional adsorption equation in spite of much effort of many researchers [83, 84]. Baumgart et al. recently showed a correlation between the domain composition and local curvature of a giant unilamellar vesicle by using high-resolution fluorescence imaging [85] and discussed the phase separation (raft formation) in lipid membranes and fission of cells from the viewpoint of the effect of line tension. Moreover, with respect to the line tension at three-phase contacts, experiments inherently have relatively large errors because of the small change in dihedral angles as a function of lens radius [86]. Further extension of the fundamental studies on the relation between molecular structure and the resultant line tension may reveal a new perspective for the fields of nanotechnology and nanoscience as well as the improved experimental techniques of line tension measurement.

Acknowledgement The authors wish to acknowledge the collaborative work of Prof. C.D. Bain and his students with regard to the study on the wetting and freezing transitions. We are also indebted to Prof. B.M. Law who provided support for the interpretation of the line tension results.

References

1. Cahn, J.W.: J. Chem. Phys. **66**, 3667 (1977)
2. Warren, C., Webb, W.W.: J. Chem. Phys. **50**, 3694 (1969)
3. Fisk, S., Widom, B.: J. Chem. Phys. **50**, 3219 (1969)
4. Moldover, M.R., Cahn, J.W.: Science **207**, 1073 (1980)
5. Kahlweit, M., Strey, R.: Angew. Chem. Int. Ed. Engl. **24**, 654 (1985)
6. Shinoda, K.: Prog. Colloid Polymer Sci. **68**, 1 (1983)
7. Kahlweit, M., Strey, R., Haase, D., Kunieda, H., Schmeling, T., Faulhaber, B., Borkovec, M., Eicke, H.-F., Busse, G., Eggers, F., Funcka, Th., Richmanna, H., Magida, L., Södermana, O., Stilbsa, P., Winklera, J., Dittricha, A., Jahn, W.: J. Colloid Interface Sci. **118**, 436 (1987)
8. Kahlweit, M., Busse, G.: J. Chem. Phys. **91**, 1339 (1989)
9. Aratono, M., Kahlweit, M.: J. Chem. Phys. **95**, 8578 (1991)
10. Aratono, M., Kahlweit, M.: J. Chem. Phys. **97**, 5932 (1992)

11. Kahlweit, M., Strey, R., Aratono, M., Busse, G., Schubert, K.V.: J. Chem. Phys. **95**, 2842 (1991)
12. Kahlweit, M., Strey, R., Busse, G.: Phys. Rev. E **47**, 4197 (1993)
13. Robert, M., Jeng, J.-F.: J. Phys. France **49**, 1821 (1988)
14. Chen, L.-J., Jeng, J.-F., Robert, M., Shukla, K.P.: Phys. Rev. A **42**, 4716 (1990)
15. Chen, L.-J., Hsu, M.-C.: J. Chem. Phys. **97**, 690 (1992)
16. Chen, L.-J., Yan, W.-J.: J. Chem. Phys. **98**, 4830 (1993)
17. Chen, L.-J., Yan, W.-J., Hsu, M.-C., Tyan, D.-L.: J. Phys. Chem. **98**, 1910 (1994)
18. Widom, B.: Langmuir **3**, 12 (1987)
19. Gomper, G., Schick, M.: Phys. Rev. Lett. **65**, 1116 (1990)
20. Brochard-Wyart, F., Di Meglio, J.M., Quéré, D., de Gennes, P.G.: Langmuir **7**, 335 (1991)
21. Ragil, K., Meunier, J., Broseta, D., Indekeu, J.O., Bonn, D.: Phys. Rev. Lett. **77**, 1532 (1996)
22. Israelachvili, J.N.: Intermolecular and Surface Forces. Academic, London (1991)
23. Bonn, D., Pauchard, L., Shahidzadeh, N., Meunier, J.: Physica **263**, 78 (1999)
24. Bertrand, E., Dobbs, H., Broseta, D., Indekeu, J.O., Bonn, D., Meunier, J.: Phys. Rev. Lett. **85**, 1282 (2000)
25. Pfohl, T., Riegler, H.: Phys. Rev. Lett. **82**, 783 (1999)
26. Aratono, M., Kawagoe, H., Toyomasu, T., Ikeda, N., Takiue, T., Matsubara, H.: Langmuir **17**, 7344 (2001)
27. Matsubara, H., Ikeda, N., Takiue, T., Aratono, M., Bain, C.D.: Langmuir **19**, 2249 (2003)
28. Wilkinson, K.M., Bain, C.D., Matsubara, H., Aratono, M.: Chem. Phys. Chem. **6**, 547 (2005)
29. Matsubara, H., Aratono, M., Wilkinson, K.M., Bain, C.D.: Langmuir **22**, 982 (2006)
30. Matsubara, H., Shigeta, T., Takata, Y., Ikeda, N., Takiue, T., Aratono, M., Sakamoto, H.: Colloids Surf. A **301**, 141, (2006)
31. Matsubara, H., Ikebe, Y., Ushijima, Y., Takata, Y., Takiue, T., Aratono, M.: Bull. Chem. Soc. Jpn. **83**, 1198 (2010)
32. Wilkinson, K.M., Qunfang, L., Bain, C.D.: Soft Matter **2**, 66 (2006)
33. Sloutskin, E., Sapir, Z., Taman, L., Ocko, B.M., Bain, C.D., Deutsch, M.: Thin Solid Films **515**, 5664 (2007)
34. Sloutskin, E., Sapir, Z., Bain, C.D., Qunfang, L., Wilkinson, K.M., Taman, L., Deutsch, M., Ocko, B.M.: Phys. Rev. Lett. **99**, 136102 (2007)
35. Ocko, B.M., Wu, X.Z., Shirota, E.B., Sinha, S.K., Deutsch, M.: Phys. Rev. E **55**, 3164 (1997)
36. Earnshaw, J.C., Hughes, C.: J. Phys. Rev. A **46**, R4494 (1992)
37. Wu, X.Z., Ocko, B.M., Sirota, E.B., Sinha, S.K., Deutsch, M., Cao, B.M., Kim, M.W.: Science **261**, 1018 (1993)
38. Wu, X.Z., Ocko, B.M., Tang, H., Sirota, E.B., Sinha, S.K., Deutsch, M.: Phys. Rev. Lett. **75**, 1332 (1995)
39. Sefler, G.A., Du, Q., Miranda, P.B., Shen, Y.R.: Chem. Phys. Lett. **235**, 347 (1995)
40. Pfohl, T., Beaglehole, D., Riegler, H.: Chem. Phys. Lett. **260**, 82 (1996)
41. Maeda, N., Yaminsky, V.V.: Phys. Rev. Lett. **84**, 698 (2000)
42. Deutsch, M., Wu, X.Z., Shirota, E.B., Shinha, S.K., Ocko, B.M., Magnussen, O.M.: Europhys. Lett. **30**, 283 (1995)
43. Gang, O., Wu, X.Z., Ocko, B.M., Sirota, E.B., Deutsch, M.: Phys. Rev. E **58**, 6086 (1998)
44. Matsubara, H., Ohtomi, E., Aratono, M., Bain, C.D.: J. Phys. Chem. B **112**, 11664 (2008)
45. Ohtomi, E., Takiue, T., Aratono, M., Matsubara, H.: Colloid Polym. Sci. **288**, 1333 (2010)
46. Rowlinson, S., Widom, B.: Molecular Theory of Capillarity. Oxford University Press, Oxford (1982)
47. Gibbs, J.W.: The Scientific Papers of J. Willard Gibbs. Dover, New York (1961)
48. Stine, K.J., Knobler, C.M., Desai, R.C.: Phys. Rev. Lett. **65**, 1004 (1990)
49. Rivière, S., Hénon, S., Meunier, J., Albrecht, G., Boissonnade, M.M., Baskin, A.: Phys. Rev. Lett. **75**, 2506 (1995)
50. Karatekin, E., Sandre, O., Brochard-Wyart, F.: Polym. Int. **52**, 486 (2003)
51. Churaev, N.V., Starov, V.M.: J. Colloid Interface Sci. **103**, 301 (1985)
52. Denkov, N.D., Petsev, D.N., Danov, K.D.: J. Colloid Interface Sci. **176**, 189 (1995)

53. Rusanov, A.I.: Colloids Surf. A **156**, 315 (1999)
54. White, L.R.: J. Chem. Soc. Faraday Trans. I **73**, 390 (1977)
55. Indekeu, J.O.: Physica (Amsterdam) **183A**, 439 (1992)
56. Dobbs, H.T., Indekeu, J.O.: Physica (Amsterdam) **201A**, 457 (1993)
57. Indekeu, J.O.: Int. J. Mod. Phys. B **8**, 309 (1994)
58. Dobbs, H.: Langmuir **15**, 2586 (1999)
59. Solomentsev, Y., White, L.R.: J. Colloid Interface Sci. **218**, 122 (1999)
60. Wang, J.Y., Betelu, S., Law, B.M.: Phys. Rev. E **63**, 031601 (2001)
61. Scheludko, A., Chakarov, V., Toshev, B.: J. Colloid Interface Sci. **82**, 83 (1981)
62. Toshev, B.V., Platikanov, D., Scheludko, A.: Langmuir **4**, 489 (1988)
63. Siegel, S., Vollhardt, D.: Thin Solid Films **284–285**, 424 (1996)
64. Miranda, J.A.: J. Phys. Chem. B **103**, 1303 (1999)
65. Wurlitzer, S., Steffen, P., Wurlitzer, M., Khattari, Z., Fischer, Th.M.: J. Chem. Phys. **113**, 3822 (2000)
66. Aveyard, R., Clint, J.H.: J. Chem. Soc. Faraday Trans. **92**, 85 (1996)
67. Faraudo, J., Bresme, F.: J. Chem. Phys. **118**, 6518 (2003)
68. Nikolov, A.D., Kralchevsky, P.A., Ivanov, I.B.: J. Colloid Interface Sci. **112**, 122 (1986)
69. Li, D., Cheng, P., Neumann, A.W.: Adv. Colloid Interface Sci. **39**, 347 (1992)
70. Dussaud, A., Vignes-Adler, M.: Langmuir **13**, 581 (1997)
71. Stöckelhuber, K.W., Radoev, B., Schulze, H.: J. Colloids Surf. A **156**, 323 (1999)
72. Wang, J.Y., Betelu, S., Law, B.M.: Phys. Rev. Lett. **83**, 3677 (1999)
73. Wang, J.Y., Betelu, S., Law, B.M.: Phys. Rev. E **63**, 31601 (2001)
74. Pompe, T., Heminghaus, S.: Phys. Rev. Lett. **85**, 1930 (2000)
75. Pompe, T.: Phys. Rev. Lett. **89**, 76102 (2002)
76. Aveyard, R., Clint, J.H., Nees, D., Paunov, V.: Colloid Surf. A **146**, 95 (1999)
77. Takata, Y., Kikuchi, Y., Matsubara, H., Takiue, T., Aratono, M.: Langmuir **21**, 8594 (2005)
78. Takata, Y., Matsubara, H., Kikuchi, Y., Takiue, T., Law, B.M., Aratono, M.: Colloid Polym. Sci. **286**, 647 (2008)
79. Ushijima, Y., Ushijima, B., Ohtomi, E., Takata, Y., Takiue, T., Aratono, M., Matsubara, H.: Colloid Surf. A **390**, 33 (2011)
80. Herminghaus, S., Fery, A., Reim, D.: Ultramicroscopy **69**, 211 (1997)
81. Fery, A., Pompe, T., Herminghaus, S.: J. Adhes. Sci. Technol. **13**, 1071 (1999)
82. Dobbs, H.: Langmuir **15**, 2586 (1999)
83. Chen, P.: Colloid Surf. A **161**, 23 (2000)
84. Widom, B.: Colloid Surf. A **239**, 141 (2004)
85. Baumgart, T., Hess, S.T., Webb, W.W.: Nature **425**, 821 (2003)
86. Tadmor, R.: Surf. Sci. **602**, 108 (2008)

Dynamics of a Complete Wetting Liquid Under Evaporation

C.-T. Pham, F. Lequeux, and L. Limat

1 Introduction

Wetting phenomena have been extensively studied theoretically and experimentally (see [1–4] for reviews and discussions) and much attention has been drawn recently to the case of the dynamics of liquid droplet under evaporation. This problem is motivated by applications (for instance coating [5, 6], deposition near contact line [7], heat exchangers [8, 9]) and by fundamental issues [10]. The local description of a moving contact line is a complicated problem for it involves a singularity of the viscous stresses due to no-slip boundary condition of the liquid on the substrate. The second phenomenon involved in the problem of evaporating contact line is the way the liquid evaporates. Two regimes shall be distinguished: on the first hand, evaporation of the liquid into its own vapor [9, 11, 12]; on the second hand, purely diffusive evaporation of the liquid in an inert surrounding gas [13–16].

In this paper, we restrict ourself to the isothermal problem of a liquid evaporating into inert gas like air. Evaporation is then driven by diffusion. We describe in details a model of contact line under evaporation and total wetting conditions [14] taking into account van der Waals interactions and the divergent nature of evaporation near the border of the liquid as evidenced by Deegan et al. [7, 17] (Sect. 2). We then apply this result to study the dynamics of an evaporating droplet in complete wetting situation (Sect. 3) and compare the results with typical scaling laws of the dynamics of retraction of small droplets found in experiments [13, 18].

C.-T. Pham (✉)
Laboratoire LIMSI, Université Paris-Sud, Orsay, France
e-mail: pham@limsi.fr

F. Lequeux
Laboratoire PPMD, ESPCI & Université P. et M. Curie, Paris, France
e-mail: francois.lequeux@espci.fr

L. Limat (✉)
Laboratoire MSC, Université Paris Diderot, Paris, France
e-mail: laurent.limat@univ-paris-diderot.fr; ldlimat@gmail.com

R.G. Rubio et al. (eds.), *Without Bounds: A Scientific Canvas of Nonlinearity and Complex Dynamics*, Understanding Complex Systems,
DOI 10.1007/978-3-642-34070-3_25,

2 Low Constant Speed Model

In this section, we study the shape of the free surface of an evaporating liquid corner moving at a *constant* velocity V along a totally wetting solid surface, both under the effect of a fluid motion $U(x,z)$ linked to pressure gradient, and of an evaporation flux $J(x)$. The edge of the liquid is set at $x = 0$ (see Fig. 1(left) for notations). We suppose we have translation invariance along the transverse direction.

Standard lubrication theory in the limit of low Reynolds numbers and small interface slope leads to a mean local velocity of the liquid given by: $\langle U \rangle = \frac{1}{h}\int_0^h U(x,z)\mathrm{d}z = -\frac{h^2}{3\eta}\frac{\partial P}{\partial x}$ where $h(x)$ is the liquid thickness, η the liquid viscosity, and the pressure term is

$$P = P_\mathrm{a} + P_\mathrm{c} + P_\mathrm{d} \tag{1}$$

with P_a, the ambient pressure, P_c the capillary pressure and P_d, the disjoining pressure (we assume van der Waals interactions) playing a role at the edge of the liquid. Both latter pressures read respectively $P_\mathrm{c} = -\gamma h_{xx}$ and $P_\mathrm{d} = +\frac{\mathscr{A}}{6\pi h^3}$; γ is the surface tension and $\mathscr{A} < 0$ the Hamaker constant. In this problem, gravity will be neglected. For a liquid moving at constant velocity V, mass conservation imposes that the local thickness $h(x - Vt)$ satisfies

$$\partial_t h + \partial_x(h\langle U\rangle) + J(x) = 0, \tag{2}$$

which leads to:

$$\frac{\partial}{\partial x}\left[h\left(\langle U\rangle - V\right)\right] + J(x) = 0 \tag{3}$$

to be combined with the previous expression of $\langle U\rangle$.

One now needs an approximation of the local evaporation rate distribution $J(x)$. For a sessile axisymmetric drop, Deegan [7] assumed an analogy between vapor diffusion in air and an electrostatic problem, the vapor concentration near the liquid surface being supposed to saturate at the mass concentration in air c^{sat}. In analogy with this work, we assume that very near the edge of the liquid $J(x)$ diverges as $J(x) = J_0 x^{-(\pi/2-\theta)/(\pi-\theta)}$ where x is the distance to the edge. This yields for very small values of angle θ:

$$J(x) \approx J_0/\sqrt{x} \tag{4}$$

in which J_0 is given by

$$J_0 = \frac{D_g}{\sqrt{\lambda}}\frac{c^{\mathrm{sat}} - c^\infty}{\rho} \tag{5}$$

where D_g is the diffusion constant of evaporated liquid in air, and ρ its mass density. The length scale λ can be either the thickness of a diffusive boundary layer, or the typical curvature of the contact line. For instance, for the sessile drops of in-plane radius R with low contact angle considered in [7] one has exactly $\lambda = 2R$. For volatile alkanes or silicon oil drops of millimetric size evaporating in ambient air one typically has $J_0 \approx 10^{-9}\ \mathrm{m}^{\frac{3}{2}}\cdot\mathrm{s}^{-1}$. Note that we are here treating the limit of a

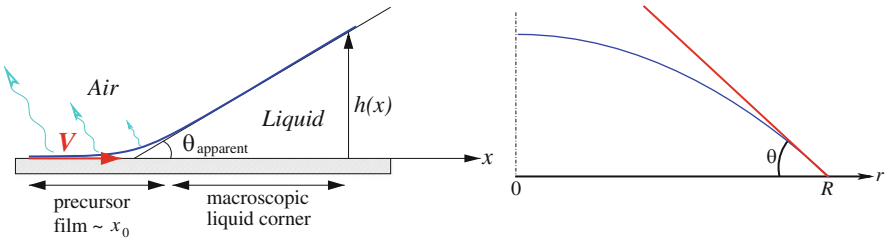

Fig. 1 (*Left*) Notations for the model studied in Sect. 2 of a liquid moving at constant speed V on a totally wetting substrate and undergoing evaporation. (*Right*) Notations used in Sect. 3: R is the droplet radius and θ the apparent contact angle of the spherical cap

liquid evaporating in the presence of air. It is also important to note that the activity of a thin film of liquid is approximately that of the bulk up to the last molecular layer of liquid.Thus the divergence of the evaporative flux holds at the border of the precursor film. In our purely diffusive model, Marangoni and thermal gradients will be neglected.

After integrating once (3) with respect to x, one gets: $(< U > -V)h = -2J_0\sqrt{x}$ that can be written as:

$$V = \frac{2J_0}{h}\sqrt{x} + \frac{\gamma}{3\eta}h^2 h_{xxx} + \frac{\mathscr{A}}{6\pi\eta}\frac{h_x}{h^2} \tag{6}$$

The local thickness of liquid $h(x)$, is supposed to vanish or at least reach microscopic values at the tip of the liquid placed by hypothesis at the location $x = 0$.

The physical meaning of this equation is that the displacement of a liquid at velocity V involves migration under capillary and disjunction pressure gradient together with evaporation itself. This adds new terms to the ordinary differential equation governing $h(x)$, considered years ago by Voinov [19], that reads in this specific case:

$$h_{xxx} = \frac{3\mathrm{Ca}}{h^2} - \frac{6\eta J_0}{\gamma}\frac{\sqrt{x}}{h^3} - \frac{\mathscr{A}}{2\pi\gamma}\frac{h_x}{h^4} \tag{7}$$

where $\mathrm{Ca} = \eta V/\gamma$ is the capillary number built upon the velocity V ($\mathrm{Ca} > 0$ in the receding case and $\mathrm{Ca} < 0$ in the advancing case).

In the framework of this model, it is convenient to set a typical horizontal length scale x_0 and a typical height h_0 that respectively read

$$x_0 = \left(\frac{|\mathscr{A}|}{12\pi J_0\eta}\right)^{\frac{2}{3}}, \qquad h_0 = x_0^{\frac{1}{2}} \times \left(\frac{|\mathscr{A}|}{2\pi\gamma}\right)^{\frac{1}{4}} = \frac{|\mathscr{A}|^{\frac{7}{12}}}{(2\pi)^{\frac{7}{12}}(6\eta J_0)^{\frac{1}{3}}\gamma^{\frac{1}{4}}} \tag{8}$$

Setting $J_0 = 10^{-9}\,\mathrm{m}^{3/2}\cdot\mathrm{s}^{-1}$, $\mathscr{A} = 10^{-19}\,\mathrm{kg}\cdot\mathrm{m}^2\cdot\mathrm{s}^{-2}$, $\eta = 10^{-3}\,\mathrm{kg}\cdot\mathrm{m}^{-1}\cdot\mathrm{s}^{-1}$ yields typical lengths $x_0 \simeq 2\,\mu\mathrm{m}$ and $h_0 \simeq 30\,\mathrm{nm}$. These values have the same

order of magnitude as those found experimentally by Kavehpour et al. [20] in the advancing regime *without* evaporation for $\mathrm{Ca} = 3 \times 10^{-4}$. The horizontal length x_0 corresponds in our model to the typical length of the precursor film at zero velocity.

Equation (7) is third order in derivatives and the uniqueness of its solutions requires the specification of three boundary conditions at the border of the domain $\varepsilon \leq x \leq L_{\max}$. At large scale $L_{\max}$, we impose zero curvature ($h_{xx}(L_{\max}) = 0$). Two other boundary conditions are needed.

A solution vanishing at $x = 0$ that connects to a macroscopic liquid corner $h_{\mathrm{mac}}(x) = \theta_{\mathrm{mac}} \cdot x$ can be found at leading order in the neighborhood of zero as

$$h(x) = \alpha\sqrt{x} \quad \text{with} \quad \alpha^4 = \frac{2}{3\pi}\frac{|\mathscr{A}|}{\gamma} \tag{9}$$

This expression yields a crossover length

$$\ell_{\mathrm{cross}} \sim \frac{1}{\theta_{\mathrm{mac}}^2}\left(\frac{2}{3\pi}\frac{|\mathscr{A}|}{\gamma}\right)^{\frac{1}{2}}. \tag{10}$$

This class of solution has been found as well by Poulard et al. [13] but appears to be non physical [14].

We can search for a second class of solutions that start flat ($h'(0) = 0$) at the origin at the given height $h(0) = h_0$. We can then obtain analytically, the expression of a precursor film the expression of which can be written as

$$H(X) = 1 + \nu_1 X^2 + cX^3 - \frac{8}{105}X^{7/2} + \frac{1}{12}\nu_1 X^4 + o(X^4) \tag{11}$$

with constants c depending on the capillary number and ν_1 insuring zero curvature at large scale. This precursor film connects to a large scale liquid corner profile, the expression of which is

$$\Theta^3(X) = \Theta_{\mathrm{m}}^3 - 9\mathrm{Ca}\left(\frac{x_0}{h_0}\right)^3 \ln\frac{X}{\lambda} + \frac{4}{\Theta_m}\left(\frac{1}{\lambda^{1/2}} - \frac{1}{X^{1/2}}\right) + \beta(X - \lambda) \tag{12}$$

where $X = x/x_0, H = h(x)/h_0, \Theta(X) = H'(X)$ with $\Theta_m \simeq 1$. Constant $\lambda \simeq 3.4$ is the matching coordinate between precursor and liquid corner. Constant β ensures the adequate boundary condition $H_{xx}(L_{\max}) = \Theta_X(L_{\max}) = 0$ (for calculations details, see [5, 14]). Both analytical solutions (9) and (12) can be confirmed numerically using shooting methods. They are plotted in Fig. 2. The agreement is very good [14].

From (12), one can deduce the following expression for the apparent contact angle θ_{app}

$$\theta_{\mathrm{app}}^3 = \theta_{\mathrm{m}}^3 - 9\mathrm{Ca}\left(\log\frac{\mathscr{L}_{\mathrm{macro}}}{\ell_{\mathrm{micro}}} + 1\right) + \frac{24J_0\eta}{\gamma\theta_{\mathrm{m}}}\frac{1}{\sqrt{\ell_{\mathrm{micro}}}} \tag{13}$$

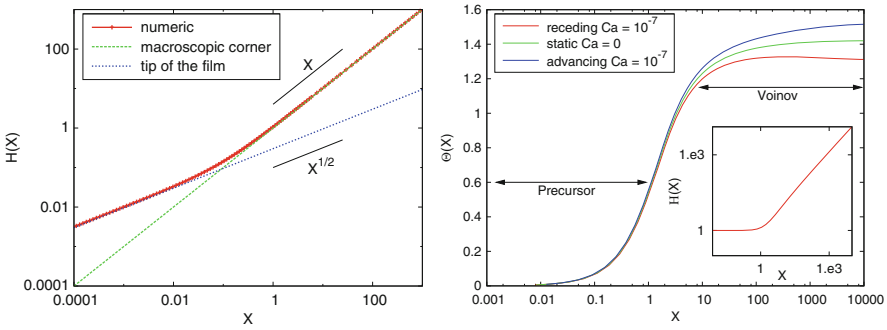

Fig. 2 Numerical solutions of (7) in non dimensional units. (*Left:*) Assuming vanishing height at origin: plot of $H(X)$ (Ca $= +10^{-7}$). Two distinct scalings are observed: linear in the macroscopic domain and parabolic in the microscopic one (see *straight lines*). (*Right:*) Assuming vanishing curvature at large distance (here $X_{\max} = 10^4$) and flat film at the edge of liquid: plot of angle Θ versus X (non dimensional unit). Inset: Corresponding $H(X)$ profile (receding case, same parameter): a macroscopic wedge is connected to a flat precursor film

or in a more simplified way

$$\theta_{\rm app}^3 = \left(1 + \frac{4}{\sqrt{3.4}}\right)\theta_{\rm m}^3 - 9{\rm Ca}\left(\log\frac{\mathscr{L}_{\rm macro}}{\ell_{\rm micro}} + 1\right) \tag{14}$$

where $\ell_{\rm micro} \simeq 3.4x_0$ is a microscopic length corresponding to the length of the precursor film, $\mathscr{L}_{\rm macro}$ a macroscopic length and

$$\theta_{\rm m}^3 = \left(\frac{h_0}{x_0}\right)^3 = \left(\frac{2\pi}{\gamma^3|\mathscr{A}|}\right)^{1/4} 6\eta J_0 \tag{15}$$

corresponding to the apparent contact angle at zero velocity [21]. This law generalizes Tanner's law in the presence of evaporation.

In a study of an evaporating meniscus in complete wetting situation where the coupling between the liquid and the gas is explicitly accounted instead of considering Deegan's electrostatic analogy as we do in this paper, Doumenc et al. derived a similar scaling for the apparent contact angle at zero velocity [16]. In this study, the authors splitted the liquid domain into different parts depending on the magnitude of the different physical effects involved in the problem (evaporation, capillary forces together with van der Waals forces). If we compare our model to theirs, our precursor film corresponds to the region they identify as the precursor film. The zero coordinate that we set as being the edge of the liquid corresponds to the beginning of their adsorbed film region. Note that the thickness we choose is one order of magnitude larger than theirs.

3 Evaporating Sessile Droplet

In this section, we will generalize our previous model and apply it to the study of an evaporating sessile droplet in total wetting condition. As already stated, the expression of the evaporative flux of a spherical cap of liquid of radius R, in the limit of small contact angle θ (see Fig. 1(right)), reads $J(r) = j_0/\sqrt{R^2 - r^2}$ with the following correspondence with previous section: $x = R - r$, $J_0 = j_0/\sqrt{2R}$ and $\mathrm{Ca} = -\eta\dot{R}/\gamma$. Substituting directly these expressions into (14) and (15) yields the following wetting law without any adjustable parameters (but a logarithmic contribution)

$$\theta^3 = \frac{A}{\sqrt{R}} + B\dot{R} \tag{16}$$

with

$$A = 6\left(\frac{\pi}{2}\right)^{1/4}\left(1 + \frac{4}{\sqrt{3.4}}\right)\frac{\eta j_0}{\gamma^{3/4}|\mathscr{A}|^{1/4}} \text{ and } B = 9\frac{\eta}{\gamma}\left(\log\frac{\mathscr{L}_{\mathrm{macro}}}{\ell_{\mathrm{micro}}} + 1\right). \tag{17}$$

This is the same kind of expression as that found by Poulard et al. using other arguments [13], hence we recover the same scaling for apparent angle at zero velocity (that is at maximum radius) $\theta_{\max} \sim R_{\max}^{-1/6}$ while experimental power law is $\theta_{\max} \sim R_{\max}^{-0.45}$.

A small sessile droplet can be considered as a spherical cap. At small contact angle θ, its volume V reads $V = \frac{\pi}{4}R^3\theta$. Under diffusive evaporation, mass conservation reads $\frac{\mathrm{d}V}{\mathrm{d}t} = -\int_0^{2\pi}\int_0^R J(r)r\mathrm{d}r\mathrm{d}\varphi = -2\pi j_0 R$. Combining these two results yields the following relation

$$3R\theta\dot{R} + R^2\dot{\theta} = -8j_0. \tag{18}$$

With (16) and (18) we then obtain a closed set of ordinary differential equations of variables R and θ that entirely governs the dynamics of evaporation of a droplet. We will now study this set of equations numerically.

Given the initial conditions $R_{\mathrm{i}} = R_{|t=0}$ and $\theta_{\mathrm{i}} = \theta_{|t=0}$, we can see using (16) that, whether $(\theta_{\mathrm{i}})^3\sqrt{R_{\mathrm{i}}}$ is larger or smaller than constant A, the droplet starts spreading then retracts, or directly starts with retraction. Experiments show that, if t_{f} is the time at which the droplet vanishes, the radius of a droplet of completely wetting alkane on mica follows the scaling $R(t) \sim (t_{\mathrm{f}} - t)^{\alpha}$ with exponent α close to $1/2$ [13,18]. During the retraction sequence, the contact angle θ has little variations up to late times before total evaporation [13]. Suppose that $R(t)$ scales like $(t_{\mathrm{f}} - t)^{\beta}$, (16) implies that $\beta = 2/3$ if θ is to remain bounded, which is not the case as we will see in the following.

We have performed numerical simulations of (16) and (18) using same physical quantities as in experiments. Results are shown in Fig. 3. The dynamics of spreading

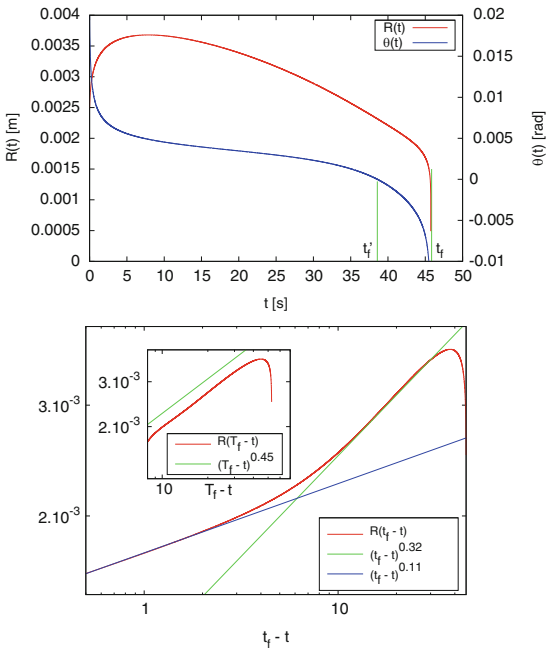

Fig. 3 (*Top*) Plot versus time $t_f - t$ of the radius R of an evaporating totally wetting droplet together with the angle θ. Time t_f corresponds to the time of vanishing radius whereas time t_f' if the time at which angle θ gets to zero. (*Bottom*) Plot of the dynamics of radius R in log–log scale. Depending on the choice of reference final time T_f, one obtains a different scaling and recovers that found in experiments

followed by the retraction sequence of the droplet is recovered with correct orders of magnitude compared with experiments. As in the experiments [13], we recover the steep decrease of the contact angle during the spreading and the beginning of the retraction. Radius vanishes at a given final time t_f. In contrast, contact angle θ vanishes at time $t_f' < t_f$ (the spherical cap then becomes flat) and eventually becomes negative which is physically incorrect. This vanishing angle singularity is intrinsic to our wetting law model but experiments by Cazabat et al. also display sharp decrease of the contact angle at late times.

If one looks carefully at the decay of the radius $R(\tau)$ with time $\tau = t_f - t$ (see Fig. 3(top)), one can see that the radius follows two regimes with distinct exponents. At the beginning of the retraction, $R(\tau) \sim \tau^{\alpha}$ with $\alpha \simeq 0.33$, then, once the values of θ becomes negative, we have $R(\tau) \sim \tau^{\beta}$ with $\beta \simeq 0.11$. These scalings are in disagreement with the experiments where exponents are close to $1/2$. Nevertheless, by choosing a shifted reference final time T_f (see inset of Fig. 3(bottom)), one can recover an exponent $\alpha' \simeq 0.45$ in agreement with experiments, as did Poulard et al. in their numerical simulations as well [13].

Note that our wetting law (16) contains a logarithmic term depending on a macroscopic scale $\mathscr{L}_{\text{macro}}$, at which contact angle is defined. Replacing the latter length scale by a fraction of radius R modifies the wetting law and shall delay the singularity (the smaller $\mathscr{L}_{\text{macro}} \sim R$, the smaller constant B). We performed numerical simulations of the dynamics using this modified wetting law and found no major changes in the dynamics: the final time of singularity is slightly shifted but the scaling exponents remain the same (data not shown).

The wetting law described by (14) only catches the early dynamics of spreading and retraction of the droplet. Indeed this analytical model was derived in the hypothesis of translational invariance along transverse direction, constant speed limit and zero curvature at large scale which is not realistic for a spherical cap. Moreover, small capillary numbers were assumed whereas speed of retraction diverges at late times. In this context, the apparent contact angle in our model cannot remain finite. Yet simple, our model shall be modified in order to properly solve the whole dynamics of evaporation.

As a comparison, note that Eggers et al. [15] numerically studied the evaporation of a sessile droplet by coupling the hydrodynamics of the droplet with a self-consistent description of evaporation from the drop and the precursor film in a similar approach as Doumenc et al. [16]. They recovered the scaling of the late time radius $R \sim (t_0 - t)^{\alpha}$ with $\alpha \simeq 1/2$. However, no wetting law for apparent contact angle was proposed. In some cases, dominant drying from the middle of the drop is even found at late times, the drops loses its spherical shape and is depleted at the center. This phenomenon is reminiscent of the negative values of apparent contact angle found in our model.

4 Conclusion

In this paper, we have described a model for completely wetting liquid under diffusive evaporation taking into account the divergent nature of the evaporative flux. A wetting law relating the apparent contact angle to the speed of the contact line was proposed and tentatively used to numerically study the dynamics of an evaporating droplet in total wetting conditions. This model correctly describes the early stages of spreading and retraction of a droplet. However, at late times, the contact angle vanishes before the radius vanishes itself, yielding non-physical scalings. Usual dynamical scalings found in experiments can only be recovered by extrapolating a final reference time.

Acknowledgement The authors acknowledge support from ANR (DEPSEC 05-BLAN-0056-01) and wish to thank G. Berteloot, A. Boudaoud, P. Colinet, A. Daerr, F. Doumenc, J. Eggers together with A. Rednikov for enlightening discussions.

References

1. de Gennes, P.-G.: Wetting: statics and dynamics. Rev. Mod. Phys. **57**, 827 (1985)
2. Bonn, D., Eggers, J., Indekeu, J., Meunier, J., Rolley, E.: Wetting and spreading. Rev. Mod. Phys. **81**, 739 (2009)
3. Starov, V.M., Velarde, M.G., Radke, C.J.: Wetting and Spreading Dynamics. CRC Press, Boca Raton (2007)

4. Velarde, M.G. (ed.): Discussion and debate: weting and spreading science - quo vadis? Eur. Phys. J. Spec. Top. **197** (2011)
5. Berteloot, G., Pham, C.-T., Daerr, A., Lequeux, F., Limat, L.: Evaporation induced flow a near contact line: consequences on coating and contact angle. Europhys. Lett. **83**, 14003 (2008)
6. Qu, D., Ramé, E., Garoff, S.: Dip-coated films of volatile liquids. Phys. Fluids **14**, 1154 (2002)
7. Deegan, R.D., Bakajin, O., Dupont, T.F., Huber, G., Nagel, S.R., Witten, T.A.: Contact line deposits in an evaporating drop. Phys. Rev. E **62**(1), 756–765 (2000)
8. Ajaev, V.S.: Spreading of thin volatile liquid dorplets on uniformly heated surfaces. J. Fluid Mech. **528**, 279 (2005)
9. Panchamgam, S.S., Gokhale, S.J., Plawsky, J.L., DasGupta, S., Wayner, P.C. Jr.: Experimental determination of the effect of disjoining pressure on shear in the contact line region of a moving evaporating thin film. J. Heat. Transf. **127**, 231 (2005)
10. Pomeau, Y.: Contact line moving on a solid. Eur. Phys. J. Spec. Top. **197**, 15 (2011)
11. Rednikov, A.Y., Colinet, P.: Vapor-liquid steady meniscus at a superheated wall: asymptotics in an intermediate zone near the contact line. Microgravity Sci. Technol. **22**, 249 (2010)
12. Semenov, S., Starov, V.M., Rubio, R.G., Agogob, H., Velarde, M.G.: Evaporation of sessile water droplets: universal behaviour in presence of contact angle hysteresis. Colloids Surf. A Physicochem. Eng. Asp. **391**, 135 (2011)
13. Poulard, C., Guéna, G., Cazabat, A.M., Boudaoud, A., Ben Amar, M.: Rescaling the dynamics of evaporating drops. Langmuir **21**, 8226–8233 (2005)
14. Pham, C.-T., Berteloot, G., Lequeux, F., Limat, L.: Dynamics of complete wetting liquid under evaporation. Europhys. Lett. **92**, 54005 (2010)
15. Eggers, J., Pismen, L.M.: Non local description of evaporating drops. Phys. Fluids **22**, 112101 (2010)
16. Doumenc, F., Guerrier, B.: A model coupling the liquid and gas phases for a totally wetting evaporative meniscus. Eur. Phys. J. Spec. Top. **197**, 281 (2011)
17. Deegan, R.D., Bakajin, O., Dupont, T.F., Huber, G., Nagel, S.R., Witten, T.A.: Capillary flow as the cause of ring stains from dried liquid drops. Nature **389**, 827 (1997)
18. Shahidzadeh-Bonn, N., Rafai, S.C., Azouni, A., Bonn, D.: Evaporating droplets. J. Fluid Mech. **549**, 307 (2006)
19. Voinov, O.V.: Hydrodynamics of wetting. Fluid Dynam. **11**, 714 (1976)
20. Kavehpour, H.P., Ovryn, B., McKinley, G.H.: Microscopic and macroscopic structure of the precursor layer in spreading viscous drops. Phys. Rev. Lett. **91**, 196104 (2003)
21. Pham, C.-T., Berteloot, G., Lequeux, F., Limat, L.: Dynamics of complete wetting liquid under evaporation (Erratum). Europhys. Lett. **93**, 69901 (2011)

Evaporation of Sessile Droplets of Liquid on Solid Substrates

S. Semenov, V.M. Starov, M.G. Velarde, and R.G. Rubio

1 Introduction

The process of evaporation of sessile droplets is of interest for both industry and academia. It is often difficult to study the evaporation process and related effects experimentally [1], as this phenomenon is controlled by a number of external conditions. Thus computer simulations are used alongside with experimental investigations to study this complex phenomenon. There are also a number of other general problems related to evaporating droplets. Some of them require a consideration of a droplet as an integral part of a wider problem, such as spray dynamics [2]. Sometimes it is required to predict the solidification in the course of evaporation including formation of hollow shells [3]. Also the residue from dried drops [4–6] has implications for a number of applications, including painting, coating processes, ink-jet printing, DNA chip manufacturing [7], formation of arrays of organic materials for video displays and photo sensors, fabrication a variety of micro-electro-mechanical (MEMS) devices [8]. The analysis of the influence of properties of solid substrates on the evaporation rate of sessile droplets can be used for production of various materials providing an optimal regime of work for air conditioners, dryers and cooling systems [9].

S. Semenov · V.M. Starov (✉)
Department of Chemical Engineering, Loughborough University, Loughborough, UK
e-mail: s.semenov@lboro.ac.uk; v.m.starov@lboro.ac.uk

M.G. Velarde
Instituto Pluridisciplinar, UCM, Paseo Juan XXIII, 1, Madrid 28040, Spain

R.G. Rubio
Department of Química Física I, Facultad de CC. Químicas, UCM, Madrid 28040, Spain

R.G. Rubio et al. (eds.), *Without Bounds: A Scientific Canvas of Nonlinearity and Complex Dynamics*, Understanding Complex Systems,
DOI 10.1007/978-3-642-34070-3_26,

2 Stages of Sessile Droplet Evaporation

Evaporation starts immediately after a deposition of a liquid droplet onto a solid substrate in non-saturated vapour atmosphere. In the case of complete wetting (equilibrium contact angle θ is zero) the evaporation process is accompanied by spreading. The whole process can be subdivided into two stages: (a) an increase of the solid–liquid contact area cause by spreading, and (b) a decrease of the solid–liquid contact area caused by evaporation. Stage (a) is usually proceeds much faster than stage (b).

In the case of partial wetting (contact angle $0° < \theta < 90°$) after a deposition of a droplet onto a solid surface, the whole process can be subdivided into the following four stages. Stage (0): a short spreading stage, when the solid–liquid contact area increases until contact angle, θ, reaches its static advancing value, θ_{ad}. This stage is accompanied by the evaporation, but due to different time scales of spreading and evaporation processes (spreading is much faster) the influence of evaporation during the spreading stage is negligible. Evaporation cannot be neglected during next stages. In the presence of contact angle hysteresis the latter process occurs in three stages [10, 11]. (i) During the first stage evaporation proceeds with a constant radius of the contact line, L, and decreasing contact angle, θ, until the contact angle reaches the static receding value, θ_r. (ii) The next stage of evaporation develops with a constant contact angle, θ_r, and decreasing radius of the contact line, L. (iii) During the third stage both the radius of the contact line, L, and the contact angle, θ, decrease until the droplet disappears. Stages (i) and (ii) are usually the longest ones, while the last third stage is the shortest one and is the most difficult for experimental investigations.

3 Dependence of Evaporation Flux on the Droplet Size

Most of the theoretical and computer simulation studies [12–17] assume the spherical shape of the cap of a sessile droplet. This is true only for small enough ($L < 1$ mm) droplets, when the capillary forces dominate over the body forces (e.g. gravity forces). In the case of diffusion controlled evaporation the latter model give the following equation for the evaporation rate of a sessile droplet:

$$\frac{dV}{dt} = -\beta L F(\theta), \tag{1}$$

$$F(\theta) = \begin{cases} (0.6366 \cdot \theta + 0.09591 \cdot \theta^2 - 0.06144 \cdot \theta^3)/sin\theta, & \theta < \pi/18 \\ (0.00008957 + 0.6333 \cdot \theta + 0.116 \cdot \theta^2 - 0.08878 \cdot \theta^3 & \\ \qquad + 0.01033 \cdot \theta^4)/sin\theta, & \theta > \pi/18 \end{cases} \tag{2}$$

where V is the droplet volume; t is time; F is a function of contact angle, derived by Picknett and Bexon [13], which equals 1 at $\theta = \pi/2$ (θ is in radians in (2));$\beta = 2\pi \frac{DM}{\rho}\left[c_{sat}(T_{surf}) - c_\infty\right]$; D is the diffusion coefficient of vapour in air; M is the molecular weight of the evaporating substance; ρ is the density of the liquid; c_{sat} is the saturated value of the molar concentration of vapour, considered as a function of uniform temperature, T_{surf}, of the droplet's surface; c_∞ is the molar vapour concentration in the ambient air far away from the droplet. Note that (1) is deduced using the model which takes into account only vapour diffusion in the surrounding air and ignores the temperature distribution along the droplet–air interface. If contact angle, θ, is constant (evaporation stage (ii) in case of contact angle hysteresis), then (1) gives the evaporation rate proportional to the first power of the contact line radius, L.

We showed earlier [18] that proportionality of the total evaporation flux, J, to the droplet perimeter has nothing to do with a distribution of the local evaporation flux, j, over the droplet surface. Let us reproduce the derivation of that statement by considering a stationary diffusion equation for vapour in air:

$$\frac{1}{r}\frac{\partial}{\partial r}\left(r\frac{\partial c}{\partial r}\right) + \frac{\partial^2 c}{\partial z^2} = 0, \tag{3}$$

where, r and z are radial and vertical coordinates, respectively; c is the molar vapour concentration. The local flux, j, in normal direction to the droplet's surface is

$$j = -D\frac{\partial c}{\partial \mathbf{n}}\Big|_{z=h(r)} = -D\left(\frac{\partial c}{\partial r}\Big|_{z=h(r)} n_r + \frac{\partial c}{\partial z}\Big|_{z=h(r)} n_z\right), \tag{4}$$

where D is the diffusion coefficient of vapour in the air; $\mathbf{n}$, n_r and n_z are unit vector normal to the liquid–air interface (pointing into the air), and its radial and vertical components, respectively; $h(r)$ is the height of the droplet surface. Let us introduce dimensionless variables using the same symbols as the original dimensional ones but with an over-bar: $\bar{z} = z/L$, $\bar{r} = r/L$, $\bar{h} = h/L$, $\bar{c} = c/\Delta c$, $\Delta c = c_{sat}(T_{surf}) - c_\infty$. Then (4) can be rewritten as:

$$j = -\frac{D\Delta c}{L}\left(\frac{\partial \bar{c}}{\partial \bar{r}}\Big|_{z=\bar{h}(\bar{r})} n_r + \frac{\partial \bar{c}}{\partial \bar{z}}\Big|_{z=\bar{h}(\bar{r})} n_z\right) = \frac{D\Delta c}{L} A(\bar{r}, \bar{z}), \tag{5}$$

where $A(\bar{r}, \bar{z}) = -\frac{\partial \bar{c}}{\partial \bar{r}}\Big|_{z=\bar{h}(\bar{r})} n_z$. Hence, the total flux is

$$J = 2\pi \int_0^L rj\sqrt{1 + \left(\frac{\partial h}{\partial r}\right)^2}\, dr = 2\pi L D\Delta c \int_0^1 \bar{r} A(\bar{r}, \bar{z})\sqrt{1 + \left(\frac{\partial \bar{h}}{\partial \bar{r}}\right)^2}\, d\bar{r}. \tag{6}$$

The latter equations show that the total flux, $J \approx L$, and the local flux $j \approx 1/L$. Note, those properties do not depend on the distribution of the local evaporation flux, j, over the droplet surface. The latter conclusions agree with the previous consideration by Guena et al. [19]. Note, that the latter properties are valid only in case of diffusion controlled evaporation.

4 Distribution of Evaporation Flux at the Droplet Surface

It was shown above that the proportionality of total evaporation flux, J, to the radius of the contact line, L, and accordingly its proportionality to the perimeter of the droplet does not necessary mean that evaporation occurs mostly at the droplet perimeter. However, a number of researches showed that in case of contact angles $\theta < 90°$ the evaporation indeed is more intensive in a vicinity of the three phase contact line. Several different principles were utilised in order to explain this phenomenon: (a) non-uniform distribution of vapour flux over the droplet surface due to the diffusion controlled process of vapour transfer to the ambient air [4–6]; (b) action of Derjaguin's (disjoining/conjoining) pressure at the three phase contact line [20–23]; (c) evaporative cooling of the liquid–gas interface (due to latent heat of vaporization) and formation of the temperature field leading to a comparatively more intensive evaporation at the three phase contact line [24].

Deegan et al. [4, 5] studied the distribution of density of vapour flux over the spherical cap of a sessile droplet, solving the diffusion equation and neglecting the latent heat of vaporization and thermocapillary flow inside the droplet. The obtained solution for the droplets with contact angles $\theta < 90°$ shows an infinite increase of the vapour flux in a vicinity of the three phase contact line. Such distribution of the flux, according to the authors, generates the flow inside the droplet, which transports particles to the edge of the droplet and results in a ring-like stain formation (coffee rings).

Starov and Sefiane [24] suggested a physical mechanism of redistribution of evaporation flux which is controlled by the temperature field rather than by the process of vapour diffusion into air. According to their model, there is convection in the ambient air, so that vapour diffusion occurs only in a boundary layer. If the thickness of the boundary layer, δ, is constant then the vapour diffusion across the layer is controlled by the difference of vapour concentrations in the ambient air and at the droplet surface. The latter is a function of the local temperature of the droplet's surface. In the model under consideration [24] the surface of a droplet is cooled by the evaporation; meanwhile due to the high heat conductivity of the substrate the temperature of the contact line is stayed equal to the ambient one. As a result the higher temperature at the three phase contact line gives higher vapour concentration and more intensive evaporation flux at the droplet's perimeter (see Fig. 1).

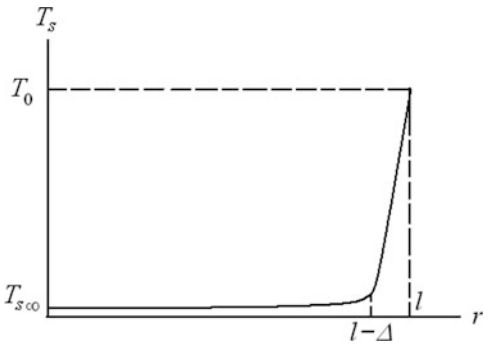

Fig. 1 Temperature distribution over the droplet surface, $T_s(r)$. r is the radial coordinate; T_0 is the temperature of the substrate; $T_{s\infty}$ is the temperature of the droplet surface at which the evaporation flux vanishes; l is the contact line radius; Δ is a tiny area within the vicinity of the three phase contact line, where evaporation mostly takes place [24]

5 Thermal Marangoni Convection

Studies of evaporation of droplets with contact angles $\theta < 120°$ were performed by Girard et al. [12, 14–17] and Hu and Larson [25–28]. Girard et al. investigated the influence of substrate heating [16, 17], air humidity [16] and Marangoni convection [12]. They concluded that contribution of Marangoni convection to the total vapour flux is negligible, whereas heating of the substrate is important. Hu and Larson investigated the process of particles deposition and ring-like stain formation during the droplet evaporation [25–27]. They concluded that the density profile of the particles deposit substantially depends on the Marangoni convection within the sessile droplet [28]. If Marangoni convection is present, then it results in a particle deposition at the droplet centre rather than at the edge. According to authors, the suppression of Marangoni convection is the one of the important conditions for ring-like deposit formation.

Ristenpart et al. [29] investigated the influence of the substrate conductivity on reversal of Marangoni circulation within evaporating sessile droplet. They neglected the thermal conductivity of the surrounding air. The authors used predefined distribution of evaporation flux over the droplet surface:

$$j(r) = j_0 \left[1 - (r/L)^2\right]^{-1/2+\theta/\pi}, \tag{7}$$

where j_0 is a constant determined by the diffusivity of vapour in the ambient air and the ambient humidity, r is the radial coordinate. This expression for $j(r)$ (a) is not applicable for contact angles $\theta > \pi/2$, and (b) introduces the singularity at the three phase contact line: $j(L)\big|_{\theta<\pi/2} = \infty$. Despite of these assumptions made by authors, their quantitative criteria for the circulation direction was experimentally confirmed.

Earlier [18, 30] we used numerical simulations to investigate instantaneous distribution of heat and mass fluxes in the system consisting of a single sessile droplet of a pure liquid, substrate, and surrounding air. Self-consistent system of equations was solved including Navier–Stokes equations inside the droplet; heat transfer equations in substrate, droplet and gas; and vapour diffusion in the surrounding air. Latent heat of vaporization and thermal Marangoni convection were taken into account. It is shown in [18, 30] that presence of Marangoni convection results in deviations from the earlier deduced laws for both local evaporation flux $j \sim L^{-1}$ and total evaporation flux, $J \sim L$. Note, the latter dependences were deduced for isothermal evaporation. If the mean temperature of the droplet surface is used instead of the temperature of the surrounding air for the vapour concentration on the droplet surface then the calculated dependences for the total evaporation flux coincide with those calculated for the isothermal case [18, 30].

6 Influence of Heat Conductivity

It is well known that evaporation process consumes heat due to the latent heat of vaporization. Because of that the droplet's surface cools down and a heat flux from the surface is generated to compensate for heat losses. As the heat conductivities of the droplet liquid and substrate material are much higher than that of air then the major part of the heat flux goes through the droplet and substrate. Thus the heat conductivities of liquid and substrate define the temperature drop at the droplet surface. From the other hand the temperature of the droplet surface defines the value of saturated vapour concentration (in case of diffusive model of evaporation) and hence the evaporation rate. Dunn et al. [31, 32] solved the coupled problem of vapour diffusion and heat transfer for the evaporation of sessile droplets of different liquids on substrates with different thermal properties. They demonstrated both experimentally and numerically that the heat conductivity of the substrate strongly influences the evaporation rate. Decreasing the heat conductivity of the substrate causes a decrease of the evaporation rate.

7 Ring-Like Stain Formation

The formation of ring-like stains during the droplet evaporation has been studied by a number of scientists. Deegan et al. [5] studied deposition of particles in a vicinity of the three phase contact line contact line and reasons for this phenomenon. The authors concluded that formation of ring-like stains requires "a weakly pinning substrate and evaporation". Hu and Larson [28] reported that formation of such deposits requires not only a pinned contact line but also suppression of Marangoni flow. They demonstrated of deposit in the centre of the droplet.

Bhardwaj et al. [6] solved numerically a complex problem of drying of droplets of colloidal solutions and deposits formation. Their model takes into account the Navier–Stokes equations, convection and conduction heat transfer equations, Marangoni convection and receding of the three phase contact line. The interaction of the free surface with the peripheral deposit and eventual depinning were also simulated. The diffusion of vapour in the atmosphere was solved numerically, providing an exact boundary condition for the evaporative flux at the droplet–air interface. The formation of different deposit patterns both theoretically and experimentally the possibility of Marangoni flow reverse and formation obtained experimentally is explained by their simulations.

8 Complete Wetting

In the case of complete wetting droplets spread out completely over a solid substrate, and contact angle decreases down to zero value. Lee et al. [33] considered process of simultaneous spreading and evaporation of sessile droplets in the case of complete wetting. In order to model the spreading they [33] considered Stokes equations under a low slope approximation. For the modelling of evaporation the proportionality of the total evaporation flux, J, to the contact line radius, L, was assumed. The whole process of spreading/evaporation was divided into two stages: (a) a first fast but short stage spreading stage, when the evaporation can be neglected, and the droplet volume, V, is approximately constant; (b) a second slower stage, when the spreading process is almost over, contact angle approximately constant, and evolution is determined by the evaporation. On the basis of this analysis the contact line radius, L, is considered as a function of the droplet volume, V, and contact angle, θ. Time derivative of $L(V, \theta)$ gives two velocities of the contact line:

$$\frac{dV(V,\theta)}{dt} = \frac{\partial L(V,\theta)}{\partial \theta}\frac{d\theta}{dt} + \frac{\partial L(V,\theta)}{\partial V}\frac{dV}{dt} = v_+ - V_-, \tag{8}$$

where v_+ is the spreading velocity, and v_- is the "shrinkage" velocity due to the evaporation:

$$v_+ = \frac{dL(V,\theta)}{dt}|_{V\approx const} = \frac{\partial L(V,\theta)}{\partial \theta}\frac{d\theta}{dt}, \tag{9}$$

$$v_- = -\frac{dL(V,\theta)}{dt}|_{\theta\approx const} = -\frac{\partial L(V,\theta)}{\partial V}\frac{dV}{dt}. \tag{10}$$

The spreading velocity of the contact line, v_+, is obtained by Starov et al. in [34]:

$$v_+ = 0.1\left(\frac{4V}{\pi}\right)^{0.3}\left(\frac{10\gamma\omega}{\mu}\right)^{0.1}\frac{1}{(t+t_0)^{0.9}}, \tag{11}$$

where γ is the surface tension of the liquid; μ is the dynamic viscosity of the liquid; ω is the effective lubrication parameter [35]; t_0 is the duration of the initial stage of spreading when the capillary regime of spreading is not applicable [34]. Equation (11) is derived from (9) using the formula for $L(t)$ obtained by Starov et al. in [35]:

$$L(t) = L_0 \left(1 + t/\tau\right)^{0.1}, \tag{12}$$

where L_0 is the droplet base radius after the very fast initial stage is over; $\tau = \frac{3\mu L_0}{10\gamma}\left(\frac{\pi\gamma L_0^3}{4V}\right)^3$; λ is the dimensionless constant [35] connected to the effective lubrication parameter ω [35]. The velocity v_- is obtained from (10) using (1):

$$v_- = \frac{\beta F(\theta) L^2}{3V}. \tag{13}$$

Substituting (11) and (13) into (8) leads to the following equation:

$$\frac{dL}{dt} = 0.1\left(\frac{4V}{\pi}\right)^{0.3}\left(\frac{10\gamma\omega}{\mu}\right)^{0.1}\frac{1}{(t+t_0)0.9}^{-}\frac{\beta F(\theta) L^2}{3V}. \tag{14}$$

The latter gives a system of two differential (1) and (14) with following boundary conditions [33]:

$$V(0) = V_0, \tag{15}$$

$$L(0) = L_0 = \left[\frac{10\gamma\omega}{\mu}\left(\frac{4V_0}{\pi}\right)^3\right]^{0.1} t_0^{0.1}, \tag{16}$$

where V_0 is the initial droplet volume and L_0 is the contact line radius after the very fast initial stage is over. Solution of this system of equation in non-dimensional form gives a universal law of process of simultaneous spreading and evaporation for the case of complete wetting, which was validated against experimental data from various literature sources [33] (see Figs. 2 and 3).

9 Partial Wetting and Contact Angle Hysteresis

Earlier in [36] we discussed the evaporation of sessile water droplets in the presence of contact angle hysteresis. Model presented in [36] describes non-isothermal diffusion limited evaporation. It takes into account latent heat of vaporization, heat transfer in solid, liquid and gas phases, and thermal Marangoni convection in water droplet. The rate of diffusion limited evaporation depends on vapour concentration in the ambient air and on concentration of the saturated vapour over the droplet's surface. The latter depends on surface temperature. Thus we decided to compare evaporation rate, J, from our computer simulations [18] with the one calculated using (1), but substituting the average temperature, T_{av}, of the droplet's surface

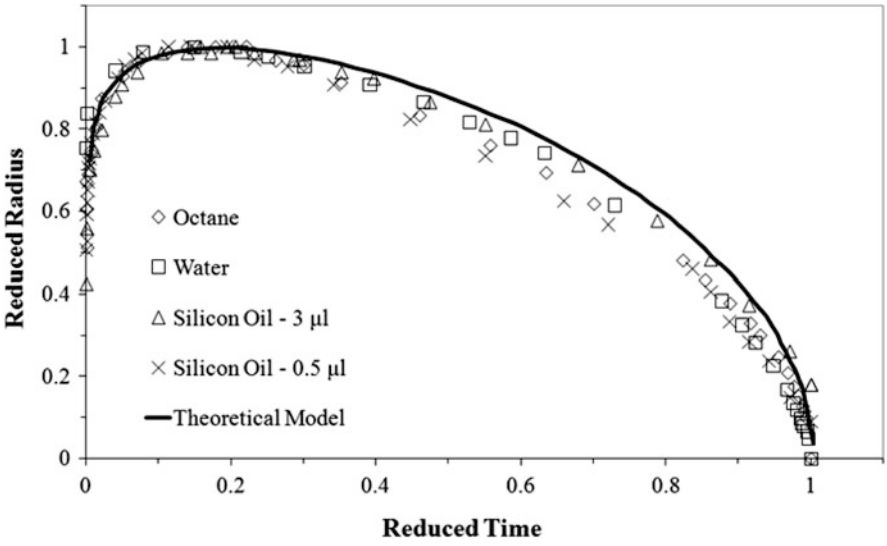

Fig. 2 Spreading/evaporation in the case of complete wetting: dimensionless radius against dimensionless time comparing different liquid droplets spreading/evaporating on solid substrates. Experimental points from various literature sources and the *solid line* according to the theoretical prediction [33]

obtained from computer simulations, instead of T_{surf}. These two evaporation rates coincide within the simulation error bar [18]. Thus (1) with new parameter β

$$\beta 2\pi \frac{DM}{\rho} \left[c_{sat}\left(T_{av}\right) - c_{\infty}\right], \tag{17}$$

where T_{av} is the average temperature of the droplet's surface, provides a very good approximation of the droplet's evaporation rate for non-isothermal case.

The average temperature, T_{av}, of the droplet's surface depends on thermal conductivities of all phases, on ambient temperature, T_{∞}, air humidity, H, and contact angle, θ, formed by the droplet in contact with a substrate. In absence of external heating or cooling of the substrate, T_{av} can be approximated with the following expression (when T_{∞} is close to 20°C) [36]:

$$T_{av} = T_{surf}\,\big|_{k_s=0\theta=\pi/2} + \frac{T_{\infty} - T_{surf}\,\big|_{k_s=0\theta=\pi/2}}{1 + F(\theta)\left[\left(k_a/k_w\right)\left(sin\theta - 0.75\theta + 4.61\right)\right]}, \tag{18}$$

where function $F(\theta)$ is defined by (2); k_a, k_w and k_s are thermal conductivities of air, water droplet and substrate, respectively; $T_{surf}\,\big|_{k_s=0\theta=\pi/2}$ is the root of (19) with respect to T_{surf}:

$$\Lambda D\left[c_{sat}\left(T_{surf}\right) - Hc_{sat}\left(T_{\infty}\right)\right] = k_a\left(T_{\infty} - T_{surf}\right), \tag{19}$$

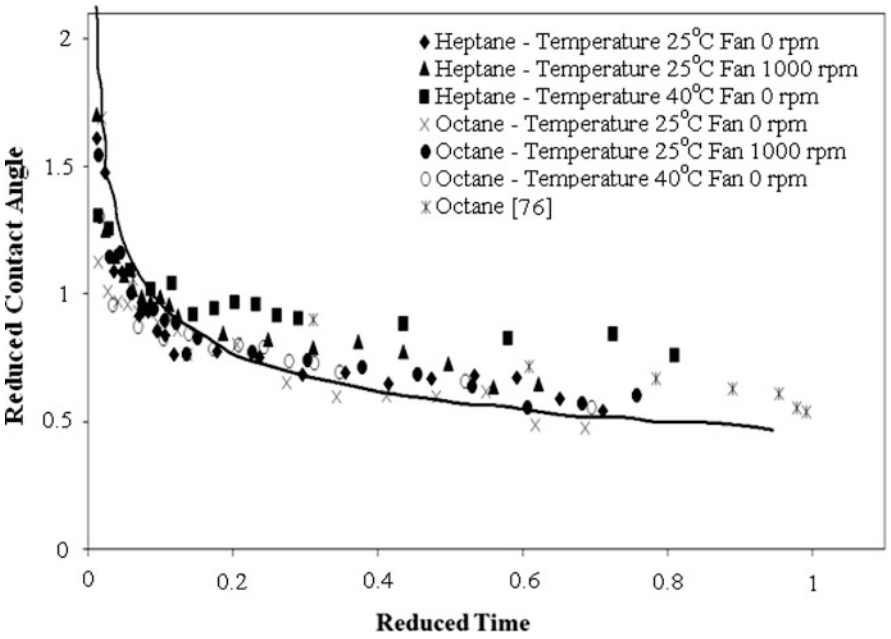

Fig. 3 Spreading/evaporation in the case of complete wetting: dimensionless contact angle against dimensionless time curve for the behaviour of the droplet radius (see Fig. 2) comparing theoretical (*solid curve*) and experimental data (*symbols*) [33]

where D is the diffusion coefficient of vapour in air, Λ is the latent heat of vaporization (in J/mol). Equation (19) represents the relation between diffusive evaporation rate and conductive heat flux through the air (air convection is neglected in [36]), in case when thermal conductivity of the substrate, k_s, is zero and contact angle is 90°, which results in absence of heat transfer through the substrate and the droplet.

Using (1) with the new parameter β, see (17), and assuming that β is almost constant during the process of droplet evaporation [36], allowed us to develop a theory describing stages of the process of sessile droplet evaporation in case of contact angle hysteresis (i), constant radius of the droplet base, $L = L_0$, but the contact angle decreases over time from the static advancing contact angle down to static receding contact angle; and (ii), constant contact angle, θ, equals to the static receding contact angle but radius of the droplet base decreases over time. Results have been compared with the experimental data from literature for evaporation of water droplets on different substrates. First, experimental data for stage (i) have been fitted with the theoretical curve by adjusting unknown parameter β. Then the same values of β have been used for plotting theoretical curves of stage (ii), which showed very good agreement with experimental data (see Fig. 4).

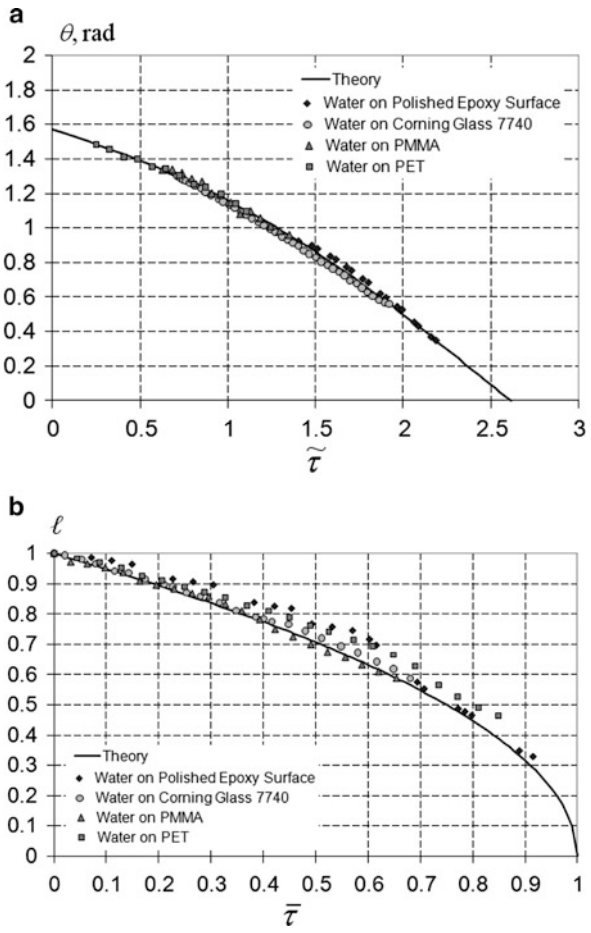

Fig. 4 Evaporation of sessile droplets of water on different substrates in case of partial wetting with contact angle hysteresis: comparison of theoretical curves (solution of (1) with β from (17)) with experimental data. (**a**) stage (i) of the evaporation process, when contact line radius is constant $L = L_0$. (**b**) stage (ii) of the evaporation process, when contact angle is constant and equal its static receding value θ_r. $\ell = L/L_0$ is the non-dimensional contact line radius. $\tilde{\tau}$ and $\bar{\tau}$ are non-dimensional times for stages (i) and (ii) respectively. Redrawn from [36]. Experimental data are taken from [10, 37, 38]

In Fig. 4 non-dimensional times are defined as follows:

$$\tilde{\tau} = \tau + B\left(\theta_{ad}\right),$$

$$\bar{\tau} = \frac{2F(\theta_r)}{3f(\theta_r)}\left(\tau - \tau_r\right),$$

where $\tau = t\beta/L_0^2$; L_0 is the value of L during the first evaporation stage (i); $B(\theta) = \int_\theta^{\pi/2} f'(\theta)/F(\theta)d\theta$; $f'(\theta) \equiv df(\theta)/d\theta$; $F(\theta)$ is defined by (2); τ_r is the value of τ at the beginning of stage (ii), when receding of the contact line starts; $f(\theta) = \frac{V}{L^3} = \frac{\pi}{3}\frac{(1-cos\theta)^2(2+cos\theta)}{sin^3\theta}$ under assumption of a spherical cap shape of the droplet.

10 Kelvin's and Kinetic Effects

Below we studied the influence of kinetic effects on evaporation of pinned sessile water droplets of submicron size on copper substrate. The model takes into account the influence of curvature of the droplet's surface (Kelvin's equation for the pressure of saturated vapour above a curved liquid–gas interface) on total evaporation rate, J.

Kinetic effects are included into model using Hertz–Knudsen–Langmuir equation, (20), for local evaporation/condensation flux at the droplet–air interface as a boundary condition for the diffusion equation of vapour in air:

$$j_m = \alpha_m \sqrt{\frac{MRT}{2\pi}} \left[c_{sat}(T) - c \right], \tag{20}$$

where j_m is the surface density of mass flux across the droplet–air interface in direction from liquid to air; α_m is the mass accommodation coefficient (probability that uptake of vapour molecules occurs upon collision of those molecules with the liquid surface); R is the universal gas constant; T and c are the local temperature in °K and molar vapour concentration at the liquid–gas interface, respectively; M is the molecular weight of the evaporating substance; c_{sat} is the molar concentration of saturated vapour at the droplet–air interface.

Equation (20) is based on the kinetic theory of gases and it links evaporation flux, j_m, with local vapour concentration, c, and local temperature, T, at the liquid–air interface.

The model also includes thermal effects: latent heat of vaporization and thermal Marangoni convection, whose presence reduced evaporation rate for less than 5% (water on copper substrate) as well as thermal conductivity in all phases. It is shown that Stefan flow, generated in air by the evaporation process, reduced evaporation rate by less than 0.2%.

Results of computer simulations are presented in Fig. 5. The model used is valid only for droplet size bigger than the radius of surface forces action, which is around 10^{-7} m $= 0.1\,\mu$m. Results for contact line radius $L < 10^{-7}$ m have no physical meaning, as additional surface forces have to be included into the model at this scale (disjoining/conjoining Derjaguin's pressure). The range of sizes $L < 10^{-7}$ m is shown only for the demonstration of curves tendencies.

Figure 5 shows that kinetic effects become important only for submicron droplets ($L < 10^{-6}$ m), therefore a deviation from the pure diffusion model of evaporation can be neglected for the droplet size bigger than 10^{-6} m. Kelvin's effect influences the evaporation rate, J, only for droplets of size $L < 1.1 \cdot 10^{-8}$ m, and can be neglected for droplets of size $L > 10^{-7}$ m.

The latter shows that a consideration of evaporation of microdroplets completely covered by the surface forces action (that is less than 10^{-7} m) should include both deviation of the saturated vapour pressure caused by the droplet curvature (Kelvin's effect) and the kinetic effects.

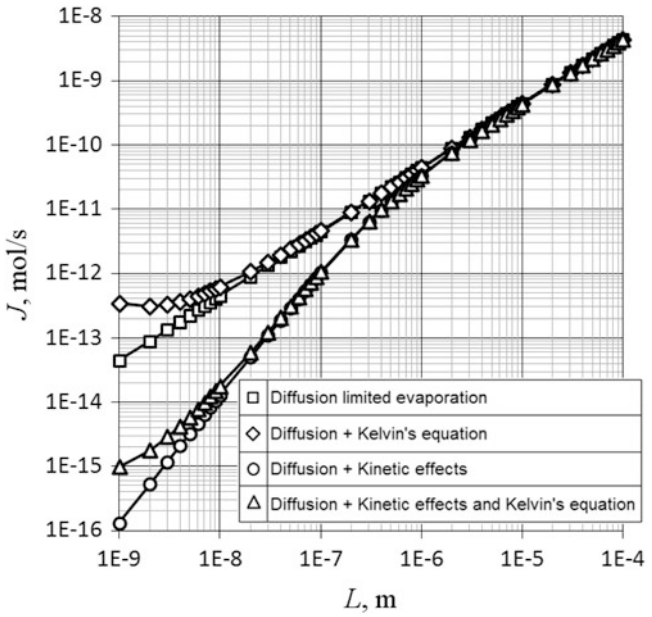

Fig. 5 Influence of Kelvin's equation and kinetic effects on evaporation rate, J, of pinned sessile droplets of water on copper substrate. L is the contact line radius

Though the influence of above mentioned effects on total evaporation flux, J, is negligible for droplets of size $L > 10^{-6}$ m, they may be important for the calculation of a local evaporation flux at the three-phase contact line.

11 Derjaguin's (Disjoining/Conjoining) Pressure

From theoretical point of view two singularities have to be coped with simultaneously [39] at the three-phase contact line. The first problem is associated with the well-known problem of a singularity at the moving three phase contact line: a singularity of the viscous stress caused by an incompatibility of no-slip boundary condition at the solid–liquid interface with boundary condition of moving liquid–air interface. The second problem is associated with the specific behaviour of the evaporation flux at the perimeter of the droplet. The latter singularity is caused by an incompatibility of a boundary condition for vapour flux at liquid–air interface with the boundary condition of no vapour penetration at the solid–air interface.

In order to overcome the problem of singularities at the three-phase contact line it is necessary to replace mathematically inconsistent boundary conditions by physically correct ones. It can be done using Derjaguin's (disjoining/conjoining) pressure concept. This approach does not introduce a three-phase contact line and,

therefore, rules out any singularity problems in a vicinity of the otherwise apparent three-phase contact line [20].

Surface forces (Derjaguin's pressure) act in a vicinity of the apparent three-phase contact line so called transition zone [20]. The presence of the Derjaguin's pressure disturbs the initial special profile of the liquid droplet in a vicinity of the three phase contact line. It is also known that a very thin adsorbed film forms on a solid surface, which is at the thermodynamic equilibrium with the vapour concentration in the surrounding humidity. That is, in the humid air, water vapour forms a thin water film on the surface of a solid substrate. Thus, a liquid–air interface of a sessile liquid droplet is actually in a contact with this adsorbed water film (or a film of other substance); thus, in this approach there is no true three-phase contact line.

First models of evaporation in a vicinity of the three phase contact line based on consideration of Derjaguin's (disjoining/conjoining) pressure action were developed by Potash and Wayner [22], and Moosman and Homsy [21], who used the Derjaguin's pressure to model the transport phenomena in an evaporating two-dimensional meniscus (both in the case of complete wetting). In [22] the authors calculated the meniscus profile, heat flux profile, and pressure gradient profile. In [23] the authors deduced a meniscus profile changes relative to the static isothermal one, as well as an evaporation flux from the interface using a perturbation theory. Both [22] and [23] demonstrated that a large heat and evaporation fluxes occur in the transition region between the capillary meniscus and the adsorbed layer. Stephan et al. [40] investigated experimentally evaporation in heat pipes with grooved walls. They confirmed the theoretical conclusions by Moosman and Homsy [21] on prediction that significant part of the evaporation flux is localized at the three-phase contact line.

Ajaev et al. [23] studied both static and dynamic values of the apparent contact angle for gravity-driven flow of a volatile liquid down of a heated inclined plane. The authors investigated macroscopic boundary conditions which could be used with a conventional continuum approach and agreed with the micro scale phenomena at the contact line. They found the profile of the liquid–vapour interface in the region of the apparent three-phase contact line and determined the dependence of the macroscopic contact angle on the temperature of the contact line and the velocity of its motion. The interface profile in the region was determined by a disjoining pressure action and asymptotically approaches the adsorbed thin liquid film. It was found that the curvature of the interface at that transition region is very high. Authors [23] also investigated the effect of evaporation on moving contact line in the case of partial wetting. They proposed a generalization of the approach of Moosman and Homsy [21] and Ajaev et al. [41, 42].

Diaz et al. [43] studied a static puddle taking into account capillarity, gravity and disjoining pressure. They found an analytical solution for the shape of the vapour–liquid interface in the transition zone between adsorbed liquid layer and capillary region.

Eggers et al. [44] studied the evolution of a droplet of pure liquid on a solid substrate in case of complete wetting and intensive evaporation. They coupled viscous flow with evaporation from droplet's surface and its precursor film. The

evaporation was limited by a diffusion of vapour into the surrounding atmosphere. Authors found that their model describes well the final stage of evaporation when drop radius goes to zero like $L\ (t_0 - t)^{\alpha}$, where α has value close to 1/2, which is in agreement with experiments.

All the above examples of disjoining pressure action at the apparent three-phase contact line gave the evidence of possibility to construct physically consistent macroscopic boundary conditions at the contact line taking into account microscopic phenomena.

References

1. Haschke, T., Lautenschlager, D., Wiechert, W., Bonaccurso, E., Butt, H.-J.: Simulation of Evaporating Droplets on AFM-Cantilevers. In: Excerpt from the Proceedings of the COMSOL Multiphysics User's Conference, Frankfurt, 2005
2. Sazhin, S.S.: Progr. Energ. Comb. Sci. **32**, 162 (2006)
3. Brenn, G.: Int. J. Heat Mass Transf. **48**, 395 (2005)
4. Deegan, R.D.: Phys. Rev. E **61**, 475 (2000)
5. Deegan, R.D., Bakajin, O., Dupont, T.F., Huber, G., Nagel, S.R., Witten, T.A.: Phys. Rev. E **62**, 756 (2000)
6. Bhardwaj, R., Fang, X., Attinger, D.: New J. Phys. **11**, 075020 (2009)
7. Dugas, V., Broutin, J., Souteyrand, E.: Langmuir **21**, 9130 (2005)
8. Hirt, C.W.: Simulating the Residue left by Evaporating Drops. Flow Science Technical Notes: FSI-08-TN80. Flow Science, Inc., Los Alamos (2008)
9. Kim, H., Kim, J.: J. Micromech. Microeng. **20**, 045008 (2010)
10. Bourges-Monnier, C., Shanahan, M.E.R.: Langmuir **11**, 2820 (1995)
11. Sefiane, K., Tadrist, L.: Int. Comm. Heat Mass Transf. **33**, 482 (2006)
12. Girard, F., Antoni, M., Sefiane, K.: Langmuir **24**, 9207 (2008)
13. Picknett, R.G., Bexon, R.: J. Colloid Interface Sci. **61**, 336 (1977)
14. Girard, F., Antoni, M., Faure, S., Steinchen, A.: Langmuir **22**, 11085 (2006)
15. Girard, F., Antoni, M., Faure, S., Steinchen, A.: Microgravity Sci. Technol. **XVIII**(3/4), 42 (2006)
16. Girard, F., Antoni, M., Faure, S., Steinchen, A.: Coll. Surf. A **323**, 36 (2008)
17. Girard, F., Antoni, M.: Langmuir **24**, 11342 (2008)
18. Semenov, S., Starov, V.M., Rubio, R.G., Velarde, M.G.: Coll. Surf. A **372**, 127 (2010)
19. Guena, G., Poulard, C., Voue, M., Coninck, J.D., Cazabat, A.M.: Coll. Surf. A **291**, 191 (2006)
20. Starov, V.M., Velarde, M.G., Radke, C.J.: Wetting and Spreading Dynamics. Taylor & Francis, Boca Raton (2007)
21. Moosman, S., Homsy, G.M.: J. Colloid Interface Sci. **73**, 212 (1980)
22. Potash, M. Jr., Wayner, P.C. Jr.: Int. J. Heat Mass Transf. **15**, 1851 (1972)
23. Ajaev, V.S., Gambaryan-Roisman, T., Stephan, P.: J. Colloid Interface Sci. **342**, 550 (2010)
24. Starov, V., Sefiane, K.: Colloids Surf. A **333**, 170 (2009)
25. Hu, H., Larson, R.G.: J. Phys. Chem. B **106**, 1334 (2002)
26. Hu, H., Larson, R.G.: Langmuir **21**, 3963 (2005)
27. Hu, H., Larson, R.G.: Langmuir **21**, 3972 (2005)
28. Hu, H., Larson, R.G.: J. Phys. Chem. B **110**, 7090 (2006)
29. Ristenpart, W.D., Kim, P.G., Domingues, C., Wan, J., Stone, H.A.: Phys. Rev. Lett. **99**, 234502 (2007)
30. Semenov, S., Starov, V., Rubio, R.G., Velarde, M.G.: Prog. Colloid Polym. Sci. **138**, 115 (2011)

31. Dunn, G.J., Wilson, S.K., Duffy, B.R., David, S., Sefiane, K.: Colloids Surf. A Physicochem. Eng. Asp. **323**, 50 (2008)
32. Dunn, G.J., Wilson, S.K., Duffy, B.R., David, S., Sefiane, K.: J. Fluid Mech. **623**, 329 (2009)
33. Lee, K.S., Cheah, C.Y., Copleston, R.J., Starov, V.M., Sefiane, K.: Colloids Surf. A **323**, 63 (2008)
34. Starov, V.M., Kostvintsev, S.R., Sobolev, V.D., Velarde, M.G., Zhdanov, S.A.: J. Colloid Interface Sci. **252**, 397 (2002)
35. Starov, V.M., Kostvintsev, S.R., Sobolev, V.D., Velarde, M.G., Zhdanov, S.A.: J. Colloid Interface Sci. **246**, 372 (2002)
36. Semenov, S., Starov, V.M., Rubio, R.G., Agogo, H., Velarde, M.G.: Colloids Surf. A Physicochem. Eng. Asp. **391**, 135–144 (2011)
37. Chen, C.-T., Tseng, F.-G., Chieng, C.-C.: Evaporation evolution of volatile liquid droplets in nanoliter wells. Sens. Actuators A **130–131**, 12–19 (2006)
38. Yildirim Erbil, H., McHale, G., Rowan, S.M., Newton, M.I.: Determination of the receding contact angle of sessile drops on polymer surfaces by evaporation. Langmuir **15**, 7378–7385 (1999)
39. Poulard, C., Guena, G., Cazabat, A.M., Boudaoud, A., Ben Amar, M.: Langmuir **21**, 8226 (2005)
40. Stephan, P.C., Busse, C.A.: Int. J. Heat Mass Transf. **35**, 383 (1992)
41. Ajaev, V.S., Homsy, G.M., Morris, S.: J. Colloid Interface Sci. **254**, 346 (2002)
42. Ajaev, V.S.: J. Colloid Interface Sci. **280**, 165 (2004)
43. Diaz, M.E., Fuentes, J., Cerro, R.L., Savage, M.D.: J. Colloid Interface Sci. **348**, 232 (2010)
44. Eggers, J., Pismen, L.M.: Phys. Fluids **22**, 112101 (2010)

Superspreading: Role of the Substrate Surface Energy

A. Nikolov and D. Wasan

1 Introduction

The quick wetting of solid surfaces with the desired liquids is necessary to many commercial processes. The trisiloxane surfactant containing 7.5–8.0 mol of ethylene oxide groups (e.g., Silwet L-77) has been found to be one of the best spreading agents with the ability to spread quickly on difficult-to-wet surfaces (e.g., hydrophobic ones like polystyrene and leaves), and is an excellent adjuvant for completely spreading an aqueous solution on leaf surfaces. Trisiloxane-ethoxylate surfactants (superspreaders) are biodegradable and understanding their ability to spread a liquid quickly on a solid surface is an important step in building a strong foundation for developing novel technologies and devices; superspreaders can be used in surface coating (e.g., to develop optical devices with desirable surface properties), heat transfer devices, painting, printing compositions, agricultural adjuvants, fabric manufacturing, cosmetics, surface cleaners, and oil removal.

Surfactants have been known to assist the spreading of liquid on a solid surface by lowering the liquid–vapor surface tension. The classical theory of wetting (e.g., Young's (1805) and Dupre (1869) equation) teaches that the resulting imbalance of forces at the contact line may cause the drop to spread outwards on a smooth horizontal substrate surface when the spreading coefficient is $S \geq 0$. The validation of the concept of the positive spreading coefficient ($S \geq 0$) requires the accurate measurement of the spreading dynamics (e.g., the decrease in the contact angle, and the surface and interfacial tension at the solution/solid interface at the droplet's spreading edge). The infrared spectroscopy (FTIR/ATR) applied by Kumar et al. [1] for monitoring the adsorption at the solid/solution is a good approach for obtaining

A. Nikolov (✉) · D. Wasan
Department of Chemical and Biological Engineering, Illinois Institute of Technology, Chicago, IL 60616, USA
e-mail: nikolov@iit.edu; wasan@iit.edu

R.G. Rubio et al. (eds.), *Without Bounds: A Scientific Canvas of Nonlinearity and Complex Dynamics*, Understanding Complex Systems,
DOI 10.1007/978-3-642-34070-3_27, © Springer-Verlag Berlin Heidelberg 2013

information for the rate and adsorption at the solid/solution interface. However, the scale of measurement for the rate of adsorption at the solid/solution interface has to be compatible with the time scale of the spreading dynamics.

A model for the spreading driven by the Marangoni flow was proposed when the spreading coefficient at the spreading edge could be ($S \leq 0$). It was assumed that the Marangoni flow was located along the drop surface–a high surface tension at the drop edge and a low surface tension at the droplet surface apex [2, 3]. In this article, we discuss the role of the Marangoni flow in enhancing spreading. It is important to notice that the two proposed concepts, the spreading due to $S \geq 0$ and the Marangoni flow, cannot apply at the same time because $S \geq 0$ requires a low surface and/or interfacial tension at the spreading edge while the Marangoni flow requires a high surface tension at the spreading edge. Put simply, the two proposed concepts for explaining superspreading are mutually exclusive.

Another option for explaining the superspreading phenomenon is to assume that the dispersed surfactant aggregates may disintegrate and the product of this disintegration somehow contributes to the formation of a bilayer (e.g., "ziplock" or self-hydrophilicity) on a substrate at the air/solid interface, air/liquid surface, and/or on the substrate solution. Such a generalized concept was proposed [4–8], but the detailed mechanism of surfactant aggregate disintegration leading to the formation of a bilayer on a substrate (or at the air/solution surface) and that enhances spreading has never been proven or presented with reliable physical evidence supporting its occurrence. The reader has to guess how and where the bilayer formed and how it triggers spreading. If the bilayer formation is the requirement for superspreading, why does the optimum of spreading rate vs. concentration exists? No experimental evidence has been presented for the role of bilayer formation on superspreading, although it has been commonly discussed in the literature.

The goal of our previously published paper was to discuss and debate the commonly presented superspreading mechanisms in the literature. The purpose of this study is to present an understanding of what drives superspreading and present a simple model to explain the experimental data reported in the literature. It was observed that the optimum in the rate of spreading vs. substrate wettability corresponds to a wetting angle between 60–65°, but this has never been explained. We would like to discuss and explain two main features: the spreading rate has a maximum vs. concentration, and the value of the concentration corresponding to a maximum rate of spreading does not depend on the substrate's wetting angle.

2 Surface Activity of Superspreader Silwet L77: Data Analyses

Superspreaders are commercial surfactants and are not a single chemical component, but rather are a mixture of siloxane polyether polymers. Superspreaders are produced by several companies and their chemical formulation and surface

activity vary. So it is not surprising that the data for the rate of spreading vs. substrate wetting nature and optimum concentrations published in the literature vary. How to choose which published data are reliable is no easy task. In this paper, we focus our attention on the commercial product Silwet L77 (with a general composition of methyl-trisiloxane with 8 ethoxylated groups capped with a methyl group). L77 is mostly used by researchers studying superspreading. Before analyzing the data on superspreading (e.g., the rate of spreading vs. optimum surfactant concentration and the role of the substrate's surface energy), we will briefly discuss the molecular state of superspreaders at the surface and in the bulk. The surface tension isotherm of superspreader L77 at room temperature (25°C) has a CAC (critical aggregation concentration) at 1.210^{-4} mol/l and this concentration is its solubility limit in an aqueous solution. Above this concentration, the superspreader molecules tend to form vesicle-type aggregates with different sizes rather than form less dispersed micelles as the classical surfactants do. The value of the surface tension at CAC is about 20–21 mN/m and the area per molecule at the surface saturation ($d\sigma/d \ln C$ =conctant) is 60–65 A^2. No pre-CAC type of aggregate was observed to form. After CAC, there was no observable change in the isotherm's slope indicating the unlikely formation of a multi-layer at the air/surfactant solution interface. The CAC value of L77 at the surface saturation is of the same order as that for a nonionic surfactant with good surface activity (e.g., hydrocarbon ethoxylated alcohol surfactant with a straight paraffin chain containing 13 carbon atoms and 30 ethylene-oxide groups has a CMC at 10^{-4} mol/l. The value of the surface tension at CMC is 43 mN/m and the area per molecule is 70–74 A^2 [9,10]. The surface tension of L77 at CAC is lower than the more conventional nonionic hydrocarbon-based surfactants, and the area per molecule is also less. These differences in the surface tension and area per molecule at the aggregation concentration are likely due to the specific molecular structure of L77. The molecular structure of L77 is like that of conventional hydrocarbon nonionic surfactants and has two parts: hydrophobic and hydrophilic. Despite the fact that L77 is a mixture of siloxane polyether polymers, the molecular structure of L77 has specific features; it enhances the surface activity at the air/surfactant interface as well as the spreading. The role of the ethoxylated chain on the spreading area has already been studied [11]. An optimum in the spreading area vs. degree of ethoxylation was observed. Trisiloxane with 8 ethoxy groups had the best spreading ability. The methyl trisiloxane chain, the hydrophobic part of the molecule, occupied the air space of the surface phase; the methyl group ending the ethoxylated chain (the hydrophilic part of the molecule) plays a role on the molecular vertical position at the surface. For example, at the optimum concentration of 0.1 wt%, the spreading rate of L77 is almost two times faster on Parafilm than on the methyl trisiloxane with the 8 ethoxylated groups end-capped with a hydroxyl group [6, 12]. The type of the end-capped group (hydrophobic or hydrophilic) anchors the molecular vertical position at the air/aqueous surface and has an impact on the surface activity (e.g., the lateral intermolecular interactions) and causes the rate of spreading of L77 to be higher compared with the same molecule end-capped with a hydroxyl group.

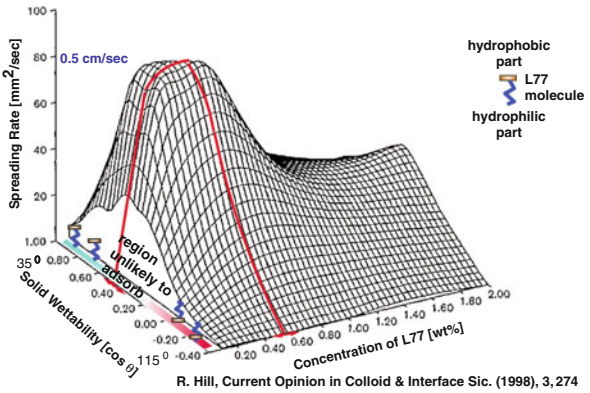

Fig. 1 Silwet L-77 spreading rate vs. concentration and substrate energy (solid wettability) and option surfactant molecule to adsorb on substrate

Many researchers investigating superspreading have assumed that the vesicle type of clusters rather than micelles are present in the bulk and that these are a requirement for superspreading (see [4, 6, 8]), however, this assumption has never been proven.

3 Superspreading: Concepts and Models

Before discussing commonly presented concepts in the literature for the mechanisms of superspreading, data for the spreading rate of L77 vs. concentration and substrate surface energy will be presented and analyzed. The data for the spreading rate of L77 vs. concentration and substrate surface energy were reported by Hill [5] and are presented in Fig. 1. The specific spreading features of the L77 superspreader are that the spreading rate has a maximum vs. surfactant concentration and vs. substrate wettability (substrate surface energy). Intriguingly, the value of the concentration corresponding to maximum rate of spreading did not depend on the substrate wettability, and the spreading rate had a maximum at a substrate wetting angle between 60–65°. The substrate wettability was quantified by the water phase's ability to wet the substrate [5].

Overall, the spreading rate for L77 (Fig. 1) had an optimum of 0.5 cm/s (or 80 mm^2/s) at a surfactant concentration of 0.45–0.50 wt% and at a substrate wettability between 60–65°.

To provide an explanation and propose a model predicting why the optimum of the spreading rate was at a substrate's wettability of 60–65° (intermedium substrate wettability) is a challenging task. The correct way to validate a proposed model or concept is to apply and predict the value of the substrate's wetting angle on the spreading optimum.

So far, no model has been presented in the literature that explains the optimum rate of spreading vs. substrate wettability. As was discussed, of the concept of the bilayer formation on the substrate/air interface or the substrate/solution interface

was proposed as possible explanation for what drives superspreading. Here, we will briefly debate the validity of this concept. More details on the validity of the bilayer concept on superspreading were recently discussed by Nikolov and Wasan [3].

Hardy [13] suggested that the presence of a precursor water film at the solid vapor interface ahead of the spreading droplet edge and fast surfactant adsorption onto the substrate/solution at the droplet meniscus causes the surface tension gradient between the precursor film and meniscus; this generates the Marangoni flow in the direction of the precursor film on the solid, causing the droplet to spread on the substrate until the surface tension gradient diminishes. Hardy's spreading concept due to the water precursor film on the substrate was modified and instead of the existence of a precursor water film on the solid/vapor substrate, it was assumed that a surfactant bilayer existed at the solid/vapor interface [6, 7]. Ruckenstein [7] proposed that the surfactant bilayer formed at the solid/vapor interface and water molecules could infiltrate into the surfactant's bilayer to promote the surface tension gradient. The weakness of this concept lies in the lack of evidence and/or physical reasons for bilayer formation on the substrate with an intermediate wettability (Fig. 1). In order to present an explanation and model describing the superspreading process, it is necessary to continuously monitor the rate of spreading and the contact angle dynamics [2].

When a droplet of L77—0.1 ml aqueous solution with a concentration of 0.1wt% (e.g., 10 times CAC)—formed on the tip of the capillary, its surface was quickly covered with surfactant molecules. When the droplet was placed on a smooth flat polystyrene surface with a water wettability of 75–80°, a humidity of 45–50% and a temperature of 25°C, the droplet began to spread quickly over the substrate in a circular manner and its initial contact radius increased. During the initial spreading time (e.g., 3–4 s), the spreading rate was fast (e.g., 0.25–0.3 cm/s) and constant. During this time, the droplet spread over 60–65% of the total area of spreading. Then, the spreading rate with time diminished; after 30–35 s, it stopped. The micrographs posted in Fig. 2 depict the initial spreading evolution of L77 at a concentration of 0.1 wt% spreading over a smooth flat polystyrene surface.

The droplet spontaneously spread over the substrate, and the droplet surface tension in the spreading direction became non-uniform. At the spreading edge, the surface concentration was expected to drop and have a high surface tension; at the apex, the surfactant concentration remained high and surface tension remained low. The advancing contact angle during the initial fast rate of spreading was 30–40° and the covered area increased by 40 cm^2 [2]. After the period of fast spreading, the rate of spreading slowly decreased; the droplet spreading rim broke into crown droplets and after 20–25 s, completely stopped. After some time, the surfactant molecules should begin to adsorb at the air/solution interface from the bulk and maybe even on the substrate also if the interactions between the substrate and surfactant molecule promote the adsorption. The optional surfactant adsorption on the substrate with an intermediate wettability (e.g. of 50–80°) and role on the spreading rate will be discussed later when the role of the substrate surface energy on spreading rate will be finalized.

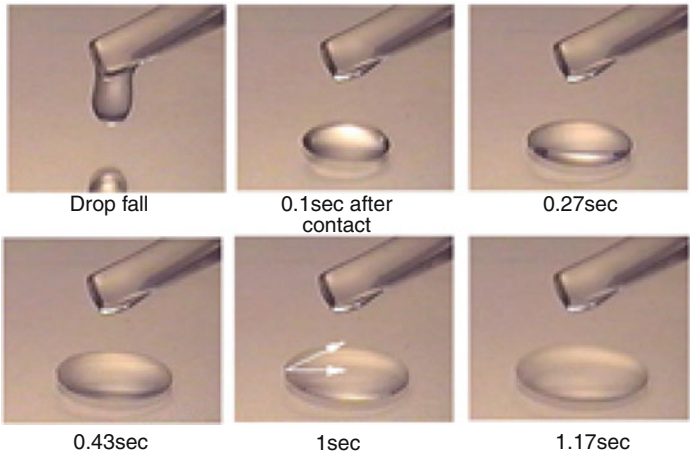

Fig. 2 The sequence of micrographs depict the early-time of Silwet L-77 droplet radial spreading: shape (curvature) and wetting over a smooth flat polystyrene surface at a concentration of 0.1 wt%, and droplet volume of 20 μl. The initial droplet constant size with substrate was about 1.7 cm

First, we will discuss the effect of the surfactant concentration on the optimum of rate of spreading. The rate of spreading during the initial time is the faster than the later rate of spreading, remains constant, and then ends with the breakup of the rim into droplets (fingers); these facts, paired with the information that the spreading rate vs. concentration had a maximum, suggest that the driving force of spreading is the Marangoni flow. It is known that the fast spreading of a liquid on a solid is driven by the surface tension gradient at the air/liquid interface, which acts as a shearing stress on the underlying liquid (the Marangoni flow) (see [14, 15]). To maintain a sufficient surface tension gradient to generate flow driven by the tangential stress on an expanding droplet surface requires an optimum in the surfactant concentration in the bulk. At low and high surfactant concentrations in the bulk, the surface gradient diminishes quickly with spreading. The forces operating per unit area on a droplet with a surfactant that is placed on a substrate with an intermediate substrate wettability are presented in Fig. 3.

Nikolov et al. [2] assumed a linear increase of the surface tension along the expanding droplet surface, and proposed a simple model for the average velocity of spreading (U_{av}) based on the lubrication approach

$$U_{av} = \frac{h}{2\eta}\left(\frac{d\sigma}{dr}\right)_{V,\Theta} - \frac{h^2}{3\eta}\frac{d}{dr}\left(\sigma\frac{d^2h}{dr^2}\right) - \frac{h\rho g}{3\eta}\frac{dh}{dr}. \quad (1)$$

The average spreading rate considers the role of the viscosity: the first term represents the role of the surface tension gradient (the driving pressure), the second term is the capillary resistance driven by the droplet curvature, and the third term is the hydrostatic pressure. Based on experimental evidence that the rate of spreading on horizontal and vertical substrates is the same as the contribution of the hydrostatic

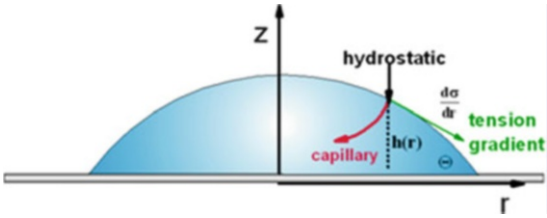

Fig. 3 The forces per unit area on a droplet with a surfactant placed on a substrate with an inter medium wettability

pressure on the spreading rate, it can be neglected [16]. A simple model based on (1) was proposed to predict the initial faster spreading rate. The model predicted well the value of the optimum velocity, assuming that the capillary term in (1) is smaller than the Marangoni flow term. The proposed simplified model did not take into consideration the effect of the droplet curvature on the Marangoni flow; the role of the substrate's wettability was neglected. As noted earlier, the data presented in Fig. 1 reveal that the spreading rate had an optimum at an intermediate substrate wettability of 60–65°. The position of the optimum of the spreading rate vs. substrate wettability was independent of the surfactant concentration, but its magnitude depends on the surfactant concentration and has an optimum at a concentration of about 0.5–0.55 wt% (Fig. 1). For example, the highest spreading rate at a substrate wettability of 60–65° was at a surfactant concentration of 0.5 wt%. This is quite intriguing because it has been proposed that the superspreader's molecule adsorption and formation on the bilayer on the substrate are necessary for superspreading to occur [4–8]. It is expected that the superspreader molecule will adsorb in different manners on hydrophobic and hydrophilic substrates. Driven by the specific molecular interactions, the hydrophobic part of a molecule tends to adsorb on a hydrophobic substrate surface. The same rule applied to the hydrophilic part of the surfactant molecule will tend to adsorb on the hydrophilic substrate rather than on the hydrophobic one.

In summary, based on the concept of specific molecular interactions, it is unlikely the molecule of L77 will adsorb on the substrate with an intermediate wettability of 60–65° where the optimum of spreading was observed.

In order to verify that the molecule of L 77 is unlikely to adsorb on the substrate with an intermediate wettability, we conducted a simple experiment. A 10 μl droplet containing an aqueous solution of L77 with a concentration of 0.4 wt%, at 25°C and a humidity of 45–50%, was placed on a smooth flat polystyrene surface. The droplet spreading was monitored and after 30–35 s, the spreading stopped. Then, the spreading surface was washed 2–3 times with Millipore purified water. The polystyrene surface was dried at room temperature for 20 min and a droplet of purified water was placed on an area where the spreading was performed; the three-phase contact angle was measured using the goniometric side-view method. The value of the measured three-phase contact angle was 75–80°. The value of the contact angle was in very good agreement with the measured value of the three-phase contact angle between the purified water drop on the polystyrene surface.

The optional bilayer formation at the air/solution surface was also examined. It is well known that an accurate measurement of the surface tension adsorption isotherm provides useful information for monitoring changes inside the surfactant adsorbed layer vs. concentration; this information includes the molecular area, structural transitions, transition from mono- to bilayer, and when the surfactant molecules tend to begin to aggregate into the bulk [17]. The detailed examination of the surface tension isotherm of L77 did not provide evidence that the bilayer could form at the air/solution surface. The formation of the bilayer at the air/surface is quite an unusual phenomenon. The assumption made by some investigators that the faster rate of spreading is driven by the bilayer's or monolayer's specific adsorption at the droplet spreading edge (e.g., the precursor layer or bilayer film) **on solid surfaces** with an *intermediate wettability* remains not only an unproven assumption, but is also a physically unrealistic phenomenon.

In summary, the formation of a surfactant bilayer at the air/solution interface or on the substrate with an intermediate wettability is unlikely to occur; it should not be considered a factor triggering the superspreading phenomenon, as was proposed in the literature by Stoebe et al. [6], Ruckenstein [7], Karapetsas et al. [8], but it has to be attributed to the adsorbed layer surface dynamic property to maintain the Marangoni flow over the droplet surface during spreading. Exploring the concept of the spreading driven by the Marangoni flow over a curved surface requires a model that predicts the superspreading vs. substrate wettability as well as the spreading rate.

4 Modeling Spreading vs. Substrate Wettability

In the case of Marangoni-driven spreading over a curved surface, rapid spreading on a substrate with a high hydrophobicity (e.g., 100–180°) is not expected because the surface area is stretched less and the Marangoni flow will diminish quickly; furthermore, it will not contribute to the direction of the spreading (Fig. 4). On a hydrophilic (water-wetted) substrate, the spreading rate is expected to be low because the liquid film on the substrate and the frictional viscous force will oppose the spreading flow. There is certainly an optimum rate of spreading vs. substrate wettability, if we assume that the surface tension gradient operates along the radial direction of the spreading. To propose a model predicting the spreading rate requires knowledge of the droplet surface curvature (shape) evolution.

Here, we will discuss the contribution of the surface tension gradient, capillary and friction on the rate of spreading vs. substrate wettability during the initial spreading time. The faster rate of spreading occurred during the initial time, and during that time the three-phase contact angle between the solution and substrate was not small. In the case of spreading on a polystyrene substrate at an optimum concentration, the advancing contact angle during the faster rate of spreading was 30–40°. The role of the droplet curvature has to be considered to evaluate the

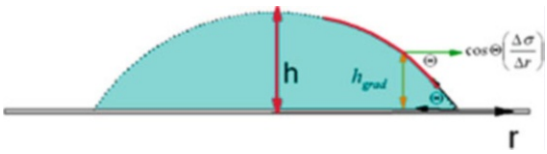

Fig. 4 The sketch depicts the surface tension gradient contribution on spreading over a curved surface

contribution of the surface tension gradient $\left(\frac{d\sigma}{dr}\right)$ on the rate of spreading. The droplet curvature depends on the substrate wettability. The degree of droplet surface stretching (a surface increase) when the droplet is placed on a substrate depends on the substrate's wettability. At a wettability of $\theta \rightarrow 180°$, the surface stretching is much less than that on the substrate with a wettability of $\theta \rightarrow 0°$. As an approximation, we assumed that, depending on the wettability of the substrate, the surface tension gradient along the radial direction of the spreading follows the droplet surface's slope and has a value the same as the substrate wetting angle θ. This assumption, however, is not quite correct. We will discuss the role of the dynamic contract angle on the spreading rate later. The contribution of the surface tension gradient on the rate of droplet spreading on a curved surface is given by the term $\cos\Theta\left(\frac{d\sigma}{dr}\right)_{V,C}$. $\cos\theta$ needs to be considered in the role of the droplet surface curvature of the gradient contribution on the spreading rate. The substrate wettability also contributes to the viscous friction. At a substrate wettability of $\theta \rightarrow 180°$, the friction term $\left(\eta\frac{\partial u}{\partial z}\right)_{V,C} \rightarrow 0$, and at $\theta \rightarrow 0°$ (a liquid film on substrate); $\left(\eta\frac{\partial u}{\partial z}\right)_{V,C} \rightarrow \infty$.

The spreading equation driven by the surface tension gradient on a curved surface due to the substrate's wettability at a constant drop volume (v) and concentration (C) is given by the expression:

$$U_{av} \approx \frac{h_{grad}}{2\eta}\left[\cos\Theta\left(\frac{d\sigma}{dr}\right)_{V,C}\right]. \tag{2}$$

For simplicity, it was assumed that the droplet shape during the faster time of the spreading was that of a spherical cap. The micrographs taken during the initial time faster spreading rate support such an assumption (Fig. 2). The parameter (h_{grad}) in (2) is the thickness of the spreading layer corresponding to $\cos\Theta\left(\frac{d\sigma}{dr}\right)_{V,C}$. The height of a droplet cap with a spherical shape can be expressed as a function of the drop radius (R) and substrate wettability (θ) with the expression: $h = R(1-\cos\Theta)$. The value of ($h > h_{grad}$), but the optimum of $U_{av}(\Theta)$, is independent of the value of (h) and contributes only to the magnitude of $U_{av}(\Theta)$. The role of $h(R)$ on the rate of spreading will be discussed later. The expression for (h) was substituted in the above equation for the average velocity of spreading, $U_{av}(\Theta)_{V,C}$:

$$U_{av}(\Theta) \approx \frac{R(1-\cos\Theta)}{2\eta}\left[\cos\Theta\left(\frac{d\sigma}{dr}\right)_{V,C}\right]. \tag{3}$$

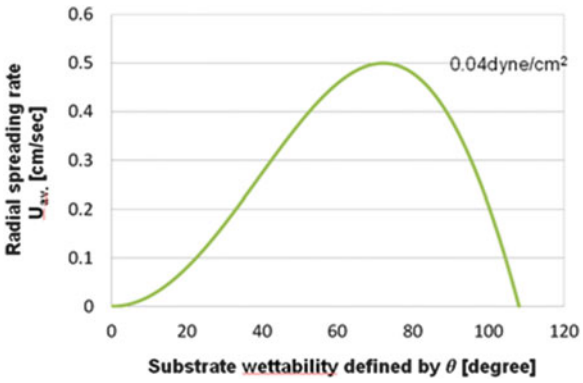

Fig. 5 The prediction of the droplet average spreading rate optimum vs. substrate wettability for droplet with surface radius of $R = 1$ cm, viscosity 10^{-2} P, and surface tension gradient 0.04 dyne/cm^2

We examined the average spreading velocity at a constant droplet volume (V) and concentration (C) vs. (θ) at a droplet surface curvature $R = 1.0$ cm and different values of $\left(\frac{d\sigma}{dr}\right)$. It had an optimum at $\theta = 60°$ (Fig. 5).

This prediction of the optimum rate of spreading vs. substrate wettability is in very good agreement with the data for the optimum rate of spreading vs. substrate wettability reported by Hill (Fig. 1). The data presented in Fig. 1 predict an optimum of the spreading rate of 0.5 cm/s (or 80 mm^2/s) of the substrate with a wettability 60–65° corresponding to a surfactant concentration of 0.5–0.55 wt%. As was expected, the value of the parameters of R (the drop surface curvature at a constant and concentration C), η and $\left(\frac{d\sigma}{dr}\right)_{V,C}$ will not contribute to the value of the optimum θ but will **contribute to the magnitude of the spreading rate at an optimum** θ. In order to validate the spreading rate vs. (θ), we substitute data for R and $\acute{\eta}$ from experiment into (3). For a droplet with a surface radius $R = 1$ cm, viscosity $\eta = 10^{-2}P$ and for $\left(\frac{d\sigma}{dr}\right)$, it was assumed that the value of 0.04 dyne/cm^2 had the corresponding surface tension gradient of 0.02 dyne/cm over 0.5 cm. The prediction of the spreading rate (velocity) vs. substrate wettability is presented in Fig. 5. The value of the spreading rate had an optimum and was 0.5 cm/s when the experimental value of the spreading rate at an optimum reported by R. Hill was also 0.5 cm/s. The (R), and respectively (h), and $\left(\frac{d\sigma}{dr}\right)$ are parameters in (3); this equation requires augmentation when using the proposed values to calculate the magnitude of the spreading rate. The optimum of the spreading rate vs. substrate wettability θ was independent of the value of these parameters and concentration, but its magnitude was a function of the value of these parameters.

Equation (3) was used to analyze the rate of spreading vs. θ for different values of the surface tension gradient over a droplet surface with the same (R). Equation (3) predicts a linear relation between the rate of spreading and the surface tension gradient (Fig. 6).

The effect of the droplet surface radius (R) on the spreading rate was also analyzed. When a larger droplet is placed on a solid at the same three-phase contact angle of the substrate and the same concentration, the local film thickness along the substrate is high and the frictional force has to be lower and spreading

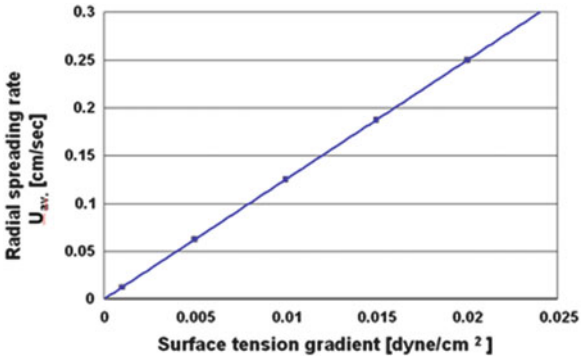

Fig. 6 Equation (3) predicts a linear relationship between the average spreading rate vs. surface tension gradient. Droplet radius: $R = 1.0\,\text{cm}$

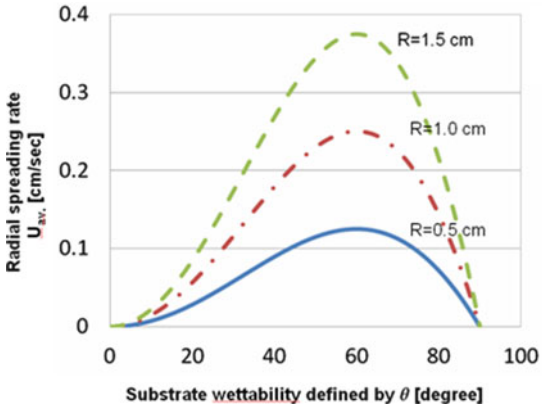

Fig. 7 The effect of the droplet surface radius R (respectively curvature $1/R$) on the spreading rate vs. substrate wettability (θ) at a surface tension gradient of $0.02\,\text{dyne/cm}^2$, and $\eta = 10^{-2}P$

fast. Figure 7 depicts the effect of the droplet surface radius (drop size) on the spreading rate vs. θ at a surface tension gradient of 0.02 dyne/cm over 0.5 cm, and $\eta = 10^{-2}P$.

At the optimum wettability, the values of the parameters (h, R, and $\left(\frac{d\sigma}{dr}\right)$) contribute only to the value of the spreading rate and not the value of θ. The questions naturally arise: is the wetting angle θ the same during the faster rate of spreading? Is the value of the surface gradient $\cos(\theta)\left(\frac{d\sigma}{dr}\right)$ over the curved surface constant? The visual observation reveals that, during the time of the faster rate of spreading, the wetting angle did not change much. However, the value of the slope over the droplet surface is unlikely to be the same as the value of the equilibrium three-phase contact angle of substrate. The contribution of the surfactant to the substrate wetting has to be considered when analyzing the rate of spreading. To correctly predict the spreading rate vs. substrate wettability, we have to consider not a water-wetting substrate (static angle), but a surfactant solution wetting the substrate during the time of the faster spreading rate. The right way to do this is to conduct an experimental observation of the wetting angle during the spreading rate. Based on our observations, superspreading on a smooth flat polystyrene substrate

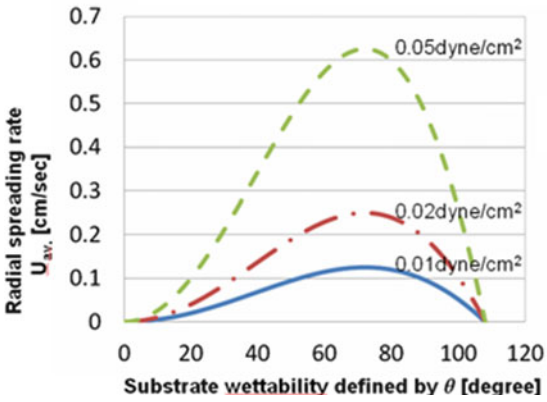

Fig. 8 Evaluation of the role of the dynamic constant angle on the droplet spreading rate. Due to the presence of the surfactant, was assumed that the value of angle wetting the substrate was reduced by factor of 0.3. The calculation was performed assuming $R = 1$ cm, surface tension gradient of 0.01, 0.02 and 0.05 dyne/cm^2, $\eta = 10^{-2}$ P and the optimum rate of spreading shifted from 60° to 75°

with a water wettability of 75° resulted in a monitored dynamic wetting angle of 40–45°. If we consider that the actual spreading angle is 30–35% less than the water-wetting substrate, the value of the optimum spreading rate shifts from $\theta = 60°$ to $\theta = 75°$ (Fig. 8).

In summary, the proposed model correctly elucidates the effect of the substrate wetting, surface tension gradient, and droplet surface curvature on the optimum rate of spreading during the time of the faster spreading rate.

The role of vesicle-type aggregates on superspreading has been discussed for some time [4–7]. Despite that, no experimental evidence has been presented to support the role of aggregates on spreading. Very recently, Karapetsas et al. [8] attempted to explain superspreading by proposing a basal adoption model. The model considers the curtailed role of the surfactant adoption dynamics from the air/solution interface to the substrate/solution interface on spreading. The aggregates' disintegration supplies the air/solution surface with surfactant molecules. The surfactant molecules adsorbed on the air/solution surface at the spreading edge transferred quickly and adsorbed on the substrate/solution interface. Marangoni stress close to the droplet edge promotes very fast spreading. The weakness of the Kakavetsis model is that the faster rate of spreading (superspreading) was observed at a substrate wettability corresponding to $\theta = 60°$. At this wettability (surface energy) of the substrate, it is unlikely that the superspreader molecules will tend to adsorb on the substrate. We noted earlier that the theory of adhesion teaches that a specific adsorption between biphilic molecules such as surfactants and substrates could occur on a substrate, either with hydrophobic or hydrophilic substrates, and is unlikely to occur on a substrate with an intermediate wettability where the optimum spreading rate was observed. The authors of the proposed model need to provide evidence for why and how the superspreader molecule tends to adsorb on the substrate (which is neither hydrophobic nor hydrophilic). However, the role of vesicle-type aggregates could play a role in superspreading, but not on the faster rate of spreading; the aggregates would instead be promoting the maximum area of

spreading. The goal of the presented research is to elucidate what drives the faster rate of spreading at the optimum substrate wettability, and not to discuss what drives the optimum of the wetting area.

5 Conclusions

The less-understood feature of the superspreading phenomenon for the role of the substrate surface energy (characterized by wetting) on the optimum rate of spreading was discussed. Observations reveal that the faster rate of spreading over the substrate occurred during the initial time. A simple model was presented to predict the optimum of the spreading rate vs. substrate wettability. The role of the surface tension gradient $\left(\frac{d\sigma}{dr}\right)_{V,C}$ over a curved surface was elucidated when the value of the wetting angle was considered. The model predicted the optimum rate of spreading vs. θ at $\theta = 60°$. This value is in good agreement with the experimental observations.

The values of R, η and $\left(\frac{d\sigma}{dr}\right)_{V,C}$ had no effect on the position of the optimum vs. θ, but contributed to the magnitude of the rate of spreading. The predicted value of the spreading rate at the optimum of wetting was also in a good agreement with the experimental observation. The effect of the surfactant on the substrate's wettability and its contribution to the surface tension gradient on the optimum spreading rate was also discussed.

Acknowledgement The authors would also like to thank Dr. Anoop Chengara from Nalco USA, Dr. Kalman Koczo and Dr. George Policello from Momentive Performance Materials USA Inc. (formerly Witco Corp.) for providing Silwet-L77 samples and fruitful discussions.

References

1. Kumar, N., Maldarelli, Ch., Couzis, A.: Colloids Surf. A Physicochem. Eng. Asp. **277**, 98 (2006)
2. Nikolov, A., Wasan, D., Chengara, A., Koczo, K., Policello, G., Kolossvary, I.: Adv. Colloid Interface Sci. **96**, 325 (2002)
3. Nikolov, A., Wasan, D.: Eur. Phys. J. Spec. Top. **197**, 325 (2011)
4. Ananthapadmanabhan, K., Goddard, E., Chandar, P.: Colloids Surf. **44**, 281 (1990)
5. Hill, R.: Curr. Opin. Colloid Interface Sci. **3**, 247 (1998)
6. Stoebe, T., Hill, R., Ward, M., Scriven, L.E., Davis, H.T.: In: Hill, R. (ed.) Silicone Surfactant, Chap. 11, pp. 275–312. Marcel Dekker, New York (1999)
7. Ruckenstein, E.: J. Colloid Interface Sci. **179**, 136 (1996)
8. Karapetsas, G., Craster, R., Matar, O.: J. Fluid Mech. **670**, 5 (2011)
9. Shinoda, K., Nakagawa, T., Tamamushi, B., Isemura, T.: Colloidal Surfactant: Some Physicochemical Properties, Chap. 2. Academic, New York (1963)
10. Schick, M.: In: Schick, M. (ed.) Nonionic Surfactant: Physical Chemistry, Chap. 13, pp. 753–834. Marcel Dekker, New York (1987)

11. Nikolov, A., Wasan, D., Koczo, K., Ploicello, G.: In: McMullan, P. (ed.) Proceeding of 5th International Symposium on Adjuvants for Agrochemicals, Memphis, vol. 2, pp. 125, 17–21 August 1998
12. Hill, R.: In: Hill, R. (ed.) Silicone Surfactant, Chap. 1, pp. 1–47. Marcel Dekker, New York (1999)
13. Hardy, W.: Colleted Work, vol. 6. Cambridge University Press, Cambridge (1936)
14. Levich, V.: Physicochemical Hydrodynamics, Chap. 7. Prentice Hall, Englewood Cliffs (1962)
15. Levich, V., Krilov, V.: Ann. Rev. Fluid Mech. **1**, 239 (1969)
16. Chengara, A., Nikolov, A., Wasan, D.: Adv. Polym. Sci. **218**, 117 (2008)
17. Defay, R., Prigogine, I., Bellemans, A., Everett, D.: Surface Tension and Adsorption, Chap. 7. Wiley, New York (1966)

Part IV
Scientific Contributions: Waves and Solitons, and Other Collective Excitations

Coupled Korteweg–de Vries Equations

R. Grimshaw

1 Introduction

In inviscid fluid flows instability can often be interpreted as a resonance between two waves. Thus, as some external parameter is varied, the phase speeds of two waves coincide at some critical parameter value. The generic unfolding of this resonance yields either a stable "kissing" configuration, or a "bubble" of instability in the space of the external parameter (see Fig. 1). There are many examples of this situation, see for instance, the monograph by Craik [1] for shear flows, or Baines and Mitsudera [2] for a discussion of the physical processes involved. Our concern here is with the unfolding of this resonance in the long-wave limit. There are two generic canonical models (see, for instance Grimshaw [3]). For the case when the corresponding wave modes coincide at criticality, the canonical model is the Boussinesq equation

$$A_{tt} - \Delta^2 A_{xx} + \frac{1}{2}\mu(A^2)_{xx} + \lambda\, A_{xxxx} = \delta A_{xx} \tag{1}$$

Here Δ is the aforementioned external parameter, δ is an unfolding parameter, while μ and λ are the nonlinear and dispersive coefficients respectively. In the linear, long-wave limit the dispersion relation for waves of speed c is just $c^2 = \Delta^2 + \delta$ which is just that sketched in Fig. 1. Resonance occurs for $\Delta = \delta = 0$, and the flow is linearly stable, or unstable, according as $\delta > 0, \delta < 0$. Equations of this form have been derived by Hickernell [4, 5] for Kelvin–Helmholtz instability, and by Helfrich and Pedlosky [6] and Mitsudera [7] for certain geophysical flows.

R. Grimshaw (✉)
Department of Mathematical Sciences, Loughborough University, Loughborough, UK
e-mail: R.H.J.Grimshaw@lboro.ac.uk

R.G. Rubio et al. (eds.), *Without Bounds: A Scientific Canvas of Nonlinearity and Complex Dynamics*, Understanding Complex Systems,
DOI 10.1007/978-3-642-34070-3_28, © Springer-Verlag Berlin Heidelberg 2013

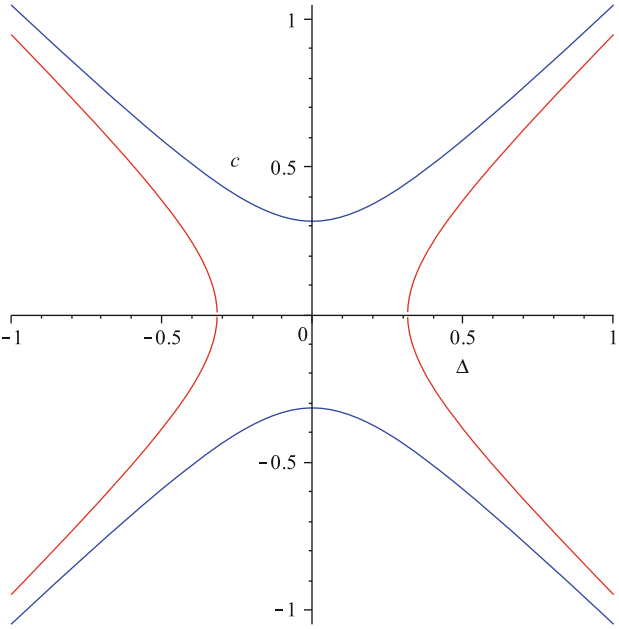

Fig. 1 Plot of the schematic dispersion relation $c^2 = \Delta^2 + \delta$; the stable case $\delta > 0$ is *blue*; the unstable case $\delta < 0$ is *red*

However, our main interest here is with the alternative scenario, when the wave modes remain *distinct* at criticality. In this case a suitable canonical model consists of coupled Korteweg–de-Vries (KdV) equations, such as

$$I_1\,(A_{1t} + \Delta_1 A_{1x} + \mu_1 A_1 A_{1x} + \lambda_1 A_{1xxx}) + \kappa A_{2x} = 0, \tag{2}$$

$$I_2\,(A_{2t} + \Delta_2 A_{2x} + \mu_2 A_2 A_{2x} + \lambda_2 A_{2xxx}) + \kappa A_{1x} = 0, \tag{3}$$

Here $\Delta_1 - \Delta_2$ is the detuning parameter, κ is an unfolding parameter, $I_{1,2}$ are normalising integrals, and $\mu_{1,2}$, $\lambda_{1,2}$ are nonlinear and dispersive coefficients respectively. In the linear long-wave limit the dispersion relation for waves of speed c is

$$(c - \Delta_1)(c - \Delta_2) = \frac{\kappa^2}{I_1 I_2}. \tag{4}$$

This is equivalent to that for the Boussinesq equation (1) if we put $\Delta_1 = -\Delta_2 = \Delta$ and $\delta = \kappa^2/I_1 I_2$. There is instability if $I_1 I_2 < 0$, and stability if $I_1 I_2 > 0$. Equations of the form (2), (3) have been derived by Mitsudera [7] and Gottwald and Grimshaw [8,9] for certain geophysical flows, and by Grimshaw [10] and Grimshaw and Skyrnnikov [11] for a three-layer stratified shear flow.

In the coupled KdV system (2), (3) the only coupling terms are those with coefficients κ. In general, there will also be cross-coupling linear dispersive terms

and nonlinear terms. That is, we can anticipate the presence of terms A_{2xxx} and A_{1xxx} in (2) and (3) respectively, and a full suite of nonlinear terms A_1A_{1x}, $(A_1A_2)_x$ and A_2A_{2x} in both equations. Our primary purpose in this paper is to demonstrate that is indeed the case for long waves in a stratified shear flow, and the outcome is the coupled system (58), (59) (see Gear and Grimshaw [12] who derived a coupled KdV system of this kind for linearly stable internal waves in a density stratified fluid). In the absence of coupling, it is well known that weakly nonlinear long waves in a stratified shear flow are described by the KdV equation (see [13–15] for instance). Here we extend the asymptotic expansion method used to derive the KdV equation to the case when there are two long waves in close resonance. The development follows that of Gear and Grimshaw [12] but now allows for a background shear flow, and hence the possibility of instability. Although our focus here is on coupled KdV equations, we note that similar systems have been studied, in which the KdV dispersion is replaced by alternative forms valid when the density stratification has some deep layers (see [16] and the references therein).

In Sect. 2.1 we present the problem formulation, and in Sect. 2.2 we describe how linear mode coupling can lead to instability. In Sect. 3 we present an outline of the asymptotic development, and in Sect. 4, we present a brief account of leapfrogging solitary waves, one of the interesting solutions of coupled KdV equations. We conclude in Sect. 5.

2 Derivation

2.1 Formulation

We assume that the fluid is inviscid and incompressible, and in the basic state has depth h, a density stratification $\rho_0(z)$ and a horizontal shear flow $u_0(z)$ in the x-direction. Further we assume that the flow is two-dimensional, and so all variables depend only on x, z where z is the vertical co-ordinate, and the time t. Using the long-wave variables

$$X = \epsilon x\,, \quad T = \epsilon t\,, \tag{5}$$

the full equations for the perturbation variables are, in standard notation, and expressed to the required order,

$$\rho_0(u_T + u_0u_X + wu_{0z}) + p_X = F_1 = -\rho_0(uu_X + wu_z) - \rho(u_T + u_0u_X + wu_{0z})\,, \tag{6}$$

$$p_z + g\rho = -\epsilon^2\rho_0(w_T + u_0w_X) + \cdots\,, \tag{7}$$

$$u_X + w_z = 0\,, \tag{8}$$

$$\zeta_T + u_0\zeta_X - w = J_1 = -u\zeta_X - w\zeta_z\,, \tag{9}$$

$$\rho_t + u_0\rho_x + w\rho_{0z} = -u\rho_X - w\rho_z\,, \tag{10}$$

and the boundary conditions are

$$w = 0\,, \quad \text{at} \quad z = -h\,, \tag{11}$$

$$p + p_0 = 0\,, \quad \text{at} \quad z = \eta\,. \tag{12}$$

$$\zeta = \eta \quad \text{at} \quad z = \eta\,. \tag{13}$$

Here we have replaced w with ϵw. The density equation (10) can be solved by $\rho_0(z) + \rho = \rho_0(z - \zeta)$, so that

$$\rho = -\rho_{0z}\zeta + \frac{\rho_{0zz}\zeta^2}{2} + \cdots\,. \tag{14}$$

Then the vertical momentum equation (7) becomes

$$p_z + \rho_0 N^2 \zeta = G_1 = -\frac{g\rho_{0zz}\zeta^2}{2} - \epsilon^2\rho_0(w_T + u_0 w_X) + \cdots\,, \tag{15}$$

where $\rho_0 N^2 = -g\rho_{0z}$. The free surface boundary conditions (12), (13) are expanded so that

$$p - g\rho_0\eta = g\rho\eta + \frac{g\rho_{0z}\eta^2}{2} + \cdots\,, \quad \zeta + \eta\zeta_z + \cdots = \eta\,, \quad \text{at} \quad z = 0\,,$$

and can then be combined to give

$$p - g\rho_0\zeta = \frac{\rho_0 N^2\zeta^2}{2} + g\rho_0\zeta\zeta_z + \cdots\,, \quad \text{at} \quad z = 0\,. \tag{16}$$

Thus the variables ρ, η are formally eliminated.

2.2 Coupled Modes

At leading linear order, the X, T-variables separate from z, and the latter yields the modal equation

$$(\rho_0 W^2\phi_z)_z + \rho_0 N^2\phi = 0\,, \tag{17}$$

$$\phi = 0 \quad \text{at} \quad z = 0\,, \quad \text{and} \quad W^2\phi_z = g\phi \quad \text{at} \quad z = 0\,. \tag{18}$$

Here $W = c - u_0$. Suppose that this has two nearly coincident solutions for c, say $c_1 = c, c_2 = c + \epsilon^2\Delta$, with two *distinct* modal functions $\phi_1(z), \phi_2(z)$. Note that it is readily shown that, when $\Delta \neq 0$,

$$\int_{-h}^{0} \rho_0[c_1 + c_2 - 2u_0]\phi_{1z}\phi_{2z}\,dz = 0, \quad \text{so that} \quad \int_{-h}^{0} \rho_0 W\phi_{1z}\phi_{2z}\,dz \approx 0\,, \tag{19}$$

where the error is $O(\epsilon^2)$.

Next, unfold the coupling by expanding u_0 as $u_0(z) + \epsilon^2 u_0^{(1)}(z)$. A similar expansion could also be done for ρ_0 but will be omitted here for simplicity. Then in the modal equation, expand ϕ as $\phi + \epsilon^2\phi^{(1)}$ and c as $c + \epsilon^2 c^{(1)}$, so that (17) becomes

$$(\rho_0 W^2\phi_z^{(1)})_z + \rho_0 N^2\phi^{(1)} = -2(\rho_0 W^{(1)} W\phi_z^{(1)})_z\,, \tag{20}$$

$$\phi_1 = 0 \quad \text{at} \quad z = 0\,, \quad \text{and} \quad W^2\phi_{1z} - g\phi_1 = -2W_1 W\phi_z \quad \text{at} \quad z = 0\,. \tag{21}$$

Here $W^{(1)} = c^{(1)} - u_0^{(1)}$ and $\phi = A_1\phi_1 + A_2\phi_2$. The compatibility condition is that the right-hand side is orthogonal to both $\phi_{1,2}$, and so

$$\int_{-h}^{0} 2\rho_0 W^{(1)} W(A_1\phi_{1z} + A_2\phi_{2z})\phi_{jz}\,dz = 0\,, \quad j = 1, 2\,, \tag{22}$$

which leads to, noting the orthogonality relation (19),

$$I_1(c^{(1)} - \Delta_1)A_1 - \kappa A_2 = 0, \qquad I_2(c^{(1)} - \Delta_2)A_2 - \kappa A_1 = 0. \tag{23}$$

Here the coefficients are defined by

$$I_j\Delta_j = 2\int_{-h}^{0} u_0^{(1)} W\phi_{jz}^2\,dz\,, \quad j = 1, 2\,, \tag{24}$$

$$\kappa = 2\int_{-h}^{0} u_0^{(1)} W\phi_{1z}\phi_{2z}\,dz\,, \quad j = 1, 2\,, \tag{25}$$

$$I_j = 2\int_{-h}^{0} W\phi_{jz}^2\,dz\,, \quad j = 1, 2\,. \tag{26}$$

The system (23) is a linear homogeneous algebraic system for $A_{1,2}$ whose determinant is zero, yielding the dispersion relation

$$I_1 I_2(c^{(1)} - \Delta_1)(c^{(1)} - \Delta_2) = \kappa^2\,. \tag{27}$$

It follows that the basic flow is unstable, that is $c^{(1)}$ is complex-valued when

$$(\Delta_1 - \Delta_2)^2 + \frac{4\kappa^2}{I_1 I_2} < 0\,. \tag{28}$$

This can only occur when $I_1 I_2 < 0$ which is thus a necessary condition for instability. In turn, this requires that the basic flow $u_0(z)$ have a critical level, that

is there exists a $z_c, -h < z_c < 0$ such that $u_0(z_c) = c$. Of course this is expected, and well-known. But when there is a critical level, in general ϕ will be singular at that level, and hence the theory described above needs a more careful examination. Also, note that instability also requires that the Richardson number $N^2/u_{0z}^2 < 1/4$, and then, in general, the singularities in ϕ are such that the integrals in (24)–(26) do not exist. The exception to this will occur when there is a layer, including z_c in which u_0 is a constant, for example a layered fluid, and in that case, the theoretical development above holds. For stable flows with no critical levels, we can assume that $c > u_0(z)$ for all z, and then $I_{1,2} > 0$. In this case, there is no real need to introduce this unfolding.

3 Asymptotic Expansion

Next we introduce the variables

$$s = X - cT, \quad \tau = \epsilon^2 T\,. \tag{29}$$

and seek a solution of the form

$$[\zeta, u, w, p] = \epsilon^2[\zeta_1, u_1, w_1, p_1] + \epsilon^4[\zeta_2, u_2, w_2, p_2] + \cdots\,. \tag{30}$$

At the leading order, we suppose that

$$\zeta_1 = A_1(s,\tau)\phi_1(z) + A_2(s,\tau)\phi_2(z)\,. \tag{31}$$

To leading order, the analogous expressions for the other variables are

$$\begin{aligned} u_1 &= A_1(W\phi_1)_z + A_2(W\phi_2)_z\,,\\ w_1 &= -A_{1s}W\phi_1 - A_{2s}W\phi_2\,,\\ p_1 &= A_1\rho_0 W^2\phi_{1z} + A_2\rho_0 W^2\phi_{2z}. \end{aligned} \tag{32}$$

In the variables s, τ, z the system (6)–(9) becomes

$$\rho_0(-Wu_s + wu_{0z}) + p_s = \tilde{F}_1 = F_1 - \epsilon^2\rho_0 u_\tau\,, \tag{33}$$

$$p_z + \rho_0 N^2\zeta = \tilde{G}_1 = -\frac{g\rho_{0zz}\zeta^2}{2} + \epsilon^2\rho_0 W w_s + 2\epsilon^2\Delta A_2(\rho_0 W\phi_{2z})_z\,, \tag{34}$$

$$u_s + w_z = 0\,, \tag{35}$$

$$-W\zeta_s - w = \tilde{J}_1 = J_1 - \epsilon^2\zeta_\tau\,. \tag{36}$$

The boundary condition (11) is unchanged, while (16) becomes

$$p - g\rho_0\zeta = H_1 = \frac{\rho_0 N^2\zeta^2}{2} + g\rho_0\zeta\zeta_z + 2\epsilon^2\Delta A_2\rho_0 W\phi_{2z} + \cdots, \quad \text{at} \quad z = 0\,. \tag{37}$$

Note that in the expressions for the second mode, W has been replaced with $W_2 - \epsilon^2\Delta$, $W_2 = c_2 - u_0$, and this generates the $\epsilon^2\Delta$ terms on the right-hand side. Using the expansion (30) we get the system

$$\rho_0(-Wu_{2s} + w_2u_{0z}) + p_{2s} = \tilde{F}_1\,, \tag{38}$$

$$p_{2z} + \rho_0 N^2\zeta_2 = \tilde{G}_1\,, \tag{39}$$

$$u_{2s} + w_{2z} = 0\,, \tag{40}$$

$$-W\zeta_{2s} - w_2 = \tilde{J}_1\,. \tag{41}$$

while the boundary conditions are

$$w_2 = 0\,, \quad \text{at} \quad z = -h\,, \tag{42}$$

$$p_2 - g\rho_0\zeta_2 = H_1\,, \quad \text{at} \quad z = 0\,, \tag{43}$$

where $F_1\,, \cdots$ etc. are evaluated at the leading order solution, $u_1\,, \cdots$. Note that eliminating u_2 yields

$$\rho_0(w_2u_{0z} + Ww_{2z}) + p_{2s} = \tilde{F}_1\,,$$

and then eliminating w_2 gives

$$-\rho_0 W^2\zeta_{2sz} + p_{2s} = F_2 = \tilde{F}_1 + \rho_0(u_{0z}\tilde{J}_1 + W\tilde{J}_{1z})\,.$$

Finally eliminating p_2 yields

$$(\rho_0 W^2\zeta_{2sz})_z + \rho_0 N^2\zeta_{2s} = I_2 = \tilde{G}_{1s} - F_{2z}\,, \tag{44}$$

with the boundary conditions

$$W\zeta_{2s} = 0 \quad \text{at} \quad z = -h\,, \tag{45}$$

$$\rho_0 W^2\zeta_{2sz} - g\rho_0\zeta_{2s} = H_2 = H_{1s} - F_2 \quad \text{at} \quad z = \eta_0\,. \tag{46}$$

The compatibility conditions are

$$\int_{-h}^{0} I_2\phi_{1,2}\,dz - [\rho_0\phi_{1,2}H_2](z = 0) = 0\,. \tag{47}$$

These can be written in the form

$$\int_{-h}^{0} \tilde{G}_{1s}\phi_{1,2}\,dz + \int_{-h}^{0} F_2\,\phi_{z1,z2}\,dz - [\rho_0 H_{1s}\phi_{1,2}](z=0) = 0\,. \tag{48}$$

When there is no shear flow, the modes $\phi_{1,2}$ are orthogonal, and these conditions are easily established. In the presence of a shear flow, they are clearly necessary conditions, but more work is needed to show that are sufficient. When only one mode is present, the derivation proceeds as follows with $A = A_1$. For two modes it is similar, with a set of similar terms for A_2 and some mixed terms.

For a single mode. the expressions for $\tilde{G}_1, F_2, H_1$ are in the Appendix. Making the substitutions into the compatibility condition (47) or (48) yields the KdV equation

$$A_\tau + \mu A A_s + \lambda A_{sss} = 0\,, \tag{49}$$

where the coefficients are given by

$$I\mu = 3\int_{-h}^{0} \rho_0 W^2 \phi_z^2\,dz\,, \tag{50}$$

$$I\lambda = \int_{-h}^{0} \rho_0 W^2 \phi^2\,dz\,, \tag{51}$$

$$I = 2\int_{-h}^{0} \rho_0 W \phi_z^2\,dz\,. \tag{52}$$

Next, when there are two modes, the corresponding expressions are also in the Appendix, and applying the compatibility condition (47) yields the coupled KdV equations

$$I_1(A_{1\tau} + \mu_1 A_1 A_{1s} + \lambda_1 A_{1sss}) + \nu_1[A_1 A_2]_s + \nu_2 A_2 A_{2s} + \lambda A_{2sss} = 0\,, \tag{53}$$

$$I_2(A_{2\tau} + \mu_2 A_2 A_{2s} + \lambda_2 A_{2sss} + \Delta A_{2s}) + \nu_2[A_1 A_2]_s + \nu_1 A_1 A_{1s} + \lambda A_{1sss} = 0\,. \tag{54}$$

The coefficients are given by (50)–(52) for $\mu_{1,2}, \lambda_{1,2}$ with indices inserted as appropriate, and by

$$\lambda = \int_{-h}^{0} \rho_0 W^2 \phi_1 \phi_2\,dz\,, \tag{55}$$

$$\nu_1 = 3\int_{-h}^{0} \rho_0 W^2 \phi_{1z}^2 \phi_{2z}\,dz\,, \tag{56}$$

$$\nu_2 = 3\int_{-h}^{0} \rho_0 W^2 \phi_{2z}^2 \phi_{1z}\,dz\,, \tag{57}$$

for $\nu_{1,2}, \lambda$.

4 Interacting Solitary Waves

To allow for possible instability, as discussed in Sect. 2.2, it is easily shown that the system (53), (54) is replaced by

$$I_1(A_{1\tau} + \Delta_1 A_{1s} + \mu_1 A_1 A_{1s} + \lambda_1 A_{1sss}) + \kappa A_{2s} + \nu_1 [A_1 A_2]_s + \nu_2 A_2 A_{2s} + \lambda A_{2sss} = 0\,, \tag{58}$$

$$I_2(A_{2\tau} + \Delta_2 A_{2s} + \mu_2 A_2 A_{2s} + \lambda_2 A_{2sss}) + \kappa A_{1s} + \nu_2 [A_1 A_2]_s + \nu_1 A_1 A_{1s} + \lambda A_{1sss} = 0\,. \tag{59}$$

The symmetry in the nonlinear coefficients ensures that the system is Hamiltonian. Indeed the Hamiltonian form is

$$J\frac{\partial \mathbf{A}}{\partial \tau} = -\frac{\partial}{\partial s}\left(\frac{\delta \mathscr{H}}{\delta \mathbf{A}}\right), \tag{60}$$

where $\mathbf{A}$ is the vector (A_1, A_2), J is the symmetric matrix

$$J = \begin{bmatrix} I_1 & 0 \\ 0 & I_2 \end{bmatrix} \tag{61}$$

and the Hamiltonian $\mathscr{H}$ is given by

$$\mathscr{H} = \int_{-\infty}^{\infty} H\, dx\,, \tag{62}$$

where

$$\begin{aligned} H = {} & \frac{I_1}{2}(\Delta_1 A_1^2 - \lambda_1 A_{1s}^2 + \frac{1}{3}\mu_1 A_1^3) + \frac{I_2}{2}(\Delta_2 A_2^2 - \lambda_2 A_{2s}^2 + \frac{1}{3}\mu_2 A_2^3) \\ & + \kappa A_1 A_2 - \lambda A_{1s} A_{2s} + \frac{1}{2}\nu_2 A_2^2 A_1 + \frac{1}{2}\nu_1 A_1^2 A_2\,. \end{aligned} \tag{63}$$

The Hamiltonian is an invariant, that is $\mathscr{H}$ is conserved, and can be interpreted as energy. Another invariant is

$$\mathscr{P} = \int_{-\infty}^{\infty} P dx, \tag{64}$$

where

$$P = I_1 A_1^2 + I_2 A_2^2, \tag{65}$$

which can be interpreted as momentum. Two other conserved quantities are the Casimirs,

$$\mathscr{A}_1 = \int_{-\infty}^{\infty} A_1\, dx, \quad \mathscr{A}_2 = \int_{-\infty}^{\infty} A_2\, dx\,, \tag{66}$$

which can be interpreted as mass. Note here, that if $I_1 I_2 < 0$ then P is sign-indefinite, and this is precisely the criterion for linear instability, see (28). On the other hand if $I_1 I_2 > 0$, then P is sign-definite, and its conservation ensures a form of stability; thus the criterion for linear stability and nonlinear stability coincide. An appropriate Poisson bracket for the Hamiltonian system (60) is

$$[F, G] = \int_{-\infty}^{\infty} \frac{\delta F}{\delta \mathbf{A}} J^{-1} \frac{\partial}{\partial x} \left(\frac{\delta G}{\delta \mathbf{A}} \right) a x, \tag{67}$$

for which all the usual properties, including the Jacobi identity, can now be readily verified.

It is not our purpose here to discuss solutions of the coupled KdV system (58), (59) in any detail. Indeed, it would seem that when compared to the single KdV equation, very little is known about the possible solution sets. Grimshaw and Iooss [17] determined the class of all steady solitary wave solutions for the reduced system (2), (3). Gear and Grimshaw [12] and Gear [18] reported numerical experiments demonstrating two principal kinds of solutions, namely either phase-locked solitary waves in each system, or leapfrogging solitary waves, analogous to those reported by Nitsche et al. [16] in a deep-fluid coupled system (see also the references therein). Leapfrogging is a term used to describe oscillatory behaviour in which solitary waves in each component of the coupled system, exchange energy with the other component in an apparently periodic manner. Malomed [19], Kivshar and Malomed [20] and Gottwald and Grimshaw [8, 9] presented an asymptotic analyses of interacting solitary waves, and leapfrogging behaviour. Recently Wright and Scheel [21] studied the stability of solitary waves in certain special coupled KdV systems, and showed that leap-frogging is a form of instability, in which the component solitary waves eventually separate. A similar conclusion was reached by Nitsche et al. [16] in a study of interacting solitary waves in three-layered fluid system with a deep middle layer.

As an indication of how leapfrogging may arise, we briefly re-examine the simplified system (2), (3), using an asymptotic analysis similar to that described by Gottwald and Grimshaw [8, 9]. An alternative approach is to use the Hamiltonian formulation directly, combined with this slowly-varying hypothesis, see Malomed [19] and Kivshar and Malomed [20]. Thus, we suppose that κ is a small parameter, and can be neglected at the leading order. Indeed when $\kappa = 0$, the system (2), (3) reduces to two uncoupled KdV equations, and then has the solitary wave solutions

$$A = a_1 \operatorname{sech}^2(\gamma_1(x - V_1 t - x_1)), \quad B = a_2 \operatorname{sech}^2(\gamma_2(x - V_2 t - x_2)), \tag{68}$$

where

$$V_1 - \Delta_1 = \frac{\mu_1 a_1}{3} = 4\lambda_1 \gamma_1^2, \; V_2 - \Delta_2 = \frac{\mu_2 a_2}{3} = 4\lambda_2 \gamma_2^2. \tag{69}$$

In the uncoupled limit, there is no connection between the solitary wave speeds $V_{1,2}$ and phases $x_{1,2}$. But in the weakly coupled case, it is clear that we require that these should be approximately equal.

For the weakly coupled system, we seek an asymptotic expansion in the form of slowly varying solitary waves, that is

$$A = a_1 \operatorname{sech}^2(\gamma_1(x - \Phi_1(t)), \quad A_2 = a_2 \operatorname{sech}^2(\gamma_2(x - \Phi_2(t)), \tag{70}$$

where

$$\mu_1 a_1 = 12\lambda_1\gamma_1^2, \quad \mu_2 a_2 = 12\lambda_2\gamma_2^2. \tag{71}$$

and

$$\Phi_{1t} = V_1 + c_1^{(1)} = \Delta_1 + \frac{\mu_1 a_1}{3} + c_1^{(1)}, \quad \Phi_{2t} = V_2 + c_2^{(1)} = \Delta_2 + \frac{\mu_2 a_2}{3} + c_2^{(1)}. \tag{72}$$

Here $a_{1,2}(t)$ are slowly varying functions of t, and $c_{1,2}^{(1)}$ are $O(\kappa)$ correction terms, determined by a direct asymptotic expansion, as described by Gottwald and Grimshaw [8, 9]. The outcome is determined by the momentum expressions

$$\begin{aligned} \frac{d}{dt}\int_{-\infty}^{\infty} \frac{I_1 A_1^2}{2}\, dx &= -\kappa \int_{-\infty}^{\infty} A_1 A_{2x}\, dx, \\ \frac{d}{dt}\int_{-\infty}^{\infty} \frac{I_2 A_2^2}{2}\, dx &= -\kappa \int_{-\infty}^{\infty} A_2 A_{1x}\, dx. \end{aligned} \tag{73}$$

The sum of these two expressions yields the momentum invariant (65). Substitution of the slowly varying solitary waves (70) into (73) yields

$$\begin{aligned} \frac{I_1 a_1 a_{1t}}{\gamma_1} &= -\kappa \frac{\partial \mathscr{J}}{\partial \Phi}, \\ \frac{I_2 a_2 a_{2t}}{\gamma_2} &= \kappa \frac{\partial \mathscr{J}}{\partial \Phi}, \end{aligned} \tag{74}$$

where

$$\mathscr{J} = \int_{-\infty}^{\infty} a_1 a_2 \operatorname{sech}^2(\gamma_1(s - \Phi))\operatorname{sech}^2(\gamma_2 s)\, ds, \quad \Phi = \Phi_1 - \Phi_2. \tag{75}$$

These are supplemented by the velocity relations (72), which can be rewritten in the form

$$\Phi_t = \Delta + \frac{\mu_1 a_1}{3} - \frac{\mu_2 a_2}{3} + c_1^{(1)} - c_2^{(1)}, \quad \Delta = \Delta_1 - \Delta_2. \tag{76}$$

The speed correction terms are found from higher-order terms in the asymptotic expansion, and are given by Grimshaw and Mitsudera [22] or Grimshaw et al. [23],

$$c_{1,2}^{(1)} = \frac{\mu_{1,2} a_{1,2}^{(s)}}{6} + \kappa \frac{\gamma_{1,2}}{a_{1,2}} \frac{\partial \mathscr{J}}{\partial a_{1,2}}, \quad \text{where} \quad \frac{\mu_{1,2} a_{1,2}^{(s)}}{3} = \text{sign}[\lambda_{1,2}] \frac{a_{1t,2t}}{a_{1,2}\gamma_{1,2}} \tag{77}$$

Here $a_{1,2}^{(s)}$ is the amplitude of the shelves generated by the failure of the slowly-varying solitary waves to conserve the mass invariants (66), and the respective signs correspond to whether the shelf lies behind or in front of the solitary wave. The second term is that expected from a Hamiltonian formulation, where we note that substitution of the *ansatz* (70) into the Hamiltonian (62), (63) yields

$$\mathscr{H} \approx \mathscr{H}_0 + \kappa \mathscr{J},$$

$$\text{where} \quad \mathscr{H}_0 = I_1 \left(\frac{2\Delta_1 a_1^2}{3\gamma_1} + \frac{2\mu_1 a_1^3}{15\gamma_1} \right) + I_2 \left(\frac{2\Delta_2 a_2^2}{3\gamma_2} + \frac{2\mu_2 a_2^3}{15\gamma_2} \right). \tag{78}$$

Note that then

$$V_{1,2} = \frac{a_{1,2}}{\gamma_{1,2}} \frac{\partial \mathscr{H}_0}{\partial a_{1,2}}. \tag{79}$$

Using the relations (71), we see that $\mathscr{J} = \mathscr{J}(a_1, a_2, \Phi)$ and so (74), (76) form three first order ordinary differential equations for the three unknowns a_1, a_2, Φ. However, (74) have the integral

$$\frac{2I_1 a_1^2}{3\gamma_1} + \frac{2I_2 a_2^2}{3\gamma_2} = \text{constant} = M_0, \tag{80}$$

which can also be deduced directly from the momentum invariant (65). Thus the system can be reduced to two first order ordinary differential equations which can then be analysed using phase plane methods.

This system remains still rather complicated, and so here we make a further simplification. Let $a_{1,2} = a_{1,2}^{(0)}, \Phi = 0$ be a steady-state equilibrium solution, and set

$$a_{1,2}(t) = a_{1,2}^{(0)} + b_{1,2}(t), \quad \text{where} \quad \Delta + \frac{\mu_1 a_1^{(0)}}{3} - \frac{\mu_2 a_2^{(0)}}{3} = 0, \tag{81}$$

where $b_{1,2}$ are small perturbations. Omitting the higher-order speed correction terms $c_{1,2}^{(1)}$, (76) becomes

$$\Phi_t = \frac{\mu_1 b_1}{3} - \frac{\mu_2 b_2}{3}, \tag{82}$$

while (74), (75) becomes

$$I_1 b_{1t} = -\kappa \gamma_1^{(0)} a_2^{(0)} \frac{\partial \mathscr{K}}{\partial \Phi},$$

$$I_2 b_{2t} = \kappa \gamma_2^{(0)} a_1^{(0)} \frac{\partial \mathscr{K}}{\partial \Phi}, \tag{83}$$

where

$$\mathscr{K}(\Phi) = \int_{-\infty}^{\infty} \operatorname{sech}^2(\gamma_1^{(0)}(s-\Phi))\operatorname{sech}^2(\gamma_2^{(0)}s)\,ds\,. \tag{84}$$

Note that $a_1^{(0)}a_2^0\mathscr{K}$ is just $\mathscr{J}$ evaluated at the equilibrium solution for the amplitudes. Also, the relation (80) becomes

$$I_1\gamma_2^{(0)}a_1^{(0)}b_1 + I_2\gamma_1^{(0)}a_2^{(0)}b_2 = \text{constant} = M_1\,, \tag{85}$$

Although the resulting system is linear in $b_{1,2}$ it is advantageous to keep the full dependence of Φ in $\mathscr{K}$. Then elimination of $b_{1,2}$ yields a single equation,

$$\Phi_{tt} - C\frac{\partial\mathscr{K}}{\partial\Phi} = 0\,, \tag{86}$$

where

$$C = \frac{\kappa}{3}\left(\frac{\mu_1\gamma_1^{(0)}a_2^{(0)}}{I_1} + \frac{\mu_2\gamma_2^{(0)}a_1^{(0)}}{I_2}\right) = 4\kappa\left(\frac{\mu_1\lambda_1\gamma_1^{(0)}\gamma_2^{(0)2}}{I_1\mu_2} + \frac{\mu_2\lambda_2\gamma_2^{(0)}\gamma_1^{(02)}}{I_2\mu_1}\right). \tag{87}$$

This reduced equation has an integral

$$\frac{\Phi_t^2}{2} - C\mathscr{K}(\Phi) = E_1\,, \tag{88}$$

which can be shown to be a consequence of the Hamiltonian invariant described above. Since $\mathscr{K}(\Phi)$ is a bounded function of $\Phi, -\infty < \Phi < \infty$, it follows that regardless of the sign of C, Φ_t^2 is also bounded, and there is nonlinear stability in all cases.

For (86) $\Phi = 0$ (when also $b_1 = b_2 = 0$) is an equilibrium point, corresponding to two phase-locked solitary waves. Near $\Phi = 0$, (86) becomes

$$\Phi_{tt} + \Omega^2\Phi \approx 0\,, \tag{89}$$

where

$$\Omega^2 = -C\frac{\partial^2\mathscr{K}}{\partial\Phi^2}(\Phi = 0) = 4C\gamma_1^{(0)}\gamma_2^{(0)}I_0$$

$$\text{and}\quad I_0 = \int_{-\infty}^{\infty} \operatorname{sech}^2(\gamma_1^{(0)}s)\operatorname{sech}^2(\gamma_1^{(0)}s)\tanh(\gamma_1^{(0)}s)\tanh(\gamma_2^{(0)}s)\,ds\,. \tag{90}$$

Since $I_0 > 0$, it follows that the steady-state equilibrium solution is *locally* stable, or unstable, according as $C > 0$, or $C < 0$. In the phase plane, the origin is then a centre or a saddle point. The former corresponds to leapfrogging, since the orbits around the centre form a family of periodic solutions with period $2\pi/\Omega$ near the

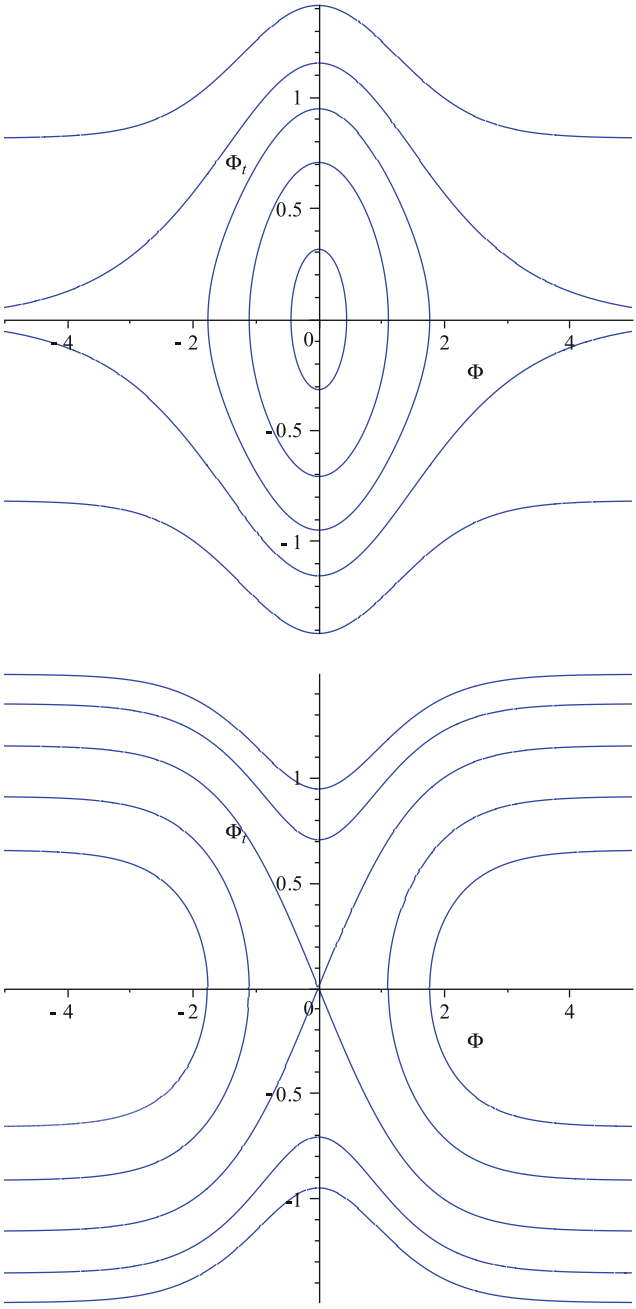

Fig. 2 Plot of the phase plane (88) for $\gamma_{1,2}^{(0)} = 1$ and $C = 0.5$ (*upper panel*) and $C = -0.5$ (*lower panel*)

origin, while the latter represents an immediate splitting apart of the two solitary waves. Note that since $I_{1,2}\lambda_{1,2} > 0$, see (51), $C > 0$ when $\kappa\mu_1\mu_2 > 0$. Using the relations (71), this corresponds to the case when the perturbation Hamiltonian $\kappa\mathscr{J} > 0, < 0$. according as either $I_{1,2} > 0$, when the system (2), (3) is linearly stable, or $I_1 I_2 < 0$, when the system (2), (3) is linearly unstable. Thus local stability of the interacting solitary waves is not related directly the linear stability of the zero state of the original system, see also [8]. The reason for this is that here instability of the coupled solitary waves is just separation, and this is not necessarily related to instability in the usual sense. When the higher-order speed correction terms $c_{1,2}^{(1)}$ are restored, the Hamiltonian part leaves the centre and saddle point classification unchanged, but the non-Hamiltonian part proportional to $a_{1,2}^{(s)}$ changes a centre into a focus, while leaving a saddle point unchanged. The focus can be stable or unstable, corresponding to either the eventual phase-locking of the leapfrogging solitary waves, or to their eventual splitting apart. These possible scenarios are discussed in more detail for related systems by Gottwald and Grimshaw [8], Wright and Scheel [21] and Nitsche et al. [16]. We conclude this brief summary of interacting solitary waves, by exhibiting in Fig. 2 a schematic phase plane defined by (88) for the reduced system (86). In the case of a saddle point, we see that the except for two exceptional orbits, all orbits pass to infinity, either as *passage*, or as *reflection*. For the case of a centre, there is a family of *periodic* orbits surrounding the centre, but this is itself bounded by a separatrix, outside which all orbits correspond to *passage*.

5 Summary

As we noted in the Introduction, coupled KdV systems can be expected to arise generically when there is a long wave resonance with near coincident phase speeds and two distinct modal functions. In this paper we have briefly reviewed the literature on such systems. In Sects. 2, 3 we have sketched the derivation for a stratified fluid, extending the derivation of Gear and Grimshaw [12] to the case when there is a background shear flow. The purpose here is to allow for the possibility that the long-wave resonance may lead to linear instability. Then in Sect. 4, we have revisited the asymptotic analysis developed in the cited literature to describe the phenomenon of leapfrogging solitary waves. It is clear that this approach has more potential to explore this phenomenon, especially when the first-order speed correction terms are restored. This was the method used by Nitsche et al. [16] to interpret their numerical results for leapfrogging solitary waves in a deep fluid context, but its exploitation in the present shallow fluid context has yet to be fully realised. In conclusion it is clear that coupled KdV systems have rich dynamics, which has not yet been fully explored.

Appendix

For a single mode

$$\tilde{G}_{1s} = (\rho_0 N^2)_z \phi^2 A A_s - \rho_0 W^2 \phi A_{sss} \,,$$

$$F_2 = -2\rho_0 W \phi_z A_\tau + (-(\rho_0 W^2)_z \phi \phi_z - \rho_0 W^2 [\phi_z^2 - \phi \phi_{zz}]) A A_s \,,$$

$$H_{1s} = (\rho_0 N^2 \phi^2 + 2\rho_0 W^2 \phi_z^2) A A_s \,.$$

$$\text{Hence} \quad \tilde{G}_{1s}\phi + F_2 \phi_z = -2\rho_0 W \phi_z^2 A_\tau - \rho_0 W^2 \phi^2 A_{sss} + K A A_s \,,$$

$$K = (\rho_0 N^2)_z \phi^3 - \rho_0 (2W W_z \phi \phi_z^2 + W^2 \phi_z^3 - W^2 \phi \phi_z \phi_{zz}) - \rho_{0z} W^2 \phi \phi_z^2 \,,$$

$$K = (\rho_0 N^2 \phi^3 + 2\rho_0 W^2 \phi_z^2 \phi)_z + M \,,$$

$$M = \rho_0 [3(W^2 \phi_z)_z \phi \phi_z - 2(W^2 \phi_z^2 \phi)_z - 2W W_z \phi \phi_z^2 - W^2 \phi_z^3 + W^2 \phi \phi_z \phi_{zz}] \,,$$

$$\text{and so} \quad M = -3\rho_0 W^2 \phi_z^2 \,.$$

$$\text{Note that} \quad H_2 = H_{1s} - F_2 = 2\rho_0 W \phi_z A_\tau + (3\rho_0 W^2 \phi_z^2 - 2\rho_0 W^2 \phi \phi_{zz}) A A_s \,,$$

$$\text{and} \quad I_2 = \tilde{G}_{1s} - F_{2z} = (2\rho_0 W \phi_z)_z A_\tau - \rho_0 W^2 \phi A_{sss} + L A A_s \,,$$

$$L = (3\rho_0 W^2 \phi_z^2)_z + D \,, \quad D = -(2\rho_0 W^2 \phi \phi_{zz})_z - \rho_0 W^2 (\phi_z^2)_z \,.$$

For two coupled modes, the calculations follow those for a single mode, and the outcome is

$$I_2 = \tilde{G}_{1s} - F_{2z} = I_2^1 + I_2^2 + I_2^{12} + (2\rho_0 W \phi_{2z})_z \Delta A_{2s} \,,$$

$$\text{where} \quad I_2^j = (2\rho_0 W \phi_{jz})_z A_{j\tau} - \rho_0 W^2 \phi_j A_{jsss} + L_j A_j A_{js} \,, \quad j = 1, 2 \,,$$

$$\text{and} \quad I_2^{12} = L_{12} [A_1 A_2]_s \,,$$

$$L_j = (3\rho_0 W^2 \phi_{jz}^2)_z + D_j \,, \quad D_j = -2(\rho_0 W^2 \phi_j \phi_{jzz})_z - \rho_0 W^2 (\phi_{jz}^2)_z \,,$$

$$L_{12} = (3\rho_0 W^2 \phi_{1z} \phi_{2z})_z + D_{12} \,,$$

$$D_{12} = -(\rho_0 W^2 [\phi_1 \phi_{2zz} + \phi_2 \phi_{1zz}])_z - \rho_0 W^2 (\phi_{1z} \phi_{2z})_z \,.$$

$$\text{Also} \quad H_2 = H_{1s} - F_2 = H^1 + H^2 + H^{12} + 2\rho_0 W \phi_{2z} \Delta A_{2s} \,,$$

$$H^j = 2\rho_0 W \phi_{jz} A_{j\tau} + (3\rho_0 W^2 \phi_{jz}^2 - 2\rho_0 W^2 \phi_j \phi_{jzz}) A_j A_{js} \,, \quad j = 1, 2 \,,$$

$$H^{12} = (3\rho_0 W^2 \phi_{1z} \phi_{2z} - \rho_0 W^2 [\phi_1 \phi_{2zz} + \phi_2 \phi_{1zz}])(A_1 A_{2s} + A_2 A_{1s}] \,.$$

Acknowledgement I am grateful for helpful discussions and advice from my colleagues at Loughborough, Azwani Alias and Karima Khusnutdinova, and from Tom Bridges at the University of Surrey.

References

1. Craik, A.D.D.: Wave Interaction in Fluid Flows, p. 332. Cambridge University Press, Cambridge (1985)
2. Baines, P.G., Mitsudera, H.: On the mechanism of shear flow instabilities. J. Fluid Mech. **276**, 327–342 (1994)
3. Grimshaw, R.: Models for instability in inviscid fluid flows due to resonance between two waves. In: Debnath, L. (ed.) Nonlinear Stability Analysis. Advances in Fluid Mechanics, vol. II, Chap. 1, pp. 1–14, 28. WIT Press, Southampton (2001)
4. Hickernell, F.: The evolution of large-horizontal scale disturbances in marginally stable, inviscid shear flows I. Solutions of the Boussinesq equation. Stud. Appl. Math. **69**, 1–21 (1983)
5. Hickernell, F.: The evolution of large-horizontal scale disturbances in marginally stable, inviscid shear flows II. Solutions of the Boussinesq equation. Stud. Appl. Math. **69**, 23–39 (1983)
6. Helfrich, K.R., Pedlosky, J.: Time-dependent islated anomolies in zonal stable, inviscid shear flows I. Derivation of the amplitude evolution equations. J. Fluid Mech. **251**, 377–409 (1993)
7. Mitsudera, H.: Eady solitary waves: a theory of type B cyclogenesis. J. Atmos. Sci. **57**, 734–745 (1994)
8. Gottwald, G., Grimshaw, R.: The formation of coherent structures in the context of blocking. J. Atmos. Sci. **56**, 3640–3662 (1999)
9. Gottwald, G., Grimshaw, R.: The effect of topography on the dynamics of interacting solitary waves in the context of atmospheric blocking. J. Atmos. Sci. **56**, 3663–3678 (1999)
10. Grimshaw, R.: Models for long-wave instability due to a resonance between two waves. In: Iooss, G., Gues, O., Nouri, A. (eds.) Trends in Applications of Mathematics to Mechanics. Monographs and Surveys in Pure and Applied Mathematics, vol. 106, pp. 183–192. Chapman & Hall/CRC, Boca Raton (2000)
11. Grimshaw, R., Skyrnnikov, Y.: Long-wave instability in a three-layer stratified shear flow. Stud. Appl. Math. **108**, 77–88 (2002)
12. Gear, J., Grimshaw, R.:. Weak and strong interactions between internal solitary waves. Stud. Appl. Math. **70**, 235–258 (1984)
13. Grimshaw, R.: Internal solitary waves. In: Grimshaw, R. (ed.) Environmental Stratified Flows, Chap. 1, pp. 1–29. Kluwer, Boston (2001)
14. Grimshaw, R.: Korteweg-de Vries equation. In: Grimshaw, R. (ed.) Nonlinear Waves in Fluids: Recent Advances and Modern Applications. CISM Courses and Lectures No. 483, Chap. 1, pp. 1–28. Springer, New York (2005)
15. Grimshaw, R.: Introduction. In: Grimshaw, R. (ed.) Solitary Waves in Fluids. Advances in Fluid Mechanics, vol. 45, pp. 1–19. WIT Press, Southampton (2007)
16. Nitsche, M., Weidman, P.D., Grimshaw, R., Ghrist, M., Fornberg, B.: Evolution of solitary waves in a two-pycnocline system. J. Fluid Mech. **642**, 235–277 (2009)
17. Grimshaw, R., Iooss, G.: Solitary waves of a coupled Korteweg-de Vries system. Math. Comput. Simul. **62**, 31–40 (2003)
18. Gear, J.: Strong interactions between solitary waves, belonging to different wave modes. Stud. Appl. Math. **72**, 95–124 (1985)
19. Malomed, B.A.: "Leapfrogging" solitons in a system of two coupled KdV equations. Wave Motion **9**, 401–411 (1987)
20. Kivshar, Y.S., Malomed, B.A.: Solitons in a system of coupled Korteweg-de Vries equations. Wave Motion **11**, 261–269 (1989)
21. Wright, J.D., Scheel, A.: Solitary waves and their linear stability in weakly coupled KdV equations. Z. Angew. Math. Phys. **58**, 136 (2007)
22. Grimshaw, R., Mitsudera, H.: Slowly-varying solitary wave solutions of the perturbed Korteweg-de Vries equation revisited. Stud. Appl. Math. **90**, 75–86 (1993)
23. Grimshaw, R., Pelinovsky, E., Tian, X.: Interaction of a solitary wave with an external force. Physica D **77**, 405–433 (1994)

Water Waves and Time Arrows in Conservative Continuum Physics

P.A. Tyvand

1 Introduction

A time arrow in a conservative physical system seems to be a paradox. Yet it is a well-known phenomenon in many-body physics. The collective behavior of many-body systems in elastic collisions exhibits a time arrow if the number of degrees of freedom is sufficiently large and the system starts from an unlikely initial state. This is the case even when each body is finite, has regular shape and performs an individual motion according to Newton's laws without dissipation.

Time arrows are implicitly established in conservative continuum physics, especially in connection with turbulence. The well-known energy cascade that transfers energy from greater turbulent vortices to smaller vortices is basically inviscid on most length scales, apart from the shortest ones. This time arrow of energy cascade can be observed in the transient degradation of smoke vortices of a campfire that is suddenly extinguished. There is no general consensus on the causality behind the non-dissipative time arrow that changes turbulent vortices into smaller ones. Bejan [1] has suggested a fully inviscid mechanism for this irreversible energy cascade in turbulence: The buckling instability of cylindrical vortices under compression, which bends the fluid cylinders and prevents their radii from increasing in time. This time arrow rests on the asymmetry of unstable compression versus stable stretching: There is no instability mechanism preventing the diameter of a vortex from decreasing when it is being stretched. The time arrow of the turbulent energy cascade is thereby explained qualitatively as an inviscid instability phenomenon. These conservative processes of fully developed turbulence contrast its dissipative onset with a balance between inertial and viscous forces.

P.A. Tyvand (✉)
Department of Mathematical Sciences and Technology, Norwegian University of Life Sciences, P.O. Box 5003, 1432 Ås, Norway
e-mail: peder.tyvand@umb.no

R.G. Rubio et al. (eds.), *Without Bounds: A Scientific Canvas of Nonlinearity and Complex Dynamics*, Understanding Complex Systems,
DOI 10.1007/978-3-642-34070-3_29,

In the present note, water waves is chosen as a field for reviewing and developing some basic notions of time arrows in conservative continuum physics. We will limit ourselves to the classical theory of nonlinear water waves, which assumes irrotational flow in an inviscid and incompressible fluid of constant density. The water waves are subject to constant free-surface pressure without surface tension.

2 Eulerian Equations of Nonlinear Water Waves

The strictly Eulerian description of nonlinear water waves captures all phenomena except for overturning waves where the surface elevation $\eta(x, y, t)$ becomes multi-valued. The governing equation for inviscid irrotational flow is

$$\nabla^2 \Phi = 0. \tag{1}$$

The exact nonlinear free-surface conditions, ignoring surface tension effects, are given by

$$\frac{\partial \eta}{\partial t} + \nabla \Phi \cdot \nabla \eta = \frac{\partial \Phi}{\partial z}, \quad z = \eta(x, y, t), \tag{2}$$

$$\frac{\partial \Phi}{\partial t} + \frac{|\nabla \Phi|^2}{2} + g\eta = 0, \quad z = \eta(x, y, t). \tag{3}$$

Φ is the velocity potential, t is time, and g is the gravitational acceleration. It is evident that the equations are conserved under the time-reversal transformation

$$(x, y, z, t, \Phi, \eta) \rightarrow (x, y, z, -t, -\Phi, \eta). \tag{4}$$

The time reversal means that the spatial coordinates are fixed and the elevation is unchanged, while the time and the velocity potential change sign. This conservation of the set of equations holds for the exact nonlinear system, and also for its linearized version. We will discuss various examples of time arrows in water waves, assuming that the full set of equations is applied.

The Lagrangian description of motion offers an alternative framework for studying water waves theoretically. It captures overturning waves, where the surface elevation becomes multi-valued and forbids a fully Eulerian description. It is also suitable for phenomena with an explicit first cause, because it numbers all particles by their initial position. The Lagrangian description of motion is physically equivalent to the Eulerian description.

The application of the full equations is essential for the time reversibility. As a contrast, some of the established simplifications of the nonlinear water-wave equations are not invariant under the time-reversal transformation. These are the type of equations that allow only one direction of wave propagation because they work with only one time derivative instead of two: The Korteweg de Vries equation for shallow-water waves and the cubic Schrödinger equation for deep-water waves.

These simplified nonlinear equations have explicit time arrows, and they may give computational advantages when we work with nonlinear wave groups. These time arrows are nevertheless artificial, because they rest on the removal of one of the two time derivatives from the full second-order mathematical problem in the time domain.

First we give two examples where free-surface nonlinearities are essential. Next we give additional examples of time arrows that arise within strictly linear theory.

3 Time Arrow in Nonlinear Wave Breaking

It ie easy to realize that a time arrow exists in the spectacular nonlinear phenomenon of breaking water waves. A plunging breaker is a wave where the tip of the crest bends over while the flow is still inviscid and irrotational. In the pioneering theoretical paper by Longuet-Higgins and Cokelet [2], the time arrow for nonlinear wave breaking with infinite water depth was initiated by an asymmetric pressure distribution $P(x, y, t)$ applied directly on the surface. The externally imposed surface pressure was traveling with the phase speed of the deep-water wave, and it lasted for half a wave period, varying harmonically with time. After that, the external pressure was turned off, while its imposed free-surface asymmetry evolved further into wave breaking. The applied external pressure broke the symmetry in time, and served as a first cause for the later evolution of wave breaking.

The process leading to wave breaking is an indirect way of revealing a time arrow. During the stage when overturning of the wave crest takes place, the time arrow becomes visible, in spite of the fact that the process is then time-reversible. The manifestation of the time arrow is delayed in time compared with its cause: the external pressure work. The final process where the tip of the plunging breaker performs an almost perfect free fall in the gravity field, is a strictly one-way process in time: It is impossible to reverse this free fall by generating an initial condition of a triple-valued surface elevation that later moves in a well-ordered manner upwards in the gravity field and evolves smoothly into a single-valued surface elevation.

Now we include an external pressure $P(x, y, t)$ in the dynamic boundary condition (3)

$$\frac{\partial \Phi}{\partial t} + \frac{|\nabla \Phi|^2}{2} + g\eta = -\frac{P(x, y, t)}{\rho}, \quad z = \eta(x, y, t). \tag{5}$$

The equations can be now be conserved under the time-reversal transformation

$$(x, y, z, t, \Phi, \eta, P) \rightarrow (x, y, z, -t, -\Phi, \eta, P). \tag{6}$$

The external pressure distribution $P(x, y, t)$ must be preserved under the time-reversal transformation in order to maintain the formal reversibility. The question

is whether it is realistic to achieve a time reversal of a real process towards wave breaking. The first cause for inviscid wave breaking is the asymmetric external pressure. To reverse this process would be to put the effect ahead of its cause, which is impossible.

We recognize two basic causes behind natural wave breaking in the sea. (1) Energy transfer from wind stress to waves in the open sea. The build-up of wave amplitude from wind may enable breaking. (2) A wave that does not break in the open sea can do so after it has entered shallow water. This is due to the concentration of energy per fluid volume, which increases the amplitude in the surface elevation.

(1) Real generation of ocean waves by turbulent wind stress has an explicit time arrow because it involves entropy production. In a fully inviscid model, one may mimic the energy input from wind stress by a variable and uneven pressure $P(x, y, t)$ applied on the surface.
(2) Tidal waves and tsunamis are transient long waves that may turn into bores due to the reduced sea depth near the coast. These bores may break when the sea depth becomes sufficiently small. The early breaking of an undular bore on a sloping beach is an inviscid phenomenon, caused by the increasing wave energy per volume of fluid. The time arrow for an individual wave is here a result of a spatial gradient in the water depth. One may say that the spatial arrow of the depth gradient serves as the cause behind the time arrow of a transient wave packet that breaks on a sloping beach. The time arrow caused by a spatial arrow is somewhat paradoxical because this time arrow might turn into periodic recurrence if the fluid depth is periodic. However, if the wave is steep enough on a periodic bottom, it will break before the depth reaches its minimum. Then there is an effective time arrow, because the possible recurrence could not be completed.

Breaking of bores on constant depth is a different phenomenon, that can only be modelled by allowing transient fluxes of mass and energy into the system. This was the procedure of Landrini and Tyvand [3] who gave an explicit first cause for the time arrow of breaking bores: A concentrated 2D bottom source turned on impulsively at time zero, maintaining a constant mass flux to develop an undular bore that can possibly break. The free-surface conditions remain fully reversible, and the time arrow is due to the steady input of energy and mass from a concentrated bottom source suddenly turned on at time zero. It is not possible to reverse this process in time, because of the accumulation of potential energy in the bore after the source has been turned on. To assume that a bore with its potential energy exists without a cause, and try to run its generation process backward in time, would be to drain energy that came from nowhere. The undular bore at constant depth therefore owes its existence to a first cause that continues as a lasting cause: The source that was suddenly turned on at time zero, and it remained constant thereafter. This causation has an explicit time arrow, even though the governing system of equations is reversible in time.

4 Time Arrow in Nonlinear Merging of Bores

A bore is a propagating change of water level in a channel. There must be a cause for the rising water level, or a source delivering the added flux of water coming in. The simplest mathematical device for generating a bore is a submerged 2D mass source that is turned on at time zero [4]. Explicitly or implicitly a time arrow will be present in all theories of undular bores. In his pioneering paper, Peregrine [5] introduced a time arrow in three implicit ways: (i) By applying a set of nonlinear shallow-water equations that are not time reversible. (ii) By giving a somewhat artificial initial condition where there is a smooth continuous transition between a uniform incoming bore and still water. (iii) By feeding net fluxes of mass and energy into the computational domain, so that the bore can progress with the given height.

The time arrow of a bore is obvious because the bore needs a steady input of energy and fluid mass. There is also a time arrow in the undulations that grow slowly with time. The time arrow of a bore is due to initial conditions and kinematic boundary flux conditions applied to the full nonlinear equations that are reversible in time.

We may search for an explicit time arrow in the nonlinear merging of two bores in a channel with constant depth. When a greater bore rides on a smaller bore from behind and overtakes it, the result will be a merged bore that is essentially dominated by the bore that came from behind. The time arrow means that bore merging is a one-way process: one bore could not split into two separate bores.

A convenient way of generating two merging bores mathematically, is to change the strength of a bottom source. The time arrow of the merging bores is then a combined effect of two primary causes with a mutual time delay. The first cause is a bottom source with a small steady flux that is started at time zero to establish an undular bore with a small height. After a certain time, the second cause is the suddenly increased steady flux of the bottom source, to producing a higher bore than the one already established. This higher, second bore propagates faster than the first bore, since its effective depth is greater. Therefore the higher second bore comes from behind and rides on the smaller first bore until it overtakes it. The computations by Bestehorn and Tyvand [6] show how two such bores merge into one common bore.

5 Time Arrow in a Cauchy–Poisson Problem

We have considered time arrows that involve free-surface nonlinearities. Now we turn our attention to time arrows that arise in linear theory of water waves. A classical case of a time arrow in linear water waves is the dispersive Cauchy–Poisson problem on infinite depth. Lamb [7, p. 384] described the large-time asymptotics of the transient wave produced by a concentrated initial elevation. There are three reasons for the time arrow in the 3D Cauchy–Poisson problem.

(1) The initial condition is a first cause for the process that follows. (2) The strong dispersion of a deep-water wave group will smear out the initial disturbance over a spatial domain that broadens with time. (3) There is outward propagation of energy from the concentrated disturbance.

It would not be possible to go backwards from a dispersed state to generate ring waves that propagate in the inward radial direction in order to form a concentrated state near the center.

It is intuitively obvious that there will be a time arrow for the ring waves generated by a stone that is thrown into a pond. During the stage of entrance of a stone thrown into a pond, the dynamic condition (5) is applicable. To reverse the stone-throwing process would be to take a wave pattern that has no cause and to combine it with a mysterious pressure distribution that has the exact variation in space and time to match the inward-going waves and finally kill them. This is impossible, because causation of this phenomenon is forward in time, which means that one cannot collect the sufficient information for a backward simulation.

A different class of Cauchy–Poisson problems are surface elevations released from rest. When a surface elevation is released from rest at $t = 0$, the process would be the same if we run it for time t positive or negative. Nevertheless, an axisymmetric ring wave from a released concentrated disturbance could not be restored fully by backward simulation based on the instant wave data at a late time. The first cause for a deep-water ring wave would not be fully detectable from the evolution at large values of time after the release. Thus a basic reason for time arrows appearing in the Cauchy–Poisson problems is that an effect cannot come before its cause.

6 A Radiation Condition Posing a Time Arrow

If the Cauchy–Poisson problem is 2D and restricted to hydrostatic shallow-water waves, there is no dispersion and no radial spreading of energy. Then the time arrow for a concentrated surface deflection released from rest at time $t = 0$ is very simple. It just expresses the fact that two equal wave pulses travel in opposite directions, away from the initial heap. There is no loss of information, and the time arrow expresses nothing but the outward propagation from the place of the first cause of released energy.

We leave the transient Cauchy–Poisson problem and go further to consider a time-periodic problem where a concentrated disturbance varies harmonically in time. Assuming that all the emitted wave energy comes from a harmonically oscillating source, one needs to formulate a radiation condition that ensures that the wave energy radiates out from the source and not into the source. Wehausen [8] pointed out that a radiation condition for a floating body is causal, which means that it guarantees that the forces on the oscillating body do not have effects that come before their causes in time.

An elementary description of a time arrow in radiation of 2D linearized water waves is given by writing the radiation conditions as follows

$$k\frac{\partial \eta}{\partial t} \pm \omega \frac{\partial \eta}{\partial x} = 0, \quad x \to \pm\infty, \tag{7}$$

where ω is the angular frequency of the forced oscillations and k is the resulting wave number for the emitted free waves at an infinite distance from the radiating object. The relevant 2D version of the general time-reversal transformation (4) can be written

$$(x, t, \eta) \to (x, -t, \eta). \tag{8}$$

We see that the radiation conditions (7) are not conserved under this transformation, which means that the radiation conditions have an explicit time arrow. Mathematically, this time arrow comes from the fact that the radiation conditions are of first order in time, while a time-reversible system requires a consistent second-order system in time. Physically, these radiation conditions are man-made algorithmic restrictions importing a time arrow into an otherwise time-reversible system. This constructed condition makes sure that the wave energy emitted by the oscillating system is transported out from the system at infinity, with no energy being imported into the system from infinity.

Alternatively, one may derive the radiation condition from a first cause: If a floating or submerged body starts its forced harmonic oscillation at time $t = 0$, then the conditions (7) appear asymptotically as $t \to \infty$ and $|x| \to \infty$.

We see that the implicit time arrow of a first cause in a time-evolving system may turn into an explicit time arrow in a time-periodic system. However, this is only true in the asymptotic limit of infinite time, which allows some of the information of the initial condition to be wiped out of the system by being transported beyond the spatial infinity where the radiation conditions are to be applied.

7 Time Arrows of Resonance and Instabilities

In a radiation problem, the phenomenon of resonance cannot be described quantitatively when we assume the flow to be oscillatory in time. Resonance will then disguise itself as an infinite amplitude. Within linear theory, resonance can therefore only be studied after we have relaxed the constraint of strictly time-periodic flow. This is important for the radiation of water waves from a submerged oscillating source in a current. At the critical frequency, it is impossible to determine a steady finite amplitude for the radiated waves unless nonlinear effects are taken into account [9].

There are time arrows both in forced resonance and in parametric resonance. However, a forced resonance that is imperfect in the sense that it misses the resonant angular frequency by a small amount $\Delta\omega$, loses its time arrow as it degenerates into

a recurrent beating phenomenon. The beating does not have a time arrow, since it is harmonic in time. It has a relatively long time period $2\pi/\Delta\omega$, and the limit $\Delta\omega = 0$ represents exact linearized resonance, where the amplitude grows steadily in time from any small initial value.

Parametric resonance is a kind of instability. In the context of hydrodynamic stability, it is obvious that an individual single mode of linearized instability has a time arrow. This is because the time reversal of an exponentially growing mode gives an anti-symmetric exponential damping in time. Hydrodynamic instability theory is mostly concerned with dissipative systems where the time arrows exist within the general system of governing equations [10]. The simplest conservative instability mechanism related to water waves is the Rayleigh–Taylor instability of an inviscid fluid. The governing equations of nonlinear Rayleigh–Taylor instability are identical to (1)–(3), with the only exception that gravity is turned in the opposite direction ($g \to -g$). This replacement changes nothing concerning the time reversibility. The full governing equations for the Rayleigh–Taylor instability are therefore reversible in time. In order to discuss the time arrow for the Rayleigh–Taylor instability, we consider the linearized dispersion relation for traveling waves, which gives imaginary phase velocities. Physically these imaginary phase velocities are rates ($\pm\sigma$) of (positive) exponential growth and (negative) damping, governed by the dispersion relation

$$\sigma = \sqrt{gk\tanh(kH)}, \tag{9}$$

where H is the thickness of the undisturbed fluid layer. The instability for a disturbance with given wave number k reveals itself as a time-reversible pair: one positive σ and one negative σ, with equal absolute values. Reversing time in the full linearized Rayleigh–Taylor instability problem simply means that the mode with exponential growth will change into a mode with exponential damping, and vice versa.

The evolution of a surface Fourier mode e^{ikx} can be expressed by the field at $t = T$ as follows

$$\eta(x,t) = \frac{(\sigma\eta(x,T) + \dot{\eta}(x,T))e^{\sigma(t-T)} + (\sigma\eta(x,T) - \dot{\eta}(x,T))e^{-\sigma(t-T)}}{2\sigma}, \tag{10}$$

$$\dot{\eta}(x,t) = \frac{(\sigma\eta(x,T) + \dot{\eta}(x,T))e^{\sigma(t-T)} - (\sigma\eta(x,T) - \dot{\eta}(x,T))e^{-\sigma(t-T)}}{2}, \tag{11}$$

where $\eta(x,t)$ is the surface deflection, and $\dot{\eta}(x,t)$ is the surface velocity.

Two particular cases are worth noting. The first particular case is

$$\text{Case (i):} \quad \sigma\eta(x,T) = \dot{\eta}(x,T). \tag{12}$$

This case gives pure exponential growth for $t > T$, and pure exponential decay if time is reversed for $t < T$. The second particular case is

$$\text{Case (ii):} \quad \sigma\eta(x,T) = -\dot{\eta}(x,T) \tag{13}$$

This case gives pure exponential decay for $t > T$, and pure exponential growth if time is reversed for $t < T$.

These two particular cases have time arrows, with exponential growth in one time direction and exponential decay in the opposite time direction. Note that these two conditions must be exactly satisfied to have any relevance. In all other cases we have $\sigma|\eta(x,T)| \neq |\dot{\eta}(x,T)|$, which gives exponential growth both in the forward direction of time as well as the backward direction of time.

The general meaning of T is a point in time from which we start or restart simulating the system either forward or backward in time. Imagine that we start a simulation of this linearized Rayleigh–Taylor system with an arbitrary initial condition at $T = 0$ and let time go forward until $T = T_1$. At $T = T_1$ we restart a backward (or forward) simulation of the system, assuming small errors in the starting conditions $(\eta(x,T_1), \dot{\eta}(x,T_1))$. These errors will blow up exponentially as we simulate the system further in time, because it is practically impossible to hit exactly the two cases (i) and (ii). This means that all forward or backward simulations of a linearized Rayleigh–Taylor system will have a time arrow in the sense that perturbations grow and accumulate. The system will in practice go irreversibly away from its initial state, in spite of being governed by mathematical equations that are explicitly time reversible. The system will soon become nonlinear, which will accelerate the processes of instability further, leading to irreversible drop formation. The time arrow of the conservative Rayleigh–Taylor instability is essentially chaotic, because it is based on the sensitivity with respect to initial conditions. This chaotic time arrow does not rely on any nonlinear effects, as it starts within linear theory.

There are other inviscid instability phenomena in continuum physics. In the theory of water waves we have the Benjamin–Feir instability, which is usually studied with a reduced system of equations that are of first order in time. This means that it has an explicit time arrow, unlike the Rayleigh–Taylor instability.

8 Time Arrow of Spiral Water Waves

Dalrymple and Dean [11] invented spiral water waves and described a rotating wavemaker that can generate such waves. Mei [12] performed a further investigation of spiral water waves. Perfect spiral waves have two intriguing properties. (i) They possess a time arrow that is detectable from the snapshot of a surface wave pattern. (ii) Their shape is steady seen from an observer in a non-inertial coordinate system that rotates with the same angular velocity as the given angular frequency of the spiral waves. No other water wave system than the spiral waves will look steady from a rotating coordinate system.

Natural spiral waves occur in geophysics, but they always have vorticity. Spiral water waves without vorticity are fundamentally algorithmic, and can only be generated by intelligent beings. It is interesting to link spiral water waves to basic

algorithmic theory [13]. All algorithms can be broken down to three types of commands: (1) Choice. (2) Sequence. (3) Repetition.

The spiral wavemaker possesses all these three characteristics: (1) The choice of rotation, either clockwise or counter-clockwise. (2) The sequence of orientation angles of the steadily rotating wavemaker. (3) The repetition of the orientation angle, with a period of 2π.

9 Time Arrow of the Impulsive Time Scale

Perhaps the least recognized time arrow of water waves is the time arrow of the incompressible impulsive time scale. It is of fundamental importance in the fields of tsunami generation and liquid sloshing starting from rest in open containers.

It is essential that the incompressible impulsive flow starts from rest with a flat free surface in the gravity field

$$\eta = 0, \ t = 0^+. \tag{14}$$

The initial dynamic condition for impulsive flow is then

$$u = v = 0, \ \ z = 0, \ t = 0^+. \tag{15}$$

We let u, v and w denote the velocity components in the x, y and z directions. The physical explanation for condition (15) is that there are no horizontal forces that can induce horizontal velocities during the sudden impulsive start. The early flow after the impulsive start is governed by the linearized free-surface conditions, which we derive from the full conditions (2)–(3) to find

$$\frac{\partial \eta}{\partial t} = w, \ \ z = 0, \tag{16}$$

$$\frac{\partial (u, v)}{\partial t} + g \nabla \eta = 0, \ \ z = 0. \tag{17}$$

It is important to note that the early impulsive flow takes the degenerate condition (15) as dynamic condition instead of (17). During the impulsive time scale after the start, the kinematic condition (16) builds up a nonzero surface deflection, while the influence of gravity is still negligible. The governing equations will then have a time arrow, as long as they are of first order in time, with the surface velocity in the kinematic condition (16) representing the only time derivative.

The second dynamic condition (17) makes the flow again reversible in time after the impulsive time scale, because it changes the system of equations from a first-order system in time into the full second-order system. Equation (17) shows that a surface particle slides freely tangentially along the free surface, accelerated with

the tangential component of the gravitational acceleration. Thus gravity converts any nonzero surface slope into horizontal acceleration of the surface particles along the projection of the surface slope. This means that it is impossible to restore a flat undisturbed free surface from an established wave field generated from an impulsive start. After the early impulsive time interval, any later gradient of the surface deflection $\eta(x, y, t)$ must generate horizontal surface acceleration as time progresses. There will be an irreversible time arrow from the flat initial surface with zero horizontal velocity, via the early impulsive build-up of a surface deflection to the continuous oscillations in surface velocity. There is a signature on the later flow from the early impulsive stage. In a finite container, this signature will persist. In an infinite fluid domain, however, this impulsive signature is likely to disappear from any finite domain as time goes.

The investigation of the time arrow due to impulsive flow has concentrated on the wavemaker problem, starting with the work by Peregrine [14]. Here the time arrow manifests itself in a dramatic way as a free-surface singularity at the waterline where the solid wall meets the initially undisturbed free surface. Waterline singularities can in principle be resolved mathematically by matched asymptotic expansions, but this is very difficult to do.

The waterline singularities of incompressible flow show that a time arrow exists. We do not discuss these waterline singularities further here, since they are only sufficient but not necessary for the existence of a time arrow. There are classes of container shapes that allow impulsive flow fields that are regular and do not contain waterline singularities.

10 Conclusions

The field of water waves is illustrative for revealing time arrows within conservative continuum physics. There are no statistical averaging procedures involved in the examples that have been shown. There is no chaotic behavior, except for the Rayleigh–Taylor instability. A basic explanation for several of these phenomena is offered by the concept of a first cause.

Let us consider a deep-water free-surface process that had a first cause at $t = 0$. If one tries to reverse this process in time from its state at a later time $t = T$, there are three obstacles: (i) The specific surface elevation $\eta(x, y, T)$ that one has to choose does not have a cause. (ii) The associated surface velocity $(\partial\eta/\partial t)(x, y, t)$ has to be chosen in perfect fit with the elevation, but there are no conditions for this choice. (iii) The sharp final state at $t = 0$ will not be attainable because of the strong dispersion, which will make the backward integration sensitive with respect to the initial state at $t = T$.

A time arrow in a conservative system may occur when the system becomes algorithmic as a result of human intervention. Basic algorithmic theory reduces all algorithms to the basic elements of selection, sequence and repetition. In the spiral water waves this means: (1) Selection is the choice of clockwise (or anti-clockwise)

direction of rotation for the wavemaker. (2) Sequence is the steadily increasing angle of rotation. (3) Repetition is the periodicity of the rotation angle.

All mathematical modeling of water waves must contain at least one algorithmic element: The choice of an initial state. This choice is explicit if the full time evolution is modelled, but it may be implicit if we are looking for an oscillatory solution of a linearized problem. The implicit algorithmic choice of an initial condition will then offer a consistent derivation of the radiation conditions at infinity.

All spiral water waves are caused by designed algorithms, so they can never be produced by natural processes alone. A snapshot of a spiral wave pattern is enough to tell which way it rotates: In the direction opposite to the outward winding of the spiral. We remark that a spiral wave pattern does not have to be produced in its center. The spiral waves can be produced by a oscillating ring source with constant radius and a continuous phase shift.

No information gets lost in a finite continuum system that is integrable and has zero entropy production. The signatures from an initial condition have to remain within a finite system. In an infinite system, information from the initial condition can be lost by outward radiation to infinity. Allowing infinite time in a spatially infinite conservative system is therefore to allow a possible loss of information. In quantum mechanics there is an interesting analogy: The physical solution of the time-dependent Schrödinger equation is reversible in time, but if ionization of an atom is modeled by allowing an electron to escape to infinity, a time arrow is introduced into the quantum mechanical system.

Will a time arrow lead to loss of information? There is no information loss in the sense of entropy production. However, the initial information may gradually be concealed. A wave in the late stage of inviscid breaking does not give full information of its origin. A merged bore does not offer full information on the individual bores that merged to form it. A late stage of a deep-water Cauchy–Poisson type initial-value problem may hide its exact initial condition. The strong deep-water dispersion is the main reason for the seemingly great loss of information in the evolution of the Cauchy–Poisson problem. In the cubic Schrödinger modeling of nonlinear deep-water waves [15], an explicit time arrow is introduced through the single time derivative. Also the Korteweg de Vries equation for shallow-water waves has an explicit time arrow through the single time derivative. The present work is restricted to the full equations for linear and nonlinear water waves.

One may ask whether this overview of time arrows in water waves applies to other fields of conservative continuum physics. Some notions of time arrows are exclusive for water waves, because of the unique free-surface nonlinearities and also the strong dispersion. Nevertheless, two of the above examples of time arrows can be carried over to standard non-dispersive waves in electromagnetics, acoustics and elastic waves: (1) The time arrow of the standard radiation condition for outgoing waves from an oscillating source or physical object. (2) The time arrow of a spiral wave. It is possible to generate spiral electromagnetic and elastic waves, although this may be difficult and perhaps not of practical use. On the other hand, spiral acoustic waves are well-known as an idealized type of model for the noise from propellers.

References

1. Bejan, A.: On the buckling property of inviscid jets and the origin of turbulence. Lett. Heat Mass Transf. **8**, 187–194 (1981)
2. Longuet-Higgins, M.S., Cokelet, E.D.: The deformation of steep surface waves on water. I. A numerical method of computation. Proc. R. Soc. Lond. A **350**, 1–26 (1976)
3. Landrini, M., Tyvand, P.A.: Generation of water waves and bores by impulsive bottom flux. J. Eng. Math. **39**, 131–170 (2001)
4. Sozer, E.M., Greenberg, M.D.: The time-dependent free surface flow induced by a submerged line source or sink. J. Fluid Mech. **284**, 225–237 (1995)
5. Peregrine, D.H.: Calculations of the development of an undular bore. J. Fluid Mech. **25**, 321–330 (1966)
6. Bestehorn, M., Tyvand, P.A.: Merging and colliding bores. Phys. Fluids **21**, 042107 (2009)
7. Lamb, H.: Hydrodynamics. Cambridge University Press, Cambridge (1932)
8. Wehausen, J.V.: Causality and the radiation condition. J. Eng. Math. **26**, 153–158 (1992)
9. Dagan, G., Miloh, T.: Free-surface flow past oscillating singularities at resonant frequency. J. Fluid Mech. **120**, 139–154 (1982)
10. Drazin, P.G., Reid, W.H.: Hydrodynamic Stability. Cambridge University Press, Cambridge (1981)
11. Dalrymple, R.A., Dean, R.G.: The spiral wavemaker for littoral drift studies. In: Proceedings of 13th Conference on Coastal Engineering, Vancouver, pp. 698–705, July 1972
12. Mei, C.C.: Shoaling of spiral waves in a circular basin. J. Geophys. Res. **78**, 977–980 (1973)
13. Böhm, C., Jacopini, G.: Flow diagrams, Turing machines and languages with only two formation rules. Comm. ACM **9**, 366–371 (1966)
14. Peregrine, D.H.: Flow due to a vertical plate moving in a channel (1972) (Unpublished note)
15. Mei, C.C.: The Applied Dynamics of Ocean Surface Waves. World Scientific, Singapore (1983)

Surface Wave Damping

M.A. Herrada, J.M. Montanero, and J.M. Vega

1 Introduction

Manuel G. Velarde has made an impressive amount of contributions to interfacial phenomena. Although none of us has worked directly with him, we have benefited from both the specific results in his published work and some discussions with him, which have been always a source of inspiration. The main goal of this paper is to account for some old and new work on the calculation of surface wave damping, which involves some phenomena (e.g., Marangoni stresses, surface viscosity, and contact line motion) that Manuel has greatly helped to uncover.

Surface wave damping is an essential ingredient for various purposes associated with the linear and weakly nonlinear descriptions of the wave dynamics. Unfortunately, the calculation of wave damping is a subtle matter, especially in finite containers. This is because several, essentially different phenomena (namely, contact line dynamics and surface contamination), may contribute to damping. The presence of these phenomena in turn may have dynamic consequences, namely they may produce essentially new dynamic behaviors. In other words, both contact line motion and the presence of surfactants may lead to qualitative (not only quantitative) changes in the surface wave dynamics response. Measurements on surface wave damping in turn may be used to identify the above mentioned sources of damping and to calculate the associated physical parameters.

M.A. Herrada
Escuela Técnica Superior de Ingenieros, Universidad de Sevilla, 41092 Sevilla, Spain

J.M. Montanero
Escuela de Ingenierías Industriales, Universidad de Extremadura, 06006 Badajoz, Spain

J.M. Vega (✉)
E.T.S.I. Aeronáuticos, Universidad Politécnica de Madrid, 28040 Madrid, Spain
e-mail: josemanuel.vega@upm.es

R.G. Rubio et al. (eds.), *Without Bounds: A Scientific Canvas of Nonlinearity and Complex Dynamics*, Understanding Complex Systems,
DOI 10.1007/978-3-642-34070-3_30, © Springer-Verlag Berlin Heidelberg 2013

2 Early Developments

The story begins with the linear theory by Stokes [1], who calculated the *viscous damping rate* of harmonic waves in a *laterally infinite liquid layer* over a flat plate. Viscous damping rate produces both temporal attenuation of standing waves and spatial attenuation of traveling waves and Stokes formulae allowed to calculate both. In fact, one of the goals of the pioneering work by Stokes was the possibility of *determining viscosity* (non-invasively) from measurements of viscous wave attenuation, as it had been pointed out by Stokes himself [2].

Stokes theory was subsequently extended to account for both *three dimensional effects* and *lateral walls* ([3] and references there in). Earlier theories usually assumed that the free surface intersects a vertical lateral wall normally. This boundary condition allows for separating variables in a fairly standard way. Assuming fixed contact line, instead, requires a more sophisticated analysis, which was undertaken by Graham-Eagle [4] (a similar solution was obtained independently by Sanz [5] for the liquid bridge geometry), after the suggestion by Benjamin and Scott [6] that it is more appropriate to assume a fixed contact line in brimful containers. Unfortunately, the attempts to match theory based on viscous dissipation and experiments in finite containers failed and promoted the search for *additional sources of damping*. Three sources were identified:

1. *Viscous dissipation.* At low viscosity, viscous dissipation in the various regions is readily estimated by a standard order of magnitude analysis. It turns out that dissipation in the oscillatory boundary layers attached to the solid walls is asymptotically dominant since it behaves as the square root of viscosity. Dissipation in the bulk behaves as the viscosity itself and dissipation in the boundary layer attached to the free surface goes to zero as the viscosity to the power $3/2$. Thus, only dissipation in the boundary layers attached to the lateral walls and the bottom of the container was accounted for in early studies.
2. *Contact line motion* is a subtle and still not well understood process. It was early recognized as a source of damping [3, 7–10]. Appropriate handling of the associated *stress singularity* (beyond the classical formulation by Moffatt [11]) to derive a *slip condition* was subsequently clarified, among others, by Huh and Scriven [12], Dussan and Davis [13], and Dussan [14]; see also [15, 16] for further references. Based on these, Hocking [17, 18] used a linear contact line motion law to derive specific damping ratio formulae, which depended on a free parameter (treated as a tunable parameter), namely a *slip length*. The resulting calculation showed a reasonable agreement with the former experiments by Benjamin and Ursell [7], Case and Parkinson [8], and Keulegan [9].
3. *Surface contamination* is also a not completely understood process. The simplest model includes *Marangoni elasticity* and *surface viscosity* (both *dilatational* and *shear*). Marangoni elasticity refers to the tangential stress on the free surface produced by surface tension gradients, as first noticed by Marangoni [19]. Surface tension gradients in turn can be induced by either temperature or surfactant concentration gradients. The effect of the latter to promote motions

along the free surface had been previously noticed by Thomson [20]; see [21, 22] for a further historical review. The concept of surface viscosity seems to have been first suggested by Plateau [23] and used by Boussinesq [24] to explain some anomalous behavior observed in the bubbles velocity. The mathematical formulation is due to Scriven [25]. As it happens with contact line motion, accounting for surface contamination in realistic conditions involves some *tunable parameters* (namely, the Marangoni elasticity and the shear and dilatational surface viscosity coefficients) that must be adjusted, especially when the nature of surfactants is completely unknown, as it usually happens in water, which is quite easily contaminated. Along this line, the effect of surface contamination on damping was recognized and modeled via phenomenological formulae [3, 26–28].

3 Isolating Effects

Combining the above mentioned effects to explain damping rate measurements required to fit tunable parameters, which made the analyses not conclusive enough. In order to isolate effects, Henderson and Miles [29] conducted a series of experiments with *ultra-pure water* (distilled, micro-filtered water was seen to be not pure enough [29]) in a *brimful cylindrical container*, with the *contact line fixed* at the upper edge of the lateral wall. Thus, both contact line motion and surface contamination were eliminated. But comparison with theory was not satisfactory.

A similar discrepancy had been simultaneously solved for the *liquid bridge configuration* by Higuera et al. [30], who included the effect of *viscous dissipation in the bulk* to the asymptotically dominant dissipation in the Stokes boundary layer, obtaining quite good agreement for the experimentally measured damping rate. As explained in [30], the reason for the necessity of including dissipation in the bulk is that the Stokes boundary layer attached to the solid supports is somewhat weak, namely, the jump of the tangential velocity across this boundary layer is somewhat small, especially when the contact line is fixed. Of course, dissipation in the bulk is higher order as viscosity goes to zero and thus it can be neglected *for sufficiently small viscosity*, but not necessarily for small, but fixed viscosity, such as that of water in centimeter devices. This emphasizes that *some care must be taken when using asymptotic results*, as some parameter goes to either zero or infinity, on actual experimental conditions, in which the parameter may be small/large, but is fixed. If discrepancies appear, a good candidate to fix them is to estimate the neglected higher order terms. Following [30], Martel and Knobloch [31] illustrated the effect, discussing the balance between viscous dissipation in the boundary layers and the bulk in a laterally unbounded layer. And Martel et al. [32] calculated the damping rate for the experimental conditions in [29], obtaining a quite good agreement in the whole range of frequencies; a similar analysis (in the light of [32]) was simultaneously performed by Miles and Henderson [33]. The theory in

[32] was extensively checked by Howell et al. [34] in a battery of fixed-contact-line experiments using several types of silicone oils, in which surface contamination was not expected.

Once the discrepancies concerning volumetric viscous damping had been solved, the additional experimental runs by Henderson and Miles [29] using contaminated water were considered by Nicolas and Vega [35], who added the effect of Marangoni elasticity with insoluble surfactant, leaving the Marangoni elasticity as a tunable parameter. The results highly improved some previous calculations in [29] (under the assumption of inextensible free surface) and matched fairly well for the whole set of measurements. As a byproduct, an estimate of the Marangoni elasticity was obtained. These results suggested that Marangoni elasticity could be considered as the main source of damping in contaminated water, as already conjectured by Van Dorn [36].

4 New Experiments on Millimetric Liquid Bridges

A liquid bridge is the configuration that appears when an isothermal liquid mass is held by capillary forces between two solid supports. This configuration is considered to be of both scientific and industrial interest in, e.g., fluid physics experiments on board of space platforms and the crystal growth technique known as floating zone. Vibrations of the liquid bridge are unavoidable in space platforms due to machinery and crew maneuvering, and have a significant effect on the liquid bridge stability and dynamics. Also, the liquid bridge configuration is useful to experimentally analyze interfacial phenomena since the free surface deformation can be measured quite precisely by optical means, using sub-pixel rendering techniques [37–39]. Its cylindrical shape scatters the light used to illuminate it, which produces a silhouette effect ideal for imaging the free surface deformation.

A liquid bridge of length L between two parallel coaxial equal disks of radii R is defined by the following nondimensional parameters: the slenderness $\Lambda = L/(2R)$, the volume $V = V^*/(\pi R^2 L)$, the Bond number $B = \rho g R^2/\sigma$, and the volumetric Ohnesorge number $C = \mu(\rho\sigma R)^{-1/2}$, where V^* is the dimensional volume, ρ is the density, σ is the surface tension, and μ is the viscosity. These properties are fairly well known for several liquids, such as hexadecane. Surface contamination will be modeled below using only the surface shear viscosity, whose nondimensionalization leads to the superficial Ohnesorge number

$$C^S = \mu^S(\rho\sigma R^3)^{-1/2}, \tag{1}$$

where μ^S is the surface shear viscosity. These parameters result from using R and $(\rho R^3/\sigma)^{1/2}$ as units for length and time, respectively, to nondimensionalize the axisymmetric governing equations and boundary conditions. With the usual notation, these are

$$(ru)_r + rw_z = 0, \tag{2}$$

$$u_t + uu_r + wu_z = -p_r + C[u_{rr} + (u/r)_r + u_{zz}], \tag{3}$$

$$w_t + uw_r + ww_z = -p_z + C[w_{rr} + w_r/r + w_{zz}], \tag{4}$$

in $0 < r < F(r,z,t), -\Lambda < z < \Lambda$, where subscripts stand hereafter for partial derivatives, and

$$F_t + F_z w - u = 0, \tag{5}$$

$$C\frac{[1-F_z^2](w_r+u_z)+2F_z(u_r-w_z)}{(1+F_z^2)^{1/2}} = C^S\left[\frac{(F\hat{v}_s)_s}{F} + \frac{F_s^2 - FF_s}{F^2}\hat{v}\right], \tag{6}$$

$$p - B\,z + \frac{FF_{zz} - 1 - F_z^2}{F(1+F_z^2)^{3/2}} - \frac{2C[u_r - F_z(w_r+u_z) + F_z^2 w_z]}{1+F_z^2} = 0, \tag{7}$$

at the free surface, $r = F$; the subscript s denotes the derivative with respect to an arch length parameter along the meridians of the free surface and $\hat{v}$ is the tangential component of the velocity along the free surface. In addition, noslip boundary conditions are applied at the supporting disks, $z = \pm\Lambda$, and the usual regularity conditions $u = w_r = p_r = 0$ are imposed at the axis $r = 0$. Explicitly imposing conservation of volume is also convenient, even though it is a consequence of the continuity equation and the kinematic compatibility boundary condition (5).

In the results quoted below, this problem is discretized as follows. The time-dependent fluid domain is mapped onto a fixed square domain ($0 \le \xi \le 1, 0 \le \eta \le 1$) through the coordinate transformation $\xi = r/F(z,t)$ and $\eta = z/(2\Lambda)$. The resulting square is discretized (after some calibration) using $n_\xi = 25$ and $n_\eta = 11$ Chebyshev collocation points along the ξ and η directions, respectively, which yields a high accuracy with a relatively small number of mesh points. The (implicit) time advancement is performed using second-order backward-differences, with a fixed time step $\Delta t = 0.05/\omega$, where ω is the nondimensional forcing frequency, see below. At each time step, the resulting set of $3n_\eta \times n_\xi + n_\xi$ discrete nonlinear equations are solved iteratively using the Newton–Raphson method implemented in the MATLAB subroutine FSOLVE. The initial guess for the iterations at each time step is the solution at the previous instant.

Liquid bridges are usually studied in microgravity conditions, but the effect of gravity is also small on ground experiments using millimetric liquid bridges. In the latter case, viscosity must be quite small to obtain small damping ratios, similar to those for larger sizes in space platforms. Water is usually avoided for various reasons, including the fact that it is easily contaminated in a somehow unpredictable way. Experimental measurements of the damping ratio in millimetric liquid bridges are scarce. Mollot et al. [40] performed in the nineties some damping measurements, but (as acknowledged by the authors) these were obtained using an experimental set-up that did not allow for a precise determination of the damping ratio. See also the more recent damping measurements by Thiessen et al. [41].

More recently, Montanero et al. [42, 43] performed a series of experiments on millimetric liquid bridges using hexadecane and compared with the current theory on viscous dissipation. The conclusion was that the natural frequencies of the free oscillations were well predicted, but the damping ratio was underestimated by a factor of about 0.6. Specifically, the so-called Cosserat one-dimensional model (which results from the full Navier–Stokes equations in the limit of slender liquid bridges) was used in [42]. A further comparison using the full Navier–Stokes equations (without any simplification) [43] did not improve the results, even modifying the formulation to account for some geometrical details of the experiment, such as a part of the injection device used in the experimental set-up to vary the liquid bridge volume. Thus, it became obvious that some physics (producing additional damping) could be lost in the theoretical model.

Contact line motion was to be excluded because the contact line appeared to be quite well attached to the edge of the supporting disks. Thus, surface contamination was the obvious candidate, which was not expected in principle in hexadecane. As explained above, modeling surface contamination requires in principle to consider the effects of Marangoni elasticity and shear and dilatational surface viscosities, which involve three free parameters (not available in the literature for hexadecane) whose determination is a subtle matter [44, 45]. Thus, these parameters must be determined by empirically fitting the available experimental data. The results in [42] were obtained in two experimental campaigns, which produced 17 experimental points with a limited precision. Thus, fitting with three free parameters would not be convincing enough. Therefore, an appropriate explanation required selecting only the effect that was most likely present. After a preliminary analysis, *the surface shear viscosity was selected*. Accounting for the remaining surface effects would require a more extensive experimental campaign, which is currently under research.

Luckily enough, surface shear viscosity alone produced a fairly good fitting [46]. This is illustrated in Fig. 1, which shows that the first natural frequency is well predicted by the simulation based on the full Navier–Stokes equations, as anticipated, but the damping rate exhibits a systematic $O(1)$ error if only viscous damping is accounted for (filled squares). Adding an appropriate value of the superficial Ohnesorge number, namely

$$C^S = 2.5 \times 10^{-2}, \tag{8}$$

instead, produces a fairly good fitting (plain squares) for all available experimental points. Note that the fitted value of the interfacial Ohnesorge number is of the order of the volumetric Ohnesorge number, $C = 2.26 \times 10^{-2}$. This was to be expected, invoking the boundary condition (6), from the experimental observation that surface contamination and volumetric viscous effects produce comparable contributions to the damping ratio. Also note that the fitted value of C^S is maintained in all runs, which is consistent with the fact that both the liquid and the disks radii were the same in all experimental runs. This value of C^S provides the following value of the surface shear viscosity of hexadecane

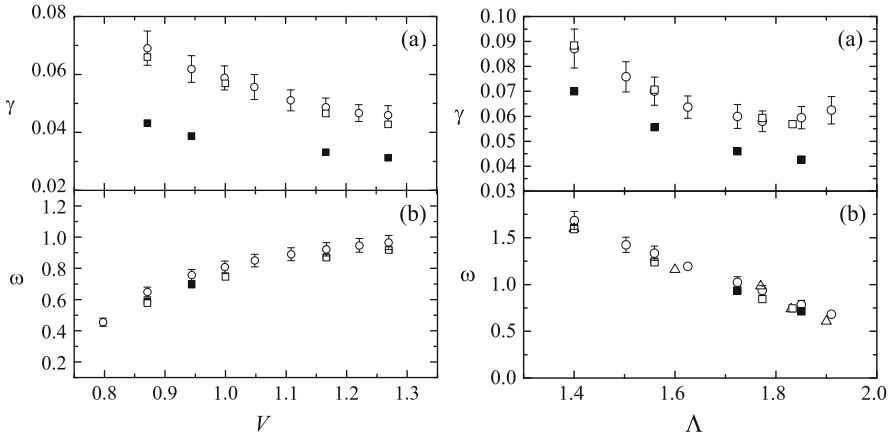

Fig. 1 Damping rate (**a**) and oscillation frequency (**b**) in a liquid bridge for the first natural mode, with $B = 0.312$ and $C = 2.26 \times 10^{-2}$: as experimentally measured (*plain circles*), and as numerically calculated with $C^S = 0$ (*filled squares*) and $C^S = 2.5 \times 10^{-2}$ (*plain squares*). *Left plots*: varying volume for $\Lambda = 1.83$; *right plots*: varying Λ for $V = 1$

$$\mu^S = (\rho\sigma R_0^3)^{1/2} C^S = 3.3 \times 10^{-3} \text{gm/sec}, \tag{9}$$

where the following experimental data have been used: $\rho = 0.773\,\text{gm/cm}^3$, $\sigma = 23.66\,\text{dyn/cm}$, and $R = 0.0985\,\text{cm}$. Thus, *a means to calculate the surface shear viscosity* results from the analysis, which is being checked using a more complete set of experimental measurements. The performance of this method (as well as the analysis of the role of additional surface contamination effects, such as dilatational viscosity and Marangoni stresses, which seems to be higher order in the present experiment but could be dominant in other configurations) requires a more complete experimental campaign, which is being planned.

In order to further check the ability of the proposed value of the surface shear viscosity to match experimental measurements, the spatial dependence of the oscillation amplitude calculated numerically is compared in Fig. 2 with its experimentally measured counterpart. Note that the agreement is again quite good.

The results quoted above suggest that some care must be taken when using millimetric liquid bridges to predict the damping ratio of larger liquid bridges. This is because of surface contamination, which does not play a significant role at larger sizes. According to (6), the ratio of the effects of shear surface viscosity to bulk viscosity is measured through the ratio

$$C^S/C = \mu^S/(\mu R),$$

which is $O(1)$ for hexadecane when R is of the order of one millimeter. Thus, if R were of the order of, say, $30\,\mu\text{m}$ (a typical size of micro-fluidic devices [47]), then C^S/C would be multiplied by 30, and interfacial effects would be dominant,

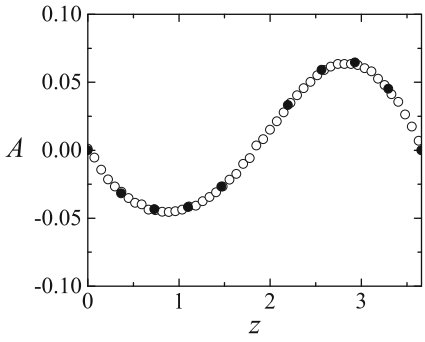

Fig. 2 Nondimensional oscillation amplitude for $\Lambda = 1.83$, $V = 1$, $\delta = 0$, $B = 0.312$, and $C = 2.26 \times 10^{-2}$: as numerically calculated with $C^S = 2.5 \times 10^{-2}$ (*filled circles*) and as experimentally measured (*plain circles*)

producing not only quantitative but also qualitative changes in the dynamical response of the device (see next section), and allowing to calculate other interfacial phenomena, such as Marangoni elasticity and surface dilatational viscosity, which were masked by shear viscosity in the experiment accounted for above.

Determining the role played by surface effects on micrometer capillary shapes is not an easy task. One must solve the experimental difficulties associated with the small spatio-temporal scales that are involved. Concerning the spatial resolution, this must be precise enough as to appropriately monitor the free surface evolution, determining the instantaneous free surface shapes with a reasonable uncertainty. Concerning the temporal scale, the free surface typically evolves with a characteristic time comparable to the capillary time, which is proportional to the capillary bridge radius to the power 3/2. This fact entails a drastic increase of the temporal resolution in the experimental analysis of micrometer configurations. The combination of high-speed imaging and a super-resolution image processing techniques allows one to meet both the spatial and temporal resolutions required to analyze surface phenomena under favorable conditions.

This is the object of our current research. We have designed and assembled an experimental setup to study surface effects on a micrometer liquid bridge, with a radius of 100 μm. A quasi-cylindrical (the Bond number is virtually zero) hexadecane liquid bridge is formed between two calibration rods of the same diameter. One of the rods is fixed, while the other one can be vibrated in the axial direction with an electrodynamic shaker with the desired amplitude and frequency. Digital images of the liquid bridge are acquired and processed to precisely determine the free surface position as a function of time; see Fig. 3, which provides some images from one of the experiments. Precise quantitative measurements will be presented elsewhere.

An additional difficulty is that the superficial Ohnesorge number is now about 0.79, which produces strongly damped oscillations whose associated free surface deformation is extremely small. In other words, resonances are no longer present. This is illustrated in Fig. 4, which provides some preliminary simulations that have been performed using the numerical tool described above. The nondimensional parameters have been chosen consistent with the experiment. Note that the

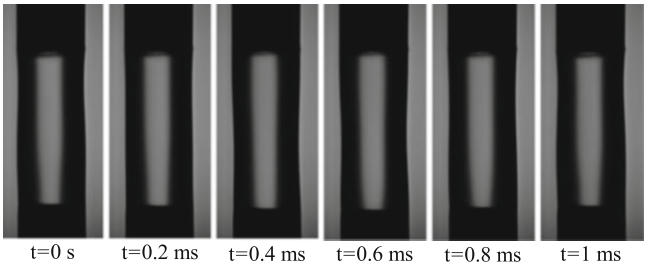

Fig. 3 Some snapshots of an experimental run in a micrometric liquid bridge for the indicated values of t

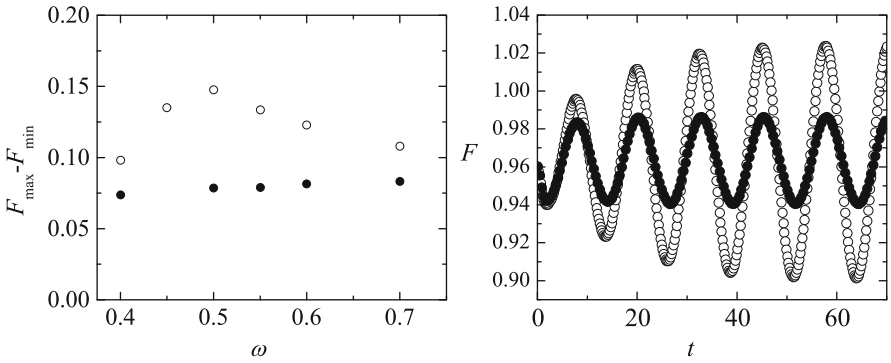

Fig. 4 Numerical simulation of the response of a liquid bridge subject to a nondimensional axial vibration amplitude $A = 0.08$, with $B = 0.0028$, $V = 0.963$, $\Lambda = 2.3$, and $C = 0.064$, comparing the cases $C^S = 0$ (*plain circles*) and $C^S = 0.79$ (*filled circles*). *Left*: Free surface deformation (measured as the difference between its maximum and minimum values, after disregarding an initial transient) vs. the nondimensional forcing frequency ω; *right*: a representative evolution for $\omega = 0.5$

resonance is completely suppressed for $C^S = 0.79$, while some weak resonance would be present at $C^S = 0$.

Summarizing, the role of surface effects at micrometric sizes is expected to be dominant, which has obvious consequences in the dynamics of microfluidic devices with interfaces [48].

5 Consequences on the Surface Wave Dynamics

Precise calculation of surface wave damping allows for obtaining an asymptotically correct, weakly nonlinear theory on surface waves dynamics at small viscosity. This is a quantitative effect. But surface contamination (which is detected through damping measurements) has additional *qualitative effects* on the dynamics. These

are associated with the generation of *viscous mean flows*, which are produced by the oscillatory boundary layers induced by the surface waves. The viscous mean flow (also called streaming flow, or acoustic streaming) was first detected by Lord Rayleigh [49] in his explanation of some anomalous accumulation of both dust in the walls of acoustic Kunt tubes and sand in the bottom of vibrating containers [50]. The generation of this mean flow in the boundary layer attached to a solid wall and a free surface was uncovered through the work by Schlichting [51] and Longuet-Higgins [52], respectively. Streaming flows have received a continuous attention in the literature in connection with a variety of fluid flows, ranging from the generation of mean motions in the ear [53] to the analysis of Langmuir circulations in the ocean [54]. The streaming flow was also used to counterbalance undesirable thermocapillary convection in materials processing in microgravity ([55] and references there in). But the streaming flow was considered in the early nineties mainly a byproduct of the oscillatory flow, and thus not included in the weakly nonlinear analyses of surface waves [56]. Nicolas and Vega [57], instead, pointed out (for the liquid bridge geometry) that *the dynamics of the surface waves themselves may be affected by the generated streaming flow*. This observation was subsequently followed to conclude that the streaming flow is also coupled in the weakly nonlinear analysis of surface waves in vibrating containers, which resulted in a complete asymptotically correct theory for both 2D large aspect ratio systems and moderate aspect ratio 3D containers, see [58–60] and references there in. A similar theory for large aspect ratio, three dimensional containers remains to be done.

Now, it turns out that surface contamination highly affects the structure of the boundary layer attached to the free surface. In other words, the new boundary layer structure produces a mean flow topology that is qualitatively different from that generated by a clean free surface, and this has qualitative consequences in the surface waves dynamics. As an example, adding Marangoni elasticity (which is expected in tap water, as explained above) allowed to explain [61] the appearance of drifting states in vertically vibrated annular containers, which had been experimentally observed by Douady et al. [62], and could not be explained in the absence of contamination [63].

6 Concluding Remarks

The various efforts to both calculating the damping rate of surface waves and explaining experimental measurements have been reviewed. In particular, the combined effects of volumetric viscous damping and interfacial effects, such as Marangoni elasticity and surface viscosity have been discussed.

Some recent experiments on millimetric liquid bridges using hexadecane showed that the role of surfactants is essential already in the scale of millimeters and could be also significant in other liquids as well. This means that surfactants will have a dominant effect in promoting damping at smaller sizes, which has obvious

implications in microfluidics. As a byproduct, a method was suggested to measure surfactant properties using micrometric liquid brides, which is currently under research.

In addition, several consequences associated with the generation of mean flows (which are well known today to affect the surface waves dynamics, both qualitatively and quantitatively) have been briefly discussed.

Acknowledgement This research was partially supported by the Spanish Ministry of Education, under Grants TRA2010-18054 and DPI2010-21103.

References

1. Stokes, G.G.: On the effect of internal friction of fluids on the motion of pendulums. Trans. Camb. Philo. Soc. **9**, 8–106 (1851)
2. Stokes, G.G.: On the theories of the internal friction of fluids in motion. Trans. Camb. Philos. Soc. **8**, 287–305 (1845)
3. Miles, J.W.: Surface-wave damping in closcd basins. Proc. R. Soc. Lond. A **297**, 459–75 (1967)
4. Graham-Eagle, J.: A new method for calculating eigenvalues with applications to gravity-capillary waves with edge constraints. Math. Proc. Camb. Philos. Soc. **94**, 553–564 (1983)
5. Sanz, A.: The influence of the outer bath in the dynamics of axisymmetric liquid bridges. J. Fluid Mech. **156**, 241–267 (1985)
6. Bejamin, T.B., Scott, J.C.: Gravity-capillary waves with edge constraints. J. Fluid Mech. **92**, 241–267 (1979)
7. Bejamin, T.B., Ursell, F.: The stability of the plane free surface of a liquid in vertical periodic motion. Proc. R. Soc. Lond. A **225**, 505–515 (1954)
8. Case, K.M., Parkinson, W.C.: Damping of surface waves in an incompressible liquid. J. Fluid Mech. **2**, 172–184 (1957)
9. Keulegan, G.H.: Energy dissipation in standing waves in rectangular basins. J. Fluid Mech. **6**, 33–50 (1959)
10. Mei, C.C., Liu, L.F.: The damping of surface gravity waves in a bounded liquid. J. Fluid Mech. **59**, 239–256 (1973)
11. Moffatt, H.K.: Viscous and resistive eddies near a sharp corner. J. Fluid Mech. **18**, 1–18 (1964)
12. Huh, C., Scriven, L.E.: Hydrodynamic model of steady movement of a solid/liquid/fluid contact line. J. Colloid Interface Sci. **36**, 85–101 (1971)
13. Dussan, V.E.B., Davis, S.H.: On the motion of a fluid-fluid interface along a solid surface. J. Fluid Mech. **65**, 71–95 (1974)
14. Dussan, V.E.B.: The moving contact line: the slip boundary condition. J. Fluid Mech. **77**, 665–684 (1976)
15. Dussan, V.E.B.: On the spreading of liquids on solid surfaces: static and dynamic contact lines. Ann. Rev. Fluid Mech. **11**, 371–400 (1979)
16. Shikhmurzaev, Y.D.: The moving contact line on a smooth solid surface. Int. J. Multiphase Flow **19**, 589–610 (1993)
17. Hocking, L.M.: The damping of capillary-gravity waves at a rigid boundary. J. Fluid Mech. **179**, 253–266 (1987)
18. Hocking, L.M.: Waves produced by a vertically oscillating plate. J. Fluid Mech. **179**, 267–281 (1987)
19. Marangoni, C.G.M.: Sull expansione dell goccie di un liquido galleggianti sulla superficie di altro liquido. Tipografia dei fratelli Fusi, Pavia (1865)
20. Thomson, J.: On certain curious motions observable at the surfaces of wine and other alcoholic liquors. Philos. Mag. **10**, 330–333 (1855)

21. Scriven, L.E., Sternling, C.V.: The Marangoni effects. Nature **187**, 186–188 (1960)
22. Ross, S., Becher, P.: The history of the spreading coefficient. J. Colloid Interface Sci. **149**, 575–579 (1992)
23. Plateau, J.A.F.: Experimental and theoretical researches into the figures of equilibrium of a liquid mass without weight. Philos. Mag. **38**, 445–455 (1869)
24. Boussinesq, J.: Existence of a superficial viscosity in the thin transition layer separating one liquid from another contiguous fluid. C. R. Hehbd. Seances Acad. Sci. **156**, 983–989 (1913)
25. Scriven, L.E.: Dynamics of a fluid interface. Chem. Eng. Sci. **12**, 98–108 (1960)
26. Dorrestein, R.: General linearized theory of the effect of surface films on water ripples, I and II. Proc. K. Ned. Akad. Wet. B **54**, 260–272, 350–356 (1951)
27. Goodrich, F.C.: The mathematical theory of capillarity, I-III. Proc. R. Soc. Lond. A **260**, 481–509 (1961)
28. Levich, V.G.: Physicochemical Hydrodynamics. Prentice-Hall, Englewood Cliffs (1962)
29. Henderson, D.M., Miles, J.W.: Surface wave damping in a circular cylinder with a fixed contact line. J. Fluid Mech. **275**, 285–299 (1994)
30. Higuera, M., Nicolas, J.A., Vega, J.M.: Linear oscillations of weakly dissipative axisymmetric liquid bridges. Phys. Fluids A **6**, 438–450 (1994)
31. Martel, C., Knobloch, E.: Damping of nearly inviscid water waves. Phys. Rev. E **56**, 5544–5548 (1997)
32. Martel, C., Nicolas, J.A., Vega, J.M.: Surface-wave damping in a brimful circular cylinder. J. Fluid Mech. **360**, 213–228 (1998) [see also Corrigendum, J. Fluid Mech. **373**, 379]
33. Miles, J.W., Henderson, D.M.: A note on interior vs. bundary layer damping on surface waves in a circular cylinder. J. Fluid Mech. **364**, 319–323 (1998)
34. Howell, D., Buhrow, B., Heath, T., McKenna, C., Hwang, W., Schatz, M.F.: Measurements of surface-wave damping in a container. Phys. Fluids **12**, 322–326 (2000)
35. Nicolas, J.A., Vega, J.M.: A note on the effect of surface contamination in water wave damping. J. Fluid Mech. **410**, 367–373 (2000)
36. Van Dorn, W.G.: Boundary conditions of oscillatory waves. J. Fluid Mech. **24**, 769–779 (1966)
37. Zitova, B., Flusser, J.: Image registration methods: a survey. Image Vis. Comput. **21**, 977–1000 (2003)
38. Song, B., Springer, J.: Determination of interfacial tension from the profile of a pendant drop using computer-aided image processing. 2. Experimental. J. Colloid Interface Sci. **184**, 77–91 (1996)
39. Vega, E.J., Montanero, J.M., Ferrera, C.: Exploring the precision of backlight optical imaging in microfluidics close to the diffraction limit. Measurement **44**, 1300–1311 (2011)
40. Mollot, D.J., Tsamopoulos, J., Chen, T.Y., Ashgriz, N.: Nonlinear dynamics of capillary bridges: experiments. J. Fluid Mech. **255**, 411–435 (1993)
41. Thiessen, D.B., Marr-Lyon, M.J., Marston, P.L.: Active electrostatic stabilization of liquid bridges in low gravity. J. Fluid Mech. **457**, 285–294 (2002)
42. Vega, E.J., Montanero, J.M.: Damping of linear oscillations in axisymmetric liquid bridges. Phys. Fluids **21**, 092101 (2009)
43. Herrada, M.A., López-Herrera, J.M., Vega, E.J., Montanero, J.M.: Numerical simulation of a liquid bridge in a coaxial gas flow. Phys. Fluids **23**, 012101 (2011)
44. Hirsa, A.H., Lopez, J.M., Miraghaie, R.: Measurement and computation of hydrodynamic coupling at an air/water interface with an insoluble monolayer. J. Fluid Mech. **443**, 271–292 (2001)
45. Hirsa, A.H., Lopez, J.M., Miraghaie, R.: Determination surface shear viscosity via deep channel flow with inertia. J. Fluid Mech. **470**, 135–149 (2003)
46. Herrada, M.A., Montanero, J.M., Vega, J.M.: The effect of surface shear viscosity on the damping of oscillations in millimetric liquid bridges. Phys. Fluids **23**, 082102 (2011)
47. Kirby, B.J.: Micro- and Nanoscale Fluid Mechanics: Transport in Microfluidic Devices. Cambridge University Press, Cambridge (2010)
48. Anna, S.L.: Interfaces and Multiphase Flows in Microfluidics. IMA Tutorial. Institute for Mathematics and its Applications, Minneapolis (2009)

49. Lord Rayleigh, J.W.S.: The circulation of air observed in Kunt's tubes, and on some allied acoustical problems. Philos. Trans. R. Soc. Lond. **175**, 1–21 (1883)
50. Faraday, M.: On the forms and states assumed by fluids in contact with vibrating elastic surfaces. Philos. Trans. R. Soc. Lond. **121**, 319–340 (1831)
51. Schlichting, H.: Berechnung ebener periodischer Grenzschichtströmungen. Phys. Z. **33**, 327–335 (1932)
52. Longuet-Higgins, M.S.: Mass transport in water waves. Philos. Trans. R. Soc. A **245**, 535–581 (1953)
53. Lighthill, J.: Acoustic streaming in the ear itself. J. Fluid Mech. **239**, 551–606 (1992)
54. Leibovich, S.: On wave-current interaction theories of Langmuir circulations. Ann. Rev. Fluid Mech. **15**, 391–427 (1983)
55. Nicolas, J.A., Rivas, D., Vega, J.M.: On the steady streaming flow due to high-frequency vibration in nearly-inviscid liquid bridges. J. Fluid Mech. **354**, 147–174 (1998)
56. Miles, J.W., Henderson, D.M.: Parametrically forced surface waves. Ann. Rev. Fluid Mech. **22**, 143–165 (1990)
57. Nicolas, J.A., Vega, J.M.: Weakly nonlinear oscillations of axisymmetric liquid bridges. J. Fluid Mech. **328**, 95–128 (1996)
58. Vega, J.M., Knobloch, E., Martel, C.: Nearly inviscid Faraday waves in annular containers of moderately large aspect ratio. Physica D **154**, 313–336 (2001)
59. Higuera, M., Vega, J.M., Knobloch, E.: Coupled amplitude-streaming flow equations for nearly inviscid Faraday waves in small aspect ratio containers. J. Nonlinear Sci. **12**, 505–551 (2002)
60. Varas, F., Vega, J.M.: Modulated surface waves in large aspect ratio, horizontally vibrated containers. J. Fluid Mech. **569**, 271–304 (2007)
61. Martin, E., Vega, J.M.: The effect of surface contamination on the drift instability of standing Faraday waves. J. Fluid Mech. **546**, 203–225 (2006)
62. Douady, S., Fauve, S., Thual, O.: Oscillatory phase modulation of parametrically forced surface waves. Europhys. Lett. **10**, 309–315 (1989)
63. Martin, E., Martel, C., Vega, J.M.: Drift instability of standing Faraday waves. J. Fluid Mech. **467**, 57–79 (2002)

Shadowgraph Contrast of Internal Wave Trains During Absorption

A. Wierschem and H. Linde

1 Introduction

The shadowgraph method is a standard technique for visualizing flow patterns. It is noninvasive and easy to implement. In general, the contrast can be generated by the deformation of an interface between media with different refractive indices and by refractive-index gradients within a medium. The simultaneous occurrence of two mechanisms for the shadowgraph contrast makes it difficult to obtain quantitative information from the light intensity distribution. In general, this is only possible where one of the two effects is negligible. Jenkins [1], and later Thess and Orszag [2] have derived a description of the shadowgraph intensity distribution for the case of a flat interface and a small refractive-index gradient within a liquid. This report discusses the visualization of internal waves, which have been described by Wierschem et al. [3] with the shadowgraph method and tackles the question what mechanism produces the shadowgraph contrast. To this end shadowgraph images obtained in reflection and in transmission are first compared to each other qualitatively. Thereafter, the shadowgraph images are compared to surface elevation measurements carried out with a laser beam.

A. Wierschem (✉)
Institute of Fluid Mechanics, Friedrich-Alexander University Erlangen-Nuremberg, Cauerstrasse 4, 91058 Erlangen, Germany
e-mail: andreas.wierschem@lstm.uni-erlangen.de

H. Linde
Strasse 201, Nr. 6, 13156 Berlin, Germany

R.G. Rubio et al. (eds.), *Without Bounds: A Scientific Canvas of Nonlinearity and Complex Dynamics*, Understanding Complex Systems,
DOI 10.1007/978-3-642-34070-3_31,

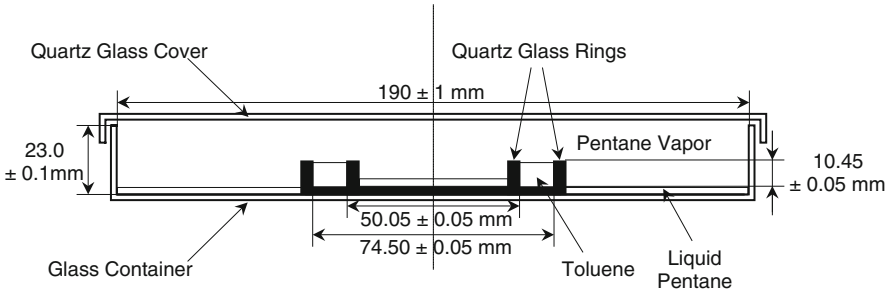

Fig. 1 Side-view of the experimental setup: two quartz-glass rings form an annular container that is placed concentrically in a circular reservoir made of glass. The annular ring is filled with toluene and the bottom of the reservoir is covered with liquid pentane

2 Experimental System and Methods

A side-view of the experimental system is sketched in Fig. 1. It consists of a cylindrical glass container in which two quartz rings are placed concentrically. The annular gap between the two quartz rings is filled with toluene. The rest of the container is covered with liquid pentane, which has a high vapor pressure at room temperature and a surface tension much lower than toluene. The vapor concentration of pentane rises rapidly until a stationary value is obtained. This gives rise to a strong concentration difference between the vapor phase and the liquid in the annular gap. This difference decreases with time due to the absorption of pentane in the liquid. Because the surface level rises due to the absorbed pentane the annular container is not filled brimfully. Further details concerning the setup and the parameters are given by Wierschem et al. [4]. In an initial stage surface waves are generated, on which has been reported elsewhere [4, 5]. The internal waves, with are of interest here, are observed at a later stage of the absorption process when the liquid in the annular container has already absorbed a considerable amount of pentane. They have been described by Wierschem et al. [3].

The internal waves have been visualized by applying the shadowgraph method. We carried out shadowgraph experiments in transmission and in reflection. The light coming from a monochromatic light source of 1 mm diameter is collimated to a parallel beam of 100 mm diameter. In the transmission mode it traverses the hydrodynamic system from underneath and then it is focused by a lens on the chip of a CCD camera. In the reflection mode, a beam splitter turns the divergent beam downwards where it is collimated by a lens. The collimated beam arrives at the free liquid surface that reflects a part of it. The reflected light is captured by a CCD camera on the other side of the beam splitter. The setups are shown in Fig. 2. In the transmission mode, the contrast could be due to surface deformation or due to a concentration modulation within the bulk. In the reflection mode, to prevent that the concentration modulation in the liquid contributes to the shadowgraph contrast, the glass bottom is covered with a thin sheet of paper that mainly acts to

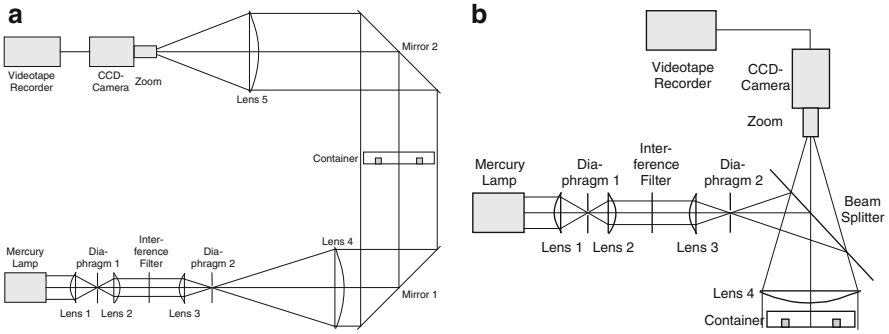

Fig. 2 Shadowgraph setup in transmission (**a**) and in reflection (**b**)

diffusely scattering the incoming light. With the focus of the camera zoom chosen beyond the surface level, the virtual image is visualized, which corresponds in principle to the image obtained in the transmission mode. In other words, this virtual image corresponds to a situation where the surface elevation serves as a lens to focus the light from a source behind the surface level.

The surface deformation provoked by the waves is detected with a laser beam reflected at the free liquid surface. The laser beam is aimed at the surface from above at a small angle with respect to the vertical and the position of the reflected beam is recorded with a CCD camera at a distance on a recording plane. From the shift of the laser spot on the recording plane, we calculate the surface deformation gradient. Integration with the phase velocity of the waves, which is obtained from simultaneous shadowgraph experiments, yields the shape of the free surface. The setup is sketched in Fig. 3a. A 0.95 mW helium–neon laser is focused by a lens of 350 mm focal distance on the liquid surface in the center of the annular container. The beam diameter at the surface is about 300 μm. The small angle between the laser beam and the surface normal is adjusted by a mirror. At about 1 m distance from the surface the reflected beam arrives at a recording plane where it is recorded with a CCD camera.

Figure 3b shows the geometry of the detection from which the surface-deformation gradient is determined in the following manner: The gradient in x-direction h_x, corresponding to the azimuth direction in the annular gap, is equal to the tangent of the inclination angle β. The reflected angle γ is twice the inclination angle. From Fig. 3b follows that the following geometrical relations hold:

$$\tan\left(\frac{\pi}{2} - \alpha_r\right) = \frac{b-h}{a}, \tag{1}$$

$$\tan\left(\frac{\pi}{2} - \alpha_r - \gamma\right) = \frac{b-h}{a+\Delta a}. \tag{2}$$

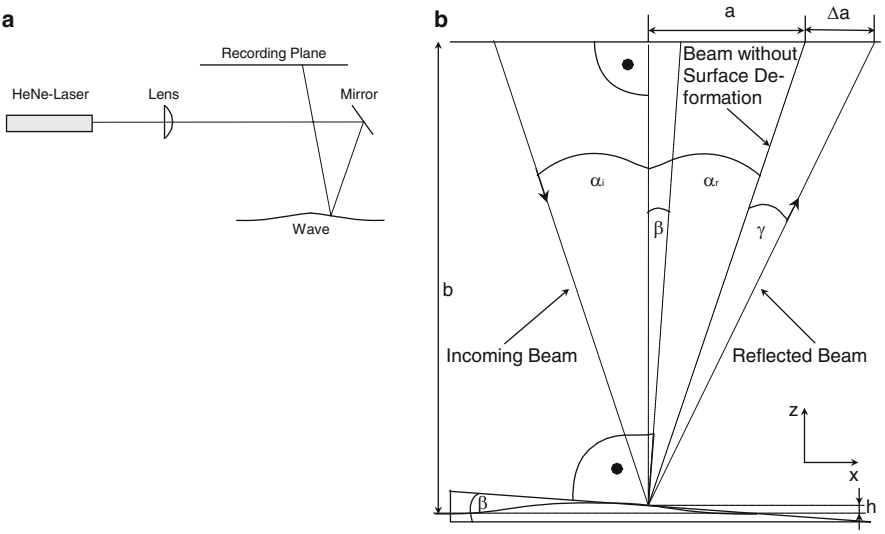

Fig. 3 Experimental setup for measuring the surface deformation with a reflected laser beam (**a**) and sketch of its geometrical properties (**b**)

Solving (2) for γ and using (1) yields:

$$\gamma = \arctan\frac{(b-h)\Delta a}{(b-h)^2 + a(a+\Delta a)}. \tag{3}$$

Replacing 2β by γ given by (3) yields for the surface deformation in x-direction:

$$h_x = -\tan\left(\frac{1}{2}\arctan\frac{(b-h)\Delta a}{(b-h)^2 + a(a+\Delta a)}\right). \tag{4}$$

This equation can be simplified for typical parameter values of our experiment. The vertical distance b between the recording plane and the surface is about 1 m and the horizontal one, a, is about 30 cm. The horizontal shift Δa a due to the deformation is less than 5 mm. Thus, the surface elevation h is in the sub-millimeter range. Therefore, on the right hand side of (4) h can be neglected relative to b and in the denominator also Δa a relative to a. The argument of the arctangent is of the order of 10^{-3}. In this case the arctangent function is equal to its argument. The same holds for the tangent function so that we finally arrive at:

$$h_x = -\frac{1}{2}\frac{b}{b^2 + a^2}\Delta a. \tag{5}$$

Because the liquid volume increases due to absorption, the surface level rises continuously. During a complete experimental run the surface level rises up to about 1 mm. Its influence on b and a can be neglected, but not that on Δa,

which point of reference also shifts. However, this shift is very small during the time a single wave passes the laser spot and thus can be neglected for a single wave. For each wave the point of reference is determined independently. The surface shape is obtained by the partial sum over the single measuring points:

$$h(t) = \sum_{t'=t_0}^{t} h_x(t')v_x(t')\Delta t', \tag{6}$$

where $\Delta t'$ denotes the time interval between the measured points, which is 0.04 s at video frequency. t_0 is the starting point of each wave and v_x is the wave velocity in the x-direction, which is measured simultaneously with the shadowgraph technique.

The neglected contributions that led to (5) are of the same order or less than the uncertainties of the parameters. The vertical and horizontal distances a and b are determined with an uncertainty of 5 mm. The displacement Δa of the center of the laser spot can be determined to within 0.12 mm. It is the main error in this experiment. Therefore, the absolute uncertainty of the gradient is $5 \cdot 10^{-5}$. The velocity is determined with an error between 0.3 and 1.7%, depending on its magnitude.

3 Results and Conclusions

Figure 4 shows space-time diagrams of the internal waves visualized with the two shadowgraph setups. Diagram (a) displays a train in the transmission mode and diagram (b) in the reflection mode. The image taken in reflection is noisier than in the transmission mode. Besides this, it shows the same qualitative characteristics, i.e. bright localized areas on an otherwise dark background traveling through the container. The sharp contrast seen in Fig. 4b is due to a larger distance between the focal plane and the surface.

To obtain the amplitude of the shadowgraph contrast, the space-time plots in the transmission mode have been demodulated. The demodulation procedure has been described by Wierschem et al. [3]. A comparison between the surface elevation amplitude as measured with the reflected laser beam and the amplitude of the shadowgraph contrast in an experimental run shows Fig. 5. The correspondence between the results of both experimental methods is in line with the interpretation that the shadowgraph contrast is mainly due to the surface deformation, which was already suggested by the shadowgraph experiment in the reflection mode.

For further quantitative comparison, we compare the shadowgraph contrast in transmission to the one that would be expected from the surface deformation, as it is measured with the reflected laser. Due to the surface inclination of the liquid with the refractive index n_L, the vertical light beam arrives at the surface under the inclination angle of the deformed surface β. There, the light ray is deflected and

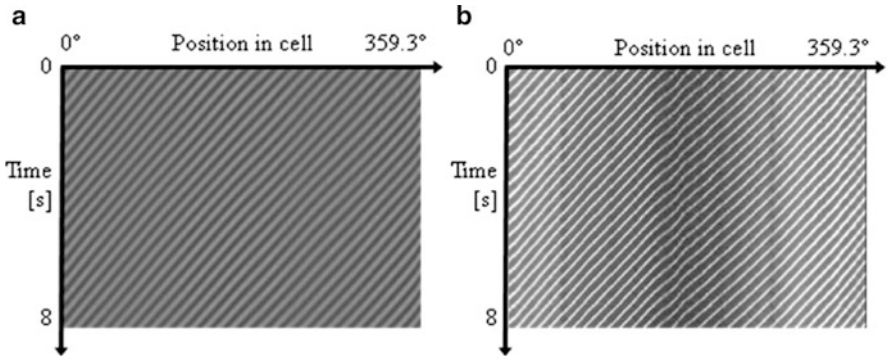

Fig. 4 Space-time diagrams along the central line of the annular container, obtained by the shadowgraph method working in transmission (**a**) and in reflection (**b**)

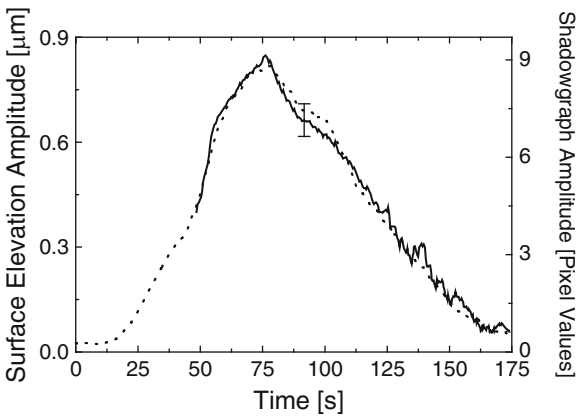

Fig. 5 Comparison between the amplitudes of the shadowgraph contrast and the surface elevation as measured with the reflected laser beam. The *solid line* displays the surface elevation and the *dotted line* the amplitude of the shadowgraph contrast at the position of the reflected beam. The *error bar* indicates the uncertainty of the surface elevation measurement

leaves the surface under an angle δ with respect to the vertical. Setting the refractive index of the air–vapor phase equal to one, Snelius' law of refraction reads:

$$n_L \sin\beta = \sin(\beta + \delta). \tag{7}$$

The experiments with the reflected laser beam have shown that the surface deformation is very small. Therefore, with $n_L > 1$, we may take all angles small and approximate the cosine by unity. Thus (7) now reads:

$$\sin\delta = (n_L - 1)\sin\beta. \tag{8}$$

Furthermore, as the angles are small the tangents become equal to the sine functions and $\sin\beta$ can be replaced by $h_x(x)$. For the deflection angle we obtain then:

$$\tan\delta = (n_L - 1)h_x. \tag{9}$$

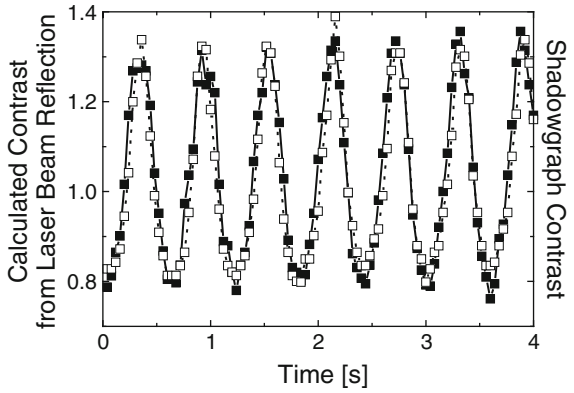

Fig. 6 Comparison of the relative intensity of the shadowgraph contrast with that calculated from the profile of the surface elevation as measured with the reflected laser beam in the case of internal waves. *Solid symbols* and *solid line* display the surface elevation while *open symbols* and *dotted line* depict the amplitude of the shadowgraph contrast at the position of the reflected beam. Both graphs have the same scaling

A ray that traverses the surface at a horizontal position x_0 arrives after a vertical distance z_1 from the liquid surface at the horizontal position x_1. The vertical distance z_1 is much larger than the surface-deformation amplitude and the later can therefore be neglected:

$$x_1 = x_0 + \Delta x = x_0 + z_1 \tan\delta = x_0 + z_1(n_L - 1)h_x(x_0). \tag{10}$$

The shadowgraph method, on the other hand, detects the light-intensity distribution. A light ray that originates at x_0 and arrives on the recording plane at x_1 contributes there to the light intensity while no light arrives at x_0. The light intensity at the point x_1 is then the sum over all points of the illuminated area that are mapped on it. This mapping changes the intensity per unit area. But, neglecting light absorption, the overall intensity remains unchanged. Thus, the product of the intensity at recording plane $I(x_1, z_1)$ and the local coordinate scale is equal to that of the former intensity at the former scale:

$$I(x_1, z_1)\Delta x_1(z_1) = I_0 \Delta x_0, \tag{11}$$

hence, the relative light intensity at the recording plane is the inverse of the Jacobian [1]. Taking the derivative of (10) we arrive at:

$$\frac{I_0}{I(x_1, z_1)} = \frac{\partial x_1}{\partial x_0} = 1 + (n_L - 1)z_1 h_{xx}(x_0). \tag{12}$$

The second derivative of the surface elevation in azimuth direction $h_{xx}(x_0)$ can be determined from the measurements with the reflected laser beam by differentiating the measured surface-elevation gradient. Figure 6 compares the intensity

relative to the homogeneous state as measured with the shadowgraph method in transmission, to that calculated with (12) from the laser-beam measurement. The scaling is the same for both measurements. The measurements are in good agreement, although a better temporal resolution would be desirable.

We conclude that the shadowgraph contrasts in the reflection mode and in the transmission mode are qualitatively the same. Even in the transmission mode its contrast is mainly produced by the surface deformation. In principle the surface deformation can be calculated from the shadowgraph images by applying (12). It is possible to deduce from the mean contrast of the shadowgraph image on the mean surface elevation and how it changes in time. On the other hand, extrapolation of this result to where the laser-beam method is not applicable is of special interest for the study of wave interaction. However, there one should only expect rather qualitative results, yet the double integration of the relative shadowgraph contrasts makes it difficult to recover the precise surface elevation from the data field due to the sensitivity of the integration to the zero-level [6].

References

1. Jenkins, D.R.: Interpretation of shadowgraph patterns in Rayleigh-Bénard convection. J. Fluid Mech. **190**, 451–469 (1988)
2. Thess, A., Orszag, S.A.: Surface tension driven Bénard-convection at infinite Prandtl number. J. Fluid Mech. **283**, 201–230 (1995)
3. Wierschem, A., Linde, H., Velarde, M.G.: Internal waves excited by the Marangoni effect. Phys. Rev. E **62**, 6522–6530 (2000)
4. Wierschem, A., Velarde, M.G., Linde, H., Waldhelm, W.: Interfacial wave motions due to Marangoni instability II. Three-dimensional surface-wave trains in annular containers. J. Colloid Interface Sci. **212**, 365–383 (1999)
5. Wierschem, A., Linde, H., Velarde, M.G.: Properties of surface wave trains excited by mass transfer through a liquid surface. Phys. Rev. E **64**, 022601 (2001)
6. Schöpf, W., Patterson, J.C., Brooker, A.M.H.: Evaluation of the shadowgraph method for the convective flow in a side-heated cavity. Exp. Fluids **21**, 331–340 (1996)

Formation of Mach-Stems on Shock Fronts and Cellular Detonations

P. Clavin

1 Introduction

Detonations are supersonic and exothermic waves propagating in reactive mixtures. They were discovered during the nineteenth century. Early experiments of the mid twentieth century showed that these reacting fronts are cellular with triple points propagating transversely in both directions in two dimensional geometry. An analytical description of this cellular structure was obtained much later in a limiting case by the nonlinear analysis of [1]. The underlying mechanism was shown to be a pulsating instability resulting from the coupling of the longitudinal (one-dimensional) dynamics of the reaction zone with the two-dimensional dynamics of the wrinkled lead shock, see [2] and [3]. The mechanism of spontaneous formation of triple points in inert shock waves is an open question.

Plane shock waves propagating in gas are known from a long time to be stable. However their relaxation mechanism is not clearly understood. The first theories and experiments considered what occurs when a plane shock propagating along a parallel channel encounters a disturbance on the wall of the channel, see [4]. Few years later, the study of [5] concerned shock waves reflected normally from perturbed flat walls. The theoretical analysis of [6] described the interaction of a cylindrical or spherical pressure wave with a shock wave. These studies reported a decay law which is not exponential in time, but follows power laws $t^{-1/2}$ or $t^{-3/2}$. No attention was payed at that time to the formation of triple points which, however, appeared clearly in all the experiments.

P. Clavin (✉)
Institut de Recherche sur les Phénomènes Hors Équilibre
Aix-Marseille Université et Centre National de la Recherche Scientifique, BP 146,
49 rue Joliot Curie, 13384 Marseille Cedex 13, France
e-mail: clavin@irphe.univ-mrs.fr

R.G. Rubio et al. (eds.), *Without Bounds: A Scientific Canvas of Nonlinearity and Complex Dynamics*, Understanding Complex Systems,
DOI 10.1007/978-3-642-34070-3_32,

The stability analysis of shock waves differs from that of usual dissipative structures. Dissipative transports are localised inside the thickness of the shock wave which is considered in the analysis as a discontinuity, separating non dissipative flows. Therefore, the damping mechanisms are resulting only from the boundary conditions at the shock waves (Rankine–Hugoniot conditions). Normal mode analyses of shock waves have been performed for general materials by DYakov [7] and Kontorovich [8]. Without natural length scale in the problem the complex linear growth rate σ is proportional to the wave number of the wrinkle k, $\sigma \propto \mathscr{D}k$, where $\mathscr{D}$ is the propagation velocity of the planar front. The complex scalar $s \equiv \sigma/(\mathscr{D}k)$ depends on the shape of the Rankine–Hugoniot curve. The case of neutral oscillatory modes, $\mathrm{Re}(s) = 0$, $\sigma = i\omega$, $\mathrm{Im}(\omega) = 0$, deserves further attention. In this case the stability property was associated with the non-divergence of the reflection coefficient of pressure waves impinging the shock from the shocked material, see Appendix 1. The stability character is then directly related to the radiating or non-radiating nature of the pressure waves which are associated with the eigenmodes.

In this context, there exist two different types of stable shock fronts, those with an exponential decay ($\mathrm{Re}(s) < 0$) and those with neutral modes ($\mathrm{Re}(s) = 0$) whose pressure waves are non-radiating. The transition separating the two types of stability in the space of parameters was not investigated for real shock waves, even though the two possibilities were mentioned very early by DYakov [7] and Kontorovich [8], and also by Majda and Rosales [9]. Surprisingly, even the case of shock waves propagating in an inert polytropic gas was not clarified. As we shall see, these shock waves have neutral non-radiating eigenmodes, contrarily to what is reported in the more modern literature without solving explicitly the problem. The confusion results from a misinterpretation of the general result of [9], see for example [10] and [11] who reported that disturbances are damped exponentially.

The formation of triple points in reacting shock fronts, called spontaneous Mach stem formation, was addressed by Majda and Rosales [9]. Their weakly nonlinear analysis showed that the formation of singularities on the reacting fronts is described by a Burgers equation. The reacting shock front being considered as a discontinuity, the patterns of cellular detonations cannot be fully represented by their analysis. The main reason is that the unsteadiness of the reacting zone is essential for introducing both an instability with an exponential growth rate and a cutoff in the wavelengths, see [2] and [1]. Furthermore, in contrast to inert shock waves, the eigenmodes of reacting shock fronts are characterised by radiating pressure waves (outgoing acoustic waves). Since the existence of these radiating pressure waves is a basic ingredient of the analysis of [9], the formation of Mach stems in inert shock waves requires a different analysis. This is the purpose of the present paper.

In the first part, we reconsider the stability of shock waves with a particular attention to polytropic gases. In the second part we performed a nonlinear analysis in the limiting case of strong shock and Newtonian limit, leading to the formation of singularities representative of a triple points. The results will be discussed in relation to the cellular structure of detonations.

2 Stability Analysis of Shock Waves

The shock wave is considered as an hydrodynamic discontinuity of zero thickness. Consider a planar shock wave standing perpendicular to the x-axis at $x = 0$. The shocked gas flows at a constant and subsonic flow velocity $\overline{u}_N > 0$ in the $x > 0$ direction. Let $x = \alpha(y,t)$ represents the perturbed shock position at transverse position y at time t in the reference frame of the unperturbed planar shock. For saving the notation we use only one transverse coordinate, the generalization to two transverse coordinates is straightforward.

2.1 Formulation

For any physical quantity f we introduce the decomposition $f = \overline{f} + \delta f$, where $\overline{f}$ represents the unperturbed solution. The upstream flow is unperturbed, and $u = \overline{u}_N + \delta u$ and $w = \delta w$ are the x and y components of the flow velocity in the shocked gas, written in the reference frame of the unperturbed shock. The flow is considered as inviscid and the heat conduction is neglected. The linearized Euler equations yield

$$\frac{1}{\overline{\rho}_N}\frac{D}{Dt}\delta\rho + \frac{\partial}{\partial x}\delta u + \frac{\partial}{\partial y}\delta w = 0, \tag{1}$$

$$\overline{\rho}_N \frac{D}{Dt}\delta u = -\frac{\partial}{\partial x}\delta p, \qquad \overline{\rho}_N \frac{D}{Dt}\delta w = -\frac{\partial}{\partial y}\delta p, \tag{2}$$

$$\frac{D}{Dt}\delta s = 0 \Rightarrow \frac{D}{Dt}\delta p = \overline{a}_N^2 \frac{D}{Dt}\delta\rho, \tag{3}$$

where p is the pressure and the material derivative D/Dt takes the simple form

$$D/Dt = \partial/\partial t + \overline{u}_N \partial/\partial x,$$

since the unperturbed flow is uniform. Eliminating $\delta\rho$ from (1) and (3) give

$$\frac{1}{\overline{\rho}_N \overline{a}_N^2}\frac{D}{Dt}\delta p + \frac{\partial}{\partial x}\delta u + \frac{\partial}{\partial y}\delta w = 0. \tag{4}$$

Eliminating δu and δw from (2) and (4) we get the d'Alembert equation for the pressure fluctuations of acoustic waves propagating in a fluid moving at constant velocity $\overline{u}_N$,

$$\frac{D^2}{Dt^2}\delta p - \overline{a}_N^2 \left(\frac{\partial^2}{\partial x^2} + \frac{\partial^2}{\partial y^2}\right)\delta p = 0. \tag{5}$$

In other words, in an homogeneous flow and in the linear approximation, all the fluctuations of pressure are associated with acoustic waves.

A boundedness condition should be used at infinity in the shocked gases, $x \to \infty$. Boundary conditions at the shock, $x = 0 : \delta u = \delta u_N(y,t)$, $\delta w = \delta w_N(y,t)$, $\delta p = \delta p_N(y,t)$, are given by the Rankine–Hugoniot relations across the wrinkled shock in Sect. 2.4, the subscript N denoting the Neumann state (just behind the shock wave).

2.2 *Pressure and Entropy–Vorticity Waves*

Due to the shock wrinkling, acoustic waves are generated by the pressure fluctuations at the Neumann state $x = 0$. Moreover isobaric shear waves and entropy fluctuations are also generated at $x = 0$, since the Hugoniot curve differs from an isentropic curve. The solution to (2) may then be decomposed into acoustic waves, superscript (a), and an entropy–vorticity wave, superscript (i), see Fig. 1. The flow velocity in the acoustic waves is obtained from (2) where the pressure is solution to (5) with the boundary condition at $x = 0$, $\delta p = \delta p_N(y,t)$. On the other hand the flow of the entropy–vorticity wave ($\delta u^{(i)}$, $\delta w^{(i)}$) is solution to (2) with $\delta p = 0$. It is an isobaric shear flow generated at the Neumann state, $x = 0$, propagating with the unperturbed flow,

$$D\delta u^{(i)}/Dt = 0, \quad D\delta w^{(i)}/Dt = 0.$$

The flow disturbances may thus be written as

$$\delta p = \delta p^{(a)}, \quad \delta u = \delta u^{(a)} + \delta u^{(i)}(y,\, t - x/\overline{u}_N), \tag{6}$$

$$\delta w = \delta w^{(a)} + \delta w^{(i)}(y,\, t - x/\overline{u}_N). \tag{7}$$

According to continuity (4), the flow of the entropy–vorticity wave is incompressible

$$\frac{\partial}{\partial x}\delta u^{(i)} + \frac{\partial}{\partial y}\delta w^{(i)} = 0, \Rightarrow \frac{\partial}{\partial t}\delta u^{(i)} = \overline{u}_N \frac{\partial}{\partial y}\delta w^{(i)}. \tag{8}$$

Density variations $\delta\rho(x,y,t)$ are obtained from the pressure fluctuations $\delta p(x,y,t)$ propagating with the acoustic waves and from the propagation (3) of the entropy fluctuations which are generated at $x = 0$ by the wrinkled shock $\delta s_N \neq 0$, $\delta p_N \neq \overline{a}_N^2 \delta\rho_N$,

$$\delta p - \overline{a}^2 \delta\rho = \delta p_N(y, t - x/\overline{u}_N) - \overline{a}_N^2 \delta\rho_N(y, t - x/\overline{u}_N). \tag{9}$$

The problem may be solved by using a normal-mode analysis

$$\alpha(y,t) = \hat{\alpha} e^{iky+\sigma t} + c.c., \qquad \delta f(x,y,t) = \tilde{f}(x) e^{iky+\sigma t} + c.c. \tag{10}$$

where k is the transverse wave vector (a real quantity), and $\sigma = s + i\,\omega$ is a complex quantity, its real part s measuring the growth rate (damping rate if $s < 0$) and its

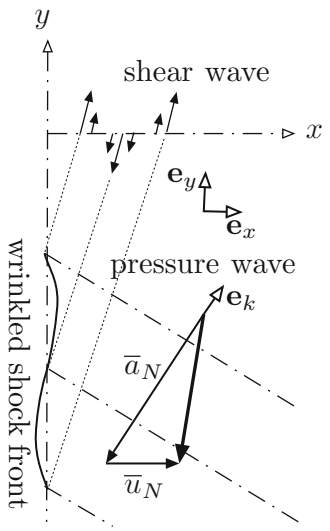

Fig. 1 Sketch of the flow field associated with an eigenmode. It is composed of an isobaric shear flow propagating at the subsonic velocity of the flow $\overline{u}_N$ and a pressure wave propagating with the sound speed $\overline{a}_N$ relatively to the shocked gas flowing with the velocity $\overline{u}_N$. In this figure the pressure wave is non-radiating since the propagation velocity of the pressure wave in the reference frame of the unperturbed shock wave is oriented toward the shock front, see (47) in Sect. 2.6.2

imaginary part ω being the frequency of oscillation in time. The pressure, solution to (5), is looked for in the form of Fourier decomposition

$$\delta p = \tilde{p}_N e^{il_\pm x + iky + \sigma t} + c.c., \tag{11}$$

where $\tilde{p}_N$ is a constant of integration obtained from the boundary condition $x = 0 : \delta p = \delta p_N(y,t) = \tilde{p}_N e^{iky+\sigma t} + c.c$. The quantities $l_\pm$ are solutions of the second-order algebraic equation associated with (5),

$$(\sigma + i l_\pm \overline{u}_N)^2 + \overline{a}_N^2 (l_\pm^2 + k^2) = 0, \tag{12}$$

resulting in,

$$\frac{i l_\pm}{|k|} = \frac{\overline{M}_N S \pm \sqrt{1+S^2}}{\sqrt{1-\overline{M}_N^2}} \quad \text{with} \quad S \equiv \frac{\sigma}{\overline{a}_N |k|} \frac{1}{\sqrt{1-\overline{M}_N^2}}, \tag{13}$$

expressing $i l_\pm$ in terms of $|k|$ and σ. Equation (13) may also be written

$$i l_\pm \overline{u}_N (1-\overline{M}_N^2) - \overline{M}_N^2 \sigma = \pm |k| \overline{u}_N \sqrt{(1-\overline{M}_N^2) + (\sigma/\overline{a}_N |k|)}. \tag{14}$$

The $\pm$ sign in (13) and (14) must be chosen to enforce boundedness of acoustic waves for $x \to \infty$, thereby requiring that the real part of $i l_\pm$ be non positive,

$$Re[\overline{M}_N S \pm \sqrt{1+S^2}] \leq 0. \tag{15}$$

This is right for unstable modes in the sense $Re(S) > 0$. However for neutral modes, $Re(S) = 0$ with $1 + S^2 < 0$, as it is the case for shock waves in a polytropic gas studied in the next section, the sign in (13) is determined in a different way, see the discussion below (42). The quantity $\sigma/(\overline{a}_N|k|)$ may be expressed in terms of $l_\pm/|k|$ from (12) or (13). In the particular case of neutral modes, $\sigma = \pm i\omega$ with $\omega > 0$ and $l_\pm$ real, this leads to the well-known result of the frequency shift by the Doppler effect,

$$\sigma = i\omega, \quad \omega > 0: \qquad \omega = \overline{a}_N\sqrt{l_\pm^2 + k^2} - \overline{u}_N l_\pm > 0, \tag{16}$$

$$\sigma = -i\omega, \quad \omega > 0: \qquad \omega = \overline{a}_N\sqrt{l_\pm^2 + k^2} + \overline{u}_N l_\pm > 0. \tag{17}$$

In the limit of infinite sound speed, $\overline{M}_N \to 0$, $\sigma/\overline{a}_N|k| \to 0$, (13) leads to the low Mach number approximation $il_\pm = \pm|k|$, $\Delta\delta p = 0$.

The velocity field associated with the acoustic modes is, according to (2),

$$\tilde{u}^{(a)} = -\frac{il_\pm\overline{u}_N}{\sigma + il_\pm\overline{u}_N}\frac{\tilde{p}_N}{\overline{\rho}_N\overline{u}_N}e^{il_\pm x}, \quad \tilde{w}^{(a)} = -\frac{ik\overline{u}_N}{\sigma + il_\pm\overline{u}_N}\frac{\tilde{p}_N}{\overline{\rho}_N\overline{u}_N}e^{il_\pm x}, \tag{18}$$

and the entropy–vorticity wave may be written as,

$$\tilde{u}^{(i)} = \left[\tilde{u}_N + \frac{il_\pm\overline{u}_N}{\sigma + il_\pm\overline{u}_N}\frac{\tilde{p}_N}{\overline{\rho}_N\overline{u}_N}\right]e^{-\sigma x/\overline{u}_N}, \tag{19}$$

$$\tilde{w}^{(i)} = \left[\tilde{w}_N + \frac{ik\overline{u}_N}{\sigma + il_\pm\overline{u}_N}\frac{\tilde{p}_N}{\overline{\rho}_N\overline{u}_N}\right]e^{-\sigma x/\overline{u}_N}, \tag{20}$$

where $\tilde{p}_N(k,\sigma)$, $\tilde{u}_N(k,\sigma)$ and $\tilde{w}_N(k,\sigma)$ are obtained by the Rankine–Hugoniot relations, see (31) and (32) below.

For strongly unstable cases, $s \equiv Re(\sigma) > 0$, the entropy–vorticity wave is damped when x increases. For strongly stable cases, $s < 0$, there is no real divergence since, according to the initial value problem for $t > 0$ and $x \le \overline{u}_N t$, the quantities $\delta u^{(i)}(y, t - x/\overline{u}_N)$ and $\delta w^{(i)}(y, t - x/\overline{u}_N)$ are bounded by the initial condition at $t = 0$ and $x = 0$, $\delta u^{(i)}(y, t = 0)$ and $\delta w^{(i)}(y, t = 0)$.

2.3 Compatibility Condition

The entropy–vorticity wave must satisfy the incompressible condition (8),

$$-\frac{(il_\pm\sigma + \overline{u}_N k^2)}{(\sigma + il_\pm\overline{u}_N)}\frac{\tilde{p}_N}{\overline{\rho}_N\overline{u}_N} - \sigma\frac{\tilde{u}_N}{\overline{u}_N} + ik\tilde{w}_N = 0. \tag{21}$$

The first term may be written in a simpler form as follows. Equation (12) yields

$$\begin{aligned} -(il_{\pm}\overline{u}_N\sigma + \overline{u}_N^2 k^2) &= \sigma^2 + il_{\pm}\sigma\overline{u}_N + (\overline{a}_N^2 - \overline{u}_N^2)(l_{\pm}^2 + k^2) \\ &= \sigma^2 + il_{\pm}\sigma\overline{u}_N - (1 - \overline{M}_N^2)(\sigma + il_{\pm}\overline{u}_N)^2 \\ &= -(\sigma + il_{\pm}\overline{u}_N)\left[il_{\pm}\overline{u}_N\left(1 - \overline{M}_N^2\right) - \sigma\overline{M}_N^2\right], \end{aligned} \tag{22}$$

where the bracket may be expressed using (14). Equation (21) may then be written

$$\pm |k|\sqrt{(1 - \overline{M}_N^2) + (\sigma^2/\overline{a}_N^2 k^2)}(\tilde{p}_N/\overline{\rho}_N\overline{u}_N) + \sigma(\tilde{u}_N/\overline{u}_N) - ik\tilde{w}_N = 0, \tag{23}$$

or, in non dimensional form,

$$\pm\sqrt{S^2 + 1}\frac{\tilde{p}_N}{\overline{\rho}_N\overline{a}_N\overline{u}_N} + S\frac{\tilde{u}_N}{\overline{u}_N} - \frac{ik\tilde{w}_N}{|k|\overline{u}_N}\frac{\overline{M}_N}{\sqrt{1 - \overline{M}_N^2}} = 0, \tag{24}$$

where the $\pm$ sign is the same as in (13) and has to be chosen to satisfy (15). In the case of neutral modes, $\sigma = i\omega$, the $\pm$ sign depends on the parameters defined below in (29), see Appendix 1. Equation (23) was first written by Buckmaster and Ludford [12], except for the $\pm$ sign. It is valid for any supersonic discontinuity when modifications to the inner structure are neglected. Equations (23) or (24) lead to an equation for the non dimensional complex growth rate $\sigma/(\overline{a}_N|k|)$, as soon as the quantities $\tilde{p}_N/(\overline{\rho}_N\overline{u}_N\overline{a}_N)$, $\tilde{u}_N/\overline{u}_N$ and $\tilde{w}_N/\overline{u}_N$ are expressed in terms of σ and k by using the Rankine–Hugoniot relations at the shock $x = 0$.

2.4 Boundary Conditions at the Shock

The conditions for the flow velocity at the Neumann state are obtained from the equation for conservation of transverse momentum and of mass (78) where $\mathscr{D}$ and u_N should be replaced by the normal shock velocity and the normal flow velocity relative to the wrinkled shock respectively. Conservation of transverse momentum leads to conservation of the transverse component of the flow velocity. This yields

$$\begin{aligned} \rho_N(u_N - \partial\alpha/\partial t - w_N\partial\alpha/\partial y) &= \rho_u(\overline{\mathscr{D}} - \partial\alpha/\partial t), \\ (\overline{\mathscr{D}} - \partial\alpha/\partial t)\cos\theta &= w_N\sin\theta + (u_N - \partial\alpha/\partial t)\cos\theta, \end{aligned} \tag{25}$$

where $\cot\theta = \partial\alpha/\partial y$, so that the second equation may be written

$$\overline{\mathscr{D}}\partial\alpha/\partial y = w_N + u_N\partial\alpha/\partial y \tag{26}$$

In the linear approximation, one gets

$$\delta\rho_N \overline{u}_N + \overline{\rho}_N(\delta u_N - \partial\alpha/\partial t) = -\rho_u \partial\alpha/\partial t, \tag{27}$$

$$\delta w_N = (\overline{\mathscr{D}} - \overline{u}_N)\partial\alpha/\partial y. \tag{28}$$

The Hugoniot relation (80) in Appendix 2 provides the slope of the Rankine–Hugoniot curve at the Neumann state $d\overline{p}_N/d\overline{\rho}_N^{-1}$. It is useful to introduce two non dimensional parameters,

$$r \equiv -\frac{(\rho_u \overline{\mathscr{D}})^2}{d\overline{p}_N/d\overline{\rho}_N^{-1}}, \qquad n \equiv \frac{\overline{\rho}_N}{\rho_u}\frac{\overline{M}_N^2}{\left(1-\overline{M}_N^2\right)}. \tag{29}$$

For wrinkled shock front, (79) in Appendix 2 is still valid when m is replaced by the normal mass flux $m = \rho_u(\overline{\mathscr{D}} - \partial\alpha/\partial t)/\sqrt{1+(\partial\alpha/\partial y)^2}$, $\delta m = -\rho_u \partial\alpha/\partial t$. Using the first equation in (29) in the form

$$\delta p_N = \frac{1}{r}\left(\frac{\rho_u}{\overline{\rho}_N}\right)^2 \overline{\mathscr{D}}^2 \delta\rho_N, \tag{30}$$

Equation (79) leads to the variations of pressure and density at the Neumann state in terms of the variation of shock velocity, $\partial\alpha/\partial t$,

$$\frac{\delta p_N}{\overline{p}_N} = -2\frac{\left(1-\frac{p_u}{\overline{p}_N}\right)}{(1-r)}\frac{\partial\alpha/\partial t}{\overline{\mathscr{D}}}, \quad \frac{\delta\rho_N}{\overline{\rho}_N} = -2\left(\frac{\overline{\rho}_N}{\rho_u}-1\right)\frac{r}{(1-r)}\frac{\partial\alpha/\partial t}{\overline{\mathscr{D}}}. \tag{31}$$

Using these results, (27) and (28) provide the variation of the flow velocity fluctuations at the Neumann state,

$$\frac{\delta u_N}{\overline{u}_N} = \left(\frac{\overline{\rho}_N}{\rho_u}-1\right)\frac{(1+r)}{(1-r)}\frac{\partial\alpha/\partial t}{\overline{\mathscr{D}}}, \quad \frac{\delta w_N}{\overline{u}_N} = \left(\frac{\overline{\rho}_N}{\rho_u}-1\right)\frac{\partial\alpha}{\partial y}. \tag{32}$$

2.5 General Case

Introducing (31) and (32) into (24), yields

$$\pm 2\overline{M}_N S\sqrt{1+S^2} = (1+r)S^2 + (1-r)n, \tag{33}$$

where the $\pm$ sign is the same as in (13). The complex linear growth rate of the normal modes, $\sigma/(\overline{a}_N|k|)$, are expressed in terms of r and n, from the solutions of the quadratic equation for S^2 corresponding to (33),

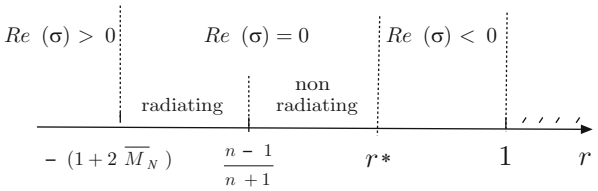

Fig. 2 General stability limits for shock waves, σ is the complex linear growth rate, $e^{\sigma t}$, the inverse of the reduced slope of the Hugoniot curve at the Neumann state r, and the parameter n are given in (29). The critical value $r*$ is given in (35)

$$aS^4 + 2bS^2 + c = 0, \tag{34}$$

$$a \equiv (1+r)^2 - 4\overline{M}_N^2, \qquad b \equiv (1-r^2)n - 2\overline{M}_N^2, \qquad c \equiv (1-r)^2 n^2 > 0.$$

The roots to be retained are those which satisfy (15) and (33). The problem reduces to discuss the roots of a quadratic equation for S^2. This simplification comes from (22) and was not used in the original works, see for example the text book of [13]. The fact that σ is proportional to $\overline{a}_N|k|$ is due to the absence of reference length scale in the problem since the shock is considered as a discontinuity in the solutions of the Euler equations.

The discussion of the general case is tedious but straightforward. The results are summarized in Fig. 2. The more striking feature is that the domain of stability with an exponential damping, $Re(\sigma) < 0$, is separated from the domain of instability with an exponential growth rate, $Re(\sigma) > 0$, by a wide domain of neutral oscillatory modes, $Re(\sigma) = 0, Im(\sigma) \neq 0$, in which at least one of the roots of (34) is negative, $S^2 < 0$. Depending on the sign of the quantity a one may have either a single neutral mode and a stable mode with an exponential relaxation, or a pair of neutral modes, as it is discussed below for polytropic gases.

The critical values $-(1+2\overline{M}_N)$ and $(n-1)/(n+1)$ for the parameter r in Fig. 2 have been obtained by DYakov [7] and Kontorovich [8]. They play an important role in the stability limits. Other authors, following Fickett and Davis [14], introduced the Gruneisen coefficient Γ instead of r. The above mentioned critical values for r correspond to the critical values $(1+\overline{M}_N)/\Gamma$ and $1/(1+\Gamma)$ for the parameter $(\frac{\overline{\rho}_N}{\rho_u} - 1)\overline{M}_N^2$.

The critical value $r*$ separating the domain of neutral oscillatory modes from the domain of exponential relaxation has not been reported before. It corresponds to the double roots $S^2 = -b/a < 0, b^2 = ac$,

$$r* = \frac{n - \sqrt{(1-\overline{M}_N^2)\left(1 - \frac{\rho_u}{\overline{\rho}_N}\right)}}{n+1}. \tag{35}$$

In the linear approximation, the amplitude of the neutral oscillatory modes in the range $-(1+2\overline{M}_N) \leq r \leq r*$ are damped as power laws in 1/t. This is shown

by the initial value problem solved by using the Laplace transform. According to (33), a square root appears in the denominator of the inversion formula of the Laplace transform. This introduces branch points in the complex plane leading to power laws when integrating along the branch cuts. The stability of shock waves characterised by neutral oscillatory normal modes has been discussed by Kontorovich [8] and Landau and Lifchitz [13] in a different manner, by considering the reflection of acoustic waves impinging the front from the shocked gases. The reflection coefficient diverges when the pressure wave of a normal mode is radiating, that is when it propagates from the shock front towards infinity in the shocked gases, see Appendix 1. Such a divergence never appears if the pressure wave of normal modes are non-radiating. Therefore the critical value $r = (n-1)/(n+1)$ was considered as the stability limit.

2.6 Polytropic Gases

For a polytropic gas, according to the Rankine–Hugoniot relations (81)–(84) in Appendix 2, the parameters r and n in (29) are related to the Mach number $\overline{M}_u \equiv \overline{\mathscr{D}}/a_u > 1$, $r = 1/\overline{M}_u^2$ and $n = \overline{M}_u^2/(\overline{M}_u^2 - 1)$, $(1-r)n = 1$. Equation (33) reduces to

$$\pm 2S\overline{M}_N\sqrt{1+S^2} = S^2\left(1+\overline{M}_u^{-2}\right)+1, \tag{36}$$

and the linear modes of shock waves in polytropic gases are neutral, $\mathrm{Re}(\sigma) = 0$, with non-radiating pressure waves since

$$\overline{M}_u > 1, \quad \gamma > 1 \quad \Rightarrow \quad (n-1)/(n+1) < r < r*,$$

see Fig. 2. A different result, $\mathrm{Re}(\sigma) < 0$, is reported by Rosales [10] and Short [11]. In order to clarify the problem, and also to prepare the nonlinear analysis it is worth re-considering in details the stability analysis of shock waves propagating in polytropic gases from the beginning.

2.6.1 Neutral Modes

Density and pressure fluctuations at the Neumann state are obtained from the linearised version (81) and (82) using $\delta M_u = -(\partial\alpha/\partial t)/\overline{a}_u$

$$\frac{\delta\rho_N}{\overline{\rho}_N} = -\frac{4}{(\gamma+1)}\frac{1}{\overline{M}_u}\frac{1}{\left[1+\frac{(\gamma-1)}{(\gamma+1)}(\overline{M}_u^2-1)\right]}\frac{\partial\alpha/\partial t}{\overline{a}_u}, \tag{37}$$

$$\frac{\delta p_N}{\overline{p}_N} = -\frac{\frac{4\gamma}{(\gamma+1)}\overline{M}_u}{\left[1+\frac{2\gamma}{(\gamma+1)}(\overline{M}_u^2-1)\right]}\frac{\partial\alpha/\partial t}{\overline{a}_u}. \tag{38}$$

Velocity fluctuations at the Neumann state are obtained from (27) and (28) using (81), (82) and (37),

$$\frac{\delta u_N}{\overline{u}_N} = \frac{\frac{2}{(\gamma+1)}[2+(\overline{M}_u^2-1)]}{\overline{M}_u^2}\frac{\partial\alpha/\partial t}{\overline{u}_N}, \qquad \frac{\delta w_N}{\overline{u}_N} = \frac{\frac{2}{(\gamma+1)}(\overline{M}_u^2-1)}{\left[1+\frac{(\gamma-1)}{(\gamma+1)}(\overline{M}_u^2-1)\right]}\frac{\partial\alpha}{\partial y}. \quad (39)$$

Equation (36) is obtained directly by introducing (38) and (39) into (24). Equation (34) then takes the form,

$$aS^4+2bS^2+1=0, \qquad S_\pm^2=[-b\pm\sqrt{b^2-a}]/a, \quad (40)$$

$$a\equiv\left(1+\overline{M}_u^{-2}\right)^2-4\overline{M}_N^2, \quad b\equiv\left(1+\overline{M}_u^{-2}\right)-2\overline{M}_N^2, \quad \sqrt{b^2-a}=2\overline{M}_N\sqrt{\overline{M}_N^2-\overline{M}_u^{-2}}$$

where $\overline{M}_N^2<1$ is expressed in terms of $\overline{M}_u^2>1$ and $(\gamma-1)>0$ by using (84) in Appendix 2. The quantity $b^2-a=4(\gamma-1)(M_N/M_u)^2(\overline{M}_u^2-1)^2/[2\gamma\overline{M}_u^2-(\gamma-1)]$ being positive, the two roots in (40) are real numbers. It is also easy to see that the quantity $b=(1-\overline{M}_u^{-2})[2\overline{M}_u^2+(\gamma-1)]/[2\gamma\overline{M}_u^2-(\gamma-1)]$ is positive and larger than a since $b-a=(1-\overline{M}_u^{-2})\overline{M}_u^{-2}[2(\gamma-1)\overline{M}_u^4+2\overline{M}_u^2-(\gamma-1)]/[2\gamma\overline{M}_u^2-(\gamma-1)]$ is positive. The quantity a may be written $a=(1-\overline{M}_u^{-2})^2[2(2-\gamma)\overline{M}_u^2-(\gamma-1)]/[2\gamma\overline{M}_u^2-(\gamma-1)]$, so that, for all values of $\overline{M}_u>1$, the condition $a>0$ is verified for $\gamma<5/3$, while the condition $a<0$ is verified for $\gamma>2$. In the interval $5/3<\gamma<2$ the quantity a is positive for sufficiently fast shocks,

$$\overline{M}_u^2>\frac{(\gamma-1)}{2(2-\gamma)}>1:\ a>0, \qquad 1<\overline{M}_u^2<\frac{(\gamma-1)}{2(2-\gamma)}:\ a<0. \quad (41)$$

The signs of the quantities a and $-b+\sqrt{b^2-a}$ being opposite, (40) yields

$$a>0:\ S_-^2<0, \quad S_+^2<0; \qquad a<0:\ S_-^2>0, \quad S_+^2<0.$$

The ratio of specific heat is $\gamma=5/3$ in monoatomic gases, and $\gamma<5/3$ in ordinary gases so that $a>0$. The relevant S solutions (40) are those that are the solutions to (36) which satisfies condition (15). Consider first the usual case $a>0$. The two solutions $S_\pm$ are purely imaginary,

$$a>0: \qquad S_+=\pm i\Omega_1, \quad S_-=\pm i\Omega_2,$$
$$\Omega_1^2=\frac{b-\sqrt{b^2-a}}{a}, \quad \Omega_2^2=\frac{b+\sqrt{b^2-a}}{a}, \quad \Omega_2>\Omega_1>1, \quad (42)$$

where the last relation $\Omega_1>1$ is easily verified since $b>a$ and $(b-a)^2>b^2-a$. The right hand side of (36) being real, the quantity $\pm S_\pm(1+S_\pm^2)^{1/2}$ should be also real. This has two consequences;

- Firstly one should have $(1+S^2) \leq 0$, $S = \pm i\,\Omega$ with $\Omega \geq 1$. This condition is verified by the two roots Ω_1 and $\Omega_2 > 1$ in (42) and the right hand side of (36) is negative.
- Secondly, with the choice $S = i\,\Omega$ one should take $\pm\sqrt{1+S^2} = i\,\sqrt{\Omega^2-1}$ in (36) and (13), while for $S = -i\,\Omega$ one should write $\pm\sqrt{1+S^2} = -i\,\sqrt{\Omega^2-1}$, in order to get a negative contribution of the left hand side of (36),

$$-2\overline{M}_N\,\Omega\,\sqrt{\Omega^2-1} = -\Omega^2\left(1+\overline{M}_u^{-2}\right)+1 < 0. \tag{43}$$

This corresponds to a single absolute value of $il_\pm$ in (13) for each Ω. One gets $il_\pm = il$ for $S = i\,\Omega$ ($\Omega > 0$, $\sigma = i\omega$, $\omega > 0$) and $il_\pm = -il$ for $S = -i\,\Omega$ where

$$\frac{l}{|k|} = \left[\frac{\overline{M}_N\,\Omega + \sqrt{\Omega^2-1}}{\sqrt{1-\overline{M}_N^2}}\right] > 0, \qquad \Omega \equiv \frac{\omega}{\overline{a}_N\,|k|}\,\frac{1}{\sqrt{1-\overline{M}_N^2}} > 0, \tag{44}$$

The frequency $\omega > 0$ expressed in terms of l and k from (44) is

$$\omega = \overline{a}_N\,\sqrt{l^2+k^2} - \overline{u}_N\,l. \tag{45}$$

which corresponds to (16) for $\sigma = i\omega$ and to (17) for $\sigma = -i\omega$. To summarize, for ordinary shock waves in gases, $a > 0$, there are two neutral oscillatory modes associated with every wavelength $2\pi/|k|$. Each of them involves a pressure wave whose frequency ω is given by (42) and satisfies (16).

Consider now the unusual case $a < 0$. The solution S_+ is still purely imaginary while the other S_- is real,

$$a<0: \qquad S_+ = \pm i\,\Omega_1, \quad \Omega_1 > 1, \quad S_- = \pm\Sigma_2, \quad \Sigma_2 > \Omega_1,$$
$$\Omega_1^2 = \frac{\sqrt{b^2-a}-b}{(-a)} > 1, \quad \Sigma_2^2 = \frac{b+\sqrt{b^2-a}}{(-a)} > \Omega_1^2. \tag{46}$$

The S_+ normal mode is neutral and oscillatory. The solution $S_- = +\Sigma_2 > 0$ has to be rejected because it would correspond to the $+$ sign in (36) and condition (15) could not be satisfied. The second normal mode is thus stable and damped exponentially, $S_- = -\Sigma_2 < 0$.

2.6.2 Non-radiating Condition

The end result does not depend on the choice of the $\pm$ sign of $\sigma = \pm i\omega$ in (11), let's take $\sigma = +i\omega \Rightarrow il_\pm = il$, see the text just above (44). Introducing the vector

$\mathbf{k} \equiv l\mathbf{e}_x + k\mathbf{e}_y$, the unit vector $\mathbf{e}_k \equiv \mathbf{k}/\sqrt{l^2+k^2}$ and the position $\mathbf{r} \equiv x\mathbf{e}_x + y\mathbf{e}_y$, $\mathbf{k}.\mathbf{r} = lx + ky$, the frequency (45) may be written $\omega = \overline{a}_N \mathbf{k}.\mathbf{e}_k - \overline{u}_N \mathbf{k}.\mathbf{e}_x$ and (11) yields

$$\delta p = \tilde{p} e^{i\mathbf{k}.[\mathbf{r}-(\overline{u}_N \mathbf{e}_x - \overline{a}_N \mathbf{e}_k)t)]} + c.c. \tag{47}$$

This shows that the propagation velocity of the pressure wave is $\overline{u}_N \mathbf{e}_x - \overline{a}_N \mathbf{e}_k$ in the referential frame of the planar front of the unperturbed shock. The acoustic wave propagates in the shocked gas with the velocity $\overline{a}_N$ in the direction $-\mathbf{e}_k$, see Fig. 1. In other word its wave vector is $-\mathbf{k}$. The component of $\overline{u}_N \mathbf{e}_x - \overline{a}_N \mathbf{e}_k$ along the x-axis is $\overline{u}_N - \overline{a}_N l/\sqrt{l^2+k^2}$. There are two possibilities:

$$\text{radiating waves} : \overline{u}_N - \overline{a}_N \frac{l}{\sqrt{l^2+k^2}} > 0$$

$$\text{non-radiating waves} : \overline{u}_N - \overline{a}_N \frac{l}{\sqrt{l^2+k^2}} < 0.$$

The radiating condition is always fulfilled for $l < 0$ while for $l > 0$ one has,

$$\text{radiating waves} : \frac{l}{|k|}\sqrt{1-\overline{M}_N^2} < \overline{M}_N, \tag{48}$$

$$\text{non-radiating waves} : \frac{l}{|k|}\sqrt{1-\overline{M}_N^2} > \overline{M}_N. \tag{49}$$

Therefore, according to (44), the pressure waves associated with the normal modes of shock waves propagating in a polytropic gas are non-radiating since $\Omega > 1$, see (42) and Fig. 1.

3 Weakly Nonlinear Analysis

The problem consists in solving the Euler equations (86)–(88) in the shocked gas, see Appendix 3. The boundary conditions at the shock front are given by the Rankine–Hugoniot equations (81)–(85) in Appendix 2 for the pressure and density, and by (25)–(26) for the components of the flow velocity. A boundedness condition is introduced at infinity. For performing a nonlinear analysis, it is more convenient to use a coordinate system attached to the front (ξ, y, t) with $\xi = x - \alpha(y,t)$, see (90) in Appendix 3, since the boundary condition at the front corresponds to $\xi = 0$.

A general method of weakly nonlinear analysis of fronts has been performed by Majda and Rosales [9]. Their analysis is based on the two following assumptions; the pressure waves associated with the normal modes are radiating, and the inner structure of the front is quasi-steady. The last assumption is not convenient for gaseous detonations and the first one does not hold for shock waves in polytropic

gas. We present below a weakly nonlinear analysis of shock waves in polytropic gas in the limit of strong shocks in the Newtonian approximation.

3.1 Strong Shocks in the Newtonian Limit

We consider the limit

$$\overline{M}_u^2 \to \infty, \qquad \overline{M}_u^2(\gamma-1) = O(1). \tag{50}$$

According to (84) in Appendix 2, the flow of the shocked gas is strongly subsonic in this limit, and it satisfies a low Mach number approximation $\overline{M}_N \ll 1$,

$$\overline{M}_N^2 \approx (\gamma-1)/2 + \overline{M}_u^{-2}, \qquad (\gamma-1) = O(\overline{M}_N^2), \qquad \overline{M}_u^{-2} = O(\overline{M}_N^2). \tag{51}$$

According to (40) and (42), the two roots Ω_1 and Ω_2 collapse and go to unity in the limit (50), $\Omega_1 \approx \Omega_2 \approx 1$, $\Omega^2 - 1 \approx (\gamma-1)/(2-\gamma) = O(\overline{M}_N^2)$, $\omega \approx \overline{a}_N|k|$. Then, according to (44), $l/|k| = O(\overline{M}_N)$, and $l\overline{u}_N/\omega = O(\overline{M}_N^2)$, the pressure wave propagates in a direction quasi parallel to the unperturbed front, and has an amplitude smaller than that of the shear wave by a factor $\overline{M}_N^2$. This is obtained from (18) and (38)–(39),

$$\frac{\tilde{u}^{(a)}/\overline{u}_N}{(\tilde{p}_N/\overline{\rho}_N\overline{u}_N^2)} \approx -\frac{l\overline{u}_N}{\omega} = O(\overline{M}_N^2), \qquad \frac{\tilde{u}_N/\overline{u}_N}{(\tilde{p}_N/\overline{\rho}_N\overline{u}_N^2)} \approx -2, \tag{52}$$

$$\tilde{w}^{(a)}/\tilde{u}^{(a)} = k/l = O(1/\overline{M}_N), \qquad \tilde{w}_N/\tilde{u}_N \approx 1/\overline{M}_N, \tag{53}$$

$$|\tilde{u}^{(a)}/\tilde{u}^{(i)}| = O(\overline{M}_N^2), \qquad |\tilde{w}^{(a)}/\tilde{w}^{(i)}| = O(\overline{M}_N^2). \tag{54}$$

Therefore, to leading order in the limit (50), the flow generated by the front wrinkling is an isobaric shear flow, with, according to (19)–(20) and (39),

$$\tilde{u}^{(i)} \approx \tilde{u}_N e^{-i\omega x/\overline{u}_N} \quad \Rightarrow \quad \delta u \approx \dot{\alpha}_t(y,\, t - x/\overline{u}_N), \tag{55}$$

$$\tilde{w}^{(i)} \approx \tilde{w}_N e^{-i\omega x/\overline{u}_N} \quad \Rightarrow \quad \delta w \approx \overline{\mathscr{D}}\alpha'_y(y,\, t - x/\overline{u}_N), \tag{56}$$

where we have introduced the short notations $\alpha'_y \equiv \partial\alpha(y,t)/\partial y$ and $\dot{\alpha}_t \equiv \partial\alpha(y,t)/\partial t$.

By using the relation $\overline{u}_N\overline{\mathscr{D}} \approx \overline{a}_N^2$, obtained from (81)–(84) to leading order, $\overline{M}_N^2\overline{M}_u^2 \approx \overline{T}_N/\overline{T}_u = \overline{a}_N^2/\overline{a}_u^2 = O(1)$, the continuity equation (8) then shows that the wrinkles of the front are solutions to the wave equation

$$\frac{\partial^2 \alpha}{\partial t^2} - \overline{a}_N^2 \frac{\partial^2 \alpha}{\partial y^2} = 0, \tag{57}$$

yielding $\omega = \overline{a}_N |k|$, in agreement with what has been said below (51). For simple waves one has simply $\dot{\alpha}_t = \pm \overline{a}_N \alpha'_y$, valid to leading order.

3.2 Perturbation Method

We perform a perturbation analysis in the limit (50) by using the small parameter ε,

$$\varepsilon \equiv |\alpha'_y| / \overline{M}_N, \qquad \overline{M}_N^2 \ll \varepsilon \ll 1. \tag{58}$$

Equation (58) means that we consider front wrinkles of small amplitude, $|\alpha'_y| = \epsilon \overline{M}_N \ll 1$. For example, the inequality in (58) is verified if we choose $\varepsilon = O(\overline{M}_N)$, $\alpha'_y = O(\overline{M}_N^2)$. In the perturbation analysis we will retain corrections of order ϵ, and neglect correction terms of order $\overline{M}_N^2$. The corrections introduced by the nonlinear terms of the type $u\partial u/\partial x$ may be evaluated from the linear approximation (55),

$$\frac{(u - \overline{u}_N)\partial u/\partial x}{\partial u/\partial t} = O(\varepsilon). \tag{59}$$

According to (54), the pressure waves introduce smaller correction terms, of order $\overline{M}_N^2$. According to (58), they are negligible in the perturbation analysis limited to correction terms of order ε. Therefore, the acoustic waves do not appear in the analysis. The nonlinear terms in pressure and density at the Neumann state coming from (85) lead to even smaller corrections that are negligible. The density variations being of the same order as that at the Neumann state, $\delta\rho/\overline{\rho}_N = O(\delta M_u/\overline{M}_u) = O(\overline{M}_N \alpha'_y)$, they are also negligible. Therefore, the flow is incompressible up to first order corrections in ε.

3.2.1 Isobaric Approximation

To simplify the presentation it is more convenient to anticipate that the pressure variations are also negligible in the analysis limited to the first order correction in ε. This will be easily proved afterwards for simple waves propagating on the shock front. The Euler equations (86)–(88) in Appendix 3, written in the reference frame attached to the flame (90), yield

$$\frac{\partial}{\partial \xi}(u - \dot{\alpha}_t - w\alpha'_y) + \frac{\partial w}{\partial y} = 0, \tag{60}$$

$$\frac{\partial u}{\partial t} + (u - \dot{\alpha}_t - w\alpha'_y)\frac{\partial u}{\partial \xi} + w\frac{\partial u}{\partial y} = 0, \tag{61}$$

$$\frac{\partial w}{\partial t} + (u - \dot{\alpha}_t - w\alpha'_y)\frac{\partial w}{\partial \xi} + w\frac{\partial w}{\partial y} = 0. \tag{62}$$

The boundary conditions are given by (25)–(26),

$$\xi = 0: \qquad (u - \dot{\alpha}_t - w\alpha'_y) = \overline{u}_N, \quad w = w_N = \overline{\mathscr{D}}\alpha'_y, \tag{63}$$

valid up to first order in ε. The terms $(\rho_u/\rho_N)\dot{\alpha}_t$ in (25) and $\delta u_N \alpha'_y$ in (26) have been neglected since, according to (81) in Appendix 1 and $|\dot{\alpha}_t| = \overline{a}_N|\alpha'_y|$, they correspond to corrections of order $\overline{M}_N^2$ in the limit (50) and (58).

Integrating (60) from $\xi = 0$, using the boundary condition (63), yield

$$u(\xi, y, t) = \overline{u}_N + \dot{\alpha}_t(y, t) + w(\xi, y, t)\alpha'_y(y, t) - \int_0^\xi \frac{\partial w}{\partial y} d\xi. \tag{64}$$

Therefore (61) and (62) take the form

$$(\frac{\partial}{\partial t} + \overline{u}_N \frac{\partial}{\partial \xi})u - \frac{\partial u}{\partial \xi}\int_0^\xi \frac{\partial w}{\partial y} d\xi + w\frac{\partial u}{\partial y} = 0, \tag{65}$$

$$(\frac{\partial}{\partial t} + \overline{u}_N \frac{\partial}{\partial \xi})w - \frac{\partial w}{\partial \xi}\int_0^\xi \frac{\partial w}{\partial y} d\xi + w\frac{\partial w}{\partial y} = 0. \tag{66}$$

3.2.2 Compatibility Condition

Without pressure term in (65)–(66), the two unknown functions $u(\xi, y, t)$ and $w(\xi, y, t)$ should satisfied a system of three equations (64)–(66). The solution implies a compatibility condition which leads to an equation for the shock front.

The quadratic terms in (64)–(66) correspond to corrections of order ε. They can be computed from the leading order terms (55)–(56) in which x is replaced by ξ. They are source terms in the equations for the flow, valid up to the first order correction in ε. Equations (61), (62) and (64), then reduce to

$$u(\xi, y, t) = \overline{u}_N + \dot{\alpha}_t(y, t) + \overline{\mathscr{D}}\alpha'_y(y, t)\alpha'_y(y, t - \xi/\overline{u}_N) - \int_0^\xi \frac{\partial w}{\partial y} d\xi \tag{67}$$

$$\frac{\partial u}{\partial t} + \overline{u}_N \frac{\partial u}{\partial \xi} = -\frac{1}{\overline{u}_N}\ddot{\alpha}_{tt}(y, t - \xi/\overline{u}_N)\dot{\alpha}_t(y, t) + \frac{1}{2}\frac{\partial H(y, t - \xi/\overline{u}_N)}{\partial t} \tag{68}$$

$$\frac{\partial w}{\partial t} + \overline{u}_N \frac{\partial w}{\partial \xi} = -\frac{\overline{\mathscr{D}}}{\overline{u}_N}\dot{\alpha}'_{ty}(y, t - \xi/\overline{u}_N)\dot{\alpha}_t(y, t) + \frac{\overline{\mathscr{D}}}{2}\frac{\partial H(y, t - \xi/\overline{u}_N)}{\partial y}, \tag{69}$$

where $H(y,t) \equiv [\dot{\alpha}_t(y,t)]^2/\overline{u}_N - \overline{\mathscr{D}}[\alpha'_y(y,t)]^2$. In the quadratic terms, the function $\alpha(y,t)$ is the leading order solution which satisfies the wave equation $\ddot{\alpha}_{tt} - \overline{a}_N^2\alpha''_{yy} = 0$. Correction terms of order ε are expected to introduce a two-time scale problem. It is convenient to not introduce this formalism too early and to wait Sect. 3.3.3. The method proceeds as follows. An expression of $(\partial u/\partial t + \overline{u}_N \partial u/\partial \xi)$ is obtained from (67) where the last term in the right hand side is computed from (69). Comparison with (68) then leads to the compatibility condition.

3.3 Result for Simple Waves

In the following we will limit the attention to simple waves, $\alpha(y,t) \propto A[(y \pm \overline{a}_N t)/l, \epsilon(a_N/l)t]$, so that, the leading order solution is $\dot{\alpha}_t = \pm\overline{a}_N\alpha'_y$ and the last term in the right hand side of (68) and (69) disappears, $H = 0$.

3.3.1 Isobaric Analysis

An expression of $(\partial u/\partial t + \overline{u}_N \partial u/\partial \xi)$ is obtained from (67)

$$\frac{\partial u}{\partial t} + \overline{u}_N \frac{\partial u}{\partial \xi} = \ddot{\alpha}_{tt}(y,t) + \overline{\mathscr{D}}\dot{\alpha}'_{yt}(y,t)\alpha'_y(y,t-\xi/\overline{u}_N) - (\frac{\partial}{\partial t} + \overline{u}_N \frac{\partial}{\partial \xi}) \int_0^\xi \frac{\partial w}{\partial y} d\xi, \tag{70}$$

where the last term in the right hand side is computed from (69),

$$(\frac{\partial}{\partial t} + \overline{u}_N \frac{\partial}{\partial \xi}) \frac{\partial w}{\partial y} = -\frac{\overline{\mathscr{D}}}{\overline{u}_N} \frac{\partial}{\partial y}[\dot{\alpha}'_{ty}(y,t-\xi/\overline{u}_N)\dot{\alpha}_t(y,t)]$$

$$(\frac{\partial}{\partial t} + \overline{u}_N \frac{\partial}{\partial \xi}) \int_0^\xi \frac{\partial w}{\partial y} d\xi - \overline{u}_N \overline{\mathscr{D}}\alpha''_{yy}(y,t) = -\frac{\overline{\mathscr{D}}}{\overline{u}_N} \frac{\partial}{\partial y} \left[\dot{\alpha}_t(y,t) \int_0^\xi \dot{\alpha}'_{ty}(y,t-\xi/\overline{u}_N) d\xi \right]$$

where the second equation in (63) has been used and where

$$\int_0^\xi \dot{\alpha}'_{ty}(y,t-\xi/\overline{u}_N) d\xi = \overline{u}_N[\alpha'_y(y,t) - \alpha'_y(y,t-\xi/\overline{u}_N)].$$

The last term of (70) may then be written

$$-\overline{u}_N \overline{\mathscr{D}}\alpha''_{yy}(y,t) + \overline{\mathscr{D}} \frac{\partial[\dot{\alpha}_t(y,t)\alpha'_y(y,t) - \dot{\alpha}_t(y,t)\alpha'_y(y,t-\xi/\overline{u}_N)]}{\partial y}. \tag{71}$$

Introducing this result into (70), and comparing the resulting expression with (68) where $\ddot{\alpha}(y,t-\xi/\overline{u}_N)$ in the right hand side is replaced by $\overline{a}_N^2\alpha''_{yy}(y,t-\xi/\overline{u}_N)$, the

terms involving the time through $t-\xi/\overline{u}_N$ cancelled, and the compatibility condition takes the form $G(y,t)=0$ where

$$G(y,t) \equiv \frac{\partial^2\alpha(y,t)}{\partial t^2} - \overline{u}_N\overline{\mathscr{D}}\frac{\partial^2\alpha(y,t)}{\partial y^2} + \overline{\mathscr{D}}\frac{\partial[\dot{\alpha}_t(y,t)\alpha'_y(y,t)]}{\partial y}. \tag{72}$$

The linear part of the compatibility condition corresponds to the linear result (57), since, according to (81) and (84), $\overline{u}_N/\overline{\mathscr{D}} = \overline{M}_N^2 + O(\overline{M}_N^4)$, $\overline{u}_N\overline{\mathscr{D}}/\overline{a}_N^2 = 1 + O(\overline{M}_N^2)$. The nonlinear term is effectively a correction of order ε as it can be checked by using $\dot{\alpha}_t = \pm\overline{a}_N\alpha'_y$ and (58).

3.3.2 Validity of the Isobaric Approximation

The pressure variations which could have been generated by the nonlinear terms of the incompressible flow $\delta p \approx \rho(\delta u)^2 \approx \overline{\rho}_N\overline{a}_N^2\alpha_y'^2$ would introduce correction terms of order ε. Therefore the pressure term should have been retained in principle in the right hand side of (61)–(62) and (68)–(69), even though there is no such small pressure corrections at the Neumann state. Following the same method as above we would have obtained an equation for the pressure of the form,

$$\frac{\partial p}{\partial\xi} + \int_0^\xi \frac{\partial^2 p}{\partial y^2}d\xi' = \overline{\rho}_N G(y,t) \quad \Rightarrow \quad \frac{\partial^2 p}{\partial\xi^2} + \frac{\partial^2 p}{\partial y^2} = 0. \tag{73}$$

The boundary condition $\xi = 0 : p = 0$ (p_N introduces smaller order terms) and the boundedness condition at infinity $\lim_{\xi\to\infty} p$ bounded, implies $p = 0$, and $G(y,t) = 0$. This proves the validity of the isobaric approximation in the weakly nonlinear analysis limited to corrections of order ε.

3.3.3 Burgers Equation

By using the relations

$$\frac{\partial(\dot{\alpha}_t\alpha'_y)}{\partial y} = \dot{\alpha}'_{ty}\alpha'_y + \dot{\alpha}_t\alpha''_{yy} = \frac{1}{2}\frac{\partial\alpha_y'^2}{\partial t} + \frac{1}{\overline{a}_N^2}\dot{\alpha}_t\ddot{\alpha}_{tt} = \frac{1}{2}\frac{\partial}{\partial t}\left[\alpha_y'^2 + \frac{\dot{\alpha}_t^2}{\overline{a}_N^2}\right] = \frac{\partial}{\partial t}\left(\frac{\partial\alpha}{\partial y}\right)^2$$

the compatibility condition $G = 0$ where $G(y,t)$ is defined in (72), takes the form

$$\frac{\partial^2\alpha}{\partial t^2} - \overline{u}_N\overline{\mathscr{D}}\frac{\partial^2\alpha}{\partial y^2} + \overline{\mathscr{D}}\frac{\partial}{\partial t}\left(\frac{\partial\alpha}{\partial y}\right)^2 = 0. \tag{74}$$

For a simple wave, this equation may be analysed by a two-time scale method. Introducing an arbitrary length scale l, for example the wavelength of the initial

wrinkles of the front, one introduces the fast time scale of the simple wave $l/\overline{a}_N$ and the slow time scale $l/(\varepsilon\overline{a}_N)$ for the evolution of the amplitude. One then looks for a solution in the form $\alpha(y,t)/(\varepsilon\overline{M}_N l) = A(\eta,\tau)$, where $\eta = (y+\overline{a}_N t)/l$ and $\tau = \epsilon\overline{a}_N t/l$ and where, according to the ordering in (58), $A = O(1)$. Using the change of variables $\partial/\partial y \to l^{-1}\partial/\partial\eta$, $\partial/\partial t \to (\overline{a}_N/l)(\partial/\partial\eta + \varepsilon\partial/\partial\tau)$, $\partial^2/\partial t^2 \to (\overline{a}_N/l)^2[\partial^2/\partial\eta^2 + 2\varepsilon(\partial/\partial\eta)\partial/\partial\tau + O(\epsilon^2)]$, (74) then reduces to a Burger equation,

$$\frac{\partial A}{\partial\tau} + \frac{1}{2}\left(\frac{\partial A}{\partial\eta}\right)^2 = 0, \tag{75}$$

which is well known to produce a singularity of the derivative $\partial A/\partial\eta$ after a finite time.

4 Conclusion

The results of the present paper are twofold. Firstly, the normal modes of shock fronts in polytropic gases are proved to be neutral with non-radiating acoustic waves. Secondly, it is found that singularities of the slope of the shock front are formed after a finite time, starting from small initial disturbances. These singular points propagate in the transverse direction at the speed of the sound wave in the shocked gas. The results are obtained for strong shocks in the Newtonian limit. They show that the mechanism of formation of the singularities is directly associated with the nonlinearities of the isobaric shear flow induced in the shocked gases by the front wrinkling. For strong shocks, the singularities are resulting from the nonlinear term in the boundary condition (63).

These results also shed light into the mechanism of formation of patterns in cellular detonations. The cellular structure is resulting from the singularities that are spontaneously formed on the lead shock front. They are fed and sustained by a longitudinal oscillatory instability of the wrinkled reaction zone described by Clavin et al. [1,2] and Daou and Clavin [3].

Appendix 1

The nature of the pressure waves (radiating or non-radiating) associated with neutral modes, $S = i\,\Omega$, $\Omega > 1$ depends on the form taken by the dispersion relation (33) when expressed in term of Ω,

$$\text{radiating waves:} \quad l/|k| = \left[\overline{M}_N\Omega - \sqrt{\Omega^2-1}\right]/\sqrt{1-\overline{M}_N^2},$$
$$2\overline{M}_N\Omega\sqrt{\Omega^2-1} = -\Omega^2(1+r) + (1-r)n > 0, \tag{76}$$

$$\text{non-radiating waves:} \quad l/|k| = \left[\overline{M}_N \Omega + \sqrt{\Omega^2 - 1}\right] / \sqrt{1 - \overline{M}_N^2},$$

$$-2\overline{M}_N \Omega \sqrt{\Omega^2 - 1} = -\Omega^2 (1 + r) + (1 - r)n < 0. \tag{77}$$

This depends on the values of the coefficients r and n which control the existence and the nature of the modes. The critical value $r = (n - 1)/(n + 1)$ separating radiating and non-radiating acoustic waves in Fig. 2, corresponds to the $\Omega = 1$ for which the right hand side of (76) and (77) changes sign. In this case, according to (15) and (33), the other mode, if any, is necessarily stable with $S < 0$.

Consider an acoustic wave impinging on the shock from the shocked gas (incoming wave). It is reflected by the shock. The reflected wave (radiating wave) has the same values of k and ω as the incident wave. Following an analysis similar to the linear analysis described above, the complex amplitudes $\tilde{p}_r$ of the reflected wave and of the wrinkles of the shock, $\tilde{\alpha}$, may be calculated in terms of the amplitude of the incident acoustic wave $\tilde{p}_i$,

$$\frac{\tilde{p}_r}{\tilde{p}_i} = -\frac{\left[2\overline{M}_N \Omega \sqrt{\Omega^2 - 1} - \Omega^2 (1 + r) + (1 - r)n\right]}{\left[-2\overline{M}_N \Omega \sqrt{\Omega^2 - 1} - \Omega^2 (1 + r) + (1 - r)n\right]}$$

$$\frac{|k|\tilde{\alpha}(\overline{\rho}_N - \rho_u)/\overline{\rho}_N}{2(1 - r)\left(\tilde{p}_i/\overline{\rho}_N \overline{a}_N^2\right)} = \frac{-i\sqrt{\Omega^2 - 1}/\sqrt{1 - \overline{M}_N^2}}{\left[-2\overline{M}_N \Omega \sqrt{\Omega^2 - 1} - \Omega^2 (1 + r) + (1 - r)n\right]}.$$

This shows that the response of the shock diverges when one of its normal mode is radiating. This occurs when the reflected wave matches the radiating eigenmode. This is why a shock is considered as unstable when one of its eigenmode is radiating, and stable in the opposite case. Shock waves in a polytropic gas are thus stable in that sense, see Sect. 2.6.2.

Appendix 2

Denoting $\mathscr{D}$ and u_N the velocity of a plane shock wave and the flow velocity of the shocked material, relative to the shock, mass conservation yields

$$m \equiv \rho_u \mathscr{D} = \rho_N u_N, \tag{78}$$

where the subscripts u and N denote the initial state of the material and the Neumann state of the shocked material, just behind the shock. Equation for the momentum conservation in the normal direction, $p_u + m^2/\rho_u = p_N + m^2/\rho_N$, yields

$$p_N - p_u = -m^2 \left(\frac{1}{\rho_N} - \frac{1}{\rho_u} \right). \tag{79}$$

Using (78), $\mathscr{D}^2 = m^2/\rho_u$, $u_N^2 = m^2/\rho_N$, and introducing the enthalpy, $h = e_T + p/\rho$, where e_T is the internal energy, conservation of energy across the shock takes the following form,

$$h_u - h_N = \frac{m^2}{2} \left(\frac{1}{\rho_N^2} - \frac{1}{\rho_u^2} \right).$$

Eliminating m by using (79), we got the Rankine–Hugoniot condition linking the density and the pressure

$$h(\rho_u, p_u) - h(\rho_N, p_N) + \frac{1}{2} \left(\frac{1}{\rho_u} + \frac{1}{\rho_N} \right) (p_N - p_u) = 0, \tag{80}$$

where the function $h(\rho, p)$ is given by the thermodynamics of the material.

For polytropic gases the Rankine–Hugoniot relations take the form

$$\frac{u_N}{\mathscr{D}} = \frac{\rho_u}{\rho_N} = \frac{(\gamma-1)M_u^2 + 2}{(\gamma+1)M_u^2}, \tag{81}$$

$$\frac{p_N}{p_u} = \frac{2\gamma M_u^2 - (\gamma-1)}{(\gamma+1)}, \tag{82}$$

$$\frac{T_N}{T_u} = \frac{[2\gamma M_u^2 - (\gamma-1)][(\gamma-1)M_u^2 + 2]}{(\gamma+1)^2 M_u^2}, \tag{83}$$

$$M_N^2 = \frac{(\gamma-1)M_u^2 + 2}{2\gamma M_u^2 - (\gamma-1)}, \tag{84}$$

where $M_u \equiv \mathscr{D}/a_u > 1$ is the propagation Mach number of the shock wave and $\gamma \equiv c_p/c_v > 1$ is the ratio of specific heats. Density, pressure and temperature at the Neumann state of wrinkled shocks are obtained from (81)–(84) by replacing M_u by the Mach number of the normal propagation velocity

$$M_u \to \frac{\mathscr{D} - \dot{\alpha}_t}{a_u \sqrt{1 + {\alpha'_y}^2}}, \qquad M_u^2 \to \frac{\mathscr{D}^2 - 2\mathscr{D}\dot{\alpha}_t + \dot{\alpha}_t^2}{a_u^2 (1 + {\alpha'_y}^2)}, \tag{85}$$

where $\dot{\alpha}_t \equiv \partial\alpha(y,t)/\partial t$ and $\alpha'_y \equiv \partial\alpha(y,t)/\partial y$.

Appendix 3

Written in 2-D geometry, the Euler equations take the form

$$\frac{1}{\rho}\frac{D}{Dt}\rho + \frac{\partial}{\partial x}u + \frac{\partial}{\partial y}w = 0, \tag{86}$$

$$\rho\frac{D}{Dt}u = -\frac{\partial}{\partial x}p, \qquad \rho\frac{D}{Dt}w = -\frac{\partial}{\partial y}p, \tag{87}$$

$$\frac{D}{Dt}s = 0, \tag{88}$$

where $s(\rho, p)$ is the entropy, and

$$\frac{D}{Dt} = \frac{\partial}{\partial t} + u\frac{\partial}{\partial x} + w\frac{\partial}{\partial y}. \tag{89}$$

Written in the reference frame attached to the front (ξ, y, t) where $\xi \equiv x - \alpha(y, t)$, the Euler equation takes the same form as (86)–(88) but with

$$\frac{D}{Dt} \to \frac{\partial}{\partial t} + (u - \dot{\alpha}_t - \alpha'_y w)\frac{\partial}{\partial \xi} + w\frac{\partial}{\partial y}, \qquad \frac{\partial}{\partial y} \to \frac{\partial}{\partial y} - \alpha'_y\frac{\partial}{\partial \xi}, \qquad \frac{\partial}{\partial x} \to \frac{\partial}{\partial \xi}. \tag{90}$$

References

1. Clavin, P., Denet, B.: Diamond patterns in the cellular front of an overdriven detonation. Phys. Rev. Lett. **88**, 044502, 1–4 (2002)
2. Clavin, P., He, L., Williams, F.A.: Multidimensional stability analysis of overdriven gaseous detonations. Phys. Fluids **9**, 3764–3785 (1997)
3. Daou, R., Clavin, P.: Instability threshold of gaseous detonations. J. Fluid Mech. **482**, 181–206 (2003)
4. Lapworth, K.: An experimental investigation of the stability of plana shock waves. J. Fluid Mech. **6**, 469–480 (1959)
5. Briscoe, M., Kovitz, A.: Experimental and theoretical study of the stability of plane shock waves reflected normally from perturbed flat walls. J. Fluid Mech. **31**, 529–546 (1968)
6. Van-Moorhem, K., George, A.: On the stability of plane shock. J. Fluid Mech. **68**, 97–108 (1975)
7. DYakov, S.P.: The stabiliy of shockwaves: investigation of the problem of stability of shock waves in arbritary media. Zh. Eksp. Teor. Fiz. **27**, 288 (1954)
8. Kontorovich, V.M.: Concerning the stability of shock waves. Zh. Eksp. Teor. Fiz. **33**, 1525 (1957)
9. Majda, A., Rosales, R.: A theory of spontaneous mach stem formation in reacting shock fronts, I. The basic perturbation analysis. SIAM J. Appl. Math. **43**, 1310–1333 (1983)
10. Rosales, R.: Stability theory for shocks in reacting media: mach stems in detonation waves. Lect. Appl. Math. **24**, 431–465 (1986)

11. Short, M., Stewart, D.S.: Cellular detonation stability. Part 1. A normal-mode linear analysis. J. Fluid Mech. **368**, 229–262 (1998)
12. Buckmaster, J.D., Ludford, G.S.S.: The effect of structure on stability of detonations. I role of the induction zone. In: Twenty-First Symposium (International) on Combustion, vol. 28, p. 1669, Combustion Institute, New York (1988)
13. Landau, L., Lifchitz, E.: Mécanique des fluides, 2nd edn. Mir, Moscow (1989)
14. Fickett, W., Davis, W.C.: Detonation. University of California Press, Berkeley (1979)

Cavity Solitons

L.A. Lugiato, F. Prati, M. Brambilla, L. Columbo, S. Barland, G. Tissoni, K.M. Aghdami, R. Kheradmand, H. Tajalli, and H. Vahed

1 Introduction

It is a pleasure to contribute this talk to the Festschrift celebrating the 70th birthday of Professor Manuel G(arcía) Velarde. One of us (LAL) is proud for a long lasting friendship with him which started when they met for the first time in a conference on statistical mechanics in Chicago in 1970. Around 1980, they had an intense scientific exchange concerning the analogy between the convective instability in a

L.A. Lugiato (✉) · F. Prati
CNISM and Dipartimento di Scienza ed Alta Tecnologia, Università dell'Insubria,
Via Valleggio 11, Como 22100, Italy
e-mail: luigi.lugiato@uninsubria.it

M. Brambilla
CNISM and Dipartimento Interateneo di Fisica, Università e Politecnico di Bari,
Via Amendola 173, 70123 Bari, Italy

L. Columbo
Dipartimento di Scienza ed Alta Tecnologia, Università dell'Insubria,
Via Valleggio 11, 22100 Como, Italy

CNR-IFN Istituto di Fotonica e Nanotecnologie, Dipartimento Interateneo di Fisica,
Università degli Studi di Bari, Via Amendola 173, 70123 Bari, Italy

S. Barland · G. Tissoni
Institut Non Lineaire de Nice Sophia Antipolis, 1361 Route des Lucioles,
Valbonne 06560, France

K.M. Aghdami
Physics Department, Payame Noor University, Mini City, Tehran 19569, Iran

R. Kheradmand
Photonics Group, Research Institute for Applied Physics and Astronomy, University of Tabriz,
Tabriz, Iran

H. Tajalli · H. Vahed
Faculty of Physics, University of Tabriz, Tabriz, Iran

R.G. Rubio et al. (eds.), *Without Bounds: A Scientific Canvas of Nonlinearity and Complex Dynamics*, Understanding Complex Systems,
DOI 10.1007/978-3-642-34070-3_33,

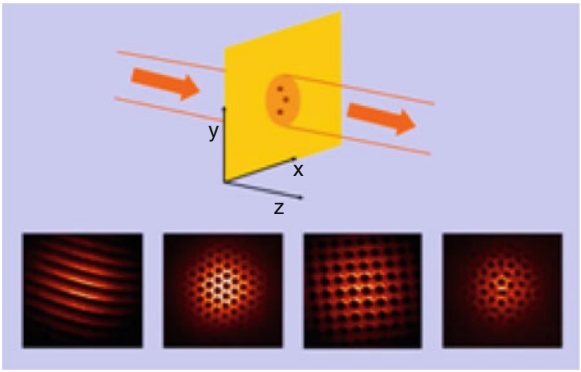

Fig. 1 The *upper part* of the figure illustrates the concept of optical pattern formation. The *lower part* shows some examples of optical patterns observed experimentally [5]

two-component liquid layer heated from below and the laser with saturable absorber [1]. Manuel and his collaborators provided very important contributions to this topic [2–4]. Later we met several times in international conferences and especially in the meetings in Brussels of the Physics Panel of the Human Capital and Mobility Programme of the European Community.

In this chapter, we present a brief outline of the topic of cavity solitons, which since more than a decade is attracting the attention of the nonlinear optics community. In order to do that, we start from the general area of optical pattern formation (Fig. 1). Let us consider a coherent laser beam with large section which propagates in the direction z. Usually the beam intensity varies slowly in the transverse directions x and y, so that the intensity distribution is close to homogeneous. However under appropriate conditions, when the beam interacts with a nonlinear medium, the interplay of nonlinearity and diffraction of radiation makes a spatial structure emerge in the beam profile. The physical principles of optical pattern formation are illustrated, for example, in [6]. The lower frames in Fig. 1 show examples of spatial patterns observed in sodium vapour [5].

In the typical optical patterns, the elements of the pattern are strongly correlated to one another (global structures). Under special conditions, however, one can form independent, isolated intensity peaks (localized structures) called cavity solitons (CS). Overviews of the subject of CS can be found in [7–9].

2 The Main Properties of Cavity Solitons

Cavity solitons are usually produced by means of optical resonators containing nonlinear materials (see Fig. 2). The energy is provided to the system by a broad-area coherent and stationary holding beam which is injected into the cavity and, in the case of semiconductor amplifiers, also by an electric current. The device is operated under parametric conditions such that the output is basically uniform. However, by injecting a localized laser pulse (writing beam), one can write a CS

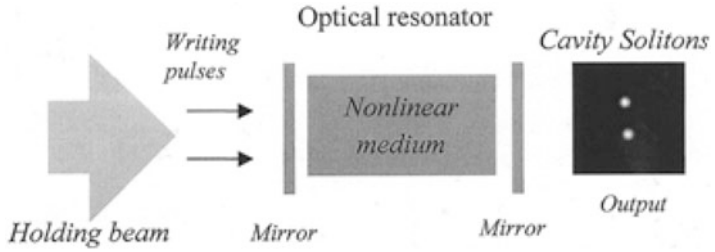

Fig. 2 A coherent, stationary, quasiplane-wave holding field drives an optical cavity containing a nonlinear medium. The injection of narrow laser pulses creates persistent localized intensity peaks in the output (cavity solitons)

where the pulse passes. It is very important that the CS persists even after the pulse, until the holding beam is kept on. In this way, by injection of several pulses one can write a number of CSs. They can be subsequently erased by again injecting pulses in the locations: where CSs lie; in most cases, the erasing pulses must be coherent and out of phase by π with respect to the writing pulse.

What are the differences between cavity solitons and standard spatial solitons? The basic difference is that spatial solitons arise in propagation in conservative Hamiltonian systems, whereas CSs are dissipative. For example, they appear in the framework of a model which is paradigmatic for optical pattern formation [10]:

$$i\frac{\partial E}{\partial t} + |E|^2 E + iE + \nabla^2 E - iE_I = 0, \quad \nabla^2 = \frac{\partial^2}{\partial x^2} + \frac{\partial^2}{\partial y^2}. \tag{1}$$

This model is equivalent to a nonlinear Schroedinger equation which includes a damping term (iE) and a driving term (iE_I). The dissipative term describes the escape of photons from the cavity, the driving term describes the electric field injected into the cavity (holding beam + writing beam). The variable E denotes the normalized intracavity electric field and the transverse Laplacian describes diffraction in the paraxial approximation.

Cavity solitons are rigid, in the sense that, once the values of the parameters of the system have been fixed, their characteristics (height, radius) are fixed. This is not the case for standard spatial solitons. Figure 3 illustrates the typical scenario for cavity solitons. The diagram shows the steady-state curve of the intracavity field as a function of the input field, for the stationary solutions which are homogeneous in the transverse plane (x, y). The curve is S-shaped, so that in principle there is bistability, however all the dotted part of the curve with positive slope is unstable against the spontaneous formation of a spatial pattern such as a roll pattern or a honeycomb pattern. In an appropriate range of values of the input field there is the possibility of forming cavity solitons.

The interest in the subject of cavity solitons was notably enhanced by their realization in semiconductor microresonators [11], because the miniaturization and the fast response of the material are promising in view of practical applications. The experiment used a broad-area driven vertical-cavity semiconductor microlaser

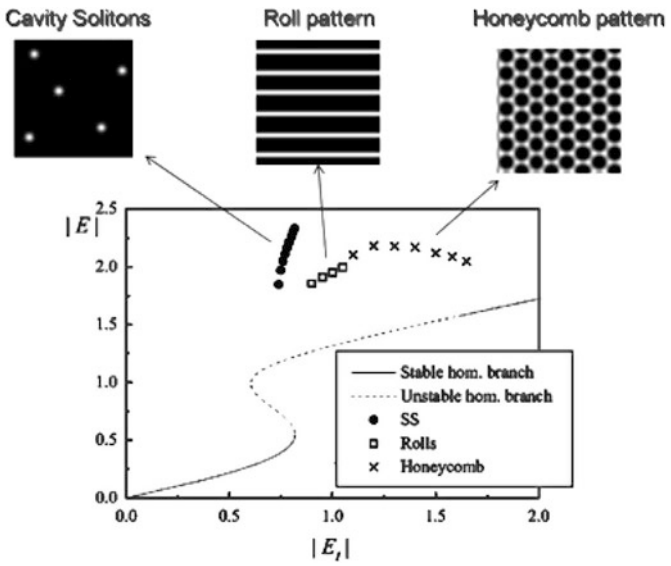

Fig. 3 Steady-state curve of intracavity field vs. input field for the homogeneous stationary solutions. In appropriate ranges of the input field one has the formation of a honeycomb pattern (*crosses*) or a roll pattern (*squares*) or cavity solitons (*circles*, the position of the *circle* indicates the value of the peak height of the CS). The three structures are shown in the upper frames (from *right* to *left*: honeycomb, roll, cavity solitons)

slightly below threshold. Two CSs were first written with the help of a writing beam and subsequently erased by flipping the phase of the writing beam by π. This result demonstrated the possibility of using CSs as pixels of information.

An extremely important property of cavity solitons is their plasticity, because they can be put in motion when they are in presence of phase or amplitude gradients in the holding beam. Usually the motion is counter gradient, for example in the case of a modulated phase profile each CS moves to the nearest local maximum of the phase landscape. As a consequence one has the possibility of realizing reconfigurable arrays of cavity solitons, Fig. 4 illustrates the theoretical simulation and the experimental realization of this phenomenon [12].

When in the device there is a defect, typically in the Bragg reflectors of the microlaser, at the position of the defect there is the spontaneous generation of a cavity soliton. A very interesting situation arises when the holding beam presents a phase gradient. This circumstance tends to set the CS in motion, so that the CS is detached from the defect and starts its motion. Once the CS is detached, the defect generates spontaneously another cavity soliton, which is then in turn detached and moves away. In this manner, the system generates spontaneously a sequence of CSs which travel, in an ordered line and at regular intervals, in the direction of the phase gradient. A numerical simulation of this effect, which has been also observed experimentally, is shown in Fig. 5 [13]. We have called this phenomenon "cavity

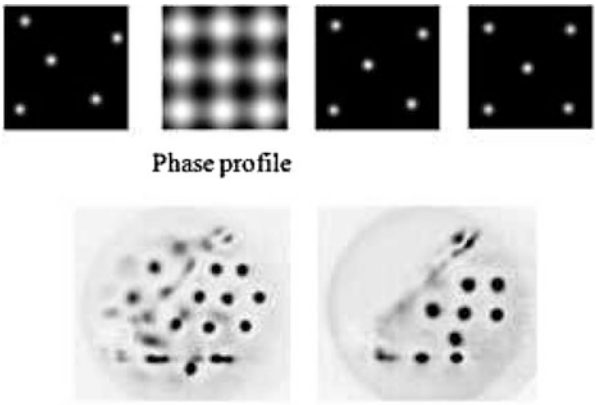

Fig. 4 *Upper row*: The leftmost frame shows the initial position of five cavity solitons, the second frame shows the phase profile of the holding beam, where the white spots correspond to the local maxima. The CSs move towards the nearest local maxima of the phase profile (third and fourth frames from the left). *Lower row*: Experimental realization of arrays of cavity solitons as reported in Ref. 11

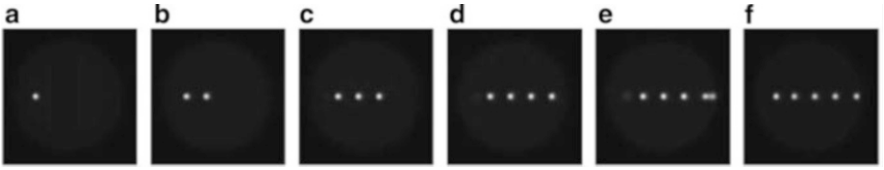

Fig. 5 Cavity soliton tap. Sequence of snapshots showing the spatiotemporal dynamics of drifting CSs in the transverse section of the device in presence of a defect. Intensity increases from *black* to *white*. The position of the defect corresponds to the high-intensity structure visible in the *first panel* and the phase gradient is directed rightwards

soliton tap", because it is similar to the case of a tap which is not completely closed so that a droplet of water hangs from it, then the gravity force makes it fall, then another droplet forms, which falls in turn, and so again and again.

In this case, if one injects the writing beam into the defect, the flux of CSs stops. Therefore, by repeatedly injecting the writing beam into the defect, one can set into motion a certain number of CSs, then stop the flux, put into motion some other CSs at will, then stop, and so on. In this way one can generate a controlled sequence of 1 and 0 which travel in the transverse plane with a velocity on the order of some kilometers per second. This principle is illustrated in Fig. 6.

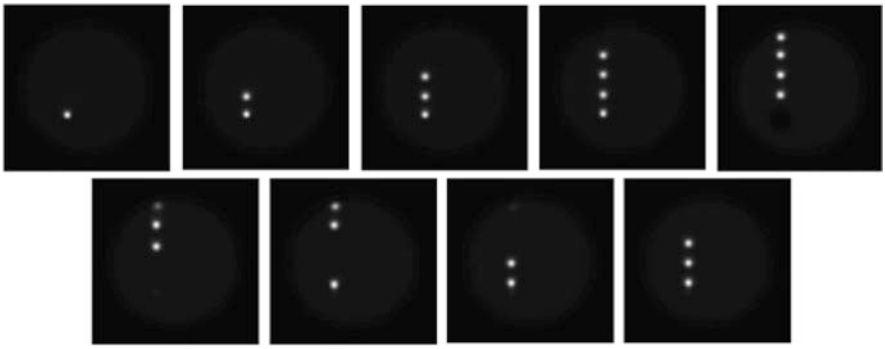

Fig. 6 Sequence of snapshots illustrating different stages of continuous creation and inhibition of CSs. The defect position corresponds to the CS in the first frame and the phase gradient is directed upwards. The injection of the writing beam starts just before frame 5 and stops after frame 6. From *left* to *right*, the frames are taken every 12 ns, starting at the fourth ns (4, 16, 28, 40, 52, 64, 76, 88, 100 ns)

3 Cavity Soliton Laser and Cavity Soliton Billiard

A considerable simplifying step was the realization of a cavity soliton laser (CSL), a device able to emit CSs even in absence of an external holding beam, so that the CSs can be seen as self-assembled microlasers existing on a dark, nonlasing background (see Fig. 7). Three types of CSL have been recently realized that have a vertical-cavity surface-emitting laser (VCSEL) as the basic element: a VCSEL with frequency selective feedback [14], two coupled VCSELs in a face-to-face configuration [15], and a monolithic VCSEL with a saturable stage integrated in the cavity [16].

The possibility of realizing a cavity soliton laser using a laser with saturable absorber was first theoretically predicted by Rosanov and his collaborators [17]. Subsequently our group analyzed a model adequate to describe a VCSEL and analyzed theoretically the behavior of a CSL of the kind realized in [16]. The dynamical equations are [18, 19]

$$\dot{F} = \left[(1 - i\alpha)\, D + (1 - i\beta)\, d - 1 + i\nabla^2\right] F, \tag{2}$$

$$\dot{D} = b_1 \left[\mu - D\left(1 + |F|^2\right) - BD^2\right], \tag{3}$$

$$d = b_2 \left[-\gamma - d\left(1 + s\,|F|^2\right) - Bd^2\right]. \tag{4}$$

The amplifying part of the device is described by the population variable D, the linewidth enhancement factor α, the pump parameter μ, and the carrier decay rate b_1; the corresponding variables and parameters for the absorber are d, β, γ,

Fig. 7 A cavity soliton laser emits a set of narrow beams (CSs), the number and position of which can be controlled. The *righthand* figure shows the shape of a CS in a cavity soliton laser

and b_2; F is the slowly varying amplitude of the electric field. The parameter s is the ratio of the saturation intensity of the amplifier to that of the absorber; the same coefficient of radiative recombination B is assumed for the two materials. Time is scaled to the photon lifetime (typically 4 ps), and space to the diffraction length (typically 4 μm). The effects of spontaneous emission noise are simulated by adding to (2) stochastic terms in the form of Gaussian white noise sources with zero mean and unit variance, uncorrelated in both time and space.

A very important point is that, since the CS arises from the interaction of light with the semiconductor, it is a composite structure which appears not only in the electric field, but also in the carrier density N of the amplifier and in the carrier density n of the absorber, which are linked in a simple way to the population variables D and d, respectively. Figure 8 shows the cavity soliton in its three distinct components which coexist.

This composite structure of the CS occurs not only in a CSL, but in any system which generates cavity solitons. Usually this composite structure is overlooked because one emphasizes the field aspects only.

Very remarkable is that, in appropriate ranges of the parameters in play, cavity solitons become self-propelled, i.e. they move spontaneously, in absence of any gradient. The motion is caused by a dynamical instability and, in absence of defects in the material, is along a straight line in a random direction and with constant velocity [20, 21].

Since the trajectory of the moving soliton bends in presence of pump boundaries, if we consider a square pump profile we realize a cavity soliton billiard. In [22] we show that the CS is reflected when it impinges the boundary and, at regime, the sum of incidence and reflection angles is 90° and the CS may cover two trajectories, one clockwise and the other counterclockwise, as shown in Fig. 9. The resulting scenario is similar to that exhibited by walking droplets in a vibrated liquid bath [23, 24].

On the other hand, in presence of defects, which act as scatterers for the CS, the trajectory may become open and may cover ergodically the entire available square section [22]. If one has just one scatterer located at an intersection of

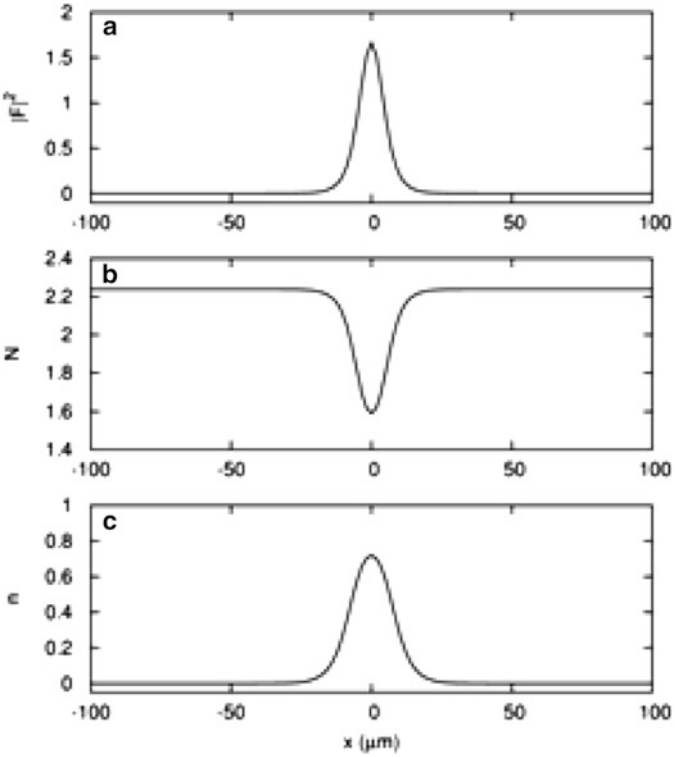

Fig. 8 The figure shows a cavity soliton in a CSL with saturable absorber, with its coexisting components in (**a**) the electric field, (**b**) the carrier density in the amplifier, in which one has a dark soliton, and (**c**) the carrier density in the absorber, in which one has a bright soliton exactly as in the electric field. The carrier densities are normalized to their transparency values

Fig. 9 (*Color online*) *Closed square* orbits of the CS. The *arrows* indicate the direction of motion of the CS. The width of the pumped region is 75 μm and the width of the integration grid is 100 μm

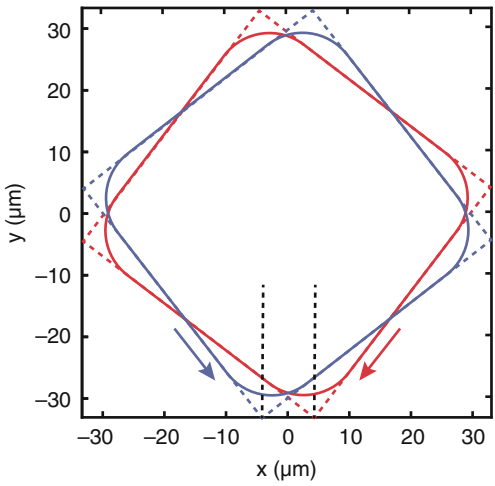

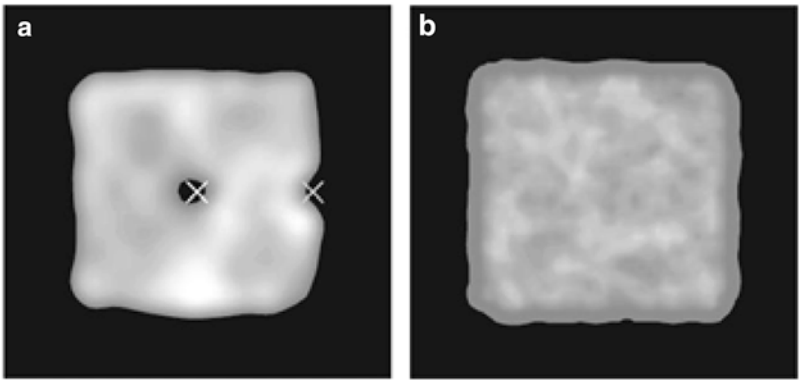

Fig. 10 (**a**) Time-averaged intensity when the CS moves in the presence of two scatterers, represented by the *white crosses*. (**b**) Time averaged intensity produced by three interacting CSs. Here the width of the pumped region is (about 188 μm). In both figures the average is over $2 \cdot 10^6$ time units

the two closed orbits it is not enough to obtain an open trajectory, because the trajectory leaves the forbidden square orbits but it ends on the other stable orbit which lies along one diagonal of the square. The desired open orbit can be realized only by putting a second scatterer in the center of the square, in such a way that the orbits on the two diagonals are also forbidden. The averaged output in the presence of the two scatterers is shown in Fig. 10a. Another method to make closed orbits unstable consists in switching on more CSs in the device. In this way the CSs interact nondestructively for at least $2 \cdot 10^6$ photon lifetimes (about 8 μs), as our computational power allowed. When two CSs are present, they can still move on periodic closed orbits, but when there are three CSs, their mutual interaction leads to open trajectories, and the average intensity profile over long times produced by the three moving CSs is substantially uniform as shown in Fig. 10b.

In the case shown by Fig. 10a, the existence of defects (scatterers) in the material is revealed by the average motion of the CS, so that the device works as a *soliton force microscope* based on the spontaneous motion of the CS. A soliton force microscope has been realized experimentally not in a cavity soliton laser, but in a device which operates with a holding beam. The CS explores the section of the device under the action of gradients in the holding beam profile, revealing the presence of defects [25]. The use of a cavity soliton laser, with the result shown in Fig. 10, paves the way to the realization of a much simpler and compact soliton force microscope.

Acknowledgement We acknowledge support from the Italian Ministry of Research (MIUR) through the Futuro in Ricerca FIRB Project PHOCOS-RBFR08E7VA.

References

1. Degiorgio, V., Lugiato, L.A.: Phys. Lett. A **77**, 167 (1980)
2. Antoranz, J.C., Velarde, M.G.: Phys. Lett. A **80**, 220 (1980); J. Stat. Phys. **24**, 235 (1981)
3. Antoranz, J.C., Gea, J., Velarde, M.G.: Phys. Rev. Lett. **47**, 1895 (1981)
4. Antoranz, J.C., Bonilla, L.L., Gea, J., Velarde, M.G.: Phys. Rev. Lett. **49**, 35 (1982)
5. Lange, W., Logvin, Yu., Ackemann, Th.: Physica D **96**, 230 (1996)
6. Lugiato, L.A., Brambilla, M., Gatti, A.: Optical pattern formation. In: Advances in Atomic, Molecular and Optical Physics, vol. 40, p. 229 ff. Academic, New York (1999)
7. Lugiato, L.A.: J. Quant. Electron. **39**, 193 (2003)
8. Lugiato, L.A., Prati, F., Tissoni, G., Brambilla, M., Barland, S., Giudici, M., Tredicce, J.: Cavity solitons in semiconductor devices. In: Akhmediev, N., Ankiewicz, A. (eds.) Dissipative Solitons: From Optics to Biology and Medicine. Lecture Notes in Physics, vol. 751, pp. 51–92. Springer, Berlin (2008)
9. Ackemann, T., Firth, W.J., Oppo, G.L.: Advances in Atomic, Molecular and Optical Systems, vol. 57, p. 323 ff. Academic, New York (2009)
10. Lugiato, L.A., Lefever, R.: Phys. Rev. Lett. **58**, 2209 (1987)
11. Barland, S., Tredicce, J.R., Brambilla, M., Lugiato, L.A., Balle, S., Giudici, M., Maggipinto, T., Spinelli, L., Tissoni, G., Knoedl, T., Miller, M., Jaeger, R.: Nature **419**, 699–702 (2002)
12. Pedaci, F., Genevet, P., Barland, S., Giudici, M., Tredicce, J.R.: Appl. Phys. Lett. **89**, 221111 (2006)
13. Caboche, E., Barland, S., Giudici, M., Tredicce, J.R., Tissoni, G., Lugiato, L.A.: Phys. Rev. A **80**, 053814 (2009)
14. Tanguy, Y., Ackemann, T., Firth, W.J.: R. Jäger, Phys. Rev. Lett. **100**, 013907 (2008)
15. Genevet, P., Barland, S., Giudici, M., Tredicce, J.R.: Phys. Rev. Lett. **101**, 123905 (2008)
16. Elsass, T., Gauthron, K., Beaudoin, G., Sagnes, I., Kuszelewicz, R., Barbay, S.: Appl. Phys. B **98**, 327 (2010)
17. Federov, S.V., Vladimirov, A.G., Khodova, G.V., Rosanov, N.N.: Phys. Rev. E **61**, 5814 (2000)
18. Bache, M., Prati, F., Tissoni, G., Kheradmand, R., Lugiato, L.A., Protsenko, I., Brambilla, M.: Appl. Phys. B **81**, 913 (2005)
19. Prati, F., Caccia, P., Tissoni, G., Lugiato, L.A., Aghdami, K.M., Tajalli, H.: Appl. Phys. B **88**, 405 (2007)
20. Fedorov, S.V., Rozanov, N.N., Shatsev, N.A.: Opt. Spectrosc. **102**, 449 (2007)
21. Prati, F., Tissoni, G., Lugiato, L.A., Aghdami, K.M., Brambilla, M.: Eur. Phys. J. D **59**, 73 (2010)
22. Prati, F., Lugiato, L.A., Tissoni, G., Brambilla, M.: Phys. Rev. A **84**, 053852 (2011)
23. Couder, Y., Protiere, S., Fort, E., Boudaoud, A.: Nature **437**, 208 (2005)
24. Eddi, A., Fort, E., Moisy, F., Couder, Y.: Phys. Rev. Lett. **102**, 240401 (2009)
25. Pedaci, F., Tissoni, G., Barland, S., Giudici, M., Tredicce, J.R.: Appl. Phys. Lett. **93**, 111104 (2008)

Three-Wave Backward Optical Solitons

C. Montes, P. Aschieri, A. Picozzi, C. Durniak, and M. Taki

1 Introduction

In nonlinear wave systems, resonance processes may give rise to solitary waves resulting from energy exchanges between dispersionless waves of different velocities. Three-wave resonant interaction in nonlinear optical systems [1], plasmas [2, 3] and gases [4] predict symbiotic three-wave solitary waves in analogy to self-induced transparency [5, 6]. The structure of them is determined by a balance between the energy exchanges rates and the velocity mismatch between the three interacting waves. The three-wave interaction problem has been the object of many theoretical studies and numerical simulations as we referred in [7, 8]. The non-conservative problem in the presence of a continuous pump has been integrated by the inverse scattering transform (IST) in the non-dissipative case [6], giving rise to backscattered solitons. Our interest has been to study this non-conservative problem in the presence of dissipation or cavity losses, because this kind of backward structuration has been experimentally obtained in stimulated Brillouin scattering of a c.w. pump wave into a backward red-shifted Stokes wave in long fiber-ring cavities. It has been shown in a Brillouin fiber-ring cavity that, spontaneous structuration of dissipative three-wave solitary waves takes place when the source is a c.w. pump [9–12]. The periodic round-trip interaction in a long lossy cavity may be associated to the non-conservative unlimited interaction [8, 11]. The nonlinear space-time

C. Montes (✉) · P. Aschieri
CNRS, Laboratoire de Physique de la Matière Condensée, Université de Nice - Sophia Antipolis, 06108 Nice Cedex 2, France
e-mail: carlos.montes@unice.fr

A. Picozzi
CNRS, Institut Carnot de Bourgogne, 21078 Dijon Cedex, France

C. Durniak · M. Taki
Laboratoire de Physique des Lasers, Atomes et Molecules, Université des Sciences et Technologies de Lille, 59655 Villeneuve d'Asq Cedex, France

R.G. Rubio et al. (eds.), *Without Bounds: A Scientific Canvas of Nonlinearity and Complex Dynamics*, Understanding Complex Systems,
DOI 10.1007/978-3-642-34070-3_34, © Springer-Verlag Berlin Heidelberg 2013

three-wave resonant model between the two optical waves and the dissipative material acoustic wave satisfactorily explains the generation and the dynamics of the backward-traveling solitary pulses in the fiber-ring cavities. Stability analysis of the inhomogeneous stationary Brillouin mirror solution in the c.w.-pumped cavity [10] exhibits a one-parameter Hopf bifurcation. Below a critical feedback, a time-dependent oscillatory regime occurs, and self-organization of a localized pulsed regime takes place. Experimental results and dynamical simulations confirm this scenario. A stable continuous family of super-luminous and sub-luminous backward-traveling dissipative solitary pulses is obtained through a single control parameter [11, 12]. A parallel analysis in an unbounded one-dimensional medium shows that the integrable three-wave super-luminous symmetrical soliton is unstable for small dissipation, and that it cascades to a turbulent multi-peak structure. The general non-symmetrical and non-integrable case is dependent only on the exponential slope of the wave front of the backscattered Stokes wave, thus providing the stable super- and sub-luminous dissipative solitary attractors [8]. An overview of the experimental results for a large set of input pump powers and Stokes feedback conditions shows a remarkable agreement with the numerical simulations of the three-wave coherent partial differential equations model [12]. We will not consider this topic here and refer the reader to a recent review article [13] where this kind of dissipative soliton has been discussed in details.

This review article is devoted to the resonant interaction of three optical waves (called pump, signal and idler) in a nonlinear quadratic material. The same mechanism, responsible for nanosecond solitary wave morphogenesis in the Brillouin-fiber-ring laser may act for picosecond backward pulse generation in a quasi-phase matched (QPM) optical parametric oscillator (OPO) [14–19]. The dissipative character will rise from the partial reinjection of one wave (in the singly resonant OPO), two waves (in the doubly resonant OPO) or to the absorption losses in a backward mirrorless OPO. The resonant condition for the wave vectors is automatically satisfied in stimulated Brillouin backscattering when the fiber ring laser contains a large number of longitudinal modes beneath the Brillouin gain curve. However, in order to achieve counter-streaming QPM matching between the three optical waves in the $\chi^{(2)}$ medium, a nonlinear susceptibility inversion grating of sub-μm period is required [20–23]. In the non-degenerate three-wave case of a backward quasi-phase matching configuration in the quadratic media where both signal and idler fields propagate backward with respect to the direction of the pump field, the first order quasi-phase-matching pitch is of order $\lambda_p/2n_p$ where n_p is the refractive index at the pump wavelength λ_p. This can be achieved for example by periodic poling techniques but up to now the polarization inverted grating of sub-μm period has been only obtained for the backward idler configuration in a $KTiOPO_4$ crystal which allows the realization of a mirrorless optical parametric oscillator (MOPO) [24] with remarkable spectral properties [25, 26]. Therefore, higher-order Bragg condition have been suggested [22]. However, the interest of the first order configuration is that the solitary waves can be spontaneously generated from noise by a c.w. pump when the quadratic material is placed inside a singly resonant OPO (where singly stands here for only one wave reinjection).

Parametric interaction of counter-propagating signal and idler waves has the unique property of automatically establishing distributed feedback without external mirrors and thus realizing sources of coherent and tunable radiation. A recent experimental demonstration of such a mirrorless optical parametric oscillator (MOPO) has been performed in a 800 nm periodically poled $KTiOPO_4$ (PPKTP) configuration [24] with a pulse pump. The forward oscillator signal is essentially a wavelength-shifted replica of the pump spectrum, and the backward generated idler pulse has a bandwidth of two orders of magnitude narrower than that of the pump [25, 26]. This sub-μm periodic configuration where QPM is achieved with a pump and signal waves propagating in the forward direction and the idler wave in the backward direction (cf. Fig. 1b) opens the way for achieving the shorter periodicity required for a QPM configuration where both signal and idler backward propagate with respect to the pump wave (cf. Fig. 1d). As we say, this doubly-backward configuration is of interest since the three-wave symbiotic solitary waves can be generated from noise in the presence of a c.w. pump when the quadratic material is placed inside an optical parametric oscillator [14–19]. With a c.w. pump the singly backward OPO yields stationarity for the backward wave. Nevertheless when the pump is a pulse, the demonstrated MOPO experimental configuration generates a coherent backward pulse in the absence of external feedback. Note that stationarity of the singly backward configuration in a c.w. pumped short length device is not contradictory with the theoretical existence of backward solitary solutions when the initial condition is localized [6]. Moreover, a coherent solitary structure can be sustained from a highly incoherent pump and a co-propagating wave [27]. This phenomenon relies on the advection between the interacting waves and leads to the formation of a novel type of three-wave parametric soliton composed of both coherent and incoherent fields. In Sect. 5 we will consider this mechanism by proposing the generation of a coherent backward pulse from an incoherent pump pulse in two BMOPO configurations, among which the first one refers to the experimental configuration demonstrated in [24–26].

We thus show that the BMOPO system is characterized, as a general rule, by the generation of a highly coherent backward field, despite the high degree of incoherence of the pump field. In substance, the incoherence of the pump is shown to be transferred to the co-moving field, which thus allows the backward field to evolve towards a highly coherent state. The incoherent pump in the BMOPO dynamics is numerically simulated with a new numerical scheme that solves the coupled wave equations in the counterpropagating configuration in the presence of group-velocity dispersion (GVD) by combining the trajectories method for the nonlinear three-wave interaction and fast Fourier transformation (FFT) to account for the GVD effects. We propose realistic experimental conditions that may be implemented with currently available technology and in which backward coherent wave generation from incoherent excitation may be observed and studied.

We have already shown, by both analytical and numerical treatments of the degenerate backward OPO in the QPM decay interaction between a c.w. pump and a backward signal wave, that the inhomogeneous stationary solutions are always unstable, whatever the cavity length and pump power values are above

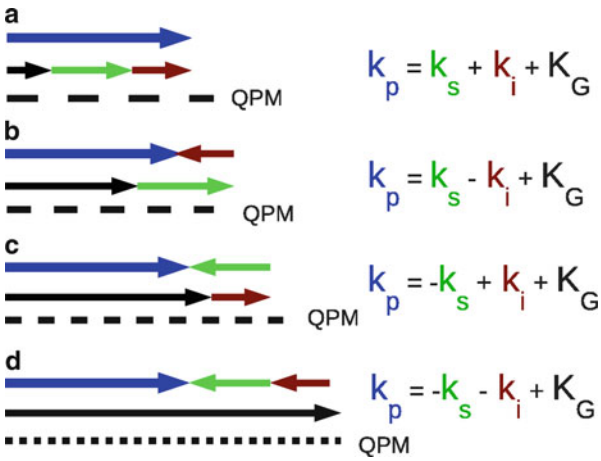

Fig. 1 Wave vector diagrams (momentum conservation) for the non-degenerate three-wave interaction in: (**a**) a three-wave forward configuration; (**b**) a singly backward idler configuration; (**c**) a singly backward signal configuration; and (**d**) a doubly backward (signal and idler) configuration. As we can see the QPM grating show a decreasing phase-reversal period for the nonlinear susceptibility represented by the *bold broken lines* under each configuration

threshold of a singly resonant OPO. Starting from any initial condition, the nonlinear dynamics exhibits self-pulsing of the backward signal with unlimited amplification and compression. Above a critical steepening of the backward pulse, dispersion may saturate this singular behavior leading to self-modulated solitary structures [17,28].

In this paper we show, by a stability analysis of the non-degenerate backward OPO [18, 19], that the previous particular behavior of unconditional temporal instability of the degenerate backward OPO is removed for a finite temporal walk-off between the counter-propagating signal and idler waves, and that we now obtain a regular Hopf bifurcation like in the Brillouin fiber-ring laser [10]. We will consider self-structuration of three-wave solitary waves in such a backward OPO with absorption losses.

For a c.w. pumped OPO near degeneracy a unique control parameter L governs the dynamical behaviour; it is shown that at a critical interaction length L_{crit} the inhomogeneous stationary solution bifurcates towards a time-dependent oscillatory solution. This critical length is finite if and only if we take into account a finite group velocity delay between both backward propagating waves $\Delta v = |v_s - v_i| \neq 0$ (or temporal *walk-off*), where v_s and v_i are the signal and idler group velocities. Moreover, for longer interaction lengths the dynamics gives rise to the generation of the backward three-wave soliton, whose stability is also ensured by this finite temporal walk-off Δv, without requiring additional saturation mechanisms like the dispersion effect. This *scenario* is confirmed by numerical simulations of the nonlinear dynamic equations, and an excellent agreement is obtained (near the degenerate configuration) for the value of L_{crit} evaluated from the stability analysis and that one obtained from the dynamical simulation.

The general fully non-degenerate configuration involves more complicated mathematics because a set of control parameters are required and we only show several dynamical behaviours resulting from the three-wave numerical model.

We will conclude this review by considering some dynamical behaviours of the backward mirrorless OPO pumped with an incoherent pulse, because up to now this configuration is the only one in which backward MOPO experiments have been performed.

The paper is organized as follows. In Sect. 2 we recall the three-wave model governing the spatio-temporal evolution of the slowly varying envelopes of the pump and the backward signal and idler waves. We also recall the analytical solutions in the form of propagating dissipative solitary waves propagating backward with respect the cw-pump under a QPM three-wave interaction. In Sect. 3 is presented the stability analysis of the nonlinear inhomogeneous stationary solutions of the non-degenerate backward OPO for finite temporal walk-off. Numerical dynamics of the self-structuration of symbiotic three-wave solitons leading to stable self-pulsing regimes is shown in Sect. 4. Finally, the numerical dynamics of the pulsed BMOPO under incoherent pump excitation is discussed in Sect. 5.

2 Three-Wave Model and Analytical Solitary-Wave Solutions

The spatio-temporal evolution of the slowly varying envelopes of the three resonant counter-streaming interacting waves $A_j(x,t)$, for a non-degenerate OPO, is given by

$$\begin{aligned}
(\partial_t + v_p\,\partial_x + \gamma_p + i\beta_p\partial_{tt})\,A_p &= -\sigma_p A_s A_i \\
(\partial_t - v_s\,\partial_x + \gamma_s + i\beta_s\partial_{tt})\,A_s &= \sigma_s A_p A_i^* \\
(\partial_t - v_i\,\partial_x + \gamma_i + i\beta_i\partial_{tt})\,A_i &= \sigma_i A_p A_s^*
\end{aligned} \tag{1}$$

where $A_p(\omega_p, k_p)$ stands for the c.w. pump wave, $A_s(\omega_s, k_s)$ for the backward signal wave, and $A_i(\omega_i, k_i)$ for the backward idler wave. The resonant conditions in one-dimensional configuration realize the energy conservation,

$$\omega_p = \omega_s + \omega_i, \tag{2}$$

and the momentum conservation,

$$k_p = -k_s - k_i + K_G, \tag{3}$$

where $K_G = 2\pi/\Lambda_{QPM}$ and Λ_{QPM} is the grating pitch for the backward quasi-phase matching (cf. Fig. 1d). The group velocities v_j $(j = p, s, i)$ as well as

the attenuation coefficients γ_j and dispersion coefficients $\beta_j \equiv v_j \beta_{2,j}/2$ are in general different for each wave. Equations (1) also hold for standard forward phase-matching configurations in which case all the signs of the velocities $v_{s,i}$ are positive (cf. Fig. 1a). For the singly backward idler (or backward signal) configuration the momentum conservation (3) must be replaced by (17). These configurations are shown in Fig. 1b, c. The nonlinear coupling coefficients are $\sigma_j = 2\pi d_{eff} v_j/(\lambda_j n_j)$, where n_j is the refractive index at frequency ω_j, wavelength λ_j and d_{eff} is the effective nonlinear susceptibility. The chromatic dispersion is also taken into account in (1); this is necessary when the generated temporal structures are sufficiently narrow. The effects of group velocity dispersion (GVD) are represented by the second derivatives with respect to time, so that the dispersion parameters are given by $\beta_j = |v_j| k_j''$ where $k_j'' = (\partial^2 k/\partial\omega^2)_j$, k being the wave vector modulus, $k = n(\omega)\omega/c$.

2.1 Solitary Wave Solution

In the absence of dispersion ($\beta_j = 0$) (1) have been extensively studied in the literature. Their solitary wave solutions have been first derived in the absence of dissipation ($\gamma_j = 0$) [2, 3, 6]. In the context of stimulated scattering in nonlinear optics, the existence of dissipative solitary waves when one of the velocities $v_{s,i}$ is zero (e.g. $v_i = 0$) has also been shown [9, 29]. More recently, Craik et al. have proved, for the particular case of degenerate three-wave interaction, that solitary waves still exist in the presence of dissipation [30]. On the basis of these previous theoretical works, we have calculated from (1) a particular analytical solution of the dissipative symbiotic solitary waves of the non-degenerate parametric three-wave interaction. Looking for a solitary wave structure induced by energy transfer from the pump wave to the signal and idler pair, we have to assume zero loss for the pump ($\gamma_p = 0$). It is the only way to keep constant the energy transfer that compensates here for the signal and the idler losses, so as to generate stationary field structures. If γ_p was not zero, the pump wave would experience an exponential decay giving rise to a vanishing energy of the three-wave structure that prevents the formation of a stationary solitary wave state.

When $\gamma_p = 0$ it is easy to find by substitution the following solution to (1):

$$\begin{aligned} A_p &= \delta - \beta \tanh\big[\Gamma(x + Vt)\big] \\ A_s &= \eta\Gamma \operatorname{sech}\big[\Gamma(x + Vt)\big] \\ A_i &= \kappa\Gamma \operatorname{sech}\big[\Gamma(x + Vt)\big] \end{aligned} \tag{4}$$

where β is the only free parameter. All other parameters depend on the material properties and on β. One finds $\delta = [\gamma_s\gamma_i/\sigma_s\sigma_i]^{1/2}$, $\Gamma = \beta[\sigma_i\sigma_s/(V-v_s)(V-v_i)]^{1/2}$, $\eta = [(V + v_p)(V - v_i)/\sigma_i\sigma_p]^{1/2}$, $\kappa = [(V + v_p)(V - v_s)/\sigma_s\sigma_p]^{1/2}$, and $V = (v_s/\gamma_s - v_i/\gamma_i)/(1/\gamma_s - 1/\gamma_i)$. This last expression shows that the velocity V of

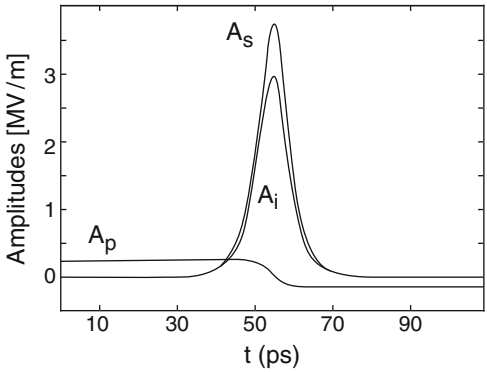

Fig. 2 Envelopes of the dissipative three-wave solitary solution

the solitary wave is fixed by the material parameters, unlike in the nondissipative case where V is undetermined [2]. Let us point out that, in order to keep Γ real, the solitary wave must be either superluminous, $V > max(v_s, v_i)$, or subluminous, $V < min(v_s, v_i)$. Note that the superluminous velocity does not contradict by any means the special theory of relativity [9] even if the velocity V becomes infinite when the signal and idler waves undergo identical losses, $\gamma_s = \gamma_i$. This can be easily explained by remembering that the velocity of this type of symbiotic solitary wave is determined by the energy transfer rate, which depends on the shape of the envelope of each component. The infinite velocity is here simply due to the fact that the width of the solitary wave Γ^{-1} also becomes infinite for $\gamma_s = \gamma_i$. However, we shall see that this symmetrical solution is not the more general one and it is not an attractor solution for a large variety of parameter values. In Sect. 4 we will present another self-similar structure for the near-degenerate backward interaction which does not present a divergence for $\gamma_s = \gamma_i$. The free wave parameter β fixes, in combination with the material parameters, the amplitude and the width of the solitary wave. According to the first equation of (4), β is determined by the initial pump amplitude $A_p = E_p(x = -\infty) = \beta + \delta$. In practice, this means that, for a given material, the solitary wave is completely determined by the pump intensity at the input face of the crystal. Note that if the losses are such that $\delta > \beta$ the solitary wave no longer exhibits a π-phase change [8], contrary to the nondissipative case [2].

Figure 2 shows a typical example of such a dissipative symbiotic solitary wave in a quasi-phase-matched backward three-wave interaction with $\lambda_p = 1\,\mu$m, $\lambda_s = 1.5\,\mu$m, $\lambda_i = 3\,\mu$m, $\Lambda_{QPM} = 2\pi/K_G = 0.233\,\mu$m, and with a pump field of amplitude $E_p = 0.25$ MV/m (i.e., a pump intensity of $I_p = 10$ kW/cm^2) propagating in a quadratic $\chi^{(2)}$ material. It is obtained with the following typical values of the parameters : $d_{eff} = 20$ pm/V, $n_p = 2.162$, $n_s = 2.142$, $n_i = 2.098$, $v_p = 1.349 \times 10^8$ m/s, $v_s = 1.371 \times 10^8$ m/s, $v_i = 1.363 \times 10^8$ m/s, and the loss coefficients $\alpha_s = 2\gamma_s/v_s = 0.23\,\text{m}^{-1}$ and $\alpha_i = 2\gamma_i/v_i = 11.5\,\text{m}^{-1}$. Note that these parameters lead to a pulse width of approximately 10 ps. Therefore, with such pulse durations one can expect that the zero pump loss approximation ($\gamma_p = 0$)

is valid in practice in the neighborhood of the solitary wave structure. Indeed, if the characteristic absorption length v_p/γ_p is much larger than the pulse width Γ^{-1}, one can anticipate that the solitary wave undergoes adiabatic reshaping during propagation so as to adapt locally its profile to the exponentially decaying pump intensity.

3 Self-pulsing in a Backward Doubly Resonant OPO

Let us point out that the self-structuration process requires backward interaction. The mechanism is similar to the Hopf bifurcation appearing in the counter-streaming Brillouin cavity [10]. Numerical simulations with the more usual forward phase-matching conditions only lead to the steady-state regime. This shows that the distributed feedback nature of the interaction plays a fundamental role in the pulse generation process. This observation is consistent with the conclusions of [23] where complex temporal pattern formation in backward-phase-matched second harmonic generation is studied and of our previous study of the degenerate backward OPO [28]. But in contrast to this last study, where no regular Hopf bifurcation was found by starting from the inhomogeneous stationary solutions, since above the threshold the perturbations always grow in time, we will show hereafter that in the non-degenerate backward OPO a regular Hopf bifurcation takes place. Below a critical parameter value, the inhomogeneous stationary solutions are stable, and above it the bifurcation leads to an also stable self-structured solitary wave. Our purpose in this section is to prove that in the non-degenerate configuration, the temporal walk-off, i.e. the group velocity delay between the signal and the idler waves, ensures a regular Hopf bifurcation and leads to a stable self-structuration of the three-wave envelopes.

For the sake of simplicity, we will focus here on the near-degenerate OPO regimes [18, 19]. However, our results are more general and can be extended to the fully non-degenerate case in a similar way. We present here several dynamical behaviours.

We start from the dimensionless form of (1) which describe the non-degenerate backward OPO in the quasi-phase-matching decay interaction between a pump and counter-propagating signal and idler waves. We write them near the degeneracy with temporal walk-off on only one field. This is not a restriction but it is more convenient for mathematical calculations. The general case can be recovered by an appropriate change of variables.

By introducing the following scalings:

$$u_p = \sqrt{1-d^2}\frac{A_p}{A_p^o},\ u_s = \sqrt{2(1-d)}\frac{A_s}{A_p^o},\ u_i = \sqrt{2(1+d)}\frac{A_i}{A_p^o},$$

$$\tau = t/\tau_o,\ \ \xi = \frac{x}{\Lambda},\ \ L = \frac{\ell}{\Lambda} \tag{5}$$

where A_p^o is the incident c.w. pump, $\tau_o = 2/(\sigma_p A_p^o)$ and $\Lambda = v_p \tau_o$ are the characteristic time and length and ℓ the cavity length, the dimensionless equations read:

$$\begin{aligned}
(\frac{\partial}{\partial \tau} + \frac{\partial}{\partial \xi} + \mu_p + i\tilde{\beta}_p \frac{\partial^2}{\partial \tau^2})u_p &= -u_s u_i \\
(\frac{\partial}{\partial \tau} - \frac{\partial}{\partial \xi} + \mu_s + i\tilde{\beta}_s \frac{\partial^2}{\partial \tau^2})u_s &= u_p u_i^* \\
(\frac{\partial}{\partial \tau} - \alpha\frac{\partial}{\partial \xi} + \mu_i + i\tilde{\beta}_i \frac{\partial^2}{\partial \tau^2})u_i &= u_p u_s^*
\end{aligned} \tag{6}$$

where $\alpha = v_i/v_p$, $v_p = v_s$, $\mu_j = \gamma_j \tau_o$, and $\tilde{\beta}_j = \beta_j/\tau_o$. The full description of the OPO dynamics is obtained by taking into account, in addition to (6), the following boundary conditions for the doubly resonant cavity

$$\begin{aligned}
&u_s(\xi = L, \tau) = \rho_s\, u_s(\xi = 0, \tau), \quad u_i(\xi = L, \tau) = \rho_i\, u_i(\xi = 0, \tau), \\
&u_p(\xi = 0, \tau) = \sqrt{1 - d^2}
\end{aligned} \tag{7}$$

where $\rho_s = \sqrt{R_s}$ and $\rho_i = \sqrt{R_i}$ are the amplitude feedback coefficients. Note that we have introduced the new coefficients $1 \pm d$ by setting $d = (\sigma_s - \sigma_i)/\sigma_p$ and assuming a near-degenerate OPO configuration, i.e., $\sigma_p \simeq \sigma_s + \sigma_i$.

3.1 Inhomogeneous Stationary Solutions

Without optical attenuation ($\mu_j = 0$) and in the absence of dispersion ($\beta_j = 0$), inhomogeneous stationary solutions $u_j^{st}(\xi)$, $j = \{p, s, i\}$ can be obtained from (6) by setting $\partial/\partial\tau = 0$. The assumption of zero loss parameters μ_j is not restrictive since the main dissipation in the OPO cavity comes from the finite feedback. In this case, the following conservation relations, also known as Manley–Rowe relations [31], hold

$$\begin{cases} |u_p^{st}|^2 - |u_s^{st}|^2 = \pm D_s^2 \\ |u_p^{st}|^2 - \alpha|u_i^{st}|^2 = \pm D_i^2 \end{cases} \tag{8}$$

For a doubly resonant OPO with the same feedback coefficient for the signal and idler fields, we have $D_s = D_i = D$. This leads to two types of stationary solutions: *(i)* $D^2 = |u_p^{st}|^2 - |u_s^{st}|^2 = |u_p^{st}|^2 - \alpha|u_i^{st}|^2$ and *(ii)* $D^2 = |u_s^{st}|^2 - |u_p^{st}|^2 = \alpha|u_i^{st}|^2 - |u_p^{st}|^2$.

In case *(i)*, the following inhomogeneous stationary solutions are obtained

$$u_p^{st}(\xi) = D\tanh^{-1}\left(\operatorname{arccotanh}(\frac{u_p^{st}(0)}{D}) + \frac{D\xi}{\sqrt{\alpha}}\right)$$
$$u_s^{st\,2} = \alpha u_i^{st\,2} = \frac{D^2}{\sinh^2\left(\operatorname{arccotanh}(\frac{u_p^{st}(0)}{D}) + \frac{D\xi}{\sqrt{\alpha}}\right)} \tag{9}$$

while in case *(ii)*,

$$u_p^{st}(\xi) = D\frac{u_p^{st}(0) - D\tan(\frac{D\xi}{\sqrt{\alpha}})}{D + u_p^{st}(0)\tan(\frac{D\xi}{\sqrt{\alpha}})} \qquad u_s^{st}(\xi) = \sqrt{\alpha}u_i^{st}(\xi) = \frac{D\sqrt{1 + \frac{u_p^{st\,2}(0)}{D^2}}}{\cos(\frac{D\xi}{\sqrt{\alpha}}) + \frac{u_p^{st}(0)}{D}\sin(\frac{D\xi}{\sqrt{\alpha}})} \tag{10}$$

where $u_p^{st}(0) = \sqrt{1-d^2}$.

Let us consider the situation of short enough OPO cavities in order to avoid total depletion of the pump inside the cavity and to benefit from the monotonous gain of the singly pumped OPO; otherwise the signal and idler fields oscillate and may return part of this intensity to the pump. This is achieved by considering $D\xi \ll 1$. Thus, to the leading order, the inhomogeneous stationary solutions (10) are

$$u_p^{st}(\xi) \simeq \frac{u_p^{st}(0) - D^2\frac{\xi}{\sqrt{\alpha}}}{1 + u_p(0)\frac{\xi}{\sqrt{\alpha}}} \qquad \text{and} \qquad u_s^{st}(\xi) = \sqrt{\alpha}u_i^{st}(\xi) \simeq \frac{D\sqrt{1 + \frac{u_p^{st\,2}(0)}{D^2}}}{1 + \frac{u_p^{st}(0)\xi}{\sqrt{\alpha}}} \tag{11}$$

Manley–Rowe relations (8) are used at $\xi = 0$ and $\xi = L$, together with the boundary conditions to determine the integration constants. A second order algebraic equation for D^2 is obtained

$$aD^4 + bD^2 - c = 0 \tag{12}$$

with

$$a = L^2/\alpha, \quad b = (1-R)(1+\sqrt{1-d^2}L/\sqrt{\alpha})^2 - 2\sqrt{1-d^2}L/\sqrt{\alpha},$$
$$c = (1-d^2)[1 - R(1+\sqrt{1-d^2}L/\sqrt{\alpha})^2]$$

Once D is determined from the above expression, $u_s(0)$ and $u_i(0)$ can be calculated via the Manley–Rowe relations (8).

Note that we will only consider the case *(ii)* configuration; case *(i)* can be analysed in a similar way.

3.2 *Stability Analysis of the Inhomogeneous Stationary Solutions*

Following [18] let us first perform the linear stability analysis of the inhomogeneous stationary solutions (10) with respect to space-time-dependent perturbations in the absence of dispersion and optical attenuation, through

$$u_j(\xi,\tau) = u_j^{st}(\xi) + \delta u_j(\xi) e^{-i\omega\tau} \quad \text{where} \quad j = p,s,i.$$

It is more convenient to introduce the new variables

$$P(\xi) = u_p^{st}(\xi), \quad S(\xi) = u_s^{st}(\xi), \quad I(\xi) = S(\xi)/\sqrt{\alpha} = u_i^{st}(\xi),$$

$$Z(\xi) = \delta u_p(\xi), \quad Y(\xi) = \delta u_s(\xi), \quad X(\xi) = \delta u_i(\xi),$$

where $P(\xi)$, $S(\xi)$ and $I(\xi)$ stand for the inhomogeneous stationary solutions and $Z(\xi)$, $Y(\xi)$ and $X(\xi)$ for the space-time-dependent perturbations. Thus, the linearized problem associated with (6) reads

$$\begin{aligned} \frac{\partial Z}{\partial \xi} - i\omega Z &= -S\left(X + \frac{Y}{\sqrt{\alpha}}\right) \\ \frac{\partial Y}{\partial \xi} + i\omega Y &= -PX - \frac{SZ}{\sqrt{\alpha}} \\ \alpha \frac{\partial X}{\partial \xi} + i\omega X &= -PY - SZ \end{aligned} \tag{13}$$

The stability analysis is performed by solving the perturbative equation (13) with the inhomogeneous stationary solutions and by taking into account the boundary conditions for the cavity. This gives rise to an eigenvalue problem with a dispersion relation for the complex frequency ω. Following [10, 28] and [18] we will look for the stability of the cavity modes with frequency $\Re(\omega) \simeq 2\pi N/L$ [N integer and L being the dimensionless length ℓ/Λ defined in (5)] yielding to mode instability whenever $\Im(\omega) > 0$.

3.2.1 Absence of Walk-Off

Let us first recall the situation in the absence of temporal walk-off; the signal and idler waves have the same group velocity leading to $\alpha = 1$ in (13). We proceed as in the degenerate case [28] and we obtain the following dispersion relation

$$a_o + b_o \sin(\omega L) + c_o \cos(\omega L) = 0 \tag{14}$$

where the expressions of a_o, b_o and c_o are given in appendix A of [18]. It should be noted that (14) generalizes the dispersion relation in [28] for the degenerate case because it applies to the doubly-resonant backward OPO. The instability of each mode is determined from (14) when $\Im(\omega) > 0$. However, in the absence of walk-off, signal and idler perturbation equations are decoupled from the pump perturbation equation, and again it leads to unconditional temporal instability. We recall that this instability leads to the generation of a localized structure exhibiting unlimited amplification and compression [17,28], whose collapse may be avoided by including the natural chromatic dispersion which is present in (1).

Since the required grating pitch for first order QPM is extremely small, we must increase the c.w. pump intensity when using higher order gratings in order to get an actual experimental configuration. Reference [21] gives a table with the threshold pump intensities and domain periods for the degenerate backward OPO in four periodic domain structures (KTP, $LiNbO_3$, GaAs/AlAs). Recently [32], it has been reported an experiment of first order QPM blue light generation at 412.66 nm, in a 20 mm long surface-poled Ti-indiffused channel waveguide in $LiNbO_3$ with c.w. pumping, using periodic domain structures as short as 1 μm. The authors have announced generation of 3.46 mW blue light for 70 mW of fundamental power. Based on such recent progresses in the poling technology of $LiNbO_3$ one can likely hope to experimentally realize the backward OPO with the allowed pump power for so short grating pitch. We will see in Sect. 5 that a periodic domain of 800 nm has been obtained in a bulk PPKTP configuration to achieve for the first time the pulsed mirrorless OPO. For example, if $\Lambda_{QPM} = 0.5\,\mu\text{m}$ we may only use a c.w. pump power ten times higher (i.e. $I_{p,0} = 1\,\text{MW/cm}^2$) for the same cavity length $\ell = 3.7\,\text{cm}$, same characteristic time $\tau_0 \simeq 0.28\,\text{ns}$, and same low finesse $\rho_s = \sqrt{R} = 0.46$ as that given in the previous example. If we consider a pulse pump of FWHM of $\Delta t = 28\,\text{ns}$ instead of a c.w. beam we can even reach $I_{p,0} = 100\,\text{MW/cm}^2$ without optical damage [33] (yielding $\tau_0 = 28\,\text{ps}$ and $\Lambda = 0.37\,\text{cm}$).

3.2.2 Finite Temporal Walk-Off

When taking into account a finite temporal walk-off $\alpha \neq 1$, (13) are more complicated as the dynamics of the pump wave and the signal-idler pair is no longer decoupled. For the sake of simplicity let us consider $D = 0$, so that $P = S = \sqrt{\alpha} I = 1/(1/\sqrt{1-d^2} + \xi/\sqrt{\alpha})$. Note that $D = 0$ requires that $c = 0$ in (12). Since $d \ll 1$, it is the second factor in the same expression of c which vanishes leading to the relation $R = 1/(1 + \sqrt{(1-d^2}L/\sqrt{\alpha})^2$. The first-order perturbed system becomes

$$\frac{d}{d\xi}\begin{pmatrix} Z \\ Y \\ X \end{pmatrix} = \begin{pmatrix} i\omega & -I & -S \\ -I & -i\omega & -P \\ -S/\alpha & -P/\alpha & -i\omega/\alpha \end{pmatrix}\begin{pmatrix} Z \\ Y \\ X \end{pmatrix}$$

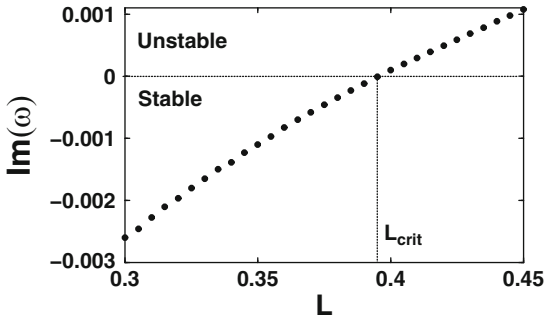

Fig. 3 Evolution of the imaginary part of the pulsation ω as a function of the length L close to the first cavity mode (with $\mathrm{Re}(\omega) \simeq 2\pi/L$). The transition from stable to unstable states is obtained for $L_{crit} \simeq 0.39$

This system of equations is numerically solved. Since the group velocity delay (temporal walk-off) of the signal and idler pair is small, we set $\alpha = v_i/v_p \simeq 1+\epsilon$. We expand the solutions up to the second order in the small parameter ϵ. The second order is necessary to match the critical parameter value obtained at the Hopf bifurcation point by the numerical integration of the normalized governing (6); the first order in ϵ being insufficient to characterize the bifurcation point.

Through the boundary conditions, we obtain the dispersion relation:

$$\begin{aligned}
&\omega^3 y_o^2 y_L + \Big[-\omega^3 y_o^2 y_L - i\omega^2 y_o L + \omega L\Big]\cos(\omega L) + \Big[i\omega^3 y_o^2 y_L + i\omega y_o - \omega^2 y_o L - 1\Big]\sin(\omega L) \\
&- \frac{i\epsilon}{8y_L(y_o\rho_o - y_L e^{-i\omega L})}\Big\{A_o e^{-2i\omega L} + B_o e^{-i\omega L} + C_o e^{i\omega L} + D_o\Big\} \\
&- \frac{i\epsilon^2}{24y_L^2(y_o\rho_o - y_L e^{-i\omega L})}\Big\{A_1 e^{-2i\omega L} + B_1 e^{-i\omega L} + C_1 e^{i\omega L} + D_1\Big\} = 0
\end{aligned} \tag{15}$$

with $y_o = 1/\sqrt{1-d^2}$, $y_L = y_o + L$, $\rho_o = y_o/y_L$ is the amplitude feedback coefficient and L stands for the dimensionless length ℓ/Λ. The expressions of the different coefficients A_o, A_1, B_o, B_1, C_o, and C_1, which are functions of $\omega = \omega_r + i\omega_i$, y_L, and y_o are given in appendix B of [18]. First we recover, as it should be, the dispersion relation (14) when $\epsilon = 0$ and $D = 0$. However, the non-degenerate backward OPO dispersion relation (15) shows that, in contrast to the degenerate case, there exist a stability domain of the inhomogeneous stationary solutions above threshold. Moreover, these solutions undergo a Hopf bifurcation, even near the degenerate configuration, for a critical length of the cavity. Figure 3 shows a typical example of a regular Hopf bifurcation with the parameters set to $d = 0.05$ and $\epsilon = 1/128$. We have plotted $\Im(\omega)$ from (15) against the propagation length L near the first cavity mode ($\Re(\omega) \simeq 2\pi/L$). As can be seen from the figure, Hopf bifurcation occurs at $L_{crit} \simeq 0.39$. For $L \leq L_{crit}$ the inhomogeneous stationary solutions are stable (see Fig. 4) whereas if $L > L_{crit}$ the perturbations are amplified generating a new oscillatory localized structure (see Figs. 5 and 6).

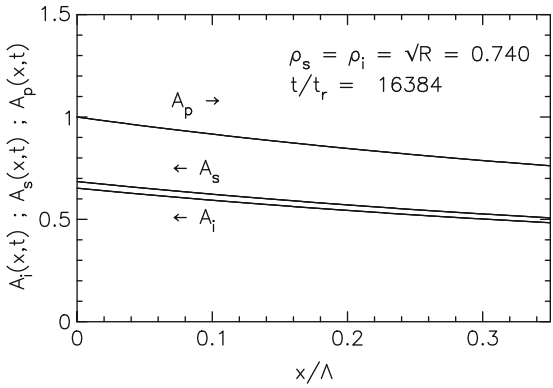

Fig. 4 Doubly resonant backward OPO: asymptotic stationary spatial profiles at round trip 16384 for $L = 0.35$ below critical length

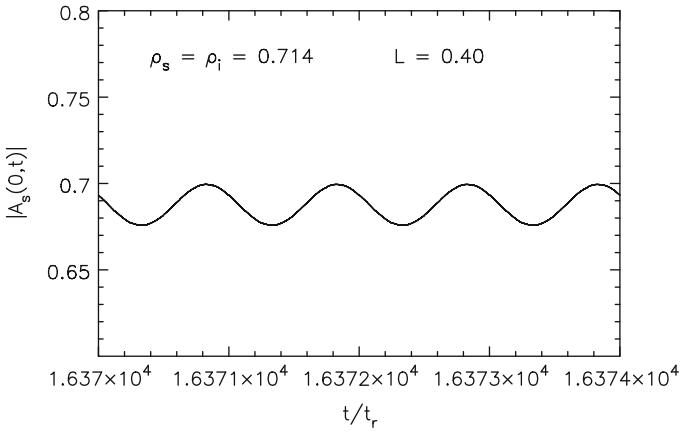

Fig. 5 Doubly resonant backward OPO: temporal oscillatory regime for $L = 0.4$ above critical length

4 Nonlinear Dynamics of the Doubly Resonant Backward OPO

In the previous section we have carried out the stability analysis of the inhomogeneous stationary solutions of the doubly resonant backward OPO near the degenerate configuration. This behavior may be generalized to the fully non-degenerate backward OPO provided that a finite temporal walk-off between the counter-propagating signal and idler waves is present. In this section we proceed as follows:

(i) We numerically check the previous analytical result in the near-degenerate OPO regime for $D = 0$;

(ii) We show that a dynamically critical bifurcation for $D \neq 0$ can be obtained with the same feedback parameter values ($\rho_s = \rho_i$) for both signal and idler waves;

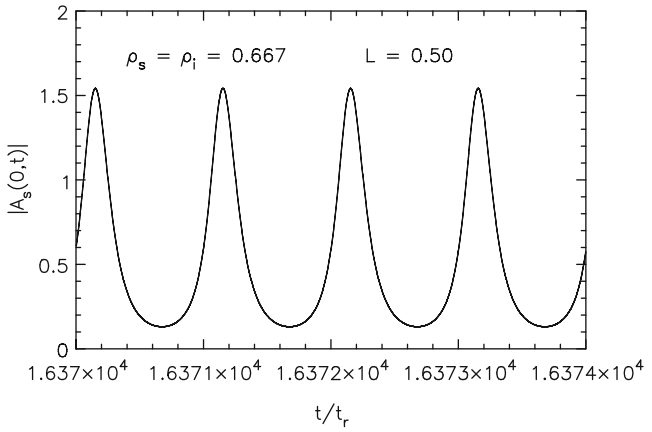

Fig. 6 Doubly resonant backward OPO: temporal pulsed regime for a length $L = 0.5$

Fig. 7 Doubly resonant backward OPO: pulse maximum amplitude *vs.* number of round trips t/t_r (where $t_r = \ell/v_s$ is the round-trip time) at the output of the backward OPO cavity exhibiting stable saturation at a constant amplitude

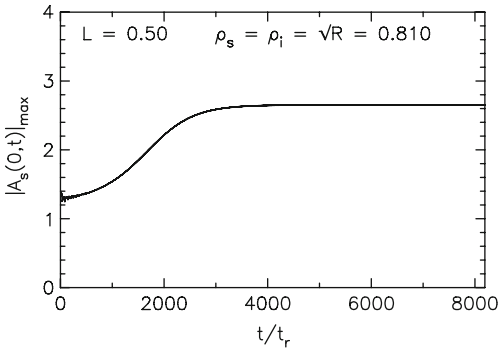

(iii) We numerically investigate the self-pulsing regime for the doubly resonant backward OPO with different feedback parameter values ($\rho_s \neq \rho_i$) including perturbative dispersion.

To this end we have numerically integrated equation (6) with the boundary conditions (7). In order to better compare the dynamical behavior with the analytical one, we first neglect dispersion ($\tilde{\beta}_j = 0,\ j = p, s, i$) which is only a perturbative effect in the non-degenerate case, but we include a small dissipation ($\mu_j = 10^{-2}$). In order to dynamically investigate the near-degenerate OPO regime for $D = 0$, we start from the approximate stationary solutions (11) with a group velocity difference (temporal walk-off) $|v_s - v_i|/v_p = 1/128$. In the near-degenerate OPO case, the feedback $R = |\rho_s|^2 = |\rho_i|^2$ is related to the dimensionless length L through the relation $u_p^2(L) - Ru_s^2(L) = D^2$, which is now simply reduced to $R = [1 + L\sqrt{(1-d^2)/\alpha}]^{-2}$. Therefore, we may investigate the near-degenerate OPO dynamics by varying the control parameter L from 0.25 to 0.5. As expected from the stability analysis, we now find a regular Hopf bifurcation of the stationary

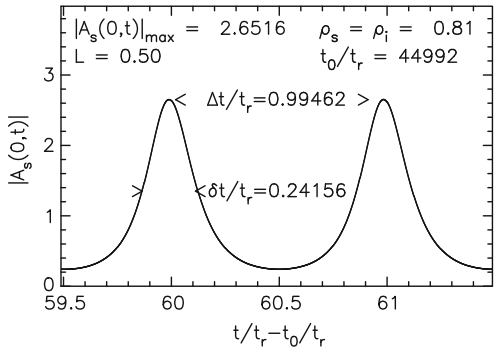

Fig. 8 Doubly resonant backward OPO: temporal evolution of a pulse train at the output of the OPO cavity. Pair of two consecutive pulses at round trip $t/t_r = 28608$ for $L = 0.5$ and $\rho_s = \rho_i = 0.81$. The amplitude is measured in $|A_{p,o}|/\sqrt{2}$ units

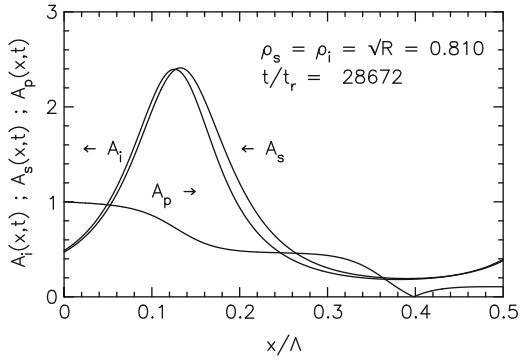

Fig. 9 Doubly resonant backward OPO: spatial profiles for the three wave amplitudes at round trip 28672

state towards a time-dependent oscillatory state for a critical length L_{crit} between 0.35 and 0.4, in contrast to the full degenerate case [28] or to the near-degenerate case $D = 0$ in the absence of temporal walk-off (cf. Sect. 3.2.1), where no Hopf bifurcation exists. The stationary spatial profiles are shown in Fig. 4 after 16384 round trips for $L = 0.35$. This stationary state bifurcates towards a stable oscillatory regime as illustrated in Fig. 5 for $L = 0.4$. For a larger length L (and correspondingly smaller feedback R) we obtain pulsed regimes as that shown in Fig. 6 whose stability is ensured by the finite temporal walk-off too, without taking into account any dispersion effect (cf. Fig. 7).

The dynamical equation (6) allow us to look further for $D \neq 0$, while the control parameter L (since R is only a function of K for $D = 0$) splits now into two control parameters L and R related through $u_p^2(L) - Ru_s^2(L) = D^2$. For $L = 0.25$ we obtain the Hopf bifurcation between $\sqrt{R} = 0.80$ and 0.81, while for $L = 0.5$ it happens between $\sqrt{R} = 0.81$ and 0.82, the pulsed regimes corresponding to lower feedback favors the localization of the structure [11]. For a typical pulsed regime at $L = 0.5$ and $\sqrt{R} = 0.81$, we show in Fig. 7 the saturation of the pulse maximum amplitude with time when starting from the stationary state, and in Fig. 8 a pair of two consecutive pulses in the asymptotic stable state (the width δt is measured in $t_r = \ell/v_s$ units). As can be seen from Fig. 9 the solitary structure is now composed of two embedded pulses of nearly identical amplitudes moving together, the constant

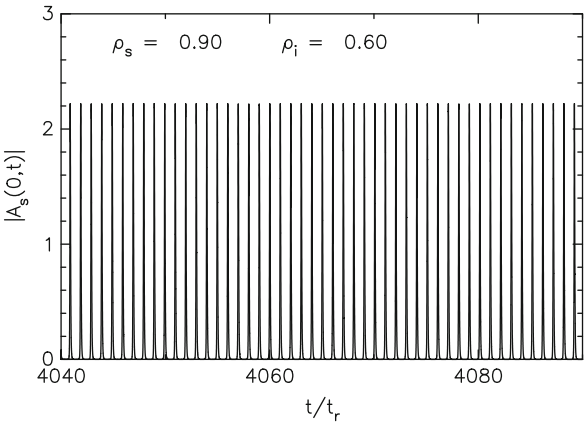

Fig. 10 Doubly resonant backward OPO: temporal amplitude signal output of the backward OPO in the stable asymptotic pulsed regime measured in cavity round trips t/t_r for $L = 1$, $\rho_s = 0.90$ $\rho_i = 0.60$ and $\tilde{\beta}_j = 10^{-6}$, $j = p, s, i$

spatial shift between them corresponds to the temporal walk-off (or different group velocities). The trapping between the signal and idler envelopes yields the new self-similar structure moving at a characteristic velocity, which is composed of the couple of embedded pulses maintaining constant spatial shift between them in spite of the different velocities of both waves.

Let us consider a physical application. In comparison to the type I (e-e) polarization interaction in $LiNbO_3$ proposed in [28] for the full-degenerate case, we may now consider a type II (e-o-e) polarization interaction in order to move away from the degeneracy and to obtain a finite group velocity delay (or temporal walk-off) between the signal and the idler waves. For the same quadratic $\chi^{(2)}$ material, same pump wave (e-polarized) at $\lambda_p = 0.775\,\mu$m, the same idler wave (e-polarized) at $\lambda_i = 1.55\,\mu$m, but now a signal wave (o-polarized) at $\lambda_s = 1.55\,\mu$m having a different refractive index, the group velocity dispersion ensures a finite temporal walk-off between both backward waves. For a first order QPM in $LiNbO_3$ the grating pitch is as small as $\Lambda_{QPM} = 2\pi/K_G = 0.177\,\mu$m. For a c.w. pump field $E_p = 0.725$ MV/m (i.e., a pump intensity of $I_p = 100$ kW/cm^2) propagating in this configuration we have the following values of the parameters [33]: $d_{eff} = 6$ pm/V, $n_p = 2.181$, $n_s = 2.212$, $n_i = 2.140$, $v_p = 1.317 \times 10^8$ m/s, $v_s = 1.323 \times 10^8$ m/s, $v_i = 1.372 \times 10^8$ m/s, $\gamma_p = 4.6 \times 10^8$ s^{-1}, and $\gamma_s = \gamma_i = 3.1 \times 10^8$ s^{-1}. The nonlinear characteristic time yields $\tau_0 = (\sigma_p A_p/2)^{-1} \simeq 0.94$ ns, and the nonlinear characteristic length $\Lambda = v_p \tau_0 = 12$ cm. We have taken cavity lengths running from 3 cm ($L = 0.25$) to 6 cm ($L = 0.5$) and we obtain a temporal width of the solitary pulses of the order of 100 ps.

Critical bifurcation parameters for doubly resonant backward OPOs with different nonlinear coupling coefficients σ_j and different feedback parameter values ($\rho_s \neq \rho_i$) may be obtained through the general dynamical equation (1) with boundary conditions (7). Figure 10 displays a typical self-pulsing regime for $\sigma_s/\sigma_p = 0.675$, $\sigma_i/\sigma_p = 0.350$, $L = 1$, $\tilde{\beta}_j = 10^{-6}$, $j = \{p, s, i\}$, $\rho_s = 0.9$ and $\rho_i = 0.6$. As can be seen from this figure the predicted stability of the self-pulsing regime is not affected by the presence of chromatic dispersion.

5 Backward Coherent Pulse from Incoherently Pumped Mirrorless OPO

The numerical dynamics of a c.w. pumped singly backward OPO, experimentally adapted for an integrated cavity or IOPO (see for example [34–38]), either for counter-propagating signal or for counter-propagating idler does not generate backward solitary structures. Even for high OPO finesses the laser output is always stationary. Note that this does not contradict the existence of backward solitons in singly counter-propagating configurations if the backward wave is initially localized [2, 3, 27]. It simply means that such solitary waves cannot be spontaneously generated from quantum noise and a c.w. pump. Nevertheless, we shall see in this section that the singly backward OPO configuration is interesting from another point of view, namely the generation of a coherent backward pulse from an incoherent pump pulse. In this section we will show that recent experimental demonstration of a backward mirrorless optical parametric oscillator (BMOPO) with a pump pulse in the quasi-phase-matched (QPM) periodic polarized $KTiOPO_4$ crystal [24–26] opens the way for achieving ultra-coherent output from a highly incoherent pump pulse. In a first time we consider a coherently phase modulated pump because in the experiments the broadening of the pump is done via a coherent chirp [25, 26].

The pump phase modulations are transferred to the co-propagating wave moving at nearby the same group velocity of the pump through the *convection-induced phase-locking mechanism* [27, 39–42]. For the highly incoherent pump we present the case of perfect group-velocity matching of the pump and the co-propagating idler wave, which may be achieved in a type I OPO for a pump at 1.060 μm, a counterpropagating signal at 1.676 μm and an idler at 2.882 μm. We will show that the degree of coherence of the backward signal field turns to be more than three orders of magnitude greater than that of the incoherent pump, with approximately the same pump power and crystal length as in the experiments.

Parametric interaction of counterpropagating optical waves has the unique property of automatically establishing distributed feedback without external cavity mirrors; the mirrorless optical parametric oscillator has been the object of several studies [21, 31, 43, 44]. The recent BMOPO experiments exhibit useful spectral properties and have been performed in a configuration of type I at $\lambda_p = 0.8616\,\mu m$, $\lambda_s = 1.2179\,\mu m$ and $\lambda_i = 2.9457\,\mu m$ with a grating period of $\Lambda_{QPM} = 0.8\,\mu m$. This singly backward configuration overcomes the extremely low sub-μm grating periodicity required for the doubly backward OPO (cf. Sects. 3 and 4).

We have already proposed two experimental configurations in type II singly resonant KTP IOPO's [40] and in a type I $\{eee\}$ singly resonant Ti:$LiNbO_3$ IOPO [42], to show the locking mechanism in standard high finesse forward propagating OPO's feeded with a c.w. pump. We will also show in this section the feasibility of coherent backward generation from an incoherent pump pulse in a mirrorless BMOPO configuration feeded with a pulse pump.

5.1 MOPO Threshold and Dynamical Equations

A theoretical model yields an estimate of the MOPO threshold for counterpropagating plane waves [21], which is reached when the spatial gain exceeds $\pi/2$:

$$I_{pth} = \frac{\varepsilon_0 c n_p n_s n_i \lambda_s \lambda_i}{2\ell^2 d_{eff}^2} \tag{16}$$

where ε_0 is the permittivity of free space, ℓ the interaction length, d_{eff} the effective quadratic nonlinear coefficient, and $n_{s,i}$, $\lambda_{s,i}$ the respective signal and idler refractive index and wavelength. For example, for a PPKTP crystal of $d_{eff} = 8\,\text{pm/V}$ we have:

$$\ell = 1\text{ cm} \implies I_{pth} = 0.64\,\text{GW/cm}^2$$
$$\ell = 6.5\text{ mm} \implies I_{pth} = 1.08\,\text{GW/cm}^2$$

The momentum mismatch for the optical parametric generation process for the singly backward QPM configuration yields now

$$k_p = \pm k_s \mp k_i + K_G, \tag{17}$$

where $(+k_s, -k_i)$ stands for backward idler propagation and $(-k_s, +k_i)$ for backward signal propagation (cf. Fig. 1 respectively Fig. 1b, c), with a resulting larger QPM grating period as that of the doubly backward OPO configuration. The schematic vector diagram and periodically domain-inverted ferroelectric crystal of the counterpropagating interaction are shown in Fig. 1, and (1) become:

$$\begin{aligned}
(\partial_t + v_p\,\partial_x + \gamma_p + i\beta_p\partial_{tt})\,A_p &= -\sigma_p A_s A_i \\
(\partial_t \pm v_s\,\partial_x + \gamma_s + i\beta_s\partial_{tt})\,A_s &= \sigma_s A_p A_i^* \\
(\partial_t \mp v_i\,\partial_x + \gamma_i + i\beta_i\partial_{tt})\,A_i &= \sigma_i A_p A_s^*.
\end{aligned} \tag{18}$$

with respectively $(+v_s, -v_i)$ for the backward idler propagation and $(-v_s, +v_i)$ for the backward signal propagation.

The input parameters in the model are the properties of the nonlinear medium and the pump amplitude at the input face, $\mathbf{A_p}(x = 0, t)$, generating outputs of $\mathbf{A_p}(x = L, t)$, and either for the backward idler configuration (Fig. 1b) $\mathbf{A_s}(x = L, t)$ and $\mathbf{A_i}(x = 0, t)$ or for the backward signal configuration (Fig. 1c) $\mathbf{A_s}(x = 0, t)$ and $\mathbf{A_i}(x = L, t)$, where $x = 0$ and $x = L$ denote the positions of the input and output faces with respect to the pump beam. For the numerical treatment of the coupled wave equations for counter-propagating interactions, the standard split-step one-directional integration algorithm, usually employed for co-propagating interactions, is not suitable due to the fact that (18) represent a problem with two simultaneous, but spatially separate, boundary conditions, i.e., the

pump wave and the copropagating wave (either the signal or the idler) are initially given at one end of the medium, while the backward wave (either the idler or the signal) is input from the other end of the medium. For such problems, there are two main appropriate numerical methods: the shooting or trajectories method and the relaxation method. For the problem at hand, the trajectories method is more convenient, whereby we eventually want to simulate a counterpropagating three-wave mixing process driven by a pump field with a quasi-random phase distribution. The trajectories method with the use of a Runge–Kutta algorithm has been extensively used for the treatment of stimulated Brillouin back-scattering problems [7, 8]. The linewidth narrowing experimentally studied in Brillouin lasers [45] has been simulated in a Brillouin fiber-ring laser with the help of this method [9]. In that case, it is the acoustic wave that absorbs the phase fluctuations of the pump and allows the backward Stokes wave to increase its coherence. In order to numerically integrate the nonlinear counterpropagation dynamics in a MOPO in the presence of group-velocity dispersion (GVD), which introduces second-order time derivatives, we have developed a new numerical scheme which combines the trajectories method with fast Fourier transformation (FFT) to account for the GVD effects in the spectral domain [46]. The scheme accurately conserves the number of photons and the Manley–Rowe invariants of (18). As in the standard split-step approach, the evolution of (18) is for each time step (typically 1 fs long) first treated by linear propagation of the fields in the Fourier domain, thereby accounting for the GVD effects and the group-velocity difference between the pump and the co-propagating wave. The originality with respect to the standard split-step schemes with multiply-repeated FFT and inverse FFT procedures where exponential spectral cut-off filtering is introduced at the edges of the spectrum, is that we here introduce smoothed exponentially-decreasing prolongations of the outgoing complex amplitudes (over a length d) in the x-space of the MOPO crystal of length L in order to render a periodic problem (cf. Fig. 11). Thus the FFT is correctly performed in the extended interaction domain of length $M = L + 2d$ without arbitrary cut-offs. Then, after inverse FFT, the backward nonlinear interaction with spatially separate boundary conditions is treated by using the trajectories method. Integration over the trajectories in the nonlinear step of the algorithm was performed by using a 4th-order fixed-step Runge–Kutta method. The space- time is discretized in 2N points with $N = 16$–18, which, for instance, when $N = 16$ allows for a total bandwidth of 35 THz with the resolution of 0.5 GHz. The algorithm is seeded by an appropriate model pump field entering from one side of the nonlinear crystal and homogeneously spatially-distributed signal and idler fields with powers corresponding to a half photon per mode and with random phases, representing quantum noise. During the field evolution, we checked that the Manley–Rowe invariants were preserved to the accuracy of better than 10^5, even after numerically evolving (18) over 6×10^6 time steps. The results obtained with our method were compared with those obtained using a 4th-order finite-difference scheme. For the chirped input pump pulse, where differentiability is ensured, the same quantitative results are obtained with both methods. The latter scheme, however, is not adapted for incoherent pulses.

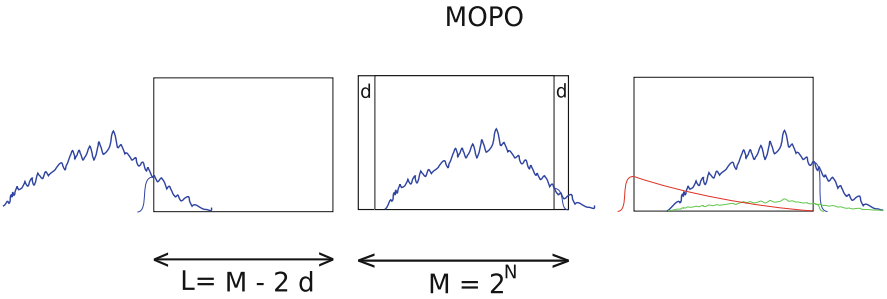

Fig. 11 Scheme for the Runge–Kutta-FFT numerical model for the backward mirrorless OPO

5.2 *BMOPO I Actual Experimental Realization*

The QPM three-wave resonant coupling in the experimental achieved backward MOPO of type I in a bulk PPKTP crystal [24–26] correspond to the following parameters [47]:

$$\lambda_p = 0.8616\,\mu\text{m};\ n_p = 1.8400;\ v_p/c = 0.5269;\ \beta_{2,p} = 0.2473\ \text{ps}^2/\text{m}$$
$$\lambda_s = 1.2179\,\mu\text{m};\ n_s = 1.8243;\ v_s/c = 0.5372;\ \beta_{2,s} = 0.1343\ \text{ps}^2/\text{m}$$
$$\lambda_i = 2.9457\,\mu\text{m};\ n_i = 1.7806;\ v_i/c = 0.5334;\ \beta_{2,i} = -0.6413\ \text{ps}^2/\text{m}$$

where

$$\Lambda_{QPM} = \left[\frac{n_p}{\lambda_p} - \frac{n_s}{\lambda_s} + \frac{n_i}{\lambda_i}\right]^{-1} = 0.8012\,\mu\text{m}$$
$$\Delta v/v_s = |v_p - v_s|/v_s = 0.0195,$$

and the counter-propagation interaction corresponds to Fig. 1b. Let us show the dynamical behaviours for a BMOPO of 6.5 mm length pumped with a 54 ps pulse duration of $I_p = 2.34\,\text{GW/cm}^2$ maximum intensity. BMOPO operation in a PPKTP crystal of period $\Lambda = 800$ nm is simulated with a linearly-chirped pump pulse with a central wavelength of 861.7 nm. The input pump amplitude is chosen to be Gaussian and given by

$$\mathbf{A_p}(x = 0, t) = \mathbf{A_p^0}\exp[i\phi_p(t)]\exp\{-2\ln 2[(t - t_0)/\Delta t_0]^2 \qquad (19)$$

The spectral and temporal shapes of the pulse are determined by the phase modulation, $\phi_p(t)$ and the FWHM temporal length, Δt_0. With a linear chirp, the phase modulation is quadratic in time, $\phi_p(t) = \alpha_2 t^2$, where the value of the chirp parameter $\alpha_2 = -0.244\,\text{rad/ps}^2$ is chosen to obtain the chirp rate of $d\omega_p/dt = -0.49\,\text{rad/ps}^2$. With this chirp, a temporal intensity FWHM of $\Delta t_0 = 52$ ps gives a FWHM spectral width of 4.04 THz.

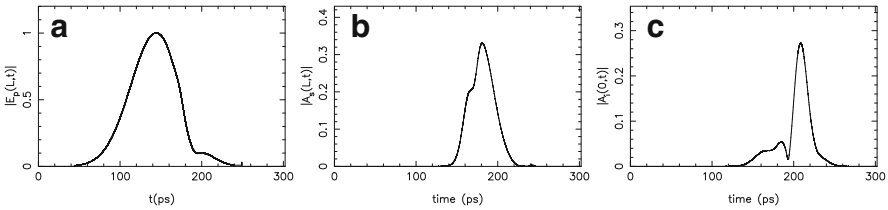

Fig. 12 BMOPO I: Temporal field amplitude output of pump (**a**), signal (**b**) and counterpropagating idler (**c**) waves in the achieved experimental configuration [26], for a pump of 52 ps temporal duration and 4.04 THz chirped pump bandwidth

As the pump pulse enters the crystal, a forward signal and a backward idler are generated with similar spectral characteristics as those obtained in the experiment [26]. The temporal pump output amplitude and output co-propagating signal and backward idler amplitudes are illustrated in Fig 12. The pump and the parametric spectra at the pump intensity of 2.34 GW/cm^2 are illustrated in Fig 13, showing a backward idler with a spectral width of $\Delta\nu_i = 51$ GHz, which is narrow compared to the widths of the pump, $\Delta\nu_p = 4.04$ THz, and the forward signal, $\Delta\nu_s = 1.78$ THz. By integrating the spectra, it is found that the conversion into parametric waves here is $I_s(L)/I_p(0) = 0.036$ for the signal and $I_i(0)/I_p(0) = 0.014$ for the idler. As expected from the convection-induced phase-locking mechanism, the phase modulation in the pump is essentially transferred to the forward signal, while the phase of the backward idler is approximately constant.

By running simulations with pump pulses of different spectral widths, it is observed that the conversion efficiency decreases as the pump spectrum broadens when the group-velocity difference between the forward wave and the pump is the same as in the experiments. This behavior is due to the nonzero convective velocity $|v_p - v_s|$ of the co-moving waves, i.e. a finite temporal walk-off, which makes the spectral components in the signal move past those in the pump. On the other hand, for perfect group-velocity matching ($v_s = v_p = 0$), there is no temporal walk-off and the conversion efficiency is constant as the pump spectrum broadens, since the pump and the signal move at the same velocity. The pump depletion, $1 - I_p(L)/I_p(0)$, and the conversion efficiencies into signal, $I_s(L)/I_p(0)$, and idler, $I_i(0)/I_p(0)$, were systematically investigated for linearly-chirped Gaussian pump pulses where the temporal pulse shape was held constant with a FWHM length of 52 ps and a peak intensity of 2.57 GW/cm^2. The spectral width was controlled by varying the chirp parameter α_2 from 0 to -0.30 rad/ps^2, corresponding to a FWHM bandwidth from the transform limit up to about 5 THz. In Fig. 14, the three lower curves show how the pump depletion and the conversion efficiency into signal and idler decrease as the pump bandwidth increases. Each point on the curves corresponds to a mean value over a set of simulations with random initial phases, i.e. the phase modulation is given by $\phi(t) = \alpha_2 t^2 + \phi_0$, where ϕ_0 is a random number. The efficiency is slightly different for each choice of ϕ_0 and the value typically varies within the vertical bar of the plus signs associated to each point. At some

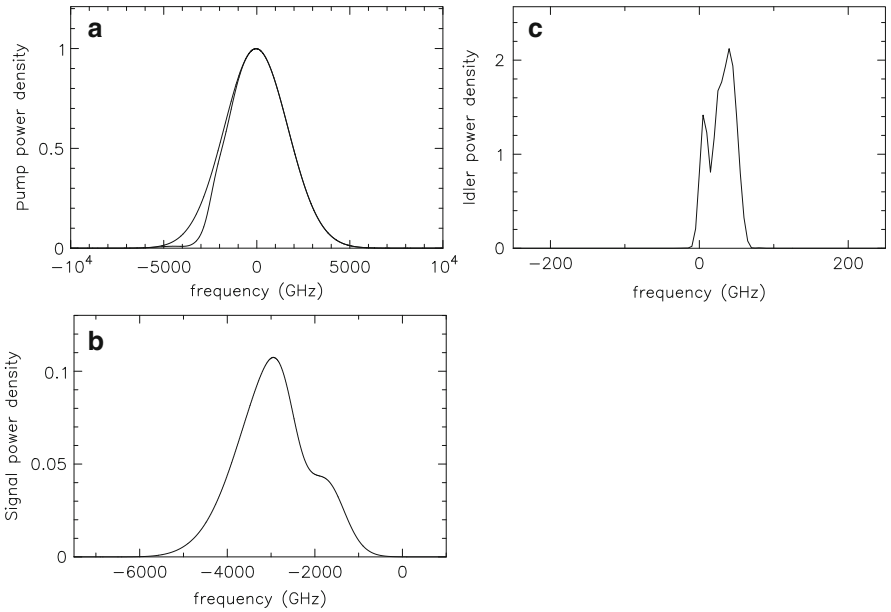

Fig. 13 (**a**) Undepleted input and depleted output pump spectrum of $\Delta\nu_p = 4.04\,\text{THz}$, (**b**) the forward signal spectrum with $\Delta\nu_f = 1.78\,\text{THz}$ and (**c**) the backward idler spectrum with $\Delta\nu_b = 51\,\text{GHz}$

points, there is an apparent increase in the efficiency with an increased pump bandwidth, which is due to the limited set of random initial phases ($n = 6$) used for the averaging. However, the main behavior is that a broader pump input spectrum decreases the efficiency of the BMOPO process when the group-velocities of the forward wave and the pump are not matched. The upper curve in Fig. 14 shows the pump depletion when the group velocities of the pump and the forward propagating wave are matched, $v_p = v_s$. This gives a direct comparison between the two cases and shows that the nonlinear interactions in a BMOPO become more efficient in the case of exact group-velocity matching. Furthermore, the pump depletion (or the conversion efficiency) then also becomes rather insensitive to the spectral quality of the pump, due to the absence of temporal walk-off.

5.3 Incoherent Pump Pulse

One question that arises is if a BMOPO can operate when it is pumped with incoherent pulses. It is not obvious that such pulses can generate a spectrally-narrow backward-propagating parametric wave which is a characteristic feature of a BMOPO. In the conventional co-propagating configuration, the generation of a

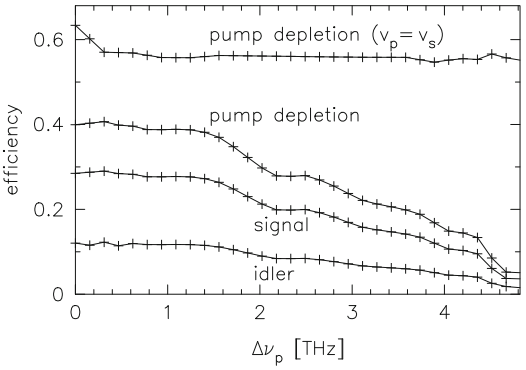

Fig. 14 Pump depletion, $1-I_p(L)/I_p(0)$, and conversion efficiencies for the signal, $I_s(L)/I_p(0)$, and for the idler, $I_i(0)/I_p(0)$, in the MOPO as function of the pump bandwidth for linearly-chirped pulses at the pump intensity of $I_p = 2.57\,\mathrm{GW/cm^2}$. The three *lower curves* correspond to the experimental condition, $|v_s - v_p|/v_s = 0.0195$, which clearly show a decrease in the efficiency as the pump bandwidth increases. The *upper curve* shows that the pump depletion is essentially independent of the pump bandwidth when $v_s - v_p = 0$

temporally coherent wave from a temporally incoherent pump has been numerically studied for i.e. parametric down-conversion [48] and has been experimentally verified for second-harmonic generation [49]. In order to answer the question in the counterpropagating BMOPO configuration, we used a pump pulse with randomly distributed phase variations, characterized by an exponential correlation function,

$$\left\langle \mathbf{A_p}(x=0,t'+t)\mathbf{A_p^*}(x=0,t)\right\rangle = \left|\mathbf{A_p}\right|^2 \exp\left(-|t|/\tau_c\right), \tag{20}$$

where $\tau_c = 1/\pi\Delta\nu_p$ is the correlation time. More precisely, we use a numerical scheme to generate a Gaussian spectrum with randomly-distributed phases and a small random variation in the amplitude, which simulates a real laser output where the amplitude exhibits small fluctuations over its Gaussian shape. In order to obtain a well-behaved Gaussian input, we impose a Gaussian profile on the Fourier spectrum and the pump amplitude is entered as the inverse Fourier transform.

As a result of the phase-locking mechanism, the transfer of phase modulation to the forward wave becomes more efficient when the group velocities of the pump and the forward parametric wave are exactly matched [39], which was already proposed for c.w. pumped forward OPO's [40–42]. This was shown in Fig. 14. For z-polarized waves in PPKTP, matching of the group velocities can be achieved by designing the experiment so that the pump and the forward wave are on different sides of the maximum on the group-velocity curve: the singly backward wave may be now the signal, the co-propagating pump and idler waves satisfying $v_p = v_i$.

However, the combination of exact group-velocity matching and quasi-phase matching requires either a very short QPM period, which is hard to fabricate,

or that the pump wavelength is substantially longer, which increases the BMOPO threshold. One example of a set of wavelengths that fulfill group-velocity matching are

$$\lambda_p = 1.0600\,\mu\text{m};\ n_p = 1.8298;\ v_p/c = 0.5341;\ \beta_p = 0.1752\ \text{ps}^2/\text{m}$$
$$\lambda_s = 1.6764\,\mu\text{m};\ n_s = 1.8129;\ v_s/c = 0.5405;\ \beta_s = 0.0290\ \text{ps}^2/\text{m}$$
$$\lambda_i = 2.8826\,\mu\text{m};\ n_i = 1.7826;\ v_i/c = 0.5341;\ \beta_i = -0.5784\ \text{ps}^2/\text{m}$$

where

$$\Lambda_{QPM} = \left[\frac{n_p}{\lambda_p} + \frac{n_s}{\lambda_s} - \frac{n_i}{\lambda_i}\right]^{-1} = 0.4567\,\mu\text{m}$$
$$\Delta v/v_s = |v_p - v_i|/v_s = 0$$

We perform the numerical dynamics from (18) with $(-v_s, +v_i)$. Around the point of group-velocity matching, the BMOPO becomes more efficient and the spectral quality of the pump can be reduced without a large effect on the conversion efficiency. This is illustrated by running a simulation with a stochastic pump with a FWHM temporal length of 50 ps and where the spectral width is increased to 23 THz. At the pump intensity of 3.5 GW/cm^2, the results are shown in Figs. 15 and 16. The BMOPO starts oscillating after $t - t_0 = 60$ ps and the conversion efficiencies are $I_b(0)/I_p(0) = 0.025$ for the signal and $I_f(L)/I_p(0) = 0.015$ for the idler. Due to the group-velocity matching, the bandwidth of the backward signal is only 23 GHz. This value is significantly smaller than the bandwidth of backward wave in Fig. 13c, even though the pump bandwidth here has been increased by almost a factor of 6. In the case of group-velocity matching under the stated operational conditions, the spectral width of the backward-generated wave is reduced by a factor of 1,000 compared to the width of the input pump spectrum. The random phase fluctuations in the pump are efficiently transferred to the forward idler, which obtains a spectral width of 10 THz.

For the experimental verification of BMOPO operation with an incoherent pump, a laser source is required that generates sub-ns pulses of energies around 100 μJ, at the same time as the pulses are incoherent. Good candidates for such a pump source are figure-eight fiber lasers operating in noise-like pulse mode with pulse lengths around 1 ns [50], which could be amplified to the required energies in fiber amplifiers.

5.4 Convection-Induced Phase-Locking Mechanism

The coherent properties of the parametric three-wave interaction driven from an incoherent pump has been the object of an analytical study where the autocorrelation functions are mathematically evaluated in the presence of dispersion [39] and the convection-induced phase-locking mechanism has been proposed for forward

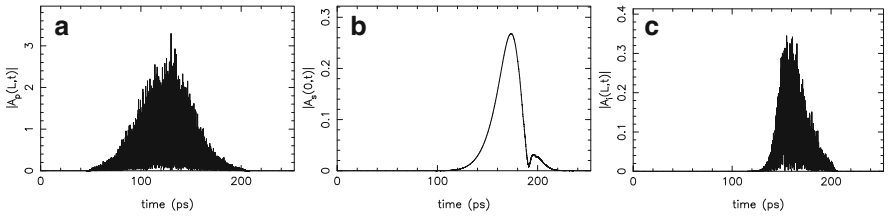

Fig. 15 Temporal evolution of the amplitudes in a BMOPO with the interacting wavelengths corresponding to exact group-velocity matching, pumped with stochastic phase modulated pulses and a bandwidth of $\Delta\nu_p = 23\,\text{THz}$: (**a**) the forward pump, (**b**) the backward signal, and (**c**) the forward idler

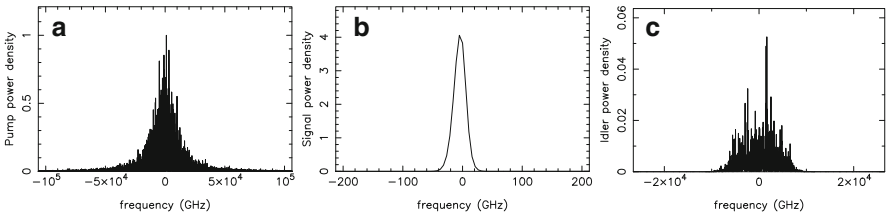

Fig. 16 (**a**) Incoherent pump spectrum with a bandwidth of $\Delta\nu_p = 23\,\text{THz}$, (**b**) the backward signal spectrum with $\Delta\nu_s = 23\,\text{GHz}$, (**c**) the forward idler spectrum with $\Delta\nu_i = 10\,\text{THz}$. Coherence gain of 1,000

OPO's configurations [40–42]. Let us present here some simple analytical arguments enlightening the convection-induced phase-locking mechanism from (18) for the singly backward signal configuration [case (c) of Fig. 1], Let us assume the dispersionless case ($\beta_j = 0$), $\sigma_s = \sigma_i = \sigma_p/2 = \sigma$, and the linear undepleted pump limit with $\gamma_p = 0$.

The incoherent pump may be modeled by a stationary single-variable stochastic function $A_p(z)$ of autocorrelation function

$$\frac{\langle A_p(z-z')A_p^*(z')\rangle}{|A_p(0)|^2} = \exp(-\frac{|z|}{\lambda_c})$$

with a coherence length λ_c in the frame traveling at its group velocity v_p,

$$z = x - v_p t,$$

the correlation time being $\tau_c \simeq 1/\pi\Delta\nu_p$, where $\Delta\nu_p$ is the incoherent (broad)-bandwidth of the pump spectrum. The role of convection in the coherence of the generated waves A_s and A_i may be analyzed by integrating the third equation (18) along the characteristic of the idler wave. Then, the second equation (18) yields

$$DA_s = \sigma^2 \int_0^t e^{-\gamma_i(t-t')} A_p(z) A_p^*(z') A_s(x',t')dt'$$

where

$$D = \partial/\partial t - v_s \partial/\partial x + \gamma_s$$

$$z' = z - (v_i - v_p)(t - t') \; ; \;\; x' = x - v_i(t - t')$$

If $v_i = v_p$ we have $z' = z$ and we can extract the pump amplitudes from the integral

$$A_p(z) A_p^*(z') = |A_p(z)|^2,$$

showing that the signal dynamics is independent of the pump phase fluctuations $\Phi_p(z)$.

This means that the rapid random phase fluctuations of the pump do not affect the signal which undergoes slow phase variations and thus evolves towards a highly coherent state during its parametric amplification.

Let us now consider the idler wave from the third equation (18):

$$A_i(x,t) = \sigma \int_0^t e^{-\gamma_i (t-t')} A_p(z') A_s^*(x', t') dt'.$$

When $v_i = v_p$ we have $z' = z$ and $A_p(z')$ becomes independent of t' which leads to an idler amplitude A_i proportional to the pump amplitude A_p i.e., the idler field absorbs the noise of the co-moving pump field. Note that this *pump-idler phase-locking mechanism* does not require an exact matching of the group-velocities $v_i = v_p$. It is indeed sufficient that

$$|v_i - v_p| \ll \lambda_c \gamma_i = v_p t_c \gamma_i,$$

to remove the pump field from the integral so that the idler field follows the pump fluctuations. This phase-locking mechanisms may be demonstrated in realistic experimental configurations as studied in details in [39].

6 Conclusions

We have shown by a stability analysis of the non-degenerate backward OPO where both the signal and idler fields propagate backward with respect to the direction of the pump field that the inhomogeneous stationary solutions regularly bifurcate towards a time-dependent oscillatory solution contrarily to the degenerate case. We obtain a regular Hopf bifurcation for a critical interaction length L_{crit}, which is finite only if a finite group velocity delay between the signal and the idler waves is taken into account.

This result has been confirmed by numerical simulations of the nonlinear dynamic equations, and an excellent agreement has been obtained near the degenerate configuration. Above L_{crit} self-structuration of symbiotic backward solitary waves—of some ps temporal duration—takes place. The finite temporal walk-off

between the backscattered signal and idler waves also ensures the stability of the solitary waves. These short stable and coherent pulses could be very interesting for optical telecommunication. However, the susceptibility inversion grating of sub-μm period required for QPM in the nonlinear quadratic materials is still a technological challenge.

We have also considered mirrorless optical parametric oscillation in a PPKTP crystal, first by using linearly-chirped pump pulses with bandwidths of up to 4 THz in order to simulate recent experiments, and second by using highly incoherent pump pulses up to 23 THz bandwidth. It has been shown that the spectral bandwidth of the backward-generated pulse is more than two orders of magnitude narrower than that of the pump. In a general situation, the gain in temporal coherence of the backward-generated wave is limited by the group-velocity mismatch between the pump and the forward-generated wave. This mismatch also limits the conversion efficiency in the BMOPO. Numerically, we proved that the same conclusions are valid regardless of the nature of the phase modulation present in the pump wave by simulating operation of a BMOPO pumped by waves containing stochastic phase distributions. Moreover, we propose a generic BMOPO configuration where exact group-velocity matching can be achieved, thereby maximizing the gain in temporal coherence in the backward-propagating wave and making the efficiency of the device insensitive to the nature of the phase modulation present in the pump wave. This opens up an intriguing possibility for narrowband generation in MOPOs pumped with incoherent beams, e.g. derived from several lasers. Albeit the realization of such a MOPO requires QPM crystals which are slightly beyond the state-of-the-art of the current poling technology, the requirements are not unrealistic and can be met with the continuing development in fabrication techniques of submicrometer-periodicity nonlinear crystals. Improved fabrication techniques could also lead to the possibility of poling longer crystals. As the threshold intensity scales inversely to the square of the length of the structured region, an increase of this length from 6.5 to 18 mm results in a threshold intensity around 100 MW/cm^2, which is comparable to that in conventional co-propagating PPKTP OPOs (cf. Fig. 1a).

Acknowledgement The authors thank G. Strömqvist, V. Pasiskevicius and C. Canalias for stimulating discussions. They also acknowledge the GDR PhoNoMi2 no. 3073 of the CNRS (Centre National de la Recherche Scientifique) devoted to Nonlinear Photonics in Microstructured Materials.

References

1. Armstrong, J.A., Jha, S.S., Shiren, N.S.: IEEE J. Quant. Elect. **QE-6**, 123–129 (1970)
2. Nozaki, K., Taniuti, T.: J. Phys. Soc. Jpn. **34**, 796–800 (1973)
3. Kaup, D.J., Reiman, A., Bers, A.: Rev. Mod. Phys. **51**, 275–309 (1979)
4. Drühl, K., Wenzel, R.G., Carlsten, J.L.: Phys. Rev. Lett. **51**, 1171 (1983)
5. McCall, S.L., Hahn, E.L.: Phys. Rev. Lett. **18**, 908 (1967)

6. Chiu, S.C.: J. Math. Phys. **19** 168–176 (1978)
7. Montes, C., Mikhailov, A., Picozzi, A., Ginovart, F.: Phys. Rev. E **55**, 1086–1091 (1997)
8. Montes, C., Picozzi, A., Bahlouol, D.: Phys. Rev. E **55**, 1092–1105 (1997)
9. Picholle, E., Montes, C., Leycuras, C., Legrand, O., Botineau, J.: Phys. Rev. Lett. **66**, 1454 (1991)
10. Montes, C., Mamhoud, A., Picholle, E.: Phys. Rev. A **49**, 1344 (1994)
11. Montes, C., Bahloul, D., Bongrand, I., Botineau, J., Cheval, G., Mamhoud, A., Picholle, E., Picozzi, A.: J. Opt. Soc. Am. B **16**, 932 (1999)
12. Botineau, J., Cheval, G., Montes, C.: Opt. Comm. **257**, 319–33 (2006)
13. Montes, C.: In: Akhmediev, N., Ankiewicz, A. (eds.) Dissipative Solitons: From Optics to Biology and Medicine. Lecture Notes in Physics (LNP), vol. 751, pp. 221–260. Springer, Berlin (2008)
14. Picozzi, A., Hælterman, M.: Opt. Lett. **23**, 1808 (1998)
15. Picozzi, A., Haelterman, M.: Phys. Rev. Lett. **84**, 5760–5762 (2000)
16. Montes, C., Picozzi, A., Hælterman, M.: In: Zakharov, V.E., Wabnitz, S. (eds.) Optical Solitons: Theoretical Challenges and Industrial Perspectives. Les Houches Workshop, Sept. 28-Oct. 2, 1998, pp. 283–292. EDP Springer, New York (1999)
17. Montes, C.: In: Porsezian, K., Kuriakos, V.C. (eds.) Optical Solitons: Theory and Experiments, Lectures Notes in Physics (LNP), vol. 613, pp. 353–371. Springer, Berlin (2003)
18. Durniak, C., Montes, C., Taki, M.: J.Opt. B Quant. Semiclass. Opt. **6**, S241–S249 (2004)
19. Montes, C., Picozzi, A., Durniak, C., Taki, M.: Eur. Phys. J. Spec. Top. **173**, 167–191 (2009)
20. Matsumoto, M., Tanaka, K.: IEEE J. Quant. Electron. **31**, 700 (1995)
21. Ding, Y.J., Khurgin, J.B.: IEEE J. Quant. Electron. **32**, 1574–1582 (1996)
22. Kang, J.U., Ding, Y.J., Burns, W.K., Melinger, J.S.: Opt. Lett. **22**, 862 (1997)
23. D'Alessandro, G., St. Russell, P., Wheeler, A.A.: Phys. Rev. A **55**, 3211 (1997)
24. Canalias, C., Pasiskevicius, V.: Nat. Photonics **1**, 459–462 (2007)
25. Strömqvist, G., Pasiskevicius, V., Canalias, C., Montes, C.: Phys. Rev. A **84**, 023845-1-4 (2011)
26. Strömqvist, G., Pasiskevicius, V., Canalias, C., Aschieri, P., Picozzi, A., Montes, C.: J. Opt. Soc. Am. **29**, 1194–1202 (2012)
27. Picozzi, A., Hælterman, M.: Phys. Rev. Lett. **86**, 2010 (2001)
28. Montes, C., Durniak, C., Taki, M., Picozzi, A.: Opt. Comm. **216**, 419–426 (2003)
29. Morozov, S.F., Piskunova, L.V., Sushchik, M.M., Freidman, G.I.: Sov. J. Quant. Electron. **8**, 576 (1978)
30. Craik, A.D.D., Nagata, M., Moroz, I.M.: Wave Motion **15**, 173 (1992)
31. Armstrong, J.A., Bloembergen, N., Ducuing, J., Pershan, N.: Phys. Rev. **127**, 1918–1939 (1962)
32. Busacca, A.C., Sones, C.L., Eason, R.W., Mailis, S.: Appl. Phys. Lett. **84**, 4430–4432 (2004)
33. Dmitriev, V.G., Gurzadyan, G.G., Nikogosyan, D.N.: Handbook of Nonlinear Optical Crystals. 74 for $LiNbO_3$ and 103 for $KTiOPO_4$. Springer, Berlin (1991)
34. Bava, G.P., Montrosset, I., Sohler, W., Suche, H.: IEEE J. Quant. Electron. **QE-23**, 42 (1987)
35. Suche, H., Sohler, W.: Integrated optical parametric oscillators (invited). Optoelectron. Devices Technol. **4**(1), 1–20 (1989)
36. Arbore, M.A., Fejer, M.M.: Opt. Lett. **22**, 151–153 (1997)
37. Hofmann, D., Herrmann, H., Schreiber, G., Grundkötter, W., Ricken, R., Sohler, W.: Continuous-wave mid-infrared optical parametric oscillators with periodically poled Ti:$LiNbO_3$ waveguide. In: 9th European Conference on Integrated Optics and Technical Exhibition ECIO'99, p. 21 (EOS - European Optical Society) (1999)
38. Hofmann, D., Herrmann, H., Schreiber, G., Haase, C., Grundkötter, W., Ricken, R., Sohler, W.: Nonlinear Guided Waves and Their Applications, FC2-1-3, p. 465 . Optical Society of America, Washington, DC (1999)
39. Picozzi, A., Montes, C., Hælterman, M.: Phys. Rev E **66**, 056605-1-14 (2002)
40. Montes, C., Picozzi, A., Gallo, K.: Opt. Comm. **237**, 437–449 (2004)
41. Picozzi, A., Aschieri, P.: Phys. Rev. E **72**, 046606-1-12 (2005)
42. Montes, C., Grundkötter, W., Suche, H., Sohler, W.: J. Opt. Soc. Am. **24**(11), 2796–2806 (2007)

43. Harris, S.E.: Appl. Phys. Lett. **9**, 114 (1966)
44. Shi, W., Ding, Y.J.: Opt. Lett. **30**, 1861–1863 (2005)
45. Smith, S.P., Zarinetchi, F., Ezekiel, S.: Opt. Lett. **16**, 393–395 (1991)
46. Montes, C., Aschieri, P., Picozzi, A., SPIE Proc. **8011**, 801136-1-10 (2011)
47. Kato, K., Takaoka, E.: Appl. Opt. **41**, 5040 (2002)
48. Piskarskas, A., Pyragaite, V., Stabinis, A.: Phys. Rev. A **82**, 053817 (2010)
49. Stabinis, A., Pyragaite, V., Tamošauskas, G., Piskarskas, A.: Phys. Rev. A **84**, 043813 (2011)
50. Özgören, K., Öktem, B., Yilmaz, S., Ilday, F.Ö., Eken, K.: Opt. Express **18**, 17647–17652 (2011)

Rivulet Structures in Falling Liquid Films

B. Scheid

1 First Visit at the Instituto Pluridisciplinar

April 1st 1998 was the day I started my Ph.D. thesis (not a joke!) supervised by Jean Claude Legros and Pierre Colinet. I do not remember when exactly I started to hear about Manuel G. Velarde (the G. is for García that should never be omitted!), but I bet it was very soon after the beginning. Pierre was finishing his postdoc with Manuel and he always looked very happy (and somehow tired) each time he came back from Madrid. So one day, I had the opportunity to visit a friend who lived there and I decided to stop by the Instituto Pluridisciplinar to check by myself what was so unique with this place. Of course my visit was coordinated by Pierre and Manuel. The goal was to meet Jan Skotheim and Uwe Thiele and discuss about the experiments I was doing at that time in Brussels with Oleg A. Kabov. Jan was a student coming from MIT and Uwe was a postdoc. We talked about rivulet structures arising in localized heated falling liquid films, as shown in Fig. 1. This collaboration lead us to a nice JFM paper on the stability analysis of a bump arising at the upper edge of the heater prior to the rivulet instability [1].

I always remember the analogy Manuel did between rivulet formation and crowd dynamics: if you have a group of people running in one direction (the hydrodynamic flow) and another group of people running in the perpendicular direction (the thermocapillary flow), we will soon see the emergence of auto-organized structure (rivulets) in which people will preferentially run to minimize their loss of energy…

That was my first experience at the Instituto Pluridisciplinar.

B. Scheid (✉)
TIPs, Université Libre de Bruxelles C.P. 165/67, 1050 Brussels, Belgium
e-mail: bscheid@ulb.ac.be

R.G. Rubio et al. (eds.), *Without Bounds: A Scientific Canvas of Nonlinearity and Complex Dynamics*, Understanding Complex Systems,
DOI 10.1007/978-3-642-34070-3_35,

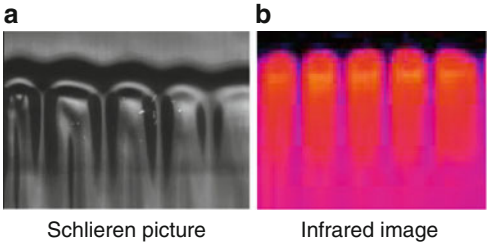

Fig. 1 Experimental images showing rivulet structures arising in a locally heated falling liquid film: the liquid arrives on a heated zone such as its surface tension decreases. A thermocapillary stress drives liquid along the interface against gravity, what produces a bump. Above criticality, this bump becomes unstable and breaks into rivulets as for the tears of wine

2 A Great Experience in Madrid

January 2002, I arrived in Madrid to work on my Ph.D. thesis with Manuel in the frame of the Marie-Curie European Network ICOPAC. I was told that Manuel usually prefers hiring postdocs than Ph.Ds. so I had to prove him he made the right choice. I did not know what to expect exactly but I felt like it was a great opportunity for me to work there. I took the office in which Jan and Uwe were sited 2 years earlier. It was facing the mountains around Madrid, very inspiring! On my desk was the thesis of Christian Ruyer-Quil. I didn't know about his work before but soon after I opened it, I understood that it was very important for the course of my own Ph.D. The first discussion I had with Manuel on the blackboard lasted only 5 min. He asked me to reschedule a meeting after changing the way I was presenting my problem. I had to use arguments! All the other meetings lasted much longer…

We were modeling wave dynamics in heated falling liquid films, with the aim to understand the occurrence of rivulet structure, not only with localized heating but also in the more general case of uniform heating. Since Manuel and Christian had already started discussing that problem, I naturally went to the FAST laboratory for 6 months with another Marie-Curie fellowship, before I came back to Madrid for 6 more months in 2003. That was probably one of the most stimulating years of my scientific career; traveling between Paris, Madrid and Brussels.

In August 2003, Manuel organized a crucial meeting with Christian, Serafim Kalliadasis and Philip Trevelyan. We spent a week during which I presented all the results of my Ph.D. that I was about writing. By the end of the week, we decided to prepare a book all together. That was the beginning of another great adventure.

3 The Book

Initially, we thought that the book could be finalized in about 2 years. It was published in 2012 [2]! So you never know, but what is sure is that Manuel was the driving force, putting us together several times in Madrid for 1 or 2 weeks

between 2003 and 2006. I keep an incredible souvenir of the productive time spent at the Instituto with Manuel, Christian and Serafim. The experience of working simultaneously on a joint project is unique and the quiet atmosphere at the Instituto plus the Madrileñan climate surely helped significantly.

The last chapter of the book is precisely about the modeling of uniformly heated falling liquid film in 2D and in 3D. Let us now recall the main step of this modeling, since it is representative of the joined effort we have all put together during this fruitful Madrileñan collaboration.

We proposed a model of four evolution equations for the film thickness h, the streamwise and transverse flow rates averaged across the film, q and p respectively, and the interfacial temperature θ, all dependent only on time t and in-plane coordinates (x,z), with x along the main flow and z in the spanwise direction. Slow time and space modulations of the basic flat-film state have been assumed, namely $\partial_t, \partial_x, \partial_z \sim \epsilon \ll 1$ where ϵ is an ordering parameter. Having posed self-similar profiles in terms of the natural similarity variable $\overline{y} = y/h$ (y being the cross-stream coordinate), namely a parabolic profile for the velocity $f_0(\overline{y}) = \overline{y} + (1/2)\overline{y}^2$ and a linear profile for the temperature $g_0(\overline{y}) = \overline{y}$, the model has been obtained by averaging along the thickness the momentum and energy equations with weights taken equal to f_0 and g_0, respectively, like in the Galerkin method (details of the procedure and results are given in [3, 4] for the 2D case). Provided the no-slip condition applies on the wall and the viscous stresses balancing the (thermo)capillary effects at the free surface, the average momentum equation at order ϵ, for the 3D case, has the form

$$\partial_t \mathbf{q} = \frac{5}{6} h\, \mathbf{i} - \frac{5}{2}\frac{\mathbf{q}}{h^2} - \frac{5}{4}\mathrm{Ma}\boldsymbol{\nabla}\theta + \frac{5}{6}\Gamma h \boldsymbol{\nabla}(\boldsymbol{\nabla}^2 h) + \frac{5}{6}\mathrm{Ct}\, h \boldsymbol{\nabla} h + \frac{9}{7}\left(\frac{\mathbf{q}\cdot\boldsymbol{\nabla} h}{h^2} - \frac{\mathbf{q}}{h}\cdot\boldsymbol{\nabla}\right)\mathbf{q} - \frac{8}{7}\frac{\boldsymbol{\nabla}\cdot\mathbf{q}}{h}\,\mathbf{q}\,, \tag{1}$$

where $\boldsymbol{\nabla} = (\partial_x, \partial_z)$, $\mathbf{q} = (q, p)$ and $\mathbf{i}$ is the streamwise unit vector. The first five terms of the r.h.s. account for the gravity acceleration, viscous shear stress, Marangoni effect, surface tension and hydrostatic pressure, respectively, and the remaining terms are due to inertia. Then, provided the temperature field is uniform at the wall and satisfies the Newton's law of cooling at the free surface, the average energy equation at order ϵ has the form

$$\partial_t \theta = 3\frac{(1 - \theta - \mathrm{Bi} h\theta)}{\mathrm{Pr}\, h^2} + \frac{7}{40}(1-\theta)\frac{\boldsymbol{\nabla}\cdot\mathbf{q}}{h} - \frac{27}{20}\frac{\mathbf{q}\cdot\boldsymbol{\nabla}\theta}{h}\,, \tag{2}$$

where the first term of the r.h.s accounts for the in-depth heat transfer and the remaining terms are due to heat convection. The system is closed by mass conservation

$$\partial_t h + \boldsymbol{\nabla}\cdot\mathbf{q} = 0\,. \tag{3}$$

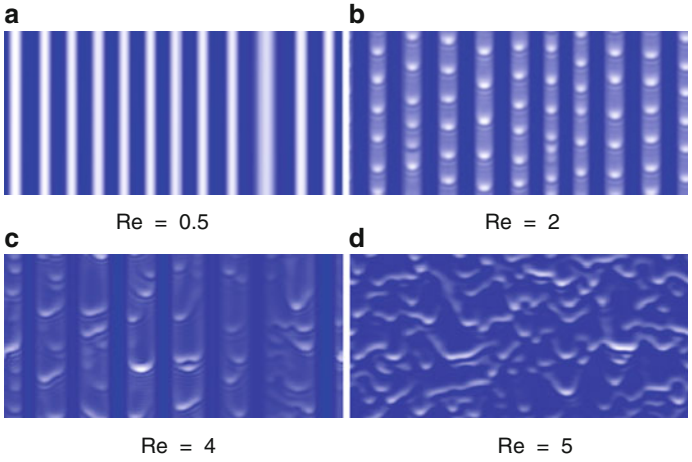

Fig. 2 Simulated wave patterns arising in uniformly heated falling liquid films for various Reynolds numbers. Water properties have been used, with $\Gamma = 3,375$, $\mathrm{Ct} = 0$, $\mathrm{Ma} = 25$ and $\mathrm{Bi} = 0.1$. Snapshots are right before rupture, except for (**d**)

The length scale and time scale are $\ell_\nu = (\nu^2/g\sin\beta)^{1/3}$ and $t_\nu = (\nu/g\sin\beta^2)^{1/3}$, with ν the kinematic viscosity and g the gravitational acceleration. The governing dimensionless groups are the Kapitza number $\Gamma = \sigma\ell_\nu/\rho\nu^2$, the inclination number $\mathrm{Ct} = \cot\beta$, the Marangoni number $\mathrm{Ma} = \gamma\Delta T\ell_\nu/\rho\nu^2$, the Biot number $\mathrm{Bi} = \alpha\ell_\nu/k$ and the Prandtl number $\mathrm{Pr} = \nu/\chi$, with ρ the density, σ the surface tension and $\gamma = -\mathrm{d}\sigma/\mathrm{d}T$ its variation with temperature, β the inclination angle of the wall from the horizontal, ΔT the temperature difference between the wall and the ambient gas, α the heat transfer coefficient at the liquid–gas interface, k the thermal conductivity and χ the thermal diffusivity. The Reynolds and Weber numbers appear implicitly through the thickness of the uniform flat film h_N as $\mathrm{Re} = g\sin\beta h_N^3/3\nu^2$ and $\mathrm{We} = \sigma/\rho g\sin\beta h_N^2$. All numbers are taken of $O(1)$, except $\Gamma \sim \mathrm{We} = O(\epsilon^{-2})$. For isothermal conditions ($\mathrm{Ma} = 0$), the present model reduces to the $O(\epsilon)$-version of the 3D model given in [5], validated against both DNS and experiments. Notice that the coefficients in the momentum and energy equations differ from unity because of the non-uniformity of the base state profiles, precisely represented by f_0 and g_0. These coefficients are necessary to recover the Benney-like equation (see e.g. [6]) through a gradient expansion of the present model in the limit $\mathrm{Re} \ll 1$.

In the case of vertical wall, we have performed simulations whose results are shown in Fig. 2 (see [7, 8] for details). For small Reynolds number ($\mathrm{Re} = 0.5$), the hydrodynamic wave amplitude is negligible as compared to the amplitude of rivulets induced by thermocapillary flow, while for large Reynolds number ($\mathrm{Re} = 5$) the hydrodynamic waves dominate the system and prevent the formation of rivulets. For intermediate Reynolds numbers, there is a region where inertia (hydrodynamic)

and thermocapillary instabilities are equally important. In this region, we found the appearance of large solitary waves channeled by rivulets aligned with the flow.

We were very excited by these results, especially as fluid flow settings where 2D pulses can be stabilized are quite rare. And everyone knows about the interest of Manuel for solitary pulses…

4 Rivulets with Negative Gravity

We also believed that the novelty of the resulting pattern showed in Fig. 2 might very well be generic for systems exhibiting a competition between monotonic and oscillatory (or wave) instabilities with anisotropy (here, due to the direction of the basic flow). In fact another competition of instabilities, embedded in (1), is also possible in case of negative gravity. This is considering an isothermal liquid film flowing underneath an inclined wall. In such a case, the dimensionless number Ct becomes negative, meaning that the hydrostatic pressure plays a destabilizing role, exactly like in the Rayleigh–Taylor instability that breaks a condensed film on a ceiling into an array of droplets. The difference with the pure Rayleigh–Taylor instability is that the flow breaks the symmetry and thus promotes the formation of rivulets, as shown in Fig. 3.

The rivulet structures shown in Fig. 3 can only be obtained for a given range of inclination numbers. This range can be identified by tuning the inclination number such that the contribution of the Rayleigh–Taylor instability to the growth rate of small perturbations is of the same order of magnitude than the contribution of the thermocapillary instability in the case of heated falling film shown in Fig. 2. This argument is inferred from the linear stability analysis of the uniform-film base-state of the system of equations (1)–(3). It consists in imposing a small harmonic disturbance writing

$$h = \overline{h}_N + \eta \exp\{\mathrm{i}\,(k\,x - c\,t) + s\,t)\}\,, \tag{4}$$

where η, k, c and s are real numbers and represent, respectively, the amplitude, the wavenumber, the phase speed and the growth rate of the disturbance; $\overline{h}_N = h_N/\ell_v$ is the dimensionless flat film thickness. Inserting this "normal mode representation" (4) into the two-dimensional form of (1)–(3) and linearizing in η yield the linear phase speed and growth rate:

$$c_{\mathrm{L}} = \overline{h}_N^2 \quad \text{and} \quad s = k^2\overline{h}_N^3\left(\frac{2}{15}\overline{h}_N^3 - \frac{1}{3}C\,t + \frac{1}{2}\frac{\mathrm{Bi\,Ma}}{\overline{h}_N(1+\mathrm{Bi}\overline{h}_N)^2} - \frac{1}{3}\Gamma,k^2\right). \tag{5}$$

The surface waves will grow for $s > 0$, i.e. for disturbance wavenumbers smaller than the critical (cut-off) wavenumber k_c obtained for $s = 0$. In (5), one can see that a negative $C\,t$ will be destabilizing with the same contribution to the growth rate than in the case of a vertical heated wall if $C\,t \sim$ BiMa, provided $\overline{h}_N \sim 1$. The angle we finally found this way to obtain rivulet structures is $\beta = 160°$, or Ct $= -2.75$.

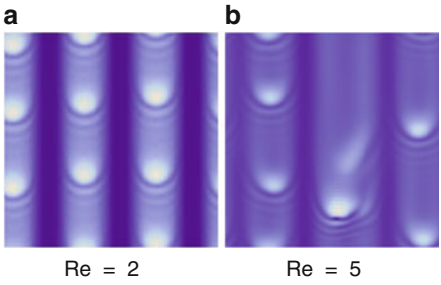

Fig. 3 Simulated wave patterns arising in falling liquid films flowing underneath an inclined wall. Water properties have been used, with $\Gamma = 3,375$, $\mathrm{Ct} = -2.75$ and $\mathrm{Ma} = 0$

Concerning the dynamics of the wave pattern consisting of solitary pulses riding rivulets, we found a fundamental difference between the rivulets formed by thermocapillary effects and those formed by negative gravity. In the former case, the rivulets grow until the thin film in between ruptures, while in the latter case, rivulet growth seems to saturate and yields stabilized pattern. This is at least what we observe for $\mathrm{Re} = 2$, in Fig. 3a, namely that the wave pattern did not change during a relatively long time. However, for $\mathrm{Re} = 5$, in Fig. 3b, the largest wave hump becomes too heavy to saturate and instead detaches after some time. No stable structure were thus observed in this case. These behaviors and the mechanism of stabilization are subject to further investigations but the aim was too show here that the field of 3D wave pattern in falling films under several configurations is still an active field of research, as illustrated for instance by a recent paper, precisely on falling films flowing down inverted substrates [9].

5 Marvelous Friendships

The aim of the present article was to show how influential has been the role of Manuel in my research activity for more than 10 years. It was not only through direct collaborations and discussions with him but also through the numerous collaborations that he has encouraged, driven by his enthusiasm to put people together in order to solve new problems. The result can not only be measured by the number of joint papers but mostly by the marvelous friendships that come out of all these collaborations. I'm thus infinitely grateful to Manuel for his indefectible support he always reserve to his friends in general and to me in particular.

References

1. Skotheim, J.M., Thiele, U., Scheid, B.: On the instability of a falling film due to localized heating. J. Fluid Mech. **475**, 1–19 (2003)
2. Kalliadasis, S., Ruyer-Quil, C., Scheid, B., Velarde, M.G.: Falling Liquid Films. Applied Mathematical Sciences, vol. 176, p. 440. Springer, London (2012)

3. Ruyer-Quil, C., Scheid, B., Kalliadasis, S., Velarde, M.G., Zeytounian, R.Kh.: Thermocapillary long waves in a liquid film flow. Part 1. Low dimensional formulation. J. Fluid Mech. **538**, 199–222 (2005)
4. Scheid, B., Ruyer-Quil, C., Kalliadasis, S., Velarde, M.G., Zeytounian, R.Kh.: Thermocapillary long waves in a liquid film flow. Part 2. Linear stability and nonlinear waves. J. Fluid Mech. **538**, 223–244 (2005)
5. Scheid, B., Ruyer-Quil, C., Manneville, P.: Wave patterns in film flows: modelling and three-dimensional waves. J. Fluid Mech. **562**, 183–222 (2006)
6. Scheid, B., Ruyer-Quil, C., Thiele, U., Kabov, O.A., Legros, J.C., Colinet, P.: Validity domain of the Benney equation including the Marangoni effect for closed and open flows. J. Fluid Mech. **527**, 303–335 (2005)
7. Scheid, B., Kalliadasis, S., Ruyer-Quil, C., Colinet, P.: Spontaneous channeling of solitary pulses in heated film flows. Europhys. Lett. **84**, 64002 (2008)
8. Scheid, B., Kalliadasis, S., Ruyer-Quil, C., Colinet, P.: Interaction of three-dimensional hydrodynamic and thermocapillary instabilities in film flows. Phys. Rev. E **78**, 066311 (2008)
9. Lin, T.-S., Kondic, L., Filippov, A.: Thin films flowing down inverted substrates: three-dimensional flow. Phys. Fluids **24**, 022105 (2012)

Towards a Theory of Degenerated Solectrons in Doped Lattices: Problems and Perspectives

A.P. Chetverikov, W. Ebeling, and M.G. Velarde

1 Introduction

In the polaron theory developed by Landau, Pekar, Fröhlich, Holstein and others, and successfully used in the study of biomolecules by Davydov, Zolotaryuk and Scott and others [1–7] the self-trapping of the electrons interacting with linear lattice oscillations (phonons) dominates. Davydov exploited the possibility of soliton excitations suitably using the above mentioned nonlinearity. He then identified quasiparticles ("electrosolitons") which move in general with subsonic velocity. Davydov in collaboration with Zolotaryuk also treated the case when the lattice bears a cubic or quartic nonlinearity [3, 5, 7]. This leads to "supersonic electrosolitons", or otherwise "lattice polarons"; excitations growing from the nonlinearity of the lattice itself.

Starting first from semiclassical considerations in several works [8–18] a closely related soliton-mediated form of supersonic charge transfer and electric conduction has been proposed by introducing the concept of "solectron" as a natural extension of both the polaron and the electrosoliton quasiparticles. In the solectron theory the soliton carrier is obtained before an excess electron is added to the system. Classical models and plasma-type Hamiltonians [8–13] and quantum-mechanical models have been studied [14, 18–22]. The quantum theory was developed within the tight-binding approximation (TBA). Besides the general methods which we

A.P. Chetverikov (✉)
Department of Physics, Saratov State University, Astrakhanskaya 83, Saratov 410012, Russia
e-mail: chetverikovap@info.sgu.ru

W. Ebeling
Institut für Physik, Humboldt-Universität Berlin, Newtonstrasse 15, Berlin 12489, Germany
e-mail: ebeling@physik.hu-berlin.de

M.G. Velarde
Instituto Pluridisciplinar, Universidad Complutense, Paseo Juan XXIII, 1, Madrid 28040, Spain
e-mail: mgvelarde@pluri.ucm.es

R.G. Rubio et al. (eds.), *Without Bounds: A Scientific Canvas of Nonlinearity and Complex Dynamics*, Understanding Complex Systems,
DOI 10.1007/978-3-642-34070-3_36, © Springer-Verlag Berlin Heidelberg 2013

developed in some earlier work [11,14–16,18] the quantum theory has been applied to two different kinds of systems:

(a) Conducting polymers, studies of hopping processes in polymers based on a TBA Hamiltonian [14,18,20–26].
(b) One- and two-dimensional plasmas and solid state plasma layers, studies of the diffusivity and the conductivity by using a plasma Hamiltonian and Pauli-type kinetic equations [12,27].

The first line of research was developed in collaboration with Larissa Brizhik, Leonor Cruzeiro, Dirk Hennig, John Kozak, Oliva Cantu Ros, and Gerd Röpke concentrating on analytical and numerical studies of solectron bound states and recently also on bisolectron bound states [21, 22, 25, 26]. The plasma approach was developed with Gerd Röpke [27, 28]. Here we will study hopping transfer of charges and hopping conductivity in plasma layers. We are using a particular method which has been developed recently in the context of applications to plasmas and charged layers in solids [19,27,29–31]. This approach is based on a generalization of the kinetic equations developed already in 1928 by Pauli [32] and the more recently developed Monte Carlo procedures of doing simulations of many particle systems [33]. As we have shown in [27] by using a particular generalization of the kinetic equations of Pauli-type, the excitations and transport processes based on the coupling of the nonlinear lattice excitations to the hopping transport of the charges may be well described by this method. This procedure is particularly useful for studying the influence of nonlinear excitations of the lattice on electric transfer, conduction and other transport properties.

Let us succinctly summarize the state of art and discuss some open tasks:

The solectron concept offers powerful methods to understand and to control the motion of charges in nonlinear atomic lattices. It is in fact a significant generalization of the polaron concept, extending the latter to nonlinear lattices [47]. This is indeed of some importance, since real atomic interactions are never strictly linear, there are always some nonlinear contributions to the atomic interactions.

In our view, so far the most important results with respect to possible practical applications are:

1. Development of tools to manipulate and control the path of charges, including the so-called vacuum-cleaner effect [20, 23, 31]. This is in fact a new way of controlling charges providing a method to overcome the spreading of probability due Schrödinger evolution and bring electrons in a controlled way from point A to point B in a lattice.
2. Studies of pair formation. It was shown that under appropriate conditions solectron pairs may be formed [21–23,25,26,34].
3. Extension of the one-dimensional solectron concept to two dimensions, i.e. the step from chains to layers [28, 30, 31]. One of the results was the detection of high energetic quasi one-dimensional solectrons running in higher-dimensional systems along the crystallographic axes [31].

Problems not yet treated include:

- Studying the influence of density of doping on physical properties [48],
- The study of nonideality effects in diffusion and conductivity,
- The quantitative treatment of percolation effects,
- The study of the influence of Fermion and Boson effects and the role of the Fermi edge (Fermi net in 2d),
- The investigation of Bose–Einstein condensation in solectron/bisolectron systems and their role in eventual superconducting systems.

As far as we can see, all known systems with high conductance—ranging from usual metals to superconducting materials—operate on the basis of degenerate charges. For this reason we will discuss here the problems which arise in generalizing the existing theory of individual solectrons and bisolectrons to many-body thermal systems.

2 The Temperature-Density Phase Plane and Solectronic Degeneration Effects

Our aim is to extend the existing theory at first in a qualitative way to finite densities and to discuss density—as well as temperature effects. Let us start with some estimates for the relative number of thermal solitons per site N_s/N as a function of temperature. There are several theoretical estimates for Toda lattices [35, 36] as well as estimates from computer simulations for Morse lattices [19]. According to the existing estimates the soliton fraction increases with $T^{1/3}$ and has maximum at certain temperature T_0 which may be in the range of a few hundred Kelvin for biomolecules [19]. For estimates we fitted the existing data with the formula

$$\frac{N_s}{N} \simeq \frac{A\tau^{1/3}}{1 + B\tau^5}, \tag{1}$$

where N is the total number of sites, $\tau = k_B T/2D$ and where $A \simeq 0.5$ and $B \simeq 0.1$ are two fitting constants. For fitting we used the results from simulations showing clearly the existence of optimal temperatures for soliton generation [19, 23]. Let us now study the role of electron density. The electron density can be given in several units, the simplest is the so-called relative occupation or fraction ν_e which is defined as the number of sites occupied by an electron relative to the total number of sites

$$\nu_e = \frac{N_e}{N}.$$

Note that in the simplest model, the electrons are always associated to one of the sites. The relative occupation is denoted as doping.

In real systems the fraction or doping may vary within wide limits, however the fraction/doping will in general not exceed the value 0.2, i.e. not more than 20% of sites are occupied (doping fraction). The number density in charges per unit volume

$$n_e = \frac{N_e}{V},$$

where V is the volume may depend on the dimension and the lattice properties. In 1d the density is given by

$$n_e = \frac{N_e}{aN},$$

where N is again the total number of lattice sites and a is the equilibrium lattice spacing. In a 2d triangular quadratic or triangular lattice the density is given by

$$n_e = \frac{N_e}{Na^2}, \qquad n_e = \frac{N_e}{Na^2(2/\sqrt{3})}.$$

Let us denote the number of solectrons by N_{se}. We assume that the number of solectrons and the number of free solitons $N - N_{se}$ are related by a Boltzmann factor.

$$\frac{N_{se}}{N - N_{se}} = \exp\left[-\frac{\epsilon_{se}}{k_B T}\right]. \tag{2}$$

Here ϵ_{se} is the energy gain in forming a solectron. This energy depends on the specific physical conditions. Following Davydov [3], the ground state energy of a strongly supersonic solectron can be estimated at

$$\epsilon_{se} \simeq \frac{v_{se}}{v_{sound}} \frac{m_e}{m_{se}} [eV], \tag{3}$$

where m_{se} and v_{se} are the mass and velocity of the solectron. For appropriate parameter values, this energy could possibly reach 0.1 eV, which is a very high value. Presumably the above given estimate is an upper bound. In our computer simulations with Morse lattices having a potential well of value D we observe solectrons in a temperature range of 0.1–1 D. Assuming wells of order 0.1–0.5 eV we arrive at temperature intervals of 0.01–0.1 eV. In the following we will assume that the ground state energy is around 0.01 eV. By using this and two smaller values for the binding energy we can estimate the fraction of solectrons as a function of temperature and density. The result is shown graphically in Fig. 1. Not that by using higher values for the binding energy, the densities of solectrons are increasing.

We will now estimate the effects of degeneration assuming that the charges are electrons or holes and are, as well as the corresponding solectrons, Fermions. Systems of Fermions show degeneration effects, if the thermal de Broglie wave length of the charges is about the distance between them. That means the degeneration effects of the charges will begin to play a role at densities satisfying the condition

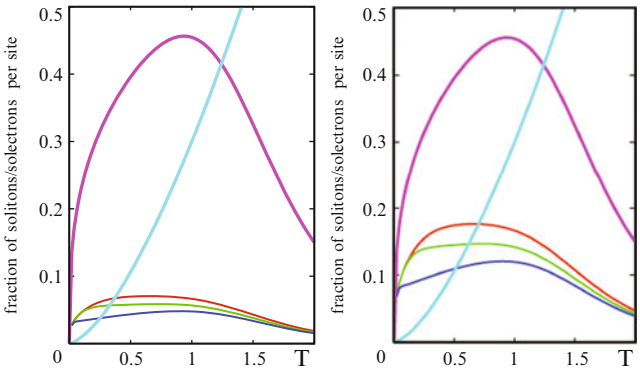

Fig. 1 Estimates of the soliton fraction per site (*upper pink curve* with maximum) and of the solectron fraction for 3 given values of the solectron binding energy (*lower three curves*: $\epsilon_{se} \simeq 0.001, 0.005, 0.01$ eV). *Left panel*: a doping of 20%, *right panel*: a rather high doping of 50%. The magenta lines going up as temperature increases show the border of degeneration effects which are to be expected only above them

$$n_{se}\Lambda_{se}^3 \simeq 1; \qquad \Lambda_{se} = \frac{h}{\sqrt{2\pi m_{se} k_B T}}, \tag{4}$$

where m_{se} is the effective mass of solectron and n_{se} as before is the solectron density. The condition of degeneracy provides us a line in the density-temperature plane

$$n_{se} = const.T^{3/2}, \tag{5}$$

which is displayed in Fig. 1. In the left panel we show the case of a quite an usual doping of 20%, the right panel we have the case of a very high doping of 50%. Only above the magenta lines the effects of degeneration may be expected.

Let us succinctly explain what we mean with a Fermi surface which is in 2d a Fermi net. The Fermi net (Fermi surface in 3d) is defined by the condition that the energy equals the Fermi energy. This corresponds to the transition to degeneration which happens at $n_{se}\Lambda_{se}^3 \simeq 1$.

If the degeneration parameter crosses unity, we expect degeneration effects (Fig. 1). The Fermi net is a set of lines on the plane where, the density corresponds to the degeneration density at the corresponding given temperature. The electron density in the field of atoms is in our case nonuniform and may have a quite complex structure and net structure schematically shown in Fig. 2. As well known from plasma physics and solid state physics most relevant processes, including transitions, diffusion and conductivity occur at the Fermi surface. Therefore it is a primary task, to explore the structure of the Fermi surface. In particular we have to study questions like: Is the Fermi surface connected (percolated) or consisting of non-connected pieces of density regions corresponding to solectrons at the Fermi energy.

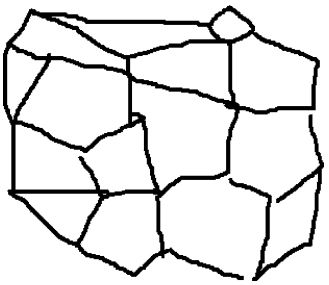

Fig. 2 The Fermi surface (Fermi net in 2d) is defined by the condition that the energy equals the Fermi energy. In other words, the density corresponds to the degeneration density at the given temperature

Our estimates show that it is not easy the cross the border of degeneration. We need strong doping or low temperatures. As far as we can see, it is quite difficult to have conditions for creating degenerate solectrons in real 2d or 3d systems. Probably we need high doping for temperatures beyond 100 K. However one should note that these estimates are conservative, the solectron mass was taken as equal to the electron mass. In reality solectrons are heavier than electrons or holes and tends to behave more classically than electrons. This question was appropriately raised by Alexandrov [37].

3 The Hamiltonian of Our Model and the Equations of Motion

We consider d-dimensional lattices of atoms ($d = 1, 2, 3$) and (added, excess) free electrons which may carry electrical currents. In applications we restrict in most cases to 1d-, or 2d-lattices in order to assess the influence of nonlinear excitations on the electrical properties. The system consists of N classical atoms and one ore several electrons. For the *heavy* atoms we assume that they obey classical Langevin dynamics. We include a phenomenological damping γ_i. In the numerical simulations we consider the lattice units with mass m. The atomic particles are described by coordinates $\mathbf{r}_j(t)$ and velocities $\mathbf{v}_j(t)$, $j = 1, \ldots, N$. We assume periodic boundary conditions. The Hamiltonian consists of three parts, the classical atom/ion Hamilton function H_i, the electron ion interaction function H_{ie} and the rest H_e, accounting for the electrons.

$$H = H_a + H_{ie} + H_e. \tag{6}$$

The atomic part is

$$H_a = \frac{m}{2} \sum_j \mathbf{v}_j^2 + \frac{1}{2} \sum_{ij} V_{ij}(\mathbf{r}_{ij}). \tag{7}$$

The atoms repel each other by strong repulsive forces. The subscript "i" denotes the number of the atom. Let us assume that the characteristic size of the atoms in the

lattice is r_0. In general we will approximate the potential of the forces between two atoms by the Morse-potential

$$V^M(r) = D\left[\exp(2B(r-\sigma)) - 2\exp(-B(r-\sigma))\right]. \tag{8}$$

We note that the characteristic frequency of oscillations around the minima is

$$m\omega_0^2 = V^M(\sigma)''. \tag{9}$$

We introduce now an electron e.g. by doping, and define in TBA the amplitude for being at site j in state n by c_{jn} and the probability to find the electron at the lattice site or atom located at x_j in state n denoted as p_{jn} by

$$p_n = c_n c_n^*. \tag{10}$$

We will show that any displacement of the atoms changes the energetic situation of the electrons, the eigenvalues as well as the transition probabilities. The electron dynamics is influenced by the lattice dynamics and as a result the electron will try to follow up these changes. This is the basic effect leading to the solectron formation. So the essential point is the running local compressions which generate a complex landscape. As shown already by Davydov [3] there exist rather deep potential wells moving (right to left or left to right) along the lattice that strongly influence the local dynamics of the electrons and are able to capture the light electrons. In the TBA the electron Hamiltonian is of hopping type [20–22]

$$H_e = \sum_{jn} E_{jn} c_{jn}^+ c_{jn} + \sum_{jj'n} t_{jj'n} c_{j'n}^+ c_{jn}. \tag{11}$$

Here j denotes the number of the atom and n the quantum numbers of the atomic states. In our adiabatic approach the atomic and the internal positions are assumed to be fixed at R_j. The representation is based on a linear combination of atomic orbitals (LCAO): $|jn>$ which are approximately given by the wave functions of a free atom at position r_j. The matrix elements are related to the operators of kinetic and potential energy. The energy levels E_{jn} fluctuate around the levels of the free atoms. The transition matrix is also a fluctuating quantity depending on the time varying atomic distances $r'_j - r_j$. In a simplified version we neglect the electron–electron interaction. Hence (11) is in fact

$$H_e = \sum_{jn} E_{jn} c_{jn}^+ c_{jn} + \sum_{jj'} t_{jj'n}(R_{j'} - R_j) c_{j'n}^+ c_{jn}, \tag{12}$$

with the matrix elements

$$E_{jn} = < jn|H_0 + V_{ej}|jn >; \qquad t_{jj'n} = < j'n|H_0 + V_{ej}|jn > . \tag{13}$$

We may simplify this expression assuming that the index n uniquely defines the state and set [20–22]

$$H_e = \sum_n E_n c_n^+ c_n + \sum_{nn'} t_{nn'}(r_{n'} - r_n) c_{n'}^+ c_n. \tag{14}$$

In order to estimate the influence of the lattice on the energy levels we consider now the electron–atom interaction.

For 1d-lattices one may consider only nearest neighbor coupling and simplify [20–22]. In the general case the energy landscape shows a complex structure and the dependence of the energy levels on the position has to be taken into account [18, 20]. In the 1d-case the linear Holstein model is

$$E_n \simeq E_n^0 + \chi_0 q_n + \chi_1 \left[q_{n+1} - q_{n-1}\right]. \tag{15}$$

Here, for convenience in notation, q_n denotes a lattice site spatial vibration (relative displacement) coordinate defined by $x_n = n\sigma + q_n/B$. There is the problem that for some values of the deviations (and typical parameter values, $\alpha = 1 - 1.75$) the exponents may take on very large values. The term E_n^0 denotes on-site energy levels of the unperturbed lattice and δE_n is the perturbation due to the lattice vibrations (harmonic as well as anharmonic modes may contribute). In the simplest case the shift is linear in the deformations [38, 39]

$$\delta E_n = \chi(q_n/B), \tag{16}$$

where the "electron-phonon coupling constant", χ, indicates that the on-site energy level E_n, i.e. the local site energy, depends on the displacement of the moving unit; q_n is dimensionless (unit: $1/B$). As shown e.g. in [38, 39], this coupling between lattice deformations and electronic states, leads for large enough values of the parameter χ to the formation of *polarons*. In view of the above given parameter values, the value of the coupling constant is in the range $\chi \simeq 0.1 - 1\,\mathrm{eV/\AA}$. Adapting these assumptions to our model without onsite contributions we have to recall that our model is translationally invariant and we are considering relative lattice displacements.

Recall also that the probability to find the electron at the lattice site or atom located at x_n, i.e. the occupation number p_n is given by (10). The discrete Schrödinger equation for the components of the wave function c_n is then

$$\begin{aligned} i\dot{c}_n \;=\; & [E_n^0 + \chi_1(q_{n+1} - q_{n-1})]c_n \\ & -V_0 \sum_k \{\exp[-\alpha(q_{n+1} - q_n)]c_{n+1} \\ & + \exp[-\alpha(q_n - q_{n-1})]c_{n-1}\}, \end{aligned} \tag{17}$$

where an over-dot denotes time derivative; the energies are dimensionless (unit: 2D).

The corresponding equations for the lattice particles are now

$$\begin{aligned}\ddot{q}_n &= \chi_1[p_{n+1} - p_{n-1}] \\ &+ \{1 - \exp[-(q_{n+1} - q_n)]\} \exp[-(q_{n+1} - q_n)] \\ &- \{1 - \exp[-(q_n - q_{n-1})]\} \exp[-(q_n - q_{n-1})] \\ &- \alpha V_0 \left\{\exp[-\alpha(q_n - q_{n-1})](c^+_{n+1} c_n + c_{n+1} c^+_n)\right. \\ &\left. + \exp[-\alpha(q_{n+1} - q_n)](c^+_n c_{n-1} + c_n c^+_{n-1})\right\}. \end{aligned} \tag{18}$$

The problem reduces, in principle, to solving coupled together both (17) and (18).

Let us study now the two-dimensional case. A standard assumption is, that the interaction is described by a pseudo-potential of polarization type. We assume that the total potential acting on an electron in the field of atoms at positions $r_1, \ldots r_N$ is

$$V_e(\mathbf{r}) = -\sum_j \frac{U_e}{[1 + (\mathbf{r} - \mathbf{r}_j)^2/h^2]^2}. \tag{19}$$

Here h is a characteristic cut-off distance and U_e the maximal polarization energy of the electron. As an estimate we may assume $U_e \simeq 0.1\,\mathrm{eV}$. In earlier work we used also a different pseudopotential approach [27]. In order to be consistent with the pseudopotential formula used above to quadratic terms we can make the choice $h \simeq 0.7\sigma$.

The eigenvalue problem is in general very complicated and practically unsolvable, so we will use the simple assumption that the eigenvalues are shifted like the polarization potential

$$E_n \simeq E^0_n - \sum_{j=1}^{N} \frac{U_e}{\left[1 + (r_n - r_j)^2/h^2\right]^2}. \tag{20}$$

The discrete Schrödinger equation for the components of the wave function c_n assumes now the form [28, 30]

$$\begin{aligned} i\dot{c}_n &= [E^0_n - \sum_{j=1}^{N} \frac{U_e}{\left[1 + (R_n - R_j)^2/h^2\right]^2}]c_n \\ &\quad -V_0 \sum_k \{\exp[-\alpha|R_k - R_n|]c_k. \end{aligned} \tag{21}$$

As before the forces between particles are supposed to be of the Morse kind and the friction and random forces accounting for a Langevin model bath in the case of a heated lattice. For convenience in the 2d lattice dynamics we use complex coordinates $Z_n = x_n + iy_n$, where x_n and y_n are Cartesian coordinates of the n-th

particle. Then the Langevin model provides the equations of motion for the lattice units

$$\frac{d^2 Z_n}{dt^2} = \sum_k \left[F^M_{nk}(Z_{nk}) + F^P_{nk}(Z_{nk}) \right] z_{nk} - \alpha V_0 \sum_k \exp\left[-\alpha |Z_{nk}|\right] (c_n^+ c_k + c_k c_n^+) + \left[-\gamma \frac{Z_n}{dt} + \sqrt{2D_v} \left(\xi_{nx} + i\xi_{ny}\right) \right], \tag{22}$$

where index n identifies a particle among all N particles of the atomic ensemble, γ is a friction coefficient, D_v defines the intensity of stochastic forces, $\xi_{nx,y}$ denotes statistically independent generators of the Gaussian noise; $Z_{nk} = Z_n - Z_k$. Further $z_{nk} = (Z_n - Z_k)/|Z_n - Z_k|$ is a unit vector defining the direction of the interaction force F^M_{nk}, corresponding to the Morse potential, and F^P_{nk}, corresponding to the polarization interaction, between the n-th and the k-th particles. The Morse interaction force F_{nk} is here given by

$$F^M_{nk} = 2B[\exp(-2B|Z_{nk}|) - \exp(-B|Z_{nk}|], \tag{23}$$

and the polarization interaction force by

$$F^P_{nk} = 4U_{ek} \frac{p_n |Z_{nk}| - p_k |Z_{kn}|}{[1 + |Z_{nk}|^2/h^2]^3}. \tag{24}$$

Note that to have dimensionless variables we may consider the spatial coordinates normalized to the length σ used in the Morse potential. Time may be normalized to the inverse frequency of linear oscillations near the minimum of the Morse potential well, ω_M^{-1}. The energy is usually scaled with $2D$, where D is the depth of the Morse potential well, a different possibility is to use V_0 as the unit of energy. Further the stiffness parameter B defines the strength of the repulsion between particles. In view of the above only those lattice units with coordinates Z_k, satisfying the condition $|Z_n - Z_k| < 1.5$, are taken into account in the sum in (41). In computer simulations the interaction of particles is considered to take place inside a rectangular cell $L_x \times L_y$ with periodic boundary conditions.

In practice some open problems remain, in particular there is the compatibility between the quantum-mechanical and the classical part of the dynamics. Due to the Langevin sources of noise and friction in the classical part of the dynamics, the dynamics is irreversible. However so far there is no proof that the final distribution corresponds to the correct Gibbs-von Neumann measures. In the following we assume a kinetic description which is irreversible from the very beginning and converges to the correct distributions. The idea we follow is due to Wolfgang Pauli who focused on p_n and not c_n hence disregarding phases. Thus the Pauli averaging excludes a complete description of coherent states hence ruling out a proper treatment of superconducting states.

4 Pauli Kinetics for Nondegenerate Solectrons on Nonlinear Heated Nonlinear Lattices

So far our analysis has been based on the Schrödinger equation for the free electrons in the TBA which is coupled to the Langevin equation for the classical lattice particles. This tacitly assumed the existence of a heat bath in which the lattice particles are embedded. In principle this picture provides a complete description of the coupled lattice–electron dynamics. The irreversibility is guaranteed by the friction-noise terms in the Langevin-equations (23). As earlier shown [14, 18, 20] we may describe this way also irreversible solitonic excitations at finite temperature. However, a serious problem here is the very long relaxation times of the electrons due to the large differences between the time scales of the electrons and the lattice particles. This leads to some difficulties in extensive computer simulations. In the standard theory of electronic transport this problem is solved by Boltzmann-type descriptions or by Fokker–Planck-type equations, which introduce an irreversible behavior [32, 40–43]. The main problem is here to give a correct description of the coupling to the heat bath [41–43]. In the TBA case, the situation is somehow simpler due to the discrete character of the electronic states, which allows a description by discrete Markov chain equations [29, 44]. The Markov approach to electron dynamics goes back to the seminal work of Pauli, Tolman, van Hove and others [32,40–43]. Pauli started from the Schrödinger equation and derived by perturbation theory a Markov chain description and an expression for the transition probabilities. He introduced an irreversible master equation expressing the balance between the transitions in an ensemble. Pauli's equation is valid for a *microcanonical* ensemble and neglects symmetry effects. Further extensions took into account the symmetry of the wave functions and offered a description compatible with the statistics of Bose–Einstein and Fermi–Dirac. Later generalizations are connected with the development of Metropolis algorithms for *canonical* ensembles [33]. Applications to hopping conduction in solids were given since the 1970s of last century by several authors [44]. First applications of the master equation formalism to electron transfer in macromolecules appear in [45]. The system we are studying here is rather difficult and seems to be too complicated to be treated in full detail. We have:

(a) Quantum electrons located in discrete states, which are coupled to a heat bath and to the classical lattice,
(b) Classical lattice particles coupled to the heat bath and to the quantum electrons.
(c) The heat bath with an unspecified nature.

Simplifying this situation we postulate here that the thermal electrons allow a Markov description. Thus we proceed from the *reversible* Schrödinger equation for the tight-binding model to an *irreversible* Pauli master equation description [32, 40–43]. Following Pauli's method [19, 29] we use here a master equation for the occupation probabilities of electrons p_n in a system with the energy levels E_n:

$$\frac{dp_n}{dt} = \sum \left[W_{nn'} p_{n'} - W_{n'n} p_n \right] . \tag{25}$$

The transition probabilities were derived by Pauli using perturbation theory for microcanonical ensembles (transitions in a narrow energy shell). Applications of this formalism to our Schrödinger equation confronts us with the problem of applicability of the perturbation approach to our basic equation. Note that the diagonal part of the interaction operator may not be small in comparison to the nondiagonal elements. We neglect here this problem and assume that we have found already an appropriate unitary transformation which makes the nondiagonal elements sufficiently small to satisfy the conditions of Pauli's perturbation approach. With this assumption the transition probabilities for the 1d-tight-binding model read in a microcanonical ensemble according to Pauli [19, 29, 32] is

$$W_{micro}(n,n') = \frac{V_0}{\hbar}\exp[-2\alpha|q_{n'}-q_n|]2\pi V_0\delta(E_n - E_{n'}), \tag{26}$$

where $n' = n \pm 1$ and $\delta(x)$ is Dirac's delta function. The transitions from state n to a state n' at one of the nearest-neighbor sites should correspond to the same energy level (or to a level within a narrow shell). In the case of a dissipative embedding, the situation is more complicated due the interaction of the electrons with the dissipative heat bath. For a canonical ensemble we assume the transition probabilities

$$W(n,n') = \frac{V_0^2}{\hbar}\exp[-2\alpha|q_n - q_{n'}|]E(n,n',\beta). \tag{27}$$

Instead of a delta-like shell we have now a Lorentz-like profile around it. In the limit of narrow profiles these expressions converge to the Pauli formula with a delta-factor. Temperature effects are to be included. When the electrons are embedded into a heat bath together with the heated lattice particles, the temperature-dependent thermal factors $E(n,n',\beta)$ are not symmetric with respect to the arguments but they are subject to the condition of detailed balance

$$\frac{W(n',n)}{W(n,n')} = \exp[\beta(E_n - E'_n)]. \tag{28}$$

In other words, the relation of the thermal factors should correspond to the relation of Boltzmann factors. The property (28) suggests the symmetry

$$E(n,n') = \exp[-\frac{\beta}{2}(E_n - E'_n)]F(n,n'), \tag{29}$$

$$F(n,n') = F((E_n - E'_n)), \tag{30}$$

where F(n,n') is an even function. There are several variants for this even function $F(x)$ which we will discuss. The simplest is defined by the phenomenological "ansatz" of the Monte-Carlo procedure, where downhill transitions are weighted with $E = 1$ and uphill transitions with a factor less than unity [33]. This corresponds to the F-function.

$$F(E_n - E_{n'}) = \exp[-\frac{\beta}{2}|E_n - E'_n|]. \tag{31}$$

Proper statistical derivations of the thermal factors may be based on certain microscopic models of the heat bath. Assuming that the heat bath is a carrier of phonons which drive transitions by a one-phonon mechanism Böttger and Bryksin [44] studied hopping systems starting from the von Neumann equation for the density matrix. The authors give the following general expression

$$F(E_n - E_{n'}) = \int_{-\infty}^{\infty} \exp[\frac{i}{\hbar}\tau|E_n - E_{n'}|]K(|\tau|)d\tau, \tag{32}$$

where $K(|\tau|)$ is a rapidly decaying memory kernel. The decay of these correlations is connected with the damping of lattice-particle motion. In the simplest case we may assume here an exponential decay with the same damping constant as appears in the above introduced Langevin dynamics. This leads to the Lorentz profile

$$F(E_n - E_{n'}) = \frac{V_0}{\hbar}\frac{\gamma}{\gamma^2 + (|E_n - E_{n'}|)/\hbar)^2}. \tag{33}$$

In the limit of small damping we come back to the delta-function in the Pauli expression for the transition probabilities.

The master equation is a useful tool for computer simulations of electron hopping processes. Since the detailed balance is obeyed, it is guaranteed that in thermal equilibrium the canonical distribution is solution of the master equation. In order to simplify our computer simulations we used so far only the simplest "ansatz", the Monte Carlo procedure. Our basic system of equations contains several approximations, however it provides a rather fast and therefore useful tool for the computer simulations of the electron–lattice dynamics in thermal systems. Figure 3 illustrates results of computer simulations based on this approach. Due to the way we treat electron relaxation effects there are differences between the methodology using the coupled Schrödinger equation and Langevin equation system (23) and that using Pauli's approach albeit they are minor differences at least for small and for intermediate values of adiabaticity $\tau \sim 1$. For large τ, the electron relaxation in the heat bath is very fast and the distribution may be approximated by a local Boltzmann- or Fermi distribution as shown in [23]. For small and intermediate values of the τ-parameter, say for $\tau \simeq 10 - 20$, the approach based on the Pauli equation (25) is most useful, since it provides informations on deviations from the adiabatic approximation. Our approximation based on the Pauli method (25) goes beyond the adiabatic approximation since the lattice dynamics and the electron dynamics are treated independently including their coupling. Recall that in a strict adiabatic approximation one assumes that the electron adapts "instantaneously" to any change in the lattice. In other words one assumes that the electrons follow in a very fast way to the new lattice configuration and may be described at any time by the canonical distribution [46]. In the new approach based on Pauli's method we take into account that the electrons need time to follow the lattice motions what

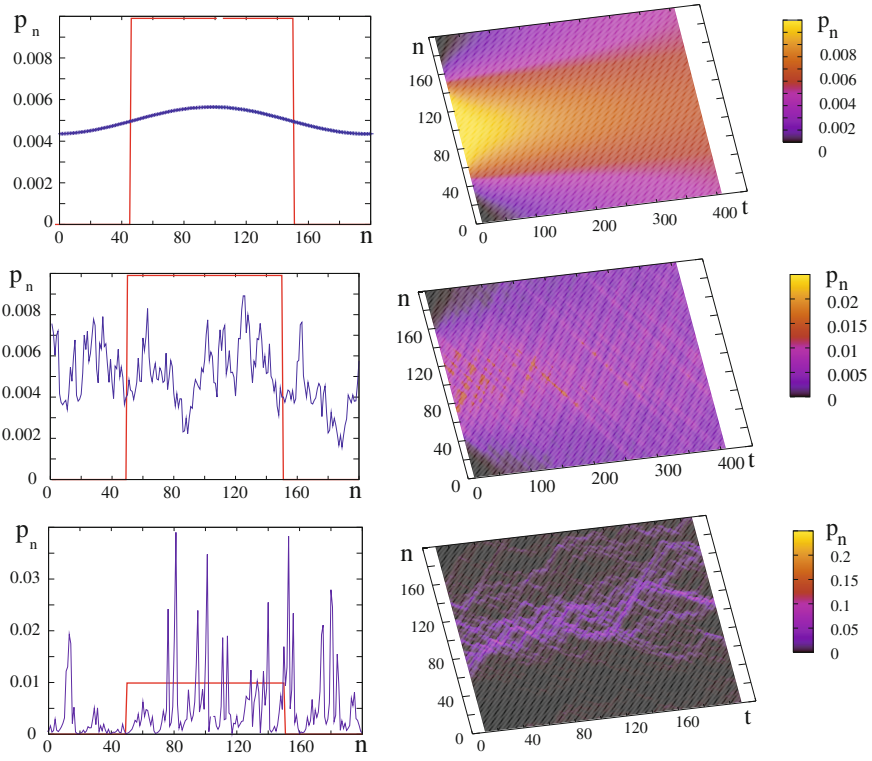

Fig. 3 Time evolution of one-dimensional probability distribution according to Pauli's equation. In the *upper panel* we see the evolution of an initial rectangular distribution, into a uniform distribution without any coupling to the lattice $T = 0$, thus illustrating an H-theorem. In the *center panel* and in the *lower panel* two temperatures different from zero are considered: *upper case*: $T = 0.01$: an initially rectangular distribution tends irreversibly towards homogeneous spreading along the lattice, the wave is weakly structured due to the excitations along the lattice; and *lower case*: $T = 0.5$: the initial rectangular distribution is spreading but at the same time becomes localized around a few peaks thus illustrating the corresponding local formation of solectrons

leads to certain delay in their response and to some deviations from the stationary solution. Qualitatively however the picture remains similar to the results obtained in adiabatic approaches. Figure 3 illustrates how the spreading of the electron density in the 1d case is diffusion-like and strongly influenced by the excitations of solitons in the lattice.

5 Kinetic Equations for Fermi Solectrons with Zero Spin

An advantage of the Pauli approach is, that it can be easily generalized to include the influence of spin and symmetry effects which we have neglected so far, except when using the Hubbard approximation. Following Pauli and Tolman [32, 40] now

we take into account that the electrons are Fermions which are not allowed to occupy a quantum state with more than one particle. In principle there exist the possibility to form bosons by pairing of two electrons but this effect we will considered later on. In a first approach we study electrons without spin, or what is equivalent we consider the case of very low density, where double occupation cannot occur due to the low probability that two electrons meet at the same place. Taking into account symmetry effects for (non-interacting) Fermions without spin the Boltzmann equilibrium distributions are to be replaced by Fermi distributions

$$p_n^0 = \frac{1}{\exp[\beta(E_n - \mu)] + 1}. \tag{34}$$

Here the "plus one" in the denominator expresses the Fermion character. The chemical potential μ marks the border between the occupied and the non-occupied states. Following a procedure described by Tolman and van Hove [40–43] the master equation may be generalized in such a way that Bosonic or Fermionic symmetry effects are included. The idea is to change the transition probabilities in dependence on the occupation of the target state. Let us explain this procedure for Fermions with zero spin. In order to include the Fermi principle we introduce the modified transition probabilities

$$\tilde{W}_{nn'} = (1 - p_n) W_{nn'}. \tag{35}$$

The prefactor reduces the probability of the transition as a function of the occupation of the target state. This way we get a nonlinear master equation

$$\frac{dp_n}{dt} = \sum \left[\tilde{W}_{nn'} p_{n'} - \tilde{W}_{n'n} p_n \right], \tag{36}$$

incorporating the Fermion character. If the spin is different from zero, the prefactor appears only for transitions to states with the same spin direction. The appearance of products like $(1 - p_n) p_{n'}$ leads to the fact that effective hopping is restricted to transitions between states near to the Fermi surface. The meaning is the following: Consider the transitions $n' \to n$. These transitions occur with the weight $p_{n'}$ if and only if the state n is free as expressed by the weight factor $(1 - p_n)$. In Fig. 4 it is demonstrated that according to this weight factor. The states near to the Fermi surface are the major contributors to transport. The new probabilities are still between zero and one i.e. $0 < p_n < 1$ but they are normalized in a different way namely

$$\sum_{n=1}^{N} p_n = N_e \tag{37}$$

where $N_e < N$ is the total number of free electrons in the system. Accordingly, p_n expresses the probability to find one electron in the state $1 \leq n \leq N$. Recall that we assume here one state per atom. This one electronic state per atom may be occupied or not. The prefactors on the r.h.s. of (36) make sure the probabilities p_n cannot grow

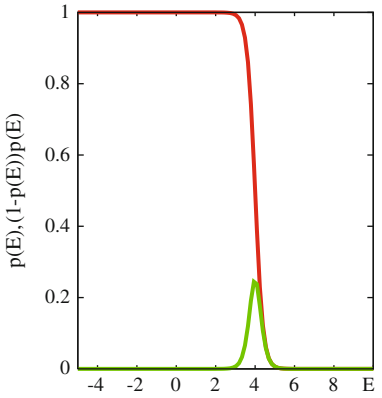

Fig. 4 The Fermi distribution $p(E)$ (upper sharply decreasing *red curve*) and the weight for transitions n' to n (*green curve* with maximum) which is depicted by the function $p(E)(1-p(E)$. The maximum corresponds to the Fermi surface on which transitions have the highest weight

larger than unity. The transition probabilities remain the same as for the Boltzmann case discussed above. The only general condition they have to satisfy is

$$\frac{W(n',n)}{W(n,n')} = \frac{\exp[-\beta E_n']}{\exp[-\beta E_n]}. \tag{38}$$

In equilibrium the normalization defines the chemical potential by

$$\sum_n \frac{1}{\exp[\beta(E_n-\mu)]+1} = N_e. \tag{39}$$

Clearly the states $E_n = \mu$ play a very special role not only in equilibrium but also for transport.

By taking into account the spin we may easily modify the distribution in such a way that two electrons may occupy the same site. This corresponds to the formation of a (small) bipolaron. However it is not trivial to take the Coulomb repulsion into account, which is significant for the formation of bipolarons.

The master equations are not closed, they still depend on the particle coordinates. The corresponding equations for the lattice particles are in the 1d case given by Chetverikov et al. [29]

$$\begin{aligned}\frac{d^2q_n}{dt^2} &= \chi_1[p_{n+1}-p_{n-1}] + \{1-\exp[-q_{n+1,n}]\}\exp[-q_{n+1,n}] \\ &- \{1-\exp[-q_{n,n-1}]\}\exp[-q_{n,n-1}] - 2\alpha V_0(\exp[-\alpha q_{n,n-1}]\sqrt{p_{n-1}p_n} \\ &+ \exp[-\alpha q_{n+1,n}]\sqrt{p_n p_{n+1}}.\end{aligned} \tag{40}$$

which are phase-averaged modifications of (18).

In the 2d case the equations of motion are more complicated. Assuming the same model about forces and friction as earlier done and using also complex coordinates $Z_n = x_n + iy_n$, where x_n and y_n are Cartesian coordinates of the n-th particle we get the Langevin equations

$$\frac{d^2 Z_n}{dt^2} = \sum_k \left[F_{nk}^M(Z_{nk}) + F_{nk}^P(Z_{nk}) \right] z_{nk} - 2\alpha' \sum_{n'} \exp\left[-\alpha' |R_n - R_{n'}| \right] \sqrt{p_n p_{n'}} + \left[-\gamma \frac{dZ_n}{dt} + \sqrt{2D_v} \left(\xi_{nx} + i\xi_{ny} \right) \right], \tag{41}$$

where as above the index n identifies a particle among all N particles of the atomic ensemble, γ is a friction coefficient, D_v defines the intensity of stochastic forces, $\xi_{nx,y}$ denotes statistically independent generators of the Gaussian noise. Note that the new Langevin equations (41) are different from the previous ones (22), since due to the phase averaging only the variables p_N and not the c_n appear. Further we note that in the classical equations of motion (40) and (41) appear two terms which couple the classical dynamics to the quantum master equations. One is due to the dependence of the energy levels on the coordinates of the atoms and the other on the dependence of the transition probabilities on the atomic distances. Furthermore let us insist on that the description by Pauli TBA equations contains less information than the standard TBA since all phases are lost and only the probabilities p_n appear in the dynamics equations.

6 Spatial Distributions, Energy Spectrum and Energy Distributions

Numerical simulations of our systems of equations (kinetic and dynamic equations) provide snapshots of the spatial distribution of Fermi solectrons on a square of 20×20 triangular lattice at $T = 0.01$. We studied 3 electron numbers $N_e = 16, 200, 300$ on a triangular lattice of 400 sites, whose fractional densities are, respectively, $\nu_e = 0.04, 0.5, 0.75$. Results are shown in Figs. 5 and 6. The corresponding probability and energy distributions are shown in Figs. 7 and 8. Note that the solectrons inside the clusters, stripes or percolated regions are degenerated. Investigating the spatial distributions shown in Figs. 5 and 10, we see interesting structures. We see clustering at the lowest density, striping at the moderate density and a kind of percolation at the highest density. The general trend is that the solectrons tend to cluster rather than remaining isolated. This means that there is a tendency to cluster, hence to pairing in space. This is a point which also needs a further analysis. We have to find the radial distribution function and expect to see a peak at small distances. This would confirm predictions made by Alexandrov [37]. From the informations we have on the energies of the Fermi particles we calculated the distributions by averaging.

Investigating the energy distributions shown in Figs. 7–10, we see also interesting structures. The general trend is that the probabilities decrease with energies. The energies are given here relative to the minimal energy and are ordered

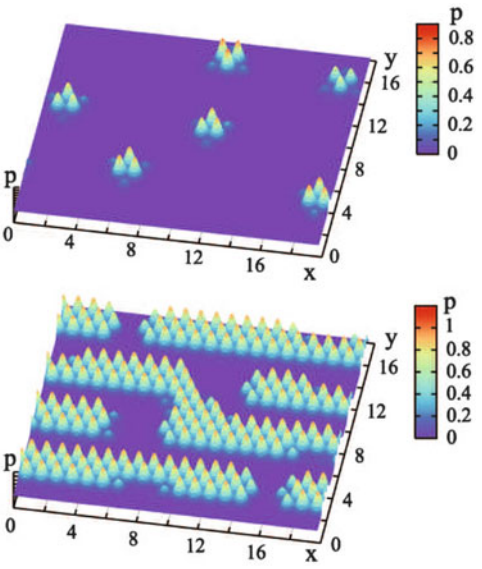

Fig. 5 Snapshot of the spatial distribution of Fermi solectrons on a versus sites 20×20 triangular lattice at a low temperature $T = 0.01$. We study 2 electron numbers $N_e = 16, 200$ on a triangular lattice of 400 sites. This corresponds to the (fractional) doping densities $\nu_e = 0.04, 0.5$. We see clustering at the lowest density and striping on the moderate density

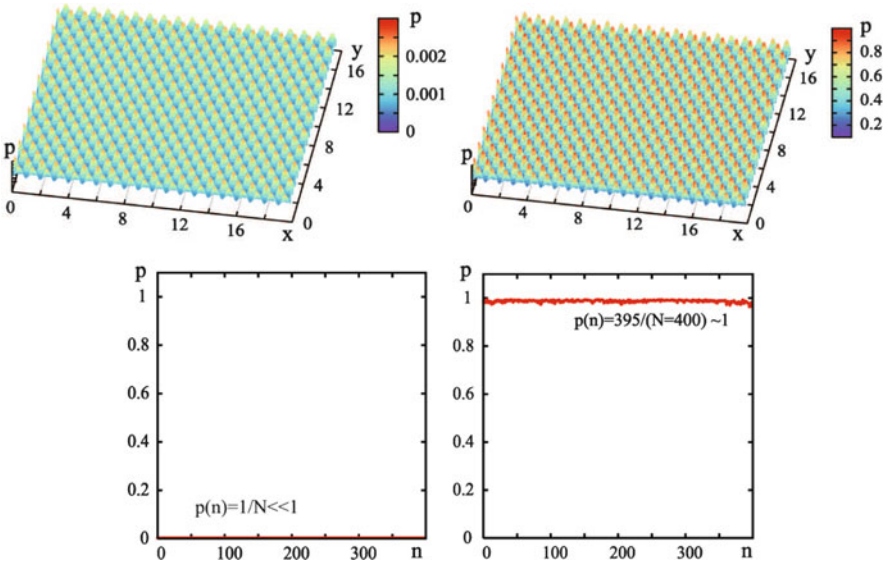

Fig. 6 Probability distribution of Fermi solectrons on a versus sites 20×20 triangular lattice at a very low temperature $T = 0.001$ for two extreme cases. *Left panel* for $N = 1$ shows the expected equal distribution of quantum probability. In the *right panel* for $N = 395$ we see a nearly equal distribution for the case of a near to full occupation

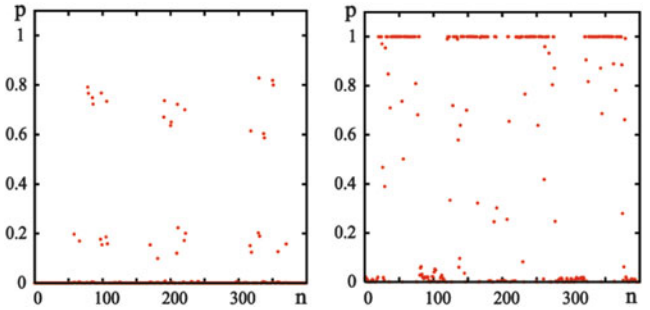

Fig. 7 Snapshot of the probability distribution of Fermi solectrons on a versus sites 20×20 triangular lattice at a very low temperature $T = 0.001$ for two intermediate densities. *Left panel* $N = 16$ and *right panel* $N = 200$

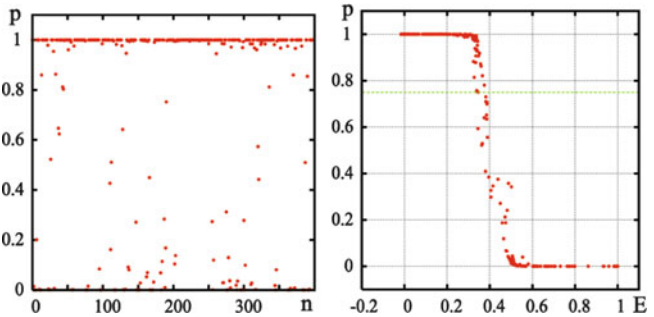

Fig. 8 Probability distribution for $\nu_e = 300/400 = 0.75$ at a low temperature $T = 0.001$. First we see versus sites and then the distribution versus energies (energy distribution). In the latter we observe (the lowest energies are left) the formation of a Fermi edge and may identify the Fermi energy

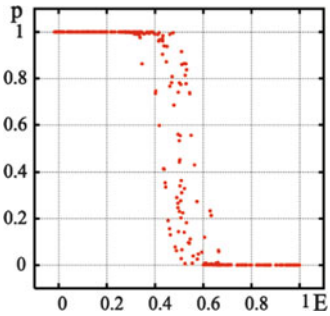

Fig. 9 Typical probability distribution versus energies (energy distribution) of Fermi solectrons at a low temperature $T = 0.001$ for the moderate doping density $\nu_e = 200/400 = 0.5$. We observe again the formation of a Fermi edge and may identify the Fermi energy

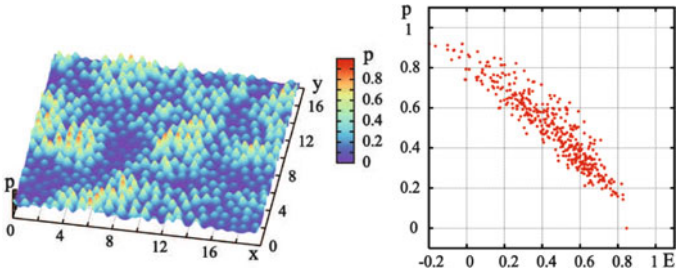

Fig. 10 Another example for the probability distribution versus energies (energy distribution) of Fermi solectrons at an intermediate temperature $T = 0.5$ for the moderate doping density $\nu_e = 200/400 = 0.5$. We observe that the Fermi distribution tends to a Boltzmann distribution. In the *left panel* we see a snapshot of the corresponding spatial electron distribution

in a way that on the left are the lowest energies for a given snapshot. At low temperatures and higher densities (region of degeneracy) a typical Fermi distribution appears which transforms at higher temperatures into a Boltzmann distribution. This transition from degeneration to Boltzmann behavior occurs at

$$n_e \Lambda_e^3 \simeq 1, \qquad \Lambda_e = \frac{h}{\sqrt{2\pi m_e k_B T}}, \qquad n_e = \frac{N_e}{Na^2/2}.$$

Besides this general trend we see an interesting fine structure including steps and gaps. This is a point which needs a further analysis. We cannot exclude the possibility that the gap-like phenomena are connected with the existence of pseudo gaps, but this needs more accurate computer simulations.

Our approximations provide a rather fast and therefore useful tool for the computer simulations of the electron–lattice dynamics in heated systems. Figures 3 and 5 illustrate results based on this approach. Due to the way we treat the electron dynamics, there are differences between the methodology using the coupled Schrödinger equation and Langevin equation system and that using Pauli's approach albeit they are minor differences. An advantage of the Pauli approach is, that it can be generalized to include the influence of spin, and Bose effects which we have neglected so far.

The qualitative difference between the Boltzmann distributions and the Fermi distributions is that Fermi distributions distinguish sharply between electrons below and above the Fermi level μ. The chemical potential (Fermi level) may be estimated from our energy distributions.

The states below the Fermi level are occupied and the states above are empty or weakly occupied. This way the Fermi level acts as the sea level in a country with many mountains. Lowering the sea level decreases the area occupied by the sea and increasing the sea level increases the area of the sea and reduces the part of the mountains. Note that transfer and transport happens only at the Fermi level (Fig. 2). Finally the "land" consists of separated islands. When this happens we have a percolation transition as seen in Fig. 11. The possible Fermi levels are

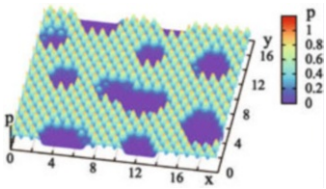

Fig. 11 Percolation is illustrated by a snapshot for a rather high level of doping density of 75% and a rather low temperature $T = 0.01$

given here by the colors. Clearly, for the given potential landscape the Fermi level $\mu \simeq -1$ hints at percolation. We see that the regions $E < \mu \simeq -1$ are connected, this is what we mean by percolation. With increasing density the Fermi level raises, and increasing Fermi levels may lead to percolation of the electronic density corresponding to a sudden increase of diffusion, conductivity and other macroscopic transport properties, from side to side of the system like, indeed, in the Italian coffee percolator when making expresso (Fig. 11). In this respect the 2d- as well as the 3d-systems are fundamentally different from the 1d-systems.

By analyzing the Pauli equation we see that due to the existence of a factor $(1-p_n)\,p_{n'}$ only the states near to the Fermi level the regions $E_n \simeq \mu$ may contribute to transport.

7 Discussion and Outlook

We have investigated the role of Fermi degeneration for a system with nonlinear anharmonic excitations. This may be significant for a theory of conducting lattices. Solitons are hard excitations of the lattice which have a long lasting time and influence the local density and this way the Fermi level. Solitons are local deformations—peaks of the density—propagating with a *supersonic* soliton velocity v_{sol} which strongly increases with the increase in the stiffness of the lattice. As the soliton velocity is much smaller than the thermal velocity of the electrons, the interaction between soliton-like waves and electrons is weak, since an effective interplay requires that the concentration of electron in the region of the soliton velocity is sufficiently high. In fact electrons captured certain time by solitonic excitations are only weakly affected by scattering processes. We have used this property for estimating the contribution of solitonic excitations to the collision frequency in [31] (Fig. 12).

An evaluation of the influence of solitons predicts for 1d-lattices a conductivity increase in the temperature region where most thermal solitons are excited. For 2d-lattices we find an eventual percolation transition to connected conducting regions. We have shown that the Fermi level of the electrons determines the percolation effects.

A few remarks are worth recalling:

(a) As our simulations show, there is a general tendency for formation of pairs. In recent work [25, 26, 34] we have shown that the soliton mediated pair

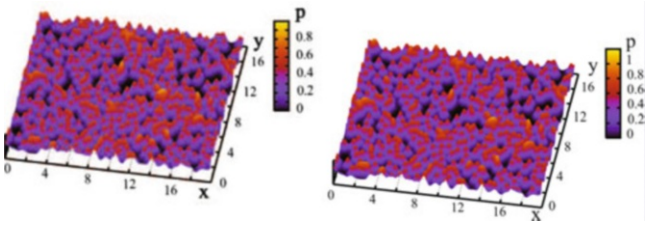

Fig. 12 The case of high temperatures: Snapshots of the electron density in a 2d Fermi system with zero spin and $N = 400$ sites at the temperature $T = 2.5$ for two different doping situations $N_e = 250$; $\nu_e = 0.625$ and $N_e = 300$; $\nu_e = 0.75$

formation is energetically favorable. However as well known this proves only, that pairs will form at $T = 0$; at higher T one has to estimate the thermodynamic probability. This is done for example by our simulations which clearly show that at moderate T, pairs can be formed. According to Alexandrov [37] the existence of local pairs is relevant for high T_c superconductors. Therefore the present study may be useful to start solving this question. However the proper treatment of pairs at finite temperatures requires first an extension of the theory to Bose systems [49].

(b) If solectrons (polarons) are dominant, the Fermi surface of the solectrons determines the electrical conductivity. That means that in order to get high conductivities, we need high enough densities of solectrons near to the Fermi surface.

(c) In certain regions (Fig. 3) bi-solectrons may be more frequent than solectrons. Note that what matters for Bose–Einstein condensation is not the Fermi levels but the lowest energy levels. Since bisolectrons are bosons, Bose condensation is then at least in principle possible. However a problem in this respect is the relatively large mass of solectrons and bisolectrons, which make it difficult to reach the conditions for Bose–Einstein condensation.

Acknowledgement The authors acknowledge fruitful discussions with A.S. Alexandrov, E. Brändas, L. Brizhik, L. Cisneros-Ake, L. Cruzeiro, F. de Moura, C. Eilbeck, J. Feder, D. Hennig, J.J. Kozak, S. Larsson, R. Lima, D.M. Newns, G. Röpke, F.M. Russell, G.A. Vinogradov and E.G. Wilson. This research was supported by the Spanish *Ministerio de Economía y Competitividad*, under Grant MAT2011-26221.

References

1. Landau, L.D.: Electron motion in crystal lattices. Phys. Z. Sowjetunion **3**, 664 (1933)
2. Pekar, S.I.: Untersuchungen über die Elektronentheorie. Akademie Verlag, Berlin (1954)
3. Davydov, A.S.: Solitons in Molecular Systems, 2nd edn. Reidel, Dordrecht (1991)
4. Brizhik, L.S., Davydov, A.S.: Soliton excitations in one-dimensional molecular systems. Physica Status Solidi B **115**, 615–630 (1983)

5. Davydov, A.S., Zolotaryuk, A.V.: Solitons in molecular systems with nonlinear nearest-neighbour interactions. Phys. Lett. **94**, 49–51 (1983); Physica Status Solidi B **115**, 115–125 (1983)
6. Scott, A.C.: Davydov's soliton. Phys. Rep. **217**, 1–67 (1992)
7. Zolotaryuk, A.V., Spatschek, K.H., Savin, A.V.: Supersonic mechanisms for charge and energy transfers in anharmonic molecular chains. Phys. Rev. B **54**, 266–277 (1996)
8. Makarov, V.A., Ebeling, W., Velarde, M.G.: Soliton-like waves on dissipative Toda lattices. Int. J. Bifurcat. Chaos **10**, 1075–1089 (2000)
9. Makarov, V.A., DelRio, E., Ebeling, W., Velarde, M.G.: Dissipative Toda-Rayleigh lattice and its oscillatory modes. Phys. Rev. E **64**, 036601-1-14 (2001)
10. Del Rio, E., Makarov, V.A., Velarde, M.G., Ebeling, W.: Mode transitions and wave propagation in a driven-dissipative Toda-Rayleigh ring. Phys. Rev. E **67**, 056208-1-9 (2003)
11. Velarde, M.G., Ebeling, W., Chetverikov, A.P.: On the possibility of electric conduction mediated by dissipative solitons. Int. J. Bifurcat. Chaos **15**, 245–251 (2005)
12. Chetverikov, A.P., Ebeling, W., Velarde, M.G.: Nonlinear ionic excitations, dynamic bound states, and nonlinear currents in a one-dimensional plasma. Contrib. Plasma Phys. **45**, 275–283 (2005)
13. Makarov, V.A., Velarde, M.G., Chetverikov, A.P., Ebeling, W.: Anharmonicity and its significance to non-Ohmic electric conduction. Phys. Rev. E **73**, 066626-1-12 (2006)
14. Velarde, M.G., Ebeling, W., Hennig, D., Neissner, C.: On soliton-mediated fast electric conduction in a nonlinear lattice with Morse interactions. Int. J. Bifurcat. Chaos **16**, 1035–1039 (2006)
15. Chetverikov, A.P., Ebeling, W., Velarde, M.G.: Thermodynamics and phase transitions in dissipative and active Morse chains. Eur. Phys. J. B **44**, 509–519 (2005)
16. Chetverikov, A.P., Ebeling, W., Velarde, M.G.: Nonlinear excitations and electric transport in dissipative Morse-Toda lattices. Eur. Phys. J. B **51**, 87–99 (2006)
17. Chetverikov, A.P., Ebeling, W., Velarde, M.G.: Dissipative solitons and complex currents in active lattices. Int. J. Bifurcat. Chaos **16**, 1613–1632 (2006)
18. Hennig, D., Neissner, C., Velarde, M.G., Ebeling, W.: Effect of anharmonicity on charge transport in hydrogen-bonded systems. Phys. Rev. B **73**, 024306-1-10 (2006)
19. Chetverikov, A.P., Ebeling, W., Velarde, M.G.: Thermal solitons and solectrons in nonlinear conducting chains. Int. J. Quant. Chem. **110**, 46–61 (2010)
20. Hennig, D., Chetverikov, A.P., Velarde, M.G., Ebeling, W.: Electron capture and transport mediated by lattice solitons. Phys. Rev. E **76**, 046602-1-9 (2007)
21. Hennig, D., Velarde, M.G., Ebeling, W., Chetverikov, A.P.: Compounds of paired-electrons lattice solitons moving with supersonic velocity. Phys. Rev. E **78**, 066606-1-9 (2008)
22. Velarde, M.G., Ebeling, W., Chetverikov, A.P., Hennig, D.: Electron trapping by solitons. Classical versus quantum mechanical approach. Int. J. Bifurcat. Chaos **18**, 521–526 (2008)
23. Ebeling, W., Velarde, M.G., Chetverikov, A.P., Hennig, D.: Anharmonicity and soliton-mediated transport. In: Russo, N., Antonchenko, V.Yu., Kryachko, E. (eds.) Selforganization of Molecular Systems, pp. 171–198. Springer, Berlin (2009)
24. Cantu-Ros, O.G., Cruzeiro, L., Velarde, M.G., Ebeling, W.: On the possibility of electric transport mediated by long living intrinsic localized modes. Eur. Phys. J. B **80**, 545–554 (2011)
25. Velarde, M.G., Brizhik, L., Chetverikov, A.P., Cruzeiro, L., Ebeling, W., Röpke, G.: Electron pairing in one-dimensional anharmonic crystal lattices. Int. J. Quant. Chem. **112**, 551–565 (2012)
26. Velarde, M.G., Brizhik, L., Chetverikov, A.P., Cruzeiro, L., Ebeling, W., Röpke, G.: Quartic lattice interactions, soliton-like excitations, and electron pairing in one-dimensional anharmonic crystals. Int. J. Quant. Chem. **112**, 2591–2598 (2012)
27. Chetverikov, A.P., Ebeling, W., Röpke, G., Velarde, M.G.: Anharmonic excitations, time correlations and electric conductivity. Contrib. Plasma Phys. **47**, 465–478 (2007)
28. Chetverikov, A.P., Ebeling, W., Röpke, G., Velarde, M.G.: Hopping transfer and stochastic dynamics of electrons in two-dimensional plasmas. Contrib. Plasma Phys. **51**, 814–829 (2011)

29. Chetverikov, A.P., Ebeling, W., Velarde, M.G.: Local electron distributions and diffusion in anharmonic lattices mediated by thermally excited solitons. Eur. Phys. J. B **70**, 217–227 (2009)
30. Chetverikov, A.P., Ebeling, W., Velarde, M.G.: Soliton-like excitations and solectrons in two-dimensional nonlinear lattices. Eur. Phys. J. B **80**, 137–145 (2011)
31. Chetverikov, A., Ebeling, W., Velarde, M.G.: Controlling fast electron transfer at the nano-scale by solitonic excitations along crystallographic axes. Eur. Phys. J. B **85**, 291–299 (2012)
32. Pauli, W.: Festschrift zum 60. Geburtstage A. Sommerfelds. Hirzel, Leipzig (1928)
33. Binder, K. (ed.): Monte Carlo Methods in Statistical Physics. Springer, Berlin (1979)
34. Brizhik, L., Chetverikov, A.P., Ebeling, W., Röpke, G., Velarde, M.G.: Electron pairing and Coulomb repulsion in one-dimensional anharmonic lattices. Phys. Rev. B **85**, 245105 (2012)
35. Muto, V., Scott, A.C., Christansen, P.L.: Thermally generated solitons in a Toda lattice model of DNA. Phys. Lett. **136**, 33–36 (1989)
36. Marchesoni, F., Lucheroni, C.: Soliton density in an infinite Toda lattice. Phys. Rev. B **44**, 5303–5305 (1991)
37. Alexandrov, A.S.: High-Temperature superconductivity: the explanation. Phys. Scripta **83**, 038301 (2011)
38. Kalosakas, G., Rasmussen, K.O., Bishop, A.R.: Charge trapping in DNA due to intrinsic vibrational hot spots. J. Chem. Phys. **118**, 3731–3736 (2003)
39. Kalosakas, G., Rasmussen, K.O., Bishop, A.R.: Nonlinear excitations in DNA: polarons and bubbles. Synth. Met. **141**, 93–97 (2004)
40. Tolman, R.: The Principles of Statistical Mechanics. Oxford University Press, Oxford (1938) [Sects. 100, 102, 105]
41. Van Hove, L.: Quantum-mechanical perturbations giving rise to a statistical transport equation. Physica **21**, 517–540 (1954)
42. Van Hove, L.: The approach to equilibrium in quantum statistics: a perturbation treatment to general order. Physica **23**, 441–480 (1957)
43. Van Hove, L.: The ergodic behaviour of quantum many-body systems. Physica **25**, 268–276 (1959)
44. Böttger, H., Bryksin, V.V.: Hopping Conduction in Solids. Akademie, Berlin (1985)
45. Schlag, E.W., Yang, D.-Y., Shen, S.-Y., Selzle, H.L., Lin, S.H., Rentzepis, P.M.: Dynamical principles in biological processes: a model of charge migration in proteins and DNA. Proc. Natl. Acad. Sci. USA **97**, 9849–9854 (2000)
46. Velarde, M.G., Chetverikov, A.P., Ebeling, W., Hennig, D., Kozak, J.J.: On the mathematical modeling of soliton-mediated long-range electron transfer. Int. J. Bifurcat. Chaos **20**, 185–194 (2010)
47. Velarde, M.G.: From *polaron* to *solectron*: the addition of nonlinear elasticity to quantum mechanics and its possible effect upon electric transport. J. Comput. Appl. Math. **233**, 1432–1445 (2010)
48. Newns, D.M., Tsuei, C.C.: Fluctuating Cu-O-Cu bond model of high-temperature superconductivity. Nat. Phys. **3**, 184–191 (2007)
49. Marouchkine, A.: Room Temperature Superconductivity. Cambridge University Press, Cambridge (2004)

Surfing Electrons in Quantum Computers?

Y. Pomeau

1 Introduction

A quoi faire la science, si l'entendement n'y est pas.
Montaigne,Essais, chap. 25[1]

Over the last years I received from Manuel electronic versions of articles by him and his coworkers [1–3] showing how an electron can be carried along by phonons propagating in atomic lattices. Lately this idea of surf has been used to experimentally transport single electrons from one quantum dot to another one [4, 5]. The two experimental papers mention a possible use of this device in a future quantum computer, an elusive machine to say the least. As I understand it, Manuel, like myself, doubt that this idea of surfing electrons could be used in quantum computers. In an e-mail exchange with him on this question (transport of electrons by surface waves from quantum dot to quantum dot) I wrote:

"Concerning the papers you sent to me [4, 5], the ones doing the experiments of electron transport by surface waves are mistaken, in my opinion, for the part concerning the coherence of the spin of the electrons: the interactions with the other electrons depend on spin and kills this coherence so fast that all this is without interest for a very hypothetical quantum computer".

[1]Montaigne made this famous statement in the chapter "Du pédantisme" of Essais. Approximately—the subtle prose of Montaigne is hard to translate—the meaning of this short sentence (a translation itself from a Greek author, Stobée), "What is the use of science if understanding is absent". By "Science" Montaigne meant "what is known" or "knowledge", the original meaning in Latin. This statement is even more remarkable if one thinks it was made before Newton's time and even before Galilei.

Y. Pomeau (✉)
Department of Mathematics, University of Arizona,Tucson, AZ 85721, USA
e-mail: pomeau@lps.ens.fr

R.G. Rubio et al. (eds.), *Without Bounds: A Scientific Canvas of Nonlinearity and Complex Dynamics*, Understanding Complex Systems,
DOI 10.1007/978-3-642-34070-3_37, © Springer-Verlag Berlin Heidelberg 2013

I believe it is of general interest to explain why transport of electrons by surfing cannot help to make quantum computers. This is based on the remark that the coherence necessary in such a device involves too the space dependent part of the quantum state, and the related phase fluctuates very fastly. This gives me also a chance to explain a few points on what is meant by quantum coherence, an often poorly understood question. The authors of [4] makes the (overoptimistic) claim: "The ability to separate the two electrons and to bring only one of them to the second quantum dot is of potential interest for the transfer of quantum information and is the essence of the quantum teleportation protocol", the issue being if the "quantum" part of the transferred information can be actually transferred.

Reference [5] gives a few more details: "To be useful in a quantum information circuit, the transfer of an electron must not cause its spin state to decohere. Coherent transfer of a collection of spins has been demonstrated over a distance of 70 mm (for a particular wafer orientation), with the potential to extend this much further and coherent oscillations of charge have been shown over a submicrometre distance. Fluctuations in the magnetic field created by nuclear spins are the main cause of dephasing in static quantum dots". A comment [6] on the two aforementionned articles emphasizes this possibility of using surfing electrons to do quantum computations. It states "Quantum information processing using photons is already a well-developed technology—the key to this steady advance being the fact that photons largely ignore each other. This is in stark contrast to electrons which, when travelling along a wire, interact with one another and quickly lose any quantum information they might be carrying". This last point is actually very unclear, not to say self contradictory. It does not explain why the "information quickly lost when traveling along a wire" is better conserved when the electrons are transported by surface waves instead (I guess) by regular electric current. As we all know, using the concept/word "information" is full of danger in physics, particularly in quantum physics, something making pertinent the statement by Montaigne I recall at the beginning. Indeed one could always argue about what is exactly meant by "quantum information". After all, we live in a world where everything is quantum, macroscopic, mesoscopic or microscopic, so that, in this world, information too is quantal as well as the rest. I shall mean by quantum information the usual sense, namely information relying on the quantum coherence of wave functions with a well defined phase difference. As we know well, a coherent phase difference is very hard to maintain, as stated in [6]: the interaction between electrons in dense matter makes lose very quickly phase information. The rate of loss of coherence is a measure of the strength of the interaction energy with the outside world, because of the Planck–Einstein relation between energy and frequency. Even a tiny interaction is enough to dephase the wave function by a random finite angle, reducing so the "information" to a purely classical one.

To explain my point, I need a bit of formalism. The idea of q-bit, at the basis of quantum computation, is that, if one can store both the phase and amplitude of quantum states, and manipulate afterwards the information so stored to make computations. This is surely a fascinating endeavour, but plagued by one major difficulty: how to keep the phase of quantum states long enough to use it in

manipulations? The loss of coherence somehow brings the state from quantum to classical and makes vanish the magic of q-bit and quantum computation. To set the stage, let us start from a system with a degenerate background state, state A and state B with the same energies (this point is not essential, one could also consider two states with different, but well-defined energies). This can be the up (u later on) and down (d) state of a spin-half electron without external magnetic field and with no interaction with other particles or fields. To understand what is the effect of such interactions, one should consider the density matrix of the two-state system, namely the matrix with diagonal real positive entries ρ_{AA} and ρ_{BB} and off-diagonal entries ρ_{AB} and $\rho_{BA} = \overline{\rho}_{AB}$, where the overline is for complex conjugation. The diagonal entries are such that $\rho_{AA} + \rho_{BB} = 1$. The diagonal entries are just the probability that the system is in the A or in the B state. Because the evolution equation of the density matrix is

$$i\hbar \frac{\mathrm{d}\rho}{\mathrm{d}t} = [H, \rho]\,,$$

where [.,.] is the commutation and H the energy operator, the evolution of the system does not link at all the eigenstates A and B if the density matrix is diagonal (that is if $\rho_{BA} = 0$). This means that, in the evolution of this system, there will be two disconnected histories, the one with the pure state $|A>$ as initial condition and the one with $|B>$ as initial condition. This is Everetts idea of separated histories [7]. When the off-diagonal term has decayed to zero, there is no difference anymore between a system in state $|A>$ with probability ρ_{AA} and state $|B>$ with probability ρ_{BB}, the word "probability" having its usual "classical" meaning. The subsequent history will not permit to return to the other state, as in a classical system which has an unique history. The only difference between quantum physics without off-diagonal and classical physics is the "existence" of an inaccessible different Universe with another history in quantum physics, although classical physics yields an unique history. In particular, once the off-diagonal term has decayed to zero, no quantum computation can be done. All this (rather standard) discussion, with no claim of originality, points to the fact that quantum information relies crucially on non zero off-diagonal terms of the density matrix. Indeed the maximum value of the off-diagonal component is reached for pure states with a well defined phase difference between state $|A>$ and state $|B>$. Notice that the decay of the off-diagonal element of the density matrix depends on macroscopic objects (or at least of "many electrons" interacting with the transported electron in the problem of surfing electrons) interacting with the system. Otherwise this would contradict the reversibility of quantum mechanics: in a macroscopic object (namely for a system with many degrees of freedom) most initial conditions are such that the off-diagonal entries of the density matrix decay to zero. For a large isolated finite system, one expects a return to non zero values of the off diagonal entries after very long times, presumably of the order of magnitude of the Poincaré recurrence time of classical mechanics at least. This also points to the dynamical meaning of the loss of phase coherence. Consider pure states with the same energy again. They bear a phase difference that may be random at time zero. In the absence of interactions

with the surrounding, this (random) phase difference will stay the same forever. Practically the off-diagonal entry of the density matrix of this isolated system will not decay to zero with time. It decays to zero when this phase fluctuates in time because of the interaction with the surrounding, so that time averages of the off-diagonal density matrix will be close to zero, provided the time scale of the average (related to the frequency resolution of the measuring devices) is longer than this typical time scale of the phase fluctuations. As argued below, in the case under consideration (electron interacting with other electrons in a conductor) the time scale of the relevant phase fluctuations is far shorter than the time resolution of any measuring device.

Consider now the transport of electron by surf on elastic waves. The theoretical predictions of [1–3] are verified in the experiments where this mode of transport is observed. Starting from a two-electrons state in the singlet spin state, by such a transport one can effectively prepare a state where one electron with a well defined spin state is in one of the dots although the other with the opposite spin state is in the other dot. The quantum coherence necessary to carry quantum computations requires to consider *two* quantum states of equal energy. Let L and R denote the left and right quantum dot. The two eigenstates under considerations are therefore $|uL, dR>$ and $|dL, uR>$, namely the state where the up spin is in the left dot and the down one in the right dot and the state where the down spin is on left and the up on right. Indeed if one forgets the location of the electrons, one finds a single (reduced) singlet state $|u, d>$, but this single state does not carry any phase relation between two states and cannot be used in quantum computations, just because it cannot be associated to the off diagonal entry of a density matrix. Indeed this singlet state looses its coherence, as stated in [4] and [5] if by interaction with nuclear spins one of the spins is reversed, to get to a multiplet state, which makes the other state needed to define quantum coherence and its eventual loss. This makes certainly an upper bound for the quantum coherence of the two-electron system. But, there is another (and far more efficient) way to loose quantum coherence between the two states $|uL, dR>$ and $|dL, uR>$, which is by changing the phase of the position part of the wave function of the electrons in each quantum dot. This is because the location of the electron in one of the dots carries also information about the phase of this wave function. The interactions with the other (field) electrons in the same dot destroy very quickly the phase coherence. This is because for a given state of the (field) electrons, the interaction with the transported (foreign) electron depends strongly on its spin polarization. Suppose to simplify the matter that the foreign electron together with the field electrons in the quantum dot make a dilute gas obeying the Boltzmann-Nordheim kinetic equation. The parameters of each collision between the field electrons and the foreign electron will depend on the spin state of the electrons. Therefore, even if the spin of the foreign electron remains unchanged after the collision, its momentum will change and so change very quickly its phase. Therefore, because its localization in one of the dots must carry position information (otherwise transport by surf or by any method is irrelevant for quantum computing), the phase associated to the off-diagonal part of the two by two density matrix will decay very quickly, with a time of the order of the coherence time of the

full wave function of a single electron, spin *and* position. In dense electron systems, like the ones in the experiments of electron surfing, this time is very short, likely in the range of the period of waves functions near the edge of the Fermi surface, much shorter than any time scale usable in electronics. I suspect that this very short time scale is often the one pertinent for the quantum coherence of electronic states envisioned for quantum computers. In this respect it is likely better, at least in principle, to use photons, interacting much more weakly with their surrounding, and so able to keep the coherence of their wave functions on decently large times. With Martine Le Berre, we suggested some years ago to use solitons states in optical fibers as bound states of many photons and to use them as carriers of quantum coherence [8], with reasonably persistent quantum coherence.

References

1. Velarde, M.G.: From polaron to solectron. J. Comput. Appl. Math. **233**, 1432–1445 (2010)
2. Cantu Ros, O.G., Cruzeiro, L., Velarde, M.G., Ebeling, W.: On the possibility of electric transport mediated by long living intrinsic localized solectron modes. Eur. Phys. J. B **80**, 545–554 (2011)
3. Velarde, M.G., Brizhik, L., Chetverikov, A.P., Cruzeiro, L., Ebeling, W., Ropke, G.: Quartic lattice interactions, soliton-like excitations, and electron pairing in one-dimensional anharmonic crystals. Int. J Quant. Chem. **112**, 2591–2598 (2012) [and references therein]
4. Hermelin, S., Takada, S., Yamamoto, M., Tarucha, S., Wieck, A. D., Saminadayar, L., Bauerle, C., Meunier, T.: Electrons surfing on a sound wave as a platform for quantum optics with flying electrons. Nature **477**, 435–438 (2011)
5. McNeil, R.P.G., Kataoka, M., Ford, C.J.B., Barnes, C.H.W., Anderson, D., Jones, G.A.C., Farrer, I., Ritchie, D.A.: On-demand single-electron transfer between distant quantum dots. Nature **477**, 439–442 (2011)
6. Gevaux, D.: Electrons surf the wave. Nat. Phys. **7**, 748 (2011)
7. Everett, H.: Relative state formulation of quantum mechanics. Rev. Mod. Phys. **29**, 454–462 (1957)
8. Pomeau, Y., Le Berre, M.: Optical soliton as quantum objects. Chaos **17**, 037118 (2007)

Collective Excitations in Superfluid Fermi Gases in the BCS-BEC Crossover

G.-X. Huang

1 Introduction

In the earlier time of the last century, Onnes [1] obtained a fermionic superfluid through cooling Hg and other metals by using liquid helium at temperature T around 4 K. Such fermionic superfluid was later successfully described by the Bardeen-Copper-Schriffer (BCS) theory. Soon after the finding of H. K. Onnes, Wolfke and Keesom [2] lowered T further to make the liquid helium enter a bosonic superfluid state, which can be described principally by the mechanism of Bose-Einstein condensation (BEC).

By continual effort of nearly 100 years, physicists are now able to obtain ultracold bosonic atomic gases with T about the order of magnitude of several tens of nK, thanks to the tremendous progress of laser cooling and trapping techniques [3–5]. Based on this achievement, the BEC of nearly ideal Bose gases (such as alkali metallic atoms ^{87}Rb, ^{23}Na), predicted by A. Einstein in 1925 [6], was at last realized in 1995 [7, 8].

Soon after this breakthrough, the ultralow temperature and superfluid state of fermionic atoms (such as ^{6}Li, ^{40}K, etc.) were also obtained [9, 10]. In addition, the crossover from BCS state to BEC was also realized by using Feshbach resonance technique [9, 10]. These important progresses make the study of ultracold atomic physics become one of very active research frontiers of physics in the beginning of twenty first century. More importantly, such study also becomes a cross point connected with many different physical disciplines, including atomic and molecular physics, nonlinear and quantum optics, statistical and condensed matter physics, etc., and even chemistry. A lot of new experimental findings are expected and new physics will be revealed and many applications are very promising [11–13].

G.-X. Huang (✉)
State Key Laboratory for Precision Spectroscopy and Department of Physics,
East China Normal University, Shanghai 200062, China
e-mail: gxhuang@phy.ecnu.edu.cn

R.G. Rubio et al. (eds.), *Without Bounds: A Scientific Canvas of Nonlinearity and Complex Dynamics*, Understanding Complex Systems,
DOI 10.1007/978-3-642-34070-3_38,

Roughly speaking, if taking the experimental realization of BEC of alkali metallic atoms in 1995 as a starting point, the research of ultracold quantum degenerate atomic gases can be divided as two main stages. (1) From 1995 to 2001, main focus is on the BEC of bosonic atomic gases and their various features and applications. Because the interaction between atoms is very weak, the most physical properties of BEC can be described by the Gross-Pitaevskii (GP) equation, and hence related studies are relatively simple in theory. (2) From 2002 to present, the focal point is moved into superfluid Fermi gases, after the degenerate fermionic atomic gases was realized and the interatomic interaction can be manipulated by using Feshbach resonance. The main research topic is the transition from BEC to BCS state, and quantum simulation of strongly correlated many-body systems.

The problem of the BCS-BEC crossover is not only of fundamental interest in condensed matter physics but also closely related to the understanding of physical mechanism for high-T_c superconductivity. Notice that the study of superfluid fermionic atomic gases is different from bosonic atomic gases due to different quantum statistical features and the role of interactions. The first important difference is that dilute Fermi gases at low temperature occupying a single spin state practically do not interact due to the suppression of s-wave scattering by Pauli exclusion principle. This provides an possibility for obtaining almost ideal Fermi gases, with potential applications to precision measurements and quantum information. The second important difference is that the superfluid in Fermi gases is resulted by interparticle interaction giving rise to paring effect [9, 10].

At low temperature, collective excitations are most important quasiparticles in a superfluid system and they can be used to characterize dominant physical property of system. Since the experimental realization of the BCS-BEC crossover, considerable interest has focused on the study of collective excitations in harmonically trapped superfluid Fermi gases. By means of the Feshbach resonance, the atom-atom interaction for dilute gases, characterized by s-wave scattering length, can be tuned from large positive to large negative values, providing a possibility to investigate and manipulate the nature of collective excitations in various superfluid regimes.

In recent years, a large body of experimental works on collective excitations in superfluid Fermi gases in the BEC-BCS crossover have been carried out, especially at Duke and Innsbruck [14–19]. Theoretically, up to now there exist two approaches on the collective excitations in superfluid Fermi gases in the BCS-BEC crossover [20–50]. One of them is microscopic theory, in which single-channel (Fermi-only) or two-channel (Fermi-Boson) model Hamiltonians with Fermi or Fermi-Boson degrees of freedom are used. Because in the experiments of superfluid Fermi gases [51–61] particles are trapped in an external potential, the inhomogeneous feature of system makes the microscopic approach not easy to handle. However, since at very low temperature the condensed fermionic atom pairs do not decay into single atoms due to the existence of energy gap in their excitation spectrum, no single fermionic atoms appear by the breaking of condensed atom pairs. The dynamics of such perfect superfluid can be well described phenomenologically by superfluid hydrodynamic equations, or an order-parameter equation called generalized Gross-Pitaevskii (GGP) equation when a suitable quantum pressure effect is taken into

account [34–36, 40–50]. Different superfluid regimes can be characterized by an equation of state, which can be obtained by a quantum Monte-Carlo simulation [62–64] or BCS energy-gap equations [32, 33]. The GGP equation captures dominant feature that the superfluid exhibits macroscopically, with its mathematical framework simple and thus easy to analyze. Consequently, it is reasonable to expect that the GGP theory is a useful theoretical tool for studying macroscopically the dynamics of superfluid Fermi gases in the BCS-BEC crossover.

In this article, we summarize the theoretical results on linear and nonlinear collective excitations in superfluid Fermi gases in the BCS-BEC crossover carried out recently at Shanghai. The rest of the article is arranged as follows. Section 2 describes the result obtained for eigenvalues and eigenfunctions of linear collective excitations for systems of three-dimensional (3D) trapping potentials with spherical and axial symmetries. Corresponding result beyond mean-field and Thomas-Fermi approximations is also provided explicitly. Furthermore, linear excitations and sound propagation in a cigar-shaped 3D superfluid Fermi gas is presented and eigenvalue problems of linear collective excitations for quasi 1D and quasi 2D systems have been solved exactly. Section 3 describes nonlinear excitations, including the dark solitons in a Q1D condensate and the bright solitons in a cigar-shaped 3D condensate. The last section contains a summary and some perspectives for further studies on the excitations in superfluid Fermi gases in future.

2 Linear Excitations

2.1 Superfluid Hydrodynamic Equations and Generalized Order Parameter Equation

We consider a system of superfluid Fermi (i.e. ^{6}Li or ^{40}K) gas in which fermionic atoms have two different internal states and atomic numbers in each internal state are the same. In ground state condensed fermionic atom pair density is $n/2$, where n is atomic density. By means of Feshbach resonance the transition from BCS to BEC regimes can be realized through tuning an applied magnetic field, and hence changing the s-wave scattering length $a_{\rm sc}$. When $a_{\rm sc} < 0$ ($a_{\rm sc} > 0$), the system is in a BCS (BEC) regime. By defining a dimensionless interaction parameter $\eta \equiv 1/(k_F a_{\rm sc})$, where $k_F = (3\pi^2 n)^{1/3}$ is Fermi wavenumber, one can distinguish several different superfluidity regimes [9, 10], i.e., BCS regime ($\eta < -1$), BEC regime ($\eta > 1$), and BEC-BCS crossover regime ($-1 < \eta < 1$). $\eta = -\infty$ ($\eta = +\infty$) is called BCS (BEC) limit and $\eta = 0$ is called unitarity limit. Both theoretical and experimental studies show that the transition from BCS regime to BEC regime is smooth [9, 10], which hints that one can study the physical property of system in various superfluid regimes in a unified way.

At zero temperature, the macroscopic dynamics of the superfluid is governed by the hydrodynamic equations [9]

$$\frac{\partial n}{\partial t} + \nabla \cdot (n\mathbf{v}) = 0, \tag{1}$$

$$m\frac{\partial \mathbf{v}}{\partial t} + \nabla\left[\frac{1}{2}m\mathbf{v}^2 + \mu(n) + V_{\text{ext}}(\mathbf{r})\right] = 0, \tag{2}$$

where $\mathbf{v}$ is atomic velocity, m is atomic mass, and $V_{\text{ext}}(\mathbf{r}) = (m/2)[\omega_\perp^2(x^2 + y^2) + \omega_z^2 z^2]$ is an external trapping potential. The equation of state (also called bulk chemical potential) under a local density approximation has the form $\mu(n) = \partial[n\varepsilon(n)]/\partial n$, where $\varepsilon(n)$ is the bulk energy per particle when the trapping potential is absent. Introducing $\varepsilon(n) = (3/5)\varepsilon_F\sigma(\eta)$, with $\varepsilon_F = \hbar^2 k_F^2/(2m)$ being Fermi energy, one obtains $\mu(n) = \varepsilon_F[\sigma - (\eta/5)(\partial\sigma/\partial\eta)]$. As a function of n, the expression of $\mu(n)$ is very complicated, which prevents us from obtaining analytical results on the dynamics of the system. A simple approach is to take a polytropic approximation, i.e., by assuming

$$\mu(n) = \mu^0\left(n/n^0\right)^\gamma \tag{3}$$

with $\gamma = (n/\mu)(\partial\mu/\partial n)_{\eta=\eta^0}$, where μ^0 and n^0 are respectively reference chemical potential and particle number density of the system, introduced here for convenience [47]. In the following we take n^0 to be the equilibrium superfluid density at the center of the trapping potential. Thus one has $\mu^0 = \varepsilon_F^0(\sigma(\eta^0) - \eta^0\sigma'(\eta^0)/5)$, with $\varepsilon_F^0 = (\hbar k_F^0)^2/(2m)$, $\eta^0 = 1/(k_F^0 a_s)$ and $k_F^0 = (3\pi n^0)^{1/3}$ [47]. There are two well known limits for the value of the polytropic index γ. One is $\gamma = 2/3$ at $\eta^0 \to -\infty$ (BCS limit) and another one is $\gamma = 1$ at $\eta^0 \to +\infty$ (BEC limit). The polytropic approximation has advantage of allowing one to obtain analytical results for various superfluid regimes in a unified way. In fact, it is quite accurate because γ is a slowly-varying function of η^0 and hence widely used in literature [32–36, 40–45].

Notice that at $T = 0$ the system consists of only condensed fermionic atom pairs. The order parameter of the condensate can be expressed as $\langle\hat{\psi}_a(\mathbf{r} - \rho/2)\hat{\psi}_b(\mathbf{r} + \rho/2)\rangle$, where $\hat{\psi}_j(\mathbf{r} \pm \rho/2)$ is the Fermi annihilation operator that destroys one fermion in the internal state j ($j = a$ or b; $a \neq b$) located at position $\mathbf{r} \pm \rho/2$. For a superfluid with velocity $\mathbf{v}_s$ the momentum of each particle is boosted by an amount $m\mathbf{v}_s$ and the order parameter $\langle\hat{\psi}_a(\mathbf{r} - \rho/2)\hat{\psi}_b(\mathbf{r} + \rho/2)\rangle$ will be multiplied by a factor $\exp(2i\phi)$ with $\phi = m\mathbf{v}_s \cdot \mathbf{r}/\hbar$. Obviously, $\Phi_s \equiv 2\phi = M\mathbf{v}_s \cdot \mathbf{r}/\hbar$ (here $M = 2m$ is pair mass) is the phase of $\langle\hat{\psi}_a(\mathbf{r} - \rho/2)\hat{\psi}_b(\mathbf{r} + \rho/2)\rangle$ and one has $\mathbf{v}_s = (\hbar/M)\nabla\Phi_s$. The change in the phase of the order parameter is independent of the relative coordinate ρ and thus we can put ρ to zero [11, 47].

Noting that pair density $n_s = n/2$ and superfluid velocity $\mathbf{v_s} = \mathbf{v}$, (1) and (2) can be written into the form

$$\frac{\partial n_s}{\partial t} + \nabla \cdot (n_s\mathbf{v_s}) = 0, \tag{4}$$

$$M\frac{\partial \mathbf{v_s}}{\partial t} + \nabla\left[\frac{M}{2}\mathbf{v}_s^2 + \mu_s(n_s) + V_{\text{ext}}^s(\mathbf{r})\right] = 0, \tag{5}$$

with $\mu_s(n_s) = 2\mu(2n_s)$ and

$$V_{\text{ext}}^s(\mathbf{r}) = \frac{1}{2}M\left[\omega_\perp^2(x^2+y^2)+\omega_z^2 z^2\right]. \tag{6}$$

If a quantum pressure term $-\hbar^2\nabla^2\sqrt{n_s}/(2M\sqrt{n_s})$ is included, (4) and (5) can be transferred into the GGP equation

$$i\hbar\frac{\partial\Psi_s}{\partial t} = \left[-\frac{\hbar^2\nabla^2}{2M} + V_{\text{ext}}^s(\mathbf{r}) + \mu_s(n_s)\right]\Psi_s, \tag{7}$$

where $\Psi_s(\mathbf{r},t) = \sqrt{n_s}\exp(i\Phi_s)$, which is the order parameter of the condensed fermionic atomic pairs. It is easy to show that in the BEC limit (i.e. $\gamma = 1$) the GGP (7) coincides exactly with the order-parameter equation obtained in [65] based on an extended BCS theory. Equation (7) was first presented in [47] and used successfully to study the interference patterns of a superfluid Fermi gas released from optical lattices below and above Feshbach resonance [53]. Nearly at same time, Salasnich and Toigo [66] derived an order parameter similar to (7) by using an extended Thomas-Fermi density functional theory. Many researches show that the GGP equation (7) is quite accurate at least between BEC and the vicinity of the unitarity regimes. In the following, the subscript "s" in (4)–(7) will be omitted.

2.2 Linear Excitations in Three Dimensions

2.2.1 Eigenvalues and Eigenfunctions for Spherically and Axially Symmetric Traps

Linear collective excitations are investigated in [42] by using the superfluid hydrodynamic equations (4) and (5). The equilibrium (ground state) solution of the system (corresponding to $\mathbf{v} = 0$ and $\partial/\partial t = 0$) satisfies $V_{\text{ext}}(\mathbf{r}) + \mu[n_G(\mathbf{r})] = \mu_G$ and $\int d^3\mathbf{r} n_G(\mathbf{r}) = N$ (N is fermionic-pair number in the condensate), which for the chemical potential (3) gives the ground-state density distribution

$$n = n^{\text{eq}}(\mathbf{r}) = n^{\text{eq}}(0)\left(1 - \frac{x^2+y^2}{R_\perp^2} - \frac{z^2}{R_z^2}\right)^{1/\gamma}, \tag{8}$$

where $n^{\text{eq}}(0) = n_0[\mu_G/(2\mu^0)]^{1/\gamma}$, $R_\perp = \left(2\mu_G/M\omega_\perp^2\right)^{1/2}$ and $R_z = \left(2\mu_G/M\omega_z^2\right)^{1/2}$ are respectively radial and axial half-lengths of the condensate at equilibrium, μ_G is the chemical potential at the ground state given by Wen et al. [50]

$$\mu_G = 2\varepsilon_F^0\left[\left(\frac{\sigma(\eta^0)-\eta^0\sigma'(\eta^0)}{5}\right)^{\frac{1}{\gamma}}\frac{\pi^{\frac{1}{2}}(1+\gamma)\Gamma(\frac{1}{\gamma}+\frac{5}{2})}{8\gamma\Gamma(\frac{1}{\gamma}+2)}\right]^{\frac{2\gamma}{2+3\gamma}}. \tag{9}$$

Setting $n(\mathbf{r},t)=n^{\rm eq}(\mathbf{r})+\delta n(\mathbf{r})\exp(-i\omega t)+$c.c. and $\mathbf{v}(\mathbf{r},t)=\delta\mathbf{v}(\mathbf{r})\exp(-i\omega t)+$ c.c. with $\delta n(\mathbf{r})$ and $\delta\mathbf{v}(\mathbf{r})$ being small quantities, we obtain the eigenvalue problem for linear excitations

$$\hat{H}_0\delta n\equiv-\frac{1}{M}\nabla\cdot\left\{n^{\rm eq}(\mathbf{r})\nabla\left[\left(\frac{\partial\mu}{\partial n}\right)_{\rm n=n^{eq}(r)}\delta n\right]\right\}=\omega^2\delta n. \tag{10}$$

(i) *Spherically symmetric trap*. In this case $\omega_z=\omega_\perp$ and hence $\lambda=1$. The orbital angular momentum l, and its projection in z axis, m, are two good quantum numbers. Therefore, the eigen equation (10) is separable in spherical polar coordinates (r,θ,φ), where $r=\left[x^2+y^2+z^2\right]^{1/2}$. The linear excitation of the system is determined by a radial expansion into a polynomial of order n_r. The eigenmodes of the excitation can be labelled by entire quantum numbers n_r, l and m, but the eigenfrequencies are independent of axial quantum number m.

By introducing $\overline{\nabla}=R_\perp\nabla$, (10) can be written into the dimensionless form

$$-\overline{\nabla}\cdot[\overline{n}^{\rm eq}(\overline{\nabla}(\overline{n}^{\rm eq})^{\gamma-1}\delta n)]=(2\overline{\omega}^2/\gamma)\delta n \tag{11}$$

with $\overline{\omega}=\omega/\omega_\perp$, $\overline{n}^{\rm eq}=n^{\rm eq}(\mathbf{r})/n^{\rm eq}(0)=(1-\overline{r}^2)^{1/\gamma}$, with $\overline{r}^2=r^2/R_\perp^2$ $(R_\perp=R_z)$. The solution of (11) has the form $\delta n=\overline{r}^l(\overline{n}^{\rm eq})^{1-\gamma}P(\overline{r})Y_{lm}(\theta,\varphi)$, where Y_{lm} are the spherical-harmonic functions and the radial function $P(\overline{r})$ can be written as $(1-x)^{1/\gamma-1}Q(x)$, where $x\equiv\overline{r}^2$ and $Q(x)$ satisfies a hypergeometric differential equation

$$x(1-x)Q''+[l+3/2-(l+3/2+1/\gamma)x]\,Q'+1/(2\gamma)(\overline{\omega}^2-l)Q=0. \tag{12}$$

Solutions of (12) are a special hypergeometric series [32] $P_{n_rl}(x)=F(-n_r,n_r+l+1/\gamma+1/2,l+3/2,\overline{r}^2)$, i.e. a classical n_sth-order Jacobi polynomials $P_{n_rl}(x)=n_rB[n_r,l+3/2]P_{n_s}^{(l+1/2|,1/\gamma-1)}(1-2x)$ with $B[x,y]$ being a beta function. The eigenvalue is given by

$$\overline{\omega}_{n_rl}^2=l+n_r\gamma(2n_r+2l+1)+2n_r, \tag{13}$$

with $n_r=0,1,2,\cdots$. and $l=0,1,2,\cdots$. We see that the eigenvalues are independent of m and hence the eigenfunctions have $2l+1$-fold degeneracy for a given l.

Notice that the above results cover several important special cases studied before. In the deep BEC regime, $\gamma=1$ and thus (13) reduces to $\overline{\omega}_{n_rl}^2=l+n_r(2n_r+2l+3)$, which was obtained by Stringari [67]. In the deep BCS region, $\gamma=2/3$ and hence (13) becomes $\overline{\omega}_{n_rl}^2=l+\frac{4}{3}n_r(n_r+l+2)$, which is the same as that obtained by Baranov and Petrov [68] (also see [69]). Especially, in the unitarity limit where $a_s=\pm\infty$ and $\gamma=2/3$, the spectrum also has the finite form of $\overline{\omega}_{n_rl}^2=l+4n_r(n_r+l+2)/3$.

(ii) *Axially symmetric trap*. In this case $\lambda \neq 1$. Solving (10) for the case of axial symmetry is not easy like for the case of the spherical symmetry. However, the axial symmetric case is more important than the spherical symmetric one because axial symmetric traps are used in almost all experiments made on the collective excitations in superfluid Fermi gases [14–19]. In this case, for the axial component of angular momentum, m is still a good quantum number. In the cylindrical coordinates $(\bar{s}, \bar{z}, \varphi)$ (here $\bar{s}^2 \equiv \bar{x}^2 + \bar{y}^2$, with $(\bar{x}, \bar{y}) = (x, y)/R_\perp$ and $\bar{z} = z/R_z$), eigenfunctions are found to have the following form [42]

$$\delta n_{n_p}^{(2n_s)}(\bar{z}, \bar{s}, \varphi) = \left(1 - \bar{s}^2 - \lambda^2 \bar{z}^2\right)^{1/\gamma - 1} \bar{s}^{|m|} P_{n_p}^{(2n_s)}(\bar{z}, \bar{s}) e^{im\varphi}, \tag{14}$$

where the coupled axial and radial function $P = P_{n_p}^{(2n_s)}(\bar{s}, \bar{z})$ satisfies the 2D partial differential equation

$$\begin{aligned} &\left(1 - \bar{s}^2 - \lambda^2 \bar{z}^2\right) \left[\frac{\partial^2}{\partial \bar{s}^2} + (1 + 2|m|) \frac{\partial^2}{\partial \bar{s}^2} + \frac{\partial^2}{\partial \bar{z}^2} \right] \\ &- \frac{2}{\gamma} \left(\bar{s} \frac{\partial}{\partial \bar{s}} + \lambda^2 \bar{z} \frac{\partial}{\partial \bar{z}} \right) + \frac{2}{\gamma} (\bar{\omega}^2 - |m|) \Bigg) P(\bar{s}, \bar{z}) = 0, \end{aligned} \tag{15}$$

and the corresponding eigenfunction takes the form

$$P_{n_p}^{(2n_s)}(\bar{z}, \bar{s}) = \sum_{k=0}^{n_p} \sum_{n=0}^{\mathrm{int}[k/2]} b_{k,n} \bar{z}^{k-2n} \bar{s}^{2n}, \tag{16}$$

where n_p is the principal quantum number for total energy. From (16) we know that for a fixed n_p, n_s is the radial quantum number for the series of modes $2n_s$ and $n_s = 0, 1, 2, \cdots, \mathrm{int}[n_p/2]$; n_z is correspondingly the axial quantum number satisfying the relation $n_z = n_p - 2n_s$ in the cylindrical coordinates.

By using techniques of decoupling and dimensionality reduction, one can generalize the solution obtained in [70] for $\gamma = 1$ to any value of γ. The detail of the calculation has been provided in the Appendix of [42]. For a fixed n_p $(= 0, 1, 2, \cdots)$, we can label the excitation spectrum $\bar{\omega}^2 = \bar{\omega}^2(n_p, |m|, \lambda^2, \gamma)$ by modes $(n_z n_s m)$. Once the coefficients $b_{k,n}$ are obtained, one can get all eigenfrequencies and eigenfunctions of the linear collective excitations. Some eigenmodes in low-excited states are listed below.

1. For $n_p = 0, 1$, one has $n_s = 0$ and $n_z = 0, 1$, respectively. The eigenfrequencies read

$$\bar{\omega}_{n_z 0m}^2 = |m| + \lambda^2 n_z (\gamma n_z - \gamma + 2)/2, \tag{17}$$

and the eigenfunctions are given by $\delta n_{n_p}^{(0)}(\bar{z}, \bar{s}) = (1 - \bar{s}^2 - \lambda^2 \bar{z}^2)^{1/\gamma - 1} e^{im\varphi}$ $b_{n_p,0} \bar{z}^{n_p} \bar{s}^{|m|}$.

2. For $n_p = 2$, we have $n_s = 0, 1$ and $n_z = 2, 0$, respectively. In this case one gets the following solutions for eigenfrequencies and the eigenfunctions

$$\begin{aligned}\overline{\omega}^2_{n_z n_s m} &= (1+\gamma)(1+|m|) + (1+\gamma/2)\lambda^2 \\ &\pm[(1+\gamma+\gamma|m|)^2 + [-2-3\gamma+\gamma^2 \\ &+(-2+\gamma)\gamma|m|]\lambda^2 + (1+\gamma/2)^2\lambda^4]^{1/2}, \end{aligned} \tag{18}$$

$$\begin{aligned}\delta n_2^{(2n_s)}(\overline{z},\overline{s}) &= (1-\overline{s}^2-\lambda^2\overline{z}^2)^{1/\gamma-1}e^{im\varphi} \\ &\times(b_{0,0}+b_{2,0}\overline{z}^2+b_{2,1}\overline{s}^2)\overline{s}^{|m|}, \end{aligned} \tag{19}$$

with $b_{2,1}/b_{0,0} = -(|m|-\overline{\omega}^2)/(2+|m|-\overline{\omega}^2)$ and $b_{2,0}/b_{0,0} = [2+2|m|+(2+|m|-\overline{\omega}^2)/\gamma] \times (|m|-\overline{\omega}^2)/(2+|m|-\overline{\omega}^2)$.

In (18), the plus sigh "+"(minus sign "−") represents either the $20m$ ($01m$) mode for $\lambda \geq 1$ or the $01m$ ($20m$) mode for $\lambda \leq 1$. In these modes, the ratio of the axial and radial amplitudes is $|b_{20}/b_{21}| = |2+2|m|+(2+|m|-\overline{\omega}^2)/\gamma| > (<)1$ for $\lambda > (<)1$. Therefore, the condensate oscillates along the z-axial (xy-plane) direction. Note that the special solutions found by Heiselberg [32] and Cozzini and Stringari [71] for the breathing modes are the special case here for $m = 0$. These $m = 0$ breathing modes have been investigated experimentally by Grimm and Thomas groups [14–17]. Figure 1 shows experimental and theoretical results of the radial and axial breathing modes with $\lambda = 0.05$. The dot-dashed lines in the figure are respectively the $1/(k_F a_{sc})$-dependence of the eigenfrequencies for the radial and axial breathing modes by using the theoretical result given above.

Our general solution provided here may give more theoretical predictions on the character of eigen-excitations of the system, including the density distributions along the BCS-BEC crossover of the radial (axial) breathing mode as a function of $1/(k_F a_{\rm sc})$ and λ. For some other concrete examples, see [42].

(iii) *Circinally symmetric case*. This corresponds a highly anisotropic trap, i.e. $\omega_z \ll \omega_\perp$ and hence $\lambda \to 0$. Equation (10) in this situation has the solution with the form $\delta n_{n_s m}(\mathbf{s}) = \overline{s}^{|m|}e^{im\varphi}P(\overline{s}^2)$, expressed by plane polar coordinates $(\overline{s},\varphi)$, where the radial function $P(x)$ ($x \equiv \overline{s}^2$) satisfies the differential equation

$$x(1-x)P'' + [(1+|m|) - (1+|m|+1/\gamma)x]P' + 1/(2\gamma)(\overline{\omega}^2 - |m|)P = 0. \tag{20}$$

The eigenfunctions of (20) are a special hypergeometric series $P_{n_s m}(x) = F(-n_s, n_s+|m|+1/\gamma, 1+|m|, \overline{s}^2)$, i.e. a classical n_sth-order Jacobi polynomials $P_{n_s m}(x) = n_s B[n_s, 1+|m|]P_{n_s}^{(|m|,1/\gamma-1)}(1-2x)$. The eigenvalues are given by

$$\overline{\omega}^2_{n_s m} = 2n_s\gamma(n_s+|m|) + 2n_s + |m|, \tag{21}$$

where the radial quantum number $n_s = 0, 1, 2, \cdots$.

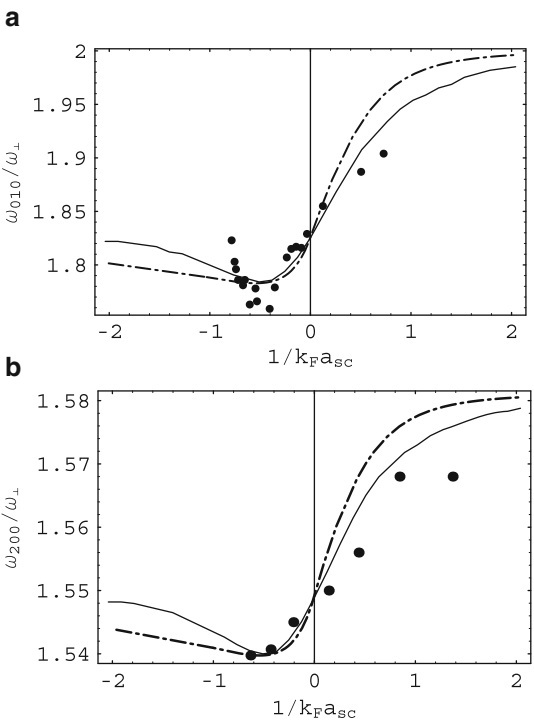

Fig. 1 $1/(k_F a_{sc})$ dependence of (**a**) the radial breathing mode frequency $\overline{\omega}_{010}$ and (**b**) the axial breathing mode frequency $\overline{\omega}_{200}$. *Dot-dashed line* is the theoretical result for the eigenfrequency with $\lambda = 0.05$, the value used in most of experiments. *Solid line* is the result of parametrization based on a Monte Carlo data [36]. *Heavy dots* are the results from experiments [15–17] in (**a**) and [14] in (**b**)

2.2.2 Excitations Beyond Mean-Field and Thomas-Fermi Approximations

In experiments of ultracold atomic physics, excitation spectra of collective modes can be measured with very high precision, which has been used to test the theoretical prediction based on various theories on the BCS-BEC crossover. A very intriguing question in the study of the BCS-BEC crossover is the presence or absence of the famous Lee-Huang-Yang terms [72, 73] in the equation of state, corresponding to beyond-mean-field terms of composite bosons. The experimental result reported by Grimm group [19] demonstrated clearly that the mean-field theory is not valid in the BCS-BEC crossover and hence a beyond the mean-field approximation is needed.

The polytropic approximation (3) for equation of state is widely used for obtaining analytical results of oscillating frequencies of collective modes. However, such approximation works well only in the BEC, BCS and unitarity limits without the contribution beyond mean-field. In [48], a perturbation method is developed for calculating the correction beyond mean-field for collective-mode frequencies of a trapped superfluid Fermi gas in the BCS-BEC crossover for a broad Feshbach resonance, generalized the work by Pitaevskii and Stringari [74] where the frequency corrections of some collective modes in a trapped Bose gas were provided beyond mean field approximation. The main idea developed in [48] is described below.

Table 1 Parameters of the equation of state in different superfluid limits

Limit	γ_0	γ_1	C_0	C_1
BCS	2/3	1/3	$\frac{\hbar^2}{2M}(3\pi^2)^{2/3}$	$\frac{4a_{sc}}{(9\pi)^{1/3}}$
BEC	1	1/2	$\frac{\pi\hbar^2 a_m}{2M}$	$\frac{32}{3\sqrt{2}}a_m^{3/2}$
Unitarity	2/3	$-1/3$	$\frac{\hbar^2}{2M}(3\pi^2)^{2/3}\xi$	$-\frac{4\zeta}{5\xi}\frac{1}{(3\pi^2)^{1/3}a_{sc}}$

Following [75], a perturbation expansion is applied to the equation of state in the BCS-BEC crossover in various regimes in term of the expansion parameter na_{sc}^3 in weak interacting regime or $1/(na_{sc}^3)$ in strong interacting regime, i.e.

$$\mu(n) = C_0 n^{\gamma_0}\left(1 + C_1 n^{\gamma_1} + \cdots\right), \tag{22}$$

where C_0, C_1, γ_0, $\gamma_1, \ldots$ are constants that are different in different superfluid regimes. For instances, near the BCS, BEC, and unitarity limits their values are already known [34–36, 76], which have been listed in Table 1. In the table, the s-wave scattering length in the BEC limit is $a_m \approx 3a_{sc}/5$ [77]; parameters ξ and ζ in the unitarity limit are given by quantum Monte Carlo calculations, i.e. $\xi \approx 0.42 \pm 0.01$ and $\zeta \approx 1$ [63, 64]. In other superfluid regimes that different the above limits, parameters of γ_0, γ_1, C_0, and C_1 are currently not known.

In the expansion of the equation of state (22), the second term on the right hand side is Lee-Huang-Yang-like term, originated generally from beyond mean field effect. Such term is assumed to be much smaller than the first term, i.e. $|C_1\rho^{\gamma_1}| \ll 1$. It is easy to get the chemical potential and condensate density in the ground state up to the first-order approximation

$$\mu_G = \mu_G^{(0)} + \mu_G^{(1)}, \tag{23}$$

$$\rho_G(\mathbf{r}) = \rho_G^{(0)}(\mathbf{r}) + \frac{\mu_G^{(1)}}{\gamma_0 C_0}\left(\rho_G^{(0)}(\mathbf{r})\right)^{1-\gamma_0} - \frac{C_1}{\gamma_0}\left(\rho_G^{(0)}(\mathbf{r})\right)^{1+\gamma_1}. \tag{24}$$

For explicit expressions of $\mu_G^{(0)}$, $\mu_G^{(1)}$ and $\rho_G^{(0)}(\mathbf{r})$, see [48].

The eigen equation (10) can be written as the form

$$(\hat{h}_0 + \hat{h}')\delta n = \omega^2 \delta n, \tag{25}$$

with $\hat{h}_0 = -\frac{1}{M}C_0\gamma_0\nabla\cdot n_G\nabla n_G^{\gamma_0-1}$ and $\hat{h}' = -\frac{1}{M}C_0C_1(\gamma_0+\gamma_1)\nabla\cdot n_G\nabla n_G^{\gamma_0+\gamma_1-1}$. Using the transformation $\Psi(\mathbf{r}) = n_G^{\gamma_0-1}(\mathbf{r})\delta n(\mathbf{r})$, (25) is converted into

$$\left(\hat{H}_0 + \hat{H}'\right)\Psi = E n_G^{1-\gamma_0}\Psi \tag{26}$$

with $\hat{H}_0 = \nabla \cdot n_G \nabla$, $\hat{H}' = C_1(1+\gamma_1/\gamma_0)\nabla \cdot n_G \nabla n_G^{\gamma_1}$, and $E = -M\omega^2/(C_0\gamma_0)$. Since both $\hat{H}_0$ and $\hat{H}'$ are Hermitian operators and $\hat{H}'$ is a small quantity, one can solve the eigen equation (26) by applying a perturbation method similar to that developed in quantum mechanics if all eigenvalues and eigenfunctions of the operator $\hat{H}_0$ can be obtained.

Making the perturbation expansion $\Psi = \Psi^{(0)} + \Psi^{(1)} + \Psi^{(2)} + \cdots$, $E = E^{(0)} + E^{(1)} + E^{(2)} + \cdots$, (26) is converted into

$$\hat{H}_0\Psi^{(k)} - E^{(0)} n_G^{1-\gamma_0}\Psi = S^{(k)}, \quad (k = 0, 1, 2, \ldots), \tag{27}$$

with $S^{(0)} = 0$, $S^{(1)} = (E^{(1)} n_G^{1-\gamma_0} - \hat{H}')\Psi^{(0)}$, $S^{(2)} = E^{(2)} n_G^{1-\gamma_0}\Psi^{(0)} + (E^{(1)} n_G^{1-\gamma_0} - \hat{H}')\Psi^{(1)}, \cdots\cdots$.

At the leading-order ($k = 0$), one has $\hat{H}_0\Psi^{(0)} - E^{(0)} n_G^{1-\gamma_0}\Psi^{(0)} = 0$. Assume $\Psi_j^{(0)}$ is an eigenfunction of $\hat{H}_0$ with eigenvalue $E_j^{(0)}$. it is easy to obtain the orthogonality relation

$$\int d^3\mathbf{r} n_G^{1-\gamma_0}\Psi_{j'}^{(0)*}\Psi_j^{(0)} = I_j \delta_{jj'}, \tag{28}$$

where $I_j = \int d^3\mathbf{r} n_G^{1-\gamma_0}\Psi_j^{(0)*}\Psi_j^{(0)}$ is the normalization constant for the jth mode.

At the next order ($k = 1$), using the leading-order solution equation (27) takes the form

$$\hat{H}_0\Psi^{(1)} - E_j^{(0)} n_G^{1-\gamma_0}\Psi^{(1)} = \left(E^{(1)} n_G^{1-\gamma_0} - \hat{H}'\right)\Psi_j^{(0)}. \tag{29}$$

Since $\hat{H}_0$ is a Hermitian operator, its eigenfunctions constitutes a complete set, and thus one can make the expansion $\Psi^{(1)} = \sum_j A_j \Psi_j^{(0)}$. Substituting this expression into (29) and applying the orthogonal relation (28) we can readily obtain A_j. Then one has the first-order corrections for the eigenvalue and eigenfunction

$$E_j^{(1)} = H'_{jj}, \tag{30}$$

$$\Psi_j^{(1)} = \sum_{j' \neq j} \frac{H'_{j'j}}{E_j - E_{j'}}\Psi_j^{(0)}, \tag{31}$$

where $H'_{j'j} = (1/I_j)\int d^3\mathbf{r}\Psi_j^{(0)*}\hat{H}'\Psi_j^{(0)}$. Similarly, explicit formulas of high-order corrections for all eigenfrequencies and eigenfunctions can be obtained.

Converting the above quantities to original ones, we obtain expressions of the eigenfrequency and eigenfunction up to the first-order correction as

$$\omega_j^2 = -\frac{C_0\gamma_0}{M}\left(E_j^{(0)} + E_j^{(1)}\right), \tag{32}$$

$$\delta n_j = n_G^{1-\gamma_0}\left(\Psi_j^{(0)} + \Psi_j^{(1)}\right). \tag{33}$$

For convenience, we introduce the dimensionless quantities $\overline{\omega}_j = \omega_j/\omega_\perp$, $\overline{\mathbf{r}} = \mathbf{r}/R_\perp$, $\overline{\nabla} = R_\perp \nabla$, $\overline{n}(\overline{\mathbf{r}}) = n(\mathbf{r})/n_G(0)$, and $\overline{\Psi}(\overline{\mathbf{r}}) = \Psi(\mathbf{r})/n_G^{\gamma_0}(0) = \overline{n}_G^{\gamma_0-1}(\overline{\mathbf{r}})\ \delta n(\mathbf{r})/n_G(0)$. Then from (32) we obtain the calculating formula for the first-order correction of $\overline{\omega}_j^2$

$$\delta\overline{\omega}_j^2 = \Delta(\lambda)\, Q_j(\lambda), \tag{34}$$

with $\Delta(\lambda) = C_1 n_G^{\gamma_1}(0;\lambda)$, and

$$Q_j(\lambda) \equiv -\frac{(\gamma_0+\gamma_1)\int d^3\overline{\mathbf{r}}\overline{n}_G^{1+\gamma_1}\overline{\Psi}_j^{(0)*}\overline{\nabla}^2\overline{\Psi}_j^{(0)}}{2\int d^3\overline{\mathbf{r}}\overline{n}_G^{1-\gamma_0}|\overline{\Psi}_j^{(0)}|^2}. \tag{35}$$

Here the integration domain in (35) is $\overline{s}^2 + \lambda^2\overline{z}^2 \le 1$. The value of $n_G(0;\lambda)$ can be obtained easily from (23) and (24) by setting $\mathbf{r} = 0$.

The key of the above perturbation theory is to solve the zero-order eigenvalue problem. Luckily, a similar eigenvalue problem has been solved exactly, and all eigenvalues $E_j^{(0)}$ and all eigenfunctions $\Psi_j^{(0)}$ have been given in [42], where j represents a group of quantum numbers. Consequently, one can apply the perturbation formulas presented above and the results in [42] to obtain explicit analytical expressions of the frequency and wavefunction corrections for various collective modes beyond mean-field approximation. For the detail of theoretical results and their comparison with experiments, see [48].

The above works are based on superfluid hydrodynamic equations (4) and (5), which are valid for Thomas-Fermi approximation (TFA), i.e. N must be large enough. When N is finite (which is the case for realistic experiments where N is typically the order of 10^5–10^6), the quantum pressure (or called surface effect [78]) contributed from the inhomogeneous distribution of condensation due to the existence of trapping potential must be taken into account. In this case, the superfluid can be described by the GGP equation (7). There are several other reasons to extend TFA: (i) At the boundary of condensate the Bogoliubov amplitudes obtained in the TFA vary quickly and hence the kinetic energy of both the condensate and excitations contributed by the boundary can not be neglected. (ii) At the boundary of the condensate singular points appear in the solution of the Bogoliubov amplitudes which makes the theory uncontrollable. (iii) The existence of the singular points results also in a divergence for coupling matrix elements describing mode-mode resonant interaction, which takes dominant role for the damping and frequency shift of collective modes in superfluid Fermi gases.

The work presented in [45] studied Bogoliubov collective excitations of harmonically trapped superfluid Fermi gases in the BCS-BEC crossover beyond TFA. Starting from a generalized Gross-Pitaevskii equation, Bogoliubov-de Gennes (BdG) equations for low-lying collective modes at zero temperature are derived. A Fetter-like variational ground state wavefunction is used to remove the non-continuity of slope at the boundary of condensate, which appears in the TFA. The BdG

equations are solved analytically and explicit expressions for all eigenvalues and eigenfunctions are obtained, which are valid for various crossover regimes and for traps with spherical and axial symmetries. The feature of these collective excitations in the BCS-BEC crossover is discussed and the theoretical result obtained agrees with available experimental data near and beyond TFA. For detail, see [45].

2.2.3 Linear Excitations and Sound Propagation in a Cigar-Shaped 3D Superfluid Fermi Gas

If the condensate is a cigar-shaped, and it is very long in axial direction, eigen excitations in the condensate are standing waves in transverse directions but are traveling waves in the axial direction, with the lowest eigenmode being a sound wave. The eigenvalue problem for linear excitations is still given by (10) with $\omega_z = 0$. Then the ground-state density is simplified into $n^{\rm eq}(r) = n^0 \left(\mu_G/2\mu^0\right)^{1/\gamma} \left(1 - r^2/R_\perp^2\right)^{1/\gamma}$. Taking $\delta n(\mathbf{r}) = \delta n(r,\varphi)\exp(ikz)$ (k is wavenumber in the axial direction), (10) is reduced into the dimensionless form

$$\overline{\nabla}_\perp \cdot \left\{ \left(1-\overline{r}^2\right)^{\frac{1}{\gamma}} \overline{\nabla}_\perp \left[\left(1-\overline{r}^2\right)^{1-\frac{1}{\gamma}} \delta n(\overline{r},\varphi) \right] \right\} - \overline{k}^2 (1-\overline{r}^2)\delta n(\overline{r},\varphi) = -\frac{2\overline{\omega}^2}{\gamma}\delta n(\overline{r},\varphi), \tag{36}$$

where $\overline{\nabla}_\perp = (\partial/\partial\overline{r}, (1/\overline{r})\partial/\partial\varphi)$, $\overline{r} = r/R_\perp$, $\overline{\omega} = \omega/\omega_\perp$, and $\overline{k} = kR_\perp$.

In order to solve above equation we introduce the following transformation $\Psi(\overline{r},\varphi) = \left(1-\overline{r}^2\right)^{1-\frac{1}{\gamma}} \delta n(\overline{r},\varphi)$, then (36) is converted into the form

$$\left(\hat{H}_0 + \hat{H}'\right)\Psi = E\, w(\overline{r},\varphi)\Psi, \tag{37}$$

where $E = -2\overline{\omega}^2/\gamma$, $w(\overline{r},\varphi) = \left(1-\overline{r}^2\right)^{\frac{1}{\gamma}-1}$, $\hat{H}_0 = \overline{\nabla}_\perp \cdot \left(1-\overline{r}^2\right)^{\frac{1}{\gamma}} \overline{\nabla}_\perp$, and $\hat{H}' = -\overline{k}^2(1-\overline{r}^2)^{\frac{1}{\gamma}}$. Notice that both $\hat{H}_0$ and $\hat{H}_1$ are Hermitian operators.

Solving the eigenvalue problem (37) for all k ($0 < k < \infty$) exactly is not available. Ghosh and Machida [40] solved (36) by a numerical diagonalization, which was first used for condensed Bose gas (i.e. for the special case of $\gamma = 1$) by Zaremba [79]. However, notice that for linear sound propagation problem we are interested in here, one needs only the result for small k. Thus one can solve (37) using the perturbation theory by taking $\hat{H}'$ as a perturbation Hamiltonian [50].

Assuming $\Psi_j = \Psi_j^{(0)} + \Psi_j^{(1)} + \Psi_j^{(2)} + \cdots$ and $E_j = E_j^{(0)} + E_j^{(1)} + E_j^{(2)} + \cdots$, (37) becomes

$$\hat{H}_0\Psi_j^{(l)} - E_j^{(0)} w(\overline{r},\varphi)\Psi_j^{(l)} = S^{(l)}, \tag{38}$$

($l = 0, 1, 2, \ldots$), with $S^{(0)} = 0$, $S^{(1)} = (E_j^{(1)} w(\overline{r},\varphi) - \hat{H}')\Psi_j^{(0)}$, $S^{(2)} = E_j^{(2)} w(\overline{r},\varphi)\Psi_j^{(0)} + (E_j^{(1)} w(\overline{r},\varphi) - \hat{H}')\Psi_j^{(1)}$, etc.

The zero-order ($l = 0$) solution of (38) can be solved exactly. The result reads

$$\Psi^{(0)}_{n_r m}(\overline{r}, \varphi) = A_{n_r m} \overline{r}^{|m|} P_{n_r}^{(\frac{1}{\gamma}-1,|m|)}(2\overline{r}^2 - 1) e^{im\varphi}, \tag{39}$$

$$E^{(0)}_{n_r m} = -\frac{2}{\gamma}\left\{|m| + 2n_r\left[\gamma(n_r + |m|) + 1\right]\right\}, \tag{40}$$

$$A^2_{n_r m} = \frac{\Gamma(n_r + 1)\Gamma(\frac{1}{\gamma} + n_r + |m|)(\frac{1}{\gamma} + 2n_r + |m|)}{\pi\Gamma(n_r + \frac{1}{\gamma})\Gamma(1 + n_r + |m|)}, \tag{41}$$

where $P_n^{(a,b)}$ is a Jacob polynomial of order n, n_r and m are radial and angular quantum numbers, respectively. The above eigenfunctions satisfy the orthogonal-normalized relation

$$\int_0^1 \int_0^{2\pi} \overline{r} d\overline{r} d\varphi \Psi^{(0)*}_{n'_r m'} \Psi^{(0)}_{n_r m}\, w(\overline{r}, \varphi) = \delta_{n_r n'_r} \delta_{m m'}. \tag{42}$$

With the zero-order solution given above as an expansion basis for $\Psi_j^{(l)}$ ($j = (n_r, m)$) we can easily solve (38) for high-order approximations ($l = 1, 2, \ldots$). The first-order solution ($l = 1$) is given by

$$E_j^{(1)} = H'_{jj}, \tag{43}$$

$$\Psi_j^{(1)} = \sum_{j' \neq j} \frac{H'_{j'j}}{E_j^{(0)} - E_{j'}^{(0)}} \Psi_{j'}^{(0)}, \tag{44}$$

where $H'_{j'j} = < \Psi_{j'}^{(0)} | \hat{H}' | \Psi_j^{(0)} > \equiv \int_0^1 \int_0^{2\pi} d\overline{r} d\varphi \overline{r}\, \Psi_{j'}^{(0)*} \hat{H}' \Psi_j^{(0)}$. The second-order solution ($l = 2$) reads

$$E_j^{(2)} = -\sum_{l \neq j} \frac{|H'_{jl}|^2}{E_l^{(0)} - E_j^{(0)}}, \tag{45}$$

$$\Psi_j^{(2)} = \sum_{l' \neq j} \frac{1}{E_{l'}^{(0)} - E_j^{(0)}} \left(E_j^{(1)} A_{l'} - \sum_{l \neq j} A_l H'_{l'l} \right) \Psi_{l'}^{(0)}. \tag{46}$$

All high-order approximation solutions can be also obtained explicitly in the same way.

Table 2 Expressions of eigenvalues of radial eigenmodes $(n_r, m) = (0,0), (1,0), (2,0)$, and $(3,0)$

	(0,0)	(1,0)	(2,0)	(3,0)
$E^{(0)}_{n_r m}$	0	$-\frac{4A_{1,1}}{\gamma}$	$-\frac{8A_{1,2}}{\gamma}$	$-\frac{12A_{1,3}}{\gamma}$
$E^{(1)}_{n_r m}/\overline{k}^2$	$-\frac{1}{A_{1,1}}$	$-\frac{A_{1,1,2}}{A_{1,4,3}}$	$-\frac{A_{1,3,8}}{A_{1,8,15}}$	$-\frac{A_{1,5,18}}{A_{1,12,35}}$
$E^{(2)}_{n_r m}/\overline{k}^4$	$\frac{\gamma^3 A_{1,2}}{4A_{1,1}A^2_{1,3,2}}$	$-\frac{\gamma^3 A_{-3,-1,25,45,-2}}{4A^3_{1,1}A^2_{1,3}A_{1,7,12}}$	$-\frac{\gamma^3 B_1}{4}$	$-\frac{\gamma^3 B_2}{4}$

Here $A_{a,b,c,d,\ldots} \equiv a + b\gamma + c\gamma^2 + d\gamma^3 + \cdots$, $B_1 \equiv A_{-5,-23,87,611,794,264}/(A_{1,5,6}A_{1,11,30}A^2_{1,3}A^2_{1,5})$, and $B_2 \equiv A_{-7,-61,153,2641,6634,4464}/(A_{1,9,20}A_{1,15,56}A^2_{1,5}A^2_{1,7})$

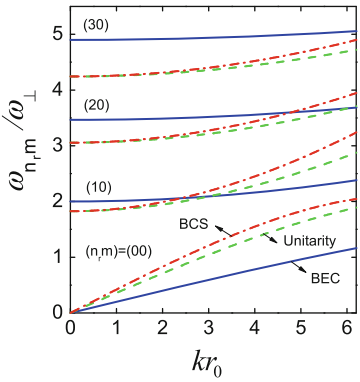

Fig. 2 Multibranch spectra of linear collective excitations for the modes of axial symmetry (i.e. $m = 0$ and $n_r = 0, 1, 2, 3$) as functions of dimensionless parameter kr_0, with $r_0 = (2\varepsilon^0_F/(M\omega^2_\perp))^{1/2}$. *Solid*, *dashed*, and *dash-dotted lines* correspond to $\eta^0 \equiv 1/(k^0_F a_s) = 5$ (near BEC limit), $\eta^0 = 0$ (unitarity limit), and $\eta^0 = -1$ (BCS regime), respectively

Up to the second-order approximation the expressions of eigenvalues and eigenfunctions are given by

$$\omega_{n_r m}(\overline{k}) = \pm\omega_\perp \left[-\frac{\gamma}{2}\left(E^{(0)}_{n_r m} + E^{(1)}_{n_r m} + E^{(2)}_{n_r m}\right)\right]^{1/2}, \tag{47}$$

$$\delta n_{sn_r m}(r, \varphi; \overline{k}) = \left(1 - \frac{r^2}{R^2_\perp}\right)^{\frac{1}{\gamma}-1}\left(\Psi^{(0)}_{n_r m} + \Psi^{(1)}_{n_r m} + \Psi^{(2)}_{n_r m}\right), \tag{48}$$

where $E^{(l)}_{n_r m}$ and $\Psi^{(l)}_{n_r m}$ are proportional to $\overline{k}^{2l}$.

In Table 2 we have listed the analytical expressions of eigenvalues up to the first three order approximations for modes of axial symmetry (i.e. $m = 0$ and $n_r = 0, 1, 2, 3$), with corresponding eigenfunctions given in the Appendix A of [50].

Shown in Fig. 2 are the dimensionless eigenfrequencies (multibranch spectrum) $\omega_{n_r m}/\omega_\perp$ for these modes as functions of dimensionless wavenumber kr_0, with $r_0 = (2\varepsilon^0_F/(M\omega^2_\perp))^{1/2}$. In the figure, solid, dashed, and dash-dotted lines correspond to $\eta^0 \equiv 1/(k^0_F a_s) = 5$ (near BEC limit), $\eta^0 = 0$ (unitarity limit), and $\eta^0 = -1$ (BCS regime), respectively. Note that the dimensionless wavenumber $\overline{k} = kR_\perp$ in the expressions of the eigenfrequencies in Table 1 is normalized by the radius of

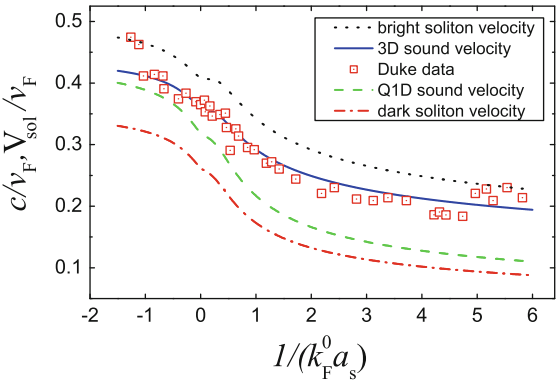

Fig. 3 The sound speed c of the cigar-shaped, but 3D superfluid gas ^{6}Li atomic gas as a function of $\eta^0 = 1/(k_F^0 a_s)$. The *solid line* is the theoretical result by using (50), whereas the *open squares* are the data measured by the Duke experiment [80]. For comparison, in the figure we have also plotted the sound speed of Q1D case (*dashed line*), the propagating velocity $V_{\rm sol}$ of the subsonic dark soliton in Q1D (*dotted-dashed line*), and the supersonic bright soliton in the present 3D case (the *dotted line*). All velocities are in unit of corresponding Fermi velocity of $v_F = (2\varepsilon 0_F/m)^{1/2}$

the condensate. However, for the comparison of the eigenfrequencies in different superfluid regimes, $kR_\perp$ is not good variable because it varies along the BCS-BEC crossover for the same k. Thus in Fig. 2 we plot the eigenfrequencies as functions of kr_0, where $r_0 = (2\varepsilon_F^0/(M\omega_\perp^2))^{1/2}$ is a fixed number for given atom-pair number N, and the trapping frequencies $\omega_\perp$, ω_z. From the figure we see that in different superfluid regimes the eigenfrequencies display different behavior. For $(n_r, m) = (0, 0)$ mode, for a given k the eigenfrequency of the BCS regime is larger than that of the uinitarity regime. In the BEC regime, the eigenfrequency is lowest. However, for $n_r \neq 0$, this property changes, which can be clearly seen from the figure. For the $(n_r, m) = (3, 0)$ mode, the eigen frequency of the BEC regime becomes largest. Such features of oscillatory frequencies of eigen collective excitations have also be found by Ghosh and Machida in their numerical approach [40], but our result is an analytical one.

The sound propagation feature can be obtained by the lowest branch dispersion relation $\omega_{00}(k)$, which is shown in Fig. 2 that satisfies $\omega_{00}(0) = 0$ (Bogoliubov spectrum). By (47) with $(n_r, m) = (0, 0)$ one obtains

$$\frac{\omega_{00}(\bar{k})}{\omega_\perp} = \left(\frac{\gamma}{2(\gamma+1)}\right)^{1/2}\left[1 - \frac{\gamma^3(2\gamma+1)\bar{k}^2}{4(1+3\gamma+2\gamma^2)^2}\right]^{1/2}\bar{k}. \tag{49}$$

Thus the sound speed of the system is

$$c = \sqrt{\frac{\gamma\mu_G}{(1+\gamma)M}}. \tag{50}$$

The solid line of Fig. 3 is the result of the sound speed (in unit of Fermi velocity $v_F = (2\varepsilon_F^0/m)^{1/2}$) of the superfluid ^{6}Li atomic gas as a function of $\eta^0 = 1/(k_F^0 a_s)$, calculated by using the experimental parameters of Joseph et al. [80]. That is, $N = 3\times 10^5$, $\omega_\perp = 2\pi \times 688\,\text{Hz}$, $\omega_z = 2\pi \times 34.4\,\text{Hz}$. Thus one has $\varepsilon_F = \hbar^2 {k_F^0}^2/2m = \hbar(6N\omega_\perp^2\omega_z)^{1/3} = k_B \times 1.4\,\mu\text{K}$ (k_B Boltzmann's constant), and hence $1/k_F^0 = 0.17\,\mu\text{m}$, and $n^0 = {k_F^0}^3/(6\pi^2) = 4\times 10^{12}\,\text{cm}^{-3}$. The experimental data measured by Joseph et al. [80] are denoted by open squares. We see that our theoretical result agrees quite well with that of Joseph et al. [80] For comparison, in Fig. 3 we have also plotted the result of the sound speed of the Q1D superfluid Fermi gas [43], which is given by the dashed line. One sees that the Q1D sound speed is obviously lower than the 3D one. The reason is that in the Q1D system there is a very strong confinement in radial direction, which results in a decrease of sound speed.

2.3 *Linear Excitations in Quasi-one and Quasi-two Dimensions*

We now consider Linear excitations in quasi-one (Q1D) system. Q1D means that the trapping potential in x and y directions is much stronger than in z direction, i.e. for harmonic potential one has $\omega_\perp >> \omega_z$ so that the condensate is not only cigar-shaped but also the motion of atoms in the x and y directions is essentially frozen and governed by the ground-state wave function (zero-point oscillation) of corresponding 2D linear harmonic oscillator. On the other hand, due to the strong confinement in the x and y directions the excitations of the system appear only in the z direction. Consequently, the superfluid velocity $\mathbf{v}$ has only z component, i.e. $\mathbf{v} = (0, 0, v_z)$.

Based on above consideration, one can set $\sqrt{n} = \sqrt{n_1(z,t)}G_0(x,y)$, where $G_0(x,y) = 1/(\pi a_\perp^2)^{1/2}\exp\left[-(x^2+y^2)/(2a_\perp^2)\right]$ is normalized ground state wave-function of the 2D harmonic oscillator of the potential $(M/2)\omega_\perp^2(x^2+y^2)$, with $a_\perp = \sqrt{\hbar/(M\omega_\perp)}$ being the oscillator length. After integrating the x and y variables, (4) and (5) becomes [43]

$$\frac{\partial n_1}{\partial t} + \frac{\partial (n_1 v_z)}{\partial z} = 0, \tag{51}$$

$$M\frac{\partial v_z}{\partial t} + \frac{\partial}{\partial z}\left[\mu_{1D}(n_1) - \mu_G + \frac{1}{2}M\omega_\perp^2\lambda^2 z^2 + \frac{1}{2}Mv_z^2\right] = 0, \tag{52}$$

where $\mu_{1D}(n_1) \equiv \hbar\omega_\perp + 2\mu^0(n_1/n_1^0)^\gamma$ is effective 1D equation of state, with $n_1^0 = n^0(\pi a_\perp^2)(\gamma+1)^{1/\gamma}$.

The ground state of the system described by (51) and (52) under the TFA reads $v_z = 0$ and

$$n_{1G}(z) = n_{1G}(0)\left[1 - \left(\frac{z}{R_z}\right)^2\right]^{1/\gamma}, \qquad (|z| \le R_z) \tag{53}$$

where $\rho_{1G}(0) = n_1^0\left[(\mu_G - \hbar\omega_\perp)/(2\mu^0)\right]^{1/\gamma}$, $R_z = [2(\mu_G - \hbar\omega_\perp)/(M\omega_\perp^2\lambda^2)]^{1/2}$, with $\mu_G = \hbar\omega_\perp + \{[N(2\mu^0)^{1/\gamma}\Gamma(1/\gamma + 3/2)\sqrt{M\omega_z^2/2}]/[n^0(\pi a_\perp^2)(\gamma + 1)^{1/\gamma}\Gamma(1/\gamma + 1)\sqrt{\pi}]\}^{2\gamma/(\gamma+2)}$ being the ground state chemical potential.

The equations of motion controlling the linear collective modes of the system can be obtained by setting $v_z(z,t) = \delta v_z(z,t)$, $n_1(z,t) = n_{1G}(z) + \delta n_1(z,t)$, where $\delta v_z(z,t)$ and $\delta n_1(z,t)$ are small perturbations. Assuming $\delta n_1(z,t) = \delta n_1(z)\exp(-i\omega t)$+c.c., $\delta v_z(z,t) = \delta v_z(z)\exp(-i\omega t)$+c.c., and eliminating δv_z and keeping only linear terms of $\delta n_1(z)$, we obtain the linear eigenvalue problem

$$-M\omega^2\delta n_1(z) = \frac{d}{dz}\left\{n_{1g}(z)\frac{d}{dz}\left[\mu'_{1D}(n_{1G})\delta n_1(z)\right]\right\}, \tag{54}$$

where $\mu'_{1D}(n_{1G}) \equiv (\partial\mu_{1D}/\partial n_1)|_{n_1=n_{1G}} = 2\mu_0\gamma n_{1G}^{\gamma-1}/(n_1^0)^\gamma$. Equation (54) can be written as the form

$$\gamma(1-\tilde{z}^2)\frac{d^2}{d\tilde{z}^2}\delta\tilde{n}_1 - 2(2\gamma-1)\tilde{z}\frac{d}{d\tilde{z}}\delta\tilde{n}_1 + 2(\omega^2/\omega_z^2 + 1 - \gamma)\delta\tilde{n}_1 = 0, \tag{55}$$

where $\tilde{z} = z/R_z$ and $\delta\tilde{n}_1 \equiv \delta n_1/n_{1G}(0)$.

Defining new variable $s = \tilde{z}^2$, (55) transforms into

$$s(1-s)\frac{d^2}{ds^2}\delta\tilde{n}_1 + \left[\frac{1}{2} - \left(\frac{5}{2} - \frac{1}{\gamma}\right)s\right]\frac{d}{ds}\delta\tilde{n}_1 + \frac{(\omega^2/\omega_z^2 - \gamma + 1)}{2\gamma}\delta\tilde{n}_1 = 0, \tag{56}$$

which is the standard form of the equation satisfied by hypergeometric function. Then we obtain the eigenfunctions

$$\delta n_1(z,t) = C\ F(-n, 3/2 - 1/\gamma + n, 1/2, z^2/R_z^2)e^{-i\omega t}, \tag{57}$$

with the eigenvalues

$$\omega^2 = \omega_z^2\left[2\gamma n^2 + n(3\gamma - 2) + \gamma - 1\right] \tag{58}$$

with $n = 0, 1, 2, \ldots$, where C is an arbitrary constant and F is hypergeometric function.

Above results cover the known one for the BEC limit ($\gamma = 1$), given by Menotti and Stringari [81]. Notice that the lowest eigenmode ($n = 0$) has the eigenfrequency $\omega^2 = \omega_z^2(\gamma - 1)$. In the BEC limit, this mode allows to exist. However, beyond the BEC limit (i.e. for $\gamma < 1$), this mode has an imaginary oscillating frequency and hence is no longer possible in the system.

An obvious character of the eigenfrequencies given by (58) has a strong γ-dependence. We see that the eigenfrequencies of the eigenmodes in the BCS regime ($\eta < -1$) is smaller than ones in the BEC regime ($\eta > 1$). In the crossover regime ($-1 < \eta < 1$) the eigenfrequencies increase as η increases. The density fluctuations $\delta\rho_1/\rho_{1g}(0)$ of the collective modes are functions of $1/(k_F a)$ and z/R_z. In general in comparison with the BCS regime, the density fluctuations are more significant in the BEC regime.

The collective modes in Q2D can be also obtained in a similar way. The Q2D means that the trapping potential in x and y directions is much weaker than in z direction, i.e. $\omega_\perp << \omega_z$ so that the condensate is disk-shaped and the motion of atoms in the z-direction is frozen and governed by the ground-state wave function (zero-point oscillation) of corresponding 1D linear harmonic oscillator. We write $V_{\rm ext}(\mathbf{r}) = M\omega_z^2\left[z^2 + \lambda^2(x^2+y^2)\right]/2$, with $\lambda \equiv \omega_\perp/\omega_z << 1$. In this case, if writing $\sqrt{n} = \sqrt{n_2(x,y,t)}G_0(z)$ with $G_0(z) = [1/(\pi a_z^2)^{1/4}]\exp\left[-z^2/(2a_z^2)\right]$ being the normalized ground state wavefunction of the 1D linear harmonic oscillator in the z-direction with the oscillator length $a_\perp = \sqrt{\hbar/(M\omega_z)}$, the superfluid hydrodynamic equations (4) and (5) becomes [43]

$$\frac{\partial}{\partial t}n_2 + \nabla_\perp \cdot (n_2 \mathbf{v}_\perp) = 0, \tag{59}$$

$$M\frac{\partial}{\partial t}\mathbf{v}_\perp + \nabla_\perp\left[\frac{1}{2}M\omega_z^2\lambda^2(x^2+y^2) + \frac{1}{2}M\mathbf{v}_\perp^2 + \mu_{2D}(n_2) - \mu_G\right] = 0, \tag{60}$$

where $n_2^0 \equiv n^0(\gamma+1)^{1/(2\gamma)}(\pi a_z^2)^{1/2}$ with $a_z = [\hbar/(M\omega_z)]^{1/2}$ being the harmonic length in z direction, and $\mu_{2D}(n_2) = \hbar\omega_z/2 + 2\mu^0(n_2/n_2^0)^\gamma$ is effective 2D equation of state.

It is easy to get the ground state distribution

$$n_{2G}(z) = n_{2G}(0)\left[1 - \frac{x^2+y^2}{R_\perp^2}\right]^{1/\gamma}, \quad (x^2+y^2 \le R_\perp^2) \tag{61}$$

where $n_{2G}(0) = n_2^0\left[(\mu_G - \hbar\omega_z/2)/(2\mu_0)\right]^{1/\gamma}$, $R_\perp = \sqrt{2(\mu_G - \hbar\omega_z/2)/(M\omega_z^2\lambda^2)}$, and $\mu_G = \hbar\omega_z/2 + \{(MN\omega_\perp^2(2\mu^0)^{1/\gamma})/[2\pi n^0(\pi a_z^2)^{1/2}(\gamma+1)^{(1/2\gamma-1)}\gamma]\}^{\gamma/(\gamma+1)}$ (ground state chemical potential).

The eigenvalue problem of linear collective excitations in the Q2D disk-shaped condensate can be obtained by assuming $\mathbf{v}_\perp(x,y,t) = \delta\mathbf{v}_\perp(x,y)\exp(-i\omega t) + \text{c.c.}$, $n_2(x,y,t) = n_{2G}(x,y) + [\delta n_2(x,y,t)\exp(-i\omega t) + \text{c.c.}]$. Equations (59) and (60) are then simplified as

$$-M\omega^2\delta n_2(x,y) = \nabla_\perp \cdot \{n_{2G}(x,y)\nabla_\perp\left[\mu_{2D}'(n_{2G}(x,y))\delta n_2(x,y)\right]\}. \tag{62}$$

To solve (62), it is convenient to introduce the polar coordinates $x = r\cos\theta$ and $y = r\sin\theta$. Then (62) can be written as the form

$$\gamma(1-\tilde{r}^2)\left(\frac{\partial^2}{\partial\tilde{r}^2}+\frac{1}{\tilde{r}^2}\frac{\partial^2}{\partial\theta^2}\right)\delta\tilde{n}_2$$
$$-\left[2(2\gamma-1)\tilde{r}-\gamma(1-\tilde{r}^2)\frac{1}{\tilde{r}}\right]\frac{\partial}{\partial\tilde{r}}\delta\tilde{n}_2+\left[2\omega^2/\omega_z^2-4(\gamma-1)\right]\delta\tilde{n}_2=0, \quad (63)$$

with $\delta\tilde{n_2}=\delta n_2/n_{2G}(0)$, and $\tilde{r}=r/R_\perp$. Solving (63) we obtain all eigenvalues and eigenfunctions of Q2D collective excitations

$$\omega^2=\omega_\perp^2\left[2n^2\gamma+n(2|m|\gamma-2+4\gamma)+2|m|\gamma-|m|+2(\gamma-1)\right], \quad (64)$$

$$\delta\tilde{n}_2(r,\theta)=C\,r^{|m|}e^{im\theta}F(-n,2+|m|-1/\gamma+n,|m|+1,(r/R_\perp)^2) \quad (65)$$

with $n=0,1,2\ldots$ and $m=0,1,2\ldots$, where C is a constant and F is hypergeometric function. Notice that when $\gamma=1$, our general result recover that obtained by Ho and Ma for the BEC limit [82]. Again the lowest eigenmode ($n=0, m=0$) is not allowed because this mode has pure imaginary oscillating frequency for $\gamma<1$. Like in the Q1D case, for a given normal mode the magnitude of the eigenfrequency in the BEC regime is larger than that in the BCS regime.

3 Nonlinear Excitations and Their Interaction

Solitons are localized wave packets arising from the balance between dispersion (or diffraction) and nonlinearity [83], and can be generally classified as being either dark or bright, relying on the details of effective nonlinearity. A dark soliton is a notch in ambient background with an associated phase slip across the notch, in contrast to a bright soliton which represents a peak in intensity. Both dark and bright solitons in trapped ultracold Bose gases have been studied intensively both experimentally and theoretically [84–93]. In particular, reduction perturbation method is successfully used to the study of 1D and high-dimensional solitons in BEC [94–97].

The experimental availability of superfluid Fermi gases provides an excellent opportunity to study soliton excitations in fermonic pair condensates, which may advance atomic optics conceptually, and more importantly, should be different from its bosonic counterpart, resulting from a different statistical property and a strong increase in interatomic interaction via Feshbach resonance, by which soliton properties can also be manipulated in a controllable way. In contrary to the intensive works on the linear collective excitations, up to now the nonlinear behavior of collective modes in superfluid Fermi gases is less explored. The work by Antezza et al. [98] investigated possible dark solitons in a superfluid Fermi gas along the BCS-BEC crossover (The dynamic evolution of dark solitons is studied by using BdG equations. See [99, 100]). However, in that work only static dark soliton

solutions are numerically provided and no dynamical behavior of the dark solitons is taken into account. In this section, we give a description of two works [49,50] where dark and bright solitons in superfluid Fermi gases are predicted. In addition, we also give a simple introduction on frequency shifts and mode coupling of collective excitations in superfluid Fermi gases [46].

3.1 Dark Soliton Excitations in Q1D Superfluid Fermi Gases

3.1.1 Q1D Approximation and Phonon Spectrum

In [49], a detailed investigation is carried out on the dynamics of the dark solitons excited in a Q1D superfluid Fermi gas in the BCS-BEC crossover. Starting from the superfluid order-parameter equation and using a method of multiple-scales, a Korteweg-de Vries (KdV) equation is derived for (shallow) dark-soliton excitations under Q1D and long wavelength approximations. The results show that the dark solitons in the superfluid Fermi gas display very different dynamic characters in different superfluid regimes. Furthermore, the head-on collision between two dark solitons is investigated by means of the Poincare-Lighthill-Kuo (PLK) method, phase shifts due to the collision is shown to have interesting features along the BCS-BEC crossover.

The GGP equation (7) (when the subscript "s" is omitted) can be written into the following form

$$\frac{\partial n}{\partial t} + \frac{\hbar}{M}\nabla \cdot (n\nabla \Phi) = 0, \tag{66}$$

$$\hbar\frac{\partial \Phi}{\partial t} + \mu(n) + \frac{M}{2}\left[\omega_\perp^2(x^2+y^2) + \omega_z^2 z^2\right] + \frac{\hbar^2}{2M}\left[(\nabla\Phi)^2 - \frac{1}{\sqrt{n}}\nabla^2\sqrt{n}\right] = 0. \tag{67}$$

We pay our attention to nonlinear excitations in a Q1D condensate. Physically, the Q1D condition implies

$$a_\perp \ll l_0, \quad \hbar\omega_z \ll \mu(n) \ll \hbar\omega_\perp, \tag{68}$$

where $l_0 = \hbar/[2M\mu(n)]^{1/2}$ is healing length. Under such condition we have: (i) The energy-level spacing for the motion of fermionic atom pairs in the transverse directions exceeds largely the interaction energy between the atom pairs. Thus at sufficiently low temperature the motion of atom pairs in the transverse directions is essentially frozen and governed by the ground-state wave function (zero-point oscillation) of corresponding harmonic-oscillator potential. (ii) Because of the strong confinement in the transverse directions, an excitation can propagate only in the axial direction, and hence the superfluid velocity has only z-component (i.e. $\Phi = \Phi(z,t)$).

For convenience, we introduce the dimensionless variables defined by $(x', y', z') = (x, y, z)/a_\perp$, $t' = \omega_\perp t$, and $n' = n/(Na_\perp^{-3})$. Then (66) and (67) are reduced into the dimensionless form

$$\frac{\partial n}{\partial t} + \nabla \cdot (n \nabla \Phi) = 0, \tag{69}$$

$$\frac{\partial \Phi}{\partial t} + U_0 n^\gamma + \frac{1}{2}\left[x^2 + y^2 + \lambda^2 z^2\right] + \frac{1}{2}\left[(\nabla \Phi)^2 - \frac{1}{\sqrt{n}}\nabla^2 \sqrt{n}\right] = 0, \tag{70}$$

with $\lambda = \omega_z/\omega_\perp \ll 1$, $U_0 = \frac{2\mu^0}{\hbar\omega_\perp} \cdot \left(\frac{N}{a_\perp^3 n^0}\right)^\gamma$, and $\int d\mathbf{r}\, n = 1$. Notice that primes are omitted in the above equations.

According to the above arguments we set $\sqrt{n_s} = G_0(x, y)\, F(z, t)$, $\Phi_s = -\mu_G t + \phi(z, t)$, where $G_0(x, y) = \exp\left[-(x^2 + y^2)/2\right]/\sqrt{\pi}$ is normalized ground state wavefunction of the 2D harmonic oscillator with the potential $(x^2 + y^2)/2$, and μ_G is dimensionless ground-state chemical potential of the condensate. Then after an integration over radial coordinates x and y (69) and (70) become

$$\frac{\partial F}{\partial t} + \frac{\partial F}{\partial z}\frac{\partial \phi}{\partial z} + \frac{1}{2}F\frac{\partial^2 \phi}{\partial z^2} = 0, \tag{71}$$

$$\left[1 - \mu_g + \frac{\partial \phi}{\partial t} + \frac{1}{2}\lambda^2 z^2 + \frac{1}{2}\left(\frac{\partial \phi}{\partial z}\right)^2\right] F + U_0 I F^{2\gamma+1} - \frac{1}{2}\frac{\partial^2 F}{\partial z^2} = 0, \tag{72}$$

with $I = 1/\left[\pi^\gamma(\gamma + 1)\right]$. The ground state solution of (71) and (72) reads $\phi =$ constant, $F(z) = [(\mu_g - 1 - \lambda^2 z^2/2)/(U_0 I)]^{1/2\gamma}$, $\mu_g = 1 + (G_0/G_1)^{2\gamma/(2+\gamma)}$, with $G_0 = \lambda\Gamma(1/\gamma + 3/2)(U_0 I)^{1/\gamma}$ and $G_1 = \Gamma(1/\gamma + 1)(2\pi)^{1/2}$.

The linear sound wave propagation in the system can be obtained by neglecting the trapping potential in the z-direction and assuming $F(z, t) = F_0 + f(z, t)$, with $F_0 = \left[(\mu_g - 1)/(I U_0)\right]^{\frac{1}{2\gamma}}$ characterizing the ground state and f describing a small perturbation (the sound wave) excited in the system. Taking $(f, \phi) = (f_0, \phi_0)\exp[i(kz - \omega t)]$+c.c., here k is wavenumber and ω is frequency, (71) and (72) gives rise to the Bogoliubov phonon spectrum

$$\omega = \frac{k}{2}\left[k^2 + 4\gamma U_0 I F_0^{2\gamma}\right]^{1/2}, \tag{73}$$

Thus the sound speed is given by $c = (\gamma U_0 I)^{1/2} F_0^\gamma$.

3.1.2 KdV Equation and Dark Soliton Excitations

For weak-nonlinear, long wavelength excitations, one can apply the standard method of multiple-scales [101] to solve (71) and (72). For the long cigar-shaped trap (i.e. $\lambda \ll 1$), one expects the variation of the order parameter along the z-direction is

slow. As a first step one can take λ as zero to make an analytical approach possible. The effect of non-zero λ is taken into account in numerical simulation.

Introducing the multi-scale variables $\rho = \epsilon\,(z - ct)$ and $\tau = \epsilon^3\,t$, where ϵ is a small parameter representing the relative amplitude of the excitations and c is sound speed, and making the asymptotic expansions

$$F = F_0 + \epsilon^2 f^{(0)} + \epsilon^4 f^{(1)} + \cdots, \tag{74}$$

$$\phi = \epsilon\,\phi^{(0)} + \epsilon^3\,\phi^{(1)} + \cdots, \tag{75}$$

Equations (71) and (72) are transferred into the following form

$$c\frac{\partial}{\partial\rho} f^{(j)} - \frac{1}{2} F_0 \frac{\partial^2}{\partial\rho^2}\phi^{(j)} = \alpha^{(j)}, \tag{76}$$

$$2\gamma\, U_0 I F_0^{2\gamma} f^{(j)} - cF_0 \frac{\partial}{\partial\rho}\phi^{(j)} = \beta^{(j)}, \tag{77}$$

where explicit expressions of $a^{(j)}$ and $\beta^{(j)}$ are lengthy and omitted.

At the lowest-order ($j = 0$), one obtains $\phi^{(0)} = (2c/F_0)\int d\rho f^{(0)}$, with $f^{(0)}$ being a yet to be determined function. In the next order ($j = 1$), one obtains the KdV equation $\partial f^{(0)}/\partial\tau + [(2+\gamma)c/F_0] f^{(0)}\partial f^{(0)}/\partial\rho - (1/8c)\partial^3 f^{(0)}/\partial\rho^3 = 0$, which can be written as

$$\frac{\partial}{\partial t} F_1 + \frac{(2+\gamma)}{F_0} c F_1 \frac{\partial F_1}{\partial Z} - \frac{1}{8c}\frac{\partial^3 F_1}{\partial Z^3} = 0 \tag{78}$$

after returning to original variables, where $F_1 = \epsilon^2 f^{(0)}$ and $Z = z - ct$. Equation (78) has the single-soliton solution

$$F_1 = -A_0\,\mathrm{sech}^2\!\left(\frac{z - V_s t - z_0}{W}\right), \tag{79}$$

where A_0 and z_0 are positive constant, $V_s = c\,[1 - (2+\gamma)A_0/(3F_0)]$ and $W = \{3F_0/[(4+2\gamma)c^2 A_0]\}^{1/2}$ are propagating velocity and spatial width of the soliton, respectively.

The phase of the order parameter under the first-order approximation is given by

$$\Phi_1(z,t) \equiv \epsilon\phi^{(0)} = -\left[\frac{6A_0}{(2+\gamma)F_0}\right]^{1/2} \tanh\left(\frac{z - V_s t - z_0}{W}\right). \tag{80}$$

Consequently, exact to the first-order approximation the order parameter of the condensate has the form

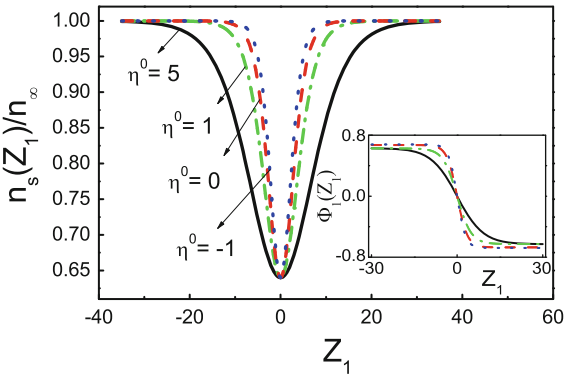

Fig. 4 Axial density profile $n(z,t) = \int\int dx\, dy |\Psi(x,y,z,t)|^2$ (normalized by $n_\infty = F_0^2$) of the dark soliton as a function of $Z_1 \equiv z - V_s t - z_0$ and the interaction parameter η^0. The *dotted*, *dashed*, *dot-dashed*, and *solid lines* correspond to $\eta^0 = -1$ (BCS regime), 0 (unitarity limit), 1 (BEC regime), and 5 (BEC limit), respectively. The inset shows the corresponding phase function Φ_1

$$\Psi(x,y,z,t) = \frac{1}{\sqrt{\pi}} F_0 \left[1 - D_0 \mathrm{sech}^2\Big(\frac{z - V_s t - z_0}{W}\Big)\right] \cdot \exp\left[-\frac{1}{2}(x^2+y^2)\right] \exp[i(-\mu_g t + \Phi_1(z,t))], \tag{81}$$

which is a dark soliton with the *grayness* $D_0 = A_0/F_0$.

Consider a ^{6}Li Fermi gas confined in a highly elongated trap with $\omega_\perp = 2\pi \times 3,000\,\mathrm{Hz}$ and $\omega_z = 2\pi$ Hz. In order to satisfy the Q1D condition in the whole BCS-BEC crossover, we choose $N = 80$. The reference Fermi energy is chosen as that of trapped, non-interacting Fermi gas, i.e. $E_F = \hbar^2 {k_F^0}^2/(2m) = \hbar(6N\omega_\perp^2\omega_z)^{1/3}$, and hence $1/k_F^0 = 0.7\,\mu\mathrm{m}$ and $n^0 = {k_F^0}^3/(3\pi^2) = 5 \times 10^{22}\,\mathrm{cm}^{-3}$.

Figure 4 shows the axial density profile $n(z,t) = \int\int dx\, dy |\Psi(x,y,z,t)|^2$ (normalized by the background density $n_\infty = F_0^2$), as a function of $Z_1 = z - V_s t - z_0$ and the interaction parameter η^0 when the dark soliton solution (81) (with $D_0 = 0.2$) is excited in the system. The dotted, dashed, dot-dashed, and solid lines correspond to $\eta^0 = -1$ (BCS regime), 0 (unitarity limit), 1 (BEC regime), and 5 ($\approx$ BEC limit), respectively. The inset shows the corresponding phase function Φ_1 given by (80). We see that the spatial width of the dark soliton W is very different in different superfluid regimes. Generally, the value of W in the BCS side is smaller than that in the BEC side; it increases as the interaction parameter η^0 increases, and becomes maximum in the BEC limit. The main physical reason for the narrower dark soliton width (and also for the faster propagating velocity) in the BCS side than that in the BEC side is due to the fact that the interaction energy between particles in the BCS side is larger than that in the BEC side. It should be pointed out that for fixed D_0, the phase difference $\Delta\Phi_1 = \Phi_1|_{Z_1=-\infty} - \Phi_1|_{Z_1=\infty}$ is different for different η^0. For a quantitative comparison, in Table 3 we have listed the values of the soliton width W,

Table 3 Values of the dark soliton width W, propagating velocity V_s, and the phase difference $\Delta\Phi_1$ for the grayness $D_0 = 0.2$ in several different superfluid regimes

	BEC limit	BEC regime	Unitarity	BCS regime
$\eta^0 = 1/(k_F^0 a_s)$	5	1	0	-1
W (μm)	4.8	2.6	1.9	1.6
V_s (mm/s)	1.4	2.5	3.7	4.5
$\Delta\Phi_1$	1.26	1.25	1.34	1.36

propagating velocity V_s, and the phase difference $\Delta\Phi_1$ for the grayness $D_0 = 0.2$ in several different superfluid regimes. We see that the soliton has generally the spatial width (propagating velocity) of order several μm (mm s^{-1}).

Numerical simulation on the dark soliton propagation in the presence of the axial trapping potential (i.e. $\lambda \neq 0$) has been carried out to check the analytical prediction. For convenience of the simulation, we define a set of new dimensionless variables $F(z,t) = [\omega_z n^0 a_\perp^3/(\omega_\perp N)]^{1/2}\chi(s,\tau)$, $t = (2\omega_\perp/\omega_z)\tau$, $z = (\omega_\perp/\omega_z)s$, and $\Phi_1(z,t) = \phi(s,\tau)$. Then (71) and (72) are transformed into

$$\frac{\partial\chi}{\partial\tau} = -2\frac{\partial\chi}{\partial s}\frac{\partial\phi}{\partial s} - \chi\frac{\partial^2\phi}{\partial s^2}, \tag{82}$$

$$\chi\frac{\partial\phi}{\partial\tau} = \frac{\partial^2\chi}{\partial s^2} - \left[s^2 + \frac{2\omega_\perp}{\omega_z}(1-\mu_g) + (\frac{\partial\phi}{\partial s})^2 + \kappa\chi^{2\gamma}\right]\chi, \tag{83}$$

with $\kappa = 4\mu^0\omega_z^{\gamma-1}/[\hbar(\gamma+1)(\pi\omega_\perp)^\gamma]$.

The ground state solution corresponds to $\partial/\partial\tau = 0$, $\phi =$ constant, and $\chi = \chi_0$. From (82) we have $\left[-d^2/ds^2 + s^2 + \kappa\chi_0^{2\gamma}\right]\chi_0 = (2\omega_\perp/\omega_z)(\mu_g - 1)\chi_0$. An imaginary time propagation method [102] is used to solve this equation, with the result represented by dotted lines presented in Fig. 5. For comparison, the ground state profile from approximated analytical (TFA) result is also plotted by solid lines. Panels (a), (b), (c), (d) are for the cases $\eta^0 = -1$ (BCS regime), $\eta^0 = 0$ (unitarity limit), $\eta^0 = 1$ (BEC regime), and $\eta^0 = 5$ (BEC limit), respectively. We see that the profile of χ_0 broadens gradually from the BEC side to the BCS side, with increasing size of the condensate. The reason of the flatten condensate profile and the large size in the BCS regime is due to the stronger interaction energy than that in the BEC regime. Additionally, we see that the TFA is a nice approximation in the BCS side, but it becomes a poor one in the BEC side, especially in the BEC limit.

The time evolution of dark soliton in the BCS-BEC crossover including the axial trapping potential is investigated numerically [49]. Such study is necessary because we need to know how the axial trapping potential affects the propagation dynamics of the dark soliton. On the other hand, in realistic ultracold Fermi gas experiments,

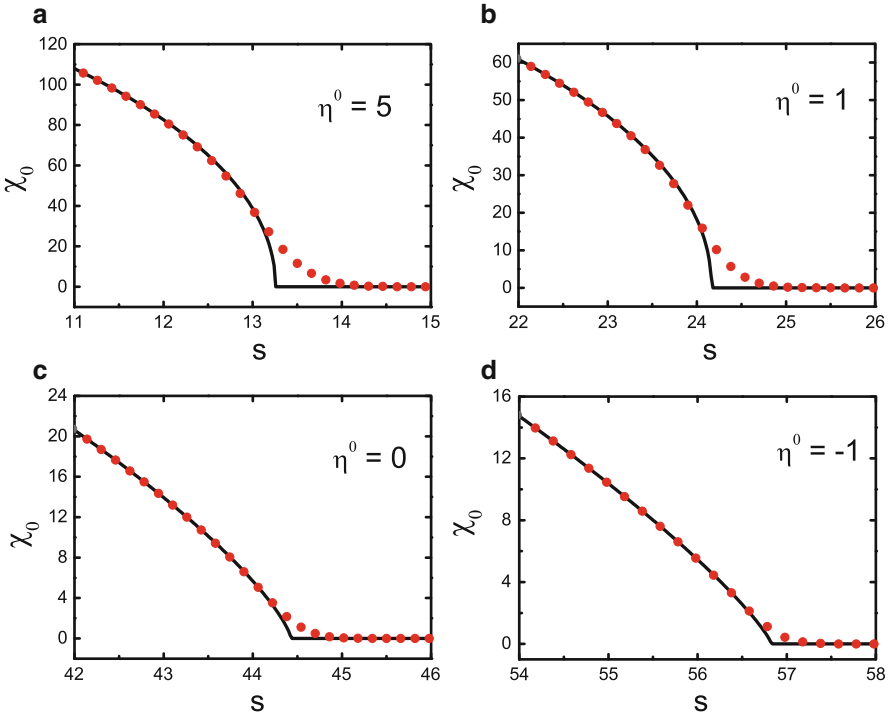

Fig. 5 Comparison of the ground state profiles between the result obtained by the numerical simulation (*dotted lines*) and that from analytical solution under TFA (*solid lines*). Panels (**a**), (**b**), (**c**), (**d**) are for the interaction parameter $\eta^0 = 5$, $\eta^0 = 1$, $\eta^0 = 0$, and $\eta^0 = -1$, respectively

the axial trapping potential always exists. For this aim, we numerically integrate (82) and (83) by using the dark soliton solution obtained above as an initial condition. In the new variables introduced in (82) and (83), the dark soliton solution given by (79) and (80) takes the form

$$\chi_{ss}(s,0) = \chi_0 \left\{ 1 - D_0 \mathrm{sech}^2 \left[\frac{\chi_0^{\gamma}(s - s_0)}{\varpi} \right] \right\}, \tag{84}$$

$$\phi_{ss}(s,0) = -\left(\frac{6D_0}{2+\gamma} \right)^{1/2} \tanh \left[\frac{\chi_0^{\gamma}(s - s_0)}{\varpi} \right], \tag{85}$$

where $\varpi = (\omega_\perp/\omega_z)^{(\gamma-1)/2}[3\pi^\gamma(\gamma+1)\hbar\omega_\perp/(4\gamma(2+\gamma)D_0\mu^0)]^{1/2}$, and s_0 is the initial soliton position.

Shown in Fig. 6 is the result of the numerical simulation for the propagation of the dimensionless soliton amplitude and phase (with grayness $D_0 = 0.1$) as functions of the dimensionless time τ and distance s along the axial direction. In the figure, panels (a), (b), (c), and (d) are for the interaction parameter $\eta^0 = 5$ (BEC limit),

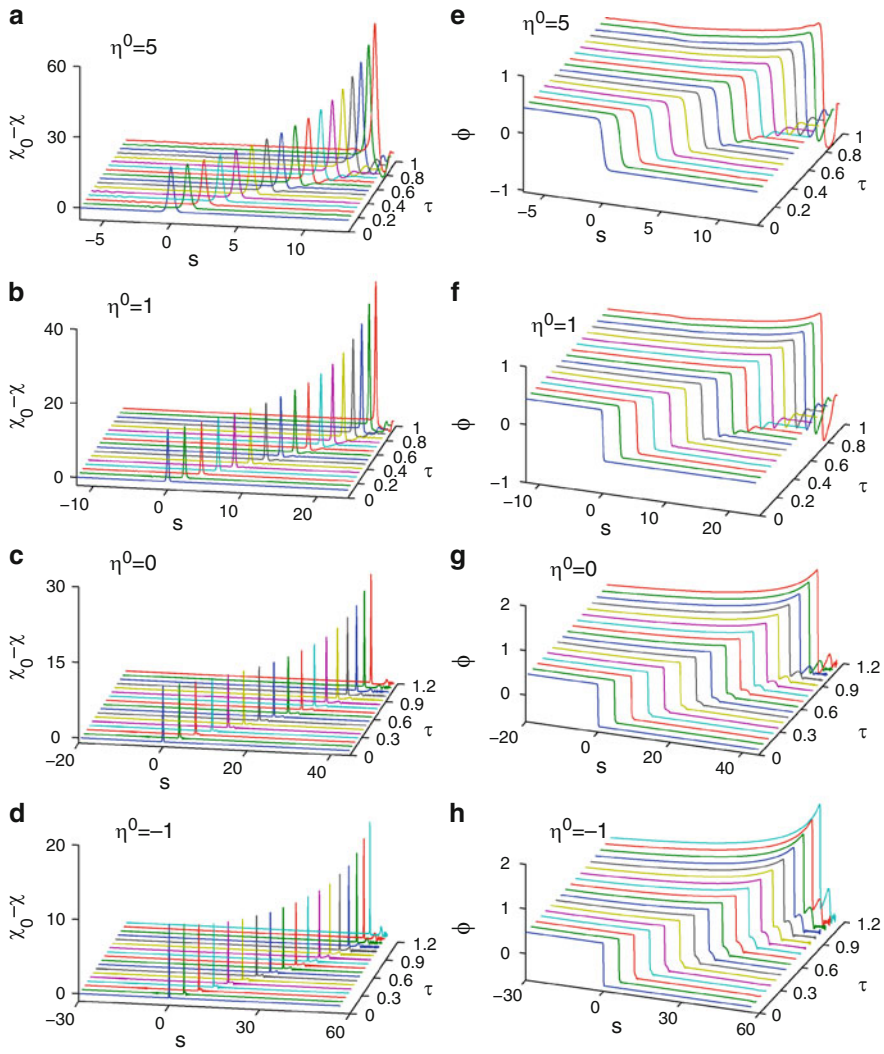

Fig. 6 Numerical result on the propagation of relative soliton amplitude $\chi_0 - \chi$ (with $D_0 = 0.1$) as a function of the dimensionless time τ and distance s. Panels (**a**), (**b**), (**c**), (**d**) are for $\eta^0 = 5$, $\eta^0 = 1$, $\eta^0 = 0$, $\eta^0 = -1$, respectively; panels (**e**)–(**h**) are results for corresponding soliton phase ϕ

$\eta^0 = 1$ (BEC regime), $\eta^0 = 0$ (unitarity limit), and $\eta^0 = -1$ (BCS regime), respectively; panels (e), (f), (g), and (h) are their corresponding soliton phase ϕ. Notice that for a better illustration the vertical coordinate in the panels (a)–(d) is the relative amplitude $\chi_0 - \chi$.

From Fig. 6 we see that there are several interesting features for the dark soliton propagation in the BCS-BEC crossover in the presence of axial trapping potential.

(i) In all superfluid regimes the relative amplitude of the dark soliton increases when the soliton approaches to the boundary of the condensate. (ii) The relative amplitude $\chi_0 - \chi$ changes drastically when η^0 passes over the crossover. In the BEC (BCS) side, $\chi_0 - \chi$ is large (small). (iii) The soliton width is much narrower in the BCS regime than that in the BEC regime. (iv) The soliton generates a small, but obvious radiation during propagation, especially when it approaches the boundary of the condensate. The radiation is in fact small-amplitude sound wave and hence propagates faster than the dark soliton. (v) The travelling velocity of the soliton in the BCS regime is much larger than that in the BEC regime. These important differences in the dark soliton propagation dynamics are obvious manifestations of different physical properties in different superfluid regimes.

3.1.3 Head-On Collisions Between Two Dark Solitons

Collisions of solitons can be divided int two classes. The first one is overtaking collision and the second one is head-on collision. The overtaking collision of the dark solitons in the BCS-BEC crossover can be studied by using the two-soliton solution of the KdV equation, which is omitted here. Here we investigate a head-on collision between two dark solitons traveling from opposite directions, which can not be described by a single KdV equation. For the case of $\lambda = 0$, such collision can be studied analytically by using the PLK method [101] to solve (71) and (72). Anticipating that there are phase shifts (i.e. shifts of soliton central positions) due to the collision, we introduce the asymptotic expansion ((74) and (75)) and the new coordinate variables

$$\xi = \epsilon(z - c_R t) + \epsilon^2 P^{(0)}(\zeta) + \cdots, \tag{86}$$

$$\zeta = \epsilon(z + c_L t) + \epsilon^2 Q^{(0)}(\xi) + \cdots \tag{87}$$

to reflect the change of travelling trajectories of the solitons, with $P^{(0)}(\zeta)$, $Q^{(0)}(\xi)$, $\cdots$ being yet to be determined functions. In order to obtain a valid asymptotic expansion, the right and left propagating wave speeds should be expanded as $c_R = c + \epsilon^2 R_1 + \cdots$ and $c_L = c + \epsilon^2 L_1 + \cdots$. Under these expansions (71) and (72) become

$$c\left(\frac{\partial}{\partial\xi} - \frac{\partial}{\partial\zeta}\right) f^{(j)} - \frac{1}{2} F_0 \left(\frac{\partial}{\partial\xi} + \frac{\partial}{\partial\zeta}\right)^2 \phi^{(j)} = M^{(j)}, \tag{88}$$

$$cF_0\left(\frac{\partial}{\partial\xi} - \frac{\partial}{\partial\zeta}\right) \phi^{(j)} - 2c^2 f^{(j)} = N^{(j)}, \tag{89}$$

where explicit expressions for $M^{(j)}$ and $N^{(j)}$ $(j = 0, 1, 2, \ldots)$ are omitted.

The first order ($j = 0$) solution of the (88) and (89) reads

$$f^{(0)} = a^{(0)}(\xi) + b^{(0)}(\zeta), \tag{90}$$

$$\phi^{(0)} = \frac{2c}{F_0}\left(\int_{+\infty}^{\xi} a^{(0)}(\xi')d\xi' - \int_{-\infty}^{\zeta} b^{(0)}(\zeta')d\zeta'\right), \tag{91}$$

where $a^{(0)}(\xi)$ (the wave travelling to the right) and $b^{(0)}(\zeta)$ (the wave travelling to the left) are yet to be determined functions. A solvability condition requires $c = \sqrt{\gamma U I F_0^{2\gamma}}$ (i.e. the linear sound speed).

At the following order ($j = 1$), we obtain the equations for $a^{(0)}(\xi)$, $b^{(0)}(\zeta)$, $P^{(0)}(\zeta)$, and $Q^{(0)}(\xi)$:

$$-R_1\frac{\partial a^{(0)}}{\partial \xi} + \frac{(\gamma+2)c}{F_0}a^{(0)}\frac{\partial a^{(0)}}{\partial \xi} - \frac{1}{8c}\frac{\partial^3 a^{(0)}}{\partial \xi^3} = 0, \tag{92}$$

$$-L_1\frac{\partial b^{(0)}}{\partial \zeta} + \frac{(\gamma+2)c}{F_0}b^{(0)}\frac{\partial b^{(0)}}{\partial \zeta} - \frac{1}{8c}\frac{\partial^3 b^{(0)}}{\partial \zeta^3} = 0, \tag{93}$$

$$\frac{\partial P^{(0)}}{\partial \zeta} = \frac{(2-\gamma)}{2F_0}b^{(0)}(\zeta), \tag{94}$$

$$\frac{\partial Q^{(0)}}{\partial \xi} = \frac{(2-\gamma)}{2F_0}a^{(0)}(\xi), \tag{95}$$

with $R_1 = -(\gamma+2)cA_0/(3F_0)$ and $L_1 = -(\gamma+2)cB_0/(3F_0)$, where A_0 and B_0 are two positive constants. Equations (92) and (93) are two KdV equations with travelling-wave coordinates ξ and ζ, respectively. Thus we have soliton solutions

$$a^{(0)}(\xi) = -A_0\,\mathrm{sech}^2\left[\left(\frac{2(\gamma+2)\mathrm{c}^2\mathrm{A}_0}{3\mathrm{F}_0}\right)^{\frac{1}{2}}\xi\right], \tag{96}$$

$$b^{(0)}(\zeta) = -B_0\,\mathrm{sech}^2\left[\left(\frac{2(\gamma+2)\mathrm{c}^2\mathrm{B}_0}{3\mathrm{F}_0}\right)^{\frac{1}{2}}\zeta\right]. \tag{97}$$

Then using (94) and (95) we immediately obtain

$$P^{(0)}(\zeta) = -\frac{2-\gamma}{2c}\left(\frac{3B_0}{2(\gamma+2)F_0}\right)^{\frac{1}{2}}\left\{\tanh\left[\left(\frac{2(\gamma+2)\mathrm{c}^2\mathrm{B}_0}{3\mathrm{F}_0}\right)^{\frac{1}{2}}\zeta\right]+1\right\}, \tag{98}$$

$$Q^{(0)}(\xi) = -\frac{2-\gamma}{2c}\left(\frac{3A_0}{2(\gamma+2)F_0}\right)^{\frac{1}{2}}\left\{\tanh\left[\left(\frac{2(\gamma+2)\mathrm{c}^2\mathrm{A}_0}{3\mathrm{F}_0}\right)^{\frac{1}{2}}\xi\right]-1\right\}. \tag{99}$$

By (98) and (99) we have the trajectories of the soliton $a_0(\xi)$ (denoted by A) and the soliton $b_0(\zeta)$ (denoted by B) given respectively by

$$\xi = \epsilon(z - c_R t) - \epsilon^2 \frac{2-\gamma}{2c}\left[\frac{3B_0}{2(\gamma+2)F_0}\right]^{\frac{1}{2}} [\tanh\theta_B(\zeta) + 1] + O(\epsilon^4), \tag{100}$$

$$\zeta = \epsilon(z + c_L t) - \epsilon^2 \frac{2-\gamma}{2c}\left[\frac{3A_0}{2(\gamma+2)F_0}\right]^{\frac{1}{2}} [\tanh\theta_A(\xi) - 1] + O(\epsilon^4), \tag{101}$$

with $c_R = c(1-\epsilon^2(\gamma+2)A_0/(3F_0)) + O(\epsilon^4)$, $c_L = c(1-\epsilon^2(\gamma+2)B_0/(3F_0)) + O(\epsilon^4)$, $\theta_A(\xi) = [2(\gamma+2)c^2A_0/(3F_0)]^{\frac{1}{2}}\,\xi$, and $\theta_B(\zeta) = [2(\gamma+2)c^2B_0/(3F_0)]^{\frac{1}{2}}\,\zeta$.

From (100) and (101) we can easily estimate the soliton phase shifts due to the head-on collision. Assume that the solitons A and B are far from each other at the initial time ($t = -\infty$); i.e., soliton A is at $\xi = 0, \zeta = -\infty$, while soliton B is at $\zeta = 0$ and $\xi = +\infty$, respectively. After the collision ($t = +\infty$), the soliton A (B) is far to the right (left) of soliton B (A), i.e., soliton A is at $\xi = 0, \zeta = +\infty$ and soliton B is at $\zeta = 0, \xi = -\infty$. Thus after the collision their corresponding phase shifts Δ_A and Δ_B are given by

$$\begin{aligned}\Delta_A &= \epsilon(z - c_R t)|_{\xi=0,\zeta=+\infty} - \epsilon(z - c_R t)|_{\xi=0,\zeta=-\infty} \\ &= \epsilon^2 \frac{2-\gamma}{c}\left[\frac{3B_0}{2(\gamma+2)F_0}\right]^{\frac{1}{2}}, \end{aligned} \tag{102}$$

$$\begin{aligned}\Delta_B &= \epsilon(z + c_L t)|_{\zeta=0,\xi=-\infty} - \epsilon(z + c_L t)|_{\zeta=0,\xi=+\infty} \\ &= -\epsilon^2 \frac{2-\gamma}{c}\left[\frac{3A_0}{2(\gamma+2)F_0}\right]^{\frac{1}{2}}, \end{aligned} \tag{103}$$

respectively. We see that the phase shift of the soliton A (B) depends on the square root of its grayness B_0/F_0 (A_0/F_0). Furthermore, the phase shifts are γ-dependent and hence they are different in different superfluid regimes in the BCS-BEC crossover. Obviously, there is a relation between the phase shifts of the two solitons, i.e.

$$\frac{\Delta_A}{(B_0/F_0)^{1/2}} = \frac{\Delta_B}{(A_0/F_0)^{1/2}} \equiv \epsilon^2 \Delta, \tag{104}$$

where

$$\Delta = \frac{2-\gamma}{c}\left[\frac{3}{2(\gamma+2)}\right]^{\frac{1}{2}}, \tag{105}$$

is a relative phase shift.

In order to test the above analytical predictions we have made a numerical simulation on the head-on collision between two dark solitons in the presence of the trapping potential in the axial direction. Figure 7 shows the result of the

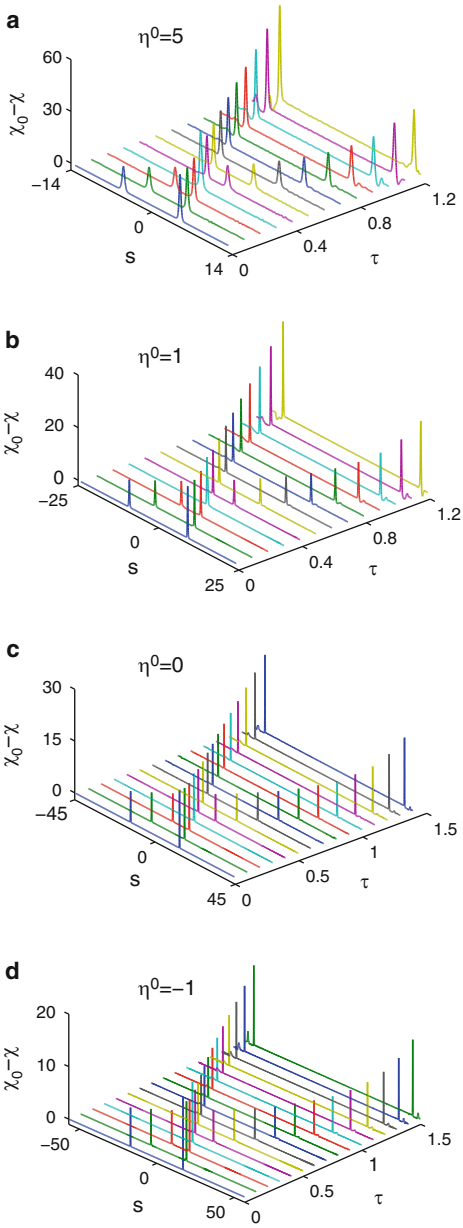

Fig. 7 Head-on collisions of two dark solitons. The relative amplitude $\chi_0 - \chi$ is plotted as a function of τ and s. Panels (**a**), (**b**), (**c**), and (**d**) are for $\eta^0 = 5$, $\eta^0 = 1$, $\eta^0 = 0$, and $\eta^0 = -1$, respectively

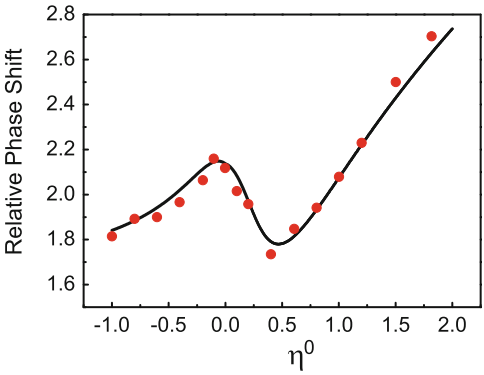

Fig. 8 Relative colliding phase shift (given by (105)) as a function of the interaction parameter η^0. The *solid circles* are from numerical simulations, while the *solid line* is by the theoretical prediction

simulation in the BCS-BEC crossover, which is based on the (82) and (83) by taking the analytical solution given above as an initial condition. In the figure, the relative amplitude $\chi_0 - \chi$ is plotted as a function of τ and s. Panels (a), (b), (c), and (d) are for $\eta^0 = 5$ (BEC limit), $\eta^0 = 1$ (BEC regime), $\eta^0 = 0$ (unitarity limit), and $\eta^0 = -1$ (BCS regime), respectively. In all panels the grayness of the soliton A (B) is chosen as $D_0^A = 0.08$ ($D_0^B = 0.15$). For a clear illustration, the initial positions of the soliton A (denoted by s_A) and the soliton B (denoted by s_B) in panels (a), (b), (c), and (d) are chosen as ($s_A = -5$, $s_B = 5$), ($s_A = -9$, $s_B = 9$), ($s_A = -13.5$, $s_B = 13, 5$), and ($s_A = -17$, $s_B = 17$), respectively. The other system parameters are the same as those used in Fig. 5. One can see that in each panel the two dark solitons, one (the soliton A) propagating to the right and the other one (the soliton B) propagating to the left, approach each other, collide, and then separate away. In various superfluid regimes in the BCS-BEC crossover, two-soliton collisions are nearly elastic.

However, the two-soliton collisions may result in phase shifts. In Fig. 6, we have shown the numerical result of the relative colliding phase shift Δ as a function of the interaction parameter η^0 (the solid circles). We see that the relative phase shift due to the head-on collision is a non-monotonic function of η^0. The phase shift is generally large (small) in the BEC (BCS) regime, but it displays a drastically change near the unitarity point $\eta^0 = 0$. The result is fairly in agreement with the analytical prediction given by the formula (105) (shown by the solid line in Fig. 8).

3.2 Bright Soliton Excitations in a Cigar-Shaped 3D Superfluid Fermi Gas

Notice that the Q1D condition (68) requires N must be small and is usually hard to realize in present Fermi-gas experiment. In the Q1D system the dispersion term in the Bogoliubov excitation spectrum comes from the quantum pressure, which results in the formation of dark solitons through the balance between interaction-induced nonlinearity and quantum pressure-induced dispersion. However, up to now all superfluid Fermi gases realized experimentally, although being cigar-shaped,

violate the Q1D condition (68). It is natural to ask the following question: Is it possible to form a soliton in such cigar-shaped, but 3D, superfluid Fermi gas with large particle number?

A definite answer to the above question is given in [50]. It is shown that it is indeed available to generate a soliton in a cigar-shaped, 3D superfluid Fermi gas when the Q1D condition (68) is breakdown. However, the soliton obtained in this case is not a dark but bright one propagating on a continuous background of the condensate. Different from the subsonic dark soliton obtained in Q1D the bright soliton is supersonic one, i.e. its propagating velocity is larger than the linear sound speed. The formation of such supersonic bright soliton is due to the balance between inter-particle interaction and a waveguide-like dispersion and hence a large particle number of the system is needed, which is explained in detail below.

The linear collective excitations in a cigar-shaped 3D superfluid Fermi gas has been described in Sect. 2.2.3. To investigate long-wavelength, weak nonlinear excitations for large N, we use the superfluid hydrodynamic equations (4) and (5). In cylindrical coordinate system, the superfluid velocity $\mathbf{v}_s = (v_r, v_\varphi, v_z)$ satisfy

$$\frac{\partial n}{\partial t} + \frac{1}{r}\frac{\partial}{\partial r}(r\, n v_r) + \frac{1}{r}\frac{\partial}{\partial \varphi}\left(n v_\varphi\right) + \frac{\partial}{\partial z}(n v_z) = 0, \tag{106}$$

$$M\frac{\partial v_\varphi}{\partial t} + \frac{1}{r}\frac{\partial}{\partial \varphi}\left[\frac{1}{2}M(v_r^2 + v_\varphi^2 + v_z^2) + \mu_s(n) + V_{\text{ext}}(r,z)\right] = 0, \tag{107}$$

$$M\frac{\partial v_r}{\partial t} + \frac{\partial}{\partial r}\left[\frac{1}{2}M(v_r^2 + v_\varphi^2 + v_z^2) + \mu_s(n) + V_{\text{ext}}(r,z)\right] = 0, \tag{108}$$

$$M\frac{\partial v_z}{\partial t} + \frac{\partial}{\partial z}\left[\frac{1}{2}M(v_r^2 + v_\varphi^2 + v_z^2) + \mu(n) + V_{\text{ext}}(r,z)\right] = 0. \tag{109}$$

For simplicity we focus our effort here to excitations with cylindrical symmetry, i.e. $\partial/\partial\varphi = 0$ and $v_\varphi = 0$. For a weak nonlinear sound wave, its linear correspondence is the mode $(n_r, m) = (0, 0)$ with vanishing wavenumber k. In order to make an analytical approach available, we assume the trapping potential is z-independent, i.e. $V_{\text{ext}}(r,z) = V_{\text{ext}}(r)$. The effect of axial inhomogeneity will be considered in later numerical simulation. Introducing the slow variables $\xi = \epsilon(z - ct)$ and $\tau = \epsilon^3 t$, where ϵ is a small parameter representing the relative amplitude of the excitation and c is an undetermined parameter, and making the asymptotic expansions $n = n^{\text{eq}} + \epsilon^2 n^{(0)} + \epsilon^4 n^{(1)} + \cdots$, $v_r = \epsilon^3 u^{(0)} + \epsilon^5 u^{(1)} + \cdots$, $v_z = \epsilon^2 w^{(0)} + \epsilon^4 w^{(1)} + \cdots$, (106)–(109) become

$$-c\frac{\partial}{\partial \xi}n^{(l)} + \frac{1}{r}\frac{\partial}{\partial r}\left[r\, n^{\text{eq}} u^{(l)}\right] + \frac{\partial}{\partial \xi}\left[n^{\text{eq}} w^{(l)}\right] = \alpha^{(l)}, \tag{110}$$

$$\frac{\partial}{\partial r}\left[\mu'\, n^{(l)}\right] = \beta^{(l)}, \tag{111}$$

$$-Mc\frac{\partial}{\partial \xi}w^{(l)} + \frac{\partial}{\partial \xi}\left[\mu'\, n^{(l)}\right] = \gamma^{(l)}, \tag{112}$$

where $\mu' \equiv \partial\mu(n)/\partial n|_{n=n^{\rm eq}}$. Explicit expressions of $\alpha^{(l)}$, $\beta^{(l)}$ and $\gamma^{(l)}$ ($l = 0, 1, \cdots$) are omitted here. For convenience, we convert (110)–(112) into the following form

$$\mu' n^{(l)} = [\mu' n^{(l)}]|_{r=0} + \int_0^r dr\ \beta^{(l)}, \tag{113}$$

$$\frac{1}{r}\frac{\partial}{\partial r}\left[r\ n^{\rm eq} u^{(l)}\right] = \alpha^{(l)} + (c - \frac{n^{\rm eq}\mu'}{Mc})\frac{\partial n^{(l)}}{\partial \xi} + \frac{n^{\rm eq}\gamma^{(l)}}{Mc}, \tag{114}$$

$$w^{(l)} = \int d\xi\ \frac{1}{Mc}\ [\mu' \frac{\partial n^{(l)}}{\partial \xi} - \gamma^{(l)}]. \tag{115}$$

Equations (113)–(115) can be solved order by order. At the lowest order ($l = 0$), from (113) we obtain $n^{(0)}(r, \xi, \tau) = (\mu'|_{r=0}/\mu')F(\xi, \tau)$, where $\mu'|_{r=0}/\mu' = (1 - r^2/R_\perp^2)^{1/\gamma - 1}$ and $F(\xi, \tau) = n^{(0)}(0, \xi, \tau)$ is an envelope function to be determined yet. By (115) we have $w^{(0)} = \mu'|_{r=0}/(Mc)F(\xi, \tau)$.

Integrating (114) (for $l = 0$) from 0 to r, we obtain

$$rn^{\rm eq}u^{(0)} = \mu'|_{r=0}\frac{\partial F}{\partial \xi}\int_0^r dr\left[\frac{cr}{\mu'} - \frac{rn^{\rm eq}}{Mc}\right]. \tag{116}$$

Because $n^{\rm eq}|_{r=R_\perp} = 0$, by (116) we obtain $\int_0^{R_\perp} dr\ [cr/\mu' - rn^{\rm eq}/(Mc)] = 0$, which yields the sound speed

$$c = \left[\frac{\int_0^{R_\perp} dr\ rn^{\rm eq}}{M\int_0^{R_\perp} dr\ r/\mu'}\right]^{1/2} = \left[\frac{\gamma\mu_G}{(1+\gamma)M}\right]^{1/2}, \tag{117}$$

agreeing exactly with (50) and also with that obtained by Capuzzi et al. [103] by using a different approach.

From (116) we obtain $u^{(0)} = -[\gamma rc/(2F_0)]\partial F/\partial \xi$, where $F_0 = n^0(\mu_g/2\mu^0)^{\frac{1}{\gamma}}$ is central number density in the ground state. With the above solution, in the next order equation (114) for $l = 1$ has the form

$$\frac{\partial}{\partial r}[rn_s^{\rm eq}u^{(1)}] = -rJ_0(r)\frac{\partial F}{\partial \tau} - rJ_1(r)\frac{\partial^3 F}{\partial \xi^3} - rJ_2(r)F\frac{\partial F}{\partial \xi} \tag{118}$$

with

$$J_0(r) = (1 - \frac{r^2}{R_\perp^2})^{\frac{1}{\gamma}-1}\left[2 + \gamma - (\gamma+1)\frac{r^2}{R_\perp^2}\right], \tag{119}$$

$$J_1(r) = -\frac{\gamma c r^2}{4(1+\gamma)}(1 - \frac{r^2}{R_\perp^2})^{\frac{1}{\gamma}-1}\left[\gamma - (\gamma+1)\frac{r^2}{R_\perp^2}\right], \tag{120}$$

$$J_2(r) = \frac{c}{F_0}(1 - \frac{r^2}{R_\perp^2})^{\frac{1}{\gamma}-2}\left[2\gamma^2 + 3\gamma + 2 - (4\gamma^4 + 5\gamma + 2)\frac{r^2}{R_\perp^2} + 2\gamma(\gamma+1)\frac{r^4}{R_\perp^4}\right]. \tag{121}$$

Integrating (118) from 0 to $R_\perp$, we obtain the envelope equation for $F(\xi,\tau)$, i.e. $\partial F/\partial\tau + \lambda_1 F\partial/\partial\xi + \lambda_2\partial^3 F/\partial\xi^3 = 0$, with $\lambda_1 = c(3\gamma+2)/(2F_0)$ and $\lambda_2 = \gamma^3 R_\perp^2 c/[8(1+\gamma)(1+3\gamma+2\gamma^2)]$. Letting $G = \epsilon^2 F$ and using the definitions of $\xi = \epsilon Z$ and $\tau = \epsilon^3 t$, the envelope equation becomes

$$\frac{\partial G}{\partial t} + \lambda_1 G\frac{\partial G}{\partial Z} + \lambda_2\frac{\partial^3 G}{\partial Z^3} = 0, \tag{122}$$

with $Z = z - ct$. Equation (122) is the KdV equation. Its single soliton solution reads

$$G = A_0\,\mathrm{sech}^2\Big(\frac{z - V_{\mathrm{sol}}t - z_0}{\sigma}\Big) \tag{123}$$

with $V_{\mathrm{sol}} = c[1+(3\gamma+2)A_0/(6F_0)]$, and $\sigma = R_\perp\{3\gamma^3 F_0/[(1+\gamma)(1+3\gamma+2\gamma^2)(3\gamma+2)A_0]\}^{1/2}$, where A_0 is a positive constant and z_0 is an arbitrary real constant depending on initial exciting condition.

Based on above results we obtain

$$n_s = F_0(1-\frac{r^2}{R_\perp^2})^{\frac{1}{\gamma}} + (1-\frac{r^2}{R_\perp^2})^{\frac{1}{\gamma}-1}A_0\,\mathrm{sech}^2\Big(\frac{z - V_{\mathrm{sol}}t - z_0}{\sigma}\Big), \tag{124}$$

$$v_z = \frac{(1+\gamma)cA_0}{F_0}\,\mathrm{sech}^2\Big(\frac{z - V_{\mathrm{sol}}t - z_0}{\sigma}\Big), \tag{125}$$

$$v_r = \frac{\gamma c A_0}{\sigma F_0}\,r\mathrm{sech}^2\Big(\frac{z - V_{\mathrm{sol}}t - z_0}{\sigma}\Big)\tanh\Big(\frac{z - V_{\mathrm{sol}}t - z_0}{\sigma}\Big), \tag{126}$$

when exact to the leading-order approximation. We see that the soliton obtained is indeed a bright one that propagates on a condensate background. This is quite different from the result in Q1D case where the soliton obtained is a dark one [49]. In addition, the bright soliton is supersonic because its propagating velocity is larger than the sound speed c, which is also different from the dark soliton in Q1D case where the soliton obtained is a subsonic one [49].

The physical reason for the occurrence of the bright soliton can be understood as follows. From the Bogoliubov spectrum (49) we know that the coefficient of k^3 (when making an expansion around $k = 0$) is negative, which is different from that obtained for Q1D case (see (73)) where the coefficient of k^3 is positive. The difference between the sign of the k^3-coefficient for the present cigar-shaped 3D system and that of the Q1D system is due to the different origin of dispersion. In the Q1D case the dispersion comes from quantum pressure, whereas in the present cigar-shaped 3D case the dispersion results from the TF distribution of ground-state wavefunction in the radial direction, which induces a dispersion for each eigenmode. It is just due to these different dispersion characters that make subsonic dark solitons occur in the Q1D system but the supersonic bright solitons possible in the present 3D system [50].

To give a quantitative picture for the feature of the bright soliton predicted above, in Table 4 we have we presented some numerical values of velocity V_{sol}, width σ of

Table 4 Numerical values of the bright soliton velocity $V_{\rm sol}$, axial width σ, and condensate radii $R_\perp$ and R_z for $A_0/F_0 = 0.1$ in several different superfluid regimes

	BEC limit	BEC regime	Unitarity	BCS regime
$\eta^0 = 1/(k_F^0 a_s)$	5	1	0	-1
$V_{\rm sol}$ (mm/s)	12	17	20	24
σ (μm)	3.5	5	6	6.5
$2R_z$(μm)	198	284	397	467
$R_\perp$(μm)	5	7	10	12

the bright soliton in terms of Duke experimental parameters [80]. The condensate radii $R_\perp$ and R_z are also given. We see that the bright soliton has different velocity and width in different superfluid regimes. When passing from the BEC to the BCS regimes, the propagating velocity and axial width of the soliton increases. This is contrast to the Q1D dark solitons, for which the soliton width in the BCS regime is smaller than that in the BEC regime.

For comparison, in Fig. 3 we have plotted the propagating velocity of the bright soliton for the present cigar-shaped 3D system (the dotted line), and that of the dark soliton for the Q1D system given (dotted-dashed line). We see clearly that the former is supersonic and the latter is subsonic.

Because the KdV equation (122) is a completely integrable model, its soliton solutions are stable to 1D perturbations. Notice that, when obtaining the KdV equation (122), weak dispersion and weak nonlinear approximations have been made and the axial trapping potential, i.e. $M\omega_z^2 z^2/2$, is not taken into account. However, this may be not the realistic case of ultracold Fermi gas experiments, where for large-amplitude and narrow-width collective excitations and for a long propagating distance, effects originated from high-order dispersion, high-order nonlinearity, and axial inhomogeneity may play significant role, and hence (these structural perturbations) will destroy the integrability of the KdV equation. For weak dispersive and weak nonlinear excitations we discussed here, the instability of solitons is mainly due to the axial inhomogeneity contributed by the axial trapping potential.

To show the influence of the axial trapping potential on the supersonic bright soliton predicted above, a numerical simulation starting from the hydrodynamics equations (106)–(109) by using the bright soliton solution (124)–(126) as an initial condition has been carried out [50]. The system parameters are chosen as $N = 1 \times 10^5$, $\omega_\perp = 2\pi \times 3,000\,\text{Hz}$, $\omega_z = 2\pi \times 100\,\text{Hz}$, and $A_0/F_0 = 0.2$. The result of the simulation for three different regimes are illustrated in Fig. 9. Panels (a), (b) and (c) in the figure correspond to bright soliton propagation in the BEC ($1/(k_F^0 a_s) = 5$), unitarity limit ($1/(k_F^0 a_s) = 0$), and BCS ($1/(k_F^0 a_s) = -1$) regimes, respectively. One can observe the following propagation features: (i) The bright soliton is fairly stable near the center of the condensate, but it becomes broadened and radiates small continuous waves when moving to the boundary of the condensate. This effect contributes mainly from the weak axial trapping potential

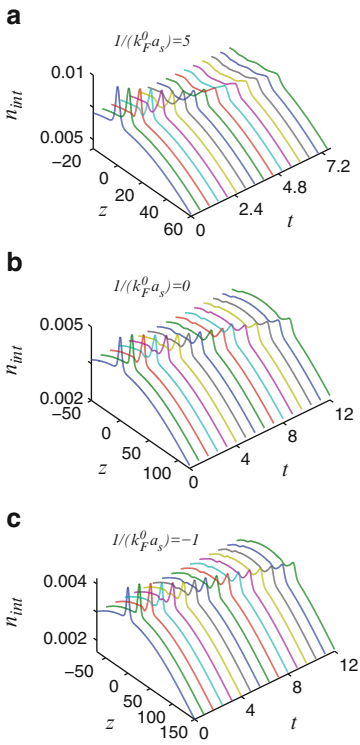

Fig. 9 Result of numerical simulation on the evolution of bright soliton as a function of dimensionless time t (in unit of 0.05 ms) and axial distance z (in unit of 0.5 μm). The vertical coordinate is the integrated density $n_{\rm int}(z) = 2\pi \int_0^{R_\perp} dr n(r, z)$. Panels (**a**), (**b**) and (**c**) correspond to the BEC regime $(1/(k_F^0 a_s) = 5)$, unitarity limit $1/(k_F^0 a_s) = 0$, BCS regime $(1/(k_F^0 a_s) = -1)$, respectively

that confines the condensate in the axial direction, not considered in the theoretical analysis given above. (ii) The soliton in the BCS regime is more stable than in the BEC regime. The reason is that, for the same N, $\omega_\perp$ and ω_z the axial length of the condensate in the BCS regime is much larger than that in the BEC regime, and hence the axial trapping potential plays less important role than in the BCS regime. (iii) During propagation, the bright soliton radiates a small dip that propagates in opposite direction. This phenomenon can be understood as follows. Because the hydrodynamics equations (106)–(109) allow two eigen sound-wave modes, one propagates with velocity c and another one propagates with velocity $-c$. Thus an initial disturbance of the system (106)–(109), though being a soliton solution of the KdV equation (122), will generally evolve into two parts that having opposite propagating directions. (iv) In different superfluid regimes the supersonic bright soliton and associated radiation has different amplitude and propagating velocity. This is a direct reflection of different physical properties of the superfluid Fermi gas that can be used to distinguish different superfluid regimes of the system.

Except for the above works, we also studied collective modes and free expansions of Q1D and Q2D ultracold Fermi gases in the BCS-BEC crossover by using a time-dependent variational analysis. We solved a superfluid order parameter equation by employing a time-dependent variational method. We took a trial wave function with the form of hybrid Gaussian-parabolic type, which not only reflects low-dimensional

character of the system but also allows an essentially analytical approach for the problem. We presented Q1D and Q2D criteria that are valid in various superfluid regimes and show clearly the relation between the maximum condensed particle number and the parameters of trapping potential as well as atom-atom interaction. We demonstrated that, due to small particle number in Q1D and Q2D condensates, the contribution to oscillating frequencies of collective modes by the quantum pressure in strong confinement direction is significant and hence a Thomas-Fermi approximation can not be used. We also showed that the free expansion of Q1D and Q2D superfluid Fermi gases in strong confinement direction is much faster than that in weak confinement direction [44].

In addition, we investigated the frequency shift and mode coupling of the collective modes of superfluid Fermi gases in the BCS-BEC crossover based on a hydrodynamic approach. We solved the superfluid hydrodynamic equations that describe the time evolution of fermionic condensates in the BCS-BEC crossover and calculated explicitly the frequency shifts of the collective modes induced by nonlinear effects using the Lindstedt-Poincaré method. The result shows that the frequency shifts display different features in different superfluid regimes. We studied the second harmonic generation of the collective modes under a phase-matching condition, which can be fulfilled by choosing appropriate parameters of the system. The analytical results obtained are checked by numerical simulations and good agreement is found. For details, see [46].

4 Conclusions and Perspectives

We have presented the recent theoretical progress made in Shanghai on the collective excitations in superfluid Fermi gases in the BCS-BEC crossover. All linear eigenvalues and eigenfunctions of 3D traps with spherical and axial symmetries have been provided and compared with experiments. Corresponding results beyond mean-field and TF approximations are also given. Furthermore, the linear excitations and the sound propagation in a cigar-shaped 3D superfluid Fermi gas have been described and the eigenvalue problems of linear collective excitations for Q1D and Q2D systems have been solved exactly. In addition, nonlinear excitations, including the dark solitons in a Q1D condensate and the bright solitons in a cigar-shaped 3D condensate have been predicted.

Although there have been tremendous progress on the understanding of collective excitations in ultracold Fermi atomic gases in the BCS-BEC crossover in last years, many important topics remain to be addressed or investigated deeply, including linear collective excitations in other external potentials (e.g. optical lattices), nonlinear (soliton) excitations in high-dimensional settings, shock waves and vortices, and so on. These studies are useful for understanding the linear and nonlinear properties of fermionic condensates and may guide experimental findings of the various linear and nonlinear excitations in superfluid Fermi atomic gases in the BCS-BEC crossover.

Acknowledgement The author thanks Professor Y.-l. Ma, Dr. W. Wen and Dr. Y. Zhou for fruitful collaborations. This work was supported by NSF-China under Grant Ns. 10434060, 10674060, 10874043, and 11174080, by the Key Development Program for Basic Research of China under Grant Nos. 2005CB724508 and 2006CB921104.

References

1. Onnes H.K.: Comm. Phys. Lab. Univ. Leiden **12**, 120 (1911)
2. Wolfke, M., Keesom, W.H.: Proc. Amsterdam **31**, 81 (1927)
3. Chu, S.: Rev. Mod. Phys. **70**, 685(1998)
4. Cohen-Tannoudji, C.: Rev. Mod. Phys. **70**, 707 (1998)
5. Phillips, W.D.: Rev. Mod. Phys. **70**, 721(1998)
6. Einstein, A.: Sitzber. Kgl. Preuss. Akad. Wiss. 3 (1925)
7. Cornell, E.A., Wieman, C.E.: Sitzber. Kgl. Preuss. Akad. Wiss. **74**, 875 (2002)
8. Ketterle, W.: Sitzber. Kgl. Preuss. Akad. Wiss. **74**, 1131 (2002)
9. Giorgini, S., Pitaevskii, L.P., Stringari, S.: Rev. Mod Phys. **80**, 1215 (2008)
10. Ketterle, W., Zwierlein, M.W.: Riv. Nuovo Cim. **31**, 247 (2008)
11. Pethick, C.J., Smith, H.: Bose-Einstein Condensation in Dilute Gases, 2nd edn. Cambridge University Press, London, 2008
12. Pitaevskii, L., Stringari, S.: Bose-Einstein Condensation. Clarendon Press, Oxford, 2003
13. Carr, L.D., DeMille, D., Krems, R.V., Ye, J.: New J. Phys. **11**, 055049 (2011)
14. Bartenstein, M., et al.: Phys. Rev. Lett. **92**, 203201 (2004)
15. Kinast, J., et al.: Phys. Rev. Lett. **92**, 150402 (2004)
16. Kinast, J., et al.: Phys. Rev. A **70**, 051401(R) (2004)
17. Kinast, J., et al.: Phys. Rev. Lett. **94**, 170404 (2005)
18. Greiner, M., et al.: Phys. Rev. Lett. **94**, 070403 (2005)
19. Altmeyer, A., et al.: Phys. Rev. Lett. **98**, 040401 (2007)
20. Holland, M., Park, J., Walser, R.: Phys. Rev. Lett. **86**, 1915 (2000)
21. Timmermans, E., et al.: Phys. Lett. A **285**, 228 (2001)
22. Ohashi, Y., Griffin, A.: Phys. Rev. Lett. **89**, 130402 (2002)
23. De Silva, T.N., Mueller, E.J.: Phys. Rev. A **72**, 063614 (2005)
24. Romans, M.W.J., Stoof, H.T.C.: Phys. Rev. Lett. **95**, 269407 (2005)
25. Liu, W.V., Wilczek, F.: Phys. Rev. Lett. **90**, 047002 (2003)
26. Pieri, P., Strinati, G.C.: Phys. Rev. Lett. **96**, 187001 (2006)
27. Yi, W., Duan, L.-M.: Phys. Rev. A **73**, 063607 (2006)
28. Yang, K., Sachdev, S.: Phys. Rev. Lett. **96**, 187001 (2006)
29. Chien, C.-C., et al.: Phys. Rev. Lett. **96**, 090402 (2006)
30. Diener, R.B., Ho, T.-L.: Phys. Rev. Lett. **96**, 010402 (2006)
31. Stringari, S.: Euro. Phys. Lett. **65**, 749 (2004)
32. Heiselberg, H.: Phys. Rev. Lett. **93**, 04040 (2004)
33. Hu, H., et al.: Phys. Rev. Lett. **93**, 190403 (2004)
34. Kim, Y.E., Zubarev, A.L.: Phys. Rev. A **70**, 033612 (2004)
35. Kim, Y.E., Zubarev, A.L.: Phys. Rev. A **77**, 011603(R) (2005)
36. Manini, N., Salasnich, L.: Phys. Rev. A **71**, 033625 (2005)
37. Combescot, R., Leyronas, X.: Phys. Rev. Lett. **93**, 138901 (2004)
38. Bulgac, A., Bertsch, G.F.: Phys. Rev. Lett. **94**, 070401 (2005)
39. Astrakharchik, G.E., et al.: Phys. Rev. Lett. **95**, 030404 (2005)
40. Ghosh, T.K., Machida, K.: Phys. Rev. A **73**, 013613 (2006)
41. Diana, G., Manini, N., Salasnich, L.: Phys. Rev. A **73**, 065601 (2006)
42. Yin, J., Ma, Y.-L., Huang, G.: Phys. Rev. A **74**, 013609 (2006)
43. Wen, W., Huang, G.: Phys. Lett. A **362**, 331 (2007)

44. Zhou, Y., Huang, G.: Phys. Rev. A **75**, 023611 (2007)
45. Ma, Y.-L., Huang, G.: Phys. Rev. A **75**, 063629 (2007)
46. Zhou, Y., Wen, W., Huang, G.: Phys. Rev. A **77**, 104527 (2008)
47. Wen, W., Zhou, Y., Huang, G.: Phys. Rev. A **77**, 033623 (2008)
48. Cao, S., Ma, Y.-l., Huang, G.: Phys. Rev. A **79**, 013620 (2009)
49. Wen, W., Huang, G.: Phys. Rev. A **79**, 023605 (2009)
50. Wen, W., Shen, S., Huang, G.: Phys. Rev. B **81**, 014528 (2010)
51. DeMacro, B., Jin, D.S.: Science **285**, 1703 (1999)
52. Jochim, S., et al.: Science **302**, 2101 (2003)
53. Chin, C., et al.: Science **305**, 1128 (2004)
54. Regal, C.A., Greiner, M., Jin, D.S.: Phys. Rev. Lett. **92**, 040403 (2004)
55. Zwierlein, M.W., et al.: Phys. Rev. Lett. **92**, 120403 (2004)
56. Zwierlein, M.W., et al.: Nature **435**, 1047 (2005)
57. Zwierlein, M.W., et al.: Science **311**, 492 (2006)
58. Partridge, G.B., et al.: Science **311**, 503 (2006)
59. Zwierlein, M.W., et al.: Nature **442**, 54 (2006)
60. Shin, Y., et al.: Phys. Rev. Lett. **97**, 030401 (2006)
61. Chin, J.K., et al.: Nature **443**, 961 (2006)
62. Astrakharchik, G.E., Boronat, J., Casulleras, J., Giorgini, S.: Phys. Rev. Lett. **93**, 200404 (2004)
63. Carlson, J., Chang, S.-Y., Pandharipande, V.R., Schmidt, K.E.: Phys. Rev. Lett. **91**, 050401 (2003)
64. Astrakharchik, G.E., Boronat, J., Casulleras, J., Giorgini, S.: Phys. Rev. Lett. **93**, 200404 (2004)
65. Pieri, P., Strinati, G.C.: Phys. Rev. Lett. **91**, 030401 (2003)
66. Salasnich, L., Toigo, F.: Phys. Rev. A **78**, 053626 (2008)
67. Stringari, S.: Phys. Rev. Lett. **77**, 2360 (1996)
68. Baranov, M.A., Petrov, D.S.: Phys. Rev. A **62**, 041601(R) (2000)
69. Bruun, G.M., Clark, C.W.: Phys. Rev. Lett. **83**, 5415 (1999)
70. Hu, B., Huang, G., Ma, Y.L.: Phys. Rev. A **69**, 063608 (2004)
71. Cozzini, M., Stringari, S.: Phys. Rev. Lett. **91**, 070401 (2003)
72. Lee, T.D., Huang, K., Yang, C.N.: Phys. Rev. *106*, 1135 (1957)
73. Yang, C.N.: arXiv:0807.0938v2 [cond-mat.stat-mech] (2008), and references therein
74. Pitaevskii, L., Stringari, S.: Phys. Rev. Lett. **81**, 4541 (1998)
75. Astrakharchik, G.E.: Phys. Rev. A **72**, 063620 (2005)
76. Astrakharchik, G.E., Boronat, J., Casulleras, J., Giorgini, S.: Phys. Rev. Lett. **93**, 200404 (2004)
77. Petrov, D.S., Salomon, C., Shlyapnikov, G.: Phys. Rev. Lett. **93**, 090404 (2004)
78. Salasnich, L., Ancilotto, F., Toigo, F.: Laser Phys. Lett. **7**, 78 (2010)
79. Zaremba, E.: Phys. Rev. A **57**, 518 (1998)
80. Joseph, J., Clancy, B., Luo, L., Kinast, J., Turlapov, A., Thomas, J.E.: Phys. Rev. Lett. **98**, 170401 (2007)
81. Menotti, C., Stringari, S.: Phys. Rev. A **66**, 043610 (2002)
82. Ho, T.-L., Ma, M.: J. Low Temp. Phys. **115**, 61 (1999)
83. Kivshar, Y.S., Agrawal, G.P.: Optical Solitons: From Fibers to Photonic Crystals. Academic, New York, 2003
84. Burger, S., Bongs, K., Dettmer, S., Ertmer, W., Sengstock, K., Sanpera, A., Shlyapnikov, G.V., Lewenstein, M.: Phys. Rev. Lett. **83**, 5198 (1999)
85. Denschlag, J., Simsarian, J.E., Feder, D.L., Clark, C.W., Collins, L.A., Cubizolles, J., Deng, L., Hagley, E.W., Helmerson, K., Reinhart, W.P., Rolston, S.L., Schneider, B.I., Phillips, W.D.: Science **287**, 97 (2000)
86. Dutton, Z., Budde, M., Slowe, C., Hau, L.V.: Science **293**, 663 (2001)
87. Anderson, B.P., Haljan, P.C., Regal, C.A., Feder, D.L., Collins, L.A., Clark, C.W., Cornell, E.A.: Phys. Rev. Lett. **86**, 2926 (2001)
88. Engels, P., Atherton, C.: Phys. Rev. Lett. **99**, 160405 (2007)
89. Khaykovich, L., Schreck, F., Ferrari, G., Bourdel, T., Cubizolles, J., Carr, L., Castin, Y., Salomon, C.: Science **296**, 1290 (2002)

90. Strecker, K.E., Partridge, G.B., Truscott, A.G., Hulet, R.G.: Nature **417**, 150 (2002)
91. Cornish, S.L., Thompson, S.T., Wieman, C.E.: Phys. Rev. Lett. **96**, 170401 (2006)
92. Eiermann, B., Anker, Th., Albiez, M., Taglieber, M., Treutlein, P., Marzlin, K.-P., Oberthaler, M.K.: Phys. Rev. Lett. **92**, 230401 (2006)
93. Kevrekidis, P.G., Frantzeskakis, D.J., Carretero-Gonzlez, R. (eds.): Emergent Nonlinear Phenomena in Bose-Einstein Condensates: Theory and Experiment. Springer, Berlin (2008), and see references therein
94. Huang, G., Velarde, M.G., Makarov, V.A.: Phys. Rev. A **64**, 013617 (2001)
95. Huang, G., Szeftel, J., Zhu, S.: Phys. Rev. A **65**, 053605 (2002)
96. Huang, G., Makarov, V.A., Velarde, M.G.: Phys. Rev. A **67**, 023604 (2003)
97. Huang, G., Deng, L., Hang, C.: Phys. Rev. E **72**, 036621(2005)
98. Antezza, M., Dalfovo, F., Pitaevskii, L.P., Stringari, S.: Phys. Rev. A **76**, 043610 (2007)
99. Liao, R., Brand, J.: Phys. Rev. A **83**, 041604 (2011)
100. Scott, R.G., Dalfovo, F., Pitaevskii, L.P., Stringari, S.: Phys. Rev. Lett. **106**, 185301 (2011)
101. Jeffery, A., Kawahawa, T.: Asymptotic Methods in Nonlinear Wave Theory. Pitman, London, 1982
102. Chin, S.A., Krotscheck, E.: Phys. Rev. E **72**, 036705 (2005)
103. Capuzzi, P., Vignolo, P., Federici, F., Tosi, M.P.: Phys. Rev. A **73**, 021603(R) (2006)

Part V
Scientific Contributions: Complex Dynamics and Stochastic Dynamics

Toward a Complex Systems Approach to Information

G. Nicolis and C. Nicolis

1 Introduction

It is a great pleasure to dedicate this short note to our colleague and friend of 47 years Manuel García Velarde, as a tribute to his brilliant contributions to science.

Manuel's work spans a wide spectrum of subjects, from statistical mechanics to the physics of fluids, interfaces, reaction–diffusion systems, neural dynamics and, more recently, condensed matter physics in connection with the soliton-mediated electric transport in lattices. In each case a common denominator is present throughout this diversity, namely, nonlinearity-induced complex collective behaviors conferring unexpected properties to the system of interest. Here we wish to present some ideas on the connection between complex systems and information theory, two concepts that have often be among Manuel's preoccupations.

One of the principal features underlying the evolution of complex systems is the multitude of the a priori available states. Clearly, the outcome of an evolution of this kind comprises an element of *unexpectedness*, reflected by the ability of the system to choose among several possible outcomes and the concomitant difficulty of the observer to localize the actual state in state space on the basis of the data that are available to him. A natural question to be raised is, then, to identify quantities serving as measures of choice and unexpectedness, thereby providing useful indicators of the complexity of the system at hand.

Now this question is reminiscent of a central problem of information and communication theories, namely, how to recognize a signal blurred by noise.

G. Nicolis (✉)
Interdisciplinary Center for Nonlinear Phenomena and Complex Systems, Université Libre de Bruxelles, Campus Plaine, CP 231, bd du Triomphe, 1050 Brussels, Belgium
e-mail: gnicolis@ulb.ac.be

C. Nicolis
Institut Royal Météorologique de Belgique, 3 av. Circulaire, 1180 Brussels, Belgium
e-mail: cnicolis.oma.be

R.G. Rubio et al. (eds.), *Without Bounds: A Scientific Canvas of Nonlinearity and Complex Dynamics*, Understanding Complex Systems,
DOI 10.1007/978-3-642-34070-3_39,

The point is that in any real world information source, living or mechanical, choice is continuously exercised. Otherwise, the messages produced would be predetermined and completely predictable and there would be no need for communication. Corresponding to the choice exercised by the message source in producing the message, there is an uncertainty at the level of the recipient of the message, which is resolved only when the recipient examines the message. Clearly, the measures we are looking for must increase with the amount of choice of the source, and, hence, with the uncertainty of the recipient as to what message the source may produce or transmit.

2 Information as an Emergent Property

A major result of information theory is that the *information entropy* [1,2]

$$S_I = -\sum_{i=1}^{N} p_i \ln p_i \tag{1}$$

where p_i is the probability of occurrence of state i, provides this measure as it possesses all the desired properties that one could reasonably assign:

(i) It takes its largest value for $p_i = 1/N$, implying that in the case of equiprobable states the uncertainty about the particular state actually realized—and hence the amount of data necessary to resolve it—is the maximum one;
(ii) Adding an impossible event α, $p_\alpha = 0$, does not change S_I;
(iii) The information entropy $S_I(A, B)$ of a composite system AB equals the entropy of subsystem A plus the conditional entropy $S_I(B|A)$ of subsystem B provided that subsystem A is in a given state.

In fact, one can show that (1) is the only quantity possessing these properties.

The deviation of information entropy from its maximum S_{max} or, more appropriately, the quantity $R = 1 - S_I/S_{max}$ is referred to as redundancy of the signal. Redundancy reflects the deviation from full randomness and contributes, clearly, to reducing errors and thus enhancing predictability [3]. In an evolving system S_I and S_{max} are both depending on time, as new states are being created. It has been conjectured that in biological evolution and in the evolution of languages R globally increases in time, in other words, that local disorder (measured by S_I) increases less rapidly than the rate of appearance of new states (measured by the time derivative of S_{max}).

To apply the above ideas to complex systems, and to use information entropy as an indicator of complexity one needs to resort to a probabilistic approach [4]. The crux is in the concept of *coarse graining*—the mapping of the dynamics into a discrete set of states. Depending on the case, these can be the states introduced in connection with a mesoscopic level description based on the master equation; or the phase space cells of a Markov partition involved in the mapping of deterministic chaos into a symbolic dynamics. The procedure can even be carried out starting

from the continuous description afforded by the Fokker–Planck equation. As an example, consider a system that admits two simultaneously stable steady states. Because of the transitions between states induced by the fluctuations, the system will spend substantial amounts of time near each of these states. Let us introduce a more abstract description in which the instantaneous state is labeled "0" or "1", according to whether the system is in the domain of attraction of the first or the second stable steady state. An observer following the evolution at regular time intervals by noticing the attraction basin in which the system is found will therefore detect a sequence like 111001100010110... which provides a description in terms of an alphabet involving only two "letters", 0 and 1.

Conversely, we are entitled on the grounds of the above arguments to view complex systems as information sources. Equation (1) allows then us to connect information entropy with different evolution scenarios. Consider, for instance, the universal phenomenon of bifurcation, one of the "elementary acts" of complexity. Prior to bifurcation the system possesses a unique macroscopic state. In the absence of internal fluctuations or environmental noise one has $N = 1,\ p_1 = 1$ in the notation of (1), hence $S_I = 0$. Switching to the other side of the bifurcation point one now has (in the case of the symmetric (pitchfork) bifurcation) two equivalent macroscopic states. In the absence of fluctuations or noise this means $N = 2,\ p_1 = p_2 = 1/2$, hence $S_I = \ln 2$. The presence of variability will modify these results slightly by an amount of the order of the variance of the process, but the essential point is that bifurcation entails a finite jump of S_I plus a small correction that can be discarded to the dominant order,

$$\Delta S_I = \ln 2 \tag{2}$$

This result is universal, as it holds for any dynamical system undergoing this type of bifurcation [5, 6]. It can be extended to other types of bifurcations, including bifurcations leading to periodic or to chaotic behavior. Notice that thermodynamic quantities and other familiar purely macroscopic observables show no universal trends across bifurcation.

On the basis of these results information may be viewed as an emergent property, arising through an evolutionary process leading from the state of "no information" to the state of "information". Fluctuations are here the natural carriers of information, as they allow the system to realize the crucial process of transition between the available states. This suggests that it would be meaningful to revisit information theory in the light of the progress in complex systems research.

3 Dynamical Entropies and Their Large Deviation Properties

As a rule, an information source produces sequences of symbols. Since we are concerned here primarily by complex systems as information sources, this means that we are letting the underlying dynamics run for a certain amount of time, map the

trajectory through the process of coarse-graining explained in Sect. 2 into a discrete sequence of states, and inquire on the restrictions imposed by the dynamics on the succession of symbols such as: constraints of word frequency, constraints of word order or, more generally, "grammatical" rules of some sort.

To handle these situations we divide the message into blocks of symbols of length n. This makes it possible to extend (1), corresponding essentially to an entropy per symbol, and define the *entropy per block* of symbols or, equivalently, the entropy associated to a portion of the system's history over a window of length n [1,2,4]:

$$S_n = -\sum_{i_1 \ldots i_n} P_n(i_1 \ldots i_n) \ln P_n(i_1 \ldots i_n) \tag{3}$$

Here $P_n(i_1 \ldots i_n)$ is the probability to generate the particular sequence $i_1 \ldots i_n$ and the sum runs over all sequences compatible with the underlying rules. Its structure depends crucially on the rules underlying the information processor. Suppose that the rules amount to choosing a particular symbol out of an alphabet of, say, L letters independently of the choice made in previous steps (for a two letter alphabet this would be equivalent to tossing a fair coin). The number of all possible sequences of length n would then be $N_n = L^n = \exp[n \ln L]$ and (3) leads to

$$\begin{aligned} P_n &\approx \exp[-n \ln L] \\ S_n &= n \ln L \end{aligned} \tag{4}$$

As can be seen, the occurrence of each particular word is penalized exponentially with respect to its length n, the rate of penalization being $\ln L$. This is a direct consequence of the adopted rules which lead to a *combinatorial explosion*, associated with the proliferation of words of increasing length. Clearly, an information source of this kind—to which one may refer as a *Bernoulli processor*—is not adequate for generating complex structures.

Suppose next that the processor generates the sequences via a Markovian stochastic process, such as in the mesoscopic level description of the fluctuations afforded by a master type equation. One can prove then the following remarkable property, known as the Shannon-McMillan-Breiman theorem [2,4].

For sufficiently large n, all sequences C of length n can be separated into two groups such that:

(i) The sum of probabilities of all the sequences of the first group is less than an arbitrarily small prescribed positive number.
(ii) For every sequence C of the second group the quantity $-(\ln P_n(C))/n$ differs from $h = \lim_{n\to\infty} \frac{S_n}{n}$ by an amount less than an arbitrarily small prescribed positive number.

The first group is clearly a low probability group, whereas the second one contains the sequences that are realized with a non-negligible probability.

The Shannon-McMillan-Breiman theorem asserts that all sequences of this latter type have approximately the same probability, given by

$$P_n \approx \exp\{-S_n\} \tag{5}$$

implying that their number is approximately

$$N_n \approx \exp\{S_n\} \tag{6}$$

Relations like (5) and (6) are referred to as *large deviation* properties [7, 8].
Now due to the presence of correlations in a typical stochastic process, S_n is always smaller that or equal to $n \ln L$. In other words, with the exception of fully uncorrelated sequences for large n the high probability group contains only a negligible small part of all sequences of length n emitted by the source whose number is

$$N_{n,max} \approx \exp\{n \ln L\}$$

We thus arrive at the important conclusion that correlations and deviations from equiprobability act like extremely efficient selectors of privileged sequences out of the huge set of all possible random sequences. Such deviations can for instance be realized if the system is not isolated but instead is put in contact with an external environment. Such conditions can lead to *nonequilibrium states* that can be sustained indefinitely because of the exchange of matter or energy between the system and the external world. Nonequilibrium is therefore the natural environment in which selection may take place.

In writing relations (5) and (6) we have assumed that the system of interest was giving rise to a stochastic process defined on a discrete (actually finite) set of states and characterized by the Markov property. In actual fact it turns out that these remarkable relations are satisfied by the much wider class of ergodic, not necessary Markovian processes.

4 Algorithmic Complexity Versus Physical Complexity. Dynamical Systems as Information Sources

The information theory view of complexity holds that rather than being described in qualitative terms, natural objects are represented as sequences of 0's and 1's stored in the memory of a computer. Likewise, statements on how things are to follow logically each other are expressed as computer programs and hence also as sequences of 0's and 1's. One is thus gradually led to the view that natural laws are algorithms implementable in the form of a computing program, that computes sets of digits as an output starting with a reference set (the initial data) provided by the experimental observations.

In the above philosophy, an object is quite naturally deemed complex when there is no short description of it. More precisely, the algorithmic complexity—also referred as Kolmogorov–Chaitin complexity, $C(K)$—of an object in its digitalized expression of binary sequence of length K, will be defined as the size of the smallest computer program (measured again in number of bits) generating it, *no matter how slow* this program might be [9, 10].

Let us give a few examples. Consider a binary sequence K data long displaying an overall regularity, e.g. 100100100... Clearly, the message in it can be considerably compressed. For instance, it could be transmitted to a computer by a very simple algorithm "Print 100 ten (or 100, or a million, ...) times". The number of binary digits K^* in such an algorithm is a small fraction of K, and as the series grows larger the algorithm size increases at a much slower rate such that K^*/K tends to zero as K tends to infinity. According to the definition this therefore implies limited algorithmic complexity. Consider next the opposite limit of a sequence of length K whose digits are set to 0 or to 1 depending on the outcome "heads" or "tails" of a (fair) coin tossing game. Clearly, this sequence can be recorded or transmitted only by reproducing it from beginning to end: its algorithmic complexity K^* is equal to its size K.

As it turns out, most of the sequences are incompressible and have a maximum algorithmic complexity. How many? To answer this question one needs to compute $C(K)$, and the quest for a result of this kind leads to a major surprise: there is no general procedure for computing it in a finite time. Far from being a temporary drawback related to the lack of sufficiently sophisticated mathematical techniques this conclusion reflects, in fact, the deep concept of undecidability discovered by Kurt Gödel in 1931: any formal system built on a set of axioms comprises statements that cannot be confirmed or rejected on the sole basis of these axioms. Translated in terms of computing this implies that there is no mechanical procedure allowing one to know whether a computer program chosen at random will or will not be executed in finite time. Gregory Chaitin reformulated this "halting problem" in terms of a halting probability, Ω and showed that Ω is an uncomputable number that cannot be compressed in any way whatsoever [10]. This "openness" in a field usually considered to be the prototype of definiteness is not unlike the existence of an unlimited, non-classifiable number of evolution scenarios of a complex system [4].

While algorithmic complexity captures certain features of natural complex systems, in its basic philosophy it is fundamentally different from the complexity one is concerned with in nature where one seeks to identify emergent patterns, concerted behavior and evolution. True, full orderliness in the form of a complete lack of variability is an extreme case of coherence in which the object is like a fossil, and its behavior can hardly be characterized as complex. On the other hand, the strong variability represented by a random sequence—a random noise—and the concomitant lack of any form of correlations is another, equally non-representative form of organization. In reality, physical complexity must somehow be sandwiched between these two extremes, and thus should not be fully identified with algorithmic complexity. The crux is the role of the dynamics and, in particular, the issue of selection. Algorithmic complexity is insensitive to the time needed to accomplish a

program (assuming that the latter will eventually halt). But in nature what matters is to produce complexity as the system of interest evolves in real time. The probability to produce a prescribed pattern/sequence out of the enormous number of the a priori possible ones is usually exceedingly small. But in a dynamical system generating complex behavior such states may be produced with probability one, being the result of a physical mechanism built into the evolution law: the problem of selection simply does not arise. In a way, under appropriate conditions dynamical systems are capable of exploring their state space continuously thereby creating information and complexity; at the same time they act like efficient selectors that reject the vast majority of possible patterns/sequences and keep only those compatible with the underlying dynamics. Furthermore, dissipation allows for the existence of attractors that have asymptotic stability and thus reproducibility. It therefore seems legitimate to state that algorithmic complexity is a static, equilibrium like concept whereas physical complexity takes its full significance in a dynamic, nonequilibrium context. To tackle physical complexity, one needs a nonequilibrium generalization of classical information theory [11–13].

5 Conclusions

The ideas summarized in this note raise the legitimate question of definition of complexity, beyond its computational aspects formalized by the concept of the Kolmogorov–Chaitin complexity. Several attempts in this direction have been reported in the literature [14, 15]. An interesting measure, on the grounds of its relation to prediction, is the amount of information necessary to estimate optimally conditional probabilities of the type $W(i_{n+1}|i_1 \cdots i_n)$ given the n-fold probabilities $P_n(i_1 \cdots i_n)$ (cf. (3)). In a quite different vein one associates complexity to "value" of some sort, for instance, the time required to actually retrieve a message from its minimal algorithmic prescription. In this view a message is complex, or *deep*, if it is implausible and can only be brought to light as a result of a long calculation [16]. This introduces the time element that is so conspicuously absent in the Kolmogorov–Chaitin complexity. Alternatively, the complexity of a system in a certain state is identified to the logarithm of the probability that this state has been reached through a particular path from time step $-n$, in the past, to the present time zero. While capturing certain aspects of physical complexity, in our view none of these definitions/measures manages to fully encompass its multiple facets. The question, how to define complexity is thus likely to remain open for some time to come. It may even turn out to be an ill-posed one. Complexity does not reflect any built-in, immediately recognizable, structure as is e.g. the case of nonlinearity. It is, rather, a set of attributes springing unexpectedly into life from the laws of nature when the appropriate conditions are met, raising in turn new issues and introducing new concepts among which information plays a special role, constituting one of the basic elements differentiating complexity research from traditional scientific disciplines and conveying to it its specificity and originality.

References

1. Shannon, C., Weaver, W.: The Mathematical Theory of Communication. University of Illinois Press, Urbana (1949)
2. Khinchine, A.: Mathematical Foundations of Information Theory. Dover, New York (1957)
3. Nicolis, J.S.: Dynamics of Hierarchical Systems. Springer, Berlin (1986)
4. Nicolis, G., Nicolis, C.: Foundations of Complex Systems, 2nd edn. World Scientific, Singapore (2012)
5. Haken, H.: Information and information gain close to nonequilibrium phase transitions. Numerical results. Z. Phys. **B62**, 255–259 (1986)
6. Nicolis, G., Altares, V.: Physics of nonequilibrium systems. In: Caglioti, G., Haken, H., Lugiato, L. (eds.) Synergetics and Dynamical Instabilities. North Holland, Amsterdam (1988)
7. Gaspard, P.: Time-reversed dynamical entropy and irreversibility in Markovian random processes. J. Stat. Phys. **117**, 599–615 (2004)
8. Touchette, H.: The large deviation approach to statistical mechanics. Phys. Rep. **478**, 1–69 (2009)
9. Chaitin, G.: Algorithmic Information Theory. Cambridge University Press, Cambridge (1987)
10. Chaitin, G.: MetaMaths – The Quest for Omega. Atlantic Books, London (2007)
11. Nicolis, G., Subba Rao, G., Subba Rao, J., Nicolis, C.: Generation of spatially asymmetric, information rich structures in far from equilibrium systems. In: Christiansen, L., Parmentier, R. (eds.) Structure, Coherence and Chaos in Dynamical Systems. Manchester University Press, Manchester (1989)
12. Nicolis, G., Nicolis, C., Nicolis, J.S.: Chaotic dynamics, Markov partitions, and Zipf's law. J. Stat. Phys. **54**, 915–924 (1989)
13. Nicolis, J.S.: Chaos and Information Processing. World Scientific, Singapore (1991)
14. Zurek, W. (ed.): Complexity, Entropy and the Physics of Information. Addison-Wesley, New York (1989)
15. Grassberger, P.: Toward a quantitative theory of self-generated complexity. Int. J. Theor. Phys. **25**, 907–938 (1986)
16. Lloyd, S., Pagels, H.: Complexity as thermodynamic depth. Ann. Phys. **188**, 186–213 (1988)

Information-Theoretical Complexity Analysis of Selected Elementary Chemical Reactions

M. Molina-Espíritu, R.O. Esquivel, and J.S. Dehesa

1 Introduction

The application of complexity concepts in physical sciences has acquired increasing interest over the last years. Since the definition of complexity is not unique, its quantitative characterization has been an important subject of research and it has received considerable attention [1–9]. For instance, Anteneodo and Plastino [10] have discussed several notions of complexity and noted that there is not yet a consensus on a precise definition. Thus, the term *complexity* has been referred to different meanings established prior to the recent attempts to use it as indicative for structure in natural systems. For example, Kolmogorov [1, 2] complexity or *algorithmic information theory* [11] are understood from the point of view of the information content of a string, which is equivalent to the length of the shortest possible self-contained representation of that string which is essentially a program. Further, *computational complexity theory* has

M. Molina-Espíritu
Departamento de Química, Universidad Autónoma Metropolitana-Iztapalapa,
09340 México D.F., México

J.S. Dehesa (✉)
Departamento de Física Atómica, Molecular y Nuclear, Universidad de Granada, 18071 Granada, Spain

Instituto Carlos I de Física Teórica y Computacional, Universidad de Granada, 18071 Granada, Spain
e-mail: dehesa@ugr.es

R.O. Esquivel
Instituto Carlos I de Física Teórica y Computacional, Universidad de Granada, 18071 Granada, Spain

Departamento de Química, Universidad Autónoma Metropolitana-Iztapalapa,
09340 México D.F., México
e-mail: esquivel@xanum.uam.mx

R.G. Rubio et al. (eds.), *Without Bounds: A Scientific Canvas of Nonlinearity and Complex Dynamics*, Understanding Complex Systems,
DOI 10.1007/978-3-642-34070-3_40,

been focused on classifying computational problems according to their inherent difficulty, measuring the amounts of resources required for the execution of algorithms [12]. In contrast, *statistical complexity theory* [8] refers to the measure of the randomness and unpredictability of a system which adequately captures the correlation of the system's components in its behavior. Roughly speaking, the larger and more intricate the correlations between the systems constituents, the more structured its underlying probability distribution. A comprehensive study of the application of complexity measures on atoms and molecules has been recently published [13].

Fundamental concepts such as *uncertainty* or *randomness* are frequently employed in the definitions of complexity, although some other concepts like *clustering*, *order*, *localization* or *organization* and also as general indicators of pattern, structure, and correlation might be also important for characterizing the complexity of systems or processes. It is not clear how the aforementioned concepts might intervene in the definitions so as to quantitatively assess the complexity of the system. However, recent proposals have formulated this quantity as a product of two factors, taking into account *order/disequilibrium* and *delocalization/uncertainty*. This is the case of the definition of López–Mancini–Calbet (*LMC*) shape complexity [8–10] that, like others, satisfies the boundary conditions by reaching its minimal value in the extreme *ordered* and *disordered* limits.

The LMC measure is constructed as the product of two important information-theoretic quantities (see below): the so-called disequilibrium D (also known as self-similarity [14] or information energy [15]), which quantifies *the departure of the probability density from uniformity* [16–18] (equiprobability) and the Shannon entropy S, which is a general measure of randomness/uncertainty of the probability density [3], and *quantifies the departure of the probability density from localizability*. Both global quantities are closely related to the measure of spread of a probability distribution. On the other hand the Fisher–Shannon product FS has been employed as a measure of atomic correlation [19] and also defined as a statistical complexity measure [20–23]. The product of the power entropy J—explicitly defined in terms of the Shannon entropy—and the Fisher information measure, I, combine both the global character (depending on the distribution as a whole) and the local one (in terms of the gradient of the distribution), to preserve the general complexity properties. As compared to the LMC complexity, aside of the explicit dependence on the Shannon entropy which serves to measure the uncertainty (localizability) of the distribution, the Fisher–Shannon complexity replaces the disequilibrium global factor D by the Fisher local one to *quantify the departure of the probability density from disorder* [4, 5] of a given system through the gradient of the distribution.

On the chemical perspective, the energetics of reactions [24] has been the focus of many quantum chemistry studies over the last decades. Particular interest has been focused on extracting information about the stationary points of the energy surface. Despite the fact that minima, maxima, and saddle points are useful mathematical features of the energy surface to reaction-path following

[25], it has been difficult to attribute too much chemical or physical meaning to these critical points [26]. Whereas the reaction rate and the reaction barrier are chemical concepts, which have been rigorously defined and experimentally studied since the early days of the transition state (TS) theory [27, 28] the structure of the TS remains as a quest of physical organic chemistry. Understanding the TS is a fundamental goal of chemical reactivity theories, which implies the knowledge of the chemical events that take place to better understand the kinetics and the dynamics of a reaction. On the other hand there has been an increasing interest to analyze the electronic structure of atoms and molecules by applying information theory (IT) [29, 30]. For instance, we have recently shown that information-theoretic measures are capable of providing simple pictorial chemical descriptions of atoms and molecules [31–33]. In more recent studies on the complexity of elementary chemical reactions [34, 35], we have employed the single information-theoretic functionals *D, L, I, J* and the composite information-theoretic measures *I-D, D-L* and *I-J* planes and Fisher–Shannon and LMC shape complexities. These measures were found to reveal all the chemically significant aspects of the course of the reaction, i.e., the reactant/product region, the bond cleavage energy region, the bond breaking/forming region and the transition state. Besides, the information-theoretic concepts of uniformity, disorder, localizability were useful to reveal the chemical phenomena of energy accumulation/releasing and to identify the mechanisms for bond forming and spin coupling.

2 Information-Theoretic Measures and Complexities: Basics

In the independent-particle approximation, the total density distribution in a molecule is a sum of the contributions from the electrons in each of the occupied orbitals. This is the case in both r- and p-spaces, position and momentum respectively. In momentum space, the total electron density, $\gamma(\mathbf{p})$, is obtained through the molecular momentals (momentum-space orbitals) $\varphi(\mathbf{p})$, and similarly for the position density, $\rho(\mathbf{r})$, through the molecular position-space orbitals $\phi(\mathbf{r})$. The momentals (atomic units are employed throughout) can be obtained by three-dimensional Fourier transformation of the corresponding orbitals (and conversely)

$$\varphi_i(\mathbf{p}) = (2\pi)^{3/2} \int d\mathbf{r} exp(-i\,\mathbf{p}) \cdot \phi_i(\mathbf{r}) \tag{1}$$

Standard procedures for the Fourier transformation of position space orbitals generated by ab-initio methods have been described [36]. The orbitals employed in ab-initio methods are linear combinations of atomic basis function and since analytic expressions are known for the Fourier transforms of such basis functions [37], the transformation of the total molecular electronic wavefunction from position to momentum space is computationally straightforward [38].

As we mentioned in the introduction, the LMC complexity is defined through the product of two relevant information-theoretic measures. So that, for a given probability density in position space, $\rho(\mathbf{r})$, the *C(LMC)* complexity is given by the authors of [8–17]:

$$C_r(LMC) = D_r e^{S_r} = D_r L_r \tag{2}$$

where D_r is the disequilibrium [14, 15]

$$D_r = \int \rho^2(\mathbf{r}) d\mathbf{r} \tag{3}$$

and S is the Shannon entropy [3]

$$S_r = -\int \rho(\mathbf{r}) ln\rho(\mathbf{r}) d\mathbf{r} \tag{4}$$

from which the exponential entropy $L_r = e^{S_r}$ is defined. Similar expressions for the LMC complexity measure in the conjugated momentum space might be defined for a distribution $\gamma(\mathbf{p})$

$$C_p(LMC) = D_p e^{S_p} = D_p L_p \tag{5}$$

It is important to mention that the *LMC* complexity of a system must comply with the following lower bound [39]:

$$C(LMC) \geq 1 \tag{6}$$

The FS complexity in position space, $C_r(FS)$, is defined in terms of the product of the Fisher information [4, 5]

$$I_r = \int \rho(\mathbf{r}) |\overrightarrow{\nabla} ln\rho(\mathbf{r})|^2 d\mathbf{r} \tag{7}$$

and the power entropy [20–23] in position space, J_r

$$J_r = \frac{1}{2\pi e} e^{\frac{2}{n} S_r} \tag{8}$$

which depends on the Shannon entropy defined above. So that, the *FS* complexity in position space is given by

$$C_r(FS) = I_r \cdot J_r \tag{9}$$

and similarly

$$C_p(FS) = I_p \cdot J_p \tag{10}$$

in momentum space.

Let us remark that the factors in the power Shannon entropy J are chosen to preserve the invariance under scaling transformations, as well as the rigorous relationship [40].

$$C(FS) \geq n \tag{11}$$

with n being the space dimensionality, thus providing a universal lower bound to FS complexity. The definition in (8) corresponds to the particular case $n = 3$, the exponent containing a factor $2/n$ for arbitrary dimensionality. See [41] for further rigorous bounds on complexity measures and uncertainty products.

It is worthwhile noting that the aforementioned inequalities remain valid for distributions normalized to unity, which is the choice that it is employed throughout this work for the 3-dimensional molecular case.

Aside of the analysis of the position and momentum information measures, we have considered it useful to study these quantities in the product rp-space, characterized by the probability density $f(\mathbf{r}, \mathbf{p}) = \rho(\mathbf{r})\gamma(\mathbf{p})$, where the complexity measures are defined as

$$C_{rp}(LMC) = D_{rp}L_{rp} = C_r(LMC)C_p(LMC) \tag{12}$$

and

$$C_{rp}(FS) = 2\pi e I_{rp}J_{rp} = 2\pi e C_r(FS)C_p(FS) \tag{13}$$

From the above two equations, it is clear that the features and patterns of both LMC and FS complexity measures in the product space will be determined by those of each conjugated space.

3 Complexity Analysis for Elementary Chemical Reactions

Our complexity study contemplates two elementary chemical reactions. Firstly, the simplest radical abstraction reaction involving a free radical (atomic hydrogen) as a reactive intermediate $H_2 + H^{\cdot} \rightarrow H^{\cdot} + H_2$. This kind of reaction involves at least two steps (S_N1 reaction type): in the first step, a new radical (atomic hydrogen in this case) is created by homolysis, and in the second one the new radical recombines with another radical species. Such homolytic bond cleavage occurs when the bond involved is not polar and there is no electrophile or nucleophile at hand to promote heterolytic patterns. Bond breaking process requires energy which should be dissipated by relaxing the structure at the TS. Evidence has been presented [32] which shows that the two-step mechanism observed for this type of reaction is completely characterized by the Shannon entropies in conjugated spaces through a concerted but yet asynchronous behaviour. Secondly, the hydrogen nucleophilic substitution (S_N2) reaction: $H_a + CH_4 \rightarrow CH_4 + H_b$. This chemical process involves only one step in contrast with the two-step S_N1 reaction [31]. In

the anionic form, the S_N2 mechanism can be depicted as $Y^- + RX \rightarrow RY + X^-$, which is characterized by being kinetically of second order. For identity S_N2 reactions it has been postulated that the observed second order kinetics is the result of passage through the well-known Walden inversion transition state where the nucleophile displaces the nucleofuge (leaving group) from the backside in a single concerted reaction step. Evidence has been presented [32] which shows that the one step mechanism observed for this type of reaction is indeed characterized by its synchronous and concerted behaviour.

The technicalities describing the ab initio calculations for the IRC of both reactions and the information-theoretical analyses for their phenomenological description has been presented elsewhere [31, 32]. Furthermore, in recent studies we have performed an information-theoretic characterization of the chemical process by use of statistical complexity concepts provided by complementary sources of information, such as the disequilibrium D, the exponential Shannon entropy L through the *C(LMC)* and also with the Fisher information I and the power Shannon entropy J through the *C(FS)* measure ((2), (5), (9) and (10)).

In previous studies [31–35], we have employed various single information-theoretic measures (Shannon, Fisher, disequilibrium) as chemical phenomenological descriptors for describing elementary reaction processes. In particular, with the Shannon and Fisher measures we described regions of chemical interest such as the bond cleavage energy region (BCER) and the bond breaking/forming one (B-B/F). From the perspective of the disequilibrium measure (D) a full description of the chemical phenomena might be predicted, i.e., the BCER, the B-B/F and the CT processes.

In the present work we extend the previous study of the two chemical reactions mentioned above by use of several two-component information-theoretic measures; namely, the information planes of disequilibrium-Shannon and Fisher–Shannon types and the complexity measures of LMC and Fisher–Shannon kinds. We find that these composite information-theoretic measures are very useful quantities to grasp the joint features of uniformity-localizability (D-L) and disorder-localizability (I-J).

3.1 Information Planes

In Figs. 1 and 2 we have plotted (in a double-logarithmic scale) the $D_r - L_r$ plane for both, the exchange and the abstraction chemical reactions, respectively. It is worth mentioning that there is a rigorous lower bound to the associated *C(LMC)* complexity, given by (6), which is valid for both spaces. From the figures we may observe that the D-L plane is clearly separated into two regions according to the inequality (valid for position, momentum as well as product spaces), and the region below the line (equality) corresponds with the forbidden region. Parallel lines to this bound represent isocomplexity regions, showing that an increase (decrease) in uncertainty, L, along them is compensated by a proportional decrease (increase) of disequilibrium, and higher deviations from this frontier are

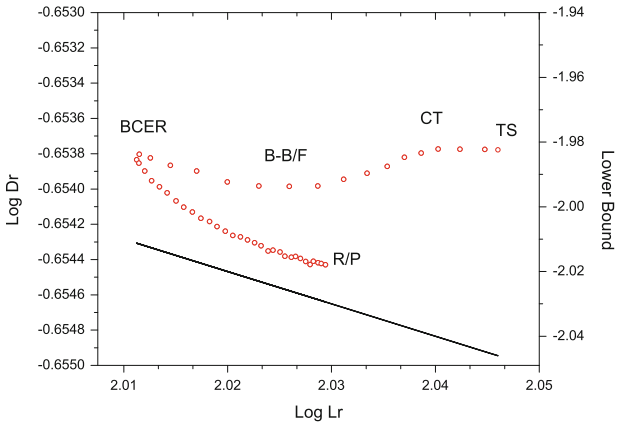

Fig. 1 Disequilibrium-Shannon plane in position space for the IRC of the hydrogenic exchange reaction

associated with greater LMC complexities. For the hydrogenic exchange reaction depicted in Fig. 1 two different tendencies are reflected for $D - L$ complexity in that one can distinguish a zone delimitated by the R/P and BCER regions in which a quasilinear tendency is observed, that is, this region appears to be more isocomplex than the rest of the chemical route as compared to the *C(LMC)* bound also shown in Fig. 1, indicating the rearranging of the ionic complex molecule when the reactives approach each other. At this stage, the information-theoretic description shows that the position space distribution augments its *localizability* by lessening its *uniformity* until the BCER is reached. Beyond this point, from BCER to B-B/F, the *informational* behavior departs from quasi-isocomplexity by diminishing *localizability* at the expense of increasing its *uniformity*. Afterwards, the position density tends to the most *delocalized* and *uniform* distribution at the IRC.

From Fig. 2 for the hydrogenic abstraction reaction we may note that from the R/P to the BCER regions the behavior is isocomplex to the *C(LMC)* bound, whereas for the rest of the IRC it behaves in a more complex manner. The general observations are that the R/P show maximum uncertainty (highly delocalized structures) and as the reaction evolves, both uniformity and uncertainty decrease up to the BCER which holds maximum disequilibrium. Then, uncertainty follows its decreasing path whereas the uniformity increases up to the B-B/F region, which shows minimum uncertainty (highly localized structures) up to the TS by lessening disequilibrium at the expense of increasing uncertainty, so as to reach a structure with maximum uniformity. The chemical analysis goes by noting that as the reaction develops (forward direction) the position space structures get distorted by loosing uniformity and gaining localizability up to the BCER in preparation for the bond cleavage. Then, from BCER up to the B-B/F region we also may observe two stages of the mechanism: first, the structures acquire both higher localizability and higher uniformity for the bond rupture at the B-B/F. In the second stage, from B-B/F

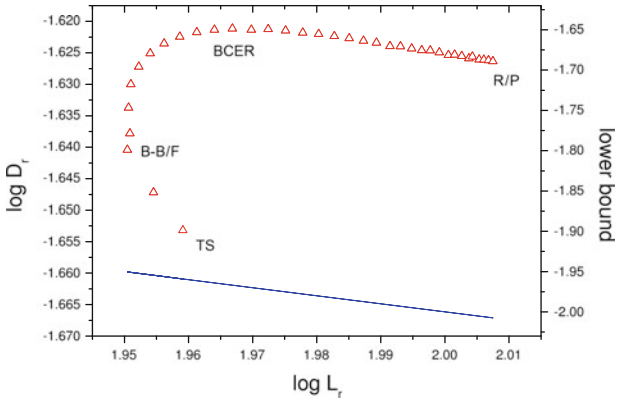

Fig. 2 Disequilibrium-Shannon plane in position space for the IRC of the hydrogenic abstraction reaction

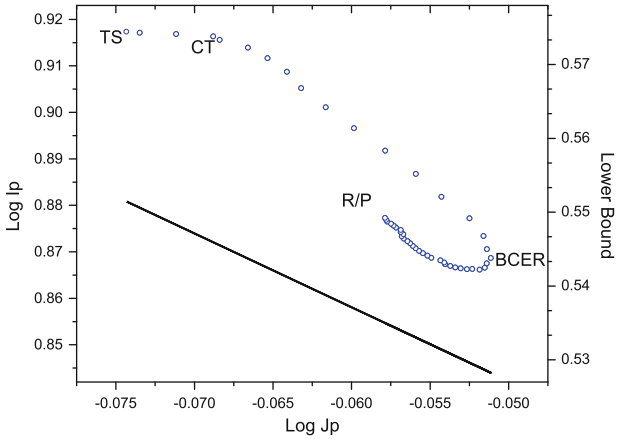

Fig. 3 Fisher–Shannon plane in momentum space for the IRC of the hydrogenic exchange reaction

to the TS, the spin coupling is achieved by gaining uniformity at the expense of augmenting uncertainty.

In Figs. 3 and 4 we have plotted (in a double-logarithmic scale) the $I_p - J_p$ plane for the exchange and the abstraction chemical reactions, respectively. Note from (11) that there is a rigorous lower bound to the associated *C(FS)* complexity, which is valid for both spaces. The analysis for the $I_r - J_r$ plane (not shown, see [35]), reveals similar features as compared to the plane above discussed in that two tendencies are clearly shown. From the R/P to the BCER, a quasi-linear behavior is observed, i.e. increase of *localizability* and *disorder*, whereas in the second stage the complexity pattern is much more intricate and is characterized by a simultaneous augment of *delocalizability* and *order* as the reaction proceeds

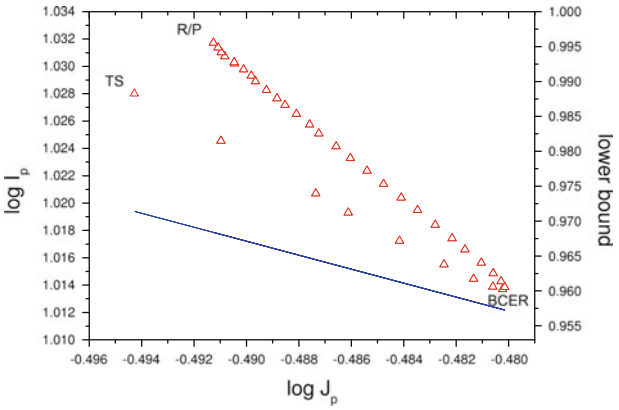

Fig. 4 Fisher–Shannon plane in momentum space for the IRC of the hydrogenic abstraction reaction

in the forward direction of the reaction. On the other hand, for the complementary space, we may note some general features from the $I_p - J_p$ plane of the exchange reaction (and the $D_p - L_p$, see [34]) from Fig. 3; namely, two energetic stages are shown: from the R/P to BCER the ionic complex is gaining energy to surmount the barrier at the TS; i.e., at the beginning of the reaction the electronic momentum distributions get delocalized by gaining *uniformity* and diminishing *order* [35], or augmenting uncertainty ($I_p - J_p$). In the second stage, the necessary energy to reach B-B/F and CT is released from the BCER to the TS by gaining momentum density *localization*, augmenting *order* or diminishing *uniformity* (see [35]). On the other hand, in Fig. 4 we have depicted the corresponding measures for the $I_p - J_p$ plane of the hydrogenic abstraction reaction wherein some general aspects are to be noted: (i) a remarkable isocomplex behavior (linearity) which is divided in two regions, from R/P to BCER and from BCER to the TS, and (ii) the B-B/F region is missing for this plane. Besides, we may note from this figure that the R/P are characterized by maximum structural order in momentum space which diminishes up to the BCER that holds maximum disorder and maximum uncertainty. Then the behavior reverts and the uncertainty as well as the disorder of the process from BCER up to the TS lessen. This last point possesses the minimum global uncertainty. From a chemical point of view, the process behaves in such a way that from R/P to BCER the energy becomes accumulated by gradually delocalizing the momentum space densities. The opposite is observed from BCER to the TS regions where the energy is being released in order to achieve the bond cleavage and the spin coupling processes as we have discussed above. It is worth mentioning that the $I_r - J_r$ plane for this reaction (not shown, see [34]) indicates an "allowed" (upper) and a "forbidden" (lower) part as we mentioned above in connection with (11), and that the R/P are characterized by maximum values for order and uncertainty. As the reaction proceeds, disorder increases at the expense of lowering uncertainty from the R/P to the B-B/F regions.

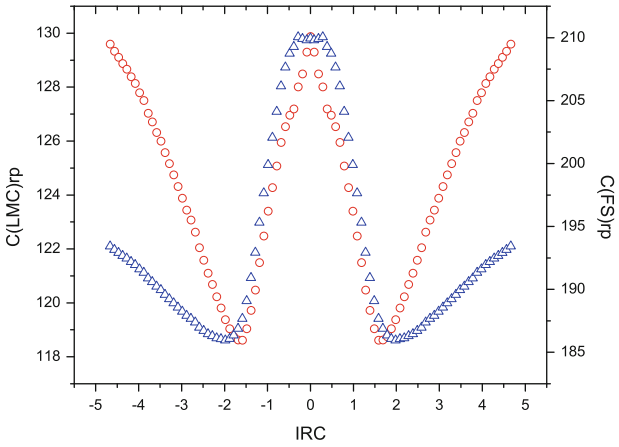

Fig. 5 *C(LMC)* (*blue open triangles*) and *C(FS)* (*red open circles*) complexity measures in the product space ($r - p$) at the IRC for the hydrogenic S_N2 exchange reaction

The latter holding highly localized densities, then disorder keeps its decreasing path at the expense of augmenting its uncertainty from the B-B/F to the TS [34].

3.2 Complexity Measures

In the search of joint patterns of *uniformity-localizability* through *C(LMC)* and *disorder-localizability* through the *C(FS)*, we have found of interest to collect all the information-theoretical features analyzed in this work through these complexities measures in the product space. So that, we can summarize the observations in that, as complementary sources of chemical information, these complexity measures reveal all the relevant chemical features at the transient region from the BCER to the TS [34, 35]. For instance, for the S_N2 exchange reaction, we have depicted in Fig. 5 the complexity measures, LMC and FS, in the product space versus the IRC. Hence, we may observe that all the concurrent processes are present, i.e., BCER, B-B/F, CT and the TS.

Moreover, by employing both, the *C(LMC)* and *C(FS)* in the joint space, we can assess the differences between the information-theoretical features of the elementary chemical reactions studied in the present work to that of their total energies at their IRC. For instance, for the hydrogenic abstraction reaction, we have depicted in Fig. 6 the *C(LMC)* and *C(FS)* complexity values in the product space as a function of the energy.

As it may be observed from the figure, the energy profile holds features of uniformity-localizability and disorder-localizability in the joint space; therefore, loosing most of the chemical features of interest; namely, the BCER and the

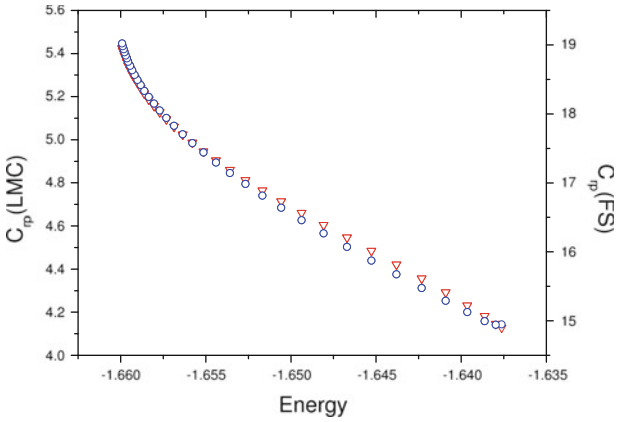

Fig. 6 *C(LMC)* (*red triangles*) and *C(FS)* (*blue circles*) in the product space ($r - p$) as a function of the total energy for the hydrogenic abstraction reaction

B-B/F. It has been shown elsewhere [34] that these features are revealed only when the particular information-theoretical aspects of uniformity, localizability and disorder are considered. In contrast, it has been observed that the behavior for the S_N2 exchange reaction [35] is totally distinct in that there are more concurrent processes in this reaction than in the abstraction reaction (S_N1) [34] and hence, the relation between the complexity measure in product space and the total energy is not as simple as in the S_N1 [34] where the *Crp(LMC)* and *Crp(FS)* complexity values as a function of the energy display a monotonic decreasing behavior for both of them.

4 Conclusions

In this work, we have investigated the complexity of the hydrogenic S_N2 exchange and the S_N1 abstraction reactions by means of various single information-theoretic functionals D, L, I, J and composite information-theoretic measures ($I-D$, $D-L$ and $I-J$ information planes) and the *Fisher–Shannon* and *LMC* shape complexity measures.

The analysis of the information-theoretic functionals of the one-particle density was performed in position (r) and momentum (p) spaces. These measures were found to reveal all the chemically significant aspects of the course of the reaction, i.e., the reactant/product region, the bond cleavage energy region, the bond breaking/forming region and the transition state. Besides, the information-theoretic concepts of *uniformity*, *disorder*, *localizability* were useful to reveal the chemical phenomena of energy accumulation/releasing.

Throughout this study we have described the phenomenological behaviour of selected elementary chemical reactions through complexity concepts. The analyses showed that information measures of Disequilibrium, Fisher and Shannon reveal all the chemical concurrent processes that undergo both reactions through concepts such as *uniformity, order* and *delocalization*. Hence, we can assign the R/P regions to chemical densities characterized by high uniform and ordered distributions, the BCER to non-uniform and low ordered local densities, the B-B/F to locally uniform distributions, the CT to globally non-uniform distributions and the TS by a locally uniform and a globally ordered distributions.

Acknowledgement We wish to thank José María Pérez-Jordá and Miroslav Kohout for kindly providing with their numerical codes. We acknowledge financial support through Mexican grants from CONACyT, PIFI, PROMEP-SEP and Spanish grants MICINN projects FIS2011-24540, FQM-4643 and P06-FQM-2445 of Junta de Andalucía. J.S.D. belongs to the Andalusian research group FQM-0207 and R.O.E. to FQM-020. R.O.E. wishes to acknowledge financial support from the Ministerio de Educación of Spain through grant SAB2009-0120 and to Prof. Marcelo Galván for his valuable support. Allocation of supercomputing time from Laboratorio de Supercómputo y Visualización at UAM, Sección de Supercomputación at CSIRC Universidad de Granada, and Departamento de Supercómputo at DGSCA-UNAM is gratefully acknowledged.

References

1. Kolmogorov, A.N.: Probl. Inf. Transm. **1**, 3 (1965)
2. Chaitin, G.: J. Altern. Complement. Med. **13**, 547 (1966)
3. Shannon, C.E., Weaver, W.: The Mathematical Theory of Communication. University of Illinois Press, Urbana (1949)
4. Fisher, R.A.: Proc. Camb. Philol. Soc. **22**, 700 (1925)
5. Frieden, B.R.: Science from Fisher Information. Cambridge University Press, Cambridge (2004)
6. Bennet, C.H.: In: Herhen, R. (ed.) The Universal Turing Machine a Half Century, Logical Depth and Physical Complexity, pp. 227–257. Oxford University Press, Oxford (1988)
7. Lloyd, S., Pagels, H.: Ann. Phys. N.Y. **188**, 186 (1988)
8. Feldman, D.P., Crutchfield, J.P.: Phys. Lett. A **238**(4–5), 244–252 (1988)
9. Lamberti, P.W., Martin, M.T., Plastino, A., Rosso, O.A.: Phys. A **334**, 119 (2004)
10. Anteonodo, C., Plastino, A.: Phys. Lett. A **223**, 348 (1996)
11. Solomonoff, R.J.: In: Emmert-Streib, F., Dehmer, M. (eds.) Algorithmic Probability: Theory and Applications, Information Theory and Statistical Learning. Springer, New York (2009). ISBN 978-0-387-84815-0
12. Arora, S., Boaz, B.: Computational Complexity: A Modern Approach. Cambridge University Press, Cambridge (2009). ISBN 978-0-521-42426-4, http://www.cs.princeton.edu/theory/complexity/
13. Angulo, J.C., Antolin, J., Esquivel, R.O.: Atomic and molecular complexities: their physical and chemical interpretations. In: Sen, K.D. (ed.) Monograph Statistical Complexity: Applications in Electronic Structure. Springer, Dordrecht (2010). ISBN: 978-90-481-3889-0
14. Carbó-Dorca, R., Arnau, J., Leyda, L.: Int. J. Quant. Chem. **17**, 1185 (1980)
15. Onicescu, O.: C. R. Acad. Sci. A **263**, 25 (1966)
16. Catalán, R.G., Garay, J., López-Ruiz, R.: Phys. Rev. E **66**, 011102 (2002)
17. Martin, M.T., Plastino, A., Rosso, O.A.: Phys. Lett. A **311**, 126 (2003)
18. López-Ruiz, R., Mancini, H.L., Calbet, X.: Phys. Lett. A **209**, 321 (1995)

19. Romera, E., Dehesa, J.S.: J. Chem. Phys. **120**, 8906 (2004)
20. Angulo, J.C., Antolin, J., Sen, K.D.: Phys. Lett. A **372**, 670 (2008)
21. Sen, K.D., Antolín, J., Angulo, J.C.: Phys. Rev. A **76**, 032502 (2007)
22. Angulo, J.C., Antolín, J.: J. Chem. Phys. **128**, 164109 (2008)
23. Antolín, J., Angulo, J.C.: Int. J. Quant. Chem. **109**, 586 (2009)
24. Hoffman, R., Shaik, S., Hiberty, P.C.: Acc. Chem. Res. **36**, 750 (2003)
25. Fukui, K.: Acc. Chem. Res. **14**, 363 (1981)
26. Shaik, S., Ioffe, A., Reddy, A.C., Pross, A.: J. Am. Chem. Soc. **116**, 262 (1994)
27. Eyring, H.: J. Chem. Phys. **3**, 107 (1935)
28. Wigner, E.: Trans. Faraday Soc. **34**, 29 (1938)
29. Esquivel, R.O., Angulo, J.C., Dehesa, J.S., Antolín, J., López-Rosa, S., Flores-Gallegos, N., Molina-Espiritu, M., Iuga, C.: Recent advances toward the nascent science of quantum information chemistry. In: Deloumeaux, P., Gorzalka, J.D. (eds.) Information Theory: New Research, Chap. 8. Nova Science, Inc., Hauppauge, NY (2012). ISBN: 978-1-62100-325-0 [references therein]
30. Esquivel, R.O., Carrera, E.M., Iuga, C., Molina-Espiritu, M., Angulo, J.C., Dehesa, J.S., López-Rosa, S., Antolín, J., Soriano-Correa, C.: Quantum information-theoretical analyses of systems and processes of chemical and nanotechnological interest. In: Quantum Mechanics/Book 3 (2012), InTech Publisher, Croatia. ISBN: 979-953-307-753-5
31. Esquivel, R.O., Flores-Gallegos, N., Iuga, C., Carrera, E., Angulo, J.C., Antolin, J.: Theor. Chem. Acc. **124**, 445 (2009)
32. Esquivel, R.O., Flores-Gallegos, N., Iuga, C., Carrera, E., Angulo, J.C., Antolin, J.: Phys. Lett. A **374**, 948 (2010)
33. López-Rosa, S., Esquivel, R.O., Angulo, J.C., Antolín, J., Dehesa, J.S., Flores-Gallegos, N.: J. Chem. Theor. Comput. **6**, 145 (2010)
34. Esquivel, R.O., Molina-Espiritu, M., Angulo, J.C., Antolin, J., Flores-Gallegos, N., Dehesa, J.S.: Mol. Phys. **109**, 2353–2365 (2011)
35. Molina-Espiritu, M., Esquivel, R.O., Angulo, J.C., Antolin, J., Dehesa, J.S.: J. Math. Chem. **50**:1882–1900 (2012)
36. Rawlings, D.C., Davidson, E.R.: J. Phys. Chem. **89**, 969 (1985)
37. Kaijser, P., Smith, V.H. Jr.: Adv. Quant. Chem. **10**, 37 (1997)
38. Kohout, M.: DGrid, version 4.6, Radebeul (2011). http://www.cpfs.mpg.de/~kohout/dgrid.html
39. López-Rosa, S., Angulo, J.C., Antolín, J.: Phys. A **388**, 2081 (2009)
40. Dembo, A., Cover, T.M., Thomas, J.A.: Information theoretic inequalities. IEEE Trans. Inform. Theory **37**, 1501–1518 (1991)
41. Guerrero, A., Sánchez-Moreno, P., Dehesa, J.S.: Phys. Rev. A **84**, 042105 (2011)

Stochastic Oscillators

V.S. Anishchenko, T.E. Vadivasova, A.V. Feoktistov, and G.I. Strelkova

1 Introduction

Studying the influence of random forces on dynamical systems is an actively developing scientific direction during the recent years. This research area can be addressed both to nonlinear dynamics and to the theory of random processes. Indeed, the response of a dynamical system (DS) to noise essentially depends both on the properties of the deterministic system and statistical characteristics of noise. Since any real system of different nature is subjected to random excitations, the influence of external noise with different characteristics on DS becomes an interesting research topic both from fundamental and applied viewpoints.

Starting with the well-known monograph by Horsthemke and Lefever [1] a significant progress has been made in studying effects of noise influence on DS. A majority of theoretical and experimental works has appeared and is now available in this direction. One can mention monographes [2, 3] and papers [4–12] where the authors explore bifurcations of noisy systems (stochastic bifurcations) and noise-induced transitions (new types of behavior that can initiate in the presence of noise only). A number of fundamental effects induced by noise in nonlinear systems has been established, such as stochastic resonance (SR) [13, 14], coherent resonance (CR) [15, 16], stochastic synchronization (SS) [17, 18].

Nonlinear dynamical systems that possess stochastic oscillations arising from random excitation (noise) can be referred to a separate class. Without external excitation, a system is in its stable equilibrium state. Such systems are called stochastic oscillators and demonstrate the above mentioned phenomena of SR,

V.S. Anishchenko (✉) · T.E. Vadivasova · A.V. Feoktistov · G.I. Strelkov
Department of Physics, Institute of Nonlinear Dynamics, Saratov State University, 410012 Saratov, Russia
e-mail: wadim@info.sgu.ru

R.G. Rubio et al. (eds.), *Without Bounds: A Scientific Canvas of Nonlinearity and Complex Dynamics*, Understanding Complex Systems,
DOI 10.1007/978-3-642-34070-3_41,

CR and SS. The following question arises: Whether all stochastic oscillators can be separated into groups with certain properties? Let try to answer this question from a general viewpoint.

It is known that deterministic dissipative oscillatory systems can be divided into non-autonomous oscillators with forced oscillations, parametric oscillators and self-sustained oscillatory systems. Forced oscillations emerge in the presence of an external force that specifies independent frequencies of oscillations. The amplitude of forced oscillations is defined by both the external force and system parameters. A system itself plays the role of a passive inertial converter. Parametric oscillations result from an external modulation of one of the oscillator parameters, that leads to the increase of energy and to the growth of the oscillation amplitude (parametric instability). This growth is bounded by the nonlinearity of a system. The amplitude of parametric oscillations is significantly larger than the external signal amplitude and their frequency is defined by the basic frequency of the oscillator, that is in a certain ratio with the external signal frequency. And finally, self-sustained oscillations are generated by an autonomous system (without external signal) that compensates the energy consumption for dissipation by means of a permanent source. Parameters of self-sustained oscillations are defined by system parameters [19].

The same classification can be applied to stochastic oscillations. One can distinguish forced stochastic oscillations that are similar to those that can be observed, for example, in a dissipative linear circuit with additive noise. It is also known that parametric noise in an oscillatory system can lead to the effect of parametric instability [9, 20]. An opposite situation can also occur when parametric noise stabilizes an equilibrium, for example, Kapitsa pendulum [21]. We deal with parametric stochastic oscillations in the case of noise-induced parametric instability. The definition of stochastic self-sustained oscillations is a more difficult question. A stochastic oscillator is a non-autonomous system. Stochastic oscillations can arise in the presence of a random force only. However, unlike forced and parametric stochastic systems, characteristics of stochastic self-sustained oscillations must be determined by system parameters and properties of a noisy signal should not be a dominant factor. Besides, a stochastic oscillator must possess the fundamental property of self-sustained oscillations—the ability of synchronization [22].

In this paper we distinguish and study two types of stochastic oscillators—parametric stochastic oscillators and excitable stochastic systems that possess a set of properties of self-sustained oscillators. We also demonstrate a qualitative difference between these oscillators.

2 Noise-Induced Parametric Instability and Properties of Parametric Stochastic Oscillators

Noise-induced parametric instability is rather well known [9, 20, 23–26]. However, in our opinion, there is no enough literature concerning a consistent comparison of

the parametric instability effect that is observed in the presence of noise sources with different characteristics. The problem on properties of stochastic parametric oscillations in nonlinear oscillators with different nonlinearity types has been unsufficiently studied. The question of whether noise-induced parametric oscillations are truly a special type of parametric oscillations or possibly possess certain properties of a self-sustained oscillatory regime has been discussed in literature [9] but it is not solved completely yet.

We consider two dynamical models of nonlinear dissipative oscillators for different characteristics of noisy parametric excitation. The first model is the Duffing oscillator with a one-well potential:

$$\ddot{x} + \alpha\dot{x} + \omega_0^2[1 + K\xi(t)]x + x^3 = 0. \tag{1}$$

The second one represents the oscillator with nonlinear friction

$$\ddot{x} + \alpha\dot{x} + \dot{x}^3 + \omega_0^2[1 + K\xi(t)]x = 0. \tag{2}$$

The latter is a simplified model of the oscillator studied [9]. Both models are written for the dimensionless variable x and dimensionless time t. In the models the random signal $\xi(t)$ modulates the parameter controlling the basic frequency of a system. ω_0 is the unperturbed basic frequency (in our calculations we set $\omega_0 = 1$), K defines the modulation factor (noise intensity), and parameter α determines linear dissipation. Systems (1) and (2) differ by a nonlinearity type. The nonlinearity leads to non-isochronous oscillations in (1), while oscillations in (2) are isochronous.

For weak noise and strong dissipation both systems (1) and (2) have a stable fixed point in the origin of coordinates (0, 0) on the plane $x,\ y = \dot{x}$, and stochastic oscillations are not observed. When the noise intensity increases, a stochastic bifurcation of the dynamical type [3] may take place and the fixed point becomes unstable. The instability threshold can be defined by considering a linear equation for a small perturbation $u(t)$ of the variable x in the vicinity of zero point:

$$\ddot{u} + \alpha\dot{u} + \omega_0^2[1 + K\xi(t)]u = 0. \tag{3}$$

The threshold value is determined by calculating the maximal Lyapunov exponent for a certain solution $u(t)$. Thus, the threshold of parametric instability is independent of a particular form of an oscillator (the main condition is a fixed point in the origin of coordinates) but can essentially depend on the nature of random signal $\xi(t)$. Properties of noise-induced stochastic parametric oscillations will also depend on a nonlinearity form of the oscillator under consideration.

We use three models of random signal $\xi(t)$: white Gaussian noise, one-dimensional and two-dimensional Ornstein–Uhlenbeck processes. The white noise is set to be $\xi(t) = \sqrt{2D}n(t)$, where $n(t)$ is a normalized Gaussian white noise ($\langle n(t)\rangle \equiv 0$; $\langle n(t)n(t+\tau)\rangle = \delta(\tau)$ is Dirac's function), and D is a constant determining the noise intensity.

An one-dimensional Ornstein–Uhlenbeck process is given by the following equation:

$$\dot{\xi}(t) + \gamma\xi(t) = \sqrt{2D}n(t), \tag{4}$$

where $n(t)$ is a normalized Gaussian white noise, $D = \text{const}$ is the noise intensity. γ is the dissipation coefficient and represents a Gaussian exponentially correlated process with the spectral power density in the Lorentzian form:

$$G_\xi(\omega) = \frac{4\sigma_\xi^2\gamma}{\gamma^2 + \omega^2}, \quad \omega > 0.$$

The maximum of the spectral power density corresponds to zero frequency. The spectrum width at the half-power level is γ (taking into account nonnegative frequencies only), and the variance is given by $\sigma_\xi^2 = D/\gamma$.

A two-dimensional Ornstein–Uhlenbeck process is determined by the following second-order equation:

$$\ddot{\xi}(t) + \gamma\dot{\xi}(t) + \omega_1^2\xi(t) = \sqrt{2D}n(t). \tag{5}$$

Here $n(t)$ is a normalized Gaussian white noise, $D = \text{const}$ is the noise intensity, and γ is the coefficient of dissipation. Besides, there is the basic frequency ω_1 that specifies the spectral maximum. For small dissipation ($\gamma \ll 1$) the process $\xi(t)$ represents a harmonic Gaussian noise with an exponentially decaying envelope of the autocorrelation function and the Lorentzian-like spectrum with the maximum at frequency ω_1:

$$G_\xi(\omega) = \frac{\sigma_\xi^2\gamma}{(\frac{\gamma}{2})^2 + (\omega - \omega_1)^2}, \quad \omega > 0.$$

The spectrum width at the half-power level is γ, and the variance is determined as $\sigma_\xi^2 = D/(\gamma\omega_1^2)$.

White noise excitation. Consider the case $\xi(t) = \sqrt{2D}n(t)$, $K = 1$, where $n(t)$ is a normalized Gaussian white noise. We fix the parameter α and increase the noise intensity D. In this case both oscillators undergo a bifurcation resulted in lossing stability by their equilibrium at the origin and in originating stochastic oscillations. We integrate (1)–(3) in the presence of parametric white noise and calculate the maximal Lyapunov exponent λ_1. Calculation results for λ_1 as a function of D are presented in Fig. 1a, b for models (1) and (2). The dependence of λ_1 of an arbitrary chosen stochastic trajectory is shown by the solid line (the choice of a trajectory is not significantly important due to the property of ergodicity). The dotted line corresponds to the Lyapunov exponent of the equilibrium at the origin, that is estimated by solving the linearized equation (3). The exponent λ_1 for an arbitrary trajectory coincides within a calculation accuracy with the exponent for the equilibrium until the fixed point is stable (because any trajectory gets into this point in some time). At some bifurcational value of D the equilibrium losses its stability and its Lyapunov exponent changes its sign. With this, the exponent of the

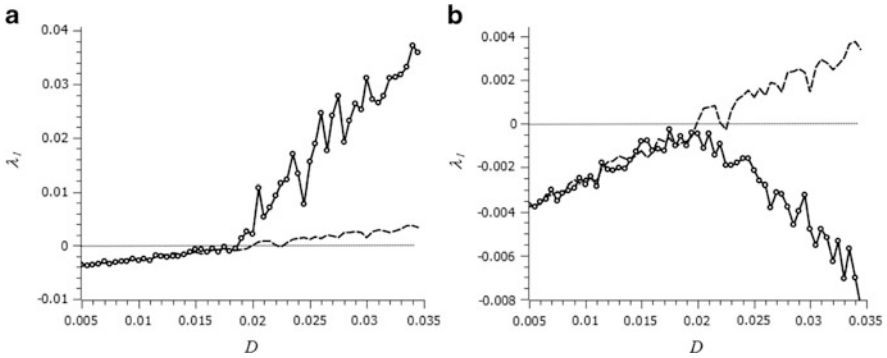

Fig. 1 Maximal Lyapunov exponent λ_1 as a function of the Gaussian white noise intensity D for oscillators (1) (**a**) and (2) (**b**) at $\alpha = 0.01$ and $K = 1$. $\lambda_1(D)$ for the trajectory starting from an arbitrary chosen nonzero initial point is shown by the *solid line*, and $\lambda_1(D)$ for the equilibrium $(0,\ 0)$ is indicated by the *dotted line*

stochastic trajectory for the oscillator (1) becomes positive, while for (2)—negative. Thus, depending on the form of nonlinearity stochastic parametric oscillations can be exponentially unstable (chaotic) as in the model (1) or stable as in (2).

The bifurcational value of D can be estimated theoretically by analyzing truncated equations for the amplitude and phase of an oscillator. In the case of linearized oscillator (3) in the presence of Gaussian white noise one can obtain stochastic differential equations (SDE) for the instantaneous amplitude and fluctuational phase component by applying standard methods of averaging and noise transformation [20, 27]. The SDE have the following forms:

$$\dot{a} = \frac{a}{2}\left(-\alpha + \frac{D}{2} + \sqrt{D}n_1(t)\right), \quad \dot{\varphi} = \frac{\sqrt{D}}{2}n_2(t). \tag{6}$$

The transformated noise sources $n_1(t)$ and $n_2(t)$ can be approximately considered as independent white Gaussian sources ($\langle n_{1,2}\rangle \equiv 0$, $\langle n_1(t)n_2(t+\tau)\rangle = \delta_{1,2}\delta(\tau)$, $\delta(\tau)$ is Dirac's function, $\delta_{1,2}$ is Kronecker symbol). It is seen from the amplitude equation that the solution $a = 0$ is stable for $D < 2\alpha$ and unstable for $D > 2\alpha$. The value $D = 2\alpha$ is bifurcational. At $\alpha = 0.01$ for that the numerical calculations were performed, the bifurcational value is $D = 0.02$ that corresponds well to the numerical results.

Phase portraits and spectra of parametric stochastic oscillations are exemplified in Fig. 2 for oscillators (1) and (2) in the presence of white noise excitation. Phase trajectories fill the phase plane area in the vicinity of the origin of coordinates, although some significant deviations from zero can also be possible because stochastic oscillations are unbounded in the presence of Gaussian noise. A stationary probability density $p(x, y)$ can be defined on a set of stochastic trajectories. The numerical estimations show that in both oscillators (1) and (2) $p(x, y)$ grows

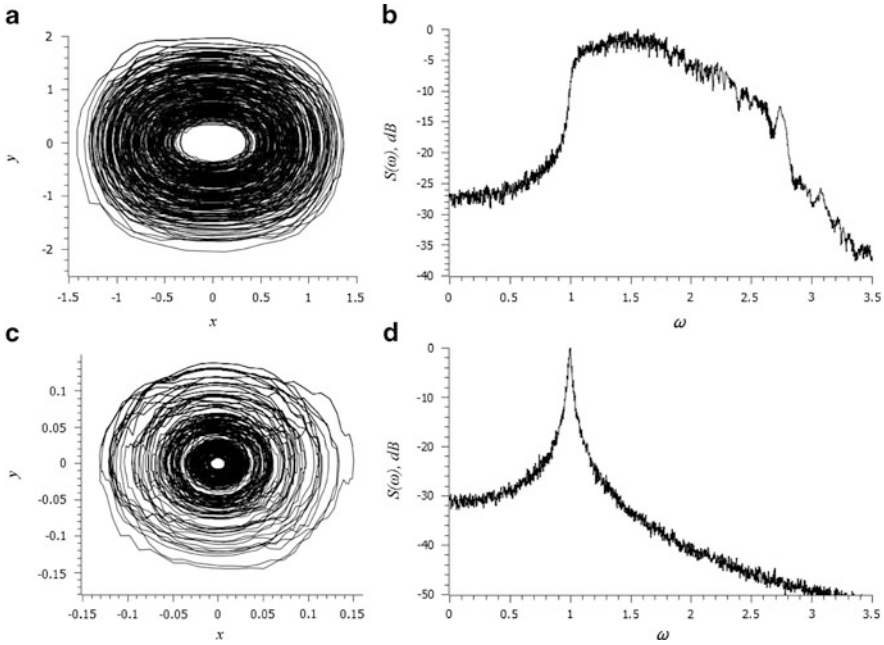

Fig. 2 Characteristics of noise-induced parametric stochastic oscillations. Phase portrait and the normalized power spectrum of $x(t)$ oscillations in system (1) (**a**), (**b**) and in system (2) (**c**), (**d**). $\alpha = 0.01$ and $K = 1$ are set for both oscillators. The normalized spectrum $S(\omega)$ is introduced as follows: $S(\omega) = 10 \lg \left(\frac{G(\omega)}{G_{max}} \right)$, where G_{max} is the maximal value of the spectral power density

infinitely when approaching the origin of coordinates.[1] The set of stochastic trajectories with the given stationary distribution density can be treated as a stochastic attractor, although there are another approaches to define an attractor of noisy DS [3,22]. The attractors presented in Fig. 2a, c cannot provide any qualitative differences in the behavior of oscillators (1) and (2), although the trajectories are unstable in (1) and stable in (2).

The spectra of oscillations of both stochastic oscillators (Fig. 2b, d) have maxima at the frequency ω_0 or in its vicinity. Otherwise they are essentially different. The spectrum of (1) is very wide and has a complex shape, while the spectrum of (2) is rather narrow and very similar to the Lorentzian. Stochastic oscillations in (1) are broadband because they are non-isochronous and strongly exponentially unstable.

[1]The phase portraits in Fig. 2a, c, do not demonstrate that. On the contrary, the neighborhood of the origin is an empty region. However, one should take into account that only sufficiently short parts of trajectories are shown in the figure and thus, one cannot judge on the probability distribution.

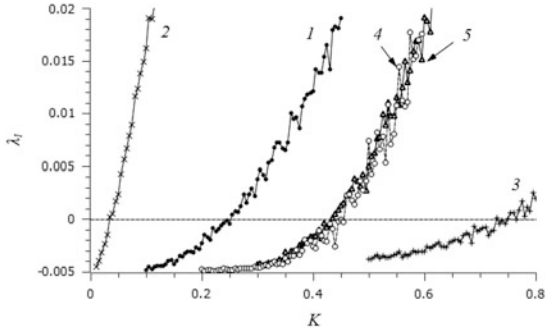

Fig. 3 Maximal Lyapunov exponent of the equilibrium as a function of the modulation amplitude K for different noisy signals. Curves 1–4 correspond to the harmonic noise (5) with different values of the spectral maximum frequency: $\omega_1 = 1$ (*curve* 1); $\omega_1 = 2$ (*curve* 2); $\omega_1 = 3$ (*curve* 3) and $\omega_1 = 0.5$ (*curve* 4). *Curve* 5 is obtained for the low-frequency noise (4). The other parameters are fixed: $\sigma_\xi = 1$, $\Delta\omega_\xi = \gamma = 0.05$ and $\alpha = 0.01$

Colored noise excitation. Influence of statistical characteristics of noise on the parametric instability threshold and properties of stochastic oscillations. As already noted, characteristics of a noisy signal, particularly, its spectral properties, can essentially influence on the threshold of parametric instability. In [20] it was indicated that a low-frequency excitation may increase own losses of an oscillator and thus, stabilizes the system, while a high-frequency excitation destabilizes it. It was also concluded that white noise has no effect at all on the stability of an equilibrium since high-frequency and low-frequency components are mutually balanced. This conclusion contradicts the numerical results presented above. Our numerical investigations show that the white noise excitation can induce stochastic oscillations.

Now we study the case of colored noise excitation by using the harmonic noise model (5) and the low-frequency noise model (4). The bifurcation of an equilibrium is found by means of the linearized equation (3) by calculating a dependence of the maximal Lyapunov exponent of the equilibrium on the modulation amplitude K. Calculation results are shown in Fig. 3. Curves 1–4 are obtained for the harmonic noise excitation (5) with different values of the spectral maximum frequency ω_1. The noise variance σ_ξ and the spectrum width at the half-power level $\Delta\omega_\xi$ are fixed as $\sigma_\xi = 1$ and $\Delta\omega_\xi = \gamma = 0.05$. Curve 5 corresponds to the low-frequency excitation (4) with the same variance $\sigma_\xi = 1$ and the spectrum width $\Delta\omega_\xi = \gamma = 0.05$. As seen from the dependences $\lambda_1(K)$, the instability arises for all the noisy signals but the bifurcational value of K (the parametric instability threshold) is significantly different for the considered cases. The harmonic noise excitation (5) at the second harmonic of the fundamental frequency $\omega_1 = 2\omega_0 = 2$ appears to be the most effective (curve 2). This case is identical to a periodic excitation. The threshold of parametric instability increases (curve 1) when the harmonic noise acts at the fundamental frequency of the oscillator ($\omega_1 = \omega_0 = 1$). Unlike the periodic force, the harmonic noise at the third harmonic $\omega_1 = 3\omega_0 = 3$

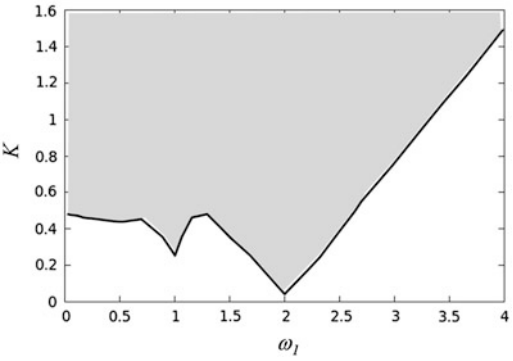

Fig. 4 The parametric instability boundary in the presence of harmonic noise (5) with $\gamma = 0.01$ and $\sigma_\xi^2 = 1$. The *dark region* corresponds to stochastic oscillations, the *white region*—to the stable equilibrium

can also lead to the parametric instability but its threshold grows further (curve 3). The instability can also be induced by the noise excitation at subharmonics of the fundamental frequency. Curve 4 in Fig. 3 corresponds to the harmonic noise at the subharmonic $\omega_1 = \frac{1}{2}\omega_0 = \frac{1}{2}$.

The obtained results testify that the equilibrium undergoes the bifurcation leading to its instability and the onset of stochastic oscillations at low-frequency noisy excitation (4). It is interesting to note that for the given values of the variance and the spectrum width of the noisy signal the dependence λ_1 on K for the low-frequency signal (4) (curve 5) fully coincides with the similar dependence for the harmonic noise (5) at subharmonic $\omega_1 = \frac{1}{2}\omega_0$ (curve 4).

For the case of harmonic noise (5) a parametric instability region is plotted on the parameter plane $(K,\ \omega_1)$ for the fixed value of the spectral linewidth $\gamma = 0.01$ and noise variance $\sigma_\xi^2 = 1$ (correspondingly $D = \gamma\omega_1^2$). Obtained results are presented in Fig. 4. The dark region in Fig. 4 corresponds to stochastic oscillations. Two tongue-like parts (Mathieu tongues) of the instability boundary can be distinguished when the noisy signal is applied at the second harmonic ($\omega_1 = 2\omega_0 = 2$) and at the basic frequency ($\omega_1 \approx 2\omega_0 = 2$). If condition $\omega_1 = 2\omega_0$ is fulfilled, the instability has the least threshold as in the case of harmonic excitation. One can assume that when α decreases, Mathieu tongues can also be observed for the noisy excitation at subharmonics of the basic frequency $\omega_1 \approx \omega_0/m, m = 2, 3, 4, \ldots$. However, they are not appeared for the chosen value of α . When increasing α, the observed tongues become less noticeable and are gradually smoothed out. Our numerical results are in a good correspondence with the results obtained in [23] by analysing the stability of linear equations for the second-order moments. In a low-frequency range ($\omega_1 < 0.1$) the process (5) cannot be considered as harmonic noise because the spectrum width becomes comparable with the characteristic frequency ω_1 and even exceeds it. For small ω_1 the parametric instability boundary marked in Fig. 4 is close to the values obtained for the low-frequency noise (4).

For all the considered cases of colored noise excitation trajectories of stochastic oscillations in oscillator (1) are exponentially unstable but trajectories in (2) are stable. Dependences of the maximal Lyapunov exponent λ_1 for an arbitrary chosen stochastic trajectory on the parameter K are exemplified in Fig. 5 for oscillators (1) and (2).

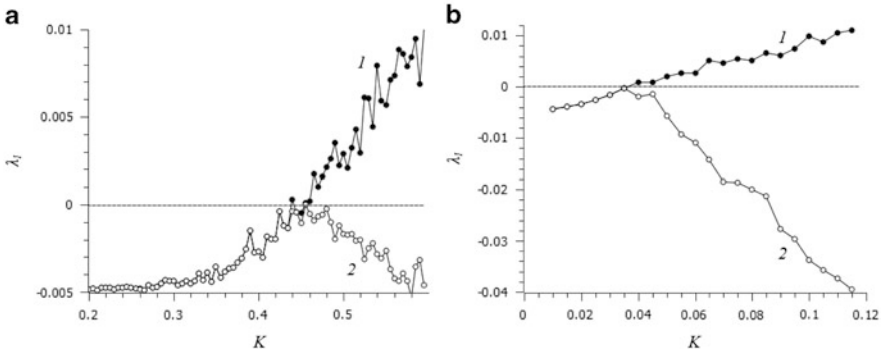

Fig. 5 Maximal Lyapunov exponent λ_1 of a stochastic trajectory versus the parameter K for oscillators (1) (*curves* 1) and (2) (*curves* 2) in the presence of low-frequency noise (4) (**a**) and harmonic noise (5) at the second harmonic of the basic frequency ($\omega_1 = 2\omega_0 = 2$) (**b**). The variance and the spectrum width of random signal $\xi(t)$ were chosen the same in both cases: $\sigma_\xi = 1$; $\Delta\omega_\xi = \gamma = 0.05$. The dissipation parameter is $\alpha = 0.01$

Our calculations show that the spectrum shape of stochastic oscillations emerging in oscillators (1) and (2) after the bifurcation of the equilibrium qualitatively depends on the character of random signal $\xi(t)$. In the presence of harmonic noise (5) (regardless of which harmonic or subharmonic of the basic frequency ω_0 the excitation is applied at) the spectrum of both oscillators demonstrates a peak at the frequency ω_0 (Fig. 6a, b). In the case of harmonic noise the spectrum width of (1) (Fig. 6a) is significantly less than in the case of white noise (Fig. 2a). In the presence of low-frequency noise excitation (4) the spectrum of stochastic oscillations in (1) becomes wide-band and a low-frequency component is noticeably manifested itself (Fig. 6c). The spectrum of stochastic oscillations in (2) is entirely located in a low-frequency range and is basically similar to the spectrum of random force. The peak at the basic frequency of the oscillator (2) cannot be practically distinguished (Fig. 6d). Therefore, although in the presence of low-frequency excitation the equilibrium losses its stability and stochastic oscillations originate in system (2), such oscillations must be rather classified as forced and not parametric ones. However, we suggest that this type of oscillations needs to be studied additionally.

Influence of an external harmonic force on parametric stochastic oscillators. Stochastic oscillations can be attributed to a stochastic self-sustained oscillatory regime if they possess the property of partial (effective in the sense of Stratonovich [27]) synchronization. In this case stochastic oscillators differ from classical deterministic oscillators only in that the latter demonstrate a strong synchronization effect without noise. For a small mismatch between the basic frequency ω_0 and an external frequency ω_2 and when a harmonic force amplitude C is increased, the effect of basic frequency locking must be indicated in the spectrum of stochastic oscillations. With this, ω_0 is shifted towards ω_2. Parametric oscillations do not demonstrate the

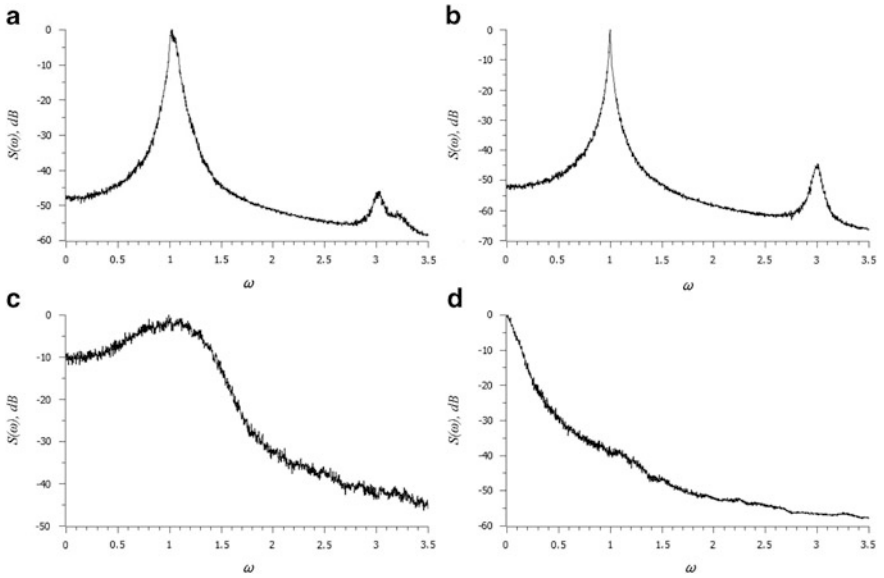

Fig. 6 Normalized power spectra of parametric stochastic oscillations $x(t)$ in oscillators (1) (**a**, **c**) and (2) (**b**, **d**) in the presence of harmonic noise (5) at the second harmonic of the basic frequency ($\omega_1 = 2\omega_0 = 2$) for $K = 0.1$ (**a**, **b**) and in the presence of low-frequency noise (4) for $K = 0.55$ (**c**, **d**). The variance and the spectrum width of random signal $\xi(t)$ were chosen the same in both cases: $\sigma_\xi = 1$; $\Delta\omega_\xi = \gamma = 0.05$. The dissipation parameter is $\alpha = 0.01$

synchronization phenomenon in the presence of harmonic excitation. An analogous suggestion can be also made for parametric stochastic oscillators with noisy excitation.

Consider oscillators (1) and (2) additively driven by an external harmonic signal. To do that the term $C \sin(\omega_2 t)$ is added to the right-hand part of the corresponding equations. C and ω_2 are the amplitude and frequency of the external force, respectively. We choose such a regime of stochastic excitation that corresponds to a well-pronounced spectral peak at the basic frequency ω_0 of an oscillator. Such a peak can be observed for the oscillator (2) in the presence of any noisy excitation, except the low-frequency signal (4). In the case of oscillator (1) one can consider the harmonic noise excitation (5) applied at the second harmonic of the basic frequency of the oscillator (1). Let the external frequency ω_2 be close to the basic frequency ω_0. Our numerical experiments in the chosen regime of external excitation as well as for another excitation signals (for example, white noise in the oscillator (2)) have shown that the basic frequency locking is not observed in the spectrum of parametric stochastic oscillations. The spectral maximum corresponding to the basic frequency of stochastic oscillations is not shifted. The obtained results are illustrated by power spectra for $x(t)$ oscillations in Fig. 7a, b. For the nonisochronous stochastic oscillator (1) the harmonic force can essentially change the spectrum shape and can lead to the appearance of narrower spectral peaks at the basic frequency

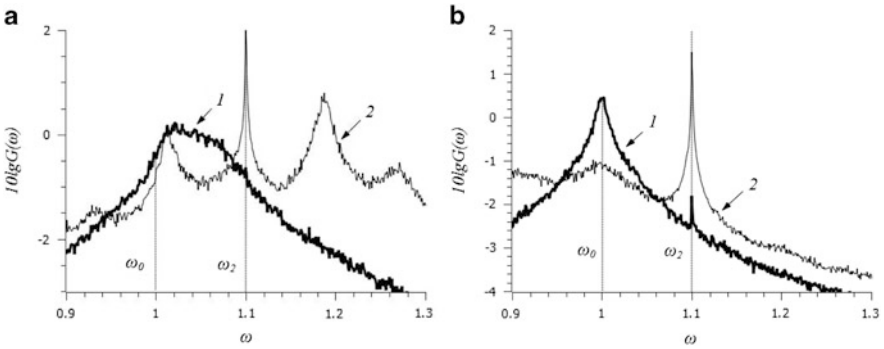

Fig. 7 Power spectra of $x(t)$ oscillations of the stochastic oscillators (1) (**a**) and (2) (**b**) additively driven by the harmonic signal at frequency ω_2. *Curves* 1 are obtained for the external signal amplitude $C = 0.001$, and *curves* 2—for $C = 0.05$. The oscillators are parametrically excited by the harmonic noise (5) at the second harmonic of the basic frequency of the oscillators. For a more convenient comparison the spectral power densities $G(\omega)$ are not normalized on their maximal value

and combination frequencies (Fig. 7a). When the external amplitude C grows, the maximum at the basic frequency of stochastic oscillations in the oscillator (2) typically decreases (is suppressed) (Fig. 7b).

3 Excitable Oscillator as an Example of a Stochastic Self-sustained Oscillator. Properties of Stochastic Self-sustained Oscillations

One of the actual problems of modern nonlinear dynamics is to study properties of so-called excitable systems. Excitable stochastic oscillators represent two-state systems, one of which is a stable equilibrium and another one (excitation state) is a transient process of return to the equilibrium. The peculiarity of excitable systems consists in the fact that the relaxation to an equilibrium takes place along phase trajectories in the form of a nearly closed loop, i.e., they are similar to the motion on a limit cycle. A system is in its equilibrium state without external forces. An external driving (kick) can pass the system to its excitation state, afterwards the system returns itself to its equilibrium. With this, there is a certain typical return time to the equilibrium. In the presence of relatively weak noise, such systems can demonstrate excitation and relaxation processes resulted in the appearance of undamped stochastic oscillations. These oscillations have a high degree of coherence (regularity) for a certain (optimal) noise intensity. This effect is called as coherent resonance (CR) [15, 16]. A considerable amount of publications is devoted to the study of excitable oscillators, ensembles of such oscillators and excitable

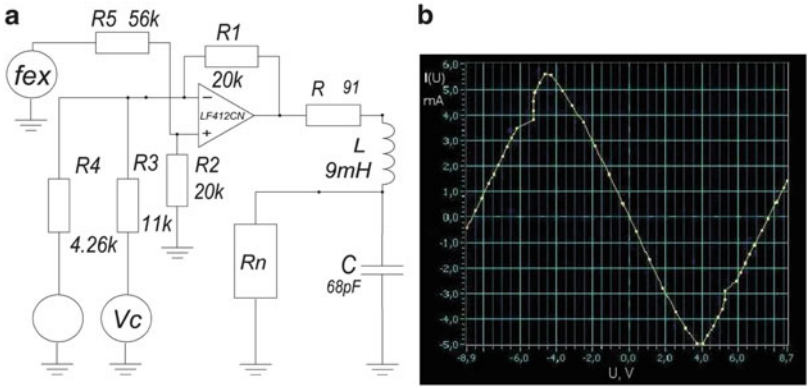

Fig. 8 Scheme of the experimental setup with noise source $\xi(t)$ and external harmonic force $F(t)$ (**a**) and the experimental voltage–current characteristic of the nonlinear element (**b**). The nominal values of scheme elements are: $R = 100\,\text{Ohm}$; $L = 6.8 \cdot 10^{-3}\,\text{H}$; $C = 6.8 \cdot 10^{-11}\,\text{F}$; $V_c = 7.2\,\text{V}$

media [28–32]. Excitable oscillatory regimes are typical for neuron activity [33], therefore, their investigation is very important from the viewpoint of understanding of how the nerve system of living organisms operates. Properties of a sequence of excitation impulses (they are called spikes in biophysics) are mostly controlled by noise presented in a system. Besides, the variation of noise parameters can serve as an ordering factor that can make the system behavior more ordered. The analysis of models of stochastic excitable systems testifies an important role that noise can play in the wildlife.

One of the classical examples of excitable systems is the FitzHugh–Nagumo oscillator (FHN) [34, 35]. It is a simplified model of the Hodgkin–Huxley neuron describing spike generation in axons of a large squid. An important fact has been established: stochastic oscillations in the CR regime can demonstrate the effect of phase-frequency synchronization [30–32]. It is known that synchronization is a characteristic feature of self-sustained oscillatory systems. A principal question arises: Could noise-induced oscillations of excitable systems be considered as a special type of self-sustained oscillations, namely, as stochastic self-sustained oscillations? To answer this question, it is necessary to find out what is the difference between stochastic oscillations in excitable systems and stochastic oscillations arising from transformations of a random external force by nonlinear systems. The last mentioned oscillations can be exemplified by parametric oscillations in the nonlinear oscillators considered above.

For our experiments we choose the original radio-technical model of an excitable system, that was suggested by FitzHugh and Nagumo. In this model a tunnel diode is used as a nonlinear element with an N-shaped voltage–current characteristic. We have slightly changed the original scheme to provide a more stable functioning of the model. Our scheme is presented in Fig. 8. It only differs by the block that models the N-type nonlinearity in a different way (Fig. 8b) [36].

The voltage–current characteristic of the nonlinear element is qualitatively similar to the characteristic of a tunnel diode, can provide a stable functioning of the scheme and, that is also quite important, allows the simplest approximation in the polynomial form $I_N(U) = g_2U^3 - g_1U$ for mathematical simulation of the dynamical system.

Model equations. Using Kirchhoff's laws we can write equations describing the system dynamics in the presence of noise source. The equations read

$$\begin{aligned} \frac{dU}{dt} &= \frac{1}{C}\left(g_1, U - g_2U^3 - I\right), \\ \frac{dI}{dt} &= \frac{1}{L}\left(V_c + U - IR\right) + \frac{A_\xi}{L}\xi(t), \end{aligned} \tag{7}$$

where the nominal values of scheme elements, supply voltage and parameters of the nonlinear characteristic are indicated in Fig. 8 caption. $A_\xi\xi(t)$ is the voltage of a wideband noisy generator with Gaussian distribution and the quantity A_ξ can be regulated. The equations (7) can be reduced to a dimensionless form by renormalizing the variables and time:

$$\begin{aligned} \varepsilon\dot{x} &= x - \alpha x^3 - y, \\ \dot{y} &= \gamma x - y + b + \sqrt{2D}n(\tau). \end{aligned} \tag{8}$$

The following designations are used:

$$U = U_0x, \quad I = U_0g_1y, \quad \tau = \frac{R}{L}t,$$
$$\varepsilon = \frac{CR}{Lg_1}, \quad s = \frac{I_0}{U_0g_1}, \quad \alpha = \frac{g_2}{g_1}U_0^2, \quad \gamma\frac{1}{Rg_1}, \quad b = \frac{V_c}{Rg_1U_0}.$$

The points denote dimensionless time τ derivatives and U_0 is some constant potential (for example, $U_0 = V_c$). The wideband Gaussian noise source in the second equation (8) is replaced by the normalized Gaussian white noise $n(\tau)$ ($< n(\tau)n(\tau + \Delta\tau) > = \delta(\Delta\tau)$, $\delta(\Delta\tau)$ is Dirac's function) with the constant intensity

$$D = \frac{A_\xi^2}{Rg_1U_0}\int_0^\infty < \xi(t)(\xi(t + \theta) > d\theta. \tag{9}$$

Consider the behavior of the experimental system excited by noise and without the external regular force (signal $F(t)$ is absent). As the noise intensity A_ξ increases, stochastic oscillations are initially induced with a sufficiently wide power spectrum (Fig. 9a). Then, a relatively narrow spectral line is formed with the maximum at a certain characteristic frequency (Fig. 9b) that corresponds to the mean frequency of spike movement. This line has a minimal width at an optimal noise intensity. When the noise intensity further grows, its width increases again. The spectral line width at

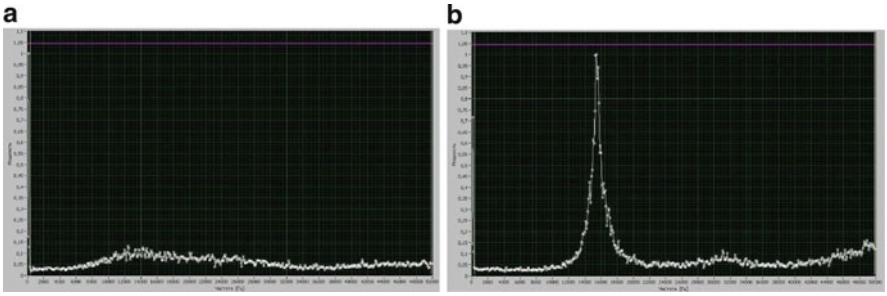

Fig. 9 Power spectra of oscillations for different values of the noise intensity: (**a**) near the threshold of oscillation origin ($A_\xi = 900$ mV), (**b**) in the regime of coherent resonance ($A_\xi = 1,300$ mV)

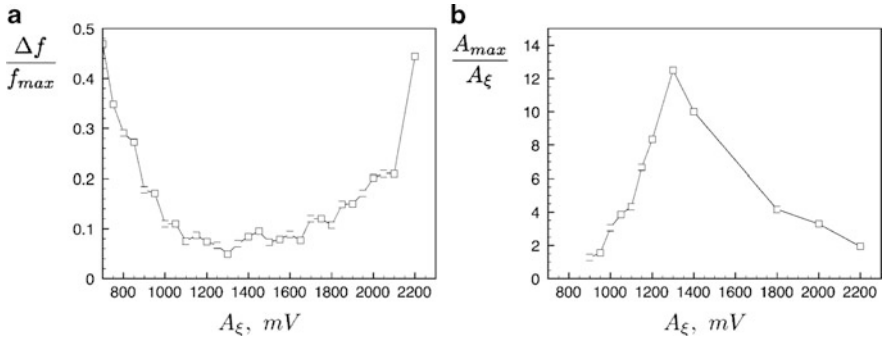

Fig. 10 Dependences of the relative spectrum width (**a**) and the normalized power spectrum density at the maximum (**b**) on the noise level A_ξ

the half-power level and the power spectrum density at the maximum frequency are experimentally measured depending on the noise intensity. The obtained results are presented in Fig. 10a, b. The experimental data clearly indicate the effect of coherent resonance when the spectrum width is minimal and hence the highest degree of oscillation coherence is achieved.

External synchronization of the FHN oscillator by a harmonic signal in the regime of coherence resonance. Now we study experimentally synchronization of stochastic oscillations in the FHN system. For this purpose the external harmonic signal $F(x)$ is added to the scheme. The noise level corresponds to the regime of coherent resonance. To reveal the synchronization effect we fix the external amplitude $A_{ex} = 510$ mV, vary the external frequency f_{ex} and measure the power spectrum of oscillations (Fig. 11). The observed effect of locking is also illustrated in Fig. 12 where the frequency ratio $\Theta = f_{ex}/f_0$ is plotted as a function of the external frequency f_{ex} for the fixed external amplitude. It is seen from the figure that there is a finite region of synchronization $f_{ex} : f_0 = 1$ (at the basic tone).

The experimental results on external and mutual synchronization of stochastic oscillations in the FHN oscillator are described in more detail in the paper [37].

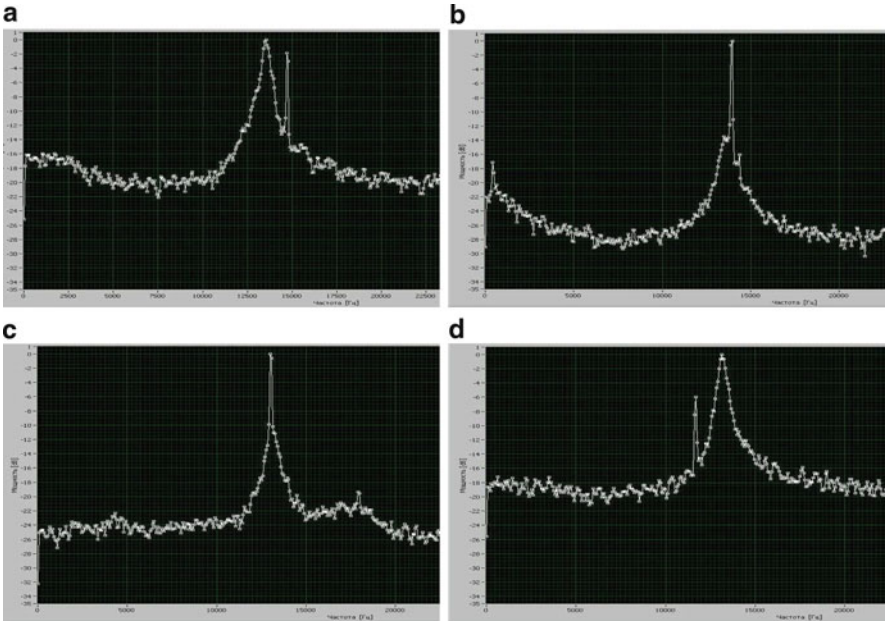

Fig. 11 Effect of frequency locking in the FHN system for different values of the external frequency: (**a**) no frequency locking is observed ($f_{ex} = 14,800$ Hz), (**b**) frequency locking when the *spectral line* of system oscillations is shifted to the right and coincides with f_{ex} ($f_{ex} = 13,950$ Hz); (**c**) frequency locking inside the synchronization region when the system frequency follows f_{ex} ($f_{ex} = 13,050$ Hz); (**d**) exit from the synchronization region ($f_{ex} = 11,700$ Hz)

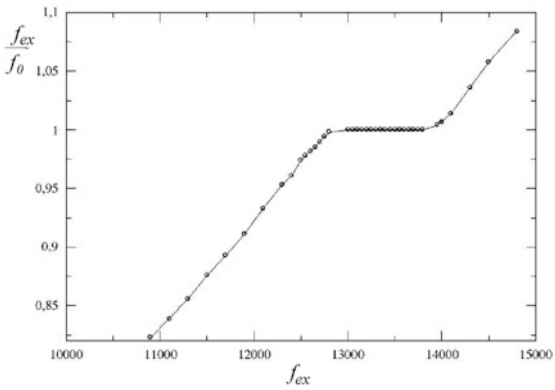

Fig. 12 Experimental dependence of the frequency ratio f_{ex}/f_0 on the external signal frequency f_{ex} for the fixed external amplitude $A_{ex} = 510$ mV

Substantiation of self-sustained oscillatory character of stochastic oscillations in the FHN system. The experimental data presented above can testify that inspite of the fact that oscillations in the FHN system can be induced and sustained only in the presence of external noise, they are characterized by a complete set of the properties peculiar to self-sustained oscillatory processes. Let us discuss this in more detail.

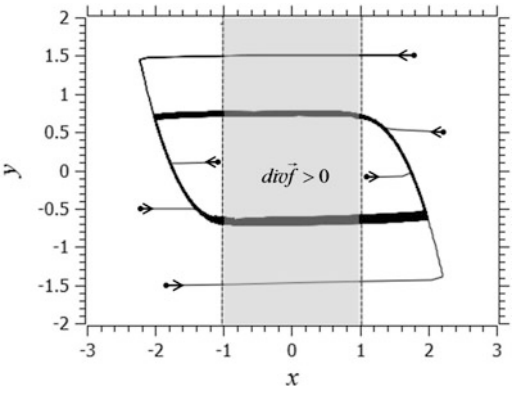

Fig. 13 Phase trajectories of the FHN system obtained numerically with different initial conditions for time $t = 500$. The *grey region* of the phase plane corresponds to the positive divergence of the vector field of system (8) and negative dissipation. System parameters are: $\varepsilon = 0.01$, $\alpha = 1/3$, $\gamma = 1$, $b = 0.5$, $D = 0.0025$

First we consider the question: Which attractor corresponds to oscillations in the regime of coherent resonance. The attractor definition of a non-autonomous system was introduced in [22] where it was shown that in this case an attractor is determined as a limit set in a functional (Hilbert) space for all possible solutions $\overrightarrow{x} = f(\overrightarrow{x_0}, \tau)$. Unfortunately, such a limit set cannot be pictured geometrically. However, if there is an attractor in the functional space, any trajectory of the FHN system tends to the same limit set of points in the phase plane. These points have a joint probability close to 1. Figure 13 presents a few phase trajectories numerically obtained for system (8) with different initial conditions. After some relaxation time, the trajectories fall on the same limit set that resembles a slightly noisy limit cycle. Thus, Fig. 13 illustrates the fact that the limit set of phase trajectories is independent on initial conditions. The FHN system has no other limit sets.

Based on the numerical data, one can conclude that the FHN system possesses an attractor. Its presence does not yet prove that the oscillatory process in the system is self-sustained. To prove that we must discuss how the energy is added to the system. The model (8) can be written in the following oscillatory form:

$$\varepsilon\ddot{x} + (3\alpha x^2 - 1 + \varepsilon)\dot{x} + (1 - \gamma)x - \alpha x^3 - b = \sqrt{2D}n(t). \tag{10}$$

We get the oscillator with the dissipation coefficient

$$\delta = \frac{3\alpha x^2 - 1}{\varepsilon} + 1 \tag{11}$$

that depends on the coordinate x and can have both positive and negative values. The vector field divergence div**f** of the system (10) is equal to the coefficient δ taken with an opposite sign and, consequently, also changes its sign depending on the x value. In the range $|x| < \sqrt{\frac{1-\varepsilon}{3\alpha}}$ the dissipation coefficient is negative and the divergence is positive. Thus, within a certain region of states the energy comes

to the system, and the excitable oscillator behaves as a self-sustained oscillator. From the physical point of view, the conditions for energy supply are fulfilled when the voltage U of oscillations corresponds to values of the negative segment of the nonlinear element G_N characteristic. At this segment the system is characterized by a negative resistance and the source energy increases the energy of oscillations.

The presented arguments testify that in the presence of noise the FHN system sustains an oscillatory regime by carrying out a synchronous nonlinear pumping of energy from a source. The numerical calculations and experimental measurements have confirmed the following important fact: the power of the oscillatory process that is proportional to $x^2(t)$ essentially exceeds the power of noise source.

4 Summary

Our numerical and experimental studies show that among stochastic oscillators two different groups of oscillators can be distinguished: parametric stochastic oscillators and stochastic self-sustained oscillators. In both cases oscillations originate only in the presence of noise. However, their properties are different.

Parametric stochastic oscillators include oscillators with noise-modulated parameters. The energy of such oscillations in the presence of dissipation is entirely replenished by a noise source. In our work we have considered two examples of dissipative parametric stochastic oscillators with different types of nonlinearity. It has been shown that the threshold of parametric instability depends on statistical characteristics of a noisy signal and especially on its spectral structure. The form of a stochastic attractor and stability of trajectories are determined by the nonlinearity of a system.

We have also studied the properties of excitable systems using as an example the FitzHugh–Nagumo oscillator. The carried out investigations convincingly demonstrate that excitable systems can be treated as stochastic oscillators. Such systems have an internal energy source and an alternating divergence of the vector field along phase trajectories on an attractor. Unlike parametric stochastic oscillators, oscillations in excitable systems can be synchronized in the sense of basic frequency locking. The presence of synchronization effect is the main reason that enables to attribute stochastic oscillations of excitable systems to self-sustained oscillatory regimes. We have demonstrated that a non-autonomous regime of the FHN system functioning realizes a self-sustained oscillatory process by converting the source energy to a regime of undamped and nearly periodic oscillations independently on initial conditions. A noise source presented in the system removes it from its stable equilibrium to the phase space region where a nonlinear process of energy pumping is switched on that leads to the origin of self-sustained oscillations.

Acknowledgement This work is supported by the Russian Ministry of Education and Sciences in the framework of the state contract N 14.B37.21.0751.

References

1. Horsthemke, W., Lefever, R.: Noise Induced Transitions. Theory and Applications in Physics, Chemistry and Biology. Springer Series in Synergetics, vol. 15. Springer, Berlin (1983)
2. Garcia-Ojalvo, J., Sancho, J.M.: Noise in Spatially Extended Systems. Springer, New York (1999)
3. Arnold, L.: Random Dynamical Systems. Springer, Berlin (2003)
4. Lefever, R., Turner, J.: Sensitivity of a Hopf bifurcation to multiplicative colored noise. Phys. Rev. Lett. **56**, 1631–1634 (1986)
5. Ebeling, W., Herzel, H., Richert, W., Schimansky-Geier, L.: Influence of noise on Duffing - Van der Pol oscillator. Z. Angew. Math. Mech. **66**, 141–146 (1986)
6. Schimansky-Geier, L., Herzel, H.: Positive Lyapunov exponents in the Kramers oscillator. J. Stat. Phys. **70**, 141–147 (1993)
7. Arnold, L., Sri Namachshivaya, N., Schenk-Yoppe, J.R.: Toward an understanding of stochastic Hopf bifurcation: A base study. Int. J. Bifurcat. Chaos **6**, 1947–1975 (1996)
8. Olarrea, J., de la Rubia, F.J.: Stochastic Hopf bifurcation: The effect of colored noise on the bifurcational interval. Phys. Rev. E **53**, 268–271 (1996)
9. Landa, P.S., Zaikin, A.A.: Noise-induced phase transitions in a pendulum with a randomly vibrating suspension axis. Phys. Rev. E **54**, 3535–3544 (1996)
10. Crauel, H., Flandol, F.: Additive noise destroys a pitchfork bifurcation. J. Dynam. Differ. Equat. **10**, 259–274 (1998)
11. Bashkirtseva, I., Ryashko, L., Schurz, H.: Analysis of noise-induced transitions for Hopf system with additive and multiplicativt random disturbances. Chaos Solitons Fractals **39**, 7–16 (2009)
12. Zakharova, A., Vadivasova, T., Anishchenko, V., Koseska, A., Kurths, J.: Stochastic bifurcations and coherencelike resonance in a self-sustained bistable noisy oscillator. Phys. Rev. E **81**, 011106 (2010)
13. Benzi, R., Sutera, A., Vulpiani, A.: The mechanism of stochastic resonance. J. Phys. A Math. Gen. **14**, L453–L457 (1981)
14. Gammaitoni, L., Marchesoni, F., Menichella-Saetta, E., Santucci, S.: Stochastic resonance in bistable systems. Phys. Rev. Lett. **62**, 349–352 (1989)
15. Pikovsky, A., Kurths, J.: Coherence resonance in a noisy driven excitable system. Phys. Rev. Lett. **78**, 775–778 (1997)
16. Lindner, B., Schimansky-Geier, L.: Analytical approach to the stochastic FizHugh-Nagumo system and coherence resonance. Phys. Rev. E **60**, 7270–7277 (1999)
17. Shulgin, B., Neiman, A., Anishchenko, V.: Mean switching frequency locking in a stochastic bistable system driven by a periodic force. Phys. Rev. Lett. **75**, 4157–4161 (1995)
18. Anishchenko, V., Neiman, A.: Stochastic synchronization. In: Schimansky-Geier, L., Pöschel, T. (eds.) Stochastic Dynamics, p. 155. Springer, Berlin (1997)
19. Andronov, A.A., Vitt, A.A., Khaikin, S.E.: Theory of Oscillations. Nauka, Moscow (1981) [in Russian]
20. Akhmanov, S.A., Dyakov, Yu.E., Chirkin, A.S.: Introduction to Statistical Radiophysics and Optics. Nauka, Moscow (1981) [in Russian]
21. Kapitsa, P.L.: Dynamical stability of a pendulum with an oscillating suspension point. J. Theor. Exp. Phys. **21**, 588–598 (1951) [in Russian]
22. Anichchenko, V., Vadivasova, T., Strelkova, G.: Stochastic self-sustained oscillations of non-autonomous system. Eur. Phys. J. Spec. Top. **187**, 109–125 (2010)
23. Bobryk, R.V., Chrzeszczyk, A.: Colored noise induced parametric resonance. Physica A **316**, 225–232 (2002)
24. Gitterman, M.: The Noisy Oscillator: The First Hundred Years, from Einstein Until Now. World Scientific, Singapore (2005)
25. Aumaître, S., Mallick, K., Petrelis, F.: Noise-induce bifurcations, multiscaling and on-off intermittency. J. Stat. Mech. **7**, 07016 (2007)

26. Sirotkin, O.L.: Izv. VUZ. Radiophys. **52**, 921–932 (2009) [in Russian]
27. Stratonovich, R.L.: Random processes in dynamical systems. In: Regular and Chaotic Dynamics. Moscow, Izhevsk (2009) [in Russian]
28. Longtin, A.: Stochastic resonance in neuron models. J. Stat. Phys. **70**, 309–327 (1993)
29. Baltanas, J.P., Casado, J.M.: Bursting behaviour of the FitzHugh-Nagumo neuron model subject to quasi-monochromatic noise. Physica D **122**, 231–240 (1998)
30. Han, S.K., Yim, T.G., Postnov, D.E., Sosnovtseva, O.V.: Interacting coherence resonance oscillators. Phys. Rev. Lett. **83**, 1771–1774 (1999)
31. Neiman, A., Schimansky-Geier, L., Cornell-Bell, A., Moss, F.: Noise-enhanced phase synchronization in excitable media. Phys. Rev. Lett. **83**, 4896–4899 (1999)
32. Hu, B., Zhou, Ch.: Phase syncronization in coupled nonidentical excitable systems and array-enhanced coherence resonance. Phys. Rev. E **61**, R1001 (2000)
33. Izhikevich, E.M.: Dynamical Systems in Neuroscience: The Geometry of Excitability and Bursting. MIT, Cambridge (2007)
34. FitzHugh, R.: Mathematical models of threshold phenomena in the nerve membrane. Bull. Math. Biophys. **17**, 257–278 (1955)
35. Scott, A.C.: The electrophysics of a nerve fiber. Rev. Mod. Phys. **47**, 487–533 (1975)
36. Makarov, V.A., del Rio, E., Ebeling, W., Velarde, M.G.: Dissipative Toda-Rayleigh lattice and its oscillatory modes. Phys. Rev. E **64**, 036601 (2001)
37. Feoktistov, A.V., Astakhov, S.V., Anishchenko, V.S.: Izv. VUZ Appl. Nonlinear Dynam. **18**, 33 (2010) [in Russian]

PDEs in Moving Time Dependent Domains

F. Cortez and A. Rodríguez-Bernal

1 Introduction

In a standard setting for many partial differential equations of mathematical physics, one usually assumes that the physical process being described occurs in a fixed domain of the physical space. This includes many equations describing the motion of fluids for example, despite the fact that particle fluids and hence fluid subdomains actually move with time. Of course there are some other problems, such as free boundary problems, in which the physical domain of the PDE changes with time. In all these problems the motion of particles or subdomains occurs according to an unknown velocity field with is actually one of the main unknowns of the problem.

In this paper we assume some intermediary situation in which each point of a given initial domain $\Omega_0 \subset \mathbb{R}^n$, moves in time according to some prescribed autonomous vector field. Hence at later times the domain Ω_0 evolves into a diffeomorphic domain $\Omega(t)$ (which is not excluded to coincide with Ω_0 itself!). In particular, topological properties of the domain are preserved along time. However the geometrical evolution of the domain can be very complex; for example one can consider the evolution of the open set Ω_0 in $\mathbb{R}^3$ with the vector field of the Lorenz equations in a chaotic regime.

Our goal is the to describe some sensible class of PDEs to be consider in such a family of moving domains. We choose then to describe balance equations in moving domains, which result from conservation principles and which have natural

F. Cortez
Department of Applied Mathematics, Universidad Complutense de Madrid, Madrid 28040, Spain

A. Rodríguez-Bernal (✉)
Department of Applied Mathematics, Universidad Complutense de Madrid, Madrid 28040, Spain

Instituto de Ciencias Matemáticas, CSIC-UAM-UC3M-UCM, Madrid 28040, Spain
e-mail: arober@mat.ucm.es

R.G. Rubio et al. (eds.), *Without Bounds: A Scientific Canvas of Nonlinearity and Complex Dynamics*, Understanding Complex Systems,
DOI 10.1007/978-3-642-34070-3_42, © Springer-Verlag Berlin Heidelberg 2013

applications to conservation of mass, momentum, energy etc. For such equations one must then give some suitable definition of solution.

After giving a convenient meaning of solution for both balance and general parabolic equations, we prove that such equations can be solved using available results.

Then we investigate, on some particular, although significative examples of equations in moving domains, basic tools in the analysis of parabolic equations such as the (weak) maximum principle and energy estimates. In particular we obtain sufficient conditions on the equations and on the moving domains, that guarantee that the solutions converge to zero as time goes to infinity.

2 Moving Domains

We assume that each point x of an original given domain (smooth open set) $\Omega_0 \subset \mathbb{R}^n$, starting at time $t = 0$ moves following a curve $t \longmapsto Y(t;x)$, in $\mathbb{R}^n$. Moreover we assume this curve is a solution of the autonomous system of ODEs

$$\begin{cases} \dot{Y}(t;x) = \mathbf{V}(Y(t;x)) \\ Y(0;x) = x \end{cases} \tag{1}$$

for some given smooth vector velocity field $\mathbf{V} : \mathbb{R}^n \longrightarrow \mathbb{R}^n$. Even more and for simplicity we assume that all solutions of (1) are defined for all $t \in \mathbb{R}$.

Hence, for $t \in \mathbb{R}$, we have a deformation map

$$\phi(t) : \mathbb{R}^n \longrightarrow \mathbb{R}^n, \quad \phi(t)z = Y(t;z)$$

which is a diffeormorphism that satisfies the group properties $\phi(0) = I$, $\phi(t+s) = \phi(t) \circ \phi(s)$ for all $t, s \in \mathbb{R}$. In particular $\phi(-t)$ is the inverse of $\phi(t)$.

Therefore, the original domain Ω_0 is deformed into the domains

$$\Omega(t) = \phi(t)\Omega_0 \qquad t \in \mathbb{R}$$

and the boundaries satisfy $\partial\Omega(t) = \phi(t)\ \partial\Omega_0$. Also, any smooth subdomain W_0 of Ω_0 is also deformed into

$$W(t) = \phi(t)W_0, \quad t \in \mathbb{R}$$

and its boundary is given by $\partial W(t) = \phi(t)\partial W_0$.

The next results gives geometrical information about the deformations above.

Lemma 1. *With the above notations, for $x_0 \in \partial\Omega_0$ then $\phi(t)x_0 \in \Omega(t)$ and*

$$D\phi(t)(x_0)$$

is an isomorphism in $\mathbb{R}^n$ *that transforms the tangent plane in* $x_0 \in \partial\Omega_0$*, that we denote* $T_{x_0}\partial\Omega_0$*, into the tangent plane to* $\partial\Omega(t)$ *at* $\phi(t)x_0$*,* $T_{\phi(t)x_0}\partial\Omega(t)$*.*

Proof. Just note that if $z(s)$ is a curve in $\partial\Omega_0$ with $z(0) = x_0$, then $z'(0) = v_0$ is a tangent vector at x_0 (and conversely). Hence, $w(s) = \phi(t)(z(s))$ is a curve in $\partial\Omega(t)$, with $w(0) = y_0$ and

$$w'(0) = D\phi(t)(x_0)v_0$$

is a tangent vector at $\partial\Omega(t)$.

We also recall the following

Definition 1. A matrix $\eta(t)$ is a fundamental matrix of the linear system

$$X'(t) = A(t)X(t) \tag{2}$$

iff each column of $\eta(t)$ is a solution of (2) and $\eta(t)$ is nonsingular.

Observe that in particular, $\eta'(t) = A(t)\eta(t)$. Then we have

Lemma 2. *If* $\eta(t)$ *is a fundamental matrix of (2), then*

$$\gamma(t) = \left(\eta^{-1}(t)\right)^* = \left(\eta^*(t)\right)^{-1}$$

is a fundamental matrix of the adjoint system

$$Y'(t) = -A^*(t)Y(t)$$

where $*$ *denotes the adjoint matrix.*

Proof. Differentiate in

$$\eta^{-1}(t) \circ \eta(t) = I$$

and use (2).

The following result is obtained from classical results in ODEs, see [5].

Proposition 1. *i) For* $x \in \mathbb{R}^n$*,* $D\phi(t)x$ *is a fundamental matrix of*

$$\dot{Z}(t) = A(t)Z(t)$$

and $D\phi(0) = I$*, where* $A(t) = D\mathbf{V}(\phi(t)x)$*.*

ii) Denote

$$|K(x,t)| = det(D\phi(t)x), \quad x \in \mathbb{R}^n$$

then we have the ***Abel–Liouville–Jacobi*** *formula*

$$\frac{\partial}{\partial t}|K(x,t)| = tr\big(D\mathbf{V}\big)(\phi(t)x)\,|K(x,t)| = div\big(\mathbf{V}\big)(\phi(t)x)\,|K(x,t)|$$

hence

$$|K(x,t)| = e^{\int_0^t div\mathbf{V}(\phi(s)x)\,ds}.$$

In particular, for $t \in [-T,T]$ *there exist* $C_1(T), C_2(T)$ *such that*

$$0 < C_1(T) \le |K(x,t)| \le C_2(T) \quad \forall x \in \Omega_0 \ \ \forall t \in [0,T]. \tag{3}$$

Remark 1. Observe that if $W_0 \subset \Omega_0$ and $W(t) = \phi(t)W_0$ then the measure of $W(t)$ satisfies

$$|W(t)| = \int_{W(t)} 1\,dy = \int_{W_0} |K(x,t)|\,dx = \int_{W_0} e^{\int_0^t div\mathbf{V}(\phi(s)(x))\,ds}\,dx.$$

In particular, if $div(\mathbf{V}) = 0$ then the measure is preserved, that is,

$$|W(t)| = |W_0| \qquad \forall\ W_0 \subset \Omega_0 \quad \forall t \in \mathbb{R}.$$

Also, if $div(\mathbf{V}) \le -d_0 < 0$ at every point, then

$$|W(t)| \le |W_0|\ \ e^{-d_0 t}$$

and we say the flow of (1) is contractive.

Finally if $div(\mathbf{V}) \ge d_0 > 0$ at every point, then

$$|W(t)| \ge |W_0|\ \ e^{d_0 t}$$

and we say the flow if expansive.

For example for a linear flow, that is, $\mathbf{V}(x) = Mx$ for a given matrix M, we have

$$div(\mathbf{V}) = tr(M) = \sum_{i=1}^{n} \mu_i = d_0$$

is the trace of M, that is the sum of all eigenvalues of M.

Then we have the following result that complements Lemma 1.

Corollary 1. *Assume* $x_0 \in \partial\Omega_0$ *and consider* $y_0 = \phi(t)x_0 \in \partial\Omega(t)$. *Then if* $\mathbf{n}(x_0)$ *is an unitary outward normal vector to* Ω_0 *at* x_0 *then*

$$N(y_0) = ((D\phi(t)x_0)^*)^{-1}\mathbf{n}(x_0)$$

is an outward vector at y_0. *That is,* $((D\phi(t))^*x_0)^{-1}$ *is a linear isomorphism in* $\mathbb{R}^n$ *that transforms the normal space at* $x_0 \in \partial\Omega_0$, *which we denote,* N_{x_0}, *into the normal space to* $\Omega(t)$ *at* $y_0 \in \partial\Omega(t)$, *which we denote* N_{y_0}.

Proof. From Lemma 1 a normal vector at $y_0 = \phi(t)(x_0) \in \partial\Omega(t)$, $\mathbf{n}$, must satisfy

$$< \mathbf{n}, D\phi(t)x_0\boldsymbol{\tau} >= 0 \quad \forall \boldsymbol{\tau} \in T_{x_0}\partial\Omega_0$$

which reads

$$< (D\phi(t)x_0)^*\mathbf{n}, \boldsymbol{\tau} >= 0 \quad \forall \boldsymbol{\tau} \in T_{x_0}\partial\Omega_0.$$

Hence we can take $\mathbf{n}$ such that $((D\phi(t)x_0)^*)\mathbf{n} = \mathbf{n}(x_0)$ which gives the result.

3 Balance Equations

The following notations will be used throughout the paper.

Definition 2. If for some $T > 0$, f is defined in

$$f : \cup_{t\in(-T,T)}\Omega(t) \times \{t\} \longrightarrow \mathbb{R}, \quad (y,t) \longmapsto f(y,t)$$

then we define $\overline{f}$ in Ω_0 as

$$\overline{f} : \Omega_0 \times (-T,T) \longrightarrow \mathbb{R}, \quad \overline{f}(x,t) = f(\phi(t)x,t)$$

Consider $W(t) = \phi(t)W_0 \subset \Omega(t)$, a sufficiently smooth region with boundary $\partial W(t)$. Then the time variation of the amount of T in $W(t)$ is given by

$$\frac{d}{dt}\int_{W(t)} T(y,t)\,dy$$

which is computed below. Note that this is the classical Reynolds Transport theorem, [3,4,6].

Proposition 2. *With the notations above, we have that*

$$\frac{d}{dt}\int_{W(t)} T(y,t)\,dy$$

can be written by either one of the following equivalent expressions

$$\int_{W_0} \frac{\partial\,\overline{T}}{\partial t}(x,t)\,|K(x,t)|\,dx + \int_{W_0} \overline{T}(x,t)\,\overline{div\mathbf{V}}(x,t)\,|K(x,t)|\,dx \tag{4}$$

or

$$\int_{W(t)} \frac{\partial T}{\partial t}(y,t)\,dy + \int_{W(t)} div_y(T(y,t)\,.\,\mathbf{V}(y))\,dy \tag{5}$$

or

$$\int_{W(t)} \frac{\partial T}{\partial t}(y,t)\,dy + \int_{\partial W(t)} T(y,t)\mathbf{V}(y)\,d\mathbf{s}. \tag{6}$$

Now we will derive the Balance Equations for the quantity $T(y,t)$. In fact we have

$$\frac{d}{dt}\int_{W(t)} T(y,t)\,dy = \int_{W(t)} f(y,t)\,dy - \int_{\partial W(t)} \mathbf{J}\,d\mathbf{s}$$

where $f(y,t)$ represents the rate of production/consumption of T per unit volume in $W(t)$ and $\mathbf{J}$ is the vector field of the flow of T across the boundary of $W(t)$. Hence the divergence theorem leads to

$$\frac{d}{dt}\int_{W(t)} T(y,t)\,dy = \int_{W(t)} f(y,t)\,dy - \int_{W(t)} div_y \mathbf{J}\,dy \tag{7}$$

Hence, (7) and the Proposition above leads to

Proposition 3. *Under the assumptions and notations above, the magnitude T satisfies the balance equations in the moving domains, if and only if the following equivalent conditions are satisfied:*

$$\frac{\partial T}{\partial t}(y,t) + div_y(T(y,t)\,.\,\mathbf{V}(y)) = f(y,t) - div_y(\mathbf{J}), \quad y \in \Omega(t),\ t > 0 \tag{8}$$

or

$$\frac{\partial}{\partial t}\overline{T}(x,t) + \overline{T}(x,t)\ \overline{div(\mathbf{V})}(x,t) = \overline{f}(x,t) - \overline{div_y(\mathbf{J})}(x,t) \quad x \in \Omega_0,\ t > 0. \tag{9}$$

Proof. First, equating (5) and (7) we get

$$\int_{W(t)} \left(\frac{\partial T}{\partial t}(y,t) + div_y(T(y,t)\mathbf{V}(y)) \right) dy = \int_{W(t)} (f(y,t) - div_y \mathbf{J})\,dy.$$

Since $W(t) = \phi(t)(W_0)$, $\phi(t)$ is a diffeormorphism and W_0 is arbitrary, we get (8).

Now, using $y = \phi(t)x$ we get in the right hand side of (7)

$$\int_{W_0} \overline{f}(x,t)\,|K(x,t)|\,dx - \int_{W_0} \overline{div_y(\mathbf{J})}(x,t)\,|K(x,t)|\,dx,$$

equating to (4) and using that W_0 is arbitrary, we get (9).

4 Boundary and Initial Conditions

As we consider Dirichlet boundary conditions and using

$$y = \phi(t)x, \qquad \Omega(t) = \phi(t)\Omega_0, \qquad \partial\Omega(t) = \phi(t)(\partial\Omega_0)$$

then

$$T(y,t) = 0 \quad \forall\ y \in \partial\Omega(t) \quad \Leftrightarrow \quad \overline{T}(x,t) = 0 \quad \forall\ x \in \partial\Omega_0$$

As for the initial condition we have, since $\phi(0) = I$,

$$T(y,0) = T_0(y) \ \ \forall\ y \in \Omega_0 \quad \Leftrightarrow \quad \overline{T}(x,0) = T_0(x) \ \ \forall\ x \in \Omega_0.$$

Thus, (8) and (9), with boundary and initial conditions read, respectively,

$$\begin{cases} \frac{\partial T}{\partial t}(y,t) + div_y(T(y,t)\,.\,\mathbf{V}(y)) = f(y,t) - div_y(\mathbf{J}) \quad y \in \Omega(t) \\ \\ T(y,t) = 0 \ \ y \in \partial\Omega(t) \quad \forall t \qquad T(y,0) = T_0(y) \quad y \in \Omega_0 \end{cases} \tag{10}$$

$$\begin{cases} \frac{\partial}{\partial t}\overline{T}(x,t) + \overline{T}(x,t)\ \ \overline{div(\mathbf{V})}(x,t) = \overline{f}(x,t) - \overline{div_y(\mathbf{J})}(x,t) \quad x \in \Omega_0 \\ \\ \overline{T}(x,t) = 0 \ \ x \in \partial\Omega_0 \quad \forall t \qquad \overline{T}(x,0) = T_0(x) \quad x \in \Omega_0. \end{cases} \tag{11}$$

In fact we use (11) to define a solution of (10), i.e.

$$T(y,t) \ \text{ satisfies } \ (10) \Leftrightarrow \overline{T}(x,t) \ \text{ satisfies } \ (11).$$

5 Balance Equations Without Diffusion

5.1 No Flux and No Diffusion: Pure Inertia

With the previous notations, assume $div_y(\mathbf{J}) = 0$ then the following problems are equivalent

$$\begin{cases} \frac{\partial}{\partial t}T(y,t) + div_y(T(y,t)\,.\,\mathbf{V}(y)) = f(y,t) \quad y \in \Omega(t) \\ \\ T(y,t) = 0 \ y \in \partial\Omega(t) \ \ \forall t \qquad T(y,0) = T_0(y) \quad y \in \Omega_0 \end{cases} \tag{12}$$

and

$$\begin{cases} \frac{\partial}{\partial t}\overline{T}(x,t) + \overline{T}(x,t)\ \overline{div(\mathbf{V})}(x,t) = \overline{f}(x,t) \quad x \in \Omega_0 \\ \overline{T}(x,t) = 0 \quad x \in \partial\Omega_0 \quad \forall t \qquad\qquad \overline{T}(x,0) = T_0(x) \quad x \in \Omega_0. \end{cases} \tag{13}$$

Then we have

Proposition 4. *With the notations above, (12) and (13) have a unique explicit solution given by*

$$T(y,t) = T_0(x)\, e^{-\int_0^t div_y \mathbf{V}(\phi(r)x)\, dr} + \int_0^t e^{-\int_s^t div_y \mathbf{V}(\phi(r)x)\, dr} f(y,s)\, ds, \quad y = \phi(t)x \in \Omega(t)$$

and

$$\overline{T}(x,t) = T_0(x)\, e^{-\int_0^t div \mathbf{V}(\phi(r)x)\, dr} + \int_0^t e^{-\int_s^t div \mathbf{V}(\phi(r)x)\, dr}\, \overline{f}(x,s)\, ds, \quad x \in \Omega_0,$$

respectively.

Proof. The solution of (13) is obtained by solving a linear nonhomogeneous ODE

$$Z'(t) + P(t)Z(t) = h(t), \quad Z(0) = Z_0$$

for each $x \in \Omega_0$. From this the solution of (12) is immediate.

Remark 2. Assume in particular that there are no source terms, that is, $f = 0$. Hence in (12) we have

$$T(y,t) = T_0(x)\, e^{-\int_0^t div_y \mathbf{V}(\phi(r)x)\, dr}, \quad y = \phi(t)x$$

Thus, if moreover $div(\mathbf{V}) = 0$ then

$$T(y,t) = T_0(x) \quad y = \phi(t)x,$$

and T remains constant along the paths of the flow.

On the other hand if the flow is expansive then $T(y,t)$ decreases along the paths of the flow, while it increases if the flow is contractive.

5.2 Flux and No Diffusion: Transport Equations

Below we use $\psi(t) = \phi^{-1}(t) = \phi(-t)$.

Proposition 5. *If we assume*

$$\mathbf{J}(y,t) = \mathbf{a}(y,t)T(y,t) \quad y \in \Omega(t)$$

with a C^1 scalar field

$$\mathbf{a} : \mathbb{R}^n \times \mathbb{R} \ \rightarrow \ \mathbb{R}$$

then the balance equations (10) and (11) read

$$\begin{cases} \frac{\partial}{\partial t} T(y,t) + div_y(T(y,t)\,.\,\mathbf{V}(y)) + \nabla_y T(y,t)\,.\,\mathbf{a}(y,t) + div_y(\mathbf{a}(y,t))T(y,t) = f(y,t) \quad y \in \Omega(t) \\ \qquad\qquad T(y,t) = 0 \quad y \in \partial\Omega(t) \ \ \forall t \qquad\qquad T(y,0) = T_0(y) \qquad y \in \Omega_0 \end{cases} \tag{14}$$

and

$$\begin{cases} \frac{\partial \overline{T}}{\partial t}(x,t) + \overline{T}(x,t)C(x,t) + \nabla_x \overline{T}(x,t)\mathbf{b}(x,t) = \overline{f}(x,t) \quad x \in \Omega_0 \\ \qquad \overline{T}(x,t) = 0 \, x \in \partial\Omega_0 \ \ \forall t \qquad \overline{T}(x,0) = T_0(x) \quad x \in \Omega_0 \end{cases} \tag{15}$$

which are equivalent, where

$$C(x,t) = \overline{div_y(\mathbf{V})}(x,t) + \overline{div_y(\mathbf{a})}(x,t), \quad \mathbf{b}(x,t) = \overline{D\psi(t)y \cdot \mathbf{a}(y,t)}.$$

Proof. Note that (14) follows by direct computation from (10) using

$$div_y(\mathbf{a}(y,t)\ T(y,t)) = \nabla_y T(y,t).\mathbf{a}(y) + T(y,t) div_y(\mathbf{a}(y,t)).$$

On the other hand, for (15) we have to write $div_y(a(y,t)T(y,t))$ in terms of x. For this we observe that since $x = \psi(t)y$ we have $T(y,t) = \overline{T}(\psi(t)y,t)$ and then

$$\frac{\partial T}{\partial y_i}(y,t) = \sum_{j=1}^{n} \frac{\partial \overline{T}}{\partial x_j}(x,t) \frac{\partial \psi_j(t)y}{\partial y_i} \tag{16}$$

and $\nabla_y T(y,t) = \nabla_x \overline{T}(x,t) D\psi(t)y$.

Thus, $\nabla_y T(y,t)\ .\ \mathbf{a}(y,t) = \nabla_x \overline{T}(x,t)\ (D\psi(t)y\ .\ \mathbf{a}(y,t))$ and hence

$$\overline{\nabla_y T(y,t)\ .\ \mathbf{a}(y,t)} = \nabla_x \overline{T}(x,t) \overline{(D\psi(t)y \cdot \mathbf{a}(y,t))} = \nabla_x \overline{T}(x,t)\mathbf{b}(x,t).$$

Now we show that under some natural geometrical conditions (15) (and hence (14)) can be solved by using characteristics. Note that we now disregard boundary conditions.

Proposition 6. *Assume that for all time and $y \in \partial\Omega(t)$, we have*

$$< \mathbf{a}(y,t), \mathbf{n_0}(y) > \leq 0$$

where $< \cdot, \cdot >$ is the scalar product and $\mathbf{n_0}(y)$ is the unit outward normal vector at y.

Then (14) and (15) have a unique solution.

Proof. For (15) we use the method of characteristics. Hence, for $x_0 \in \Omega_0$ we define curves defined on some interval I containing 0

$$s \longmapsto X(s) \in \Omega_0, \quad X(0) = x_0, \qquad s \longmapsto t(s) \in \mathbb{R}^+, \quad t(0) = 0,$$

and $s \longmapsto Z(s) = \overline{T}(X(s), t(s))$. Then

$$\frac{d}{ds} Z(s) = \nabla_x \overline{T}(X(s), t(s)) X'(s) + \frac{\partial}{\partial t} \overline{T}(X(s), t(s)) t'(s).$$

So from (15) we choose

$$t'(s) = 1, \quad t(0) = 0,$$

$$X'(s) = \mathbf{b}(X(s), t(s)), \quad X(0) = x_0$$

which gives $t(s) = s$ and

$$X'(t) = \mathbf{b}(X(t), t), \quad X(0) = x_0 \in \Omega_0, \tag{17}$$

which has a solution because $\mathbf{b} \in C^1(\mathbb{R}^n)$.

Hence, from (17) and (15)

$$\begin{cases} \frac{d}{dt} Z(t) + C(X(t), t) Z(t) = \overline{f}(X(t), t) \\ Z(0) = T_0(x_0) \end{cases}$$

whose solution is given by

$$Z(t) = T_0(x_0) e^{-\int_0^t C(X(r), r)\, dr} + \int_0^t e^{-\int_s^t C(X(r), r)\, dr} \overline{f}(X(s), s)\, ds. \tag{18}$$

In the computation above we need the solution of (17) not to leave Ω_0. Thus, if $X(t)$ reaches the boundary of Ω_0 at time t_0 at the point $y_0 = x(t_0) \in \partial\Omega_0$, the tangent vector to the characteristic curve at this point is $X'(t_0) = \mathbf{b}(x_0, t_0)$, and therefore if it points inward, that is, if

$$< \mathbf{b}(x_0, t_0), \mathbf{n}(x_0) > \leq 0 \tag{19}$$

then it will remain in Ω. Note now that from (19)

$$< \mathbf{b}(x_0, t_0), \mathbf{n}(x_0) > = < D\psi(t_0) y_0 . \mathbf{a}(y_0, t_0), \mathbf{n}(x_0) > = < \mathbf{a}(y_0, t_0), (D\psi(t_0) y_0)^* \mathbf{n}(x_0) > =$$

$$= < \mathbf{a}(y_0, t_0), ((D\phi(t_0) x_0)^*)^{-1} \mathbf{n}(x_0) > = < \mathbf{a}(y_0, t_0), N(y_0) > \leq 0$$

where we have used Corollary 1 and the assumption of this Proposition.

With this (18) gives the values of the solution in the moving domain.

6 Balance Equations with Diffusion

Recalling the equivalent equations (10) and (11) we have

Proposition 7. *Assume the flux vector field is given by*

$$\mathbf{J}(y,t) = -k\nabla_y T(y,t) \quad y \in \Omega(t)$$

for some $k > 0$*, then (10) and (11) read*

$$\begin{cases} \frac{\partial}{\partial t}T(y,t) + \nabla_y T(y,t).\mathbf{V}(y) + T(y,t)div(\mathbf{V})(y) - k\Delta T(y,t) = f(y,t) \quad t \in \Omega(t) \\ \\ T(y,t) = 0 \quad y \in \partial\Omega(t) \ \ \forall t \qquad\qquad T(y,0) = T_0(y) \qquad y \in \Omega_0 \end{cases} \tag{20}$$

and

$$\begin{cases} \frac{\partial \overline{T}(x,t)}{\partial t} + \overline{T}(x,t)\overline{div(\mathbf{V})}(x,t) - k\left(\sum_{k,i=1}^{n} a_{k,i}(x,t)\frac{\partial^2 \overline{T}(x,t)}{\partial x_k \partial x_i} + \sum_{i=1}^{n}\frac{\partial \overline{T}(x,t)}{\partial x_i}.s_i(x,t)\right) = \overline{f}(x,t) \\ \\ \overline{T}(x,t) = 0 \; x \in \partial\Omega_0 \ \ \forall t \qquad \overline{T(x,0)} = T_0(x) \quad x \in \Omega_0 \end{cases} \tag{21}$$

where

$$a_{k,i}(x,t) = \sum_{j=1}^{n} \frac{\partial \psi_k(t)y}{\partial y_j} \cdot \frac{\partial \psi_i(t)y}{\partial y_j} = \nabla_y \psi_k . \nabla_y \psi_i \ \ , \ y = \phi(t)x$$

and

$$s_i(x,t) = \sum_{j=1}^{n} \frac{\partial^2 \psi_i(t)y}{\partial y_j^2} = \Delta_y \psi_i(t)y \quad y = \phi(t)x.$$

Proof. Clearly $div_y(\mathbf{J}) = -k\Delta T(y,t)$ for $y \in \Omega(t)$ and we get (20). Now for (21), we have from (16),

$$\nabla_y T(y,t) = \nabla_x \overline{T}(x,t).D\psi(t)y.$$

Hence,

$$div_y(-k\nabla_y T(y,t)) = -k\ div_y(\nabla_x \overline{T}(x,t) D\psi(t)y) =$$

$$-k\ div_y\left(\sum_{i=1}^{n}\frac{\partial\ \overline{T}(x,t)}{\partial x_i}\cdot\frac{\partial \psi_i(t)y}{\partial y_1},\ldots,\sum_{i=1}^{n}\frac{\partial\ \overline{T}(x,t)}{\partial x_i}\cdot\frac{\partial \psi_i(t)y}{\partial y_n}\right).$$

Now observe that

$$\frac{\partial}{\partial y_j}\left(\sum_{i=1}^{n}\frac{\partial\,\overline{T}(x,t)}{\partial x_i}\cdot\frac{\partial\,\psi_i(t)y}{\partial y_j}\right)\sum_{i=1}^{n}\left(\frac{\partial}{\partial y_j}\left(\frac{\partial\,\overline{T}(x,t)}{\partial x_i}\right)\cdot\frac{\partial\,\psi_i(t)y}{\partial y_j}+\frac{\partial\,\overline{T}(x,t)}{\partial x_i}\cdot\frac{\partial^2\,\psi_i(t)y}{\partial y_j^2}\right) \tag{22}$$

and by (16), we get

$$\frac{\partial}{\partial y_j}\left(\frac{\partial\,\overline{T}(x,t)}{\partial x_i}\right)=\sum_{k=1}^{n}\frac{\partial^2\,\overline{T}(x,t)}{\partial x_k\,\partial x_i}\frac{\partial\,\psi_k(t)y}{\partial y_j}$$

and we get in (22)

$$\sum_{i=1}^{n}\left(\left(\sum_{k=1}^{n}\frac{\partial^2\,\overline{T}(x,t)}{\partial x_k\partial x_i}\cdot\frac{\partial\psi_k(t)y}{\partial y_j}\right)\frac{\partial\psi_i(t)y}{\partial y_j}+\frac{\partial\,\overline{T}(x,t)}{\partial x_i}\cdot\frac{\partial^2\psi_i(t)y}{\partial y_j^2}\right).$$

Therefore

$$-div_y(-k\nabla_y T(y,t))=-k\sum_{j=1}^{n}\sum_{i=1}^{n}\left(\sum_{k=1}^{n}\frac{\partial^2\,\overline{T}(x,t)}{\partial x_k\partial x_i}\cdot\frac{\partial\psi_k(t)y}{\partial y_j}\right)\cdot\frac{\partial\psi_i(t)y}{\partial y_j}$$

$$-k\sum_{j=1}^{n}\sum_{i=1}^{n}\frac{\partial\,\overline{T}(x,t)}{\partial x_i}\frac{\partial^2\psi_i(t)y}{\partial y_j^2}$$

which leads to

$$-k\;div_y\left(\sum_{i=1}^{n}\frac{\partial\,\overline{T}(x,t)}{\partial x_i}\cdot\frac{\partial\psi_i(t)y}{\partial y_1},\ldots,\sum_{i=1}^{n}\frac{\partial\,\overline{T}(x,t)}{\partial x_i}\cdot\frac{\partial\psi_i(t)y}{\partial y_n}\right)=$$

$$-k\sum_{k,i=1}^{n}\frac{\partial^2\,\overline{T}(x,t)}{\partial x_k\partial x_i}\cdot\left(\sum_{j=1}^{n}\frac{\partial\psi_k(t)y}{\partial y_j}\cdot\frac{\partial\psi_i(t)y}{\partial y_j}\right)-k\sum_{i=1}^{n}\frac{\partial\overline{T}(x,t)}{\partial x_i}\cdot\left(\sum_{j=1}^{n}\frac{\partial^2\psi_i(t)y}{\partial y_j^2}\right).$$

and we get the result.

Concerning the main part in (21) we have the following

Proposition 8. *With the notations above, the term*

$$\sum_{k,i=1}^{n}a_{k,i}(x,t)\frac{\partial^2\,\overline{T}}{\partial x_k\,\partial x_i}(x,t)$$

can be written in divergence form.

Proof. Just note that

$$\sum_{k,i=1}^{n} a_{k,i}(x,t)\frac{\partial^2 \overline{T}(x,t)}{\partial x_k \partial x_i} = \sum_{i=1}^{n}\frac{\partial}{\partial x_i}\left(\sum_{k=1}^{n}\frac{\partial \overline{T}(x,t)}{\partial x_i}.a_{k,i}(x,t)\right) - \sum_{i=1}^{n}\frac{\partial \overline{T}(x,t)}{\partial x_i}\,.c_i(x,t)$$

with

$$c_i(x,t) = \sum_{k=1}^{n}\frac{a_{k,i}(x,t)}{\partial x_i}$$

Remark 3. Note that now (21) can be written as

$$\begin{cases} \frac{\partial \overline{T}(x,t)}{\partial t} + \overline{T}(x,t)\overline{div(\mathbf{V})}(x,t) - k\left(div(B(x,t)) - \sum_{i=1}^{n}\frac{\partial \overline{T}(x,t)}{\partial x_i}d_i(x,t)\right) = \overline{f}(x,t) \\ \\ \overline{T}(x,t) = 0 \; x \in \partial\Omega_0 \;\; \forall t \qquad \overline{T}(x,0) = T_0(x) \quad x \in \Omega_0 \end{cases}$$

with

$$\mathbf{B} = (B_i)_{i=1,\ldots,n} = A(x,t)\nabla_x \overline{T}(x,t)$$
$$A(x,t) = (a_{k,i}(x,t)), \quad d_i(x,t) = s_i(x,t) - c_i(x,t).$$

7 Parabolic PDEs in Moving Domains

Now we consider general parabolic equations in moving domains. That means that the equations are not necessarily balance equations. Hence, we consider

$$\begin{cases} \frac{\partial}{\partial t}T(y,t) - k\Delta_y T(y,t) + \sum_{i=1}^{n}\frac{\partial T}{\partial y_i}(y,t)\,.\,g_i(y,t) + c(y,t)T(y,t) = f(t,y) \quad y \in \Omega(t) \\ T(y,t) = 0 \;\; y \in \partial\Omega(t) \;\; \forall t \qquad T(y,0) = T_0(y) \quad y \in \Omega_0 \end{cases} \tag{23}$$

with $k > 0$ and given smooth $c(y,t)$ and $\mathbf{g}(y,t) = (g_i(y,t),\ldots,g_n(y,t))$. Note that this equation contains (20) as a particular case.

Then we have the following result whose proof follows from the computation in the sections above.

Proposition 9. *With the notations above (23) is equivalent to*

$$\begin{cases} \frac{\partial \overline{T}}{\partial t}(x,t) - kdiv(B(x,t)) + \nabla_x \overline{T}(x,t).\big(\mathbf{h}(x,t) - \mathbf{d}(x,t)\big) + \overline{c}(x,t)\overline{T}(x,t) = \overline{f}(x,t) \quad x \in \Omega_0 \\ \overline{T}(x,t) = 0 \;\; x \in \partial\Omega_0 \;\; \forall t \qquad \overline{T}(x,0) = T_0(x) \quad x \in \Omega_0 \end{cases} \tag{24}$$

with

$$B(x,t) = A(x,t)\nabla_x \overline{T}(x,t), \quad A(x,t) = (a_{k,i}(x,t)), \quad a_{k,i}(x,t) = \sum_{j=1}^{n} \frac{\partial \psi_k(t)y}{\partial y_j} \cdot \frac{\partial \psi_i(t)y}{\partial y_j},$$

$$d_i(x,t) = s_i(x,t) - c_i(x,t), \quad s_i(x,t) = \Delta_y \psi_i(t)y, \quad c_i(x,t) = \sum_{k=1}^{n} \frac{a_{k,i}(x,t)}{\partial x_i}$$

$$\mathbf{h}(x,t) = (\overline{\mathbf{g}}(x,t) \cdot \nabla_y \psi_1(t)y, \ldots, \overline{\mathbf{g}}(x,t) \cdot \nabla_y \psi_n(t)y), \quad y = \phi(t)x.$$

Now we are in a position to proof that (23) is well posed.

Proposition 10. *Under the assumptions above, if the initial data satisfies*

$$T_0 \in L^2(\Omega_0)$$

then (24) and (23) have a unique solution.

Proof. Observe that in (24)

$$A(x,t) = D\psi(t)y.(D\psi(t)y)^t \qquad y = \phi(t)x.$$

Then we show below that this is a positive definite matrix. In fact for $\xi \in \mathbb{R}^n$, $\xi \neq 0$, we have

$$< A(x,t)\xi, \xi > = < (D\psi(t)y)^t \xi, (D\psi(t)y)^t \xi > = \left\| (D\psi(t)y)^t \xi \right\|^2 > 0.$$

since $(D\psi(t)y)^t$ is non singular. Also, from (3), the eigenvalues of $D\phi(t)$ are bounded and bounded away from 0 for all $t \in [0,T]$ and so are the eigenvalues of $D\psi(t)$. Therefore there exist $\alpha = \alpha(T) > 0$ such that $\|(D\psi(t)y)^t \xi\|^2 \geq \alpha \|\xi\|^2$.

Using this, the smoothness of the coefficients and the results in [1, 2], we get that (24) has a unique smooth solution and so does (23).

8 Maximum Principle

In this section we show that the parabolic equations in moving domains possess the maximum principle. We will show this on the particular example of the heat equation

$$\begin{cases} \frac{\partial T}{\partial t}(y,t) - \Delta T(y,t) + a(y,t)\, T(y,t) = 0 \quad y \in \Omega(t) \\ \\ T(y,t) = 0 \;\; y \in \partial\Omega(t) \;\; \forall t \qquad T(y,0) = T_0(y) \quad y \in \Omega_0 \end{cases} \tag{25}$$

with a sufficiently smooth coefficient $a(y,t)$. Then we have

Proposition 11. *With the assumption above, if*

$$T_0 \in L^2(\Omega_0), \quad T_0(x) \geq 0 \quad x \in \Omega_0$$

and

$$\alpha(t) \leq a(y,t) \quad \forall y \in \Omega(t) \quad \forall t$$

for some smooth $\alpha(t)$*. Then*

$$T(y,t) \geq 0, \quad y \in \Omega(t), \quad t \geq 0.$$

Proof. We multiply (25) by the negative part of T, $T^-(y,t)$, and integrate in $\Omega(t)$, to get

$$\int_{\Omega(t)} \frac{\partial T}{\partial t}(y,t)\,.\,T^-(y,t)\,dy - \int_{\Omega(t)} \Delta T(y,t)\,.\,T^-(y,t)\,dy + \int_{\Omega(t)} a(y,t).\,T(y,t).\,T^-(y,t)\,dy = 0.$$

Using (6) for $(T^-)^2$ and the fact that $T^-(y,t) = 0$ in $\partial\Omega(t)$, because $T(y,t) = 0$ in $\partial\Omega(t)$, we have

$$\frac{1}{2}\frac{d}{dt}\int_{\Omega(t)} (T^-)^2(y,t)\,dy + \int_{\Omega(t)} |\nabla T^-(y,t)|^2\,dy + \int_{\Omega(t)} a(y,t)(T^-)^2(y,t)\,dy = 0.$$

Hence

$$\frac{1}{2}\frac{d}{dt}\,\|T^-(.,t)\|^2_{L^2(\Omega(t))} + \alpha(t)\,\|T^-(.,t)\|^2_{L^2(\Omega(t))} \leq 0$$

and taking $\bar{F}(t) = \|T^-(.,t)\|^2_{L^2(\Omega(t))}$, we have

$$\frac{d}{dt}\bar{F}(t) + 2\alpha(t)\bar{F}(t) \leq 0$$

and Gronwall's lemma leads to $\bar{F}(t) \leq \left\|T_0^-\right\|_{L^2(\Omega_0)} e^{-2\int_0^t \alpha(s)\,ds} = 0$, since $T_0^- = 0$ in Ω_0. Therefore $T^-(y,t) = 0$ for $y \in \Omega(t)$ and $t \geq 0$ as claimed.

9 Energy Estimates

In this section we derive suitable energy estimates for the heat equation in a moving domain

$$\begin{cases} \frac{\partial T}{\partial t}(y,t) - \Delta T(y,t) + a(y,t)\,T(y,t) = 0 \quad y \in \Omega(t) \\ \\ T(y,t) = 0 \;\; y \in \partial\Omega(t) \quad \forall t \qquad T(y,0) = T_0(y) \quad y \in \Omega_0 \end{cases} \tag{26}$$

with a smooth enough $a(y,t)$. First, we have for nonnegative solutions

Proposition 12. *Assume*

$$T_0 \in L^2(\Omega_0) \quad T_0(x) \geq 0, \quad x \in \Omega_0$$

and

$$\alpha(t) \leq a(y,t) \quad \forall y \in \Omega(t) \quad \forall t.$$

for some smooth $\alpha(t)$ *such that*

$$\liminf_{t\to\infty} \frac{1}{t} \int_0^t \alpha(s)\, ds > \alpha_0 > 0.$$

Then

$$\int_{\Omega(t)} T(y,t)\, dy \leq e^{-\int_0^t \alpha(t)\, ds} \int_{\Omega_0} T_0(x)\, dx \xrightarrow[t\to\infty]{} 0.$$

Proof. From (6)

$$\frac{d}{dt} \int_{\Omega(t)} T(y,t)\, dy = \int_{\Omega(t)} \frac{\partial T}{\partial t}(y,t)\, dy + \int_{\partial\Omega(t)} T(y,t)\mathbf{V}(y)\, d\mathbf{s}$$

and since T vanishes on the boundary, we have

$$\frac{d}{dt} \int_{\Omega(t)} T(y,t)\, dy = \int_{\Omega(t)} \frac{\partial T}{\partial t}(y,t)\, dy.$$

Using this, we integrate in (26) in $\Omega(t)$, to get

$$\int_{\Omega(t)} \frac{\partial T}{\partial t}(y,t)\, dy - \int_{\Omega(t)} \Delta T(y,t)\, dy + \int_{\Omega(t)} a(y,t)\, T(y,t)\, dy = 0.$$

Now Green's formula leads to

$$\frac{d}{dt} \int_{\Omega(t)} T(y,t)\, dy - \int_{\partial\Omega(t)} \frac{\partial T}{\partial \mathbf{n}}(y,t)\, d\mathbf{s} + \int_{\Omega(t)} a(y,t)\, T(y,t)\, dy = 0.$$

By the maximum principle we know that $T(y,t) \geq 0$ for $y \in \Omega(t)$ and $t \geq 0$, and then for $y \in \partial\Omega(t)$ we have $\frac{\partial T}{\partial \mathbf{n}}(y,t) \leq 0$ and then

$$\frac{d}{dt} \int_{\Omega(t)} T(y,t)\, dy + \int_{\Omega(t)} a(y,t)\, T(y,t)\, dy \leq 0.$$

Hence, denoting $\bar{Y}(t) = \int_{\Omega(t)} T(y,t)\,dy$ we have

$$\frac{d\bar{Y}}{dt}(t) + \alpha(t)\bar{Y}(t) \leq 0$$

and Gronwall's lemma gives

$$\bar{Y}(t) = \int_{\Omega(t)} T(y,t)\,dy \leq e^{-\int_0^t \alpha(t)\,ds} \int_{\Omega_0} T_0(x)\,dx \xrightarrow[t\to\infty]{} 0.$$

since, by assumption

$$\liminf_{t\to\infty} \frac{1}{t}\int_0^t \alpha(s)\,ds > \alpha_0 > 0$$

and then

$$e^{-\int_0^t \alpha(s)\,ds} = e^{-t\left(\frac{1}{t}\int_0^t \alpha(s)\,ds\right)} \leq e^{-\alpha_0 t} \xrightarrow[t\to\infty]{} 0.$$

for $t >> 1$.

Now without assuming sign on the solutions, we have

Proposition 13. *With the notations above, assume*

$$T_0 \in L^2(\Omega_0)$$

and the function

$$\gamma(t) = \alpha(t) - C_0(\Omega(t)),$$

is such that for some $\alpha_1 > 0$,

$$\liminf_{t\to\infty} \frac{1}{t}\int_0^t \gamma(s)\,ds > \alpha_1 > 0,$$

where $C_0(\Omega(t))$ *is the Poncairè constant in* $\Omega(t)$.

Then

$$0 \leq \int_{\Omega(t)} T^2(y,t)\,dy \leq e^{-2\int_0^t \gamma(s)\,ds} \int_{\Omega(t)} T_0^2(x)\,dx \xrightarrow[t\to\infty]{} 0.$$

Proof. Multiply (26) by $T(y,t)$ and integrate in $\Omega(t)$, to get

$$\int_{\Omega(t)} \frac{\partial T}{\partial t}(y,t)T(y,t)\,dy - \int_{\Omega(t)} \Delta T(y,t)T(y,t)\,dy + \int_{\Omega(t)} a(y,t)\,T^2(y,t)\,dy = 0.$$

Using (6), the boundary conditions and the Green's formula we have

$$\frac{1}{2}\frac{d}{dt}\int_{\Omega(t)} T^2(y,t)\,dy + \int_{\Omega(t)} |\nabla T(y,t)|^2\,dy + \int_{\Omega(t)} a(y,t)T^2(y,t)\,dy = 0.$$

Now the Poincarè inequality in $\Omega(t)$ gives for any smooth function vanishing on $\partial\Omega(t)$,

$$\|\nabla u\|^2_{L^2(\Omega(t))} \geq C_0(\Omega(t))\,\|u\|^2_{L^2(\Omega(t))}.$$

This and the assumption on $a(y,t)$ leads to

$$\frac{1}{2}\frac{d}{dt}\|T(.,t)\|^2_{L^2(\Omega(t))} + \gamma(t)\,\|T(.,t)\|^2_{L^2(\Omega(t))} \leq 0. \tag{27}$$

Thus, denoting $\bar{Z}(t) = \|T(.,t)\|^2_{L^2(\Omega(t))}$, (27) reads

$$\frac{d}{dt}\bar{Z}(t) + 2\gamma(t)\bar{Z}(t) \leq 0$$

and Gronwall's lemma yields

$$\bar{Z}(t) \leq \|T_0\|^2_{L^2(\Omega_0)}\, e^{-2\int_0^t \gamma(s)\,ds} \xrightarrow[t\to\infty]{} 0.$$

since by assumption

$$\liminf_{t\to\infty} \frac{1}{t}\int_0^t \gamma(s)\,ds > \alpha_1 > 0$$

and then

$$e^{-\int_0^t \gamma(s)\,ds} = e^{-t\left(\frac{1}{t}\int_0^t \gamma(s)\,ds\right)} \leq e^{-\alpha_1 t} \xrightarrow[t\to\infty]{} 0$$

for $t >> 1$.

Acknowledgement Partially supported by Project MTM2009-07540, MEC and GR58/08 Grupo 920894, UCM, Spain.

References

1. Amann, H.: Linear and Quasilinear Parabolic Problems, vol. 89. Birkhauser Verlag, Berlin (1995)
2. Amann, H.: Nonhomogeneous linear and quasilinear elliptic and parabolic boundary value problems Function spaces, differential operators and nonlinear analysis, (Friedrichroda, 1992). Teubner **133**, 9–126 (1993)
3. Chorin, A.J., Marsden, J.E.: A Mathematical Introduction to Fluid Mechanics. Springer, Berlin (1979)

4. Duvaut, G.: Mécanique Des Milieux Continus. Masson, Paris (1990)
5. Hartman, P.: Ordinary Differential Equations. Wiley, New York (1964)
6. Ladyzhenskaya, O.A.: The Mathematical Theory of Viscous Incompressible Flow. Gordon and Breach, New York (1969)

Asymptotic Scaling for Euclidean Lattices

R.A. Garza-López and J.J. Kozak

1 Introduction

In an earlier contribution to a volume celebrating the legacy of Professor Manuel G(arcía) Velarde [1], V. Balakrishnan and one of the present authors (JJK) presented an exact analytic expression for the mean time to absorption (or mean walk length) for a particle performing an unbiased, nearest-neighbor random walk on a finite, nth generation Sierpinski gasket embedded in d Euclidean dimensions with a trap at one vertex. Earlier we had obtained an exact expression for the mean walk length, $T^{(n)}$, on the gasket embedded in $d = 2$ dimensions (see Fig. 1),

$$T^{(n)} = \left[3^n 5^{n+1} + 4(5^n) - 3^n\right] / \left(3^{n+1} + 1\right), \tag{1}$$

where n denotes the generation index of the gasket, and the mean is over a set of starting points of the walk distributed uniformly over all the other sites of the gasket [2]. For the nth generation Sierpinski gasket embedded in $d = 3$ (the Sierpinski "tower") the exact expression is given by

$$T^{(n)} = 9\left[4^n 6^{n+1} + 5(6^n) - 4^n\right] / 5\left(4^{n+1} + 2\right), \tag{2}$$

and for the case of a tower embedded in an arbitrary number of Euclidean dimensions d the exact result is:

R.A. Garza-López
Department of Chemistry and Seaver Chemistry Laboratory, Pomona College, Claremont, CA 91711, USA
e-mail: rgarza@pomona.edu

J.J. Kozak (✉)
DePaul University, 243 South Wabash Ave., Chicago, Illinois 60604-2301, USA
e-mail: kozak@depaul.edu

R.G. Rubio et al. (eds.), *Without Bounds: A Scientific Canvas of Nonlinearity and Complex Dynamics*, Understanding Complex Systems,
DOI 10.1007/978-3-642-34070-3_43, © Springer-Verlag Berlin Heidelberg 2013

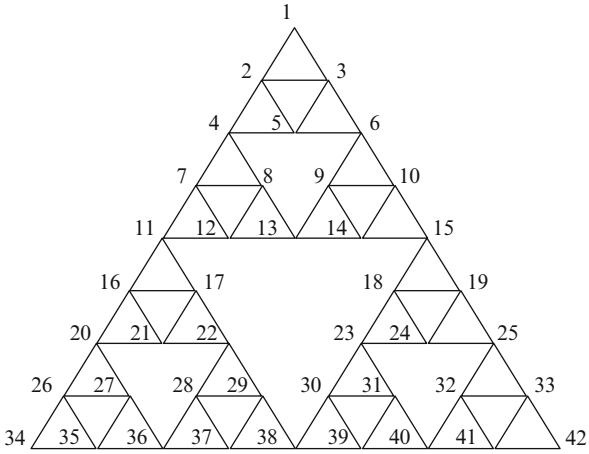

Fig. 1 The generation $n = 3$ Sierpinski gasket ($N = 42$)

$$T^{(n)} = d^2\left[(d+1)^n(d+3)^{n+1} + (d+2)(d+3)^n - (d+1)^n\right]/(d+2)\left[(d+1)^{n+1} + d - 1\right]. \quad (3)$$

Subsequently, Bentz, Turner and one of the authors (JJK) obtained for the Sierpinski gasket and tower the eigenvalue spectrum of the stochastic master equation corresponding to this Markovian problem, and derived exact analytic expressions for recurrence relations among the eigenvalues [3].

The reason that analytic expressions could be obtained for the finite, nth generation Sierpinski gasket in arbitrary Euclidean dimension is that the figure is a self-similar fractal. Once the scaling relation was discovered, the mathematics unfolded naturally. The triangular Euclidean lattice ($d = 2$) that is the starting template for constructing the Sierpinski gasket (via site decimation) is not self-similar (see Fig. 2). So, there is no reason to suppose that an exact analytic expression for the mean walk length $T^{(n)}$ could be obtained. However, over 40 years ago in a tour de force of mathematical physics, Elliot Montroll derived an expression for $T^{(n)}$ for $d = 2$ dimensional random walks on an infinite, periodic lattices of uniform connectivity. For the triangular lattice an expression was obtained that was *asymptotically* correct [4],

$$T = N/(N-1)\left[\left(\sqrt{3}/2\pi\right) N \ln N + 0.235214021N - 0.251407596\right], \quad (4)$$

where N is the total number of lattice points and the valence v (or connectivity) of all lattice sites is $v = 6$. Extensive numerical calculations have confirmed the accuracy of Montroll's result.

We now come to the question posed in this contribution. Is it possible that if one were to "set up" the triangular lattice problem in a manner similar to the design of the Sierpinski gasket problem [2], could one find evidence for "scaling" in the asymptotic limit of large N?

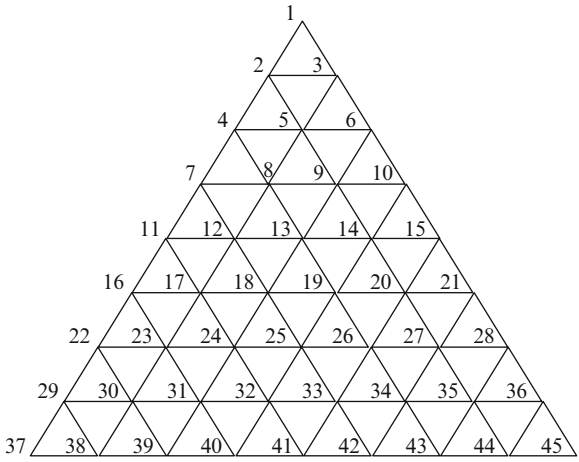

Fig. 2 The triangular lattice template ($N = 45$)

2 Formulation and Results

We follow the design of the $d = 2$ Sierpinski gasket problem described in [2]. Interior sites of the triangular lattice have the valence $v = 6$, sites on the boundary of the lattice have valence $v = 4$, and vertex sites have $v = 2$. Note that, in contrast to Montroll's formulation, the triangular lattices considered in this study do *not* have a uniform valence v, and they are *not* periodic. A deep trap is placed at one vertex (for definiteness, at the "top"). Mobilizing the theory of finite Markov processes, *exact* numerical results are obtained for the mean walk length for triangular lattices of increasing size. For emphasis, we reiterate that the results reported here are numerically exact [4]; otherwise any claims of "scaling" would be problematical.

The observation made in [2] that led, eventually, to the exact result, (2) [via a resummation procedure which amounted to an exact real-space renormalization] related to scaling on the gasket. Consider the simplest case, the three sites at the "top", the trap labeled "1" and sites "2" and "3" (see Fig. 1). For this case, denoted $n = 0$ in [2], the (exact) site specific mean walk length from both sites 2 and 3 is

$$T_2 = T_3 = 2,$$

Overall, $T^{(n=0)} = 2$. The first gasket generation $n = 1$, sites 1 to 6, gives (see Fig. 1),

$$T_2 = T_3 = 8,$$

$$T_4 = T_6 = 10,$$

so that, $T^{(1)} = 46/5$. The first generation that is representative of the gasket is $n = 2$, sites 1 to 15, yields

$$T_2 = T_3 = 26,$$

$$T_4 = T_6 = 40,$$

$$T_5 = 34,$$

$$T_7 = T_8 = T_9 = T_{10} = 48,$$

$$T_{11} = T_{12} = T_{13} = T_{14} = T_{15} = 50,$$

and $T^{(2)} = 608/14$.

The numerical values above show that

$$T_4^{(1)} = 10 = 5T_2^{(0)},$$

$$T_{11}^{(2)} = 50 = 5T_3^{(1)} = 5^2T_2^{(0)},$$

$$T_4^{(2)} = 40 = 5T_2^{(1)},$$

$$T_{13}^{(2)} = 50 = 5T_5^{(1)}.$$

These results and corresponding results for larger gaskets (higher generation indices n), led to the following observation, quoted directly from [2]: "Doubling the chemical distance systematically increases the mean time to reach a given point for the first time by a factor of five: on a given structure (in a given generation), the mean time to hit any of the four points two lattice constants away from any site, and along the same directions as its four nearest-neighbor sites, is equal to five time steps. Exactly the same scale factor occurs in the case of the two corner sites L and R with coordination number two. This scaling is exact on the Sierpinski gasket, and is essentially the statement that the random walk dimension of the gasket [5] is $d_w = \ln 5/\ln 2$." Reference [5] in the quote is [6] in this study.

Consider now the data reported in Table 1. Displayed there are the values of $T^{(n)}$ *versus* the generation index n for successive triangular lattices with site connectivity as specified above. Here, the generation index n (an integer) is the shortest chemical distance from any site on the base of a given triangular lattice to the vertex at the top. See Fig. 3 for an explicit numeration. The total number N of lattice sites at each generation is given by

$$N^{(n)} = (n+1)(n+2)/2. \tag{5}$$

For future reference,

$$N^{(2n)} = (n+1)(2n+1). \tag{6}$$

Taking advantage of the insight on scaling (above quote) we present in Table 2 values of the scaling ratio

$$\text{Ratio} = 5T^{(n)}/T^{(2n)} \tag{7}$$

Listed in tandem are values of the scaling ratio calculated using the numerically-exact values of $T^{(n)}$ reported in Table 1, and values of the ratio calculated using Montroll's asymptotic result, (4).

Table 1 Values of the mean walk length $T^{(n)}$ *vs* the generation index *n*

n	N	$T^{(n)}$	n	N	$T^{(n)}$
1	3	2	17	171	1286.369479
2	6	9.8	18	190	1467.525195
3	10	23.047619	19	210	1662.076736
4	15	44.674216	20	231	1870.199245
5	21	74.935121	21	253	2092.059022
6	28	114.513788	22	276	2327.814377
7	36	163.977799	23	300	2577.616364
8	45	223.811851	24	325	2841.609416
9	55	294.438615	25	351	3119.931905
10	66	376.232702	26	378	3412.716633
11	78	469.530428	27	406	3996.384509
12	91	574.636897	28	435	4042.178688
13	105	691.831301	29	465	4379.097411
14	120	821.370975	30	496	4730.961811
15	136	963.494573	31	528	5097.882441
16	153	1118.424604	32	561	5479.966272

N is the total number of lattice sites at generation *n*

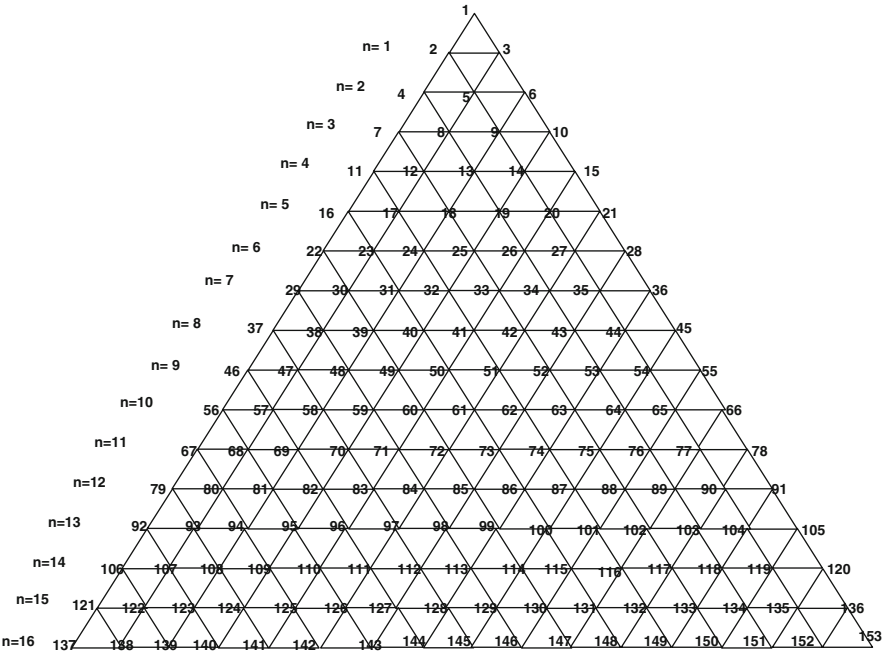

Fig. 3 The $N = 153$ triangular lattice. The generation index *n* is listed to the left of the figure

Table 2 Values of the scaling ratio $5T^{(n)}/T^{(2n)}$ *vs* the generation index n

n	Exact	Montroll
6	0.996402	1.223900
7	0.998196	1.198177
8	1.000576	1.178100
9	1.003181	1.165341
10	1.005862	1.154432
11	1.008522	1.145814
12	1.011111	1.138888
13	1.013608	1.133242
14	1.016000	1.128583
15	1.018286	1.124701
16	1.020467	1.121439

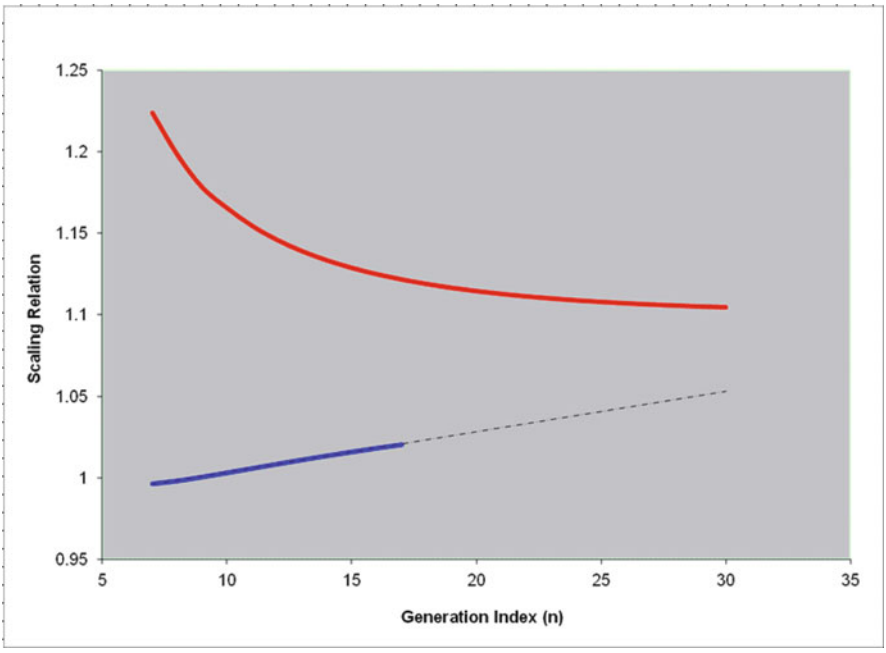

Fig. 4 The scaling ratio $5T^{(n)}/T^{(2n)}$ *versus* the generation index n. Exact results in *blue*, Montroll's results in *red*

A plot of these two ratios for generations $n = 6$ to $n = 15$ is displayed in Fig. 4. Although the ratios generated using Montroll's asymptotic result appear to be monotonically decreasing, the curve "turns around" and approaches asymptotically the (exact) limiting value of 5/4, a result which can be seen at once using the relations (5) and (6) in concert with Montroll's (4). The convergence to this limiting value is painfully slow; see Table 3.

Table 3 Values of the ratio $5T^{(n)}/T^{(2n)}$ using Montroll's (4) for large $n = 10^p$

p	Montroll
1	1.165341
2	1.107156
3	1.139024
4	1.163397
5	1.179497
6	1.190611
7	1.198705
8	1.204859
9	1.209694
10	1.213593
100	1.246250
500	1.249248
1000	1.249624

3 Discussion

We have considered an unbiased, nearest-neighbor, random walk on a finite, nth generation triangular lattice in $d = 2$ with a deep trap at one vertex. We have shown that a scaling relation developed for the self-similar fractal, the Sierpinski gasket, also holds for this Euclidean lattice. Specifically, if you double the chemical distance n on a given triangular lattice (the shortest path from any point on the base of the lattice to the trap at the vertex), one finds that the scaling relation, Ratio $= 5T^{(n)}/T^{(2n)}$, is satisfied in the limit of *asymptotically large* n. This result stands in contrast to the results presented in [1,2]; there, recognition of scaling on the Sierpinksi gasket could be coupled with a resummation procedure to derive an *exact*, closed-form analytic expression for $T^{(n)}$ valid for *arbitrary* n, that is, for finite lattices of any size. This distinction highlights the fundamental qualitative difference between the results presented in [1,2] and those presented here.

There is, however, an exact analytic result that can be derived from our numerical results. Montroll showed that, irrespective of the dimensionality of the Euclidean lattice, provided the connectivity v was the same for all N lattice sites, if the mean walk length $T_M^{(n)}$ is determined for the v sites that are nearest neighbor to the trap, then

$$T_M^{(n)} = N - 1.$$

Notice that the right-hand side must be an integer. This result amounts to an invariance relation which can be used to assess the accuracy of results obtained in numerical studies, either ones based on Monte Carlo simulations or (as here) via implementation of the theory of finite Markov processes. In terms of the generation index n, the above result can be written

$$T_M^{(n)} = (n+1)(n+2)/2 - 1.$$

Table 4 Mean walk length $T_{1,2}^{(n)}$ from the (two) sites nearest neighbor to the trap *vs* the generation index *n*

n	N	$T_{1,2}^{(n)}$	n	N	$T_{1,2}^{(n)}$
1	3	2	17	171	458
2	6	8	18	190	512
3	10	17	19	210	569
4	15	29	20	231	629
5	21	44	21	253	692
6	28	62	22	276	758
7	36	83	23	300	827
8	45	107	24	325	899
9	55	134	25	351	974
10	66	164	26	378	1,052
11	78	197	27	406	1,133
12	91	233	28	435	1,217
13	105	272	29	465	1,304
14	120	314	30	496	1,394
15	136	359	31	584	1,487
16	153	407	32	632	1,583

The class of triangular Euclidean lattices considered in this study is *not* of uniform connectivity; interior points are $v = 6$, points on the boundary are $v = 4$ and vertex points are $v = 2$. Nevertheless, we find that the numerical results for $T_{1,2}^{(n)}$ presented in Table 4 satisfy

$$T_{1,2}^{(n)} = 3n(n+1)/2 - 1.$$

Insofar as the authors are aware, this is the first example of an invariance relation for Euclidean lattices of variable connectivity.

Acknowledgement The authors are pleased to be able to contribute to the volume celebrating the seminal contributions of Professor Manuel G(arcía) Velarde. To one of us he has long been a friend and to both of us an inspiration. This research was funded in part by the Sontag Fellowship from Pomona College.

References

1. Kozak, J.J., Balakrishnan, V.: Int. J. Bifurcat. Chaos **12**, 2379 (2002)
2. Kozak, J.J., Balakrishnan, V.: Phys. Rev. E **65**, 021105 (2002)
3. Bentz, J.L., Turner, J.W., Kozak, J.J.: Phys. Rev. E **82**, 011137 (2010)
4. Montroll, E.: J. Math. Phys. **10**, 753 (1969)
5. Kozak, J.J.: Adv. Chem. Phys. **115**, 245–406 (2000)
6. Havlin, S., Ben-Avraham, D.: Adv. Phys. **36**, 695 (1987)

Part VI
Scientific Contributions: Bio- and Neuro-physical Problems

Present Day Biology seen in the Looking Glass of Physics of Complexity

P. Schuster

1 The Mathematics of Darwin's Selection

Darwin's principle of natural selection is based on three prerequisites: (i) multiplication, (ii) variation, and (iii) limitation of resources. Multiplication follows some mechanism of reproduction that may also take care for variation since no process can occur with ultimate precision and replication errors called mutations yield variants. A nontrivial condition for replication is that a sufficiently large fraction of error copies has to be able to survive in order to sustain an evolutionary process. Limitation of resources is simply a consequence of our finite world. As shown in this section the Darwinian principle can be readily expressed in mathematical form by means of ordinary differential equations (ODEs).

In 1838, 21 years before the publication of the famous *Origin of Species* [12], the Belgium mathematician Pierre-François Verhulst [80] published a kinetic differential equation, which presumably was not known to Darwin and to most other scientists. The Verhulst or logistic equation describes population growth in ecosystems with finite resources:

$$\frac{dN}{dt} = N \cdot r \left(1 - \frac{N}{K}\right) \quad \text{and} \quad N(t) = N(0)\,\frac{K}{N(0) + \big(K - N(0)\big)\,e^{-rt}}\,. \quad (1)$$

The population size N counts the number of individuals $\mathbf{I}$ in the population Υ and its time dependence is the solution of the ODE (1): $[\mathbf{I}]_t = N(t)$. $N(0)$ is the population size at time $t = 0$, r is the growth parameter also called *Malthusian* parameter after the English economist Robert Malthus, and K is the *carrying*

P. Schuster (✉)
Institute für Theoretische Chemie der Universität Wien, Währingerstrasse 17, 1090 Wien, Austria

The Santa Fe Institute, 1399 Hyde Park Road, Santa Fe, NM 87501, USA
e-mail: pks@tbi.univie.ac.at

R.G. Rubio et al. (eds.), *Without Bounds: A Scientific Canvas of Nonlinearity and Complex Dynamics*, Understanding Complex Systems,
DOI 10.1007/978-3-642-34070-3_44,

capacity, the maximal population size that can be sustained by the ecosystem. The interpretation is straightforward: Populations grow by reproduction and the population size increases proportionally to the number of individuals already present times the Malthusian parameter, $N(t)\cdot r$. Growth requires resources, their limitations is taken into account by the third factor, $\big(1-N(t)/K\big)$, which approaches zero if the population size reaches the carrying capacity, and then no further growth of the total population size is possible. The solution of Verhulst equation is called the *logistic curve*. In the early phase of growth, $N(t) \ll K$ (Fig. 1; upper plot, red curve), the logistic curve starts with unlimited exponential growth and, beginning in the range around 20% saturation, i.e. populations sizes of $N(t) \geq 0.2\,K$, the effect of finite resources becomes significant.

The Verhulst model of constrained growth is dealing with *multiplication*, the first factor of Darwin's principle. It is implicitly contained in the term leading to exponential growth. In order to visualize selection the population Υ is now partitioned into subpopulations of n classes of individuals $\mathbf{I}_j$ $(j = 1,\ldots,n)$ with $[\mathbf{I}_j] = N_j$ and $N(t) = \sum_{j=1}^{n} N_j(t)$ [68] where each variant has its own specific Malthusian parameter or *fitness value* denoted by f_j $(j = 1,\ldots,n)$. The result is the *selection equation* (2), which describes the evolution of the total population size and the distribution of variants within the population:

$$\frac{dN_j}{dt} = N_j\left(f_j - \frac{N}{K}\,\phi(t)\right);\; j = 1,\,\ldots\,,\,n \quad \text{with} \quad \phi(t) = \frac{1}{N(t)}\sum_{i=1}^{n} f_i\,N_i(t)\,. \tag{2}$$

Equation (2) is solved by means of normalized variables $x_j(t) = N_j(t)/N(t)$ and integrating factor transformation $z_k(t) = x_k(t)\exp\big(\int_0^t \phi(\tau)d\tau\big)$ (see [94, p.322ff.]):

$$\frac{dx_j}{dt} = x_j\Big(f_j - \phi(t)\Big),\; j = 1,\,\ldots\,,\,n\,;\; x_j(t) = \frac{x_j(0)\cdot\exp(f_j\,t)}{\sum_{i=1}^{n} x_j(0)\cdot\exp(f_i\,t)},\; j = 1,\,\ldots\,,\,n\,. \tag{2a}$$

The size of the subpopulations is obtained through multiplication by the total population size

$$N_j(t) = N(t)\cdot x_j(t) = N(t)\cdot\frac{N(0)\cdot\exp(f_j\,t)}{\sum_{i=1}^{n} N_j(0)\cdot\exp(f_i\,t)};\; j = 1,\,\ldots\,,\,n\,, \tag{2b}$$

and hence, the knowledge of the time dependence of population size, $N(t)$, is required. It can be obtained by means of the integral $\Phi(t) = \int_0^t \phi(\tau)d\tau$

$$N(t) = N(0)\,\frac{K}{N(0) + \big(K - N(0)\big)\,e^{-\Phi(t)}}\,. \tag{1a}$$

Herein $\exp\big(-\Phi(t)\big)$ replaces $\exp(-rt)$ in the solution of the Verhulst equation. The course of selection in the variables N_j and x_j is the same [26] and the restriction

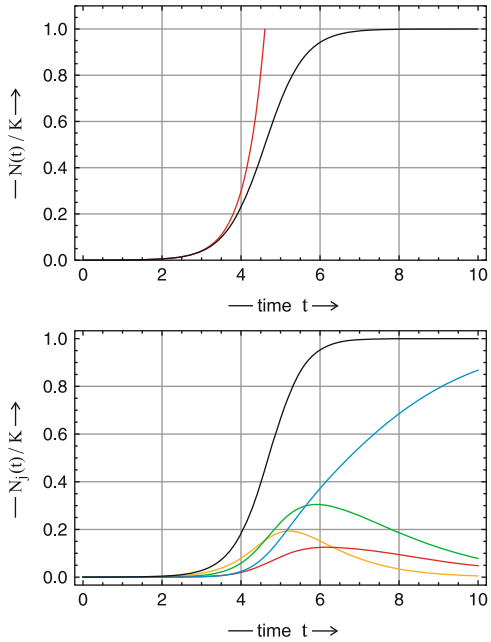

Fig. 1 Solution curves of the logistic equation. *Upper plot*: The *black curve* illustrates growth in population size from a single individual to a population at the carrying capacity of the ecosystem (1). For comparison the *red curve* represents the results for unlimited exponential growth, $N(t) = N(0)\exp(rt)$. Parameters: $r = 2$, $N(0) = 1$, and $K = 10,000$.
Lower plot: Growth and internal selection is illustrated in a population with four variants (2), $n = 4$. Color code: N *black*, N_1 *yellow*, N_2 *green*, N_3 *red*, N_4 *blue*. Parameters: fitness values $f_j = (1.75, 2.25, 2.35, 2.80)$, $N_j(0) = (0.8888, 0.0888, 0.0020, 0.0004)$, $K = 10,000$. The parameters were adjusted such that the curves for the total populations size $N(t)$ in the two plots (almost) coincide

to constant population size, $N = K$, leaves the results unchanged unless $N(t)$ vanishes or diverges, or in other words unless the population dies out or explodes. A typical example is shown in Fig. 2. The interpretation of the solution curves (2b) is straightforward: For sufficiently long times the sum in the denominator is dominated by the term containing the exponential with the highest fitness value, $f_m = \max\{f_j; j = 1, \ldots, n\}$, all variables except N_m vanish and the fittest variant is selected: $\lim_{t\to\infty}[N_m] = N$. Finally, the time derivative of the mean fitness, $d\phi(t)/dt = \mathrm{var}\{f\} \geq 0$, encapsulates optimization in Darwinian evolution: $\phi(t)$ is optimized during natural selection (see, e.g., [68]). The equation for selection is rather simple, derivation and analysis of the solutions are both straightforward, and everything needed was standard mathematics at Darwin's time.

Mechanisms creating new variants are not part of the nineteenth century model of evolution. Recombination and mutation were unknown and new variants appear spontaneously in the population like the *deus ex machina* in the ancient antique theater. Figure 2 illustrates selection at constant population size and the growth of

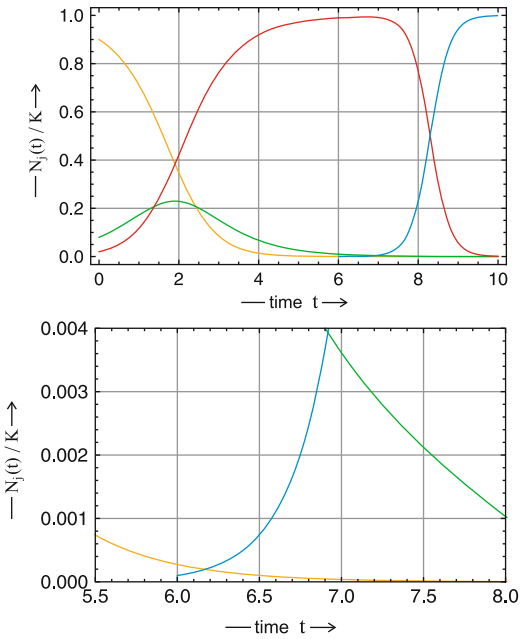

Fig. 2 Solution curve of the selection equation. The system is studied at constant maximal population size, $N = K$, and the plots represent calculated changes of the variant distributions with time. The *upper plot* shows selection among three species $\mathbf{I}_1$ (*yellow*), $\mathbf{I}_2$ (*green*), and $\mathbf{I}_3$ (*red*), and then the appearance of a fourth, fitter variant $\mathbf{I}_4$ (blue) at time $t = 6$, which takes over and becomes selected thereafter. The *lower plot* presents an enlargement of the upper plot around the point of spontaneous creation of the fourth species ($\mathbf{I}_4$). Parameters: fitness values $f_j = (1, 2, 3, 7)$; $x_j(0) = (0.9, 0.08, 0.02, 0)$, and $x_4(6) = 0.0001$

a spontaneously created advantageous variant. With spontaneous input of variants the simple mathematical model described here encapsulates all three preconditions of Darwin's natural selection and reflects in essence the state of knowledge of the evolutionists in the second half of nineteenth century.

2 Mutation, Quasispecies, and Error Thresholds

Mutation has been introduced by Hugo De Vries as a principle to create variation at the beginning of the twentieth century [13] but the mechanistic explanation as incorporation of wrong digits during a copying process has not been possible before the advent of molecular biology (For a historical account on the concept of mutation see [8]). In order to introduce mutations into selection dynamics Manfred Eigen [23] conceived a kinetic model based on stoichiometric equations, which handles correct replication and mutation as parallel reactions

$$(\mathbf{A}) + \mathbf{X}_i \xrightarrow{Q_{ji}\, f_i} \mathbf{X}_j + \mathbf{X}_i \,;\; i, j = 1, \ldots, n \,. \tag{3}$$

The material required to synthesize molecules is denoted by $\mathbf{A}$ and put in parentheses in order to indicate that it is present in excess and its concentration is constant: $[\mathbf{A}] = a_0$. Accordingly, the concentration of $\mathbf{A}$ can be absorbed as a constant factor into the rate parameter: $k_i\,[\mathbf{A}] = k_i\, a_0 = f_i$. The factor Q_{ji} represents the frequency at which sequence $\mathbf{X}_j$ is obtained as an error copy of $\mathbf{X}_i$. Accordingly, Q_{ii} is the fraction of correctly reproduced copies of $\mathbf{X}_i$.

Individuals are specified as genotypes or polynucleotide sequences $\mathbf{X}_i$, which form together a population $\Upsilon = \{\mathbf{X}_i; i = 1, \ldots, n\}$ where they are present in time dependent concentrations $[\mathbf{X}_i] = c_i = x_i\, c$ with $c = \sum_{i=1}^{n} c_i$. Equation (3) designates one polynucleotide sequence, $\mathbf{X}_i$, as template whereas the second one, $\mathbf{X}_j$, is the product. In the language of chemical kinetics the template $\mathbf{X}_i$ is a catalyst, in case of correct direct copying when template and product are the same molecule it is an autocatalyst. Template action is illustrated in Fig. 3: Completing the template strand to a full double helix synthesizes a complementary molecule or a minus-strand. Replication occurs, in essence, by two different mechanisms: (i) complementary or $\pm$-replication and (ii) double strand replication. In the first case the process occurs in two steps like manufacturing a positive and a negative in silver based photography—a minus strand is synthesized on the plus strand and vice versa a plus strand is produced on the minus strand—and it is straightforward to prove that after an initial approach towards internal stationarity of the two strands the $\pm$-ensemble grows exponentially with a rate parameter $\sqrt{f_+\, f_-}$ and the ratio of the two strands becomes $[\mathbf{X}_+]/[\mathbf{X}_-] = \sqrt{f_-/f_+}$ [23]. Here, we shall assume that internal equilibrium has been established and we shall treat $\pm$-ensembles as single entities. Complementary replication is found with several classes of RNA viruses and with in vitro evolution of RNA molecules. Commonly, only a single enzyme or very few enzymes are required and the accuracy of the copying process is limited to about one error in a few thousand nucleobases because the system lacks proofreading. Extensive kinetic studies on RNA replication by means of a virus specific RNA replicase were performed [4–6] and conditions were derived under which the many step reaction can be replaced successfully by the single over-all reaction (3): The replicase has to be present in excess. As mentioned in the caption of Fig. 3, complementary replication of single stranded DNA is used in applications of polymerase chain reaction (PCR). Direct replication of DNA double strands is the basis of multiplication of organisms in nature from bacteria to men. The process follows a simple principle: The double strand is separated into the two strands on the fly and both are completed to yield new double helices by adding nucleobases consecutively on both sides. In reality, double strand replication of DNA is highly complex and involves about twenty different enzymes. Nevertheless, even in this case the single step mechanism (3) leads to a suitable description of the over-all replication kinetics.

In normalized coordinates the mechanism (3) corresponds to a differential equation called *mutation-selection* equation, which has the form

$$\frac{dx_j}{dt} = \sum_{i=1}^{n} Q_{ji}\, f_i\, x_i - x_j\, \phi(t)\,;\; j = 1, \ldots, n\;;\; \sum_{i=1}^{n} x_i = 1\,. \tag{4}$$

The finite size constraint or dilution flux $\phi(t) = \sum_{i=1}^{n} f_i x_i$ is precisely the same as in the mutation-free case (2), and the same techniques can be used to solve the differential equation (see [46, 79] and [94, p322ff.]). *Exact* solutions of (4) are derived in terms of eigenvalues λ_k and eigenvectors $\mathbf{b}_k$ of the $n \times n$ *value matrix* $\mathrm{W} = \mathrm{Q} \cdot \mathrm{F} = \{W_{ji} = Q_{ji} f_i\}$, where the mutation frequencies are subsumed

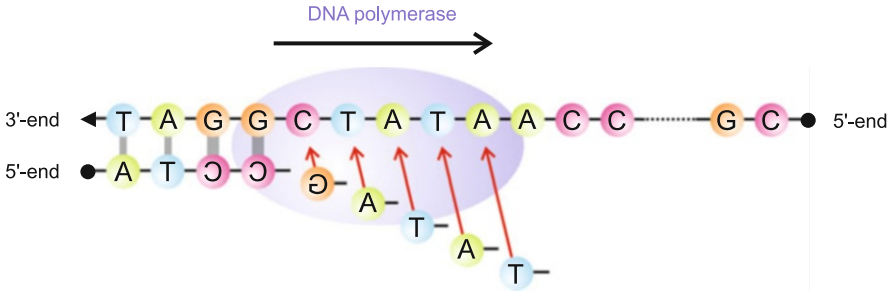

Fig. 3 The principle of DNA and RNA polymerization. Complementarity of nucleobases in Watson-Crick base pairs is the principle of all polynucleotide replication. Template induced polymerization of DNA and RNA always proceeds in the direction from the 5'-end to the 3'-end of the synthesized strand. The process that comes closest to the sketch is template induced DNA polymerization by a thermostable polymerase from a thermophilic bacterium, *Thermus aquaticus* or *Thermus thermophilus* [62]. Polymerization requires *primers*, which are oligonucleotides that bind specifically to the single stranded DNA and which provide a free 3'-OH group that allows to start polymerization. After the double helix has been completed the two strands are separated by heating, subsequent cooling leads to binding of primers and the next polymerization round begins. Polymerase chain reaction (PCR) amplification of DNA stretches is a standard technique in molecular biology (see e.g. [32])

in the *mutation matrix* $\mathrm{Q} = \{Q_{ji}\}$ and the fitness values are the elements of a diagonal matrix $\mathrm{F} = \{F_{ij} = f_i \cdot \delta_{i,j}\}$ called *fitness matrix* or *fitness landscape*. Transformation of W yields the diagonal matrix Λ that contains the eigenvalues as elements

$$\begin{aligned} &\mathrm{B}^{-1} \cdot \mathrm{W} \cdot \mathrm{B} = \Lambda = \{\lambda_k;\, k = 0, 1, \ldots, n-1\} \quad \text{with} \\ &\mathrm{B} = \{b_{ij};\, i, j = 1, \ldots, n\} \text{ and } \mathrm{B}^{-1} = \mathrm{H} = \{h_{ij};\, i, j = 1, \ldots, n\}\,. \end{aligned} \tag{5}$$

The individual components of the eigenvectors are obtained through solving the differential equation $d\boldsymbol{\zeta}/dt = \Lambda\,\boldsymbol{\zeta}$

$$\boldsymbol{\zeta}(t) = \exp(\Lambda t) \cdot \boldsymbol{\zeta}(0) \text{ or } \zeta_k(t) = \zeta_k(0)\, \exp(\lambda_k t)\,;\; k = 0, 1, \ldots, n\,.$$

The solutions are readily expressed in the original variables $x_j(t)$

$$x_j(t) = \frac{\sum_{k=0}^{n-1} b_{jk}\, \zeta_k(0)\, \exp(\lambda_k\, t)}{\sum_{i=1}^{n} \sum_{k=0}^{n-1} b_{ik}\, \zeta_k(0)\, \exp(\lambda_k\, t)}\,. \tag{6}$$

For sufficiently long times the term with the largest eigenvalue λ_0 dominates the summations and we find for the stationary solutions

$$\bar{x}_j(t) = \frac{b_{j0}\, \zeta_0(0)\, \exp(\lambda_0\, t)}{\sum_{i=1}^{n} b_{i0}\, \zeta_0(0)\, \exp(\lambda_0\, t)}\,. \tag{7}$$

The stationary distributions of mutants in populations, $\bar{\Upsilon} = (\bar{x}_i; i = 1, \ldots, n)$, have been called *quasispecies* since they represent the genetic reservoirs of asexually reproducing species. A typical quasispecies commonly consists of a fittest genotype, the *master sequence* and its frequent mutants (For details see [25–27]). Several important properties of the quasispecies follow from the applicability of Perron-Frobenius theorem to the value matrix[1] [72]: (i) The largest eigenvalue is real and positive, $\lambda_0 > 0$, (ii) a strictly positive right eigenvector $\mathbf{b}_0$ and a strictly positive left eigenvector $\mathbf{h}_0$ are associated with λ_0, (iii) $\lambda_0 > |\lambda_k|$ holds for all eigenvalues $\lambda_k \neq \lambda_0$, and (iv) the largest eigenvalue is non-degenerate, i.e. the eigenvectors associated with λ_0 are unique (up to constants factors) and λ_0 is a simple root of the characteristic polynomial of matrix W. Item (ii) is of particular relevance for the mutation-selection problem: All n variants of the population $(\mathbf{X}_k; k = 1, \ldots, n)$ are present at strictly positive concentrations in the quasispecies or, in other words, no variant vanishes in the approach towards the stationary distribution.

In order to gain more insight into error propagation over generations we introduce a mutation rate per site and generation, $p_k^{(i)}$, which denotes the error frequency at position k of the sequence $\mathbf{X}_i$. For the diagonal elements of the mutation matrix Q describing correct replication we find:

$$Q_{ii} = (1 - p_1^{(i)})\,(1 - p_2^{(i)}) \ldots (1 - p_\nu^{(i)}) = (1 - \bar{p}^{(i)})^\nu \,, \tag{8}$$

where ν is the chain length and $\bar{p}^{(i)}$ the mean mutation rate of the polynucleotide $\mathbf{X}_i$. The structure of (8) implicitly assumes independence of nucleobase incorporation as suggested by Fig. 3. For the elements leading to mutants the factor $(1 - p_k^{(i)})$ is simply replaced by $p_k^{(i)}$ at every nucleobase where a mutation occurs. We are now in the position to calculate stationary populations as a function of the mutation rate: $\bar{\Upsilon}(p)$. In order to be able to derive analytical expressions we apply the *uniform mutation rate model*, which assumes that the mutation rate per site and generation, p, is independent of the particular template $\mathbf{X}_i$ and the position k on the polynucleotide sequence, and get for the elements of the matrix Q:

$$Q_{ii} = (1 - p)^\nu \quad \text{and} \quad Q_{ji} = (1 - p)^{\nu - d_{ij}}\, p^{d_{ij}} \;\text{ for } i \neq j \,, \tag{9}$$

where the Hamming distance between sequences is expressed by $d_{ji} = d_{\mathrm{H}}(\mathbf{X}_i, \mathbf{X}_j)$.[2] Mutational backflow from mutants to the master sequence is neglected,

[1] Perron-Frobenius theorem in its strict form holds for *primitive* matrices. A square non-negative matrix $\mathrm{T} = \{t_{ij}; i, j = 1, \ldots, n; t_{ij} \geq 0\}$ is called primitive if there exists a positive integer m such that T^m is strictly positive: $\mathrm{T}^m > 0$, which implies $\mathrm{T}^m = \{t_{ij}^{(m)}; i, j = 1, \ldots, n; t_{ij}^{(m)} > 0\}$. In terms of mutations the matrices Q and W are primitive if every pair of sequences $\mathbf{X}_i$ and $\mathbf{X}_j$ is connected by a finite-length path of consecutive mutations.

[2] The Hamming distance d_{H} counts the number of positions in which two aligned sequences differ [41].

and this is denoted in the variables by the superscript '$^{(0)}$' indicating a kind of zeroth order perturbation approximation [23, 76]. For the master sequence we find:

$$\frac{dx_m^{(0)}}{dt} = x_m^{(0)}\,(W_{mm} - \phi(t)) = x_m^{(0)}\,(Q_{mm}\,f_m - \phi(t))\ . \tag{10}$$

From the stationarity condition, $dx_m^{(0)}/dt = 0$, we obtain for the quasispecies $\bar{\Upsilon}^{(0)}$:

$$\begin{aligned} \bar{x}_m^{(0)} &= \frac{Q_{mm} - \sigma_m^{-1}}{1 - \sigma_m^{-1}} \quad \text{with} \quad \sigma_m = f_m \Big/ \overline{f}_{-m} \ \text{and} \ \overline{f}_{-m} = \frac{\sum_{i=1, i\neq m}^{n} f_i x_i}{1 - x_m}\ , \\ \bar{x}_j^{(0)} &= \frac{f_m}{f_m - f_j}\,\varepsilon^{d_{jm}}\,\bar{x}_m^{(0)} \quad \text{with} \quad \varepsilon = \frac{p}{1-p}\ . \end{aligned} \tag{11}$$

An accurate computation of the mean value $\overline{f}_{-m}$ is quite involved because it requires a knowledge of the distribution of mutants in form of the x_l-values. An exception makes the single peak fitness landscape, where all sequences except the master sequence have the same fitness: $f_m = f_0$ and $f_j = f_s\ \forall\ j = 1, \ldots, n$; $j \neq m$ with the trivial result $\overline{f}_{-m} = f_s$.

Although (11) is only a zeroth order approximation, it describes the dependence of the quasispecies on the mutation rate p remarkably well for sufficiently long polynucleotides (Fig. 4 shows the case $\nu = 50$). According to (11) the stationary concentration of the master sequence vanishes at some critical mutation rate:

$$\bar{x}_m = 0 \Longrightarrow (1 - p_{\text{cr}})^{\nu} = \sigma_m^{-1} \ \text{and} \ p_{\text{cr}} = 1 - \sigma_m^{-1/\nu}\ . \tag{12}$$

The master sequence and all its mutants—because of $\bar{x}_j^{(0)}(p) \propto \varepsilon^{d_{jm}}\,\bar{x}_m^{(0)}(p)$—vanish at this point. Making use of the approximation $\ln(1 - x) \approx -x$ we find two relations for the error threshold

$$p_{\text{cr}} = \frac{\ln \sigma_m}{\nu} \quad \text{and} \quad \nu_{\text{cr}} = \frac{\ln \sigma_m}{\nu}\ , \tag{45.12'}$$

which were used in various applications from developing new antiviral strategies [21] to questions concerning the primordial origin of replication [27, 28].

Because of Perron-Frobenius the exact solution of the mutation-selection equation (4) cannot vanish at the critical error rate $p = p_{\text{cr}}$. Instead it undergoes a remarkably sharp transition to the uniform distribution $\Upsilon^{(\mathbb{I})}$: $x_i = 1/n\ \forall\ i = 1, \ldots, n$. Since n becomes very large already for moderately small chain length—$n = 4^{\nu}$ for the natural **AUGC**-alphabet, the stationary concentration in the uniform distribution is extremely small $\bar{x}_0 = n^{-1}$ and accordingly the approach by perturbation theory is a good approximation.

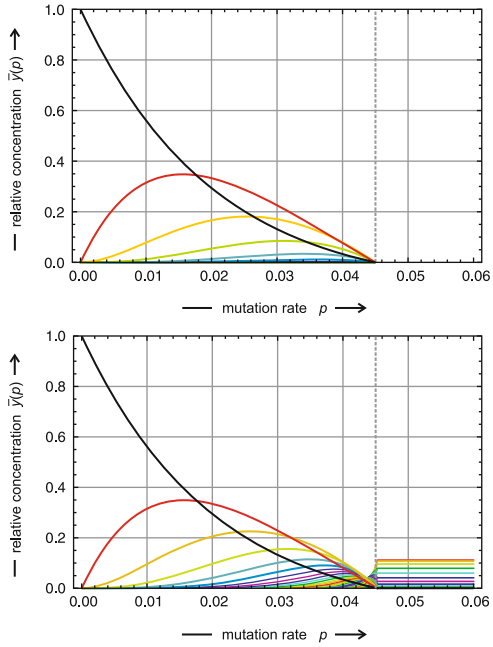

Fig. 4 The quasispecies as a function of the mutation rate p. The plot shows the stationary mutant distribution of sequences of chain length $\nu = 50$ on a single-peak fitness landscape as a function of the point mutation rate p. The upper part contains the approximation by perturbation theory according to (11) and is compared with the exact results presented in the lower part of the figure. Individual sequences are grouped into classes $\Gamma_k^{(m)} \equiv \{\mathbf{X}_i | d_{\mathrm{H}}(\mathbf{X}_i, \mathbf{X}_m) = k\}$ containing all mutants with Hamming distance k form the master sequence (see Sect. 3). Plotted are the stationary concentration of entire mutant classes, $\bar{y}_k = \sum_{i \in \Gamma_k} \bar{x}_i$: $\bar{y}_0$ (black) is the concentration of the master sequence, $\mathbf{X}_m \equiv \mathbf{X}_0$ and $\bar{y}_0 = \bar{x}_0$, $\bar{y}_1$ (*red*) is the sum of the concentrations of all one-error mutants of the master sequence, $\bar{y}_2$ (*yellow*) that of all two-error mutants, $\bar{y}_3$ (*green*) that of all three-error mutants, and so on. In the perturbation approach the entire population vanishes at a critical mutation rate p_{cr} called the error threshold (which is indicated by a *broken gray line* at $p_{\mathrm{cr}} = 0.04501$) whereas a sharp transition to the uniform distribution is observed with the exact solutions. In the uniform distribution the concentration of class k is given by $\binom{\nu}{k}/2^{\nu}$ with a largest value of $\bar{y}_{25} = 0.1123$ and a smallest value of $\bar{y}_0 = \bar{y}_{50} = 8.8818 \times 10^{-16}$. Choice of parameters: $f_0 = 10$, $f = f_k = 1 \; \forall \; k = 1, \ldots, \nu$ referring to classes $\Gamma_k^{(0)}$, and hence $\overline{f}_{-0} = 1$

It has to be pointed out that modeling by means of differential equations becomes obsolete beyond the error threshold. Population sizes in nature and in laboratory experiments commonly vary between a few thousand and 10^{15} individuals. These numbers are tiny compared to the possible numbers of different sequences in sequence space: $|\mathscr{Q}| = \kappa^{\nu}$ with κ being the number of digits in the alphabet—$2^{50} = 1.13 \times 10^{15}$ and $4^{50} = 1.27 \times 10^{30}$. What actually happens at the error threshold can be studied by means of stochastic models and computer simulation [24, 36, 45, 55, 66]: Because of error accumulation all members of the population go extinct after some time and the evolution of the population is determined by *random*

replication where no correlation exists between the template and the copies in future generations. The stochastic process is similar to a linear birth-and-death process on the population level [70]. The population is no longer stationary but migrates in sequence space and the migration is in analogy to a diffusion process.

3 Sequence Space and Fitness Landscape

The metaphor of a fitness landscape is due to Sewall Wrigh [88]: Populations are optimizing fitness by climbing on a mountain landscape under the condition that no downward steps are allowed (Fig. 5). Species occupy local maxima of the fitness landscape. The process creating variation is recombination rather than mutation, which was not yet properly understood in the first half of the twentieth century. The support of the landscape is a recombination space of genotypes [75] in analogy to a sequence space. Both spaces share the combinatorial principle and high-dimensionality. Wright's metaphor is illustrative but is has been strongly criticized by his contemporaries, in particular by Ronald Fisher (see, e.g., [73]). In Wright's time the problem with the landscape metaphor was twofold: (i) the space upon which evolution takes place could not be handled, and (ii) fitness was an abstract quantity in the center of population genetics but nobody had at hand a concept for the determination of fitness independently of the outcome of the evolutionary process. Later molecular biology shed light on the process of inheritance, the nature of mutation and recombination became explainable at the molecular level, and the stage for a scientific analysis of Wright's metaphor was set. Determining the fitness of variants, however, remained a great challenge and substantial progress has been made only recently. Fitness can be measured now in the case of RNA evolution in vitro [3] and in virus evolution [51]. It can be expected that further progress will bring the landscape into the focus of evolutionary thinking.

Originating from the application of quantum mechanics to molecular motions the Born-Oppenheimer approximation gave rise to molecular *hypersurfaces* upon which nuclear motion takes place. Meanwhile the landscape concept became also an integral part of biophysics and in other areas of physics and chemistry. In particular, conformational landscapes of biopolymers have been and are successfully applied to the folding problem of proteins [56, 87]. Nucleic acid structures, in particular RNA in the simplified form of secondary structures, turned out to provide a sufficiently simple model for the study of basic features of sequence-structure mappings [59, 60]. What renders nucleic acids accessible to mathematical analysis is the straightforward and unique base pairing logic, which dominates intramolecular and intermolecular interactions and accounts for the major fraction of the free energy of folding. Base pairing logic, for example, allows for the application of combinatorics in counting of structures with predefined structural features or properties [44, 81].

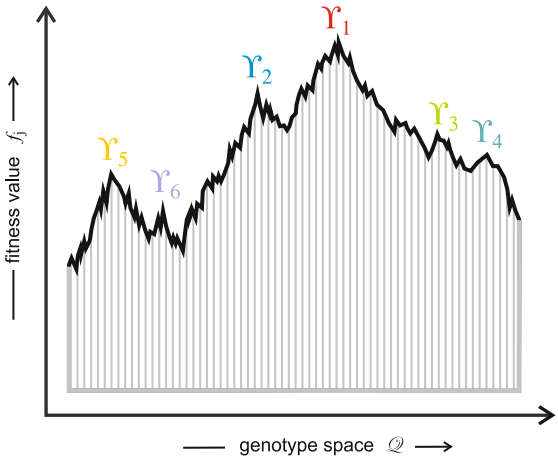

Fig. 5 Sewall Wright's fitness landscape. The landscape has been introduced as a metaphor to illustrate evolution [88]. Populations or subpopulations of species are climbing on landscape with multiple peaks and optimize fitness in a non-descending or adaptive walk until they occupy local maxima. Genotype space in Wright's original concept is recombination space and as such it is high-dimensional

3.1 Sequence-Structure Mappings

In structural biology the relation between biopolymer sequences and functions is conventionally spit into two parts: (i) the mapping of sequences into structures and (ii) the prediction or assignment of function for known structures (Fig. 6). If function is encapsulated in a scalar quantity, for example in a reaction rate parameter or a fitness value, the second mapping corresponds to a landscape with structure space as support:

$$\mathbf{X} \longrightarrow \mathbf{S} = \Phi(\mathbf{X}) \longrightarrow f = \Psi(\mathbf{S}) \,. \tag{13}$$

The function itself gives rise to the dynamics of a process involving a population of sequences or genotypes. The underlying concept is based on the assumption that structures can be calculated from sequences either directly or by means of an algorithm. Function manifests itself in the structure and should therefore be predictable. As it turned out after some spectacular successes in the early days (see, e.g., [82]) both steps are feasible but the mappings are highly complex and not fully understood yet. The alternative way to determine parameters consists of an inversion of conventional kinetics: The measured time dependence of concentrations is the input and parameters are fit to the data either by trial and error or systematically by means of inverse methods involving regularization techniques [30].

The conventional problem in structural biology is to find the structures into which a sequences folds under predefined conditions [92, 93]. Solutions to the inverse problem, finding a sequence that folds into a given structure are important for the design of molecules in synthetic biology. An inverse folding algorithm has been developed for RNA secondary structures [43] (for a recent variant see [1]) and turned out to by a very useful tool for studying sequence-structure mappings. In particular, these mappings are not invertible: Many sequences fold into the

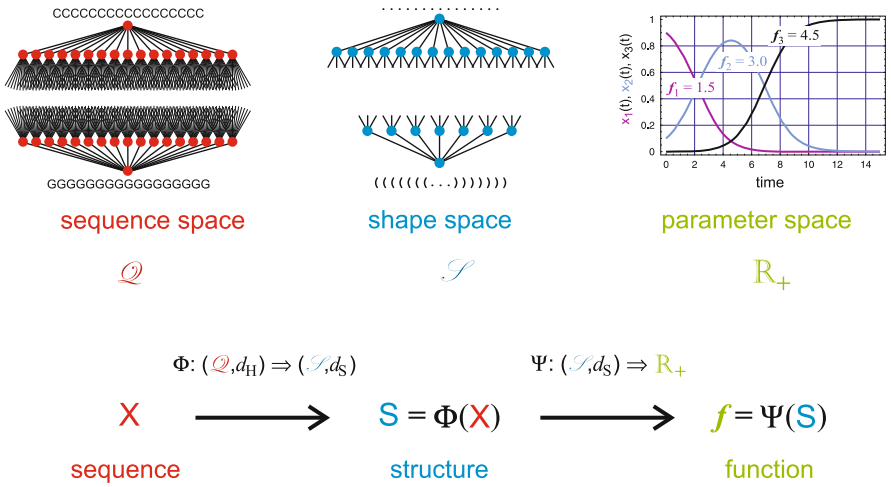

Fig. 6 The paradigm of structural biology. The relations between sequences, structures, and functions involve three spaces: (i) the sequence space $\mathcal{Q}$ with the Hamming distance d_H as metric, (i) the shape space $\mathcal{S}$ with a structure distance d_S as metric, and (iii) the parameter space $\mathbb{R}_+^m$ for m parameters. Properties and functions are viewed as the result of two consecutive mappings: Φ maps sequences into structures, Ψ assigns parameters to structures and thereby determines molecular function (The insert shows fitness values f_k and selection as example). The sequence space $\mathcal{Q}$ has a remarkable symmetry: All sequences are equivalent in the sense that the occupy topologically identical positions having the same number of nearest, next nearest, etc., neighbors linked in the same way (An example of a sequence space is shown in Fig. 7). The shape space $\mathcal{S}$ refers here to RNA secondary structures. The elements of shape space can be classified by the number of base pairs and then there is a unique *smallest* element, the open chain, and depending on ν one *largest* element for odd ν or two largest elements for even ν—one with the unpaired nucleobase on the 5'-end and one with it on the 3'-end. Parameter space in chemical kinetics is commonly multi-dimensional and the elements are rate parameters, commonly nonnegative real numbers $f_k \in \mathbb{R}_+$; $k = 1, \ldots$

same structure, and the notion of *neutral network* has been created for the graph representing the preimage of a given structure in sequence space [69]:

$$\Phi(\mathbf{X}_j) = \mathbf{S}_k \implies G_k = \Phi^{-1}(\mathbf{S}_k) \equiv \{\mathbf{X}_j | \Phi(\mathbf{X}_j = \mathbf{S}_k\}\,, \tag{14}$$

The neutral set G_k is converted into the neutral network $\mathcal{G}_k$ through connecting all pairs of sequences with Hamming distance $d_H = 1$. Figure 8 shows a sketch of a typical neutral network in sequence space. The network consists of several components with one, the so-called *giant component* being much larger than the others. Neutral networks are characterized by a (mean) degree of neutrality

$$\bar{\lambda}_k = \frac{\sum_{j|\mathbf{X}_j \in G_k} \lambda_j^{(k)}}{|G_k|}\,, \tag{15}$$

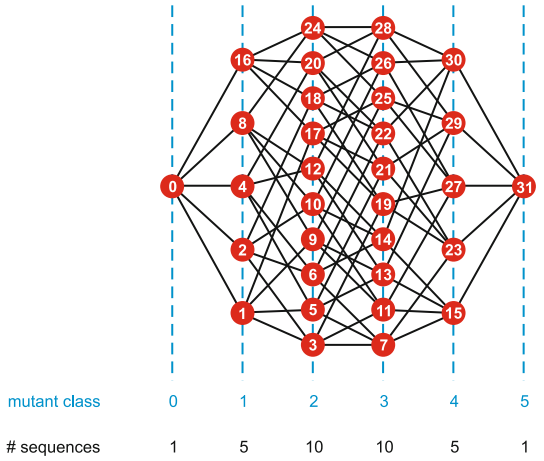

Fig. 7 Classes in sequence space. The sketch shows the space of binary sequences of chain length $\nu = 5$, $\mathscr{Q}_5^{(2)}$, which is a hypercube of dimension 5 housing $2^5 = 32$ sequences. The reference sequence, commonly the master sequence, is denoted by $\mathbf{X}_m \equiv \mathbf{X}_0$. It is the only element of the mutant class $\Gamma_0^{(m)} \equiv \Gamma_0$ where the superscript denotes the reference (that is omitted in case it is zero). Individual sequences are characterized by their decadic equivalents, e.g., $13 \equiv$ (**CGGCG**) with $\mathbf{C} = \mathbf{0}$ and $\mathbf{G} = \mathbf{1}$. The index k of the mutant class Γ_k counts the number of **G**s or **1**s

wherein $\lambda_j^{(k)}$ is the local fraction of neutral nearest neighbors of sequence $\mathbf{X}_j$ in sequence space (An example is shown in Fig. 8).

Application of random graph theory [31] in order to derive results for neutral networks [59] yields among other things a theorem on connectedness: A neutral network is connected if the degree of neutrality exceeds the critical value $\bar{\lambda}_k > \lambda_{\text{cr}} = 1 - \kappa^{-1/(\kappa-1)}$. The only parameter in this equation is κ, the size of the nucleobase alphabet. For a binary or two letter alphabet we find $\lambda_{\text{cr}} = 1/2$ and for four letters as in nature $\lambda_{\text{cr}} = 0.370$. Connectedness is important for the evolution of populations, which migrate in random walk like manner on neutral networks [36, 45]. Although random graph theory provides an appropriate reference for neutral networks, deviations from the ideal case are found and they contain information on the specific properties of RNA shape space [39]. Indeed, special features of RNA structures have direct impact on the distribution of neutral sequences in sequence space. Readily interpretable structural features may give rise to two or four equally sized giant components, or to three components with a size ratio 1:2:1. Structures with such distributions of sequences in sequence space are formed preferentially when there is an excess of one nucleobase—for example more **G** than **C** or more **C** than **G** in the two letter alphabet {**C**, **G**}—and accordingly the deviation from a homogeneous distribution is large in the sense that the *middle of sequence space* where $\mathbf{C}/\mathbf{G} = 1$ is depleted of sequences belonging to the neutral network. Without going into further details we may conclude here that neutral networks of RNA structures exhibit features that make them different from random

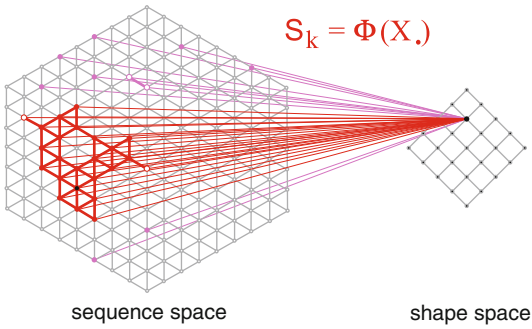

Fig. 8 Sequence-structure mapping. The sketch shows the neutral network G_k as preimage of structure $\mathbf{S}_k$ in sequence space. The giant component (*red*) is flanked by disconnected components (*red violet*). The number of neutral neighbors varies considerably. In the sketch we find: eight isolated sequences with zero neighbors ($\lambda_j^{(k)} = 0$), four sequences with one neighbor ($\lambda_j^{(k)} = 1/6$; marked *white*), three sequences with two neighbors ($\lambda_j^{(k)} = 1/3$), three sequences with three neighbors ($\lambda_j^{(k)} = 1/2$), nine sequences with four neighbors ($\lambda_j^{(k)} = 2/3$), six sequences with five neighbors ($\lambda_j^{(k)} = 5/6$), and one sequence with the maximum number of neighbors, six on this lattice ($\lambda_j^{(k)} = 1$; marked *black*). The network in total has a (mean) degree of neutrality of $\bar{\lambda}_k = 0.446$

graphs but, nevertheless, random graph theory is suitable as reference for them. Other features of the RNA model are dealing with suboptimal structures: Every molecule has a sequence specific spectrum of suboptimal states, which determine molecular properties when they lie within reach of the thermal energy, and kinetic effects may give rise to metastability of states when they are separated from the ground state by sufficiently high energy barriers [67].

The total number of physically acceptable RNA structures formed by all sequences with a certain chain length ν, N_S, can be counted by means of combinatorics [44] or estimated by an asymptotic expression

$$\tilde{N}_S(\nu) \;=\; 1.4848\,\nu^{-3/2}\,1.84892^{\nu} \tag{16}$$

that represents an upper bound, which becomes exact in the limit of long sequences. Alternatively, for a given nucleobase alphabet the number of structures can be obtained through exhaustive enumeration [38, 39, 66]. For $\nu = 100$ one counts $N_S = 6.89 \times 10^{23}$ whereas the asymptotic expression (16) yields $\tilde{N}_S = 7.3 \times 10^{23}$. Although the number of possible RNA secondary structures grows exponentially with chain length, it is tiny compared to the number of possible sequences, which is $n = 4^{100} = 1.6 \times 10^{60}$ for the same chain length ($\nu = 100$). Even for a small chain length $\nu = 17$ and 1.7×10^{10} possible sequences we count $N_S = 530$ structures out of which 414 are realized in the **AUGC**-alphabet and hence we are dealing with

many orders of magnitude more sequences than structures: Inevitably, the mapping from sequence space into structures exhibits a remarkably high degree of neutrality.

The structures in the local environment of a sequence in sequence space determine the accessibility through evolutionary dynamics. A measure for the sensitivity to mutations of a given structure is the autocorrelation in sequence space as a function of h being the Hamming distance from the reference:

$$\rho(h) \;=\; 1 - \frac{\langle d_{\mathrm{S}}^2(h)\rangle}{\langle d_{\mathrm{S}}^2\rangle} \text{ with } \langle d_{\mathrm{S}}^2(h)\rangle \equiv \left\langle d_{\mathrm{S}}^2\Big(\Phi(\mathbf{X}_j),\Phi(\mathbf{X}_k)\Big)\right| d_{\mathrm{H}}(\mathbf{X}_j,\mathbf{X}_k) = h\Big\rangle . \tag{17}$$

Herein, d_{S} is the structure distance, in $\langle d_{\mathrm{S}}^2(h)\rangle$ the average is taken over all sequences at Hamming distance $d_{\mathrm{H}} = h$ form the reference sequence, i.e. over the error class Γ_h, and in $\langle d_{\mathrm{S}}^2\rangle$ the average is taken over the entire sequence space [35]. The autocorrelation of structures in sequence space, $\rho(h)$, is a measure of the decaying memory on the structure of the reference sequence along a path progressing into sequence space: A short correlation length ℓ means that only a few steps away from any reference sequence the same average distribution of structures is encountered everywhere in sequence space. In particular, the correlation length ℓ measures the distance at which the fraction of reference structures in the environment of a sequence has shrunk to $1/e \approx 0.367879$. For secondary structures of **AUGC**-sequences the correlation length for $\nu = 100$ is about $\ell \approx 7.5$ and for $\nu = 17$ (the chain length of the sequence example $\mathbf{X}_0$ chosen here) it amounts only to $\ell \approx 2$. In other words, going to error class three and higher, $\Gamma_{k\geq 3}$, we can expect to find practically no differences in the distribution of structures with respect to the initially chosen reference sequence.

In order to illustrate the typical form of the local environment in a biopolymer landscape we choose a small RNA of chain length $\nu = 17$ with the sequence $\mathbf{X}_0 \equiv$ **AGCUUACUUAGUGCGCU** as example.[3] At 0 °C the sequence forms the minimum free energy structure $\mathbf{S}_0 = \Phi(\mathbf{X}_0)$, which consists of an hairpin with six base pairs and an internal loop that separates two stacks with three base pairs each (Fig. 9; black structure), and the free energy of structure formation is: $\Delta G_0^{(0)} = -6.39$ kcal/mole. The molecule is relatively stable and has three low lying suboptimal conformations with free energies at 0.29, 0.38, and 0.67 kcal/mole above the minimum free energy structure. These three states differ from the ground state through opening of one or both external base pairs (see e.g. Fig. 9), all three suboptimal configurations are lying within reach of thermal energy and therefore contribute to the partition function of the molecule. The Hamming distance one neighborhood of $\mathbf{X}_0$ consists of $17 \times 3 = 51$ sequences, which form 16 different structures. Out of the 51 sequences 15 form the same minimum free energy structure as $\mathbf{X}_0$ and 10 have also the same minimum free energy implying a local degree of neutrality of $\lambda_0^{(0)} = 0.29$ for structures and $\lambda_0^{(\Delta G)} = 0.19$ for the free energies,

[3] All polynucleotide sequences are written from the 5'-end at the lhs to the 3'-end on the rhs.

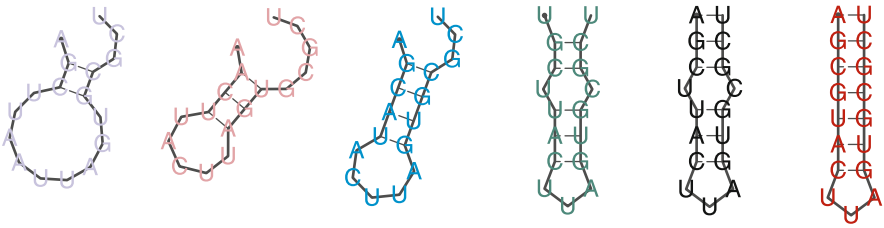

Fig. 9 Selected RNA structures. Shown are examples of RNA structures in the one-error neighborhood of sequence $\mathbf{X}_0$ ordered by the numbers of base pairs. In total, the $3 \times 17 = 51$ sequences form two different structures with two base pairs (1,8; the numbers in parentheses refer to the occurrence of the individual structures), four structures with three base pairs (1,1,2,3), three structure with four base pairs (1,2,3), four structures with five base pairs (1,1,3,4), two structures with six base pairs (2,15), and one structure with seven base pairs (3). The three structures on the rhs have a common folding pattern and differ only by closing and opening of a base pair: (i) the two bases in the internal loop and (ii) the outermost base pair

respectively. The plot of the free energies of folding $\Delta G_0^{(0)}$ for all 51 mutants in Fig. 10 is a perfect illustration of the ruggedness of the free energy landscape: The stability range of the one-error mutants goes from marginal stability at position 2, **G** → **U**, to more than twice the absolute free energy of the reference at position 4, **U** → **G**.

The message of the model studies on sequence-structure mappings and parameter landscapes derived from RNA secondary structures is twofold: The mappings and landscapes are (i) rugged in the sense that nearby lying sequences may give rise to very different structures and stabilities, and (ii) neutral meaning that an appreciable fraction of individual sequences leads to the same structures with practically identical properties. What has been shown here for free energies of folding into minimum free energy structures is valid also for many other functions [34] and thus represents a generic property of biopolymers.

3.2 From Sequences and Structures to Genotypes and Phenotypes

Genotypes or genomes are RNA or DNA sequences. The phenotype comprises structures and functions, both of which are dependent on the specific experimental or environmental setup. The simplest system capable of selection and mutation consists of RNA molecules in a medium that sustains replication. Then, genotype and phenotype are simply the RNA sequence and structure, respectively. In case of evolution experiments with the bacteriophage Qβ the functional requirements are a result of the replication mechanism [4–6]. In order to be replicated the Qβ-virus RNA molecules must carry an accessible recognition site for binding to the enzyme

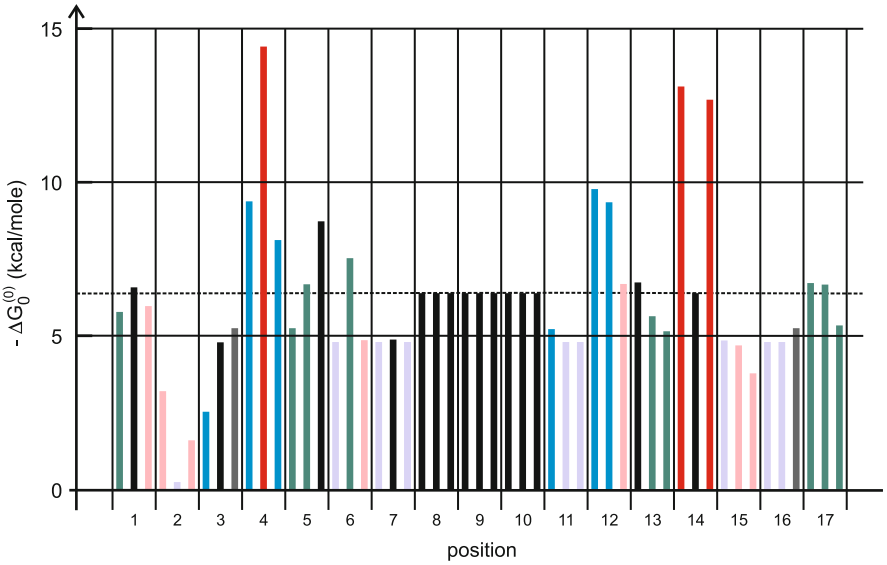

Fig. 10 Free energy landscape of a small RNA. Free energies of folding, $-\Delta G_0^{(0)}$ at 0 °C, are plotted for the individual point mutations, which are grouped according to their positions along the sequence (from 5'- to 3'-end). The color code refers to the number of base pairs in the structures (see Fig. 9): *powder blue* for two base pairs, *pink* for three base pairs, *sky blue* for four base pairs, *grass green* for five base pairs, *black* for six base pairs as in the reference structure, and *red* for seven base pairs. Mutations in the hairpin loop—positions 8, 9, 10—do not change the structure. All calculations were performed with the Vienna RNA Package, version 1.8.5 [43]

Qβ-replicase [2, 83], replication involves a complementary or plus-minus strand copying mechanism, and hance both strands must carry the recognition site. The replication rate parameters for plus-strand and minus strand synthesis are $f_j^{(+)}$ and $f_j^{(-)}$, and after internal equilibration the plus-minus ensemble grows exponentially with an overall fitness constant, which is the geometric mean of the fitness values of both strands: $f_j = \sqrt{f_j^{(+)} f_j^{(-)}}$. Thus, the phenotype in the case of Qβ-replication in the test tube is the ensemble consisting of both strands.

Outside plant cells viroids are *naked*, cyclic, and especially stable RNA molecules whose sequences are the viroid genotypes. Viroid RNAs are multiplied through transcription by the host cell machinery and carry specific recognition sites at which transcription is initiated. Replication of *Potato spindle tuber viroid* (PSTV), for example, starts predominantly at two specific sites with the closely related sequences GGAGCG**A** at position $\mathbf{A}_{111}$ and GGGGCG**A** at position $\mathbf{A}_{325}$ of the viroid RNA with a chain length of $\nu = 359$ nucleotides [33]—the two positions are almost on opposite sides of the cyclic RNA, 214 or 145 nucleotides apart. Viroid RNAs have many loops and bulges that serve two purposes: (i) They allow

for *melting*[4] of the viroid RNA since a fully double stranded molecule would be too stable to be opened, and (ii) they carry the recognition sites and motifs for replication and system trafficking [16, 90], which have also been studied on the 3D structural level [91]. Although viroid reproduction in nature requires a highly specific host cell and there was a common agreement that viroids in general are highly species specific, recent attempts to replicate *Avocado sunblotch viroid* in yeast cells have been successful [14]. The viroid phenotype is already quite involved: It has a structural component that guarantees high RNA stability outside the host cell, but at the same time the structure has to be sufficiently flexible in order to allow for opening of the structure and processing the RNA inside the cell. Like the Qβ RNA, viroid RNA carries specific recognition sites for initiation and control of the reproduction cycle.

Viruses, in essence, are like viroids but the complexity of the life cycle is increased by three important factors: (i) virus DNAs or RNAs carry genes that are translated in the host cell, yield virus specific factors, and accordingly viruses have genetic control on the evolution of these coding regions, (ii) the virus capsid may contain functional protein molecules, for example replicases, in addition to the virus specific genetic material, and (iii) viruses are coated by virus specific proteins or proteins and membranes (For a recent treatise of virus evolution see, e.g., [20]). Because of the relative simplicity compared to cellular life, fast replication, and high mutation rates virus evolution has been modeled in some detail and the quasispecies concept was found to be particularly suitable for virus populations (see, e.g., [9, 17–19, 29, 53, 63, 64]). Although plenty of fitness data are available, which deal with very few genetic loci or alleles, comprehensive large scale studies are practically non existing. A very recent exception is a large scale study on HIV-1 [51]: In essence, the expectations derived from theoretical studies—ruggedness, neutrality, and the importance of high dimensionality—are confirmed, although the correlation lengths appear to be longer than expected.

Bacterial phenotypes are currently to complex for a comprehensive analysis at the molecular level. An exception are the particulary small and cell-wall free bacteria of the genus *Mycoplasma*. In particular, *Mycoplasma genitalium* is a parasitic bacterium and was considered to be the smallest organism for quite some time.[5] Its genome consists of one circular chromosome with 582,970 base pairs and 521 genes of which 482 encode for proteins. Extensive studies aiming at full systems biology of a cellular organism were performed on the some what larger species *Mycoplasma pneumoniae* with a genome size of $\nu \approx 816,000$ base pairs [40, 52, 89]. For larger organisms—ordinary bacteria of about tenfold size and small eukaryotic cells—flux balance analysis [57] rather than full molecular systems biology has been

[4]The notion melting a stacking region of a polynucleotide means opening of the double helix in order to yield the two single strands. The analogy to the melting process comes from the fact that rising temperature leads to opening of stacks.

[5]The smallness record is currently hold by *Nanoarchaeum equitans* with a genome size of 490,885 base pairs.

performed (An early example of flux balance analysis of *Escherichia coli* is found in [22]). Another approach to complex phenotypes is based on completely annotated genomes and information on gene interactions mainly coming from proteomics. A gene interaction network has been worked out recently for a small eukaryotic cell with roughly 6,000 genes [10] and it is overwhelmingly complex.

4 Evolutionary Dynamics on Realistic Landscapes

As outlined in the previous Sect. 3.1 two features are fundamental for *realistic landscapes*: (i) ruggedness and (ii) neutrality. They were not only found with landscapes derived from RNA but also with those from proteins [42]. The Japanese population geneticist Motoo Kimura realized that a large number of mutations has no influence on fitness [49] and conceived a theory of evolution that is based on neutrality. Kimura's theory describes *random selection*, which is a stochastic process that is induced by replication and leads to almost homogeneous populations of a particular sequences chosen at random. Still the interplay of ruggedness and neutrality is not completely understood yet [11], and almost all information comes from computer simulations using ad hoc model landscapes[36, 37, 45].

Models for rugged fitness landscapes have been proposed, the most popular example is the Nk-model due to Stuart Kauffman [47, 48, 84] that is based on individual loci on a genome and interactions between them: N is the number of loci and k is the number of interacting loci. A random element, which is drawn from a predefined probability distribution—commonly the normal distribution—and which defines the interaction network, is added to the otherwise deterministic model: N and k are fixed and not subjected to variation. Here, a different approach is proposed that starts out from the nucleotide sequence of a genome rather than from genes and alleles and consequently it is directly anchored in sequence space. Ruggedness and neutrality are introduced by means of tunable parameters, d and λ, and pseudorandom numbers are used to introduce random scatter, which reflects the current ignorance with respect to detailed fitness values and which is thought to be replaced by real data when they become available in the near future.

4.1 Realistic Rugged Landscapes (RRL)

A new type of landscapes, the *realistic rugged landscape* (RRL), is introduced and analyzed here. Ruggedness is modeled by assigning fitness differences at random within a band of fitness values with adjustable width d. The highest fitness value is attributed to the master sequence $\mathbf{X}_m \doteq \mathbf{X}_0$, $f_m = f_0$, and the fitness values are obtained by means of the equation

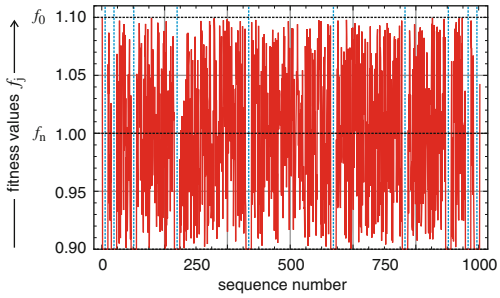

Fig. 11 A realistic rugged fitness landscape. The landscapes for 1,024 binary sequences of chain length $\nu = 10$ is constructed according to (18). The band width of random scatter was chosen to be maximal, $d = 1$, and $s = 637$ was applied. The *broken blue lines* separate different mutant classes

$$f(\mathbf{X}_j) = f_j = \begin{cases} f_0 & \text{if } j = 0\,, \\ f_s + 2d(f_0 - f_s)\left(\eta_j^{(s)} - 0.5\right) & \text{if } j = 1,\ldots,\kappa^\nu\,, \end{cases} \tag{18}$$

where $\eta_j^{(s)}$ is the j-th output random number from a pseudorandom number generator with a uniform distribution of numbers in the range $0 \le \eta_j^{(s)} \le 1$ that has been started with the seed s,[6] which will be used to characterize a particular distribution of fitness values (Fig. 11). The parameter d determines the amount of scatter around the mean value $\bar{f}_{-0} = f_s$, which is independent of d: $d = 0$ yields the single peak landscape, and $d = 1$ leads to fully developed or maximal scatter where individual fitness values f_j can reach the value f_0. Two properties of realistic rugged landscapes fulfilled by fitness values relative to the mean except the master, $\varphi_j = f_j - f_s \,\forall\, j = 0,\ldots,\kappa^\nu$, are relevant: (i) the ratio of two relative fitness values of sequences within the mutant cloud is independent of the scatter d and (ii) the ratio of the relative fitness values of a sequence from the cloud and the master sequence is proportional to the scatter d:

$$\frac{\phi_j}{\phi_k} = \frac{\eta_j^{(s)} - 0.5}{\eta_k^{(s)} - 0.5}\,;\; j,k = 1,\ldots,\kappa^\nu \text{ and} \tag{19a}$$

$$\frac{\phi_j}{\phi_0} = 2\,d\left(\eta_j^{(s)} - 0.5\right);\; j = 1,\ldots,\kappa^\nu\,. \tag{19b}$$

These properties allow for an investigation of the role of random scatter without changing the fitness relations with the error classes.

[6]The seed s indeed determines all details of the landscape, which is completely defined by s and the particular type of the pseudorandom number generator as well as by f_0, f_s, and d. Here we use the pseudorandom number generator *Legacy* of the software package *Mathematica* [86].

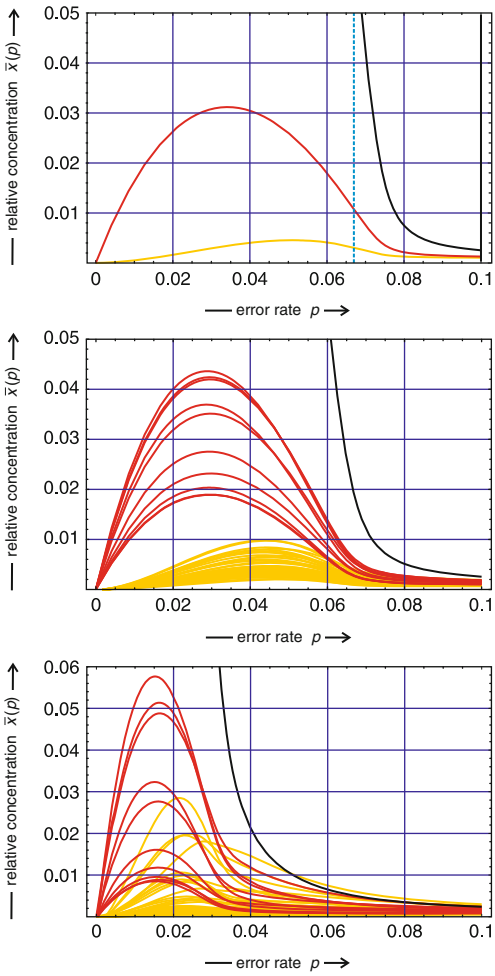

Fig. 12 Quasispecies on *realistic* model landscapes with different random scatter d. Shown are the stationary concentrations $\bar{x}_j(p)$ on a landscape with $s = 491$ for $d = 0$ (*upper plot*), $d = 0.5$ (*middle plot*), and $d = 0.9375$ (*lower plot*). In the topmost plot the curves for all sequences in class Γ_1 coincide, and so do the curves in class Γ_2 since zero scatter, $d = 0$, has been chosen. The error threshold calculated by perturbation theory lies at $p_{\mathrm{cr}} = 0.066967$ (*blue broken line*). Other parameters: $\nu = 10$, $f_0 = 2.0$, and $f_s = 1.0$. Color code: Γ_0 *black*, Γ_1 *red*, and Γ_2 *yellow*

We are now in a position to explore whether or not the results derived from simple single peak model landscapes and reported in Sect. 2 are representative for mutation-selection dynamics on realistic landscapes. The influence of random scatter on quasispecies and error thresholds on landscapes of sequences of chain length $\nu = 10$ has been studied in detail.[7] Despite the short chain length of $\nu = 10$ the plots in Fig. 12 reflect the threshold phenomena rather well, the width of the transition to the uniform distribution is hardly changing, and the decay of the concentration of the master sequence is shifted towards smaller p-values with

[7]The chain length for which diagonalization of the value matrix W can be routinely performed lies at rather small chain lengths around the $\nu = 10$ giving rise to a matrix size of 1000×1000. It has been shown that such a short chain length is sufficient to yield representative results provided the fitness parameters f_0 and f_s are chosen appropriately (Fig. 12).

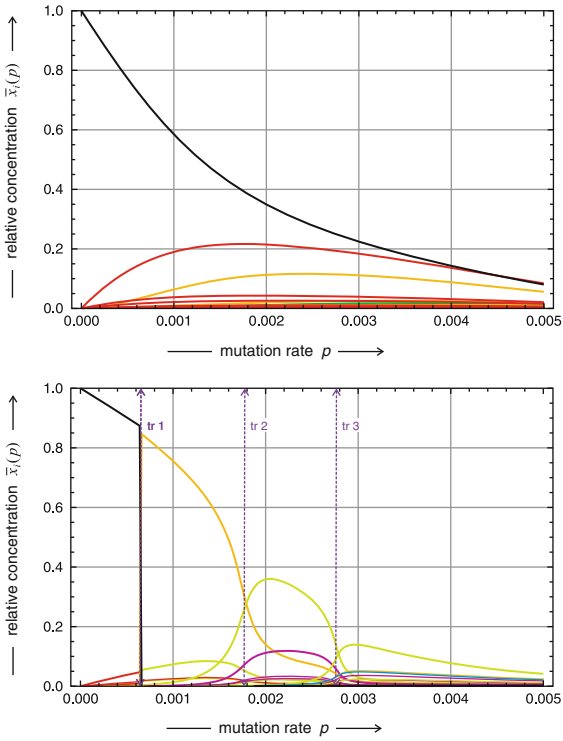

Fig. 13 Quasispecies on *realistic* model landscapes with different random seeds s. Shown are the stationary concentrations $\bar{x}_j(p)$ on landscapes with $s = 919$ and $d = 1$ (*upper plot*), and $s = 637$ and $d = 1$ (*lower plot*). The *upper plot* shows a *strong quasispecies* that is stable from $p = 0$ up to the error threshold at $p = p_{\mathrm{cr}} = 0.0084$. The landscape in the lower plot sustains four different quasispecies, which are separated by three transitions: tr1, $\Upsilon_{\mathbf{0}} \leftrightarrow \Upsilon_{\mathbf{1003}}$ at $p = 0.0007$; tr2, $\Upsilon_{\mathbf{1003}} \leftrightarrow \Upsilon_{\mathbf{923}}$ at $p = 0.0018$; and tr3, $\Upsilon_{\mathbf{923}} \leftrightarrow \Upsilon_{\mathbf{247}}$ at $p = 0.0028$. The error threshold lies at $p_{\mathrm{cr}} = 0.0083$ (outside the plot). Other parameters: $\nu = 10$, $f_0 = 1.1$, and $f_s = 1.0$. Color code: Γ_0 *black*, Γ_1 *red*, Γ_2 *yellow*, Γ_3 *green*, Γ_4 *cyan*, Γ_5 *blue*, Γ_6 *magenta*, Γ_7 *chartreuse*, Γ_8 *yellow*, Γ_9 *red*, and Γ_{10} *black*

increasing d. For moderate random scatter ($d = 0.5$; middle plot) the curves for the sequences of the individual classes form bands, which do not overlap before the quasispecies approaches the error threshold. At large scatter (bottom plot) the bands start to overlap already at small p-values.

Differences between individual landscapes at moderate band width d—according to different seeds s—concerns only the distribution of curves within the bands. At large band widths $d \to 1$, however, qualitatively different behavior may be observed (Fig. 13). Some landscapes sustain the same quasispecies for the entire range of ordered replication from $p = 0$ up to the error threshold at $p = p_{\mathrm{cr}}$ (upper plot in the figure) and point at a remarkable stability of the stationary mutant distribution, which is expressed in the term *strong quasispecies* that has been coined for such a scenario. On the majority of landscapes transitions between different quasispecies are observed (lower plot in the figure). These transitions occur at error rates where

the difference in fitness between the two master sequences is compensated by the mutational backflow [71] (13 years later this phenomenon was called *survival of the flattest* [85]). At mutation rates p below the transition the master sequence with the higher fitness value and weaker mutational backflow dominates, and above the transition the sequence with lower fitness but stronger mutational backflow is prevailing. The position of the transition, $p = p_{\mathrm{tr}}$, can be calculated by means of perturbation theory in the spirit of (10), the expressions, however, are rather complicated and we refer therefore here only to the literature [71].

The evolutionary dynamics on a given landscape can often be predicted from a few special fitness values. The occurrence of strong quasispecies, for example, requires four nearest neighbor sequences with high fitness values, which form a cluster coupled by strong mutational backflow (Fig. 14): One of these sequences is the master sequence $\mathbf{X}_0$, one or two sequences are situated in error class Γ_1 and the fourth sequences is in error class Γ_2. It turned to be sufficient if one of the two error class Γ_1 sequences has an especially high fitness value. In the strong quasispecies shown in Fig. 13 the sequences and their fitness values are: $\mathbf{X}_0$ with $f_0 = 1.1$ (by definition), $\mathbf{X}_4$ with $f_4 = 1.0966$, $\mathbf{X}_{512}$ with $f_{512} = 0.9296$, and $\mathbf{X}_{516}$ with $f_{516} = 1.0970$, and the sequences with the high fitness values are present at the highest concentrations ($\mathbf{X}_0$ black, $\mathbf{X}_4$ red, and $\mathbf{X}_{516}$ yellow) (Fig. 14).

4.2 Rugged and Neutral Landscapes (RNL)

In case of neutral fittest sequences of Hamming distances $d_{\mathrm{H}} = 1$ or $d_{\mathrm{H}} = 2$ replication-mutation networks are formed and we shall denote them as *master pairs* or *master clusters*. An important issue of the realistic landscape approach is the random positioning of neutral master sequences in sequence space, which can be achieved by means of the same random number generator that is used to compute the random scatter of the other fitness values obtained from pseudorandom numbers with a uniform distribution in the interval $0 \le \eta \le 1$:

$$f(\mathbf{X}_j) = \begin{cases} f_0 & \text{if } j = 0\,, \\ f_0 & \text{if } \eta_j^{(s)} \ge 1-\lambda\,, \\ f_s + \frac{2d}{1-\lambda}(f_0 - f_s)\left(\eta_j^{(s)} - 0.5\right) & \text{if } \eta_j^{(s)} < 1-\lambda\,, \\ & j = 1,\ldots,\kappa^{\nu};\ j \ne m\,. \end{cases} \tag{20}$$

The rugged and neutral fitness landscape (20) is a straightforward extension of the purely rugged fitness landscape (18) meeting the condition that several master sequences with fitness f_0 exist. There are two limiting cases: (i) $\lim \lambda \to 0$ yielding the non-neutral random landscape (18) and (ii) $\lim \lambda \to 1$ leading to the fully neutral case of Motoo Kimura [50]. The fraction of neutral mutants is determined by the fraction of random numbers, which fall into the range $1 - \lambda < \eta \le 1$, and

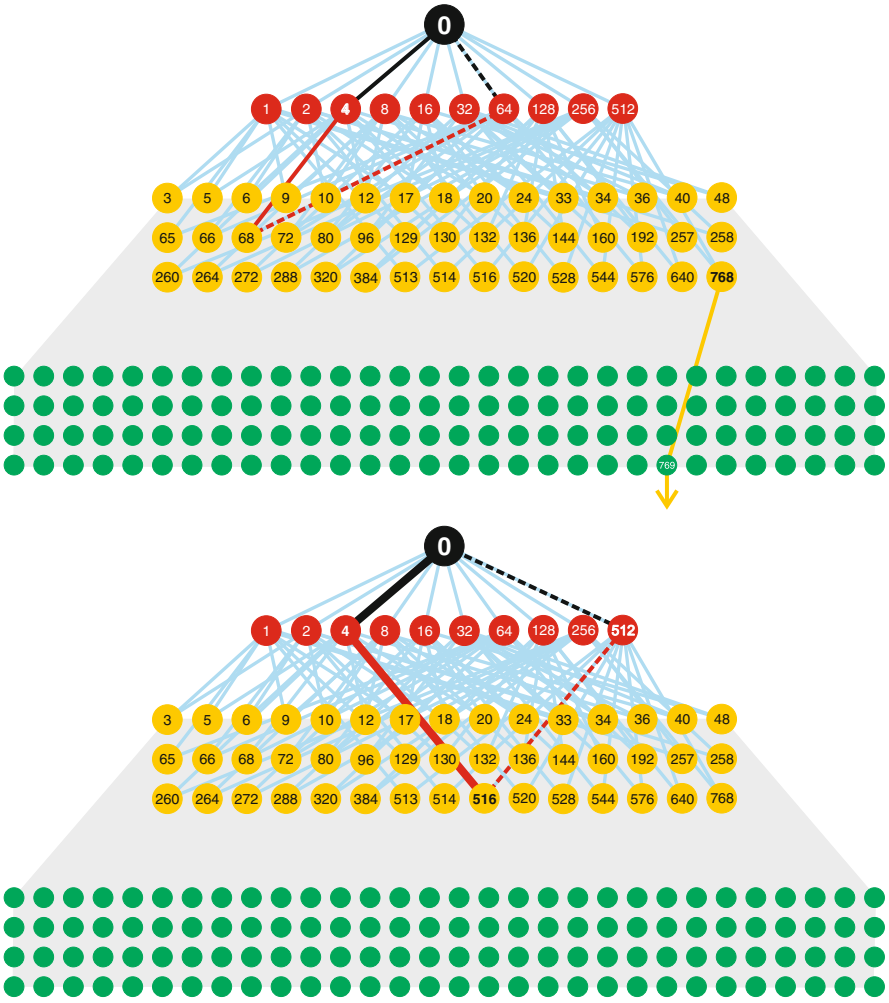

Fig. 14 Mutation flow in quasispecies. The sketch shows two typical situations in the distribution of fitness values in sequence space. In the upper diagram ($s = 637$) the fittest two-error mutant, $\mathbf{X}_{768}$, has its fittest nearest neighbor, $\mathbf{X}_{769}$, in the three-error class Γ_3, and the fittest sequence in the one-error neighborhood of $\mathbf{X}_4$ (being the fittest sequence in the one-error class), $\mathbf{X}_{68}$, is different from $\mathbf{X}_{768}$, the mutational flow is not sufficiently strong to couple $\mathbf{X}_0$, $\mathbf{X}_4$, and $\mathbf{X}_{68}$, and transitions between different quasispecies are observed (Fig. 13). The lower diagram ($s = 919$) shows the typical fitness distribution for a strong quasispecies: The fittest two-error mutant, $\mathbf{X}_{516}$, has its fittest nearest neighbor, $\mathbf{X}_4$, in the one-error class Γ_1 and it coincides with the fittest one-error mutant. Accordingly, the three sequences ($\mathbf{X}_0$, $\mathbf{X}_4$, and $\mathbf{X}_{516}$) are strongly coupled by mutational flow and a strong quasispecies is observed (Fig. 13). Sequence $\mathbf{X}_{512}$ is also part of this cluster but because of low fitness plays no role in this particular case

apart from statistical fluctuations this fraction is λ. At small values of the degree of neutrality λ isolated peaks of highest fitness f_0 will appear in sequence space. Increasing λ will result in the formation of neutral networks or clusters of sequences with highest fitness.

Replication without mutation on purely neutral landscapes is a stochastic process that leads to selection of one randomly chosen sequence. Mutation changes the outcome of the evolutionary process. Depending on the Hamming distance between the neutral sequences either a group of master sequences coupled by selection dynamics is formed or random selection takes place and only one sequence survives in the sense of Kimura's theory. The case of vanishing mutation rates, $\lim p \to 0$, has been analyzed for two neutral sequences [71], $\mathbf{X}_j$ and $\mathbf{X}_k$, at different Hamming distance $d_{\mathrm{H}}(\mathbf{X}_j, \mathbf{X}_k)$:

(i) $d_{\mathrm{H}} = 1$: $\lim_{p\to 0} \frac{\bar{x}_j}{\bar{x}_k} = 1$ or $\lim_{p\to 0} \bar{x}_j = \lim_{p\to 0} \bar{x}_k = 1/2$,
(ii) $d_{\mathrm{H}} = 2$: $\lim_{p\to 0} \frac{\bar{x}_j}{\bar{x}_k} = \alpha$ or $\lim_{p\to 0} \bar{x}_j = \alpha/(1+\alpha)$, $\lim_{p\to 0} \bar{x}_k = 1/(1+\alpha)$, with some value $0 \le \alpha \le 1$, and
(iii) $d_{\mathrm{H}} \ge 3$: $\lim_{p\to 0} \bar{x}_1 = 1$, $\lim_{p\to 0} \bar{x}_2 = 0$ or $\lim_{p\to 0} \bar{x}_1 = 0$, $\lim_{p\to 0} \bar{x}_2 = 1$.

The mutational flow apparently counteracts successfully random selection provided the Hamming distance is short enough. It is remarkable that the mutational flow prevails even in the limit $p \to 0$ and thus selects one particular state at $p = 0$ where all combinations of concentrations $[\mathbf{X}_j] + [\mathbf{X}_k] = 1$ are solutions on an equal footing because of degeneracy.

In order to check the role of the predictions for the limit $p \to 0$ in the case of nonzero mutation rates we search for appropriate test cases by inspection of landscapes according to (20). For small degrees of neutrality we found indeed suitable neutral clusters on the landscapes ($s = 637, \lambda = 0.01$; Fig. 15) and ($s = 877, \lambda = 0.01$; Fig. 16). In full agreement with the exact result we find that two fittest sequences of Hamming distance $d_{\mathrm{H}} = 1$ are selected as a strongly coupled pair with equal frequency of both members and numerical results show that strong coupling does not occur only for small mutation rates but extends over the whole range of p-values from $p = 0$ up to the error threshold $p = p_{\mathrm{cr}}$ (Fig. 15). Examples for the case $d_{\mathrm{H}} = 2$ are also found on random neutral landscapes and again the exact result for vanishing mutation rate holds up to the error threshold. The existence of neutral nearest and next nearest neighbors manifest itself by the lack of a unique consensus sequence of the population has an important consequence for phylogeny reconstruction (see Fig. 17).

Neutral networks may comprise several sequences and then, all neutral nearest neighbor sequences form a strongly coupled master cluster in reproduction. The distribution of individual members of the cluster in the limit $p \to 0$ are readily obtained by diagonalization of the adjacency matrix.[8] The components of the largest

[8]The adjacency matrix of a graph, A, is a symmetric square matrix that has an entry $a_{jk} = a_{kj} = 1$ whenever the graph has an edge between the nodes for $\mathbf{X}_j$ and $\mathbf{X}_k$ and zero entries everywhere else.

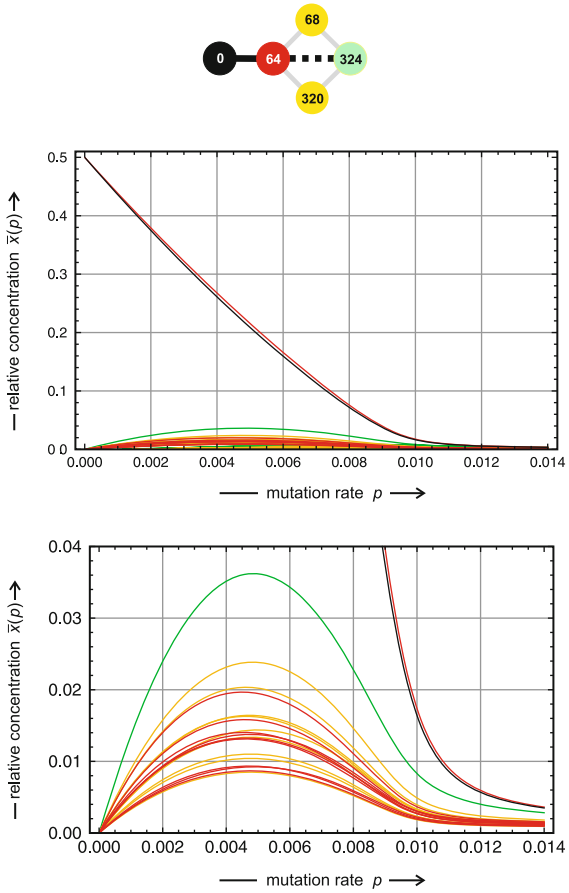

Fig. 15 Quasispecies on a realistic landscape with two neutral nearest neighbor sequences. The landscape ($s = 367, \lambda = 0.01$) sustains two neighboring sequences of highest fitness ($f_0 = 1.1$) forming a master pair of Hamming distance $d_H = 1$, $\mathbf{X}_0$ and $\mathbf{X}_{64}$. The master pair is surrounded by 18 single point mutations (*red* and *yellow*) in the quasispecies $\Upsilon_{\mathbf{0.64}}$. A third neutral sequence $\mathbf{X}_{324}$ (*green*) is situated at Hamming distance $d_H = 3$ and $d_H = 2$ from the two master sequences $\mathbf{X}_0$ and $\mathbf{X}_{64}$, respectively, and it is more abundant than the single point mutations $\mathbf{X}_{68}$ and $\mathbf{X}_{320}$. The sketch at the top shows the network of the five coupled sequences. The plots shows the dependence of the joint quasispecies on the point mutation rate p The plot at the bottom is an enlargement of the plot in the middle. The concentrations of the two master sequences are practically identical for all mutations rates. Color code: master sequences (*black* and *red*), the colors are standard colors for all sequences centered around $\mathbf{X}_m = \mathbf{X}_0$ (see caption of Fig. 13). Further parameters: $n = 10$, $f_0 = 1.1$, $f_s = 1.0$, $d = 0.5$

eigenvector are proportional to the concentrations of elements of the replication network. Increasing the degree of neutrality λ gives rise to the formation of larger neutral networks. Commonly there is a *giant cluster* and many small clusters as predicted by random graph theory and sketched in Fig. 8.

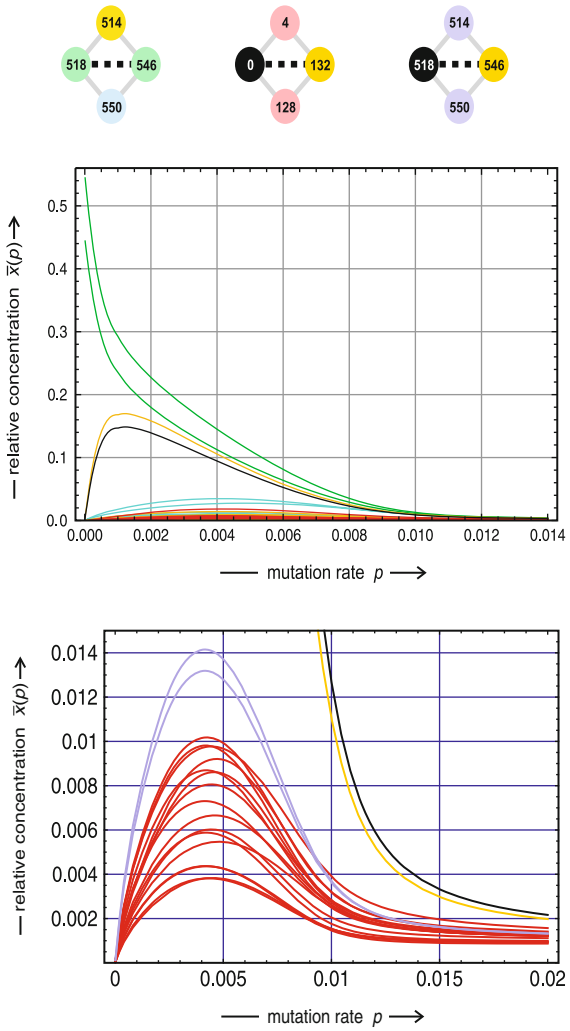

Fig. 16 Quasispecies on a realistic landscape with two neutral next nearest neighbor sequences. The landscape ($s = 877, \lambda = 0.01$) sustains two nest nearest neighbor sequences of highest fitness ($f_0 = 1.1$) forming a master pair of Hamming distance $d_H = 2$, $\mathbf{X}_{518}$ and $\mathbf{X}_{546}$. There is also a second neutral network of the same type on this landscape that involves the two Hamming distance $d_H = 2$ sequences $\mathbf{X}_0$ and $\mathbf{X}_{132}$. The sketch on top of the figure shows the two networks, the diagram on the rhs gives the color code for the enlargement in the plot at the bottom of the figure. The middle part of the figure presents the solution curves for the quasispecies $\Upsilon_{\mathbf{518,546}}$, which contains the cluster $\{\mathbf{X}_0, \mathbf{X}_{132}\}$ in the mutant cloud. The plot at the bottom is an enlargement, shows the quasispecies $\Upsilon_{\mathbf{518,546}}$ centered around **518** and restricted to the master pair and all one error mutants (*red*). The curves for the two intermediate sequences $\mathbf{X}_{514}$ and $\mathbf{X}_{550}$ are highlighted in pastel blue (see rightmost diagram at the top of the figure). Color code for the plot in the middle: master sequences (*green*), the colors are standard colors for all sequences centered around $\mathbf{X}_0$ (see caption of Fig. 13). Further parameters: $n = 10$, $f_0 = 1.1$, $f_s = 1.0$, $d = 0.5$

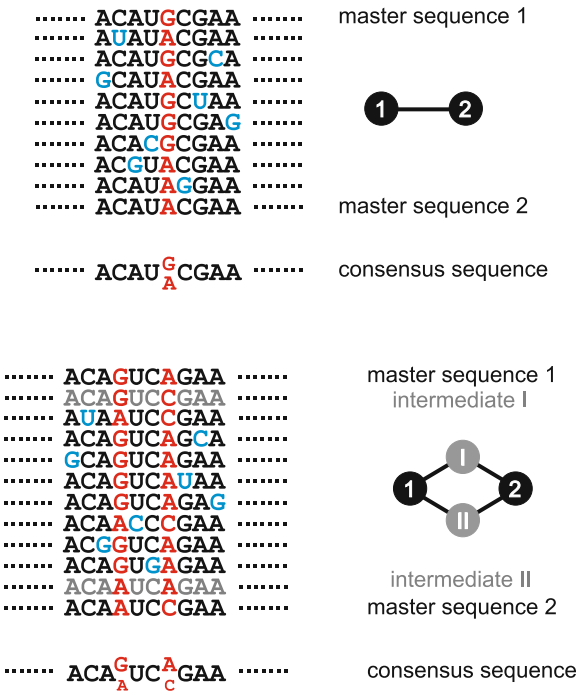

Fig. 17 Quasispecies and consensus sequences in case of neutrality. The upper part of the figure shows a sketch of sequences in the quasispecies of two fittest nearest neighbor sequences ($d_H = 1$). The consensus sequence is not unique and differs in a single position where both nucleotides appear with equal frequency. In the lower part the two master sequences have Hamming distance $d_H = 2$ and differ in two positions. The two sequences are present at some ratio α that is determined by the fitness values of other neighboring sequences, and the nucleobases corresponding to the differences in the two master sequences appear with the same ratio α

5 Perspectives and Limitations of the Kinetic Approach

The conventional synthetic theory of evolution considers reproduction of organisms rather than molecules [54]. In contrast, the kinetic theory of evolution [23, 25, 26] is dealing with the evolutionary processes at the molecular level. Correct reproduction and mutation are implemented as parallel reactions and various detailed mechanisms of reproduction can be readily incorporated into the kinetic differential equations. An extensively investigated example is RNA replication by means of an enzyme from the bacteriophage Qβ [4–6, 83]. The detailed kinetic analysis reveals precise conditions for the applicability of the mutation-selection model (4): Given activated nucleobases are available in excess the RNA concentration has to be smaller than the concentration of the replication enzyme. Provided the mechanism of reproduction is known, it can be implemented straightforwardly into replication kinetics based on ordinary differential equations (ODEs) [58, pp. 29–75]. This is true likewise for epigenetic effects, which may require the use of delay differential equations. Furthermore, the kinetic theory rather than the conventional population genetics approach is the appropriate basis for molecular evolution and molecular phylogeny, since these concepts deal with genes and genomes as molecules within cells and organisms and not with the organisms themselves. The molecular approach is able to account for complex dynamical interactions, and this is indispensable, because evolution does not care for elegance, simplicity, symmetry or optimality, the only thing that matters is efficiency.

Explicit consideration of mutations as parallel reactions to error-free reproduction is manifested in the structure of stationary populations, no ad hoc assumptions are required for the appearance of mutants. In addition, high mutation rates as found, for example, in test tube evolution experiments [3, 7, 74] and in virus reproduction [20] do not represent a problem and are handled equally well as low mutation rates. The kinetic model relates evolutionary dynamics directly to fitness landscapes, which have a straightforward physical interpretation and are accessible experimentally. Unclear, ambiguous, and wrong results are obtained with simple models of fitness landscapes and they demonstrate that an understanding of evolution is impossible without sufficient knowledge on the molecular basis of fitness. In simple systems fitness is a property that can be determined by the methods of physics and chemistry, and thus independently of evolutionary dynamics. The current explosion of harvested data provides a new source of molecular information that can be used for the computation of fitness values under sufficiently simple conditions.

The quasispecies is the stationary solution of a deterministic, differential equation based model that, in principle, is bound to constant population size. Analysis of the basic ODEs, however, has shown that the results in relative concentrations (x_i; $\sum_{i=1}^{n} x_i = 1$) are generally valid as long as the population does neither die out ($\sum_{i=1}^{n} N_i \to 0$) nor explode ($\sum_{i=1}^{n} N_i \to \infty$) [26]. Then, particle numbers are not normalizable and the structure of the population cannot be predicted from solutions of (4). Nevertheless, quasispecies may still exist for vanishing populations but any rigorous treatment has to start out from the original kinetic equations with population size being treated as a variable. Variants with zero fitness are compatible with the error threshold phenomenon [77, 78] but the prerequisites for the conventional calculation of the quasispecies are no longer fulfilled—not every sequence can be reached from every sequence by a finite chain of point mutations and Perron-Frobenius theorem does not hold.

Another question is hard to answer at present: Do populations in nature ever reach a stationary state? In vitro evolution experiments can be carried out in such a way that stationarity or mutation equilibrium is achieved, but is this true also in nature? In virus infections specific mutants appear also within the infected host but on the other hand the effect of infection and the course of disease is rather similar with comparable hosts indicating that viruses are in a comparable state at least at the beginning of an infection.

Two other problems are quite general in biological modeling in particular on the molecular level: (i) Most models assume spatial homogeneity whereas cells are highly structured objects with limited diffusion, active transport, and spatial localization of molecular players, and (ii) many results are derived from differential equations, which are based on the use of continuous variables, and thereby it is implicitly assumed that populations are very large. In principle, the definition of continuous space and time requires infinite population size and this is a reasonable and well justified assumption in chemistry but not in biology where sample sizes may be very small. Examples are the often extremely small concentrations of regulatory molecules. Systematic studies on the very small bacterium *Mycoplasma*

pneumoniae in the spirit of systems biology [40, 52, 89] have shown that in extreme cases only one molecule per hundreds or even thousands of bacterial cells is present at a given instant in the population. Also the assumption of a homogeneous space is questionable: There is very little free diffusion in real cells and even bacterial cells have a very rich spatial structure. Stochasticity plays an important role and discrete stochastic rather than deterministic continuous variables should be applied more in the future. Also a combination of stochastic events with ODE modeling between individual jumps might well be suitable for modeling in systems biology.

Finally we mention another general problem for evolutionary models. Using conventional modeling with ODEs all populations would extend over whole sequence space. A drastic example is the uniform distribution of sequences, which is predicted at mutation rates above the error threshold. Coverage of sequence space can never occur in a finite world: Even for small RNA molecules of tRNA size we would need a population size of $N = 10^{46}$ individuals in order to have one molecule for every possible sequence whereas the largest populations in in vitro experiments with RNA hardly exceed $N = 10^{15}$ molecules. What we have instead are clones of sequences migrating through sequence space (see, for example, [15, 36, 37, 45]. Truncation of fitness landscapes has been suggested recently as a possible solution to the problem [61]. Alternatively, one could leave the full landscape and truncate populations through setting all concentrations less than one molecule per reaction volume equal to zero and eliminate the corresponding variables [65]. New variables come into play when their concentration exceeds this truncation threshold similarly as occurring in stochastic processes.

Acknowledgement The author wishes to acknowledge support by the University of Vienna, Austria and the Santa Fe Institute, USA.

References

1. Aguirre-Hernandéz, R., Hoos, H.H., Condon, A.: Computational RNA secondary structure design: empirical complexity and improved methods. BMC Bioinformat. **8**, e34 (2007)
2. Biebicher, C.K., Luce, R.: In vitro recombination and terminal elongation of RNA by Qβ replicase. The EMBO J. **11**(13), 5129–5135 (1992)
3. Biebricher, C.K.: Darwinian selection of self-replicating RNA molecules. In: Hecht, M.K., Wallace, B., Prance, G.T. (eds.) Evolutionary Biology, vol. 16, pp. 1–52. Plenum Publishing Corporation, New York (1983)
4. Biebricher, C.K., Eigen, M., William, C., Gardiner, J.: Kinetics of RNA replication. Biochemistry **22**, 2544–2559 (1983)
5. Biebricher, C.K., Eigen, M., William, C., Gardiner, J.: Kinetics of RNA replication: plus-minus asymmetry and double-strand formation. Biochemistry **23**, 3186–3194 (1984)
6. Biebricher, C.K., Eigen, M., William, C., Gardiner, J.: Kinetics of RNA replication: competition and selection among self-replicating RNA species. Biochemistry **24**, 6550–6560 (1985)
7. Biebricher, C.K., Gardiner, W.C. Jr: Molecular evolution of RNA in vitro. Biophys. Chem. **66**, 179–192 (1997)

8. Carlson, E.A.: Mutation. The History of an Idea from Darwin to Genomics. Cold Spring Harbor Laboratory Press, Cold Spring Harbor, NY (2011)
9. Ciota, A.T., Kramer, L.D.: Insights into arbovirus evolution and adaptation from experimental studies. Viruses **2010**(2), 2594–2617 (2010)
10. Costanzo, M., Baryshnikova, A., Bellay, J., Kim, Y., Spear, E.D., Sevier, C.S., Ding, H., Koh, J.L.Y., Toufighi, K., Mostafavi, S., Prinz, J., Onge, R.P.S., Van der Sluis, B., Makhnevych, T., Vizeacoumar, F.J., Alizadeh, S., Bahr, S., Brost, R.L., Chen, Y., Cokol, M., Deshpande, R., Li, Z., Li, Z.-Y., Liang, W., Marback, M., Paw, J., San Luis, B.-J., Shuteriqi, E., Tong, A.H.Y., van Dyk, N., Wallace, I.M., Whitney, J.A., Weirauch, M.T., Zhong, G., Zhu, H., Houry, W.A., Brudno, M., Ragibizadeh, S., Papp, B., Pál, C., Roth, F.P., Giaver, G., Nislow, C., Troyanskaya, O.G., Bussey, H., Bader, G.D., Gingras, A.-C., Morris, Q.D., Kim, P.M., Kaiser, C.A., Myers, C.L., Andrews, B.J., Boone, C.: The genetic landscape of a cell. Science **317**, 425–431 (2010)
11. Crutchfield, J.P., Schuster, P. (eds.): Evolutionary Dynamics – Exploring the Interplay of Accident, Selection, Neutrality and Function. Oxford University Press, New York (2003)
12. Darwin, C.: On the Origin of Species by Means of Natural Selection of the or the Preservation of Favoured Races in the Struggle for Life, 1st edn. John Murray, London (1859)
13. De Vries, H.: Species and Varieties. Their Origin by Mutation. The Open Court Publishing Company, Chicago (1904)
14. Delan-Forino, C., Maurel, M., Torchet, C.: Replication of *avocado sunblotch viroid* in the yeast *saccaromyces cerevisiae*. J. Virol. **85**, 3229–3238 (2011)
15. Derrida, B., Peliti, L.: Evolution in a flat fittness landscape. Bull. Math. Biol. **53**, 355–382 (1991)
16. Ding, B., Itaya, A.: Viroid: a useful model for studying the basic principles of infection and RNA biology. Molecular Plant Microbe Interac. **20**, 7–20 (2007)
17. Domingo, E., Escarmis, C., Lázaro, E., Manrubia, S.C.: Quasispecies dynamics and RNA virus extinction. Virus Res. **107**, 129–139 (2005)
18. Domingo, E., Holland, J.J.: RNA virus mutations and fitness for survival. Annu. Rev. Microbiol. **51**, 151–178 (1997)
19. Domingo, E., Menédez-Arias, L., Holland, J.J.: RNA virus fitness. Rev. Med. Virol. **7**, 87–96 (1997)
20. Domingo, E., Parrish, C.R., John H.J. (eds.): Origin and Evolution of Viruses, 2nd edn. Elsevier, Academic, Amsterdam (2008)
21. Domingo, E. (ed.): Virus entry into error catastrophe as a new antiviral strategy. Virus Res. **107**(2), 115–228 (2005)
22. Edwards, J.S., Ibarra, R.U., Palsson, B.Ø.: *In silico* predictions of *escherichia coli* metabolic capabilities are consistent with experimental data. Nat. Biotechnol. **19**, 125–130 (2001)
23. Eigen, M.: Selforganization of matter and the evolution of biological macromolecules. Naturwissenschaften **58**, 465–523 (1971)
24. Eigen, M., McCaskill, J., Schuster, P.: The molecular quasispecies. Adv. Chem. Phys. **75**, 149–263 (1989)
25. Eigen, M., Schuster, P.: The hypercycle. A principle of natural self-organization. Part A: Emergence of the hypercycle. Naturwissenschaften **64**, 541–565 (1977)
26. Eigen, M., Schuster, P.: The hypercycle. A principle of natural self-organization. Part B: The abstract hypercycle. Naturwissenschaften **65**, 7–41 (1978)
27. Eigen, M., Schuster, P.: The hypercycle. A principle of natural self-organization. Part C: The realistic hypercycle. Naturwissenschaften **65**, 341–369 (1978)
28. Eigen, M., Schuster, P.: Stages of emerging life – Five principles of early organization. J. Mol. Evol. **19**, 47–61 (1982)
29. Elena, S.F., Ricard, S.V., Sardanyés, J.: Simple genomes, complex interactions: Epistasis in RNA virus. Chaos **20**, 026106 (2010)
30. Engl, H.W., Flamm, C., Kügler, P., Lu, J., Müller, S., Schuster, P.: Inverse problems in systems biology. Inverse Problems **25**, 123014 (2009)
31. Erdős, P., Rényi, A.: On random graphs. I. Publicationes Mathematicae **6**, 290–295 (1959)

32. Erlich, H.A. (ed.): PCR Technology. Principles and Applications for DNA Amplification. Stockton, New York (1989)
33. Fels, A., Hu, K., Riesner, D.: Transcription of potato spindle tuber viroid by RNA polymerase II starts predominantly at two specific sites. Nucleic Acids Res. **29**, 4589–4597 (2001)
34. Fontana, W., Griesmacher, T., Schnabl, W., Stadler, P.F., Schuster, P.: Statistics of landscapes based od free energies, replication and degradation rate constants of RNA secondary structures. Mh. Chem. **122**, 795–819 (1991)
35. Fontana, W., Konings, D.A.M., Stadler, P.F., Schuster, P.: Statistics of RNA secondary structures. Biopolymers **33**, 1389–1404 (1993)
36. Fontana, W., Schuster, P.: Continuity in evolution. On the nature of transitions. Science **280**, 1451–1455 (1998)
37. Fontana, W., Schuster, P.: Shaping space. The possible and the attainable in RNA genotype-phenotype mapping. J. Theor. Biol. **194**, 491–515 (1998)
38. Grüner, W., Giegerich, R., Strothmann, D., Reidys, C., Weber, J., Hofacker, I.L., Schuster, P.: Analysis of RNA sequence structure maps by exhaustive enumeration. I. Neutral networks. Mh. Chem. **127**, 355–374 (1996)
39. Grüner, W., Giegerich, R., Strothmann, D., Reidys, C., Weber, J., Hofacker, I.L., Schuster, P.: Analysis of RNA sequence structure maps by exhaustive enumeration. II. Structures of neutral networks and shape space covering. Mh. Chem. **127**, 375–389 (1996)
40. Güell, M., van Noort, V., Yus, E., Chen, W.-H., Leigh-Bell, J., Michalodimitrakis, K., Yamada, T., Arumugam, M., Doerks, T., Kühner, S., Rode, M., Suyama, M., Schmidt, S., Gavin, A.-C., Bork, P., Serrano, L.: Transcriptome complexity in a genome-reduced bacterium. Science **326**, 1268–1271 (2009)
41. Hamming, R.W.: Coding and Information Theory, 2nd edn. Prentice-Hall, Englewood Cliffs (1986)
42. Hayashi, Y., Aita, T., Toyota, H., Husimi, Y., Urabe, I., Yomo, T.: Experimental rugged fitness landscape in protein sequence space. PLoS One **1**, e96 (2006)
43. Hofacker, I.L., Fontana, W., Stadler, P.F., Bonhoeffer, L.S., Tacker, M., Schuster, P.: Fast folding and comparison of RNA secondary structures. Mh. Chemie **125**, 167–188 (1994)
44. Hofacker, I.L., Schuster, P., Stadler, P.F.: Combinatorics of RNA secondary structures. Discr. Appl. Math. **89**, 177–207 (1998)
45. Huynen, M.A., Stadler, P.F., Fontana, W.: Smoothness within ruggedness. The role of neutrality in adaptation. Proc. Natl. Acad. Sci. USA **93**, 397–401 (1996)
46. Jones, B.L., Enns, R.H., Rangnekar, S.S.: On the theory of selection of coupled macromolecular systems. Bull. Math. Biol. **38**, 15–28 (1976)
47. Kauffman, S., Levin, S.: Towards a general theory of adaptive walks on rugged landscapes. J. Theor. Biol. **128**, 11–45 (1987)
48. Kauffman, S.A., Weinberger, E.D.: The N-k model of rugged fitness landscapes and its application to the maturation of the immune response. J. Theor. Biol. **141**, 211–245 (1989)
49. Kimura, M.: Evolutionary rate at molecular level. Nature **217**, 624–626 (1968)
50. Kimura, M.: The Neutral Theory of Molecular Evolution. Cambridge University Press, Cambridge (1983)
51. Kouyos, R.D., Leventhal, G.E., Hinkley, T., Haddad, M., Whitcomb, J.M., Petropoulos, C.J., Bonhoeffer, S.: Exploring the complexity of the HIV-1 fitness landscape. PLoS Genet. **8**, e1002551 (2012)
52. Kühner, S., van Noort, V., Betts, M.J., Leo-Macias, A., Batisse, C., Rode, M., Yamada, T., Maier, T., Bader, S., Beltran-Alvarez, P., Castaño-Diez, D., Chen, W.-H., Devos, D., Güell, M., Norambuena, T., Racke, I., Rybin, V., Schmidt, A., Yus, E., Aebersold, R., Herrmann, R., Böttcher, B., Frangakis, A.S., Russell, R.B., Serrano, L., Bork, P., Gavin, A.-C.: Proteome organization in a genome-reduced bacterium. Science **326**, 1235–1240 (2009)
53. Lauring, A.S., Andino, R.: Quasispecies theory and the behavior of RNA viruses. PLoS Pathogens **6**, e1001005 (2010)
54. Maynard Smith, J.: Evolutionary Genetics, 2nd edn. Oxford University Press, Oxford (1998)

55. McCaskill, J.S.: A stochastic theory of macromolecular evolution. Biol. Cybern. **50**, 63–73 (1984)
56. Onuchic, J.N., Luthey-Schulten, Z., Wolynes, P.G.: Theory of protein folding: the energy landscape perspective. Annu. Rev. Phys. Chem. **48**, 545–600 (1997)
57. Orth, J.D., Thiele, I., Palsson, B.Ø.: What is flux balance analysis? Nat. Biotechnol. **28**, 245–248 (2010)
58. Phillipson, P.E., Schuster, P.: In: Modeling by Nonlinear Differential Equations. Dissipative and Conservative Processes. World Scientific Series on Nonlinear Science A, vol. 69. World Scientific, Singapore (2009)
59. Reidys, C., Stadler, P.F., Schuster, P.: Generic properties of combinatory maps. Neutral networks of RNA secondary structure. Bull. Math. Biol. **59**, 339–397 (1997)
60. Reidys, C.M., Stadler, P.F.: Combinatorial landscapes. SIAM Rev. **44**, 3–54 (2002)
61. Saakian, D.B., Biebricher, C.K., Hu, C.-K.: Phase diagram for the Eigen quasispecies theory with a trancated fitness landscape. Phys. Rev. E **79**, 041905 (2009)
62. Saiki, R.K., Gelfand, D.H., Stoffel, S., Scharf, S.J., Higuchi, R., Horn, G.T., Mullis, K.B., Erlich, H.A.: Primer-directed enzymatic amplification of DNA with a thermostable DNA polymerase. Science **239**, 487–491 (1988)
63. Sardanyés, J., Elena, S.F.: Error threshold in RNA quasispecies models with complementation. J. Theor. Biol. **265**, 278–286 (2010)
64. Sardanyés, J., Elena, S.F.: Quasispecies spatial models for RNA viruses with different replication models and infection strategies. PLoS One **6**, e24884 (2011)
65. Schuster, P.: How does complexity arise in evolution. Nature's recipe for mastering scarcity, abundance, and unpredictability. Complexity **2**(1), 22–30 (1996)
66. Schuster, P.: Molecular insight into the evolution of phenotypes. In: Crutchfield, J.P., Schuster, P. (eds.) Evolutionary Dynamics – Exploring the Interplay of Accident, Selection, Neutrality, and Function, pp. 163–215. Oxford University Press, New York (2003)
67. Schuster, P.: Prediction of RNA secondary structures: from theory to models and real molecules. Rep. Progress Phys. **69**, 1419–1477 (2006)
68. Schuster, P.: Mathematical modeling of evolution. Solved and open problems. Theory Biosci. **130**, 71–89 (2011)
69. Schuster, P., Fontana, W., Stadler, P.F., Hofacker, I.L.: From sequences to shapes and back: a case study in RNA secondary structures. Proc. Roy. Soc. Lond. B **255**, 279–284 (1994)
70. Schuster, P., Sigmund, K.: Random selection – A simple model based on linear birth and death processes. Bull. Math. Biol. **46**, 11–17 (1984)
71. Schuster, P., Swetina, J.: Stationary mutant distribution and evolutionary optimization. Bull. Math. Biol. **50**, 635–660 (1988)
72. Seneta, E.: Non-negative Matrices and Markov Chains, 2nd edn. Springer, New York (1981)
73. Skipper, R.A. Jr: The persistence of the R.A. Fisher – Sewall Wright controversy. Biol. Philosophy **17**, 341–367 (2002)
74. Spiegelman, S.: An approach to the experimental analysis of precellular evolution. Quart. Rev. Biophys. **4**, 213–253 (1971)
75. Stadler, B.R.M., Stadler, P.F., Shpak, M., Wagner, G.P.: Recombination spaces, metrics, and pretopologies. Z. Phys. Chem. **216**, 217–234 (2002)
76. Swetina, J., Schuster, P.: Self-replication with errors - A model for polynucleotide replication. Biophys. Chem. **16**, 329–345 (1982)
77. Takeuchi, N., Hogeweg, P.: Error-thresholds exist in fitness landscapes with lethal mutants. BMC Evolution. Biol. **7**, 15:1–15:11 (2007)
78. Tejero, H., Marín, A., Moran, F.: Effect of lethality on the extinction and on the error threshold of quasispecies. J. Theor. Biol. **262**, 733–741 (2010)
79. Thompson, C.J., McBride, J.L.: On Eigen's theory of the self-organization of matter and the evolution of biological macromolecules. Math. Biosci. **21**, 127–142 (1974)
80. Verhulst, P.F.: Notice sur la loi que la population pursuit dans son accroisement. Corresp. Math. Phys. **10**, 113–121 (1838)

81. Waterman, M.S.: Secondary structures of single stranded nucleic acids. Adv. Math. Suppl. Studies **I**, 167–212 (1978)
82. Watson, J.D., Crick, F.H.C.: A structure for deoxyribose nucleic acid. Nature **171**, 737–738 (1953)
83. Weissmann, C.: The making of a phage. FEBS Lett. **40**, S10–S18 (1974)
84. Welch, J.J., Waxman, D.: The nk model and population genetics. J. Theor. Biol. **234**, 329–340 (2005)
85. Wilke, C.O., Wang, J.L., Ofria, C.: Evolution of digital organisms at high mutation rates leads to survival of the flattest. Nature **412**, 331–333 (2001)
86. Wolfram Research, Inc., Champaign, IL. *Wolfram Mathematica 8.0.0.0* (2010)
87. Wolynes, P.G.: Energy landscapes and solved protein-folding problems. Phil. Trans. Roy. Soc. A **363**, 453–467 (1997)
88. Wright, S.: The roles of mutation, inbreeding, crossbreeding and selection in evolution. In: Jones, D.F. (ed.) International Proceedings of the Sixth International Congress on Genetics, vol. 1, pp. 356–366. Brooklyn Botanic Garden, Ithaca (1932)
89. Yus, E., Maier, T., Michalodimitrakis, K., van Noort, V., Yamada, T., Chen, W.-H., Wodke, J.A., Güell, M., Martínez, S., Bourgeois, R., Kühner, S., Raineri, E., Letunic, I., Kalinina, O.V., Rode, M., Herrmann, R., Gutiérez-Gallego, R., Russell, R.B., Gavin, A.-C., Bork, P., Serrano, L.: Impact of genome reduction on bacterial metabolism and its regulation. Science **326**, 1263–1268 (2009)
90. Zhong, X., Archual, A.J., Amin, A.A., Ding, B.: A genomic map of viroid RNA motifs critical for replication and system trafficking. The Plant Cell **30**, 35–47 (2008)
91. Zhong, X., Leontis, N., Qian, S., Itaya, A. Qi, Y., Boris-Lawrie, K., Ding, B.: Tertiary structural and functional analyses of a viroid RNA motif s critical for replication and system trafficking. The Plant Cell **30**, 35–47 (2008)
92. Zuker, M.: The use of dynamic programming algorithms in RNA secondary structure prediction. In: Waterman, M.S. (ed.) Mathematical Methods for DNA Sequences, pp. 159–184. CRC, Boca Raton (FL) (1989)
93. Zuker, M., Stiegler, P.: Optimal computer folding of larger RNA sequences using thermodynamics and auxiliary information. Nucl. Acids Res. **9**, 133–148 (1981)
94. Zwillinger, D.: Handbook of Differential Equations, 3rd edn. Academic, San Diego (1998)

Dissipative Structures and Biological Evolution

E.J. Brändas

1 Introduction

In this commemorative volume we honor Professor M. G. Velarde (MGV) on account of his remarkable achievements in the new and exciting domain of Complex Systems and Non-Linear Dynamics in general and the study of novel electric transport mechanisms in particular, for recent references see e.g. [1–3]. Our trajectories first crossed during a workshop, under the chairmanship of Profs. I. Prigogine and G. Nicolis, to discuss the European Commission's working document on Prospects in the Science of Complexity in European Research within the Fourth Framework Programme in 1994. In these panel reports fundamental problems in complex systems research were laid down with particular emphasis on viewing phenomena from the microscopic scale to the macroscopic one including the emergence of selforganization in the information technology and the biology sectors.

At this time MGV had just started to lay the fundaments of the highly regarded Instituto Pluridisciplinar besides receiving many awards, i.e. Honorary Doctorate, the Rammal Medal, the Dupont Science Prize, election (later Council Member) to membership of the Academia Europaea etc. My own contribution to meet the criteria for an invitation to review and elaborate on future specific platforms with scientific specialists and DG XII (Directorate-General for Science, Research and Development) probably originated from the fact that I was one of the first recipients of a European Commission (EG-SCIENCE) grant in Sweden [4], a somewhat overriding yet unfamiliar privilege that took the administration of the oldest University in Scandinavia with unexpected surprise! Fortunately I was permitted to accept the grant after guarantees were made that the new type of funding should not cause the University any extra costs.

E.J. Brändas (✉)
Ångström Laboratory, Institute for Quantum Chemistry, Department of Chemistry,
Uppsala University, Box 518, S-751 20 Uppsala, Sweden
e-mail: Erkki.Brandas@kemi.uu.se

R.G. Rubio et al. (eds.), *Without Bounds: A Scientific Canvas of Nonlinearity and Complex Dynamics*, Understanding Complex Systems,
DOI 10.1007/978-3-642-34070-3_45,

Another "crossing" occasion relates to the Workshop organized at les Trielles in honor of Ilya Prigogine on the occasion of his 85:th birthday [5]. In this tribute to the founder of dissipative dynamics and the Brussels-Austin School one may appreciate the various approaches and strategies from "bottom-up" and "top-down", in particular the concept of a coherent-dissipative structure, *CDS*, as an example of the former and of dissipative solitons as representing the latter.

As Program Director of the Uppsala Graduate Research School, Advanced Instrumentation and Measurements, [6], AIM being an associate member of the FANTOM International Research School [7], MGV was invited to lecture during the General FANTOM/AIM Study Week: *Dynamical processes and structure formation*. Now his research outline incorporated a liable connection between the dissipative soliton and high-T_C superconductivity, an idea today being further developed into the original conception of the *solectron* [1–3]. The relationship continued via other meetings like MGV's series of Madrid Meetings as well as various Solvay Symposia. In particular our Madrid-host confronted us as invited discussion partners to sign a declaration in his "black guest book" which by now should contain an illustrious list of research ideas extrapolated via the provoked expectations and imaginings, thoughts and dreams of the contributor in order to anticipate the challenges of tomorrow!

In order to comment on my reflexive vestiges in the aforementioned guest book I will, in this tribute, remind of some recent issues, see e.g. [8] for more details. In an ascending strategical perspective, complexity does emerge calling further attention to "complex-enough" systems that borderline on biological organization. In the artistic mode of science including its symbolic significance the present turmoil of scientific interpretation requests a new beginning, i.e. a conceptual renaissance of philosophical communication and motivated functionality. To begin with we need to consider general questions of the following nature: what is the proper framework for a *bona fide* science of biology? While physical progress is governed by natural laws (teleomatic principles), biology is teleonomically goal-directed due to the influence of an evolved program. In this vein one might ask whether biology naturally and logically supervenes (characterization of a relation that emergent properties bear on their base properties) on physics (physicalism)? How do we come to terms with the contradictory issues troubling micro-macro correlates? To exemplify the latter we need only to mention concepts like causality, unidirectional and irreversible time, the controversial nature of the second law not to mention the frenetic avoidance of Gödel's inconsistency theorem(s) (the assertion of the inherent limitations of all non-trivial axiomatic systems) in most enduring philosophical agendas. In more detail we will advance queries like

what distinguishes living matter from inanimate systems?
do we have a law of microscopic self-organization?
can physical teleomatic laws be transformed into teleonomic rules?
what is the role of temperature in biological systems?
what is the role of gravity in biology?
how to incorporate Gödel's incompleteness theorem?

These in turn lead directly to follow-up questions, i.e. in what manner do we develop new biological natural laws based on self-referentiability, and will mentalistic-materialistic construals generate mind-body analogies or more specifically structure-matter readings and finally will this environ new positions on artificial intelligence, AI, and lead to true sentience? As already indicated in the questions enlisted in italic above, supplementary theoretical details of a more general accord must be examined and developed, such as

can we profusely merge quantum- and thermal correlations?
what are the cosmological teleological consequences?
can decoherence be prohibited and what does this mean?
can classical and quantum mechanics coexist under common laws?

In the following sections we will briefly discuss this programme as well as call attention to various situations were we have been able to initiate some steps forward.

2 Complex Forms and the Global Superposition Principle

In order to examine the four questions at the end of the introduction, we will revisit our extended approach to a generalized theoretical formulation via so-called complex symmetric forms. As the present tribute will not allow any detailed accounts in regard to our quest for completeness, we will generally refer to a recent review [8] and references therein. To begin in a most general fashion we will consider abstract a particle-antiparticle system characterized by the kets in terms of the coordinate $\mathbf{x}$ and linear momentum $\mathbf{p}$, time t and energy $E = mc^2$ and m is the mass and c the velocity of light (spin is left although it may be incorporated)

$$|\mathbf{x},\ ict\rangle\,, \qquad |\mathbf{p},\ iE/c\rangle\,, \tag{1}$$

which for a free particle would amount to the general scalar product

$$\langle \mathbf{x},\ -ict\,|\mathbf{p}\ ,\ iE/c\rangle = (2\pi\hbar)^{-2} e^{\frac{i}{\hbar}(\mathbf{p}\cdot\mathbf{x}-Et)}. \tag{2}$$

The minus sign in the "bra" in (2) implies that we have taken a more general scalar product including all four dimensions. Since furthermore our construction should be complex symmetric [8], we have included a minus sign before *ict*. The conjugate operators defined in (1) and (2) are related as usual e.g.

$$E_{\text{op}} = i\hbar\frac{\partial}{\partial t}; \qquad \mathbf{p} = -i\hbar\nabla \tag{3}$$

and

$$\tau = T_{\text{op}} = -i\hbar\frac{\partial}{\partial E}; \qquad \mathbf{x} = i\hbar\nabla_p. \tag{4}$$

Since we consider operator identifications, i.e. with operator spectra distributed over the full real axis and possibly generalized by analytic continuation to appropriate complex half planes there are no contradictions associated with their definitions [8]. Employing the operators above one obtains

$$\widehat{\mathscr{H}} = |m,\ \bar{m}\rangle \begin{pmatrix} m & -i\,\mathbf{p}/c \\ -i\,\mathbf{p}/c & -m \end{pmatrix} \left\langle \begin{matrix} m^* \\ \overline{m}^* \end{matrix} \right| , \tag{5}$$

with $|m\rangle = |\mathbf{p}, iE/c\rangle$ and $|\bar{m}\rangle = |\mathbf{p}, -iE/c\rangle$ (note the complex conjugation in the bra-position, required to characterize a complex symmetric form [8]) and

$$\widehat{\mathscr{T}} = |\,\tau,\ \bar{\tau}\rangle \begin{pmatrix} c\tau & -i\mathbf{x} \\ -i\mathbf{x} & c\tau \end{pmatrix} \left\langle \begin{matrix} \tau^* \\ \overline{\tau}^* \end{matrix} \right| , \tag{6}$$

with $|\tau\rangle = |\mathbf{x}, ict\rangle$ and $|\bar{\tau}\rangle = |\mathbf{x}, -ict\rangle$. Since our formulation is very general we could of course have introduced a new scalar product like the c-product [9], but since orthogonal and unitary transformations reside alongside each other a new symbol might only add to the confusion. Although there are many times convenient to adhere to "real" representation in conjunction with our fourvector representations yet the "complex conjugate" is a reminder that we are dealing with biorthogonal constructions. From the ansatz above we derive the following results. Solving the general secular equation corresponding to (1)–(6) yields trivially with $\beta = \frac{p}{mc} = \frac{v}{c}$ the well-known relations of special relativity (note that the group velocity is compatible with special relativity)

$$m = \frac{m_0}{\sqrt{1-\beta^2}};\ \tau = \frac{\tau_0}{\sqrt{1-\beta^2}};\ x = \frac{x_0}{\sqrt{1-\beta^2}}.$$

The key is the complex form above that mimics the Minkowski metric combining particle-anti-particle dynamics in accordance with Lorentz invariance. Note that the interpretation here is different in comparison with the classical formulation in that the relativistic contractions above carries a realistic interpretation beyond merely measurements. Another bonus is that the superposition principle of (5), (6) is valid irrespective of whether we exploit classical or quantum observables as base ingredient. Finally we note the interplay between conjugate operators (variables), which becomes of crucial importance in the general theory, see more below.

Before ending this section we emphasize that gravitational interactions are easily included analogously (G is the gravitational constant, r the radial operator (variable) and μ the gravitational radius for massive object with mass M).

$$\widehat{\mathscr{H}} = |m,\ \bar{m}\rangle \begin{pmatrix} m(1-\kappa(r)) & -i\,\mathbf{p}/c \\ -i\,\mathbf{p}/c & -m(1-\kappa(r)) \end{pmatrix} \left\langle \begin{matrix} m^* \\ \overline{m}^* \end{matrix} \right|$$

$$m\kappa(r) = m\mu/r;\ \mu = \frac{G\cdot M}{c^2}. \tag{7}$$

One can show, see e.g. [8,10], that the ansatz (7) above, for a spherical black-hole object leads to the celebrated Schwarzschild gauge with singularities appearing at the Schwarzschild radius $r_0 = 2\mu$ via coupling between the gravitationally modified conjugate operators (variables), i.e.

$$-c^2 ds^2 = -c^2 dt^2 (1 - 2\kappa(r)) + dr^2 (1 - 2\kappa(r))^{-1}. \tag{8}$$

The singular behavior in the covariant formulation above stems from a Jordan block (of Segré characteristic of order 2) cf. the formula below

$$\widehat{\mathscr{H}} = |m,\, \bar{m}\rangle \begin{pmatrix} m(1-\kappa(r)) & -im\kappa(r) \\ -im\kappa(r) & -m(1-\kappa(r)) \end{pmatrix} \left\langle \begin{matrix} m^* \\ \overline{m}^* \end{matrix} \right|, \tag{9}$$

where in comparison with (7) we have included proper boundary conditions for the spherical system. Not only do we find that the operator matrix (9) is not diagonalizable for $r = r_0 = 2\mu$, i.e. Jordan block formation at the Schwarzschild radius (here a "true" singularity and not dependent as in the classical case on the coordinate system), but also that, photons (rest mass zero) interacts with massive objects gravitationally twice as much as prescribed by Newtonian theories. In addition follows the renown Einstein laws, the gravitational redshift and the time delay. For more on the associated cosmological scenario, see also [10].

As already stated we find that, see the last sentence in italic at the end of the introduction, that our formulation supports a global superposition principle, where quantum realizations (based on operators) coexist with classical idealizations (variables), from which further significant physical modeling becomes attainable. Another twist of fate appears from the close relation between (9) and the Gödel theorems of mathematical logic asserting the inherent limitations of all non-trivial axiomatic systems [8, 10]. Since the Jordan block signifies a curve crossing (in the complex form) decoherence to a unique state (classical or quantum) is protected or code forbidden (leaving the law of decoherence inoperative). Note that "decoherence" here is more general than usual since the states under consideration may be both classical and quantum and hence if general decoherence is forbidden hence it certainly protects decoherence to a classical realization.

3 Subdynamics and Interpretations

In order to come to terms with the challenges phrased in the introduction one needs to diagnose the dilemma confronting theoretical descriptions of physical events, i.e. problems related to irreversible behavior and the associated time asymmetry of entropic increase. In this assessment lies a basic explanation of thermodynamics from the viewpoint of statistical mechanics, including the emergence of temporal asymmetry from perfectly time symmetric microscopic dynamics. This cliffhanger, moreover, persists in the cosmological picture, which, notwithstanding the emergence of modern Big Bang models, is far from adequately resolved [11].

As is very well known to the present community of researchers, I. Prigogine, in his theory of time irreversibility [12], offered a radical solution to the puzzle of the violation of time symmetry, *viz.* without taking recourse to any approximations like course graining he took irreversibility to be a fundamental fact due to dynamics alone. We also know that, while speaking of intrinsic irreversibility he did attract outspoken criticism from the environment of scientists and philosophers. Although it may still be premature to finally assess the vision and foresight of Ilya Prigogine, there have appeared over time various fundamental and also critical objections to his programme of open dissipative systems, see e.g. [13,14]. Even if some disagreement were imprecisely formulated [15] the main difference between the construal to be briefly considered below, see e.g. [8] for details, and the one of the Brussels School rests in the non probability interpretation of the former, while the latter rests on the conceptual understanding of the theory of probability.

In short we bring attention to an alternative subdynamics derivation that has its origin in quantum mechanics, namely the utilization of the dilation group through a mathematical theorem due to Balslev and Combes [16]. Via a re-derivation of the Nakajima-Zwanzig Generalized Master Equation [17, 18] in a retarded-advanced formulation [13] it becomes straightforward to calculate the relevant residue contributions of the non-hermitean collision operator as well as evaluating associated creation- and destruction operators via apposite analytic continuation rigorously obtained from the aforementioned mathematical theorem [16]. The subsequent limit on the real axis yields the dissipativity condition for quantum mechanical systems with an absolutely continuous spectrum. As already indicated Prigogine's causal dynamics [12] differs with the present formulation in that we advocate (i) a retarded-advanced dynamics permitting the conversion of the time evolution into contracted semigroups with the positivity preserving condition (probabilistic interpretation) relaxed [14], (ii) the latter in turn carries with it an inevitable objective loss of information, (iii) and, as has been amply demonstrated [8, 10, 19], an analytic extension via Bloch thermalization enabling microscopic self-organization through integrated quantum-thermal correlations [19, 20]. This development begets a new concept, *viz.* the Coherent Dissipative Structure, *CDS*, which perpetuates microscopic selforganization including a rich variation of timescales as well as code protection against decoherence [8, 10, 20].

There is no room here to discuss in more detail the non-probabilistic formulation and its generalization to incorporating complex enough biological systems. We will, however in the next section, demonstrate its significance as regards biological organization and in so doing connect with the queries listed in the introduction.

4 Complex Enough Systems

As discernable by our attention to the above generalized formulation, we have maintained the position of one leg in an operationalist's rationale based on abstract operators extended by analytic continuation [8] and at the same time another leg

in a realist's thinking (for a recent discussion of the division of researchers into two camps in the field of quantum foundations, see [21]) in that the description goes beyond traditional readings of relationships between observable quantities. The attestation to hold such a view derives from the concurrent interplay between appropriate conjugate operators, their compatibility and consistency accounting for tangible assertions of e.g. Einstein's laws of relativity. In this understanding lies also a surprising relation with Gödel's theorem and the appearance of so-called Jordan blocks in the dynamics as well as the possibility to combine classical and quantum formulations on a global platform [8, 10]. By necessity the development sanctions non-probabilistic interpretations, which on a deeper level leads to vital consequences in the support of an authentic and relevant subdynamics.

We will devote the rest of this section to biological order, organization and evolution. We have previously discussed the generalization of the "complex symmetric" theory at several occasions, so we will abbreviate the argument. To sum up we emphasize (i) that we have incorporated a constructive integration of quantum- and thermal correlations, which (ii) under appropriate boundary conditions, involving the temperature, lead to the emergence of so-called coherent-dissipative structure, *CDS*, i.e. an optimal spatio-temporal structure formed by specific relationships between time-, size- and temperature scales and (iii) the realization that *CDS* suggests microscopic self-organization, the emergence of higher order codes that including Gödel-like self-referential traits providing code protection to decoherence and, counteracting wavefunction collapse in the case of quantum mechanics. As already brought up above, we will extend the discussion to incorporate hierarchies of complexity levels. In particular we will show that flexible and robust treatments of so-called dissipative systems are viable within our analytic approach, but first some definitions.

We will define an open or dissipative system as follows: *a system in which there exists a flow of entropy due to exchange of energy or matter with the environment*. To go beyond standard considerations of systems traditionally classified somewhat ambiguously as condensed matter, we will in addition deliberate on a specific order or organization that will be significant for both condensed matter and complex enough biological systems.This leads unequivocally to the conditions for the above mentioned *coherent-dissipative structure*, *CDS*, by stipulating that *(a) they are created or destroyed by integrated quantum- and thermal correlations, (b) they exchange energy with an (partially) entangled environment and (c) they can not have a size smaller than a critical one*.

Important developments in this direction is Yang's concept of ODLRO (Off-Diagonal Long-Range Order), see [22], and Coleman's concept of the extreme state, see [23]. The intimate connections between these ideas are most simply expressed as the possibility for a macroscopic system to exhibit ODLRO and for instance acquire anomalous properties like e.g. superconductivity out of a strongly correlated extreme configuration as predicted by quantum chemical laws (before employing the so-called thermodynamic limit). Since the latter can be derived and generalized as a quantum statistical degenerate structure, we have here at the same

time a connection with MGV's solectron [2] and a starting point for our work on dissipative dynamics.

Summarizing the basics relevant for the present microscopic development, we consider suitable system operators, or properly reduced density matrices. Subsequent dynamical evolution derives under apposite boundary conditions [8, 10] the aforesaid *CDS*-ordering-assembly, sustaining characteristic non-exponential decay as well as signaling microscopic self-organization. This understanding relates realistic temperature- and inclusive timescales via the Bloch equation. Although it is sometimes customary to bring together time and temperature into a complex parameter, it is important to point out that the extended dynamics relies on the Liouville Equation, while thermalization needs a separate analytic structure based on the energy super-operator, see e.g. [8,10,19]. Hence thermalization of the system operator yields temperature-regulated correlations and the appearance of canonical Jordan forms with sizeable Segré characteristics, n, i.e. the dimension of the largest Jordan block in the degenerate representation.

To establish the proper time scales, one needs to consider the generator of the dynamics, providing Hamiltonian and Liouvillian isometric and contractive evolution, see [8, 10] for technical details. The dimension n is monitored by the physico-chemical conditions of the dissipative system and as has been shown in several articles [8,10,19,20], the theoretical formulation centers on the transformation $\mathbf{B}$ given by

$$\mathbf{B} = \frac{1}{\sqrt{n}} \begin{pmatrix} 1 & \omega & \omega^2 & \cdot & \omega^{n-1} \\ 1 & \omega^3 & \omega^6 & \cdot & \omega^{3(n-1)} \\ \cdot & \cdot & \cdot & \cdot & \cdot \\ \cdot & \cdot & \cdot & \cdot & \cdot \\ 1 & \omega^{2n-1} & \omega^{2(2n-1)} & \cdot & \omega^{(n-1)(2n-1)} \end{pmatrix} ; \; \omega = e^{i\pi/n}, \tag{10}$$

which connects a preferred orthonormal basis $\boldsymbol{h} = h_1, h_2, \ldots h_n$, on e.g. local sites representing pairs of light carriers in a nuclear skeleton, cf. superconductivity, base pairs (or a group) of DNA, elements of protein structures or neural sites in related to functions of the brain in biological systems etc., to a canonical basis

$$\boldsymbol{f} = f_1, f_2, \ldots f_n,$$

with special properties and unique dynamics, and in tandem also to a coherent basis

$$\boldsymbol{g} = g_1, g_2, \ldots g_n,$$

which condense the system operator to proper measure-gauging subspaces which will communicate an encoding option for ontogenetic evolution via the *CDS*, see more below. Hence the tandem becomes

$$|\boldsymbol{h}\rangle \, \mathbf{B} = |\boldsymbol{g}\rangle \; ; \; |\boldsymbol{h}\rangle \, \mathbf{B}^{-1} = |\boldsymbol{f}\rangle \; . \tag{11}$$

Incidentally we note, see [8, 10, 19, 20], that the unitary transformation **B** connects the complex symmetric expression **Q** and the canonical form $\mathbf{J}_n(0)$

$$\mathbf{Q} = \mathbf{B}^{-1}\mathbf{J}_n(0)\mathbf{B};\ Q_{kl} = \exp\left\{\frac{i\pi}{n}(k+l-2)\right\}(\delta_{kl} - \frac{1}{n}), \tag{12}$$

where

$$\mathbf{J}_n(0) = \begin{pmatrix} 0\,1\,0\,\cdot\,\cdot\,0 \\ 0\,0\,1\,\cdot\,\cdot\,0 \\ 0\,0\,0\,1\,\cdot\,0 \\ \cdot\,\cdot\,\cdot\,\cdot\,\cdot\,\cdot \\ 0\,0\,\cdot\,\cdot\,0\,1 \\ 0\,0\,\cdot\,\cdot\,0\,0 \end{pmatrix} \tag{13}$$

The underlying relations obtained from the derivation of the *CDS* via Bloch thermalization and identified as a Jordan block, disguised as **Q** in complex symmetric form, while the original density matrix becomes diagonal under the transformation **B**. Although we have many examples of successful mappings of *CDS* structures in condensed matter systems, see e.g. [20], we will finish the discussion by focusing on biological ordering as emanating from the transformation **B** in (10). By inspection one finds that **B** exhibits an interesting factorization property, i.e. the columns show a particular recurring structure involving precisely correlated groups of sites and, conditional on the value of n, all conceivable factors develop as closed cyclic structures. We will exhibit the cyclic order by displaying e.g. $\sqrt{12}\mathbf{B}$, i.e. an array for $n = 12$ inserted in (10) above. The dimension of the vectors is displayed in parenthesis. We have eliminated the first vector of one-dimensional units (1), which leaves the diagram with only 11 columns.

$$\begin{array}{ccccccccccc} & & & & (2) & & & & & & \\ & & & & (2) & & & & & & \\ & & (3) & & (2) & & (3) & & & & \\ & (4) & (3) & & (2) & & (3) & (4) & & & \\ (12)\ (6) & (4) & (3)\ (12) & & (2) & (12) & (3) & (4) & (6)\ (12) & & \\ (6) & (4) & (3) & & (2) & & (3) & (4) & (6) & & \\ & (4) & (3) & & (2) & & (3) & (4) & & & \\ & & & & (2) & & & & & & \end{array}$$

Generalizing we might e.g. consider a sequence $s_1 s_2 s_3 \ldots s_k$ of positive integers with the numbering, i.e. being the product of the first primes raised to the corresponding values in the sequence, cf. the Gödel encoding, getting

$$n(s_1 s_2 s_3 \ldots s_k) = 2^{s_1} \cdot 3^{s_2} \cdot 5^{s_3} \cdots p_k^{s_k}.$$

The corresponding cyclic diagram to this Gödel numeral becomes ($n_k = n/k$)

$$
\begin{array}{ccccccccccc}
 & & & & (n_{\frac{n}{2}}) & & & & & & \\
 & & & (n_{pk}) & (\cdot) & (n_{pk}) & & & & & \\
 & & \cdot & \cdot & \cdot & \cdot & \cdot & & & & \\
 & & & (\cdot) & (n_{\frac{n}{2}}) & (\cdot) & & & & & \\
 & & \cdot & \cdot & \cdot & \cdot & \cdot & & & & \\
(n) & (n_2) & \cdot & (n_{pk}) & \cdot & (n_{pk}) & \cdot & (n_2) & (n) & & \\
 & (n_2) & \cdot & (n_{pk}) & \cdot & (n_{pk}) & \cdot & (n_2) & & & \\
 & & \cdot & \cdot & (n_{\frac{n}{2}}) & \cdot & \cdot & & & & \\
 & & & (\cdot) & \cdot & (\cdot) & & & & & \\
 & & \cdot & \cdot & (\cdot) & \cdot & \cdot & & & & \\
 & & & (n_{pk}) & (n_{\frac{n}{2}}) & (n_{pk}) & & & & &
\end{array}
\tag{14}
$$

Note that in (14), the cyclic structure is interspersed with non-cyclic n-dimensional columns when the column number is not a divisor of n (for instance when $n > p_k$ where p_k is the largest prime above). There are many interesting cases; e.g. if n is a prime number we have no cycle structure at all and if $n = m!$ we have an uninterrupted number cyclical columns up-to row m and from then on the appearance of recurrence becomes sparse compared to columns denoted by (n).

Before concluding this venture and in particular this section we recapitulate a few themes. First, the essential conception comes from the possibility to map biological order onto *CDS* spatio-temporal orderliness. These maps encompass information stored in the system operator via the transformation **B**, and which is communicated *mutatis mutandis* via the *CDS* to the environment. The unbiased code protection to "classical" dynamics leads strictly to suitable time scales for biological ordering. The map also suggests various ways of encoding depending on the levels of organization under study. Since the world usually partitions into a mental- and a materialistic part it is obvious that the present *CDS* structure signifies both a teleomatic element (based on natural law) and a teleonomic constituent (governed by an evolved program), for more details see [24].

5 Conclusion

It is obvious that we have only been able to give an abridged survey of our ideas to incorporate a unified picture of physics, i.e. whether the different branches of science can be reduced to physical theory. In this bottom-up approach we have also noted the prerequisite for coming across top-down strategies, the latter well exemplified by the concept of the dynamic bound state of the electron by solitons, the so-called solectron, see [1–3], in electric transport phenomena.

To round off the discussion we return to the conjectures voiced in the introduction. Although we have not explicitly given the requirements for a living state, for details see [24], we have here tried to give the physical base for a *bona fide* science of biology, i.e. the anticipation of so-called teleonomic processes regulated by an

evolved program. Furthermore we have referred to the importance of the Gödel indeterminacy theorem(s) and the analogy between self-references and emerging Jordan blocks in the equations of motion. We have also described microscopic selforganization and the importance of temperature in biological systems via precise incorporation of thermal- and quantum correlations. Further consequences regarding inferences from gravity, artificial intelligence, universal superposition and decoherence code protection have been detailed in [8, 10, 24].

With these remembrances the author wants to thank MGV for his vivacious interest in always trying to tempt his environment to discuss science on the broadest stage yet appropriately confining the proposals to the proper depth as he did instigate as the policy at the Instituto Pluridisciplinar.

Acknowledgement The present contribution has been presented as a tribute to Professor Manuel G. Velarde in connection with his retirement from the Instituto Pluridisciplinar de la Universidad Complutense de Madrid and on account of his significant achievements in the new and exciting domain of Complex Systems and Non-Linear Dynamics. The present research has, over the years, been supported by the Swedish Natural Science Research Council, the Swedish Foundation for Strategic Research, The European Commission and the Nobel Foundation.

References

1. Henning, D., Velarde, M.G., Ebeling, W., Chetverikov, A.: Phys. Rev. E **78**, 066606 (2008)
2. Velarde, M.G.: J. Comput. Appl. Math. **233**, 1432 (2010)
3. Cantu Ros, O.G., Cruzeiro, L., Velarde, M.G., Ebeling, W.: Eur. Phys. J. B **80**, 545 (2011)
4. Brändas, E.: Samarbete i Europa. RÅDSLAGET (Information from the Natural Sciences Research Council), Nr.6, 4 (1989)
5. Antoniou, I., Goldbeter, A., Lefever, R. (eds.) Complexity: microscopic and macroscopic aspects. Int. J. Quant. Chem. **98** (2004)
6. Boström, R., Brändas, E., Kullander, S.: Promoting University-Industry Links by a New Type of PhD Education: The AIM Graduate School. Conference Proceedings, Vienna, 4–6, November 1998 ESA 432, p. 181. Academic and Industrial Cooperation in Space (1998)
7. Koopmans, M.: International Research School FANTOM, Triennial Reports 1998–2000; 2001–2003, Universiteitsdrukkerij, Gronningen, The Netherlands (2000; 2003)
8. Brändas, E.J.: In: Nicolaides, C.A., Brändas, E.J. (eds.) Unstable States in the Continuous Spectra, Part II: Interpretation, Theory and Application, Adv. Quant. Chem. vol. 63, p. 33. Elsevier, Amsterdam, (2012)
9. Moiseyev, N.: Non-Hermitean Quantum Mechanics. Cambridge University Press, Cambridge (2011)
10. Brändas, E.J.: In: Hoggan, P., Brändas, E.J., Maruani, J., Piecuch, P., Delgado-Barrio, G. (eds.) Advances in the Theory of Quantum Systems in Chemistry and Physics, vol. 21, p. 3. Springer, Dordrecht (2012)
11. Sklar, L.: Physics and Chance. Cambridge University Press, Cambridge (1993)
12. Prigogine, I.: The End of Certainty. Time, Chaos and the New Laws of Nature. The Free Press, Simon & Schuster Inc., New York (1996)
13. Obcemea, Ch., Brändas, E.: Ann. Phys. **151**, 383 (1983)
14. Kumicák, J., Brändas, E.: Int. J. Quant. Chem. **32**, 669 (1987); ibid. **46**, 391 (1993)
15. Brändas, E.J., Antoniou, I.E.: Int. J. Quant. Chem. **46**, 419 (1993)
16. Balslev, E., Combes, J.M.: Commun. Math. Phys. **22**, 280–294 (1971)

17. Nakajima, S.: Progr. Theoret. Phys. **20**, 948 (1958)
18. Zwanzig, R.: J. Chem. Phys. **33**, 1338 (1960)
19. Brändas, E., Chatzidimitriou-Dreismann, C.A.: Int. J. Quant. Chem. **40**, 649–673 (1991)
20. Brändas, E.: Complex symmetry, Jordan Blocks and microscopic selforganization: an examination of the limits of quantum theory based on nonself-adjoint extensions with illustrations from chemistry and physics. In: Russo, N., Antonchenko, V.Ya., Kryachko, E. (eds.) Self-Organization of Molecular Systems: From Molecules and Clusters to Nanotubes and Proteins. NATO Science for Peace and Security Series A: Chemistry and Biology, pp. 49–87. Springer Science+Business Media B. V., Dordrecht (2009)
21. Hardy, L., Spekkens, R.: Phys. Canada **66**, 73 (2010)
22. Yang, C.N.: Rev. Mod. Phys. **34**, 694–704 (1962)
23. Coleman, A.J.: Rev. Mod. Phys. **35**, 668–686 (1963)
24. Brändas, E.: Int. J. Quant. **111**, 215; ibid. 1321 (2011)

Nonlinear Models for Protein Folding and Function

L. Cruzeiro

1 Introduction

The first time that I attended a meeting at the group of Manuel G(arcía) Velarde was in November 2008 and I am very glad indeed that I went. The meetings, with informal but intense seminars, where all aspects of the research can be discussed, are both lively and informative. I was immediately interested in Manuel's idea that electrons can surf on nonlinear waves (the solectron concept) and have learned a lot from these meetings that include also guest speakers who provide extra expertise and different outlooks to the core research work. In spite of the many contributions by many people, it is fair to say that the whole solectron project lives because of Manuel's commitment to it and the hope is that someday (soon) solectrons will be observed experimentally, either in already existing materials or in materials specially designed to sustain them. In the meantime, I am sure that we will all continue to learn a lot about charge and energy transport in condensed matter just by researching the solectron.

While solectrons have now joined my personal list of research interests, protein folding and function remains at the top of that list. From a physical point of view, proteins are polymers whose units are the amino acids. Even a small protein, with something like 60 amino acids, possesses approximately one thousand atoms which interact via covalent bonds, hydrogen bonds, electrostatic interactions and van der Waals interactions. Despite the inherent complexity of such a system, proteins, in cells, are capable of folding reproducibly to a well defined three-dimensional structure (the native structure) that is generally irregular and lacks symmetry. How do proteins do it? The current orthodox answer to this question

L. Cruzeiro (✉)
CCMAR and Department of Physics, FCT, University of Algarve, Campus de Gambelas, 8005-139 Faro, Portugal
e-mail: lhansson@ualg.pt

R.G. Rubio et al. (eds.), *Without Bounds: A Scientific Canvas of Nonlinearity and Complex Dynamics*, Understanding Complex Systems,
DOI 10.1007/978-3-642-34070-3_46,

is to assume that the native structure of proteins corresponds to the minimum of the free energy, the so-called thermodynamic hypothesis, first proposed by Anfinsen [1]. According to thermodynamic hypothesis protein folding is a process in which the protein's free energy is minimized and which is simply driven by thermal agitation. There are two types of experimental evidence for this hypothesis, namely, (1) the reversible unfolding experiments, first performed by Anfinsen on bovine pancreatic ribonuclease (RNase) [1], and later by many other authors on different proteins, and, very importantly, (2) the realization soon after Anfinsen's folding experiments of the synthesis of RNase by the solid phase method [2], later followed by the chemical synthesis of other proteins. Both types of experiments seem to indicate that the amino acid sequence (the primary sequence of proteins) constitutes all the necessary and sufficient information needed for a protein to fold to the native state. In the late 1980s the thermodynamics hypothesis was complemented by the hypothesis that the free energy landscape of proteins is funnel-shaped [3–5] in order to explain how proteins can solve the problem of finding the native state among the configurational maze of possibilities, in a comparatively fast manner (a problem known as Levinthal's paradox); the answer provided by the funnel hypothesis is that, if the free energy landscape is funnel-shaped, with the native state lying at the bottom, any downward path will lead to the native conformation so that proteins do not have to explore an enormous number of configurations in the search for the native state. More recent concepts, like the kinetic hub [6] have been added, which do not seem to challenge the thermodynamic hypothesis. However, in spite of the improvements in the accuracy of force fields [7–9] and in the power of computer facilities (http://folding.stanford.edu/) [10,11], and in spite of the many announcements of a solution for protein folding "just around the corner" [12–15] it has not yet been possible to predict a protein structure solely from its amino acid sequence.

The opposite view, that protein folding is a non-equilibrium, kinetic process, is as old as the thermodynamic hypothesis. Levinthal was the first to propose it and to design an experiment that confirmed his proposal: he showed that the protein alkaline phosphatase synthesized in mutants of *E. coli* at 44°C does not show activity, even when the temperature is brought down to 25°C, and also that when those proteins were synthesized at 25°C, they had activity, even when the temperature was increased [16]. I.e., he showed that alkaline phosphatase can assume two forms, one active and the other not, and that both forms are stable between 25°C and 44°C. Since then, and in spite of the "rather special conditions that must hold for kinetic control to be observable" [17], direct experimental evidence for a kinetic control of protein folding has been demonstrated in a number of other proteins, such as proteases, subtilisin, serpins, influenza Hemagglutinin, Luciferase and prions [17–22]. Thus, contrary to most computational work on protein folding, the hypothesis explored here is that the native state is just one of the many kinetic traps in which proteins can find themselves in [23]. This hypothesis is also supported by previous computational work [24–27] which shows that a protein from a given CATH [29] class can be forced into artificial, non-native structures that belong to other CATH classes and maintain these structures for at least 50 nanoseconds. Because such alternative structures have never been

found experimentally, within the thermodynamic hypothesis they should be very unstable for the proteins considered, contrary to what is observed in the computer simulations; on the other hand, within a kinetically controlled folding mechanism, these results favour a *multi-funnel-shaped* free energy landscape, in which many different conformations of the same protein, in the same thermodynamic conditions, have very similar free energies and in which the native conformation is not necessarily the global minimum (which is itself very ill-defined).

In a multi-funnel free energy landscape, each protein has equal probability of assuming structures very different from, and yet as thermodynamically stable as, the native structure, and the thermodynamic hypothesis cannot explain folding to a well defined three dimensional structure. Instead, protein folding must follow a well defined pathway, as first proposed by Levinthal [16]; however, and equally importantly, *folding must always start from the same well-defined initial conformation*. Thus, a question that arises when we consider folding as a kinetic process in a multi-funnel free energy landscape is: what is the initial structure that proteins have when they are synthesized? Experimentally, it has not yet been possible to determine the structure of nascent chains, that is, the structure proteins have as they come out of the ribosomal tunnel but it is known that only fully extended and helical structures fit into the tunnel dimensions [28]. While a fully extended polypeptide provides many more possibilities for folding pathways, an initial structure in the form of a helix can constrain the configurational maze and lead to fewer and more defined pathways, consequently, in [27] it was suggested that the conformation that *all* proteins have immediately after synthesis in cells, is helical and it was also proposed that the first step in folding is the bending of this initial helix at specific amino acid sites.

The aim of the present study is to make a comparison between the kinetic pathways followed by two proteins when their initial structure is a helix and when their initial structure is fully extended. To that end, two proteins, representative of the mainly α and α/β CATH [29] protein classes, were selected and pathways to the native state were generated using Targeted Molecular Dynamics (TMD) [30]. In TMD simulations, harmonic restraints are added to the protein force field in order to drive an initial protein conformation to a given target conformation [30,31]. TMD simulations were first applied to the T $\leftrightarrow$ R transition of the protein insulin [30] and have since been used to study a variety of other problems, including the conformational changes associated with the functioning of a molecular motor [32], the elucidation of the reaction steps in the full catalytic cycle of a protein involved in an electron transfer process [33], as well as in protein folding [34]. Thus, TMD simulations have generally shown their usefulness in the modeling of large conformational changes. In the present study, TMD simulations are used to generate folding pathways in order to make a preliminary comparison of the efficiency of folding from an initial helical conformation, proposed previously to be the conformation of proteins immediately after synthesis [27], relative to a fully extended conformation which has also been identified as experimentally possible [28].

2 Numerical Simulations

Two proteins, one representative of the mainly α CATH class [29] and the other representative of the α/β CATH class, were chosen and their native structures were obtained from the Protein Data Bank (PDB) [35]. The first protein (PDB1BDD [36], 60 amino acids, 941 atoms, mainly α) has a native structure constituted by three α-helices, while the second protein (PDB1IGD [37], 61 amino acids, 927 atoms, α/β) has a native structure that includes one α-helix and a β-sheet. Two initial conformations, both of which have been identified as viable experimentally [28], were taken for each of the two proteins, namely, one conformation in which the backbone is fully extended and a second conformation in which the backbone is folded into an ideal α-helix. The energy minimized versions of these two conformations were used as initial conditions for the TMD simulations. The potential energy function used in all simulations was the ff99SB force field [38], with an implicit solvent, implemented in AMBER 9 [39], which has been shown to give a better representation of protein secondary structure than previous versions [40], whose mathematical expression is as follows:

$$V = \sum_{\text{bonds}} K_r(r - r_{eq})^2 + \sum_{\text{angles}} K_\theta(\theta - \theta_{eq})^2 + + \sum_{\text{dihedrals}} \frac{V_n}{2}[1 + \cos(n\phi - \gamma)] + \sum_{i<j}\left[\frac{A_{ij}}{R_{ij}^{12}} - \frac{B_{ij}}{R_{ij}^{6}}\right] + \sum_{i<j}\left[\frac{q_i q_j}{\epsilon R_{ij}}\right]. \quad (1)$$

The energy functional V includes harmonic potentials for bond stretching (first term) and angle bending (second term), a truncated Fourier series to represent torsions (third term), a Lennard-Jones potential to represent hydrogen-bonds and other nonbonded interactions (fourth term) and electrostatic interactions between atoms that are more than two covalent bonds away from each other (fifth term). Potential energy functionals such as (1), as well as the many parameters they depend on, have been fitted to a variety of experimental data and continue to be improved [7–9, 38, 40], but their approximate validity is reflected in the successes that practical applications by the pharmaceutical and biotechnology industries have had.

For each initial conformation, 20 independent TMD trajectories to the native state were generated by changing the seeds of the random forces in the Langevin thermal baths, with $T = 298$ K in all cases. In TMD simulations the harmonic forces that drive the initial conformations to the native structure arise from the following term added to the atomic potential energy function (1):

$$U_{\text{TMD}} = \frac{1}{2} k N \left(\text{RMSD}_N(t) - \text{RMSD}_{\text{target}}(t)\right)^2 \quad (2)$$

where N is the number of atoms used to calculate the root mean square deviation per atom (RMSD), $\text{RMSD}_N(t)$ being the RMSD, with respect to the native structure,

Table 1 RMSD, in Å, between the native state and the two initial conformations of the two proteins

Protein	Initially extended	Initially α-helix
mainly α (1BDD)	55.78	21.54
α/β (1IGD)	59.76	24.46

of the conformation the protein has at time t, and $\text{RMSD}_{\text{target}}(t)$ being the target RMSD at that time. In the simulations reported here, $k = 100\,\text{kcal/mol/Å}^2$ and N is the total number of carbons, nitrogens and oxygens in the backbone of the two proteins selected.

In TMD simulations, $\text{RMSD}_{\text{target}}(t)$ is a linear function of time, being completely defined by the values at two time instants. Here, these two times are (1) its initial value, $\text{RMSD}_{\text{target}}(t = 0)$, given in Table 1, and (2) its final value, set to 0.1 Å in all trajectories. As shown in Table 1, for both proteins, the α-helical conformation is more than 2.4 times closer to the native structure than the fully extended conformation. Preliminary simulations starting from the α-helical conformation showed that the total potential energy (including the TMD term) does not vary much until $\text{RMSD}_N \approx 6$ Å and so, in order to make the simulations with the two different initial conformations as equivalent as possible, in all the TMD simulations presented here, two $\text{RMSD}_{\text{target}}(t)$ functions were used, i.e., the first 0.1 ns were spent in the convergence of the initial conformation to within 6 Å of the native structure, that is, $\text{RMSD}_{\text{target}}(t = 0.1\text{ ns}) = 6$ Å, and 0.4 ns were allowed for the further convergence to within 0.1 Å of the native conformation. In this way, a slower rate of change of the RMSD is imposed in the final stages of convergence to the native state, allowing more time for the side chains to adjust and avoid steric overlaps, and, most importantly, making the rate of RMSD change in this latter stage the same for all simulations. The overall duration of each TMD simulation was 0.5 ns, comparable to other TMD protein folding simulations [34].

Each of the two initial conformations was taken as an initial condition in 20 independent TMD simulations, as detailed above. Figure 1 shows the average over the 20 trajectories and the corresponding standard deviations of the total potential energy as a function of instantaneous value of RMSD_N for the mainly α 1BDD protein [36]. The curve in red is for the trajectories starting with a α-helical conformation and the curve in green is for the trajectories starting with a fully extended backbone conformation. Included in the values displayed in Fig. 1 is the contribution of the TMD term (2) which, however, only starts to rise above 0.3% of the total potential energy when the RMSD distance to the native structure becomes less than 0.6 Å. This means that, although *the local dynamics* is dominated by the TMD forces that drive the initial backbone fold to the native backbone fold, *the global energetics* of these folding pathways is determined essentially by the atomic interactions in the ff99SB AMBER potential (1) [38].

Figure 1 shows that the pathways from the initially extended conformations are populated by protein conformations which have, on average, a potential energy that

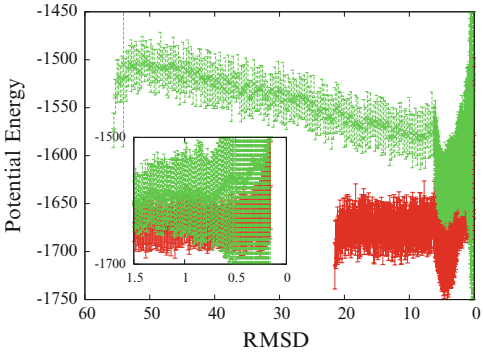

Fig. 1 Total potential energy (kcal/mol) as a function of the RMSD distance to the native structure of the mainly α 1BDD [36] protein. Average values over 20 independent TMD simulations are shown, together with the corresponding standard deviations. The starting conformation is fully extended for the *green* curves and an α-helix for the *red* curves. The inset is an enlargement of the final stages of convergence to the native structure

is much greater than the conformations that arise when the initial conformation is α-helical; indeed, even in the final stages of approach to the native state, the protein conformations sampled in the pathways from an extended initial structure to the native state have potential energies at least 40 kcal/mol above the conformations sampled when the initial conformation is a helix. Furthermore, contrary to what was found in previous folding simulations [34] and also below for the α/β 1IGD protein, all pathways of the mainly α 1BDD protein lead to conformations with a perfectly folded backbone which is at least within 0.3 Å of the native structure.

To test further the hypotheses put forward in [27], another protein, the α/β 1IGD protein [37], whose native structure includes both an α-helix and a four stranded β-sheet, was also considered. As reported previously for chymotrypsin inhibitor 2 [34], many of the TMD folding simulations of the α/β 1IGD protein lead to final structures that, although apparently close to the native structure, differ from it by entangled backbone folds such as those highlighted by the red circles in Fig. 2. Indeed, inspection of the trajectories with the Visual Molecular Dynamics (VMD) software [41] reveals that 12 (14) of the 20 TMD simulations starting with a fully extended (α-helical) conformation lead to such entangled final structures. These entanglements can be resolved by letting the chains go through each other, an artificial process enabled by the TMD term (2) but of course penalized by extremely large values of the potential energy. Thus, in Fig. 3 the averages are made over viable pathways only, that is, over the TMD trajectories in which such backbone entanglements did not occur. Although the TMD term contributes a little more than before to the overall energetics of the pathways, its total amount only rises above 1% when the RMSD distance to the native structure goes below 1 Å, with the larger values being associated with entangled structures. Figure 3 shows that, also for the α/β 1IGD protein, the viable pathways from an initial α-helix to the native state are much less energetic than the corresponding ones from a fully extended structure,

Fig. 2 The native fold of the α/β 1IGD protein is depicted on the left and on the right the *red circles* highlight two of the most common backbone entanglements that arose in the TMD simulations of this protein. The figures were made with the VMD software [41]

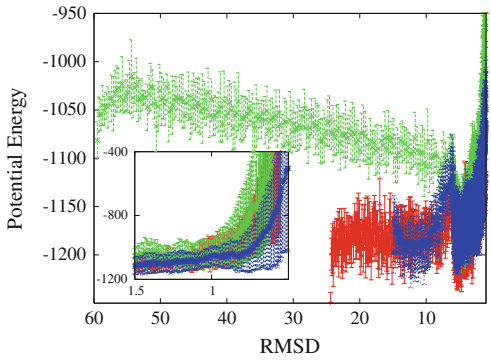

Fig. 3 Total potential energy (kcal/mol) as a function of the RMSD distance to the native structure of the α/β 1IGD [37] protein. Average values together with the corresponding standard deviations are shown using the non-entangled TMD trajectories (see text). The starting conformation is fully extended for the *green curves*, an α-helix for the *red curves* and the embrio (see text and Fig. 4) for the *blue curves*. The inset shows the final stages of convergence to the native structure

with the conformations covered by the latter having a potential energy more than 130 kcal/mol greater than the former to start with, and with their values only merging when the RMSD distance to the native structure is approximately 6 Å.

In [27] it is suggested that the initial conformation of *all* proteins is a helix and that **the first step** in the folding of *all* proteins is the bending of this helix at specific amino acid sites. In the case of proteins whose secondary structure is just a set of helix bundles, as in the mainly α 1BDD protein [36], this first step is the only major step in their folding pathways. VMD [41] animations of the TMD trajectories of the 1BDD protein do show pathways of this sort when the initial conformation is α-helical. (When the initial conformation is fully extended, on the other hand, the formation of the α-helices constitutes the last step, coming after the backbone has

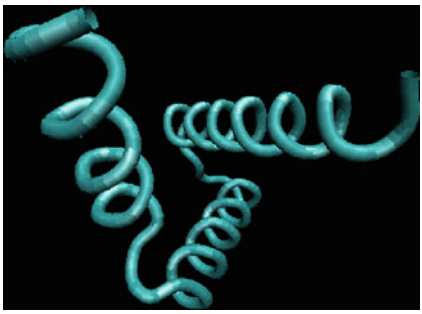

Fig. 4 The putative embrio (see text) built from the native fold of the α/β 1IGD protein by substituting the native β-sheets by α-helices. This figure was made with the software VMD [41]

folded to the native tertiary structure). For proteins whose native secondary structure includes both helices and sheets, as is the case of the α/β 1IGD protein, it was further suggested [27] that the formation of the β-sheets takes place after the first step of bending of the initial helix and is triggered by destabilizing interactions between the amino acid side chains that are thrown together by that first step. VMD [41] animations of the TMD trajectories of the α/β 1IGD protein starting from the α-helical conformation reveal pathways that start off in that manner but in which the helical portions very quickly become distorted because the convergence to the right secondary structure is mixed with the convergence to the right tertiary fold. This is to be expected because of the unspecific character of the TMD term (2). In order to test, in a more direct way, the effect that an intermediate all-helical conformation has on the folding efficiency of the α/β 1IGD protein, such a putative intermediate was generated by substituting the β-sheets in the native structure of 1IGD by α-helices, as shown in Fig. 4. In the kinetic process proposed in [27], the structure of this intermediate not only influences the pathway but also determines the nature of the final, native, structure of the protein and for these two reasons it is here called an *embrio*.

Further TMD simulations were run by first driving an initial α-helix to the embrio, and then by driving the embrionic conformations to the native structure of 1IGD. As the RMSD between the α-helix and the embrio is 23.78 Å and the RMSD between the embrio and the native 1IGD structure is 15.05 Å, in order to keep approximately the same rate of change of RMSD as before, the first simulations had a duration of 0.05 ns and the second simulations had a duration of 0.45 ns. In the first 0.05 ns all 20 trajectories converge to within 0.1 Å of the embrio structure; furthermore, 17 out of the 20 trajectories from the embrio to the native state lead to un-entangled final structures. Figure 3, in which the potential energies of the protein conformations in these 17 viable folding pathways are displayed in blue, shows that the α-helix $\rightarrow$ embrio $\rightarrow$ native trajectories provide, on average, the lowest energy folding pathways for the α/β 1IGD protein.

3 Discussion

The folding pathways analyzed in this study were generated by TMD simulations, in which the total time from initial condition to final state is set a priori, and thus cannot be used to estimate kinetic rates. In fact, the interest here was to find pathways from the initial structure to the native state through the protein conformational space and TMD was used merely as a tool to generate such pathways. Thus, although the evolution from one conformation to another in those pathways is due to the artificial TMD terms (2), the fact that the restraint energy of each protein conformation sampled is, for most part of the trajectory, less than 1% of the total AMBER potential energy (1) for that conformation means that we *can* neglect the TMD terms in the analysis of the relative energetics of the pathways sampled. And from the point of view of the energetics, the simulations reported here indicate that, of the two nascent chains that have been identified as experimentally possible [28], that in the form of a helix is to be preferred to a fully extended conformation.

The a priori advantage of a helix as an initial condition is that a more constrained structure at the beginning limits the number of possible pathways to the native state and pathways must be well defined in a kinetically controlled folding process. But table I shows that helical initial structures have also a second advantage: they are generally closer to the native structure. Furthermore, from a topological point of view, the advantage of an initial alpha-helical conformation for the efficient folding of all-α proteins is immediately apparent. On the other hand, in the case of the α/β-protein 1IGD, an initial helical structure, in spite of being closer to the native state in terms of RMSD, is not necessarily an advantage as the simulations showed that only 30% of the direct pathways lead to a correctly folded native state (the percentage being actually marginally better (40%) when the initial structure is fully extended). These results also provide a glimpse of the many entangled states that can be expected to arise if protein folding is just a random search of the native structure, driven by thermal noise, especially if the initial structure is also arbitrary. If, however, we introduce a well defined intermediate/transient structure in the folding pathway from an initial helix, the odds of reaching the native structure in a reproducible manner can dramatically increase: with the roughly built embrio tentatively considered here (see Fig. 4) the probability of reaching the native state when starting from a helical conformation became 85%! This is because in the embrio, the amino acids are organized in helical pieces which are much less free to roam the conformational space that is accessible to the more random chains that arise in the absence of the embrio. Another important point concerning the embrio structure is the rule used to build it, namely, the bending of the initial helix at the same sites where turns are found in the final native state of 1IGD, which implicitly assumes that the first step in the folding of this α/β protein is the formation of an all-α structure. According to that rule, all proteins, no matter which class their native structure belongs to, first fold to an all-α structure and other classes only arise when the helices that are brought together in this first step are not stable, (for example, because the interactions between their side chains are globally repulsive).

The embrio proposed here plays the role of an intermediate. In a review about the "molten globule" concept [42], Ptitsyn comments on how the dogma according to which there are no protein intermediates in protein folding persisted well into the 1980s, in spite of ample experimental evidence to the contrary. In fact, intermediates have been identified in the folding of many proteins [43–45] and may even be present in proteins that fold in an apparently two-state process [43, 45]. While according to the thermodynamic hypothesis any trajectory from the high free energy states to the global free energy minimum leads to the native state, and not just one, but many intermediates should exist, each set characterizing a different folding trajectory, in a kinetically controlled folding process, essentially one pathway must be followed and the intermediates must be correspondingly well defined, as is observed experimentally.

Implicit in this kinetic approach to protein folding is the notion that folding in vitro is fundamentally different from folding in vivo because the initial structures proteins have are different in the two cases. While it was first assumed that denatured states of proteins were essentially structureless [1], evidence is accumulating for that they largely preserve the secondary structure of the native state [46]. Thus while here it is assumed that the initial structure for folding in vivo is an alpha-helix (with the embrio being a universal intermediate) [27], the initial structure from which a protein re-folds following chemical or thermal denaturation is possibly an open structure that preserves much of its previously formed native secondary structure. In this view, the initial structures in in vitro experiments vary from protein to protein, something that can account for the difficulty in extracting universal rules for folding from such experiments.

The purpose of the simulations reported here is to perform a *feasibility* test of the kinetic folding mechanism first proposed in [27] according to which all protein have a helical structure as they come out of the ribosomal tunnel and the first step in the folding of all proteins is the bending of this initial helix at specific amino acid sites, with the consequent formation of a compact core, here called an embrio. As pointed out in [27] such a kinetic mechanism means that ribosomes are not just synthesizing machines, but they also have chaperone activity, a suggestion that is confirmed by recent experiments [47]. The simulations here do not prove the kinetic mechanism but they do demonstrate that it can lead to low energy pathways and therefore that it is a viable mechanism to explain reproducible folding to the native state.

4 The VES Hypothesis and Solectrons

According to the kinetic mechanism proposed in [27] and explored here, the first step in the folding of *all* proteins, immediately after they are synthesized in the ribosome, is the bending of the initial helix at specific amino acid sites. As it happens, there is a formal connection between this proposal and the solectron concept, which is through the *VES hypothesis* [25, 27, 48]. According to the VES hypothesis the initial triggers of protein conformational changes are vibrational

excited states (VES). There are many sources of VES for a protein in solution: excited states of water molecules can be transferred to the protein [49] and the binding of water molecules, or ions, and other ligands can create excited vibrational states in peptide groups [50]. According to the VES hypothesis, conformational changes take place when the energy stored in VES is transferred to the classical degrees of freedom of the protein leading to the domain motions such as helical rotations, hinge oscillations, etc, that characterize conformational changes [51]. A model for this kind of energy transfer must contain a quantum Hamiltonian, to describe the VES and a classical part to describe the conformational degrees of freedom, just as the solectron Hamiltonian includes a term to describe the electrons (which, like VES, are quantum particles) and a term that describes the motions of the lattice sites, usually treated as classical degrees of freedom. One very important difference between the two systems is that while the number of electrons is conserved in the usual transport processes, VES in proteins have a short lifetime that can be just a few picoseconds [52] and the transfer of their energy to the conformational degrees of freedom involves the annihilation of the quantum particle [23], a non-conservative process for which models are being developed [53, 54]. However, the short-term dynamics of the two systems, before the annihilation of the vibrational excited states occurs, i.e. when the quantum particles (electrons or VES) move under the influence of the classical degrees of freedom, is formally similar and much can be learn about the one when studying the other. This cross-fertilization between the research work on protein folding and function and the research on solectrons is continuously explored in the collaboration with the group of Manuel G(arcía) Velarde.

Acknowledgement Many of these simulations were performed at the Milipeia cluster of the Laboratory for Advanced Computing of the University of Coimbra, Portugal.

References

1. Anfinsen, C.B.: Science **181**, 223 (1973)
2. Butte, B., Merrifield, R.B.: J. Biol. Chem. **246**, 1922–1941, (1971)
3. Bryngelson, J.D., Onuchic, J.N., Socci, N.D., Wolynes, P.G.: Proteins **21**, 167 (1995)
4. Onuchic, J.N., Luthey-Schulten, Z., Wolynes, P.G.: Ann. Rev. Phys. Chem. **48**, 545 (1997)
5. Dill, K.A., Chan, H.-S.: Nat. Struct. Biol. **4**, 10 (1997)
6. Bowman, G.R., Pande, V.S.: Proc. Natl. Acad. Sci. USA **107**, 10890 (2010)
7. Case, D.A., et al.: J. Computat. Chem. **26**, 1668 (2005)
8. Christen, M., et al.: J Computat. Chem **26**, 1719 (2005)
9. Brooks, B.R., et al.: J. Computat. Chem. **30**, 1545 (2009)
10. Allen, F., et al.: IBM Syst. J. **40**, 310 (2001)
11. Shaw, D.E., et al.: Proceedings of the Conference on High Performance Computing Networking, Storage and Analysis, SC09. ACM, New York (2009)
12. Anfinsen, C.B.: Biochim. Biophys. Acta **1000**, 197 (1989)
13. Berendsen, H.J.C.: Science **282**, 642 (1998)
14. Horowitz, P.M.: Nat. Biotechnol. **17**, 136 (1999)

15. Service, R.F.: Science **321**, 784 (2008)
16. Levinthal, C.: J. Chim. Phys. **65**, 44 (1968)
17. Baker, D., Agard, D.A.: Biochemistry **33**, 7505 (1994)
18. Prusiner, S.B.: Science **216**, 136 (1982)
19. Prusiner, S.B.: Science **252**, 1515 (1991)
20. Baker, D., Sohl, J.L., Agard, D.A.: Nature **356**, 263 (1992)
21. Sohl, J.L., Jaswal, S.S., Agard, D.A.: Nature **395**, 817 (1998)
22. Gettins, P.G.W.: Chem. Rev. **102**, 4751 (2002)
23. Cruzeiro-Hansson, L., Silva, P.A.S.: J. Biol. Phys. **27**, S6 (2001)
24. Cruzeiro, L.: http://arxiv.org/abs/0712.2034 (2008)
25. Cruzeiro, L.: J. Phys. Org. Chem. **21**, 549 (2008)
26. Cruzeiro, L., Lopes, P.A.: Mol. Phys. **107**, 1485 (2009)
27. Cruzeiro, L.: Protein folding. In: Springborg, M. (ed.) Specialist Periodical Reports Chemical Modelling. Applications and Theory, vol. 7, p. 89. Royal Society of Chemistry, London (2010)
28. Ellis, J.P., Culviner, P.H., Cavagnero, S.: Prot. Sci. **18**, 2003 (2009)
29. Orengo, C.A., et al.: Structure **5**, 1093 (1997)
30. Schlitter, J., Engels, M., Krüger, P., Jacoby, E., Wollmer, A.: Mol. Simul. **10**, 291 (1994)
31. Apostolakis, J., Ferrara, P., Caflisch, A.: J. Chem. Phys. **110**, 2099 (1999)
32. Ovchinnikov, V., Trout, B.L., Karplus, M.: J. Mol. Biol. **395**, 815 (2010)
33. Negri, A., Rodríguez-Larrea, D., Marco, E., Jiménez-Ruiz, A., Sánchez-Ruiz, J.M., Gago, F.: Proteins: Struc. Funct. Bioinf. **78**, 36 (2010)
34. Apostolakis, J., Ferrara, P., Caflisch, A.: Proteins: Struct, Funct. Gen. **39**, 252 (2000)
35. Berman, H.M., et al.: Nucl. Acids Res. **28**, 235 (2000)
36. Gouda, H., et al.: Biochemistry **31**, 9665 (1992)
37. Gallagher, T., Alexander, P., Bryan, P., Gillilan, G.L.: Biochemistry **33**, 4721 (1994)
38. Hornak, V., et al.: Proteins **65**, 712 (2006)
39. Case, D.A., et al.: AMBER 9. University of California, San Francisco (2006)
40. Wickstrom, L., Okur, A., Simmerling, C.: Biophys. J. **97**, 853 (2009)
41. Humphrey, W., Dalke, A., Schulten, K.: J. Molec. Graph. **14**, 33 (1996)
42. Ptitsyn, O.B.: TiBS **20**, 376 (1995)
43. Roder, H., Colón, W.: Curr. Opt. Struct. Biol. **7**, 15 (1997)
44. Englander, S.W.: Annu. Revs. Biophys. Biomol. Struct. **29**, 213 (2000)
45. Brockwell, D.J., Radford, S.E.: Curr. Opt. Struct. Biol. **17**, 30 (2007)
46. Shortle, D., Ackerman, M.S.: Science **293**, 487 (2001)
47. Kaiser, C.M., Goldman, D.H., Chodera, J.D., Tinoco, I. Jr., Bustamante, C.: Science **334**, 1723 (2011)
48. Cruzeiro, L.: J. Phys.: Condens. Matter **17**, 7833 (2005)
49. Sieler, G., Schweitzer-Stenner, R.: J. Am. Chem. Soc. **119**, 1720 (1997)
50. Careri, G., Wyman, J.: Proc. Natl. Acad. Sci. USA **81**, 4386 (1984)
51. Flores, S., Echols, N., Milburn, D., Hespenheide, B., Keating, K., Lu, J., Wells, S., Yu, E.Z., Thorpe, M., Gerstein, M.: Nuc. Acid Res. **34**, D296 (2006)
52. Edler, J., Hamm, P.: J. Chem. Phys. **117**, 2415 (2002)
53. Silva, P.A.S., Cruzeiro-Hansson, L.: Phys. Lett. A **315/6**, 447 (2003)
54. Silva, P.A.S., Cruzeiro, L.: Phys. Rev. E **74**, 021920 (2006)

Study of Cardiac Defibrillation Through Numerical Simulations

J. Bragard, S. Marin, E.M. Cherry, and F.H. Fenton

1 Introduction

Ventricular fibrillation (VF) is a serious medical condition that requires immediate intervention. During VF, the electrical activity of the heart is disorganized, leading to localized and ineffective contraction that renders the heart unable to pump blood properly. Cardiac defibrillation [1, 2] consists of the application of a very strong electric shock to restore the correct function of the heart. Unfortunately, defibrillation is not always successful. Computational studies can help to elucidate the mechanisms underlying defibrillation. In this study, we construct a realistic model of the electrical activity taking place inside the ventricles of the heart. Next, we set the parameter values of the model to produce fibrillatory dynamics. Then, we test the defibrillation procedure directly on the numerical model.

The numerical model contains two primary fields, the extracellular and intracellular electric potentials. These fields are governed by partial differential equations that must be solved simultaneously (one is a stiff reaction-diffusion equation and the other is the Poisson equation). In Sect. 2, we discuss the basic equations that govern the problem. In Sect. 3, we explain the algorithm used to solve these equations efficiently. In particular, the equations are solved in parallel with the Poisson equation solved by Krylov iterative techniques implemented with the PETSc package [3]. The performance of the algorithm and how it scales with the number of processors also

J. Bragard (✉) · S. Marin
Department of Physics and Applied Mathematics, University of Navarra, 31080 Pamplona, Spain
e-mail: jbragard@unav.es

E.M. Cherry
Rochester Institute of Technology, School of Mathematical Sciences, Rochester, NY, USA
e-mail: elizabeth.cherry@rit.edu

F.H. Fenton
Department of Biomedical Sciences, Cornell University, Ithaca, NY, USA
e-mail: fhf3@cornell.edu

R.G. Rubio et al. (eds.), *Without Bounds: A Scientific Canvas of Nonlinearity and Complex Dynamics*, Understanding Complex Systems,
DOI 10.1007/978-3-642-34070-3_47, © Springer-Verlag Berlin Heidelberg 2013

are addressed. In Sect. 4, we analyze the results of the application of strong electric shocks using several initial conditions. From these results, it is possible to determine the energy needed for successful defibrilation. In the conclusions, we suggest ideas for future studies aimed at designing milder defibrillatory shocks.

2 Governing Equations

The most commonly used model to describe the electrical activity of the heart during defibrillation is the bidomain model. This model was derived from the basic Kirchhoff laws applied to cardiac tissue and cardiomyocyte membrane dynamics by Leslie Tung [4]. The spatial domains where the equations are solved are shown in Fig. 1. The two fundamental fields of these equations are the intracellular electrical potential u_i and the extracellular electrical potential u_e. The two can be combined to derive the transmembrane potential $V = u_i - u_e$, which is the quantity most accessible for direct experimental measurement.

2.1 Bidomain Model

The complete mathematical expressions for the model are as follows [5–7]:

$$\frac{\partial s}{\partial t} = f(V, s) \qquad x \in H \quad (1)$$

$$\frac{\partial V}{\partial t} + I_{ion}(V, s) = \nabla \cdot (M_i \nabla V) + \nabla \cdot (M_i \nabla u_e) \qquad x \in H \quad (2)$$

$$\nabla \cdot ((M_i + M_e)\nabla u_e) = -\nabla \cdot (M_i \nabla V) - I_{ext} \qquad x \in H \quad (3)$$

$$\nabla \cdot (M_T \nabla u_T) = 0 \qquad x \in T \quad (4)$$

where s is a state vector that contains all the variables associated with the description of ionic currents across the membrane, where all ion transport takes place [2]. The mathematical description of the opening and closing of the ion channels is described by a set of differential equations (1). The time scales associated with these equations vary from 0.1 ms up to 1 s and higher. Furthermore, the vector function $f(V, s)$ in (1) is highly nonlinear. Consequently, the equations are stiff and are challenging to solve from the numerical point of view. Equation (2) is a nonlinear parabolic equation (reaction–diffusion) that relates the local activity of the membrane at each point in space to that of its neighbors and M_i is the electrical conductivity tensor of rank two. In general the conductivity tensor is neither homogeneous nor isotropic. Typical values for the conductivities [8] are $D_{\parallel}^{(i)} = 10^{-3}$, $D_{\perp}^{(i)} = 6.75 \times 10^{-5}$, $D_{\parallel}^{(e)} = 1.5 \times 10^{-3}$, and $D_{\parallel}^{(e)} = 1.575 \times 10^{-4}$, all in units of cm^2/ms; these correspond to the

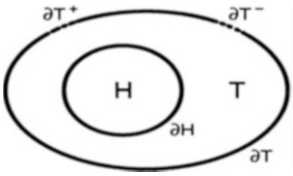

Fig. 1 Heart (H) and torso (T) mathematical domain definitions

orthotropic tensors (M_i and M_e) [7]. Although we provide the equations associated with the torso for completeness, we do not include a detailed torso model in the present study. Therefore, here the value for the electrical conductivity in the domain where only the extracellular tissue is present is taken as isotropic and is fixed to the conductivity of blood (i.e. $D_{\parallel}^{(T)} = D_{\perp}^{(T)} = 4. \times 10^{-3}\,\mathrm{cm}^2/\mathrm{ms}$). The large difference between the conductivities along the fibers ($\parallel$) and perpendicular to the fibers ($\perp$) allows for a significant difference in the speed of electrical wave propagation.

Equation (3) is the Poisson equation (elliptic PDE) that relates the current inside the heart to the extracellular electrical potential. Time does not appear explicitly in the Poisson equation and it must be solved simultaneously with (2) at every time. Finally, (4) is a Laplace equation (Poisson equation without the source term) and it must also be solved inside this domain simultaneously with the other equations. The term I_{ext} allows for the introduction of external current as happens during a defibrillation event.

In the present study, we use the three-dimensional geometry corresponding to the rabbit heart ventricles [9].

To solve (1)–(4), the following boundary conditions are imposed:

$$(M_i \nabla V + M_i \nabla u_e) \cdot n_H = 0 \qquad x \in \partial H \tag{5}$$

$$(M_e \nabla u_e) \cdot n_H = -(M_T \nabla u_T) \cdot n_T \qquad x \in \partial H \tag{6}$$

$$u_e = u_T \qquad x \in \partial H \tag{7}$$

$$(M_T \nabla u_T) \cdot n_T = 0 \qquad x \in \partial T \tag{8}$$

These equations express the current conservation condition at the boundaries.

2.2 Membrane Models

From a dynamical point of view, the heart, like the brain, is an excitable medium. This means that a perturbation that overcomes a certain threshold produces an action potential (nonlinear response) that propagates as a wave throughout the entire domain with a characteristic shape and velocity. The challenge from the biological

point of view is to correctly describe and model the dynamics of the opening and closing of the ion channels embedded in the cell membrane that collectively give rise to the action potential. This task started from the seminal work of Hodgkin and Huxley in describing the dynamics of the squid giant axon in the 1950s [10]. More recently, a large number of mathematical models of ventricular myocytes are available in the literature [11]. For example, the Beeler-Reuter [12] model contains eight variables including the membrane potential, the intracellular calcium concentration, and six gating variables. Luo and Rudy produced two widely used models of mammalian ventricular myocytes (LR1 and LR2) [13,14], with the more recent containing 24 variables and the detailed descriptions of 12 transmembrane currents. In 1998, Fenton and Karma [15] reduced the BR and LR1 models into a simplified three-variable model able to represent quite faithfully the propagation of the action potential without the numerical burden associated with the large numbers of variables in the original models. In 2004, Cherry and Fenton [16] improved the previous model by Fenton-Karma by adding a fourth variable to provide more flexibility in accounting for action potential shape. In 2010, Cantalapiedra et al. [17, 18] developed a five-variable model containing a specific formulation for the transient outward K^+ current, which is important in describing action potentials associated with the Brugada syndrome. In general, selecting a model for simulating the electrical activity of the heart requires finding the appropriate balance of model complexity and computational speed. In this work, we use a reduced version of the Cantalapiedra et al. model [17,18] given in the Appendix.

3 Numerical Method

To solve (1)–(8) numerically, it is necessary to discretize space and time. For the spatial discretization, the finite volume method is used [19]. This method is preferred because it conserves exactly the charges moving from a reference volume to the next. The time discretization uses a simple forward Euler method that parallelizes easily:

$$\nabla \cdot ((M_i + M_e)\nabla u_e^n) = -\nabla \cdot (M_i \nabla V^n) - I_{ext}^n \tag{9}$$

$$\frac{V^{n+1} - V^n}{\delta t} = -I_{ion}(V^n, s^n)\nabla \cdot (M_i \nabla V^n) + \nabla \cdot (M_i \nabla u_e^n) \tag{10}$$

$$\frac{s^{n+1} - s^n}{\delta t} = f(V^n, s^n) \tag{11}$$

The most costly part of the computation comes from (9), which we solve using the Poisson solver PETSc package [3]. The spatial discretization of the equation leads to a system of the form

$$Ax = b, \tag{12}$$

Table 1 Propagation velocity of electrical waves in cm/s for different spatial and temporal discretizations

Δx (cm)	$\delta t = 0.005$ ms	$\delta t = 0.01$ ms	$\delta t = 0.02$ ms	$\delta t = 0.05$ ms
0.01	35.3	35.2	35	34.3
0.02	34.3	34.2	34	33.3
0.04	31	30.9	30.7	30

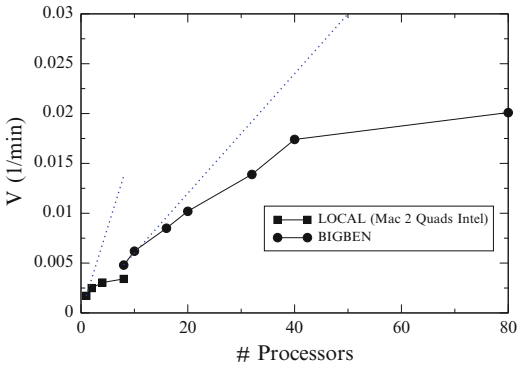

Fig. 2 Scalability of the 3D code with the number of processors. The horizontal axis indicates the number of processors, the vertical axis indicates the inverse time spent for a given reference simulation (speed in min^{-1}). The two *dashed blue lines* indicate how the speed would increase in the ideal case (i.e. double the speed when double the number of processors)

where A is a large sparse positive semi-definite constant matrix and the vector x contains the unknowns u_e of every discretized volume of the system.

We tested three different iterative methods: biconjugate gradient stabilized (BCG–STAB), conjugate gradient (CG), and generalized minimum residual (GMRES). All are based on Krylov subspace methods. These methods use projection processes onto Krylov subspaces to get an approximate solution at every step of the iterative process [20].

To improve the efficiency of this method, it is necessary to apply a preconditioner. In this case the preconditioner has been made using an additive Schwarz method (ASM) with an incomplete factorization ILU(0) applied in each block, where the zero index refers to the fact that the sparsity of the preconditioner is the same as the sparsity of the matrix A. Although all three methods give appropriate accuracy, GMRES with the preconditioner gives the best results in term of computational speed, so we use this method.

We verified the numerical consistency of the results by changing the spatial discretization Δx and the time steps δt. In simulations using one spatial dimension, we measured the propagation velocity of electrical waves at different discretizations. The results are shown in Table 1.

For the three-dimensional simulations, we chose $\Delta x = 0.02$ cm and $\delta t = 0.02$ ms, which is a good trade-off between accuracy and CPU cost (see Table 1). The code was parallelized with message passing interface (MPI) in Fortran [21] and run locally on a dual-quad Mac Intel (see square symbols in Fig. 2) and also on large clusters at the Pittsburgh Supercomputing Center and Purdue University (see circle symbols in Fig. 2).

An important characteristic for parallel codes is how the speed (inverse of computation time) varies with respect to the number of processors. Figure 2 shows how the 3D code scales with the number of processors used. It is clear that the scaling is much better for the large clusters than for the local Intel/Quad workstation because communication among the processors is much faster for the clusters, which substantially improves the scaling of computation speed. As the number of processors increases, the time spent communicating among processes represents an increased fraction of the workload, causing the performance gain from using additional processors to be more modest. Performance levels off for a fairly small number of processors because the rabbit ventricles are themselves rather small; larger computational domains can benefit more easily from more processors.

4 Results of the Defibrillation Simulations

The main objective of the present study is to quantify the efficacy of defibrillatory shocks at various energies using our numerical model. We use the rabbit ventricular anatomical model [9] in conjunction with the membrane model detailed in the Appendix. The parameter values used with the membrane model are given in Table 2. For these parameter values, a disorganized electrical state corresponding to VF is achieved, as shown in Fig. 3.

4.1 Model Initial Conditions

We simulated the model for 3 s, as shown in Fig. 3. During this time the full dynamical state of the system was saved every 300 ms. These 10 saved states were then used as 10 uncorrelated initial conditions for testing the defibrillation procedure. Indeed, we verified that the absolute value of the Pearson correlation coefficient between any two fields was below 0.2, which indicates that they are uncorrelated.

The conventional medical procedure for defibrillation consists of applying a very strong electric field through two electrodes placed on the patient torso. Here, in our numerical model, two plane electrodes are placed at the limits of the cubic integration domain in the extracellular region, with the load anode (injecting positive charge) located close to the left ventricle (LV) and the load cathode located close to the right ventricle (RV), as depicted in Fig. 3.

Figure 4 shows four stages of a successful defibrillatory shock.

4.2 Dose-Response Curve

In this study, we used monophasic shocks 12 ms in duration. Five levels of shock intensity were tested corresponding to inter-electrode electric field strengths of

Table 2 Parameter values for the four-variable model

Parameter	Value	Parameter	Value	Parameter	Value
g_{fi}	$5\,\text{ms}^{-1}$	V_c	0.13	β_1	5
g_{si}	$0.01\,\text{ms}^{-1}$	V_{fi}	1	β_2	10
g_{so}	$0.022\,\text{ms}^{-1}$	V_1	0.3	τ_{w1}	180 ms
g_{ito}	$1\,\text{ms}^{-1}$	V_r	0.2	τ_{w2}	40 ms
τ_{s1}	10 ms	τ_{r1}	7 ms		
τ_{s2}	39.2 ms	τ_{r2}	5 ms		

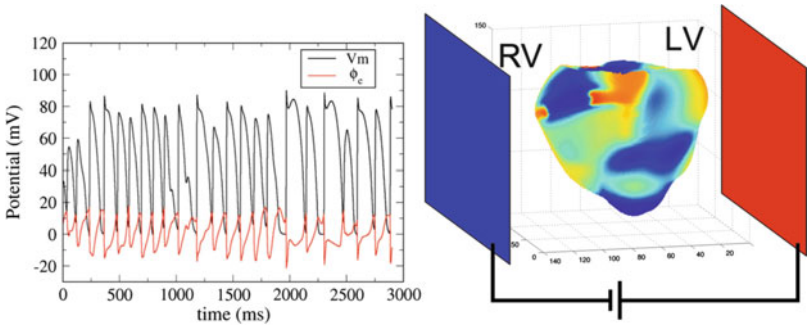

Fig. 3 *Left*: Time evolution of the membrane potential V_m and the extracellular potential (denoted here by ϕ_e) measured in the middle of the ventricular septum. Note that here V_m is given in dimensional units (mV) and has been rescaled and shifted for plotting purposes so that the resting state is 0 mV. *Right*: Setup used in this study for quantifying defibrillation efficacy

3.625, 7.25, 10.875, 14.5, and 18.125 V/cm. Using the 10 different initial conditions, we calculated statistics for the success rate. After the 12-ms shock was applied, the system evolved for 600 ms. Then the outcome of the numerical experiment was classified as follows. If the activity stopped directly, it was considered a success (score 1). If disorganized activity remained after 600 ms, it was considered a failure (score 0). If only a single beat (ectopic beat) was observed, it was scored at 0.5. The results of all the simulation are shown in Fig. 5. The analysis of the results can be made using the well-known dose-response curve [22]:

$$P(I) = \frac{1}{1 + \exp[k(I_{50} - I)]} \tag{13}$$

where P indicates the probability of success as a function of the dose intensity I.

A direct fit of the curve given by (13) using the data of Fig. 5 results in the following values: $I_{50} = 6.6\,(\text{V/cm})$ and $k = 0.45\,(\text{cm/V})$. This means that an energy associated with an electric field above 6.6 V/cm would provide a 50% chance of efficacious defibrillation. The latter is in good agreement with values found in the literature [23].

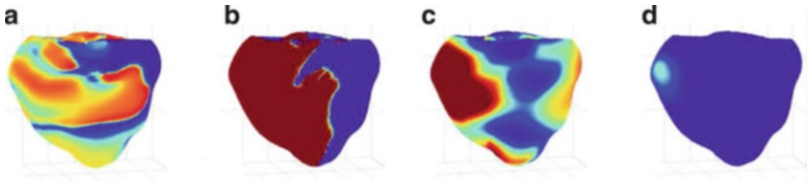

Fig. 4 Four successive snapshots during successful defibrillation using a monophasic shock of 12 ms duration. (**a**) Electrical activity before the shock; (**b**) Strong polarized activity during the shock; (**c**) Activity 50 ms after the shock ending; (**d**) Nearly all activity has disappeared 100 ms after the shock ending

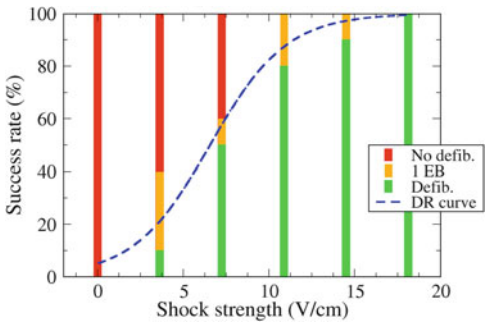

Fig. 5 Defibrillation success rate as a function of electrical shock strength as obtained through the 50 numerical simulations. The *dashed curve* (dose-response curve) represents the best fit of the data through (13). EB: extra beat. DR: dose-response

5 Conclusions and Further Work

In this study we developed a parallel numerical code to simulate the electrical activity of the heart and applied the code to study defibrillation. We found that the shock strength needed to defibrillate the numerical heart agree well with what has been reported experimentally and clinically [23]. Our next step is optimize our defibrillation protocol using additional numerical simulations. Our objective is to reduce the energy content of the shock, thereby reducing the risk of irreversible tissue damage. Experimental results achieving lower energy by applying multiple low-energy shocks rather than a single high-energy shock have been published recently by Fenton et al. [24]. Additional energy reductions are expected to result from optimizing such parameters as electrode positions and polarity; number, duration, and frequency of shocks; and shock waveform.

Appendix

Below we give the detailed formulations of the transmembrane currents used in this study. The membrane potential V is written in dimensionless form and is re-scaled in the range [0, 1]. Note that the hyperbolic tangent functions were evaluated using lookup tables to improve performance.

$$I_{ion} = J_{fi} + J_{si} + J_{so} + J_{to} \tag{14}$$

$$J_{fi} = -g_{fi}\ s\,(V - V_c)\,(V_{fi} - V)\Theta(V - V_c)\ , \tag{15}$$

$$J_{si} = -g_{si}\ w\{1 + \tanh[\beta_1(V - V_1)]\}\{1 + \tanh[\beta_2(1 - V)]\}\Theta(V - V_c)\ , \tag{16}$$

$$J_{so} = g_{so}\ \left\{\frac{V}{V_c}\,[1 - \Theta(V - V_c)] + \Theta(V - V_c)\right\}\ , \tag{17}$$

$$J_{to} = g_{ito}\ r\,s\,V\ , \tag{18}$$

where $\Theta(x)$ is the usual Heaviside function and where the differential equations for the three ionic gate variables are written as follows:

$$\frac{\partial s}{\partial t} = \frac{\Theta(V_c - V) - r}{\tau_{s_1} + (\tau_{s_2} - \tau_{s_1})\Theta(V_c - V)} \tag{19}$$

$$\frac{\partial r}{\partial t} = \frac{\Theta(V - V_r) - r}{\tau_{r_1} + (\tau_{r_2} - \tau_{r_1})\Theta(V - V_r)} \tag{20}$$

$$\frac{\partial w}{\partial t} = \frac{\Theta(V_c - V) - w}{\tau_{w_1} + (\tau_{w_2} - \tau_{w_1})\Theta(V_c - V)} \tag{21}$$

The time constants that appear in (15)–(21) are fitted to reproduce specific mesoscopic characteristics of heart tissue, such as action potential duration (APD) and the conduction velocity (CV) restitution curves, as well as action potential (AP) shapes. The present model is a simplification of the model proposed by Cantalapiedra et al. [17, 18].

Acknowledgement The first author (J.B.) is indebted to Prof. M.G. Velarde, who was his PhD advisor, for his time, guidance, patience, and good mood in teaching him science. Financial support from the Spanish Ministry of Economy is acknowledged through project number FIS2011-28820-C02-02, and the "Salvador Madariaga" program (Spanish mobility program: PR2011-0168). This work used the Extreme Science and Engineering Discovery Environment (XSEDE), which is supported by National Science Foundation (USA) grant number OCI-1053575.

References

1. Efimov, I.R., Kroll, M.W., Tchou, P.J.: Cardiac Bioelectric Therapy. Springer, New York (2009)
2. Keener, J., Sneyd, J.: Mathematical Physiology. Springer, New York (1998)
3. Balay, S., Buschelman, K., Eijkhout, V., Gropp, W.D., Kaushik, D., Knepley, M.G., McInnes, L.C., Smith, B.F., Zhang, H.: PETSc Users Manual. Argonne National Laboratory (2008)
4. Tung, L.: A bi-domain model for describing ischemic myocardial d-c potentials. PhD. Thesis, MIT, Cambridge (1978)
5. Hanslien, M., Sundnes, J., Lines, G.T.: Numerical simulations of cardiac arrhythmias and defibrillation. In: Skallerud, B., Andersson, H.I. (eds.) MekIT'05 - Third National Conference on Computational Mechanics, Trondheim, Norway, May 11–12, pp. 135–144. Tapir Academic Press, Trondheim (2005)

6. Henriquez, C.S.: Simulating the electrical behavior of cardiac tissue using the bidomain model. Crit. Rev. Biomed. Eng. **21**, 1–77 (1993)
7. Sachse, F.B.: Computational Cardiology. Springer, Berlin (2004)
8. Aguel, F., Eason, J., Trayanova, N.A.: Advances in modeling cardiac defibrillation. IJBC. **13**(12), 3791–3803 (2003)
9. Vetter, F.J., McCulloch, A.D.: Three-dimensional analysis of regional cardiac function. Prog. Bioph. Mol. Biol., **69**(2), 157–183 (1998)
10. Hodgkin, A., Huxley, A.: A quantitative description of membrane current and its application to conduction and excitation in nerve. J. Physiol. **117**, 500–544 (1952)
11. Clayton, R.H., Bernus, O., Cherry, E.M., Dierckx, H., Fenton, F.H., Mirabella, L., Panfilov, A.V., Sacjse, F.B., Seemann, G., Zhang, H.: Models of cardiac tissue electrophysiology: progress, challenges and open questions. Progr. Bioph. Mol. Biol. **104**, 22–48 (2011)
12. Beeler, G.W., Reuter, H.: Reconstruction of the action potential of ventricular myocardial fibers. J. Physiol. **268**, 177–210 (1977)
13. Luo, C.H., Rudy, Y.: A model of the ventricular cardiac action potential: depolarization, repolarization, and their interaction. Circ. Res. **68**, 1501–1526 (1991)
14. Luo, C.H., Rudy, Y.: A dynamical model of the cardiac ventricular action potential: I. Simulations of ionic currents and concentration changes. Circ. Res. **74**, 1071–1096 (1994)
15. Fenton, F., Karma, A.: Vortex dynamics in three-dimensional continuous myocardium with fiber rotation: filament instability and fibrillation. Chaos **8**(1), 20–47 (1998)
16. Cherry, E., Fenton, F.: Suppression of alternans and conduction blocks despite steep APD restitution: electrotonic, memory, and conduction velocity restitution effects. Am. J. Physiol. Heart Circ. **286**, H2332–H2341 (2004)
17. Cantalapiedra, I.R., Peñaranda, A., Echebarria, B., Bragard, J.: Phase-2 reentry in cardiac tissue: role of the slow calcium pulse. Phys. Rev. E **82(1)**, 1907 (2010)
18. Peñaranda, A., Cantalapiedra, I.R., Bragard, J., Echebarria, B.: Cardiac dynamics: a simplified model for action potential propagation. Theor. Biol. Med. Model. **9**, art. 50. doi:10.1186/1742-4682-9-50. Published: Nov 29, 2012
19. Press, W., Flannery, B., Teukolvsky, S., Vetterling, W.: Numerical recipes in FORTRAN: the art of scientific computing. Cambridge University Press, Cambridge (1992)
20. Saad, Y.: Iterative Methods for Sparse Linear System. Springer, New York (2002)
21. Pacheco, P.: Parallel programing with MPI. Morgan Kaufmann, Los Altos (1997)
22. Stroobandt, R.X., Barold, S.S., Sinnaeve, A.F.: Implantable cardioverter-defibrillators step by step. Wiley-Blackwell, Chichester (2009)
23. Wharton, J.M., Wolf, P.D., Smith, W.M., Chen, P.S., Frazier, D.W., Yabe, S., Danieley, N., Ideker, R.E.: Cardiac potential and potential gradient fields generated by single, combined, and sequential shocks during ventricular defibrillation. Circulation **85**, 1510–1523 (1992)
24. Luther, S., Fenton, F.H., Kornreich, B.G., Squires, A., Bittihn, P., Hornung, D., Zabel, M., Flanders, J., Gladuli, A., Campoy, L., Cherry, E.M., Luther, G., Hasenfuss, G., Krinsky, V.I., Pumir, A., Gilmour, R.F. Jr., Bodenschatz, E.: Low-energy control of electrical turbulence in the heart. Nature **475**, 235–239 (2011)

Morphogenesis and Complexity of the Tumor Patterns

E. Izquierdo-Kulich and J.M. Nieto-Villar

1 Introduction

Cancer is a generic name given to a group of malignant cells which have lost their specialization and control over normal growth. These groups of malignant cells are nonlinear dynamic systems which self-organize in time and space, far from thermodynamic equilibrium, and exhibit high complexity [1] robustness [2] and adaptability [3].

Transition phenomena, far from being in thermodynamic equilibrium, are related due to bifurcations, to states characterized by correlations that affect the macroscopic behavior of the tumor. Coherence in tumor cells is associated with simultaneous reinforcement of fluctuations. A recent work shows that tumors operate close to an instability threshold [4]. This study shows that tumor cell populations live close to this threshold at a certain level of genetic instability.

An important characteristic of complex dynamic systems is their stability in front of external perturbations. We have recently demonstrated that dynamic systems may or may not be controlled by the effect of periodic external fluctuations, according to the type of dynamic systems' complexity [5]. In other words, the sensitivity of the system to external fluctuations depends on its robustness [3].

In spite of achievements in molecular biology and genomics, the growth mechanism for tumor cells and the nature of its robustness are still unknown. Tumor cell robustness enables a system to maintain its functionality in the face of various external and internal perturbations [6, 7]. Tumor cells exhibit two aspects of robustness: functional redundancy, which is enabled by cellular heterogeneity, and

E. Izquierdo-Kulich · J.M. Nieto-Villar (✉)
M.V. Lomonosov Chemistry Chair, Faculty of Chemistry, H. Poincaré Group of Complex Systems, Physics Faculty, Department of Chemical-Physics, University of Havana, Havana 10400, Cuba
e-mail: elenaik@fq.uh.cu; nieto@fq.uh.cu

R.G. Rubio et al. (eds.), *Without Bounds: A Scientific Canvas of Nonlinearity and Complex Dynamics*, Understanding Complex Systems,
DOI 10.1007/978-3-642-34070-3_48,

feedback-control systems [6,7]. Controlling cell robustness by reducing heterogeneity is a potential strategy for the development of drugs and therapies.

Tumor cell heterogeneity is manifested by the irregularity of the tumor boundaries. Fractal geometry proves to be useful for describing the pathological architecture of tumors and for yielding insights into the mechanisms of tumor growth [8].

Mathematical models represent a manner for formalizing the knowledge of living systems obtained through theoretical biology. Mathematical modeling of tumor growth makes possible the description of its most important regularities and is useful in providing effective guidelines for cancer therapy, drug development, and clinical decision-making [9, 10].

The goal of this chapter is to give a theoretical framework the mathematical modeling of tumor growth, based on a stochastic and thermodynamics approaches that allows improving our understanding of the origin of tumor cell heterogeneity and thus its robustness. The plan of the paper is the following: In Sect. 2, we propose a mechanism for the apoptosis regulation by $p53$ sustained oscillations. This mechanism was developed taking into account the experimental results reported being related with the oscillation in the amount of $p53$ that is present in the damaged cells [11–14] and the role of oscillation in the biological system. A mesoscopic approach to be used, to establish cancer's therapeutic strategies is obtained from the proposed mechanism [15].

In Sect. 3, formalism is obtained from the master equation (ME) to obtain the mesoscopic model which describes the tumor growth dynamics in absence of external fluctuations, taking into account that the tumor grows in a limited area. The microscopic variable considered to describe the state of the system is the total number of tumor cells, and the macroscopic variables are the expected value of the radius and the fractal dimension, which is a result of internal fluctuations.

In Sect. 4, a mathematical model was obtained to describe the relation between the tissue morphology of cervix carcinoma and both dynamic processes of mitosis and apoptosis, and an expression to quantify the tumor aggressiveness, which in this context is associated with the tumor growth rate. The proposed model was applied to Stage III cervix carcinoma in vivo studies. Finally, in the Sect. 5, the entropy production rate was determined for avascular tumor growth. The proposed formula relates the fractal dimension of the tumor contour with the quotient between mitosis and apoptosis rate, which can be used to characterize the degree of proliferation of tumor cells. The entropy production rate was determined for fourteen tumor cell lines as a physical function of cancer robustness.

2 A Mesoscopic Approach to Model Regulation of Apoptosis by $p53$

Three decades of $p53$ research have led to many advances in understanding the function of $p53$ in relation to longevity and aging [16], metabolism regulation [17], tumor suppression and apoptosis process, which are important aspects because

many human cancers show resistance to apoptosis [18, 19]. The apoptosis process consists in the programmed cellular death which occurs when DNA damage is detected, but can not be repaired. In this scenario, the cell may reproduce in a mutated form, later appearing as cancer.

Experimental studies of $p53$ and $Mdm2$ behavior in response to DNA damage show damped oscillation of $p53$ concentration at cell population level and undamped oscillation of $p53$ in single cells [11–14]. Although the oscillatory behavior is ubiquitous for biological systems [20–22], the significance of $p53$ oscillations still remains unclear [14].

To obtain a mechanism to predict the dynamics of $p53$ at cellular level associated to the apoptosis process, the following considerations were made: (1) the $p53$ activation is stimulated by a virtual species Dm, which is associated with the DNA damage level; (2) $p53$ stimulates the synthesis of $Mdm2$; (3) $Mdm2$ stimulates the $p53$ degradation and (4) the level of Dm decreases with the increased $p53$ level. The increase in $p53$ retards the mitosis processes while the damage is repaired [14]. This proposed mechanism is shown in Fig. 1.

We assumed that each p processes at microscopic level occurs with a transition probability per unit time Wp, which must be supposed a priory. So, the following facts were established:

(1) the synthesis of $p53$ via DNA has a transition probability given by $W1 = \Phi_1.\Omega$, where Φ_1 is the $p53$ basal synthesis rate constant; (2) the degradation of $p53$ because of the $Mdm2$ action, $W2 = K.\Omega^{-1}.p53.Mdm2$, where K is the $p53$ degradation rate constant; (3) The synthesis of $Mdm2$ is stimulated by $p53$, $W3 = A.p53$, where A is the $Mdm2$ synthesis rate constant; (4) the inhibition of $Mdm2$, $W4 = B.\Omega^{-1}.Mdm2.Dm$, where B is the $Mdm2$ inhibition rate constant; (5) the synthesis of Dm is stimulated by the damage magnitude, $W5 = \Phi_2.\Omega$, where Φ_2 is a rate constant associated to the damage level and (6) the damage inhibition caused by the $p53$ action is, $W6 = C.p53$, where C is a rate constant associated to damage reparation because of the $p53$ action.

From the transition probability per unit time established a priori, the obtained Fokker-Planck equation (FPE) [23, 24], expressed as a function of the macroscopic variables. From the established considerations, we obtained that the dynamic behavior of the system [15] is given by the following system ordinary differential equations:

$$\frac{d\,[p53]}{dt} = \Phi_1 - K\,[p53]\,[Mdm2] \tag{1}$$

$$\frac{d\,[Mdm2]}{dt} = A\,[p53] - B\,[Mdm2]\,[Dm] \tag{2}$$

$$\frac{d\,[Dm]}{dt} = \Phi_2 - C\,[p53] \tag{3}$$

With the purpose of analyzing the model predictions we selected as control parameters the B constant associated to $Mdm2$ degradation, and the Φ_2 constant

Fig. 1 Proposed mechanism

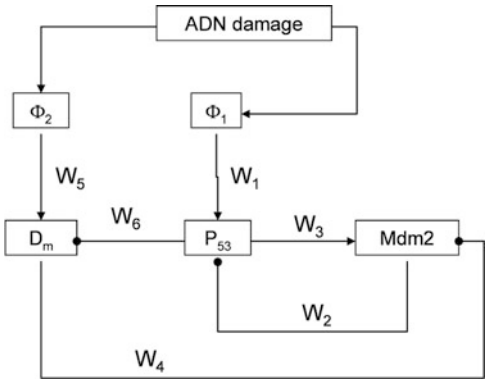

related to the damage level of DNA. In order to simplify, the rest of the constants are assumed equal to 1; thus (1)–(3) are written:

$$\frac{dx}{dt} = 1 - xy \tag{4}$$

$$\frac{dy}{dt} = x - Byz \tag{5}$$

$$\frac{dz}{dt} = \Phi_2 - x \tag{6}$$

where the corresponding stationary state is:

$$x_{ss} = \Phi_2, y_{ss} = \frac{1}{\Phi_2}, z_{ss} = \frac{\Phi_2^2}{B} \tag{7}$$

If the stationary state is substituted in the Jacobian Θ

$$\Theta = \begin{bmatrix} -Ky & -Kx & 0 \\ A & -Bz & -By \\ -C & 0 & 0 \end{bmatrix} \tag{8}$$

we arrive to the characteristic equation as a function of the eigenvalues

$$B + 2\Phi_2\lambda + \frac{1 + \Phi_2^3}{\Phi_2}\lambda^2 + \lambda^3 = 0 \tag{9}$$

and we find that the periodic oscillations occur because of a supercritical Andronov-Hopf bifurcation [25], where:

$$B_c = 2 + 2\Phi_2^3 \tag{10}$$

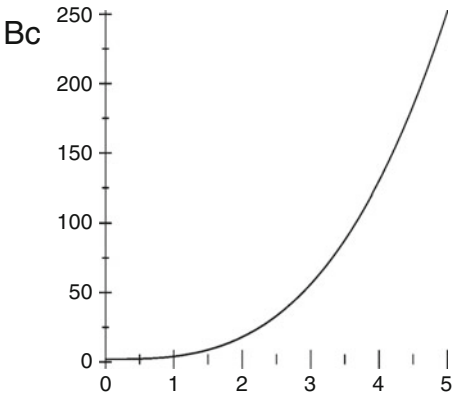

Fig. 2 Bifurcation diagram ($B_c = 2 + 2\Phi_2^3$)

Taken into account that the oscillations number of $p53$ and the probability of apoptosis process depend of level damage, we considered as hypothesis that the apoptosis process is controlled and induced by the sustained oscillations of $p53$, whereas this process doesn't occur when the oscillations are damped, indicating the survival of the mutated cells.

The bifurcation diagram obtained from (10) is shown in Fig. 2, where the survival or apoptosis cells are described as a function of control parameters. In this case, when $B < Bc$, $p53$ shows damped oscillations (Fig. 3a) and the stimulated process is the cells' survival, while when $B > Bc$, the stimulated process is the cells apoptosis, which is just regulated by the $p53$ sustained oscillations (Fig. 3b). If the hypothesis proposed is correct, the obtained bifurcation diagram can be used to establish different therapy strategies against cancer based on the stimulation of apoptosis.

The protein $Mdm2$, which is the biological regulator of $p53$, is overexpressed in certain types of cancer [26]. Taking into account the bifurcation diagram and the established hypothesis, if the value of the parameter B, which represents the $Mdm2$ degradation, is increased in such way that $B > Bc$, the apoptosis process is stimulated and regulated through sustained oscillations. This theoretical result may correspond to therapeutic strategies recently established by other authors, which proposed a therapy based on the inhibition of $Mdm2$ [26–28].

The apoptosis process has been associated with high levels of $p53$, which is based on the experimental results which show $p53$ increase with damage level [29]. In this sense, the absence of $p53$ observed in certain cancers, seems to corroborate this hypothesis. Nevertheless, other types of cancer show high level of $p53$, which is correlated with a poor prognosis [30, 31]. According to the proposed model, apoptosis can only occur when $\Phi_2 < \Phi_{2,c}$ for a given value of B, i.e. the cell survival is induced when the level of $p53$ is too high, which can explain why a high level of $p53$ is not always associated to apoptosis.

We considered as hypothesis that the apoptosis occurs as a result of a non-linear self-organized process far from thermodynamic equilibrium. Based on it, a

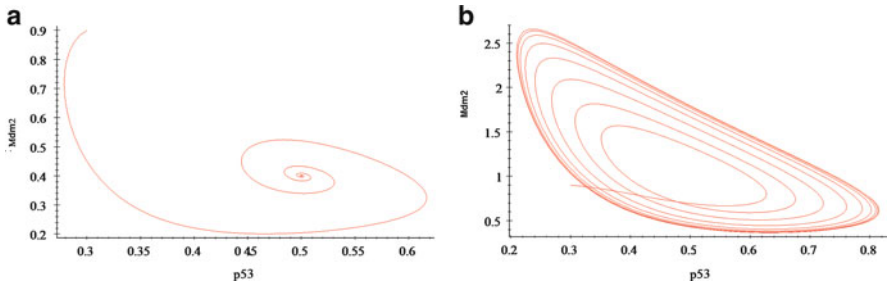

Fig. 3 (**a**) (*left*): Phase plane x, y corresponding to predicted dynamical behaviour; $B < B_c$, damped oscillation, stable focus. (**b**) (*right*): Phase plane x, y corresponding to predicted dynamical behaviour; $B > B_c$, undamped oscillation, limit cycle

stochastic formalism that allows a better understanding of the regulation processes of apoptosis through $p53$ sustained oscillations is proposed, where the obtained deterministic model predicts the reported qualitative experimental results related with the $p53$ oscillations when there is a DNA damage. It also predicts that it is necessary a strict regulation of $p53$ level for stimulating the apoptosis process, which depends of both the $Mdm2 - p53$ and the inhibition of $Mdm2$ negative feed-back loops.

3 Morphogenesis of the Tumor Patterns

Most of the mathematical models presented in literature assume by default that they can describe the phenomenological features of the tumor growth using analogue systems. Such models include the Gompertzinan model [32, 33], the logistic model [34], the prey-predator model [35], and so on. On the other hand, such models are focused on some kind of therapy, such as; immunotherapy [36], radiotherapy [9], and combinatory therapy [37] or drug administrations [38].

In recent studies [39], experimental evidence has shown been found that the main mechanism responsible for tumor growth is the competition for space, and not for nutrients, between the tumor and the host cells, and that the tumor shows a linear growth in time.

In the previous work [40], a mesoscopic model for tumor growth was has been presented, considering only the effect of internal fluctuations, in order to improve our understanding of the origin of tumor cells heterogeneity. In this case, this stochastic formalism allows us not only to reproduce, but also to obtain a better understanding of the experimental results presented by Brú [39]. In fact, the internal fluctuations give an explanation as to the "super-rough" dynamics of tumor growth, where the change of microscopic entities size is taken into account.

Another important feature of the mesoscopic model [40] is that it allows us to predict a range of values for the critical exponents and the fractal dimensions corresponding to the experimental findings presented by Brú [39] for different tumor cell cultures.

Our hypothesis is that the rugosity of the interface between the tumor and the host is primarily the result of two main effects. One of them is related to the fact that the reproduction and death of cells at the interface occurs with a particular probability, and therefore it is the results of internal fluctuations [40]; the other is associated with the randomness of the environment, in particular the interaction between the tumor and the immune systems and the host, and for that reason it is also associated with the external fluctuations.

Our objective is to extend the study of the morphogenetic basis of two-dimensional tumor patterns. In Sect. 3.1, formalism is obtained from the master equation (ME) to obtain the mesoscopic model which describes the tumor growth dynamics in absence of external fluctuations, taking into account that the tumor grows in a limited area. The microscopic variable considered to describe the state of the system is the total number of tumor cells, and the macroscopic variables are the expected value of the radius and the fractal dimension, which is a result of internal fluctuations.

3.1 Mesoscopic Model

To obtain a mathematical model to predict avascular tumor growth, the following considerations were made:

1. The total number of cells n is the microscopic variable that describes the behavior of the system, and macroscopic variables considered were the tumor radius r and the fractal dimension of the interface d_f, related by the expression:

$$n = \frac{\pi r^2}{\Omega} \tag{11}$$

$$d_f = 2 - 0.5G\,(y) \tag{12}$$

$$y = \lim_{l \to 1} \frac{\Delta \ln (w)}{\Delta \ln (l)} \tag{13}$$

where Ω is the area occupied by the cell or cell colony in the contour, w is an adimensional magnitude that expresses the height difference between two points in the contour separated by an adimensional distance l, and $G(y)$ is a linear function of y.

Geometrically, a tumor has the shape shown in Fig. 4, in which the distance between the center of the tumor and the point at the interface more distant from the center H, the expected value of the tumor radius R, and the difference between the maximum heights of two points in the contour W are useful variables.

2. As the contour rugosity is a property of the tumor, not all the surface of radius H is covered by tumor cells. If it is considered that internal fluctuations scale with the area occupied by the microscopic entities that characterize the tumor (tumor cells or tumor cell colonies) then the percentage of the host area occupied by tumor cells depends on the relation between the size of the entity and the expected value of the area occupied by the tumor, expressed by:

$$\frac{R^2}{H^2} = f\left(\frac{\Omega}{R^2}\right) \tag{14}$$

where f is a function of the relation $\frac{\Omega}{R^2}$ with the following properties:

$$\lim_{\frac{\Omega}{R^2}\to 0} f\left(\frac{\Omega}{R^2}\right) = 1 \Longrightarrow W = 0, \quad d_f = 1 \tag{15}$$

and

$$\lim_{\frac{\Omega}{R^2}\to \infty} f\left(\frac{\Omega}{R^2}\right) = 0 \Longrightarrow W = \infty, \quad d_f = 2 \tag{16}$$

3. Because the change of n depends of the proliferation death of the contour cells and if (11) is considered, then the transition probability per unit time $T_r\left[t^{-1}\right]$ is assumed as:

$$T_r = \mu n^{0.5} \tag{17}$$

while the transition probability per unit of time T_d associated to the apoptosis of cells on the interface is supposed as:

$$T_d = b\,(1 + F_a)\,n^{0.5} \tag{18}$$

where:

$$\begin{aligned} b &= cte \\ F_a &= \frac{r^2}{D^2} \\ &= \frac{n}{N} \end{aligned} \tag{19}$$

In (17) and (18) $\mu\left[t^{-1}\right]$ is the cell reproduction rate constant, and $k_d\left[t^{-1}\right]$ is the cell death rate constant. The death rate constant k_d includes a correction term

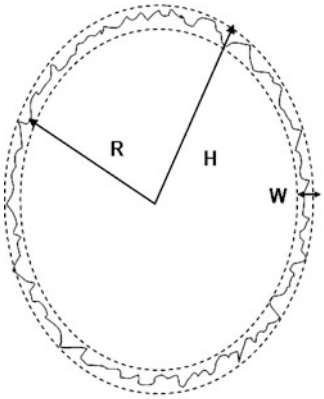

Fig. 4 Geometric representation of the tumor

F_a, which represents the relation between the tumor radius r and a characteristic length D of the area and takes into account the finite area of the host. The term F_a is equivalent to the relation between the total number of cells and the total sites which can be occupied.

Considering the transition probabilities (17) and (18) the master equation ME [23, 24] which describes the probability behavior $P\,(n;t)$ of having n cells in time t is written as:

$$\begin{aligned}\frac{\partial P\,(n;t)}{\partial t} &= \left(\mathbf{E}_n^{-1}-1\right)\mu n^{0.5}P\,(n;t)\\ &\quad+\left(\mathbf{E}_n^{+1}-1\right)b\left(1+\frac{n}{N}\right)n^{0.5}P\,(n;t)\\ P\,(n_0;0) &= 1\end{aligned} \tag{20}$$

where E_n^a is the step operator.

Since the reproduction or death of a single cell produces a negligible effect on the system:

$$\frac{\Delta n}{n}\approx 0 \tag{21}$$

Then the variable n could be considered continuous. If the step operator is expressed in its differential form:

$$\begin{aligned}\mathbf{E}_n^{-1} &= 1-\frac{\partial}{\partial n}+\frac{1}{2}\frac{\partial^2}{\partial n^2}\\ \mathbf{E}_n^{+1} &= 1+\frac{\partial}{\partial n}+\frac{1}{2}\frac{\partial^2}{\partial n^2}\end{aligned} \tag{22}$$

Then the Fokker-Planck equation (FPE) is obtained [23,24] for $P\,(n,t)$:

$$\frac{\partial P\,(n;t)}{\partial t} = -\frac{\partial}{\partial n}\left[\mu n^{0.5} - b\left(1+\frac{n}{N}\right)n^{0.5}\right]P\,(n;t) + \frac{1}{2}\frac{\partial^2}{\partial n^2}\left[\mu n^{0.5} + b\left(1+\frac{n}{N}\right)n^{0.5}\right]P\,(n;t) \tag{23}$$

If we take into account the following relations between the probability related to the microscopic $P(n;t)$ and the one related to the macroscopic variables $P(r;t)$ [23]:

$$\partial P\,(n;t)\,\partial n = \partial P\,(r;t)\,\partial r \tag{24}$$

Then the FPE related to the behavior of the macroscopic variable is:

$$\frac{\partial P\,(r;t)}{\partial t} = -\frac{\partial}{\partial r}\left[\psi - \eta\left(1+\frac{r^2}{D^2}\right) - \frac{\Omega}{2r^2}\left(\psi+\eta\left(1+\frac{r^2}{D^2}\right)\right)\right]P\,(r;t) + \frac{\partial^2}{\partial r^2}\left[\frac{\Omega}{2r}\left(\psi+\eta\left(1+\frac{r^2}{D^2}\right)\right)\right]P\,(r;t) \tag{25}$$

in which the relations among macroscopic and microscopic rate constants are:

$$\psi = \left(\frac{\Omega}{4}\right)^{0.5}\mu$$
$$\eta = \left(\frac{\Omega}{4}\right)^{0.5} b \tag{26}$$

In FPE (25), the first term on the right is a convective term related to the expected or deterministic value, while the second term is a diffusive term related to the fluctuations value. Taking into account that the macroscopically observed cell size Ω is independent of the tumor size r^2, we can consider that:

$$\psi - \eta\left(1+\frac{r^2}{D^2}\right) >> \frac{\Omega}{2r^2}\left(\psi+\eta\left(1+\frac{r^2}{D^2}\right)\right) \tag{27}$$

in such a way that (25) can be written as:

$$\frac{\partial P\,(r;t)}{\partial t} = -\frac{\partial}{\partial r}\left[\psi - \eta\left(1+\frac{r^2}{D^2}\right)\right]P\,(r;t) + \frac{\partial^2}{\partial r^2}\left[\frac{\Omega}{2r}\left(\psi+\eta\left(1+\frac{r^2}{D^2}\right)\right)\right]P\,(r;t) \tag{28}$$

From the FPE (28) the expected radius of the tumor R is obtained [41]:

$$\begin{aligned} \frac{dR}{dt} &= \psi - \eta\left(1 + \frac{r^2}{D^2}\right) \\ \frac{dR}{dt} &= V - \eta\frac{r^2}{D^2} \\ R\,(0) &= R_0 > 0 \end{aligned} \tag{29}$$

where $V = \psi - \eta\ \left[L.t^{-1}\right]$ is the tumor growth rate macroscopically observed during the linear growth stage by mitosis and apoptosis processes [39].

For variance σ associated to the internal fluctuations we obtain from (28):

$$\begin{aligned} \frac{d\sigma}{dt} &= -2\frac{\eta R}{D^2}\sigma + \frac{\Omega}{2R}\left(\psi - \eta\left(1 + \frac{R^2}{D^2}\right)\right) \\ \sigma\,(0) &= \sigma_0 > 0 \end{aligned} \tag{30}$$

The system of ordinary differential equations given by (29) and (30) represents the mesoscopic model which describes the tumor dynamics in absence of external fluctuations considering the finite host area.

The stability analysis [42] shows that the radius grows to a stable stationary state, also called dormant tumor stage [43].

4. The tumor fractal dimension depends on the physiological condition of active cells at the interface, and it must include the reproduction and death rate constants. To determine the characteristic fractal dimension of the tumor, the right side of (30) is equalled to zero, so:

$$\begin{aligned} \frac{d\sigma}{dt} &= 0 \\ D &= H \end{aligned} \tag{31}$$

and the variance is expressed as:

$$\sigma = \frac{H^2}{4}\frac{\Omega}{R^2}\left(\frac{\psi}{\eta} + 1 + \frac{R^2}{H^2}\right) \tag{32}$$

As the height difference between two points at the interface is equivalent to the magnitude of internal fluctuations, expressed by the square root of the variance [44], the following adimensional expression is obtained from (32):

$$w^2 = \frac{l^2}{4}\left(\frac{\psi}{\eta} + 1 + L^2\right) \tag{33}$$

where:

$$w = \frac{\sigma^{0.5}}{H}, l = \frac{\Omega^{0.5}}{R}, L^2 = f\left(l^2\right) \tag{34}$$

In (34) $f\left(l^2\right)$ is, according to the pre-established considerations, a scale down function which takes into account the fact that internal fluctuations will depend on the size of the microscopic entities and the size of the system.

Also, as there is a linear relation between the expected value of the radius and the perimeter, the adimensional variable l is equivalent to the distance between two interface points. Consequently, the following scaling relation can be assumed:

$$L^2 = 1 - l^2 \tag{35}$$

So, (33) is expressed as:

$$w^2 = \frac{l^2}{4}\left(\frac{\psi}{\eta} + 2 + l^2\right) \tag{36}$$

Substituting (36) in (13) gives:

$$\begin{aligned} y &= \lim_{l\to 1} \frac{\Delta \ln\left(\frac{l^2}{4}\left(\frac{\psi}{\eta} + 2 + l^2\right)\right)}{\Delta \ln l} \\ &= \lim_{l\to 1}\left(\frac{d \ln\left(\frac{l^2}{4}\left(\frac{\psi}{\eta} + 2 + l^2\right)\right)}{dl}\right)\left(\frac{d \ln l}{dl}\right)^{-1} \\ &= \frac{\psi + \eta}{\eta} = \frac{\mu + b}{b} \end{aligned} \tag{37}$$

the fractal dimension is given by:

$$d_f = 2 - \frac{1}{2}\left(C_1\left(\frac{\mu + b}{b}\right) + C_2\right) \tag{38}$$

where constants C_1 and C_2 are evaluated taking into account the interval of values physically possible that can be obtained by the relation between the reproduction and endogenous death rate constants. Then two extreme cases appear:

$$\frac{\psi}{\eta} = 1 \Longrightarrow d_f = 2 \tag{39}$$

Because when $\frac{\psi}{\eta} = 1$ the tumor does not grow so the fractal dimension is equal to the surface dimension, and:

$$\frac{\psi}{\eta} = 2 \Longrightarrow d_f = 2 \tag{40}$$

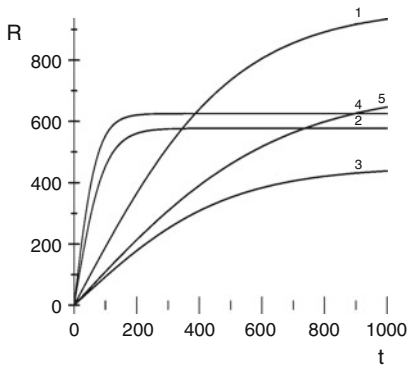

Fig. 5 Predicted dynamics. 1. HT colon adenocarcinoma; 2. C-33 cervis carcinoma; 3. Saos 2 osteosarcoma; 4. AT5 primary human foreskin fibroblasts; 5. 313 mouse fibroblasts [41]

Table 1 Aggressiveness index V for tumor in vitro

Cell line	f^p	V^*	ψ	η
HT colon adenocarcinoma	1.13	1.93	3.9643	2.0343
C-33 cervix carcinoma	1.25	6.10	24.4	18.3
Saos 2 osteosarcoma	1.31	0.94	5.5411	4.6011
AT5 primary human foreskin fibroblasts	1.23	8.72	31.004	22.284
313 mouse fibroblasts	1.20	1.10	3.3	2.2

*Experimental results reported by Brú [39]

since when $\frac{\psi}{\eta} = 1$ the contour roughness is zero and the fractal dimension is equal to the topological dimension of the contour of a circle of radius H. Taking into account both extreme conditions given by (39) and (40) the following expression is proposed to determine fractal dimension d_f as a function of the quotient between mitosis and apoptosis rates [41], which quantifies the tumor capacity to invade and infiltrate healthy tissue [45]:

$$d_f = \frac{5 - \frac{\psi}{\eta}}{\frac{\psi}{\eta} + 1} \tag{41}$$

To applied the proposed model in for tumor in vitro, five tumor cell lines shown in Fig. 4 were selected. The features of theses cells are reported by Brú [39]. Table 1 shows the linear growth rates $V\left[\mu\text{m.h}^{-1}\right]$, their fractal dimension d_f [39], as well as the reproduction ψ and death η rate constants of these cells, predicted by the model.

As can be seen, in the absence of external fluctuations, the stochastic formalism allows formulating a macroscopic model that on the one hand describes the linear growth of the tumor radius in time and on the other hand its evolution until reaching a stable stationary state, which seems to be associated with tumor dormant state.

On one hand, it has been experimentally demonstrated that once the tumor appears, which is considered as a self-organising systems, spatial and temporally far from thermodynamic equilibrium, it shows a linear growth in the host [39] until reaching a critical size; then, for reasons not yet clarified, it stops growing for a

period known as the dormant state [46]. After this, the tumor metastasizes, invading other organs, and this is main cause of death for cancer patients.

In summary, in this work, a stochastic formalism that allows a better understanding of the morphogenesis of the tumor pattern formation dynamics has been developed. The stochastic formalism developed not only reproduces the experimental results observed by Brú [39] but clarifies the physics of the complexity observed of the tumor patterns.

4 Diagnosis of a Tumor Malignancy and Aggressiveness

In general, benign tumors are well differentiated, while malignant neoplasms or cancer are composed of undifferentiated cells. Malignant tumors are locally invasive, infiltrating the surrounding normal tissues and the metastasis is frequently present [47].

A mesoscopic formalism was used to obtain a theoretical equation that describes the relation between the fractal dimension of the tumor interface and the quotient between mitosis and apoptosis rates [41], which quantifies the tumor capacity to invade and infiltrate healthy tissue [45]. Another result was an empirical scale-up equation that simulates the macroscopic morphology of the tumor [40].

The diagnosis of a tumor malignancy and aggressiveness is a key factor in establishing an adequate therapy. The morphology of this tissue is too complex to be described using Euclidian geometry [45, 48, 49]. Conversely, the morphology of the tumor pattern can be characterized by its fractal dimension [40], in relation to the cell density. Thus, experimental studies have been conducted to determine the relation between tissue fractal dimension [8, 50, 51], cell fractal dimension [52], interface fractal dimension, and others aspects of tumor malignancy and prognosis, [53–56]. Most of these studies are based on statistical correlations and do not arrive at conclusive results.

We propose in this section a new mesoscopic model to describe the behavior of cells inside the tumor. In this section will: 4.1 establish a relationship between the fractal dimension of the cell pattern, the fractal dimension of the interface, and the quotient between mitosis and apoptosis rates; 4.2 develop an equation to describe the dynamic behavior of the tumor from the cell pattern fractal dimension, which can explain the Gompertzian dynamics; 4.3 propose indexes to quantify invasion and proliferation capacities of in vitro tumors.

4.1 Relation Between Cell Pattern Fractal Dimension and Dynamic Quotient

A mesoscopic formalism [23] is used to obtain the relation between the cell pattern's fractal dimension and the mitosis-apoptosis quotient [57]. The following

suppositions was established: i) the system is an area Ω of tissue inside the tumor where there are not necrosis; ii) the microscopic variable is the number n of tumoral cells with individual area α presents on Ω; iii) the macroscopic variable is the fraction of tissue Φ composed by tumoral cells; iv) the relation between n and Φ is given by:

$$\Phi = \frac{n\alpha}{\Omega}; \tag{42}$$

v) the transition probability per unit of time $T_{n+1/n}$ associated to cells reproduction depends of the constant rate $u\left[t^{-1}\right]$ and it is established a priori as:

$$T_{n+1/n} = un; \tag{43}$$

vi) the transition probability per unit of time $T_{n-1/n}$ related to cells dead depends of the constant rate $b\left[t^{-1}\right]$ and the available space Ω, and this probability is

$$T_{n-1/n} = b\left(1 + \frac{n\alpha}{\Omega}\right)n; \tag{44}$$

vii) because of the area Ω is considered constant due to limitation of space, the number n of cells are in a stationary state.

Considering the transition probabilities (43) and (44) the master equation ME [23, 24], which describes the probability behavior $P(n;t)$ of having n cells in time t, is written as:

$$\begin{aligned}\frac{\partial P\,(n;t)}{\partial t} &= \left(E^{-1} - 1\right)unP\,(n;t) \\ &\quad + \left(E^{+1} - 1\right)b\left(1 + \frac{n\alpha}{\Omega}\right)nP\,(n;t) \\ P\,(n_0;0) &= 1\end{aligned} \tag{45}$$

where E^a is the step operator.

The behavior of the expected value $\langle\Phi\rangle$ and the variance σ_Φ are deduced through the solution of the master equation (45). Due to the non-linearity of this ME (in the sense of its transition probability per time unit), an exact analytic solution is not possible [23], and so it is necessary to use approximate methods. In this case the first two terms of Van Kampen's expansion will be used [23, 24]. Taking into account the established suppositions we obtained:

$$0 = \left(u\langle\Phi\rangle - b\langle\Phi\rangle\left(1 + \langle\Phi\rangle\right)\right) \tag{46}$$

$$0 = 2\left(u - b - 2b\langle\Phi\rangle\right)\sigma_\Phi + \left(\frac{\alpha}{\Omega}\right)\left(u\langle\Phi\rangle + b\left(1 + \langle\Phi\rangle\right)\langle\Phi\rangle\right) \tag{47}$$

and consequently:

$$\langle \Phi \rangle = (k-1) \tag{48}$$

$$\sigma_{\Phi} = \varepsilon \frac{\left((k+1)\langle \Phi \rangle + \langle \Phi \rangle^2\right)}{2\left(1-k+2\langle \Phi \rangle\right)} \tag{49}$$

where:

$$k = \frac{u}{b} \tag{50}$$

$$\varepsilon = \frac{\alpha}{\Omega} \tag{51}$$

According to (50), the parameter k is related to the relation between mitosis and apoptosis rate, and therefore it is called dynamic quotient. This quotient physically represents the proliferation index of a tumor. The parameter ε (51) is related to the observation scale of the system, and therefore it is called mesoscopic scale factor; it describes the relation between the size of an individual tumoral cell and the size of observed tissue inside the tumor.

In order to characterize the pattern cells morphology from (48) and (49), the variance σ is written as a function of a parameter, which can be related to the fractal dimension D_f of the cells pattern at the microscopic level. That is why we selected ε in such way that the magnitude of internal fluctuations is similar to the magnitude of the expected value. Then, we considered:

$$\Phi_{n\to 1} \sim \varepsilon \tag{52}$$

so (49) can be rewritten as:

$$\sigma_{\Phi\to 1} = \varepsilon \frac{\left((k+1)\varepsilon + \varepsilon^2\right)}{2\left(1-k+2\varepsilon\right)} \sim \varepsilon^a \tag{53}$$

To obtain a as a theoretical function of the dynamic quotient k and the fractal dimension D_f, we took into account that D_f is calculated using the box counting method within a limit where the size of the observed box is equivalent to the size of an individual cell. Therefore, a is calculated according to the following relation [41]:

$$a = \lim_{\varepsilon\to 1}\left(\frac{d\ln\left(\left(\varepsilon\frac{\left((k+1)\varepsilon+\varepsilon^2\right)}{2(1-k+2\varepsilon)}\right)\right)}{d\varepsilon}\right)\left(\frac{d\ln\varepsilon}{d\varepsilon}\right)^{-1}$$

$$a = \frac{(5.5-k\,(k+0.5))}{3-0.5k\,(k-1)} \tag{54}$$

As the system is considered in a stationary stable state, the probability function $P(n;t)$ is normal or Gaussian [23, 24], in such way that, when internal fluctuations are appreciable, this function can be written as:

$$P_{\Phi\sim\varepsilon} \sim \frac{1}{(2\pi\varepsilon^a)^{0.5}} \exp\left(-\frac{(\langle\varepsilon\rangle-\varepsilon)^2}{2\varepsilon^a}\right). \tag{55}$$

If $P_{\Phi\sim\varepsilon}$ is visualized from the ensemble viewpoint [23, 24], the expected value of $P_{\Phi\sim\varepsilon}$ is a measure of the pattern cell density $\rho(Z)$ observed on an area $\Omega = Z^2$, where Z is a characteristic length. Therefore:

$$\rho(Z) \sim \int \frac{1}{(2\pi\varepsilon^a)^{0.5}} \exp\left(-\frac{(\langle\varepsilon\rangle-\varepsilon)^2}{2\varepsilon^a}\right) P(\varepsilon)\, d\varepsilon$$

$$\rho(Z) \sim \frac{1}{(Z^a)^{0.5}} \tag{56}$$

All tumors have two basic components: (1) cells that constitute their parenchyma, and (2) supportive stroma made up of connective tissue and blood vessels [47]. The amount λ of parenchyma, which is proportional to the number of cells, can be estimated as:

$$\lambda \sim \rho(Z)\,\Omega$$

$$\lambda \sim \frac{1}{(Z^a)^{0.5}} Z^2 \sim Z^D \tag{57}$$

From (54), (56) and (58), the following theoretical equation is obtained:

$$D = \frac{1}{2}\frac{k(5-2k)+13}{(k+2)(3-k)} \tag{58}$$

4.2 Dynamics Behavior of the Tumor

To determine the relation between λ and other macroscopic variables associated with the tumor growth, the following assumptions are: i) the observed macroscopic variable r is a virtual line, which is the tumor radius; ii) the microscopic variable m is the number of cells of length l inside the virtual line:

$$r = ml; \tag{59}$$

iii) the transition probability per unit of time $T_{m+1/m}$ associated with cells proliferation depends only on the mitosis constant rate $u\left[t^{-1}\right]$ associated with interface cells, and it is established a priori as:

$$T_{m+1/m} = u; \tag{60}$$

iv) the transition probability per unit of time $T_{m-1/m}$ associated with the death of interface cells depends on the apoptosis constant rate $b\left[t^{-1}\right]$ and the relation between r and the value Ω^*, related to the finite size of the host. This probability is written as:

$$T_{n-1/n} = b\left(1 + \frac{r}{\Omega^*}\right). \tag{61}$$

The master equation ME, obtained from the assumed transition probability per unit of time (60) and (61), describes the behavior of the probability $P\,(m;t)$ of having m number of cells in time t, is:

$$\begin{aligned} \frac{\partial P\,(m;t)}{\partial t} &= \left(E^{+1} - 1\right) uP\,(m;t) + \left(E^{-1} - 1\right) b\left(1 + \frac{r}{\Omega^*}\right) P\,(m;t) \\ P\,(m;0) &= 1. \end{aligned} \tag{62}$$

The ME (62) is linear and therefore its solution is a function of normal or Gaussian distribution [23,24]. The expected value of the tumor radius R is given by:

$$\begin{aligned} \frac{dR}{dt} &= \left(\psi - \eta - \eta\frac{R}{\Omega^*}\right) \\ R\,(0) &= R_0, \end{aligned} \tag{63}$$

where ψ and $\eta\left[L.t^{-1}\right]$ are the macroscopic parameters associated with mitosis and apoptosis rates, respectively, and they are related to the microscopic rates by:

$$\psi = ul, \tag{64}$$

$$\eta = bl. \tag{65}$$

To obtain the solution of (62) we defined the following dimensional variables and parameters:

$$\phi = \frac{R}{\Omega^*}; \tag{66}$$

$$\tau^* = \frac{\eta}{\Omega^*}t; \tag{67}$$

$$k_c = \frac{\psi}{\eta}, \tag{68}$$

where the adimensional parameter k_c is the dynamic quotient on the tumor-host interface and $\frac{\eta}{\Omega^*}\left[t^{-1}\right]$ is the inverse of a constant related to the time that the tumor takes to achieve its maximum radius value. Then we obtain to the expected value:

$$\begin{aligned} \frac{d\phi}{d\tau^*} &= (k_c - 1 - \phi) \\ \phi(0) &\approx 0 \end{aligned} \tag{69}$$

where the exact solution of (69) is:

$$\phi\left(\tau^*\right) = (k_c - 1)\left(1 - \exp\left(-\tau^*\right)\right). \tag{70}$$

Taking into account the fractal morphology of the tumor patterns, an expression which describes the evolution of the parenchyma tumor can be obtained:

$$x = \left((k-1)\left(1 - \exp\left(-\tau^*\right)\right)\right)^{D_f} \tag{71}$$

where x is an adimensional variable describing the quotient between the parenchyma size and the maximum value of λ when $t \to \infty$.

Equation (71) is an exact solution of the following differential equation:

$$\frac{dx}{d\tau} = Dx\left((k-1)\,x^{-\frac{1}{D}} - 1\right) \tag{72}$$

If we define a variable y

$$y = \ln x \tag{73}$$

then the equation can be expressed as

$$\frac{dy}{d\tau} = D_f\left((k-1)\left(\exp\left(-\frac{y}{D_f}\right) - 1\right)\right) \tag{74}$$

If the right side of equation is expanded in a power series of y and only the first two terms are hold, turns into:

$$\begin{aligned} \frac{dx}{dt} &= -A_1 x \ln\frac{x}{A_2} \\ A_1 &= (k-1) \\ A_2 &= (k-1)^D \end{aligned} \tag{75}$$

Equation (75), describing the approximate tumor growth, is analogous to the Gompertz model, which has been successfully used for the mathematical description of many types of cancer [45]. The predicted behaviour from both (75) and (72) are show on the Fig. 6.

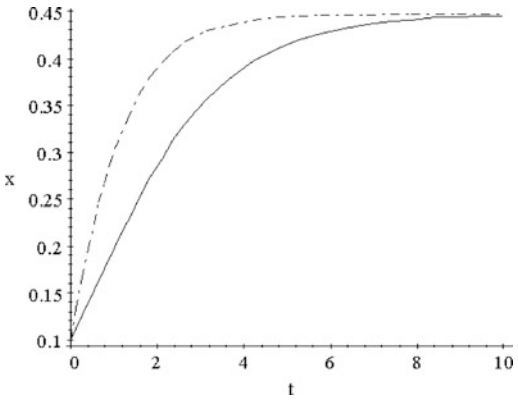

Fig. 6 (– –) Dynamics predicted from (72) (–) Gompertz dynamics from (75)

The next step is to find a relation between the macroscopic morphology of the tumor, described by the interface fractal dimension d_f and the microscopic morphology described by the cell pattern fractal dimension D_f. According to the linear master equation the temporal behavior of the radius variance is given by:

$$\frac{d\sigma}{dt} = -2\frac{\eta}{\Omega^*}\sigma + l\left(\psi + \eta + \eta\frac{R}{\Omega^*}\right) \tag{76}$$

If the equation is expressed as a function of the adimensional variables and parameters

$$\begin{aligned} \tau &= \frac{2\eta}{\Omega^*} \\ \beta &= \frac{\sigma}{(\Omega^*)^2} \\ \epsilon &= \frac{2l}{\Omega^*} \end{aligned} \tag{77}$$

and as there is a linear relation between the expected value R of the tumor radius and the expected value P_e of the tumor perimeter the equation is expressed as:

$$\begin{aligned} \frac{d\beta}{d\tau} &= -\beta + \epsilon_m\left(k_c + 1 + \gamma\right) \\ \beta\left(0\right) &= 0 \end{aligned} \tag{78}$$

where ϵ_m is the macroscopic scale factor on the interface, related to the interface scale of observation γ is an adimentional variable related to the distance between two points on the interface and $\beta^{0.5}$ is an adimensional variable related to the height difference h between these points. As $\gamma = \phi$ we write:

$$\gamma\left(\tau\right) = \left(k_c - 1\right)\left(1 - \exp\left(-\tau\right)\right) \tag{79}$$

the exact solution of equation is:

$$\beta(\tau) = 2k_c\epsilon_m - \epsilon_m\left(\frac{k_c - 1 - \gamma}{k_c - 1}\right)\left((k_c - 1)\ln\left(\frac{k_c - 1 - \gamma}{k_c - 1}\right) + 2k_c\right) \tag{80}$$

the term $\ln\left(\frac{k_c-1-\gamma}{k_c-1}\right)$ in equation is expanded in a power series of γ and the first term is taken the we arrive to the following expression:

$$\beta \sim \left(\epsilon_m\gamma\frac{3k_c - \gamma - 1}{k_c - 1}\right) \tag{81}$$

To characterize the roughness of the tumor-host interface the distance γ must be appreciable in comparison with the observation scale:

$$\beta \sim \epsilon_m \tag{82}$$

and the local roughness exponent α_{loc} can be estimated as:

$$\alpha_{loc} = \lim_{\epsilon_m \to 1}\left(\frac{d\ln\left(h_{\gamma\to\epsilon_m}\right)}{d\epsilon_m}\right)\left(\frac{d\ln\epsilon_m}{d\epsilon_m}\right)^{-1}$$

$$\alpha_{loc} = \frac{6k_c - 5}{6k_c - 4} \tag{83}$$

Taking into account that the exponent α_{loc} is related to the interface fractal dimension d_f according to

$$d_f = 2 - \alpha_{loc} \tag{84}$$

the following equation is obtained to relate the fractal dimension d_f to the dynamic quotient on the interface k_c

$$d_f = 1.5\frac{k_c - 0.5}{1.5k_c - 1} \tag{85}$$

if it is assumed that the dynamic quotient k_c on the interface is equal to the dynamic quotient k inside the tumor, i. e. $k = k_c$ the relation between the macroscopic morphology pattern and the microscopic morphology pattern inside the tumor is given by:

$$d_f = \frac{1.0045\left(D_f + 6.6667\times 10^{-2}\sqrt{D_f^2 - 2.2D_f + 1.29} - 1.22\right)}{D_f - 1.2411} \tag{86}$$

4.3 Morphogenesis and Aggressiveness of Cervix Carcinoma

The cervix epithelium is a biological tissue which is kept under constant cell renewal [47]. The replication of the stem cells (Fig. 7a) produces well-differentiated cells (Fig. 7b) which replace the apoptosis cells that are on the epithelium surface (Fig. 7c). Due to the papilloma virus, the stem cells mutate and they produce not-differentiated cells (Fig. 7d) which divide out of control.

The cervix carcinoma is visualized as a two-dimensional region (Fig. 8) where tumor cells T proliferate and invade non-tumor tissue N, which usually is inflamed as a response to the invasion [59, 60]. The considered system to obtain the model is an area of arbitrary size Ω inside the tumor, which corresponds to the observed image used for diagnosis.

The microscopic variable is the total number of cells n inside Ω, and is suppose to change due to the following processes: i) the production of epithelium cells caused by the division of stem cells, where the transition probability per unit of time $W_{1,n+1/n}$ is written as:

$$W_{1,n+1/n} = M; \tag{87}$$

ii) the mitosis process, whose transition probability per unit of time $W_{2,n+1/n}$ is given by:

$$W_{2,n+1/n} = k_1 n \tag{88}$$

and iii) the apoptosis due to the competition for space and nutrients, and the action of regulatory mechanisms, where the transition probability $W_{3,n-1/n}$ is assumed as:

$$W_{3,n-1/n} = \frac{k_2}{\Omega} n^2. \tag{89}$$

where M is a rate constant $\left[t^{-1}\right]$ associated with the division of stem cells, k_1 is the mitosis rate constant $\left[t^{-1}\right]$, and k_2 is the apoptosis rate constant $\left[t^{-1}\right]$.

The master equation [23] that describes the temporal behavior of the probability $P\,(n;t)$ of having cells n at time t is written from the transition probabilities per unit of time established a priori:

$$\begin{aligned} \frac{\partial P\,(n;t)}{\partial t} &= \left(E^{-1}-1\right) MP\,(n;t) \\ &\quad + \left(E^{-1}-1\right) k_1 n P\,(n;t) \\ &\quad + \left(E^{+1}-1\right) \frac{k_2}{\Omega} n^2 P\,(n;t) \\ P\,(1;0) &= 1. \end{aligned} \tag{90}$$

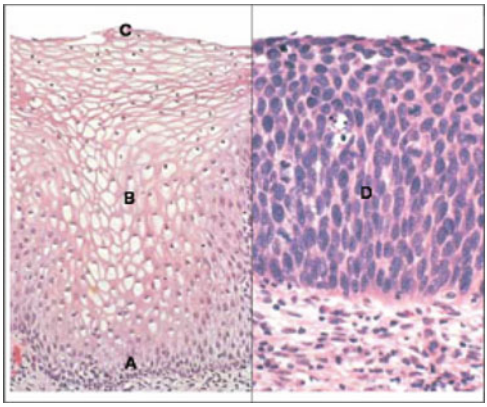

Fig. 7 Normal tissue and cervix carcinoma in situ

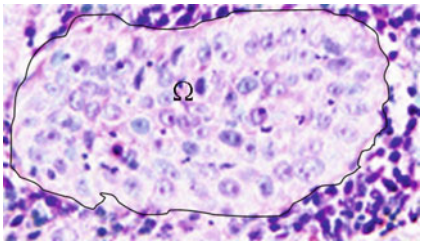

Fig. 8 Histopatological imagen of cervix carcinoma

If Ω is selected sufficiently large in such way that n can be considered as a continuous variable, then the step operator E^a can be expressed as [24]:

$$E^a = 1 + a\frac{\partial}{\partial n} + a^2\frac{\partial^2}{\partial n^2} + \ldots., \tag{91}$$

and substituting (91) in (90), the following Fokker-Planck equation is obtained:

$$\frac{\partial P\,(n;t)}{\partial t} = -\frac{\partial}{\partial n}\left[\left(M + k_1 n - \frac{k_2}{\Omega}n^2\right)P\,(n;t)\right] + \frac{1}{2}\frac{\partial^2}{\partial n^2}\left[\left(M + k_1 n + \frac{k_2}{\Omega}n^2\right)P\,(n;t)\right]. \tag{92}$$

The observed macroscopic variable is defined as the percentage x of Ω which is occupied by the cells:

$$x \equiv \epsilon\frac{n}{\Omega^*}, \tag{93}$$

where $\Omega = \frac{\Omega}{\epsilon}$ and ϵ is a constant which is related to the size of individual cell; taking into account the following relation between the probability $P\,(n;t)$ and the probability $\Pi\,(x;t)$ associated with the macroscopic variable [23]:

$$P\,(n;t)\,\partial n = \Pi\,(x;t)\,\partial x, \tag{94}$$

a change of variable was carried out on the Fokker-Planck equation (92), in such way that:

$$\frac{\partial \Pi(x;t)}{\partial t} = -\frac{\partial}{\partial x}\left[\left(M + k_1 x - k_2 x^2\right)\Pi(x;t)\right] + \frac{1}{2}\frac{1}{\Omega^*}\frac{\partial^2}{\partial x^2}\left[\left(M + k_1 x + k_2 x^2\right)\Pi(x;t)\right]. \tag{95}$$

is obtained.

Equation (95) is non-linear; therefore it is not possible to obtain an exact solution. Nevertheless, an approximate analytical solution can be obtained when we consider the dynamic behavior of the system in the vicinity of the stationary state, where $\Pi(x;t)$ is normal or Gaussian [23, 24]. In this case, the expected value is given by the differential equation:

$$\begin{aligned} \frac{d\langle x\rangle}{dt} &= M + k_1\langle x\rangle - k_2\langle x\rangle^2 \\ \langle x\rangle_{t=0} &= x_0, \end{aligned} \tag{96}$$

and the variance σ associated with the internal fluctuations is expressed as:

$$\begin{aligned} \frac{d\sigma}{dt} &= 2\left(k_1 - 2k_2\langle x\rangle\right)\sigma + \frac{1}{\Omega^*}\left(M + k_1\langle x\rangle + k_2\langle x\rangle^2\right) \\ \sigma(0) &= \sigma_0. \end{aligned} \tag{97}$$

Defining the non-dimensional time τ and non-dimensional parameters α and β:

$$\tau = tM \tag{98}$$

$$\alpha = \frac{k_1}{M}, \tag{99}$$

$$\beta = \frac{k_2}{M}, \tag{100}$$

the differential equations (96) and (97) are written as:

$$\begin{aligned} \frac{d\langle x\rangle}{d\tau} &= 1 + \alpha\langle x\rangle - \beta\langle x\rangle^2 \\ \langle x\rangle_{t=0} &= x_0, \end{aligned} \tag{101}$$

$$\begin{aligned}\frac{d\sigma}{d\tau} &= 2\left(\alpha - 2\beta\left\langle x\right\rangle\right)\sigma + \frac{1}{\Omega^*}\left(1 + \alpha\left\langle x\right\rangle + \beta\left\langle x\right\rangle^2\right)\\ \sigma\left(0\right) &= \sigma_0,\end{aligned} \tag{102}$$

where:

$$\Pi\left(x;\tau\right) = \frac{1}{\left(2\pi\sigma\right)^{0.5}}\exp\left(-\frac{\left(x - \left\langle x\right\rangle\right)^2}{2\sigma}\right) \tag{103}$$

Equations (101)–(103) describe the mesoscopic temporal behavior of the system in the vicinity of the stationary state [23].

As the temporal averages are constant in the stationary state, we can assume that the stochastic process is ergodic [23, 24], in such way that temporal averages are equivalent to spatial averages. If the probability $\Pi^s\left(x\right) = \lim_{\tau\to\infty}\Pi\left(x;\tau\right)$ is visualized by an ensemble then the expected value $\left\langle\Pi^s\left(x\right)\right\rangle$ is proportional to the cell density inside Ω^*, so [57]:

$$\begin{aligned}\rho &= \left\langle\Pi^s\left(x\right)\right\rangle\\ &= \int\left(\Pi^s\left(x\right)\right)\Pi^s\left(x\right)dx\\ &= \frac{1}{\left(2\pi\exp\left(1\right)\sigma\right)^{0.5}}\end{aligned} \tag{104}$$

If the mathematical definition of box counting fractal dimension D_f is taken into account [8], then we arrive to:

$$\begin{aligned}D_f &\equiv \lim_{x\to 1}\left(\lim_{\Omega\to x}\frac{d\ln\rho}{d\ln\frac{1}{x}}\right)\\ &\equiv \lim_{x\to 1}\left(\lim_{\Omega^*\to x}\frac{d\ln\left(2\pi\exp\left(1\right)\sigma\right)}{d\ln x}\right)\end{aligned} \tag{105}$$

where it was considered that the minimum box size is $x = 1$ corresponding to one individual cell and the system is visualized in a mesoscopic scale, where $\Omega^* \to x$ [57].

In order to express D_f as a function of the parameters α and β, it is necessary to write σ as a function of x. For this, the following differential equation is obtained from (101) and (102):

$$\begin{aligned}\frac{d\sigma}{dx} &= \frac{2\left(\alpha - 2.0\beta x\right)\sigma + \frac{1}{\Omega^*}\left(1 + \alpha x + \beta x^2\right)}{1 + \alpha x - \beta x^2}\\ \sigma\left(0\right) &= 0,\end{aligned} \tag{106}$$

where the series solution of (106) is:

$$\sigma(x) \approx \left(\frac{1}{\Omega^*}\right)x + \frac{\alpha}{\Omega^*}x^2 + \left(-\frac{0.000\,01}{\Omega^*}\left(\alpha^2 + 66666.\beta\right)\right)x^3 + \left(-.\,333\,33\frac{\beta}{\Omega^*}\alpha\right)x^4 + O\left(x^5\right) \tag{107}$$

Substituting (107) in (104) the following approximate relation among D_f, α, and β is obtained:

$$D_f \simeq \frac{1 + 2\alpha - 2\beta}{1 + \alpha - .\,666\,67\beta} \tag{108}$$

where the pattern cells fractal dimension D_f can be calculated with a suitable software for image processing. Besides D_f, another morphological parameter is necessary to be determined, because there are two unknown quantities, α and β. If we assume that $\langle x\rangle^s$ is associated with the percentage of black pixels λ of the binary histopathological images of the tumor tissue, where the nucleus cells are black, then:

$$\lambda \equiv \langle x\rangle^s \equiv \frac{1}{2}\left(\frac{\alpha}{\beta} + \sqrt{\left(\frac{\alpha}{\beta}\right)^2 + \frac{4.0}{\beta}}\right) \tag{109}$$

Therefore, the dynamic parameters α and β can be estimated from the morphological parameters λ and D_f, according to:

$$\alpha = \frac{.\,666\,67D - 2 + \lambda^2 - \lambda^2 D}{(\lambda D + 2 - 2\lambda - .\,666\,67D)\,\lambda} \tag{110}$$

$$\beta = \frac{\lambda D - \lambda + 2 - D}{(.\,666\,67D - \lambda D - 2 + 2\lambda)\,\lambda} \tag{111}$$

The histopathological image of a cervix carcinoma tissue and both, its corresponding black and white binary image and the cell pattern are shown in Fig. 9.

In this context, the tumor aggressiveness is related to the tumor growth rate V, which depends on the values of α and β. In order to obtain an expression to quantify the aggressiveness, the temporal behavior of x is obtained from the analytical exact solution of the differential equation (101) for $x(0) = 1$:

$$x(\tau) = \frac{1}{2}\left(\frac{\alpha}{\beta} + \frac{\sqrt{(\alpha^2 + 4\beta)}}{\beta}\left(\tanh\left(\frac{1}{2}\tau\sqrt{(\alpha^2 + 4\beta)} + \gamma\right)\right)\right) \tag{112}$$

where $\gamma = \operatorname{arctanh}\frac{2\beta - \alpha}{\sqrt{(\alpha^2 + 4\beta)}}$.

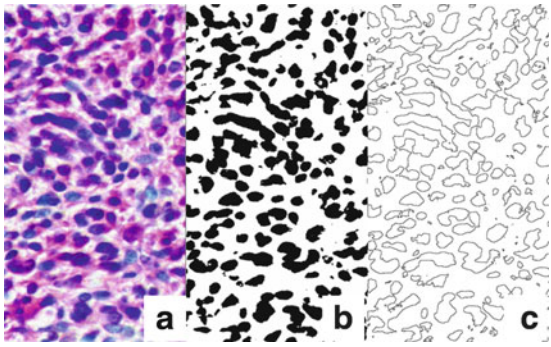

Fig. 9 Histopathological image of cervix carcinoma (**a**), its binary image (**b**) and cell patterns (**c**)

If the tumor growth rate V is defined as $\frac{dx(\tau)}{d\tau}$, then V can be obtained from the temporal derivative of (112) :

$$V(\tau) = -\frac{0.25}{\beta}\left(\alpha^2 + 4.0\beta\right)\left(\tanh^2\left(\gamma + 0.5\tau\sqrt{\alpha^2 + 4.0\beta}\right) - 1.0\right) \tag{113}$$

As V changes with the time τ, the aggressiveness index is related to the value of V for an arbitrary time $\tau = \phi$. Taking into account that V reaches its maximum value when $x(\tau) \simeq \frac{\langle x\rangle^s}{2}$, ϕ is selected from the solution of the equation:

$$\frac{\langle x\rangle^s}{2} = \frac{1}{2}\left(\frac{\alpha}{\beta} + \frac{\sqrt{(\alpha^2 + 4\beta)}}{\beta}\left(\tanh\left(\frac{1}{2}\phi\sqrt{(\alpha^2 + 4\beta)} + \gamma\right)\right)\right) \tag{114}$$

in such way that:

$$\phi = \frac{2}{\sqrt{\alpha^2 + 4\beta}}\left(\operatorname{arctanh}\frac{(\alpha - 2\beta)}{\sqrt{\alpha^2 + 4\beta}} - \operatorname{arctanh}\frac{\alpha - 1.0\beta\sqrt{\frac{1}{\beta^2}(\alpha^2 + 4.0\beta)}}{4\sqrt{\alpha^2 + 4.0\beta}}\right) \tag{115}$$

Substituting $\tau = \phi$ in (113) we proposed an index Ψ to quantify the cervix carcinoma aggressiveness:

$$\Psi = .125\frac{\alpha^2 + \alpha\sqrt{(\alpha^2 + 4.0\beta)} + 6.0\beta}{\beta} \tag{116}$$

where Ψ represents the maximum cell proliferation rate in a region Ω inside the tumor and, therefore, it must be related to the tissue growth rate.

The proposed formalism was applied to quantify the cervix carcinoma aggressiveness in vivo [59, 60]. For this, 35 cases of stage III patients were selected, and

considered the patients' age as the clinical parameter. The histopathological images of both the tumor tissues and healthy cervix epithelium tissues, which were treated with hematoxilin-eocin tincion, were taken with a microscope Olympus CX21FS (×40) and an 8 mega pixels Canon digital camera. Each image was processed with the ImageJ 1.40g software by Wayne Rasband, National Institute of Health, USA (http:rsb.info.nih.gov/ij/). For each case, 9 images were analyzed, where the maximum relative error associated to both λ and D_f was 2% and 4.5%, respectively.

The average values of λ and D_f corresponding to each case were used to estimate both the experimental value of α and β from (115) and (116). As the only considered clinical variable was the patient age g and many factor are known to influence the cancer aggressiveness [60, 61] cases were grouped according to their ages and g, α and β averages were calculated for each group. Then we applied statistical methods using the software STATGRAPHICS Plus 5.1 with the objective to study the correlation among g, α and β. The obtained results are shown on Figs. 10 and 11.

The value of α average taking all cases is 0.9024, slightly greater than the one corresponding to a healthy epithelium cervix ($\alpha = 0.888\,5$). Nevertheless, the total average β is 0.035 for tumor tissues, whereas $\beta = 0.2163$ for the healthy tissues; the calculated apoptosis rate was significantly smaller in the tumor tissues. It is well-known that the expression of the protein $p53$ is inhibited by papilloma virus gene E6 and, as $p53$ plays an important role in the DNA reparation and the induction of the apoptosis process [61, 62] we must expect that the calculated apoptosis rate of the tumor cells must be smaller than the one corresponding to healthy cells, as it was found in this study.

The obtained statistical model for the relation between g and α is:

$$\alpha = \frac{1}{(0.781604 + 0.00760981g)} \tag{117}$$

The statistical analysis indicated that there is a significant statistical relation at the 95% confidence level, with a correlation coefficient of 0.812723, indicating a moderately strong relationship between α and g. The standard deviation of the residuals is 0.135176 and the statistical Durbin-Watson indicated that there is not serial correlation between residues. Therefore, the statistical model was accepted. According to this result, in this study we found that α decreases with the patient age, and it is interesting to observe that α corresponding to younger patient ($g \leq 45$) is greater than of a healthy cervix.

For the relation between β and g we found the statistical model:

$$\beta = 0.0309435 + \frac{0.280417}{g} \tag{118}$$

where the correlation coefficient is 0.20212, indicating a relatively weak relationship between β and g and there is not a significant statistical relations between and

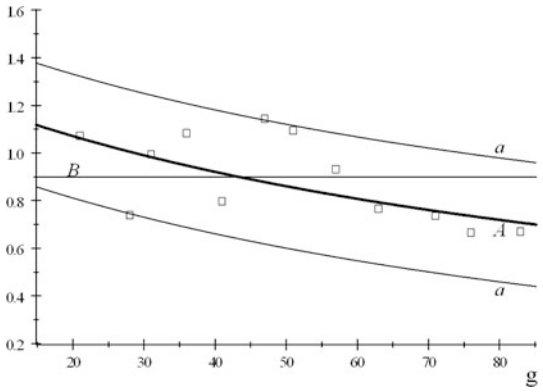

Fig. 10 Experimental behaviour between α and patient age

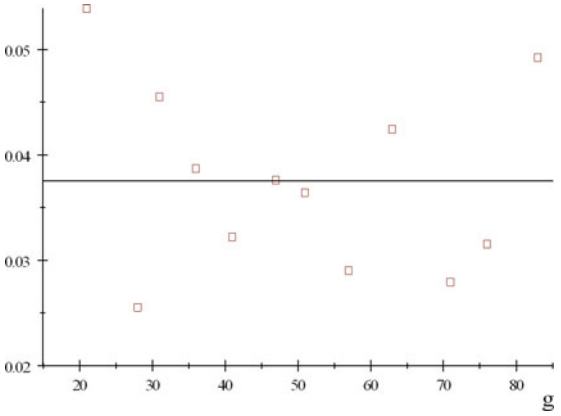

Fig. 11 Experimental behaviour between β and patient age

at the 90% or higher confidence level. Therefore, the statistical model (118) was rejected, and it is considered:

$$\begin{aligned} \beta &= \langle \beta \rangle \\ &= 0.035 \end{aligned} \tag{119}$$

Equations (117) and (118) were substituted in (116) to find the relation between both proposed aggressiveness index Ψ and the patient's age g. The obtained quantitative predictions are showed on Fig. 12.

The obtained behavior predicts the following facts: i) the tumor tissue of cervix carcinoma has a growth rate at stage III ranging from 2.2 to 4.5 bigger than the corresponding to a healthy tissue. This result is logical if it is considered that the invasion of the normal tissue only is possible if the tumoral cells growth faster than the normal cells and ii) cervix carcinoma in older women is less aggressive, which corresponds with the clinical observation [58]. This fact can be explained as a result

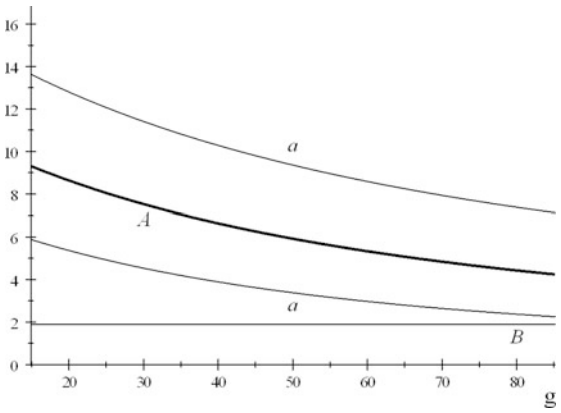

Fig. 12 Experimental behaviour of ψ with respect to patient age a

that the tumor mitosis rate decreased with age, according to the quantitative results obtained from the proposed equations. Therefore, we do not find enough evidence to reject the proposed model, at least for the cases in vivo considered in this study. Nevertheless, it is important to point out that this model has limitations, because only the patient's age was considered as a clinical factor, and there are many others such as the immune response, virus type, sociological aspects, clinical stage, etc., which can influence the aggressiveness and prognosis [63].

5 Entropy Production Rate for Avascular Tumor Growth

We know from classic thermodynamics that if the constraints of a system are the temperature T and the pressure P; the entropy production can be evaluated using Gibbs's free energy [64], as:

$$\delta S_i = -\frac{1}{T} dG_{TP} \tag{120}$$

If the time derivative of (5.1) is taken, we have that:

$$\frac{\delta S_i}{dt} = -\frac{1}{T}\frac{dG_{TP}}{dt} \tag{121}$$

where represents the entropy production rate. The term can be developed by means of the chain rule as a function of the degree of advance of the reaction as:

$$\frac{dG_{TP}}{dt} = \left(\frac{\partial G}{\partial \xi}\right)_{TP} \frac{d\xi}{dt} \tag{122}$$

where $\left(\frac{\partial G}{\partial \xi}\right)_{TP}$ according to De Donder and Van Rysselberghe [65] represents the affinity A, with opposed sign, and the term $\frac{d\xi}{dt}$ is the reaction rate. Taking into account (121) and (122), we get:

$$\frac{\delta S_i}{dt} = \dot{S}_i = \frac{1}{T} A \dot{\xi} \tag{123}$$

The affinity can be calculated as [64]:

$$A = RT \ln \left(\frac{K_c}{\Pi C_k^{\nu(k)}} \right) \tag{124}$$

where $K_c = K^+ / K^-$ is the *Guldberg-Waage* constant (K^+ and K^- are the forward and backward rate constants), C_k is the concentration of the component k, whose stoichiometric coefficient is $\nu(k)$, and are rate constants. The reaction rate $\dot{\xi}$ can be evaluated according to the difference between the forward and backward reaction rates $\dot{\xi}^+$ and $\dot{\xi}^-$, as:

$$\begin{aligned} \dot{\xi} &= \dot{\xi}^+ - \dot{\xi}^- \\ &= k^+ \Pi C_{k(+)}^{\nu(k)} - k^- \Pi C_{k(-)}^{\nu(k)} \end{aligned} \tag{125}$$

Substituting (125), (124) and (123) is obtained [66]:

$$\dot{S}_i = \frac{1}{T} \left(\dot{\xi}^+ - \dot{\xi}^- \right) \ln \frac{\dot{\xi}^+}{\dot{\xi}^-} \tag{126}$$

If (126) is applied to describe the tumor, taking into account the results presented in Sect. 3 we obtained [67]:

$$\begin{aligned} \dot{S}_i &\approx R \left(\psi - \eta \right) \ln \frac{\psi}{\eta} \\ &= R \left(\psi - \eta \right) \ln \left(\frac{5 - d_f}{1 + d_f} \right) \end{aligned} \tag{127}$$

In the expression (127) it was included two properties observed in tumour growth. The first is its growth rate $V = (\psi - \eta)$, which is associated to their invasive capacity. The second is its complexity, a morphology characteristic, such as fractal dimension of the tumor interface d_f, which quantifies the tumor capacity to invade and infiltrate the healthy tissue.

The entropy production rate was determined by tumor cell lines as a physical function of cancer robustness and results are shown in Table 2 [67]. $\dot{S}_i$

Table 2 Entropy production rate for tumor in vitro

Cell line	d_f^*	Growth rate V^* $\left[\frac{\mu m}{h}\right]$	$\dot{S}_i$ $\left[\frac{J.\mu m}{mol.K.h}\right]$
Mv1Lu	1.23	11.50	50.11
AT5	1.23	8.72	38.05
B16	1.13	5.83	30.08
C-33A	1.25	6.40	27.26
Vero C	1.18	5.10	23.77
McA3D	1.09	3.73	19.45
C6	1.21	2.90	13.46
HT-29	1.13	1.93	9.64
CarB	1.20	2.06	9.39
HT-29M6	1.12	1.85	9.31
3T3K-ras	1.32	1.89	7.23
HeLa	1.30	1.34	5.32
3T3	1.20	1.10	4.99
Saos 2	1.34	0.94	3.49

*Experimental results reported by Brú [39]

Acknowledgement This paper was supported in part by Spanish Agency of International Cooperation for Development (AECID, projects: D/023653/09 and D/030752/10). We would like to thank to Prof. M. G. Velarde for inviting us to write the manuscript. Finally, it is a pleasure to thank Mrs. María J. Martín Espada for the skilled typing of the manuscript and her patience.

References

1. Deisboeck, T.S., Berens, M.E., Kansal, A.R., Torquato, S., Stemmer-Rachamimov, A.O., Chiocca, E.A.: Pattern of self-organization in tumour systems: complex growth dynamics in a novel brain tumour spheroid model. Cell Proliferat. **34**, 115–134 (2001)
2. Kitano, H.: Towards a theory of biological robustness. Mol. Syst. **3**, 137 (2007)
3. Rockmore, D.: Cancer complex nature. Santa Fe Institute Bulletin (SFI) **20**, 18–21 (2005)
4. Sole, R.V.: Phase transitions in unstable cancer cell populations. SFI Working paper 03-02-028
5. Betancourt-Mar, J.A., Nieto-Villar, J.M.: Theoretical models for chronotherapy: periodic perturbations in funnel chaos type. Math. Biosci. Eng. **4**, 177–186 (2007)
6. Kitano, H.: Cancer robustness: tumour tactics. Nature **426**, 125 (2003)
7. Kitano, H.: Cancer as a robust system: implications for anticancer therapy. Nature **4**, 227–235 (2004)
8. Baish, J.W., Jain, R.K.: Perspectives in cancer research. Can. Res. **60**, 3683–3688 (2000)
9. Ribba, B.A., Colin, T., Schnell, S.: Multiscale mathematical model of cancer, and its use in analyzing irradiation therapies. Theoret. Biol. Med. Modelling **3**, 1–19 (2006)
10. Roose, T., Chapmanm, S.J., Main, D.K.: Mathematical models of avascular tumor growth. SIAM Rev. **49**, 179–208 (2007)
11. Bar-Or, R.L., Maya, R., Segel, L.A., Alon, U., Levine, A.J., Oren, M.: Generation of oscillations by the p53-Mdm2 feedback loop: a theoretical and experimental study. PNAS **97**, 11250–11255 (2000)
12. Geva-Zatorsky, N., Dekel, E., Batchelor, E., Lahav, G., Alon, U.: Fourier analysis and systems identification of the p53 feedback loop. PNAS **107** 13550–13555 (2010)

13. Geva-Zatorsky, N., Rosenfeld, N., Itzkovitz, S., Milo, R., Sigal, A.: Oscillations and variability inthe p53 system. Mol. Syst. Biol. **2**, 33 (2006)
14. Wee, K.B., Surana, U., Aguda, B.D.: Oscillations of the p53-Akt network: implications on cell survival and death. PLoS One **4**, e4407 (2009)
15. Izquierdo-Kulich, E., Nieto-Villar, J.M.: A mesoscopic approach to model regulation of apoptosis by p53. Revista Cubana de Física **28**, 119–122 (2011)
16. Kirkwood, T.B.L.: Systems biology of ageing and longevity. Phil. Trans. R. Soc. B **64** (2011)
17. Vousden, K., Prives, C.: Blinded by light: the growing complexity of p53. Cell **413** (2009)
18. Lane, D., Levine, A.: p53 research: the past thirty years and the next thirty years. Cold Spring Harb. Perspect. Biol. (2010). doi:10.1101/cshperspect.a000893
19. Fulda, S.: Evasion of apoptosis as a cellular stress response in cancer. Int. J. Cell. Biol. **2010**, 6 (2010). Article ID 370835. doi:10.1155/2010/370835
20. Goldbeter, A.: Biological rhythms as temporal dissipative structures. Adv. Chem. Phys. **135** (2007)
21. Nicolis, G., Deams, D.: Probabilistic and thermodynamic aspects of dynamical systems. Chaos **8**, 311–320 (1998)
22. Nicolis, G., Prigogine, I.: Self Organization in Non-Equilibrium Systems. Wiley, New York (1977)
23. Van Kampen, N.G.: Stochastic Processes in Physics and Chemistry. North-Holland, Amsterdam (1992)
24. Gardiner, C.W.: Handbook of Stochastic Methods. Springer, Berlin (2004)
25. Murray, J.D.: Mathematical Biology I. An Introduction, 3rd edn. Springer, Berlin (2002)
26. Azmi, A.S., et al.: MI-219-zinc combination: a new paradigm. Oncogene **30**, 117 (2011)
27. Vu, B.T., Vassilev, L.T.: Current topics in microbiology an immunology. **348**, 151 (2011)
28. Wang, H., et al.: A small-molecules inhibitor of MdmX activates p53 and induces apoptosis. Mol. Can. Theor. **10**, 69 (2010)
29. Batchelor, E., Mock, C.S., Bhan, I., Loewer, A., Lahav, G.: Recurrent initiation: a mechanism for triggering p53 pulses in response to DNA damage. Mol. Cell **30**, 277 (2008)
30. Lacroix, M., Toillon, R.A., Lecrercq, G.: p53 and brest cancer, an update. Endocrine-related Can. **13**, 293 (2006)
31. Starzynska, T., et al.: Accumulation of p53 in relation to long-term prognosis in colorectal carcinoma. Eur. J. Gastroenterol. Hepatol. **9**, 183 (1997)
32. Castorina, P., Zappala, D.: Tumor Gompertzian growth by cellular energetic balance, arXiv:q-bio.CB/0407018 v2 21 Dec (2004)
33. Clatz, O., et al.: Brain tumor growth simulation. INRIA Rapport de recherche **5187**, 1–45 (2004)
34. Voitikova, M.V.: Strange attractors in inmunology of tumor growth. arXiv:chao-dyn/9708015, vol. 21 (1997)
35. Kuang, Y., Nagy, J.D., Elser, J.J.: Biological stoichiometry of tumor dynamics: mathematical models and analysis. Discrete Continuous Dyn. Syst. Ser B **4**, 221–240 (2004)
36. Rodríguez-Pérez, D., et al.: Tumors under periodic therapy: role of the inmune response time delay. arXvi:q-bio/0604008v1 (q-bio.TO) 7 April (2006)
37. de Pillis, L.G., Gu, W., Radunskaya, A.E.: Mixed immunotherapy and chemotherapy of tumors: modelling, applications and biological iterpretations. J. Theor. Biol. **238**, 841–862 (2006)
38. Magni, P., Simeoni, M., Poggesi, I., Rocchetti, M., De Nicolao, G.: A mathematical model to study the effects of drugs administration on tumor growth dynamics. Math. Biosc. **200**, 127–151 (2006)
39. Brú, A., Albertos, S., Subiza, J.L., García-Asenjo, J.L., Brú, I.: The universal dynamics of tumor growth. Biophys. J. **85**, 2948–2961 (2003)
40. Izquierdo Kulich, E., Nieto Villar, J.M.: Mesoscopic model of tumor growth. MBE **2**, 687–698 (2007)
41. Izquierdo Kulich, E., Nieto Villar, J.M.: Morphogenesis of the tumor patterns. MBE **5**, 299–313 (2008)

42. Anishchenko, V., Astakhov, V., Neiman, A., Vadivasova, T., Schimansky-Geier, L.: Nonlinear Dynamics of Chaotic and Stochastic Systems. Springer, Berlin (2007)
43. Kuznetsov, V., et al.: Nonlinear dynamics of immunogenic tumors: parameter estimation and global bifurcation analysis. Bull. Math. Biol. **56**, 295–231 (1994)
44. Barabási, A.L., Stanley, H.E.: Fractal Concepts in Surface Growth. Cambridge University Press, Cambridge (1995)
45. Norton, L.: Conceptual and practical implications of breast tissue geometry: toward a more effective, less toxic therapy. Oncologist **10**, 370–381 (2005)
46. Steeg, P.S.: Tumor metastasis: mechanistic insights and clinical challenges. Nat. Med. **12**, 895–904 (2006)
47. Robbins & Cotran (eds.): Pathologic Basis of Disease. Elsevier, Amsterdam (2005)
48. Chen, C.C., Daponte, J.S., Fox, M.D.: Fractal feature analysis and classification in medical images. IEEE Trans. Med. Imag. **8**, 133–142 (1989)
49. Luzi, P., Bianciardi, G., Miracco, C., Desanti, M.M., Del Vecchio, M.T., Alia, L., Tosi, P.: Fractal analysis in human pathology. Ann. NY Acad. Sci. **879**, 255–257 (1999)
50. Cross, S.S.: Fractals in pathology. J. Pathol. **182**, 1–8 (1997)
51. Elston, C., Ellis, I.O.: Pathological prognostic factors in breast cancer. I. The value of histological grade in breast cancer: experience from a large study with long-term follow-up. Histopathology **19**, 403–410 (1991)
52. Sedivy, R., Windischberger, Ch., Svozil, K., Moser, E., Breitenecker, G.: Fractal analysis: an objective method for identifying atypical nuclei in dysplastic lesions of the cervix uteri. Gynecologic Oncol. **75**, 78–83 (1999)
53. Landini, G., Rippin, J.W.: Fractal dimensions of the epithelial connective tissue interfaces in premalignant and malignant epithelial lesions of the floor of the mouth. Anal. Quant. Cytol. Histol. **15**, 144–149 (1993)
54. Landini, G., Rippin, J.W.: How important is tumour shape? Quantification of the epithelial connective tissue interface in oral lesions using local connected fractal dimension analysis. J. Patol. **179**, 210–217 (1996)
55. Sabo, E., Boltenko, A., Sova, Y., Stein, A., Kleinhaus, S., Resnick, M.B.: Microscopic analysis and significance of vascular architectural complexity in renal cell carcinoma. Clin. Can. Res. **7**, 533–537 (2001)
56. Tejera, E., Brizuela, N., Rieumont, J., Nieto-Villar, J.M.: Fractal analysis in epigenetic differentiation of Leukemic cells. Harmon. Fractal Image Anal., 74–75 (2004). http://www.fch.vutbr.cz/lectures/imagesci/download_ejournal/18_E.Tejera.pdf
57. Izquierdo Kulich, E., Amigó de Quesada, M., Pérez Amor, C.M., Lopes-Texeira, M., Nieto-Villar, J.M.: The dynamics of tumor growth and cells pattern. Math. Biosci. Eng. **6**, 547–559 (2009)
58. Izquierdo Kulich, E., Amigó de Quesada, M., Pérez Amor, C.M., Casanella Saint-Blanclard, O., Nieto-Villar, J.M.: Predicción de la agresividad del cáncer de cervix a partir de la morfología del tejido tumoral. Revista Cubana de Física **26**, 246–250 (2009)
59. Izquierdo Kulich, E., Amigó de Quesada, M., Pérez Amor, C.M., Nieto-Villar, J.M.: Morphogenesis and aggressiveness of cervix carcinoma. Math. Biosci. Eng. **8**, 987–997 (2011)
60. Frank, S.A.: Dynamics of Cancer. H. Allen Orr; Princenton, Series in evolutionary biology (2007)
61. Tsang, R.W., Fyles, A.W., Li, Y., Rajaraman, M.M., Chapman, W., Pintilie, M., Wong, C.S.: Tumor proliferation and apoptosis in human uterine cervix carcinoma. I: correlations between tumor proliferation and apoptosis. Radiother. Oncol. **50**, 85–92 (1999)
62. Toledo Cuevas, E.M., García Carrancá, A.: p53 and human papillomavirus in the carcinogenesis of the uterine cervix. Rev. Invest. Clin. **48**, 59–68 (1996)
63. Prempree, T., Patanaphan, V., Sewchand, W., Scott, R.M.: The influence of patients' age and tumor grade on the prognosis of carcinoma of the cervix. Cancer **51**, 764–777 (1983)
64. Prigogine, I.: Introduction to Thermodynamics of Irreversible Processes. Wiley, New York (1961)

65. De Donder, Th., Van Rysselberghe, P.: Thermodynamic Theory of Affinity. H. Milford, Oxford University Press, London (1936)
66. Nieto-Villar, J.M., Quintana, R., Rieumont, J.: Entropy production rate as a Lyapunov function in chemical systems: Proof. Physica Scripta **68**, 163–165 (2003)
67. Izquierdo Kulich, E., Alonso Becerra, E., Nieto-Villar, J.M.: Entropy Production rate for avascular tumor growth. J. Modern Phys. **2**, 615–620 (2011)

Quantitative Neuroimaging: What You can Say and What You can Believe About the Brain

M. Desco

1 Quantitative Neuroimaging. Introduction to the Problem

For many years, medical images have been simple pictures examined by a doctor at the lightbox. With the introduction of modern image modalities (X-Ray Computed Tomography, Positron Emission Tomography, Magnetic Resonance Imaging), imaging has turned into a measuring instrument able to provide quantitative information about many aspects of biological systems, including brain function.

Nowadays we can quantify many different properties or features of the brain. Regarding anatomy, the volume of the different structures can be accurately measured, and its shapes quantitatively characterized. White matter tracts can be located and depicted, and its degree of structuring can be measured using magnetic resonance diffusion imaging. Regarding function, there is an impressive span of techniques to measure features such as electrical activity, blood flow, number and localization of different neuroreceptors, energy metabolism (glucose consumption), etc.

Procedures to extract numbers from brain images can be collectively called quantification or post-processing algorithms. A few years ago, the only way for many researchers to extract quantitative information from the images was to develop their own algorithms. At this moment, the situation is completely different because of the widespread availability of algorithms and software packages intended to provide such quantitative information in a semiautomatic way (Fig. 1). These algorithms are usually applied following "pipelines", which depend on the particular

M. Desco (✉)
Instituto de Investigación Sanitaria Gregorio Marañón, Universidad Carlos III de Madrid, Madrid, Spain
e-mail: desco@hggm.es

R.G. Rubio et al. (eds.), *Without Bounds: A Scientific Canvas of Nonlinearity and Complex Dynamics*, Understanding Complex Systems,
DOI 10.1007/978-3-642-34070-3_49,

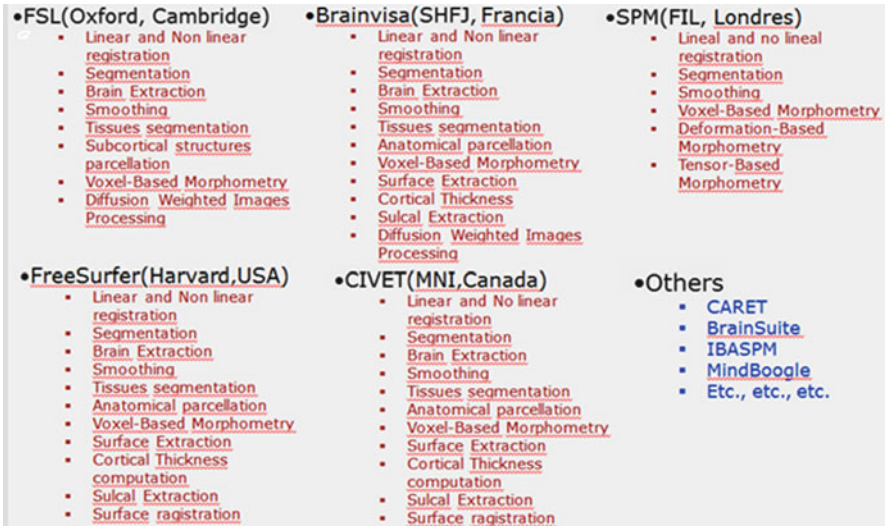

Fig. 1 Table representing different software packages (*in black*) and the algorithms they offer (*in red*), together with smaller complementary processing tools (*in blue*). This is just a survey of the more common ones; it is possible to download from Internet hundreds of other algorithms and packages

type of analysis the user wishes to conduct. Most of these pipelines are fairly complex and involve many steps performing advanced mathematical methods for image geometrical warping, kinetic modeling, automatic identification of structures (segmentation), shape and volume quantification, etc. As an example, Fig. 2 shows one possible pipeline for structural (morphological) assessment of brain magnetic resonance images. It is not uncommon to make use of components from different software packages to implement a given workflow, in such a way that the user has to develop some pieces of software to implement the connectors.

There is a significant overlap between software packages, since several of them are intended to achieve similar goals and contain equivalent algorithms. However, one puzzling fact is that they do not necessarily reach identical outcomes, since their approachesarediverse. Subtle differences between algorithms and assumptions realized with each approach may lead to noticeable differences in the results. Unfortunately, it is not easy to discern which packages are more accurate or reliable, since the ground truth remains unknown. There are reports about alteration of the results derived from using different versions of the software or even different operating systems (Windows, Linux) [1]. In practice, it is mostly matter of taste to choose one or another package, and there are "schools" of followers of the different approaches. Sometimes, researchers make use of new in-house developed approaches, which they consider more advanced from a technical standpoint. Being this a positive fact that promote new advances in the field, it also has a negative side, as it contributes to the publication of inconsistent results that cannot be easily compared with previous ones.

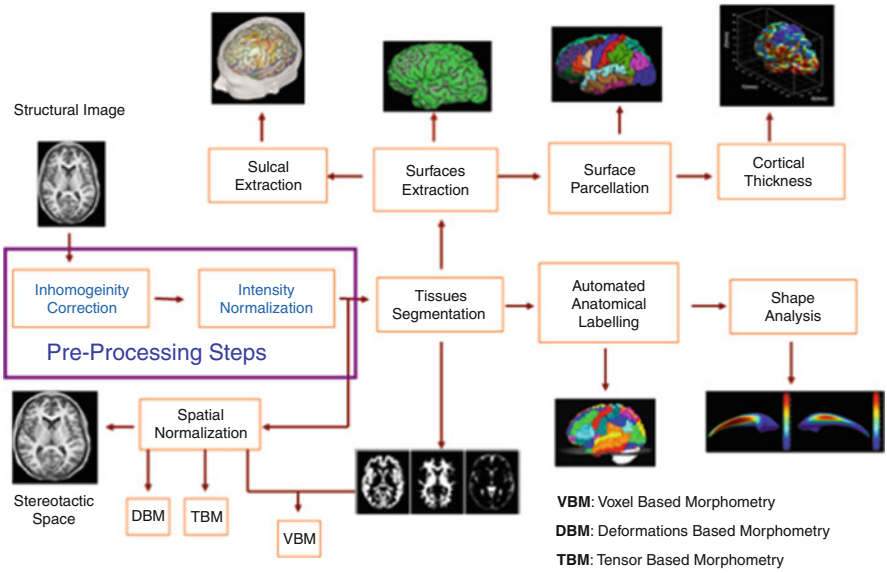

Fig. 2 Example of pipeline to process structural magnetic resonance images of the brain. It includes many sophisticated mathematical methods to correct image artifacts, to identify tissues and structures (segmentation, parcellation), to render 3D images, to quantify geometrical differences between different brains (voxel, deformation- and tensor-based morphometry), or to force a spatial matching of images from different subjects (normalization)

To sum up, any researcher interested in the brain who has relevant questions from a medical or biological point of view has to face the fact that there is a large (although still manageable) number of available imaging techniques, together with a huge (unmanageable) number of packages, algorithms and post-processing techniques, all of them apparently able to perform the different tasks involved in quantification processes. Even worse, the final results achieved with each of these competing approaches are frequently inconsistent.

To further support this standpoint, we could mention the work titled "Puzzlingly high correlations in fMRI studies of emotion, personality, and social cognition" [2], where the authors state that "[. . .] we are led to conclude that a disturbingly large, and quite prominent segment of social neuroscience research is using seriously defective research methods [. . .] producing a profusion of numbers that should not be believed".

Of course, it is not my purpose to transmit the idea that this exciting research field is so seriously defective that it should be rejected as a whole. But it is evident that something is going wrong, and it is of the utmost importance to identify the problems in order to enable further scientific progress by producing reliable and replicable results instead of creating confusion.

2 An Example: The Assessment of Mental Processes Through fMRI Studies

The non-invasive study of regional brain activity is an extraordinarily interesting tool to assess brain function under different cognitive or pathological situations. Electrical (EEG-based) approaches show some advantages, such as its excellent temporal resolution, but its potential is severely limited by significant shortcomings, mainly derived from its low spatial resolution (unless invasive direct cortical recordings are obtained). Brain activity has also been assessed by means of nuclear imaging techniques, particularly positron emission tomography (PET) which offers a relatively good spatial resolution. The most common approach is to study the uptake of ^{18}F-Fluoro-desoxy-glucose (FDG), a radioactive labeled analogue of glucose whose distribution reveals the map of brain energy consumption. This compound is widely available because of its use in clinical oncology, but its long uptake period (about half an hour) prevents performing fast experiments and severely restricts its application to assess brain function. Another approach is the use of ^{15}O-water as a radioactive tracer. Its distribution reflects regional cerebral blood flow, and its short radioactive half-life (about 2 s) allows for much faster studies than ^{18}F-based radiotracers (half-life of about 110 min). Nevertheless, the short life of ^{15}O heavily hampers its practical application, as it can only be used in the very few places where a cyclotron is available near a PET camera, at an immoderate cost. Finally, another drawback of all nuclear imaging techniques is the use of ionizing radiation, potentially harmful for the subject, which prevents replication of studies and limits its use on healthy volunteers.

In the early 1990s a new contrast mechanism was introduced in MRI: the so-called “BOLD” (blood-oxygen-level-dependent) contrast opened a new sub-modality within MRI, known as fMRI (functional MRI). This variety of MRI allows assessing cerebral regional blood flow with relatively good spatial resolution (millimeters) and acceptable temporal resolution (few seconds). These features, together with the absence of ionizing radiation, make this technique very suitable for experimental research on brain function, and its use in Neuroscience has grown exponentially. Presently, almost any state-of-the-art clinical MRI scanner can be used to obtain fMRI studies.

The process that links BOLD contrast to brain activity is relatively indirect: through a mechanism called “neurovascular coupling”, brain activity induces an increase in regional blood flow, in order to boost the energy supply to the activated area. This increase in blood flow usually exceeds the actual requirements, in such a way that the blood oxygenation level raises and consequently the proportion of oxy-hemoglobin versus deoxy-hemoglobin increases too. This difference can be sensed with MRI because of the different magnetic properties between both forms of hemoglobin (deoxy-hemoglobin is paramagnetic, oxy-hemoglobin is not).A good review of the topic of fMRI and its limitations can be found in [3].

Interestingly, the changes in image intensity derived from the BOLD effect are tiny and impossible to notice with the naked eye (Fig. 3). This makes it necessary

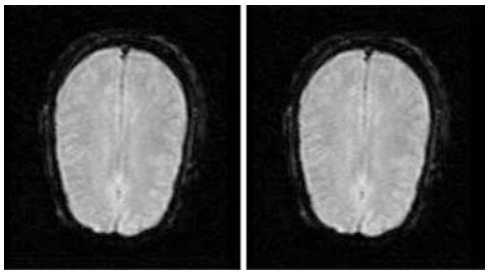

Fig. 3 fMRI images of a brain slice in activated (*left*) and rest (*right*) states. Notice how the difference is negligible with the naked eye

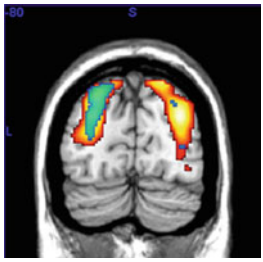

Fig. 4 Statistical Parametric Map resulting from an fMRI experiment. Areas in *red* color represent activation areas in a group of mathematically-gifted children when performing certain cognitive task (as compared to a control task). Areas in *green* depict activation under the same circumstances in an aged-matched control group. Color intensity represents the p-level of the statistical comparison, overimposed on an average high-quality structural image. (Data taken from [4])

to apply statistical techniques to detect the differences. The procedure consists in repeating a number of times a so-called "paradigm", in which the subject alternates (at least) two states, usually called "activation" and "rest". Statistical tests on the subtraction image (activation minus rest) allow the researcher to detect small differences which are solely due to the "activation" state. These "real" differences consistently add up in a coherent way while noise only grows with the square root of the number of repetitions, thus leading to an increased the signal-to-noise ratio. Statistically significant differences are usually over imposed on a good-quality anatomical image following a process called "statistical parametric mapping (SPM)" (Figs. 4 and 5).

Sometimes, paradigms are more sophisticated than just comparing two states, and require a more complex statistical assessment, based on Analysis of Variance (ANOVA). It is interesting to note that the assumption of additivity of the effects which underlies the whole analysis is more likely to be violated when dealing with complex designs.The entire workflow is fairly complex, and includes numerous adjustable parameters in the different processing steps (Fig. 5).

Many fMRI studies lead to very consistent results, particularly when mapping relatively low-level sensorial or motor functions, analyzed through straightforward paradigms. However, things become harder when dealing with more complex

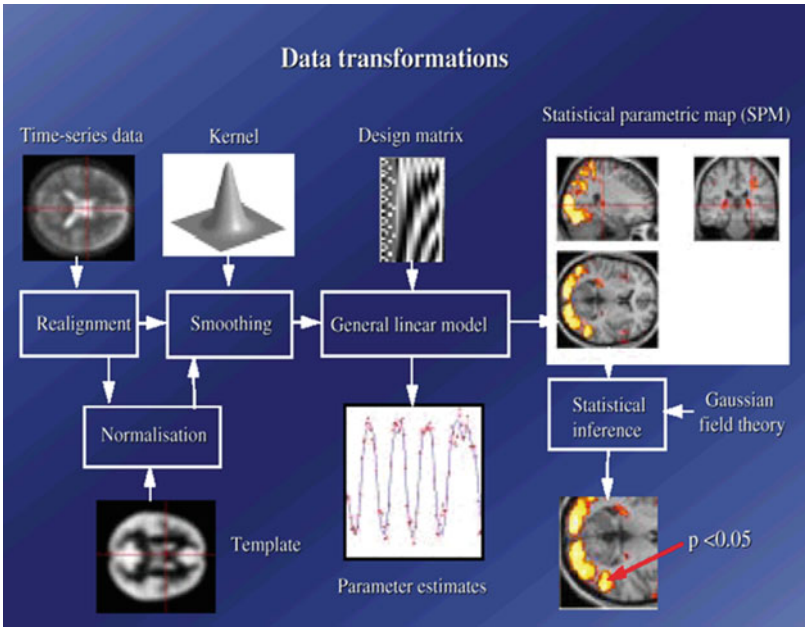

Fig. 5 Workflow of fMRI image processing with the SPM free software package ([http://www.fil.ion.ucl.ac.uk/spm/]). Each step (represented in *squares*) has several parameters that may require tuning for different types of experiments

paradigms involving higher mental functions. It is easy to find contradictory results in the literature, together with studies which suffer from severe methodological flaws or propose too speculative conclusions which do not derive from the actual results obtained. To illustrate these problems we can cite two examples, presented at the Human Brain Mapping Conference in 2005 [5]. The first one intended to study the perception of "Beauty", by assessing "Specific Activation of Aesthetic Judgment of Affective Pictures". In this study eleven subjects saw 300 photographs from the International Affective Picture System for 3 s. Each picture was rated as beautiful, ugly, or neutral. The authors conclude that the main effect of beauty is associated with one system of neural activations, whereas making an aesthetic judgment is associated with other neural structures.

Besides the paradigm itself, which is debatable, the main flaw in this study is the extremely low number of pixels reported as associated to the perception of beauty (Fig. 6). Most authors would never publish a result like this, especially considering that the minuscule size of the areas detected makes them very sensitive to any change in the processing parameters, particularly the degree of smoothing applied.

The second example is a study titled "Virtuous and evil: an fMRI study of different moral circumstance". In this case, besides the debatable identification between "good and bad" words and a moral circumstance, the authors concluded

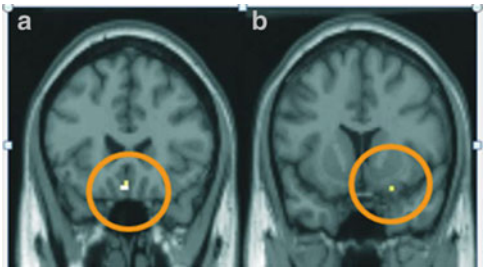

Fig. 6 Orbital activation purportedly associated with the main effect of beauty. Notice the small size of the reported activations

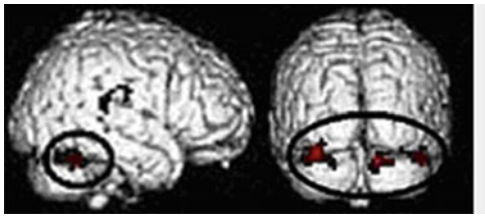

Fig. 7 One of the results reported in a study on moral circumstance with fMRI. Activation appears at the cerebellum, according to the authors

that "It also suggests morality is a behavior internalizing the social rules, but also an inherent behavior". In the reported results (Fig. 7) the authors report "activation" in the cerebellum, derived from being exposed to evil words.

Stretching the situation to the limits, we can witness how some commercial companies sell fMRI services, for instance for lie detection. Some of them claim that, for an affordable price, they can elucidate whether you vote democrat or republican, you are homo- or heterosexual, you are prone to be a criminal, etc. As a matter of fact, economy moves the world and no opportunity of making money will be wasted because of "subtle" technical problems or "superfluous" validations.

3 The Roots of the Problem

The reasons for the sometimes dubious reliability of quantitative neuroimaging results of studies assessing complex mental processes come from two main sources: Firstly the fact that imaging implies anatomical localization and secondly, the use of what could be called "accommodating" methodology. In the following sections we discuss these two sources of unreliability.

3.1 Localization of Brain Functions

Imaging implies, by definition, spatial localization. Regarding low-level brain functions, the existence of a topographical distribution is well known since a long time ago, because of the consequences of head traumas. The studies of

Penfield-Rasmussen in 1930 provided a very detailed and nice description of the localization of sensory and motor functions,introducing the idea of their famous "homunculus".

In this way, a strict localization of these low-level functions of the brain is widely accepted. However, what about higher-level mental activities? Should we assume that religion, courage, friendliness, anxiety, etc. are localized in certain regions of the brain? Probably, most researchers would answer this question negatively.

An example can illustrate this point: Consider a personal computer running a word processing software and somebody asking which is the "computer area" responsible for setting the margins of the document. It is not necessary to be an expert in Computer Science to see that such a question makes no sense, because many (almost all) the computer components are implied in that task. Similarly, it is evident that no hardware component has to be necessarily blamed if the program "hangs". Nowadays, everybody would identify these issues as software-related, because there is a clear awareness of the difference between hardware and software. Actually, software engineering is a discipline completely different from "regular" engineering. Surprisingly, in the case of the human brain, a much more complex 'computer' than a PC, questions similar to these are not uncommon. This may be because the notion of "cerebral software" simply does not yet exist. The closer concepts to that idea in neuroscience are those relative to brain circuitry, still very related to the brain "hardware". Of course, this upcoming new discipline studying the "brain operating system" has little to do with what present psychology studies.

Another important question is to what extent we can assume an exact homology between subjects for functions with a clear spatial localization. The noticeable intersubject anatomical variations in the cerebral cortex makes it impossible to accept the existence of a perfect spacial correspondence between different subjects. Therefore, it is hard to determine the scale, or degree of detail, at which we can accept the existence of such intersubject homology.

Brain plasticity is another fascinating feature of the brain that contributes to our difficulties with imaging. Brain plasticity can be defined as the capacity of the central nervous system to reorganize itself even performing structural changes as a reaction to environmental feedback. This amazing ability constitutes the basis for the rehabilitation after brain injuries. It is well known that not all brain functions can be easily relocated to a different area and that plasticity decreases with age. There are classical works about the activation of primary visual cortex in blind subjects when performing a reading task in Braille alphabet [6], or activation of the auditory cortex in congenitally deaf people when they view signs or sign-like movements [7]. Thus, even primary sensory areas, whose anatomical localization was first discovered and is more consistent among subjects, can be recruited for other tasks, particularly in young people.

Looking back at the history of Medicine and Neuroscience, we can realize that this fascination for localizing functions in the brain has been recurrent. By the dawn of the nineteenth century, phrenologists attempted to locate different mental faculties on the brain (actually, on the skull), obviously on very weak scientific grounds [8] Again, by the dawn of the twentieth century and thanks to the discovery of X-rays, there was an attempt to characterize and detect criminals

by over imposing and averaging skull X-ray films. Nowadays, by the dawn of the twenty-first century, those nave efforts are ridiculed in the light of modern science, while at the same time scientists make efforts to locate morality, make a commercial case of fMRI-based lie detection or use powerful mathematical techniques to average and superimpose brain images of different subjects. History is condemned to repeat itself.

3.2 'Accommodating' Methodologies

Postprocessing of neuroimaging studies to draw quantitative results makes use of a complex methodology, which relies on many experimental and statistical hypotheses. Researchers have an opportunity to tune the results thanks to the myriad of parameters involved, whose selection and validation is rarely explained in their papers as it is not usually required by the journals, even the most prestigious.

As in any statistical design, data are supposed to be collected through an unbiased random sampling, assumption which seldom holds in practice. The statistical conclusions reached in these types of analyses are also very demanding in terms of mathematical assumptions. Most designs require data independence, linearity, additivity, normality, homoscedasticity, no interaction, no colinearity, absence of confounded effects, etc. It takes a substantial effort and a long time to verify all these conditions, whose fulfillment most of the times cannot be assessed with a simple yes or no, but with an intermediate degree of certainty. This explains why, in practice, many authors do not spend enough time validating the assumptions involved in the models used.

Another crucial difficulty involved in statistical neuroimaging studies is how to choose a proper p-value threshold to accept a result as statistically significant. The huge number of regions (or even individual pixels) simultaneously tested lead to the arduous problem of how to correct the significance level for the multiple comparisons performed. Several statistical strategies are available to address this issue, but they lead to different results and it is not uncommon that just uncorrected results are provided, under the argument that exploratory analyses do not require such a correction. This originates a strong bias towards positive results. In a recent review of this problem [9] the authors conclude that "After more than 25 years of research in this field, further progress requires stronger guarantees of reliability for the ensuing results". In the meantime, the problem of choosing a sensible p-value threshold for neuroimaging studies remains largely unsolved.

There is a remarkable paper on Biostatistics titled "Data Torturing" [10] which explains how subtle statistical manipulations can be used to obtain the desired results. From that paper, "If you torture your data long enough, they will tell you whatever you want to hear" and "like other forms of torture, it leaves no incriminating marks when done skillfully". Neuroimaging designs are very prone to this type of manipulation because they usually comprise many variables, strongly associated, together with few cases (subjects).This leads to instability of the

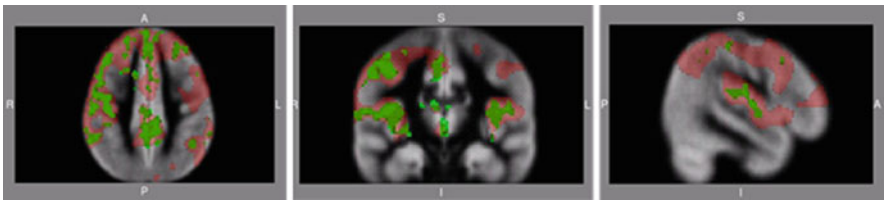

Fig. 8 SPM representation of the result of a PET experiment comparing two groups of patients (data not published). In *red*, significant areas detected when applying a smoothing of 12 mm, in *green* the smoothing was 4 mm

mathematical methods in such a way that small variations of some parameters may drastically change the outcome.

Besides these problems, which are common to many complex biostatistical designs, modern neuroimaging processing algorithms have numerous tunable parameters whose values need adjustment. By tuning these parameters the researcher has many opportunities for "steering" the analysis towards preconceived ideas or, at least, to force obtaining "statistically significant" results. As an example, Fig. 8 shows a quantitative analysis of a PET neuroimaging study comparing two groups of patients with schizophrenia. In this case we could report the areas in red or green (or any intermediate result), depending on the degree of smoothing selected by the operator (4–12 mm). It is remarkable that many published studies use different smoothing values within this range with no further explanation.Notice the huge difference in number and size of "detected" areas, depending on the actual decision made by the operator.

There are many examples in the scientific literature which may further illustrate this problem. A relatively classic work [11] performed a meta-analysis of 15 studies assessing volume deficits in brain structures in patients with schizophrenia. All the studies made use of the same technical approach (voxel-based morphometry, VBM). Only two out of 50 areas reported consistently appeared in more than 50% of the studies, while 9 of the regions appeared in only one study. This diversity of results was mainly attributed to different choices of parameters during the automated process. In more recent reviews on this topic, things do not seem to have improved significantly. In [12] the authors concludes that "There is limited high quality evidence supporting grey or white matter changes in schizophrenia, which has previously been obscured by a large volume of conflicting lower quality evidence".

In summary, the exceedingly sophisticated algorithms and procedures required to process quantitative neuroimaging studies are plenty of tunable parameters whose values may drastically change the outcome of the study. Setting aside the possibility of interested manipulations, it is clear that comprehensive explanations should be required by the journal reviewers before publishing this type of studies, at least in order to allow for a confirmatory replication of the results by other groups. Regrettably, this is not yet the case.

4 Conclusions

We should revisit the title of this work "Quantitative neuroimaging: What you can say and what you can believe about the brain" before attempting to reach some conclusions. It is clear that we can say many things about the brain and its functioning using neuroimaging. Powerful techniques and quantification algorithms allow us to measure with amazing precision many aspects of brain physiology and to characterize many psychological or cognitive processes. However, a high level of caution is necessary when interpreting the results. Many authors do not report on the assumptions they have used, on the exact set of parameters used, or on the depth of the validations they have performed on their data. These omissions may explain the extreme variability of results we can find in the scientific literature, and the difficulty to replicate studies. The inspired title of the work "If neuroimaging is the answer, what is the question?" [13] gives us a clue on how to proceed. If research is conducted on the grounds of sounding biological hypotheses, which are validated or rejected with neuroimaging techniques, then Neuroscience will benefit from these new powerful techniques. If its power is used to set up "data fishing" expeditions or to support preconceived ideas, then it will be progressively more difficult to distinguish real scientific advances from noise, only useful to increase the curriculum of the authors. This conclusion is in line with the editorial opinion of many prestigious journals [14].

References

1. Gronenschild, E.H., Habets, P., Jacobs, H.I., Mengelers, R., Rozendaal, N., van Os, J., Marcelis, M.: The effects of FreeSurfer version, Workstation Type, and Macintosh operating system version on anatomical volume and cortical thickness measurements. PLoS One **7**, e38234 (2012)
2. Vul, E., Harris, C., Winkielman, P., Pashler, H.: Puzzlingly high correlations in fMRI studies of emotion, personality, and social cognition. Perspect. Psychol. Sci. **4**, 274–290 (2009)
3. Logothetis, N.K.: What we can do and what we cannot do with fMRI. Nature **453**, 869–878 (2008)
4. Desco, M., Navas-Sánchez, F.J., Sánchez-González, J., Reig, S., Robles, O., Franco, C., Guzmán-de-Villoria, J.A., García-Barreno, P., Arango, C.: Mathematically gifted adolescents use more extensive and more bilateral areas of the fronto-parietal network than controls during executive functioning and fluid reasoning tasks. Neuroimage **57**, 281–292 (2011)
5. 11th Annual Meeting of the Organization for Human Brain Mapping. Toronto (2005)
6. Sadato, N., Pascual-Leone, A., Grafman, J., Ibáñez, V., Deiber, M.P., Dold, G., Hallett, M.: Activation of the primary visual cortex by Braille reading in blind subjects. Nature **11**, 380, 526–528 (1996)
7. Bavelier, D., Brozinsky, C., Tomann, A., Mitchell, T., Neville, H., Liu, G.: Impact of early deafness and early exposure to sign language on the cerebral organization for motion processing. J. Neurosci. **21**, 8931–8942 (2001)
8. Renner, C.: History of phrenology. Hist. Sci. Med. **45**, 249–256 (2011)
9. Ioannidis, J.P.: Excess significance bias in the literature on brain volume abnormalities. arch. Gen. Psychiatry **68**, 773–80 (2011)

10. Mills, J.L.: Data torturing. New Engl. J. Med. **14**, 329, 1196–1199 (1993)
11. Honea, R., Crow, T.J., Passingham, D., Mackay, C.E.: Regional deficits in brain volume in schizophrenia: a meta-analysis of voxel-based morphometry studies. Am. J. Psych. **162**, 2233–2245 (2005)
12. Shepherd, A.M., Laurens, K.R., Matheson, S.L., Carr, V.J., Green, M.J.: Systematic meta-review and quality assessment of the structural brain alterations in schizophrenia. Neurosci. Biobehav. R **36**, 1342–1356 (2012)
13. Kosslyn, S.M.: If neuroimaging is the answer, what is the question? Philos. Trans. R Soc. Lond. B Biol. Sci. **29** 354(1387), 1283–1294 (1999)
14. Nemeroff, C.B., Kilts, C.D., Berns, G.S.: Functional brain imaging: twenty-first cebtury phrenology or psychobiological advance for the millenium? [EDITORIAL]. Am. J. Psychiatry **156**, 671–673 (1999)

Part VII
Scientific Contributions: Geophysical Flows and Other Geo-problems

Strong Flows of Bottom Water in Abyssal Channels of the Atlantic

E.G. Morozov

1 Introduction

Due to the cold temperatures in Antarctica cold water mass is formed over the Antarctic slope as a result of mixing of the cold and dense Antarctic Shelf Water with the lighter, warmer, and more saline Circumpolar Deep Water [1]. Antarctic Shelf Water is formed over the Antarctic shelf in the autumn-winter season due to the cooling of relatively fresh Antarctic Surface Water and increased salinity caused by the ice formation. The salinity of the mixed water is relatively high and its temperature is low; thus, the resulting water mass with increased density descends and reaches the ocean floor. The water resulting from this process is called Antarctic Bottom Water. Formation of Antarctic Bottom Water is confined to a few regions along the perimeter of the Antarctic slope. In the Atlantic Ocean, the regions of dominating Antarctic Bottom Water formation are in the southern and western parts of the Weddell Sea.

Antarctic Bottom Water occupies a bottom layer approximately 1,000 m thick. The thickness decreases in the northern direction. Munk and Wunsch [2] estimated that without mixing, Antarctic Bottom Water would fill the entire ocean within a few thousand years and turn it into a stagnant pool of cold water. Only a thin upper layer of warm water (approximately 100 m thick) would remain at the surface due to wind mixing. Internal tide is the main source of ocean mixing, especially at hot spots over slopes of bottom topography.

In this paper we analyze the propagation of Antarctic Bottom water in the Atlantic Ocean. Antarctic Bottom Water (AABW) is the coldest and deepest layer of the South Atlantic. According to the definition, AABW is the water with potential temperature cooler than 2°C [3]. During the World Ocean Circulation Experiment

E.G. Morozov (✉)
Shirshov Institute of Oceanology, Nakhimovsky prospekt 36, 117851, Moscow, Russia
e-mail: egmorozov@mail.ru

R.G. Rubio et al. (eds.), *Without Bounds: A Scientific Canvas of Nonlinearity and Complex Dynamics*, Understanding Complex Systems,
DOI 10.1007/978-3-642-34070-3_50, © Springer-Verlag Berlin Heidelberg 2013

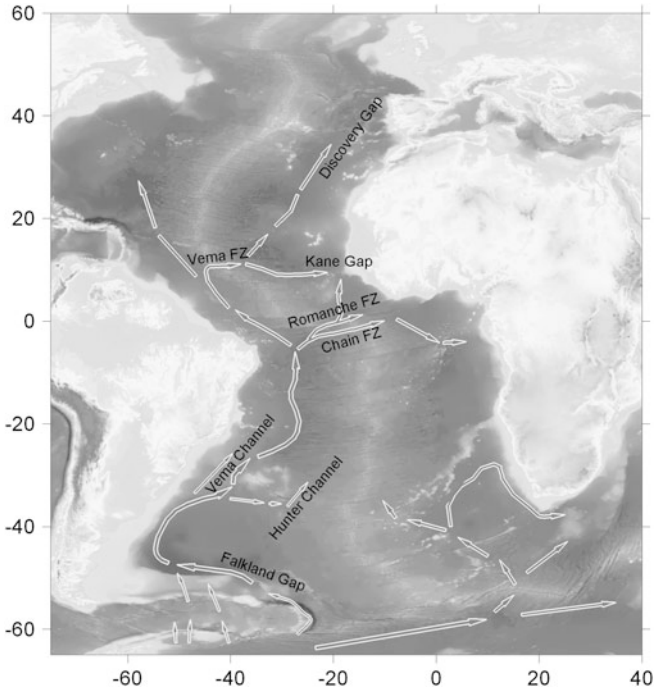

Fig. 1 Scheme of antarctic bottom flow in the Atlantic Ocean

(WOCE) one of the WOCE core projects was focused on the role of deep passages that make possible the far northward propagation of AABW. The pathways of AABW in the Atlantic Ocean are shown in Fig. 1. Everywhere, AABW occupies the bottom position in the oceanic stratification.

2 Vema Channel

The Rio Grande Rise is the boundary between the Argentine Basin in the south and the Brazil Basin in the north. It is a high topographic obstacle for bottom water propagation to the north. There are two meridional gaps in the Rio Grande Rise at 39°W and 28°W (Vema and Hunter channels, respectively). The depth in the Vema Channel exceeds 4,600 m, while the background depths are approximately 4,200 m. The Hunter Channel is much shallower and the greatest depth does not exceed 4,000 m.

Numerous observations in the Vema and Hunter channels indicate that the role of the Vema Channel for the transport of Antarctic Bottom Water is dominating compared with the Hunter Channel in the east and the Santos Plateau in the

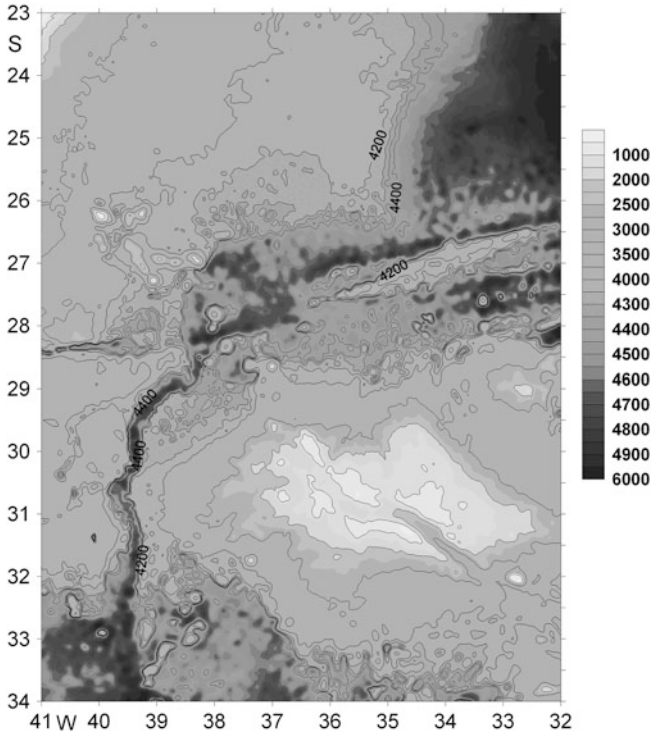

Fig. 2 Bottom topography of the Vema Channel

west. Approximately 7 Sverdrups of the total flow of Antarctic Bottom Water is transported across the Rio Grande Rise and Santos Plateau (1 Sv is $10^6\,m^3/s$). On the average, two thirds of this volume passes through the Vema Channel. The remaining part of bottom water flows over the Santos Plateau and through the Hunter Channel.

The bottom topography around the Vema Channel is shown in Fig. 2. The Vema Channel is the deepest passage for Antarctic Bottom Water. Therefore, the coldest part of this water (Weddell Sea Deep Water) can flow from the Argentine Basin in the equatorward direction only through this channel. The shallowest spot in the Vema Channel is the Vema Sill. The depth of this sill is approximately 4,614 m and the width of the channel in the narrowest point is 18 km.

According to the moored measurements at anchored buoy stations, the mean transport of Antarctic Bottom Water (layer below 2°C isotherm) through the Vema Channel is estimated at 3.5 Sv. The greatest velocities reach $60\,cm\,s^{-1}$. However, the instantaneous transport measured by LADCP instruments (five profiles) appears lower and fluctuates between 2.5 and 3.5 Sv. Usually, the jet core is vertically mixed in a layer approximately 150 m thick. Owing to the Ekman friction the coldest core

of the flow in the Vema Channel is usually displaced to the eastern slope of the channel.

The most intense studies in the Vema Channel were carried out along the so-called "standard" section across the channel at a latitude of 31°12' S. There were 22 expeditions to this location. The current measurements in this channel and in particular a section in 2009 using lowered acoustic Doppler current profiler (LADCP) demonstrated the existence of a counter-current of Antarctic Bottom Water above 4,200 m directed to the south. A conclusion that not all bottom water that flows in the Vema Channel discharges into the Brazil Basin was made even earlier based on hydrographic CTD measurements [4].

In 2010, a Russian expedition carried out the measurements of the currents in the region where Antarctic Bottom Water flows from the Vema Channel to the Brazil Basin at a latitude of 26°40' S. Let us compare the sections at the standard section (31°12' S) and in the northern part of the channel. The sections are presented in Fig. 3. The black line shows the location of the zero isotherm of potential temperature. In the extreme northern part, the channel becomes deeper and narrower. In the northern part, the isotherms of the temperature greater than 2°C do not reach the slopes of the channel as in the south. This means that the flow with a temperature of $\theta = 2$°C and even with a temperature of $\theta = 0.2$°C becomes wider. Using the available data we can compare only the water flows with temperatures less than $\theta < 0$°C. The mean velocities of the flow with such temperatures at the standard section are 23 cm/s, while at the northern section they decrease to 11 cm/s. Antarctic Bottom Water with higher temperatures flows above the western slope of the channel with velocities exceeding 20 cm/s, but we could not extend the section to the west in this expedition for a more precise calculation of the transport.

The square of the standard section for the water below 0°C is $6 \cdot 10^6$ m^2, while in the north the similar square (below 0°C) is almost four times smaller ($1.4 \cdot 10^6$ m^2). A large amount of the coldest water does not reach the northern section remaining beyond the topographic obstacles and mixes with the overlying waters. The transport of water with temperatures less than 0°C across the standard section is 1.4 Sv, while the transport across the northern section is 0.16 Sv, which is almost 10 times smaller.

We studied the time variation of the bottom flow in the Vema Channel. During the period from 1979 to 2003, a temperature increase was observed in the coldest jet in the Vema Channel. The temperature increased from –0.18°C to –0.12°C. In the end of 2004, this warming stopped and temperature fluctuations with an amplitude of 0.02°C were observed. Thus, we observed a general warming trend of Weddell Sea Deep Water with slight fluctuations over a period greater than 30 years.

We studied the variability of the flow along the Vema Channel over a distance of 700 km. The temperature in the jet increases, while the flow propagates from south to north in the Vema Channel due to mixing with the overlying North Atlantic Deep Water.

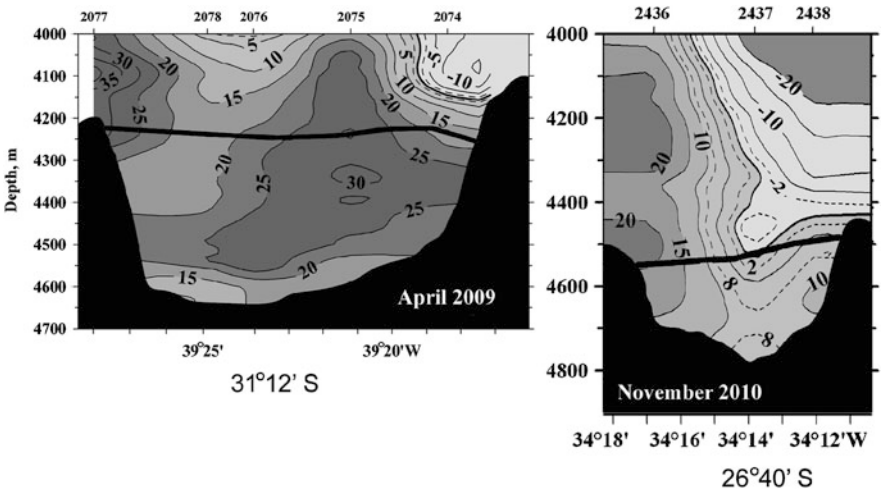

Fig. 3 Distributions of velocities normal to the sections. Positive values indicate flow to the north. The currents across the standard section are shown on the left (31°12' S). The currents in the northern part of the channel are shown on the right (26°40' S). The heavy line shows isotherm 0°C

3 Romanche and Chain Fracture Zones

The bottom topography of the Atlantic Ocean allows propagation of Antarctic Bottom Water to the northern latitudes of the East Atlantic only through the Romanche and Chain fracture zones (at the equator) and the Vema Fracture Zone (11° N) [5, 6]. Other small and shallower passages are less significant.

The Romanche Fracture Zone is a deep passage in the Mid-Atlantic Ridge 800 km long and 10–40 km wide (Fig. 4). Together with the Chain Fracture Zone they form an equatorial pathway for Antarctic Bottom Water to the East Atlantic. The main sill across the Romanche Fracture Zone is located at a depth of 4,359 m (13°40' W). The Vema Deep (7,856 m) is the deepest place in the Romanche Fracture Zone. The Chain Fracture Zone is located south of the equator, 200 km south of the Romanche Fracture Zone. The main sill of the Chain Fracture Zone is located at a depth of 4,050 m (12°22' W). Both fracture zones are the channels for the water flow between the Brazil and Guinea basins

The Antarctic Bottom Water ($\theta < 2°C$) flow through the Romanche and Chain fracture zones based on moored velocity measurements is estimated at 0.5 Sv in each channel [7]. The mean velocities are 10–20 cm s^{-1}. Velocities measured by current meters on moorings in 1991–1992 and using LADCP measurements in 2009 are very close. The bottom water passing through the Romanche and Chain fracture zones spreads only to the southeastern and equatorial parts of the Atlantic. Its further propagation to the north is almost limited by the Kane Gap.

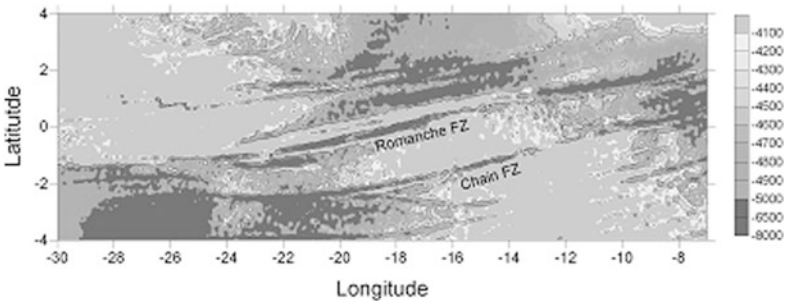

Fig. 4 Bottom topography of the Romanche and Chain fracture zones

4 Vema Fracture Zone

During the German expedition in 1927–1929 on R/V *Meteor*, Wüst [3] found cold abyssal waters with potential temperature $\theta = 1.74°C$ at the bottom of the Gambia Abyssal Plain. He suggested that these waters were of the Antarctic origin. He attributed their existence to the penetration through the Romanche Fracture Zone (known already by that time) and a fracture in the Mid-Atlantic Ridge presumptively located near 7–13° N. Only in 1956, deep sounding from R/V *Vema* revealed a deep fracture near 11°N, which was later called the Vema Fracture Zone. The fracture occurs between 43.5° and 41° W and connects the Demerara and Gambia abyssal plains. The width of the fracture zone is 8–10 km and the maximum depth is approximately 5,200 m. Three sills of the fracture zone have depths 4,690, 4,650, and 4,710 m.

In 2006, an expedition with CTD and LADCP measurements onboard R/V *Akademik Ioffe* visited the region of the main sills. The Antarctic Bottom Water ($\theta < 2°C$) flow through the Vema Fracture Zone (11° N) based on the measurements with a lowered velocity profiler was estimated at 0.5 Sv. The mean velocity is $10\,cm\,s^{-1}$, while the greatest velocity reaches $30\,cm\,s^{-1}$. Numerous observations in the North Atlantic indicate that the Vema Fracture Zone is the main pathway for Antarctic Bottom Water to the Northeast Atlantic.

5 Further Propagation of Antarctic Bottom Water to the Northeast Atlantic

In this section, we analyze the inflow of bottom waters to the Northeast Atlantic from the Vema, Romanche, and Chain fracture zones and their further propagation in the basin. The present-day concept was for the first time suggested in [8]. They wrote that the bottom waters propagating through the Romanche Fracture Zone spreads only in the equatorial and southeastern part of the Atlantic Ocean and do

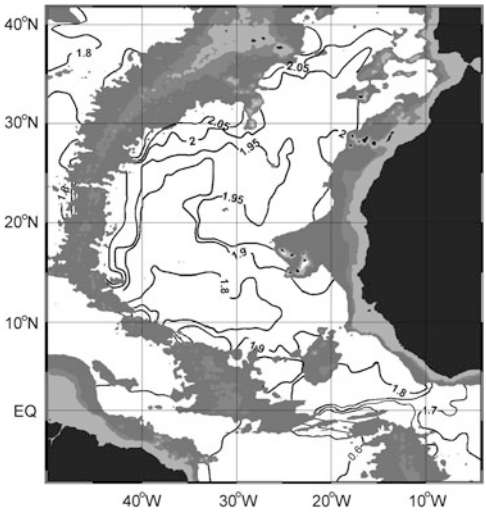

Fig. 5 Scheme of Antarctic waters spreading in the bottom layer of the Atlantic. Distribution of potential temperature (°C) at the bottom in the eastern part of the North Atlantic based on the WODB-2005 data. Only the stations deeper than 4,000 km were used. *Gray shade* shows the location of isobaths above 4 km

not propagate to the north through the Kane Gap, whereas the Vema Fracture Zone is the main pathway for bottom waters into the northeastern Atlantic.

On the basis of a large amount of measurements before 1991, a scheme of Antarctic Bottom Water (with potential temperature $\theta < 2°C$) spreading in the Northeast was suggested in [5]. According to this scheme, Antarctic Bottom Water that propagated to the Gambia Abyssal Plain in the East Atlantic through the Vema Fracture Zone splits into two branches. One branch transports bottom waters to the northeast and the other to the southeast. We suggest an improved scheme of the distribution of potential temperature at the bottom based on recent measurements, which appeared after 1991, with inclusion of all available historical data based of CTD-measurements during the WOCE experiment (Fig. 5).

One branch of the bottom water flow from the Vema Fracture Zone in the Gambia Abyssal Plane is directed to the north and northeast and the waters of the Antarctic origin fill the deepest parts of the Northeast Atlantic basins including the Canary Basin. The flow reaches the Discovery Gap at 37°N. This topographic feature is the boundary for the further northward transport of bottom water with potential temperatures below 2°C.

The second branch is directed from the Vema Fracture Zone to the southeast; the slopes of the Mid-Atlantic Ridge and Sierra Leone Rise are constraints for this flow from the south. This branch reaches the Kane Gap near the coast of Guinea.

According to the CTD casts made in the last 20 years, the waters with potential temperature less than $\theta = 1.85°C$ from the Romanche and Vema fracture zones merge in the region around the Kane Gap. Waters with $\theta = 1.80°C$ are located north and south of the Kane Gap. Since the waters with temperatures $\theta = 2.00°C$ and cooler are not separated over the Kane Gap the exchange of Antarctic Bottom Water through this passage is possible.

Antarctic Bottom Water transports through the Romanche and Chain fracture zones are of the order of 1 Sv, which is almost the same as the water transport through the Vema Fracture Zone. We believe that it may be explained by stronger mixing in the Romanche and Chain Fracture Zones compared to the Vema Fracture Zone. This can be seen from enhanced transformation of bottom water properties in the equatorial channels. In particular before the entrance to the Romanche and Vema fracture zones, the minimum values of potential temperature at the bottom are 0.68°C and 1.33°C, respectively [5]. The difference between the smallest values of potential temperature in these fracture zones becomes insignificant after they outflow to the East Atlantic from the fracture zones: $\theta = 1.66°$ (in Romanche) and $\theta = 1.69°$ (in Vema) [9].

Despite the fact that the bottom waters of the Antarctic origin propagated from the Brazil Basin they conserve all distinguishing indicators of Antarctic Bottom Water: low salinity, low concentration of dissolved oxygen, and high concentration of nutrients [10]. However, some authors use other names for Antarctic Bottom Water in the Northeast Atlantic.

Let us give a physical explanation why strong mixing occurs in the equatorial channel, which results in the isolation of different basins east of the Mid-Atlantic Ridge. This fact is explained by different intensities of mixing of Antarctic waters with the overlying North Atlantic Deep Water due to internal tides generated over the slopes of the Mid-Atlantic Ridge.

Morozov [11] calculated the amplitudes of internal tidal waves in the World Ocean based on the integrated results of measurements and model calculations. According to these estimates, the amplitude of internal tidal waves reaches almost 50 m in the Romanche Fracture Zone region at the equator and only slightly exceeds 20 m in the Vema Fracture Zone region at 11°N.

Figure 6 shows a chart of amplitudes of internal tides in the Atlantic Ocean. Due to such strong difference in the amplitudes of waves in these regions, mixing of deep water masses will differ strongly. The main mixing occurs over the slopes of the submarine ridge, where amplitudes of internal waves are the greatest. Internal tides are intensely generated in the regions of strong barotropic tides if the currents are normal to the ridge. Generation is intensified if the inclination of the bottom coincides with the inclinations of characteristic curves of internal tides, which depend on stratification [11]. The conditions that favor strong generation of internal tides are much better in the region of equatorial channels than in the Vema Fracture Zone.

We summarize that mixing in the equatorial region of the East Atlantic is greater than in the region of the Vema Fracture Zone. This strong mixing is caused by a strong barotropic tide in the equatorial region of the East Atlantic compared to the region of the Mid-Atlantic Ridge near the Vema Fracture Zone.

Strong mixing in the equatorial channels explains the difference in the contribution of the equatorial channels and Vema Fracture Zone to the bottom water mass composition in the Northeast Atlantic. Without strong mixing in the equatorial region, the influence of the Romanche and Vema fracture zones on the Northeast Atlantic seems to be equal. Antarctic Bottom Water transports through the

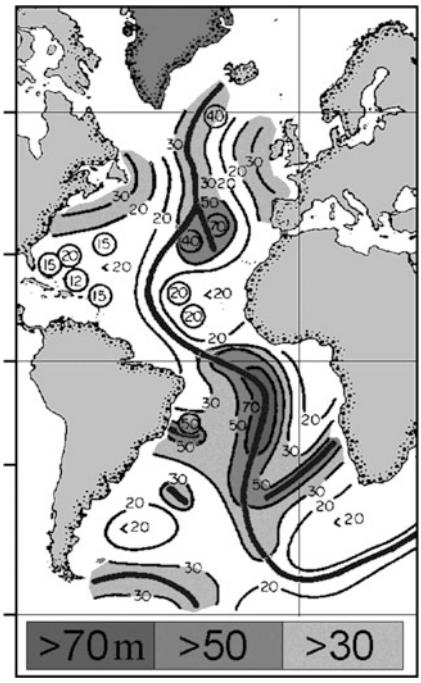

Fig. 6 Contour lines of amplitudes of internal tide in meters [11]. *Thick lines* show submarine ridges. *Numerals in circles* denote actual measurements of amplitudes of internal tide. The internal tide amplitude exceeds 50 m in the Romanche Fracture Zone region and only slightly exceeds 20 m in the Vema Fracture Zone region

Romanche and Chain fracture zones are of the order of 1 Sv, which is almost the same as the water transport through the Vema Fracture Zone. The difference between the smallest values of potential temperature of bottom water is insignificant after the water outflows to the East Atlantic: $\theta = 1.66°$ (in the Romanche FZ) and $\theta = 1.69°$ (in the Vema FZ). The depths of the main sills in the channels do not differ greatly: 4,359 m (Romanche FZ) and 4,571 m (Vema FZ).

Despite the fact that depths of the Kane Gap allow propagation of Antarctic Bottom Water and only 1.8°C isotherm is separated over the passage, the transport of bottom water through this channel is not strong.

Strong mixing with overlying waters results in strong transformation of properties of Antarctic Bottom Water after its outflow from the equatorial channels. In addition, the region of strong mixing includes also the Kane Gap, which makes this passage almost impossible for the strong northerly flow of bottom waters. Strong mixing closes this pathway for the flow of bottom water transported through the equatorial fracture zones. On the other hand, mixing conditions in the Vema Fracture Zone region are not as strong as in the equatorial East Atlantic and bottom water inflows are less transformed through the Vema Fracture Zone filling the entire Northeast Atlantic abyssal depths.

Different intensity of mixing results in different stratification at the outflow from the channels. Brunt-Väisälä frequency east of the Romanche Fracture Zone is $N = 0.14.10^{-3}\mathrm{s}^{-1}$, while east of the Vema Fracture Zone it is equal to $N = 0.80.10^{-3}\mathrm{s}^{-1}$.

6 Kane Gap

The Kane Gap is located between the Grimaldi Mountains, which are a part of the Sierra Leone Rise and the Guinea Plateau near the African Continent. The gap connects Gambia Abyssal Plain and Sierra Leone Basin. The sill depth in the gap is 4,502 m [12]. This depth was confirmed by the echo sounder measurements in our expeditions.

According to the scheme of Antarctic Bottom Water spreading in the Northeast Atlantic, the Kane Gap occupies the middle position between the Antarctic Bottom Water that propagated to the East Atlantic through the Vema Fracture Zone and the Antarctic Bottom Water that propagated through the Romanche and Chain fracture zones. Waters with potential temperature less than $\theta = 1.80°C$ are separated near the Kane Gap. The lowest temperatures measured over the sill in the Kane Gap were made in October 2009 at the western slope of the gap (1.846°C). South and north of the Kane Gap potential temperatures at the bottom are cooler.

In May 2009, the currents measured with LADCP were directed to the south at all depths below 2,500 m. Thus, the bottom transport was directed from the Gambia Abyssal Plain to the Sierra Leone Basin. In October 2009, measurements with an LADCP profiler demonstrated that the flow was directed to the northwest. Thus, the flow was opposite to the one recorded in May 2009. This result agrees with the idea discussed in [13] based on the photographs of the bottom, from which they concluded that the bottom flow in the Kane Gap is directed to the north.

The temperature stratification of the flow is similar to the flow in the Vema Channel. The coolest and densest water of the flow is displaced to the western wall of the gap due to the Ekman friction.

The total transport below 1.9°C potential temperature isotherm based on LADCP measurements fluctuates between zero and 0.2 Sv based on our measurements in different years (2009–2011). Thus, the bottom water from the Vema Fracture Zone influences at least the northern part of the Sierra Leone Basin, while the bottom water from the Romanche Fracture Zone can spread to the north through the Kane Gap and influence the adjacent southern region of Cape Verde Basin. However, the bottom water transport is not very strong and can be influenced by tides.

7 Discovery Gap

The northward propagation of bottom waters from the Canary Basin to the northeastern Atlantic occurs through the Discovery Gap. This passage is considered the terminal point of AABW spreading to the north in the sense that this is the water with a potential temperature less than 2°C, This is a narrow passage in the East Azores Fracture Zone at 37°N between the Madeira and Iberian abyssal basins. Our knowledge of the flow through this passage is based on the research described in [14] who named the passage “Discovery Gap”. The passage is 150 km long. Its

narrowest place is located at 37°20'N, 15°40'W. The width of the narrowest gap is 10 km and the depth of the sill is 4,800 m. The flow was measured from six moorings and supplemented by tracking floats at a depth of 4,700 m. The measured mean velocities were 5 cm s^{-1}. The flux of bottom water colder than potential temperature $\theta = 2.05$°C was estimated at 0.2 Sv. Numerous CTD measurements around the Discovery Gap indicate that water with potential temperature below 2°C does not propagate through this passage.

During the last 29 years since the previous measurements in 1982 the temperature at the bottom of the Discovery Gap increased by 0.02°C from 2.025°C in 1982 to 2.002°C in 2011. Unlike the current measurements in 1982, the measurements in 2011 did not demonstrate clearly manifested northerly flow of the bottom water. A fluctuating flow was observed in 2011. One core displaced to the eastern slope was directed to the northeast with velocities of approximately 5 cm/s and the second core with slightly greater velocities was directed to the southwest and displaced to the western slope.

8 Conclusions

This Chapter is a review of recent field studies of bottom transport of bottom through the main abyssal channels of the Atlantic Ocean. The expeditions carried out in the last 10 year made measurements with CTD-casts and moored current meters. A strong flow of bottom water in the Vema Channel was analyzed. The mean velocities are 30 cm/s. After the Vema Channel, Antarctic Bottom water slowly flows in the Brazil Basin and then splits into two flows. Part of the water flows through the Romanche and Chain fracture zones to the east. The other part flows to the northwest to the North American Basin. Part of the northwestern flow turns to the east and spreads through the Vema Fracture Zone into the Northeast Atlantic.

References

1. Orsi, A.H., Johnsson, G.C., Bullister, J.L.: Circulation, mixing, and production of Antarctic bottom water. Prog. Oceanograp. **43**, 55–109 (1999)
2. Munk, W.H., Wunsch, C.: Abyssal recipes II: energetics of tidal and wind mixing. Deep-Sea Res. **45**, 1977–2010 (1998)
3. Wüst, G.: Schichtung und Zirkulation des Atlantischen Ozeans, Das Bodenwasser und die Stratosphre. In: Defant, A. (ed.) Wissenschaftliche Ergebnisse, Deutsche Atlantische Expedition auf dem Forschungs – und Vermessungsschiff "Meteor" 6(1), 1925–1927, p. 411. Walter de Gruyter & Co, Berlin (1936)
4. McDonagh, E.L., Arhan, M., Heywood, K.J.: On the circulation of bottom water in the region of the Vema Channel. Deep-Sea Res. **49**, 1119–1139 (2002)
5. McCartney, M.S., Bennet, S.L., Woodgate-Jones, M.E.: Eastward flow through the Mid-Atlantic ridge at 11°N and its influence on the abyss of the Eastern basin. J. Phys. Oceanogr. **21**(8), 1089–1121 (1991)

6. Messias, M.-J., Andrie, C., Memery, L., Mercier, H.: Tracing the North Atlantic Deep Water through the Romanche and Chain fracture zones with chlorofluoromethanes. Deep-Sea Res. **46**, 1247–1278 (1999)
7. Mercier, H., Speer, K.G.: Transport of bottom water in the Romanche fracture zone and the Chain fracture zone. J. Phys. Oceanogr. **28**(5), 779–790 (1998)
8. Mantyla, A.W., Reid, J.L.: Abyssal characteristics of the World Ocean waters. Deep-Sea Res. **30**(8), 805–833 (1983)
9. Morozov, E.G., Demidov, A., Tarakanov, R., Zenk, W.: Abyssal Channels in the Atlantic Ocean: Water Structure and Flows. Springer, Berlin (2010)
10. van Aken, H.M.: The hydrography of the mid-latitude northeast Atlantic Ocean I: the deep water masses. Deep-Sea Res. **47**, 757–788 (2000)
11. Morozov, E.G.: Semidiurnal internal wave global field. Deep-Sea Res. **42**, 135–148 (1995)
12. Smith, W.H.F., Sandwell, D.T.: Global sea floor topography from satellite altimetry and ship depth soundings. Science **277**, 1956–1962 (1997)
13. Hobart, M.A., Bunce, E.T., Sclater, J.G.: Bottom water flow through the Kane Gap, Sierra Leone Rise, Atlantic Ocean. J. Geophys. Res. **80**, 5083–5088 (1975)
14. Saunders, P.M.: Flow through discovery gap. J. Phys. Oceanogr. **17**, 631–643 (1987)

Global Climate Change and Local Severe Weather Phenomena: Is There a Possible Synthesis Among These Apparent Antitheses?

F. Stel and D.B. Giaiotti

1 Introduction

Climate change is one of the major concerns of post modern world.[1] Climate, here considered as the average state of the coupled ocean-atmosphere system, continuously changed in the past and will continuously change in the future. Under the mathematical point of view, the reasons of this chaotic and everlasting transformation, a sort of mechanical samsara, are written in the equations that describe the system, in particular into the advection term, which brings with it the germs of non linearity. Under the physical point of view, the reasons of the ceaseless change relies within the equilibrium between incoming and out coming energy, in particular in the way in which energy is redistributed in the oceanic-atmospheric system. Even if science is not a matter of democracy, it is relevant to underline that nowadays the large majority of Scientists are confident that current climate is changing and the ocean-atmospheric system that is moving toward a higher energy state. The index used to quantify the intensity and timing of state's change is average temperature, even if average temperature barely represents a threat for people or environment.

The reasons why temperature is chosen as "the" index to quantify climate change are many: one of these is that in the World there is a relatively large number of relatively long temperature time series, then we can have a useful baseline to compare current climate with past climates. Another relevant advantage of

[1]The expression "post modern" is borrowed from Zygmunt Baumann's "Liquid modernity" (2000, Polity Pr, 228 pages).

F. Stel (✉) · D.B. Giaiotti
Arpa FVG – Regional Center for Environmental Modelling, via Cairoli, 14, I-33057 Palmanova (UD), Italy
e-mail: fulvio.stel@arpa.fvg.it

R.G. Rubio et al. (eds.), *Without Bounds: A Scientific Canvas of Nonlinearity and Complex Dynamics*, Understanding Complex Systems,
DOI 10.1007/978-3-642-34070-3_51, © Springer-Verlag Berlin Heidelberg 2013

temperature is that, being directly related to the amount of available energy, it gives us exactly the information we are interested is, i.e., if Earth is earning or loosing energy, moreover, just being temperature the measure of available energy, there are a lot of proxy relationships based on energy that can be used to infer temperature trends for the periods when there are no direct temperature measurements (e.g., tree rings, oxygen isotopes in ice cores, etc.). Temperature, moreover, is quite easily determined, without ambiguities, by numerical models and can be easily compared with the in situ available time series as a form of calibration for the climatic numerical models or projected into the future to guess what might happen to the climate.

Nevertheless, in spite of its countless good qualities, temperature is affected by the awful drawback not to be directly related with all the atmospheric phenomena we are interested in. In other words, even if global and/or local temperature is growing, this will not automatically mean that the number of tornadoes will globally and/or locally increase as well as the number of thunderstorms, floods, hail falls, draughts, etc. The reason for this apparent paradox, i.e., available energy rises but relevant events which often requires a lot of energy do not necessarily become more frequent or severe, is that significant weather is mainly related to atmospheric flows rather than bulk available energy. In turn, this is caused by the fact that, even if energy reaches Earth in radiative form, it is redistributed (then equilibrium is kept) mechanically through the meridional perturbations of geostrophic flow. In other words, even if it is true that intense atmospheric phenomena are characterized by a high energy density, the local increase in energy density is produced by mechanisms that are not directly related to the energy off-set represented by the average temperature which is, very likely, going to increase in the next years. Trends in the frequency and/or intensity of flash floods in a specific area instead of dry spells, then, will be related to the way in which atmospheric flows change more than to the local and/or global trends in temperature [1]. Moreover, even average temperature should be more correctly considered as an effect of oceanic-atmospheric global circulation than as a consequence of the direct radiative forcing [2, 3].

This is not a new paradigm, indeed, because already C. G. Rossby [4], in 1939, pointed out that changes in global average temperature have to be a consequence of changes in average flow patterns [5], nevertheless, probably even thanks to the wonder of successes achieved by atmospheric and coupled oceanic and atmospheric numerical models, the causal relationship between dynamics and temperature fade as time went by, becoming less evident in researchers minds. More generally, people barely remembered that numerical models do not reproduce full reality, but only some of its behaviours. This oversight increased the risk to be trapped into the so called shadowgraphy mirage (Velarde, personal communication), confusing reality behaviour (the shadow) with reality itself[2] (the subject whose shadow

[2]Here "reality" and "reality representation" are assumed, with a significant abuse of language, to have the same meaning.

is reproduced). This kind of oversight is not new in the history of science, in fact it happened, as an example, to Astronomy in the late sixteenth century, with the Tychonic System (a conceptual model, indeed), which was capable to reproduce some of the observed planets behaviour, but it was not a correct representation of reality. Even nowadays, however, we can fall in the same trap. As an example, current state-of-the-art meteorological numerical models can, through wise parametrizations (conceptual models, indeed), quite effectively reproduce the observed rain patterns, even if associated with different dynamical conditions; but in spite of their success in reproducing rain patterns, the same parametrizations often fail to reproduce correctly the boundary layer properties. Such a failure can become extremely relevant when just those boundary layer properties play a fundamental role for a correct description of rain patterns, as is the case for intense orographic rain [6].

The "shadowgraphy mirage", as will be shown in a while, is a crucial aspect that has to be clearly kept in mind dealing with the local effects of global climate change, in particular when we are interested in severe local effects. These events, in fact, are characterized by a relevant release of energy, often occurring by way of intense convection, in a relatively short amount of time, which is by far negligible when compared with the climate change characteristic time, as it is marked by average temperature. This pristine evidence raise immediately two questions: the first is if we already have the conceptual tools to say something about the frequency and intensity of events occurring in spatial and temporal scales several orders of magnitude different from that of global climate change; the second question is if it is worth to spent efforts trying to answer to the first one. Give a response to the latter question is relatively easy, in fact almost the majority of atmospheric damages inflicted to people, property and environment are caused by local severe weather events [7]. Moreover, as an effect of globalization, nowadays local damages can produce long range disturbances more frequently than in the past, this because of the increased degree of connection in Societies which, in turn, have become more sensitive to this kind of events [8]. Giving a response to the first question is a little bit more tricky and would require a whole new chapter.

2 The Characteristic Environment of Local Severe Weather Events

Severe weather events [9] pertain to small scale (say a few kilometres) and high time frequency (say a few hours), while climate change belongs to very low frequency and, because of the lack of information at small spatial scales, it is quite well understood only at large scales. Moreover, the most effective, and probably only, tools we have are numerical models that can describe climate behaviour with a satisfying level of confidence only at a spatial scale of several tens of kilometres and with a time resolution of years. The question then is how can we use these large

nets to capture such small, but dangerous, fishes? There is not a unique answer to this question, but we can say that there are at least two ways in which we can face this problem, both based on the physical mechanisms that produce the onset and evolution of severe weather events [10, 11].

When related to deep moist convection, severe weather events, requires three ingredients to occur [12]. The first ingredient is represented by the onset of convection, i.e., the initial vertical displacement of a significant portion of the air mass that moves it away from its original position and, thermodynamically speaking, away from its unstable equilibrium. The second ingredient is represented by the presence of a sufficient amount of thermodynamic energy in the unstable air mass, that might sustain an independent and organized vertical motion of the air mass portions. The third ingredient is represented by the presence in the air mass of a sufficient shear, i.e., a variation of wind speed and direction with altitude, that might prevent the development of damping mechanisms (hydrodynamic load, among others) and supply the horizontal vorticity that, in turn, would favour a long-lasting convection. The role of the first two ingredients is quite obvious and we will spend only a few more words describing which variable is almost often used to quantify the amount of available energy, that is the "convective available potential energy", because it would be relevant for the technical possibility to determine this quantity in climate numerical models.

Convective available potential energy, in detail, is a quantity which is directly related to the maximum kinetic energy that a volume of air can acquire attaining the thermodynamic instability and releasing the energy present in the air mass. Moreover, this quantity can be easily determined using only the vertical thermal atmospheric profiles. Mathematically speaking, this quantity springs out straightforwardly from the vertical component of the simplified Navier-Stokes equation, i.e.,

$$\rho \frac{dw}{dt} = -\frac{\partial p}{\partial z} - g\rho.$$

This equation assumes a very useful form, just considering a small volume subject to the displacement and changing the density variable with temperature variable using the ideal gal law, i.e.,

$$\frac{dw}{dt} = -g\frac{T_0 - T}{T_0},$$

where T is the temperature of the displaced parcel and T_0 is the temperature of the environment in which the parcel moves.

A solution of this equation has the following form

$$\tfrac{1}{2}\int_{LFC}^{EL} dw^2 = -g\int_{LFC}^{EL} \frac{(T_0 - T)}{T_0} dz,$$

where the integration limits are the level of free convection (LFC, the level at which the air parcel starts to buoy) and the equilibrium level (EL, the level at which there is no more buoyancy). In this solution, the term

$$g \int_{LFC}^{EL} \frac{(T_0 - T)}{T_0} dz = CAPE,$$

is the convective available potential energy (CAPE). As formerly stated, this quantity depends only from the thermal field[3] and temperature should be, in principle, quite well reproduced by climatic numerical models. Thanks to the CAPE index we can say that, even if it is not reasonable to use currently available climatic models to see directly if the frequency and intensity of local severe weather events will change, it might be reasonable and feasible to use the same numerical models to see if the frequency and intensity of the environments prone to severe weather events under the point of view of available energy would change in the future [13, 14].

The role of the third ingredient, i.e., the wind shear, is a little bit less intuitive and will be described in more detail right now. In fact, when a volume of air begins to buoy, releasing its CAPE, condensation often occurs and water droplets, as well as ice crystals, begin to fall down in the air mass with theirs terminal velocity. With this downward uniform movement, these hydrometeors increase the pressure on the rising parcel by an amount equal to their weight per unit of parcel surface. This local increase in pressure is called hydrometeors loading and, if the amount of condensation is enough large, it can completely dump the vertical motion. However, the dumping effect of hydrometeors loading can be avoided if the upward displacement is not exactly vertical but slanted, in this way the dynamic high pressure is exerted far away from the base of the convective current, that in turn can continue to develop.

Another relevant effect of wind shear on the development of convection is related to the enhancing of vertical vorticity, described by the vertical component of vorticity in a rotating system

$$\frac{d}{dt}(\zeta + f) = -(\zeta + f)\left(\frac{\partial u}{\partial x} + \frac{\partial v}{\partial y}\right) + \left(\frac{\partial w}{\partial y}\eta - \frac{\partial w}{\partial x}\xi\right) + \left(\frac{\partial \alpha}{\partial y}\frac{\partial p}{\partial x} - \frac{\partial \alpha}{\partial x}\frac{\partial p}{\partial y}\right) + Fr,$$

where the η and ξ horizontal components of vorticity, directly related to the vertical variation of wind field, can be transformed in horizontal vorticity by horizontal variations of vertical velocity, clearly related to upward motions. This increased vorticity, in turn, can be further enhanced by convergence or by baroclinic effects, producing the intense local vortexes called tornadoes.

[3] In reality, CAPE depends even from the initial temperature and moisture of the rising parcel, because these two variables modify the level of free convection (LFC), which is pivotal for the determination of CAPE. In other words, CAPE can change, for the same vertical thermal profile, just chosing a different risilg parcel on the same column of air. Moreover, the air parcels that starts convection are often near to the ground, and the lowest levels are badly reproduced by numerical models, climatic ones in particular, and strongly depend from the way in wich land use, orography and gerography are reproduced by the numerical models. This is an extra, non negligible, problem to face.

3 Impacts of Global Climate Change on Severe Weather Events

Currently, the majority of attempts made to infer the variation in frequency and intensity of local severe weather events due to the global climate change are carried out looking for the way in which environmental conditions prone to local severe weather events are going to change in the future. In general, attention is often devoted to CAPE and shear, because these quantities are directly related to severe convection and, in principle, they can be retrieved by the currently available global and regional climate models. An approach parallel to the CAPE and wind shear approach is that based on the first ingredient, that is convection onset, and, more generally, on the knowledge of physical climatology. Analysing the flow patterns associated to the occurrence of severe weather events in a specific area, in fact, it is possible to see that they cluster in definite and distinct classes (among others, Giaiotti et al. [15]). In this way it is possible to move the quest for the variations in frequency and intensity of severe weather events to the quest for the variations in frequency and intensity of the large scale flow patterns associated to the occurrence of these phenomena. This connection is often manifested by the relationship between large scale flow index and local (sometimes very local) phenomena like hail, as it is shown in Fig. 1 [16].

Dealing with hail, in particular, it is amazing how a very local meteorological phenomenon produced by the microphysical interactions between supercooled water droplets and ice crystals might, as shown in the above picture, be in a tight connection with the hemispheric centres of pressure represented by the Island low and Azores high. This connection, would not be possible without an interplay between large scale flows and orography.[4] Similar connections between severe convective events and large scale flows can be found in other areas of the World and might represent, once physically understood, a useful proxy to infer the future trends of these events.

Even if all the above described approaches are promising and can supply right now hints on what might be expected in the different areas of the World for some classes of severe weather events, they are undermined by the above mentioned "shadowgraphy" effect. In fact, even if currently available numerical models are capable to reproduce correctly the observed average temperature trends, unfortunately they do not reproduce correctly the observed values of CAPE and shear [17], overestimating it over sea (e.g., in the Mediterranean area) and underestimating it over land or in general over areas characterized by complex orography, like the Alpine chain. The reasons of this systematic effect are still not clear, but they might be related both to an incorrect parametrization of the radiative budget near to the

[4]This connection between NAO and hail days is not general, but peculiar of the Friuli Venezia Giulia Region (northeastern Italy), in fact other areas do not show such a behaviour, as is the case of other alpine areas. In the latter cases, probably, the onset of hail storms is less related to large scale flows and is more connected with peculiar effects.

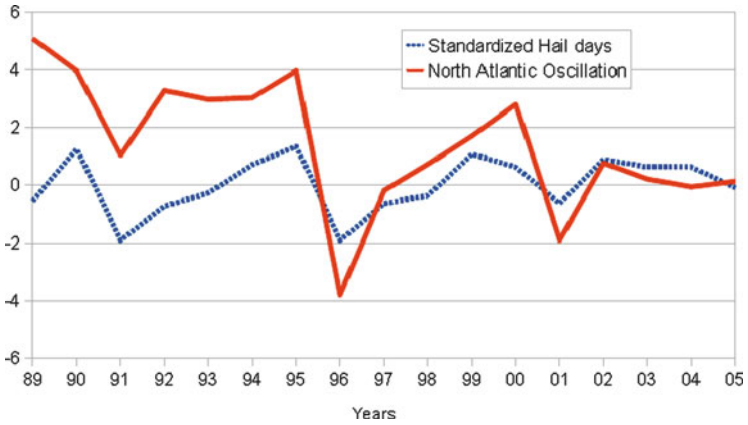

Fig. 1 Trends of hail days (normalized) over Friuli Venezia Giulia and of North Atlantic Oscillation (NAO; Hurrel, 2003)

Earth's surface (boundary layer parametrization), or to an incorrect description of the large scale flows ([18], then to a resulting poor representation of the interaction between flows and complex orography. The fact that even the large scale flows might be incorrectly represented puts severe threats not only to the CAPE-shear technique, but even to the possibility to adopt the complementary approach of physical climatology and the onset ingredient.

4 Conclusions

What we know about future climates comes out from complex tools called numerical climate models. These tools might in principle be used even to infer information on the future trend of local severe weather events in defined areas of our planet. At least two approaches, based on the so called "ingredients" of local severe weather events, can be adopted to face this challenge but, even if these approaches might in principle work, their adoption is undermined by the fact that state-of-the-art climate numerical models barely reproduce the needed variables even if they reproduce correctly the observed past trends of temperature and rain. This apparent paradox probably reveals a significant point that has to be analysed in detail, in fact this might be caused by imperfect parametrizations that, when tuned, can reproduce correctly only some of the main atmospheric behaviours, in spite of others, among which there are those directly connected with the onset and development of local severe weather events. If this is the case, we might have been trapped by a "shadowgraphy mirage", confusing a shadow with its physical reality. Even if this had to be the case, however numerical climate models have the capability to be improved, through the adoption of more correct physical parametrizations. This amelioration would produce direct

benefits, with a more robust determination of the already well reproduced variables (temperature and rain, in particular), but even indirect benefits, supplying correct information on the variables needed for the determination of the future trends of local severe weather events. Mirages, in fact, do not represent a threat if we realize what they are.

Acknowledgement Authors are deeply in debt with Prof. M. G. Velarde for the interesting and stimulating discussions that often started from very practical questions and, generally, moved in the realm of Social Sciences, literature and Politics, returning back, unexpectedly, to the solution of the former practical question.

References

1. Paeth, H., Hense, A., Glowienka-Hense, R., Voss, S., Cubasch, U.: The North Atlantic Oscillation as an indicator for green-house gas induced climate change. Climate Dyn. **15**, 953–960 (1999)
2. Seager, R., Battisti, D.S., Yin, J., Gordon, N., Naik, N.H., Clement, A.C., Cane, M.A.: Is the Gulf Stream responsible for Europe's mild winters? Quart. J. Roy. Meteor. Soc. **128**(586), 2563–2586 (2002)
3. Seager, R., Battisti, D.S.: Challenges to our understanding of the general circulation: abrupt climate change. In: Schneider, T., Sobel, A.S. (eds.) The Global Circulation of the Atmosphere: Phenomena, Theory, Challenges, pp. 331–371. Princeton University Press, Princeton (2007)
4. Rossby, C.G.: Relation between variations in the intensity of the zonal circulation of the atmosphere and the displacements of the semi-permanent centers of action. J. Mar. Res. **2**, 38–55 (1939)
5. Palmer, T.: Nonlinear dynamics and climate change: Rossby's legacy. Bull. Am. Meteo. Soc. **79**, 1411–1423 (1998)
6. Gallai, I., Giaiotti, D.B., Gladich, I., Stel, F.: On the onset and evolution of deep moist convection over areas characterized by complex orography: the case of Friuli Venezia Giulia. FORALPS Technical Report, 6. Universit degli Studi di Trento, Dipartimento di Ingegneria Civile e Ambientale, Trento, Italy, pp. 20 (2008)
7. Platt, R.H.: Disasters and Democracy: The Politics of Extreme Natural Events, pp. 320. Island, Washington, DC (1999)
8. Doswell III, C.A.: Societal impacts of severe thunderstorms and tornadoes: lessons learned and implications for Europe. Atmos. Res. **67–68**, 135–152 (2003)
9. Orlanski, I.: A rational subdivision of scales for atmospheric processes. Bull. Am. Meteo. Soc. **56**, 527–553 (1975)
10. Brooks, H.E., Doswell III, C.A., Cooper, J.: On the environment of tornadic and non tornadic mesocyclones. Wea. Forecast. **9**, 606–618 (1994)
11. Giaiotti, D.B., Giovannoni, M., Pucillo, A., Stel, F.: The climatology of tornadoes and waterspouts in Italy. Atmos. Res. **83**, 534–241 (2007)
12. Johns, R.H., Doswell III, C.A.: Severe local storms forecasting. Wea. Forecast. **7**, 588–612 (1992)
13. Riemann-Campe, K., Fraedrich, K., Lunkeit, F.: Global climatology of Convective Available Potential Energy (CAPE) and Convective Inhibition (CIN) in ERA-40 reanalysis. Atmos. Res. **93**, 534–545 (2009)
14. Brooks, H.E.: Proximity soundings for severe convective for Europe and the United States from reanalysis data. Atmos. Res. **93**, 546–553 (2009)

15. Giaiotti, D.B., Steinacker, R., Stel, F.: Atmospheric Convection: Research and Operational Forecasting Aspects, pp. 235. Springer Verlag GmbH, Wien (2007)
16. Giaiotti, D.B., Stel, F.: The climatology of hail in the plain of Friuli Venezia Giulia. Atmos. Res. **67–68**, 247–259 (2003)
17. Marsh, P.T., Brooks, H.E., Karoly, D.J.: Preliminary investigations into the severe thunderstorms environment of Europe simulated by the Community Climate System Model 3. Atmos. Res. **93**, 607–618 (2009)
18. Lucarini, V., Calmanti, S., Dell'Aquila, A., Ruti, P.M., Speranza, A.: Intercomparison of the northern hemisphere winter mid-latitude atmospheric variability of the IPCC models. Climate Dyn. **28**, 7–8 (2007)

A Time-Space Description of the Analysis Produced by a Data Assimilation Method

K.P. Belyaev and C.A.S. Tanajura

1 Introduction

The assimilation of geophysical data into dynamical models of the ocean and the atmosphere has become one of the most attractive scientific areas during last decade. This was mostly caused by the demands on improvements of weather and climate predictability, by the increase on computational resources, and by substantial developments in the observational system of the ocean and the atmosphere.

In general, the data assimilation (DA) schemes can be classified as variational or sequential. The variational scheme assimilates the available data in a time window by finding the model initial condition that provides a trajectory with minimum errors with respect to the data. If new data come after assimilation, the scheme should be repeated independently of the previous solution. This scheme is theoretically well posed but rather complicated for realisation, particularly for non-linear models, since it requires the use of iterative schemes and the calculation of the model adjoint operator. The update or sequential scheme produces the objective analysis by correcting the model forecast or first guess. This correction is calculated by minimising the errors of the estimate with respect to the true value. The analysis is used as the model initial condition for the calculation of the first guess in the next time step. This scheme is much easier for realisations despite some theoretical uncertainties.

K.P. Belyaev (✉)
Russian Academy of Science, Shirshov Institute of Oceanology (SIORAS),
Nakhimovsky 36, Moscow 117799, Russia
e-mail: kbel55@yahoo.com

C.A.S. Tanajura
Dept. Geophysics and Geology, Federal University of Bahia, CPGG, Campus Ondina,
Travessa Barão de Jeremoabo, s/n, 40170-29 Salvador, BA, Brazil
e-mail: cast@ufba.br

R.G. Rubio et al. (eds.), *Without Bounds: A Scientific Canvas of Nonlinearity and Complex Dynamics*, Understanding Complex Systems,
DOI 10.1007/978-3-642-34070-3_52,

The majority of the sequential DA algorithms is based on the control theory of filtration of stochastic processes and statistical estimations. After the classical work of N. Wiener, A. Kolmogorov, and other great mathematicians of the twentieth century, a feasible sequential scheme was proposed by Kalman [3]. It is referred to in the literature as the Kalman filter [4]. Reviews about the Kalman filter theory and applications on geophysical research have been presented by Ghil and Malanotte-Rizzoli [5], Cohen [6], and others, i.e. [10]. During the last years, extensions of the Kalman filter, such as the generalisation to non-linear models and the use of non-Gaussian error distributions, have been proposed. These extensions can be found, for instance, in Evensen [7]. In addition, simpler forms of the Kalman filter algorithm, such as the statistical interpolation scheme, have been quite used in ocean data assimilation (e.g., [8,9]).

Despite the recent developments, the extended Kalman filter schemes are still an open area. The feasibility of the standard Kalman filter method for the operational atmosphere and ocean data assimilation remains questionable, mainly because of its high computational cost. Also, approximations are required for its realisation. This creates a serious gap between theory and applications, and adds difficulties to investigate the numerical behaviour of the scheme. Another limitation of the Kalman filter scheme is the lack of initial and/or boundary conditions for the covariance function of the error.

In Belyaev et al. [11], another contribution on the sequential DA methods has been presented. It is also based on the Kalman filter theory, but it is able to solve some of the aforementioned problems. Its feasibility and physical relevance have been demonstrated in a recent study as well [12,13]. The limitations of the method have been discussed in those works.

The main goal of the present study is to further develop the DA method derived in those papers for practical applications in atmosphere and ocean circulation problems. Another goal is to discuss the quality of the estimated fields and better understand the time-space structure of the analysis and of the error between the model and the observations.

The present work utilises the eigenvalues and eigenvectors decomposition for the analysis error covariance matrix, referred to in the scientific literature as the canonical covariance matrix representation. This method is very similar to the well-known empirical orthogonal function (EOF) decomposition and principal components, widely used in the data analysis of the atmosphere and ocean variability. However, this approach is not commonly used in DA studies.

Most of the DA methods based on the probability theory and statistics, such as the Kalman filter approach, the statistical interpolation or the method of successive corrections, exploit the analysis covariance. If, for instance, a variable is observed at a point A at time t but it is not observed at a point B at time t (or at time τ different of t), then, in order to make any conclusion about this variable at a point B at time t (or τ), it is necessary to know the connection of the variable between the points A and B at time t (or at times t and τ). This connection is mathematically expressed through the covariance. However, the representation of the covariance of a scalar variable with spatial and temporal dependence is rather difficult, since, in general, it

requires a four-dimensional function. For vector variables, it would require an even higher dimensional function. The canonical decomposition allows to identify the pattern and magnitude of this connection in a physically reasonable and transparent way. It decreases the dimension of the function that describes the covariance.

The present study uses the ocean general circulation model (OGCM) MOM3 from the Geophysical Fluid Dynamics Laboratory (GFDL/NOAA), USA, as a tool to investigate the DA scheme. A new model, MOM4, has become recently available. However, from the qualitative point of view, the results obtained in this work would be the same with MOM3 or MOM4. Here, the observational data used in the assimilation experiments and in the validation procedure are from the Pilot Research Moored Array for Tropical Atlantic (PIRATA) database [14].

The structure of this work is the following. Section 2 briefly describes the OGCM, the PIRATA data and the DA technique. Section 3 presents the strategy of the canonical decomposition of the covariance matrix of the analyses error as a development of the DA technique. Section 4 discusses the experiments and the main results. In the end of this paper, there are two appendixes. Both of them present some mathematical details of the DA method for completion and to help understanding the method and the present work.

2 The OGCM, the PIRATA Data and the DA Technique

2.1 The OGCM

MOM3 [15, 16] is a primitive equation hydrostatic ocean model in z-coordinate. It uses finite differences over a staggered Arakawa B-grid in space and an implicit scheme in time.

In the present study, the model horizontal resolution was set to $1.5° \times 1.41°$ (longitude $\times$ latitude) over the globe for each of the 15 vertical layers. The model has no explicit mixed layer parameterisation. The latter is resolved by considering non-uniform vertical resolution, in which the number of layers in the upper ocean is much greater than below. For the configuration used in the present study, the first 10 layers cover the upper 500 m. The horizontal diffusion coefficients were 10^8 °C $cm^{-1}s^{-1}$ for heat, $10^6 cms^{-1}$ for momentum, and the same for salinity. The vertical diffusion coefficients were 10^2 °C $cm^{-1}s^{-1}$ and $10^6 cms^{-1}$. Time-step in the model was 3,600 s.

The OGCM was initialised at rest with climatological salinity-temperature structure from Levitus data, and it was integrated for 5 years forced by climatological atmosphere heat, momentum, and freshwater fluxes through its surface boundary [17]. This was the spin-up run. Starting from the result of the spin-up run, the model was forced by the National Centre for Environmental Prediction (NCEP)/National Center for Atmospheric Research (NCAR) reanalyses [1] momentum fluxes, climatological freshwater fluxes, and observed sea surface temperature from January 1, 1996 until December 31, 2000.

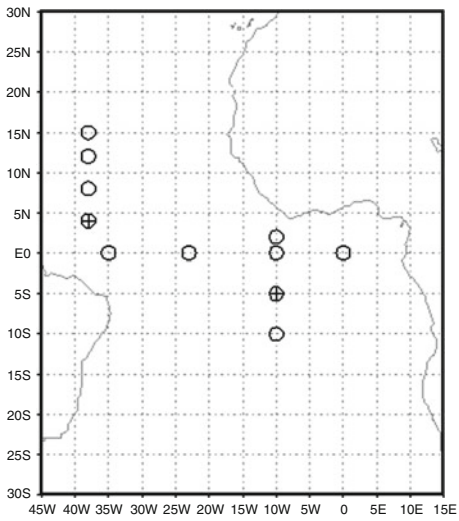

Fig. 1 PIRATA mooring location in ATLANTIC

2.2 The PIRATA Data

The PIRATA array is today composed by 15 Atlas moored buoys located in the tropical Atlantic (Fig. 1). Several meteorological variables are measured at the surface, including precipitation, wind direction and magnitude and air temperature. Vertical profiles of the ocean temperature are measured at 11 levels, from surface to 500 m. More recently, salinity measurements have been taken at 3 levels. Daily mean data are transmitted via the ARGOS satellite system and they are freely available in the internet.

For the data assimilation experiments in the present work, only the temperature vertical profiles were used. It should be emphasized that no filtering or other smoothing of the data time series was done, but time and vertical linear interpolation were performed to fill in gaps of the data and easy the realization of the assimilation experiments.

2.3 The DA Technique

The DA method considered here will be referred to as the Fokker-Planck (FP) assimilation scheme. It is based on the Kalman filter theory, but it uses the FP equation to calculate the evolution of the error covariance. The method was presented in details in [11], and its feasibility and practical applications were discussed in [12,13]. Here, only a brief description is presented. Also, to avoid unjustified references and to simplify the understanding of this paper, some mathematical and technical aspects

of the FP method are presented in two appendixes. The analysis of the unknown variable $\xi(t,\bar{x})$ produced by the method at time t and position $\bar{x}$ is

$$\hat{\xi}(t,\bar{x}) = \xi_m(t,\bar{x}) + \int_0^t \sum_{i=1}^{N(\tau)} \alpha(\tau,\bar{x},\bar{x}_i)\theta(\tau,\bar{x}_i)d\tau, \tag{1}$$

where $\bar{x}_i$ is the position of an observation; the bar is introduced to distinguish the 3-dimensional spatial point from its coordinate; τ is time, $\tau \leq t$; $\xi_m(t,\bar{x})$ and $\xi_0(t,\bar{x}_i)$ are the values of the variable given by the model (first guess) and the observation, respectively; $\theta(t,\bar{x}_i) = \xi_0(t,\bar{x}_i) - \xi_m(t,\bar{x}_i)$ is the error of the model variable known only at the observational points; $\alpha(\tau,\bar{x},\bar{x}_i)$ is the optimal weight coefficient; $N(\tau)$ is the number of observations used in the assimilation at time τ. Without loss of generality, the observational data are assumed to be available continuously in time, while their spatial distribution is discrete. Also, the observational values are assumed to be perfect, i.e., there is no difference between the observed value and the true value. The weight coefficients α are unknown and should be determined from other equations.

Formula (1) has a clear physical interpretation. It shows that in order to estimate the unknown variable ξ at an arbitrary grid point or to correct the model variable at this point, it is sufficient to: (i) calculate the differences between the model variable and the observations at all available observational points; (ii) then multiply these differences by the weight coefficients taking into account the location of both the observation and the analysis grid point; and (iii) finally add this to the model value. This linear form of the optimal estimator is commonly used [2,5].

To obtain the Kalman-gain matrix $A(t)$ the following equation is used

$$K(t,\bar{x},\bar{x}_i) = \int_0^t \sum_{j=1}^{N(\tau)} \alpha(\tau,\bar{x},\bar{x}_j)K_0(\tau,t,\bar{x}_i\bar{x}_j)d\tau, \tag{2}$$

or in matrix form

$$\underline{K}(t) = \int_0^t A(\tau)\underline{K_0}(\tau,t)\,d\tau, \tag{3}$$

where $K_0(\tau,t,\bar{x}_i\bar{x}_j)d\tau$ is the covariance between the errors of the estimated variable taken at the points $\bar{x}_i\bar{x}_j)$ and at times τ,t, respectively, and $K(t,\bar{x}_i\bar{x})$ is the covariance between the estimated variables at an analysis grid point $\bar{x}$ and an observational point $\bar{x}_i$.

The determination of the covariance matrices $\underline{K_0}(\tau,t)$ and $\underline{K}(t)$ is a key-problem of the Kalman-filter theory. However, if these matrices are known, the optimal estimation is found linearly and uniquely from formulas (1)–(3).

In [11], it was proposed to obtain $\underline{K_0}(\tau, t)$ by using the FP equation

$$\frac{\partial p}{\partial t} = -\frac{\partial (ap)}{\partial s} + \frac{1}{2}\frac{\partial^2 (bp)}{\partial s^2}, \tag{4}$$

where $p = p(t, s)$ is the joint conditional probability density function between the error of the analysis at two arbitrary (observational) points; s is a two-dimensional vector with the values of those errors; and a and b are parameters that depend on s and t, known as the drift vector and the diffusion matrix, respectively. The solution of this equation, the density distribution p, uniquely defines the covariance between any pair of errors, which can be inserted into formulas (2) and (3).

The drift vector and the diffusion matrix are approximated from the model output and the data. The main idea is given here in the appendixes.

3 Further Developments of the DA Technique

In this section some new ideas on the development of the DA technique are discussed. They are mostly connected with the simplification of the method.

Equation (4) defines only a conditional probability of the error. It means that the real unconditional probability can be determined only if the probability at the previous time step or at the initial time is known. The initial probability of the error is known uniquely only at those points where the observations are available. Indeed, comparing the model and the observed data, it is possible to define the error, and hence, to set up the distribution for this error.

If no prior information about the observational error is considered, this density distribution function will be simply the Dirac-function centred at the time in which the observation is taken. If there is additional information about the observational error, the full distribution of the error will be given as a convolution of this known distribution and the δ-function. In any case, the set up of the initial condition of the density is necessary, and this requires information about the errors. Therefore, the covariance matrix $\underline{K_0}(\tau, t)$ can be defined uniquely for any pair of observational points. However, the lack of information creates uncertainties about the covariance matrix $\underline{K}(t)$.

In general, there are two ways to define $\underline{K}(t)$. One way is to subjectively set up the initial conditions for the FP equation. This is physically equivalent to set up an a priori distribution of the error before the experiment. The second way is to define $\underline{K}(t)$ knowing $\underline{K_0}(\tau, t)$. The second way seems preferable. It does not need any additional assumptions and it reduces the problem to a simple linear interpolation. However, to obtain a good estimation of $\underline{K}(t)$, it is necessary to have a dense observational network.

Now one way is proposed to realise this scheme. Matrix $\underline{K_0}(\tau, t)$ is a positive-determined diagonally-dominated matrix and, hence, it has a full set of eigenvectors,

which are linearly independent, orthogonal and have a length equalled one. Let this set be $g_1(t), g_2(t) \ldots, g_{N(t)}(t)$ and $\lambda_1, \lambda_2 \ldots, \lambda_{N(t)}(t)$ be the corresponding eigenvalues for a moment$t$. After multiplication both parts of equality (2.b) on vector $g_1(t)$ for any index 1, one obtains the formula

$$\lambda_1 \hat{g}_1 = A(t)\lambda_1 g_1(t) + F(t),$$

where $\hat{g}_1(t) = K(t)g_1(t)$ and $F(t)$ is known function which includes the previously corrected values. As it was mentioned if data at moment t are updated this function is zero.

Vector $\hat{g}_1(t)$ has the following properties:

- It must coincide with vector $g_1(t)$ at all observational points;
- It should vanish at arbitrary grid points $\bar{x}$ if the distance between $\bar{x}$ and any observational point exceeds some limit value or cut-off radius;
- It should be continue and smooth function of the distance between grid point $\bar{x}$ and arbitrary observational point.

These requirements leave some space to construct the vector $\hat{g}_1(t)$ through the known vectors $g_1(t), g_2(t) \ldots, g_{N(t)}(t)$ and eigenvalues $\lambda_1, \lambda_2 \ldots, \lambda_{N(t)}(t)$. However, if a scheme of interpolation is chosen, this is done uniquely. In this study the scheme of interpolation or construction of vector $\hat{g}_1(t)$ is used as follows:

$$\hat{g}_1(t) = \left[\sum_{j=1}^{N(t)} \gamma_j^1 g_j(t) \right] (R - R_0)^{-1}$$

where R is the distance between grid point $\bar{x}$ and observational point $\bar{x}_j$ where eigenvector g_j is defined and known, R_0 is the cut-off radius, which is a parameter of the scheme and γ_j^1 are the coefficients of simple linear interpolation in space from point $\bar{x}_j$ to point $\bar{x}$. Namely, they are the solution of the linear system

$$x = \sum \gamma_j x_j, \qquad \sum \gamma_j y_j, \qquad z = \sum \gamma_j z_j,$$

where $x,\ y,\ z$ are co-ordinates of grid point $\bar{x}$, and $x_j,\ y_j,\ z_j$ are the co-ordinates of observational point $\bar{x}_j$. If R exceeds R_0, $\hat{g}_1(t)$ is prescribed zero. This scheme is simple, uniquely defines the vector $\hat{g}_1(t)$ at any grid points and provides the holding of requirements (a)–(c). When vector $\hat{g}_1(t)$ is defined for each eigennumber $l,\ 0 < l \leq N(t)$, there is no problem to find out the Kalman gain matrix $A(t)$ The problem of its definition is reduced to a simple linear system of equation which defines the unique solution, because the matrix of the system is non-degenerated. And, ultimately, having defined the Kalman gain, the assimilated amendment is found by (1). This completes the DA scheme description.

4 The Experiments and Results

The scheme described above has been applied in conjunction with OCM MOM3 as follows: Spin up run of MOM3 forced by climatological wind stress and heat fluxes from NCEP for 4 years started from climatological temperature-salinity atlas and zero currents.

Forced run of MOM3 by reanalysed wind stress and heat fluxes NCEP from 1996–1999 years (also 4 years).

Assimilated and control run in parallel (twin experiments). Assimilated run starts from initial fields obtained after forced run and assimilates PIRATA data as it was mentioned before. This run has been continued one month (January 2000). Model was forced by reanalysed atmosphere field for 2000 January. In parallel, the same scheme but without assimilation has been performed. Further these two experiments will be referred as assimilation and control, respectively.

In the assimilation run data were assimilated daily, from 9 buoys, on each level independently. The scheme of a buoy location is presented in Fig. 1. Also, in Fig. 1 the location of two another buoys are shown, marked by crosses. Data from those buoys had not been assimilated but used for comparison of the corrected temperature profiles with real data. Now the results of experiments are discussed. Figure 2 shows the experiments results on day January 15 on level 40 m. Figure 2a presents the model assimilation run, Fig. 2b presents the model control run, and Fig. 2c shows their difference, assimilation minus control. The first view on these figures shows that after assimilation the resulted field becomes much more dynamical and varied. The temperature difference after assimilation ranged from 22°C up to 28°C while in control run this variability is smaller, maximum is only 26°C. In general, the temperature on the sea surface is higher after assimilation. Assimilation increases the temperature of upper ocean level significantly underestimated by the model. The difference of two runs (Fig. 2c) clearly demonstrates the non-homogeneity of the assimilation impact, its concentration near the observational point position, but spreading far beyond them. The assimilation process grabs the whole tropical zone and fills out 20°S and 25°N despite all stations lie in between 10°S and 20°N. Everywhere this difference is positive. The opposite situation occurs below the mixed layer. Figure 3 demonstrates the temperature structure on the same day Janeiro 15 on level 200 m. Figure 3a presents the model assimilation run, Fig. 3b presents the model control run, and Fig. 3c shows their difference. The structure of the difference is very similar as in Fig. 2c, but with the opposite sign. Also, in general the impact of assimilation is less pronounced, grabs smaller area and gives less amendment. However, this impact physically is even stronger, because it involves larger volume of water. The accumulated results of assimilation are very well presented by comparison the assimilated and non-assimilated temperature profiles shown in Fig. 4a, b. Two points have been chosen for demonstration, one had co-ordinates 330W, 0N(equator), and another had position 350W 5 S. They are shown in Fig. 1 by crosses, as it was mentioned above. In the first of this point there are no observations, but there are observations in vicinities points. Among these

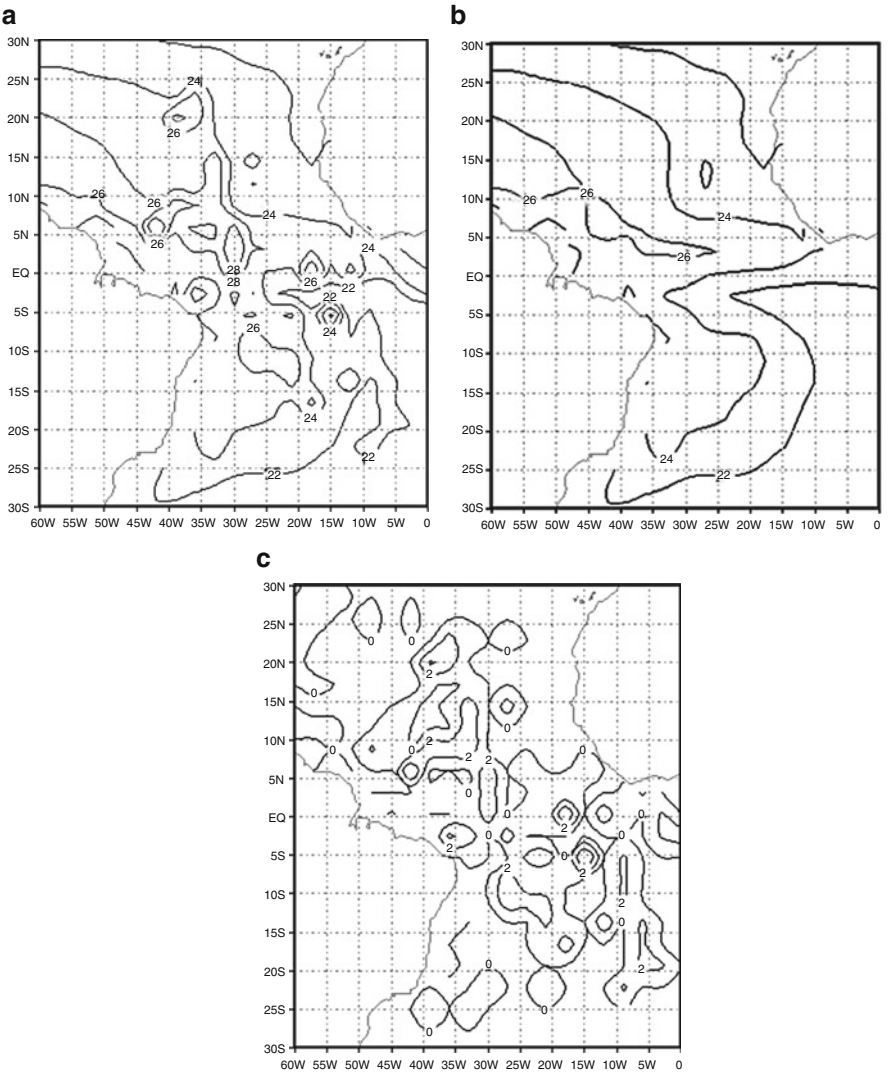

Fig. 2 Model run on January 15, 40 m depth, temperature. **(a)** Assimilation, **(b)** control, **(c)** difference **(a)–(b)**

two vicinity points, one of them with co-ordinates 337W, 0 was used in assimilation while another was not. And point with coordinates 35°W 5°S was not used in assimilation process at all.

These figures show the model deficiency versus observations. In Fig. 4a curve (a) marked by black circles represents the model control temperature profile, while curve (b) marked by open circles represents in assimilated counterpart and curve (c) marked by is real temperature. It is clearly seen that model substantially

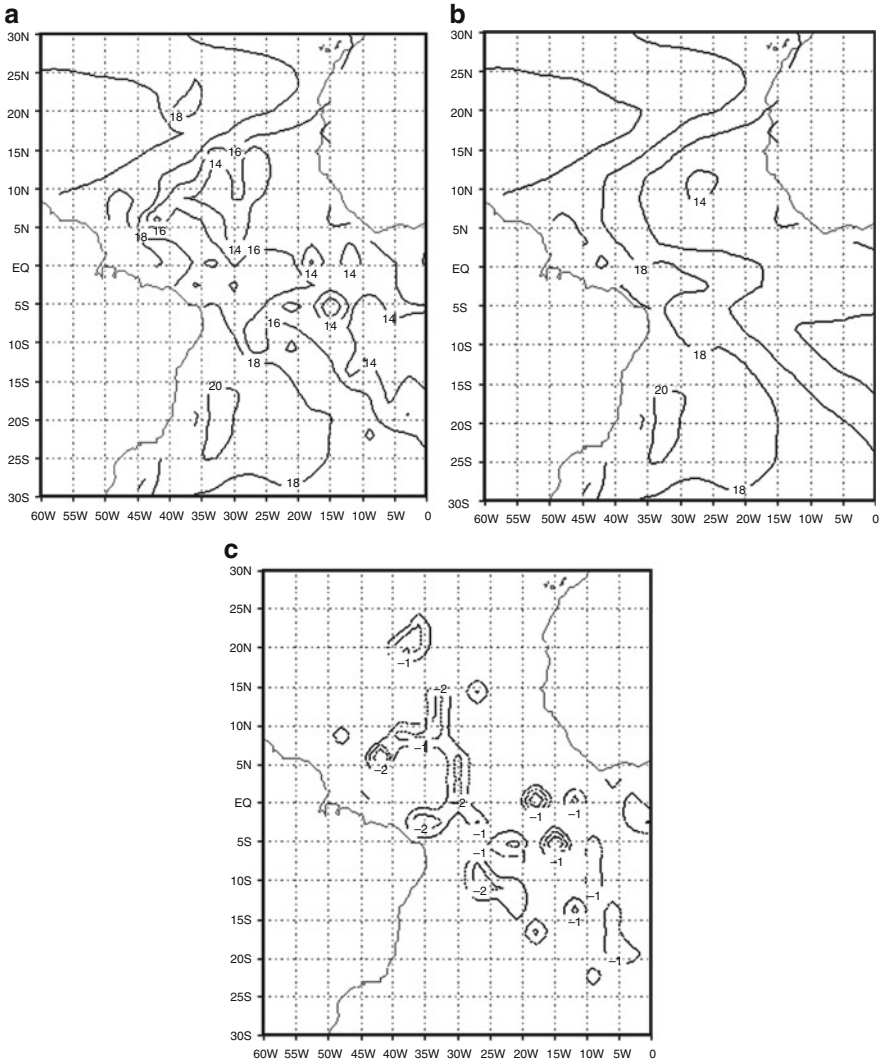

Fig. 3 Model run on January 15, 200 m depth. The same as in Fig. 2

overestimated the real diffusion and creates the temperature profile smoother than it is in reality. The major thermocline part in assimilated curve is pronounced much better, and profile becomes crunched below mixed layer. However, the mixed layer part is very well pronounced at all three curves. Control run does not take into account any data, so this may be explained by pure coincidence. From these pictures it is possible to make a conclusion that natural data show the prevalence an advection process over diffusion. This detail was already cited in [12, 13] but confirmed again in the study. In Fig. 4b only modelled and assimilated data are shown. A point where

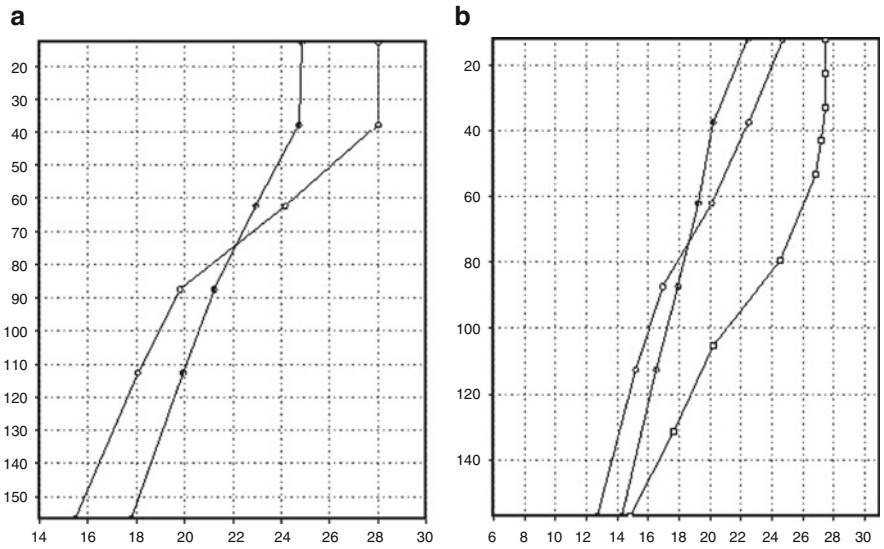

Fig. 4 Assimilated and non-assimilated temperature profiles at two spatial points 30 W, 0 N; 35°W 5°S: **(a)** assimilated, **(b)** non-assimilated

these two profiles are compared has no direct measurements, natural observation are interpolated into this point. Figure 4b also demonstrates that a tendency to overestimate a diffusion conserves in control run, mixed layer expressed badly and major thermocline simulated very weakly. The assimilated run partially fixes these disadvantages but does not overcome them fully. Particularly, it is necessary to note that the mixed layer step is pronounced insufficiently, and the crunch of the major thermocline is also not very realistic. However, the assimilated profile looks much better and physically more relevant then its control counterpart.

The next figures show how the assimilation process occurs in details. As it was said above, the main idea of this presentation is based on the canonical decomposition of covariance matrix. In present study 9 moorings were used, hence the covariance matrix has the dimension 9×9 , and all eigenvalues of this matrix are real and positive for any time moment. Let, $\lambda_1,\ \lambda_2, \ldots\ \lambda_9$ be the eigennumbers taken with respect to their order, $g_1,\ g_2, \ldots\ g_9$ be the corresponding eigenvectors and $g_0 = \sum_{i=1}^{9} \lambda_i g_i$ be the summarised eigenvector, which accumulates the impact of all covariance matrix. Figure 5a–e presents the eigenvectors $g_1,\ g_4,\ g_7,\ g_9,\ g_0$ for day January 10 and for 200 m depth. From these figures one may see the localisation of an impact of the assimilation and its magnitudes. There is understood, that its localisation matches the position of observational points, but absolutely unclear a priory a spatial-temporal variability of this influence as well as its relatively contribution in accumulative impact. The resulted action can be broken down into specific local influence relatively each entered observation. These observations may affect differently, either to be relatively isolated, as it is seen in Fig. 5c, d or may

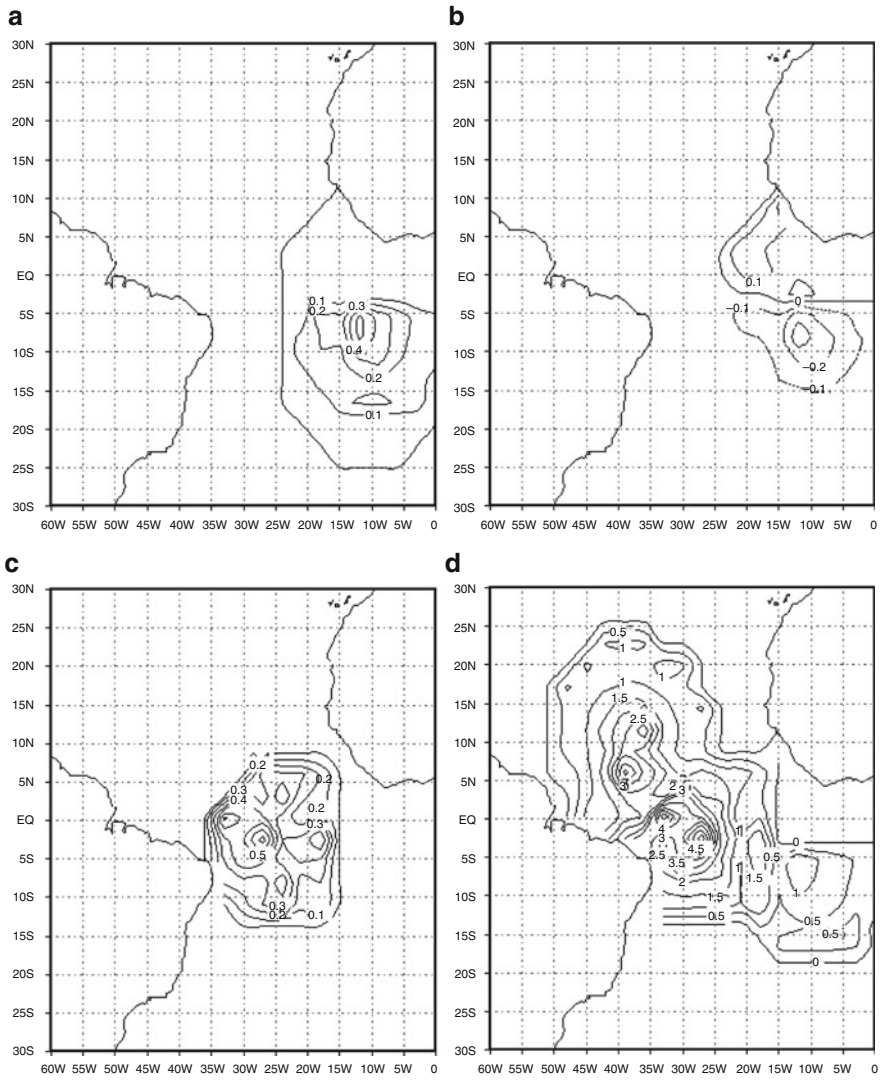

Fig. 5 The eigenvectors structure **(a–d)** for January 10, 200 m depth

impact in conjunctions, as it is clearly seen in Fig. 5a, b. Magnitude of those impacts also varies from 0.1 until around 2. The summary effect is shown in Fig. 5e. One may see the zones of more strong and weaker influence, non-homogeneously distributed over the domain, zone of maximum effect, near the observational point with coordinate 0, 330W and zone of very weak impact near the continent in Guinea Bay.

Situation is different on the mixed layer. Figure 6 presents the same values but taken on the 40 m depth. Figure 6a–d contain the same eigenvectors, as in Fig. 5. One

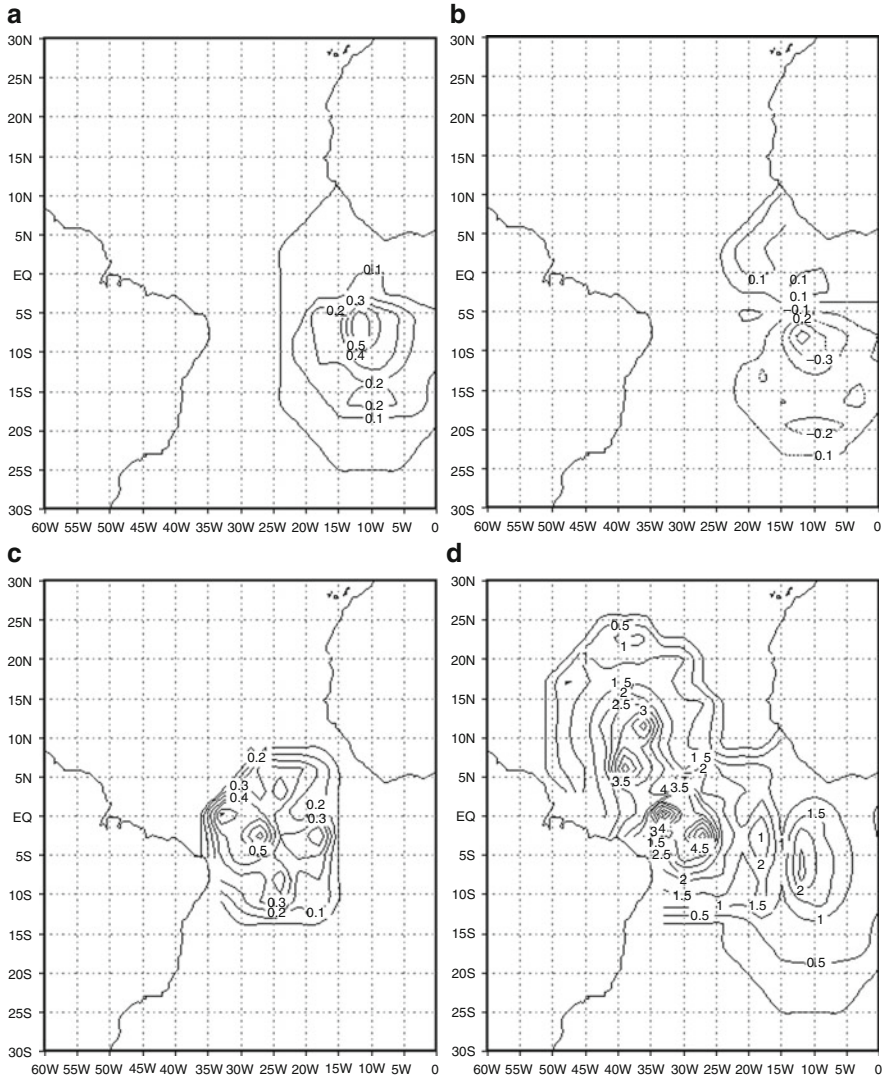

Fig. 6 The eigenvectors structure **(a–d)** for January 10, 40 m depth

may see that the magnitudes of covariance in sea top are higher and their influence enlarges much longer then it occurs for below eigenvectors. This is reasonable, the dynamic on sea surface is greater and covariance reflects this dynamic. It interest to note, for instance zone of the negative covariance near the continent in Guinea Bay appeared in Fig. 6b, for eigenvector g_4. This does not exist in previous Fig. 5b, but seems to be important part in the summary effect.

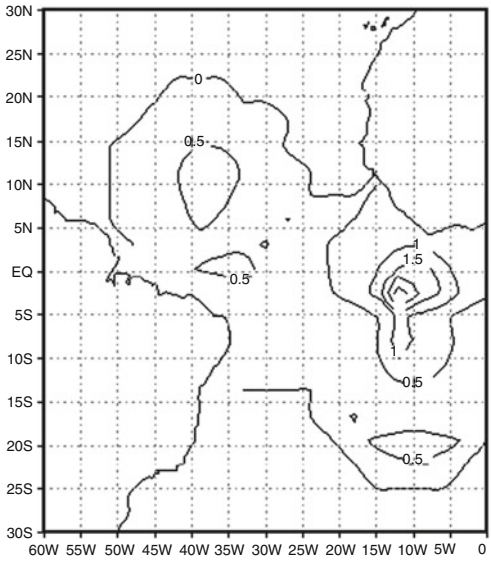

Fig. 7 Difference between Fig. 5 and Fig. 6

To highlight the variability of the covariance with respect to depth, the difference between these two figures in presented in Fig. 7. Only the difference between resulted vectors g_0 is shown. This difference is almost everywhere negative, which demonstrates the domination of impact on sea surface. However, it is extremely non-homogeneous. There are three well-pronounced cores, in Guinea Bay, in Southern part of Eastern Atlantic and in Northern part of Western Atlantic. However, a weak difference occurs in Equatorial Atlantic, which seems strange, because the major part of data observed here. This paradox can be explained by the following reason- the covariance near the observations reaches maximum and close to variance of the error in the observational points. This variance depends on the model skill to simulate the temperature and does not clearly produce this dependence with the depth. But the spread of this error mostly depends on the model dynamic, which strongly differs with depth. It shifts the maximum of difference from directly observed points to their transport outside of the observations.

Finally, the time-variability of eigenvector over one month is studied. Figure 8 presents the difference between accumulated vector g_0 after 20 days of assimilation and 10 days of assimilation on level 40 m. This difference is well pronounced, covers the same domain, which is natural, everywhere is negative. The last circumstance is also reasonable. During the time with the continuing assimilation the error of modelling decreases (see [12]), the variance of the error falls and, the covariance being enhanced by variance falls as well. However, this error remains valuable and this is confirmed by Fig. 9. Other levels do not shown but the situation there is similar. The main conclusion from this figure is that the time variability of the covariance of the error even within one month is substantial.

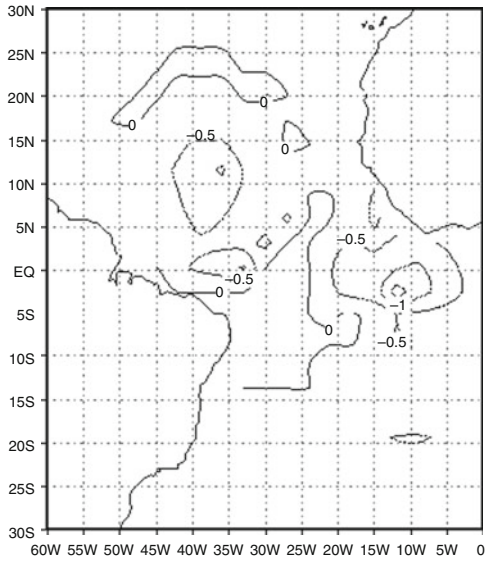

Fig. 8 The difference between accumulated vectors after 20 days of assimilation and 10 days of assimilation on level 40 m

Appendix 1. Mathematical Basis of the Data Assimilation Scheme

This paragraph deals with the mathematical foundation of the DA scheme used throughout the paper. Its full math. description and explanation is contained in [11, 13]. However, this paragraph highlights some moments which are important for the current study from the mathematical point of view. Let the true (unknown) variable ξ be satisfied the equation

$$\frac{\partial \xi}{\partial t} = \Lambda(t,\ \xi) + \eta(t), \tag{5}$$

while its model counterpart is given as

$$\frac{\partial \xi_m}{\partial t} = \Lambda(t,\ \xi_m). \tag{6}$$

In formulas (5) and (6), ξ and ξ_m are tri-dimensional fields, depending also on time, t denotes the time, $\Lambda(t,\ \xi)$ is a known operator, in generally non-linear, acting on the given functional space and $\eta(x,\ t)$ is a random variable, with zero mean for any spatial point x and with covariance satisfying for any arbitrary two time-moments $t,\ \tau$ to the relation , where δ is the Dirac function, R is a known function and E is a symbol of mathematical expectation. The expression $R(|x - y)|$ means that function R depends only on the distance between two spatial points x and y. Let the observed variable ξ_0 be given on the same space as the true variable ξ and let its be

linked by the relation $\xi = \xi_0 + \varphi$, where φ is the error of observation (instrumental error). Random variable φ is supposed to be independent on $\eta(t)$, also with zero mean and the covariance given as $E\varphi(x,t)\varphi(y,\tau) = Q(|x-y)|\,\delta(t-\tau)$, where Q is known. Let θ denote the summarised error or modelling, i.e. $\theta = \xi - \xi_m$ and $\theta_0 = \xi_0 - \xi_m$ is an observed error, i.e. the error between observation and model simulation. According to (5) and (6)

$$\frac{\partial\theta}{\partial t} = \Lambda(t, \xi_m + \theta) - \Lambda(\xi_m) + \eta(t). \tag{7}$$

Definition. Operator $\Lambda(t, f)$, where f is a function on a given functional space is called unbiased (relatively family of distribution Φ) if for any random variable η (from this family) the condition $E\eta = 0$ implies the condition $E\Lambda(t,\eta) = 0$ for any moment t.

Note 1. Obviously, any linear operator is unbiased. The inverse statement is not valid. For instance, if η is a Gaussian random variable with zero mean and $\Lambda(t, f) = f^3$ is one-dimensional operator, then $E\Lambda(t,\eta) = 0$ but operator is non-linear.

Note 2. The indication relatively which distribution the operator is unbiased is essential. The operator may be unbiased relatively one family of distribution but not unbiased relatively others. But this makes pure theoretical interest and is minor significant in applications.

Two obvious equalities hold for an unbiased operator. 1. $\Lambda(t,0) = 0$. 2. If the operator $\Lambda(t,\eta)$ can be expanded as $\Lambda(t,\eta) = a(t)\eta + \Psi$, where $a(t)$ is non-random, η and Ψ are random and $E\eta = 0$, then $E\Psi = 0$.

The main statement follows the formula (7) and equalities 1 and 2.

Statement. If the model operator Λ satisfying (5) and (6) is unbiased then the following equation holds for the model error θ

$$\frac{\partial\theta\xi}{\partial t} = \Lambda(t,\ \theta) + \vartheta(t), \tag{8}$$

where $\vartheta(t)$ is a random variable with zero mean, which includes the non-linear part of operator and all stochastic noise.

Appendix 2. On the Definition of the Coefficients of the Fokker-Planck Equation

Equation (8) in finite-differential approximation is presented as follows

$$\frac{\theta(t_{n+1}) - \theta(t_n)}{\lambda_n} = \Lambda\left[t_n, \theta(t_n)\right] + \vartheta(t_n), \tag{9}$$

where $\theta = t_0 < t_1 < \ldots < t_n < \ldots < T$ is an arbitrary breaking down the time interval [0,T], T may coincide with infinity, and $\lambda_n = t_{n+1} - t_n$ is a length of n-th interval. With fixed discretisation the sequence of random variables $\theta^n = \theta(t_1), \ldots, \theta(t_n), \ldots$ is a Markov chain. Following [18], the series of sequences θ^n when n goes to infinity and $\lambda_n \to 0$, converges under some reasonable conditions to a stochastic diffusion process $\theta(t)$ given by stochastic differential equation (Langeiven equation)

$$d\theta = a(t, \theta)dt + B(t, \theta)dW, \tag{10}$$

where $a(t, \theta)$ and $B(t, \theta)$ are drift vector and diffusion matrix, respectively, and W is a symbolic notation of the Wiener process. As it was shown [12], in this specific case, $a(t, \theta) = \Lambda(t, \theta)$ and $B(t, \theta) = E\vartheta\vartheta^T = \sum$ is a covariance matrix of summary noise, included the non-linear part of operator. These formulas give the method how to calculate the coefficients $a(t, s)$ and $B(t, s)$ as a function of variable s. Indeed, having a sample of arbitrary variable s at moment $t - dt$ it is sufficient to calculate the $\Lambda(t, s)$ as a model output at moment t. As this sample, the model variable ξ_m can be chosen. Because the sampled variable has to have a zero mean, a deviation $\xi_m - < \xi_m >$ can be taken, where symbol $<>$ means the spatial average. This variable is inserted into the model operator and the model output will be used to estimate a drift vector a. More technically complicated but the same idea is utilised to get the covariance matrix $\sum$. Details of this scheme, with using the histogram technique are presented in [11].

References

1. Kalnay, E., et al.: The NCEP/NCAR reanalysis project. Bull. Am. Meteor. Soc. **77**, 437–472 (1996)
2. Hamill, T.M., Snyder, C.: A hybrid ensemble Kalman Filter-3D variational analysis scheme. Mon. Wea. Rev. **128**, 2906–2919 (2000).
3. Kalman, R.: A new approach to linear filtering and prediction problems. Trans. ASME, Ser. D, J. Basic Eng. **82**, 35–45 (1960)
4. Jazwinski, A.H.: Stochastic Processes and Filtering Theory. Academic, New York (1970)
5. Ghil, M., Malanotte-Rizzoli, P.: Data assimilation in meteorology and oceanography. Adv. Geophys. **33**, 141–266 (1991)
6. Cohn, S.: An introduction to estimation theory. J. Meteor. Soc. Jpn. **75**(1B), 257–288 (1997)
7. Evensen, G.: The ensemble Kalman filter: theoretical formulation and practical implementation. Ocean Dyn. **53**, 343–367 (2003)
8. Ott, E., Hunt, B.R., Szunyogh, I., Zimin, A.V., Kostelich, E.J., Corazza, M., Kalnay, E., Patil, D.J., Yorke, J.A.: A local ensemble Kalman Filter for atmospheric data assimilation. Tellus **56**(A), 415–428 (2004)
9. Derber, J., Rosati, A.: A global data assimilation system. J. Phys. Oceanogr. **19**, 1333–1347 (1989)
10. Barker, D.M., Huang, W., Guo, Y.-R., Bourgeois, A., Xiao, X.N.: A three-dimensional variational data assimilation system for MM5: implementation and initial results. Mon. Wea. Rev. **132**, 897–914 (2004)

11. Belyaev, K.P., Tanajura, C.A.S., O'Brien, J.J.: A data assimilation method with an ocean circulation model and its application to the tropical Atlantic. Appl. Math. Modell. **25**, 655–670 (2001)
12. Tanajura, C.A.S., Belyaev, K.: On the oceanic impact of the data assimilation method in coupled-ocean-land atmosphere model. Ocean Dyn. **52**, 123–132 (2002)
13. Tanajura, C.A.S., Belyaev, K.: A sequential data assimilation method based on the properties of a diffusion-type process. Appl. Math. Modell. **33**, 115–135 (2009)
14. Servain, J., et al.: A pilot research moored array in the tropical Atlantic (PIRATA). Bull. Am. Meteor. Soc. **29**, 2019–2031 (1998)
15. Bryan, K.: A numerical method for the study of the World. Ocean. J. Comp. Phys. **4**, 347–376 (1969)
16. Pacanowski, R.C., Griffies, S.M.: The MOM3 manual, NOAA/Geophysical Fluid Dynamics Laboratory (1999)
17. Conkright, M.E., et al.: World ocean database: documentation and quality control. NOAA/NODC Inter. Rep. **14** (1998)
18. Gikhman, I.I., Skorokhod, A.V.: Introduction to the Theory of Random Processes. Dover, New York (1996)

Challenges of Biomass in a Development Model Based on Renewable Energies

F. Cuadros, A. González-González, A. Ruiz-Celma, F. López-Rodríguez, J. García-Sanz-Calcedo, J.A. García, and A. Mena

1 Introduction

All living matter on earth—biomass—lives on a surface layer known as biosphere. Biomass represents only a tiny fraction of the total mass of the planet, but on a human scale it represents a vast energy source that is continuously being renewed through Photosynthesis. The original source of that energy is the Sun.

Energy stored in plants is naturally recycled through a series of physical and chemical processes that take place between themselves, the ground, the surrounding atmosphere, and other living things, until it is mostly radiated again, from earth to space, as low-temperature heat (Longwave Infrared Radiation).

If the cyclical process is interfered and some of the energy is captured when it is being stored as biomass, then a fuel (*biofuel*) that can burn or transform its energy to generate final useful energy (heat, electricity, or motion) will be acquired. A significant advantage is added to the process: burning biomass does not imply generating any more heat or more CO_2 than it would be generated by natural processes (decomposition, respiration, fermentation, etc…). In any case, CO_2 balance is zero, since plants return CO_2 consumed during their growth back to

F. Cuadros (✉) · A. González-González · A. Ruiz-Celma · F. López-Rodríguez
School of Industrial Engineering, University of Extremadura, Avda. Elvas s/n., 06006-Badajoz, Spain
e-mail: cuadros1@unex.es

J. García-Sanz-Calcedo
CUM, Avda. Santa Teresa de Jornet, 38, 06800-Mérida, Spain

J.A. García
Agrifood Technological Centre of Extremadura (CTAEX). Ctra. Villafranco a Balboa km 1.2, 06195-Villafranco del Guadiana, Spain

A. Mena
Higher Technical School of Engineering, Univertisy of Huelva, Ctra. Huelva-Palos de la Frontera, 21819-La Rábida, Spain

R.G. Rubio et al. (eds.), *Without Bounds: A Scientific Canvas of Nonlinearity and Complex Dynamics*, Understanding Complex Systems,
DOI 10.1007/978-3-642-34070-3_53,

the environment at the end of their life. The term biofuel describes a wide range of energy sources and it is applied to any solid, liquid or gas produced from organic materials, either directly from plants or indirectly from industrial, commercial, domestic or agricultural residues. Biofuels may result from a large number of raw materials (provided they are of organic nature) and produced as a wide variety of final types [1].

A first classification of biomass can be established as:

1. Natural biomass, which occurs in nature without human intervention.
2. Residual biomass, generated by any human activity. It includes agricultural, livestock, agro-industrial, and organic residues.
3. Produced biomass (energy crops), which is grown to be further transformed into fuel. Biomass conversion into useful energy takes place through several technologies, which are also primarily based on thermochemical and biochemical processes. Table 1 shows an outline of preferred technologies in biomass transformation processes [2].

   Biomass use as a source of production of useful final energy is a common objective of the European Union's agricultural, energy, and environmental policies.

Agricultural policy:

(a) Biomass represents a valid alternative to replace traditional crops whose financial viability depends on retaining the production subsidies referred to in the Common Agricultural Policy (CAP).
(b) Removal of agricultural crop residues and waste from forestry work helps meet the CAP agri-environmental measures for countryside and environment conservation and sustainability.
(c) Biomass shows more stable prices, which will revise upwards according to the development of primary energy prices.

Energy policy:

(a) Biomass helps meet objectives of reducing dependence on foreign energy, which is currently around 50% in the EU, and over 80% in Spain.
(b) Biomass means energy that due to its renewable nature does not become exhausted, as is expected to happen with fossil fuels.

Environmental policy: the use of biomass helps meet the Kyoto protocol for the reasons listed below.

a) Energy crops consume fewer amounts of fertilizers, and usually require less or no pesticide treatment that pollutes the environment.
b) Collection and use of agricultural, forestry and agro-industrial crop residues and pruning for energy use, prevents its burning, dumping or uncontrolled burial.
c) The usage of biomass to replace fossil fuels avoids greenhouse gas emissions that contribute to global warming.

Despite all these advantages, the use of biomass as fuel or for electricity generation barely meant an insignificant percentage of primary energy consumption

Table 1 Biomass transformation processes for energy purposes, technologies used and final energy output

Transformation process	Technology used	Output product
	Combustion	Vapour Heat Electricity
Thermochemical	Gasification	Vapour Heat Electricity Methane
	Pyrolysis	Charcoal Biocoal Combustible gas
Biochemical	Fermentation and anaerobic digestion	Ethanol Water for irrigation Biogas Compost

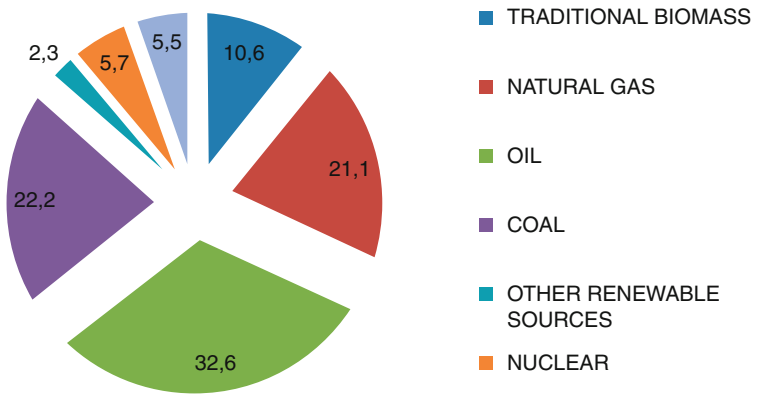

Fig. 1 World annual primary energy consumption as sorted by different types of source (http://www.bp.com)

to national statistics. Figure 1 shows contribution of biomass to global primary energy consumption in 2000, according to UN estimates (http://www.bp.com). Global application of this resource is exclusively focused to heat generation.

It is difficult to come up with a reliable estimation of biomass consumption, since a biomass world market with a role similar to OPEC for oil does not yet exist. Biomass industries are locally managed, and no financial transactions are recorded.

The European Union (EU) was the first region in the world to show a firm commitment to renewable energy, setting ambitious targets on the White Paper on Renewable Energy published in 1997. The main challenge set by Europe in 2010

was to reach 12% of its primary energy consumption through renewable sources. In order to achieve this percentage, biomass should play a major role in the European energy system, progressively displacing other fossil fuels for (mainly) electricity, heat and motion generation.

However, results have been different. Thus, Spain's National Renewable Energy Action Plan, published in late 1999 [3], established a biomass contribution to total primary energy consumption in 2010 to 6,650 ktoe (6,000 ktoe for solid biomass, 500 ktoe for biofuels, and 150 ktoe for biogas). In 2005, Spain's Renewable Energies Plan (REP) [4] revised downwards these goals, as biomass development was not as significant as expected. This Plan established for 2010 a share of solid biomass for primary energy of 5,040.3 ktoe (582,5 for thermal applications and 4,457.8 ktoe for electrical applications).

Nowadays, as shown in the next section, numbers indicate that we are still far from biomass taking off and entering neither the European energy market, nor our own Spanish market. The situation is even worse in the rest of the world. The use of biomass as energy source is essentially implemented as heat generation, same as 500,000 years ago. Something is changing, however, especially in Europe, but the pace of global change is not enough for biomass to make a significant contribution to the development of a system based on renewable energy sources.

The effort that R&D is developing globally is also remarkable. According to the Scopus database (http://www.info.scopus.com/researchtrends/archive/RT13/bib$_-$mes$_-$13.html), the number of scientific publications (articles, reviews, and conference papers) on biomass has increased from about 4,400 in 1996 to about 12,000 in 2008. This means that an initial stage of pre-industrial research and development has taken place, but the final step to implementing large-scale industrial projects has not occurred yet.

Why cannot biomass development reach the percentage required in order to achieve the objectives set out in the European White Paper and the Spanish Renewable Energy Plan? In our view, biomass difficulties to enter current energy markets can be summarized into three main aspects:

1. Biomass, as opposed to solar, wind, hydraulic energy sources, has an owner and therefore a price.
2. Biomass comes in many forms and is delivered through large areas of land, which makes its collection difficult and very expensive. Being highly divided, energy density per hectare is very low and costs allotted to its collection and transport to the conversion plant need then to be added.
3. Net profits of biomass energy conversion into electricity are still very low in general.

The present paper focuses on the discussion of several problems associated with the use of biomass as primary energy source for generating electricity and heat. As a result, a series of possible solutions, some of which are currently being developed at the University of Extremadura, are suggested.

2 Biomass Status in Europe and Spain

If data referring 2008 are accounted for, the percentage contribution of renewables to total primary energy consumption in Spain was 7.7% (http://epp.eurostat.ec.europa.eu). Data corresponding to 2009 shows a contribution of renewables to total primary energy consumption in Spain of 9.4% (http://www.idae.es, http://www.eurobserv-er.org), which concurs with the European average in the same sector. Provisional data for 2010 show some significant contributions of Spanish renewable energy, coming close to 10.7% (http://www.idae.es). In Europe, the contribution of renewables to electricity production in 2007 was 20% and, later in 2010, this percentage was expected to approach 30% (http://epp.eurostat.ec.europa.eu). Meanwhile in Spain, the amount of electricity generated from renewable sources in 2010 was 32.6% of the total. This improvement of renewable energies in Spain denotes a shift in energy models and their future—mainly biomass—implies their use and integration into the building, urban planning and transport sectors.

The barometer EurObser'ER (http://www.eurobserv-er.org) presents some preliminary data for 2009 comparing Spain's 4,315 ktoe (4.315 Mtoe) contribution of solid biomass to total consumption of primary energy, to the European total of 72.77 Mtoe. This represents primary energy consumption in the form of solid biomass of 0.094 toe/(inhabitantyear), while the European average was estimated at 0.145 toe/(inhabitantyear). That is, in Spain the average consumption of biomass per year is 35% lower than the corresponding European average.

As for the use of biomass to generate electricity, transformation profits must be taken into consideration. Therefore, biomass Lower Heating Value (LHV), which is estimated at around 3,000 kcal/kg (12.5 MJ/kg), must be initially established. This value corresponds to a type of wood showing moisture content achievable by natural means. To achieve an electrical output of 1 MW performing an average of 7,600 h per year, 8,000–10,000 tons of this sort of wood is required. The plant produces an overall performance of about 25% [5].

Based on a provisional basis, the above mentioned reference (http://www.eurobserv-er.org) provides some preliminary data regarding power generation in Europe in 2009 of 62.2 TWh gross, using wood as primary energy. Assuming an overall performance of 25% in the transformation of biomass to electricity, biomass consumption for this purpose was around 248.8 TWh. In order to transform TWh to conventional units referring primary energy consumption (ktoe), an appropriate conversion factor must be implemented. According to reference [4], 1 TWh is equivalent to 86 ktoe. Thus, the consumption of biomass for electricity generation in 2009 in Europe was 21 398.8 ktoe (21.4 Mtoe). Since the total biomass consumption in Europe during 2009 was 72.77 Mtoe, it can be inferred that the percentage of biomass used in Europe for electricity generation is approximately 29% of total biomass. The remaining 71% is used to generate heat. It should be noted, in this regard, the role played by Germany, Sweden and Finland, as these three countries account for almost half of all biomass electricity in Europe. At the other end,

countries such as Romania, Estonia and Latvia show very little electrical power supplied by biomass.

In Spain, and on a provisional basis, the gross production of biomass electricity was of 2.14 TWh in 2009 (http://www.eurobserv-er.org). After proper calculations, as described in the previous paragraph, this amount corresponds to the consumption of primary energy (biomass) of 8.56 TWh, equivalent to 735.82 ktoe. Since solid biomass total consumption in Spain in 2009 was 4,315 ktoe (http://www.eurobserv-er.org), the percentage of biomass in Spain dedicated to electricity production is only 17%. The remaining 83% is used for heat generation.

It is evident that such quantities indicate a low biomass development, especially in electrical applications, both in Europe and Spain. Such slow growth occurs despite the high percentage of renewables represented in the national electricity market (32.6% of the total, as previously shown). Therefore, identification of barriers that slow down the development of biomass is necessary, as well as trying to overcome such barriers with designed actions on all areas: institutional, business, research and development, programming, etc. . .

3 Barriers to Biomass Development

In order for biofuels to gain greater market share, they must be available (in quantity, quality and price) and easily distributed (transported). But there are several drawbacks, some of which are mentioned below [4].

In the case of forest residues, costs arising from cleaning, chipping and transportation activities substantially exceed the benefits achieved by its energy potential. It is also difficult to ensure a stable and homogeneous production of large biomass amounts in a given area. Finally, forest residues have other traditional and industrial uses, which make their energy use more complicated.

As for agricultural waste, they are seasonal and, similarly to forest residues, it is necessary to apply a series of pre-treatments such as chipping (in the particular case of wood wastes) or compaction (if crops) to reduce transportation costs. Furthermore, their distribution and the small scale of most farms are other problems to take into consideration.

The level of waste generated by the forest industry is initially high, but its production fluctuates and its availability becomes influenced by the same industrial activity generating it. By contrast, wastes from agrifood industry come from a great variety of sources, and generally, retain a high moisture content, which complicates its handling for energy use by conventional combustion technologies. In the case of residual biomass with high moisture content, it is highly advisable to use biodegradation techniques (anaerobic digestion and fermentation) in order to extract energy from this type of waste.

To properly develop, energy crops (herbaceous or wood) need a legislative and support framework in order to provide farmers confidence towards changing their traditional activity for the production of such type of crops. The lack of crops energy

performance-based practices and projects in action leads to uncertainty regarding its financing. Currently, costs associated with cultivation and collection of this type of product are too high. In addition, investment cost associated with power plants fuelled by energy crops is much higher than conventional plants. All these elements decrease the economic viability of projects to the point of unprofitability.

Universities and research centres must undertake R&D actions to achieve greater incursion of such technologies in the Spanish energy system. At the same time, projects validating biomass energy, environmental and economic profitability are necessary.

The next section reports on a series of actions that are being developed at the University of Extremadura in order to contribute to biomass development in the region.

4 Some Proposals from the University of Extremadura

4.1 Assessing the Energy Potential of Forest Biomass in the Northern Province of Cáceres (Extremadura, Spain)

As above mentioned, one of the main hindrances to biomass energy management lies on the difficulty of ensuring a steady supply for thermal or electric power generation. The viability of a project would thus largely depend on both availability and management of the biomass resource. However, identifying and assessing the potential of different forest species for energy purposes is a main concern for most developed regions worldwide in order to replace fossil fuels and therefore to contribute to biosphere sustainability.

Around 50% of the area in central regions of Spain is mainly covered by *dehesa* woodland, featured by medium wood density approaching 40% wooded area and a secondary vegetation cover mostly represented by diverse pasture species. The remaining area (11–12%) corresponds to several shrub species and primarily *Pinus pinaster* woods [5].

A recent work on the assessment of the energy potential of the main forestry biomass wastes in the province of Cáceres (Spain) can be found in the scientific literature [6]. GIS-based techniques were used not only for the geographic mapping of biomass resources, but also as an inestimable tool for operation and management activities.

The methodology followed a four-stage procedure: (i) Determination of the theoretic biomass potential in terms of the previous location and estimate of the annual quantities of biomass generated by the most representative forestry species in the area under study; (ii) Available biomass potential was obtained via the selection of the main forestry species in the region on the basis of the two following aspects: extension of their regional distribution and difficulties in the collection process due to steep terrain or some other drawbacks; (iii) Energetic characterisation of biomass

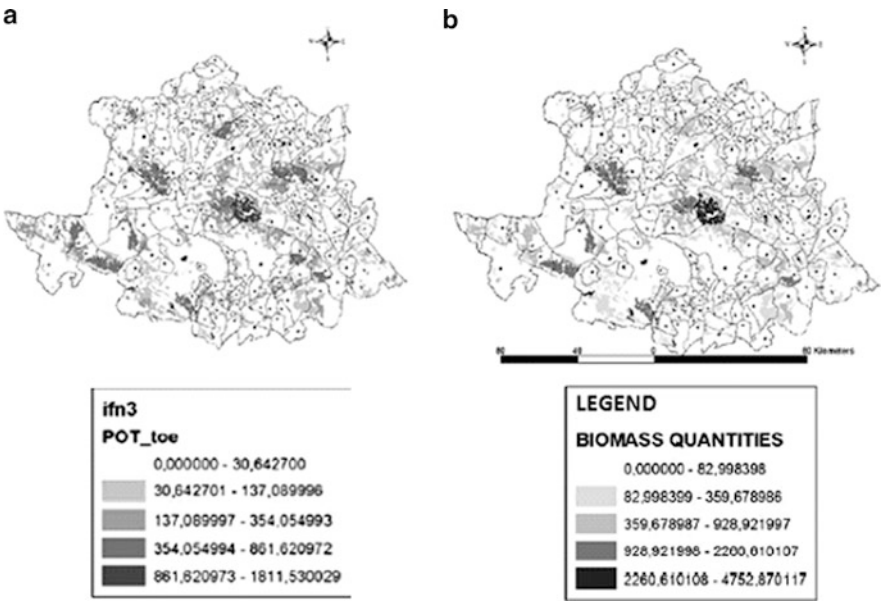

Fig. 2 Global energy potential (**a**) and annual amount of forest biomass (**b**) in the area under study (northern Cáceres)

and determination of technical feasibility for power production—i.e. determination of technologically exploitable potential—; (iv) Finally, consideration of the fact operations are based on the environmentally exploitable potential, since the biomass derives from conventional forestry activities and from clearing of underbrush in access tracks for fire prevention.

As a result, it was asserted that there is a vast biomass potential in the northern area of the province of Cáceres, with rates approaching 463,000 gross t/year, which would yield an equivalent energy potential of around 139,000 toe/year. Steep slopes (sometimes exceeding 20%) play a drastic role in biomass collection, and lead to a 50% reduction of the biomass potential. Figure 2a, b represent the global energy potential from forest residues in the province of Cáceres and the amount of forest biomass collectable from slightly sloped areas, respectively. Optimal locations for forest-biomass-supplied energy plants are shown in Fig. 3. Note that figures represent potential quantities, provided that actual values might strongly depend on the frequency the forestry activities that generate the residual biomass are performed. In view of these data, and linked to the policies on conservation and maintenance of *dehesa* (and some other types of woodland), to the development of new techniques for forestry biomass exploitation as well as to the continual supply of good quality biomass, it could be concluded that forestry wastes might—at least partially—come to replace current fossil fuels in Extremadura and Spain.

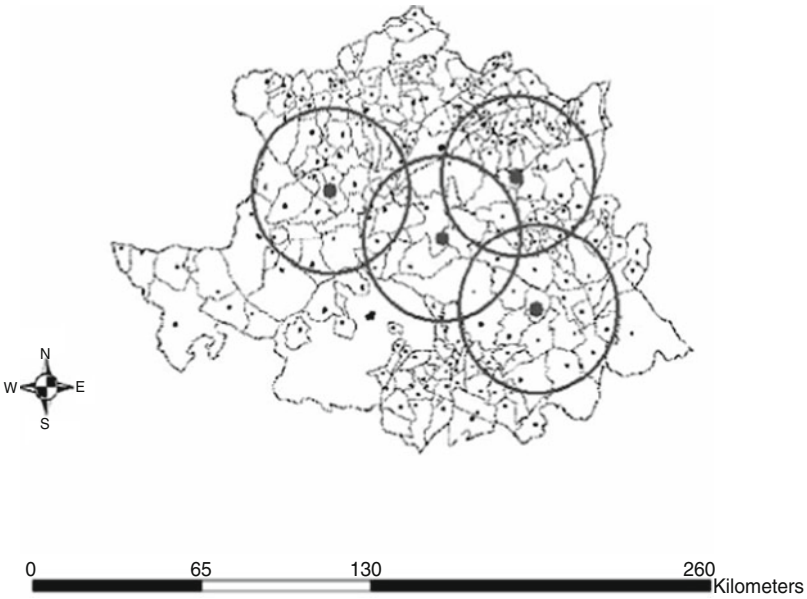

Fig. 3 Optimal locations suggested for forest-biomass-supplied energy plants in northern Cáceres

4.2 Use of Biomass in Services Sector. Installation of a Biomass Boiler at Zafra Regional Hospital (Badajoz)

Demonstration facilities for the general public are another relevant measure for the development and consolidation of biomass in the energy market. This point is enhanced if they are installed in buildings devoted to public care and administration, like Hospitals and Health Centres.

The installation of specific facilities for the production of thermal energy from biomass in buildings associated to the tertiary sector is one of main current challenges faced by the renewable energy sector, which has successfully emerged in terms of solar energy collection, but remains underdeveloped in Spain with respect to the particular case of biomass [7, 8].

A 430 kW biomass boiler for heat and domestic hot water production was installed to operate as complementary equipment to the conventional existing units in Zafra Hospital (Badajoz) by November 2009. It is made of sheet steel with a three-step vertical flue cleaning system and operates at 4 bar. It is designed as a modulating-cascade type, equipped with automatic ignition and ash-pusher device. Moreover, it incorporates a specific set for solid-particle retrieval based on cyclone effect.

The biomass fuel is introduced into the boiler from a storage silo by an endless screw, so that thermal energy is transferred to the water stream of the primary hydraulic circuit.

In order to regulate the heating energy demand—and therefore to achieve a greater efficiency—a 2000 l buffer tank was installed as heat sink to prevent multiple burner startup. This way, the setup performance was optimized and operating life of facilities was extended (Fig. 4).

For the sake of efficiency, the facility is equipped with a remote control panel so that operating parameters are monitored in real-time.

If the corresponding subvention from the Regional Government is accounted for (Decree 60/2007 April 10th), the feasibility analysis of the installation sets investment payback time as 5–6 years, as shown in Table 2.

The energy balance of the installation was carried out according to the energy demand reported for the preceding 5 years (see Table 3). The installation had to meet the annual heating demand of the Hospital, which is quantified as 812,515.5 kWh (0.07 toe/year equivalent fossil fuel savings, approximately). Note that calculations were made assuming the efficiency of the biomass heating facility as 10% lower than that of any other conventional diesel boiler.

Carbon dioxide emissions due to biomass combustion are taken as neutral. With regard to the rest of contaminants, emissions are negligible. This way, the pollution charge associated to conventional diesel boilers is equivalent to the avoided charge associated to the substitution by a biomass boiler (see Table 4). As can be observed, positive increment of emissions is only reported for *particles*, which account for all solid or liquid constituents present in the atmosphere whose size ranges from that of a simple molecule up to 100 microns.

It should be noted that part of the hospital staff-managers and maintenance staff-showed initial reluctance to the installation of the biomass equipment, which was a shortcoming for the direct implementation of this technology. More than 3 months of continuous operation of the biomass boiler had been needed to verify that collection, load and unload activities do not require neither additional efforts nor further increase of the daily workload of maintenance personnel, and therefore to overcome the remaining obstacles that had impeded regular operation of the installation.

Seven months after installation of the biomass boiler, the main conclusions might be stated as follows:

Hospitals are shown to be suitable buildings for the installation of biomass facilities, provided their high energy consumption rates regarding hot domestic water as well as heating and cooling requirements. Such specific energy needs would allow biomass systems continuous operation throughout the whole year, thus favouring both depreciation of the installation and a drastic reduction of contaminant emissions to the atmosphere. The permanent presence of maintenance staff in the room where the biomass boiler is located eases the additional operations derived from the maintenance of this type of installation, mainly due to furnace cleaning and ash removal. However, specific lifelong training programs for maintenance staff

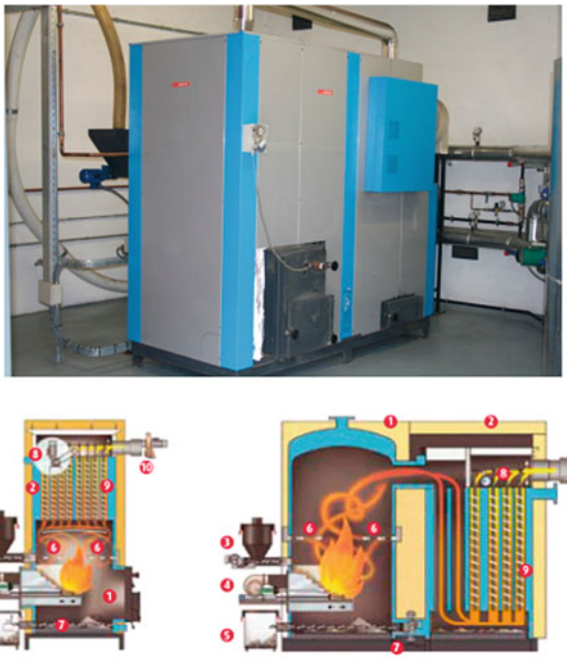

Fig. 4 Biomass boiler installed at Zafra Hospital and operating scheme

Table 2 Economic balance of the biomass installation at Zafra Hospital

Subvention	51,600 euros
Cost of installation	125,400 euros
Annual fuel savings	23,131.04 euros
Investment payback time	5.4 years
Savings over useful life (10 years)	231,310.40 euros

Table 3 Energy balance of the biomass installation at Zafra Hospital

Thermal energy demand	812,515.5 kWh
Useful power	430 kW
Temperature	84°C
Efficiency	80%

are crucial for the implementation and development of renewable energy units in hospitals.

It has been observed that acting on the supply and demand of fuel as well as promoting renewable energy sources through the use of biomass in public buildings would help the consolidation of a local biomass market.

Table 4 Environmental balance of the biomass installation at Zafra Hospital

NO_2 (kg)	–5,852.81
SO_2 (kg)	–303.537
CO (kg)	–1,249.17
CO_2 (kg)	–242,829.6
Particles (kg)	140.72

Furthermore, it has been proved that biomass facilities might also be used for educational purposes regarding awareness and demonstrations on environmental issues aimed at general public, so that current prejudices about this type of installations could be mitigated.

On another note, regarding the installation of biomass units in Health facilities, olive stones have been documented to achieve advantageous use with respect to conventional wood pellets provided lower market price, proper homogeneity and lower rates of residual ash after combustion.

Some other studies on the energy, environmental and economic analysis of public buildings in the Spanish Autonomous Communities Extremadura and Andalusia—Health Centres and Hospitals—are currently being developed [9]. The viability of acclimatization of public buildings in extreme weather locations by implementing measures to minimize energy consumption (bio-acclimatization) using abundant renewable energy sources (mainly biomass as well as solar thermal and photovoltaic) is therefore stated.

4.3 Biogas Production from Agrifood Industry Wastes

Anaerobic digestion (AD) is a biological degradation process by which organic matter, in the absence of oxygen and due to the action of specific sets of bacteria, is broken down into a series of gaseous products known as “biogas” (CH4, CO2, H2, H2S, etc.), a digested effluent (a mixture of mineral elements like N, P, K or Ca) and some other nondegradable compounds. Such process can therefore be regarded as a suitable biological treatment for residual biomass with high moisture content.

The biogas shows a high percentage of methane, CH4 (between 50% and 80%, which makes it suitable for energetic exploitation by combustion in engines, turbines or boilers, either alone or mixed with another fuel.

The AD is featured by the existence of four consecutive stages in the substratum degradation process (hydrolysis, acidogenesis, acetogenesis and methanogenesis) and the action of five main populations of microorganisms (hydrolytic, acidogenic, acetogenic, hydrogenofilic-methanogenic and acetoclastic bacteria).

A schematic diagram of the laboratory-scaled experimental setup used for the anaerobic digestion experiments is shown in Fig. 5. The reactor was a CSTR type (continuous-flow stirred-tank reactor) with about 6 l operating volume. It was controlled by an automaton which regulates the substratum feeding supply, the operating temperature as well as the agitation stage inside the reactor.

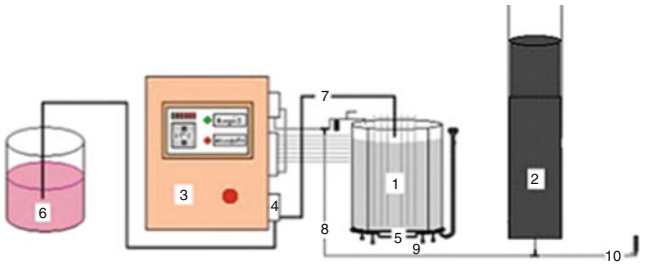

(1) Digester; (2) Gasometer; (3) Control System; (4) Feeding valve; (5) Heating plates; (6) Food tank; (7) Food current; (8) Biogas reciculation current; (9) Sampling; (10) Gas flares.

Fig. 5 Continuous-flow strirred-tank reactor (CSTR) anaerobic digester

Experiments were conducted within the mesophilic range of temperature, keeping temperature at 38°C by ceramic heating elements installed in the lower part of the digester. The biodigester was fed using a peristaltic dosing pump that sucks the substrate from a glass container equipped with a magnetic stirrer to guarantee homogeneity of the substratum before being introduced into the digester. The reactor content was agitated by the recirculation of part of the biogas produced by another peristaltic pump. The biogas generated during the process was collected in a gasometer, which is a device devoted not only to provide direct visual readout of the accumulated volume of biogas, but also to guarantee safe biogas storage, hence preventing fire hazard, bad odor, etc. The volume of biogass inside the digester was controlled by an overflow spillway, so that the digested effluent was collected and stored by a cone separator. Finally, sampling operations in the digester were carried out by specific valves installed in its lower section.

The following paragraphs report on a summary of the main results achieved from diverse types of residual material at the Laboratory for Alternative Energy Sources in the University of Extremadura.

4.3.1 Anaerobic Digestion of Wastes from the Municipal Slaughterhouse in Badajoz

The optimal operating parameters to achieve large biogas volumes as well as highest degradation of wastes were:

- Temperature: 37–38°C.
- Inoculum feeding rate: 350 ml/day, which leads to 17 days Hydraulic Residence Time (HRT).
- Concentration of solids in the substrate: 6%.

10.6 l/day biogas production rate was achieved, which approaches 30.8 Nm3 biogas/m3 degraded substrate, or 1.9 l biogas/l digester day.

Regarding the level of degradation of the wastes, 75.3% and 97.8% reductions were achieved for the Chemical Oxygen Demand (COD) of the effluent sludge and

for the liquid fraction of such degraded effluent, respectively [10]. According to those results, the authors estimated an investment payback time between 5 and 7 years for the construction of a biogas production plant to operate with this type of wastes—as accounting for economic aids provided by Spanish regulations for this kind of projects—.

4.3.2 Codigestion of Wastes from Agrifood Industry and Iberian Pig Slaughterhouse Operations

A series of experiments using different proportions of slaughterhouse and tomato industry wastes were conducted to yield the forthcoming results. The average composition of the output products were observed as: (i) 6% solids (viscera, fats, stomachs, etc.), 93% washing water and 1% blood for slaughterhouse wastes; (ii) 10% solids (7.14% peels and seeds, 2.86% sludge) and 90% water for wastes from tomato processing activities.

Results are listed in Table 5. The following features were noted as concentration of tomato in the substratum was increased:

- Both alkalinity and the concentration of volatile fat acids (VFA) decreased. The gradual reduction of those parameters allowed the rate VFA/alkalinity to remain within the optimal interval, which accounted for stability and self-regulation (for each of the selected substrata) in the biological reactions involved.
- Biogas production decreased. Nevertheless, volumes of produced biogas were larger for each co-substratum than for any experiment regarding the specific degradation of wastes from tomato processing industry.
- The degradation of the substratum remained at around 72–78%.
- The HRT could be reduced by feeding higher volumes of the residual mixture [11]. This was due to the fact that tomato residues showed a lower biodegrading potential. This way, when increasing the concentration of tomato in the feeding substratum, higher feeding rates were needed to reach the optimal organic charge (as lower quantities of the input inoculum would be degraded).
- On another note, it could be stated that codigestion leads to an increase of the pH in the reaction medium (up to 7.5–7.8) if compared with pH values observed for separated experiments with slaughterhouse wastes or residues from tomato processing activities.

4.4 Solar Drying Processes and Pelletizing of Wet Residual Biomass Conducted at the University of Extremadura

Another basic technique devoted to reduce the moisture content of biomass samples is thermal drying. This process increases biomass heating power and, at the same time, allows achieve a reduction in the associated handling costs. The main

Table 5 Experimental results for the anaerobic codigestion of slaughterhouse wastes and residues from tomato processing industry

%Slaughterhouse/ %tomato	Inoculum feeding flow ml/day	HRT days	m^3biogas/m^3inoculum day	%Degradation OCD
100%/0%	250	24	22.53 ± 1.48	73.29 ± 2.49
80%/20%	200	30	22.75 ± 2.02	72.83 ± 3.34
60%/40%	750	8	22.26 ± 2.04	73.34 ± 4.27
40%/60%	600	10	23.02 ± 5.33	78.02 ± 3.65
0%/100%	600	10	5.45 ± 0.83	63.46 ± 5.28

drawback lies in the high energy intensity involved in such operation (between 4,500–9,200 kJ/kg evaporated water, depending on the specific technology, the features of the product and operation stages), hence the high exploitation costs, which might hinder economic feasibility. At this point, solar energy plays a relevant role as an alternative energy source.

Solar radiation shows two main drawbacks:

1. *The energy density of radiation is low*, which makes drying air operate at low temperatures (< 60°C). Due to this, as well as to minimization of operating costs, the best configuration to perform the drying process is that of a thin layer on an appropriate mounting device. The concentration mode would allow operation with significantly higher drying air temperatures, although at the expense of higher costs for specific equipment.
2. *The intensity of radiation depends on time*, which requires control strategies involving the use of intermediate storage systems, profuse ventilation during high solar exposure periods, etc.

The study of the kinetics of the drying process, together with the associated energy-exergy analyses, are crucial tasks for the design of the solar drying device as well as for the estimate of its load-unload intervals. As an example, some interesting experimental results obtained at the University of Extremadura concerning several types of biomass residual products (peels and seeds from tomato processing industry) are presented in the present work [12]. Figure 6 represents an operating scheme of the laboratory-scaled convective dryer used to perform experiments in steady regime.

Results for the analysis of the kinetics of the drying process are shown in Fig. 7, which represents the drying curves as well as the dependence of drying velocity on operating time.

The following mathematical model for the convective drying of industrial tomato wastes at low temperatures was obtained by using nonlinear regression (together with multiple regressions) techniques:

$$\mathrm{MR} = \exp\left\{\left(-0.0001104 - 5.81\cdot 10^{-8}T - 1.81\cdot 10^{-8}T^2 + 6.8536\cdot 10^{-5}V\right)\right.$$
$$\left. t^{(0.51783+0.001308T-0.0001533T^2+0.27373V)}\right\} \quad (1)$$

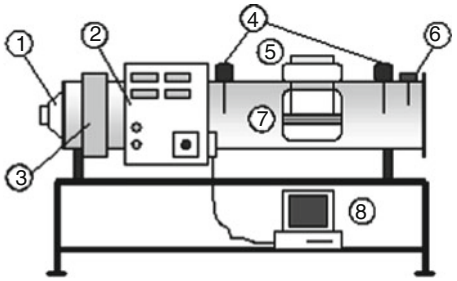

(1) Fan. (2) Operating control. (3) Resistance battery. (4) Relative humi ditr and temperature sensors. (5) Digital balance. (6) Flow sesnsor. (7) Drying chamber traus. (8) Computer.

Fig. 6 Laboratory-scaled convective dryer

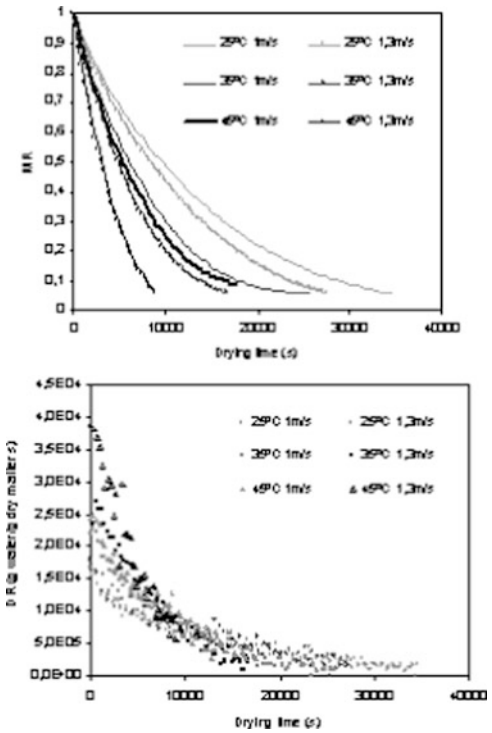

Fig. 7 *Top*: Experimental drying curves. *Bottom*: Drying velocity as a function of operating time

t being the drying time (s), T the drying air temperature (°C) and V the speed of drying air parallel to sample surface (m/s). The goodness of the fit was guaranteed as $r^2_{med} = 0.9961$ [12].

The energy analysis of the process allows the determination of available thermal power (kJ/s), thermal power used (kJ/s) and percentage ratio used/available energies. All experiments showed energy ratios below 20%, which confirmed the availability of remaining drying power in the air stream leaving the dryer.

An exergy analysis of the process allowed the quantification of both exergetic loss and time fluctuations in exergetic efficiency. Setting low drying temperatures led to more satisfactory exergetic efficiency, even at the expense of longer operating periods.

It should be noted that studies on laboratory-scaled convective drying experiments do not account for direct solar radiation on samples, which notably accelerates the drying process at industrial scale. The quantification of this phenomenon is quite complex, provided the influence of the intensity of solar radiation and of the colour of the absorbing surface and the instantaneous moisture content of the product.

Experimental results were used to determine the average operating ratio during the summer term (according to availability of this type of residual biomass) as 22 kg/m^2 day.

After drying operations had been carried out, the product needed to undergo densification. Pelletizing is regarded as one of the most efficient densification processes to recover agricultural and biological wastes [13]. Before dried tomato residues (with diverse moisture contents, i.e. 20.52%, 24.81%, 28.95%, 34.20% and 37.79%) were subjected to such process, samples were crushed in a blade mill *Euro tools*, *220* V/*1.5* kW/*50* Hz/*2 850* rpm, in order to ensure suitable granulometry. Particle size distribution of crushed samples was determined with the use of a sieve tower *Retsch Test sieve model AS 200.*

Experiments were conducted with a laboratory-scaled pelletizer *Euro tools*, *380* V/*15* kW/*50* Hz. Residual biomass was introduced into a flat matrix under the action of (constant pressure) pressing rollers. The raw material passed through the matrix while being compressed, so that pellets were manufactured according to the characteristic diameter of the matrix (namely 6 mm for the experiments herein described). Samples were finally cut as suitably cylinder-shaped units of the expected length. Laboratory samples of the final product are shown in Fig. 8.

A series of physic-chemical properties of pellets manufactured from tomato processing industry wastes (peels and seeds) were analyzed. Samples were selected according to various moisture contents, provided this parameter plays a relevant role in quality tests of densified residues.

Particle and apparent densities, hardness and durability of pellets were observed to increase as moisture content of the biomass residue was raised. A significant decrease of those magnitudes was seen as moisture content of dried (by direct solar radiation) samples exceeded 30%, which was set as the maximum suitable moisture content of biomass samples to guarantee quality of the final product.

The improvement of the densification operations of these residues by using some kind of binding substances to optimize the process and the features of the final product will be the subject of future work [14].

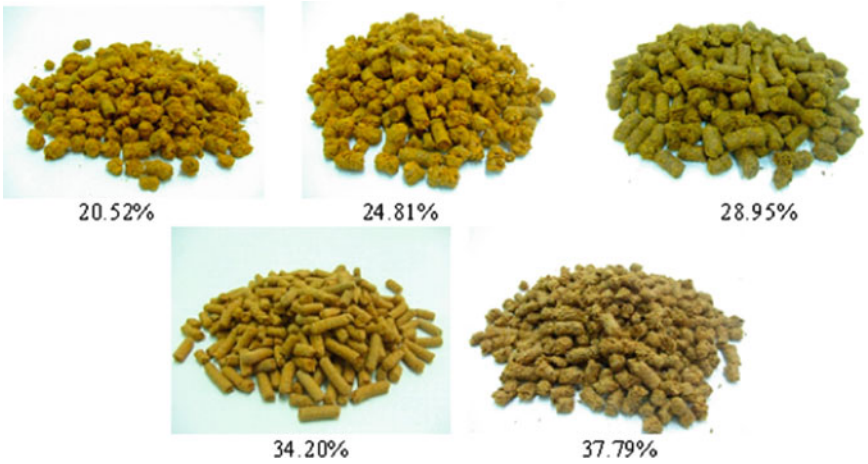

Fig. 8 Sample pellets manufactured at laboratory for different moisture content percentages

4.5 New Energy Crops

Tobacco can be mentioned as an example of search for new energy crops. In fact, Extremadura has extensive experience in tobacco cultivation. Following CAP's (Common Agricultural Policy) conditions, new alternatives to tobacco farmers in Extremadura need to be offered, so that they can attain more sustainable living conditions and enable their establishment in rural areas. Usage of tobacco as biomass to generate energy through a process of digestion or anaerobic co-digestion could be regarded as a novel application.

The idea of tobacco as a plant that requires an expensive and demanding crop is widely spread, and it is certainly true when leaf production is intended for the tobacco industry. However, tobacco plants can be grown by implementing a similar method to forage such as alfalfa, with a high density planting, which can reach high productions: above 150 t/ha of green biomass with a high moisture content not lower than 80%, and therefore with a maximum of 20% dry matter.

Once crops have been established, tobacco plants can be successively cut, provided after each cut, plants sprout again at a growth rate that can be harvested after reaching 60–70 cm. Four or five cuts can be made over one growing season, which may extend to the end of October. Therefore, the potential of tobacco growing for biomass production is based on its crop high productivity.

Since cut plants need to be removed as soon as possible to allow saplings regrowth, collected biomass barely lowers its amount of water. High water content makes tobacco impossible to be used in thermochemical processes (combustion, pyrolysis and gasification). However, tobacco plants can actually be used as feedstock in anaerobic biodigestion processes.

This process shows many advantages. Some of them are as follows:

- Waste energy recovery in an ecological way is ensured.
- Large amounts of energy are produced.
- Recycling organic matter for further energy use is allowed.
- High quality compost (which may be organic, depending on the nature of the feeding waste product) is produced.
- No odour emissions.
- A CO_2-neutral fuel is obtained.

Tobacco anaerobic digestion tests have been conducted in a semi-continuous mode. The experimental setup is outlined in Fig. 9. It consists of a 2 l capacity glass reactor that is kept continuously stirred at a temperature of 38°C. The inoculum is initially inserted together with the tobacco and water mixture and the reactor is closed with a lid that has five openings (four of which are sealed and the fifth one to allow feeding) and the output for produced gas. Generated biogas is channelled towards wash bottles to capture CO_2, thus obtaining exclusively methane. As methane moves forward to the water containers, it displaces a volume equal to the volume of produced methane. In order to stabilize pH and to optimize the production of methane, substrate must be neutralized using lime, before injection into the reactor.

Preliminary results from two tobacco dry methanation tests, diluted by 80% and 50% respectively, in pressurized water and with an active biomass inoculum, were of 770 l biogas/kg organic matter (50 biogas Nm^3/t substrate-tobacco biomass-), in the case of 80% dilution (KOMPOGAS. Private communication, 2008).

Anaerobic digestion experiments were conducted in the laboratories of the University of Extremadura for three different tobacco/water mixture ratios, i.e. 20%/80%, 15%/85% and 10%/90%. Using these substrates and setting HRT as 20 days, it is possible to obtain average tobacco yields of 21, 54.7 and 51 m^3 CH4/m^3 respectively, as well as percentage reduction in the initial Chemical Oxygen Demand (COD) of 46, 62.8 and 4%. According to such results, the optimal tobacco/water ratio was set as 15%/85.

Therefore, there are alternatives to the tobacco CMO Reform, whose implementation began in 2006, and which has generated negative consequences in the tobacco growing area of Cáceres. The surface of tobacco has declined and is expected to continue falling, remaining to finally remain around 50–60% (about 6,000 ha) of the acreage of traditional tobacco. This decrease will mean a highly detrimental economic impact for the area, as well as direct job losses to farmers. It will also represent a significant loss for economic and employment activity generated in the area.

4.6 Search for Alternative Bioenergy Sources

Annual cellulose production by plants through photosynthesis is estimated as $4 \cdot 10^{10}$ t [15], of which only 2% are used for combustion and other industrial processes.

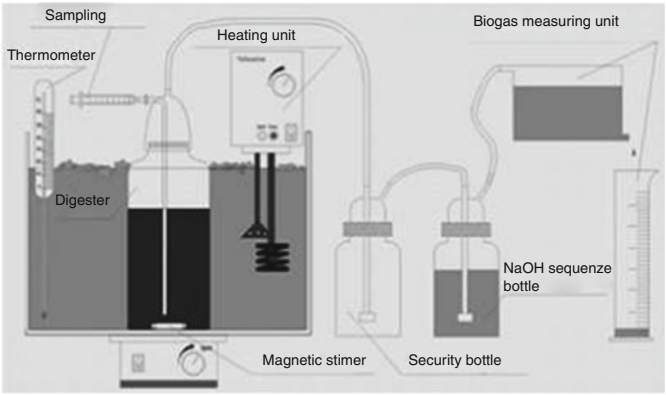

Fig. 9 Anaerobic digester in semicontinuous configuration

Lignocellulose is a major component of various wastes from industries, forestry, agriculture and a large percentage of urban waste. It shows a great bioenergy potential since mostly consists of glucose polymers, a molecule that can be used both for bioethanol production through fermentation processes, as for methane production in anaerobic digestion processes. However, the main obstacle to its energy use is the difficulty to obtain glucose from cellulose since its structure is highly resistant to all kinds of treatments, chemical, physical as well as enzymatic. The limiting step, therefore, lies in the pre-treatment to be applied to cellulose in order to release glucose right before its conversion into ethanol or biogas.

There are many treatments, both physical and chemical, to break the crystalline structure of cellulose and consequently, to make molecules more accessible to the action of enzymes that degrade them. Such treatments are, in general, quite effective but have the disadvantage of requiring high energy (physical) or producing large waste quantities (chemicals) that must be neutralized at the end of the process. Biological treatments show none of these problems, but are very slow and show low energy efficiency, so that they are currently not viable. Therefore, research has focused on optimizing all types of pre-treatments and in case of biological ones on increasing their speed and efficiency.

Among biological processes, the most studied is that associated with fungus *Trichoderma Reesei*, which is featured by its ability to degrade cellulose. It is able to produce the three major types of cellulose, and is resistant to chemical inhibitors and stable at low pH and at temperatures up to 50°C, which eases its industrial use.

As for the degradation of lignocellulose residues, another line of research with a promising future is the study of the bacterium *Clostridium Thermocellum*, which is able to grow efficiently on cellulosic substrates. This bacterium has the advantage that in addition to degrading cellulose is capable of producing ethanol from derived sugars, all in the same reactor and in a single step, although it can only efficiently use β-1, 3 and β-1.4-glucans and it prefers longer-chain cellodextrins. Nowadays, the genetic engineering process is being improved by enhancing the microorganism and by trying to fully understand the mechanisms that favour its dual function [16].

More recently, it has been noticed that enzymes present in microorganisms that develop in the intestinal tracts of termites are miniature bioreactors, capable of fragmenting the complex polymer chain of cellulose and xylan in much smaller sugar units that feed termites. In the biotechnology field, these enzymes could be incorporated to fermentation processes, which would yield waste wood biofuels and other agrifood waste. This research restriction lays on the complexity of the insects' microbial population and the complex symbiotic relationships between microorganisms in the intestinal tract of termites. They are able to transform 95% of the ingested cellulose into fermentable sugars, which makes it particularly interesting to study the microflora residing in their intestinal tract, as well as the possibility of discovering new celluloses which significantly increase the yield of treatments biological cellulose for energy purposes.

Acknowledgement This work was supported in part by Govertment of Extremadura through project PCJ 100201 and GR10045. A. González-González thanks the Ministry of Education and Science the grant of the FPU. Reference AP2008-02546.

References

1. Boyle, G. (ed.): Renewable energy. Power for a Sustainable Future. Oxford University Press, Oxford (1996)
2. McKendry, P.: Energy production from biomass (part 2): conversion technologies. Bioresource Technol **83**(1), 47–54 (2002)
3. Plan for the Promotion of Renewable Energies. Ministry for Industry and Energy. IDAE (1999)
4. Plan for the Promotion of Renewable Energies 2005-2010. Available at http://www.idae.es/index.php/mod.documentos/mem.descarga?file=/documentos_PER_2005-2010_8_de_gosto-2005_Completo.(modificacionpag_63)_Copia_2_301254a0.pdf [Updated 2013 April 2]
5. Osorio, S.: Recursos de la biomasa y su aplicación industrial. http://drago.intecca.uned.es/download/d3d3LmludGVjY2EudW5lZC5lcw%3D%3D_53006_20090526101335u_SORUNEDLugoMayo2009.pdf. Accessed 2 April 2013
6. López-Rodríguez, F., Pérez-Atanet, C., Cuadros, F., Ruiz-Celma, A.: Spatial assessment of the bioenergy potential of forest residues in the western province of Spain, Cáceres. Biomass Bioenergy **33**(10), 1358–1366 (2009)
7. García Sanz–Calcedo, J.: Centros de salud de alta eficiencia energética y medioambiental. 20th Congress of the International Federation of Hospital Engineering, Barcelona (October 2008)
8. IDAE. Biomasa: Edificios. Madrid (2007)
9. García Sanz–Calcedo, J.: Análisis sobre la sensibilidad energética y medioambiental de los parámetros funcionales en los Centros de Salud de Extremadura. PhD Thesis, University of Extremadura (2009)
10. Marcos, A., Al-Kassir, A., Mohamad, A.A., Cuadros, F., López-Rodríguez, F.: Combustible gas production (methane) and biodegradation of solid and liquid mixtures of meat industry wastes. Appl. Energy **87**, 1729–1735 (2010)
11. González–González, A., Cuadros, F., Amaya, J., Ruiz–Celma, A., Delgado, M.T., Galán, A.M.V., López-Rodríguez, F.: Primeros resultados de la co-digestin anaerobia de residuos de matadero con residuos de la industria del tomate. XII Encuentro Inter-Bienal del Grupo Especializado de Termodinmica (GET), Las Palmas de Gran Canaria, Spain (September 2010)

12. Ruiz-Celma, A., Cuadros, F., López-Rodríguez, F., Redrado, A.: Thin layer drying behaviour of industrial tomato by-products in a convective dryer at low temperatures. Res J Biotechnol **8**(2), 50–56 (2013)
13. Barrer, P.C.: Biomass transport systems. Encyclopedia of agriculture. In: Heldman (ed.) Food and Biological Engineering, pp. 94–98. Dekker, New York (2003)
14. Celma, A.R., Delgado, M.T., Galán, A.M.V., Blázquez, F.C., González, A.G., Rodríguez, F.L.: Caracterizacin de pellet de residuos de tomate industrial. XII Encuentro Inter-Bienal del Grupo Especializado de Termodinmica (GET). Las Palmas de Gran Canaria, Spain (September 2010)
15. Barceló, J., Nicolás, G., Sabater, B., Sánchez, R.: Fisiología Vegetal, 4 edn. Pirámide, Madrid (1987)
16. Bhat, M.K., Bhat, S.: Cellulose degrading enzymes and their potential industrial applications. Biotechnoly Adv. **15** 583–620 (1997)

Part VIII
Science for the Lay Audience

Swings of Science: From Complexity to Simplicity and Back

L.M. Pismen

1 Introduction

I start with the lines by Boris Pasternak, given here in my poor translation:

> *In the end, one cannot do but to fall like into herecy into unheard-of simplicity.*
> *But we will not be spared if we fail keeping it concealed:*
> *people need it most of all but they better understand complexity.*

People need simplicity, to grasp the essence of things, maybe in a single moment of revelation—but they better understand complexity, being evolved to endure challenges of complex environment.

From the very beginning of civilization, man tried to introduce order—and thereby "unheard-of simplicity" into the infinite complexity of the surrounding world. The order, in its simplicity, had been, however, always fragile and hard to sustain, as it was overpowered by ever present ambient complexity, as well as by internal complexity of man who never stops at simple explanations and simple rules.

2 Swings of Religions

We see this swinging motion, from complexity to simplicity and back, already in the evolution of religions, which had served historically, in many ways, the same epistemological purpose that science is serving today (I do not say anything on other functions of religion). Primitive magical, shamanic rituals took the complex world as is, as a "black box", if we use a modern term. There was a fairy in every tree, and

L.M. Pismen (✉)
Department of Chemical Engineering and Minerva Center for Nonlinear Physics of Complex Systems, Technion – Israel Institute of Technology, 32000 Haifa, Israel
e-mail: pismen@technion.ac.il

R.G. Rubio et al. (eds.), *Without Bounds: A Scientific Canvas of Nonlinearity and Complex Dynamics*, Understanding Complex Systems,
DOI 10.1007/978-3-642-34070-3_54,

a nymph in every stream, and practical benefits could be obtained by placating the spirits, without insight into their nature.

More order was introduced by ancient religions with their hierarchical pantheons and codified rituals, and eventually by the monotheism with the unique God as the source and the cause of everything. The tetragrammaton, the unpronounceable sacred name, is formed as the active form of the verb "to be", loosely translated as "he bringeth into existence". A direct line can be drawn from here to the dream of modern physics, "the theory of everything". When we read now the first chapter of the Book of Genesis, it sounds not unlike the theory of phase transitions in early Universe, as explained to a pastoral tribe, followed by an account of creation of living forms going in about the same order as the theory of evolution. Other unified religio-philosophical systems have been created in the "axial age" in India, China, and Greece. This was the period, centered around 500 BC, during which, according to Karl Jaspers [1], "*the spiritual foundations of humanity were laid simultaneously and independently*".

Complexity has found its way back when the unified systems were expanded and elaborated in diverse ways: in Judaism, first by prophets and further by talmudic scholars and eventually, back to magic, by kabbalists and Hasidic mystics; in Christianity, by expanding the unique God to Trinity and veneration of a multitude of saints; in Buddhism, by proliferation of schools and the cult of bodhisattvas. It was counteracted by retrograde simplification, in islam, returning to the ethos of desert tribes, and in various iconoclastic and puritanical movements throughout Christian history, and eventually in totalitarian ideologies of twentieth century.

In our time, we see proliferation of sectarian and esoteric beliefs, as well as all shades of traditional religions unrestricted, thanks to globalization, by geography or ethnicity. Science remains a thin crust over the molten lava of ignorance. The society at large views science rather like a hog from a fable who does not care that the oak will wilt when its roots are dug under, but only needs the oak's acorns to remain available. The fruits of science, from communication tools to weapons, are eagerly used by the same forces, from terrorists to preachers to pop stars, who undermine its roots.

3 Swings of Elements

3.1 Thales to Dalton

In science, starting with its pre-scientific origins, the quest for simplicity is seen, first of all, in a quest for elementary entities in Nature. The great idea of Thales, not unlike religious visions of his time, was that *water* is the foundation of all. By comparison, the symmetry-breaking transition in the first chapter of the book of Genesis also involved waters, separated by a domain wall—the firmament of heaven. This far-reaching universality was later relaxed to a rational Aristotelian system of

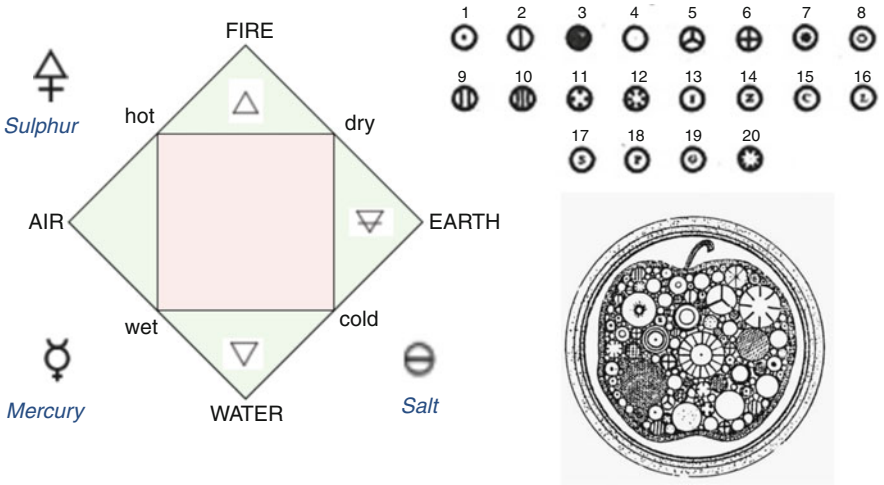

Fig. 1 *Left*: Aristotelian and medieval elements. *Upper right*: Dalton's elements. *Lower right*: symbolic presentation of composition of matter [2]

four classical elements, earth, water, air, and fire, or five, including quintessence, which dominated for almost two millenia. Alchemists, more practically minded, added *Tria Prima*, crucial for their transmutation activities: sulfur, mercury, and salt, with a number of "mundane" elements on the top of that.

In the new age, a completely different empirically based principle was suggested for identification of elements: they were defined as substances that could not be split into simpler constituent parts. This was the basis of John Dalton's system of elements; their number was not restricted, and kept expanding throughout the rational nineteenth century (Fig. 1).

The notion of elements was naturally compatible with the atomic hypothesis going back to Leucippus and Democritus in the fifth century BC: to each indivisible element corresponded an indivisible atom. and compound species, with their specific properties, could be assembled by combining atoms, as seen in a symbolic artist's rendering in Fig. 2. The existence of atoms had not yet been proven, and many prominent scientists, Like Wilhelm Ostwald, Ernst Mach, and Dmitry Mendeleev, still believed in infinite divisibility of matter at the break of the twentieth century, well after the discovery of radioactivity which made atoms both real and not really atomic but divisible.

3.2 Mendeleev to Bohr

This was particularly ironic in the case of Mendeleev, who has organized the multitude of elements known at the time into his famous periodic table. While

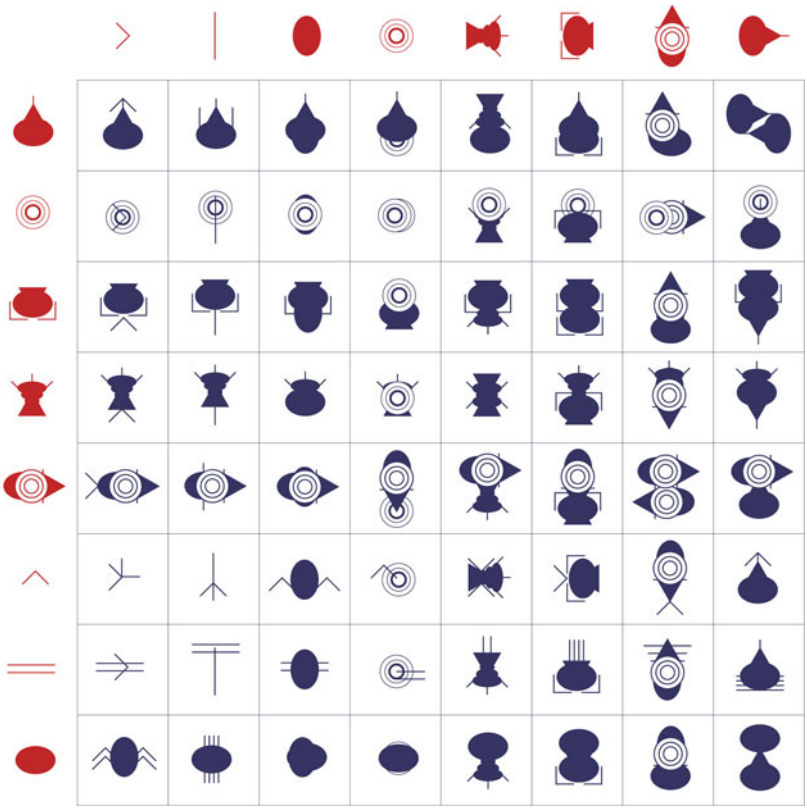

Fig. 2 Assembling elements into variegated structures [3]. Courtesy TM/R Design

the elements were ostensibly ordered in the periodic table by their atomic mass, Mendeleev took liberty to switch places of some elements to fit the periodic change of their chemical properties, and to leave empty spaces—thereby predicting the elements unknown at the time, which later were discovered to add to the glory of his genius. This was an amazing breakthrough: what was really important was not the atomic mass thoroughly measured by nineteenth century chemists, but just the innocuous natural number assigned to the element in the periodic table. The reason has become shortly clear through the discovery by Rutherford of the structure of the atom that consists of a nucleus with the charge equal to its number in Mendeleev's table, surrounded by the matching number of electrons. Rutherford called the positively charged nuclear particles protons, and inferred existence of neutral particles of a comparable mass, neutrons, to account for the difference between the atomic mass and the charge.

The periodicity of chemical properties was explained by a bold hypothesis of Niels Bohr allowing electrons to move around the nucleus along a fixed discrete sets of orbits, in defiance of laws of classical electrodynamics, which predicted that electron should gradually lose energy, and fall eventually onto the nucleus.

3.3 Rutherford to Strings

This was the moment of unheard-of simplicity: only three elementary particles remained; electron, proton and neutron; but we were not spared, as "weird"—from the contemporaries' point of view—quantum mechanics came forth to explain the inconsistencies of Bohr's model. Complexity kept creeping in: Dirac's relativistic quantum theory required an antiparticle partner for each particle, and by the mid twentieth century accelerators produced a cornucopia of baryons and mesons, arbitrarily named and obeying no particular order. The new coup of simplicity came with the establishment of the Standard Model; the new set of elements were quarks and leptons, neatly organized in three generations; all particles predicted theoretically to fit this scheme have been later discovered experimentally, except the quintessence of the scheme, the elusive Higgs boson.

This order is being endangered again by hypothetical supersymmetric partners of all particles and murky dark matter and dark energy. Finally, the string theory with its zillions of versions, realized, perhaps, in a zillion worlds of the multiverse, kills the dream of finding a unique single principle governing the complex world. A multitude of outcomes renders this theory immune to empirical falsification, which, if we follow the definition by Karl Popper [4], removes it out of the realm of science, back into the ancient world of metaphysics and magic.

4 Swings of Cosmology

4.1 Aristoteles to Newton

The macroworld of cosmology, which, as we now believe, is deeply related to the microworld of elementary particles, has also passed through its cycles of simplicity and complexity. The neat Aristotelian system of seven planets rotating around the quiescent Earth was supplemented by Ptolemean epicycles to better fit observational data; this was simplified by Heliocentric system of Copernicus. Young Kepler came with a fantastic scheme of nesting the five Platonic solids, each encased in a sphere, to produce six layers, corresponding to the orbits of the six known planets (Fig. 3). He thought at the time that he had revealed God's geometrical plan for the universe. The perfect geometry of a circle or a sphere came, however into contradiction with refined astronomical measurements of Tycho Brahe. To explain them, Kepler came to an idea of elliptical orbits; he created a formula in which a planet's rate of motion is inversely proportional to its distance from the Sun which, as a symbol of God the Father, was the source of the motive force in the solar system. The laws of planetary motion were soon rationally explained by Newton's theory of gravitation. Though Newton was no less mystically inclined, he concentrated his esoteric views in his passion to alchemy rather than in mathematical and physical work we admire to this day.

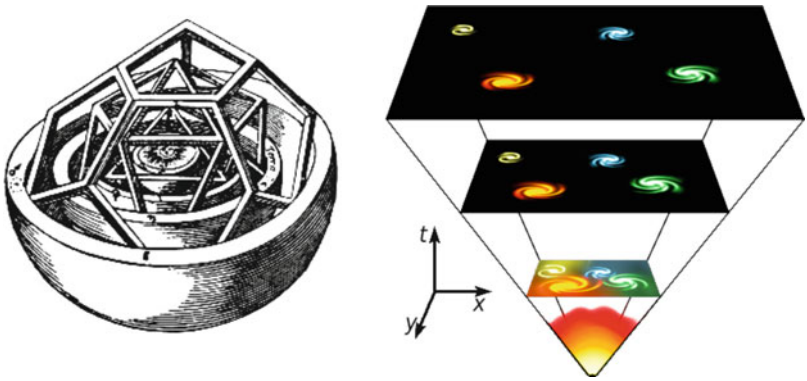

Fig. 3 *Left*: Kepler's nesting of the five Platonic solids. *Right*: Universe expanding from Big Bang

4.2 Universe to Multiverse

This theory reigned supreme even after the Sun was demoted to the status of a run-of-the-mill insignificant star in a run-of-the-mill galaxy, and the cosmological question has shifted to the structure of the Universe as a whole. The first trouble surfaced in the experiment by Albert Michelson and Edward Morley proving that the speed of light—which was thought at the time to be transmitted through the ether filling up the space, as sound is transmitted through air—remains invariant, independently of the direction of its propagation relative to the moving observer. This made it necessary to consider time on the same footing as spatial coordinates. The paradox was resolved by Einstein's special relativity theory—but Einstein claimed that he was not aware of these experiments and was driven only by mathematical beauty and logic—by the quest for simplicity.

Since then, the cosmological question turned into the question of the structure of *spacetime*. Still, no observations had contradicted Newton's gravitation theory in 1916 when Einstein came with his general relativity theory, which has reduced Newton's gravitation to pure geometry. Einstein became world-famous after his theory was confirmed by measuring small deviations of the orbit of Mercury. For him, this was rather a non-event. What significance has this tiny measurement compared to the great edifice of the theory? When asked what he would do if the experiment had not confirmed the theory, Einstein ostensibly said: "*I would pity poor God*"—poor God indeed, who has not created the world according to this beautiful plan.

The Universe was now understood as spacetime governed by Einstein's relativity, which expands following its creation at Big Bang (Fig. 3). The word itself was ironically coined by Fred Hoyle, who believed in an alternative scenario of continuous creation of matter, finally disproved by the discovery in the 1960s of the cosmic microwave background radiation—the remainder of Big Bang.

The ultimate fate of the Universe, and the nature of Big Bang itself remain, however, so far unclear, and complexity is bursting out into the picture of a bubbling multiverse where anything is possible. The contradicting modern and postmodern attitudes can be seen in two statements of the same prominent scientist, John Archibald Wheeler [5]: First: "*Omnibus ex nihil ducendis sufficit unum*" (one principle suffices to obtain everything from nothing). Second: "*Physics has to give up its impossible ideal of a proud unbending immutability and adopt the more modest mutability of its sister sciences, biology and geology*". The first, is Einstein's uncompleted quest; the second, a retreat from Einstein's challenge to God.

4.3 From Order to Chaos

Our world seems to have been more stable in the past, both ontologically and politically, and it probably had never been more stable than at the time when it stood on the firm ground of the laws of Newtonian mechanics, developed into a beautiful mathematical structure by the brilliant French and German mathematicians of the Age of Enlightenment. The social and moral ground had been firm then as well, even though occasionally trembled by revolutions.

Deterministic laws, should, in principle, allow computation of all future states of the system. Laplace's daemon should have been able to accomplish this task [6]:

> *An intellect which at a certain moment would know all forces that set nature in motion, and all positions of all items of which nature is composed, if this intellect were also vast enough to submit these data to analysis, it would embrace in a single formula the movements of the greatest bodies of the universe and those of the tiniest atom; for such an intellect nothing would be uncertain and the future just like the past would be present before its eyes.*

Alas, even with the gravitation laws intact and no quantum uncertainty, the future of a gravitating many-body system is uncertain. In his research on the three-body problem, Henri Poincaré [7] became the first to describe a chaotic deterministic system. The solar system itself is intrinsically chaotic. It is rendered unstable by weak multibody interactions, as proven in mid twentieth century by Vladimir Arnold—thankfully, on exceedingly long times of Arnold diffusion [8].

5 Turbulence

5.1 A Question to God

This brings us to the ultimate revenge of complexity: even when the basic laws are firmly established, behavior of large systems including many interacting parts may become practically unpredictable. This problem became particularly acute in such a

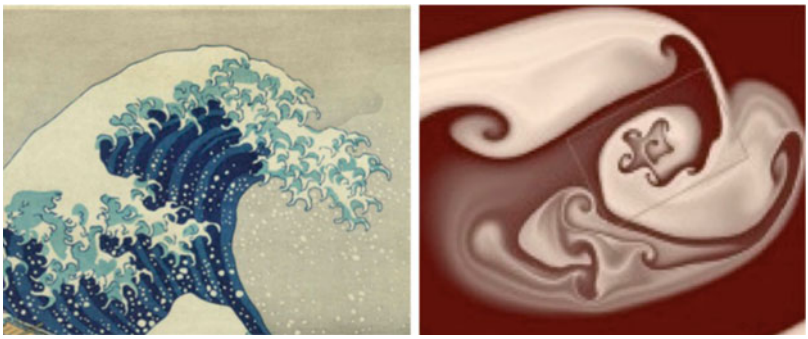

Fig. 4 *Left*: Hokusai, The Wave (fragment). *Right*: Fractal Kelvin-Helmholtz breakup [9] (fragment)

mundane everyday phenomenon as turbulent fluid motion. An apocryphal quotation from Werner Heisenberg says:

> *When I meet God, I am going to ask him two questions: Why relativity? And why turbulence? I really believe he will have an answer for the first.*

A similar witticism has been attributed to Horace Lamb:

> *I am an old man now, and when I die and go to heaven there are two matters on which I hope for enlightenment. One is quantum electrodynamics, and the other is the turbulent motion of fluids. And about the former I am rather optimistic.*

"Enlightenment" supposes a simple answer to a complicated question, like a rabbi challenged to explain the essence of the Torah while standing on one foot. Why to think that it might be possible at all? No fundamental questions are involved here; no one doubts the Navier–Stokes equation, which well describes hydrodynamics of a Newtonian fluid moving with a velocity much smaller than the speed of sound. The problem of turbulence has, however, philosophical depth: the equation, apparently deterministic, should, in principle, allow computation of all future states of the system, as the daemon of Laplace claimed to do. This is, of course, impossible, even without intervention of quantum uncertainty, as we all know not only from frustrating weather forecasts, but even from a failure to predict the outcome of such a simple mechanical process as flipping a coin. No reasonable physicist attempts precise prediction; in many cases—those, of course, which do not concern us personally—statistical description is satisfactory.

The challenging feature of turbulence that it is not plainly random, but has elements of structure, as seen, for example, both in the famous drawing by Hokusai and in a modern simulation [9] (Fig. 4). The attempts to "understand" turbulence, i.e. to reduce it to simpler "elementary" entities went accordingly from two directions, from statistics—maybe somewhat organized, and structures—maybe somewhat distorted and fluent.

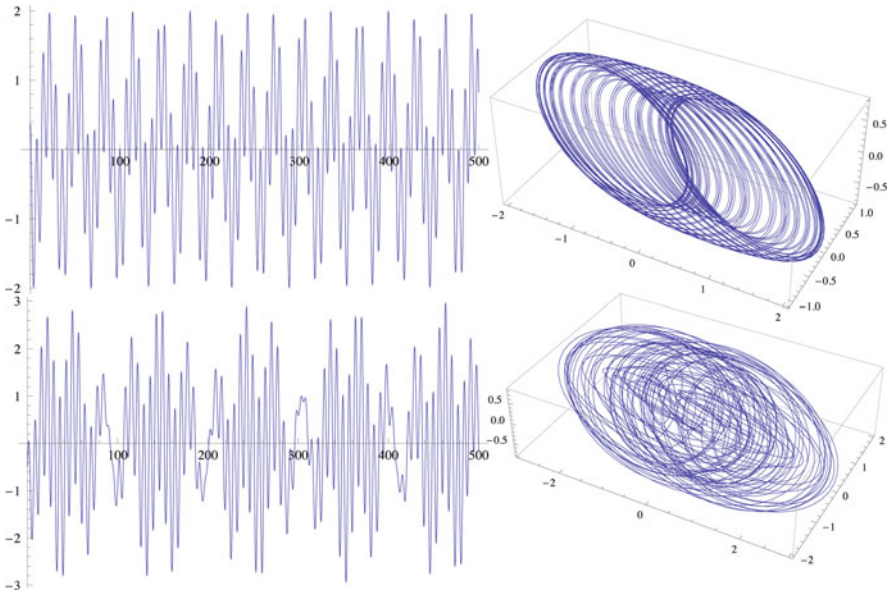

Fig. 5 Quasiperiodic motion: superposition of two (above) and three (below) oscillating modes

5.2 Origin of Turbulence

The first direction is associated with Lev Landau and Andrey Kolmogorov. Landau was tuned to generic phenomena, he might have dismissed as "sick" some curiosities of behavior of complex systems which now find their way to covers of Physical Review Letters and Nature. Many complex flow patterns arising near the onset of hydrodynamic turbulence were dismissed as a "turbulence crisis", and attention was concentrated on "developed turbulence" formed by superposition of a large number of waves. Landau envisaged transition to turbulence as a gradual excitation of a large number of waves. One can see in Fig. 5 that already a superposition of three oscillating modes looks chaotic to the eye. In developed turbulence a great many waves of different length and matching frequency coexist, and energy is transmitted from longer to shorter ones, as can be seen even in the Hokusai drawing; it is expressed by Lewis Fry Richardson [10] in a paraphrase of Jonathan Swift:

> *Big whirls have little whirls that feed on their velocity,*
> *and little whirls have lesser whirls, and so on to viscosity.*

Quantitatively it leads to the famous Kolmogorov's 5/3 law of the energy distribution among the modes of different wavelengths [11].

There were a lot of corrections to this simple picture. Nonlinear interactions among the modes and their localization had to be taken into account; a diagram technique similar to that developed by Feynman in quantum electrodynamics was

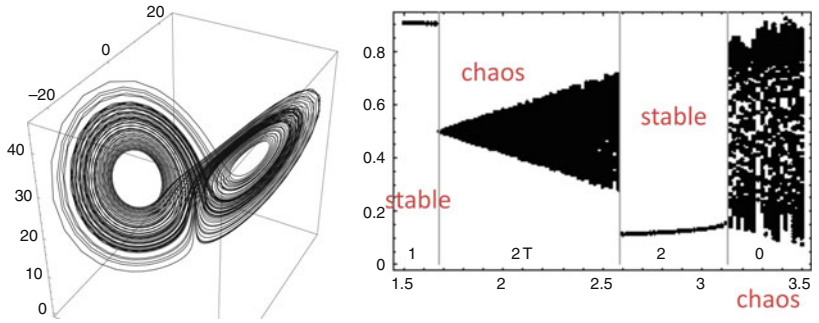

Fig. 6 *Left*: Trajectories of the Lorenz system. *Right*: Transitions in the respective Poincaré map. Transition to chaos according to the Pomeau–Manneville scenario takes place at the borders of Region 2 [19]

applied. I recall one distinguished scientist saying about another one that the latter's merit is in bringing this method to a conclusive dead end. Nevertheless, the work in this direction is still pursued.

Kolmogorov reportedly chuckled at Landau's scenario saying that he is probably unaware of more complex dynamical systems. It has been known already to Poincaré that very simple systems, like two coupled pendula, can exhibit unpredictable chaotic behavior—but the scientific community, let alone general public, failed to appreciate this. Kolmogorov, Arnold, and Jürgen Moser showed that weak interactions near resonances can make motion around the tori unstable.

One of the problems in Kolmogorov's student seminar in mid 1950s was to prove using this theory a practical impossibility of weather forecast. For Edward Lorenz, a meteorologist, the forecast problem was particularly acute. He devised in 1963 a toy mathematical model of thermal convection [12] that showed chaotic behavior, with trajectories switching erratically between circling either of the two stationary points (Fig. 6). The work remained unnoticed till late 1970s when chaos came into fashion.

5.3 Turbulence made Simple

The Lorenz system was an example of a very simple system capable to behave chaotically. This does not surprise us anymore: the question we can ask now is why far more complex systems are most commonly well behaved. This was still, however, not the end of the quest for simplicity. A system of differential equations can be turned into a still simpler iterative equation by constructing a Poincaré map; the complexity of behavior is retained, and can be investigated far more easily—a pocket calculator, one of those in use $30+$ years ago, would suffice to find out change of behavior in different parametric regions. An important feature of the

Lorenz map is a possibility of long chaotic transients and, on the contrary, long quiet sequences bursting into chaos. This is the way to turbulence through intermittency of Yves Pomeau and Paul Manneville [13].

Other simple chaotic systems designed in the 1970s showed the phenomenon of repeated period doubling leading eventually to chaos. Differential equation systems behaving in this way are qualitatively equivalent to the simplest iterative map of all—the famous logistic map. Mitchell Feigenbaum [14] discovered transition to chaos via the period doubling cascade while trying to help his pocket calculator to faster compute many iterations of this map. The cascade is commonly known by his name, although it was described earlier by Robert May [15] and the related renormalization group discovered independently by Charles Tresser and Pierre Coullet [16]. This scenario was considered at the time as a universal way to chaos—but with time, as usual, complexity creeped back again, and scenarios of transition to chaos turned out to be too numerous to be universal.

5.4 Coherent Structures

Studies of toy models prompted an alternative approach to turbulence: discerning *coherent structures* which follow relatively simple dynamic equations and remain more or less persistent while evolving in time [17]. The vortices seen in Fig. 4 give an example of structures of this kind, and more ephemeral structures can be discerned in turbulent flows, as familiar to us in cloud and smoke patterns. Nobody has given, however, a working definition of a coherent structure, and their persistence time is usually quite limited.

Although we doubt that even God knows turbulence theory, practical computations of turbulent flows are gradually improving. We keep listening to weather forecasts with attention, and forgive failures, taking note that short-range forecasts gain reliability as computers become more powerful and data banks swell.

6 Patterns

6.1 Unity in Variety

There are great many other structures or patterns in Nature, often persisting in time and having similar appearance in completely different settings [18, 19]. Hexagonal convection patterns is a common form, first seen in experiments of Bénard [20], but also sculpted by Nature in solidified lava flows—and in ephemeral cloud patterns on different scales (Fig. 7). More fancy patterns generated by same process were seen in the laboratory.

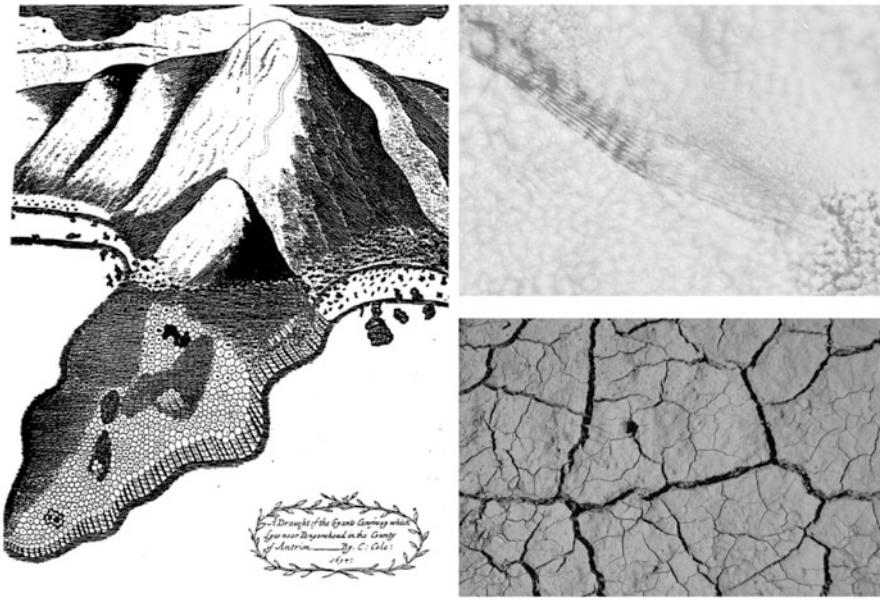

Fig. 7 Hexagonal patterns in Nature. *Left*: Rendering of Devil's causeway in Ireland (1642). *Upper right*: cloud patterns (NASA image). *Lower right*: cracks in soil (author's photo)

Another way to generate a variety of patterns, discovered by Faraday [21] but brought to sophistication in our days, is vibrating a fluid layer; a layer of sand can serve the same purpose. Patterns of sand created by the action of wind and water currents are common in Nature as we all know, and more patterns are seen in rocks and cracked soil.

Quite often, the same system—be it convection, vibration, or chemical reactions—is capable to generate different patterns, and quite often, different systems generate the same patterns. Both convective and chemical patterns may look similar to desert vegetation patterns or to patterns of animal coats.

Chemical reactions can produce waves rather than steady patterns, both in fluids and on surfaces. Chemical surface patterns on shorter scales are sculpted by crystalline structure, distorting round spirals to a squared form or imposing a decorated hexagonal structure. Spiral waves are ubiquitous, and are seen in different physical settings, and on immensely different scales. In shells and flowers, it reflects a radial growth pattern, and in the hurricane cloud pattern, the earth rotation, but in chemical patterns, as well as in slime, it results from spontaneous symmetry breaking. Spiral forms also commonly appear as a result of instabilities of fluid flows and wave breaking. Another common structure seen in chemical, crystalline, hydrodynamic, and living patterns, is dendritic.

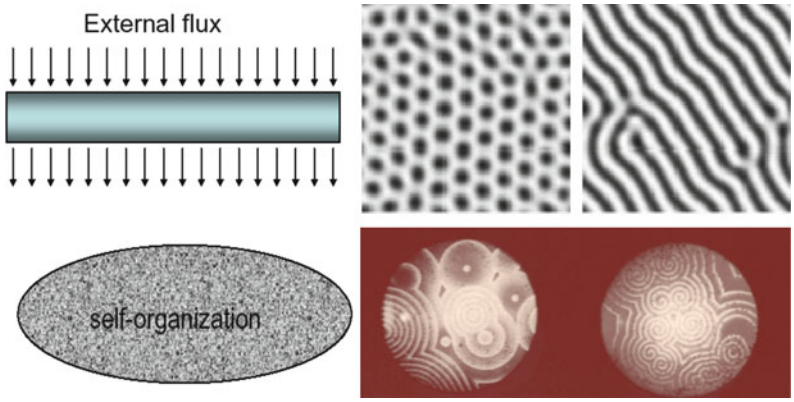

Fig. 8 *Left*: Spontaneous symmetry breaking in an isotropic open system subject to uniform external fluxes. *Right*: the various chemical patterns

6.2 Turing Patterns

The general principle governing the creation of a great variety of patterns is spontaneous symmetry breaking in non-equilibrium systems subject to external matter or energy fluxes (Fig. 8). They are often called Turing patterns after his famous 1952 paper [22]. The general recipe for a pattern is to have a combination of a short-range activator and a long-range inhibitor. The principle is simple: the inhibitor excited by the activator locally, spreads sidewise, and depresses growth nearby; for example, animals attracted by local abundance of grass, depress the surroundings; this pattern spreads over the available terrain. Both activator and inhibitor can be either chemical or biological species, or, in a more abstract form, other physical agents, and the scale of the pattern is determined by the relevant spreading ranges.

This is another breakthrough of simplicity: A simple system of two reaction-diffusion equations: first, a nonlinear activator equation, and second, an inhibitor equation, which can be linear, can generate various patterns and waves in different applications, both in chemistry and biology.

6.3 Genetic Code

But is it really a way complex living forms can be created? Life is not spontaneous; this is recognized at least since the notion of spontaneous generation from non-living matter e.g. insects from putrefying earth, going back to pre-Aristotelian Greek philosophers, has been finally disproved by Pasteur. Living things develop following

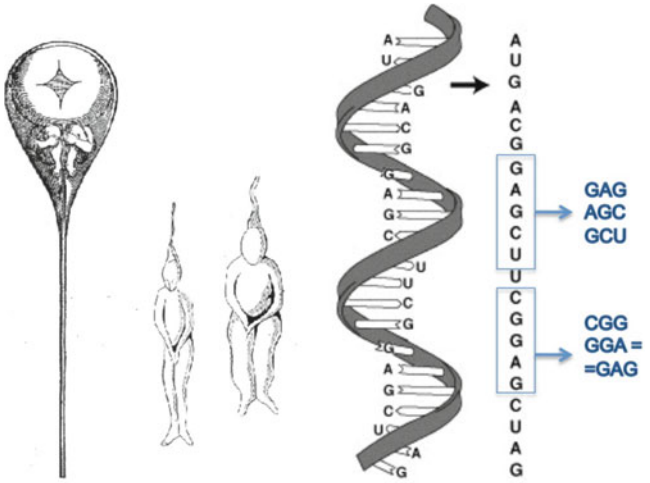

Fig. 9 *Left*: Homunculus in the sperm, drawn by N. Hartsoecker (1695). *Right*: Genetic code in the double spiral, read according to G. Gamov

a predetermined plan—long believed to be set by Almighty—but where is hidden this plan?

Quite an absurd answer was given by spermists of the early modern age: there is a tiny *homunculus* hidden in the sperm (Fig. 9). This engenders infinite complexity: is there a chain of homunculi "all the way down"? A far simpler plan has been discerned in Mendel's study of variation in peas, as he set the basis of modern genetics while working unnoticed in a quiet monastery garden. The "homunculi" turned out to be tightly compressed in double spirals of DNA carrying genetic information. This was a triumph of a unique simple principle beneath the infinite variety of forms. Only four "letters"—bases attached to the spiral backbone—suffice to encode the order of aminoacids assembled into protein molecules. The design ensures stability of hereditary forms, and at the same time is sufficiently flexible to allow new forms to develop by recombination and mutation of genes, as shown in a symbolic artist's rendering in Fig. 10.

As related by Francis Crick [23], the great physicist George Gamow tried to deduce the precise way this code is structured. It follows from simple combinatorics that if each amino acid is coded by a combination of overlapping triplets bases in any order (as sketched in Fig. 9), four "letters" are just enough to code twenty aminoacids in a unique way. This would immediately explain why there are four bases and twenty aminoacids, not more and not less.

Alas, Nature is not as rational as the physicist sees it; there is no overlap, the order of bases counts, and the code is highly degenerate: some combinations of bases do not code any aminoacids, and the correspondence between base triplets and aminoacids is not one-to-one. And, alas, Gamow, unlike Einstein, could not pity God who has not followed his beautiful design. It is hard to tell, which features

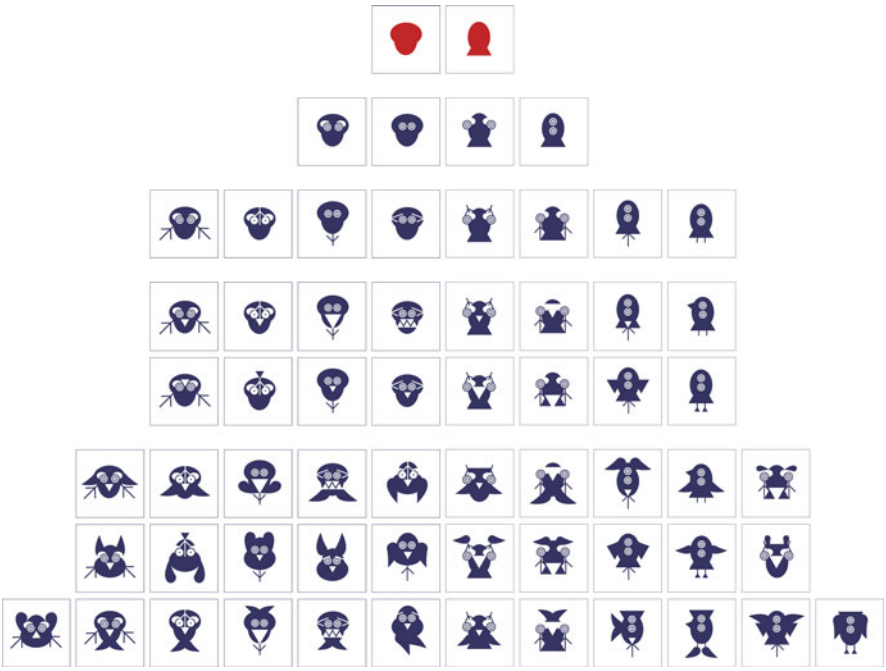

Fig. 10 Evolution of variegated complex forms [3]. Courtesy TM/R Design

are essential and which came about just as a result of random play of evolution. A close analogy is found in the Hebrew language where most roots are triplets of letters; their order counts, of course; some triplets have more than one meaning, and many others have no meaning at all.

6.4 Development and Signaling

Complexity kept creeping in as thousands and thousands of biologists, biochemists, and biophysicists, driven by the desire to understand the inner workings of life—maybe to be able to extend it eternally—and sustained by grants more generous than in other branches of science (except, perhaps, the megalomanic edifice at CERN)—have been struggling during the half-century since the discovery of the double spiral, trying to uncover detailed mechanisms of translation of the molecular code into the living form.

The chemistry of life turned out to be immensely complex, maybe unnecessarily so—but Nature may be not aware of Occam's razor, and cares for robustness and stability more than for rational and economic design. There is far less universality here than the physicist would like to see.

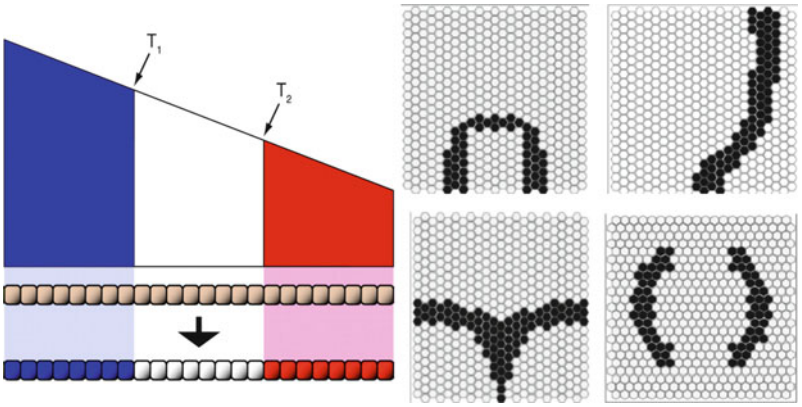

Fig. 11 *Left*: Wolpert's *French flag* model [26]. *Right*: Simulated patterns in crossed signaling gradients coupled with signals emitted by cells [27]. A quarter of the morphogenetic field is shown, with signal sources originating on the left and below

Turing's mechanism does not work in living forms and patterns; even animal coat patterns are not created in this way, in spite of a superficial semblance achieved in simulations. When a living organism develops from a seed or an egg, the cells do not specialize by spontaneous symmetry breaking, but are directed my morphogen gradients [24]. Patterns are not created by a simple activator-inhibitor scheme, but involve a great number of chemical interactions. Even segmentation, common in animals, does not work by Turing: particular chemical interactions are implemented to build up each segment—which may be the only way to insure that the number of segments be independent of the size of the animal [25].

The simplest patterning scheme generates Wolpert's *French flag* model [26]. The target gene is expressed in the middle (white) interval, where the signal level is above the threshold T_2 of an activated link but below the threshold T_1 of a depressing link in the genetic scheme (Fig. 11). In many cases, *e.g.* in the *Drosophila* egg, two axes (anterior–posterior and ventral–dorsal) are set by diffusing morphogens, leaving only left-right symmetry, which may be further weakly broken. A combination of external crossed gradients with signals emitted by cells themselves may create a variety of asymmetric patterns [27]; some examples are shown in Fig. 11.

7 Conclusion

One has to distinguish between simplicity through rude simplification and simplicity through understanding the roots and causes; between complexity through mix-up and failure of analysis and complexity through interactions and enrichment. Simplicity that we need most, that which human intuition is able to comprehend,

drives scientific insight; it is dressed in refining details when applied to practical problems and is understood in its complex realizations.

This refinement, unfortunately, deprives us of the light of sudden comprehension; great aims disappear into unreachable distance, like Kafka's castle. Where the ancient alchemist thrived to find the philosopher's stone—which would be in our terms a catalyst for all reactions, both chemical and nuclear, the modern chemical engineer is happy to improve performance of a particular kind of a catalyst for a particular process. Where the elixir of life was sought, we are happy to find a drug reducing mortality in a single variation of cancer.

There is probably no way to make complexity simple again.

References

1. Jaspers, K.T.: The Origin and Goal of History. Reprint. Greenwood, Greenwood (1977)
2. Pismen, L.M.: From the Miracle to the Number (in Russian). Pedagogika, Moscow (1973)
3. Timerman, E., Timerman, A.: The Elements. Klaudpress, San Francisco (2002)
4. Popper, K.: The Logic of Scientific Discovery. Routledge, London (1959)
5. Misner, C.W., Thorne, K.S., Zurek, W.H.: John Wheeler, relativity, and quantum information. Phys. Today **62**, 40 (2009)
6. Laplace, P.S.: A Philosophical Essay on Probabilities. Dover, New York (1951)
7. Poincaré, J.H.: Sur le problme des trois corps et les quations de la dynamique. Divergence des series de M. Lindstedt". Acta Mathematica **13**, 1 (1890)
8. Arnold, V.I.: Instability of dynamical systems with several degrees of freedom. Dokl. Akad. Nauk SSSR **156**, 9 (1964)
9. Fontane, J., Joly, L., Reinaud, J.N.: Fractal Kelvin-Helmholtz breakups. Phys. Fluids **20**, 091109-1 (2008)
10. Richardson, L.F.: Weather Prediction by Numerical Process, 2nd edn. Cambridge University Press, Cambridge (2007)
11. Kolmogorov, A.N.: The local structure of turbulence in incompressible viscous fluid for very large Reynolds numbers. Dokl. Akad. Nauk SSSR **30**, 299 (1941)
12. Lorenz, E.N.: J. Atmos. Sci. **20**, 130 (1963)
13. Pomeau, Y., Manneville, P.: J. Physique Lett. **40**, L609 (1979)
14. Feigenbaum, M.J.: Quantitative universality for a class of non-linear transformations. J. Stat. Phys. **19**, 25 (1978)
15. May, R.M.: Simple mathematical-models with very complicated dynamics. Nature **261**, 459 (1976)
16. Tresser, C., Coullet, P.: Preturbulent states and renormalization group for simple models. Rep. Math. Phys. **17**, 189 (1980)
17. Sirovich, L.: Turbulence and the dynamics of coherent structures. 1. Coherent structures. Quart. Appl. Math. **45**, 561 (1987)
18. Cross, M.C., Hohenberg, P.: Pattern formation outside of equilibrium. Rev. Mod. Phys. **65**, 851 (1993)
19. Pismen, L.M.: Patterns and Interfaces in Dissipative Dynamics. Springer Series in Synergetics, Springer, Berlin (2006)
20. Bénard, H.: Les tourbillons cellulaires dans une nappe liquide transportent de la chaleur par convection en regime permanent. Ann. Chim. Phys. **7**(Ser. 23), 62 (1900)
21. Faraday, M.: Philos. Trans. R. Soc. Lond. **121**, 299 (1831)
22. Turing, A.M.: The chemical basis of morphogenesis. Philos. Trans. R. Soc. Lond. Ser. B **237**, 37 (1952)

23. Crick, F.: What Mad Pursuit. Basic Books, London (1998)
24. Nusslein-Volhard, C.: Coming to Life: How Genes Drive Development. Kales, Carlsbad (2008)
25. Pourquie, O.: Vertebrate somitogenesis: a novel paradigm for animal segmentation? Int. J. Dev. Biol. **47**, 597 (2003)
26. Wolpert, L.: Positional information and spatial pattern of cellular differentiation. J. Theor. Biol. **25**, 1 (1969)
27. Pismen, L.M., Simakov, D.S.A.: Genesis of two-dimensional patterns in cross-gradient fields. Phys. Rev. E **84**, 061917 (2011)

MANUEL G. VELARDE

A DECADE OF SCIENCE FOR THE PEOPLE IN SPAIN: LA BARRACA DE LA CIENCIA

1. INTRODUCTION

Science is part of Culture and today scientific illiteracy is plain illiteracy. On the other hand in the fight for survival or just as a consumer the citizen needs a fair amount of knowledge on electricity, electronics, computers,... in order to make adequate choice among the "goods" available at least in developped countries. At higher levels we also see the role of science and eventually technology in improving food processing, modern farming, medical care adn hygiene at large, ... and even affecting international politics. Star Wars, or SDI in the more appropriate jargon, and its huge budget seems to have been crucial in the positive progression of peace talks between the superpowers in Geneva. SDI was to a major extent based on laser science and technology.

Intelligence or Intelligence Capacity, Talent is a gift received from our parents but its use can only be adequately implemented with Culture. Educated people are not more intelligent but they are better equipped for "survival" and progress.

Unfortunately there are countries with none or little tradition in Science. There occasional catastrophes originated in inadequate use of technology lead to accusing science of wrong doings. Are the scientists responsible for the wrong doings with nuclear energy or pesticides? They are not. Rather politicians and speculators or military dictators are the responsible people to blame. Scientific knowledge and culture at large open new ways, new possibilities and it is up to us whether or not we use them correctly.

To improve the Cultural Level of our society we must make Science and Technology accessible to the laity. Magazines like Scientific American, American Scientist, New Scientist, La Recherche, etc., are playing an important role in this respect. However, do they rearch the laity?

My guess is that public lecturing at Elementary and High Schools, ... TV and Radio programmes about Science and Tecnology could play a much more crucial role than magazines. There seems to be tendency

today (it is only a personal guess) to gather information and culture in the passive rather than active way. Reading a book or an article in a magazine demands an effort that relatively few citizens (again a personal guess) perform. It is so easy to watch TV and to believe what the speaker says!

2. Spain and UNED, the Spanish Open University

U.N.E.D., the Spanish State University for Distance Education (learning) has over one hundred thousand students and some sixty branches distributed around the country with headquarters in Madrid. Students range from regular post-high school youngsters to workers and eventually graduates from other universities. From the legal standpoint it delivers the standard diploma in Humanities, the Sciences and even Engineering. At the same time it offers non-curricular courses to elementary and high-school teachers and the laity.

The Uned local branches are Centers with strong local economic and social support. Thus it is a valuable network in the country for a programme of public lecturing.

Radio broadcasting is used but TV is not yet used. Students are assumed to contact their nearest Center where either some regular evening classes are given or else they meet instructors to discuss the material they are supposed to study at home. In Physics, for instance, the Berkeley Book Series is used for Mechanics, Waves, Statistical and Quantum Physics. The books by M. Alonso and E. J. Finn, D. Halliday and R. Resnick, or P. A. Tippler are used for freshmen together with the four book set by L. D. Landau and A. Kitaigorodski, Physics for Everyone. The latter set is also used by students that prepare the University Admission Examination and by laity following a non-curricular course on Physics (for everyone). Other possibilities offered include lab work at the Centers or at Headquarters in Madrid (this began quite recently and in a reduced scale only).

3. My experience of science for the laity. Part One: a decade of lecture series in Madrid

In 1975 as a professor of physics at a regular state university in Madrid (at Unviersidad Autonoma de Madrid) I accepted the duty of giving the Admission Examination to High School students. Then I realized that succes and failure where crucially related to the socio-economic background and high school location of the candidates. Satellite, dormitory type of neighborhoods where low income citizen live in a highly

dense state tend to have teachers of low scientific status with rather meager dedication and motivation. It is an unfortunate fact, although again my guess that nowadays the working class does not value education as much as the higher educated people and thus have a tendency to disregard both the quality control in the selection and tenure of the teachers and the pressure on the individual action to improve his or her level of knowledge. Youngsters have then a tendency to go the easy way in the high school thus leading to failure in the university admission examination. On top of this physics and the sciences are genrally given with little if any laboratory practice. Science is thus uninteresting to a large part of the high school students.

Then I decided to act upon both the high school teachers and the students by offering public lectures with demonstrations and using multimedia (slides, films and transparencies). As the *curriculum* is fairly conservative, traditional in presenting physics (mechanics, optics, electricity and so on) I decided to bring in the lectures topics of present-day interest, the kind of topics that mass media refer to or the kind of subject that is hot in research and novel technological applications. With well over sixty lecturers in ten series of public lectures on Frontiers of Science (1976-1986) and five series of lectures on applied-oriented matters, Science and Technology for the Benefit of Mankind (1983-87) I acted in Madrid generally in downtown lecture halls of easy accessibility. The last three years we had the sponsorship of the Lord Mayor of Madrid and lectures were delivered at a city public hall with capacity of three hundred fifty seats. I was amazed by the enormous success these lectures leading on occasion to the closing of the auditorium and the building due to overcrowding.

In the Frontiers of Science series we covered topics such as liquid crystals, ultrahigh vacuum, turbulence, plasmas, superconductivity, modern spectroscopy, biophysics, lasers, ecology, photonics, nuclear fusion, fundamental particles and interactions, scientific aspects of medical care (frontiers in medicine), computer sciences, science and philosophy, polymers, crystallography, modern aspects of catalysis, solar energy and renewable energy sources, astrophysics, cosmology, ferroelectricity, etc.

In the applied-oriented series we focussed attention to matters of direct relevance to the daily life of the laity at cities or in the country side. Topics discussed included solar energy uses in the city and at home, electricity at home, food processing advances, laser applications, optical fibers, uses of renewable energies (wind, waves, biomass) etc.

Summing-up, in this programme we have had an estimated average audience of two to three hundred participants per lecture for a total number of ninety lectures alltogether. On the other hand, I have myself, given well over twenty public lectures in Madrid at different other places than those belonging to the two series of lectures mentionned above.

4. My experience of science for the laity. Part Two "La barraca de la ciencia" or itinerant public lecturing with demonstrations

Three years after joining Uned in 1980 I started a public lecture programme touring different parts of Spain. Since then I have visited as many as seventy five places (cities, towns and villages of all kind) and I have delivered well over one hundred and fifty lectures with a duration of two to three hours per lecture. These lectures included demonstrations and demanded cooperation of participants, students and even the laity.

Most of the lectures were delivered at public schools and in many places have been seminal for activities developped by school teachers. Crucial for the implementation and success of the lectures have been the collaboration of Directors, Secretaries and colleagues from the Uned Centers. Generally, at every place they took the responsability of adequately choosing the villages, schools and Town Halls where there was interest in my lectures and took the necessary steps to secure a large audience of students and laity.

In order to combine timeliness, and attractivity to the audience as well as relation to my actual research work I made the choice of three topics: (i) Lasers, (ii) Fluids and (iii) Evolution (Physics versus Biology and other disciplines).

Lasers includes an account of science fiction (Leonardo da Vinci, F. Bacon, H.G. Welles, "Buck Rogers", Ian Fleming, A.N. Tolstoy, etc.), science history (Einstein, Basov, Prokhorov, Towness, Schawlow, Gould, Maiman, Javan, Patel, etc.), a discussion of differences and similarities between lasers and light bulbs or neon (fluorescence) tubes, a description of a laser -inside (He-Ne, in particular), sketchy presentation of laser action (just a bit of theory of cooperative phenomena, pumping and stimulated emission), ray and wave optics and a description of applications ranging from medical care to biochemistry, industry and military uses. I also give an account of the economic impact of lasers all over the world (research, production and use). The whole presentation lasts about three hours but the duration depends very much in my guess about the feelings of people present in the audience.

Fluids includes an account of molecular diffusion processes, convection, interfacial pheomena, combustion, and turbulence. I also give a description of differences between Newtonian and non-Newtoninan fluids. Different dimensionless groups (Reynolds, Bond, Rayleigh, Strouhal, etc.) are introduced to explain the role of similarity in fluid physics and the heuristic description of physical phenomena. Emphasis is given to the role of fluid flow and fluids in our daily life.

Evolution is a public lecture about the onset of ordering and dissipative structures (structure both in anatomy and function) of special

relevance to our understanding of biology *i.e.* on how today physicists view Darwin's ideas. Thus I comment on non-equilibrium thermodynamics, phase transitions, cooperative and nonlinear phenomena. Emphasis is given to the subject of order through fluctuations and feedback mechanisms. Illustration is provided with examples using simple nonlinear discrete maps and their seemingly unexpected features like oscillations and eventually deterministic chaos and the appearance of fractals. Evolution, has mostly been delivered at evening sessions in a thougt-provocative way by presenting to the laity some of my philosophical, ideological views as a naural scientist which I believe are the current views in the scientific community at the end of the Twentieth Century.

5. The precursors: medieval "juglares", La Barraca and las Misiones Pedagogicas

In March 1932 with the strong support of Minister, University Professor and Educator Fernando de los Rios and with a budget of one hundred thousand pesetas, the Spanish (Republican) Government created La Barraca an Itinerant Drame Group made of university people and directed by Federico Garcia Lorca and Eduardo Ugarte. This itinerant group of some twenty people and four trucks toured Spain until April 14, 1936. They performed plays by Cervantes, Calderón de la Barca, Lope de Vega, Tirso de Molina, Lope de Rueda and Antonio Machado. With the exception of the latter all the authors belonged to the Golden Century (approximately the XVII) in the Spanisch Literature and Arts.

At about the same time, December 1931, and until the Spring of 1936, under the inspiration and leadership of Manuel Bartolomé Cossio another itinerant Group of Misiones Pedagogicas (Educative Actions) was touring the country. The Patronato (Board) was created on May 29, 1931 by the Spanish (Republican) Government with the "Mission" of bridging the gap between the cultural life of the cities and the cultural dessert of the villages in the country side. However, more than to provide a systematic approach to culture the members of Misiones, a bunch of intelectuals and educators, aimed at entertaining the peasants and other pariticipants with poetry, songs and plays from Golden Century or even Mediaeval writers. They also brought books (created small librairies), reproductions of paintings and musical recordings, and delivered public lectures on various topics of modern scientific or technological relevance.

Both La Barraca and Misiones Pedagogicas were reminiscent of the itinerant Mediaeval Juglares that toured the country with legends and "romances". Their success was based on the fraternal collaboration of school teachers and local authorities.

I reinvented the itinerant action with Science and as it is difficult to invent something really new under the Sun, I share with both groups many features including the fact that I have travelled with a small trailer

full of lab equipment and multimedia material, generally accompanied by one to three collaborators. Alltogether some ten collaborators have participated to different degree in my Barraca de la Ciencia.

6. Conclusion and outlook

Summing-up, with a rather large number of public lectures with demonstrations I have tremendously enjoyed myself. I believe a lot of people have also enjoyed with my presentations. Did I efficiently transmit the message that Science is part of Culture? Did I make scientific topics accessible to the audience? I guess so. However there has been no systematic study of the results of my activity although quite a number of laymen and colleagues have expressed their satisfaction and acknowledgment of what I have done over the years. To many regions I have returned twice, three or four times and this together with quite a number of follow-up activities by school colleagues (the after-effect) is a measure, albeit a qualitative one only of the success of my activity.

May I conclude with the claim that in our present society with TV, Radio and all that there is indeed still room (or necessity) for an action like that developped decades ago by La Barraca and Las Misiones Pedagogicas or recently by my Barraca de la Ciencia provided we approach culture in the most naive and perhaps deep sense: something that with pleasure lifts the human beings well above its irrational (less rational) animal ancestors and partners. For this purpose there is no need, strictly speaking, of a network like the Uned Centers in Spain. However, something similar and eventually Ministry support may help.

Acnowledgments

Contrary to Lorca's Barraca and Cossio's Misiones Pedagogicas I have not benefited from systematic institutional or Ministry economic support. Life is indeed different now from what it was in the thirties in Spain. On the other hand I wonder if government support may limit the freedom of action, choice of place where to act and topics of presentation. I have benefited, however, from the random economic sponsorship of Uned Centers, elementary and high school directors, Mayors and other local Institutions. Occasionally I have acted for free and more than once I received payment in the old fashion way with food, olive oil and other "goods" that peasants know are worth bringing home. These friends are too numerous to be listed here. They have my gratitude and if I may single out just one this would be the High School Teacher Ricardo Fernández-Cruz for his friendship, encouragement and collaboration over the decade that we have been working together.

APPENDIX

MAP OF SPAIN WITH INDICATION OF REGIONS VISITED BY "LA BARRACA DE LA CIENCIA" LIST OF PLACES AND ESTIMATE OF AUDIENCE

Fig. 1 is a map of Spain illustrating with black spots the different regions visited by "La Barraca de la Ciencia". Estimating that on the average two hundred participants attended my lectures (note, however, that on several ocassions I have had over thousand people in large theaters) I can say that with some one hundred and fifty presentations

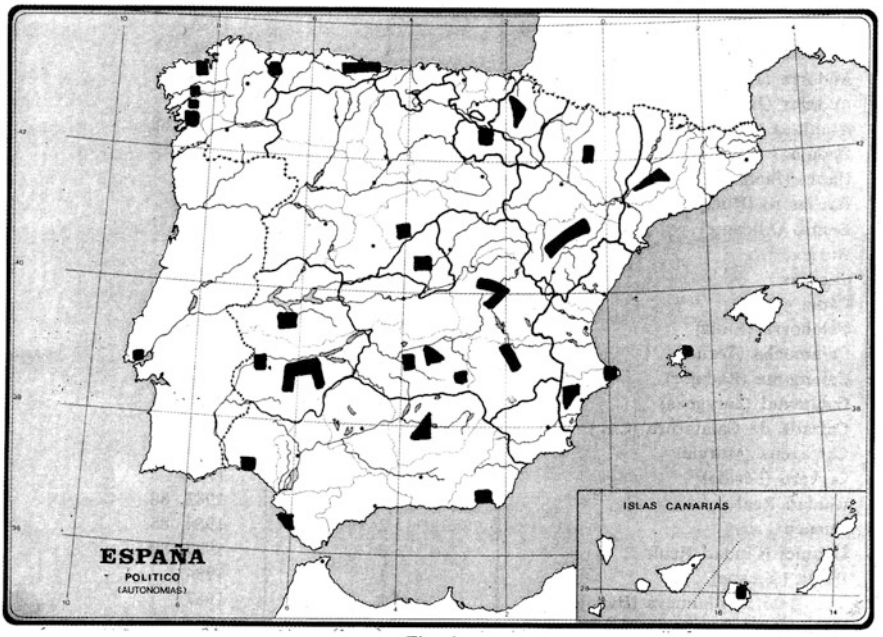

Fig. 1.

I have lectured to some thirty thousand people. This figure is to be supplemented with the estimated number given earlier for the series of lectures in Madrid where I have been only one among many other lecturers. Some of these participants, mostly youngsters, are presumably going to be leaders in the future. They may bring new ideas to society when they reach responsability.

ISSN: 0391-805X

ACCADEMIA NAZIONALE DEI LINCEI

ATTI DEI CONVEGNI LINCEI

83

Colloquio sul tema:

LA DIMENSIONE SCIENTIFICA DELLO SVILUPPO CULTURALE

PROMOSSO DALL'UNESCO E DALL'ACCADEMIA EUROPEA
SOTTO GLI AUSPICI DELL'ACCADEMIA NAZIONALE DEI LINCEI

(Roma, 30 settembre - 2 ottobre 1987)

(ESTRATTO)

ROMA
ACCADEMIA NAZIONALE DEI LINCEI
1990

A decade of hands-on science at the schools of Friul (Udine province, Friuli-Venezia-Giulia): Toccare l'aria e sentire la terra tremare.

M.G. Velarde

Back in 2002, when I was on duty as Rector of the International Center for Mechanical Sciences (CISM, www.cism.it) in Udine, Friuli-Venezia-Giulia (FVG, Italy), I had the idea of focusing as a research scientist on the education of children in the bracket 10-12 years old. This was indeed a natural follow-up to my experience with the "Barraca de la Ciencia" in Spain. It is at that age bracket when brain wiring, the software, the synaptic networking and the complex neuron dynamics, is making the change from "childhood" to "youth". My idea was that then their *instability*, their *criticality* makes brains highly responsive to inputs and "experiences".

How can a research scientist be of use? On the one hand, the obvious, is by bringing knowledge at the frontier. On the other hand, by bringing *methodology* or, in other words, **attitude towards problems**, including attitude towards life, to social behavior, and beyond, thus leading to experiences that include problem solving, team work and collaboration. After all the development of (modern) **science** goes together with that of (modern) **democracy**, save anomalous situations brought by dictatorial political ideology.

Is there truth in Science? Is the Scientist looking after truth? My personal experience is that the answer to both questions above is NO. Or else the concept of "truth" demands clarification. **Scientists first look for evidence** (in Nature, in the Lab carrying on experiments that can be repeated -in most cases- by others), **then create theories, models that accommodate and explain data and bring predictability of data not yet gathered!, and, finally, try to get consensus with the peers**. With more knowledge, definitions change.

In Science we do not demand unanimous consensus for ever. Thinks about Aristotle, Galileo, Newton, Maxwell, Boltzmann, Planck, Einstein,... whose science had truth? There is room for the dissident! It is because we all scientists do not recite the same (scientific) creed that progress is possible. It is the creative unorthodox that brings progress, that is new ideas, new ways of looking at evidence, old and new

Instituto Pluridisciplinar, UCM, Madrid, Spain, e-mail: mgvelarde@pluri.ucm.es

evidence in the lab or in Nature, new theories. Education should be an adventure instead of a sentence.

I toured the FVG Region visiting Rotary Clubs (I am a Rotarian), Lions Clubs, and other service clubs around. Eventually I was real lucky as I found two extraordinary persons who believed in my project of introducing at each school a meteorological unit and a seismological unit in a few. The life of the FVG Region is most sensitive to weather conditions and earthquakes. They were Adriana Ronco-Villota (a Lioness and a retired High School teacher in the Humanities) and Mario Malgarotto (a Rotarian and a retired Electrical Engineer from Telecom who played quite a significant role in maintaining phone communication when in 1976 a major earthquake devastated the FVG region). Children-students were supposed to self-organize themselves so that one would measure temperature, another would measure relative humidity, etc thus gathering data for subsequent analysis by the group. Teachers were supposed to help but the group leaders should appear "spontaneously". After seeking the collaboration of the FVG Meteorological Agency and other relevant institutions and individuals, the project started and in 2012 reached its tenth anniversary. Adriana and Mario, collaborating with a team of strongly motivated teachers and experts, offer the opportunity to the students to annually attend a kind of conference where they are exposed to technical talks and where, as plenary speakers, they are able to present their "experiences". Attendance reaches every year some three hundred participants.

Udine , 26 aprile 2012

"Toccare l'aria e
sentire la terra tremare"

"con l'occhio della ragione "

PROGETTO DIDATTICO SPERIMENTALE

Creando nelle scuole una squadra di studenti addetti ad una piccola stazione meteosismologica si avvicinano i giovani alla scienza attraverso l'analisi e la misurazione dei fenomeni meteorologici naturali più evidenti, per capirne cause ed effetti.

I ragazzi, lavorando in equipe, diventano responsabili e autonomi, comprendendo il senso della concretezza, della praticità, del lavoro collettivo, della disciplina e della solidarietà; aumentano il livello culturale dialogando con l'Europa e il mondo.

Utilizzano il computer nella raccolta dati e nella comunicazione anche con la consultazione del sito dell'OSMER -ARPA.

Service culturale e scientifico per interagire attivamente fra giovani ; protagonisti e artefici del loro lavoro e del mondo che li circonda.

Vari club service "Adottano" le scuole fornendo materiale e sostegno nella realizzazione del Progetto con la collaborazione attiva e costante degli insegnanti .

Udine Agorà
Udine Castello
Udine Duomo
Udine Host
Udine Lionello

Udine
Udine Nord
Udine Patriarcato

INNER WHEEL

FIDAPA

SOROPTIMIST

UNESCO Udine

meteo.FVG
ARPA FVG - OSMER
Osservatorio meteorologico regionale

con la partecipazione

AUDITORIUM
PALAZZO DELLA REGIONE
via Sabbadini -UDINE

Referenti Gruppo Promotore :
adrierrevillotta@yahoo.it
m.malgarotto@alice.it

Programma

Ore 9.00
Saluto delle autorità

Ore 9.15
Introduzione al convegno
prof. Manuel. G. Velarde
Ordinario di fisica Università di Madrid

Ore 9.30
10 anni di storia del Progetto Didattico

Ore 9.40
E x allievi: Ricordi del Progetto

Ore 9.50
Capannina meteorologica
e strumentazione
dott. Sergio Nordio- Previsore OSMER

Ore 10.00
Parliamo di sismologia
Ing. Stefano Grimaz
doc. Sismologia applicata Università UD

Ore 10.20
Illustrazione di un sismografo

Ore 10.30
Video Canzone - Premio Città di Castello
Scuola Manzoni

Ore 10.40
"Science Magic"
dott. Fulvio Stel - Fisico dell'Arpa
Centro Regionale di Modellistica Ambientale

Ore10.50
Proverbi Friulani
Scuola Fermi

Ore 11.00
Meteorologia nell'arte
Scuola Mills

Ore 11.10
Temporale Virtuale

Ore 11.20
Conclusioni del Convegno
prof. Manuel .G.Velarde

Ore 11.30
Riconoscimenti agli insegnanti

Consegna l'Assessore Regionale
dott. Roberto Molinaro

Moderatore : Piero Villotta
Presidente Ordine giornalisti

2002 -Il prof. M. Velarde Rettore del CISM di UD espone la sua idea
2002 -alcuni club service di Ud accettano la sfida
2003–,consegnati i primi strumenti con il supporto scientifico dell'Osmer .
2003 - ARPA e OSMER insegnano nelle scuole a studenti e insegnanti l'uso degli strumenti .
2004 - sala Aiace - conferenza stampa sui problemi didattici e scientifici delle scuole .
2005 - docenti e studenti collaborano attivamente
2005 – discussione dati attraverso internet
2006 – progetto al Congresso Europeo di Meteorologia a Lubiana .
2006 -sostituzione e consegna strumenti
2007 - realizzazione di cortometraggi nelle scuole
2007 – consegna sismografo e computer ad una scuola
2007- Sito internet per docenti e studenti
2008 – corso di informatica per docenti . Creato Blog ad uso delle scuole partecipanti
2008 - progetto all'Università di Udine, XVIII° ediz giornate Diffusione Cultura .
2008-"Tutti su per terra"manifestazione laboratorio scientifico didattico per studenti
2009 - questionario conoscitivo/gradimento della sperimentazione per docenti e studenti
2009 – verifica dei dati raccolti ed elaborati statisticamente
2009- convegno sulla sismologia- relatori docenti dell'Università di Udine
2010- consegna del secondo sismografo
2010-"Tutti su per terra"manifestazione laboratorio scientifico didattico all'aperto
2010- presentazione al Forum del Mediterraneo
2011- convegno meteosismologia

Fig. 1 Tenth anniversary Conference program flyer (2002-2012).